

FIBER-OPTIC COMMUNICATION SYSTEMS

WILEY SERIES IN MICROWAVE AND OPTICAL ENGINEERING

KAI CHANG, Editor
Texas A&M University

A complete list of the titles in this series appears at the end of this volume.

FIBER-OPTIC COMMUNICATION SYSTEMS

Fourth Edition

Govind P. Agrawal

The Institute of Optics
University of Rochester
Rochester, New York



WILEY

A JOHN WILEY & SONS, INC., PUBLICATION

Copyright © 2010 by John Wiley & Sons, Inc. All rights reserved.

Published by John Wiley & Sons, Inc., Hoboken, New Jersey.

Published simultaneously in Canada.

No part of this publication may be reproduced, stored in a retrieval system, or transmitted in any form or by any means, electronic, mechanical, photocopying, recording, scanning, or otherwise, except as permitted under Section 107 or 108 of the 1976 United States Copyright Act, without either the prior written permission of the Publisher, or authorization through payment of the appropriate per-copy fee to the Copyright Clearance Center, Inc., 222 Rosewood Drive, Danvers, MA 01923, (978) 750-8400, fax (978) 750-4470, or on the web at www.copyright.com. Requests to the Publisher for permission should be addressed to the Permissions Department, John Wiley & Sons, Inc., 111 River Street, Hoboken, NJ 07030, (201) 748-6011, fax (201) 748-6008, or online at <http://www.wiley.com/go/permission>.

Limit of Liability/Disclaimer of Warranty: While the publisher and author have used their best efforts in preparing this book, they make no representations or warranties with respect to the accuracy or completeness of the contents of this book and specifically disclaim any implied warranties of merchantability or fitness for a particular purpose. No warranty may be created or extended by sales representatives or written sales materials. The advice and strategies contained herein may not be suitable for your situation. You should consult with a professional where appropriate. Neither the publisher nor author shall be liable for any loss of profit or any other commercial damages, including but not limited to special, incidental, consequential, or other damages.

For general information on our other products and services or for technical support, please contact our Customer Care Department within the United States at (800) 762-2974, outside the United States at (317) 572-3993 or fax (317) 572-4002.

Wiley also publishes its books in a variety of electronic formats. Some content that appears in print may not be available in electronic formats. For more information about Wiley products, visit our web site at www.wiley.com.

Library of Congress Cataloging-in-Publication Data:

Agrawal, G. P. (Govind P.), 1951--

Fiber-optic communication systems with cd / Govind P. Agrawal. — 4th ed.

p. cm. — (Wiley series in microwave and optical engineering ; 222)

ISBN 978-0-470-50511-3 (hardback)

1. Optical communications. 2. Fiber optics. I. Title.

TK5103.59.A37 2010

621.382'75—dc22

2010023284

Printed in the United States of America.

10 9 8 7 6 5 4 3 2 1

To the memory of my Parents

To Anne, Sipra, Caroline, and Claire

Contents

Preface	xv
1 Introduction	1
1.1 Historical Perspective	1
1.1.1 Need for Fiber-Optic Communications	2
1.1.2 Evolution of Lightwave Systems	4
1.2 Basic Concepts	8
1.2.1 Analog and Digital Signals	8
1.2.2 Channel Multiplexing	11
1.2.3 Modulation Formats	13
1.3 Optical Communication Systems	16
1.4 Lightwave System Components	17
1.4.1 Optical Fibers as a Communication Channel	18
1.4.2 Optical Transmitters	18
1.4.3 Optical Receivers	19
Problems	20
References	21
2 Optical Fibers	24
2.1 Geometrical-Optics Description	24
2.1.1 Step-Index Fibers	25
2.1.2 Graded-Index Fibers	27
2.2 Wave Propagation	29
2.2.1 Maxwell's Equations	29
2.2.2 Fiber Modes	31
2.2.3 Single-Mode Fibers	34
2.3 Dispersion in Single-Mode Fibers	38
2.3.1 Group-Velocity Dispersion	39
2.3.2 Material Dispersion	40
2.3.3 Waveguide Dispersion	41
2.3.4 Higher-Order Dispersion	43
2.3.5 Polarization-Mode Dispersion	44
2.4 Dispersion-Induced Limitations	46
2.4.1 Basic Propagation Equation	46

2.4.2	Chirped Gaussian Pulses	47
2.4.3	Limitations on the Bit Rate	50
2.4.4	Fiber Bandwidth	54
2.5	Fiber Losses	55
2.5.1	Attenuation Coefficient	55
2.5.2	Material Absorption	57
2.5.3	Rayleigh Scattering	58
2.5.4	Waveguide Imperfections	58
2.6	Nonlinear Optical Effects	59
2.6.1	Stimulated Light Scattering	59
2.6.2	Nonlinear Phase Modulation	64
2.6.3	Four-Wave Mixing	67
2.7	Fiber Design and Fabrication	67
2.7.1	Silica Fibers	68
2.7.2	Plastic Optical Fibers	71
2.7.3	Cables and Connectors	72
Problems	74
References	75
3	Optical Transmitters	79
3.1	Semiconductor Laser Physics	79
3.1.1	Spontaneous and Stimulated Emissions	80
3.1.2	Nonradiative Recombination	81
3.1.3	Optical Gain	82
3.1.4	Feedback and Laser Threshold	84
3.1.5	Longitudinal Modes	85
3.1.6	Laser Structures	86
3.2	Single-Mode Semiconductor Lasers	87
3.2.1	Distributed Feedback Lasers	88
3.2.2	Coupled-Cavity Semiconductor Lasers	90
3.2.3	Tunable Semiconductor Lasers	91
3.2.4	Vertical-Cavity Surface-Emitting Lasers	93
3.3	Laser Characteristics	94
3.3.1	CW Characteristics	95
3.3.2	Modulation Bandwidth	98
3.3.3	Relative Intensity Noise	100
3.3.4	Spectral Linewidth	102
3.4	Optical Signal Generation	104
3.4.1	Direct Modulation	104
3.4.2	External Modulation	106
3.5	Light-Emitting Diodes	110
3.5.1	CW Characteristics	110
3.5.2	Modulation Response	112
3.5.3	LED Structures	113
3.6	Transmitter Design	115
3.6.1	Source–Fiber Coupling	115

3.6.2	Driving Circuitry	118
3.6.3	Reliability and Packaging	119
Problems		121
References		122
4 Optical Receivers		128
4.1	Basic Concepts	128
4.1.1	Responsivity and Quantum Efficiency	128
4.1.2	Rise Time and Bandwidth	130
4.2	Common Photodetectors	131
4.2.1	$p-n$ Photodiodes	132
4.2.2	$p-i-n$ Photodiodes	133
4.2.3	Avalanche Photodiodes	137
4.2.4	MSM Photodetectors	143
4.3	Receiver Design	144
4.3.1	Front End	144
4.3.2	Linear Channel	145
4.3.3	Decision Circuit	147
4.3.4	Integrated Receivers	148
4.4	Receiver Noise	151
4.4.1	Noise Mechanisms	151
4.4.2	$p-i-n$ Receivers	153
4.4.3	APD Receivers	154
4.5	Coherent Detection	158
4.5.1	Local Oscillator	158
4.5.2	Homodyne Detection	159
4.5.3	Heterodyne Detection	160
4.5.4	Signal-to-Noise Ratio	160
4.6	Receiver Sensitivity	161
4.6.1	Bit-Error Rate	162
4.6.2	Minimum Received Power	164
4.6.3	Quantum Limit of Photodetection	166
4.7	Sensitivity Degradation	167
4.7.1	Extinction Ratio	167
4.7.2	Intensity Noise	169
4.7.3	Timing Jitter	171
4.8	Receiver Performance	173
Problems		175
References		177
5 Lightwave Systems		182
5.1	System Architectures	182
5.1.1	Point-to-Point Links	182
5.1.2	Distribution Networks	184
5.1.3	Local-Area Networks	185
5.2	Design Guidelines	187

5.2.1	Loss-Limited Lightwave Systems	187
5.2.2	Dispersion-Limited Lightwave Systems	189
5.2.3	Power Budget	190
5.2.4	Rise-Time Budget	191
5.3	Long-Haul Systems	194
5.3.1	Performance-Limiting Factors	194
5.3.2	Terrestrial Lightwave Systems	196
5.3.3	Undersea Lightwave Systems	198
5.4	Sources of Power Penalty	200
5.4.1	Modal Noise	201
5.4.2	Mode-Partition Noise	202
5.4.3	Reflection Feedback and Noise	204
5.4.4	Dispersive Pulse Broadening	208
5.4.5	Frequency Chirping	209
5.4.6	Eye-Closure Penalty	210
5.5	Forward Error Correction	212
5.5.1	Error-Correcting Codes	212
5.5.2	Coding Gain	213
5.6	Computer-Aided Design	214
Problems		216
References		218
6	Multichannel Systems	223
6.1	WDM Lightwave Systems	223
6.1.1	High-Capacity Point-to-Point Links	224
6.1.2	Wide-Area and Metro-Area Networks	228
6.1.3	Multiple-Access WDM Networks	230
6.2	WDM Components	232
6.2.1	Tunable Optical Filters	233
6.2.2	Multiplexers and Demultiplexers	238
6.2.3	Add-Drop Multiplexers and Filters	242
6.2.4	Star Couplers	244
6.2.5	Wavelength Routers	246
6.2.6	WDM Transmitters and Receivers	248
6.3	System Performance Issues	251
6.3.1	Heterowavelength Linear Crosstalk	251
6.3.2	Homowavelength Linear Crosstalk	253
6.3.3	Nonlinear Raman Crosstalk	255
6.3.4	Stimulated Brillouin Scattering	257
6.3.5	Cross-Phase Modulation	259
6.3.6	Four-Wave Mixing	261
6.3.7	Other Design Issues	262
6.4	Time-Division Multiplexing	264
6.4.1	Channel Multiplexing	264
6.4.2	Channel Demultiplexing	266
6.4.3	System Performance	268

6.5 Subcarrier Multiplexing	269
6.5.1 Analog and Digital SCM Systems	270
6.5.2 Multiwavelength SCM Systems	273
6.5.3 Orthogonal Frequency-Division multiplexing	275
6.6 Code-Division Multiplexing	277
6.6.1 Time-Domain Encoding	278
6.6.2 Frequency-Domain Encoding	280
6.6.3 Frequency Hopping	281
Problems	283
References	285
7 Loss Management	295
7.1 Compensation of Fiber Losses	295
7.1.1 Periodic Amplification Scheme	296
7.1.2 Lumped Versus Distributed Amplification	298
7.1.3 Bidirectional Pumping Scheme	299
7.2 Erbium-Doped Fiber Amplifiers	300
7.2.1 Pumping and Gain Spectrum	300
7.2.2 Two-Level Model	302
7.2.3 Amplifier Noise	305
7.2.4 Multichannel Amplification	307
7.3 Raman Amplifiers	310
7.3.1 Raman Gain and Bandwidth	310
7.3.2 Raman-Induced Signal Gain	312
7.3.3 Multiple-Pump Raman Amplification	313
7.3.4 Noise Figure of Raman Amplifiers	316
7.4 Optical Signal-To-Noise Ratio	318
7.4.1 Lumped Amplification	318
7.4.2 Distributed Amplification	319
7.5 Electrical Signal-To-Noise Ratio	321
7.5.1 ASE-Induced Current Fluctuations	321
7.5.2 Impact of ASE on SNR	322
7.5.3 Noise Buildup in an Amplifier Chain	323
7.6 Receiver Sensitivity and <i>Q</i> Factor	325
7.6.1 Bit-Error Rate	325
7.6.2 Relation between <i>Q</i> Factor and Optical SNR	327
7.7 Role of Dispersive and Nonlinear Effects	328
7.7.1 Noise Growth through Modulation Instability	328
7.7.2 Noise-Induced Signal Degradation	330
7.7.3 Noise-Induced Energy Fluctuations	332
7.7.4 Noise-Induced Timing Jitter	333
7.8 Periodically Amplified Lightwave Systems	334
7.8.1 Numerical Approach	335
7.8.2 Optimum Launched Power	337
Problems	339
References	340

8 Dispersion Management	345
8.1 Dispersion Problem and Its Solution	345
8.2 Dispersion-Compensating Fibers	347
8.2.1 Conditions for Dispersion Compensation	348
8.2.2 Dispersion Maps	349
8.2.3 DCF Designs	350
8.3 Fiber Bragg Gratings	354
8.3.1 Constant-Period Gratings	354
8.3.2 Chirped Fiber Gratings	356
8.3.3 Sampled Gratings	360
8.4 Dispersion-Equalizing Filters	363
8.4.1 Gires–Tournois Filters	363
8.4.2 Mach–Zehnder Filters	366
8.4.3 Other All-Pass Filters	367
8.5 Optical Phase Conjugation	369
8.5.1 Principle of Operation	369
8.5.2 Compensation of Self-Phase Modulation	370
8.5.3 Generation of Phase-Conjugated Signal	371
8.6 Channels at High Bit Rates	375
8.6.1 Tunable Dispersion Compensation	375
8.6.2 Higher-Order Dispersion Management	379
8.6.3 PMD Compensation	382
8.7 Electronic Dispersion Compensation	385
8.7.1 Basic Idea behind GVD Precompensation	385
8.7.2 Precompensation at the Transmitter	386
8.7.3 Dispersion Compensation at the Receiver	392
Problems	397
References	399
9 Control of Nonlinear Effects	407
9.1 Impact of Fiber Nonlinearity	407
9.1.1 System Design Issues	408
9.1.2 Semianalytic Approach	411
9.1.3 Soliton and Pseudo-linear Regimes	414
9.2 Solitons in Optical Fibers	416
9.2.1 Properties of Optical Solitons	416
9.2.2 Loss-Managed Solitons	419
9.3 Dispersion-Managed Solitons	423
9.3.1 Dispersion-Decreasing Fibers	423
9.3.2 Periodic Dispersion Maps	424
9.3.3 Design Issues	427
9.3.4 Timing Jitter	430
9.3.5 Control of Timing Jitter	432
9.4 Pseudo-linear Lightwave Systems	434
9.4.1 Origin of Intrachannel Nonlinear Effects	435
9.4.2 Intrachannel Cross-Phase Modulation	437

9.4.3	Intrachannel Four-Wave Mixing	441
9.5	Control of Intrachannel Nonlinear Effects	444
9.5.1	Optimization of Dispersion Maps	444
9.5.2	Phase-Alteration Techniques	448
9.5.3	Polarization Bit Interleaving	449
Problems	451
References	453
10	Advanced Lightwave Systems	459
10.1	Advanced Modulation Formats	460
10.1.1	Encoding of Optical Signals	460
10.1.2	Amplitude and Phase Modulators	462
10.2	Demodulation Schemes	464
10.2.1	Synchronous Heterodyne Demodulation	464
10.2.2	Asynchronous Heterodyne Demodulation	466
10.2.3	Optical Delay Demodulation	467
10.3	Shot Noise and Bit-Error Rate	470
10.3.1	Synchronous Heterodyne Receivers	470
10.3.2	Asynchronous Heterodyne Receivers	472
10.3.3	Receivers with Delay Demodulation	475
10.4	Sensitivity Degradation Mechanisms	476
10.4.1	Intensity Noise of Lasers	476
10.4.2	Phase Noise of Lasers	478
10.4.3	Signal Polarization Fluctuations	480
10.4.4	Noise Added by Optical Amplifiers	483
10.4.5	Fiber Dispersion	484
10.5	Impact of Nonlinear Effects	485
10.5.1	Nonlinear Phase Noise	486
10.5.2	Effect of Fiber Dispersion	489
10.5.3	Compensation of Nonlinear Phase Noise	490
10.6	Recent Progress	494
10.6.1	Systems with the DBPSK format	494
10.6.2	Systems with the DQPSK format	496
10.6.3	QAM and Related formats	497
10.6.4	Systems Employing Orthogonal FDM	499
10.7	Ultimate Channel Capacity	501
Problems	503
References	504
11	Optical Signal Processing	511
11.1	Nonlinear Techniques and Devices	511
11.1.1	Nonlinear Optical Loop Mirrors	512
11.1.2	Parametric Amplifiers	516
11.1.3	Nonlinear Effects in Semiconductor Optical Amplifiers	522
11.1.4	Bistable Optical Devices	526
11.2	All-Optical Flip-Flops	529

11.2.1 Semiconductor Lasers and SOAs	529
11.2.2 Coupled Semiconductor Lasers and SOAs	531
11.3 Wavelength Converters	533
11.3.1 XPM-Based Wavelength Converters	533
11.3.2 FWM-Based Wavelength Converters	537
11.3.3 Passive Semiconductor Waveguides	540
11.3.4 SOA-Based Wavelength Converters	542
11.4 Ultrafast Optical Switching	544
11.4.1 Time-Domain Demultiplexing	545
11.4.2 Data-Format Conversion	549
11.4.3 Packet Switching	552
11.5 Optical Regenerators	553
11.5.1 Fiber-Based 2R Regenerators	553
11.5.2 SOA-Based 2R Regenerators	559
11.5.3 Fiber-Based 3R Regenerators	560
11.5.4 SOA-Based 3R Regenerators	562
11.5.5 Regeneration of Phase-Encoded Signals	565
Problems	568
References	569
A System of Units	578
B Acronyms	580
C General Formula for Pulse Broadening	584
D Software Package	587
Index	589

Preface

Since the publication of the first edition of this book in 1992, the state of the art of fiber-optic communication systems has advanced dramatically despite the relatively short period of only 18 years between the first and fourth editions. The highest capacity of commercial fiber-optic links available in 1992 was only 2.5 Gb/s. A mere 4 years later, with the advent of wavelength-division multiplexing (WDM), systems with the total capacity of 40 Gb/s became available commercially. By 2001, the capacity of commercial WDM systems exceeded 1.6 Tb/s. At the same time, the capacity of transoceanic lightwave systems installed worldwide exploded. A global network covering 250,000 km with a capacity of 2.56 Tb/s (64 WDM channels at 10 Gb/s over 4 fiber pairs) was planned in 2001 and became operational by 2004 (currently operated by VSNL, an Indian telecommunication company). Although the pace slowed down after 2001 for a few years with the bursting of the so-called “telecom bubble,” progress in the design of lightwave systems continued and accelerated after 2006 with the advent of phase-based modulation formats, 100-Gb Ethernet, and orthogonal frequency-division multiplexing.

The third edition of this book appeared in 2002. It has been well received by the scientific community involved with lightwave technology as well as by the educational community, judging from book’s adoption as a textbook for courses offered at many universities worldwide. Because of the rapid advances that have occurred over the last 8 years, the publisher and I deemed it necessary to bring out the fourth edition if the book were to continue to provide a comprehensive and up-to-date account of fiber-optic communication systems. The result is in your hands. The primary objective of the book remains the same. Specifically, it should be able to serve both as a textbook and a reference monograph. For this reason, the emphasis is on the physical understanding, but the engineering aspects are also discussed throughout the text.

Because of the large amount of material that needed to be added to provide comprehensive coverage, the book size has increased considerably compared with the first edition. Although all chapters have been updated, the major changes have occurred in Chapters 7–11. I have taken this opportunity to rearrange the material such that it is better suited for a two-semester course on optical communications. In particular, the chapter on WDM systems has been moved earlier and now appears as Chapter 6. With this arrangement, Chapters 1 to 6 provide the basic foundation, while Chapters 7 to 11 cover the issues related to the design of advanced lightwave systems. More specifically, after the introduction of the elementary concepts in Chapter 1, Chapters 2–4 are devoted to the three primary components of a fiber-optic communications—

optical fibers, optical transmitters, and optical receivers. Chapters 5 and 6 then focus on the design issues relevant for single-channel and multichannel systems, respectively. Chapters 7 and 8 are devoted to the advanced techniques used for the management of fiber losses and chromatic dispersion, respectively. Chapter 9 focuses on the impact of nonlinear effects and techniques used to manage them such as the use of optical solitons and pseudo-linear propagation through enhanced dispersion. Chapters 10 and 11 are new to the fourth edition. Chapter 10 focuses primarily on the coherent and self-coherent lightwave systems making use of the novel phase-based modulation formats. Chapter 11 is devoted to all-optical signal processing with emphasis on wavelength conversion and optical regeneration. The contents of the book reflect the state of the art of lightwave systems in 2010.

The primary role of this book is as a graduate-level textbook in the field of *optical communications*. An attempt is made to include as much recent material as possible so that students are exposed to the recent advances in this exciting field. The book can also serve as a reference text for researchers already engaged in or wishing to enter the field of optical fiber communications. The reference list at the end of each chapter is more elaborate than what is common for a typical textbook. The listing of recent research papers should be useful for researchers using this book as a reference. At the same time, students can benefit from it if they are assigned problems requiring reading of the original research papers. A set of problems is included at the end of each chapter to help both the teacher and the student. Although written primarily for graduate students, the book can also be used for an undergraduate course at the senior level with an appropriate selection of topics. Parts of the book can be used for several other related courses. For example, Chapter 2 can be used for a course on optical waveguides, and Chapters 3 and 4 can be useful for a course on optoelectronics.

Many universities in the United States and elsewhere offer a course on optical communications as a part of their curriculum in electrical engineering, physics, or optics. I have taught such a course since 1989 to the graduate students of the Institute of Optics, and this book indeed grew out of my lecture notes. I am aware that it is used as a textbook by many instructors worldwide—a fact that gives me immense satisfaction. I am acutely aware of a problem that is a side effect of an enlarged revised edition. How can a teacher fit all this material in a one-semester course on *optical communications*? I have to struggle with the same question. In fact, it is impossible to cover the entire book in one semester. The best solution is to offer a two-semester course covering Chapters 1 through 6 during the first semester, leaving the remainder for the second semester. However, not many universities may have the luxury of offering a two-semester course on optical communications. The book can be used for a one-semester course provided that the instructor makes a selection of topics. For example, Chapter 3 can be skipped if the students have taken a laser course previously. If only parts of Chapters 7 through 11 are covered to provide students a glimpse of the recent advances, the material can fit in a single one-semester course offered either at the senior level for undergraduates or to graduate students.

The book features a compact disk (CD) on the back cover provided by the Optiwave Corporation. The CD contains a state-of-the art software package suitable for designing modern lightwave systems. It also contains additional problems for each chapter that can be solved by using the software package. Appendix D provides more details about

the software and the problems. It is my hope that the CD will help to train the students and will prepare them better for an industrial job.

A large number of persons have contributed to this book either directly or indirectly. It is impossible to mention all of them by name. I thank my graduate students and the students who took my course on optical communication systems and helped improve my class notes through their questions and comments. Thanks are due to many instructors who not only have adopted this book as a textbook for their courses but have also pointed out the misprints in previous editions, and thus have helped me in improving the book. I am grateful to my colleagues at the Institute of Optics for numerous discussions and for providing a cordial and productive atmosphere. I appreciated the help of Karen Rolfe, who typed the first edition of this book and made numerous revisions with a smile. Last, but not least, I thank my wife, Anne, and my daughters, Sipra, Caroline, and Claire, for understanding why I needed to spend many weekends on the book instead of spending time with them.

Govind P. Agrawal

Rochester, NY

April 2010

Chapter 1

Introduction

A communication system transmits information from one place to another, whether separated by a few kilometers or by transoceanic distances. Information is often carried by an electromagnetic carrier wave whose frequency can vary from a few megahertz to several hundred terahertz. Optical communication systems use high carrier frequencies (~ 100 THz) in the visible or near-infrared region of the electromagnetic spectrum. They are sometimes called lightwave systems to distinguish them from microwave systems, whose carrier frequency is typically smaller by five orders of magnitude (~ 1 GHz). Fiber-optic communication systems are lightwave systems that employ optical fibers for information transmission. Such systems have been deployed worldwide since 1980 and have revolutionized the field of telecommunications. Indeed, lightwave technology, together with microelectronics, led to the advent of the “information age” during the 1990s. This book describes fiber-optic communication systems in a comprehensive manner. The emphasis is on the fundamental aspects, but relevant engineering issues are also discussed. In this introductory chapter we present the basic concepts and provide the background material. Section 1.1 gives a historical perspective on the development of optical communication systems. Section 1.2 covers concepts such as analog and digital signals, channel multiplexing, and modulation formats. Relative merits of various lightwave systems are discussed in Section 1.3. The last section focuses on the building blocks of a fiber-optic communication system.

1.1 Historical Perspective

The use of light for communication purposes dates back to antiquity if we interpret optical communications in a broad sense [1]. Most civilizations have used mirrors, fire beacons, or smoke signals to convey a single piece of information (such as victory in a war). Essentially the same idea was used up to the end of the eighteenth century through signaling lamps, flags, and other semaphore devices. The idea was extended further, following a suggestion of Claude Chappe in 1792, to transmit mechanically coded messages over long distances (~ 100 km) by the use of intermediate relay stations [2], acting as *regenerators* or *repeaters* in the modern-day language. Figure 1.1

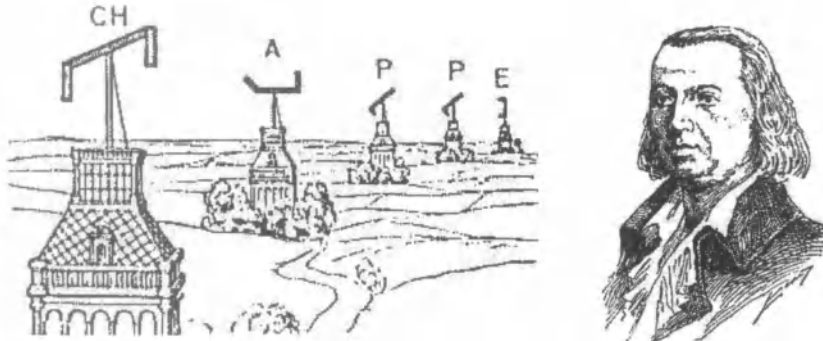


Figure 1.1: Schematic illustration of the optical telegraph and its inventor Claude Chappe. (After Ref. [2]; ©1944 American Association for the Advancement of Science; reprinted with permission.)

shows the basic idea schematically. The first such “optical telegraph” was put in service between Paris and Lille (two French cities about 200 km apart) in July 1794. By 1830, the network had expanded throughout Europe [1]. The role of light in such systems was simply to make the coded signals visible so that they could be intercepted by the relay stations. The opto-mechanical communication systems of the nineteenth century were inherently slow. In modern-day terminology, the effective bit rate of such systems was less than 1 bit per second ($B < 1 \text{ b/s}$).

1.1.1 Need for Fiber-Optic Communications

The advent of telegraphy in the 1830s replaced the use of light by electricity and began the era of electrical communications [3]. The bit rate B could be increased to $\sim 10 \text{ b/s}$ by the use of new coding techniques, such as the *Morse code*. The use of intermediate relay stations allowed communication over long distances ($\sim 1000 \text{ km}$). Indeed, the first successful transatlantic telegraph cable went into operation in 1866. Telegraphy used essentially a digital scheme through two electrical pulses of different durations (dots and dashes of the Morse code). The invention of the telephone in 1876 brought a major change inasmuch as electric signals were transmitted in analog form through a continuously varying electric current [4]. Analog electrical techniques were to dominate communication systems for a century or so.

The development of worldwide telephone networks during the twentieth century led to many advances in the design of electrical communication systems. The use of coaxial cables in place of wire pairs increased system capacity considerably. The first coaxial-cable system, put into service in 1940, was a 3-MHz system capable of transmitting 300 voice channels or a single television channel. The bandwidth of such systems is limited by the frequency-dependent cable losses, which increase rapidly for frequencies beyond 10 MHz. This limitation led to the development of microwave communication systems in which an electromagnetic carrier wave with frequencies in the range of 1–10 GHz is used to transmit the signal by using suitable modulation techniques.

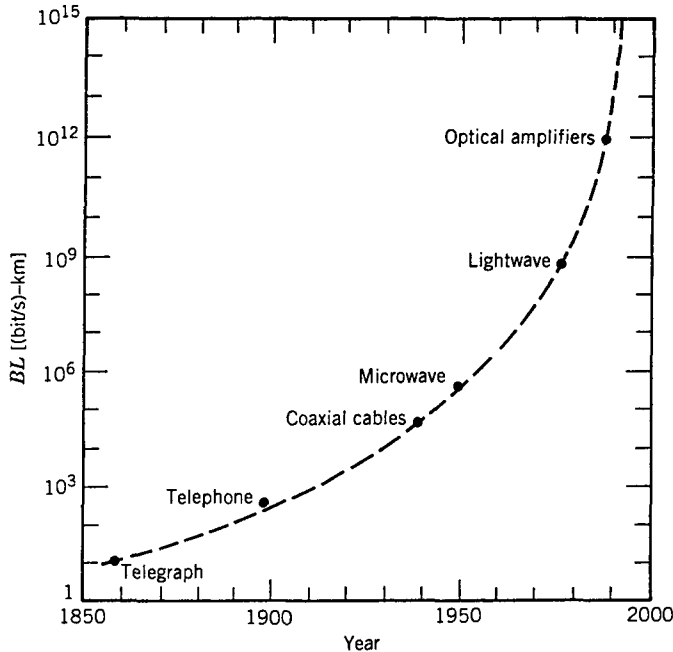


Figure 1.2: Increase in bit rate–distance product BL during the period 1850–2000. The emergence of a new technology is marked by a solid circle.

The first microwave system operating at the carrier frequency of 4 GHz was put into service in 1948. Since then, both coaxial and microwave systems have evolved considerably and are able to operate at bit rates ~ 100 Mb/s. The most advanced coaxial system was put into service in 1975 and operated at a bit rate of 274 Mb/s. A severe drawback of such high-speed coaxial systems is their small *repeater spacing* (~ 1 km), which makes the system relatively expensive to operate. Microwave communication systems generally allow for a larger repeater spacing, but their bit rate is also limited by the carrier frequency of such waves. A commonly used figure of merit for communication systems is the *bit rate–distance product*, BL , where B is the bit rate and L is the repeater spacing. Figure 1.2 shows how the BL product has increased through technological advances during the last century and a half. Communication systems with $BL \sim 100$ (Mb/s)-km were available by 1970 and were limited to such values because of fundamental limitations.

It was realized during the second half of the twentieth century that an increase of several orders of magnitude in the BL product would be possible if optical waves were used as the carrier. However, neither a coherent optical source nor a suitable transmission medium was available during the 1950s. The invention of the laser and its demonstration in 1960 solved the first problem [5]. Attention was then focused on finding ways for using laser light for optical communications. Many ideas were advanced during the 1960s [6], the most noteworthy being the idea of light confinement using a sequence of gas lenses [7].

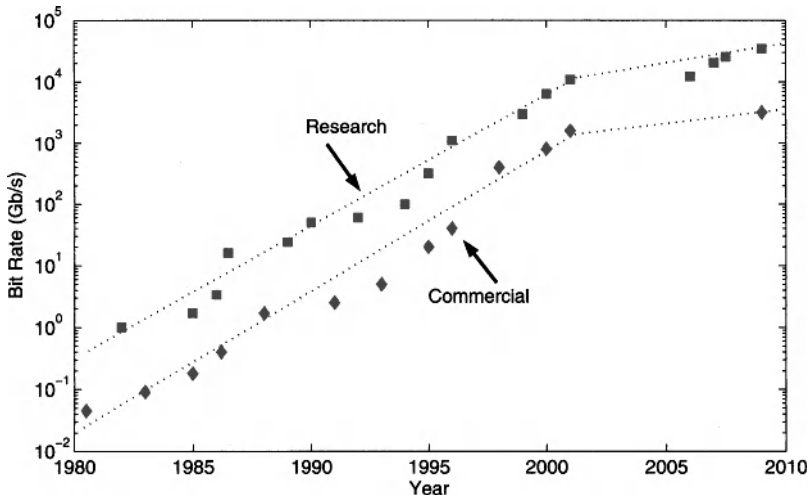


Figure 1.3: Increase in the capacity of lightwave systems realized after 1980. The dotted lines indicate a nearly exponential growth in the bit rate for both the research and commercial systems. Note the change in the slope after 2001.

It was suggested in 1966 that optical fibers might be the best choice [8], as they are capable of guiding the light in a manner similar to the guiding of electrons in copper wires. The main problem was the high losses of optical fibers—fibers available during the 1960s had losses in excess of 1000 dB/km. A breakthrough occurred in 1970 when fiber losses could be reduced to below 20 dB/km in the wavelength region near 1 μm [9]. At about the same time, GaAs semiconductor lasers, operating continuously at room temperature, were demonstrated [10]. The simultaneous availability of *compact* optical sources and a *low-loss* optical fibers led to a worldwide effort for developing fiber-optic communication systems [11]. Figure 1.3 shows the increase in the capacity of lightwave systems realized after 1980 through several generations of development [12]. As seen there, the commercial deployment of lightwave systems followed the research and development phase closely. The progress has indeed been rapid as evident from an increase in the bit rate by a factor of 100,000 over a period of less than 30 years. Transmission distances have also increased from 10 to 10,000 km over the same time period. As a result, the bit rate–distance product of modern lightwave systems can exceed by a factor of 10⁷ compared with the first-generation lightwave systems.

1.1.2 Evolution of Lightwave Systems

The research phase of fiber-optic communication systems started around 1975. The enormous progress realized over the 25-year period extending from 1975 to 2000 can be grouped into several distinct generations. Figure 1.4 shows the increase in the *BL* product over this time period as quantified through various laboratory experiments [13]. The straight line corresponds to a doubling of the *BL* product every year. In every

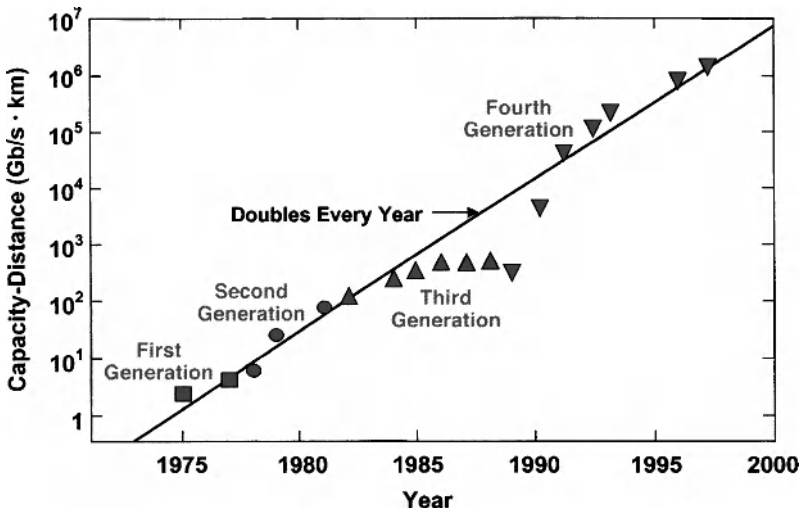


Figure 1.4: Increase in the BL product over the period 1975 to 1980 through several generations of lightwave systems. Different symbols are used for successive generations. (After Ref. [13]; ©2000 IEEE; reprinted with permission.)

generation, BL increases initially but then begins to saturate as the technology matures. Each new generation brings a fundamental change that helps to improve the system performance further.

The first generation of lightwave systems operated near $0.8 \mu\text{m}$ and used GaAs semiconductor lasers. After several field trials during the period 1977–79, such systems became available commercially in 1980 [14]. They operated at a bit rate of 45 Mb/s and allowed repeater spacings of up to 10 km. The larger repeater spacing compared with 1-km spacing of coaxial systems was an important motivation for system designers because it decreased the installation and maintenance costs associated with each repeater.

It was clear during the 1970s that the repeater spacing could be increased considerably by operating the lightwave system in the wavelength region near $1.3 \mu\text{m}$, where fiber loss is below 1 dB/km. Furthermore, optical fibers exhibit minimum dispersion in this wavelength region. This realization led to a worldwide effort for the development of InGaAsP semiconductor lasers and detectors operating near $1.3 \mu\text{m}$. The second generation of fiber-optic communication systems became available in the early 1980s, but the bit rate of early systems was limited to below 100 Mb/s because of dispersion in multimode fibers [15]. This limitation was overcome by the use of *single-mode* fibers. A laboratory experiment in 1981 demonstrated transmission at 2 Gb/s over 44 km of single-mode fiber [16]. The introduction of commercial systems soon followed. By 1987, second-generation lightwave systems, operating at bit rates of up to 1.7 Gb/s with a repeater spacing of about 50 km, were commercially available.

The repeater spacing of the second-generation lightwave systems was limited by the fiber losses at the operating wavelength of $1.3 \mu\text{m}$ (typically 0.5 dB/km). Losses

of silica fibers become minimum near $1.55\text{ }\mu\text{m}$. Indeed, a 0.2-dB/km loss was realized in 1979 in this spectral region [17]. However, the introduction of third-generation lightwave systems operating at $1.55\text{ }\mu\text{m}$ was considerably delayed by a large fiber dispersion near $1.55\text{ }\mu\text{m}$. Conventional InGaAsP semiconductor lasers could not be used because of pulse spreading occurring as a result of simultaneous oscillation of several longitudinal modes. The dispersion problem can be overcome either by using dispersion-shifted fibers designed to have minimum dispersion near $1.55\text{ }\mu\text{m}$ or by limiting the laser spectrum to a single longitudinal mode. Both approaches were followed during the 1980s. By 1985, laboratory experiments indicated the possibility of transmitting information at bit rates of up to 4 Gb/s over distances in excess of 100 km [18]. Third-generation lightwave systems operating at 2.5 Gb/s became available commercially in 1990. Such systems are capable of operating at a bit rate of up to 10 Gb/s [19]. The best performance is achieved using dispersion-shifted fibers in combination with lasers oscillating in a single longitudinal mode.

A drawback of third-generation $1.55\text{-}\mu\text{m}$ systems is that the signal is regenerated periodically by using electronic repeaters spaced apart typically by $60\text{--}70\text{ km}$. The repeater spacing can be increased by making use of a homodyne or heterodyne detection scheme because its use improves receiver sensitivity. Such systems are referred to as coherent lightwave systems. Coherent systems were under development worldwide during the 1980s, and their potential benefits were demonstrated in many system experiments [20]. However, commercial introduction of such systems was postponed with the advent of fiber amplifiers in 1989.

The fourth generation of lightwave systems makes use of *optical amplification* for increasing the repeater spacing and of *wavelength-division multiplexing* (WDM) for increasing the bit rate. As seen from Figures 1.3 and 1.4, the advent of the WDM technique around 1992 started a revolution that resulted in doubling of the system capacity every 6 months or so and led to lightwave systems operating at a bit rate of 10 Tb/s by 2001. In most WDM systems, fiber losses are compensated periodically using erbium-doped fiber amplifiers spaced $60\text{--}80\text{ km}$ apart. Such amplifiers were developed after 1985 and became available commercially by 1990. A 1991 experiment showed the possibility of data transmission over $21,000\text{ km}$ at 2.5 Gb/s , and over $14,300\text{ km}$ at 5 Gb/s , using a recirculating-loop configuration [21]. This performance indicated that an amplifier-based, all-optical, submarine transmission system was feasible for intercontinental communication. By 1996, not only transmission over $11,300\text{ km}$ at a bit rate of 5 Gb/s had been demonstrated by using actual submarine cables [22], but commercial transatlantic and transpacific cable systems also became available. Since then, a large number of submarine lightwave systems have been deployed worldwide.

Figure 1.5 shows the international network of submarine systems around 2005 [23]. The $27,000\text{-km}$ fiber-optic link around the globe (known as FLAG) became operational in 1998, linking many Asian and European countries [24]. Another major lightwave system, known as *Africa One* was operating by 2000; it circles the African continent and covers a total transmission distance of about $35,000\text{ km}$ [25]. Several WDM systems were deployed across the Atlantic and Pacific oceans during 1998–2001 in response to the Internet-induced increase in the data traffic; they increased the total capacity by orders of magnitudes. Indeed, such a rapid deployment led to a worldwide overcapacity that resulted in the bursting of the so-called “telecom bubble” in 2001.



Figure 1.5: International undersea network of fiber-optic communication systems around 2005. (After Ref. [23]; ©2005 IEEE; reprinted with permission.)

The change in the slopes of dotted lines in Figure 1.3, occurring around 2001, reflects this reality.

The emphasis of most WDM lightwave systems is on increasing their capacity by transmitting more and more channels through the WDM technique. With increasing signal bandwidth, it is often not possible to amplify all channels using a single amplifier. As a result, new amplification schemes (such as distributed Raman amplification) have been developed for covering the spectral region extending from 1.45 to 1.62 μm . This approach led in 2000 to a 3.28-Tb/s experiment in which 82 channels, each operating at 40 Gb/s, were transmitted over 3000 km. Within a year, the system capacity could be increased to nearly 11 Tb/s (273 WDM channels, each operating at 40 Gb/s) but the transmission distance was limited to 117 km [26]. In another record experiment, 300 channels, each operating at 11.6 Gb/s, were transmitted over 7380 km, resulting in a BL product of more than 25,000 (Tb/s)-km [27]. Commercial terrestrial systems with the capacity of 3.2 Tb/s, transmitting 80 channels (each at 40 Gb/s) with the use of Raman amplification, were available by the end of 2003. Given that the first-generation systems had a capacity of 45 Mb/s in 1980, it is remarkable that the capacity jumped by a factor of more than 70,000 over a period of 25 years.

The fifth generation of fiber-optic communication systems is concerned with extending the wavelength range over which a WDM system can operate simultaneously. The conventional wavelength window, known as the C band, covers the wavelength range 1.53–1.57 μm . It is being extended on both the long- and short-wavelength sides, resulting in the L and S bands, respectively. The Raman amplification technique can be used for signals in all three wavelength bands. Moreover, a new kind of fiber, known as the *dry fiber* has been developed with the property that fiber losses are small over the entire wavelength region extending from 1.30 to 1.65 μm [28]. Availability of such fibers and new amplification schemes may lead to lightwave systems with thousands of WDM channels.

The focus of current fifth-generation systems is on increasing the spectral efficiency of WDM systems. The idea is to employ advanced modulation formats in which information is encoded using both the amplitude and phase of the optical carrier [29]. Although such formats were developed and are used commonly for microwave systems, their use for lightwave systems attracted serious attention only after 2001. It has allowed one to increase the spectral efficiency, typically limited to below 0.8 b/s/Hz for the fourth-generation systems, to >8 b/s/Hz. In a 2010 experiment [30], a new record was established when 64-Tb/s transmission was realized over 320 km using 640 WDM channels that spanned both the C and L bands with 12.5-GHz channel spacing. Each channel contained two polarization-multiplexed 107-Gb/s signals coded with a modulation format known as quadrature amplitude modulation.

Even though the fiber-optic communication technology is barely 30 years old, it has progressed rapidly and has reached a certain stage of maturity. This is also apparent from the publication of a large number of books on optical communications and WDM networks since 2000 [31]–[47]. The fourth edition of this book (first edition published in 1992) is intended to present an up-to-date account of fiber-optic communications systems with emphasis on recent developments.

1.2 Basic Concepts

This section introduces a few basic concepts common to all communication systems. We begin with a description of analog and digital signals and describe how an analog signal can be converted into digital form. We then consider time- and frequency-division multiplexing of input signals, and conclude with a discussion of various modulation formats.

1.2.1 Analog and Digital Signals

In any communication system, information to be transmitted is generally available as an electrical signal that may take *analog* or *digital* form [48]. In the analog case, the signal (e.g., electric current) varies continuously with time, as shown schematically in Figure 1.6(a). Familiar examples include audio and video signals resulting when a microphone converts voice or a video camera converts an image into an electrical signal. By contrast, the digital signal takes only a few discrete values. In the *binary representation* of a digital signal only two values are possible. The simplest case of a binary digital signal is one in which the electric current is either on or off, as shown in Figure 1.6(b). These two possibilities are called “bit 1” and “bit 0” (*bit* is a contracted form of *binary digit*). Each bit lasts for a certain period of time T_B , known as the bit period or *bit slot*. Since one bit of information is conveyed in a time interval T_B , the bit rate B , defined as the number of bits per second, is simply $B = T_B^{-1}$. A well-known example of digital signals is provided by computer data. Each letter of the alphabet together with other common symbols (decimal numerals, punctuation marks, etc.) is assigned a code number (ASCII code) in the range 0–127 whose binary representation corresponds to a 7-bit digital signal. The original ASCII code has been extended to represent 256 characters transmitted through 8-bit bytes. Both analog and digital signals

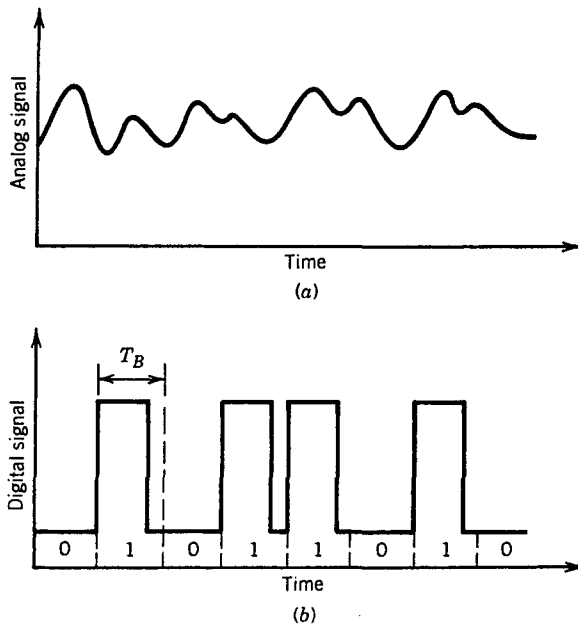


Figure 1.6: Representation of (a) an analog signal and (b) a digital signal.

are characterized by their bandwidth, which is a measure of the spectral contents of the signal. The *signal bandwidth* represents the range of frequencies contained within the signal and is determined mathematically through its Fourier transform.

An analog signal can be converted into digital form by sampling it at regular intervals of time [48]. Figure 1.7 shows the conversion method schematically. The sampling rate is determined by the bandwidth Δf of the analog signal. According to the sampling theorem [49], a bandwidth-limited signal can be fully represented by discrete samples, without any loss of information, provided that the sampling frequency f_s satisfies the *Nyquist criterion* [50], $f_s \geq 2\Delta f$. The first step consists of sampling the analog signal at the right frequency. The sampled values can take any value in the range $0 \leq A \leq A_{\max}$, where A_{\max} is the maximum amplitude of the given analog signal. Let us assume that A_{\max} is divided into M discrete (not necessarily equally spaced) intervals. Each sampled value is quantized to correspond to one of these discrete values. Clearly, this procedure leads to additional noise, known as *quantization noise*, which adds to the noise already present in the analog signal.

The effect of quantization noise can be minimized by choosing the number of discrete levels such that $M > A_{\max}/A_N$, where A_N is the root-mean-square noise amplitude of the analog signal. The ratio A_{\max}/A_N is called the dynamic range and is related to the *signal-to-noise ratio* (SNR) by the relation

$$\text{SNR} = 20 \log_{10}(A_{\max}/A_N), \quad (1.2.1)$$

where SNR is expressed in decibel (dB) units. Any ratio R can be converted into decibels by using the general definition $10 \log_{10} R$ (see Appendix A). Equation (1.2.1)

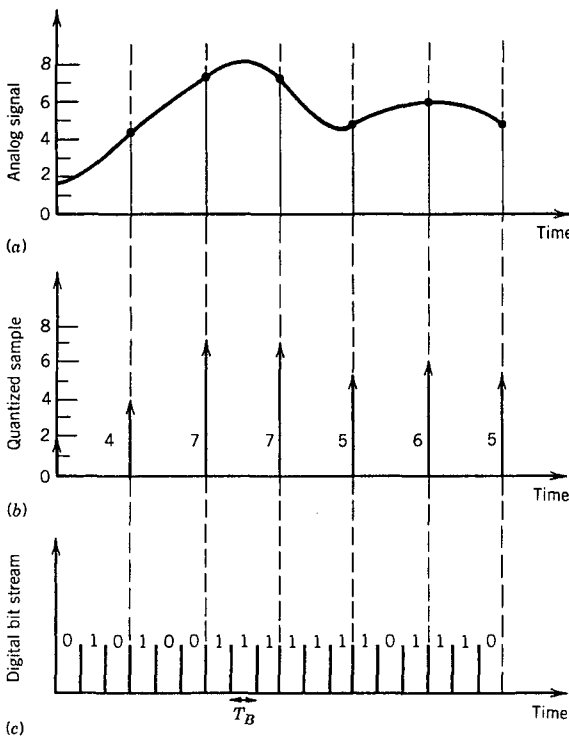


Figure 1.7: Three steps of (a) sampling, (b) quantization, and (c) coding required for converting an analog signal into a binary digital signal.

contains a factor of 20 in place of 10 simply because the SNR for electrical signals is defined with respect to the electrical power, whereas A is related to the electric current (or voltage).

The quantized sampled values can be converted into digital format by using a suitable conversion technique. In one scheme, known as *pulse-position modulation*, pulse position within the bit slot is a measure of the sampled value. In another, known as *pulse-duration modulation*, the pulse width is varied from bit to bit in accordance with the sampled value. These techniques are rarely used in practical optical communication systems, since it is difficult to maintain the pulse position or pulse width to high accuracy during propagation inside the fiber. The technique used almost universally, known as *pulse-code modulation* (PCM), is based on a binary scheme in which information is conveyed by the absence or the presence of pulses that are otherwise identical. A binary code is used to convert each sampled value into a string of 1 and 0 bits. The number of bits m needed to code each sample is related to the number of quantized signal levels M by the relation

$$M = 2^m \quad \text{or} \quad m = \log_2 M. \quad (1.2.2)$$

The bit rate associated with the PCM digital signal is thus given by

$$B = mf_s \geq (2\Delta f) \log_2 M, \quad (1.2.3)$$

where the Nyquist criterion, $f_s \geq 2\Delta f$, was used. By noting that $M > A_{\max}/A_N$ and using Eq. (1.2.1) together with $\log_2 10 \approx 3.33$,

$$B > (\Delta f/3) \text{SNR}, \quad (1.2.4)$$

where the SNR is expressed in decibel (dB) units.

Equation (1.2.4) provides the minimum bit rate required for digital representation of an analog signal of bandwidth Δf and a specific SNR. When $\text{SNR} > 30$ dB, the required bit rate exceeds $10(\Delta f)$, indicating a considerable increase in the bandwidth requirements of digital signals. Despite this increase, the digital format is almost always used for optical communication systems. This choice is made because of the superior performance of digital transmission systems. Lightwave systems offer such an enormous increase in the system capacity (by a factor $\sim 10^5$) compared with microwave systems that some bandwidth can be traded for improved performance.

As an illustration of Eq. (1.2.4), consider the digital conversion of an audio signal generated in a telephone. The analog audio signal contains frequencies in the range 0.3–3.4 kHz with a bandwidth $\Delta f = 3.1$ kHz and has a SNR of about 30 dB. Equation (1.2.4) indicates that $B > 31$ kb/s. In practice, a digital audio channel operates at 64 kb/s. The analog signal is sampled at intervals of 125 μ s (sampling rate $f_s = 8$ kHz), and each sample is represented by 8 bits. The required bit rate for a digital video signal is higher by more than a factor of 1000. The analog television signal has a bandwidth ~ 4 MHz with a SNR of about 50 dB. The minimum bit rate from Eq. (1.2.4) is 66 Mb/s. In practice, a digital video signal requires a bit rate of 100 Mb/s or more unless it is compressed by using a standard format (such as MPEG-2).

1.2.2 Channel Multiplexing

As seen in the preceding discussion, a digital voice channel operates at 64 kb/s. Most fiber-optic communication systems are capable of transmitting at a rate of more than 1 Gb/s. To utilize the system capacity fully, it is necessary to transmit many channels simultaneously through multiplexing. This can be accomplished through *time-division* multiplexing (TDM) or *frequency-division* multiplexing (FDM). In the case of TDM, bits associated with different channels are interleaved in the time domain to form a composite bit stream. For example, the bit slot is about 15 μ s for a single voice channel operating at 64 kb/s. Five such channels can be multiplexed through TDM if the bit streams of successive channels are delayed by 3 μ s. Figure 1.8(a) shows the resulting bit stream schematically at a composite bit rate of 320 kb/s.

In the case of FDM, the channels are spaced apart in the frequency domain. Each channel is carried by its own carrier wave. The carrier frequencies are spaced more than the channel bandwidth so that the channel spectra do not overlap, as seen Figure 1.8(b). FDM is suitable for both analog and digital signals and is used in broadcasting of radio and television channels. TDM is readily implemented for digital signals and is commonly used for telecommunication networks. It is important to realize that

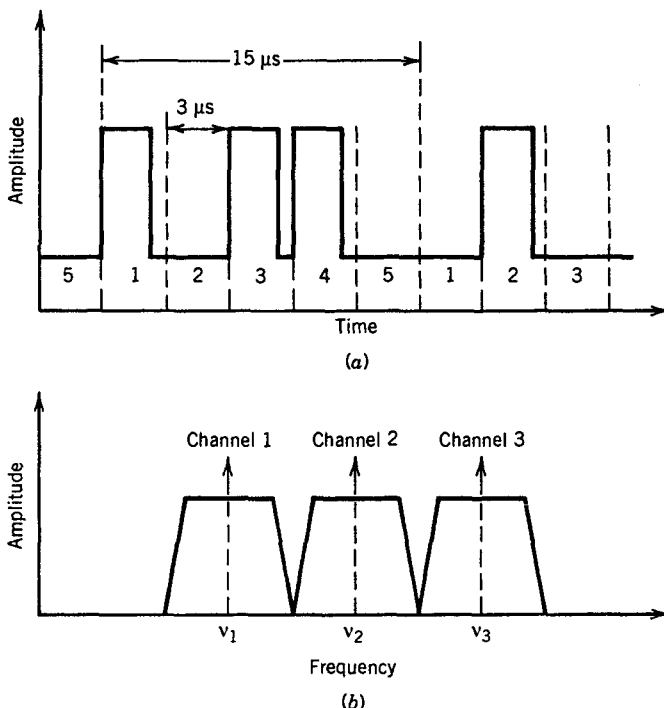


Figure 1.8: (a) Time-division multiplexing of five digital voice channels operating at 64 kb/s; (b) frequency-division multiplexing of three analog signals.

TDM and FDM can be implemented in both the electrical and optical domains; optical FDM is often referred to as WDM. Chapter 6 is devoted to optical-domain multiplexing techniques. This section covers electrical TDM, which is employed universally to multiplex a large number of voice channels into a single electrical bit stream.

The concept of TDM has been used to form *digital hierarchies*. In North America and Japan, the first level corresponds to multiplexing of 24 voice channels with a composite bit rate of 1.544 Mb/s (hierarchy DS-1), whereas in Europe 30 voice channels are multiplexed, resulting in a composite bit rate of 2.048 Mb/s. The bit rate of the multiplexed signal is slightly larger than the simple product of 64 kb/s with the number of channels because of extra control bits that are added for separating (demultiplexing) the channels at the receiver end. The second-level hierarchy is obtained by multiplexing 4 DS-1 TDM channels. This results in a bit rate of 6.312 Mb/s (hierarchy DS-2) for North America or Japan and 8.448 Mb/s for Europe. This procedure is continued to obtain higher-level hierarchies. For example, at the fifth level of hierarchy, the bit rate becomes 565 Mb/s for Europe and 396 Mb/s for Japan.

The lack of an international standard in the telecommunication industry during the 1980s led to the advent of a new standard, first called the *synchronous optical network* (SONET) and later termed the *synchronous digital hierarchy* or SDH [51]–[53]. It defines a synchronous frame structure for transmitting TDM digital signals. The basic

Table 1.1 SONET/SDH bit rates

SONET	SDH	B (Mb/s)	Channels
OC-1		51.84	672
OC-3	STM-1	155.52	2,016
OC-12	STM-4	622.08	8,064
OC-48	STM-16	2,488.32	32,256
OC-192	STM-64	9,953.28	129,024
OC-768	STM-256	39,813.12	516,096

building block of the SONET has a bit rate of 51.84 Mb/s. The corresponding optical signal is referred to as OC-1, where OC stands for optical carrier. The basic building block of the SDH has a bit rate of 155.52 Mb/s and is referred to as STM-1, where STM stands for a *synchronous transport module*. A useful feature of the SONET and SDH is that higher levels have a bit rate that is an exact multiple of the basic bit rate. Table 1.1 lists the correspondence between SONET and SDH bit rates for several levels. The SDH provides an international standard that appears to be well adopted. Indeed, lightwave systems operating at the STM-64 level ($B \approx 10$ Gb/s) are available since 1996 [19]. Commercial STM-256 (OC-768) systems operating near 40 Gb/s became available by 2002.

1.2.3 Modulation Formats

The first step in the design of an optical communication system is to decide how the electrical signal would be converted into an optical bit stream. Normally, the output of an optical source such as a semiconductor laser is modulated by applying the electrical signal either directly to the optical source or to an external modulator. There are two choices for the modulation format of the resulting optical bit stream. These are shown in Figure 1.9 and are known as the *return-to-zero* (RZ) and *nonreturn-to-zero* (NRZ) formats. In the RZ format, each optical pulse representing bit 1 is shorter than the bit slot, and its amplitude returns to zero before the bit duration is over. In the NRZ format, the optical pulse remains on throughout the bit slot and its amplitude does not drop to zero between two or more successive 1 bits. As a result, pulse width varies depending on the bit pattern, whereas it remains the same in the case of RZ format. An advantage of the NRZ format is that the bandwidth associated with the bit stream is smaller than that of the RZ format by about a factor of 2 simply because on-off transitions occur fewer times. However, its use requires tighter control of the pulse width and may lead to bit-pattern-dependent effects if the optical pulse spreads during transmission. The NRZ format is often used in practice because of a smaller signal bandwidth associated with it.

The use of the RZ format in the optical domain began to attract attention around 1999 after it was found that its use may help the design of high-capacity lightwave systems [54]–[56]. By now, this format is used almost exclusively for WDM channels designed to operate at 40 Gb/s or more. An example of the usefulness of the RZ format is provided by the so-called pseudo-linear systems [57] that employ relatively short op-

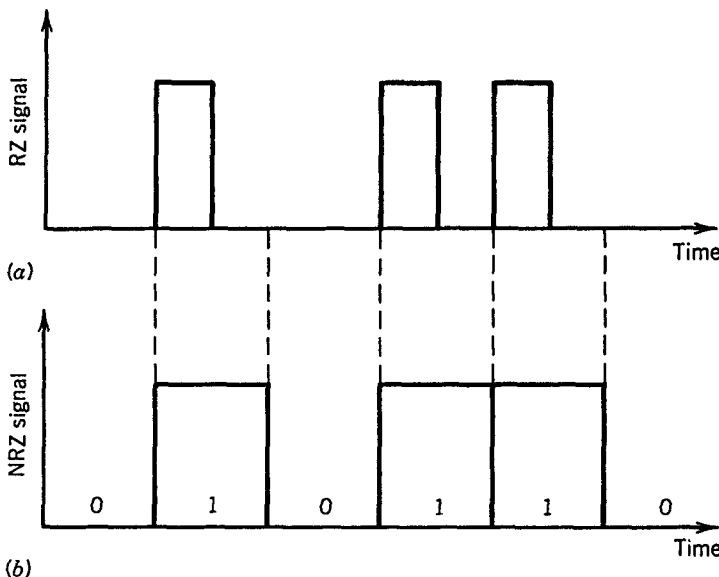


Figure 1.9: Digital bit stream 010110... coded by using (a) return-to-zero (RZ) and (b) nonreturn-to-zero (NRZ) formats.

tical pulses that spread over multiple bit slots quickly as they propagate down the fiber link. This spreading reduces the peak power and lowers the impact of several nonlinear effects that may prove detrimental otherwise. Pulses are eventually compressed back to their original width using a dispersion-management technique. Such systems typically employ an interesting variant of the RZ format, known as the chirped RZ (or CRZ) format, in which optical pulses are prechirped before they are launched into the fiber.

An important issue is related to the choice of the physical variable that is modulated to encode the data on the optical carrier. The optical carrier wave before modulation is of the form

$$\mathbf{E}(t) = \hat{\mathbf{e}} a \cos(\omega_0 t - \phi) = \hat{\mathbf{e}} \operatorname{Re}[a \exp(i\phi - i\omega_0 t)], \quad (1.2.5)$$

where \mathbf{E} is the electric field vector, $\hat{\mathbf{e}}$ is the polarization unit vector, a is the amplitude, ω_0 is the carrier frequency, and ϕ is the phase. The spatial dependence of \mathbf{E} is suppressed for simplicity of notation. One may choose to modulate the amplitude a , the frequency ω_0 , or the phase ϕ . In the case of analog modulation, the three modulation choices are known as amplitude modulation (AM), frequency modulation (FM), and phase modulation (PM). As shown schematically in Figure 1.10, The same modulation techniques can be applied in the digital case and are called amplitude-shift keying (ASK), frequency-shift keying (FSK), and phase-shift keying (PSK), depending on whether the amplitude, frequency, or phase of the carrier wave is shifted between the two levels of a binary digital signal. The simplest technique consists of simply changing the signal power between two levels, one of which is set to zero, and is often called *on-off keying* (OOK) to reflect the on-off nature of the resulting optical signal. Until recently, OOK was the format of choice for most digital lightwave systems.

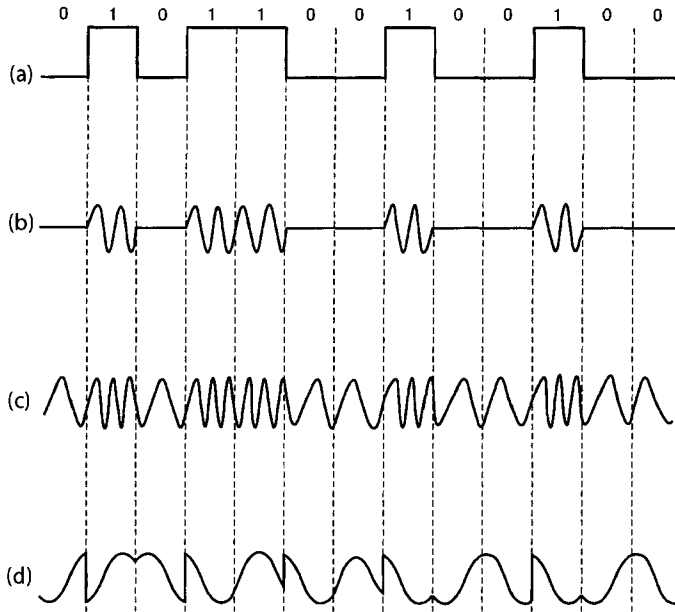


Figure 1.10: (a) An electrical bit stream and the resulting electric field patterns when it is converted to optical domain using (b) ASK, (c) FSK, (d) PSK modulation formats.

Although the use of FSK and PSK formats was explored during the 1980s in the context of coherent lightwave systems [20], these formats were nearly abandoned during the 1990 because of the complexities associated at the receiving end. The situation changed after 2000 when it was realized that the use of PSK is essential for improving the spectral efficiency of WDM systems. Modern WDM systems employ advanced modulation formats in which information is encoded using both the amplitude and phase of the optical carrier [29]. The basic idea behind the new formats can be understood by employing the complex notation for the electric field in Eq. (1.2.5) and introducing the so-called phasor as $A = a e^{i\phi}$. Figure 1.11 shows four modulation formats in the constellation diagrams, where the real and imaginary parts of A are plotted along the x and y axes, respectively. The first two configurations represent the standard binary ASK and PSK formats in which either the amplitude or the phase of electric field takes two values marked by circles. The third one shows the quadrature PSK (or QPSK) format in which the optical phase takes four possible values. This case, discussed in considerable detail in Chapter 10, two bits are transmitted during each time slot, and the effective bit rate is halved. Borrowing from the microwave communication terminology [48], the effective bit rate is called the *symbol rate* (or baud). The last example in Figure 1.11 shows how the symbol concept can be extended to multilevel signaling such that each symbol carries 4 bits or more. An additional factor of two can be gained if one transmits two orthogonally polarized symbols simultaneously during each symbol slot.

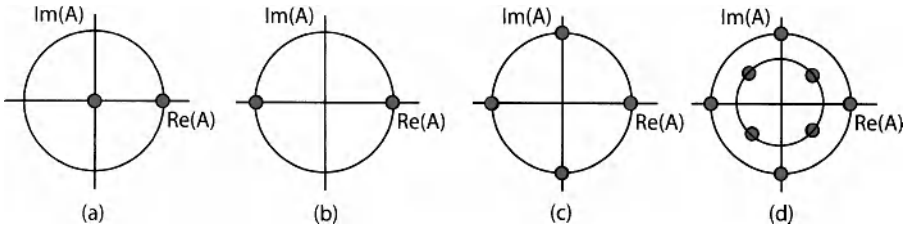


Figure 1.11: Constellation diagrams for (a) ASK, (b) PSK, (c) QPSK, and (d) multilevel QPSK formats.

1.3 Optical Communication Systems

As mentioned earlier, optical communication systems differ in principle from microwave systems only in the frequency range of the carrier wave used to carry the information. The optical carrier frequencies are typically ~ 200 THz, in contrast with the microwave carrier frequencies (~ 1 GHz). An increase in the information capacity of optical communication systems by a factor of up to 10,000 is expected simply because of such high carrier frequencies used for lightwave systems. This increase can be understood by noting that the bandwidth of the modulated carrier can be up to a few percent of the carrier frequency. Taking, for illustration, 1% as the limiting value, optical communication systems have the potential of carrying information at bit rates ~ 1 Tb/s. It is this enormous potential bandwidth of optical communication systems that is the driving force behind the worldwide development and deployment of lightwave systems. Current state-of-the-art systems operate at bit rates ~ 10 Gb/s, indicating that there is considerable room for improvement.

Figure 1.12 shows a generic block diagram of an optical communication system. It consists of a transmitter, a communication channel, and a receiver, the three elements common to all communication systems. Optical communication systems can be classified into two broad categories: *guided* and *unguided*. As the name implies, in the case of guided lightwave systems, the optical beam emitted by the transmitter remains spatially confined. This is realized in practice by using optical fibers, as discussed in Chapter 2. Since all guided optical communication systems currently use optical fibers, the commonly used term for them is fiber-optic communication systems. The term *lightwave system* is also used for fiber-optic communication systems, although it should generally include both guided and unguided systems.

In the case of unguided optical communication systems, the optical beam emitted by the transmitter spreads in space, similar to the spreading of microwaves. However, unguided optical systems are less suitable for broadcasting applications than microwave systems because optical beams spread mainly in the forward direction (as a result of their short wavelength). Their use generally requires accurate pointing between the transmitter and the receiver. In the case of terrestrial propagation, the signal in unguided systems can deteriorate considerably by scattering within the atmosphere. This problem, of course, disappears in *free-space communications* above the earth atmosphere (e.g., intersatellite communications). Although free-space optical communica-

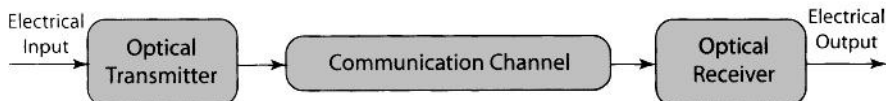


Figure 1.12: A generic optical communication system.

tion systems are needed for certain applications and have been studied extensively [58], most terrestrial applications make use of *fiber-optic communication systems*. This book does not consider unguided optical communication systems.

The application of fiber-optic transmission is possible in any area that requires transfer of information from one place to another. However, fiber-optic communication systems have been developed mostly for telecommunications applications. This is understandable in view of the worldwide telephone networks used to transmit not only voice signals but also computer data and fax messages. The telecommunication applications can be broadly classified into two categories, *long-haul* and *short-haul*, depending on whether the optical signal is transmitted over relatively long or short distances compared with typical intercity distances (~ 100 km). Long-haul telecommunication systems require high-capacity trunk lines and benefit most by the use of fiber-optic lightwave systems. Indeed, the technology behind optical fiber communication is often driven by long-haul applications. Each successive generation of lightwave systems is capable of operating at higher bit rates and over longer distances. Periodic regeneration of the optical signal by using repeaters is still required for most long-haul systems. However, considerable increase in both the repeater spacing and the bit rate, compared with those of coaxial systems, has made the use of lightwave systems very attractive for long-haul applications. Furthermore, the use of WDM with optical amplifiers has reduced the overall cost while increasing system capacity. As seen in Figure 1.5, a large number of transoceanic lightwave systems have already been installed to create an international fiber-optic network.

Short-haul telecommunication applications cover intracity and local-loop traffic. Such systems typically operate at low bit rates over distances of less than 50 km. The use of single-channel lightwave systems for such applications is not very cost-effective. For this reason, the use of WDM has become relevant even for short-haul systems. With the advent of the Internet in the 1990s, data traffic involving transmission of video and still images has become much more common and, by now such traffic consumes more bandwidth than the traditional telephone traffic. The use of Internet protocol involving packet switching is increasing continuously. Only modern fiber-optic WDM systems can meet the rapidly growing bandwidth requirements. Multichannel lightwave systems and their applications are discussed in Chapter 6.

1.4 Lightwave System Components

The generic block diagram of Figure 1.12 applies to a fiber-optic communication system, the only difference being that the communication channel is an optical fiber cable. The other two components, the optical transmitter and the optical receiver, are designed

to meet the needs of such a specific communication channel. In this section we discuss the general issues related to the role of optical fiber as a communication channel and to the design of transmitters and receivers. The objective is to provide an introductory overview, as the three components are discussed in detail in Chapters 2–4.

1.4.1 Optical Fibers as a Communication Channel

The role of a communication channel is to transport the optical signal from transmitter to receiver without distorting it. Most lightwave systems use optical fibers as the communication channel because silica fibers can transmit light with losses as small as 0.2 dB/km. Even then, optical power reduces to only 1% after 100 km. For this reason, fiber losses remain an important design issue and determines the repeater or amplifier spacing of a long-haul lightwave system. Another important design issue is *fiber dispersion*, which leads to broadening of individual optical pulses with propagation. If optical pulses spread significantly outside their allocated bit slot, the transmitted signal is severely degraded. Eventually, it becomes impossible to recover the original signal with high accuracy. The problem is most severe in the case of multimode fibers, since pulses spread rapidly (typically at a rate of ~ 10 ns/km) because of different speeds associated with different fiber modes. It is for this reason that most optical communication systems use single-mode fibers. Material dispersion (related to the frequency dependence of the refractive index) still leads to pulse broadening (typically <0.1 ns/km), but it is small enough to be acceptable for most applications and can be reduced further by controlling the spectral width of the optical source. Nevertheless, as discussed in Chapter 2, material dispersion sets the ultimate limit on the bit rate and the transmission distance of fiber-optic communication systems.

1.4.2 Optical Transmitters

The role of an *optical transmitter* is to convert the electrical signal into optical form and to launch the resulting optical signal into the optical fiber. Figure 1.13 shows the block diagram of an optical transmitter. It consists of an optical source, a modulator, and a channel coupler. Semiconductor lasers or light-emitting diodes are used as optical sources because of their compatibility with the optical-fiber communication channel; both are discussed in detail in Chapter 3. The optical signal is generated by modulating the optical carrier wave. Although an external modulator is sometimes used, it can be dispensed with in some cases, since the output of a semiconductor optical source can be modulated directly by varying the injection current. Such a scheme simplifies the transmitter design and is generally cost-effective. The coupler is typically a microlens that focuses the optical signal onto the entrance plane of an optical fiber with the maximum possible efficiency.

The *launched power* is an important design parameter. One can increase the amplifier (or repeater) spacing by increasing it, but the onset of various *nonlinear effects* limits how much the input power can be increased. The launched power is often expressed in “dBm” units with 1 mW as the reference level. The general definition is (see

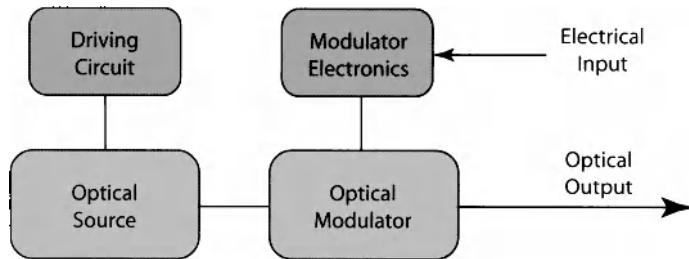


Figure 1.13: Components of an optical transmitter.

Appendix A)

$$\text{power (dBm)} = 10\log_{10}\left(\frac{\text{power}}{1 \text{ mW}}\right). \quad (1.4.1)$$

Thus, 1 mW is 0 dBm, but 1 μW corresponds to -30 dBm. The launched power is rather low (< -10 dBm) for light-emitting diodes but semiconductor lasers can launch powers ~ 10 dBm. As light-emitting diodes are also limited in their modulation capabilities, most lightwave systems use semiconductor lasers as optical sources. The bit rate of optical transmitters is often limited by electronics rather than by the semiconductor laser itself. With proper design, optical transmitters can be made to operate at a bit rate of up to 40 Gb/s. Chapter 3 is devoted to a complete description of optical transmitters.

1.4.3 Optical Receivers

An *optical receiver* converts the optical signal received at the output end of the optical fiber back into the original electrical signal. Figure 1.14 shows the block diagram of an optical receiver. It consists of a coupler, a photodetector, and a demodulator. The coupler focuses the received optical signal onto the photodetector. Semiconductor photodiodes are used as photodetectors because of their compatibility with the whole system; they are discussed in Chapter 4. The design of the demodulator depends on the modulation format used by the lightwave system. The use of FSK and PSK formats generally requires heterodyne or homodyne demodulation techniques discussed in Chapter 10. Most lightwave systems employ a scheme referred to as “intensity modulation with direct detection” (IM/DD). Demodulation in this case is done by a decision circuit that identifies bits as 1 or 0, depending on the amplitude of the electric signal. The accuracy of the decision circuit depends on the SNR of the electrical signal generated at the photodetector.

The performance of a digital lightwave system is characterized through the *bit-error rate* (BER). Although the BER can be defined as the number of errors made per second, such a definition makes the BER bit-rate dependent. It is customary to define the BER as the average probability of incorrect bit identification. Therefore, a BER of 10^{-6} corresponds to on average one error per million bits. Most lightwave systems specify a BER of 10^{-9} as the operating requirement; some even require a BER as small

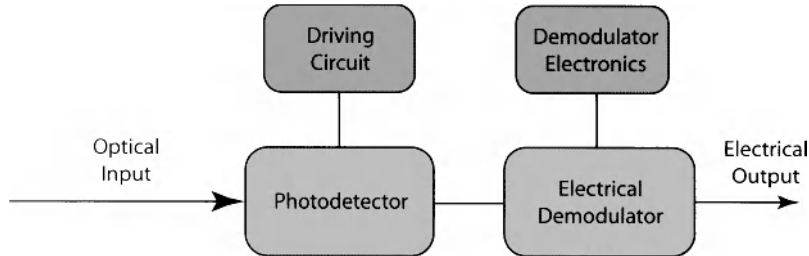


Figure 1.14: Components of an optical receiver.

as 10^{-14} . The error-correction codes are sometimes used to improve the raw BER of a lightwave systems.

An important parameter for any receiver is the *receiver sensitivity*. It is usually defined as the minimum average optical power required to realize a BER of 10^{-9} . Receiver sensitivity depends on the SNR, which in turn depends on various noise sources that corrupt the signal received. Even for a perfect receiver, some noise is introduced by the process of photodetection itself. This is referred to as the *quantum noise* or the *shot noise*, as it has its origin in the particle nature of electrons. Optical receivers operating at the shot-noise limit are called quantum-noise-limited receivers. No practical receiver operates at the quantum-noise limit because of the presence of several other noise sources. Some of the noise sources such as *thermal noise* are internal to the receiver. Others originate at the transmitter or during propagation along the fiber link. For instance, any amplification of the optical signal along the transmission line with the help of optical amplifiers introduces the so-called *amplifier noise* that has its origin in the fundamental process of spontaneous emission. Chromatic dispersion in optical fibers can add additional noise through phenomena such as intersymbol interference and mode-partition noise. The receiver sensitivity is determined by a cumulative effect of all possible noise mechanisms that degrade the SNR at the decision circuit. In general, it also depends on the bit rate as the contribution of some noise sources (e.g., shot noise) increases in proportion to the signal bandwidth. Chapter 4 is devoted to noise and sensitivity issues of optical receivers by considering the SNR and the BER in digital lightwave systems.

Problems

- 1.1 Calculate the carrier frequency for optical communication systems operating at 0.88, 1.3, and $1.55 \mu\text{m}$. What is the photon energy (in eV) in each case?
- 1.2 Calculate the transmission distance over which the optical power will attenuate by a factor of 10 for three fibers with losses of 0.2, 20, and 2000 dB/km . Assuming that the optical power decreases as $\exp(-\alpha L)$, calculate α (in cm^{-1}) for the three fibers.

- 1.3 Assume that a digital communication system can be operated at a bit rate of up to 1% of the carrier frequency. How many audio channels at 64 kb/s can be transmitted over a microwave carrier at 5 GHz and an optical carrier at $1.55 \mu\text{m}$?
- 1.4 A 1-hour lecture script is stored on the computer hard disk in the ASCII format. Estimate the total number of bits assuming a delivery rate of 200 words per minute and on average 5 letters per word. How long will it take to transmit the script at a bit rate of 1 Gb/s?
- 1.5 A $1.55\text{-}\mu\text{m}$ digital communication system operating at 1 Gb/s receives an average power of -40 dBm at the detector. Assuming that 1 and 0 bits are equally likely to occur, calculate the number of photons received within each 1 bit.
- 1.6 An analog voice signal that can vary over the range 0–50 mA is digitized by sampling it at 8 kHz. The first four sample values are 10, 21, 36, and 16 mA. Write the corresponding digital signal (a string of 1 and 0 bits) by using a 4-bit representation for each sample.
- 1.7 Sketch the variation of optical power with time for a digital NRZ bit stream 010111101110 by assuming a bit rate of 2.5 Gb/s. What is the duration of the shortest and widest optical pulse?
- 1.8 A $1.55\text{-}\mu\text{m}$ fiber-optic communication system is transmitting digital signals over 100 km at 2 Gb/s. The transmitter launches 2 mW of average power into the fiber cable, having a net loss of 0.3 dB/km. How many photons are incident on the receiver during a single 1 bit? Assume that 0 bits carry no power, while 1 bits are in the form of a rectangular pulse occupying the entire bit slot (NRZ format).
- 1.9 A $0.8\text{-}\mu\text{m}$ optical receiver needs at least 1000 photons to detect the 1 bits accurately. What is the maximum possible length of the fiber link for a 100-Mb/s optical communication system designed to transmit -10 dBm of average power? The fiber loss is 2 dB/km at $0.8 \mu\text{m}$. Assume the NRZ format and a rectangular pulse shape.
- 1.10 A $1.3\text{-}\mu\text{m}$ optical transmitter is used to obtain a digital bit stream at a bit rate of 2 Gb/s. Calculate the number of photons contained in a single 1 bit when the average power emitted by the transmitter is 4 mW. Assume that the 0 bits carry no energy.

References

- [1] G. J. Holzmann and B. Pehrson, *The Early History of Data Networks*, Wiley, Hoboken, NJ, 2003.
- [2] D. Koenig, "Telegraphs and Telegrams in Revolutionary France," *Scientific Monthly*, 431 (1944). See also Chap. 2 of Ref. [1].
- [3] A. Jones, *Historical Sketch of the Electrical Telegraph*, Putnam, New York, 1852.
- [4] A. G. Bell, U.S. Patent No. 174,465 (1876).
- [5] T. H. Maiman, *Nature* **187**, 493 (1960).
- [6] W. K. Pratt, *Laser Communication Systems*, Wiley, New York, 1969.
- [7] S. E. Miller, *Sci. Am.* **214** (1), 19 (1966).

- [8] K. C. Kao and G. A. Hockham, *Proc. IEE* **113**, 1151 (1966); A. Werts, *Onde Electr.* **45**, 967 (1966).
- [9] F. P. Kapron, D. B. Keck, and R. D. Maurer, *Appl. Phys. Lett.* **17**, 423 (1970).
- [10] I. Hayashi, M. B. Panish, P. W. Foy, and S. Sumski, *Appl. Phys. Lett.* **17**, 109 (1970).
- [11] A. E. Willner, Ed., *IEEE J. Sel. Topics Quantum Electron.* **6**, 827 (2000). Several historical articles in this millennium issue cover the development of lasers and optical fibers. See, for example, the articles by Z. Alferov, W. A. Gambling, T. Izawa, D. Keck, H. Kogelnik, and R. H. Rediker.
- [12] A. H. Gnauck, R. W. Tkach, A. R. Chraplyvy, and T. Li, *J. Lightwave Technol.* **26**, 1032 (2008).
- [13] H. Kogelnik, *IEEE J. Sel. Topics Quantum Electron.* **6**, 1279 (2000).
- [14] R. J. Sanferrare, *AT&T Tech. J.* **66**, 95 (1987).
- [15] D. Gloge, A. Albanese, C. A. Burrus, E. L. Chinnock, J. A. Copeland, A. G. Dentai, T. P. Lee, T. Li, and K. Ogawa, *Bell Syst. Tech. J.* **59**, 1365 (1980).
- [16] J. I. Yamada, S. Machida, and T. Kimura, *Electron. Lett.* **17**, 479 (1981).
- [17] T. Miya, Y. Terunuma, T. Hosaka, and T. Miyoshita, *Electron. Lett.* **15**, 106 (1979).
- [18] A. H. Gnauck, B. L. Kasper, R. A. Linke, R. W. Dawson, T. L. Koch, T. J. Bridges, E. G. Burkhardt, R. T. Yen, D. P. Wilt, J. C. Campbell, K. C. Nelson, and L. G. Cohen, *J. Lightwave Technol.* **3**, 1032 (1985).
- [19] K. Nakagawa, *Trans. IECE Jpn. Pt. J* **78B**, 713 (1995).
- [20] R. A. Linke and A. H. Gnauck, *J. Lightwave Technol.* **6**, 1750 (1988); P. S. Henry, *Coherent Lightwave Communications*, IEEE Press, New York, 1990.
- [21] N. S. Bergano, J. Aspell, C. R. Davidson, P. R. Trischitta, B. M. Nyman, and F. W. Kerfoot, *Electron. Lett.* **27**, 1889 (1991).
- [22] T. Otani, K. Goto, H. Abe, M. Tanaka, H. Yamamoto, and H. Wakabayashi, *Electron. Lett.* **31**, 380 (1995).
- [23] N. S. Bergano, *J. Lightwave Technol.* **23**, 4125 (2005).
- [24] T. Welsh, R. Smith, H. Azami, and R. Chrisner, *IEEE Commun. Mag.* **34** (2), 30 (1996).
- [25] W. C. Marra and J. Schesser, *IEEE Commun. Mag.* **34** (2), 50 (1996).
- [26] K. Fukuchi, T. Kasamatsu, M. Morie, R. Ohhira, T. Ito, K. Sekiya, D. Ogasahara, and T. Ono, *Proc. Optical Fiber Commun. Conf.*, Paper PD24 (2001).
- [27] G. Vareille, F. Pitel, and J. F. Marcerou, *Proc. Optical Fiber Commun. Conf.*, Paper PD22 (2001).
- [28] G. A. Thomas, B. L. Shraiman, P. F. Glodis, and M. J. Stephan, *Nature* **404**, 262 (2000).
- [29] P. J. Winzer and R. J. Essiambre, *J. Lightwave Technol.* **24**, 4711 (2006).
- [30] X. Zhou, J. Yu, M.-F. Huang, et al., *Proc. Opt. Fiber Commun. Conf.*, Paper PDPB9 (2010).
- [31] K. M. Sivalingam and S. Subramaniam, Eds., *Optical WDM Networks: Principles and Practice*, Kluwer Academic, Norwell, MA, 2000.
- [32] J. Chesnoy, Ed., *Undersea Fiber Communication System*, Academic Press, Boston, 2002.
- [33] R. L. Freeman, *Fiber Optic Systems for Telecommunications*, Wiley, Hoboken, NJ, 2002.
- [34] I. P. Kaminow and T. Li, Eds., *Optical Fiber Telecommunications IV*, Academic Press, Boston, 2002.
- [35] C. G. Omidyar, H. G. Shiraz, and W. D. Zhong, Eds., *Optical Communications and Networks*, World Scientific, Singapore, 2004.
- [36] A. K. Dutta, N. K. Dutta, and M. Fujiwara, Eds., *WDM Technologies: Optical Networks*, Academic Press, Boston, 2004.

- [37] J. C. Palais, *Fiber Optic Communications*, 5th ed., Prentice Hall, Upper Saddle River, NJ, 2004.
- [38] E. Forestieri, Ed., *Optical Communication Theory and Techniques*, Springer, Mew York, 2004.
- [39] K.-P. Ho, *Phase-Modulated Optical Communication Systems*, Springer, Mew York, 2005.
- [40] B. Mukherjee, *Optical WDM Networks*, Springer, Mew York, 2006.
- [41] H.-G. Weber and M. Nakazawa, Eds., *Ultrahigh-Speed Optical Transmission Technology*, Springer, New York, 2007.
- [42] I. P. Kaminow, T. Li, and A. E. Willner, Eds., *Optical Fiber Telecommunications V*, vols. A and B, Academic Press, Boston, 2008.
- [43] L. N. Binh, *Digital Optical Communications*, CRC Press, Boca Raton, FL, 2008.
- [44] C. DeCusatis, *Handbook of Fiber Optic Data Communication*, 3rd ed., Academic Press, Boston, 2008.
- [45] J. Senior, *Optical Fiber Communications: Principles and Practice*, 3rd ed., Prentice Hall, Upper Saddle River, NJ, 2009.
- [46] R. Ramaswami, K. Sivarajan, and G. Sasaki, *Optical Networks: A Practical Perspective*, 3rd ed., Morgan Kaufmann, San Francisco, 2009.
- [47] G. E. Keiser, *Optical Fiber Communications*, 4th ed., McGraw-Hill, New York, 2010.
- [48] M. Schwartz, *Information Transmission, Modulation, and Noise*, 4th ed., McGraw-Hill, New York, 1990.
- [49] C. E. Shannon, *Proc. IRE* **37**, 10 (1949).
- [50] H. Nyquist, *Trans. AIEE* **47**, 617 (1928).
- [51] R. Ballart and Y.-C. Ching, *IEEE Commun. Mag.* **27** (3), 8 (1989).
- [52] T. Miki, Jr. and C. A. Siller, Eds., *IEEE Commun. Mag.* **28** (8), 1 (1990).
- [53] S. V. Kartalopoulos, *Understanding SONET/SDH and ATM*, IEEE Press, Piscataway, NJ, 1999.
- [54] M. I. Hayee and A. E. Willner, *IEEE Photon. Technol. Lett.* **11**, 991 (1999).
- [55] R. Ludwig, U. Feiste, E. Dietrich, H. G. Weber, D. Breuer, M. Martin, and F. Kuppers, *Electron. Lett.* **35**, 2216 (1999).
- [56] M. Nakazawa, H. Kubota, K. Suzuki, E. Yamada, and A. Sahara, *IEEE J. Sel. Topics Quantum Electron.* **6**, 363 (2000).
- [57] R.-J. Essiambre, G. Raybon, and B. Mikkelsen, in *Optical Fiber Telecommunications*, Vol. 4B, I. P. Kaminow and T. Li, Eds., Academic Press, Boston, 2002, Chap. 6.
- [58] S. G. Lambert and W. L. Casey, *Laser Communications in Space*, Artec House, Norwood, MA, 1995.

Chapter 2

Optical Fibers

The phenomenon of *total internal reflection*, responsible for guiding of light in optical fibers, has been known since 1854 [1]. Although glass fibers were made in the 1920s [2]–[4], their use became practical only in the 1950s, when the use of a cladding layer led to considerable improvement in their guiding characteristics [5]–[7]. Before 1970, optical fibers were used mainly for medical imaging over short distances [8]. Their use for communication purposes was considered impractical because of high losses (~ 1000 dB/km). However, the situation changed drastically in 1970 when, following an earlier suggestion [9], the loss of optical fibers was reduced to below 20 dB/km [10]. Further progress resulted by 1979 in a loss of only 0.2 dB/km near the $1.55\text{-}\mu\text{m}$ spectral region [11]. The availability of low-loss fibers led to a revolution in the field of lightwave technology and started the era of fiber-optic communications. Several books devoted entirely to optical fibers cover numerous advances made in their design and understanding [12]–[19]. This chapter focuses on the role of optical fibers as a communication channel in lightwave systems. In Section 2.1 we use geometrical-optics description to explain the guiding mechanism and introduce the related basic concepts. Maxwell’s equations are used in Section 2.2 to describe wave propagation in optical fibers. The origin of fiber dispersion is discussed in Section 2.3, and Section 2.4 considers limitations on the bit rate and the transmission distance imposed by fiber dispersion. Section 2.5 focuses on loss mechanisms in optical fibers, whereas Section 2.6 is devoted to the nonlinear effects. Section 2.7 covers manufacturing details and includes a discussion of fiber cables.

2.1 Geometrical-Optics Description

In its simplest form an optical fiber consists of a cylindrical core of silica glass surrounded by a cladding whose refractive index is lower than that of the core. Because of an abrupt index change at the core–cladding interface, such fibers are called *step-index fibers*. In a different type of fiber, known as *graded-index fiber*, the refractive index decreases gradually inside the core. Figure 2.1 shows schematically the index profile and the cross section for the two kinds of fibers. Considerable insight in the guiding

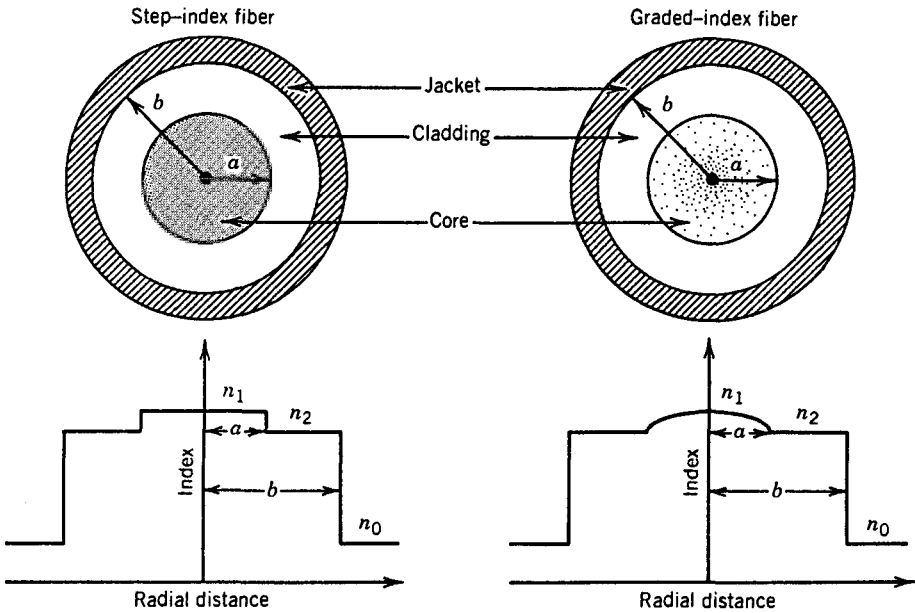


Figure 2.1: Cross section and refractive-index profile for step-index and graded-index fibers.

properties of optical fibers can be gained by using a ray picture based on geometrical optics [20]. The geometrical-optics description, although approximate, is valid when the core radius a is much larger than the light wavelength λ . When the two become comparable, it is necessary to use the wave-propagation theory of Section 2.2.

2.1.1 Step-Index Fibers

Consider the geometry of Figure 2.2, where a ray making an angle θ_i with the fiber axis is incident at the core center. Because of refraction at the fiber-air interface, the ray bends toward the normal. The angle θ_r of the refracted ray is given by [20]

$$n_0 \sin \theta_i = n_1 \sin \theta_r, \quad (2.1.1)$$

where n_1 and n_0 are the refractive indices of the fiber core and air, respectively. The refracted ray hits the core-cladding interface and is refracted again. However, refraction is possible only for an angle of incidence ϕ such that $\sin \phi < n_2/n_1$. For angles larger than a *critical angle* ϕ_c , defined by [20]

$$\sin \phi_c = n_2/n_1, \quad (2.1.2)$$

where n_2 is the cladding index, the ray experiences total internal reflection at the core-cladding interface. Since such reflections occur throughout the fiber length, all rays with $\phi > \phi_c$ remain confined to the fiber core. This is the basic mechanism behind light confinement in optical fibers.

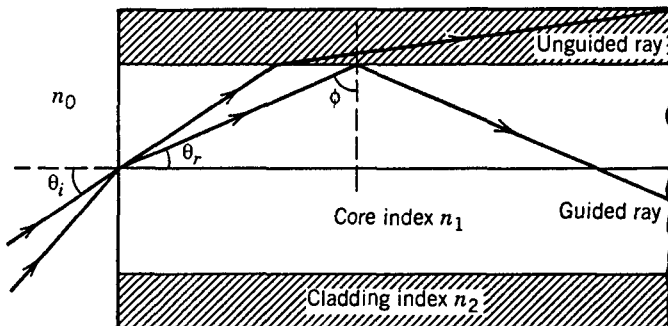


Figure 2.2: Light confinement through total internal reflection in step-index fibers. Rays for which $\phi < \phi_c$ are refracted out of the core.

One can use Eqs. (2.1.1) and (2.1.2) to find the maximum angle that the incident ray should make with the fiber axis to remain confined inside the core. Noting that $\theta_r = \pi/2 - \phi_c$ for such a ray and substituting it in Eq. (2.1.1), we obtain

$$n_0 \sin \theta_i = n_1 \cos \phi_c = (n_1^2 - n_2^2)^{1/2}. \quad (2.1.3)$$

In analogy with lenses, $n_0 \sin \theta_i$ is known as the *numerical aperture* (NA) of the fiber. It represents the light-gathering capacity of an optical fiber. For $n_1 \simeq n_2$ the NA can be approximated by

$$\text{NA} = n_1(2\Delta)^{1/2}, \quad \Delta = (n_1 - n_2)/n_1, \quad (2.1.4)$$

where Δ is the fractional index change at the core-cladding interface. Clearly, Δ should be made as large as possible in order to couple maximum light into the fiber. However, such fibers are not useful for the purpose of optical communications because of a phenomenon known as multipath dispersion or *modal dispersion* (the concept of fiber modes is introduced in Section 2.2).

Multipath dispersion can be understood by referring to Figure 2.2, where different rays travel along paths of different lengths. As a result, these rays disperse in time at the output end of the fiber even if they were coincident at the input end and traveled at the same speed inside the fiber. A short pulse (called an *impulse*) would broaden considerably as a result of different path lengths. One can estimate the extent of pulse broadening simply by considering the shortest and longest ray paths. The shortest path occurs for $\theta_i = 0$ and is just equal to the fiber length L . The longest path occurs for θ_i given by Eq. (2.1.3) and has a length $L/\sin \phi_c$. By taking the velocity of propagation $v = c/n_1$, the time delay is given by

$$\Delta T = \frac{n_1}{c} \left(\frac{L}{\sin \phi_c} - L \right) = \frac{L n_1^2}{c n_2} \Delta. \quad (2.1.5)$$

The time delay between the two rays taking the shortest and longest paths is a measure of broadening experienced by an impulse launched at the fiber input.

We can relate ΔT to the information-carrying capacity of the fiber measured through the bit rate B . Although a precise relation between B and ΔT depends on many details,

such as the pulse shape, it is clear intuitively that ΔT should be less than the allocated bit slot ($T_B = 1/B$). Thus, an order-of-magnitude estimate of the bit rate is obtained from the condition $B\Delta T < 1$. By using Eq. (2.1.5) we obtain

$$BL < \frac{n_2}{n_1^2} \frac{c}{\Delta}. \quad (2.1.6)$$

This condition provides a rough estimate of a fundamental limitation of step-index fibers. As an illustration, consider an unclad glass fiber with $n_1 = 1.5$ and $n_2 = 1$. The bit rate-distance product of such a fiber is limited to quite small values since $BL < 0.4$ (Mb/s)-km. Considerable improvement occurs for cladded fibers with a small index step. Most fibers for communication applications are designed with $\Delta < 0.01$. As an example, $BL < 100$ (Mb/s)-km for $\Delta = 2 \times 10^{-3}$. Such fibers can communicate data at a bit rate of 10 Mb/s over distances up to 10 km and may be suitable for some local-area networks.

Two remarks are in order concerning the validity of Eq. (2.1.6). First, it is obtained by considering only rays that pass through the fiber axis after each total internal reflection. Such rays are called *meridional rays*. In general, the fiber also supports *skew rays*, which travel at angles oblique to the fiber axis. Skew rays scatter out of the core at bends and irregularities and are not expected to contribute significantly to Eq. (2.1.6). Second, even the oblique meridional rays suffer higher losses than paraxial meridional rays because of scattering. Equation (2.1.6) provides a conservative estimate since all rays are treated equally. The effect of intermodal dispersion can be considerably reduced by using graded-index fibers, which are discussed in the next subsection. It can be eliminated entirely by using the single-mode fibers discussed in Section 2.2.

2.1.2 Graded-Index Fibers

The refractive index of the core in graded-index fibers is not constant but decreases gradually from its maximum value n_1 at the core center to its minimum value n_2 at the core-cladding interface. Most graded-index fibers are designed to have a nearly quadratic decrease and are analyzed by using α -profile, given by

$$n(\rho) = \begin{cases} n_1[1 - \Delta(\rho/a)^\alpha]; & \rho < a, \\ n_1(1 - \Delta) = n_2; & \rho \geq a, \end{cases} \quad (2.1.7)$$

where a is the core radius. The parameter α determines the index profile. A step-index profile is approached in the limit of large α . A parabolic-index fiber corresponds to $\alpha = 2$.

It is easy to understand qualitatively why intermodal or multipath dispersion is reduced for graded-index fibers. Figure 2.3 shows schematically paths for three different rays. Similar to the case of step-index fibers, the path is longer for more oblique rays. However, the ray velocity changes along the path because of variations in the refractive index. More specifically, the ray propagating along the fiber axis takes the shortest path but travels most slowly as the index is largest along this path. Oblique rays have a large part of their path in a medium of lower refractive index, where they travel faster. It is therefore possible for all rays to arrive together at the fiber output by a suitable choice of the refractive-index profile.

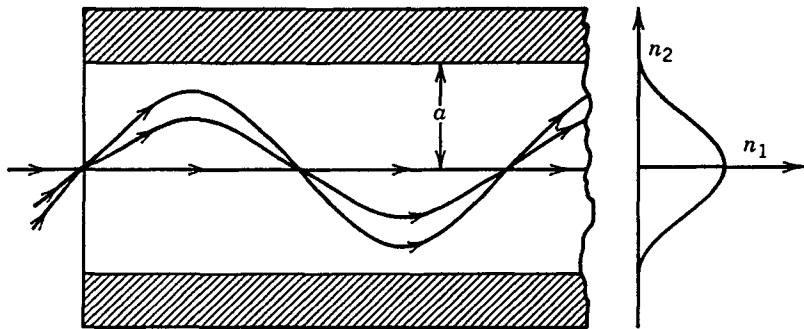


Figure 2.3: Ray trajectories in a graded-index fiber.

Geometrical optics can be used to show that a parabolic-index profile leads to nondispersive pulse propagation within the *paraxial approximation*. The trajectory of a paraxial ray is obtained by solving [20]

$$\frac{d^2\rho}{dz^2} = \frac{1}{n} \frac{dn}{d\rho}, \quad (2.1.8)$$

where ρ is the radial distance of the ray from the axis. By using Eq. (2.1.7) for $\rho < a$ with $\alpha = 2$, Eq. (2.1.8) reduces to an equation of harmonic oscillator and has the general solution

$$\rho = \rho_0 \cos(pz) + (\rho'_0/p) \sin(pz), \quad (2.1.9)$$

where $p = (2\Delta/a^2)^{1/2}$ and ρ_0 and ρ'_0 are the position and the direction of the input ray, respectively. Equation (2.1.9) shows that all rays recover their initial positions and directions at distances $z = 2m\pi/p$, where m is an integer (see Figure 2.3). Such a complete restoration of the input implies that a parabolic-index fiber does not exhibit intermodal dispersion.

The conclusion above holds only within the paraxial and the geometrical-optics approximations, both of which must be relaxed for practical fibers. Intermodal dispersion in graded-index fibers has been studied extensively with wave-propagation techniques [13]–[15]. The quantity $\Delta T/L$, where ΔT is the maximum multipath delay in a fiber of length L , is found to vary considerably with α . Figure 2.4 shows this variation for $n_1 = 1.5$ and $\Delta = 0.01$. The minimum dispersion occurs for $\alpha = 2(1 - \Delta)$ and depends on Δ as [21]

$$\Delta T/L = n_1 \Delta^2 / 8c. \quad (2.1.10)$$

The limiting bit rate–distance product is obtained by using the criterion $\Delta T < 1/B$ and is given by

$$BL < 8c/n_1 \Delta^2. \quad (2.1.11)$$

The right scale in Figure 2.4 shows the BL product as a function of α . Graded-index fibers with a suitably optimized index profile can communicate data at a bit rate of 100 Mb/s over distances up to 100 km. The BL product of such fibers is improved by nearly three orders of magnitude over that of step-index fibers. Indeed, the first

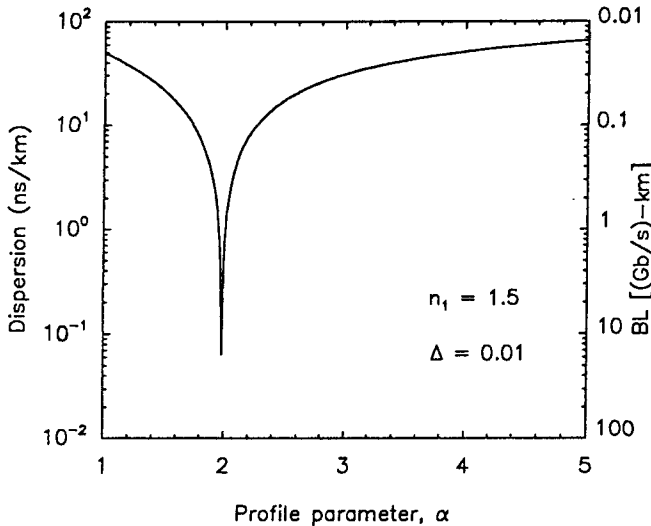


Figure 2.4: Variation of intermodal dispersion $\Delta T/L$ with the profile parameter α for a graded-index fiber. The scale on the right shows the corresponding bit rate–distance product.

generation of lightwave systems used graded-index fibers. Further improvement is possible only by using single-mode fibers whose core radius is comparable to the light wavelength. Geometrical optics cannot be used for such fibers.

Although graded-index fibers are rarely used for long-haul links, the use of graded-index *plastic* optical fibers for data-link applications has attracted attention in recent years. Such fibers exhibit high losses (>20 dB/km) but they can be used to transmit data at bit rates 1 Gb/s or more over short distances (1 km or less) because of a graded-index profile (see Section 2.7.2 for further details).

2.2 Wave Propagation

In this section we consider propagation of light in step-index fibers using Maxwell's equations for electromagnetic waves. These equations are introduced in Section 2.2.1 and solved in Section 2.2.2 to obtain optical modes that are guided inside a fiber. Section 2.2.3 focuses on how a step-index fiber can be designed to support only a single mode and discusses the properties of such single-mode fibers.

2.2.1 Maxwell's Equations

Like all electromagnetic phenomena, propagation of optical fields in fibers is governed by *Maxwell's equations*. For a nonconducting medium without free charges, these equations take the form [22] (in SI units; see Appendix A)

$$\nabla \times \mathbf{E} = -\partial \mathbf{B} / \partial t, \quad (2.2.1)$$

$$\nabla \times \mathbf{H} = \partial \mathbf{D} / \partial t, \quad (2.2.2)$$

$$\nabla \cdot \mathbf{D} = 0, \quad (2.2.3)$$

$$\nabla \cdot \mathbf{B} = 0, \quad (2.2.4)$$

where \mathbf{E} and \mathbf{H} are the electric and magnetic field vectors, respectively, and \mathbf{D} and \mathbf{B} are the corresponding flux densities. The flux densities are related to the field vectors by the constitutive relations [22]

$$\mathbf{D} = \epsilon_0 \mathbf{E} + \mathbf{P}, \quad \mathbf{B} = \mu_0 \mathbf{H} + \mathbf{M}, \quad (2.2.5)$$

where ϵ_0 is the vacuum permittivity, μ_0 is the vacuum permeability, and \mathbf{P} and \mathbf{M} are the induced electric and magnetic polarizations, respectively. For optical fibers $\mathbf{M} = 0$ because of the nonmagnetic nature of silica glass.

Evaluation of the electric polarization \mathbf{P} requires a microscopic quantum-mechanical approach. Although such an approach is essential when the optical frequency is near a medium resonance, a phenomenological relation between \mathbf{P} and \mathbf{E} can be used far from medium resonances. This is the case for optical fibers in the wavelength region 0.5–2 μm , a range that covers the low-loss region of optical fibers that is of interest for fiber-optic communication systems. In general, the relation between \mathbf{P} and \mathbf{E} can be nonlinear. Although the nonlinear effects in optical fibers are of considerable interest [23] and are covered in Section 2.6, they can be ignored in a discussion of fiber modes. \mathbf{P} is then related to \mathbf{E} by the relation

$$\mathbf{P}(\mathbf{r}, t) = \epsilon_0 \int_{-\infty}^{\infty} \chi(\mathbf{r}, t - t') \mathbf{E}(\mathbf{r}, t') dt'. \quad (2.2.6)$$

The linear susceptibility χ is, in general, a second-rank tensor but reduces to a scalar for an isotropic medium such as silica glass. Optical fibers become slightly birefringent because of unintentional variations in the core shape or in local strain; such birefringent effects are considered in Section 2.2.3. Equation (2.2.6) assumes a spatially local response. However, it includes the delayed nature of the temporal response, a feature that is responsible for chromatic dispersion.

Equations (2.2.1) through (2.2.6) provide a general formalism for studying wave propagation in optical fibers. In practice, it is convenient to use a single field variable \mathbf{E} . By taking the curl of Eq. (2.2.1) and using Eqs. (2.2.2) and (2.2.5), we obtain the wave equation

$$\nabla \times \nabla \times \mathbf{E} = -\frac{1}{c^2} \frac{\partial^2 \mathbf{E}}{\partial t^2} - \mu_0 \frac{\partial^2 \mathbf{P}}{\partial t^2}, \quad (2.2.7)$$

where the vacuum speed of light c is defined as usual by $\mu_0 \epsilon_0 = 1/c^2$. By introducing the Fourier transform of $\mathbf{E}(\mathbf{r}, t)$ through the relation

$$\tilde{\mathbf{E}}(\mathbf{r}, \omega) = \int_{-\infty}^{\infty} \mathbf{E}(\mathbf{r}, t) \exp(i\omega t) dt, \quad (2.2.8)$$

as well as a similar relation for $\mathbf{P}(\mathbf{r}, t)$, and by using Eq. (2.2.6), Eq. (2.2.7) can be written in the frequency domain as

$$\nabla \times \nabla \times \tilde{\mathbf{E}} = \epsilon(\mathbf{r}, \omega) (\omega^2 / c^2) \tilde{\mathbf{E}}, \quad (2.2.9)$$

where the frequency-dependent dielectric constant is defined as

$$\epsilon(\mathbf{r}, \omega) = 1 + \tilde{\chi}(\mathbf{r}, \omega), \quad (2.2.10)$$

and $\tilde{\chi}(\mathbf{r}, \omega)$ is the Fourier transform of $\chi(\mathbf{r}, t)$. In general, $\epsilon(\mathbf{r}, \omega)$ is complex. Its real and imaginary parts are related to the *refractive index* n and the *absorption coefficient* α by the definition

$$\epsilon = (n + i\alpha c/2\omega)^2. \quad (2.2.11)$$

By using Eqs. (2.2.10) and (2.2.11), n and α are related to $\tilde{\chi}$ as

$$n = (1 + \text{Re } \tilde{\chi})^{1/2}, \quad \alpha = (\omega/nc) \text{Im } \tilde{\chi}, \quad (2.2.12)$$

where Re and Im stand for the real and imaginary parts, respectively. Both n and α are frequency dependent. The frequency dependence of n is referred to as *chromatic dispersion* of the medium. In Section 2.3, fiber dispersion is shown to limit the performance of fiber-optic communication systems in a fundamental way.

Two further simplifications can be made before solving Eq. (2.2.9). First, ϵ can be taken to be real and replaced by n^2 because of low optical losses in silica fibers. Second, since $n(\mathbf{r}, \omega)$ is independent of the spatial coordinate \mathbf{r} in both the core and the cladding of a step-index fiber, one can use the identity

$$\nabla \times \nabla \times \tilde{\mathbf{E}} \equiv \nabla(\nabla \cdot \tilde{\mathbf{E}}) - \nabla^2 \tilde{\mathbf{E}} = -\nabla^2 \tilde{\mathbf{E}}, \quad (2.2.13)$$

where we used Eq. (2.2.3) and the relation $\tilde{\mathbf{D}} = \epsilon \tilde{\mathbf{E}}$ to set $\nabla \cdot \tilde{\mathbf{E}} = 0$. This simplification is made even for graded-index fibers. Equation (2.2.13) then holds approximately as long as the index changes occur over a length scale much longer than the wavelength. By using Eq. (2.2.13) in Eq. (2.2.9), we obtain

$$\nabla^2 \tilde{\mathbf{E}} + n^2(\omega) k_0^2 \tilde{\mathbf{E}} = 0, \quad (2.2.14)$$

where the free-space wave number k_0 is defined as

$$k_0 = \omega/c = 2\pi/\lambda, \quad (2.2.15)$$

and λ is the vacuum wavelength of the optical field oscillating at the frequency ω . Equation (2.2.14) is solved next to obtain the optical modes of step-index fibers.

2.2.2 Fiber Modes

The concept of the mode is a general concept in optics occurring also, for example, in the theory of lasers. An *optical mode* refers to a specific solution of the wave equation (2.2.14) that satisfies the appropriate boundary conditions and has the property that its spatial distribution does not change with propagation. The fiber modes can be classified as guided modes, leaky modes, and radiation modes [14]. As one might expect, signal transmission in fiber-optic communication systems takes place through the guided modes only. The following discussion focuses exclusively on the guided modes of a step-index fiber.

To take advantage of the cylindrical symmetry, Eq. (2.2.14) is written in the cylindrical coordinates ρ , ϕ , and z as

$$\frac{\partial^2 E_z}{\partial \rho^2} + \frac{1}{\rho} \frac{\partial E_z}{\partial \rho} + \frac{1}{\rho^2} \frac{\partial^2 E_z}{\partial \phi^2} + \frac{\partial^2 E_z}{\partial z^2} + n^2 k_0^2 E_z = 0, \quad (2.2.16)$$

where for a step-index fiber of core radius a , the refractive index n is of the form

$$n = \begin{cases} n_1; & \rho \leq a, \\ n_2; & \rho > a. \end{cases} \quad (2.2.17)$$

For simplicity of notation, the tilde over $\tilde{\mathbf{E}}$ has been dropped and the frequency dependence of all variables is implicitly understood. Equation (2.2.16) is written for the axial component E_z of the electric field vector. Similar equations can be written for the other five components of \mathbf{E} and \mathbf{H} . However, it is not necessary to solve all six equations since only two components out of six are independent. It is customary to choose E_z and H_z as the independent components and obtain E_ρ , E_ϕ , H_ρ , and H_ϕ in terms of them. Equation (2.2.16) is easily solved by using the method of separation of variables and writing E_z as

$$E_z(\rho, \phi, z) = F(\rho)\Phi(\phi)Z(z). \quad (2.2.18)$$

By using Eq. (2.2.18) in Eq. (2.2.16), we obtain the three ordinary differential equations:

$$d^2 Z/dz^2 + \beta^2 Z = 0, \quad (2.2.19)$$

$$d^2 \Phi/d\phi^2 + m^2 \Phi = 0, \quad (2.2.20)$$

$$\frac{d^2 F}{d\rho^2} + \frac{1}{\rho} \frac{dF}{d\rho} + \left(n^2 k_0^2 - \beta^2 - \frac{m^2}{\rho^2} \right) F = 0. \quad (2.2.21)$$

Equation (2.2.19) has a solution of the form $Z = \exp(i\beta z)$, where β has the physical significance of the propagation constant. Similarly, Eq. (2.2.20) has a solution $\Phi = \exp(im\phi)$, but the constant m is restricted to take only integer values since the field must be periodic in ϕ with a period of 2π .

Equation (2.2.21) is the well-known differential equation satisfied by the Bessel functions [24]. Its general solution in the core and cladding regions can be written as

$$F(\rho) = \begin{cases} AJ_m(p\rho) + A'Y_m(p\rho); & \rho \leq a, \\ CK_m(q\rho) + C'I_m(q\rho); & \rho > a, \end{cases} \quad (2.2.22)$$

where A , A' , C , and C' are constants and J_m , Y_m , K_m , and I_m are different kinds of Bessel functions [24]. The parameters p and q are defined by

$$p^2 = n_1^2 k_0^2 - \beta^2, \quad (2.2.23)$$

$$q^2 = \beta^2 - n_2^2 k_0^2. \quad (2.2.24)$$

Considerable simplification occurs when we use the boundary condition that the optical field for a guided mode should be finite at $\rho = 0$ and decay to zero at $\rho = \infty$. Since $Y_m(p\rho)$ has a singularity at $\rho = 0$, $F(0)$ can remain finite only if $A' = 0$. Similarly

$F(\rho)$ vanishes at infinity only if $C' = 0$. The general solution of Eq. (2.2.16) is thus of the form

$$E_z = \begin{cases} AJ_m(p\rho) \exp(im\phi) \exp(i\beta z); & \rho \leq a, \\ CK_m(q\rho) \exp(im\phi) \exp(i\beta z); & \rho > a. \end{cases} \quad (2.2.25)$$

The same method can be used to obtain H_z which also satisfies Eq. (2.2.16). Indeed, the solution is the same but with different constants B and D , that is,

$$H_z = \begin{cases} BJ_m(p\rho) \exp(im\phi) \exp(i\beta z); & \rho \leq a, \\ DK_m(q\rho) \exp(im\phi) \exp(i\beta z); & \rho > a. \end{cases} \quad (2.2.26)$$

The other four components E_ρ , E_ϕ , H_ρ , and H_ϕ can be expressed in terms of E_z and H_z by using Maxwell's equations. In the core region, we obtain

$$E_\rho = \frac{i}{p^2} \left(\beta \frac{\partial E_z}{\partial \rho} + \mu_0 \frac{\omega}{\rho} \frac{\partial H_z}{\partial \phi} \right), \quad (2.2.27)$$

$$E_\phi = \frac{i}{p^2} \left(\frac{\beta}{\rho} \frac{\partial E_z}{\partial \phi} - \mu_0 \omega \frac{\partial H_z}{\partial \rho} \right), \quad (2.2.28)$$

$$H_\rho = \frac{i}{p^2} \left(\beta \frac{\partial H_z}{\partial \rho} - \epsilon_0 n^2 \frac{\omega}{\rho} \frac{\partial E_z}{\partial \phi} \right), \quad (2.2.29)$$

$$H_\phi = \frac{i}{p^2} \left(\frac{\beta}{\rho} \frac{\partial H_z}{\partial \phi} + \epsilon_0 n^2 \omega \frac{\partial E_z}{\partial \rho} \right). \quad (2.2.30)$$

These equations can be used in the cladding region after replacing p^2 by $-q^2$.

Equations (2.2.25) through (2.2.30) express the electromagnetic field in the core and cladding regions of an optical fiber in terms of four constants A , B , C , and D . These constants are determined by applying the boundary condition that the tangential components of \mathbf{E} and \mathbf{H} be continuous across the core-cladding interface. By requiring the continuity of E_z , H_z , E_ϕ , and H_ϕ at $\rho = a$, we obtain a set of four homogeneous equations satisfied by A , B , C , and D [17]. These equations have a nontrivial solution only if the determinant of the coefficient matrix vanishes. After considerable algebraic details, this condition leads us to the following eigenvalue equation [17]–[19]:

$$\begin{aligned} \left[\frac{J'_m(pa)}{p J_m(pa)} + \frac{K'_m(qa)}{q K_m(qa)} \right] & \left[\frac{J'_m(pa)}{p J_m(pa)} + \frac{n_2^2}{n_1^2} \frac{K'_m(qa)}{q K_m(qa)} \right] \\ & = \frac{m^2}{a^2} \left(\frac{1}{p^2} + \frac{1}{q^2} \right) \left(\frac{1}{p^2} + \frac{n_2^2}{n_1^2} \frac{1}{q^2} \right), \end{aligned} \quad (2.2.31)$$

where a prime indicates differentiation with respect to the argument.

For a given set of the parameters k_0 , a , n_1 , and n_2 , the eigenvalue equation (2.2.31) can be solved numerically to determine the propagation constant β . In general, it may have multiple solutions for each integer value of m . It is customary to enumerate these solutions in descending numerical order and denote them by β_{mn} for a given m ($n = 1, 2, \dots$). Each value β_{mn} corresponds to one possible mode of propagation of the optical field whose spatial distribution is obtained from Eqs. (2.2.25)–(2.2.30). Since the field distribution does not change with propagation except for a phase factor and satisfies all boundary conditions, it is an optical mode of the fiber. In general, both E_z and

H_z are nonzero (except for $m = 0$), in contrast with the planar waveguides, for which one of them can be taken to be zero. Fiber modes are therefore referred to as *hybrid modes* and are denoted by HE_{mn} or EH_{mn} , depending on whether H_z or E_z dominates. In the special case $m = 0$, HE_{0n} and EH_{0n} are also denoted by TE_{0n} and TM_{0n} , respectively, since they correspond to transverse-electric ($E_z = 0$) and transverse-magnetic ($H_z = 0$) modes of propagation. A different notation LP_{mn} is sometimes used for weakly guiding fibers [25] for which both E_z and H_z are nearly zero (LP stands for linearly polarized modes).

A mode is uniquely determined by its propagation constant β . It is useful to introduce a quantity $\bar{n} = \beta/k_0$, called the *mode index* or *effective index* and having the physical significance that each fiber mode propagates with an effective refractive index \bar{n} whose value lies in the range $n_1 > \bar{n} > n_2$. A mode ceases to be guided when $\bar{n} \leq n_2$. This can be understood by noting that the optical field of guided modes decays exponentially inside the cladding layer since [24]

$$K_m(q\rho) = (\pi/2q\rho)^{1/2} \exp(-q\rho) \quad \text{for } q\rho \gg 1. \quad (2.2.32)$$

When $\bar{n} \leq n_2$, $q^2 \leq 0$ from Eq. (2.2.24) and the exponential decay does not occur. The mode is said to reach cutoff when q becomes zero or when $\bar{n} = n_2$. From Eq. (2.2.23), $p = k_0(n_1^2 - n_2^2)^{1/2}$ when $q = 0$. A parameter that plays an important role in determining the cutoff condition is defined as

$$V = k_0 a (n_1^2 - n_2^2)^{1/2} \approx (2\pi/\lambda) a n_1 \sqrt{2\Delta}. \quad (2.2.33)$$

It is called the normalized frequency ($V \propto \omega$) or simply the V parameter. It is also useful to introduce a normalized propagation constant b as

$$b = \frac{\beta/k_0 - n_2}{n_1 - n_2} = \frac{\bar{n} - n_2}{n_1 - n_2}. \quad (2.2.34)$$

Figure 2.5 shows a plot of b as a function of V for a few low-order fiber modes obtained by solving the eigenvalue equation (2.2.31). A fiber with a large value of V supports many modes. A rough estimate of the number of modes for such a multimode fiber is given by $V^2/2$ [21]. For example, a typical multimode fiber with $a = 25 \mu\text{m}$ and $\Delta = 5 \times 10^{-3}$ has $V \simeq 18$ at $\lambda = 1.3 \mu\text{m}$ and would support about 162 modes. However, the number of modes decreases rapidly as V is reduced. As seen in Figure 2.5, a fiber with $V = 5$ supports seven modes. Below a certain value of V all modes except the HE_{11} mode reach cutoff. Such fibers support a single mode and are called single-mode fibers. The properties of single-mode fibers are described next.

2.2.3 Single-Mode Fibers

Single-mode fibers support only the HE_{11} mode, also known as the fundamental mode of the fiber. The fiber is designed such that all higher-order modes are cut off at the operating wavelength. As seen in Figure 2.5, the V parameter determines the number of modes supported by a fiber. The cutoff condition of various modes is also determined by V . The fundamental mode has no cutoff and is always supported by a fiber.

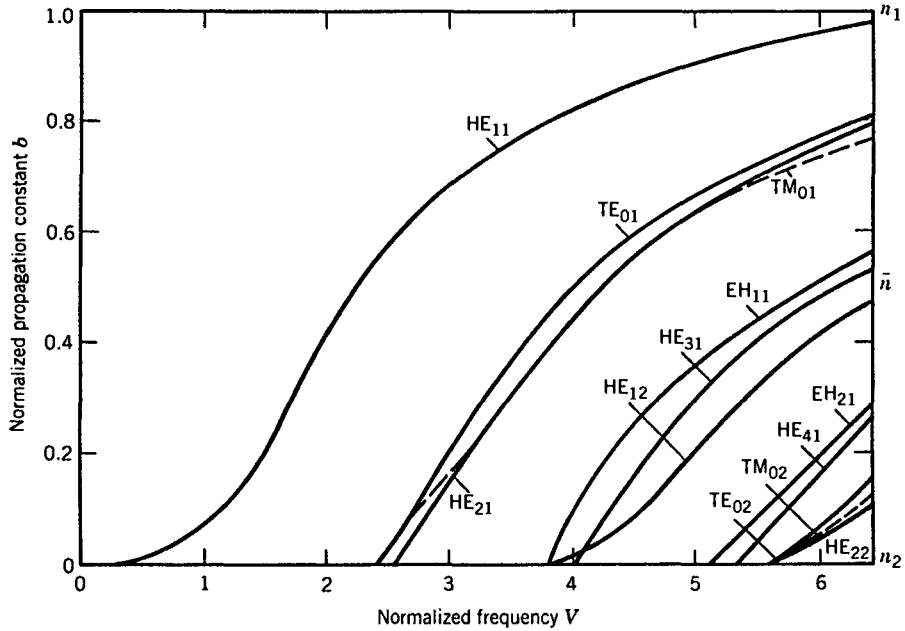


Figure 2.5: Normalized propagation constant b as a function of normalized frequency V for a few low-order fiber modes. The right scale shows the mode index \bar{n} . (After Ref. [26]; ©1981 Academic Press; reprinted with permission.)

Single-Mode Condition

The *single-mode condition* is determined by the value of V at which the TE_{01} and TM_{01} modes reach cutoff (see Figure 2.5). The eigenvalue equations for these two modes can be obtained by setting $m = 0$ in Eq. (2.2.31) and are given by

$$pJ_0(pa)K'_0(qa) + qJ'_0(pa)K_0(qa) = 0, \quad (2.2.35)$$

$$pn_2^2 J_0(pa)K'_0(qa) + qn_1^2 J'_0(pa)K_0(qa) = 0. \quad (2.2.36)$$

A mode reaches cutoff when $q = 0$. Since $pa = V$ when $q = 0$, the cutoff condition for both modes is simply given by $J_0(V) = 0$. The smallest value of V for which $J_0(V) = 0$ is 2.405. A fiber designed such that $V < 2.405$ supports only the fundamental HE_{11} mode. This is the single-mode condition.

We can use Eq. (2.2.33) to estimate the core radius of single-mode fibers used in lightwave systems. For the operating wavelength range 1.3–1.6 μm , the fiber is generally designed to become single mode for $\lambda > 1.2 \mu\text{m}$. By taking $\lambda = 1.2 \mu\text{m}$, $n_1 = 1.45$, and $\Delta = 5 \times 10^{-3}$, Eq. (2.2.33) shows that $V < 2.405$ for a core radius $a < 3.2 \mu\text{m}$. The required core radius can be increased to about 4 μm by decreasing Δ to 3×10^{-3} . Indeed, most telecommunication fibers are designed with $a \approx 4 \mu\text{m}$.

The mode index \bar{n} at the operating wavelength can be obtained by using Eq. (2.2.34), according to which

$$\bar{n} = n_2 + b(n_1 - n_2) \approx n_2(1 + b\Delta) \quad (2.2.37)$$

and by using Figure 2.5, which provides b as a function of V for the HE₁₁ mode. An analytic approximation for b is [15]

$$b(V) \approx (1.1428 - 0.9960/V)^2 \quad (2.2.38)$$

and is accurate to within 0.2% for V in the range 1.5–2.5.

The field distribution of the fundamental mode is obtained by using Eqs. (2.2.25)–(2.2.30). The axial components E_z and H_z are quite small for $\Delta \ll 1$. Hence, the HE₁₁ mode is approximately linearly polarized for weakly guiding fibers. It is also denoted as LP₀₁, following an alternative terminology in which all fiber modes are assumed to be linearly polarized [25]. One of the transverse components can be taken as zero for a linearly polarized mode. If we set $E_y = 0$, the E_x component of the electric field for the HE₁₁ mode is given by [15]

$$E_x = E_0 \begin{cases} [J_0(p\rho)/J_0(pa)] \exp(i\beta z); & \rho \leq a, \\ [K_0(q\rho)/K_0(qa)] \exp(i\beta z); & \rho > a, \end{cases} \quad (2.2.39)$$

where E_0 is a constant related to the power carried by the mode. The dominant component of the corresponding magnetic field is given by $H_y = n_2(\epsilon_0/\mu_0)^{1/2}E_x$. This mode is linearly polarized along the x axis. The same fiber supports another mode linearly polarized along the y axis. In this sense a single-mode fiber actually supports two orthogonally polarized modes that are degenerate and have the same mode index.

Fiber Birefringence

The degenerate nature of the orthogonally polarized modes holds only for an ideal single-mode fiber with a perfectly cylindrical core of uniform diameter. Real fibers exhibit considerable variation in the shape of their core along the fiber length. They may also experience nonuniform stress such that the cylindrical symmetry of the fiber is broken. Degeneracy between the orthogonally polarized fiber modes is removed because of these factors, and the fiber acquires birefringence. The degree of modal birefringence is defined by

$$B_m = |\bar{n}_x - \bar{n}_y|, \quad (2.2.40)$$

where \bar{n}_x and \bar{n}_y are the mode indices for the orthogonally polarized fiber modes. Birefringence leads to a periodic power exchange between the two polarization components. The period, referred to as the *beat length*, is given by

$$L_B = \lambda/B_m. \quad (2.2.41)$$

Typically, $B_m \sim 10^{-7}$, and $L_B \sim 10$ m for $\lambda \sim 1 \mu\text{m}$. From a physical viewpoint, linearly polarized light remains linearly polarized only when it is polarized along one of the principal axes. Otherwise, its state of polarization changes along the fiber length from linear to elliptical, and then back to linear, in a periodic manner over the length L_B . Figure 2.6 shows schematically such a periodic change in the state of polarization for a fiber of constant birefringence B . The *fast axis* in this figure corresponds to the axis along which the mode index is smaller. The other axis is called the *slow axis*.

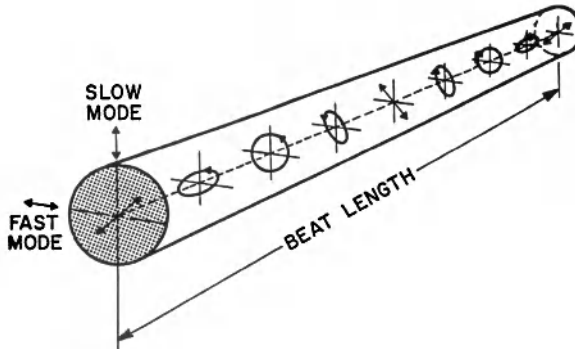


Figure 2.6: State of polarization in a birefringent fiber over one beat length. Input beam is linearly polarized at 45° with respect to the slow and fast axes.

In conventional single-mode fibers, birefringence is not constant along the fiber but changes randomly, both in magnitude and direction, because of variations in the core shape (elliptical rather than circular) and the anisotropic stress acting on the core. As a result, light launched into the fiber with linear polarization quickly reaches a state of arbitrary polarization. Moreover, different frequency components of a pulse acquire different polarization states, resulting in pulse broadening. This phenomenon is called *polarization-mode dispersion* (PMD) and becomes a limiting factor for optical communication systems operating at high bit rates. It is possible to make fibers for which random fluctuations in the core shape and size are not the governing factor in determining the state of polarization. Such fibers are called *polarization-maintaining* fibers. A large amount of birefringence is introduced intentionally in these fibers through design modifications so that small random birefringence fluctuations do not affect the light polarization significantly. Typically, $B_m \sim 10^{-4}$ for such fibers.

Spot Size

Since the field distribution given by Eq. (2.2.39) is cumbersome to use in practice, it is often approximated by a Gaussian distribution of the form

$$E_x = A \exp(-\rho^2/w^2) \exp(i\beta z), \quad (2.2.42)$$

where w is the *field radius* and is referred to as the *spot size*. It is determined by fitting the exact distribution to the Gaussian function or by following a variational procedure [27]. Figure 2.7 shows the dependence of w/a on the V parameter. A comparison of the actual field distribution with the fitted Gaussian is also shown for $V = 2.4$. The quality of fit is generally quite good for values of V in the neighborhood of 2. The spot size w can be determined from Figure 2.7. It can also be determined from an analytic approximation accurate to within 1% for $1.2 < V < 2.4$ and given by [27]

$$w/a \approx 0.65 + 1.619V^{-3/2} + 2.879V^{-6}. \quad (2.2.43)$$

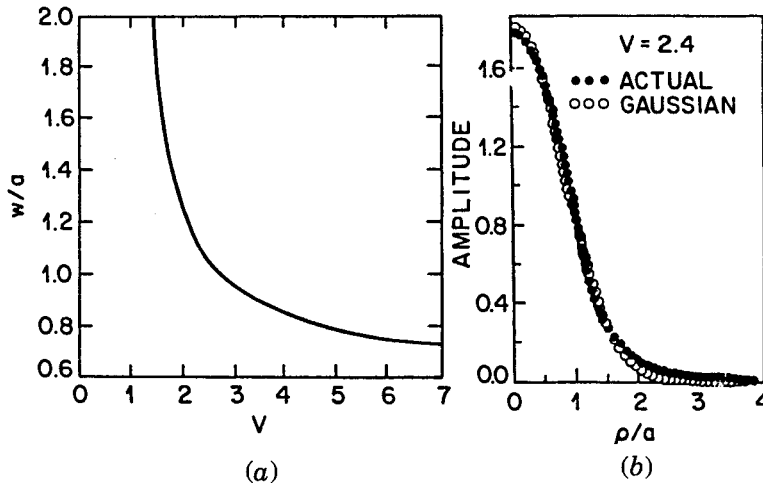


Figure 2.7: (a) Normalized spot size w/a as a function of the V parameter obtained by fitting the fundamental fiber mode to a Gaussian distribution; (b) quality of fit for $V = 2.4$. (After Ref. [27]; ©1978 OSA; reprinted with permission.)

The effective mode area, defined as $A_{\text{eff}} = \pi w^2$, is an important parameter for optical fibers as it determines how tightly light is confined to the core. It will be seen later that the nonlinear effects are stronger in fibers with smaller values of A_{eff} .

The fraction of the power contained in the core can be obtained by using Eq. (2.2.42) and is given by the *confinement factor*

$$\Gamma = \frac{P_{\text{core}}}{P_{\text{total}}} = \frac{\int_0^a |E_x|^2 \rho d\rho}{\int_0^\infty |E_x|^2 \rho d\rho} = 1 - \exp\left(-\frac{2a^2}{w^2}\right). \quad (2.2.44)$$

Equations (2.2.43) and (2.2.44) determine the fraction of the mode power contained inside the core for a given value of V . Although nearly 75% of the mode power resides in the core for $V = 2$, this percentage drops down to 20% for $V = 1$. For this reason most telecommunication single-mode fibers are designed to operate in the range $2 < V < 2.4$.

2.3 Dispersion in Single-Mode Fibers

It was seen in Section 2.1 that intermodal dispersion in multimode fibers leads to considerable broadening of short optical pulses (~ 10 ns/km). In the geometrical-optics description, such broadening was attributed to different paths followed by different rays. In the modal description it is related to the different mode indices (or group velocities) associated with different modes. The main advantage of single-mode fibers is that intermodal dispersion is absent simply because the energy of the injected pulse is transported by a single mode. However, pulse broadening does not disappear altogether. The group velocity associated with the fundamental mode is frequency dependent because of chromatic dispersion. As a result, different spectral components

of the pulse travel at slightly different group velocities, a phenomenon referred to as *group-velocity dispersion* (GVD), *intramodal dispersion*, or simply *fiber dispersion*. Intramodal dispersion has two contributions, material dispersion and waveguide dispersion. We consider both of them and discuss how GVD limits the performance of lightwave systems employing single-mode fibers.

2.3.1 Group-Velocity Dispersion

Consider a single-mode fiber of length L . A specific spectral component at the frequency ω would arrive at the output end of the fiber after a time delay $T = L/v_g$, where v_g is the *group velocity*, defined as [20]

$$v_g = (d\beta/d\omega)^{-1}. \quad (2.3.1)$$

By using $\beta = \bar{n}k_0 = \bar{n}\omega/c$ in Eq. (2.3.1), one can show that $v_g = c/\bar{n}_g$, where \bar{n}_g is the *group index* given by

$$\bar{n}_g = \bar{n} + \omega(d\bar{n}/d\omega). \quad (2.3.2)$$

The frequency dependence of the group velocity leads to pulse broadening simply because different spectral components of the pulse disperse during propagation and do not arrive simultaneously at the fiber output. If $\Delta\omega$ is the spectral width of the pulse, the extent of pulse broadening for a fiber of length L is governed by

$$\Delta T = \frac{dT}{d\omega} \Delta\omega = \frac{d}{d\omega} \left(\frac{L}{v_g} \right) \Delta\omega = L \frac{d^2\beta}{d\omega^2} \Delta\omega = L\beta_2 \Delta\omega, \quad (2.3.3)$$

where Eq. (2.3.1) was used. The parameter $\beta_2 = d^2\beta/d\omega^2$ is known as the GVD parameter. It determines how much an optical pulse would broaden on propagation inside the fiber.

In some optical communication systems, the frequency spread $\Delta\omega$ is determined by the range of wavelengths $\Delta\lambda$ emitted by the optical source. It is customary to use $\Delta\lambda$ in place of $\Delta\omega$. By using $\omega = 2\pi c/\lambda$ and $\Delta\omega = (-2\pi c/\lambda^2)\Delta\lambda$, Eq. (2.3.3) can be written as

$$\Delta T = \frac{d}{d\lambda} \left(\frac{L}{v_g} \right) \Delta\lambda = DL\Delta\lambda, \quad (2.3.4)$$

where

$$D = \frac{d}{d\lambda} \left(\frac{1}{v_g} \right) = -\frac{2\pi c}{\lambda^2} \beta_2. \quad (2.3.5)$$

D is called the *dispersion parameter* and is expressed in units of ps/(km-nm).

The effect of dispersion on the bit rate B can be estimated by using the criterion $B\Delta T < 1$ in a manner similar to that used in Section 2.1. By using ΔT from Eq. (2.3.4) this condition becomes

$$BL|D|\Delta\lambda < 1. \quad (2.3.6)$$

Equation (2.3.6) provides an order-of-magnitude estimate of the BL product offered by single-mode fibers. The wavelength dependence of D is studied in the next two subsections. For standard silica fibers, D is relatively small in the wavelength region

near $1.3 \mu\text{m}$ [$D \sim 1 \text{ ps}/(\text{km}\cdot\text{nm})$]. For a semiconductor laser, the spectral width $\Delta\lambda$ is 2–4 nm even when the laser operates in several longitudinal modes. The BL product of such lightwave systems can exceed 100 (Gb/s)-km. Indeed, $1.3\text{-}\mu\text{m}$ telecommunication systems typically operate at a bit rate of 2 Gb/s with a repeater spacing of 40–50 km. The BL product of single-mode fibers can exceed 1 (Tb/s)-km when single-mode semiconductor lasers are used to reduce $\Delta\lambda$ below 1 nm.

The dispersion parameter D can vary considerably when the operating wavelength is shifted from $1.3 \mu\text{m}$. The wavelength dependence of D is governed by the frequency dependence of the mode index \bar{n} . From Eq. (2.3.5), D can be written as

$$D = -\frac{2\pi c}{\lambda^2} \frac{d}{d\omega} \left(\frac{1}{v_g} \right) = -\frac{2\pi}{\lambda^2} \left(2 \frac{d\bar{n}}{d\omega} + \omega \frac{d^2\bar{n}}{d\omega^2} \right), \quad (2.3.7)$$

where Eq. (2.3.2) was used. If we substitute \bar{n} from Eq. (2.2.37) and use Eq. (2.2.33), D can be written as the sum of two terms,

$$D = D_M + D_W, \quad (2.3.8)$$

where the *material dispersion* D_M and the *waveguide dispersion* D_W are given by

$$D_M = -\frac{2\pi}{\lambda^2} \frac{dn_{2g}}{d\omega} = \frac{1}{c} \frac{dn_{2g}}{d\lambda}, \quad (2.3.9)$$

$$D_W = -\frac{2\pi\Delta}{\lambda^2} \left[\frac{n_{2g}^2}{n_2\omega} \frac{Vd^2(Vb)}{dV^2} + \frac{dn_{2g}}{d\omega} \frac{d(Vb)}{dV} \right]. \quad (2.3.10)$$

Here n_{2g} is the group index of the cladding material and the parameters V and b are given by Eqs. (2.2.33) and (2.2.34), respectively. In obtaining Eqs. (2.3.8)–(2.3.10) the parameter Δ was assumed to be frequency independent. A third term known as differential material dispersion should be added to Eq. (2.3.8) when $d\Delta/d\omega \neq 0$. Its contribution is, however, negligible in practice.

2.3.2 Material Dispersion

Material dispersion occurs because the refractive index of silica, the material used for fiber fabrication, changes with the optical frequency ω . On a fundamental level, the origin of material dispersion is related to the characteristic resonance frequencies at which the material absorbs the electromagnetic radiation. Far from the medium resonances, the refractive index $n(\omega)$ is well approximated by the *Sellmeier equation* [28]

$$n^2(\omega) = 1 + \sum_{j=1}^M \frac{B_j \omega_j^2}{\omega_j^2 - \omega^2}, \quad (2.3.11)$$

where ω_j is the resonance frequency and B_j is the oscillator strength. Here n stands for n_1 or n_2 , depending on whether the dispersive properties of the core or the cladding are considered. The sum in Eq. (2.3.11) extends over all material resonances that contribute in the frequency range of interest. In the case of optical fibers, the parameters B_j and ω_j are obtained empirically by fitting the measured dispersion curves to Eq. (2.3.11)

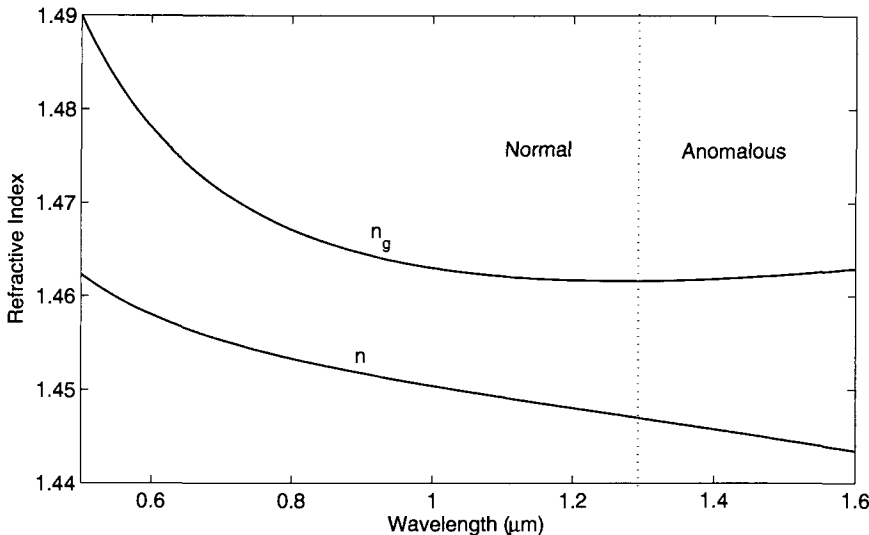


Figure 2.8: Variation of refractive index n and group index n_g with wavelength for fused silica.

with $M = 3$. They depend on the amount of dopants and have been tabulated for several kinds of fibers [12]. For pure silica these parameters are found to be $B_1 = 0.6961663$, $B_2 = 0.4079426$, $B_3 = 0.8974794$, $\lambda_1 = 0.0684043 \mu\text{m}$, $\lambda_2 = 0.1162414 \mu\text{m}$, and $\lambda_3 = 9.896161 \mu\text{m}$, where $\lambda_j = 2\pi c/\omega_j$ with $j = 1$ to 3 [28]. The group index $n_g = n + \omega(dn/d\omega)$ can be obtained by using these parameter values.

Figure 2.8 shows the wavelength dependence of n and n_g in the range 0.5 – $1.6 \mu\text{m}$ for fused silica. Material dispersion D_M is related to the slope of n_g through Eq. (2.3.9). It turns out that $dn_g/d\lambda = 0$ at $\lambda = 1.276 \mu\text{m}$, the value marked by the dotted vertical line in Figure 2.8. This wavelength is called the *zero-dispersion wavelength* λ_{ZD} because $D_M = 0$ at $\lambda = \lambda_{\text{ZD}}$. The dispersion parameter D_M is negative below λ_{ZD} (normal dispersion) and becomes positive above that (anomalous dispersion). In the wavelength range 1.25 – $1.66 \mu\text{m}$ it can be approximated by an empirical relation

$$D_M \approx 122(1 - \lambda_{\text{ZD}}/\lambda). \quad (2.3.12)$$

It should be stressed that $\lambda_{\text{ZD}} = 1.276 \mu\text{m}$ only for pure silica. It can vary in the range 1.28 – $1.31 \mu\text{m}$ for optical fibers whose core and cladding are doped to vary the refractive index because λ_{ZD} also depends on the core radius a and the index step Δ through the waveguide contribution to the total dispersion.

2.3.3 Waveguide Dispersion

The contribution of waveguide dispersion D_W to the dispersion parameter D is given by Eq. (2.3.10) and depends on the V parameter of the fiber. It turns out that D_W is negative in the entire wavelength range 0 – $1.6 \mu\text{m}$. On the other hand, D_M is negative for wavelengths below λ_{ZD} and becomes positive above that. Figure 2.9 shows D_M ,

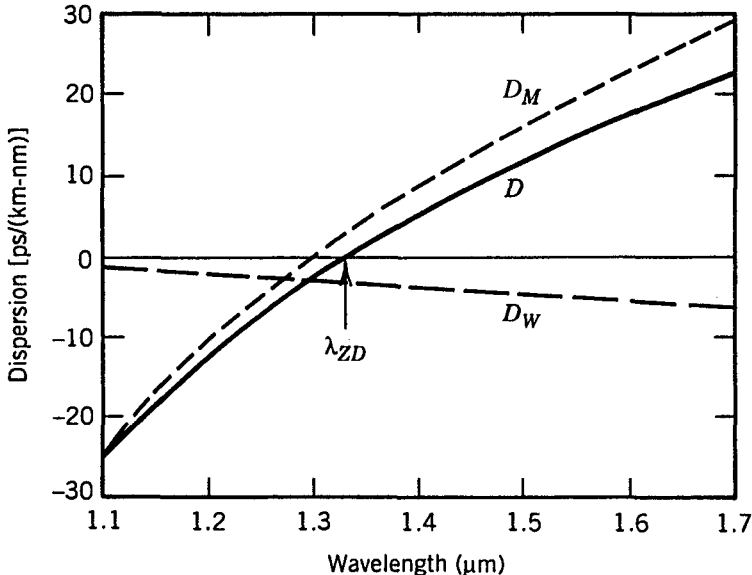


Figure 2.9: Total dispersion D and relative contributions of material dispersion D_M and waveguide dispersion D_W for a conventional single-mode fiber. The zero-dispersion wavelength shifts to a higher value because of the waveguide contribution.

D_W , and their sum $D = D_M + D_W$, for a typical single-mode fiber. The main effect of waveguide dispersion is to shift λ_{ZD} by an amount 30–40 nm so that the total dispersion is zero near 1.31 μm . It also reduces D from its material value D_M in the wavelength range 1.3–1.6 μm that is of interest for optical communication systems. Typical values of D are in the range of 15 to 18 ps/(km-nm) near 1.55 μm . This wavelength region is of considerable interest for lightwave systems because fiber losses become minimum near 1.55 μm (see Section 2.5). High values of D limit the performance of 1.55- μm lightwave systems.

Since the waveguide contribution D_W depends on fiber parameters such as the core radius a and the index difference Δ , it is possible to design the fiber such that λ_{ZD} is shifted into the vicinity of 1.55 μm [29], [30]. Such fibers are called *dispersion-shifted* fibers. It is also possible to tailor the waveguide contribution such that the total dispersion D is relatively small over a wide wavelength range extending from 1.3 to 1.6 μm [31]–[33]. Such fibers are called *dispersion-flattened* fibers. Figure 2.10 shows typical examples of the wavelength dependence of D for standard (conventional), dispersion-shifted, and dispersion-flattened fibers. The design of dispersion-modified fibers involves the use of multiple cladding layers and a tailoring of the refractive-index profile [29]–[35]. Waveguide dispersion can also be used to produce dispersion-decreasing fibers in which GVD decreases along the fiber length because of axial variations in the core radius. In another kind of fibers, known as the *dispersion-compensating* fibers, GVD is made normal and has a relatively large magnitude. Table 2.1 lists the dispersion characteristics of several commercially available fibers.

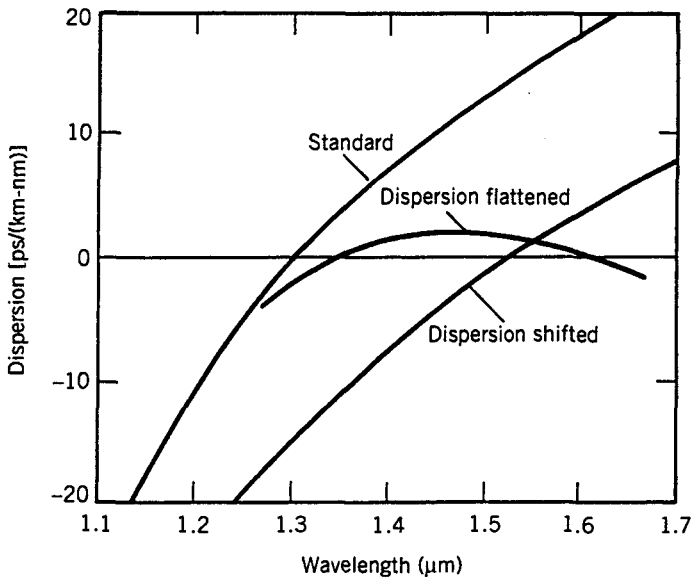


Figure 2.10: Typical wavelength dependence of the dispersion parameter D for standard, dispersion-shifted, and dispersion-flattened fibers.

2.3.4 Higher-Order Dispersion

It appears from Eq. (2.3.6) that the BL product of a single-mode fiber can be increased indefinitely by operating at the zero-dispersion wavelength λ_{ZD} where $D = 0$. The dispersive effects, however, do not disappear completely at $\lambda = \lambda_{ZD}$. Optical pulses still experience broadening because of higher-order dispersive effects. This feature can be understood by noting that D cannot be made zero at all wavelengths contained within the pulse spectrum centered at λ_{ZD} . Clearly, the wavelength dependence of D will play a role in pulse broadening. Higher-order dispersive effects are governed by the *dispersion slope* $S = dD/d\lambda$. The parameter S is also called a *differential-dispersion* parameter. By using Eq. (2.3.5) it can be written as

$$S = (2\pi c/\lambda^2)^2 \beta_3 + (4\pi c/\lambda^3) \beta_2, \quad (2.3.13)$$

where $\beta_3 = d\beta_2/d\omega \equiv d^3\beta/d\omega^3$ is the third-order dispersion parameter. At $\lambda = \lambda_{ZD}$, $\beta_2 = 0$, and S is proportional to β_3 .

The numerical value of the dispersion slope S plays an important role in the design of modern WDM systems. Since $S > 0$ for most fibers, different channels have slightly different GVD values. This feature makes it difficult to compensate dispersion for all channels simultaneously. To solve this problem, new kind of fibers have been developed for which S is either small (reduced-slope fibers) or negative (reverse-dispersion fibers). Table 2.1 lists the values of dispersion slopes for several commercially available fibers.

It may appear from Eq. (2.3.6) that the limiting bit rate of a channel operating at $\lambda = \lambda_{ZD}$ will be infinitely large. However, this is not the case since S or β_3 becomes

Table 2.1 Characteristics of several commercial fibers

Fiber Type and Trade Name	A_{eff} (μm^2)	λ_{ZD} (nm)	D (C band) [ps/(km-nm)]	Slope S [ps/(km-nm 2)]
Corning SMF-28	80	1302–1322	16 to 19	0.090
OFS AllWave	80	1300–1322	17 to 20	0.088
Draka ColorLock	80	1300–1320	16 to 19	0.090
Corning Vascade	100	1300–1310	18 to 20	0.060
OFS TrueWave-RS	50	1470–1490	2.6 to 6	0.050
Corning LEAF	72	1490–1500	2.0 to 6	0.060
Draka TeraLight	65	1430–1440	5.5 to 10	0.052

the limiting factor in that case. We can estimate the limiting bit rate by noting that for a source of spectral width $\Delta\lambda$, the effective value of dispersion parameter becomes $D = S\Delta\lambda$. The limiting bit rate–distance product can now be obtained by using Eq. (2.3.6) with this value of D . The resulting condition becomes

$$BL|S|(\Delta\lambda)^2 < 1. \quad (2.3.14)$$

For a multimode semiconductor laser with $\Delta\lambda = 2$ nm and a dispersion-shifted fiber with $S = 0.05$ ps/(km-nm 2) at $\lambda = 1.55$ μm , the BL product approaches 5 (Tb/s)-km. Further improvement is possible by using single-mode semiconductor lasers.

2.3.5 Polarization-Mode Dispersion

A potential source of pulse broadening is related to fiber birefringence. As discussed in Section 2.2.3, small departures from perfect cylindrical symmetry lead to birefringence because of different mode indices associated with the orthogonally polarized components of the fundamental fiber mode. If the input pulse excites both polarization components, it becomes broader as the two components disperse along the fiber because of their different group velocities. This phenomenon is called the PMD and has been studied extensively because it limits the performance of modern lightwave systems [36]–[47].

In fibers with constant birefringence (e.g., polarization-maintaining fibers), pulse broadening can be estimated from the time delay ΔT between the two polarization components during propagation of the pulse. For a fiber of length L , ΔT is given by

$$\Delta T = \left| \frac{L}{v_{gx}} - \frac{L}{v_{gy}} \right| = L|\beta_{1x} - \beta_{1y}| = L(\Delta\beta_1), \quad (2.3.15)$$

where the subscripts x and y identify the two orthogonally polarized modes and $\Delta\beta_1$ is related to the difference in group velocities along the two principal states of polarization [36]. Equation (2.3.1) was used to relate the group velocity v_g to the propagation constant β . Similar to the case of intermodal dispersion discussed in Section 2.1.1, the quantity $\Delta T/L$ is a measure of PMD. For polarization-maintaining fibers, $\Delta T/L$ is

quite large (~ 1 ns/km) when the two components are equally excited at the fiber input but can be reduced to zero by launching light along one of the principal axes.

The situation is somewhat different for conventional fibers in which birefringence varies along the fiber in a random fashion. It is intuitively clear that the polarization state of light propagating in fibers with randomly varying birefringence will generally be elliptical and would change randomly along the fiber during propagation. In the case of optical pulses, the polarization state will also be different for different spectral components of the pulse. The final polarization state is not of concern for most light-wave systems as photodetectors used inside optical receivers are insensitive to the state of polarization unless a coherent detection scheme is employed. What affects such systems is not the random polarization state but pulse broadening induced by random changes in the birefringence. This is referred to as *PMD-induced* pulse broadening.

The analytical treatment of PMD is quite complex in general because of its statistical nature. A simple model divides the fiber into a large number of segments. Both the degree of birefringence and the orientation of the principal axes remain constant in each section but change randomly from section to section. In effect, each fiber section can be treated as a phase plate using a Jones matrix [36]. Propagation of each frequency component associated with an optical pulse through the entire fiber length is then governed by a composite Jones matrix obtained by multiplying individual Jones matrices for each fiber section. The composite Jones matrix shows that two principal states of polarization exist for any fiber such that, when a pulse is polarized along them, the polarization state at fiber output is frequency independent to first order, in spite of random changes in fiber birefringence. These states are analogous to the slow and fast axes associated with polarization-maintaining fibers. An optical pulse not polarized along these two principal states splits into two parts which travel at different speeds. The differential group delay ΔT is largest for the two principal states of polarization.

The principal states of polarization provide a convenient basis for calculating the moments of ΔT . The PMD-induced pulse broadening is characterized by the root-mean-square (RMS) value of ΔT , obtained after averaging over random birefringence changes. Several approaches have been used to calculate this average. The variance $\sigma_T^2 \equiv \langle (\Delta T)^2 \rangle$ turns out to be the same in all cases and is given by [38]

$$\sigma_T^2(z) = 2(\Delta\beta_1)^2 l_c^2 [\exp(-z/l_c) + z/l_c - 1], \quad (2.3.16)$$

where l_c is the correlation length defined as the length over which two polarization components remain correlated; its value can vary over a wide range from 1 m to 1 km for different fibers, typical values being ~ 10 m.

For short distances such that $z \ll l_c$, $\sigma_T = (\Delta\beta_1)z$ from Eq. (2.3.16), as expected for a polarization-maintaining fiber. For distances $z > 1$ km, a good estimate of pulse broadening is obtained using $z \gg l_c$. For a fiber of length L , σ_T in this approximation becomes

$$\sigma_T \approx (\Delta\beta_1) \sqrt{2l_c L} \equiv D_p \sqrt{L}, \quad (2.3.17)$$

where D_p is the PMD parameter. Measured values of D_p vary from fiber to fiber in the range of 0.01 to 10 ps/km^{1/2}. Fibers installed during the 1980s have relatively large PMD such that $D_p > 0.1$ ps/km^{1/2}. In contrast, modern fibers are designed to have low PMD, and typically $D_p < 0.1$ ps/km^{1/2} for them. Because of the \sqrt{L} dependence,

PMD-induced pulse broadening is relatively small compared with the GVD effects. Indeed, $\sigma_T \sim 1$ ps for fiber lengths ~ 100 km and can be ignored for pulse widths > 10 ps. However, PMD becomes a limiting factor for lightwave systems designed to operate over long distances at high bit rates [40]–[47]. Several schemes have been developed for compensating the PMD effects (see Section 8.6.3).

Several other factors need to be considered in practice. The derivation of Eq. (2.3.16) assumes that the fiber link has no elements exhibiting polarization-dependent loss or gain. The presence of polarization-dependent losses can induce additional broadening [42]. Also, the effects of second and higher-order PMD become important at high bit rates (40 Gb/s or more) or for systems in which the first-order effects are eliminated using a PMD compensator [46].

2.4 Dispersion-Induced Limitations

The discussion of pulse broadening in Section 2.3.1 is based on an intuitive phenomenological approach. It provides a first-order estimate for pulses whose spectral width is dominated by the spectrum of the optical source. In general, the extent of pulse broadening depends on the width and the shape of input pulses [48]. In this section we discuss pulse broadening by using the wave equation (2.2.14).

2.4.1 Basic Propagation Equation

The analysis of fiber modes in Section 2.2.2 showed that each frequency component of the optical field propagates in a single-mode fiber as

$$\tilde{\mathbf{E}}(\mathbf{r}, \omega) = \hat{\mathbf{x}} F(x, y) \tilde{B}(0, \omega) \exp(i\beta z), \quad (2.4.1)$$

where $\hat{\mathbf{x}}$ is the polarization unit vector, $\tilde{B}(0, \omega)$ is the initial amplitude, and β is the propagation constant. The field distribution $F(x, y)$ of the fundamental fiber mode can be approximated by the Gaussian distribution given in Eq. (2.2.42). In general, $F(x, y)$ also depends on ω , but this dependence can be ignored for pulses whose spectral width $\Delta\omega$ is much smaller than ω_0 , a condition satisfied by pulses used in lightwave systems. Here ω_0 is the frequency at which the pulse spectrum is centered; it is referred to as the carrier frequency.

Different spectral components of an optical pulse propagate inside the fiber according to the simple relation

$$\tilde{B}(z, \omega) = \tilde{B}(0, \omega) \exp(i\beta z). \quad (2.4.2)$$

The amplitude in the time domain is obtained by taking the inverse Fourier transform and is given by

$$B(z, t) = \frac{1}{2\pi} \int_{-\infty}^{\infty} \tilde{B}(z, \omega) \exp(-i\omega t) d\omega. \quad (2.4.3)$$

The initial spectral amplitude $\tilde{B}(0, \omega)$ is just the Fourier transform of the input amplitude $B(0, t)$.

Pulse broadening results from the frequency dependence of β . For pulses for which $\Delta\omega \ll \omega_0$, it is useful to expand $\beta(\omega)$ in a Taylor series around the carrier frequency ω_0 and retain terms up to third order. In this quasi-monochromatic approximation,

$$\beta(\omega) = \bar{n}(\omega) \frac{\omega}{c} \approx \beta_0 + \beta_1(\Delta\omega) + \frac{\beta_2}{2}(\Delta\omega)^2 + \frac{\beta_3}{6}(\Delta\omega)^3, \quad (2.4.4)$$

where $\Delta\omega = \omega - \omega_0$ and $\beta_m = (d^m \beta / d\omega^m)_{\omega=\omega_0}$. From Eq. (2.3.1) $\beta_1 = 1/v_g$, where v_g is the group velocity. The GVD coefficient β_2 is related to the dispersion parameter D by Eq. (2.3.5), whereas β_3 is related to the dispersion slope S through Eq. (2.3.13). We substitute Eqs. (2.4.2) and (2.4.4) in Eq. (2.4.3) and introduce a *slowly varying amplitude* $A(z, t)$ of the pulse envelope as

$$B(z, t) = A(z, t) \exp[i(\beta_0 z - \omega_0 t)]. \quad (2.4.5)$$

The amplitude $A(z, t)$ is found to be given by

$$\begin{aligned} A(z, t) &= \frac{1}{2\pi} \int_{-\infty}^{\infty} d(\Delta\omega) \tilde{A}(0, \Delta\omega) \\ &\times \exp \left[i\beta_1 z \Delta\omega + \frac{i}{2} \beta_2 z (\Delta\omega)^2 + \frac{i}{6} \beta_3 z (\Delta\omega)^3 - i(\Delta\omega)t \right], \end{aligned} \quad (2.4.6)$$

where $\tilde{A}(0, \Delta\omega) \equiv \tilde{B}(0, \omega)$ is the Fourier transform of $A(0, t)$.

By calculating $\partial A / \partial z$ and noting that $\Delta\omega$ is replaced by $i(\partial A / \partial t)$ in the time domain, Eq. (2.4.6) can be written as [23]

$$\frac{\partial A}{\partial z} + \beta_1 \frac{\partial A}{\partial t} + \frac{i\beta_2}{2} \frac{\partial^2 A}{\partial t^2} - \frac{\beta_3}{6} \frac{\partial^3 A}{\partial t^3} = 0. \quad (2.4.7)$$

This is the basic propagation equation that governs pulse evolution inside a single-mode fiber. In the absence of dispersion ($\beta_2 = \beta_3 = 0$), the optical pulse propagates without change in its shape such that $A(z, t) = A(0, t - \beta_1 z)$. Transforming to a reference frame moving with the pulse and introducing the new coordinates

$$t' = t - \beta_1 z \quad \text{and} \quad z' = z, \quad (2.4.8)$$

the β_1 term can be eliminated in Eq. (2.4.7) to yield

$$\frac{\partial A}{\partial z'} + \frac{i\beta_2}{2} \frac{\partial^2 A}{\partial t'^2} - \frac{\beta_3}{6} \frac{\partial^3 A}{\partial t'^3} = 0. \quad (2.4.9)$$

For simplicity of notation, we drop the primes over z' and t' in this and the following chapters whenever no confusion is likely to arise.

2.4.2 Chirped Gaussian Pulses

As a simple application of Eq. (2.4.9), consider the propagation of chirped Gaussian pulses inside optical fibers by choosing the initial field as

$$A(0, t) = A_0 \exp \left[-\frac{1+iC}{2} \left(\frac{t}{T_0} \right)^2 \right], \quad (2.4.10)$$

where A_0 is the peak amplitude. The parameter T_0 represents the half-width at $1/e$ intensity point. It is related to the full-width at half-maximum (FWHM) of the pulse by the relation

$$T_{\text{FWHM}} = 2(\ln 2)^{1/2} T_0 \approx 1.665 T_0. \quad (2.4.11)$$

The parameter C governs the frequency chirp imposed on the pulse. A pulse is said to be chirped if its carrier frequency changes with time. The frequency change is related to the phase derivative and is given by

$$\delta\omega(t) = -\frac{\partial\phi}{\partial t} = \frac{C}{T_0^2} t, \quad (2.4.12)$$

where ϕ is the phase of $A(0, t)$. The time-dependent frequency shift $\delta\omega$ is called the *chirp*. The spectrum of a chirped pulse is broader than that of the unchirped pulse. This can be seen by taking the Fourier transform of Eq. (2.4.10) so that

$$\tilde{A}(0, \omega) = A_0 \left(\frac{2\pi T_0^2}{1+iC} \right)^{1/2} \exp \left[-\frac{\omega^2 T_0^2}{2(1+iC)} \right]. \quad (2.4.13)$$

The spectral half-width (at $1/e$ intensity point) is given by

$$\Delta\omega_0 = (1+C^2)^{1/2} T_0^{-1}. \quad (2.4.14)$$

In the absence of frequency chirp ($C = 0$), the spectral width satisfies the relation $\Delta\omega_0 T_0 = 1$. Such a pulse has the narrowest spectrum and is called *transform-limited*. The spectral width is enhanced by a factor of $(1+C^2)^{1/2}$ in the presence of linear chirp, as seen in Eq. (2.4.14).

The pulse-propagation equation (2.4.9) can be easily solved in the Fourier domain. Its solution is given by

$$A(z, t) = \frac{1}{2\pi} \int_{-\infty}^{\infty} \tilde{A}(0, \omega) \exp \left(\frac{i}{2} \beta_2 z \omega^2 + \frac{i}{6} \beta_3 z \omega^3 - i\omega t \right) d\omega, \quad (2.4.15)$$

where $\tilde{A}(0, \omega)$ is given by Eq. (2.4.13) for the Gaussian input pulse. Let us first consider the case in which the carrier wavelength is far away from the zero-dispersion wavelength so that the contribution of the β_3 term is negligible. The integration in Eq. (2.4.15) can be performed analytically with the result

$$A(z, t) = \frac{A_0}{\sqrt{Q(z)}} \exp \left[-\frac{(1+iC)t^2}{2T_0^2 Q(z)} \right], \quad (2.4.16)$$

where $Q(z) = 1 + (C - i)\beta_2 z / T_0^2$. This equation shows that a Gaussian pulse remains Gaussian on propagation but its width, chirp, and amplitude change as dictated by the factor $Q(z)$. The width changes with z as $T_1(z) = |Q(z)|T_0$, and chirp changes from its initial value C to become $C_1(z) = C + (1+C^2)\beta_2 z / T_0^2$.

Changes in the pulse width are quantified through the broadening factor

$$\frac{T_1}{T_0} = \left[\left(1 + \frac{C\beta_2 z}{T_0^2} \right)^2 + \left(\frac{\beta_2 z}{T_0^2} \right)^2 \right]^{1/2}. \quad (2.4.17)$$

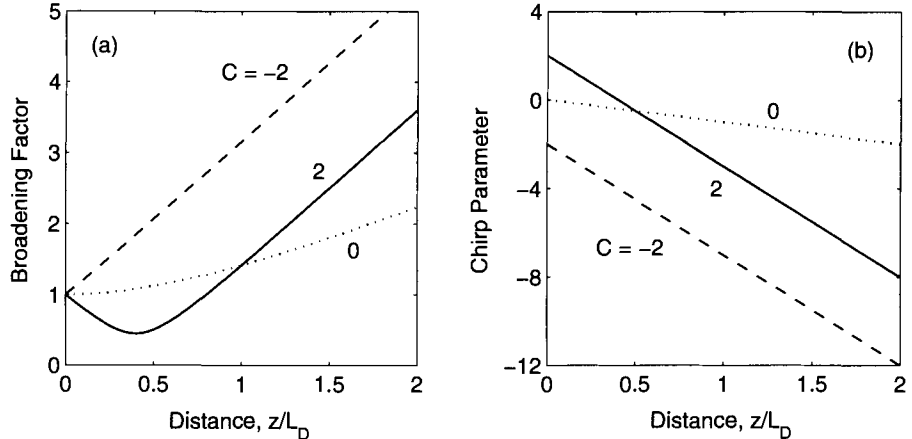


Figure 2.11: Broadening factor (a) and the chirp parameter (b) as functions of distance for a chirped Gaussian pulse propagating in the anomalous-dispersion region of a fiber. Dashed curves correspond to the case of an unchirped Gaussian pulse. The same curves are obtained for normal dispersion ($\beta_2 > 0$) if the sign of C is reversed.

Figure 2.11 shows (a) the broadening factor T_1/T_0 and (b) the chirp parameter C_1 as a function of $\xi = z/L_D$ in the case of anomalous dispersion ($\beta_2 < 0$). Here, $L_D = T_0^2/|\beta_2|$ is the so-called *dispersion length*. An unchirped pulse ($C = 0$) broadens monotonically by a factor of $(1 + \xi^2)^{1/2}$ and develops a negative chirp such that $C_1 = -\xi$ (the dotted curves). Chirped pulses, on the other hand, may broaden or compress depending on whether β_2 and C have the same or opposite signs. When $\beta_2 C > 0$, a chirped Gaussian pulse broadens monotonically at a rate faster than that of the unchirped pulse (the dashed curves). The reason is related to the fact that for $\beta_2 C < 0$, the pulse width initially decreases and becomes minimum at a distance

$$z_{\min} = [|C|/(1 + C^2)] L_D. \quad (2.4.18)$$

The minimum value depends on the chirp parameter as

$$T_1^{\min} = T_0/(1 + C^2)^{1/2}. \quad (2.4.19)$$

Physically, when $\beta_2 C < 0$, GVD-induced chirp counteracts the initial chirp, and the net chirp decreases until it vanishes at $z = z_{\min}$.

Equation (2.4.17) can be generalized to include higher-order dispersion governed by β_3 in Eq. (2.4.15). The integral can still be performed in closed form in terms of an Airy function [49]. However, the pulse no longer remains Gaussian on propagation and develops a tail with an oscillatory structure. Such pulses cannot be properly characterized by their FWHM. A proper measure of the pulse width is the RMS width of the pulse defined as

$$\sigma = [\langle t^2 \rangle - \langle t \rangle^2]^{1/2}, \quad (2.4.20)$$

where the angle brackets denote averaging with respect to the intensity profile, i.e.,

$$\langle t^m \rangle = \frac{\int_{-\infty}^{\infty} t^m |A(z, t)|^2 dt}{\int_{-\infty}^{\infty} |A(z, t)|^2 dt}. \quad (2.4.21)$$

The broadening factor defined as σ/σ_0 , where σ_0 is the RMS width of the input Gaussian pulse ($\sigma_0 = T_0/\sqrt{2}$) can be calculated following the analysis of Appendix C and is given by [48]

$$\frac{\sigma^2}{\sigma_0^2} = \left(1 + \frac{C\beta_2 L}{2\sigma_0^2}\right)^2 + \left(\frac{\beta_2 L}{2\sigma_0^2}\right)^2 + (1+C^2)^2 \left(\frac{\beta_3 L}{4\sqrt{2}\sigma_0^3}\right)^2, \quad (2.4.22)$$

where L is the fiber length.

The foregoing discussion assumes that the optical source used to produce the input pulses is nearly monochromatic such that its spectral width under CW conditions satisfies $\Delta\omega_L \ll \Delta\omega_0$, where $\Delta\omega_0$ is given by Eq. (2.4.14). This condition is not always satisfied in practice. To account for the source spectral width, we must treat the optical field as a stochastic process and consider the coherence properties of the source through the mutual coherence function [20]. Appendix C shows how the broadening factor can be calculated in this case. When the source spectrum is Gaussian with an RMS spectral width σ_ω , the broadening factor is obtained from [48]

$$\frac{\sigma^2}{\sigma_0^2} = \left(1 + \frac{C\beta_2 L}{2\sigma_0^2}\right)^2 + (1+V_\omega^2) \left(\frac{\beta_2 L}{2\sigma_0^2}\right)^2 + (1+C^2+V_\omega^2)^2 \left(\frac{\beta_3 L}{4\sqrt{2}\sigma_0^3}\right)^2, \quad (2.4.23)$$

where $V_\omega = 2\sigma_\omega\sigma_0$ is a dimensionless parameter. Equation (2.4.23) provides an expression for dispersion-induced broadening of Gaussian input pulses under quite general conditions. We use it in the next section to find the limiting bit rate of optical communication systems.

2.4.3 Limitations on the Bit Rate

The limitation imposed on the bit rate by fiber dispersion can be quite different depending on the source spectral width. It is instructive to consider the following two cases separately.

Optical Sources with a Large Spectral Width

This case corresponds to $V_\omega \gg 1$ in Eq. (2.4.23). Consider first the case of a lightwave system operating away from the zero-dispersion wavelength so that the β_3 term can be neglected. The effects of frequency chirp are negligible for sources with a large spectral width. By setting $C = 0$ in Eq. (2.4.23), we obtain

$$\sigma^2 = \sigma_0^2 + (\beta_2 L \sigma_\omega)^2 \equiv \sigma_0^2 + (DL\sigma_\lambda)^2, \quad (2.4.24)$$

where σ_λ is the RMS source spectral width in wavelength units. The output pulse width is thus given by

$$\sigma = (\sigma_0^2 + \sigma_D^2)^{1/2}, \quad (2.4.25)$$

where $\sigma_D \equiv |D|L\sigma_\lambda$ provides a measure of dispersion-induced broadening.

We can relate σ to the bit rate by using the criterion that the broadened pulse should remain inside the allocated bit slot, $T_B = 1/B$, where B is the bit rate. A commonly used criterion is $\sigma \leq T_B/4$; for Gaussian pulses at least 95% of the pulse energy then remains within the bit slot. The limiting bit rate is given by $4B\sigma \leq 1$. In the limit $\sigma_D \gg \sigma_0$, $\sigma \approx \sigma_D = |D|L\sigma_\lambda$, and the condition becomes

$$BL|D|\sigma_\lambda \leq \frac{1}{4}. \quad (2.4.26)$$

This condition should be compared with Eq. (2.3.6) obtained heuristically; the two become identical if we interpret $\Delta\lambda$ as $4\sigma_\lambda$ in Eq. (2.3.6).

For a lightwave system operating exactly at the zero-dispersion wavelength, $\beta_2 = 0$ in Eq. (2.4.23). By setting $C = 0$ as before and assuming $V_\omega \gg 1$, Eq. (2.4.23) can be approximated by

$$\sigma^2 = \sigma_0^2 + \frac{1}{2}(\beta_3 L \sigma_\omega^2)^2 \equiv \sigma_0^2 + \frac{1}{2}(SL\sigma_\lambda^2)^2, \quad (2.4.27)$$

where Eq. (2.3.13) was used to relate β_3 to the dispersion slope S . The output pulse width is thus given by Eq. (2.4.25) but now $\sigma_D \equiv |S|L\sigma_\lambda^2/\sqrt{2}$. As before, we can relate σ to the limiting bit rate by the condition $4B\sigma \leq 1$. When $\sigma_D \gg \sigma_0$, the limitation on the bit rate is governed by

$$BL|S|\sigma_\lambda^2 \leq 1/\sqrt{8}. \quad (2.4.28)$$

This condition should be compared with Eq. (2.3.14) obtained heuristically by using simple physical arguments.

As an example, consider the case of a light-emitting diode with $\sigma_\lambda \approx 15$ nm. By using $D = 17$ ps/(km-nm) at 1.55 μ m, Eq. (2.4.26) yields $BL < 1$ (Gb/s)-km. However, if the system is designed to operate at the zero-dispersion wavelength, BL can be increased to 20 (Gb/s)-km for a typical value $S = 0.08$ ps/(km-nm²).

Optical Sources with a Small Spectral Width

This case corresponds to $V_\omega \ll 1$ in Eq. (2.4.23). As before, if we neglect the β_3 term and set $C = 0$, Eq. (2.4.23) can be approximated by

$$\sigma^2 = \sigma_0^2 + (\beta_2 L / 2\sigma_0)^2 \equiv \sigma_0^2 + \sigma_D^2. \quad (2.4.29)$$

A comparison with Eq. (2.4.25) reveals a major difference between the two cases. In the case of a narrow source spectrum, dispersion-induced broadening depends on the initial width σ_0 , whereas it is independent of σ_0 when the spectral width of the optical source dominates. In fact, σ can be minimized by choosing an optimum value of σ_0 . The minimum value of σ is found to occur for $\sigma_0 = \sigma_D = (|\beta_2|L/2)^{1/2}$ and is given by $\sigma = (|\beta_2|L)^{1/2}$. The limiting bit rate is obtained by using $4B\sigma \leq 1$ and leads to the condition

$$B\sqrt{|\beta_2|L} \leq \frac{1}{4}. \quad (2.4.30)$$

The main difference from Eq. (2.4.26) is that B scales as $L^{-1/2}$ rather than L^{-1} . Figure 2.12 compares the decrease in the bit rate with increasing L for $\sigma_\lambda = 0, 1$, and 5 nm using $D = 16$ ps/(km-nm). Equation (2.4.30) was used in the case $\sigma_\lambda = 0$.

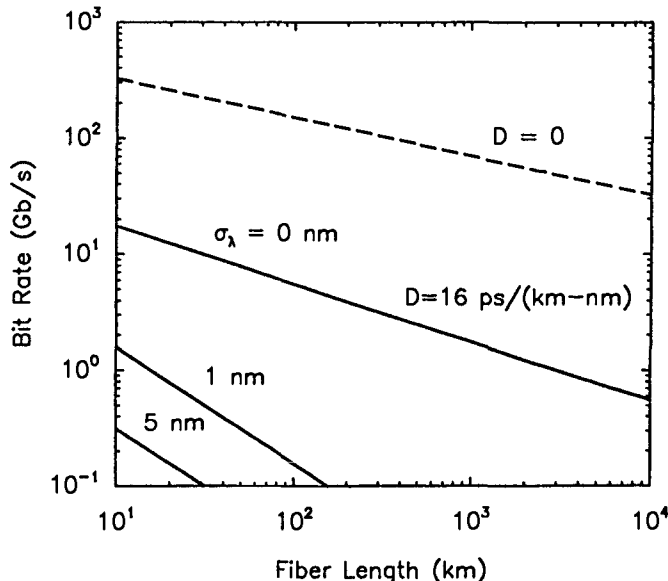


Figure 2.12: Limiting bit rate of single-mode fibers as a function of the fiber length for $\sigma_\lambda = 0$, 1, and 5 nm. The case $\sigma_\lambda = 0$ corresponds to the case of an optical source whose spectral width is much smaller than the bit rate.

For a lightwave system operating close to the zero-dispersion wavelength, $\beta_2 \approx 0$ in Eq. (2.4.23). Using $V_\omega \ll 1$ and $C = 0$, the pulse width is then given by

$$\sigma^2 = \sigma_0^2 + (\beta_3 L / 4\sigma_0^2)^2 / 2 \equiv \sigma_0^2 + \sigma_D^2. \quad (2.4.31)$$

Similar to the case of Eq. (2.4.29), σ can be minimized by optimizing the input pulse width σ_0 . The minimum value of σ occurs for $\sigma_0 = (|\beta_3|L/4)^{1/3}$ and is given by

$$\sigma = (\frac{3}{2})^{1/2} (|\beta_3|L/4)^{1/3}. \quad (2.4.32)$$

The limiting bit rate is obtained by using the condition $4B\sigma \leq 1$, or

$$B(|\beta_3|L)^{1/3} \leq 0.324. \quad (2.4.33)$$

The dispersive effects are most forgiving in this case. When $\beta_3 = 0.1 \text{ ps}^3/\text{km}$, the bit rate can be as large as 150 Gb/s for $L = 100 \text{ km}$. It decreases to only about 70 Gb/s even when L increases by a factor of 10 because of the $L^{-1/3}$ dependence of the bit rate on the fiber length. The dashed line in Figure 2.12 shows this dependence by using Eq. (2.4.33) with $\beta_3 = 0.1 \text{ ps}^3/\text{km}$. Clearly, the performance of a lightwave system can be improved considerably by operating it near the zero-dispersion wavelength of the fiber and using optical sources with a relatively narrow spectral width.

Effect of Frequency Chirp

The input pulse in all preceding cases has been assumed to be an unchirped Gaussian pulse. In practice, optical pulses are often non-Gaussian and may exhibit considerable

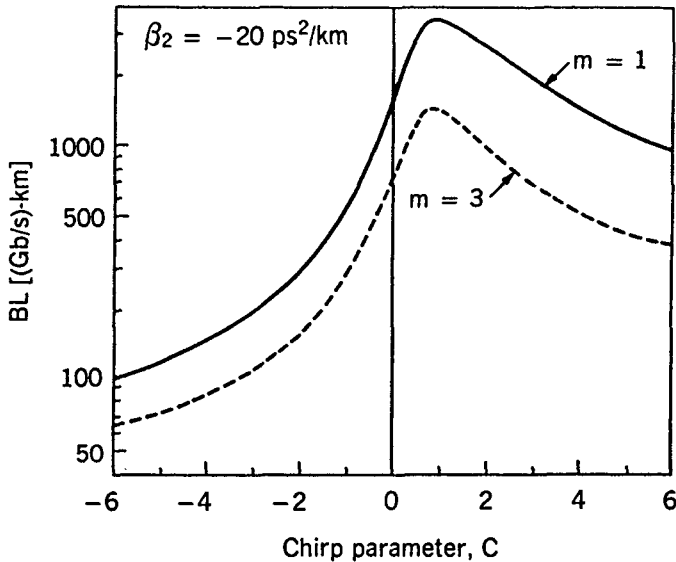


Figure 2.13: Dispersion-limited BL product as a function of the chirp parameter for Gaussian (solid curve) and super-Gaussian (dashed curve) input pulses. (After Ref. [50]; ©1986 OSA; reprinted with permission.)

chirp. A super-Gaussian model has been used to study the bit-rate limitation imposed by fiber dispersion for a NRZ-format bit stream [50]. In this model, Eq. (2.4.10) is replaced by

$$A(0, T) = A_0 \exp \left[-\frac{1+iC}{2} \left(\frac{t}{T_0} \right)^{2m} \right], \quad (2.4.34)$$

where the parameter m controls the pulse shape. Chirped Gaussian pulses correspond to $m = 1$. For large value of m the pulse becomes nearly rectangular with sharp leading and trailing edges. The output pulse shape can be obtained by solving Eq. (2.4.9) numerically. The limiting bit rate-distance product BL is found by requiring that the RMS pulse width does not increase above a tolerable value. Figure 2.13 shows the BL product as a function of the chirp parameter C for Gaussian ($m = 1$) and super-Gaussian ($m = 3$) input pulses. In both cases the fiber length L at which the pulse broadens by 20% was obtained for $T_0 = 125$ ps and $\beta_2 = -20 \text{ ps}^2/\text{km}$. As expected, the BL product is smaller for super-Gaussian pulses because such pulses broaden more rapidly than Gaussian pulses. The BL product is reduced dramatically for negative values of the chirp parameter C . This is due to enhanced broadening occurring when $\beta_2 C$ is positive (see Figure 2.11). Unfortunately, C is generally negative for directly modulated semiconductor lasers with a typical value of -6 at $1.55 \mu\text{m}$. Since $BL < 100 \text{ (Gb/s)}\text{-km}$ under such conditions, fiber dispersion limits the bit rate to about 2 Gb/s for $L = 50 \text{ km}$. This problem can be overcome by employing the technique dispersion management (see Chapter 8).

2.4.4 Fiber Bandwidth

The concept of fiber bandwidth originates from the general theory of time-invariant linear systems [51]. If the optical fiber can be treated as a *linear system*, its input and output powers should be related by a general relation

$$P_{\text{out}}(t) = \int_{-\infty}^{\infty} h(t-t') P_{\text{in}}(t') dt'. \quad (2.4.35)$$

For an impulse $P_{\text{in}}(t) = \delta(t)$, where $\delta(t)$ is the delta function, and $P_{\text{out}}(t) = h(t)$. For this reason, $h(t)$ is called the *impulse response* of the linear system. Its Fourier transform,

$$H(f) = \int_{-\infty}^{\infty} h(t) \exp(2\pi i f t) dt, \quad (2.4.36)$$

provides the frequency response and is called the *transfer function*. In general, $|H(f)|$ falls off with increasing f , indicating that the high-frequency components of the input signal are attenuated by the fiber. In effect, the optical fiber acts as a *bandpass filter*. The *fiber bandwidth* $f_{3\text{dB}}$ corresponds to the frequency $f = f_{3\text{dB}}$ at which $|H(f)|$ is reduced by a factor of 2 or by 3 dB:

$$|H(f_{3\text{dB}})/H(0)| = \frac{1}{2}. \quad (2.4.37)$$

Note that $f_{3\text{dB}}$ is the optical bandwidth of the fiber as the optical power drops by 3 dB at this frequency compared with the zero-frequency response. In the field of electrical communications, the bandwidth of a linear system is defined as the frequency at which electrical power drops by 3 dB.

Optical fibers cannot generally be treated as linear with respect to power, and Eq. (2.4.35) does not hold for them [52]. However, this equation is approximately valid when the source spectral width is much larger than the signal spectral width ($V_{\omega} \gg 1$). In that case, we can consider propagation of different spectral components independently and add the power carried by them linearly to obtain the output power. For a Gaussian spectrum, the transfer function $H(f)$ is found to be given by [53]

$$H(f) = \left(1 + \frac{if}{f_2}\right)^{-1/2} \exp\left[-\frac{(f/f_1)^2}{2(1+if/f_2)}\right], \quad (2.4.38)$$

where the parameters f_1 and f_2 are given by

$$f_1 = (2\pi\beta_2 L\sigma_{\omega})^{-1} = (2\pi|D|L\sigma_{\lambda})^{-1}, \quad (2.4.39)$$

$$f_2 = (2\pi\beta_3 L\sigma_{\omega}^2)^{-1} = [2\pi(S+2|D|/\lambda)L\sigma_{\lambda}^2]^{-1}, \quad (2.4.40)$$

and we used Eqs. (2.3.5) and (2.3.13) to introduce the dispersion parameters D and S .

For lightwave systems operating far away from the zero-dispersion wavelength ($f_1 \ll f_2$), the transfer function is approximately Gaussian. By using Eqs. (2.4.37) and (2.4.38) with $f \ll f_2$, the fiber bandwidth is given by

$$f_{3\text{dB}} = (2 \ln 2)^{1/2} f_1 \approx 0.188(|D|L\sigma_{\lambda})^{-1}. \quad (2.4.41)$$

If we use $\sigma_D = |D|L\sigma_\lambda$ from Eq. (2.4.25), we obtain the relation $f_{3\text{dB}}\sigma_D \approx 0.188$ between the fiber bandwidth and dispersion-induced pulse broadening. We can also get a relation between the bandwidth and the bit rate B by using Eqs. (2.4.26) and (2.4.41). The relation is $B \leq 1.33f_{3\text{dB}}$ and shows that the fiber bandwidth is an approximate measure of the maximum possible bit rate of dispersion-limited lightwave systems. In fact, Figure 2.12 can be used to estimate $f_{3\text{dB}}$ and its variation with the fiber length under different operating conditions.

For lightwave systems operating at the zero-dispersion wavelength, the transfer function is obtained from Eq. (2.4.38) by setting $D = 0$. The use of Eq. (2.4.37) then provides the following expression for the fiber bandwidth

$$f_{3\text{dB}} = \sqrt{15}f_2 \approx 0.616(SL\sigma_\lambda^2)^{-1}. \quad (2.4.42)$$

The limiting bit rate can be related to $f_{3\text{dB}}$ by using Eq. (2.4.28) and is given by $B \leq 0.574f_{3\text{dB}}$. Again, the fiber bandwidth provides a measure of the dispersion-limited bit rate. As a numerical estimate, consider a $1.55\text{-}\mu\text{m}$ lightwave system employing dispersion-shifted fibers and multimode semiconductor lasers. By using $S = 0.05\text{ ps}/(\text{km}\cdot\text{nm}^2)$ and $\sigma_\lambda = 1\text{ nm}$ as typical values, $f_{3\text{dB}}L \approx 32\text{ THz-km}$. By contrast, the bandwidth-distance product is reduced to 0.1 THz-km for standard fibers with $D = 18\text{ ps}/(\text{km}\cdot\text{nm})$.

2.5 Fiber Losses

Section 2.4 shows that fiber dispersion limits the performance of optical communication systems by broadening optical pulses as they propagate inside the fiber. Fiber losses represent another limiting factor because they reduce the signal power reaching the receiver. As optical receivers need a certain minimum amount of power for recovering the signal accurately, the transmission distance is inherently limited by fiber losses. In fact, the use of silica fibers for optical communications became practical only when losses were reduced to an acceptable level during the 1970s. With the advent of optical amplifiers in the 1990s, transmission distances could exceed thousands of kilometers by compensating accumulated losses periodically. However, low-loss fibers are still required since spacing among amplifiers is set by fiber losses. This section is devoted to a discussion of various loss mechanisms in optical fibers.

2.5.1 Attenuation Coefficient

Under quite general conditions, changes in the average optical power P of a bit stream propagating inside an optical fiber are governed by Beer's law:

$$dP/dz = -\alpha P, \quad (2.5.1)$$

where α is the attenuation coefficient. Although denoted by the same symbol as the absorption coefficient in Eq. (2.2.11), α in Eq. (2.5.1) includes not only material absorption but also other sources of power attenuation. If P_{in} is the power launched at the input end of a fiber of length L , the output power P_{out} from Eq. (2.5.1) is given by

$$P_{\text{out}} = P_{\text{in}} \exp(-\alpha L). \quad (2.5.2)$$

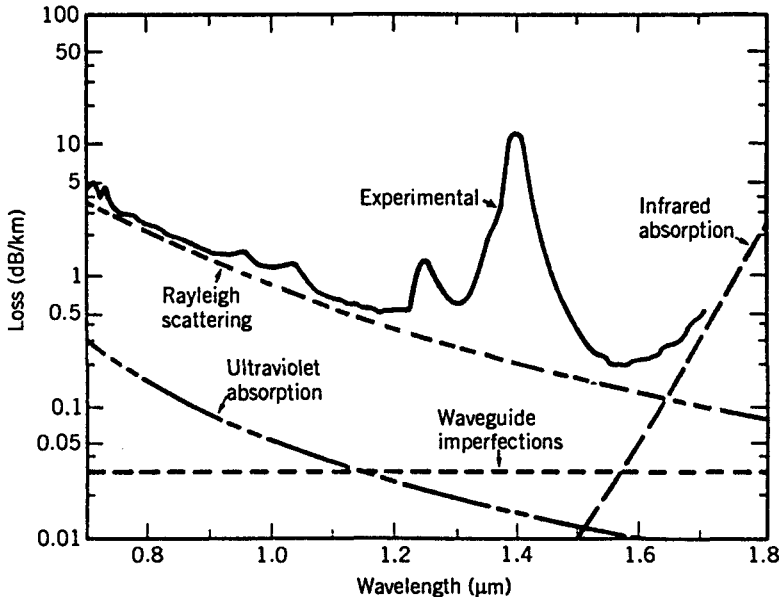


Figure 2.14: Loss spectrum of a single-mode fiber produced in 1979. Wavelength dependence of several fundamental loss mechanisms is also shown. (After Ref. [11]; ©1979 IEE; reprinted with permission.)

It is customary to express α in units of dB/km by using the relation

$$\alpha \text{ (dB/km)} = -\frac{10}{L} \log_{10} \left(\frac{P_{\text{out}}}{P_{\text{in}}} \right) \approx 4.343\alpha, \quad (2.5.3)$$

and refer to it as the fiber-loss parameter.

Fiber losses depend on the wavelength of transmitted light. Figure 2.14 shows the loss spectrum $\alpha(\lambda)$ of a single-mode fiber made in 1979 with $9.4\text{-}\mu\text{m}$ core diameter, $\Delta = 1.9 \times 10^{-3}$, and $1.1\text{-}\mu\text{m}$ cutoff wavelength [11]. The fiber exhibited a loss of only about 0.2 dB/km in the wavelength region near $1.55\text{ }\mu\text{m}$, the lowest value first realized in 1979. This value is close to the fundamental limit of about 0.16 dB/km for silica fibers. The loss spectrum exhibits a strong peak near $1.39\text{ }\mu\text{m}$ and several other smaller peaks. A secondary minimum is found to occur near $1.3\text{ }\mu\text{m}$, where the fiber loss is below 0.5 dB/km. Since fiber dispersion is also minimum near $1.3\text{ }\mu\text{m}$, this low-loss window was used for second-generation lightwave systems. Fiber losses are considerably higher for shorter wavelengths and exceed 5 dB/km in the visible region, making it unsuitable for long-haul transmission. Several factors contribute to overall losses; their relative contributions are also shown in Figure 2.14. The two most important among them are material absorption and Rayleigh scattering.

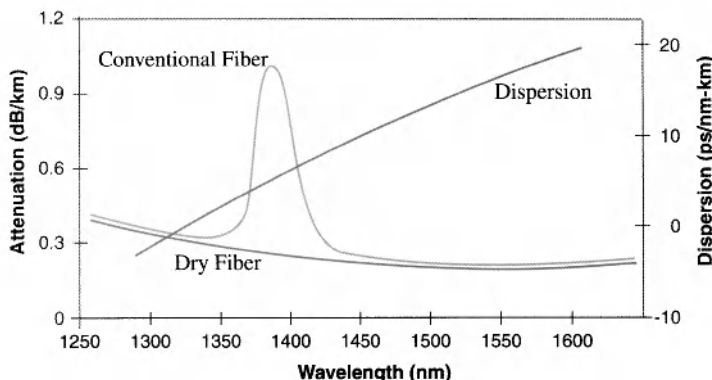


Figure 2.15: Loss and dispersion of a dry fiber. Loss of a conventional fiber is shown by the gray line for comparison.)

2.5.2 Material Absorption

Material absorption can be divided into two categories. Intrinsic absorption losses correspond to absorption by fused silica (material used to make fibers) whereas extrinsic absorption is related to losses caused by impurities within silica. Any material absorbs at certain wavelengths corresponding to the electronic and vibrational resonances associated with specific molecules. For silica (SiO_2) molecules, electronic resonances occur in the ultraviolet region ($\lambda < 0.4 \mu\text{m}$), whereas vibrational resonances occur in the infrared region ($\lambda > 7 \mu\text{m}$). Because of the amorphous nature of fused silica, these resonances are in the form of absorption bands whose tails extend into the visible region. Figure 2.14 shows that intrinsic material absorption for silica in the wavelength range $0.8\text{--}1.6 \mu\text{m}$ is below 0.1 dB/km . In fact, it is less than 0.03 dB/km in the wavelength window $1.3\text{--}1.6 \mu\text{m}$ used commonly for lightwave systems.

Extrinsic absorption results from the presence of impurities. Transition-metal impurities such as Fe, Cu, Co, Ni, Mn, and Cr absorb strongly in the wavelength range $0.6\text{--}1.6 \mu\text{m}$. Their amount should be reduced to below 1 part per billion to obtain a loss level below 1 dB/km . Such high-purity silica can be obtained by using modern techniques. The main source of extrinsic absorption in state-of-the-art silica fibers is the presence of water vapors. A vibrational resonance of the OH ion occurs near $2.73 \mu\text{m}$. Its harmonic and combination tones with silica produce absorption at the $1.39\text{-}, 1.24\text{-}$, and $0.95\text{-}\mu\text{m}$ wavelengths. The three spectral peaks seen in Figure 2.14 occur near these wavelengths and are due to the presence of residual water vapor in silica. Even a concentration of 1 part per million can cause a loss of about 50 dB/km at $1.39 \mu\text{m}$. The OH concentration is reduced to below 10^{-8} in modern fibers to lower the $1.39\text{-}\mu\text{m}$ peak to below 1 dB . In a new kind of fiber, known as the *dry fiber*, the OH concentration is reduced to such low levels that the $1.39\text{-}\mu\text{m}$ peak almost disappears [54]. Figure 2.15 shows the loss and dispersion profiles of such a fiber (OFS AllWave fiber in Table 2.1). Such fibers can be used to transmit WDM signals over the entire wavelength range of 1.3 to $1.65 \mu\text{m}$.

2.5.3 Rayleigh Scattering

Rayleigh scattering is a fundamental loss mechanism arising from local microscopic fluctuations in density. Silica molecules move randomly in the molten state and freeze in place during fiber fabrication. Density fluctuations lead to random fluctuations of the refractive index on a scale smaller than the optical wavelength λ . Light scattering in such a medium is known as *Rayleigh scattering* [20]. The scattering cross section varies as λ^{-4} . As a result, the intrinsic loss of silica fibers from Rayleigh scattering can be written as

$$\alpha_R = C/\lambda^4, \quad (2.5.4)$$

where the constant C is in the range 0.7–0.9 (dB/km)- μm^4 , depending on the constituents of the fiber core. These values of C correspond to $\alpha_R = 0.12$ –0.16 dB/km at $\lambda = 1.55 \mu\text{m}$, indicating that fiber loss in Figure 2.14 is dominated by Rayleigh scattering near this wavelength.

The contribution of Rayleigh scattering can be reduced to below 0.01 dB/km for wavelengths longer than 3 μm . Silica fibers cannot be used in this wavelength region, since infrared absorption begins to dominate the fiber loss beyond 1.6 μm . Considerable effort has been directed toward finding other suitable materials with low absorption beyond 2 μm [55]–[58]. Fluorozirconate (ZrF_4) fibers have an intrinsic material absorption of about 0.01 dB/km near 2.55 μm and have the potential for exhibiting loss much smaller than that of silica fibers. State-of-the-art fluoride fibers, however, exhibit a loss of about 1 dB/km because of extrinsic losses. Chalcogenide and polycrystalline fibers exhibit minimum loss in the far-infrared region near 10 μm . The theoretically predicted minimum value of fiber loss for such fibers is below 10^{-3} dB/km because of reduced Rayleigh scattering. However, practical loss levels remain higher than those of silica fibers [58].

2.5.4 Waveguide Imperfections

An ideal single-mode fiber with a perfect cylindrical geometry guides the optical mode without energy leakage into the cladding layer. In practice, imperfections at the core-cladding interface (e.g., random core-radius variations) can lead to additional losses which contribute to the net fiber loss. The physical process behind such losses is *Mie scattering* [20], occurring because of index inhomogeneities on a scale longer than the optical wavelength. Care is generally taken to ensure that the core radius does not vary significantly along the fiber length during manufacture. Such variations can be kept below 1%, and the resulting scattering loss is typically below 0.03 dB/km.

Bends in the fiber constitute another source of scattering loss [59]. The reason can be understood by using the ray picture. Normally, a guided ray hits the core-cladding interface at an angle greater than the critical angle to experience total internal reflection. However, the angle decreases near a bend and may become smaller than the critical angle for tight bends. The ray would then escape out of the fiber. In the mode description, a part of the mode energy is scattered into the cladding layer. The bending loss is proportional to $\exp(-R/R_c)$, where R is the radius of curvature of the fiber bend and $R_c = a/(n_1^2 - n_2^2)$. For single-mode fibers, $R_c = 0.2$ to 0.4 μm typically, and the

bending loss is negligible ($< 0.01 \text{ dB/km}$) for bend radius $R > 5 \text{ mm}$. Since most macroscopic bends exceed $R = 5 \text{ mm}$, macrobending losses are negligible in practice.

A major source of fiber loss, particularly in cable form, is related to the random axial distortions that invariably occur during cabling when the fiber is pressed against a surface that is not perfectly smooth. Such losses are referred to as *microbending losses* and have been studied extensively [60]–[64]. Microbends cause an increase in the fiber loss for both multimode and single-mode fibers and can result in an excessively large loss ($\sim 100 \text{ dB/km}$) if precautions are not taken to minimize them. For single-mode fibers, microbending losses can be minimized by choosing the V parameter as close to the cutoff value of 2.405 as possible so that mode energy is confined primarily to the core. In practice, the fiber is designed to have V in the range 2.0–2.4 at the operating wavelength. Many other sources of optical loss exist in a fiber cable. These are related to splices and connectors used in forming the fiber link and are often treated as a part of the cable loss; microbending losses can also be included in the total cable loss.

2.6 Nonlinear Optical Effects

The response of any dielectric to light becomes nonlinear for intense electromagnetic fields, and optical fibers are no exception. Even though silica is intrinsically not a highly nonlinear material, the waveguide geometry that confines light to a small cross section over long fiber lengths makes nonlinear effects quite important in the design of modern lightwave systems [23]. We discuss in this section the nonlinear phenomena that are most relevant for fiber-optic communications.

2.6.1 Stimulated Light Scattering

Rayleigh scattering, discussed in Section 2.5.3, is an example of elastic scattering for which the frequency (or the photon energy) of scattered light remains unchanged. By contrast, the frequency of scattered light is shifted downward during inelastic scattering. Two examples of inelastic scattering are *Raman scattering* and *Brillouin scattering* [65]. Both of them can be understood as scattering of a photon to a lower energy photon such that the energy difference appears in the form of a phonon. The main difference between the two is that optical phonons participate in Raman scattering, whereas acoustic phonons participate in Brillouin scattering. Both scattering processes result in a loss of power at the incident frequency. However, their scattering cross sections are sufficiently small that loss is negligible at low power levels.

At high power levels, the nonlinear phenomena of stimulated Raman scattering (SRS) and stimulated Brillouin scattering (SBS) become important. The intensity of the scattered light in both cases grows exponentially once the incident power exceeds a threshold value [66]. SRS and SBS were first observed in optical fibers during the 1970s [67]–[70]. Even though SRS and SBS are quite similar in their origin, different dispersion relations for acoustic and optical phonons lead to the following differences between the two in single-mode fibers [23]: (i) SBS occurs only in the backward direction whereas SRS can occur in both directions; (ii) The scattered light is shifted in frequency by about 10 GHz for SBS but by 13 THz for SRS (this shift is called

the Stokes shift); and (iii) the Brillouin gain spectrum is extremely narrow (bandwidth < 100 MHz) compared with the Raman-gain spectrum that extends over 20–30 THz. The origin of these differences lies in a relatively small value of the ratio v_A/c ($\sim 10^{-5}$), where v_A is the acoustic velocity in silica and c is the velocity of light.

Stimulated Brillouin Scattering

The physical process behind Brillouin scattering is the tendency of materials to become compressed in the presence of an electric field—a phenomenon termed electrostriction [65]. For an oscillating electric field at the pump frequency Ω_p , this process generates an acoustic wave at some frequency Ω . Spontaneous Brillouin scattering can be viewed as scattering of the pump wave from this acoustic wave, resulting in creation of a new wave at the pump frequency Ω_s . The scattering process must conserve both the energy and the momentum. The energy conservation requires that the Stokes shift Ω equals $\omega_p - \omega_s$. The momentum conservation requires that the wave vectors satisfy $\mathbf{k}_A = \mathbf{k}_p - \mathbf{k}_s$. Using the dispersion relation $|k_A| = \Omega/v_A$, where v_A is the acoustic velocity, this condition determines the acoustic frequency as [23]

$$\Omega = |k_A|v_A = 2v_A|k_p|\sin(\theta/2), \quad (2.6.1)$$

where $|k_p| \approx |k_s|$ was used and θ represents the angle between the pump and scattered waves. Note that Ω vanishes in the forward direction ($\theta = 0$) and is maximum in the backward direction ($\theta = \pi$). In single-mode fibers, light can travel only in the forward and backward directions. As a result, SBS occurs in the backward direction with a frequency shift $\Omega_B = 2v_A|k_p|$. Using $k_p = 2\bar{n}\lambda_p/\lambda_p$, where λ_p is the pump wavelength, the *Brillouin shift* is given by

$$v_B = \Omega_B/2\pi = 2\bar{n}v_A/\lambda_p, \quad (2.6.2)$$

where \bar{n} is the mode index. Using $v_A = 5.96$ km/s and $\bar{n} = 1.45$ as typical values for silica fibers, $v_B = 11.1$ GHz at $\lambda_p = 1.55$ μm. Equation (2.6.2) shows that v_B scales inversely with the pump wavelength.

Once the scattered wave is generated spontaneously, it beats with the pump and creates a frequency component at the beat frequency $\omega_p - \omega_s$, which is automatically equal to the acoustic frequency Ω . As a result, the beating term acts as source that increases the amplitude of the sound wave, which in turn increases the amplitude of the scattered wave, resulting in a positive feedback loop. SBS has its origin in this positive feedback, which ultimately can transfer all power from the pump to the scattered wave. The feedback process is governed by the following set of two coupled equations [65]:

$$\frac{dI_p}{dz} = -g_B I_p I_s - \alpha_p I_p. \quad (2.6.3)$$

$$-\frac{dI_s}{dz} = +g_B I_p I_s - \alpha_s I_s \quad (2.6.4)$$

where I_p and I_s are the intensities of the pump and Stokes fields, g_B is the SBS gain, and α_p and α_s account for fiber losses.

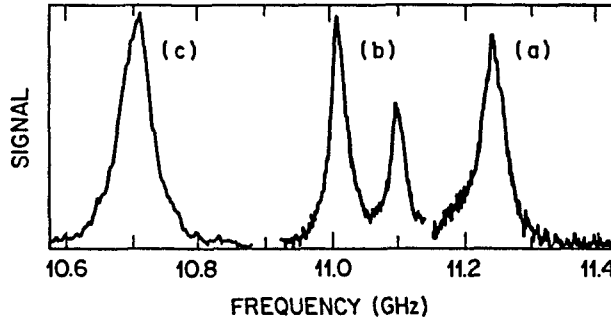


Figure 2.16: Brillouin-gain spectra measured using a 1.525- μm pump for three fibers with different germania doping: (a) silica-core fiber; (b) depressed-cladding fiber; (c) dispersion-shifted fiber. Vertical scale is arbitrary. (After Ref. [70]; ©1986 IEE; reprinted with permission.)

The SBS gain g_B is frequency dependent because of a finite damping time T_B of acoustic waves (the lifetime of acoustic phonons). If the acoustic waves decay as $\exp(-t/T_B)$, the Brillouin gain has a Lorentzian spectral profile given by [69]

$$g_B(\Omega) = \frac{g_B(\Omega_B)}{1 + (\Omega - \Omega_B)^2 T_B^2}. \quad (2.6.5)$$

Figure 2.16 shows the Brillouin gain spectra at $\lambda_p = 1.525 \mu\text{m}$ for three different kinds of single-mode silica fibers. Both the Brillouin shift ν_B and the gain bandwidth $\Delta\nu_B$ can vary from fiber to fiber because of the guided nature of light and the presence of dopants in the fiber core. The fiber labeled (a) in Figure 2.16 has a core of nearly pure silica (germania concentration of about 0.3% per mole). The measured Brillouin shift $\nu_B = 11.25 \text{ GHz}$ is in agreement with Eq. (2.6.2). The Brillouin shift is reduced for fibers (b) and (c) of a higher germania concentration in the fiber core. The double-peak structure for fiber (b) results from inhomogeneous distribution of germania within the core. The gain bandwidth in Figure 2.16 is larger than that expected for bulk silica ($\Delta\nu_B \approx 17 \text{ MHz}$ at $\lambda_p = 1.525 \mu\text{m}$). A part of the increase is due to the guided nature of acoustic modes in optical fibers. However, most of the increase in bandwidth can be attributed to variations in the core diameter along the fiber length. Because such variations are specific to each fiber, the SBS gain bandwidth is generally different for different fibers and can exceed 100 MHz; typical values are $\sim 50 \text{ MHz}$ for λ_p near 1.55 μm .

The peak value of the Brillouin gain in Eq. (2.6.5) occurs for $\Omega = \Omega_B$ and depends on various material parameters such as the density and the elasto-optic coefficient [65]. For silica fibers $g_B \approx 5 \times 10^{-11} \text{ m/W}$. The threshold power level for SBS can be estimated by solving Eqs. (2.6.3) and (2.6.4) and finding at what value of I_p , I_s grows from noise to a significant level. The threshold power $P_{\text{th}} = I_p A_{\text{eff}}$, where A_{eff} is the effective mode area, satisfies the condition [66]

$$g_B P_{\text{th}} L_{\text{eff}} / A_{\text{eff}} \approx 21, \quad (2.6.6)$$

where L_{eff} is the effective interaction length defined as

$$L_{\text{eff}} = [1 - \exp(-\alpha L)]/\alpha, \quad (2.6.7)$$

and α represents fiber losses. For optical communication systems L_{eff} can be approximated by $1/\alpha$ as $\alpha L \gg 1$ in practice. Using $A_{\text{eff}} = \pi w^2$, where w is the spot size, P_{th} can be as low as 1 mW depending on the values of w and α [69]. Once the power launched into an optical fiber exceeds the threshold level, most of the light is reflected backward through SBS. Clearly, SBS limits the launched power to a few milliwatts because of its low threshold.

The preceding estimate of P_{th} applies to a narrowband CW beam as it neglects the temporal and spectral characteristics of the incident light. In a lightwave system, the signal is in the form of a bit stream. For a single short pulse whose width is much smaller than the phonon lifetime, no SBS is expected to occur. However, for a high-speed bit stream, pulses come at such a fast rate that successive pulses build up the acoustic wave, similar to the case of a CW beam, although the SBS threshold increases. The exact value of the average threshold power depends on the modulation format (RZ versus NRZ) and is typically ~ 5 mW. It can be increased to 10 mW or more by increasing the bandwidth of the optical carrier to > 200 MHz through phase modulation. SBS does not produce interchannel crosstalk in WDM systems because the 10-GHz frequency shift is much smaller than typical channel spacing.

Stimulated Raman Scattering

Spontaneous Raman scattering occurs in optical fibers when a pump wave is scattered by the silica molecules. It can be understood using the energy-level diagram shown in Figure 2.17(b). Some pump photons give up their energy to create other photons of reduced energy at a lower frequency; the remaining energy is absorbed by silica molecules, which end up in an excited vibrational state. An important difference from Brillouin scattering is that the vibrational energy levels of silica dictate the value of the Raman shift $\Omega_R = \omega_p - \omega_s$. As an acoustic wave is not involved, spontaneous Raman scattering is an isotropic process and occurs in all directions.

Similar to the SBS case, the Raman scattering process becomes stimulated if the pump power exceeds a threshold value. SRS can occur in both the forward and backward directions in optical fibers. Physically speaking, the beating of the pump and with the scattered light in these two directions creates a frequency component at the beat frequency $\omega_p - \omega_s$, which acts as a source that derives molecular oscillations. Since the amplitude of the scattered wave increases in response to these oscillations, a positive feedback loop sets in. In the case of forward SRS, the feedback process is governed by the following set of two coupled equations [23]:

$$\frac{dI_p}{dz} = -g_R I_p I_s - \alpha_p I_p, \quad (2.6.8)$$

$$\frac{dI_s}{dz} = g_R I_p I_s - \alpha_s I_s, \quad (2.6.9)$$

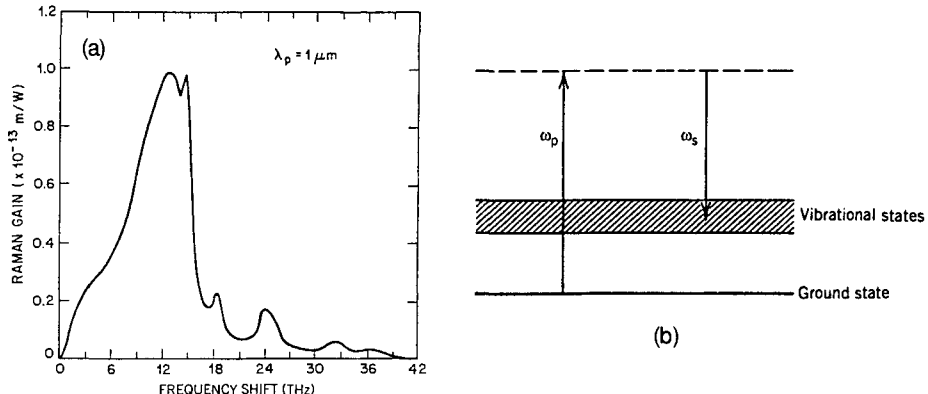


Figure 2.17: (a) Raman gain spectrum of fused silica at $\lambda_p = 1 \mu\text{m}$ and (b) energy levels participating in the SRS process. (After Ref. [67]; ©1972 AIP; reprinted with permission.)

where g_R is the SRS gain. In the case of backward SRS, a minus sign is added in front of the derivative in Eq. (2.6.9), and this set of equations becomes identical to the SBS case.

The spectrum of the Raman gain depends on the decay time associated with the excited vibrational state. In the case of a molecular gas or liquid, the decay time is relatively long ($\sim 1 \text{ ns}$), resulting in a Raman-gain bandwidth of $\sim 1 \text{ GHz}$. In the case for optical fibers, the bandwidth exceeds 10 THz. Figure 2.17 shows the Raman-gain spectrum of silica fibers. The broadband and multiphoton nature of the spectrum is due to the amorphous nature of glass. More specifically, vibrational energy levels of silica molecules merge together to form a band. As a result, the Stokes frequency ω_s can differ from the pump frequency ω_p over a wide range. The maximum gain occurs when the Raman shift $\Omega_R \equiv \omega_p - \omega_s$ is about 13 THz. Another major peak occurs near 15 THz while minor peaks persist for values of Ω_R as large as 35 THz. The peak value of the Raman gain g_R is about $1 \times 10^{-13} \text{ m/W}$ at a wavelength of $1 \mu\text{m}$. This value scales linearly with ω_p (or inversely with the pump wavelength λ_p), resulting in $g_R \approx 6 \times 10^{-13} \text{ m/W}$ at $1.55 \mu\text{m}$.

Similar to the case of SBS, the threshold power P_{th} is defined as the incident power at which half of the pump power is transferred to the Stokes field at the output end of a fiber of length L . It is estimated from [66]

$$g_R P_{\text{th}} L_{\text{eff}} / A_{\text{eff}} \approx 16, \quad (2.6.10)$$

where g_R is the peak value of the Raman gain. As before, L_{eff} can be approximated by $1/\alpha$. If we replace A_{eff} by πw^2 , where w is the spot size, P_{th} for SRS is given by

$$P_{\text{th}} \approx 16\alpha(\pi w^2)/g_R. \quad (2.6.11)$$

If we use $\pi w^2 = 50 \mu\text{m}^2$ and $\alpha = 0.2 \text{ dB/km}$ as the representative values, P_{th} is about 570 mW near $1.55 \mu\text{m}$. It is important to emphasize that Eq. (2.6.11) provides an order-of-magnitude estimate only as many approximations are made in its derivation.

As channel powers in optical communication systems are typically below 10 mW, SRS is not a limiting factor for single-channel lightwave systems. However, it affects the performance of WDM systems considerably; this aspect is covered in Chapter 6.

Both SRS and SBS can be used to advantage while designing optical communication systems because they can amplify an optical signal by transferring energy to it from a pump beam whose wavelength is suitably chosen. SRS is especially useful because of its extremely large bandwidth. Indeed, the Raman gain is used routinely for compensating fiber losses in modern lightwave systems (see Chapter 7).

2.6.2 Nonlinear Phase Modulation

The refractive index of silica was assumed to be power independent in the discussion of fiber modes in Section 2.2. In reality, all materials behave nonlinearly at high intensities and their refractive index increases with intensity. The physical origin of this effect lies in the anharmonic response of electrons to optical fields, resulting in a nonlinear susceptibility [65]. To include nonlinear refraction, we modify the core and cladding indices of a silica fiber as [23]

$$n'_j = n_j + \bar{n}_2(P/A_{\text{eff}}), \quad j = 1, 2, \quad (2.6.12)$$

where \bar{n}_2 is the *nonlinear-index coefficient*, P is the optical power, and A_{eff} is the effective mode area introduced earlier. The numerical value of \bar{n}_2 is about $2.6 \times 10^{-20} \text{ m}^2/\text{W}$ for silica fibers and varies somewhat with dopants used inside the core. Because of this relatively small value, the nonlinear part of the refractive index is quite small ($< 10^{-12}$ at a power level of 1 mW). Nevertheless, it affects modern lightwave systems considerably because of long fiber lengths. In particular, it leads to the phenomena of self- and cross-phase modulations.

Self-Phase Modulation

If we use first-order perturbation theory to see how fiber modes are affected by the nonlinear term in Eq. (2.6.12), we find that the mode shape does not change but the propagation constant becomes power dependent. It can be written as [23]

$$\beta' = \beta + k_0 \bar{n}_2 P / A_{\text{eff}} \equiv \beta + \gamma P, \quad (2.6.13)$$

where $\gamma = 2\pi\bar{n}_2/(A_{\text{eff}}\lambda)$ is an important nonlinear parameter with values ranging from 1 to $5 \text{ W}^{-1}/\text{km}$ depending on the values of A_{eff} and the wavelength. Noting that the optical phase increases linearly with z as seen in Eq. (2.4.1), the γ term produces a nonlinear phase shift given by

$$\phi_{\text{NL}} = \int_0^L (\beta' - \beta) dz = \int_0^L P(z) dz = \gamma P_{\text{in}} L_{\text{eff}}, \quad (2.6.14)$$

where $P(z) = P_{\text{in}} \exp(-\alpha z)$ accounts for fiber losses and L_{eff} is defined in Eq. (2.6.7).

In deriving Eq. (2.6.14) P_{in} was assumed to be constant. In practice, time dependence of P_{in} makes ϕ_{NL} to vary with time. In fact, the optical phase changes with time

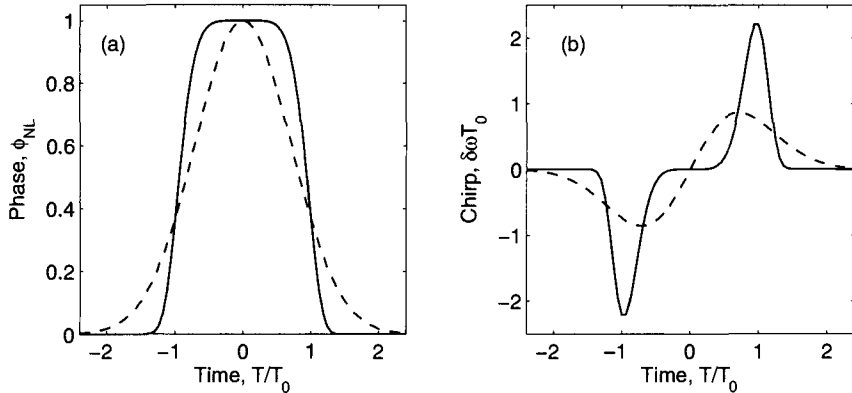


Figure 2.18: Temporal variation of SPM-induced (a) phase shift ϕ_{NL} and (b) frequency chirp for Gaussian (dashed curve) and super-Gaussian (solid curve) pulses.

in exactly the same fashion as the optical signal. Since this nonlinear phase modulation is self-induced, the nonlinear phenomenon responsible for it is called *self-phase modulation* (SPM). It should be clear from Eq. (2.4.12) that SPM leads to frequency chirping of optical pulses. In contrast with the linear chirp considered in Section 2.4, the frequency chirp is proportional to the derivative dP_{in}/dt and depends on the pulse shape.

Figure 2.18 shows variation of (a) the nonlinear phase shift ϕ_{NL} and (b) the frequency chirp across the pulse for $\gamma P_{in} L_{eff} = 1$ in the cases of a Gaussian pulse ($m = 1$) and a super-Gaussian pulse ($m = 3$). The SPM-induced chirp affects the pulse shape through GVD and often leads to additional pulse broadening [23]. In general, spectral broadening of the pulse induced by SPM [71] increases the signal bandwidth considerably and limits the performance of lightwave systems.

If fiber losses are compensated periodically using optical amplifiers, ϕ_{NL} in Eq. (2.6.14) should be multiplied by the number of amplifiers N_A because the SPM-induced phase accumulates over multiple amplifiers. To reduce the impact of SPM in lightwave systems, it is necessary that $\phi_{NL} \ll 1$. If we use $\phi_{NL} = 0.1$ as the maximum tolerable value and replace L_{eff} by $1/\alpha$ for long fibers, this condition can be written as a limit on the input peak power as

$$P_{in} < 0.1\alpha / (\gamma N_A). \quad (2.6.15)$$

For example, if $\gamma = 2 \text{ W}^{-1}/\text{km}$, $N_A = 10$, and $\alpha = 0.2 \text{ dB/km}$, the input peak power is limited to below 2.2 mW. Clearly, SPM can be a major limiting factor for long-haul lightwave systems.

Cross-Phase Modulation

The intensity dependence of the refractive index in Eq. (2.6.12) can also lead to another nonlinear phenomenon known as *cross-phase modulation* (XPM). It occurs when two or more optical channels are transmitted simultaneously inside an optical fiber using

the WDM technique. In such systems, the nonlinear phase shift for a specific channel depends not only on the power of that channel but also on the power of other channels [72]. The phase shift for the j th channel becomes

$$\phi_j^{\text{NL}} = \gamma L_{\text{eff}} \left(P_j + 2 \sum_{m \neq j} P_m \right), \quad (2.6.16)$$

where the sum extends over the number of channels. The factor of 2 in Eq. (2.6.16) has its origin in the form of the nonlinear susceptibility [23] and indicates that XPM is twice as effective as SPM for the same amount of power. The total phase shift depends on the powers in all channels and would vary from bit to bit depending on the bit pattern of the neighboring channels. If we assume equal channel powers, the phase shift in the worst case in which all channels simultaneously carry 1 bits and all pulses overlap is given by

$$\phi_j^{\text{NL}} = (\gamma/\alpha)(2M - 1)P_j. \quad (2.6.17)$$

It is difficult to estimate the impact of XPM on the performance of multichannel lightwave systems. The reason is that the preceding discussion has implicitly assumed that XPM acts in isolation without dispersive effects and is valid only for CW optical beams. In practice, pulses in different channels travel at different speeds. The XPM-induced phase shift can occur only when two pulses overlap in time. For widely separated channels they overlap for such a short time that XPM effects are virtually negligible. On the other hand, pulses in neighboring channels will overlap long enough for XPM effects to accumulate. These arguments show that Eq. (2.6.17) cannot be used to estimate the limiting input power.

A common method for studying the impact of SPM and XPM uses a numerical approach. Equation (2.4.9) can be generalized to include the SPM and XPM effects by adding a nonlinear term. The resulting equation is known as the nonlinear Schrödinger equation and has the form [23]

$$\frac{\partial A}{\partial z} + \frac{i\beta_2}{2} \frac{\partial^2 A}{\partial t^2} = -\frac{\alpha}{2}A + i\gamma|A|^2A, \quad (2.6.18)$$

where we neglected the third-order dispersion and added the term containing α to account for fiber losses. This equation is quite useful for designing lightwave systems and will be used in later chapters.

Since the nonlinear parameter γ depends inversely on the effective mode area, the impact of fiber nonlinearities can be reduced considerably by enlarging A_{eff} . As seen in Table 2.1, A_{eff} is about $80 \mu\text{m}^2$ for standard fibers but reduces to $50 \mu\text{m}^2$ for dispersion-shifted fibers. A new kind of fiber known as large effective-area fiber (LEAF) has been developed for reducing the impact of fiber nonlinearities. The nonlinear effects are not always detrimental for lightwave systems. Numerical solutions of Eq. (2.6.18) show that dispersion-induced broadening of optical pulses is considerably reduced in the case of anomalous dispersion [73]. In fact, an optical pulse can propagate without distortion if the peak power of the pulse is chosen to correspond to a fundamental soliton. Techniques used to control the nonlinear effects are discussed in Chapter 9.

2.6.3 Four-Wave Mixing

The power dependence of the refractive index seen in Eq. (2.6.12) has its origin in the third-order nonlinear susceptibility denoted by $\chi^{(3)}$ [65]. The nonlinear phenomenon, known as *four-wave mixing* (FWM), also originates from $\chi^{(3)}$. If three optical fields with carrier frequencies ω_1 , ω_2 , and ω_3 copropagate inside the fiber simultaneously, $\chi^{(3)}$ generates a fourth field whose frequency ω_4 is related to other frequencies by a relation $\omega_4 = \omega_1 \pm \omega_2 \pm \omega_3$. Several frequencies corresponding to different plus and minus sign combinations are possible in principle. In practice, most of these combinations do not build up because of a phase-matching requirement [23]. Frequency combinations of the form $\omega_4 = \omega_1 + \omega_2 - \omega_3$ are often troublesome for multichannel communication systems since they can become nearly phase-matched when channel wavelengths lie close to the zero-dispersion wavelength. In fact, the degenerate FWM process for which $\omega_1 = \omega_2$ is often the dominant process and impacts the system performance most.

On a fundamental level, a FWM process can be viewed as a scattering process in which two photons of energies $\hbar\omega_1$ and $\hbar\omega_2$ are destroyed, and their energy appears in the form of two new photons of energies $\hbar\omega_3$ and $\hbar\omega_4$. The *phase-matching condition* then stems from the requirement of momentum conservation. Since all four waves propagate in the same direction, the phase mismatch can be written as

$$\Delta = \beta(\omega_3) + \beta(\omega_4) - \beta(\omega_1) - \beta(\omega_2), \quad (2.6.19)$$

where $\beta(\omega)$ is the propagation constant for an optical field with frequency ω . In the degenerate case, $\omega_2 = \omega_1$, $\omega_3 = \omega_1 + \Omega$, and $\omega_4 = \omega_1 - \Omega$, where Ω represents the channel spacing. Using the Taylor expansion in Eq. (2.4.4), we find that the β_0 and β_1 terms cancel, and the phase mismatch is simply $\Delta = \beta_2\Omega^2$. The FWM process is completely phase matched when $\beta_2 = 0$. When β_2 is small ($< 1 \text{ ps}^2/\text{km}$) and channel spacing is also small ($\Omega < 100 \text{ GHz}$), this process can still occur and transfer power from each channel to its nearest neighbors. Such a power transfer not only results in the power loss for the channel but also induces interchannel crosstalk that degrades the system performance severely. Modern WDM systems avoid FWM by using the technique of dispersion management in which GVD is kept locally high in each fiber section even though it is low on average (see Chapter 8). Commercial dispersion-shifted fibers are designed with a dispersion of about $4 \text{ ps}/(\text{km-nm})$, a value found large enough to suppress FWM.

FWM can also be useful for lightwave systems (see Chapter 11). It is often used for demultiplexing individual channels when time-division multiplexing is used in the optical domain. It can also be used for wavelength conversion. FWM in optical fibers is sometimes used for generating a spectrally inverted signal through the process of *optical phase conjugation*. As discussed in Chapter 8, this technique is useful for dispersion compensation.

2.7 Fiber Design and Fabrication

In this section we discuss the engineering aspects of optical fibers made using either silica glass or a suitable plastic material. Manufacturing of fiber cables, suitable for

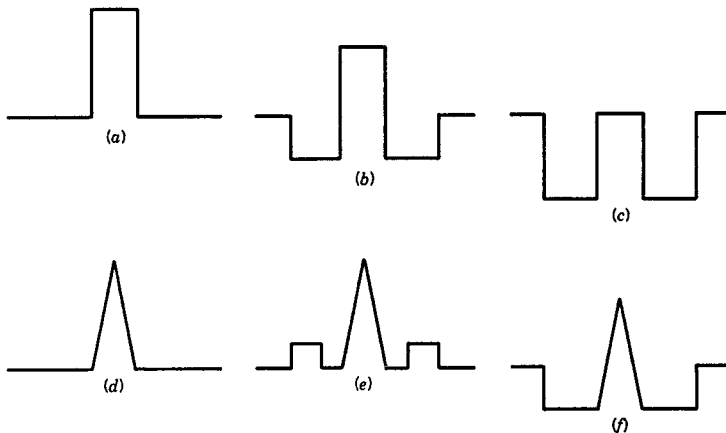


Figure 2.19: Several index profiles used in the design of single-mode fibers. Upper and lower rows correspond to standard and dispersion-shifted fibers, respectively.

use in an actual lightwave system, involves sophisticated technology with attention to many practical details available in several books [74]–[76]. We begin with silica fibers and then consider plastic fibers. Both types of materials have been used in recent years to make microstructured fibers discussed in a separate subsection.

2.7.1 Silica Fibers

In the case of silica fibers, both the core and the cladding are made using silicon dioxide (SiO_2) or silica as the base material. The difference in their refractive indices is realized by doping the core, or the cladding, or both with a suitable material. Dopants such as GeO_2 and P_2O_5 increase the refractive index of silica and are suitable for the core. On the other hand, dopants such as B_2O_3 and fluorine decrease the refractive index of silica and are suitable for the cladding. The major design issues are related to the refractive-index profile, the amount of dopants, and the core and cladding dimensions [77]–[81]. The diameter of the outermost cladding layer has the standard value of $125 \mu\text{m}$ for all communication-grade silica fibers.

Figure 2.19 shows typical index profiles that have been used for different kinds of fibers. The top row corresponds to standard fibers which are designed to have minimum dispersion near $1.3 \mu\text{m}$ with a cutoff wavelength in the range 1.1 – $1.2 \mu\text{m}$. The simplest design [Figure 2.19(a)] consists of a pure-silica cladding and a core doped with GeO_2 to obtain $\Delta \approx 3 \times 10^{-3}$. A commonly used variation [Figure 2.19(b)] lowers the cladding index over a region adjacent to the core by doping it with fluorine. It is also possible to have an undoped core by using a design shown in Fig 2.20(c). The fibers of this kind are referred to as doubly clad or *depressed-cladding fibers* [77]. They are also called W fibers, reflecting the shape of the index profile. The bottom row in Figure 2.19 shows three index profiles used for dispersion-shifted fibers for which the zero-dispersion wavelength is chosen in the range 1.45 – $1.60 \mu\text{m}$ (see Table 2.1). A triangular index profile with a depressed or raised cladding is often used for this purpose [78]–[80]. The

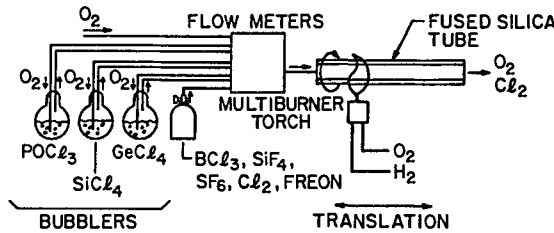
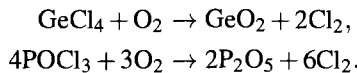


Figure 2.20: MCVD process commonly used for fiber fabrication. (After Ref. [82]; ©1985 Academic Press; reprinted with permission.)

refractive indices and the thickness of different layers are optimized to design a fiber with desirable dispersion characteristics [81]. Sometimes as many as four cladding layers are used for dispersion-flattened fibers (see Figure 2.10).

Fabrication of telecommunication-grade silica fibers involves two stages. In the first stage a vapor-deposition method is used to make a *cylindrical preform* with the desired refractive-index profile. The preform is typically 1 m long and 2 cm in diameter and contains core and cladding layers with correct relative dimensions. In the second stage, the preform is drawn into a fiber by using a precision-feed mechanism that feeds the preform into a furnace at the proper speed.

Several methods can be used to make the preform. The three commonly used methods [82]–[84] are modified chemical-vapor deposition (MCVD), outside-vapor deposition (OVD), and vapor-axial deposition (VAD). Figure 2.20 shows a schematic diagram of the MCVD process. In this process, successive layers of SiO_2 are deposited on the inside of a fused silica tube by mixing the vapors of SiCl_4 and O_2 at a temperature of about 1800°C . To ensure uniformity, a multiburner torch is moved back and forth across the tube length using an automatic translation stage. The refractive index of the cladding layers is controlled by adding fluorine to the tube. When a sufficient cladding thickness has been deposited, the core is formed by adding the vapors of GeCl_4 or POCl_3 . These vapors react with oxygen to form the dopants GeO_2 and P_2O_5 :



The flow rate of GeCl_4 or POCl_3 determines the amount of dopant and the corresponding increase in the refractive index of the core. A triangular-index core can be fabricated simply by varying the flow rate from layer to layer. When all layers forming the core have been deposited, the torch temperature is raised to collapse the tube into a solid rod of preform.

The MCVD process is also known as the *inner-vapor-deposition method*, as the core and cladding layers are deposited inside a silica tube. In a related process, known as the *plasma-activated chemical vapor deposition* process [85], the chemical reaction is initiated by a microwave plasma. By contrast, in the OVD and VAD processes the core and cladding layers are deposited on the outside of a rotating mandrel by using the technique of *flame hydrolysis*. The mandrel is removed prior to sintering. The porous soot boule is then placed in a sintering furnace to form a glass boule. The central hole

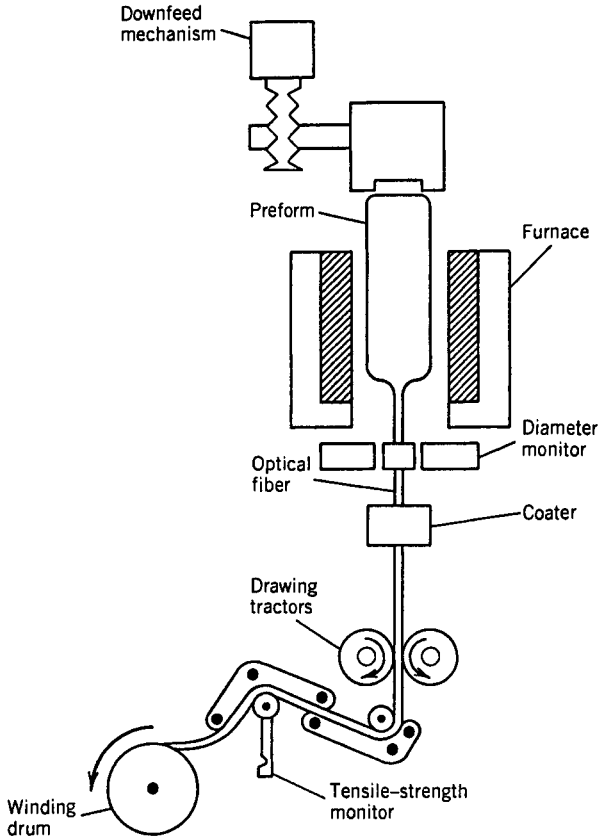


Figure 2.21: Apparatus used for fiber drawing.

allows an efficient way of reducing water vapors through dehydration in a controlled atmosphere of $\text{Cl}_2\text{-He}$ mixture, although it results in a central dip in the index profile. The dip can be minimized by closing the hole during sintering.

The fiber drawing step is essentially the same irrespective of the process used to make the preform [86]. Figure 2.21 shows the drawing apparatus schematically. The preform is fed into a furnace in a controlled manner where it is heated to a temperature of about 2000°C . The melted preform is drawn into a fiber by using a precision-feed mechanism. The fiber diameter is monitored optically by diffracting light emitted by a laser from the fiber. A change in the diameter changes the diffraction pattern, which in turn changes the photodiode current. This current change acts as a signal for a servocontrol mechanism that adjusts the winding rate of the fiber. The fiber diameter can be kept constant to within 0.1% by this technique. A polymer coating is applied to the fiber during the drawing step. It serves a dual purpose, as it provides mechanical protection and preserves the transmission properties of the fiber. The diameter of the coated fiber is typically $250 \mu\text{m}$, although it can be as large as $900 \mu\text{m}$ when multiple coatings are used. The tensile strength of the fiber is monitored during its winding

on the drum. The winding rate is typically 0.2–0.5 m/s. Several hours are required to convert a single preform into a fiber of about 5 km length. This brief discussion is intended to give a general idea. The fabrication of optical fiber generally requires attention to a large number of engineering details discussed in several texts [74]–[75].

2.7.2 Plastic Optical Fibers

The interest in plastic optical fibers grew during the 1990s as the need for cheaper fibers capable of transmitting data over short distances (typically <1 km) became evident [87]–[95]. Such fibers have a relatively large core (diameter as large as 1 mm), resulting in a high numerical aperture and high coupling efficiency, but they exhibit high losses (typically exceeding 20 dB/km). For this reason, they are used to transmit data at bit rates of up to 10 Gb/s over short distances (1 km or less). In a 1996 demonstration, a 10-Gb/s signal was transmitted over 0.5 km with a bit-error rate of less than 10^{-11} [88]. Graded-index plastic optical fibers provide an ideal solution for transferring data among computers and are becoming increasingly important for the Gigabit Ethernet and other Internet-related applications requiring bit rates in excess of 1 Gb/s.

As the name implies, plastic optical fibers use plastics in the form of organic polymers for making both the core and the cladding. The commonly used polymers for this purpose are polymethyl methacrylate (PMMA), polystyrene, polycarbonate, and an amorphous fluorinated polymer poly(perfluoro-butenevinyl ether), or PFBVE, known commercially as CYTOP [92]. The PMMA plastic was used to make step-index fibers as early as 1968. By 1995, the technology had advanced enough that it was possible to make graded-index plastic fibers with a relatively large bandwidth [87]. Since then, considerable progress has been made in making new types of plastic fibers with relatively low losses even in the wavelength region near $1.3\text{ }\mu\text{m}$ [91]–[95]. The core diameter of plastic fibers can vary from $10\text{ }\mu\text{m}$ to 1 mm depending on the application. In the case of low-cost applications, the core size is typically $120\text{ }\mu\text{m}$, while the cladding diameter approaches $200\text{ }\mu\text{m}$.

Manufacturing of modern plastic fibers follows the same two-step process used for silica fibers in the sense that a preform is prepared first with the correct refractive-index profile and is then converted into the fiber form. An important technique used for making the preform for graded-index plastic fibers is known as the interfacial gel polymerization method [87]. In this technique, one begins with a hollow cylinder made of the polymer (such as PMMA) destined to be used for the cladding. This hollow cylinder is filled with a mixture of the monomer from which the cladding polymer was made, a dopant with higher refractive index than that of the cladding polymer, a chemical compound that helps in initiating the polymerization process, and another chemical known as the chain-transfer agent. The filled cylinder is heated to a temperature close to 95°C and rotated on its axis for a period of up to 24 hours. The polymerization of the core begins near the inner wall of the cylinder because of the so-called gel effect and then gradually moves toward the center of the tube. At the end of the polymerization process, one ends up with a graded-index preform in the form of a solid cylinder.

The fiber-drawing step is identical to that used for silica fibers. The drawing apparatus, similar to that shown in Figure 2.21 is used for this purpose. The main difference is that the melting temperature of plastics is much lower than that of silica (about 200°C

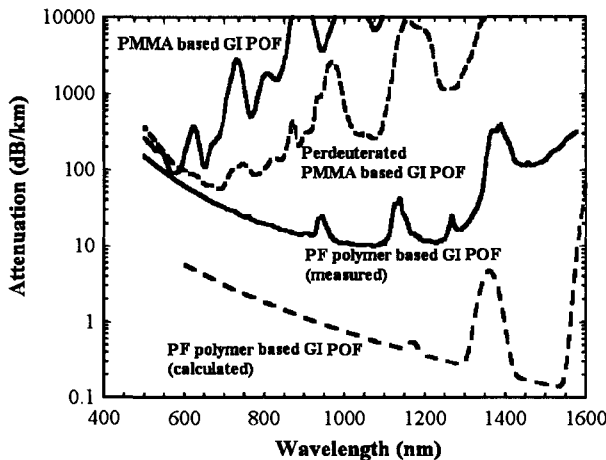


Figure 2.22: Loss spectra of several plastic optical fibers. The dotted curve shows the theoretical limit. (After Ref. [94]; ©2006 IEEE.)

in place of 1800°C). The fiber diameter is continuously monitored using a suitable optical technique, and another plastic coating is applied to the fiber. This top plastic coating protects the fiber against microbending and facilitates its handling.

Figure 2.22 shows the loss spectra of several plastic fibers. A PMMA fiber exhibits losses that typically exceed 100 dB. In contrast, losses of modern PFBVE fibers remain close to 20 dB/km over a wide wavelength range extending from 800 to 1,300 nm and have the potential of being reduced to below 10 dB/km with further optimization. Similar to the case of silica fibers, material absorption can be divided into intrinsic and extrinsic categories. Intrinsic absorption losses in plastic fibers result from the vibrational modes of various molecular bonds within the organic polymer used to make the fiber. Even though the vibrational frequencies of these modes lie in the wavelength region beyond $2\ \mu\text{m}$, their harmonics introduce considerable losses for all plastic fibers even in the near-infrared and visible region. Extrinsic absorption is related to the presence of impurities within the fiber core. Transition-metal impurities such as Fe, Co, Ni, Mn, and Cr absorb strongly in the wavelength range $0.6\text{--}1.6\ \mu\text{m}$. Even a trace amount as small as a few parts per billion can add losses in excess of 10 dB/km. Similar to the case of silica fibers, any residual water vapor results in a strong peak near 1,390 nm. This problem is less severe for PFBVE fibers because fluoropolymers do not absorb water easily.

2.7.3 Cables and Connectors

Cabling of optical fibers is necessary to protect them from deterioration during transportation and installation [96]. Cable design depends on the type of application. For some applications it may be enough to buffer the fiber by placing it inside a plastic jacket. For others the cable must be made mechanically strong by using strengthening elements such as steel rods.

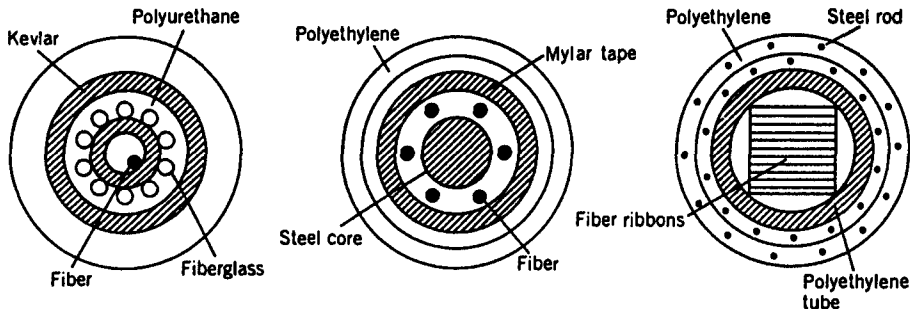


Figure 2.23: Typical designs for heavy-duty fiber cables.

A light-duty cable is made by surrounding the fiber by a buffer jacket of hard plastic. A tight jacket can be provided by applying a buffer plastic coating of 0.5–1 mm thickness on top of the primary coating applied during the drawing process. In an alternative approach the fiber lies loosely inside a plastic tube. Microbending losses are nearly eliminated in this loose-tube construction, since the fiber can adjust itself within the tube. This construction can also be used to make multifiber cables by using a slotted tube with a different slot for each fiber.

Heavy-duty cables, needed for submarine applications among other things, use steel or a strong polymer such as Kevlar to provide the mechanical strength. Figure 2.23 shows schematically three kinds of cables. In the loose-tube construction, fiberglass rods embedded in polyurethane and a Kevlar jacket provide the necessary mechanical strength (left drawing). The same design can be extended to multifiber cables by placing several loose-tube fibers around a central steel core (middle drawing). When a large number of fibers need to be placed inside a single cable, a ribbon cable is used (right drawing). The ribbon is manufactured by packaging typically 12 fibers between two polyester tapes. Several ribbons are then stacked into a rectangular array that is placed inside a polyethylene tube. The mechanical strength is provided by using steel rods in the two outermost polyethylene jackets. The outer diameter of such fiber cables is typically in the range of 1 to 1.5 cm.

Connectors are needed to use optical fibers in any actual lightwave system. They can be divided into two categories. A permanent joint between two fibers is known as a fiber splice, and a detachable connection between them is realized by using a fiber connector. Connectors are used to link fiber cable with the transmitter (or the receiver), while splices are used to join two fiber segments permanently. The main issue in the use of splices and connectors is related to the loss. Some power is always lost, as the two fiber ends are never perfectly aligned in practice. Splice losses below 0.1 dB are routinely realized by using the technique of fusion splicing [97]. Connector losses are generally larger. State-of-the-art connectors provide an average loss of about 0.3 dB [98]. The technology behind the design of splices and connectors is quite sophisticated. For details, the reader is referred to Ref. [99], a book devoted entirely to this issue.

Problems

- 2.1** A multimode fiber with a 50- μm core diameter is designed to limit the intermodal dispersion to 10 ns/km. What is the numerical aperture of this fiber? What is the limiting bit rate for transmission over 10 km at 0.88 μm ? Use 1.45 for the refractive index of the cladding.
- 2.2** Use the ray equation in the paraxial approximation [Eq. (2.1.8)] to prove that intermodal dispersion is zero for a graded-index fiber with a quadratic index profile.
- 2.3** Use Maxwell's equations to express the field components E_ρ , E_ϕ , H_ρ , and H_ϕ in terms of E_z and H_z and obtain Eqs. (2.2.27)–(2.2.30).
- 2.4** Derive the eigenvalue equation (2.2.31) by matching the boundary conditions at the core–cladding interface of a step-index fiber.
- 2.5** A single-mode fiber has an index step $n_1 - n_2 = 0.005$. Calculate the core radius if the fiber has a cutoff wavelength of 1 μm . Estimate the spot size (FWHM) of the fiber mode and the fraction of the mode power inside the core when this fiber is used at 1.3 μm . Use $n_1 = 1.45$.
- 2.6** A 1.55- μm unchirped Gaussian pulse of 100-ps width (FWHM) is launched into a single-mode fiber. Calculate its FWHM after 50 km if the fiber has a dispersion of 16 ps/(km-nm). Neglect the source spectral width.
- 2.7** Derive an expression for the confinement factor Γ of single-mode fibers defined as the fraction of the total mode power contained inside the core. Use the Gaussian approximation for the fundamental fiber mode. Estimate Γ for $V = 2$.
- 2.8** A single-mode fiber is measured to have $\lambda^2(d^2n/d\lambda^2) = 0.02$ at 0.8 μm . Calculate the dispersion parameters β_2 and D .
- 2.9** Show that a chirped Gaussian pulse is compressed initially inside a single-mode fiber when $\beta_2 C < 0$. Derive expressions for the minimum width and the fiber length at which the minimum occurs.
- 2.10** Estimate the limiting bit rate for a 60-km single-mode fiber link at 1.3- and 1.55- μm wavelengths assuming transform-limited, 50-ps (FWHM) input pulses. Assume that $\beta_2 = 0$ and $-20 \text{ ps}^2/\text{km}$ and $\beta_3 = 0.1 \text{ ps}^3/\text{km}$ and 0 at 1.3- and 1.55- μm wavelengths, respectively. Also assume that $V_\omega \ll 1$.
- 2.11** A 0.88- μm communication system transmits data over a 10-km single-mode fiber by using 10-ns (FWHM) pulses. Determine the maximum bit rate if the LED has a spectral FWHM of 30 nm. Use $D = -80 \text{ ps}/(\text{km-nm})$.
- 2.12** Use Eq. (2.4.23) to prove that the bit rate of an optical communication system operating at the zero-dispersion wavelength is limited by $BL|S|\sigma_\lambda^2 < 1/\sqrt{8}$, where $S = dD/d\lambda$ and σ_λ is the RMS spectral width of the Gaussian source spectrum. Assume that $C = 0$ and $V_\omega \gg 1$ in the general expression of the output pulse width.
- 2.13** Repeat Problem 2.12 for the case of a single-mode semiconductor laser for which $V_\omega \ll 1$ and show that the bit rate is limited by $B(|\beta_3|L)^{1/3} < 0.324$. What is the limiting bit rate for $L = 100 \text{ km}$ if $\beta_3 = 0.1 \text{ ps}^3/\text{km}$?

- 2.14** An optical communication system is operating with chirped Gaussian input pulses. Assume that $\beta_3 = 0$ and $V_\phi \ll 1$ in Eq. (2.4.23) and obtain a condition on the bit rate in terms of the parameters C , β_2 , and L .
- 2.15** A $1.55\text{-}\mu\text{m}$ optical communication system operating at 5 Gb/s is using Gaussian pulses of width 100 ps (FWHM) chirped such that $C = -6$. What is the dispersion-limited maximum fiber length? How much will it change if the pulses were unchirped? Neglect laser linewidth and assume that $\beta_2 = -20 \text{ ps}^2/\text{km}$.
- 2.16** A $1.3\text{-}\mu\text{m}$ lightwave system uses a 50-km fiber link and requires at least $0.3 \mu\text{W}$ at the receiver. The fiber loss is 0.5 dB/km. Fiber is spliced every 5 km and has two connectors of 1-dB loss at both ends. Splice loss is only 0.2 dB. Determine the minimum power that must be launched into the fiber.
- 2.17** A $1.55\text{-}\mu\text{m}$ continuous-wave signal with 6-dBm power is launched into a fiber with $50\text{-}\mu\text{m}^2$ effective mode area. After what fiber length would the nonlinear phase shift induced by SPM become 2π ? Assume $\bar{n}_2 = 2.6 \times 10^{-20} \text{ m}^2/\text{W}$ and neglect fiber losses.
- 2.18** Calculate the threshold power for stimulated Brillouin scattering for a 50-km fiber link operating at $1.3 \mu\text{m}$ and having a loss of 0.5 dB/km. How much does the threshold power change if the operating wavelength is changed to $1.55 \mu\text{m}$, where the fiber loss is only 0.2 dB/km? Assume that $A_{\text{eff}} = 50 \mu\text{m}^2$ and $g_B = 5 \times 10^{-11} \text{ m/W}$ at both wavelengths.
- 2.19** Calculate the power launched into a 40-km-long single-mode fiber for which the SPM-induced nonlinear phase shift becomes 180° . Assume $\lambda = 1.55 \mu\text{m}$, $A_{\text{eff}} = 40 \mu\text{m}^2$, $\alpha = 0.2 \text{ dB/km}$, and $\bar{n}_2 = 2.6 \times 10^{-20} \text{ m}^2/\text{W}$.
- 2.20** Find the maximum frequency shift occurring because of the SPM-induced chirp imposed on a Gaussian pulse of 20-ps width (FWHM) and 5-mW peak power after it has propagated 100 km. Use the fiber parameters of the preceding problem but assume $\alpha = 0$.

References

- [1] J. Tyndall, *Proc. Roy. Inst.* **1**, 446 (1854).
- [2] J. L. Baird, British Patent 285,738 (1927).
- [3] C. W. Hansell, U.S. Patent 1,751,584 (1930).
- [4] H. Lamm, *Z. Instrumentenk.* **50**, 579 (1930).
- [5] A. C. S. van Heel, *Nature* **173**, 39 (1954).
- [6] B. I. Hirschowitz, L. E. Curtiss, C. W. Peters, and H. M. Pollard, *Gastro-enterology* **35**, 50 (1958).
- [7] N. S. Kapany, *J. Opt. Soc. Am.* **49**, 779 (1959).
- [8] N. S. Kapany, *Fiber Optics: Principles and Applications*, Academic Press, San Diego, CA, 1967.
- [9] K. C. Kao and G. A. Hockham, *Proc. IEE* **113**, 1151 (1966); A. Werts, *Onde Electr.* **45**, 967 (1966).
- [10] F. P. Kapron, D. B. Keck, and R. D. Maurer, *Appl. Phys. Lett.* **17**, 423 (1970).

- [11] T. Miya, Y. Terunuma, T. Hosaka, and T. Miyoshita, *Electron. Lett.* **15**, 106 (1979).
- [12] M. J. Adams, *An Introduction to Optical Waveguides*, Wiley, New York, 1981.
- [13] T. Okoshi, *Optical Fibers*, Academic Press, San Diego, CA, 1982.
- [14] A. W. Snyder and J. D. Love, *Optical Waveguide Theory*, Chapman & Hall, London, 1983.
- [15] L. B. Jeunhomme, *Single-Mode Fiber Optics*, Marcel Dekker, New York, 1990.
- [16] E. G. Neumann, *Single-Mode Fibers*, Springer, New York, 1988.
- [17] D. Marcuse, *Theory of Dielectric Optical Waveguides*, 2nd ed., Academic Press, San Diego, CA, 1991.
- [18] G. Cancellieri, *Single-Mode Optical Fibers*, Pergamon Press, Elmsford, NY, 1991.
- [19] J. A. Buck, *Fundamentals of Optical Fibers*, 2nd ed., Wiley, Hoboken, NJ, 2004.
- [20] M. Born and E. Wolf, *Principles of Optics*, 7th ed., Cambridge University Press, New York, 1999.
- [21] J. Gower, *Optical Communication Systems*, 2nd ed., Prentice Hall, London, 1993.
- [22] P. Diament, *Wave Transmission and Fiber Optics*, Macmillan, New York, 1990, Chap. 3.
- [23] G. P. Agrawal, *Nonlinear Fiber Optics*, 4th ed., Academic Press, San Diego, CA, 2001.
- [24] M. Abramowitz and I. A. Stegun, Eds., *Handbook of Mathematical Functions*, Dover, New York, 1970, Chap. 9.
- [25] D. Gloge, *Appl. Opt.* **10**, 2252 (1971); **10**, 2442 (1971).
- [26] D. B. Keck, in *Fundamentals of Optical Fiber Communications*, M. K. Barnoski, Ed., Academic Press, San Diego, CA, 1981.
- [27] D. Marcuse, *J. Opt. Soc. Am.* **68**, 103 (1978).
- [28] I. H. Malitson, *J. Opt. Soc. Am.* **55**, 1205 (1965).
- [29] L. G. Cohen, C. Lin, and W. G. French, *Electron. Lett.* **15**, 334 (1979).
- [30] C. T. Chang, *Electron. Lett.* **15**, 765 (1979); *Appl. Opt.* **18**, 2516 (1979).
- [31] L. G. Cohen, W. L. Mammel, and S. Lumish, *Opt. Lett.* **7**, 183 (1982).
- [32] S. J. Jang, L. G. Cohen, W. L. Mammel, and M. A. Shaifi, *Bell Syst. Tech. J.* **61**, 385 (1982).
- [33] V. A. Bhagavatula, M. S. Spotz, W. F. Love, and D. B. Keck, *Electron. Lett.* **19**, 317 (1983).
- [34] P. Bachamann, D. Leers, H. Wehr, D. V. Wiechert, J. A. van Steenwijk, D. L. A. Tjaden, and E. R. Wehrhahn, *J. Lightwave Technol.* **4**, 858 (1986).
- [35] B. J. Ainslie and C. R. Day, *J. Lightwave Technol.* **4**, 967 (1986).
- [36] C. D. Poole and J. Nagel, in *Optical Fiber Telecommunications III*, Vol. A, I. P. Kaminow and T. L. Koch, Eds., Academic Press, San Diego, CA, 1997, Chap. 6.
- [37] F. Bruyère, *Opt. Fiber Technol.* **2**, 269 (1996).
- [38] P. K. A. Wai and C. R. Menyuk, *J. Lightwave Technol.* **14**, 148 (1996).
- [39] M. Karlsson, *Opt. Lett.* **23**, 688 (1998).
- [40] G. J. Foschini, R. M. Jopson, L. E. Nelson, and H. Kogelnik, *J. Lightwave Technol.* **17**, 1560 (1999).
- [41] M. Midrio, *J. Opt. Soc. Am. B* **17**, 169 (2000).
- [42] B. Huttner, C. Geiser, and N. Gisin, *IEEE J. Sel. Topics Quantum Electron.* **6**, 317 (2000).
- [43] M. Shtaif and A. Mecozzi, *Opt. Lett.* **25**, 707 (2000).
- [44] M. Karlsson, J. Brentel, and P. A. Andrekson, *J. Lightwave Technol.* **18**, 941 (2000).
- [45] Y. Li and A. Yariv, *J. Opt. Soc. Am. B* **17**, 1821 (2000).
- [46] J. M. Fini and H. A. Haus, *IEEE Photon. Technol. Lett.* **13**, 124 (2001).
- [47] R. Khosravani and A. E. Willner, *IEEE Photon. Technol. Lett.* **13**, 296 (2001).
- [48] D. Marcuse, *Appl. Opt.* **19**, 1653 (1980); **20**, 3573 (1981).

- [49] M. Miyagi and S. Nishida, *Appl. Opt.* **18**, 678 (1979); **18**, 2237 (1979).
- [50] G. P. Agrawal and M. J. Potasek, *Opt. Lett.* **11**, 318 (1986).
- [51] M. Schwartz, *Information, Transmission, Modulation, and Noise*, 4th ed., McGraw-Hill, New York, 1990, Chap. 2.
- [52] M. J. Bennett, *IEE Proc.* **130**, Pt. H, 309 (1983).
- [53] D. Gloge, K. Ogawa, and L. G. Cohen, *Electron. Lett.* **16**, 366 (1980).
- [54] G. A. Thomas, B. L. Shraiman, P. F. Glodis, and M. J. Stephan, *Nature* **404**, 262 (2000).
- [55] P. Kloczek and G. H. Sigel, Jr., *Infrared Fiber Optics*, Vol. TT2, SPIE, Bellingham, WA, 1989.
- [56] T. Katsuyama and H. Matsumura, *Infrared Optical Fibers*, Bristol, Philadelphia, 1989.
- [57] J. A. Harrington, Ed., *Infrared Fiber Optics*, SPIE, Bellingham, WA, 1990.
- [58] M. F. Churbanov, *J. Non-Cryst. Solids* **184**, 25 (1995).
- [59] E. A. J. Marcatili, *Bell Syst. Tech. J.* **48**, 2103 (1969).
- [60] W. B. Gardner, *Bell Syst. Tech. J.* **54**, 457 (1975).
- [61] D. Marcuse, *Bell Syst. Tech. J.* **55**, 937 (1976).
- [62] K. Petermann, *Electron. Lett.* **12**, 107 (1976); *Opt. Quantum Electron.* **9**, 167 (1977).
- [63] K. Tanaka, S. Yamada, M. Sumi, and K. Mikoshiba, *Appl. Opt.* **16**, 2391 (1977).
- [64] W. A. Gambling, H. Matsumura, and C. M. Rodgal, *Opt. Quantum Electron.* **11**, 43 (1979).
- [65] R. W. Boyd, *Nonlinear Optics*, 3rd ed., Academic Press, Boston, 2008.
- [66] R. G. Smith, *Appl. Opt.* **11**, 2489 (1972).
- [67] R. H. Stolen, E. P. Ippen, and A. R. Tynes, *Appl. Phys. Lett.* **20**, 62 (1972).
- [68] E. P. Ippen and R. H. Stolen, *Appl. Phys. Lett.* **21**, 539 (1972).
- [69] D. Cotter, *Electron. Lett.* **18**, 495 (1982); *J. Opt. Commun.* **4**, 10 (1983).
- [70] R. W. Tkach, A. R. Chraplyvy, and R. M. Derosier, *Electron. Lett.* **22**, 1011 (1986).
- [71] R. H. Stolen and C. Lin, *Phys. Rev. A* **17**, 1448 (1978).
- [72] A. R. Chraplyvy, D. Marcuse, and P. S. Henry, *J. Lightwave Technol.* **2**, 6 (1984).
- [73] M. J. Potasek and G. P. Agrawal, *Electron. Lett.* **22**, 759 (1986).
- [74] T. Li, Ed., *Optical Fiber Communications*, Vol. 1, Academic Press, San Diego, CA, 1985, Chaps. 1–4.
- [75] T. Izawa and S. Sudo, *Optical Fibers: Materials and Fabrication*, Kluwer Academic, Boston, 1987.
- [76] D. J. DiGiovanni, S. K. Das, L. L. Blyler, W. White, R. K. Boncek, and S. E. Golowich, in *Optical Fiber Telecommunications*, Vol. 4A, I. Kaminow and T. Li, Eds., Academic Press, San Diego, CA, 2002, Chap. 2.
- [77] M. Monerie, *IEEE J. Quantum Electron.* **18**, 535 (1982); *Electron. Lett.* **18**, 642 (1982).
- [78] M. A. Saifi, S. J. Jang, L. G. Cohen, and J. Stone, *Opt. Lett.* **7**, 43 (1982).
- [79] Y. W. Li, C. D. Hussey, and T. A. Birks, *J. Lightwave Technol.* **11**, 1812 (1993).
- [80] R. Lundin, *Appl. Opt.* **32**, 3241 (1993); *Appl. Opt.* **33**, 1011 (1994).
- [81] S. P. Survaiya and R. K. Shevgaonkar, *IEEE Photon. Technol. Lett.* **8**, 803 (1996).
- [82] S. R. Nagel, J. B. MacChesney, and K. L. Walker, in *Optical Fiber Communications*, Vol. 1, T. Li, Ed., Academic Press, San Diego, CA, 1985, Chap. 1.
- [83] A. J. Morrow, A. Sarkar, and P. C. Schultz, in *Optical Fiber Communications*, Vol. 1, T. Li, Ed., Academic Press, San Diego, CA, 1985, Chap. 2.
- [84] N. Niizeki, N. Ingaki, and T. Edahiro, in *Optical Fiber Communications*, Vol. 1, T. Li, Ed., Academic Press, San Diego, CA, 1985, Chap. 3.
- [85] P. Geittner, H. J. Hagemann, J. Warnier, and H. Wilson, *J. Lightwave Technol.* **4**, 818 (1986).

- [86] F. V. DiMarcello, C. R. Kurkjian, and J. C. Williams, in *Optical Fiber Communications*, Vol. 1, T. Li, Ed., Academic Press, San Diego, CA, 1985, Chap. 4.
- [87] Y. Koike, T. Ishigure, and E. Nihei, *J. Lightwave Technol.* **13**, 1475 (1995).
- [88] U. Fiedler, G. Reiner, P. Schnitzer, and K. J. Ebeling, *IEEE Photon. Technol. Lett.* **8**, 746 (1996).
- [89] W. R. White, M. Dueser, W. A. Reed, and T. Onishi, *IEEE Photon. Technol. Lett.* **11**, 997 (1999).
- [90] T. Ishigure, Y. Koike, and J. W. Fleming, *J. Lightwave Technol.* **18**, 178 (2000).
- [91] A. Weinert, *Plastic Optical Fibers: Principles, Components, and Installation*, Wiley, New York, 2000.
- [92] J. Zubia and J. Arrue, *Opt. Fiber Technol.* **7**, 101 (2001).
- [93] W. Daum, J. Krauser, P. E. Zamzow, and O. Ziemann, *POF—Plastic Optical Fibers for Data Communication*, Springer, New York, 2002.
- [94] Y. Koike and T. Ishigure, *J. Lightwave Technol.* **24**, 4541 (2006).
- [95] Y. Koike and S. Takahashi, in *Optical Fiber Telecommunications*, Vol. 5A, I. P. Kaminow, T. Li, and A. E. Willner, Eds., Academic Press, Boston, 2008, Chap. 16.
- [96] H. Murata, *Handbook of Optical Fibers and Cables*, Marcel Dekker, New York, 1996.
- [97] S. C. Mettler and C. M. Miller, in *Optical Fiber Telecommunications II*, S. E. Miller and I. P. Kaminow, Eds., Academic Press, San Diego, CA, 1988, Chap. 6.
- [98] W. C. Young and D. R. Frey, in *Optical Fiber Telecommunications II*, S. E. Miller and I. P. Kaminow, Eds., Academic Press, San Diego, CA, 1988, Chap. 7.
- [99] C. M. Miller, S. C. Mettler, and I. A. White, *Optical Fiber Splices and Connectors*, Marcel Dekker, New York, 1986.

Chapter 3

Optical Transmitters

The role of the optical transmitter is to convert an electrical input signal into the corresponding optical signal and then launch it into the optical fiber serving as a communication channel. The major component of optical transmitters is an optical source. Fiber-optic communication systems employ semiconductor optical sources such as light-emitting diodes (LEDs) and semiconductor lasers because of several advantages offered by them. These advantages include compact size, high efficiency, good reliability, right wavelength range, small emissive area, and possibility of direct modulation at relatively high frequencies. The use of semiconductor lasers became practical after 1970, when continuous operation of such lasers at room temperature became possible [1]. Since then, semiconductor lasers have been developed extensively. They are also known as laser diodes or injection lasers, and their properties have been discussed in several recent books [2]–[12]. This chapter is devoted to LEDs and semiconductor lasers with emphasis on their applications in lightwave systems. After introducing the basic concepts in Section 3.1, we describe in Section 3.2 the techniques used for forcing a semiconductor laser to operate in a single mode. The steady-state, modulation, and noise characteristics of semiconductor lasers are discussed in Section 3.3. The encoding of data through direct or external modulation is the focus of Section 3.4. The use of LEDs as an optical source is discussed in Section 3.5. The design issues related to optical transmitters are covered in Section 3.6.

3.1 Semiconductor Laser Physics

Under normal conditions, all materials absorb light rather than emit it. The absorption process can be understood by referring to Figure 3.1(a), where the energy levels E_1 and E_2 correspond to the ground state and the excited state of atoms of the absorbing medium. If the photon energy $\hbar\nu$ of the incident light of frequency ν is about the same as the energy difference $E_g = E_2 - E_1$, the photon is absorbed by the atom, which ends up in the excited state. Incident light is attenuated as a result of many such absorption events occurring inside the medium.

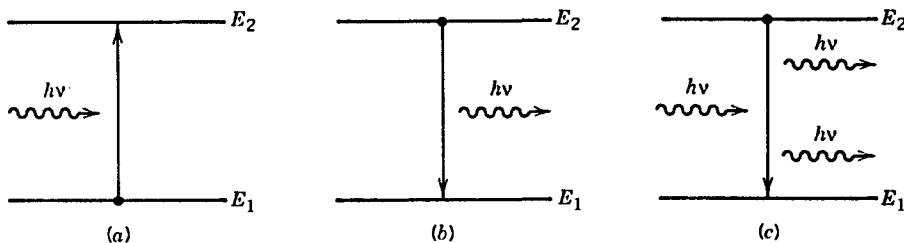


Figure 3.1: Three fundamental processes occurring between the two energy states of an atom: (a) absorption; (b) spontaneous emission; and (c) stimulated emission.

3.1.1 Spontaneous and Stimulated Emissions

If an atom is in the excited state, it eventually returns to its normal “ground” state and emits light in the process. Light emission can occur through two fundamental processes known as *spontaneous emission* and *stimulated emission*. Both are shown schematically in Figure 3.1. In the case of spontaneous emission, photons are emitted in random directions with no phase relationship among them. Stimulated emission, by contrast, is initiated by an existing photon. The remarkable feature of stimulated emission is that the emitted photon matches the original photon not only in energy (or in frequency), but also in its other characteristics, such as the direction of propagation. All lasers, including semiconductor lasers, emit light through the process of stimulated emission and are said to emit coherent light. In contrast, LEDs emit light through the incoherent process of spontaneous emission.

In a semiconductor laser, atoms participating in the process of stimulated emission are arranged in a crystal lattice. As a result, individual energy levels associated with a single atom merge and form energy bands. The two bands relevant for our discussion are the valence and conduction bands representing, respectively, the topmost band filled with electrons and the first band that is nearly empty of electrons. It is common to represent these bands in an $E-k$ diagram shown schematically in Figure 3.2, where $k = p/\hbar$ is the wave number of an electron with momentum p and energy E . If some of the electrons are raised to the conduction band through electrical pumping, the empty states left behind in the valence band represent holes. Light is produced when an electron near the bottom of the conduction band recombines with a hole in the valence band. The photon emitted during this recombination process carries an energy $h\nu \approx E_g$, where E_g is the bandgap energy of the semiconductor. Using $\nu = c/\lambda$, one can conclude that a semiconductor laser can operate only in a certain wavelength region near $\lambda = hc/E_g$. For a semiconductor laser to emit light near $1.55\text{ }\mu\text{m}$, its bandgap must be about 0.8 eV wide.

Semiconductor lasers operating in the wavelength range $1.3\text{--}1.6\text{ }\mu\text{m}$ were developed during the 1980s and are used almost exclusively for fiber-optic communications. They make use of a quaternary compound $\text{In}_{1-x}\text{Ga}_x\text{As}_y\text{P}_{1-y}$ that is grown in a layer form on InP substrates using a suitable epitaxial growth technique. The lattice constant of each layer should remain matched to that of InP to maintain a well-defined lattice structure so that defects are not formed at the interfaces between any two layers with

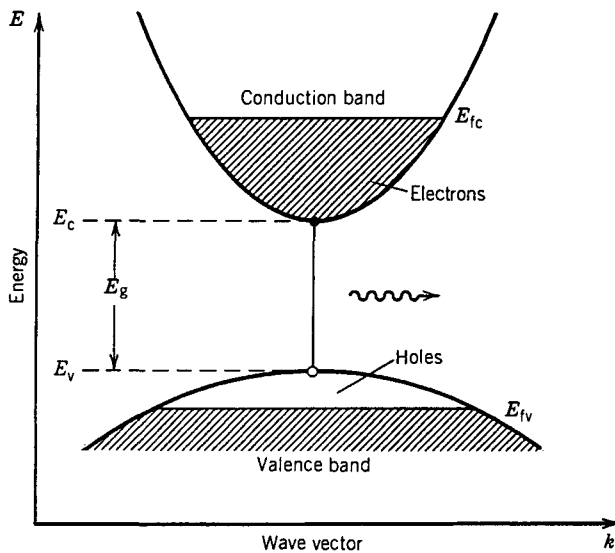


Figure 3.2: Conduction and valence bands of a semiconductor. Electrons in the conduction band and holes in the valence band recombine to emit photons.

different bandgaps. The fractions x and y cannot be chosen arbitrarily but are related as $x/y = 0.45$ to ensure matching of the lattice constant. The bandgap of the quaternary compound can be expressed in terms of y only by the empirical relation [2]

$$E_g(y) = 1.35 - 0.72y + 0.12y^2, \quad (3.1.1)$$

where $0 \leq y \leq 1$. The smallest bandgap occurs for $y = 1$. The corresponding ternary compound $\text{In}_{0.55}\text{Ga}_{0.45}\text{As}$ emits light near $1.65 \mu\text{m}$ ($E_g = 0.75 \text{ eV}$). By a suitable choice of the mixing fractions x and y , $\text{In}_{1-x}\text{Ga}_x\text{As}_y\text{P}_{1-y}$ lasers can be designed to operate in the wide wavelength range $1.0\text{--}1.65 \mu\text{m}$ that includes the region $1.3\text{--}1.6 \mu\text{m}$ important for optical communication systems.

3.1.2 Nonradiative Recombination

In any semiconductor, electrons and holes can also recombine nonradiatively. Nonradiative recombination mechanisms include recombination at traps or defects, surface recombination, and the Auger recombination [3]. The last mechanism is especially important for semiconductor lasers emitting light in the wavelength range of 1.3 to $1.6 \mu\text{m}$ because of a relatively small bandgap of the active layer [2]. In the Auger recombination process, the energy released during electron–hole recombination is given to another electron or hole as kinetic energy rather than producing light.

From the standpoint of device operation, all nonradiative processes are harmful, as they reduce the number of electron–hole pairs that emit light. Their effect is quantified

through the *internal quantum efficiency*, defined as

$$\eta_{\text{int}} = \frac{\tau_{\text{nr}}}{\tau_{\text{rr}} + \tau_{\text{nr}}}. \quad (3.1.2)$$

where τ_{rr} and τ_{nr} are the radiative and nonradiative recombination times associated with the carriers. These two recombination times vary from semiconductor to semiconductor. In general, τ_{rr} and τ_{nr} are comparable for direct-bandgap semiconductors, whereas τ_{nr} is a small fraction ($\sim 10^{-5}$) of τ_{rr} for semiconductors with an indirect bandgap. A semiconductor is said to have a direct bandgap if the conduction-band minimum and the valence-band maximum occur for the same value of the electron wave number (see Figure 3.2). The probability of radiative recombination is large in such semiconductors, since it is easy to conserve both energy and momentum during electron–hole recombination. By contrast, indirect-bandgap semiconductors require the assistance of a phonon for conserving momentum during electron–hole recombination. This feature reduces the probability of radiative recombination and increases τ_{rr} considerably compared with τ_{nr} in such semiconductors. As evident from Eq. (3.1.2), $\eta_{\text{int}} \ll 1$ under such conditions. Typically, $\eta_{\text{int}} \sim 10^{-5}$ for Si and Ge, the two semiconductors commonly used for electronic devices. Both are not suitable for optical sources because of their indirect bandgap. For direct-bandgap semiconductors such as GaAs and InP, $\eta_{\text{int}} \approx 0.5$ and approaches 1 when stimulated emission dominates.

It is useful to define a quantity known as the *carrier lifetime* τ_c such that it represents the total recombination time of charged carriers in the absence of stimulated recombination. It is defined by the relation

$$1/\tau_c = 1/\tau_{\text{rr}} + 1/\tau_{\text{nr}}. \quad (3.1.3)$$

In general, τ_c depends on the carrier density N if Auger recombination is not negligible. It is often expressed in the form $\tau_c^{-1} = A_{\text{nr}} + BN + CN^2$, where A_{nr} is the nonradiative coefficient, B is the spontaneous radiative recombination coefficient, and C is the Auger coefficient.

3.1.3 Optical Gain

Semiconductor lasers are pumped electrically using a p – n junction. Such a pumping can be realized in practice by using a three-layer structure in which a central core layer is sandwiched between the p -type and n -type cladding layers, both of which are doped so heavily that the Fermi-level separation $E_{fc} - E_{fv}$ exceeds the bandgap energy E_g (see Figure 3.2) under forward biasing of the p – n junction. Figure 3.3 shows the three-layer structure of a typical semiconductor laser together with its physical dimensions. The whole laser chip is typically under 1 mm in all three dimensions, resulting in an ultracompact design.

The central core layer in Figure 3.3 is made of the semiconductor that emits light and is called the “active” layer. The cladding layers are made using a semiconductor whose bandgap is larger than that of the active layer. The bandgap difference between the two semiconductors helps to confine electrons and holes to the active layer. At the same time, the active layer has a slightly larger refractive index than the surrounding cladding layers and acts as a planar waveguide whose number of modes can be

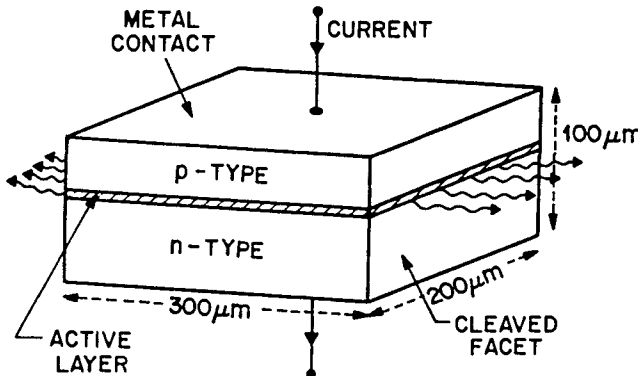


Figure 3.3: Schematic of a broad-area semiconductor laser. The active layer (hatched region) is sandwiched between *p*-type and *n*-type cladding layers with a larger bandgap.

controlled by changing the active-layer thickness. The main point is that such a heterostructure design helps to confine both the injected carriers (electrons and holes) and the light generated within the active layer through electron–hole recombination. A third feature is that the two cladding layers are transparent to the emitted light by virtue of their higher bandgap, thereby resulting in a low-loss structure. These features have made semiconductor lasers practical for a wide variety of applications.

When the injected carrier density in the active layer exceeds a certain value, population inversion is realized and the active region exhibits optical gain. An input signal propagating inside the active layer is then amplified by a factor of $\exp(gL)$, where g is the *gain coefficient* and L is the active-layer length. The calculation of g requires the rates at which photons are absorbed and emitted through stimulated emission and depends on details of the band structure associated with the active material. In general, g is calculated numerically. Figure 3.4(a) shows the gain calculated for a $1.3\text{-}\mu\text{m}$ InGaAsP active layer at different values of the injected carrier density N . For $N = 1 \times 10^{18} \text{ cm}^{-3}$, $g < 0$, as population inversion has not yet occurred. As N increases, g becomes positive over a spectral range that increases with N . The peak value of the gain, g_p , also increases with N , together with a shift of the peak toward higher photon energies. The variation of g_p with N is shown in Figure 3.4(b). For $N > 1.5 \times 10^{18} \text{ cm}^{-3}$, g_p varies almost linearly with N . Figure 3.4 shows that the optical gain in semiconductors increases rapidly once population inversion is realized. It is because of such a high gain that semiconductor lasers can be made with physical dimensions of less than 1 mm.

The nearly linear dependence of g_p on N suggests an empirical approach in which the peak gain is approximated by

$$g_p(N) = \sigma_g(N - N_T), \quad (3.1.4)$$

where N_T is the transparency value of the carrier density and σ_g is the gain cross section; σ_g is also called the *differential gain*. Typical values of N_T and σ_g for InGaAsP lasers are in the range $1.0\text{--}1.5 \times 10^{18} \text{ cm}^{-3}$ and $2\text{--}3 \times 10^{-16} \text{ cm}^2$, respectively [2]. As

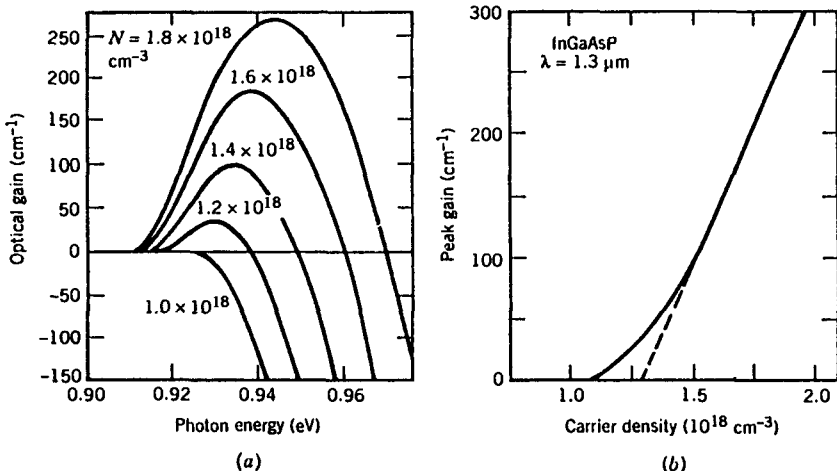


Figure 3.4: (a) Gain spectra at several carrier densities for a 1.3-μm laser. (b) Variation of peak gain g_p with N . Dashed line shows the linear fit in the high-gain region.

seen in Figure 3.4(b), the approximation (3.1.4) is reasonable in the high-gain region where g_p exceeds 100 cm⁻¹; most semiconductor lasers operate in this region. The use of Eq. (3.1.4) simplifies the analysis considerably, as band-structure details do not appear directly. The parameters σ_g and N_T can be estimated from numerical calculations such as those shown in Figure 3.4(b) or can be measured experimentally.

Semiconductor lasers with a larger value of σ_g generally perform better, since the same amount of gain can be realized at a lower carrier density or, equivalently, at a lower injected current. In quantum-well semiconductor lasers, σ_g is typically larger by about a factor of 2. The linear approximation in Eq. (3.1.4) for the peak gain can still be used in a limited range. A better approximation replaces Eq. (3.1.4) with $g_p(N) = g_0[1 + \ln(N/N_0)]$, where $g_p = g_0$ at $N = N_0$ and $N_0 = eN_T \approx 2.718N_T$ by using the definition $g_p = 0$ at $N = N_T$ [3].

3.1.4 Feedback and Laser Threshold

The optical gain alone is not enough for laser operation. The other necessary ingredient is *optical feedback*, which converts any amplifier into an oscillator. In most lasers the feedback is provided by placing the gain medium inside a Fabry-Perot (FP) cavity formed by using two mirrors. Semiconductor lasers do not require external mirrors because the two cleaved facets can act as mirrors (see Figure 3.3) because of a relatively large index difference across the air-semiconductor interface. The facet reflectivity normal to this interface is given by

$$R_m = \left(\frac{n-1}{n+1} \right)^2, \quad (3.1.5)$$

where n is the refractive index of the gain medium. Typically, $n = 3.5$, resulting in 30% facet reflectivity. Even though the FP cavity formed by two cleaved facets is relatively lossy, the gain in a semiconductor laser is large enough that high losses can be tolerated.

A simple way to obtain the threshold condition is to study how the amplitude of an optical mode changes during one round trip inside the FP cavity. Assume that the mode has initially an amplitude A_0 , frequency ν , and propagation constant $\beta = \bar{n}(2\pi\nu)/c$, where \bar{n} is the mode index. After one round trip, its amplitude increases by $\exp[2(g/2)L]$ because of gain (g is the power gain) and its phase changes by $2\beta L$, where L is the length of the laser cavity. At the same time, its amplitude decreases by $\sqrt{R_1 R_2} \exp(-\alpha_{\text{int}}L)$ because of reflection at the laser facets and because of internal losses α_{int} resulting from free-carrier absorption and interface scattering. The facet reflectivities R_1 and R_2 can be different if facets are coated to change their natural reflectivity. In the steady state, the mode should remain unchanged after one round trip, that is,

$$A_0 \exp(gL) \sqrt{R_1 R_2} \exp(-\alpha_{\text{int}}L) \exp(2i\beta L) = A_0. \quad (3.1.6)$$

By equating the amplitude and the phase on two sides, we obtain

$$g = \alpha_{\text{int}} + \frac{1}{2L} \ln \left(\frac{1}{R_1 R_2} \right) = \alpha_{\text{int}} + \alpha_{\text{mir}} = \alpha_{\text{cav}}, \quad (3.1.7)$$

$$2\beta L = 2m\pi \quad \text{or} \quad \nu = \nu_m = mc/2\bar{n}L, \quad (3.1.8)$$

where m is an integer. Equation (3.1.7) shows that the gain g equals total cavity loss α_{cav} at the threshold and beyond. It is important to note that g is not the same as the material gain g_m shown in Figure 3.4. The optical mode extends beyond the active layer while the gain exists only inside it. As a result, $g = \Gamma g_m$, where Γ is the confinement factor of the active region with typical values < 0.4 .

3.1.5 Longitudinal Modes

The phase condition in Eq. (3.1.8) shows that the laser frequency ν must match one of the frequencies in the set ν_m , where m is an integer. These frequencies correspond to the *longitudinal modes* and are determined by the optical length $\bar{n}L$. The spacing $\Delta\nu_L$ between the longitudinal modes is constant. In fact, it is the same as the free spectral range associated with any FP resonator and is given by $\Delta\nu_L = c/2n_g L$ when material dispersion is included [2], where n_g is the group index. Typically, $\Delta\nu_L = 150$ GHz for $L = 250$ μm .

A semiconductor laser generally emits light in several longitudinal modes of the cavity simultaneously. As seen in Figure 3.5, the gain spectrum $g(\omega)$ of semiconductor lasers is wide enough (bandwidth ~ 10 THz) that many longitudinal modes of the FP cavity experience gain simultaneously. The mode closest to the gain peak becomes the dominant mode. Under ideal conditions, the other modes should not reach threshold since their gain always remains less than that of the main mode. In practice, the difference is extremely small (~ 0.1 cm $^{-1}$) and one or two neighboring modes on each side of the main mode carry a significant portion of the laser power together with the main mode. Since each mode propagates inside the fiber at a slightly different speed

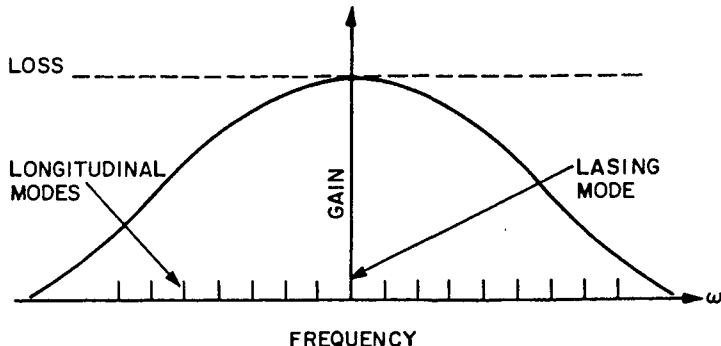


Figure 3.5: Schematic of gain and loss profiles in semiconductor lasers. Vertical bars show the location of longitudinal modes.

because of group-velocity dispersion, the multimode nature of a semiconductor laser often limits the bit rate of lightwave systems operating near $1.55 \mu\text{m}$. Performance can be improved by designing lasers such that they oscillate in a single longitudinal mode. Such lasers are discussed in Section 3.2.

3.1.6 Laser Structures

The simplest structure of a semiconductor laser consists of a thin active layer (with a thickness of $0.1 \mu\text{m}$ or less) sandwiched between the *p*-type and *n*-type cladding layers of another semiconductor with a higher bandgap. Such lasers are called *broad-area* lasers since the current is injected over a relatively broad area covering the entire width of the laser chip (see Figure 3.3). The laser light is emitted from the two cleaved facets in the form of an elliptic spot of dimensions $\sim 1 \times 100 \mu\text{m}^2$. In the transverse direction perpendicular to the junction plane, the spot size is $\sim 1 \mu\text{m}$ because the active layer supports only the fundamental TE_0 and TM_0 modes. In practice, the gain is slightly larger for the TE_0 mode, and the laser light is polarized in the junction plane. Since no confinement mechanism exists in the lateral direction (parallel to the junction plane), emitted light spreads over the entire width of a broad-area laser, resulting in a highly elliptical beam. Such lasers suffer from a number of deficiencies and are rarely used in practice. The major drawbacks are a relatively high threshold current and a spatial pattern that changes in an uncontrollable manner with the current. These problems can be solved by introducing a mechanism for light confinement in the lateral direction.

The light-confinement problem is solved in the so-called *index-guided* semiconductor lasers by introducing an index step Δn_L in the lateral direction so that a rectangular waveguide is formed. Figure 3.6 shows two commonly used designs. In a *ridge-waveguide laser* (Figure 3.6a), a ridge is formed by etching most of the top cladding layer [2]. A silica layer is then deposited to block the current flow so that the current enters only through the ridge. Since the cladding material used for the ridge has a much larger refractive index than silica, the mode index is also higher under the ridge, resulting in an index step $\Delta n_L \sim 0.01$. This index difference guides the optical mode in

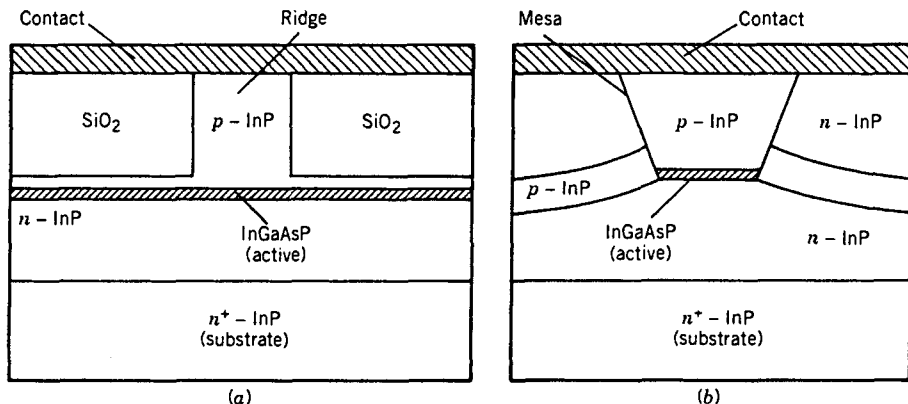


Figure 3.6: Schematic cross section of (a) a ridge-waveguide laser and (b) a buried-heterostructure laser.

the lateral direction. The magnitude of the index step is sensitive to many fabrication details, such as the ridge width and the proximity of the silica layer to the active layer. Although this scheme offers only weak lateral confinement, the relative simplicity of the ridge-waveguide design and the resulting low cost make this design attractive for some applications.

In strongly index-guided semiconductor lasers, the active region is buried on all sides by several layers of lower refractive index (typical dimensions $\sim 0.1 \times 1 \mu\text{m}^2$). Such lasers are called *buried heterostructure* (BH) lasers (see Figure 3.6b). Several different kinds of BH lasers have been developed. They are known under names such as etched-mesa BH, planar BH, double-channel planar BH, and V-grooved or channelled substrate BH lasers, depending on the fabrication method used to realize the laser structure [2]. They all allow a relatively large index step ($\Delta n_L > 0.1$) in the lateral direction and, as a result, permit strong mode confinement. Because of a large built-in index step, the spatial distribution of the emitted light is inherently stable, provided that the laser is designed to support a single spatial mode. In practice, a BH laser operates in a single mode if the active-region width is reduced to below $2 \mu\text{m}$. The spot size still remains elliptical with typical dimensions of $2 \times 1 \mu\text{m}^2$. Because of small spot-size dimensions, the output beam diffracts considerably in both the lateral and transverse directions as it leaves the laser. An elliptic spot size and a large divergence angle make it difficult to couple light into the fiber efficiently. A spot-size converter is sometimes used to improve the coupling efficiency.

3.2 Single-Mode Semiconductor Lasers

As discussed earlier, semiconductor lasers oscillate in several longitudinal modes simultaneously because of a relatively small gain difference ($\sim 0.1 \text{ cm}^{-1}$) between two neighboring modes of the cavity. The resulting spectral width (2–4 nm) is acceptable for some applications but becomes a concern for many others. This section is devoted

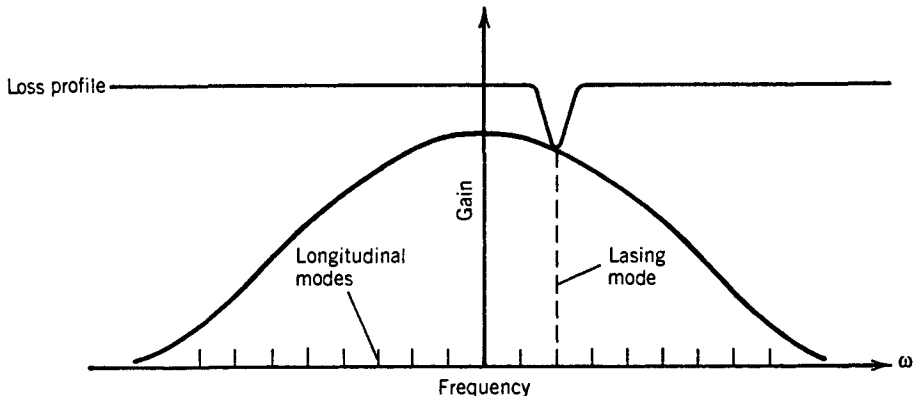


Figure 3.7: Gain and loss profiles for semiconductor lasers oscillating predominantly in a single longitudinal mode.

to techniques that can be used to design semiconductor lasers such that they emit light predominantly in a single longitudinal mode [13]–[20].

The basic idea is to design the laser such that losses are different for different longitudinal modes of the cavity, in contrast with FP lasers whose losses are mode-independent. Figure 3.7 shows the gain and loss profiles schematically for such a laser. The longitudinal mode with the smallest cavity loss reaches threshold first and becomes the dominant mode. Other neighboring modes are discriminated by their higher losses. The power carried by these side modes is usually a small fraction (<1%) of the total emitted power. The performance of a single-mode laser is often characterized by the *mode-suppression ratio* (MSR), defined as $\text{MSR} = P_{\text{mm}}/P_{\text{sm}}$, where P_{mm} is the main-mode power and P_{sm} is the power of the most dominant side mode. The MSR should exceed 1,000 (or 30 dB) for a good single-mode laser.

3.2.1 Distributed Feedback Lasers

Distributed feedback (DFB) semiconductor lasers were developed during the 1980s and are used routinely for WDM lightwave systems [15]–[20]. The feedback in DFB lasers, as the name implies, is not localized at the facets but is distributed throughout the cavity length. This is achieved through an internal built-in grating that leads to a periodic variation of the mode index. Feedback occurs by means of *Bragg diffraction*, a phenomenon that couples the waves propagating in the forward and backward directions. Mode selectivity of the DFB mechanism results from the *Bragg condition*: The coupling occurs only for wavelengths λ_B satisfying

$$\Lambda = m(\lambda_B/2\bar{n}), \quad (3.2.1)$$

where Λ is the grating period, \bar{n} is the average mode index, and the integer m represents the order of Bragg diffraction. The coupling between the forward and backward waves is strongest for the first-order Bragg diffraction ($m = 1$). For a DFB laser operating at

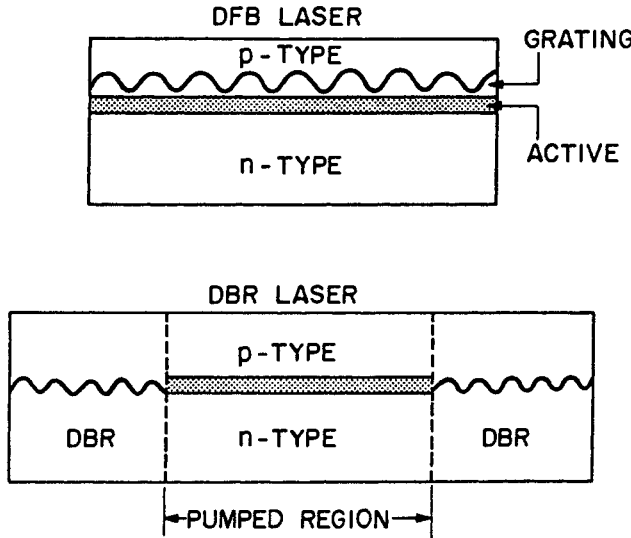


Figure 3.8: DFB and DBR laser structures. The shaded area shows the active region and the wavy line indicates the presence of a Bragg grating.

$\lambda_B = 1.55 \mu\text{m}$, Λ is about 235 nm if we use $m = 1$ and $\bar{n} = 3.3$ in Eq. (3.2.1). Such gratings can be made by using a holographic technique [2].

From the standpoint of device operation, semiconductor lasers employing the DFB mechanism can be classified into two broad categories: DFB lasers and *distributed Bragg reflector* (DBR) lasers. Figure 3.8 shows two kinds of laser structures. Though the feedback occurs throughout the cavity length in DFB lasers, it does not take place inside the active region of a DBR laser. In effect, the end regions of a DBR laser act as mirrors whose reflectivity is maximum for a wavelength λ_B satisfying Eq. (3.2.1). The cavity losses are therefore minimum for the longitudinal mode closest to λ_B and increase substantially for other longitudinal modes (see Figure 3.7). The MSR is determined by the gain margin defined as the excess gain required by the most dominant side mode to reach threshold. A gain margin of $3\text{--}5 \text{ cm}^{-1}$ is generally enough to realize an $\text{MSR} > 30 \text{ dB}$ for DFB lasers operating continuously [16]. However, a larger gain margin is needed ($> 10 \text{ cm}^{-1}$) when DFB lasers are modulated directly. *Phase-shifted DFB lasers* [15], in which the grating is shifted by $\lambda_B/4$ in the middle of the laser to produce a $\pi/2$ phase shift, are often used, since they are capable of providing a much larger gain margin than that of conventional DFB lasers. Another design that has led to improvements in the device performance is known as the *gain-coupled DFB laser* [21]. In these lasers, both the optical gain and the mode index vary periodically along the cavity length.

Fabrication of DFB semiconductor lasers requires advanced technology with multiple epitaxial growths [18]. The principal difference from FP lasers is that a grating is etched onto one of the cladding layers surrounding the active layer. A thin *n*-type waveguide layer with a refractive index intermediate to that of the active layer and the

substrate acts as a grating. The periodic variation of the thickness of the waveguide layer translates into a periodic variation of the mode index \bar{n} along the cavity length and leads to a coupling between the forward and backward propagating waves through Bragg diffraction.

A holographic technique is often used to form a grating with a pitch of $\sim 0.2 \mu\text{m}$. It works by forming a fringe pattern on a photoresist deposited on the wafer surface by interfering two optical beams and then etching the pattern chemically. In the alternative electron-beam lithographic technique, an electron beam writes the desired pattern on the electron-beam resist. Both methods use chemical etching to form grating corrugations, with the patterned resist acting as a mask. Once the grating has been etched onto the substrate, multiple layers are grown by using an epitaxial growth technique. A second epitaxial regrowth is needed to make a BH device such as that shown in Figure 3.6(b). Despite the technological complexities, DFB lasers are routinely produced commercially. They are used in nearly all $1.55\text{-}\mu\text{m}$ optical communication systems operating at bit rates of 2.5 Gb/s or more. DFB lasers are reliable enough that they have been used since 1992 in all transoceanic lightwave systems.

3.2.2 Coupled-Cavity Semiconductor Lasers

In a *coupled-cavity* semiconductor laser [2], single-mode operation is realized by coupling the laser cavity to an external cavity, which feeds a portion of the exiting light back into the laser cavity. The feedback from the external cavity is not necessarily in phase with the field inside the laser cavity because of the phase shift occurring in the external cavity. The in-phase feedback occurs only for those laser modes whose wavelength nearly coincides with one of the longitudinal modes of the external cavity. In effect, the effective reflectivity of the laser facet facing the external cavity becomes wavelength-dependent and leads to low losses for certain wavelengths. The longitudinal mode that is closest to the gain peak and has the lowest cavity loss becomes the dominant mode.

Several kinds of coupled-cavity schemes have been developed for making single-mode laser; Figure 3.9 shows three of them. A simple scheme couples the light from a semiconductor laser to an external grating [Figure 3.9(a)]. It is necessary to reduce the natural reflectivity of the cleaved facet facing the grating through an antireflection coating to provide a strong coupling. Such lasers are called *external-cavity* semiconductor lasers and have attracted considerable attention because of their tunability [13]. The wavelength of the single mode selected by the coupled-cavity mechanism can be tuned over a wide range (typically 50 nm) simply by rotating the grating. Wavelength tunability is a desirable feature for lasers used in WDM lightwave systems. A drawback of the laser shown in Figure 3.9(a) from the system standpoint is its nonmonolithic nature, which makes it difficult to realize the mechanical stability required of optical transmitters.

A monolithic design for coupled-cavity lasers is offered by the cleaved-coupled-cavity laser [14] shown in Figure 3.9(b). Such lasers are made by cleaving a conventional multimode semiconductor laser in the middle so that the laser is divided into two sections of about the same length but separated by a narrow air gap (with a width of $\sim 1 \mu\text{m}$). The reflectivity of cleaved facets ($\sim 30\%$) allows enough coupling between

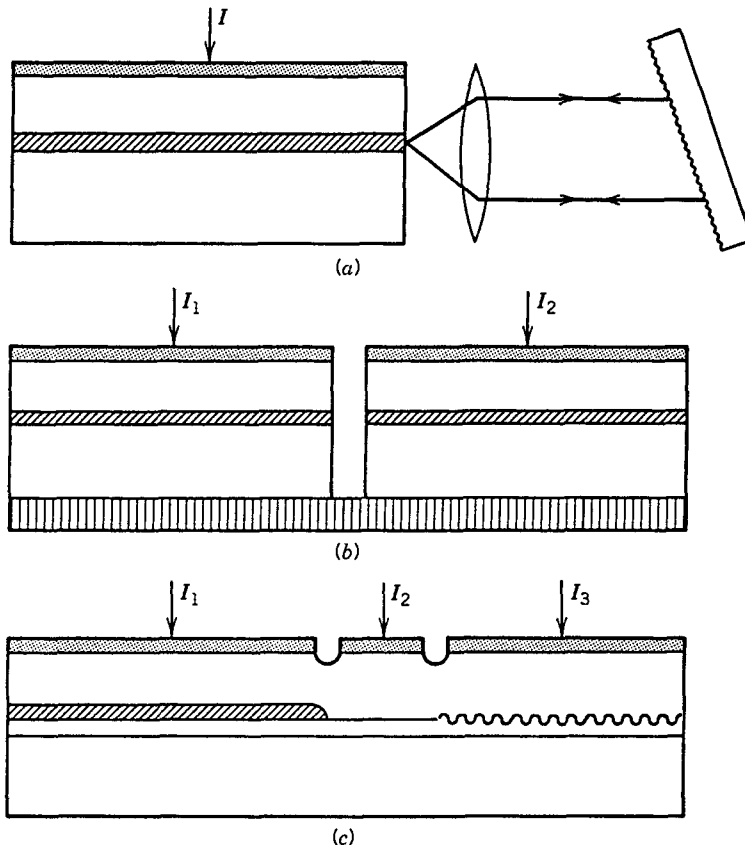


Figure 3.9: Coupled-cavity laser structures: (a) external-cavity laser; (b) cleaved-coupled-cavity laser; (c) multisection DBR laser.

the two sections as long as the gap is not too wide. It is even possible to tune the wavelength of such a laser over a tuning range ~ 20 nm by varying the current injected into one of the cavity sections acting as a mode controller. However, tuning is not continuous, since it corresponds to successive mode hops of about 2 nm.

3.2.3 Tunable Semiconductor Lasers

Modern WDM lightwave systems require single-mode, narrow-linewidth lasers whose wavelength remains fixed over time. DFB lasers satisfy this requirement but their wavelength stability comes at the expense of tunability. The large number of DFB lasers used inside a WDM transmitter make the design and maintenance of such a lightwave system expensive and impractical. The availability of semiconductor lasers whose wavelength can be tuned over a wide range solves this problem [11].

Multisection DFB and DBR lasers were developed during the 1990s to meet the somewhat conflicting requirements of stability and tunability [22]–[31]. Figure 3.9(c)

shows a typical laser structure. It consists of three sections, referred to as the active section, the phase-control section, and the Bragg section. Each section can be biased independently by injecting different amounts of currents. The current injected into the Bragg section is used to change the Bragg wavelength ($\lambda_B = 2n\Lambda$) through carrier-induced changes in the refractive index n . The current injected into the phase-control section is used to change the phase of the feedback from the DBR through carrier-induced index changes in that section. The laser wavelength can be tuned almost continuously over the range 10–15 nm by controlling the currents in the phase and Bragg sections. By 1997, such lasers exhibited a tuning range of 17 nm and output powers of up to 100 mW with high reliability [26].

Several other designs of tunable DFB lasers have been developed in recent years. In one scheme, the built-in grating inside a DBR laser is chirped by varying the grating period Λ or the mode index \bar{n} along the cavity length. As seen from Eq. (3.2.1), the Bragg wavelength itself then changes along the cavity length. Since the laser wavelength is determined by the Bragg condition, such a laser can be tuned over a wavelength range determined by the grating chirp. In a simple implementation of the basic idea, the grating period remains uniform, but the waveguide is bent to change the effective mode index \bar{n} . Such multisection DFB lasers can be tuned over 5–6 nm while maintaining a single longitudinal mode with high side-mode suppression [22].

In another scheme, a superstructure or sampled grating is used for the DBR section of a multisection laser [23]–[25]. In such gratings, the amplitude or the phase of the coupling coefficient is modulated in a periodic fashion along the grating length. As a result, the reflectivity peaks at several wavelengths whose interval is determined by the modulation period. Such multisection DBR lasers can be tuned discretely over a wavelength range exceeding 100 nm. By controlling the current in the phase-control section, a quasi-continuous tuning range of 40 nm was realized in 1995 with a superstructure grating [23]. The tuning range can be extended considerably by using a four-section device in which another DBR section is added to the left side of the device shown in Figure 3.9(c). Each DBR section supports its own comb of wavelengths but the spacing in each comb is not the same. The coinciding wavelength in the two combs becomes the output wavelength that can be tuned over a wide range (analogous to the Vernier effect).

In a different design, referred to as a tunable twin-guide laser [31], a tuning layer is added vertically within a standard DFB structure and two different sampled gratings are employed for tuning, as shown schematically in Figure 3.10. Such a device is much simpler to fabricate and operate than the three- or four-section DBR designs. The resulting laser can be tuned over a 40-nm wavelength range while maintaining a relatively large output power (~ 10 mW) and a high side-mode suppression ratio (> 30 dB). Since the active and tuning layers are separated by a passive n -type InP layer, such a device consists of two vertically stacked p - i - n diodes that can be biased independently. At the same time, the active and tuning layers act as cladding layers for the middle InP layer (with a higher refractive index) that forms an optical waveguide such that the intensity of the optical mode peaks in this middle layer. Because a good fraction of the optical mode resides in both the active and tuning layers, the two electrically isolated diodes are optically coupled in the vertical direction, thus allowing a wide tuning of the mode wavelength through the Vernier effect implemented with the two sampled gratings.

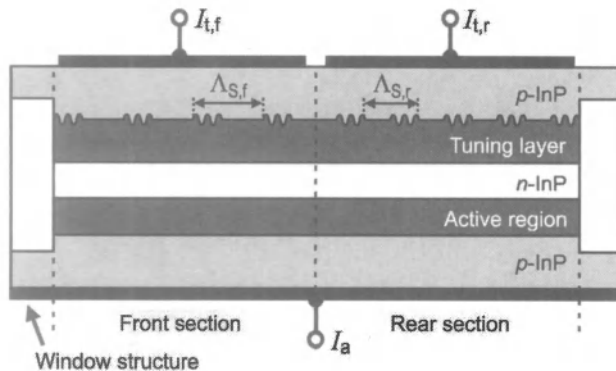


Figure 3.10: Schematic of a twin-guide laser in which a vertically integrated tuning layer with two sampled gratings is employed for tuning. (After Ref. [31]; ©2007 IEEE.)

3.2.4 Vertical-Cavity Surface-Emitting Lasers

A new class of semiconductor lasers, known as *vertical-cavity surface-emitting lasers* (VCSELs), emerged during the 1990s with many potential applications [32]–[43]. VCSELs operate in a single longitudinal mode by virtue of an extremely small cavity length ($\sim 1 \mu\text{m}$), for which the mode spacing exceeds the gain bandwidth. They emit light in a direction normal to the active-layer plane, in a manner analogous to that of a surface-emitting LED. Moreover, the emitted light is in the form of a circular beam that can be coupled into a single-mode fiber with high efficiency. These properties result in a number of advantages that are leading to rapid adoption of VCSELs for lightwave communications.

As seen in Figure 3.11, fabrication of VCSELs requires growth of multiple thin layers on a substrate. The active region, in the form of one or several quantum wells, is surrounded by two high-reflectivity (>99.5%) DBR mirrors that are grown epitaxially on both sides of the active region to form a high-Q microcavity [34]. Each DBR mirror is made by growing many pairs of alternating GaAs and AlAs layers, each $\lambda/4$ thick, where λ is the wavelength emitted by the VCSEL. A wafer-bonding technique is sometimes used for VCSELs operating in the $1.55\text{-}\mu\text{m}$ wavelength region to accommodate the InGaAsP active region [37]. Chemical etching or a related technique is used to form individual circular disks (each corresponding to one VCSEL) whose diameter can be varied over a wide range (typically $5\text{--}20 \mu\text{m}$). The entire two-dimensional array of VCSELs can be tested without requiring separation of lasers because of the vertical nature of light emission. As a result, the cost of a VCSEL can be much lower than that of an edge-emitting laser. VCSELs also exhibit a relatively low threshold ($\sim 1 \text{ mA}$ or less). Their only disadvantage is that they cannot emit more than a few milliwatts of power because of a small active volume. For this reason, they are mostly used for local-area and data-communication applications and have virtually replaced LEDs. Early VCSELs were designed to emit near $0.8 \mu\text{m}$ and operated in multiple transverse modes because of their relatively large diameters ($\sim 10 \mu\text{m}$).

In recent years, VCSEL technology has advanced enough that VCSELs can be de-

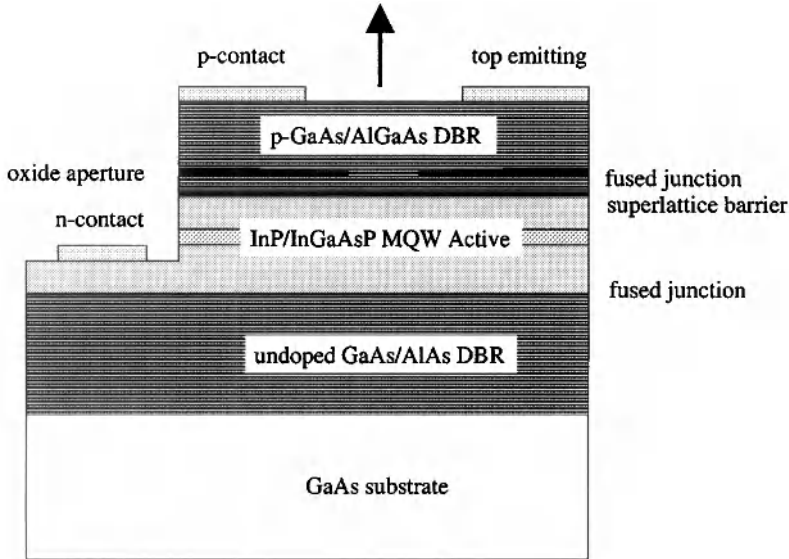


Figure 3.11: Schematic of a $1.55\text{-}\mu\text{m}$ VCSEL made by using the wafer-bonding technique. (After Ref. [37]; ©2000 IEEE.)

signed to operate in a wide wavelength range extending from 650 to 1,600 nm [41]. Their applications in the 1.3- and $1.55\text{-}\mu\text{m}$ wavelength windows require that VCSELs operate in a single transverse mode. By 2001, several techniques had emerged for controlling the transverse modes of a VCSEL, the most common being the oxide-confinement technique in which an insulating aluminum-oxide layer, acting as a dielectric aperture, confines both the current and the optical mode to a $<3\text{-}\mu\text{m}$ -diameter region (see Figure 3.11). Such VCSELs operate in a single mode with narrow linewidth and can replace a DFB laser in many lightwave applications as long as their low output power is acceptable. They are especially useful for data transfer and local-loop applications because of their low-cost packaging. VCSELs are also well suited for WDM applications for two reasons. First, one can make two-dimensional VCSEL arrays such that each laser operates at a different wavelength. Second, VCSEL wavelengths can be tuned over a wide range ($>50\text{ nm}$) using the micro-electro-mechanical system (MEMS) technology [35].

3.3 Laser Characteristics

The operation of semiconductor lasers is well described by a set of rate equations that govern the interaction of photons and electrons inside the active region. In this section we use the rate equations to discuss both the continuous-wave (CW) and modulation characteristics. The last two subsections focus on the intensity noise and spectral bandwidth of semiconductor lasers.

3.3.1 CW Characteristics

A rigorous derivation of the rate equations generally starts from Maxwell's equations. The rate equations can also be written heuristically by considering various physical phenomena through which the number of photons, P , and the number of electrons, N , change with time inside the active region. For a single-mode laser, these equations take the form [2]

$$\frac{dP}{dt} = GP + R_{\text{sp}} - \frac{P}{\tau_p}, \quad (3.3.1)$$

$$\frac{dN}{dt} = \frac{I}{q} - \frac{N}{\tau_c} - GP, \quad (3.3.2)$$

where the net rate of stimulated emission G is defined as

$$G = \Gamma v_g g_m = G_N(N - N_0), \quad (3.3.3)$$

and R_{sp} is the rate of spontaneous emission into the lasing mode. Note that R_{sp} is much smaller than the total spontaneous-emission rate. The reason is that spontaneous emission occurs in all directions over a wide spectral range (40–50 nm) but only a small fraction of it, propagating along the cavity axis and emitted at the laser frequency, actually contributes to Eq. (3.3.1). In fact, R_{sp} and G are related as $R_{\text{sp}} = n_{\text{sp}} G$, where n_{sp} is the spontaneous emission factor introduced in Section 3.1 and is about 2 for semiconductor lasers [2]. The variable N in the rate equations represents the number of electrons rather than the carrier density; the two are related by the active volume V . In Eq. (3.3.3), v_g is the group velocity, Γ is the confinement factor, and g_m is the material gain at the mode frequency. From Eq. (3.1.4), G varies linearly with N with $G_N = \Gamma v_g \sigma_g / V$ and $N_0 = N_T V$.

The last term in Eq. (3.3.1) takes into account the loss of photons inside the cavity. The parameter τ_p is referred to as the *photon lifetime*. It is related to the *cavity loss* α_{cav} introduced in Eq. (3.1.7) as

$$\tau_p^{-1} = v_g \alpha_{\text{cav}} = v_g (\alpha_{\text{mir}} + \alpha_{\text{int}}). \quad (3.3.4)$$

The three terms in Eq. (3.3.2) indicate the rates at which electrons are created or destroyed inside the active region. The carrier lifetime τ_c includes the loss of electrons owing to both spontaneous emission and nonradiative recombination.

The P - I curve characterizes the emission properties of a semiconductor laser, as it indicates not only the threshold level but also the current that needs to be applied to obtain a certain amount of power. Figure 3.12 shows the P - I curves of a $1.3\text{-}\mu\text{m}$ InGaAsP laser at temperatures in the range $10\text{--}130^\circ\text{C}$. At room temperature, the threshold is reached near 20 mA, and the laser can emit 10 mW of output power from each facet at 100 mA of applied current. The laser performance degrades at high temperatures. The threshold current is found to increase exponentially with temperature, that is,

$$I_{\text{th}}(T) = I_0 \exp(T/T_0), \quad (3.3.5)$$

where I_0 is a constant and T_0 is a characteristic temperature often used to express the temperature sensitivity of threshold current. For InGaAsP lasers T_0 is typically in the

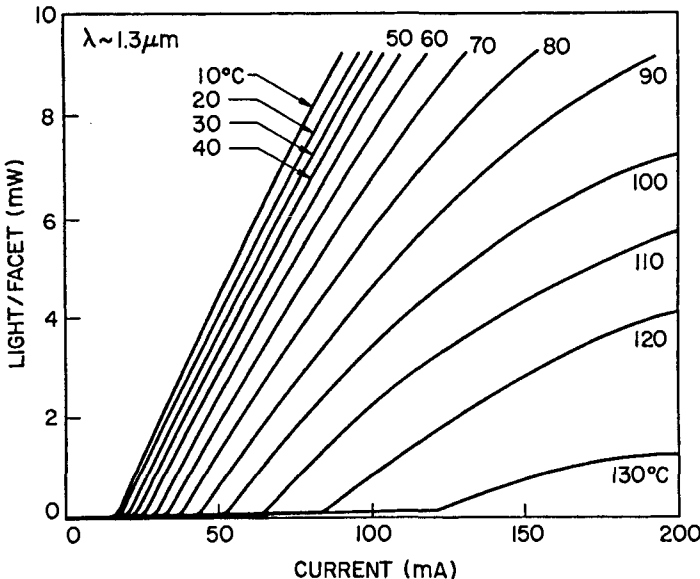


Figure 3.12: P - I curves at several temperatures for a $1.3\text{-}\mu\text{m}$ buried heterostructure laser.

range 50–70 K. By contrast, T_0 exceeds 120 K for GaAs lasers. Because of the temperature sensitivity of InGaAsP lasers, it is often necessary to control their temperature through a built-in thermoelectric cooler.

The rate equations can be used to understand most of the features seen in Figure 3.12. In the case of CW operation at a constant current I , the time derivatives in Eqs. (3.3.1) and (3.3.2) can be set to zero. The solution takes a particularly simple form if spontaneous emission is neglected by setting $R_{\text{sp}} = 0$. For currents such that $G\tau_p < 1$, $P = 0$ and $N = \tau_c I / q$. The threshold is reached at a current for which $G\tau_p = 1$. The carrier population is then clamped to the threshold value $N_{\text{th}} = N_0 + (G_N \tau_p)^{-1}$. The threshold current is given by

$$I_{\text{th}} = \frac{qN_{\text{th}}}{\tau_c} = \frac{q}{\tau_c} \left(N_0 + \frac{1}{G_N \tau_p} \right). \quad (3.3.6)$$

For $I > I_{\text{th}}$, the photon number P increases linearly with I as

$$P = (\tau_p/q)(I - I_{\text{th}}). \quad (3.3.7)$$

The emitted power P_e is related to P by the relation

$$P_e = \frac{1}{2}(v_g \alpha_{\text{mir}})\hbar\omega P. \quad (3.3.8)$$

The derivation of Eq. (3.3.8) is intuitively obvious if we note that $v_g \alpha_{\text{mir}}$ is the rate at which photons of energy $\hbar\omega$ escape from the two facets. The factor of $\frac{1}{2}$ makes P_e the power emitted from each facet for a FP laser with equal facet reflectivities. For FP

lasers with coated facets or for DFB lasers, Eq. (3.3.8) needs to be suitably modified [2]. By using Eqs. (3.3.4) and (3.3.7) in Eq. (3.3.8), the emitted power is given by

$$P_e = \frac{\hbar\omega}{2q} \frac{\eta_{\text{int}}\alpha_{\text{mir}}}{\alpha_{\text{mir}} + \alpha_{\text{int}}} (I - I_{\text{th}}), \quad (3.3.9)$$

where the internal quantum efficiency η_{int} is introduced phenomenologically to indicate the fraction of injected electrons that is converted into photons through stimulated emission. In the above-threshold regime, η_{int} is almost 100% for most semiconductor lasers.

A quantity of practical interest is the slope of the P - I curve for $I > I_{\text{th}}$; it is called the *slope efficiency* and is defined as

$$\frac{dP_e}{dI} = \frac{\hbar\omega}{2q} \eta_d \quad \text{with} \quad \eta_d = \frac{\eta_{\text{int}}\alpha_{\text{mir}}}{\alpha_{\text{mir}} + \alpha_{\text{int}}}. \quad (3.3.10)$$

The quantity η_d is called the *differential quantum efficiency*, as it is a measure of the efficiency with which light output increases with an increase in the injected current. One can define the external quantum efficiency η_{ext} as

$$\eta_{\text{ext}} = \frac{\text{photon-emission rate}}{\text{electron-injection rate}} = \frac{2P_e/\hbar\omega}{I/q} = \frac{2q}{\hbar\omega} \frac{P_e}{I}. \quad (3.3.11)$$

By using Eqs. (3.3.9) through (3.3.11), η_{ext} and η_d are found to be related by

$$\eta_{\text{ext}} = \eta_d (1 - I_{\text{th}}/I). \quad (3.3.12)$$

Generally, $\eta_{\text{ext}} < \eta_d$ but becomes nearly the same for $I \gg I_{\text{th}}$. Similar to the case of LEDs, one can define the total quantum efficiency (or wall-plug efficiency) as $\eta_{\text{tot}} = 2P_e/(V_0 I)$, where V_0 is the applied voltage. It is related to η_{ext} as

$$\eta_{\text{tot}} = \frac{\hbar\omega}{qV_0} \eta_{\text{ext}} \approx \frac{E_g}{qV_0} \eta_{\text{ext}}, \quad (3.3.13)$$

where E_g is the bandgap energy. Generally, $\eta_{\text{tot}} < \eta_{\text{ext}}$ as the applied voltage exceeds E_g/q . For GaAs lasers, η_d can exceed 80% and η_{tot} can approach 50%. The InGaAsP lasers are less efficient with $\eta_d \sim 50\%$ and $\eta_{\text{tot}} \sim 20\%$.

The exponential increase in the threshold current with temperature can be understood from Eq. (3.3.6). The carrier lifetime τ_c is generally N -dependent because of Auger recombination and decreases with N as N^2 . The rate of Auger recombination increases exponentially with temperature and is responsible for the temperature sensitivity of InGaAsP lasers. Figure 3.12 also shows that the slope efficiency decreases with an increase in the output power (bending of the P - I curves). This decrease can be attributed to junction heating occurring under CW operation. It can also result from an increase in internal losses or current leakage at high operating powers. Despite these problems, the performance of DFB lasers improved substantially during the 1990s [18]. DFB lasers emitting >100 mW of power at room temperature in the $1.55\text{-}\mu\text{m}$ spectral region were fabricated by 1996 using a strained multiquantum-well (MQW) design [44]. Such lasers exhibited <10 mA threshold current at 20°C and emitted ~ 20 mW of power at 100°C while maintaining a MSR of >40 dB. By 2003, DFB lasers capable of delivering more than 200 mW of power with a wavelength stability of <3 pm became available [45].

3.3.2 Modulation Bandwidth

Output power of a DFB laser can be modulated directly if the applied current varies with time. The question is how fast this current can be modulated before the laser fails to respond to current variations. The modulation response of semiconductor lasers is studied by solving the rate equations (3.3.1) and (3.3.2) with a time-dependent current of the form

$$I(t) = I_b + I_m f_p(t), \quad (3.3.14)$$

where I_b is the bias current, I_m is the current, and $f_p(t)$ represents the shape of the current pulse. Two changes are necessary for a realistic description. First, Eq. (3.3.3) for the gain G must be modified to become [2]

$$G = G_N(N - N_0)(1 - \epsilon_{NL}P), \quad (3.3.15)$$

where ϵ_{NL} is a nonlinear-gain parameter that leads to a slight reduction in G as P increases. The physical mechanism behind this reduction can be attributed to several phenomena, such as spatial hole burning, spectral hole burning, carrier heating, and two-photon absorption [46]–[49]. Typical values of ϵ_{NL} are $\sim 10^{-7}$. Equation (3.3.15) is valid for $\epsilon_{NL}P \ll 1$. The factor $1 - \epsilon_{NL}P$ should be replaced by $(1 + P/P_s)^{-b}$, where P_s is a material parameter, when the laser power exceeds far above 10 mW. The exponent b equals $\frac{1}{2}$ for spectral hole burning [47] but can vary over the range 0.2–1 because of the contribution of carrier heating [49].

The second change is related to an important property of semiconductor lasers. It turns out that whenever the optical gain changes as a result of changes in the carrier population N , the refractive index also changes. From a physical standpoint, amplitude modulation in semiconductor lasers is always accompanied by phase modulation because of carrier-induced changes in the mode index \bar{n} . Phase modulation can be included through the equation [2]

$$\frac{d\phi}{dt} = \frac{1}{2}\beta_c \left[G_N(N - N_0) - \frac{1}{\tau_p} \right], \quad (3.3.16)$$

where β_c is the amplitude-phase coupling parameter, commonly called the *linewidth enhancement factor*, as it leads to an enhancement of the spectral width associated with a single longitudinal mode. Typical values of β_c for InGaAsP lasers are in the range 4–8, depending on the operating wavelength [50]. Lower values of β_c occur in MQW lasers, especially for strained quantum wells [3].

In general, the nonlinear nature of the rate equations makes it necessary to solve them numerically. A useful analytic solution can be obtained for the case of small-signal modulation in which the laser is biased above threshold ($I_b > I_{th}$) and modulated such that $I_m \ll I_b - I_{th}$. The rate equations can be linearized in that case and solved analytically, using the Fourier transform technique, for an arbitrary form of $f_p(t)$. The small-signal modulation bandwidth can be obtained by considering the response of semiconductor lasers to sinusoidal modulation at the frequency ω_m so that $f_p(t) = \sin(\omega_m t)$. The laser output is also modulated sinusoidally. The general solution of Eqs. (3.3.1) and (3.3.2) is given by

$$P(t) = P_b + |p_m| \sin(\omega_m t + \theta_m), \quad (3.3.17)$$

$$N(t) = N_b + |n_m| \sin(\omega_m t + \psi_m), \quad (3.3.18)$$

where P_b and N_b are the steady-state values at the bias current I_b , $|p_m|$ and $|n_m|$ are small changes occurring because of current modulation, and θ_m and ψ_m govern the phase lag associated with the small-signal modulation. In particular, $p_m \equiv |p_m| \exp(i\theta_m)$ is given by [2]

$$p_m(\omega_m) = \frac{P_b G_N I_m / q}{(\Omega_R + \omega_m - i\Gamma_R)(\Omega_R - \omega_m + i\Gamma_R)}, \quad (3.3.19)$$

where

$$\Omega_R = [GG_N P_b - (\Gamma_P - \Gamma_N)^2 / 4]^{1/2}, \quad \Gamma_R = (\Gamma_P + \Gamma_N) / 2, \quad (3.3.20)$$

$$\Gamma_P = R_{sp}/P_b + \epsilon_{NL} G P_b, \quad \Gamma_N = \tau_c^{-1} + G_N P_b. \quad (3.3.21)$$

Ω_R and Γ_R are the frequency and the damping rate of relaxation oscillations. These two parameters play an important role in governing the dynamic response of semiconductor lasers. In particular, the efficiency is reduced when the modulation frequency exceeds Ω_R by a large amount.

It is common to introduce a power-transfer function as

$$H(\omega_m) = \frac{p_m(\omega_m)}{p_m(0)} = \frac{\Omega_R^2 + \Gamma_R^2}{(\Omega_R + \omega_m - i\Gamma_R)(\Omega_R - \omega_m + i\Gamma_R)}. \quad (3.3.22)$$

The modulation response is flat [$H(\omega_m) \approx 1$] for frequencies such that $\omega_m \ll \Omega_R$, peaks at $\omega_m = \Omega_R$, and then drops sharply for $\omega_m \gg \Omega_R$. These features are observed experimentally for all semiconductor lasers [51]–[55]. Figure 3.13 shows the modulation response of a 1.55-μm DFB laser at several bias levels [54]. The 3-dB modulation bandwidth, f_{3dB} , is defined as the frequency at which $|H(\omega_m)|$ is reduced by 3 dB (by a factor of 2) compared with its direct-current (dc) value. Equation (3.3.22) provides the following analytic expression for f_{3dB} :

$$f_{3dB} = \frac{1}{2\pi} \left[\Omega_R^2 - \Gamma_R^2 + 2(\Omega_R^4 + \Omega_R^2 \Gamma_R^2 + \Gamma_R^4)^{1/2} \right]^{1/2}. \quad (3.3.23)$$

For most lasers, $\Gamma_R \ll \Omega_R$, and f_{3dB} can be approximated by

$$f_{3dB} \approx \frac{\sqrt{3}\Omega_R}{2\pi} \approx \left(\frac{3G_N P_b}{4\pi^2 \tau_p} \right)^{1/2} = \left[\frac{3G_N}{4\pi^2 q} (I_b - I_{th}) \right]^{1/2}, \quad (3.3.24)$$

where Ω_R was approximated by $(GG_N P_b)^{1/2}$ in Eq. (3.3.21) and G was replaced by $1/\tau_p$ since gain equals loss in the above-threshold regime. The last expression was obtained by using Eq. (3.3.7) at the bias level.

Equation (3.3.24) provides a remarkably simple expression for the modulation bandwidth. It shows that f_{3dB} increases with an increase in the bias level as $\sqrt{P_b}$ or as $(I_b - I_{th})^{1/2}$. This square-root dependence has been verified for many DFB lasers exhibiting a modulation bandwidth of up to 30 GHz [51]–[54]. Figure 3.13 shows how f_{3dB} can be increased to 24 GHz for a DFB laser by biasing it at 80 mA [54]. A modulation bandwidth of 25 GHz was realized in 1994 for a packaged 1.55-μm In-GaAsP laser specifically designed for high-speed response [52]. The injection-locking technique is sometimes used to improve the modulation response of DFB lasers [56].

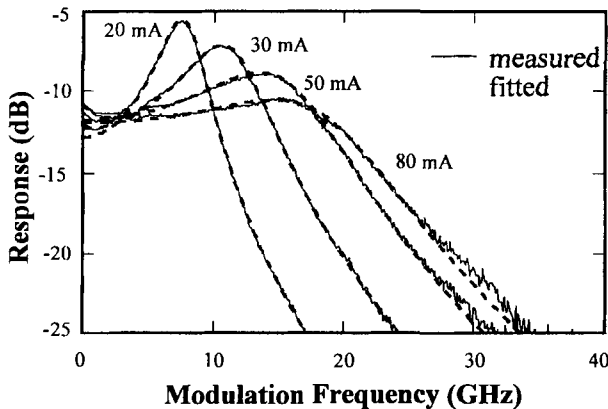


Figure 3.13: Measured (solid curves) and fitted (dashed curves) modulation response of a 1.55- μm DFB laser as a function of modulation frequency at several bias levels. (After Ref. [54]; ©1997 IEEE.)

3.3.3 Relative Intensity Noise

The output of a semiconductor laser exhibits fluctuations in its intensity, phase, and frequency even when the laser is biased at a constant current with negligible current fluctuations. The two fundamental noise mechanisms are spontaneous emission and electron–hole recombination (shot noise). Noise in semiconductor lasers is dominated by spontaneous emission. Each spontaneously emitted photon adds to the coherent field (established by stimulated emission) a small field component whose phase is random, and thus perturbs both the amplitude and phase in a random manner. Moreover, such spontaneous-emission events occur randomly at a high rate ($\sim 10^{12} \text{ s}^{-1}$) because of a relatively large value of R_{sp} in semiconductor lasers. The net result is that the intensity and the phase of the emitted light exhibit fluctuations over a time scale as short as 100 ps. Intensity fluctuations lead to a limited *signal-to-noise ratio* (SNR), whereas phase fluctuations lead to a finite spectral linewidth when semiconductor lasers are operated at a constant current. Since such fluctuations can affect the performance of lightwave systems, it is important to estimate their magnitude [57].

The rate equations can be used to study laser noise by adding a noise term, known as the *Langevin force*, to each of them [58]. Equations (3.3.1), (3.3.2), and (3.3.16) then become

$$\frac{dP}{dt} = \left(G - \frac{1}{\tau_p} \right) P + R_{\text{sp}} + F_P(t), \quad (3.3.25)$$

$$\frac{dN}{dt} = \frac{I}{q} - \frac{N}{\tau_c} - GP + F_N(t), \quad (3.3.26)$$

$$\frac{d\phi}{dt} = \frac{1}{2} \beta_c \left[G_N(N - N_0) - \frac{1}{\tau_p} \right] + F_\phi(t), \quad (3.3.27)$$

where $F_P(t)$, $F_N(t)$, and $F_\phi(t)$ are the Langevin forces. They are assumed to be Gaus-

sian random processes with zero mean and to have a correlation function of the form (the Markovian approximation)

$$\langle F_i(t)F_j(t') \rangle = 2D_{ij}\delta(t - t'), \quad (3.3.28)$$

where $i, j = P, N$, or ϕ , angle brackets denote the ensemble average, and D_{ij} is called the *diffusion coefficient*. The dominant contribution to laser noise comes from only two diffusion coefficients $D_{PP} = R_{sp}P$ and $D_{\phi\phi} = R_{sp}/4P$; others can be assumed to be nearly zero [59].

The intensity-autocorrelation function is defined as

$$C_{pp}(\tau) = \langle \delta P(t)\delta P(t + \tau) \rangle / \bar{P}^2, \quad (3.3.29)$$

where $\bar{P} \equiv \langle P \rangle$ is the average value and $\delta P = P - \bar{P}$ represents a small fluctuation. The Fourier transform of $C_{pp}(\tau)$ is known as the *relative-intensity-noise* (RIN) spectrum and is given by

$$\text{RIN}(\omega) = \int_{-\infty}^{\infty} C_{pp}(\tau) \exp(-i\omega\tau) dt. \quad (3.3.30)$$

The RIN can be calculated by linearizing Eqs. (3.3.25) and (3.3.26) in δP and δN , solving the linearized equations in the frequency domain, and performing the average with the help of Eq. (3.3.28). It is given approximately by [2]

$$\text{RIN}(\omega) = \frac{2R_{sp}\{(\Gamma_N^2 + \omega^2) + G_N\bar{P}[G_N\bar{P}(1 + N/\tau_c R_{sp}\bar{P}) - 2\Gamma_N]\}}{\bar{P}[(\Omega_R - \omega)^2 + \Gamma_R^2][(\Omega_R + \omega)^2 + \Gamma_R^2]}, \quad (3.3.31)$$

where Ω_R and Γ_R are the frequency and the damping rate of relaxation oscillations. They are given by Eq. (3.3.21), with P_b replaced by \bar{P} .

Figure 3.14 shows the calculated RIN spectra at several power levels for a typical 1.55-μm InGaAsP laser. The RIN is considerably enhanced near the relaxation-oscillation frequency Ω_R but decreases rapidly for $\omega \gg \Omega_R$, since the laser is not able to respond to fluctuations at such high frequencies. In essence, the semiconductor laser acts as a bandpass filter of bandwidth Ω_R to spontaneous-emission fluctuations. At a given frequency, RIN decreases with an increase in the laser power as P^{-3} at low powers, but this behavior changes to P^{-1} dependence at high powers.

The autocorrelation function $C_{pp}(\tau)$ is calculated using Eqs. (3.3.30) and (3.3.31). The calculation shows that $C_{pp}(\tau)$ follows relaxation oscillations and approaches zero for $\tau > \Gamma_R^{-1}$ [60]. This behavior indicates that intensity fluctuations do not remain correlated for times longer than the damping time of relaxation oscillations. The quantity of practical interest is the SNR defined as \bar{P}/σ_p , where σ_p is the root-mean-square (RMS) noise. From Eq. (3.3.29), $\text{SNR} = [C_{pp}(0)]^{-1/2}$. At power levels above a few milliwatts, the SNR exceeds 20 dB and improves linearly with the power as

$$\text{SNR} = \left(\frac{\epsilon_{NL}}{R_{sp}\tau_p} \right)^{1/2} \bar{P}. \quad (3.3.32)$$

The presence of ϵ_{NL} indicates that the nonlinear form of the gain in Eq. (3.3.15) plays a crucial role. This form needs to be modified at high powers. Indeed, a more accurate treatment shows that the SNR eventually saturates at a value of about 30 dB and becomes power-independent [60].

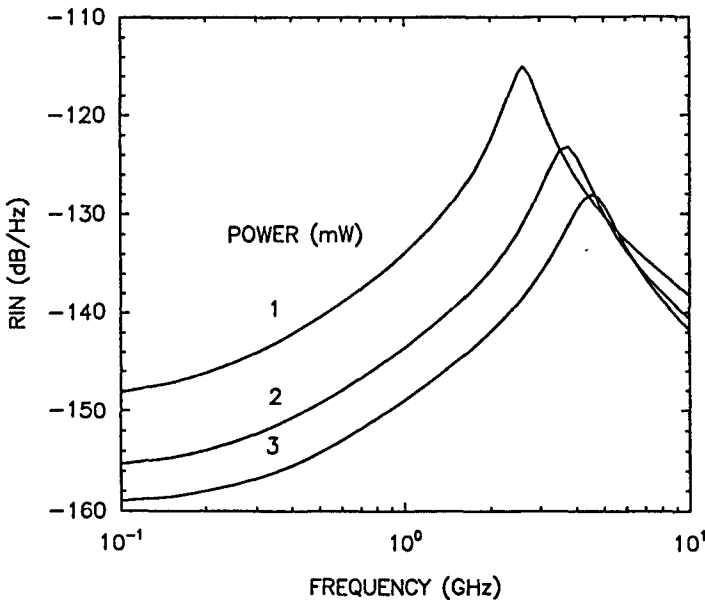


Figure 3.14: RIN spectra at several power levels for a typical 1.55- μm semiconductor laser.

So far, the laser has been assumed to oscillate in a single longitudinal mode. In practice, even DFB lasers are accompanied by one or more side modes. Even though side modes remain suppressed by more than 20 dB on the basis of the average power, their presence can affect the RIN significantly. In particular, the main and side modes can fluctuate in such a way that individual modes exhibit large intensity fluctuations, but the total intensity remains relatively constant. This phenomenon is called *mode-partition noise* (MPN) and occurs due to an anticorrelation between the main and side modes [2]. It manifests through the enhancement of RIN for the main mode by 20 dB or more in the low-frequency range 0–1 GHz; the exact value of the enhancement factor depends on the MSR [61]. In the case of a VCSEL, the MPN involves two transverse modes [62]. In the absence of fiber dispersion, MPN would be harmless for optical communication systems, as all modes would remain synchronized during transmission and detection. However, in practice all modes do not arrive simultaneously at the receiver because they travel at slightly different speeds. Such a desynchronization not only degrades the SNR of the received signal but also leads to intersymbol interference.

3.3.4 Spectral Linewidth

The spectrum of emitted light is related to the field-autocorrelation function $\Gamma_{EE}(\tau)$ through a Fourier-transform relation similar to Eq. (3.3.30), that is,

$$S(\omega) = \int_{-\infty}^{\infty} \Gamma_{EE}(t) \exp[-i(\omega - \omega_0)\tau] d\tau, \quad (3.3.33)$$

where $\Gamma_{EE}(t) = \langle E^*(t)E(t+\tau) \rangle$ and $E(t) = \sqrt{P} \exp(i\phi)$ is the optical field. If intensity fluctuations are neglected, $\Gamma_{EE}(t)$ is given by

$$\Gamma_{EE}(t) = \langle \exp[i\Delta\phi(t)] \rangle = \exp[-\langle \Delta\phi^2(\tau) \rangle / 2], \quad (3.3.34)$$

where the phase fluctuation $\Delta\phi(\tau) = \phi(t+\tau) - \phi(t)$ is taken to be a Gaussian random process. The phase variance $\langle \Delta\phi^2(\tau) \rangle$ can be calculated by linearizing Eqs. (3.3.25) through (3.3.27) and solving the resulting set of linear equations. The result is [59]

$$\langle \Delta\phi^2(\tau) \rangle = \frac{R_{sp}}{2\bar{P}} \left[(1 + \beta_c^2 b) \tau + \frac{\beta_c^2 b}{2\Gamma_R \cos \delta} [\cos(3\delta) - e^{-\Gamma_R \tau} \cos(\Omega_R \tau - 3\delta)] \right], \quad (3.3.35)$$

where

$$b = \Omega_R / (\Omega_R^2 + \Gamma_R^2)^{1/2} \quad \text{and} \quad \delta = \tan^{-1}(\Gamma_R / \Omega_R). \quad (3.3.36)$$

The spectrum is obtained by using Eqs. (3.3.33) through (3.3.35). It is found to consist of a dominant central peak located at ω_0 and multiple satellite peaks located at $\omega = \omega_0 \pm m\Omega_R$, where m is an integer. The amplitude of satellite peaks is typically less than 1% of that of the central peak. The physical origin of the satellite peaks is related to relaxation oscillations, which are responsible for the term proportional to b in Eq. (3.3.35). If this term is neglected, the autocorrelation function $\Gamma_{EE}(\tau)$ decays exponentially with τ . The integral in Eq. (3.3.33) can then be performed analytically, and the spectrum is found to be Lorentzian. The spectral linewidth $\Delta\nu$ is defined as the full-width at half-maximum (FWHM) of this Lorentzian line and is given by [59]

$$\Delta\nu = R_{sp} (1 + \beta_c^2) / (4\pi\bar{P}), \quad (3.3.37)$$

where $b = 1$ was assumed as $\Gamma_R \ll \Omega_R$ under typical operating conditions. The linewidth is enhanced by a factor of $1 + \beta_c^2$ as a result of the amplitude-phase coupling governed by β_c in Eq. (3.3.27); β_c is called the linewidth enhancement factor for this reason.

Equation (3.3.37) shows that $\Delta\nu$ should decrease as \bar{P}^{-1} with an increase in the laser power. Such an inverse dependence is observed experimentally at low power levels (<10 mW) for most semiconductor lasers. However, often the linewidth is found to saturate to a value in the range of 1–10 MHz at a power level above 10 mW. Figure 3.15 shows such linewidth-saturation behavior for several 1.55-μm DFB lasers [63]. It also shows that the linewidth can be reduced considerably by using a MQW design for the DFB laser. The reduction is due to a smaller value of the parameter β_c realized by such a design.

The linewidth can also be reduced by increasing the cavity length L , since R_{sp} decreases and P increases at a given output power as L is increased. Although not obvious from Eq. (3.3.37), $\Delta\nu$ can be shown to vary as L^{-2} when the length dependence of R_{sp} and P is incorporated. As seen in Figure 3.15, $\Delta\nu$ is reduced by about a factor of 4 when the cavity length is doubled. The 800-μm-long MQW-DFB laser is found to exhibit a linewidth as small as 270 kHz at a power output of 13.5 mW [63]. It is further reduced in strained MQW lasers because of relatively low values of β_c , and a value of about 100 kHz has been measured in lasers with $\beta_c \approx 1$ [70]. It should be stressed, however, that the linewidth of most DFB lasers is typically 5–10 MHz when operating

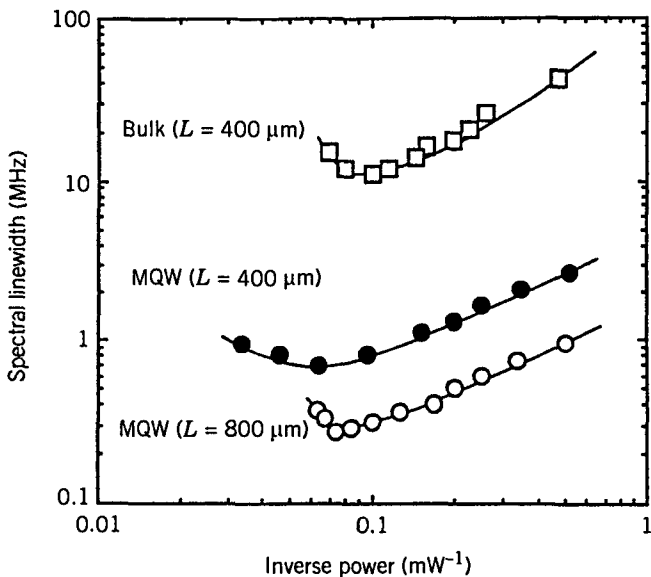


Figure 3.15: Measured linewidth as a function of emitted power for several $1.55-\mu\text{m}$ DFB lasers. Active layer is 100 nm thick for the bulk laser and 10 nm thick for MQW lasers. (After Ref. [63]; ©1991 IEEE.)

at a power level of 10 mW . Figure 3.15 shows that as the laser power increases, the linewidth not only saturates but also begins to rebroaden. Several mechanisms such as current fluctuations, $1/f$ noise, nonlinear gain and index changes, and interaction with weak side modes have been invoked to explain this saturation. The linewidth of most DFB lasers is small enough that it is not a limiting factor for lightwave systems.

3.4 Optical Signal Generation

The first step in the design of an optical communication system is to decide how the electrical data would be converted into an optical signal with the same information. The original electrical data can be in an analog form, but it is invariably converted into a digital bit stream (with the RZ or NRZ format) consisting of a pseudorandom sequence of 0 and 1 bits. Two techniques, known as (a) direct modulation and (b) external modulation, can be used to generate the corresponding optical bit stream. Both of them are discussed in this section.

3.4.1 Direct Modulation

In the case of direct modulation, the laser source itself is biased close to its threshold and driven by the electrical bit stream that increases the applied current considerably above the lasers threshold to create optical pulses representing digital bits (the so-called

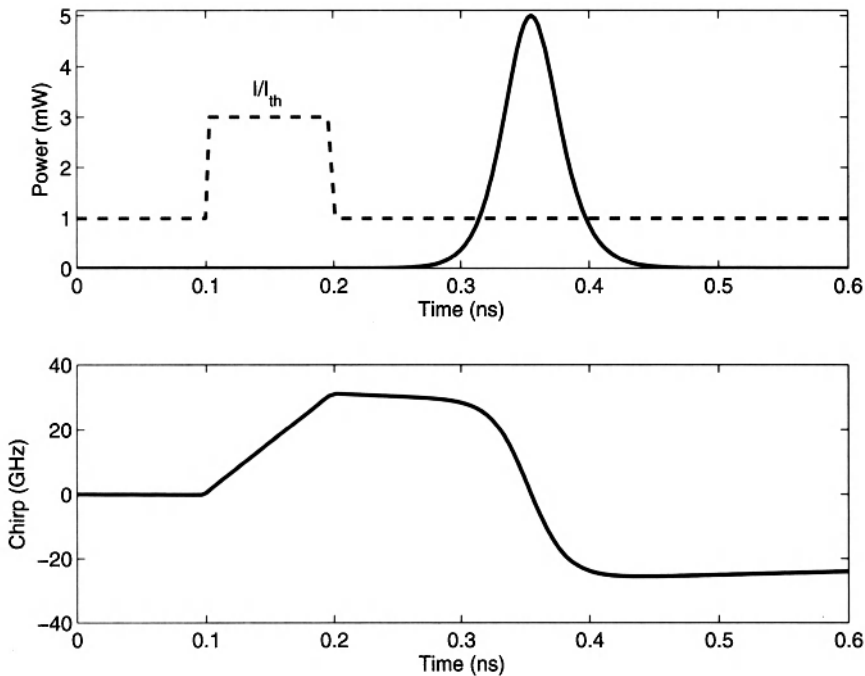


Figure 3.16: Simulated modulation response of a semiconductor laser to 100-ps rectangular current pulses (dashed curve). The bottom trace shows the frequency chirp imposed on the pulse ($\beta_c = 5$).

large-signal modulation). The important question is how closely the optical pulse mimics the shape of optical pulse. To answer this question, the two rate equations, Eqs. (3.3.1) and (3.3.2), must be solved numerically with $I(t) = I_b + I_m f_p(t)$, where $f_p(t)$ represents the shape of electrical pulses. Figure 3.16 shows, as an example, the shape of the emitted optical pulse for a laser biased at $I_b = I_{th}$ and modulated at 10 Gb/s using rectangular current pulses of duration 100 ps and amplitude $I_m = 3I_{th}$. The optical pulse does not have sharp leading and trailing edges because of a limited modulation bandwidth of the laser. It is also delayed considerably because it takes time for the optical power to build up from its initially negligible values. Even though the resulting optical pulse is not an exact replica of the applied electrical pulse, its overall shape and width are such that this semiconductor lasers can be used for direct modulation at 10 Gb/s.

As discussed in Section 3.3.2, amplitude modulation in semiconductor lasers is accompanied by phase modulation and temporal phase variations can be studied by solving Eq. (3.3.16). A time-varying phase is equivalent to transient changes in the mode frequency from its steady-state value v_0 . Such a pulse is called chirped. The frequency chirp $\delta v(t)$ is obtained from Eq. (3.3.16) and is given by

$$\delta v(t) = \frac{1}{2\pi} \frac{d\phi}{dt} = \frac{\beta_c}{4\pi} \left[G_N(N - N_0) - \frac{1}{\tau_p} \right]. \quad (3.4.1)$$

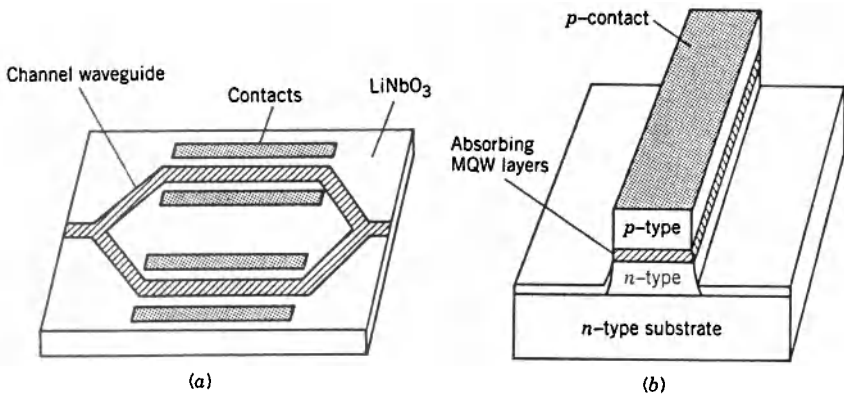


Figure 3.17: Two kinds of external modulators: (a) LiNbO_3 modulator in the Mach–Zehnder configuration; (b) semiconductor modulator based on electroabsorption.

The bottom trace in Figure 3.13 shows the frequency chirp across the optical pulse. The mode frequency first shifts toward the blue side near the leading edge and then toward the red side near the trailing edge of the optical pulse [64]. Such a frequency shift implies that the pulse spectrum is considerably broader than that expected in the absence of frequency chirp, a feature that degrades system performance through excessive broadening of optical pulses during their transmission through a fiber link.

Since frequency chirp is often the limiting factor for lightwave systems operating near $1.55 \mu\text{m}$, several methods have been used to reduce its magnitude [66]–[70]. These include pulse-shape tailoring, injection locking, and coupled-cavity schemes. A direct way to reduce the frequency chirp is to design semiconductor lasers with small values of the linewidth enhancement factor β_c . The use of quantum wells or quantum dots reduces β_c by a factor of 2 or so. A further reduction occurs for strained quantum wells [69]. Indeed, $\beta_c \approx 1$ has been measured in modulation-doped strained MQW lasers [70]. Such lasers exhibit low chirp under direct modulation.

3.4.2 External Modulation

At bit rates of 5 Gb/s or higher, the frequency chirp imposed by direct modulation becomes large enough that direct modulation of semiconductor lasers is rarely used. For such high-speed transmitters, the laser is biased at a constant current to provide the CW output, and an optical modulator placed next to the laser converts the CW light into a data-coded pulse train with the right modulation format.

Two types of optical modulators developed for lightwave system applications are shown in Figure 3.17. An important class of optical modulators makes use of the electro-optic effect inside a LiNbO_3 waveguide such that the effective mode index changes in response to an applied voltage across it [71]. Such a simple device modulates the phase of light passing through it and is useful as a phase modulator. To construct an intensity modulator, phase modulation is converted into amplitude modulation with the help of a Mach–Zehnder (MZ) interferometer [72]–[76]. Two titanium-

diffused LiNbO₃ waveguides form the two arms of a MZ interferometer (see Figure 3.17). In the absence of an external voltage, the optical fields in the two arms of the MZ interferometer experience identical phase shifts and interfere constructively. The additional phase shift introduced in one of the arms through voltage-induced index changes destroys the constructive nature of the interference and reduces the transmitted intensity. In particular, no light is transmitted when the phase difference between the two arms equals π , because of destructive interference occurring in that case. As a result, the electrical bit stream applied to the modulator produces an optical replica of the bit stream.

A LiNbO₃ modulator is rarely used in ASK lightwave systems that simply turn the light on and off to encode the information because of considerable insertion losses that invariably occur when CW light from the laser source is coupled into the LiNbO₃ waveguide inside an external modulator. The electroabsorption modulator (EAM) shown in Figure 3.17 solves this problem because it is made with the same InP material used to make the laser source, and both of them can be integrated on the same InP substrate [77]–[90].

An EAM makes use of the Franz–Keldysh effect, according to which the bandgap of a semiconductor decreases when an electric field is applied across it. Thus, a transparent semiconductor layer begins to absorb light when its bandgap is reduced electronically by applying an external voltage. An extinction ratio of 15 dB or more can be realized for an applied reverse bias of a few volts at bit rates of up to 40 Gb/s. Although some chirp is still imposed on coded pulses, it can be made small enough not to be detrimental for the system performance.

An advantage of EAMs is that they are made using the same semiconductor material that is used for the laser, and thus the two can be easily integrated on the same chip. Low-chirp transmission at a bit rate of 5 Gb/s was demonstrated as early as 1994 by integrating an EAM with a DBR laser [78]. By 1999, 10-Gb/s optical transmitters with an integrated EAM were available commercially and were used routinely for WDM lightwave systems [81]. By 2001, such integrated modulators could be operated at a bit rate of 40 Gb/s [83], and such devices became available commercially soon after [90]. Moreover, EAMs exhibit the potential of operating at bit rates of up to 100 Gb/s [82].

Figure 3.18 shows schematically the basic idea behind modulator-integrated DFB laser. The DFB laser on the left provides the CW signal at a fixed wavelength (determined by the grating) that is modulated by the EAM on the right. The middle section is designed to isolate the two devices electrically while inducing minimum losses. The facets of the whole device are coated such that the left facet has a high reflectivity (>90%), while the right facet has as low reflectivity as possible (<1%).

The fabrication of modulator-integrated lasers requires attention to many details. In general, the active core layers in the laser and modulator sections should be made using different compositions with different bandgaps so that they can be optimized for each device separately. Two different approaches are used for this purpose. In one scheme, the waveguides for the laser and modulator are butt-joined using separate epitaxial growth steps for each of them. First, the layers are grown for one device, say the laser. Then a mask is used to remove the epitaxial layers from the modulator region, and new layers are regrown. Although this approach offers the maximum flexibility for optimizing each device separately, the vertical alignment of the layers in the two

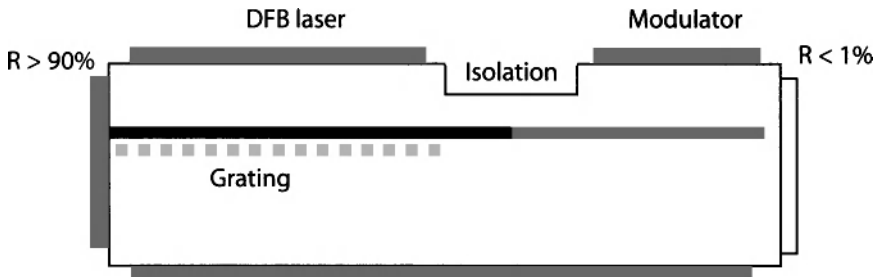


Figure 3.18: Schematic of a modulator-integrated DFB laser. The DFB laser on the left provides the CW light that is modulated by the EAM on the right. The middle section is designed to isolate the two devices electrically with minimum losses.

sections is relatively difficult and affects the yield. In the much simpler, selective-area growth technique, both devices (laser and modulator) are formed in a single epitaxial growth, but the oxide pads placed on the wafer prior to growth allow one to shift the laser wavelength toward the red side by more than 100 nm. The wavelength shift results from a change in the Bragg wavelength of the laser grating occurring because of changes in the effective mode index induced by the oxide pads. This technique is commonly used in practice for making modulator-integrated lasers.

The performance of modulator-integrated DFB lasers is limited by the optical and electrical crosstalk between the laser and modulator sections. Typically, the separation between the electrical contacts used for the two devices is less than 0.2 mm. Any leakage from the modulator contact to the laser contact can change the dc bias of the laser in a periodic manner. Such unwanted laser-current changes shift the laser wavelength and produce frequency chirp because the laser frequency changes with time. Since laser frequency can shift by more than 200 MHz/mA, the middle section should provide an isolation impedance of 800Ω or more [9]. Although such values are easily realized at low modulation frequencies, this level of isolation is difficult to achieve at microwave frequencies approaching 40 GHz. In one approach, the FM efficiency of the laser is controlled by reducing the chirp parameter β_c for the laser.

The optical crosstalk between the laser and modulator results from the residual reflectivity of the output facet (see Figure 3.18). This residual reflectivity is seen by the laser only when the modulator is on because in the off state, the laser light is totally absorbed by the modulator before it reaches the output facet. As a result, the laser gain, and hence the emission wavelength, are slightly different during each on-off cycle of the modulator. This is an additional source of frequency chirping. It can be nearly eliminated if the front facet has a residual reflectivity of less than 0.01%. However, it is hard to realize antireflection coatings of this quality in practice.

In general, frequency chirp associated with the laser and modulator sections is a limiting factor for modulator-integrated DFB lasers. Typically, the chirp parameter β_c exceeds 2 in the on state and changes to below -2 in the off state when the reverse voltage of about 3 V is applied. In a novel approach, chirp was reduced by designing the quantum wells of the modulator to be relatively shallow [84]. More specifically,

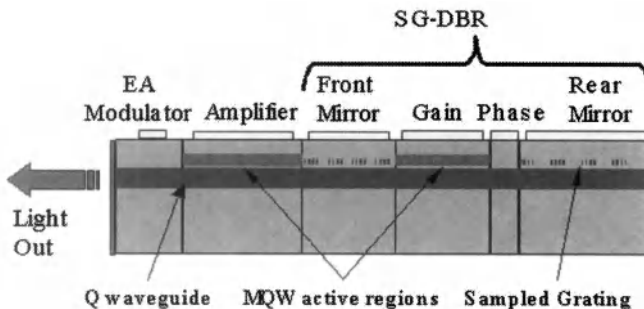


Figure 3.19: Schematic of a DBR laser integrated with an EAM and an amplifier. Both the front and rear DBRs were designed a sampled grating (SG) to enhance the tuning range of the laser. (After Ref. [85]; ©2002 IEEE.)

the bandgap difference between the barrier and quantum-well layers was reduced from 0.2 to close to 0.1 eV. The measured values of β_c were below 0.7 for such devices in the entire 0–3 V range of the reverse bias, resulting in improved performance when the device was used in a lightwave system operating at 10 Gb/s. Physically speaking, frequency chirp is due to changes in the refractive index occurring because of the pileup of electrons and holes inside the quantum wells. Since the carrier escape time is reduced considerably in shallow quantum wells, the carrier density does not build up to high values, resulting in a lower chirp.

Integration of DBR lasers with an EAM provides certain advantages and is being pursued for realizing tunable optical sources. In one 2002 experiment, a four-section DBR laser fabricated with a sampled grating was integrated with a modulator and an amplifier [85], resulting in a six-section structure shown schematically in Figure 3.19. Such a monolithically integrated device was tunable over 40 nm, while maintaining an extinction ratio better than 10 dB [85]. Since then, considerable progress has been made in realizing widely tunable transceivers capable of operating at bit rates of up to 40-Gb/s [87]. Such devices integrate an optical receiver with the laser transmitter on the same chip and can be used over a wavelength range covering the entire the C band.

Some applications require a transmitter capable of emitting a pulse train at high repetition rates such that a short optical pulse is present in each bit slot. Examples of such applications include optical time-division multiplexing and WDM systems designed with advanced modulation formats (see Chapter 10). An EAM modulator can be used for generating short optical pulses suitable for such applications. The EAM in this case acts as a saturable absorber and is employed to realize mode locking of the semiconductor lasers. A DFB laser, integrated monolithically with a MQW modulator, was used as early as 1993 to generate a 20-GHz pulse train [77]. The 7-ps output pulses were nearly transform-limited because of an extremely low chirp associated with the modulator. A 40-GHz train of 1.6 ps pulses was produced in 1999 using an EAM [80]. By 2007, such monolithic mode-locked semiconductor lasers were available in a packaged form [88].

3.5 Light-Emitting Diodes

In some local-area networks, a coherent source is not required, and one can employ a light-emitting diode (LED), a less expensive and longer-lasting optical source with a relatively wide optical spectrum [93]. The basic structure of an LED is similar to that of semiconductor lasers in the sense that both employ an active layer sandwiched between two cladding layers and pumped using a forward-biased p - n junction. The main difference is that stimulated emission does not occur because a population inversion is not realized. Rather, radiative recombination of electron–hole pairs in the active layer generates light through spontaneous emission, some of which escapes from the device and can be coupled into an optical fiber. The emitted light is incoherent with a relatively wide spectral width (30–60 nm) and a relatively large angular spread.

3.5.1 CW Characteristics

It is easy to estimate the internal power generated by spontaneous emission. At a given current I the carrier-injection rate is I/q . In the steady state, the rate of electron–hole pairs recombining through radiative and nonradiative processes is equal to the carrier-injection rate I/q . Since the internal quantum efficiency η_{int} determines the fraction of electron–hole pairs that recombine through spontaneous emission, the rate of photon generation is simply $\eta_{\text{int}}I/q$. The internal optical power is thus given by

$$P_{\text{int}} = \eta_{\text{int}}(\hbar\omega/q)I, \quad (3.5.1)$$

where $\hbar\omega$ is the photon energy, assumed to be nearly the same for all photons. If η_{ext} is the fraction of photons escaping from the device, the emitted power is given by

$$P_e = \eta_{\text{ext}}P_{\text{int}} = \eta_{\text{ext}}\eta_{\text{int}}(\hbar\omega/q)I. \quad (3.5.2)$$

The quantity η_{ext} is called the *external quantum efficiency*. It can be calculated by taking into account internal absorption and the total internal reflection at the semiconductor–air interface. As seen in Figure 3.20, only light emitted within a cone of angle θ_c , where $\theta_c = \sin^{-1}(1/n)$ is the critical angle and n is the refractive index of the semiconductor material, escapes from the LED surface. Internal absorption can be avoided by using heterostructure LEDs in which the cladding layers surrounding the active layer are transparent to the radiation generated. The external quantum efficiency can then be written as

$$\eta_{\text{ext}} = \frac{1}{4\pi} \int_0^{\theta_c} T_f(\theta)(2\pi \sin \theta) d\theta, \quad (3.5.3)$$

where we have assumed that the radiation is emitted uniformly in all directions over a solid angle of 4π . The Fresnel transmissivity T_f depends on the incidence angle θ . In the case of normal incidence ($\theta = 0$), $T_f(0) = 4n/(n+1)^2$. If we replace for simplicity $T_f(\theta)$ by $T_f(0)$ in Eq. (3.5.3), η_{ext} is given approximately by

$$\eta_{\text{ext}} = n^{-1}(n+1)^{-2}. \quad (3.5.4)$$

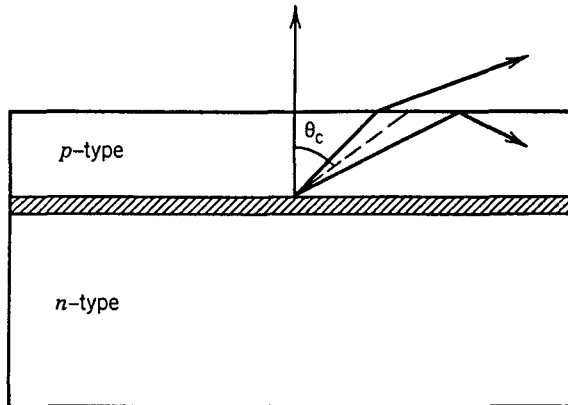


Figure 3.20: Total internal reflection at the output facet of an LED. Only light emitted within a cone of angle θ_c is transmitted, where θ_c is the critical angle for the semiconductor-air interface.

By using Eq. (3.5.4) in Eq. (3.5.2), we obtain the power emitted from one facet. If we use $n = 3.5$ as a typical value, $\eta_{\text{ext}} = 1.4\%$, indicating that only a small fraction of the internal power becomes the useful output power. A further loss in useful power occurs when the emitted light is coupled into an optical fiber. Because of the incoherent nature of the emitted light, an LED acts as a *Lambertian source* with an angular distribution $S(\theta) = S_0 \cos \theta$, where S_0 is the intensity in the direction $\theta = 0$. The coupling efficiency for such a source [93] scales with the numerical aperture (NA) as $(\text{NA})^2$. Since NA for optical fibers falls typically in the range 0.1–0.3, only a few percent of the emitted power is coupled into the fiber (100 μW or less), even though the internal power can easily exceed 10 mW.

A measure of the LED performance is the total quantum efficiency η_{tot} , defined as the ratio of the emitted optical power P_e to the applied electrical power, $P_{\text{elec}} = V_0 I$, where V_0 is the voltage drop across the device. By using Eq. (3.5.2), η_{tot} is given by

$$\eta_{\text{tot}} = \eta_{\text{ext}} \eta_{\text{int}} (\hbar \omega / q V_0). \quad (3.5.5)$$

Typically, $\hbar \omega \approx q V_0$, and $\eta_{\text{tot}} \approx \eta_{\text{ext}} \eta_{\text{int}}$. The total quantum efficiency η_{tot} , also called the *power-conversion efficiency* or the *wall-plug efficiency*, is a measure of the overall performance of the device.

Another quantity sometimes used to characterize the LED performance is the *responsivity* defined as the ratio $R_{\text{LED}} = P_e / I$. From Eq. (3.5.2),

$$R_{\text{LED}} = \eta_{\text{ext}} \eta_{\text{int}} (\hbar \omega / q). \quad (3.5.6)$$

A comparison of Eqs. (3.5.5) and (3.5.6) shows that $R_{\text{LED}} = \eta_{\text{tot}} V_0$. Typical values of R_{LED} are $\sim 0.01 \text{ W/A}$. The responsivity remains constant as long as the linear relation between P_e and I holds. In practice, this linear relationship holds only over a limited current range [94]. Figure 3.21(a) shows the power-current (P - I) curves at several temperatures for a typical 1.3- μm LED. The responsivity of the device decreases at high currents above 80 mA because of the bending of the P - I curve. One reason for

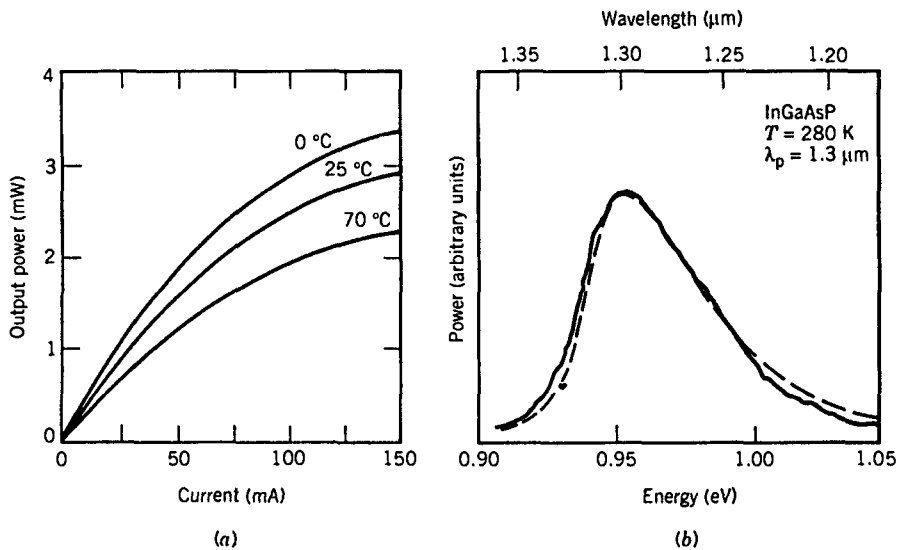


Figure 3.21: (a) Power–current curves at several temperatures; (b) spectrum of the emitted light for a typical 1.3- μm LED. The dashed curve shows the theoretically calculated spectrum. (After Ref. [94]; ©1981 American Institute of Physics.)

this decrease is related to the increase in the active-region temperature. The internal quantum efficiency η_{int} is generally temperature-dependent because of an increase in the nonradiative recombination rates at high temperatures.

The LED spectrum is related to the rate of spontaneous emission given approximately by

$$R_{\text{spon}}(\omega) = A_0(\hbar\omega - E_g)^{1/2} \exp[-(\hbar\omega - E_g)/k_B T], \quad (3.5.7)$$

where A_0 is a constant, k_B is the Boltzmann constant, and E_g is the bandgap. It is easy to deduce that $R_{\text{spon}}(\omega)$ peaks when $\hbar\omega = E_g + k_B T/2$ and has a full-width at half-maximum (FWHM) $\Delta\nu \approx 1.8k_B T/h$. At room temperature ($T = 300 \text{ K}$) the FWHM is about 11 THz. In practice, the spectral width is expressed in nanometers by using $\Delta\nu = (c/\lambda^2)\Delta\lambda$ and increases as λ^2 with an increase in the emission wavelength λ . As a result, $\Delta\lambda$ is larger for InGaAsP LEDs emitting at 1.3 μm by about a factor of 1.7 compared with GaAs LEDs. Figure 3.21(b) shows the output spectrum of a typical 1.3- μm LED and compares it with the theoretical curve obtained by using Eq. (3.5.7). Because of a large spectral width ($\Delta\lambda = 50\text{--}60 \text{ nm}$), LEDs are suitable primarily for local-area networks and are often used in combination with plastic fibers to reduce the overall system cost.

3.5.2 Modulation Response

The modulation response of LEDs depends on carrier dynamics and is limited by the carrier lifetime τ_c . It can be determined by using the carrier rate equation (3.3.2) after

dropping the last term resulting from stimulated emission. The resulting equation is

$$\frac{dN}{dt} = \frac{I}{q} - \frac{N}{\tau_c}. \quad (3.5.8)$$

It can be easily solved in the Fourier domain owing to its linear nature. Consider sinusoidal modulation of the injected current in the form

$$I(t) = I_b + I_m \exp(i\omega_m t), \quad (3.5.9)$$

where I_b is the bias current, I_m is the modulation current, and ω_m is the modulation frequency. Since Eq. (3.5.8) is linear, its general solution can be written as

$$N(t) = N_b + N_m \exp(i\omega_m t), \quad (3.5.10)$$

where $N_b = \tau_c I_b / q$ and N_m is given by

$$N_m(\omega_m) = \frac{\tau_c I_m / q}{1 + i\omega_m \tau_c}. \quad (3.5.11)$$

The modulated power P_m is related to $|N_m|$ linearly. One can define the LED transfer function $H(\omega_m)$ as

$$H(\omega_m) = \frac{N_m(\omega_m)}{N_m(0)} = \frac{1}{1 + i\omega_m \tau_c}. \quad (3.5.12)$$

The *3-dB modulation bandwidth* f_{3dB} is defined as the frequency at which $|H(\omega_m)|$ is reduced by 3 dB, or by a factor of 2. The result is

$$f_{3dB} = \sqrt{3}(2\pi\tau_c)^{-1}. \quad (3.5.13)$$

Typically, τ_c is in the range of 2–5 ns for InGaAsP LEDs. The corresponding LED modulation bandwidth is in the range of 50–140 MHz. Note that Eq. (3.5.13) provides the optical bandwidth because f_{3dB} is defined as the frequency at which optical power is reduced by 3 dB. The corresponding electrical bandwidth is the frequency at which $|H(\omega_m)|^2$ is reduced by 3 dB and is given by $(2\pi\tau_c)^{-1}$.

3.5.3 LED Structures

The LED structures can be classified as surface-emitting or edge-emitting, depending on whether the LED emits light from a surface that is parallel to the junction plane or from the edge of the junction region. Both types can be made using either a *p*-*n* homojunction or a heterostructure design in which the active region is surrounded by *p*- and *n*-type cladding layers. The heterostructure design leads to superior performance, as it provides a control over the emissive area and eliminates internal absorption because of the transparent cladding layers.

Figure 3.22 shows schematically a surface-emitting LED design referred to as the *Burrus-type* LED [95]. The emissive area of the device is limited to a small region whose lateral dimension is comparable to the fiber-core diameter. The use of a gold stud avoids power loss from the back surface. The coupling efficiency is improved by

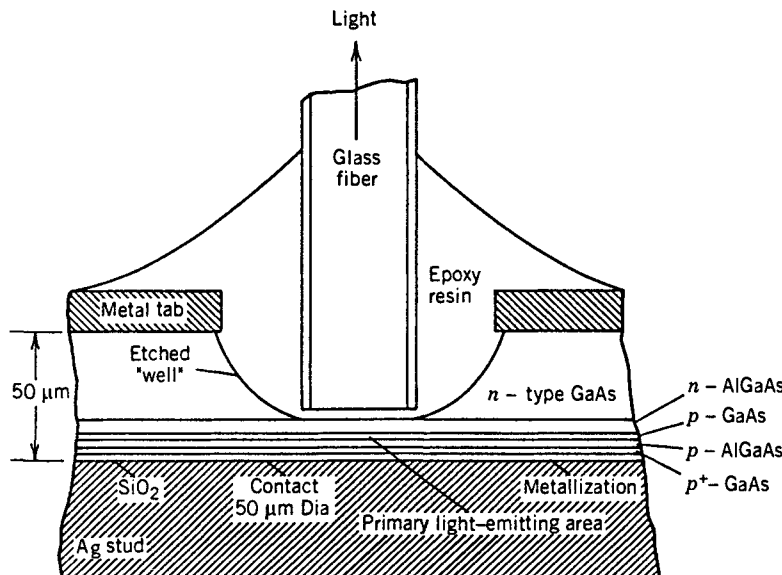


Figure 3.22: Schematic of a surface-emitting LED with a double-heterostructure geometry.

etching a well and bringing the fiber close to the emissive area. The power coupled into the fiber depends on many parameters, such as the numerical aperture of the fiber and the distance between fiber and LED. The addition of epoxy in the etched well tends to increase the external quantum efficiency as it reduces the refractive-index mismatch. Several variations of the basic design exist in the literature. In one variation, a truncated spherical microlens fabricated inside the etched well is used to couple light into the fiber. In another variation, the fiber end is itself made in the form of a spherical lens. With a proper design, surface-emitting LEDs can couple up to 1% of the internally generated power into an optical fiber.

The edge-emitting LEDs employ a design identical to that used for semiconductor lasers. In fact, a semiconductor laser is converted into an LED by depositing an antireflection coating on its output facet to suppress lasing action. Beam divergence of edge-emitting LEDs differs from surface-emitting LEDs because of waveguiding in the plane perpendicular to the junction. Surface-emitting LEDs operate as a Lambertian source with angular distribution $S_e(\theta) = S_0 \cos \theta$ in both directions. The resulting beam divergence has a FWHM of 120° in each direction. In contrast, edge-emitting LEDs have a divergence of only about 30° in the direction perpendicular to the junction plane. Considerable light can be coupled into a fiber of even low numerical aperture (<0.3) because of reduced divergence and high radiance at the emitting facet. The modulation bandwidth of edge-emitting LEDs is generally larger (~ 200 MHz) than that of surface-emitting LEDs because of a reduced carrier lifetime at the same applied current. The choice between the two designs is dictated, in practice, by a compromise between cost and performance.

In spite of a relatively low output power and a low bandwidth of LEDs compared

with those of lasers, LEDs are useful for low-cost applications requiring data transmission at a bit rate of 100 Mb/s or less over a few kilometers. For this reason, several new LED structures were developed during the 1990s [96]–[101]. In one design, known as resonant-cavity LED [96], two metal mirrors are fabricated around the epitaxially grown layers, and the device is bonded to a silicon substrate. In a variant of this idea, the bottom mirror is fabricated epitaxially by using a stack of alternating layers of two different semiconductors, while the top mirror consists of a deformable membrane suspended by an air gap [97]. The operating wavelength of such an LED can be tuned over 40 nm by changing the air-gap thickness. In another scheme, several quantum wells with different compositions and bandgaps are grown to form a MQW structure [98]. Since each quantum well emits light at a different wavelength, such LEDs can have an extremely broad spectrum (extending over a 500-nm wavelength range) and are useful for local-area WDM networks.

3.6 Transmitter Design

So far this chapter has focused on the properties of optical sources. Although an optical source is a major component of optical transmitters, it is not the only component. Other components include a modulator for converting electrical data into optical form (if direct modulation is not used) and an electrical driving circuit for supplying current to the optical source. This section covers the design of optical transmitters with emphasis on the packaging issues [102]–[110].

3.6.1 Source–Fiber Coupling

The design objective for any transmitter is to couple as much light as possible into the optical fiber. In practice, the coupling efficiency depends on the type of optical source (LED versus laser) as well as on the type of fiber (multimode versus single mode). The coupling can be very inefficient when light from an LED is coupled into a single-mode fiber. As discussed briefly in Section 3.5.1, the coupling efficiency for an LED changes with the numerical aperture, and can become $< 1\%$ in the case of single-mode fibers. In contrast, the coupling efficiency for edge-emitting lasers is typically 40–50% and can exceed 80% for VCSELs because of their circular spot size. A small piece of fiber (known as a pigtail) is included with the transmitter so that the coupling efficiency can be maximized during packaging; a splice or connector is used to join the pigtail with the fiber cable.

Two approaches have been used for source–fiber coupling. In one approach, known as direct or *butt coupling*, the fiber is brought close to the source and held in place by epoxy. In the other, known as *lens coupling*, a lens is used to maximize the coupling efficiency. Each approach has its own merits, and the choice generally depends on the design objectives. An important criterion is that the coupling efficiency should not change with time; mechanical stability of the coupling scheme is therefore a necessary requirement.

An example of butt coupling is shown in Figure 3.23(a), where the fiber is brought in contact with a surface-emitting LED. The coupling efficiency for a fiber of numerical

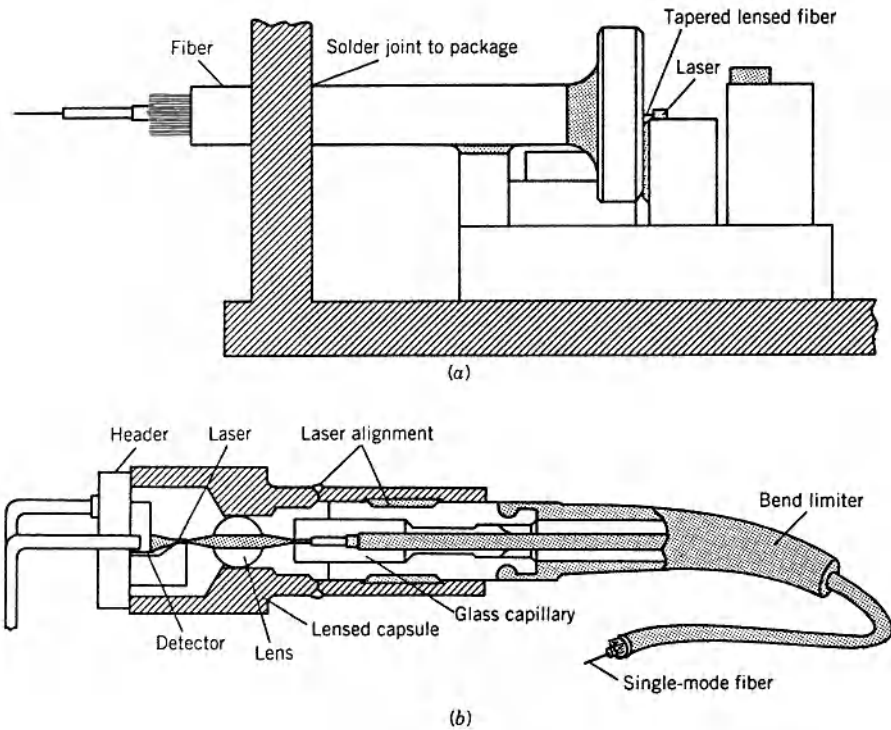


Figure 3.23: Transmitters employing (a) butt-coupling and (b) lens-coupling designs. (After Ref. [104]; ©1989 AT&T; reprinted with permission.)

aperture NA is given by [103]

$$n_c = (1 - R_f)(NA)^2, \quad (3.6.1)$$

where R_f is the reflectivity at the fiber front end. R_f is about 4% if an air gap exists between the source and the fiber but can be reduced to nearly zero by placing an index-matching liquid. The coupling efficiency is about 1% for a surface-emitting LED and roughly 10% for an edge-emitting LED. Some improvement is possible in both cases by using fibers that are tapered or have a lensed tip. An external lens also improves the coupling efficiency but only at the expense of reduced mechanical tolerance.

The coupling of a semiconductor laser to a single-mode optical fiber is more efficient than that of an LED. The butt coupling provides only about 10% efficiency, as it makes no attempt to match the mode sizes of the laser and the fiber. Typically, index-guided InGaAsP lasers have a mode size of about $1\text{ }\mu\text{m}$, whereas the mode size of a single-mode fiber is in the range $6\text{--}9\text{ }\mu\text{m}$. The coupling efficiency can be improved by tapering the fiber end and forming a lens at the fiber tip. Figure 3.23(a) shows such a butt-coupling scheme for a commercial transmitter. The fiber is attached to a jewel, and the jewel is attached to the laser submount by using an epoxy [104]. The fiber tip is aligned with the emitting region of the laser to maximize the coupling efficiency.

(typically 40%). The use of a lensed fiber can improve the coupling efficiency, and values close to 100% have been realized with an optimum design [105]–[107].

Figure 3.23(b) shows a lens-coupling approach for transmitter design. The coupling efficiency can exceed 70% for such a confocal design in which a sphere is used to collimate the laser light and focus it onto the fiber core. The alignment of the fiber core is less critical for the confocal design because the spot size is magnified to match the fiber's mode size. The mechanical stability of the package is ensured by soldering the fiber into a ferrule which is secured to the body by two sets of laser alignment welds. One set of welds establishes proper axial alignment, while the other set provides transverse alignment.

The laser–fiber coupling issue remains important, and several new schemes have been developed in recent years [108]–[112]. In one approach, a *silicon optical bench* is used to align the laser and the fiber [108]. In another, a *silicon micromirror*, fabricated with the micro-machining technology, is used for optical alignment [109]. In a different approach, a *spot-size converter* is employed for maximizing the coupling efficiency. Coupling efficiencies of up to 80% were realized by 1997 by integrating a spot-size converter with InP semiconductor lasers [110]. A lensed, graded-index, oval-core fiber has also provided higher coupling efficiency compared with conventional lensed fibers [111].

An important problem that needs to be addressed in designing an optical transmitter is related to the extreme sensitivity of semiconductor lasers to optical feedback [2]. Even a relatively small amount of feedback (< 0.1%) can destabilize the laser and affect the system performance through phenomena such as linewidth broadening, mode hopping, and RIN enhancement [113]–[117]. Attempts are made to reduce the feedback into the laser cavity by using antireflection coatings. Feedback can also be reduced by cutting the fiber tip at a slight angle so that the reflected light does not hit the active region of the laser. Such precautions are generally enough to reduce the feedback to a tolerable level. However, it becomes necessary to use an *optical isolator* between the laser and the fiber in transmitters designed for more demanding applications. One such application corresponds to lightwave systems operating at high bit rates and requiring a narrow-linewidth DFB laser.

Most optical isolators make use of the *Faraday effect*, which governs the rotation of the plane of polarization of an optical beam in the presence of a magnetic field: The rotation is in the same direction for light propagating parallel or antiparallel to the magnetic field direction. Optical isolators consist of a rod of Faraday material such as yttrium iron garnet (YIG), whose length is chosen to provide 45° rotation. The YIG rod is sandwiched between two polarizers whose axes are tilted by 45° with respect to each other. Light propagating in one direction passes through the second polarizer because of the Faraday rotation. By contrast, light propagating in the opposite direction is blocked by the first polarizer. Desirable characteristics of optical isolators are low insertion loss, high isolation (> 30 dB), compact size, and a wide spectral bandwidth of operation. A very compact isolator can be designed if the lens in Figure 3.23(b) is replaced by a YIG sphere so that it serves a dual purpose [118]. As light from a semiconductor laser is already polarized, a signal polarizer placed between the YIG sphere and the fiber can reduce the feedback by more than 30 dB.

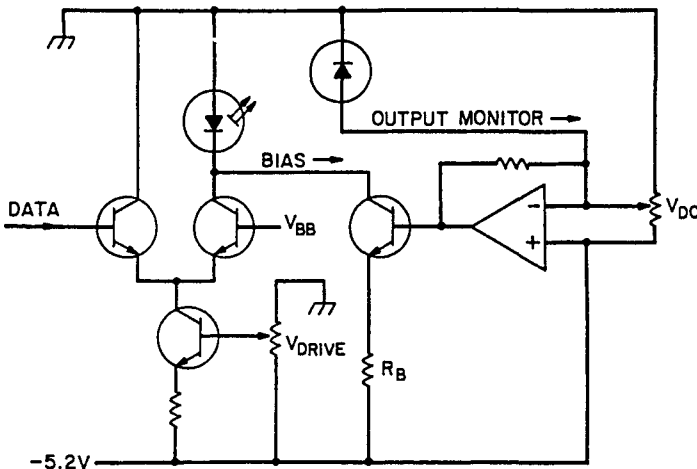


Figure 3.24: Driving circuit for a laser transmitter with feedback control to keep the average optical power constant. A photodiode monitors the output power and provides the control signal. (After Ref. [102]; ©1988 Academic Press; reprinted with permission.)

3.6.2 Driving Circuitry

The purpose of driving circuitry is to provide electrical power to the optical source and to modulate the light output in accordance with the signal that is to be transmitted. Driving circuits are relatively simple for LED transmitters but become increasingly complicated for high-bit-rate optical transmitters employing semiconductor lasers as an optical source [102]. In the case of direct modulation (see Section 3.4.1), semiconductor lasers are biased near threshold and then modulated through an electrical time-dependent signal. In this case, the driving circuit is designed to supply a constant bias current as well as modulated electrical signal. Furthermore, a servo loop is often used to keep the average optical power constant.

Figure 3.24 shows a simple driving circuit that controls the average optical power through a feedback mechanism. A photodiode monitors the laser output and generates the control signal that is used to adjust the laser bias level. The rear facet of the laser is generally used for the monitoring purpose (see Figure 3.23). In some transmitters a front-end tap is used to divert a small fraction of the output power to the detector. The bias-level control is essential, since the laser threshold is sensitive to the operating temperature. The threshold current also increases with aging of the transmitter because of gradual degradation of the semiconductor laser.

The driving circuit shown in Figure 3.24 adjusts the bias level dynamically but leaves the modulation current unchanged. Such an approach is acceptable if the slope efficiency of the laser does not change with aging. As discussed in Section 3.3.1 and seen in Figure 3.13, the slope efficiency of the laser generally decreases with an increase in temperature. A thermoelectric cooler is often used to stabilize the laser temperature. An alternative approach consists of designing driving circuits that use dual-loop feedback circuits and adjust both the bias current and the modulation current

automatically [119].

The electrical components used in the driving circuit determine the rate at which the transmitter output can be modulated. For lightwave transmitters operating at bit rates above 1 Gb/s, electrical parasitics associated with various transistors and other components often limit the transmitter performance. The performance of high-speed transmitters can be improved considerably by using monolithic integration of the laser with the driver. Since optical and electrical devices are fabricated on the same chip, such monolithic transmitters are referred to as *optoelectronic integrated-circuit* (OEIC) transmitters. The OEIC approach was first applied to integration of GaAs lasers, since the technology for fabrication of GaAs electrical devices is relatively well established [120]–[122]. The technology for fabrication of InP OEICs evolved rapidly during the 1990s [123]–[127]. A 1.5- μm OEIC transmitter capable of operating at 5 Gb/s was demonstrated in 1988 [123]. By 1995, 10-Gb/s laser transmitters were fabricated by integrating 1.55- μm DFB lasers with field-effect transistors made with the InGaAs/InAlAs material system. Since then, OEIC transmitters with multiple lasers on the same chip have been developed for WDM applications (see Chapter 6).

The concept of monolithic integration can be extended to build single-chip transmitters by adding all functionality on the same chip. Considerable effort has been directed toward developing such OEICs, often called *photonic integrated circuits*, which integrate on the same chip multiple optical components, such as lasers, detectors, modulators, amplifiers, filters, and waveguides [128]–[131]. Such integrated circuits had reached the commercial stage by 2008.

3.6.3 Reliability and Packaging

An optical transmitter should operate reliably over a relatively long period of time (10 years or more) in order to be useful as a major component of lightwave systems. The reliability requirements are quite stringent for undersea lightwave systems, for which repairs and replacement are prohibitively expensive. By far the major reason for failure of optical transmitters is the optical source itself. Considerable testing is performed during assembly and manufacture of transmitters to ensure a reasonable lifetime for the optical source. It is common [102] to quantify the lifetime by a parameter t_F known as *mean time to failure* (MTTF). Its use is based on the assumption of an exponential failure probability [$P_F = \exp(-t/t_F)$]. Typically, t_F should exceed 10^5 hours (about 11 years) for the optical source. Reliability of semiconductor lasers has been studied extensively to ensure their operation under realistic operating conditions [132]–[138].

Both LEDs and semiconductor lasers can stop operating suddenly (catastrophic degradation) or may exhibit a gradual mode of degradation in which the device efficiency degrades with aging [133]. Attempts are made to identify devices that are likely to degrade catastrophically. A common method is to operate the device at high temperatures and high current levels. This technique is referred to as burn-in or *accelerated aging* [132] and is based on the assumption that under high-stress conditions weak devices will fail, while others will stabilize after an initial period of rapid degradation. The change in the operating current at a constant power is used as a measure of device degradation. Figure 3.25 shows the change in the operating current of a 1.3- μm InGaAsP laser aged at 60°C under a constant output power of 5 mW from each facet.

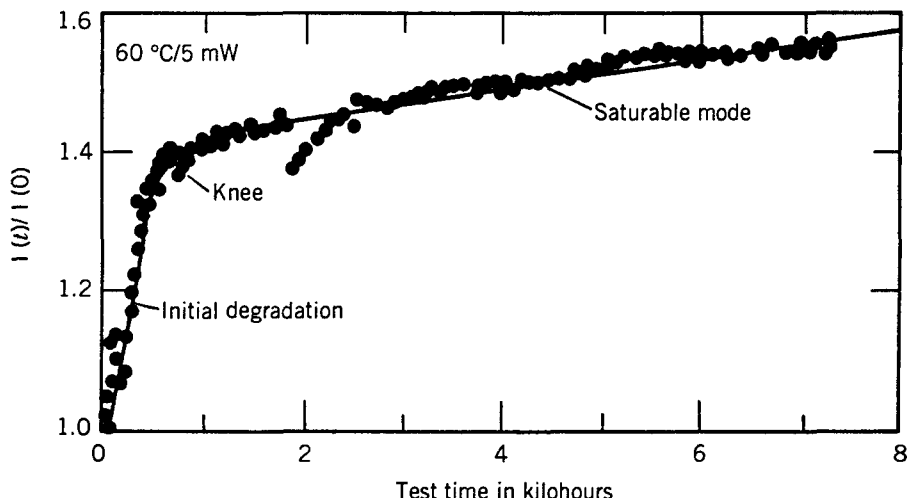


Figure 3.25: Change in current as a function of time for a 1.3- μm InGaAsP laser aged at 60°C with 5 mW of output power. (After Ref. [134]; ©1985 AT&T; reprinted with permission.)

The operating current for this laser increases by 40% in the first 400 hours but then stabilizes and increases at a much reduced rate indicative of gradual degradation. The degradation rate can be used to estimate the laser lifetime and the MTTF at the elevated temperature. The MTTF at the normal operating temperature is then extrapolated by using an Arrhenius-type relation $t_F = t_0 \exp(-E_a/k_B T)$, where t_0 is a constant and E_a is the activation energy with a typical value of about 1 eV [133]. Physically, gradual degradation is due to the generation of various kinds of defects (dark-line defects, dark-spot defects) within the active region of the laser or LED [2].

Extensive tests have shown that LEDs are normally more reliable than semiconductor lasers under the same operating conditions. The MTTF for GaAs LEDs easily exceeds 10^6 hours and can be $> 10^7$ hours at 25°C [133]. The MTTF for InGaAsP LEDs is even larger, approaching a value $\sim 10^9$ hours. By contrast, the MTTF for InGaAsP lasers is generally limited to 10^6 hours at 25°C [134]–[136]. Nonetheless, this value is large enough that semiconductor lasers can be used in undersea optical transmitters designed to operate reliably for a period of 25 years. Because of the adverse effect of high temperatures on device reliability, most transmitters use a thermoelectric cooler to maintain the source temperature near 20°C even when the outside temperature may be as high as 80°C.

Even with a reliable optical source, a transmitter may fail in an actual system if the coupling between the source and the fiber degrades with aging. Coupling stability is an important issue in the design of reliable optical transmitters. It depends ultimately on the packaging of transmitters. Although LEDs are often packaged nonhermetically, an hermetic environment is essential for semiconductor lasers. It is common to package the laser separately so that it is isolated from other transmitter components. Figure 3.23 showed two examples of laser packages. In the butt-coupling scheme, an epoxy is used to hold the laser and fiber in place. Coupling stability in this case depends

on how epoxy changes with aging of the transmitter. In the lens-coupling scheme, laser welding is used to hold various parts of the assembly together. The laser package becomes a part of the transmitter package, which includes other electrical components associated with the driving circuit. The choice of transmitter package depends on the type of application; a dual-in-line package or a butterfly housing with multiple pins is typically used.

Testing and packaging of optical transmitters are two important parts of the manufacturing process [135], and both of them add considerably to the cost of a transmitter. The development of low-cost packaged transmitters is necessary, especially for local-area and local-loop applications.

Problems

- 3.1** Find the composition of the quaternary alloy InGaAsP for making semiconductor lasers operating at 1.3- and 1.55- μm wavelengths.
- 3.2** The active region of a 1.3- μm InGaAsP laser is 250 μm long. Find the active-region gain required for the laser to reach threshold. Assume that the internal loss is 30 cm^{-1} , the mode index is 3.3, and the confinement factor is 0.4.
- 3.3** Derive the eigenvalue equation for the transverse-electric (TE) modes of a planar waveguide of thickness d and refractive index n_1 sandwiched between two cladding layers of refractive index n_2 . (*Hint:* Follow the method of Section 2.2.2 using Cartesian coordinates.)
- 3.4** Use the result of Problem 3.3 to find the single-mode condition. Use this condition to find the maximum allowed thickness of the active layer for a 1.3- μm semiconductor laser. How does this value change if the laser operates at 1.55 μm ? Assume $n_1 = 3.5$ and $n_2 = 3.2$.
- 3.5** Solve the rate equations in the steady state and obtain the analytic expressions for P and N as a function of the injection current I . Neglect spontaneous emission for simplicity.
- 3.6** A semiconductor laser is operating continuously at a certain current. Its output power changes slightly because of a transient current fluctuation. Show that the laser power will attain its original value through an oscillatory approach. Obtain the frequency and the damping time of such relaxation oscillations.
- 3.7** A 250- μm -long InGaAsP laser has an internal loss of 40 cm^{-1} . It operates at 1.55 μm in a single mode, with the modal index 3.3 and the group index 3.4. Calculate the photon lifetime. What is the threshold value of the electron population? Assume that the gain varies as $G = G_N(N - N_0)$ with $G_N = 6 \times 10^3 \text{ s}^{-1}$ and $N_0 = 1 \times 10^8$.
- 3.8** Determine the threshold current for the semiconductor laser of Problem 3.7 by taking 2 ns as the carrier lifetime. How much power is emitted from one facet when the laser is operated twice above threshold?
- 3.9** Consider the laser of Problem 3.7 operating twice above threshold. Calculate the differential quantum efficiency and the external quantum efficiency for the

laser. What is the device (wall-plug) efficiency if the external voltage is 1.5 V? Assume that the internal quantum efficiency is 90%.

- 3.10** Calculate the frequency (in GHz units) and the damping time of the relaxation oscillations for the laser of Problem 3.7 operating twice above threshold. Assume that $G_P = -4 \times 10^4 \text{ s}^{-1}$, where G_P is the derivative of G with respect to P . Also assume that $R_{\text{sp}} = 2/\tau_p$.
- 3.11** Determine the 3-dB modulation bandwidth for the laser of Problem 3.7 biased to operate twice above threshold. What is the corresponding 3-dB electrical bandwidth?
- 3.12** The threshold current of a semiconductor laser doubles when the operating temperature is increased by 50°C. What is the characteristic temperature of the laser?
- 3.13** Derive an expression for the 3-dB modulation bandwidth by assuming that the gain G in the rate equations varies with N and P as

$$G(N, P) = G_N(N - N_0)(1 + P/P_s)^{-1/2}.$$

Show that the bandwidth saturates at high operating powers.

- 3.14** Solve the rate equations (3.3.1) and (3.3.2) numerically by using $I(t) = I_b + I_m f_p(t)$, where $f_p(t)$ represents a rectangular pulse of 200-ps duration. Assume that $I_b/I_{\text{th}} = 0.8$, $I_m/I_{\text{th}} = 3$, $\tau_p = 3 \text{ ps}$, $\tau_c = 2 \text{ ns}$, and $R_{\text{sp}} = 2/\tau_p$. Use Eq. (3.3.15) for the gain G with $G_N = 10^4 \text{ s}^{-1}$, $N_0 = 10^8$, and $\epsilon_{\text{NL}} = 10^{-7}$. Plot the optical pulse shape and the frequency chirp. Why is the optical pulse much shorter than the applied current pulse?
- 3.15** Complete the derivation of Eq. (3.3.31) for the RIN. How does this expression change if the gain G is assumed of the form of Problem 3.15?
- 3.16** Calculate the autocorrelation $C_{pp}(\tau)$ by using Eqs. (3.3.30) and (3.3.31). Use it to derive an expression for the SNR of the laser output.
- 3.17** Show that the external quantum efficiency of a planar LED is given approximately by $\eta_{\text{ext}} = n^{-1}(n+1)^{-2}$, where n is the refractive index of the semiconductor-air interface. Consider Fresnel reflection and total internal reflection at the output facet. Assume that the internal radiation is uniform in all directions.
- 3.18** Prove that the 3-dB optical bandwidth of a LED is related to the 3-dB electrical bandwidth by the relation $f_{3\text{dB}}(\text{optical}) = \sqrt{3}f_{3\text{dB}}(\text{electrical})$.

References

- [1] Z. Alferov, *IEEE J. Sel. Topics Quantum Electron.* **6**, 832 (2000).
- [2] G. P. Agrawal and N. K. Dutta, *Semiconductor Lasers*, 2nd ed., Van Nostrand Reinhold, New York, 1993.
- [3] S. L. Chuang, *Physics of Optoelectronic Devices*, 2nd ed., Wiley, Hoboken, NJ, 2008.
- [4] L. A. Coldren and S. W. Corzine, *Diode Lasers and Photonic Integrated Circuits*, Wiley, New York, 1995.

- [5] G. P. Agrawal, Ed., *Semiconductor Lasers: Past, Present, and Future*, AIP Press, Woodbury, NY, 1995.
- [6] E. Kapon, Ed., *Semiconductor Lasers*, Part I and II, Academic Press, San Diego, CA, 1999.
- [7] W. W. Chow and S. W. Koch, *Semiconductor-Laser Fundamentals*, Springer, New York, 1999.
- [8] M. Dutta and M. A. Stroscio, Eds., *Advances in Semiconductor Lasers and Application to Optoelectronics*, World Scientific, Singapore, 2000.
- [9] D. A. Ackerman, J. E. Johnson, L. J. P. Ketelsen, L. E. Eng, P. A. Kiely, and T. G. B. Mason, *Optical Fiber Telecommunications*, Vol. 4A, I. P. Kaminow and T. Li, Eds., Academic Press, Boston, 2002, Chap. 12.
- [10] T. Suhara, *Semiconductor Laser Fundamentals*, CRC Press, 2004.
- [11] C. Ye, *Tunable Semiconductor Diode Lasers*, World Scientific, Singapore, 2007.
- [12] S. L. Chuang, G. Liu, and T. K. Kondrakko, in *Optical Fiber Telecommunications*, Vol. 5A, I. P. Kaminow, T. Li, and A. E. Willner, Eds., Academic Press, Boston, 2008, Chap. 12.
- [13] R. Wyatt and W. J. Devlin, *Electron. Lett.* **19**, 110 (1983).
- [14] W. T. Tsang, Ed., *Semiconductors and Semimetals*, Vol. 22B, Academic Press, Boston, 1985, Chap. 4.
- [15] S. Akiba, M. Usami, and K. Utaka, *J. Lightwave Technol.* **5**, 1564 (1987).
- [16] G. P. Agrawal, in *Progress in Optics*, Vol. 26, E. Wolf, Ed., North-Holland, Amsterdam, 1988, Chap. 3.
- [17] J. Buus, *Single Frequency Semiconductor Lasers*, SPIE Press, Bellingham, WA, 1991.
- [18] N. Chinone and M. Okai, in *Semiconductor Lasers: Past, Present, and Future*, G. P. Agrawal, Ed., AIP Press, Woodbury, NY, 1995, Chap. 2.
- [19] G. Morthier and P. Vankwikelberge, *Handbook of Distributed Feedback Laser Diodes*, Artech House, Norwood, MA, 1995.
- [20] J. E. Carroll, J. E. Whiteaway, and R. G. Plumb, *Distributed Feedback Semiconductor Lasers*, INSPEC, London, 1998.
- [21] J. Hong, C. Blaauw, R. Moore, S. Jatar, and S. Doziba, *IEEE J. Sel. Topics Quantum Electron.* **5**, 442 (1999).
- [22] H. Hillmer, A. Grabmaier, S. Hansmann, H.-L. Zhu, H. Burkhard, and K. Magari, *IEEE J. Sel. Topics Quantum Electron.* **1**, 356 (1995).
- [23] H. Ishii, F. Kano, Y. Tohmori, Y. Kondo, T. Tamamura, and Y. Yoshikuni, *IEEE J. Sel. Topics Quantum Electron.* **1**, 401 (1995).
- [24] P.-J. Rigole, S. Nilsson, I. Bäckbom, T. Klinga, J. Wallin, B. Stålnacke, E. Berglind, and B. Stoltz, *IEEE Photon. Technol. Lett.* **7**, 697 (1995); **7**, 1249 (1995).
- [25] G. Albert, F. Delorme, S. Grossmaire, S. Slempkes, A. Ougazzaden, and H. Nakajima, *IEEE J. Sel. Topics Quantum Electron.* **3**, 598 (1997).
- [26] F. Delorme, G. Albert, P. Boulet, S. Grossmaire, S. Slempkes, and A. Ougazzaden, *IEEE J. Sel. Topics Quantum Electron.* **3**, 607 (1997).
- [27] L. Coldren, *IEEE J. Sel. Topics Quantum Electron.* **6**, 988 (2000).
- [28] L. A. Coldren, G. A. Fish, Y. Akulova, J. S. Barton, and C. W. Coldren, *J. Lightwave Technol.* **22**, 193 (2004).
- [29] J. Buus, M.-C. Amann, and D. J. Blumenthal, *Tunable Laser Diodes and Related Optical Sources*, 2nd ed., IEEE Press, Piscataway, NJ, 2005.
- [30] J. Klamkin, J. M. Hutchinson, J. T. Getty, L. A. Johansson, E. J. Skogen, and L. A. Coldren, *IEEE J. Sel. Topics Quantum Electron.* **11**, 931 (2005).

- [31] R. Todt, T. Jacke, R. Meyer, R. Laroy, G. Morthier, and M.-C. Amann, *IEEE J. Sel. Topics Quantum Electron.* **13**, 1095 (2007).
- [32] C. J. Chang-Hasnain, in *Semiconductor Lasers: Past, Present, and Future*, G. P. Agrawal, Ed., AIP Press, Woodbury, NY, 1995, Chap. 5.
- [33] A. E. Bond, P. D. Dapkus, and J. D. O'Brien, *IEEE J. Sel. Topics Quantum Electron.* **5**, 574 (1999).
- [34] C. Wilmsen, H. Temkin, and L.A. Coldren, Eds., *Vertical-Cavity Surface-Emitting Lasers*, Cambridge University Press, New York, 1999.
- [35] C. J. Chang-Hasnain, *IEEE J. Sel. Topics Quantum Electron.* **6**, 978 (2000).
- [36] K. Iga, *IEEE J. Sel. Topics Quantum Electron.* **6**, 1201 (2000).
- [37] A. Karim, S. Björlin, J. Piprek, and J. E. Bowers, *IEEE J. Sel. Topics Quantum Electron.* **6**, 1244 (2000).
- [38] H. Li and K. Iga, *Vertical-Cavity Surface-Emitting Laser Devices*, Springer, New York, 2001.
- [39] Y. Matsui, D. Vakhshoori, P. Wang, P. Chen, C.-C. Lu, M. Jiang, K. Knopp, S. Burroughs, and P. Tayebati, *IEEE J. Quantum Electron.* **39**, 1037 (2003).
- [40] C.-K. Lin, D. P. Bour, J. Zhu, W. H. Perez, M. H. Leary, A. Tandon, S. W. Corzine, and M. R. T. Tan, *IEEE J. Sel. Topics Quantum Electron.* **9**, 1415 (2003).
- [41] F. Koyama, *J. Lightwave Technol.* **24**, 4502 (2006).
- [42] E. Söderberg, J. S. Gustavsson, P. Modh, A. Larsson, Z. Zhang, J. Berggren, and M. Hammar, *J. Lightwave Technol.* **25**, 2791 (2007).
- [43] P. Debernardi, B. Kögel, K. Zogal, P. Meissner, M. Maute, M. Ortsiefer, G. Böhm, and M.-C. Amann, *IEEE J. Quantum Electron.* **44**, 391 (2008).
- [44] T. R. Chen, J. Ungar, J. Iannelli, S. Oh, H. Luong, and N. Bar-Chaim, *Electron. Lett.* **32**, 898 (1996).
- [45] M. Funabashi, H. Nasu, T. Mukaihara, T. Kimoto, T. Shinagawa, T. Kise, K. Takaki, T. Takagi, M. Oike, T. Nomura, and A. Kasukawa, *IEEE J. Sel. Topics Quantum Electron.* **10**, 312 (2004).
- [46] G. P. Agrawal, *IEEE J. Quantum Electron.* **23**, 860 (1987).
- [47] G. P. Agrawal, *IEEE J. Quantum Electron.* **26**, 1901 (1990).
- [48] G. P. Agrawal and G. R. Gray, *Proc. SPIE* **1497**, 444 (1991).
- [49] C. Z. Ning and J. V. Moloney, *Appl. Phys. Lett.* **66**, 559 (1995).
- [50] M. Osinski and J. Buus, *IEEE J. Quantum Electron.* **23**, 9 (1987).
- [51] H. Ishikawa, H. Soda, K. Wakao, K. Kihara, K. Kamite, Y. Kotaki, M. Matsuda, H. Sudo, S. Yamakoshi, S. Isozumi, and H. Imai, *J. Lightwave Technol.* **5**, 848 (1987).
- [52] P. A. Morton, T. Tanbun-Ek, R. A. Logan, N. Chand, K. W. Wecht, A. M. Sergent, and P. F. Sciortino, *Electron. Lett.* **30**, 2044 (1994).
- [53] E. Goutain, J. C. Renaud, M. Krakowski, D. Rondi, R. Blondeau, and D. Decoster, *Electron. Lett.* **32**, 896 (1996).
- [54] S. Lindgren, H. Ahlfeldt, L. Backlin, L. Forssen, C. Vieider, H. Elderstig, M. Svensson, L. Granlund, L. Andersson, B. Kerzar, B. Broberg, O. Kjebon, R. Schatz, E. Forzelius, and S. Nilsson, *IEEE Photon. Technol. Lett.* **9**, 306 (1997).
- [55] C.-W. Hu, F.-M. Lee, T.-C. Peng, T.-M. Ou, M.-C. Wu, and Y.-H. Huang, *J. Lightwave Technol.* **24**, 2906 (2006).
- [56] H.-K. Sung, E. K. Lau, and M. C. Wu, *IEEE J. Sel. Topics Quantum Electron.* **13**, 1215 (2007).
- [57] G. P. Agrawal, *Proc. SPIE* **1376**, 224 (1991).

- [58] M. Lax, *Rev. Mod. Phys.* **38**, 541 (1966); *IEEE J. Quantum Electron.* **3**, 37 (1967).
- [59] C. H. Henry, *IEEE J. Quantum Electron.* **18**, 259 (1982); **19**, 1391 (1983); *J. Lightwave Technol.* **4**, 298 (1986).
- [60] G. P. Agrawal, *Electron. Lett.* **27**, 232 (1991).
- [61] G. P. Agrawal, *Phys. Rev. A* **37**, 2488 (1988).
- [62] J. Y. Law and G. P. Agrawal, *IEEE Photon. Technol. Lett.* **9**, 437 (1997).
- [63] M. Aoki, K. Uomi, T. Tsuchiya, S. Sasaki, M. Okai, and N. Chinone, *IEEE J. Quantum Electron.* **27**, 1782 (1991).
- [64] R. A. Linke, *Electron. Lett.* **20**, 472 (1984); *IEEE J. Quantum Electron.* **21**, 593 (1985).
- [65] G. P. Agrawal and M. J. Potasek, *Opt. Lett.* **11**, 318 (1986).
- [66] R. Olshansky and D. Fye, *Electron. Lett.* **20**, 928 (1984).
- [67] G. P. Agrawal, *Opt. Lett.* **10**, 10 (1985).
- [68] N. A. Olsson, C. H. Henry, R. F. Kazarinov, H. J. Lee, and K. J. Orlowsky, *IEEE J. Quantum Electron.* **24**, 143 (1988).
- [69] H. D. Summers and I. H. White, *Electron. Lett.* **30**, 1140 (1994).
- [70] F. Kano, T. Yamanaka, N. Yamamoto, H. Mawatan, Y. Tohmori, and Y. Yoshikuni, *IEEE J. Quantum Electron.* **30**, 533 (1994).
- [71] G. P. Agrawal, *Applications of Nonlinear Fiber Optics*, 2nd ed., Academic Press, San Diego, CA, 2008.
- [72] E. L. Wooten, K. M. Kiss, A. Yi-Yan, E. J. Murphy, D. A. Lafaw, P. F. Hallemeier, D. Maack, D. V. Attanasio, D. J. Fritz, G. J. McBrien, and D. E. Bossi, *IEEE J. Sel. Topics Quantum Electron.* **6**, 69 (2000).
- [73] N. Courjal, H. Porte, J. Hauden, P. Mollier and N. Grossard, *J. Lightwave Technol.* **22**, 1338 (2004).
- [74] S. Oikawa, F. Yamamoto, J. Ichikawa, S. Kurimura and K. Kitamura, *J. Lightwave Technol.* **23**, 2756 (2005).
- [75] F. Lucchi, D. Janner, M. Belmonte, S. Balsamo, M. Villa, S. Giurgola, P. Vergani, V. Pruneri, *Opt. Express* **15**, 10739 (2007).
- [76] A. Mahapatra and E. J. Murphy, in *Optical Fiber Telecommunications*, Vol. 4A, I. P. Kaminow, T. Li, and A. E. Willner, Eds., Academic Press, San Diego, CA, 2008, Chap. 6.
- [77] M. Aoki, M. Suzuki, H. Sano, T. Kawano, T. Ido, T. Taniwatari, K. Uomi, and A. Takai, *IEEE J. Quantum Electron.* **29**, 2088 (1993).
- [78] G. Raybon, U. Koren, M. G. Young, B. I. Miller, M. Chien, T. H. Wood, and H. M. Presby, *Electron. Lett.* **30**, 1330 (1994).
- [79] H. Takeuchi, K. Tsuzuki, K. Sato, M. Yamamoto, Y. Itaya, A. Sano, M. Yoneyama, and T. Otsuji, *IEEE J. Sel. Topics Quantum Electron.* **3**, 336 (1997).
- [80] A. D. Ellis, R. J. Manning, I. D. Phillips, and D. Nessel, *Electron. Lett.* **35**, 645 (1999).
- [81] Y. Kim, S. K. Kim, J. Lee, Y. Kim, J. Kang, W. Choi, and J. Jeong, *Opt. Fiber Technol.* **7**, 84 (2001).
- [82] Y. Akage, K. Kawano, S. Oku, R. Iga, H. Okamoto, Y. Miyamoto, and H. Takeuchi, *Electron. Lett.* **37**, 299 (2001).
- [83] H. Kawanishi, Y. Yamauchi, N. Mineo, Y. Shibuya, H. Murai, K. Yamada, and H. Wada, *IEEE Photon. Technol. Lett.* **13**, 964 (2001).
- [84] Y. Miyazaki, H. Tada, T. Aoyagi, T. Nashimuraand, and Y. Mitsui, *IEEE J. Quantum Electron.* **38**, 1075 (2002).
- [85] Y. A. Akulova, G. A. Fish, P. C. Koh, C. L. Schow, P. Kozodoy, A. P. Dahl, S. Nakagawa, M. C. Larson, M. P. Mack, T. A. Strand, C. W Coldren, E. Hegblom, S. K. Penniman, T. Wipiejewski, and L. C. Coldren, *IEEE J. Sel. Topics Quantum Electron.* **8**, 1349 (2002).

- [86] B. K. Saravanan, T. Wenger, C. Hanke, P. Gerlach, M. Peschke, T. Knoedl, and R. Macaluso, *IEEE Photon. Technol. Lett.* **18**, 862 (2006).
- [87] J. W. Raring and L. A. Coldren, *IEEE J. Sel. Topics Quantum Electron.* **13**, 3 (2007).
- [88] R. Kaiser and B. Hüttl, *IEEE J. Sel. Topics Quantum Electron.* **13**, 125 (2007).
- [89] H. Fukano, Y. Akage, Y. Kawaguchi, Y. Suzuki, K. Kishi, T. Yamanaka, Y. Kondo, and H. Yasaka, *IEEE J. Sel. Topics Quantum Electron.* **13**, 1129 (2007).
- [90] H. G. Yun, K. S. Choi, Y. H. Kwon, J. S. Choe, and J. T. Moon, *IEEE Trans. Adv. Packag.* **31**, 351 (2008).
- [91] W. Wang, D. Chen, H. R. Fetterman, Y. Shi, W. H. Steier, L. R. Dalton, and P.-M. Chow, *Appl. Phys. Lett.* **67**, 1806 (1995).
- [92] H. Zhang, M. C. Oh, A. Szep, W. H. Steier, C. Zhang, L. R. Dalton, H. Erlig, Y. Chang, D. H. Chang, and H. R. Fetterman, *Appl. Phys. Lett.* **78**, 3136 (2001).
- [93] J. Gower, *Optical Communication Systems*, 2nd ed., Prentice-Hall, Upper Saddle River, NJ, 1993.
- [94] H. Temkin, G. V. Keramidas, M. A. Pollack, and W. R. Wagner, *J. Appl. Phys.* **52**, 1574 (1981).
- [95] C. A. Burrus and R. W. Dawson, *Appl. Phys. Lett.* **17**, 97 (1970).
- [96] S. T. Wilkinson, N. M. Jokerst, and R. P. Leavitt, *Appl. Opt.* **34**, 8298 (1995).
- [97] M. C. Larson and J. S. Harris, Jr., *IEEE Photon. Technol. Lett.* **7**, 1267 (1995).
- [98] I. J. Fritz, J. F. Klem, M. J. Hafich, A. J. Howard, and H. P. Hjalmarson, *IEEE Photon. Technol. Lett.* **7**, 1270 (1995).
- [99] T. Whitaker, *Compound Semicond.* **5**, 32 (1999).
- [100] P. Bienstman and R. Baets, *IEEE J. Quantum Electron.* **36**, 669 (2000).
- [101] P. Sipila, M. Saarinen, M. Guina, V. Vilokkinen, M. Toivonen, and M. Pessa, *Semicond. Sci. Technol.* **15**, 418 (2000).
- [102] P. W. Shumate, in *Optical Fiber Telecommunications II*, S. E. Miller and I. P. Kaminow, Eds., Academic Press, Boston, 1988, Chap. 19.
- [103] T. P. Lee, C. A. Burrus, and R. H. Saul, in *Optical Fiber Telecommunications*, Vol. 2, S. E. Miller and I. P. Kaminow, Eds., Academic Press, Boston, 1988, Chap. 12.
- [104] D. S. Alles and K. J. Brady, *AT&T Tech. J.* **68**, 183 (1989).
- [105] H. M. Presby and C. A. Edwards, *Electron. Lett.* **28**, 582 (1992).
- [106] R. A. Modavis and T. W. Webb, *IEEE Photon. Technol. Lett.* **7**, 798 (1995).
- [107] K. Shiraishi, N. Oyama, K. Matsumura, I. Ohisi, and S. Suga, *J. Lightwave Technol.* **13**, 1736 (1995).
- [108] P. C. Chen and T. D. Milster, *Laser Diode Chip and Packaging Technology*, Vol. 2610, SPIE Press, Bellingham, WA, 1996.
- [109] M. J. Daneman, O. Sologaard, N. C. Tien, K. Y. Lau, and R. S. Muller, *IEEE Photon. Technol. Lett.* **8**, 396 (1996).
- [110] B. Hubner, G. Vollrath, R. Ries, C. Gréus, H. Janning, E. Ronneberg, E. Kuphal, B. Kempf, R. Gobel, F. Fiedler, R. Zengerle, and H. Burkhard, *IEEE J. Sel. Topics Quantum Electron.* **3**, 1372 (1997).
- [111] K. Shiraishi, H. Yoda, T. Endo, and I. Tomita, *IEEE Photon. Technol. Lett.* **16**, 1104 (2004).
- [112] Z. Jing, P. V. Ramana, J. L. Hon-Shing, Z. Qingxin, J. Chandrappan, T. C. Wei, J. M. Chinq, C. T. W. Liang, and K. D. Lee, *IEEE Photon. Technol. Lett.* **20**, 1375 (2008).
- [113] G. P. Agrawal, *IEEE J. Quantum Electron.* **20**, 468 (1984).
- [114] G. P. Agrawal and T. M. Shen, *J. Lightwave Technol.* **4**, 58 (1986).

- [115] A. T. Ryan, G. P. Agrawal, G. R. Gray, and E. C. Gage, *IEEE J. Quantum Electron.* **30**, 668 (1994).
- [116] G. H. M. van Tartwijk and D. Lenstra, *Quantum Semiclass. Opt.* **7**, 87 (1995).
- [117] K. Petermann, *IEEE J. Sel. Topics Quantum Electron.* **1**, 480 (1995).
- [118] T. Sugie and M. Saruwatari, *Electron. Lett.* **18**, 1026 (1982).
- [119] F. S. Chen, *Electron. Lett.* **16**, 7 (1980).
- [120] O. Wada, T. Sakurai, and T. Nakagami, *IEEE J. Quantum Electron.* **22**, 805 (1986).
- [121] T. Horimatsu and M. Sasaki, *J. Lightwave Technol.* **7**, 1613 (1989).
- [122] M. Dagenais, R. F. Leheny, H. Temkin, and P. Battacharya, *J. Lightwave Technol.* **8**, 846 (1990).
- [123] N. Suzuki, H. Furuyama, Y. Hirayama, M. Morinaga, K. Eguchi, M. Kushibe, M. Funamizu, and M. Nakamura, *Electron. Lett.* **24**, 467 (1988).
- [124] K. Pedrotti, *Proc. SPIE* **2149**, 178 (1994).
- [125] O. Calliger, A. Clei, D. Robein, R. Azoulay, B. Pierre, S. Biblemont, and C. Kazmierski, *IEE Proc.* **142**, Pt. J, 13 (1995).
- [126] R. Pu, C. Duan, and C. W. Wilmsen, *IEEE J. Sel. Topics Quantum Electron.* **5**, 201 (1999).
- [127] K. Shuke, T. Yoshida, M. Nakano, A. Kawatani, and Y. Uda, *IEEE J. Sel. Topics Quantum Electron.* **5**, 146 (1999).
- [128] T. L. Koch and U. Koren, *IEEE J. Quantum Electron.* **27**, 641 (1991).
- [129] M. N. Armenise and K.-K. Wong, Eds., *Functional Photonic Integrated Circuits*, SPIE Proc. Series, Vol. 2401, SPIE Press, Bellingham, WA, 1995.
- [130] W. Metzger, J. G. Bauer, P. C. Clemens, G. Heise, M. Klein, H. F. Mahlein, R. Matz, H. Michel, and J. Rieger, *Opt. Quantum Electron.* **28**, 51 (1996).
- [131] D. F. Welch, C. H. Joyner, D. Lambert, P. W. Evans, and M. Raburn, in *Optical Fiber Telecommunications*, Vol. 5A, I. P. Kaminow, T. Li, and A. E. Willner, Eds., Academic Press, Boston, 2008, Chap. 10.
- [132] F. R. Nash, W. B. Joyce, R. L. Hartman, E. I. Gordon, and R. W. Dixon, *AT&T Tech. J.* **64**, 671 (1985).
- [133] N. K. Dutta and C. L. Zipfel, in *Optical Fiber Telecommunications*, Vol. 2, S. E. Miller and I. P. Kaminow, Eds., Academic Press, Boston, 1988, Chap. 17.
- [134] B. W. Hakki, P. E. Fraley, and T. F. Eltringham, *AT&T Tech. J.* **64**, 771 (1985).
- [135] M. Fallahi and S. C. Wang, Eds., *Fabrication, Testing, and Reliability of Semiconductor Lasers*, Vol. 2863, SPIE Press, Bellingham, WA, 1995.
- [136] O. Ueda, *Reliability and Degradation of III-V Optical Devices*, Artec House, Boston, 1996.
- [137] N. W. Carlson, *IEEE J. Sel. Topics Quantum Electron.* **6**, 615 (2000).
- [138] T. Takeshita, T. Tadokoro, R. Iga, Y. Tohmori, M. Yamamoto, and M. Sugo, *IEEE Trans. Electron Dev.* **54**, 456 (2007).

Chapter 4

Optical Receivers

The role of an optical receiver is to convert the optical signal back into electrical form and recover the data transmitted through the lightwave system. Its main component is a photodetector that converts light into electricity through the photoelectric effect. The requirements for a photodetector are similar to those of an optical source. It should have high sensitivity, fast response, low noise, low cost, and high reliability. Its size should be compatible with the fiber-core size. These requirements are best met by photodetectors made of semiconductor materials. This chapter focuses on photodetectors and optical receivers [1]–[9]. We introduce in Section 4.1 the basic concepts behind the photodetection process and discuss in Section 4.2 several kinds of photodetectors commonly used for optical receivers. The components of an optical receiver are described in Section 4.3 with emphasis on the role played by each component. Section 4.4 deals with various noise sources that limit the signal-to-noise ratio in optical receivers. Sections 4.5 and 4.6 are devoted to receiver sensitivity and its degradation under nonideal conditions. The performance of optical receivers in actual transmission experiments is discussed in Section 4.7.

4.1 Basic Concepts

The fundamental mechanism behind the photodetection process is optical absorption. This section introduces basic concepts such as responsivity, quantum efficiency, rise time, and bandwidth that are common to all photodetectors and are used to characterize them.

4.1.1 Responsivity and Quantum Efficiency

Consider the semiconductor slab shown schematically in Figure 4.1. If the energy hv of incident photons exceeds the bandgap energy, an electron–hole pair is generated each time a photon is absorbed by the semiconductor. Under the influence of an electric field set up by an applied voltage, electrons and holes are swept across the semiconductor, resulting in a flow of electric current. The photocurrent I_p is directly proportional to

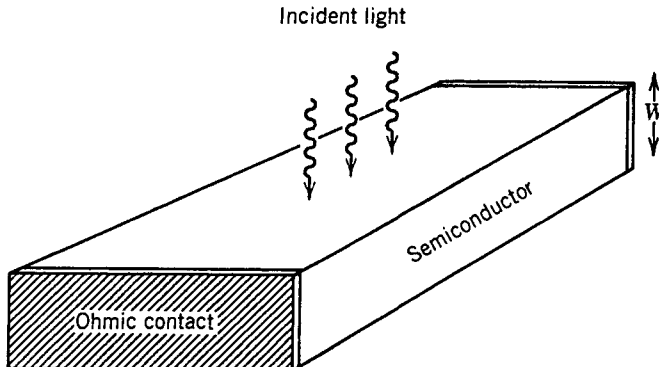


Figure 4.1: A semiconductor slab used as a photodetector.

the incident optical power P_{in} , i.e.,

$$I_p = R_d P_{\text{in}}. \quad (4.1.1)$$

The constant R_d is referred to as the *responsivity* of the photodetector because more current is produced at a given input power for larger values of R_d ; it is expressed in units of ampere/watts (A/W).

The responsivity R_d can be expressed in terms of a fundamental quantity η , called the *quantum efficiency* and defined as

$$\eta = \frac{\text{electron generation rate}}{\text{photon incidence rate}} = \frac{I_p/q}{P_{\text{in}}/\hbar\nu} = \frac{\hbar\nu}{q} R_d, \quad (4.1.2)$$

where Eq. (4.1.1) was used. The responsivity R_d is thus given by

$$R_d = \frac{\eta q}{\hbar\nu} \approx \frac{\eta \lambda}{1.24}, \quad (4.1.3)$$

where $\lambda \equiv c/\nu$ is expressed in micrometers. The responsivity of a photodetector increases with the wavelength λ simply because more photons are present for the same optical power. Such a linear dependence on λ is not expected to continue forever because eventually the photon energy becomes too small to generate electrons. In semiconductors, this happens for $\hbar\nu < E_g$, where E_g is the bandgap. The quantum efficiency η then drops to zero.

The dependence of η on λ enters through the absorption coefficient α . If the facets of the semiconductor slab in Figure 4.1 are assumed to have an antireflection coating, the power transmitted through the slab of width W is $P_{\text{tr}} = \exp(-\alpha W)P_{\text{in}}$. The absorbed power can be written as

$$P_{\text{abs}} = P_{\text{in}} - P_{\text{tr}} = [1 - \exp(-\alpha W)]P_{\text{in}}. \quad (4.1.4)$$

Since each absorbed photon creates an electron-hole pair, the quantum efficiency η is given by

$$\eta = P_{\text{abs}}/P_{\text{in}} = 1 - \exp(-\alpha W). \quad (4.1.5)$$

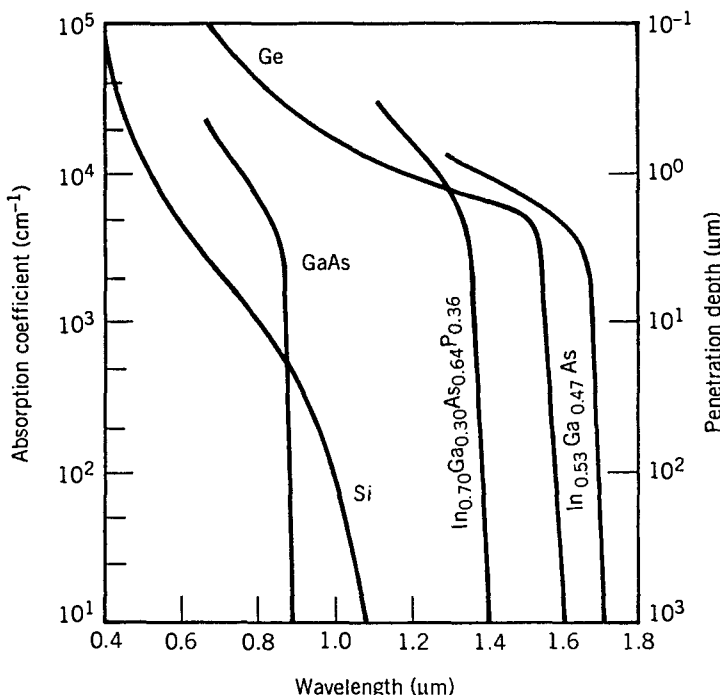


Figure 4.2: Wavelength dependence of the absorption coefficient for several semiconductor materials. (After Ref. [2]; ©1979 Academic Press; reprinted with permission.)

As expected, η becomes zero when $\alpha = 0$. On the other hand, η approaches 1 if $\alpha W \gg 1$.

Figure 4.2 shows the wavelength dependence of α for several semiconductor materials commonly used to make photodetectors for lightwave systems. The wavelength λ_c at which α becomes zero is called the cutoff wavelength, as that material can be used for a photodetector only for $\lambda < \lambda_c$. As seen in Figure 4.2, indirect-bandgap semiconductors such as Si and Ge can be used to make photodetectors even though the absorption edge is not as sharp as for direct-bandgap materials. Large values of α ($\sim 10^4 \text{ cm}^{-1}$) can be realized for most semiconductors, and η can approach 100% for $W \sim 10 \mu\text{m}$. This feature illustrates the efficiency of semiconductors for the purpose of photodetection.

4.1.2 Rise Time and Bandwidth

The *bandwidth* of a photodetector is determined by the speed with which it responds to variations in the incident optical power. It is useful to introduce the concept of *rise time* T_r , defined as the time over which the current builds up from 10 to 90% of its final value when the incident optical power is changed abruptly. Clearly, T_r will depend on

the time taken by electrons and holes to travel to the electrical contacts. It also depends on the response time of the electrical circuit used to process the photocurrent.

The rise time T_r of a linear electrical circuit is defined as the time during which the response increases from 10 to 90% of its final output value when the input is changed abruptly (a step function). When the input voltage across an RC circuit changes instantaneously from 0 to V_0 , the output voltage changes as

$$V_{\text{out}}(t) = V_0[1 - \exp(-t/RC)], \quad (4.1.6)$$

where R is the resistance and C is the capacitance of the RC circuit. The rise time is found to be given by

$$T_r = (\ln 9)RC \approx 2.2\tau_{RC}, \quad (4.1.7)$$

where $\tau_{RC} = RC$ is the time constant of the RC circuit.

The rise time of a photodetector can be written by extending Eq. (4.1.7) as

$$T_r = (\ln 9)(\tau_{\text{tr}} + \tau_{RC}), \quad (4.1.8)$$

where τ_{tr} is the transit time and τ_{RC} is the time constant of the equivalent RC circuit. The transit time is added to τ_{RC} because it takes some time before the carriers are collected after their generation through absorption of photons. The maximum collection time is just equal to the time an electron takes to traverse the absorption region. Clearly, τ_{tr} can be reduced by decreasing W . However, as seen from Eq. (4.1.5), the quantum efficiency η begins to decrease significantly for $\alpha W < 3$. Thus, there is a trade-off between the bandwidth and the responsivity (speed versus sensitivity) of a photodetector. Often, the RC time constant τ_{RC} limits the bandwidth because of electrical parasitics. The numerical values of τ_{tr} and τ_{RC} depend on the detector design and can vary over a wide range.

The bandwidth of a photodetector is defined in a manner analogous to that of a RC circuit and is given by

$$\Delta f = [2\pi(\tau_{\text{tr}} + \tau_{RC})]^{-1}. \quad (4.1.9)$$

As an example, when $\tau_{\text{tr}} = \tau_{RC} = 100$ ps, the bandwidth of the photodetector is below 1 GHz. Clearly, both τ_{tr} and τ_{RC} should be reduced below 10 ps for photodetectors needed for lightwave systems operating at bit rates of 10 Gb/s or more.

Together with the bandwidth and the responsivity, the dark current I_d of a photodetector is the third important parameter. Here, I_d is the current generated in a photodetector in the absence of any optical signal and originates from stray light or from thermally generated electron–hole pairs. For a good photodetector, the dark current should be negligible ($I_d < 10$ nA).

4.2 Common Photodetectors

The semiconductor slab of Figure 4.1 is useful for illustrating the basic concepts but such a simple device is rarely used in practice. This section focuses on reverse-biased p – n junctions that are commonly used for making optical receivers. Metal–semiconductor–metal (MSM) photodetectors are also discussed briefly.

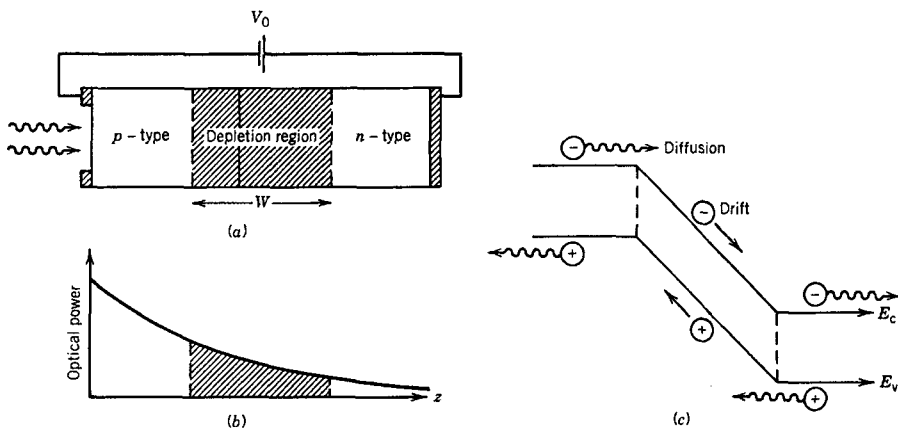


Figure 4.3: (a) A p - n photodiode under reverse bias; (b) variation of optical power inside the photodiode; (c) energy-band diagram showing carrier movement through drift and diffusion.

4.2.1 p - n Photodiodes

A reverse-biased p - n junction consists of a region, known as the *depletion region*, that is essentially devoid of free charge carriers and where a large built-in electric field opposes flow of electrons from the n -side to the p -side (and of holes from p to n). When such a p - n junction is illuminated with light on one side, say the p -side (see Figure 4.3), electron–hole pairs are created through absorption. Because of the large built-in electric field, electrons and holes generated inside the depletion region accelerate in opposite directions and drift to the n - and p -sides, respectively. The resulting flow of current is proportional to the incident optical power. Thus a reverse-biased p - n junction acts as a photodetector and is referred to as the p - n photodiode.

Figure 4.3(a) shows the structure of a p - n photodiode. As shown in Figure 4.3(b), optical power decreases exponentially as the incident light is absorbed inside the depletion region. The electron–hole pairs generated inside the depletion region experience a large electric field and drift rapidly toward the p - or n -side, depending on the electric charge [Figure 4.3(c)]. The resulting current flow constitutes the photodiode response to the incident optical power in accordance with Eq. (4.1.1). The responsivity of a photodiode is quite high ($R \sim 1 \text{ A/W}$) because of a high quantum efficiency.

The bandwidth of a p - n photodiode is often limited by the transit time τ_{tr} in Eq. (4.1.9). If W is the width of the depletion region and v_d is the drift velocity, the transit time is given by

$$\tau_{tr} = W/v_d. \quad (4.2.1)$$

Typically, $W \sim 10 \mu\text{m}$, $v_d \sim 10^5 \text{ m/s}$, and $\tau_{tr} \sim 100 \text{ ps}$. Both W and v_d can be optimized to minimize τ_{tr} . The depletion-layer width depends on the acceptor and donor concentrations and can be controlled through them. The velocity v_d depends on the applied voltage but attains a maximum value (called the *saturation velocity*) $\sim 10^5 \text{ m/s}$ that depends on the material used for the photodiode. The RC time constant τ_{RC} can be

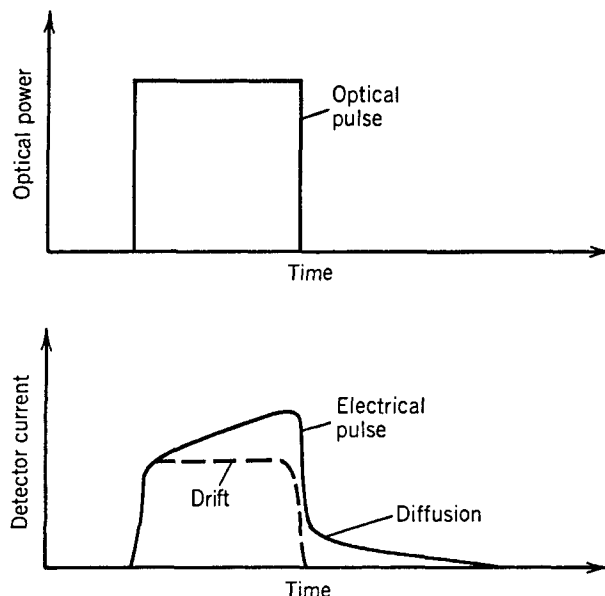


Figure 4.4: Response of a p - n photodiode to a rectangular optical pulse when both drift and diffusion contribute to the detector current.

written as

$$\tau_{RC} = (R_L + R_s)C_p, \quad (4.2.2)$$

where R_L is the external load resistance, R_s is the internal series resistance, and C_p is the parasitic capacitance. Typically, $\tau_{RC} \sim 100$ ps, although lower values are possible with a proper design. Indeed, modern p - n photodiodes are capable of operating at bit rates of up to 40 Gb/s.

The limiting factor for the bandwidth of p - n photodiodes is the presence of a diffusive component in the photocurrent. The physical origin of the diffusive component is related to the absorption of incident light outside the depletion region. Electrons generated in the p -region have to diffuse to the depletion-region boundary before they can drift to the n -side; similarly, holes generated in the n -region must diffuse to the depletion-region boundary. Diffusion is an inherently slow process; carriers take a nanosecond or longer to diffuse over a distance of about 1 μm . Figure 4.4 shows how the presence of a diffusive component can distort the temporal response of a photodiode. The diffusion contribution can be reduced by decreasing the widths of the p - and n -regions and increasing the depletion-region width so that most of the incident optical power is absorbed inside it. This is the approach adopted for p - i - n photodiodes, discussed next.

4.2.2 p - i - n Photodiodes

A simple way to increase the depletion-region width is to insert a layer of undoped (or lightly doped) semiconductor material between the p - n junction. Since the middle

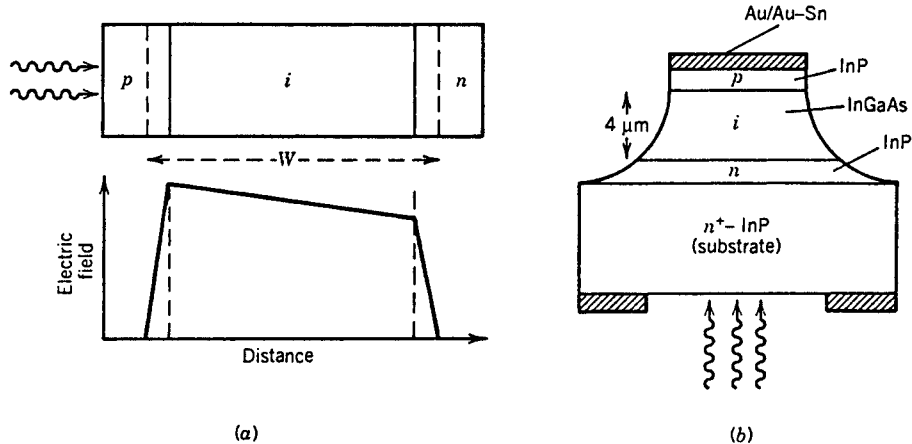


Figure 4.5: (a) A *p*-*i*-*n* photodiode together with the electric-field distribution under reverse bias; (b) design of an InGaAs *p*-*i*-*n* photodiode.

layer consists of nearly intrinsic material, such a structure is referred to as the *p*-*i*-*n* photodiode. Figure 4.5(a) shows the device structure together with the electric-field distribution inside it under reverse-bias operation. Because of its intrinsic nature, the middle *i*-layer offers a high resistance, and most of the voltage drop occurs across it. As a result, a large electric field exists in the *i*-layer. In essence, the depletion region extends throughout the *i*-region, and its width *W* can be controlled by changing the middle-layer thickness. The main difference from the *p*-*n* photodiode is that the drift component of the photocurrent dominates over the diffusion component simply because most of the incident power is absorbed inside the *i*-region of a *p*-*i*-*n* photodiode.

Since the depletion width *W* can be tailored in *p*-*i*-*n* photodiodes, a natural question is how large *W* should be. As discussed in Section 4.1, the optimum value of *W* depends on a compromise between speed and sensitivity. The responsivity can be increased by increasing *W* so that the quantum efficiency η approaches 100% [see Eq. (4.1.5)]. However, the response time also increases, as it takes longer for carriers to drift across the depletion region. For indirect-bandgap semiconductors such as Si and Ge, typically *W* must be in the range 20–50 μm to ensure a reasonable quantum efficiency. The bandwidth of such photodiodes is then limited by a relatively long transit time ($\tau_{tr} > 200$ ps). By contrast, *W* can be as small as 3–5 μm for photodiodes that use direct-bandgap semiconductors, such as InGaAs. The transit time for such photodiodes is $\tau_{tr} \sim 10$ ps. Such values of τ_{tr} correspond to a detector bandwidth $\Delta f \sim 10$ GHz if we use Eq. (4.1.9) with $\tau_{tr} \gg \tau_{RC}$.

The performance of *p*-*i*-*n* photodiodes can be improved considerably by using a double-heterostructure design. Similar to the case of semiconductor lasers, the middle *i*-type layer is sandwiched between the *p*-type and *n*-type layers of a different semiconductor whose bandgap is chosen such that light is absorbed only in the middle *i*-layer. A *p*-*i*-*n* photodiode commonly used for lightwave applications uses InGaAs for the middle layer and InP for the surrounding *p*-type and *n*-type layers [10]. Figure 4.5(b)

Table 4.1 Characteristics of common $p-i-n$ photodiodes

Parameter	Symbol	Unit	Si	Ge	InGaAs
Wavelength	λ	μm	0.4–1.1	0.8–1.8	1.0–1.7
Responsivity	R_d	A/W	0.4–0.6	0.5–0.7	0.6–0.9
Quantum efficiency	η	%	75–90	50–55	60–70
Dark current	I_d	nA	1–10	50–500	1–20
Rise time	T_r	ns	0.5–1	0.1–0.5	0.02–0.5
Bandwidth	Δf	GHz	0.3–0.6	0.5–3	1–10
Bias voltage	V_b	V	50–100	6–10	5–6

shows such an InGaAs $p-i-n$ photodiode. Since the bandgap of InP is 1.35 eV, InP is transparent for light whose wavelength exceeds 0.92 μm . By contrast, the bandgap of lattice-matched $\text{In}_{1-x}\text{Ga}_x\text{As}$ material with $x = 0.47$ is about 0.75 eV (see Section 3.1.1), a value that corresponds to a cutoff wavelength of 1.65 μm . The middle InGaAs layer thus absorbs strongly in the wavelength region 1.3–1.6 μm . The diffusive component of the detector current is eliminated completely in such a heterostructure photodiode simply because photons are absorbed only inside the depletion region. The front facet is often coated using suitable dielectric layers to minimize reflections. The quantum efficiency η can be made almost 100% by using an InGaAs layer 4–5 μm thick. InGaAs photodiodes are quite useful for lightwave systems and are often used in practice. Table 4.1 lists the operating characteristics of three common $p-i-n$ photodiodes.

Considerable effort was directed during the 1990s toward developing high-speed $p-i-n$ photodiodes capable of operating at bit rates exceeding 10 Gb/s [10]–[21]. Bandwidths of up to 70 GHz were realized as early as 1986 by using a thin absorption layer ($< 1 \mu\text{m}$) and by reducing the parasitic capacitance C_p with a small size, but only at the expense of a lower quantum efficiency and responsivity [10]. By 1995, $p-i-n$ photodiodes exhibited a bandwidth of 110 GHz for devices designed to reduce τ_{RC} to near 1 ps [15].

Several techniques have been developed to improve the efficiency of high-speed photodiodes. In one approach, a Fabry–Perot (FP) cavity is formed around the $p-i-n$ structure to enhance the quantum efficiency [11]–[14], resulting in a laser-like structure. As discussed in Section 3.1.5, a FP cavity has a set of longitudinal modes at which the internal optical field is resonantly enhanced through constructive interference. As a result, when the incident wavelength is close to a longitudinal mode, such a photodiode exhibits high sensitivity. The wavelength selectivity can even be used to advantage in wavelength-division multiplexing (WDM) applications. A nearly 100% quantum efficiency was realized in a photodiode in which one mirror of the FP cavity was formed by using the Bragg reflectivity of a stack of AlGaAs/AlAs layers [12]. This approach was extended to InGaAs photodiodes by inserting a 90-nm-thick InGaAs absorbing layer into a microcavity composed of a GaAs/AlAs Bragg mirror and a dielectric mirror. The device exhibited 94% quantum efficiency at the cavity resonance with a bandwidth of 14 nm [13]. By using an air-bridged metal waveguide together with an undercut mesa

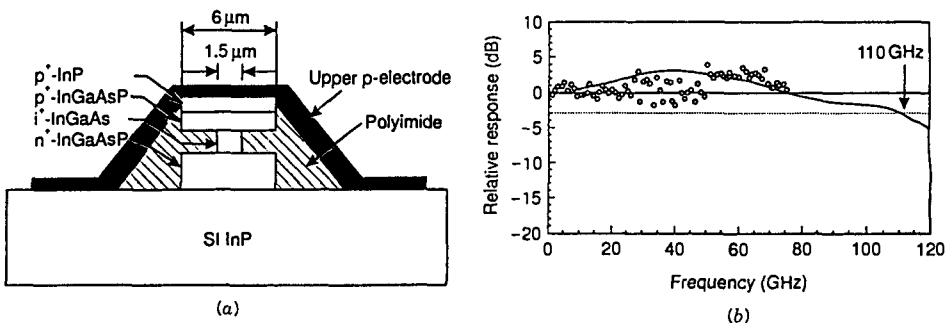


Figure 4.6: (a) Schematic cross section of a mushroom-mesa waveguide photodiode and (b) its measured frequency response. (After Ref. [17]; ©1994 IEEE; reprinted with permission.)

structure, a bandwidth of 120 GHz has been realized [14]. The use of such a structure within a FP cavity should provide a $p-i-n$ photodiode with a high bandwidth and high efficiency.

Another approach to realize efficient high-speed photodiodes makes use of an optical waveguide into which the optical signal is edge coupled [16]–[21]. Such a structure resembles an unpumped semiconductor laser except that various epitaxial layers are optimized differently. In contrast with a semiconductor laser, the waveguide can be made wide to support multiple transverse modes in order to improve the coupling efficiency [16]. Since absorption takes place along the length of the optical waveguide ($\sim 10 \mu\text{m}$), the quantum efficiency can be nearly 100% even for an ultrathin absorption layer. The bandwidth of such *waveguide photodiodes* is limited by τ_{RC} in Eq. (4.1.9), which can be decreased by controlling the waveguide cross-section-area. Indeed, a 50-GHz bandwidth was realized in 1992 for a waveguide photodiode [16].

The bandwidth of waveguide photodiodes can be increased to 110 GHz by adopting a mushroom-mesa waveguide structure [17]. Such a device is shown schematically in Figure 4.6. In this structure, the width of the i -type absorbing layer was reduced to 1.5 μm while the p - and n -type cladding layers were made 6 μm wide. In this way, both the parasitic capacitance and the internal series resistance were minimized, reducing τ_{RC} to about 1 ps. The frequency response of such a device at the 1.55- μm wavelength is also shown in Figure 4.6. It was measured by using a spectrum analyzer (circles) as well as taking the Fourier transform of the short-pulse response (solid curve). Clearly, waveguide $p-i-n$ photodiodes can provide both a high responsivity and a large bandwidth. Waveguide photodiodes have been used for 40-Gb/s optical receivers [19] and have the potential for operating at bit rates as high as 100 Gb/s [18].

The performance of waveguide photodiodes can be improved further by adopting an electrode structure designed to support traveling electrical waves with matching impedance to avoid reflections. Such photodiodes are called traveling-wave photodetectors [21]. In a GaAs-based implementation of this idea, a bandwidth of 172 GHz with 45% quantum efficiency was realized in a traveling-wave photodetector designed with a 1- μm -wide waveguide [22]. By 2000, such an InP/InGaAs photodetector exhibited a bandwidth of 310 GHz in the 1.55- μm spectral region [23].

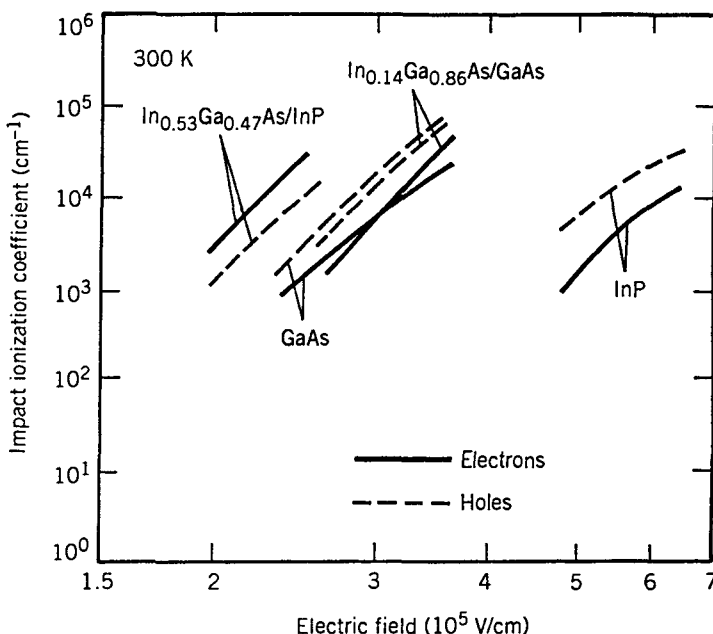


Figure 4.7: Impact-ionization coefficients of several semiconductors as a function of the electric field for electrons (solid line) and holes (dashed line). (After Ref. [25]; ©1977 Elsevier; reprinted with permission.)

4.2.3 Avalanche Photodiodes

All detectors require a certain minimum current to operate reliably. The current requirement translates into a minimum power requirement through $P_{\text{in}} = I_p/R_d$. Detectors with a large responsivity R_d are preferred since they require less optical power. The responsivity of $p-i-n$ photodiodes is limited by Eq. (4.1.3) and takes its maximum value $R_d = q/h\nu$ for $\eta = 1$. Avalanche photodiode (APDs) can have much larger values of R_d , as they are designed to provide an internal current gain in a way similar to photomultiplier tubes. They are used when the amount of optical power that can be spared for the receiver is limited.

The physical phenomenon behind the internal current gain is known as the *impact ionization* [24]. Under certain conditions, an accelerating electron can acquire sufficient energy to generate a new electron–hole pair. In the band picture (see Figure 3.2) the energetic electron gives a part of its kinetic energy to another electron in the valence band that ends up in the conduction band, leaving behind a hole. The net result of impact ionization is that a single primary electron, generated through absorption of a photon, creates many secondary electrons and holes, all of which contribute to the photodiode current. Of course, the primary hole can also generate secondary electron–hole pairs that contribute to the current. The generation rate is governed by two parameters, α_e and α_h , the *impact-ionization coefficients* of electrons and holes, respectively. Their numerical values depend on the semiconductor material and on the electric field

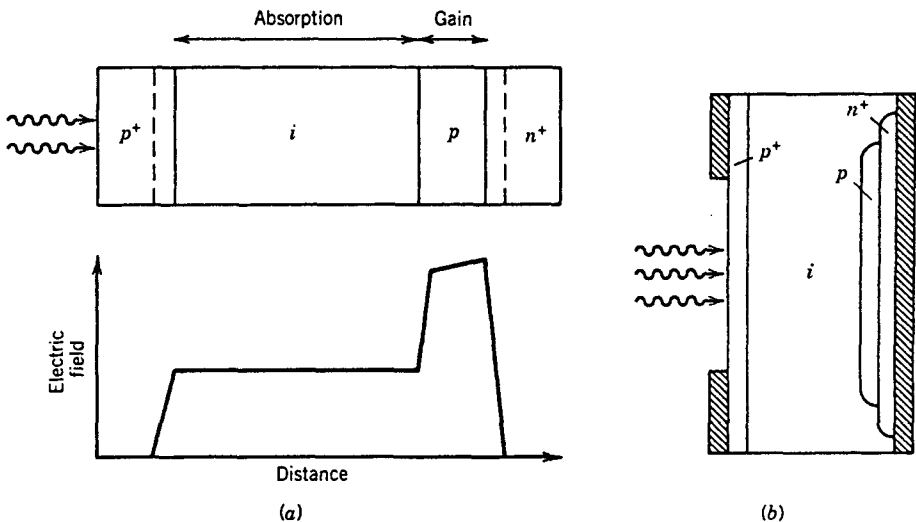


Figure 4.8: (a) An APD together with the electric-field distribution inside various layers under reverse bias; (b) design of a silicon reach-through APD.

that accelerates electrons and holes. Figure 4.7 shows α_e and α_h for several semiconductors [25]. Values $\sim 1 \times 10^4 \text{ cm}^{-1}$ are obtained for electric fields in the range $2\text{--}4 \times 10^5 \text{ V/cm}$. Such large fields can be realized by applying a high voltage ($\sim 100 \text{ V}$) to the APD.

APDs differ in their design from that of $p-i-n$ photodiodes mainly in one respect: an additional layer is added in which secondary electron-hole pairs are generated through impact ionization. Figure 4.8(a) shows the APD structure together with the variation of electric field in various layers. Under reverse bias, a high electric field exists in the p -type layer sandwiched between i -type and n^+ -type layers. This layer is referred to as the *multiplication layer*, since secondary electron-hole pairs are generated here through impact ionization. The i -layer still acts as the depletion region in which most of the incident photons are absorbed and primary electron-hole pairs are generated. Electrons generated in the i -region cross the gain region and generate secondary electron-hole pairs responsible for the current gain.

The current gain for APDs can be calculated by using the two rate equations governing current flow within the multiplication layer [24]:

$$\frac{di_e}{dx} = \alpha_e i_e + \alpha_h i_h, \quad (4.2.3)$$

$$-\frac{di_h}{dx} = \alpha_e i_e + \alpha_h i_h, \quad (4.2.4)$$

where i_e is the electron current and i_h is the hole current. The minus sign in Eq. (4.2.4) is due to the opposite direction of the hole current. The total current,

$$I = i_e(x) + i_h(x), \quad (4.2.5)$$

remains constant at every point inside the multiplication region. If we replace i_h in Eq. (4.2.3) by $I - i_e$, we obtain

$$di_e/dx = (\alpha_e - \alpha_h)i_e + \alpha_h I. \quad (4.2.6)$$

In general, α_e and α_h are x dependent if the electric field across the gain region is nonuniform. The analysis is considerably simplified if we assume a uniform electric field and treat α_e and α_h as constants. We also assume that $\alpha_e > \alpha_h$. The avalanche process is initiated by electrons that enter the gain region of thickness d at $x = 0$. By using the condition $i_h(d) = 0$ (only electrons cross the boundary to enter the n -region), the boundary condition for Eq. (4.2.6) is $i_e(d) = I$. By integrating this equation, the *multiplication factor* defined as $M = i_e(d)/i_e(0)$ is given by

$$M = \frac{1 - k_A}{\exp[-(1 - k_A)\alpha_e d] - k_A}, \quad (4.2.7)$$

where $k_A = \alpha_h/\alpha_e$. The APD gain is quite sensitive to the ratio of the impact-ionization coefficients. When $\alpha_h = 0$ so that only electrons participate in the avalanche process, $M = \exp(\alpha_e d)$, and the APD gain increases exponentially with d . On the other hand, when $\alpha_h = \alpha_e$, so that $k_A = 1$ in Eq. (4.2.7), $M = (1 - \alpha_e d)^{-1}$. The APD gain then becomes infinite for $\alpha_e d = 1$, a condition known as the *avalanche breakdown*. Although higher APD gain can be realized with a smaller gain region when α_e and α_h are comparable, the performance is better in practice for APDs in which either $\alpha_e \gg \alpha_h$ or $\alpha_h \gg \alpha_e$ so that the avalanche process is dominated by only one type of charge carrier. The reason behind this requirement is discussed in Section 4.4, where issues related to the receiver noise are considered.

Because of the current gain, the responsivity of an APD is enhanced by the multiplication factor M and is given by

$$R_{APD} = MR_d = M(\eta q/h\nu), \quad (4.2.8)$$

where Eq. (4.1.3) was used. It should be mentioned that the avalanche process in APDs is intrinsically noisy and results in a gain factor that fluctuates around an average value. The quantity M in Eq. (4.2.8) refers to the average APD gain. The noise characteristics of APDs are considered in Section 4.4.

The intrinsic bandwidth of an APD depends on the multiplication factor M . This is easily understood by noting that the transit time τ_{tr} for an APD is no longer given by Eq. (4.2.1) but increases considerably simply because generation and collection of secondary electron-hole pairs take additional time. The APD gain decreases at high frequencies because of such an increase in the transit time and limits the bandwidth. The decrease in $M(\omega)$ can be written as [25]

$$M(\omega) = M_0[1 + (\omega\tau_e M_0)^2]^{-1/2}, \quad (4.2.9)$$

where $M_0 = M(0)$ is the low-frequency gain and τ_e is the effective transit time that depends on the ionization coefficient ratio $k_A = \alpha_h/\alpha_e$. For the case $\alpha_h < \alpha_e$, $\tau_e = c_A k_A \tau_{tr}$, where c_A is a constant ($c_A \sim 1$). Assuming that $\tau_{RC} \ll \tau_e$, the APD bandwidth is given approximately by $\Delta f = (2\pi\tau_e M_0)^{-1}$. This relation shows the *trade-off* between

Table 4.2 Characteristics of common APDs

Parameter	Symbol	Unit	Si	Ge	InGaAs
Wavelength	λ	μm	0.4–1.1	0.8–1.8	1.0–1.7
Responsivity	R_{APD}	A/W	80–130	3–30	5–20
APD gain	M	—	100–500	50–200	10–40
k -factor	k_A	—	0.02–0.05	0.7–1.0	0.5–0.7
Dark current	I_d	nA	0.1–1	50–500	1–5
Rise time	T_r	ns	0.1–2	0.5–0.8	0.1–0.5
Bandwidth	Δf	GHz	0.2–1	0.4–0.7	1–10
Bias voltage	V_b	V	200–250	20–40	20–30

the APD gain M_0 and the bandwidth Δf (speed versus sensitivity). It also shows the advantage of using a semiconductor material for which $k_A \ll 1$.

Table 4.2 compares the operating characteristics of Si, Ge, and InGaAs APDs. As $k_A \ll 1$ for Si, silicon APDs can be designed to provide high performance and are useful for lightwave systems operating near $0.8 \mu\text{m}$ at bit rates $\sim 100 \text{ Mb/s}$. A particularly useful design, shown in Figure 4.8(b), is known as reach-through APD because the depletion layer reaches to the contact layer through the absorption and multiplication regions. It can provide high gain ($M \approx 100$) with low noise and a relatively large bandwidth. For lightwave systems operating in the wavelength range $1.3\text{--}1.6 \mu\text{m}$, Ge or InGaAs APDs must be used. The improvement in sensitivity for such APDs is limited to a factor below 10 because of a relatively low APD gain ($M \sim 10$) that must be used to reduce the noise (see Section 4.4.3).

The performance of InGaAs APDs can be improved through suitable design modifications to the basic APD structure shown in Figure 4.8. The main reason for a relatively poor performance of InGaAs APDs is related to the comparable numerical values of the impact-ionization coefficients α_e and α_h (see Figure 4.7). As a result, the bandwidth is considerably reduced, and the noise is also relatively high (see Section 4.4). Furthermore, because of a relatively narrow bandgap, InGaAs undergoes tunneling breakdown at electric fields of about $1 \times 10^5 \text{ V/cm}$, a value that is below the threshold for avalanche multiplication. This problem can be solved in heterostructure APDs by using an InP layer for the gain region because quite high electric fields ($> 5 \times 10^5 \text{ V/cm}$) can exist in InP without tunneling breakdown. Since the absorption region (*i*-type InGaAs layer) and the multiplication region (*n*-type InP layer) are separate in such a device, this structure is known as SAM, where SAM stands for *separate absorption and multiplication* regions. As $\alpha_h > \alpha_e$ for InP (see Figure 4.7), the APD is designed such that holes initiate the avalanche process in an *n*-type InP layer, and k_A is defined as $k_A = \alpha_e / \alpha_h$. Figure 4.9(a) shows a mesa-type SAM APD structure.

One problem with the SAM APD is related to the large bandgap difference between InP ($E_g = 1.35 \text{ eV}$) and InGaAs ($E_g = 0.75 \text{ eV}$). Because of a valence-band step of about 0.4 eV , holes generated in the InGaAs layer are trapped at the heterojunction interface and are considerably slowed before they reach the multiplication region (InP layer). Such an APD has an extremely slow response and a relatively small bandwidth.

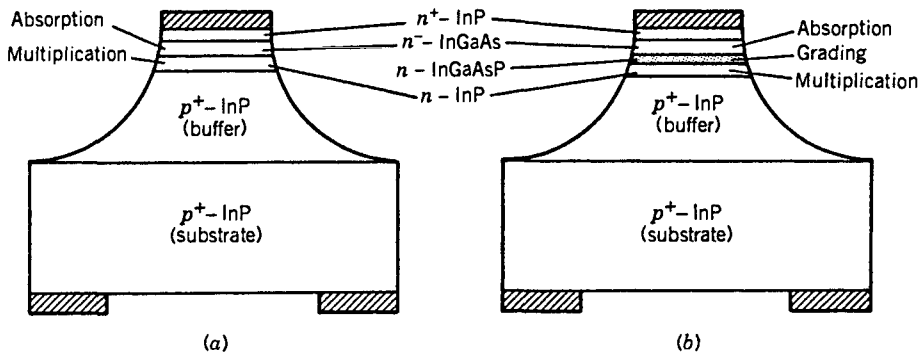


Figure 4.9: Design of (a) SAM and (b) SAGM APDs containing separate absorption, multiplication regions.

The problem can be solved by using another layer between the absorption and multiplication regions whose bandgap is intermediate to those of InP and InGaAs layers. The quaternary material InGaAsP, the same material used for semiconductor lasers, can be tailored to have a bandgap anywhere in the range 0.75–1.35 eV and is ideal for this purpose. It is even possible to grade the composition of InGaAsP over a region of 10–100 nm thickness. Such APDs are called SAGM APDs, where SAGM indicates *separate absorption, grading, and multiplication* regions [26]. Figure 4.9(b) shows the design of an InGaAs APD with the SAGM structure. The use of an InGaAsP grading layer improves the bandwidth considerably. As early as 1987, a SAGM APD exhibited a gain-bandwidth product $M\Delta f = 70$ GHz for $M > 12$ [27]. This value was increased to 100 GHz in 1991 by using a charge region between the grading and multiplication regions [28]. In such SAGCM APDs, the InP multiplication layer is undoped, while the InP charge layer is heavily n -doped. Holes accelerate in the charge layer because of a strong electric field, but the generation of secondary electron–hole pairs takes place in the undoped InP layer. SAGCM APDs improved considerably during the 1990s [29]–[33]. A gain–bandwidth product of 140 GHz was realized in 2000 using a 0.1- μ m-thick multiplication layer that required <20 V across it [33]. Such APDs are quite suitable for making a compact 10-Gb/s APD receiver.

A different approach to the design of high-performance APDs makes use of a superlattice structure [34]–[39]. The major limitation of InGaAs APDs results from comparable values of α_e and α_h . A superlattice design offers the possibility of reducing the ratio $k_A = \alpha_h/\alpha_e$ from its standard value of nearly unity. In one scheme, the absorption and multiplication regions alternate and consist of thin layers (~ 10 nm) of semiconductor materials with different bandgaps. This approach was first demonstrated for GaAs/AlGaAs multiquantum-well (MQW) APDs and resulted in a considerable enhancement of the impact-ionization coefficient for electrons [34]. Its use is less successful for the InGaAs/InP material system. Nonetheless, considerable progress has been made through the so-called *staircase* APDs, in which the InGaAsP layer is compositionally graded to form a sawtooth kind of structure in the energy-band diagram that looks like a staircase under reverse bias. Another scheme for making high-speed

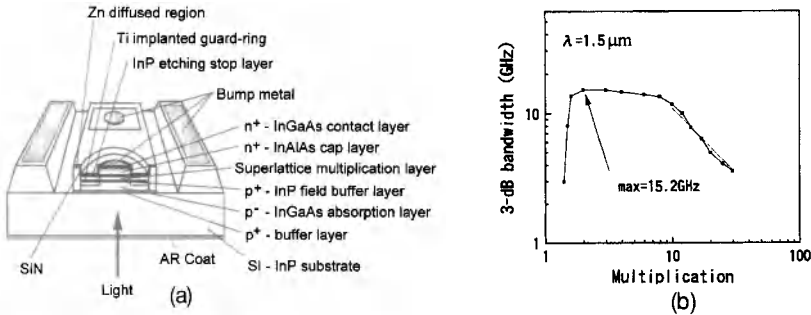


Figure 4.10: (a) Device structure and (b) measured 3-dB bandwidth as a function of M for a superlattice APD. (After Ref. [39]; ©2000 IEEE; reprinted with permission.)

APDs uses alternate layers of InP and InGaAs for the grading region [34]. However, the ratio of the widths of the InP to InGaAs layers varies from zero near the absorbing region to almost infinity near the multiplication region. Since the effective bandgap of a quantum well depends on the quantum-well width (InGaAs layer thickness), a graded pseudo-quaternary compound is formed as a result of variation in the layer thickness.

The most successful design for InGaAs APDs uses a superlattice structure for the multiplication region of a SAM APD. A superlattice consists of a periodic structure such that each period is made using two ultrathin (~ 10 -nm) layers with different bandgaps. In the case of $1.55\text{-}\mu\text{m}$ APDs, alternate layers of InAlGaAs and InAlAs are used, the latter acting as a barrier layer. An InP field-buffer layer often separates the InGaAs absorption region from the superlattice multiplication region. The thickness of this buffer layer is quite critical for the APD performance. For a 52-nm-thick field-buffer layer, the gain-bandwidth product was limited to $M\Delta f = 120$ GHz [35] but increased to 150 GHz when the thickness was reduced to 33.4 nm [38]. These early devices used a mesa structure. During the late 1990s, a planar structure was developed for improving the device reliability [39]. Figure 4.10 shows such a device schematically together with its 3-dB bandwidth measured as a function of the APD gain. The gain-bandwidth product of 110 GHz is large enough for making APDs operating at 10 Gb/s. Indeed, such an APD receiver was used for a 10-Gb/s lightwave system with excellent performance.

The gain-bandwidth limitation of InGaAs APDs results primarily from using the InP material system for the generation of secondary electron-hole pairs. A hybrid approach in which a Si multiplication layer is incorporated next to an InGaAs absorption layer may be useful provided the heterointerface problems can be overcome. In a 1997 experiment, a gain-bandwidth product of more than 300 GHz was realized by using such a hybrid approach [40]. The APD exhibited a 3-dB bandwidth of over 9 GHz for values of M as high as 35 while maintaining a 60% quantum efficiency.

Most APDs use an absorbing layer thick enough (about $1 \mu\text{m}$) that the quantum efficiency exceeds 50%. The thickness of the absorbing layer affects the transit time τ_{tr} and the bias voltage V_b . In fact, both of them can be reduced significantly by using a thin absorbing layer ($\sim 0.1 \mu\text{m}$), resulting in improved APDs provided that a high

quantum efficiency can be maintained. Two approaches have been used to meet these somewhat conflicting design requirements. In one design, a FP cavity is formed to enhance the absorption within a thin layer through multiple round trips. An external quantum efficiency of $\sim 70\%$ and a gain-bandwidth product of 270 GHz were realized in such a $1.55\text{-}\mu\text{m}$ APD using a 60-nm-thick absorbing layer with a 200-nm-thick multiplication layer [41]. In another approach, an optical waveguide is used into which the incident light is edge coupled [42]. Both of these approaches reduce the bias voltage to near 10 V, maintain high efficiency, and reduce the transit time to ~ 1 ps. Such APDs are suitable for making 10-Gb/s optical receivers.

4.2.4 MSM Photodetectors

In a different kind of photodetector, known as a metal–semiconductor–metal (MSM) photodetector, a semiconductor absorbing layer is sandwiched between two metal electrodes. As a result, a Schottky barrier is formed at each metal–semiconductor interface that prevents the flow of electrons from the metal to the semiconductor. Similar to a $p-i-n$ photodiode, electron–hole pairs generated through the absorption of light flow toward the metal contacts, resulting in a photocurrent that is a measure of the incident optical power, as indicated in Eq. (4.1.1). However, in contrast with a $p-i-n$ photodiode or APD, no $p-n$ junction is required. In this sense, an MSM photodetector employs the simplest design.

For practical reasons, it is difficult to sandwich a thin semiconductor layer between two metal electrodes. This problem can be solved by placing the two metal contacts on the same (top) side of an epitaxially grown absorbing layer using an *interdigitated* electrode structure with a finger spacing of about $1\ \mu\text{m}$ [43]. Figure 4.11(a) show the basic design. In modern devices, the concentric ring structure shown in Figure 4.11(b) is often used in place of finger-shaped electrodes. The resulting planar structure has an inherently low parasitic capacitance and thus allows high-speed operation (up to 300 GHz) of MSM photodetectors. If the light is incident from the electrode side, the responsivity of a MSM photodetector is reduced because some light is blocked by the opaque electrodes. This problem can be solved through back illumination if the substrate is transparent to the incident light.

GaAs-based MSM photodetectors were developed throughout the 1980s and exhibit excellent operating characteristics [43]. The development of InGaAs-based MSM photodetectors, suitable for lightwave systems operating in the range $1.3\text{--}1.6\ \mu\text{m}$, started in the late 1980s, with most progress made during the 1990s [44]–[54]. The major problem with InGaAs is its relatively low *Schottky-barrier height* (about 0.2 eV). This problem was solved by introducing a thin layer of InP or InAlAs between the InGaAs layer and the metal contact. Such a layer, called the *barrier-enhancement layer*, improves the performance of InGaAs MSM photodetectors drastically. The use of a 20-nm-thick InAlAs barrier-enhancement layer resulted in 1992 in $1.3\text{-}\mu\text{m}$ MSM photodetectors exhibiting 92% quantum efficiency (through back illumination) with a low dark current [45]. A packaged device had a bandwidth of 4 GHz despite a large $150\ \mu\text{m}$ diameter. If top illumination is desirable for processing or packaging reasons, the responsivity can be enhanced by using semitransparent metal contacts. In one experiment, the responsivity at $1.55\ \mu\text{m}$ increased from 0.4 to 0.7 A/W when the thickness of

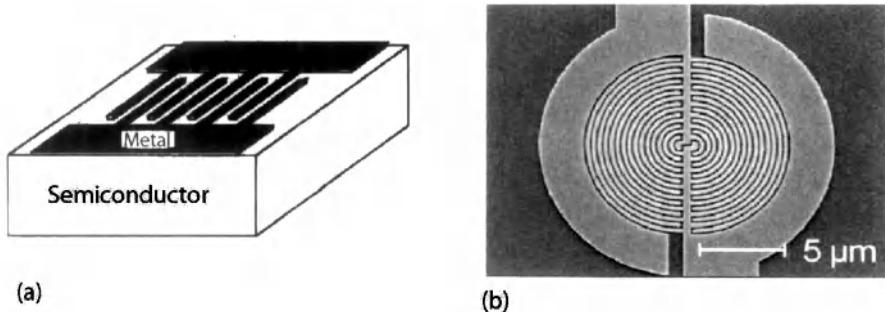


Figure 4.11: (a) Finger-shaped and (b) ring-shaped electrode structures used for MSM photodetectors. (After Ref. [53]; ©1999 IEEE.)

gold contact was reduced from 100 to 10 nm [46]. In another approach, the structure is separated from the host substrate and bonded to a silicon substrate with the interdigitized contact on bottom. Such an “inverted” MSM photodetector then exhibits high responsivity when illuminated from the top [47].

The temporal response of MSM photodetectors is generally different under back and top illuminations [48]. In particular, the bandwidth Δf is larger by about a factor of 2 for top illumination, although the responsivity is reduced because of metal shadowing. The performance of a MSM photodetector can be further improved by using a graded superlattice structure. Such devices exhibit a low dark-current density, a responsivity of about 0.6 A/W at 1.3 μm , and a rise time of about 16 ps [51]. In 1998, a 1.55- μm MSM photodetector exhibited a bandwidth of 78 GHz [52]. By 2002, the use of a traveling-wave configuration resulted in a GaAs-based device operating near 1.3 μm with a bandwidth >230 GHz [54]. The planar structure of MSM photodetectors is also suitable for monolithic integration, an issue covered in the next section.

4.3 Receiver Design

The design of an optical receiver depends on the modulation format used by the transmitter. Since most lightwave systems employ the binary intensity modulation, we focus in this chapter on digital optical receivers. Figure 4.12 shows a block diagram of such a receiver. Its components can be arranged into three groups—the front end, the linear channel, and the decision circuit.

4.3.1 Front End

The front end of a receiver consists of a photodiode followed by a preamplifier. The optical signal is coupled onto the photodiode by using a coupling scheme similar to that used for optical transmitters (see Section 3.6.1); butt coupling is often used in practice. The photodiode converts the optical bit stream into an electrical time-varying signal. The role of the preamplifier is to amplify the electrical signal for further processing.

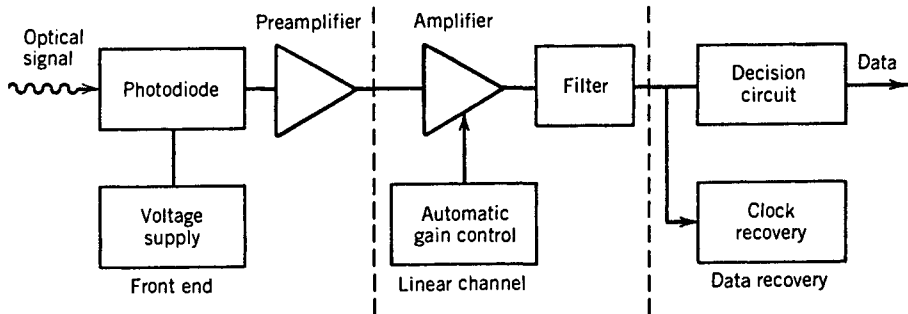


Figure 4.12: Diagram of a digital optical receiver showing various components. Vertical dashed lines group receiver components into three sections.

The design of the front end requires a trade-off between speed and sensitivity. Since the input voltage to the preamplifier can be increased by using a large load resistor R_L , a high-impedance front end is often used [see Figure 4.13(a)]. Furthermore, as discussed in Section 4.4, a large R_L reduces the thermal noise and improves the receiver sensitivity. The main drawback of high-impedance front end is its low bandwidth given by $\Delta f = (2\pi R_L C_T)^{-1}$, where $R_s \ll R_L$ is assumed in Eq. (4.2.2) and $C_T = C_p + C_A$ is the total capacitance, which includes the contributions from the photodiode (C_p) and the transistor used for amplification (C_A). The receiver bandwidth is limited by its slowest component. A high-impedance front end cannot be used if Δf is considerably less than the bit rate. An equalizer is sometimes used to increase the bandwidth. The equalizer acts as a filter that attenuates low-frequency components of the signal more than the high-frequency components, thereby effectively increasing the front-end bandwidth. If the receiver sensitivity is not of concern, one can simply decrease R_L to increase the bandwidth, resulting in a low-impedance front end.

Transimpedance front ends provide a configuration that has high sensitivity together with a large bandwidth. Its dynamic range is also improved compared with high-impedance front ends. As seen in Figure 4.13(b), the load resistor is connected as a feedback resistor around an inverting amplifier. Even though R_L is large, the *negative feedback* reduces the effective input impedance by a factor of G , where G is the amplifier gain. The bandwidth is thus enhanced by a factor of G compared with high-impedance front ends. Transimpedance front ends are often used in optical receivers because of their improved characteristics. A major design issue is related to the stability of the feedback loop. More details can be found in Refs. [4]–[9].

4.3.2 Linear Channel

The linear channel in optical receivers consists of a high-gain amplifier (the main amplifier) and a low-pass filter. An equalizer is sometimes included just before the amplifier to correct for the limited bandwidth of the front end. The amplifier gain is controlled automatically to limit the average output voltage to a fixed level irrespective of the incident average optical power at the receiver. The low-pass filter shapes the

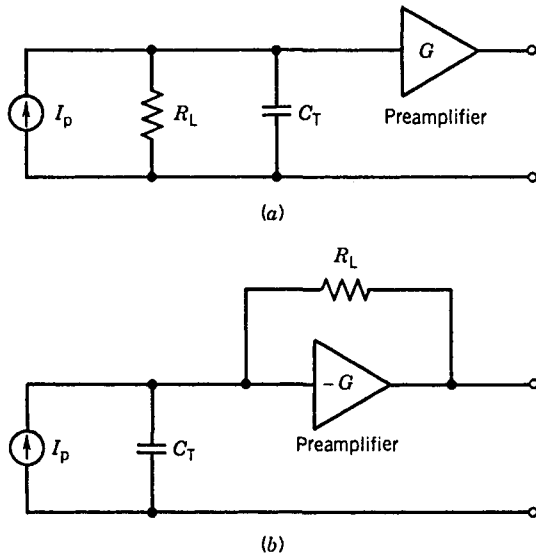


Figure 4.13: Equivalent circuit for (a) high-impedance and (b) transimpedance front ends in optical receivers. The photodiode is modeled as a current source in both cases.

voltage pulse. Its purpose is to reduce the noise without introducing much *intersymbol interference* (ISI). As discussed in Section 4.4, the receiver noise is proportional to the receiver bandwidth and can be reduced by using a low-pass filter whose bandwidth Δf is smaller than the bit rate. Since other components of the receiver are designed to have a bandwidth larger than the filter bandwidth, the receiver bandwidth is determined by the low-pass filter used in the linear channel. For $\Delta f < B$, the electrical pulse spreads beyond the allocated bit slot. Such a spreading can interfere with the detection of neighboring bits, a phenomenon referred to as ISI.

It is possible to design a low-pass filter in such a way that ISI is minimized [1]. Since the combination of preamplifier, main amplifier, and the filter acts as a linear system (hence the name *linear channel*), the output voltage can be written as

$$V_{\text{out}}(t) = \int_{-\infty}^{\infty} z_T(t-t') I_p(t') dt', \quad (4.3.1)$$

where $I_p(t)$ is the photocurrent generated in response to the incident optical power ($I_p = R_d P_{\text{in}}$). In the frequency domain,

$$\tilde{V}_{\text{out}}(\omega) = Z_T(\omega) \tilde{I}_p(\omega), \quad (4.3.2)$$

where Z_T is the total impedance at the frequency ω and a tilde represents the Fourier transform. Here, $Z_T(\omega)$ is determined by the transfer functions associated with various receiver components and can be written as [3]

$$Z_T(\omega) = G_p(\omega) G_A(\omega) H_F(\omega) / Y_{\text{in}}(\omega), \quad (4.3.3)$$

where $Y_{\text{in}}(\omega)$ is the input admittance and $G_p(\omega)$, $G_A(\omega)$, and $H_F(\omega)$ are transfer functions of the preamplifier, the main amplifier, and the filter. It is useful to isolate the frequency dependence of $\tilde{V}_{\text{out}}(\omega)$ and $\tilde{I}_p(\omega)$ through normalized spectral functions $H_{\text{out}}(\omega)$ and $H_p(\omega)$, which are related to the Fourier transform of the output and input pulse shapes, respectively, and write Eq. (4.3.2) as

$$H_{\text{out}}(\omega) = H_T(\omega)H_p(\omega), \quad (4.3.4)$$

where $H_T(\omega)$ is the total transfer function of the linear channel and is related to the total impedance as $H_T(\omega) = Z_T(\omega)/Z_T(0)$. If the amplifiers have a much larger bandwidth than the low-pass filter, $H_T(\omega)$ can be approximated by $H_F(\omega)$.

The ISI is minimized when $H_{\text{out}}(\omega)$ corresponds to the transfer function of a *raised-cosine filter* and is given by [3]

$$H_{\text{out}}(f) = \begin{cases} \frac{1}{2}[1 + \cos(\pi f/B)], & f < B, \\ 0, & f \geq B, \end{cases} \quad (4.3.5)$$

where $f = \omega/2\pi$ and B is the bit rate. The impulse response, obtained by taking the Fourier transform of $H_{\text{out}}(f)$, is given by

$$h_{\text{out}}(t) = \frac{\sin(2\pi Bt)}{2\pi Bt} \frac{1}{1 - (2Bt)^2}. \quad (4.3.6)$$

The functional form of $h_{\text{out}}(t)$ corresponds to the shape of the voltage pulse $V_{\text{out}}(t)$ received by the decision circuit. At the decision instant $t = 0$, $h_{\text{out}}(t) = 1$, and the signal is maximum. At the same time, $h_{\text{out}}(t) = 0$ for $t = m/B$, where m is an integer. Since $t = m/B$ corresponds to the decision instant of the neighboring bits, the voltage pulse of Eq. (4.3.6) does not interfere with the neighboring bits.

The linear-channel transfer function $H_T(\omega)$ that will result in output pulse shapes of the form (4.3.6) is obtained from Eq. (4.3.4) and is given by

$$H_T(f) = H_{\text{out}}(f)/H_p(f). \quad (4.3.7)$$

For an ideal bit stream in the nonreturn-to-zero (NRZ) format (rectangular input pulses of duration $T_B = 1/B$), $H_p(f) = B \sin(\pi f/B)/\pi f$, and $H_T(f)$ becomes

$$H_T(f) = (\pi f/2B) \cot(\pi f/2B). \quad (4.3.8)$$

Equation (4.3.8) determines the frequency response of the linear channel that would produce output pulse shape given by Eq. (4.3.6) under ideal conditions. In practice, the input pulse shape is far from being rectangular. The output pulse shape also deviates from Eq. (4.3.6), and some ISI invariably occurs.

4.3.3 Decision Circuit

The data-recovery section of optical receivers consists of a decision circuit and a clock-recovery circuit. The purpose of the latter is to isolate a spectral component at $f = B$ from the received signal. This component provides information about the bit slot

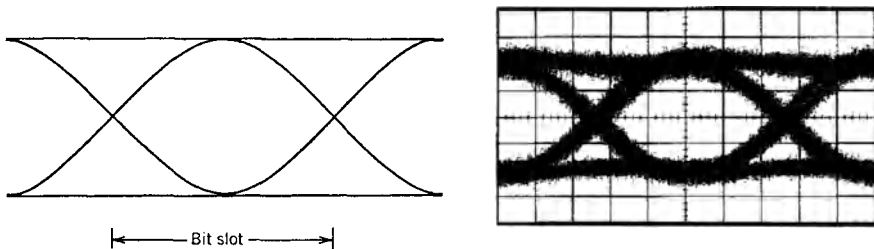


Figure 4.14: Ideal and degraded eye patterns for the NRZ format.

($T_B = 1/B$) to the decision circuit and helps to synchronize the decision process. In the case of RZ (return-to-zero) format, a spectral component at $f = B$ is present in the received signal; a narrow-bandpass filter such as a surface-acoustic-wave filter can isolate this component easily. Clock recovery is more difficult in the case of NRZ format because the signal received lacks a spectral component at $f = B$. A commonly used technique generates such a component by squaring and rectifying the spectral component at $f = B/2$ that can be obtained by passing the received signal through a high-pass filter.

The decision circuit compares the output from the linear channel to a threshold level, at sampling times determined by the clock-recovery circuit, and decides whether the signal corresponds to bit 1 or bit 0. The best sampling time corresponds to the situation in which the signal level difference between 1 and 0 bits is maximum. It can be determined from the *eye diagram* formed by superposing 2–3-bit-long electrical sequences in the bit stream on top of each other. The resulting pattern is called an eye diagram because of its appearance. Figure 4.14 shows an ideal eye diagram together with a degraded one in which the noise and the timing jitter lead to a partial closing of the eye. The best sampling time corresponds to maximum opening of the eye.

Because of noise inherent in any receiver, there is always a finite probability that a bit would be identified incorrectly by the decision circuit. Digital receivers are designed to operate in such a way that the error probability is quite small (typically $< 10^{-9}$). Issues related to receiver noise and decision errors are discussed in Sections 4.4 and 4.5. The eye diagram provides a visual way of monitoring the receiver performance: Closing of the eye is an indication that the receiver is not performing properly.

4.3.4 Integrated Receivers

All receiver components shown in Figure 4.12, with the exception of the photodiode, are standard electrical components and can be easily integrated on the same chip by using the integrated-circuit (IC) technology developed for microelectronic devices. Integration is particularly necessary for receivers operating at high bit rates. By 1988, both Si and GaAs IC technologies have been used to make integrated receivers up to a bandwidth of more than 2 GHz [55]. Since then, the bandwidth has been extended to 10 GHz.

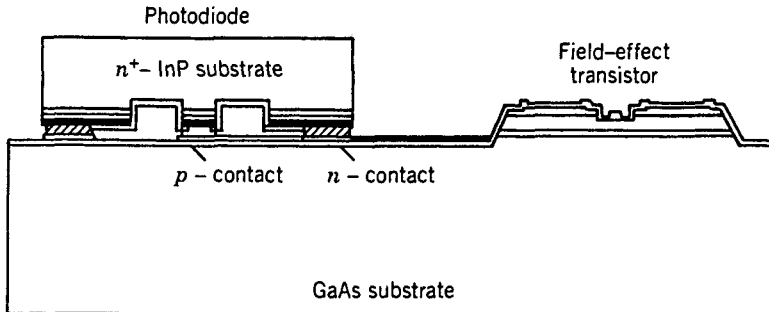


Figure 4.15: Flip-chip OEIC technology for integrated receivers. The InGaAs photodiode is fabricated on an InP substrate and then bonded to the GaAs chip through common electrical contacts. (After Ref. [59]; ©1988 IEE; reprinted with permission.)

Considerable effort has been directed at developing monolithic optical receivers that integrate all components, including the photodetector, on the same chip by using the *optoelectronic integrated-circuit* (OEIC) technology [56]–[78]. Such a complete integration is relatively easy for GaAs receivers, and the technology behind GaAs-based OEICs is quite advanced. The use of MSM photodiodes has proved especially useful as they are structurally compatible with the well-developed *field-effect-transistor* (FET) technology. This technique was used as early as 1986 to demonstrate a four-channel OEIC receiver chip [58].

For lightwave systems operating in the wavelength range 1.3–1.6 μm , InP-based OEIC receivers are needed. Since the IC technology for GaAs is much more mature than for InP, a hybrid approach is sometimes used for InGaAs receivers. In this approach, called *flip-chip OEIC technology* [59], the electronic components are integrated on a GaAs chip, whereas the photodiode is made on top of an InP chip. The two chips are then connected by flipping the InP chip on the GaAs chip, as shown in Figure 4.15. The advantage of the flip-chip technique is that the photodiode and the electrical components of the receiver can be independently optimized while keeping the parasitics (e.g., effective input capacitance) to a bare minimum.

The InP-based IC technology has advanced considerably during the 1990s, making it possible to develop InGaAs OEIC receivers [60]–[78]. Several kinds of transistors have been used for this purpose. In one approach, a $p-i-n$ photodiode is integrated with the FETs or high-electron-mobility transistors (HEMTs) side by side on an InP substrate [61]–[65]. By 1993, HEMT-based receivers were capable of operating at 10 Gb/s with high sensitivity [64]. The bandwidth of such receivers has been increased to >40 GHz, making it possible to use them at bit rates above 40 Gb/s [65]. A waveguide $p-i-n$ photodiode has also been integrated with HEMTs to develop a two-channel OEIC receiver.

In another approach [66]–[71], the heterojunction-bipolar transistor (HBT) technology is used to fabricate the $p-i-n$ photodiode within the HBT structure itself through a common-collector configuration. Such transistors are often called *heterojunction phototransistors*. OEIC receivers operating at 5 Gb/s (bandwidth $\Delta f = 3$ GHz) were made

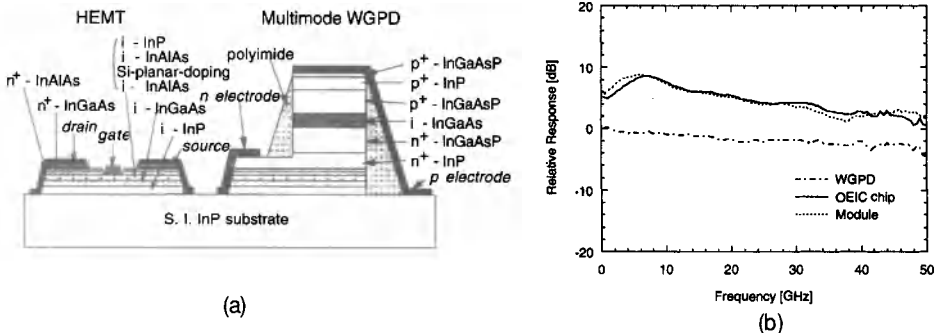


Figure 4.16: (a) Epitaxial-layer structure and (b) frequency response of an OEIC receiver module made using a waveguide photodetector (WGPD). (After Ref. [19]; ©2000 IEEE; reprinted with permission.)

by 1993 [66]. By 1995, OEIC receivers making use of the HBT technology exhibited a bandwidth of up to 16 GHz, together with a high gain [68]. Such receivers can be used at bit rates of more than 20 Gb/s. Indeed, a high-sensitivity OEIC receiver module was used in 1995 at a bit rate of 20 Gb/s in a 1.55- μm lightwave system [69]. Even a decision circuit can be integrated within the OEIC receiver by using the HBT technology [70].

A third approach to InP-based OEIC receivers integrates a MSM or a waveguide photodetector with an HEMT amplifier [72]–[75]. By 1995, a bandwidth of 15 GHz was realized for such an OEIC by using modulation-doped FETs [73]. By 2000, such receivers exhibited bandwidths of more than 45 GHz with the use of waveguide photodiodes [19]. Figure 4.16 shows the frequency response together with the epitaxial-layer structure of such an OEIC receiver. This receiver had a bandwidth of 46.5 GHz and exhibited a responsivity of 0.62 A/W in the 1.55- μm wavelength region. It had a clear eye opening at bit rates of up to 50 Gb/s.

Similar to the case of optical transmitters (Section 3.6), packaging of optical receivers is also an important issue [79]–[83]. The fiber–detector coupling issue is quite critical since only a small amount of optical power is typically available at the photodetector. The optical-feedback issue is also important since unintentional reflections fed back into the transmission fiber can affect system performance and should be minimized. In practice, the fiber tip is cut at an angle to reduce the optical feedback. Several different techniques have been used to produce packaged optical receivers capable of operating at bit rates as high as 10 Gb/s. In one approach, an InGaAs APD was bonded to the Si-based IC by using the flip-chip technique [79]. Efficient fiber–APD coupling was realized by using a *slant-ended fiber* and a microlens monolithically fabricated on the photodiode. The fiber ferrule was directly laser welded to the package wall with a double-ring structure for mechanical stability. The resulting receiver module withstood shock and vibration tests and had a bandwidth of 10 GHz.

Another hybrid approach makes use of a *planar-lightwave-circuit* platform containing silica waveguides on a silicon substrate. In one experiment, an InP-based OEIC receiver with two channels was flip-chip bonded to the platform [80]. The resulting

module could detect two 10-Gb/s channels with negligible crosstalk. GaAs ICs have also been used to fabricate a compact receiver module capable of operating at a bit rate of 10 Gb/s [81]. By 2000, fully packaged 40-Gb/s receivers were available commercially [83]. For local-loop applications, a low-cost package is needed. Such receivers operate at lower bit rates but they should be able to perform well over a wide temperature range extending from -40 to 85°C .

4.4 Receiver Noise

Optical receivers convert incident optical power P_{in} into electric current through a photodiode. The relation $I_p = RP_{\text{in}}$ in Eq. (4.1.1) assumes that such a conversion is noise free. However, this is not the case even for a perfect receiver. Two fundamental noise mechanisms, shot noise and thermal noise [84]–[86], lead to fluctuations in the current even when the incident optical signal has a constant power. The relation $I_p = RP_{\text{in}}$ still holds if we interpret I_p as the average current. However, electrical noise induced by current fluctuations affects the receiver performance. The objective of this section is to review the noise mechanisms and then discuss the signal-to-noise ratio (SNR) in optical receivers. The p - i - n and APD receivers are considered in separate subsections, as the SNR is also affected by the avalanche gain mechanism in APDs.

4.4.1 Noise Mechanisms

The shot noise and thermal noise are the two fundamental noise mechanisms responsible for current fluctuations in all optical receivers even when the incident optical power P_{in} is constant. Of course, additional noise is generated if P_{in} is itself fluctuating because of noise produced by optical amplifiers. This section considers only the noise generated at the receiver; optical noise is discussed in Section 4.7.2.

Shot Noise

Shot noise is a manifestation of the fact that an electric current consists of a stream of electrons that are generated at random times. It was first studied by Schottky [87] in 1918 and has been thoroughly investigated since then [84]–[86]. The photodiode current generated in response to a constant optical signal can be written as

$$I(t) = I_p + i_s(t), \quad (4.4.1)$$

where $I_p = R_d P_{\text{in}}$ is the average current and $i_s(t)$ is a current fluctuation related to shot noise. Mathematically, $i_s(t)$ is a stationary random process with *Poisson statistics* (approximated often by Gaussian statistics). The autocorrelation function of $i_s(t)$ is related to the spectral density $S_s(f)$ by the *Wiener–Khinchin theorem* [86]

$$\langle i_s(t)i_s(t+\tau) \rangle = \int_{-\infty}^{\infty} S_s(f) \exp(2\pi if\tau) df, \quad (4.4.2)$$

where angle brackets denote an ensemble average over fluctuations. The spectral density of shot noise is constant and is given by $S_s(f) = qI_p$ (an example of *white noise*).

Note that $S_s(f)$ is the *two-sided* spectral density, as negative frequencies are included in Eq. (4.4.2). If only positive frequencies are considered by changing the lower limit of integration to zero, the *one-sided* spectral density becomes $2qI_p$.

The noise variance is obtained by setting $\tau = 0$ in Eq. (4.4.2), i.e.,

$$\sigma_s^2 = \langle i_s^2(t) \rangle = \int_{-\infty}^{\infty} S_s(f) df = 2qI_p \Delta f, \quad (4.4.3)$$

where Δf is the *effective noise bandwidth* of the receiver. The actual value of Δf depends on receiver design. It corresponds to the intrinsic photodetector bandwidth if fluctuations in the photocurrent are measured. In practice, a decision circuit may use voltage or some other quantity (e.g., signal integrated over the bit slot). One then has to consider the transfer functions of other receiver components such as the preamplifier and the low-pass filter. It is common to consider current fluctuations and include the total transfer function $H_T(f)$ by modifying Eq. (4.4.3) as

$$\sigma_s^2 = 2qI_p \int_0^{\infty} |H_T(f)|^2 df = 2qI_p \Delta f, \quad (4.4.4)$$

where $\Delta f = \int_0^{\infty} |H_T(f)|^2 df$ and $H_T(f)$ is given by Eq. (4.3.7). Since the dark current I_d also generates shot noise, its contribution is included in Eq. (4.4.4) by replacing I_p by $I_p + I_d$. The total shot noise is then given by

$$\sigma_s^2 = 2q(I_p + I_d)\Delta f. \quad (4.4.5)$$

The quantity σ_s is the root-mean-square (RMS) value of the noise current induced by shot noise.

Thermal Noise

At a finite temperature, electrons move randomly in any conductor. Random thermal motion of electrons in a resistor manifests as a fluctuating current even in the absence of an applied voltage. The load resistor in the front end of an optical receiver (see Figure 4.13) adds such fluctuations to the current generated by the photodiode. This additional noise component is referred to as thermal noise. It is also called *Johnson noise* [88] or *Nyquist noise* [89] after the two scientists who first studied it experimentally and theoretically. Thermal noise can be included by modifying Eq. (4.4.1) as

$$I(t) = I_p + i_s(t) + i_T(t), \quad (4.4.6)$$

where $i_T(t)$ is a current fluctuation induced by thermal noise. Mathematically, $i_T(t)$ is modeled as a stationary Gaussian random process with a spectral density that is frequency independent up to $f \sim 1$ THz (nearly white noise) and is given by

$$S_T(f) = 2k_B T / R_L, \quad (4.4.7)$$

where k_B is the *Boltzmann constant*, T is the absolute temperature, and R_L is the load resistor. As mentioned before, $S_T(f)$ is the two-sided spectral density.

The autocorrelation function of $i_T(t)$ is given by Eq. (4.4.2) if we replace the subscript s by T . The noise variance is obtained by setting $\tau = 0$ and becomes

$$\sigma_T^2 = \langle i_T^2(t) \rangle = \int_{-\infty}^{\infty} S_T(f) df = (4k_B T / R_L) \Delta f, \quad (4.4.8)$$

where Δf is the effective noise bandwidth. The same bandwidth appears in the case of both shot and thermal noises. Note that σ_T^2 does not depend on the average current I_p , whereas σ_s^2 does.

Equation (4.4.8) includes thermal noise generated in the load resistor. An actual receiver contains many other electrical components, some of which add additional noise. For example, noise is invariably added by electrical amplifiers. The amount of noise added depends on the front-end design (see Figure 4.13) and the type of amplifiers used. In particular, the thermal noise is different for field-effect and bipolar transistors. Considerable work has been done to estimate the amplifier noise for different front-end designs [4]. A simple approach accounts for the amplifier noise by introducing a quantity F_n , referred to as the *amplifier noise figure*, and modifying Eq. (4.4.8) as

$$\sigma_T^2 = (4k_B T / R_L) F_n \Delta f. \quad (4.4.9)$$

Physically, F_n represents the factor by which thermal noise is enhanced by various resistors used in pre- and main amplifiers.

The total current noise can be obtained by adding the contributions of shot noise and thermal noise. Since $i_s(t)$ and $i_T(t)$ in Eq. (4.4.6) are independent random processes with approximately Gaussian statistics, the total variance of current fluctuations, $\Delta I = I - I_p = i_s + i_T$, can be obtained simply by adding individual variances. The result is

$$\sigma^2 = \langle (\Delta I)^2 \rangle = \sigma_s^2 + \sigma_T^2 = 2q(I_p + I_d)\Delta f + (4k_B T / R_L)F_n\Delta f. \quad (4.4.10)$$

Equation (4.4.10) can be used to calculate the SNR of the photocurrent.

4.4.2 *p-i-n* Receivers

The performance of an optical receiver depends on the SNR. The SNR of a receiver with a *p-i-n* photodiode is considered here; APD receivers are discussed in the following subsection. The SNR of any electrical signal is defined as

$$\text{SNR} = \frac{\text{average signal power}}{\text{noise power}} = \frac{I_p^2}{\sigma^2}, \quad (4.4.11)$$

where we used the fact that electrical power varies as the square of the current. By using Eq. (4.4.10) in Eq. (4.4.11) together with $I_p = R_d P_{\text{in}}$, the SNR is related to the incident optical power as

$$\text{SNR} = \frac{R_d^2 P_{\text{in}}^2}{2q(R_d P_{\text{in}} + I_d)\Delta f + 4(k_B T / R_L)F_n\Delta f}, \quad (4.4.12)$$

where $R = \eta q/h\nu$ is the responsivity of the *p-i-n* photodiode.

Thermal-Noise Limit

In most cases of practical interest, thermal noise dominates receiver performance ($\sigma_T^2 \gg \sigma_s^2$). Neglecting the shot-noise term in Eq. (4.4.12), the SNR becomes

$$\text{SNR} = \frac{R_L R_d^2 P_{\text{in}}^2}{4k_B T F_n \Delta f}. \quad (4.4.13)$$

Thus, the SNR varies as P_{in}^2 in the thermal-noise limit. It can also be improved by increasing the load resistance. As discussed in Section 4.3.1, this is the reason why most receivers use a high-impedance or transimpedance front end. The effect of thermal noise is often quantified through a quantity called the *noise-equivalent power* (NEP). The NEP is defined as the minimum optical power per unit bandwidth required to produce $\text{SNR} = 1$ and is given by

$$\text{NEP} = \frac{P_{\text{in}}}{\sqrt{\Delta f}} = \left(\frac{4k_B T F_n}{R_L R_d^2} \right)^{1/2} = \frac{h\nu}{\eta q} \left(\frac{4k_B T F_n}{R_L} \right)^{1/2}. \quad (4.4.14)$$

Another quantity, called *detectivity* and defined as $(\text{NEP})^{-1}$, is also used for this purpose. The advantage of specifying NEP or the detectivity for a *p-i-n* receiver is that it can be used to estimate the optical power needed to obtain a specific value of SNR if the bandwidth Δf is known. Typical values of NEP are in the range 1–10 pW/Hz^{1/2}.

Shot-Noise Limit

Consider the opposite limit in which the receiver performance is dominated by shot noise ($\sigma_s^2 \gg \sigma_T^2$). Since σ_s^2 increases linearly with P_{in} , the shot-noise limit can be achieved by making the incident power large. The dark current I_d can be neglected in that situation. Equation (4.4.12) then provides the following expression for SNR:

$$\text{SNR} = \frac{R_d P_{\text{in}}}{2q\Delta f} = \frac{\eta P_{\text{in}}}{2h\nu\Delta f}. \quad (4.4.15)$$

The SNR increases linearly with P_{in} in the shot-noise limit and depends only on the quantum efficiency η , the bandwidth Δf , and the photon energy $h\nu$. It can be written in terms of the number of photons N_p contained in the “1” bit. If we use $E_p = P_{\text{in}} \int_{-\infty}^{\infty} h_p(t) dt = P_{\text{in}}/B$ for the pulse energy of a bit of duration $1/B$, where B is the bit rate, and note that $E_p = N_p h\nu$, we can write P_{in} as $P_{\text{in}} = N_p h\nu B$. By choosing $\Delta f = B/2$ (a typical value for the bandwidth), the SNR per bit is simply given by ηN_p . In the shot-noise limit, a SNR of 20 dB can be realized if $N_p = 100$ and $\eta \approx 1$. By contrast, several thousand photons are required to obtain SNR = 20 dB when thermal noise dominates the receiver. As a reference, for a 1.55-μm receiver operating at 10 Gb/s, $N_p = 100$ when $P_{\text{in}} \approx 130$ nW.

4.4.3 APD Receivers

Optical receivers that employ an APD generally provide a higher SNR for the same incident optical power. The improvement is due to the internal gain that increases the

photocurrent by a multiplication factor M so that

$$I_p = MR_d P_{\text{in}} = R_{\text{APD}} P_{\text{in}}, \quad (4.4.16)$$

where $R_{\text{APD}} \equiv MR_d$ is the APD responsivity, enhanced by a factor of M compared with that of $p-i-n$ photodiodes. The SNR should improve by a factor of M^2 if the receiver noise were unaffected by the internal gain mechanism of APDs. Unfortunately, this is not the case, and the SNR improvement is considerably reduced.

Shot-Noise Enhancement

Thermal noise remains the same for APD receivers, as it originates in the electrical components that are not part of the APD. This is not the case for shot noise. The APD gain results from generation of secondary electron-hole pairs through the process of impact ionization. Since such pairs are generated at random times, an additional contribution is added to the shot noise associated with the generation of primary electron-hole pairs. In effect, the multiplication factor itself is a random variable, and M appearing in Eq. (4.4.16) represents the average APD gain. Total shot noise can be calculated by using Eqs. (4.2.3) and (4.2.4) and treating i_e and i_h as random variables [90]. The result is

$$\sigma_s^2 = 2qM^2 F_A (R_d P_{\text{in}} + I_d) \Delta f. \quad (4.4.17)$$

where F_A is the *excess noise factor* of the APD and is given by [90]

$$F_A(M) = k_A M + (1 - k_A)(2 - 1/M). \quad (4.4.18)$$

The dimensionless parameter $k_A = \alpha_h/\alpha_e$ if $\alpha_h < \alpha_e$ but is defined as $k_A = \alpha_e/\alpha_h$ when $\alpha_h > \alpha_e$. In other words, k_A is in the range $0 < k_A < 1$. In general, F_A increases with M . However, although F_A is at most 2 for $k_A = 0$, it keeps on increasing linearly ($F_A = M$) when $k_A = 1$. The ratio k_A should be as small as possible for achieving the best performance from an APD [91].

If the avalanche-gain process were noise free ($F_A = 1$), both I_p and σ_s would increase by the same factor M , and the SNR would be unaffected as far as the shot-noise contribution is concerned. In practice, the SNR of APD receivers is worse than that of $p-i-n$ receivers when shot noise dominates because of the excess noise generated inside the APD. It is the dominance of thermal noise in practical receivers that makes APDs attractive. In fact, the SNR of APD receivers can be written as

$$\text{SNR} = \frac{I_p^2}{\sigma_s^2 + \sigma_T^2} = \frac{(MR_d P_{\text{in}})^2}{2qM^2 F_A (R_d P_{\text{in}} + I_d) \Delta f + 4(k_B T / R_L) F_n \Delta f}, \quad (4.4.19)$$

where Eqs. (4.4.9), (4.4.16), and (4.4.17) were used. Figure 4.17 shows the dependence of SNR on received power P_{in} for three values of APD gain M using $R_d = 1 \text{ A/W}$, $I_d = 1 \text{ nA}$, $k_A = 0.7$, and $\sigma_T = 1 \mu\text{A}$ for a receiver with a 30-GHz bandwidth.

Several features are noteworthy in Figure 4.17. Noting that $M = 1$ case corresponds to the use of a $p-i-n$ photodiode, it is evident that the SNR is in fact degraded for an APD receiver when input powers are relatively large. Any improvement in SNR occurs only for low input power levels (below -20 dBm). The reason behind this

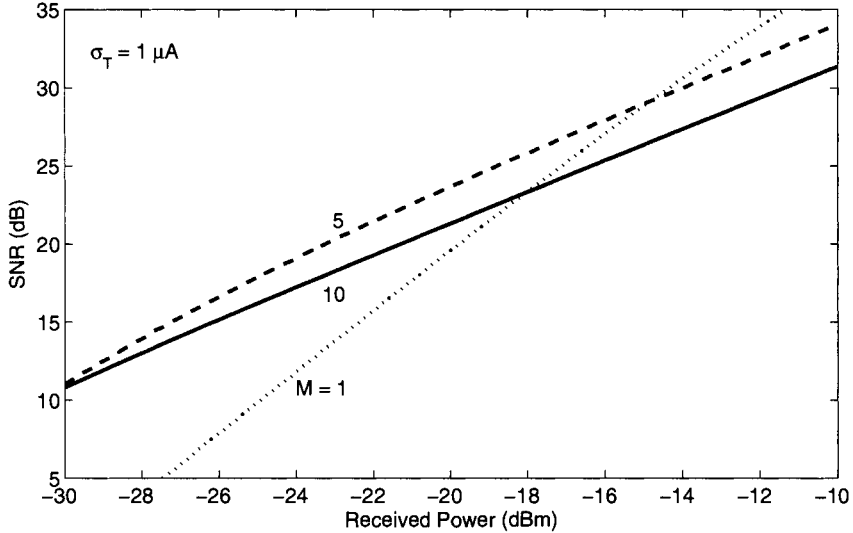


Figure 4.17: Increase in SNR with received power P_{in} for three values of APD gain M for a receiver with a bandwidth of 30 GHz. The $M = 1$ case corresponds to a $p-i-n$ photodiode.

behavior is related to the enhancement of shot noise in APD receivers. At low power levels, thermal noise dominates over shot noise, and the APD gain helps. However, as the APD gain increases, shot noise begins to dominate over thermal noise, and APD performs worse than a $p-i-n$ photodiode under the same operating conditions. To make this point clear, we consider the two limits separately.

In the thermal-noise limit ($\sigma_s \ll \sigma_T$), the SNR becomes

$$\text{SNR} = (R_L R_d^2 / 4k_B T F_n \Delta f) M^2 P_{\text{in}} \quad (4.4.20)$$

and is improved, as expected, by a factor of M^2 compared with that of $p-i-n$ receivers [see Eq. (4.4.13)]. By contrast, in the shot-noise limit ($\sigma_s \gg \sigma_T$), the SNR is given by

$$\text{SNR} = \frac{R_d P_{\text{in}}}{2qF_A \Delta f} = \frac{\eta P_{\text{in}}}{2h\nu F_A \Delta f} \quad (4.4.21)$$

and is reduced by the excess noise factor F_A compared with that of $p-i-n$ receivers [see Eq. (4.4.15)].

Optimum APD Gain

Equation (4.4.19) shows that for a given P_{in} , the SNR of APD receivers is maximum for an optimum value M_{opt} of the APD gain M . It is easy to show that the SNR is maximum when M_{opt} satisfies the following cubic polynomial:

$$k_A M_{\text{opt}}^3 + (1 - k_A) M_{\text{opt}} = \frac{4k_B T F_n}{q R_L (R_d P_{\text{in}} + I_d)} . \quad (4.4.22)$$

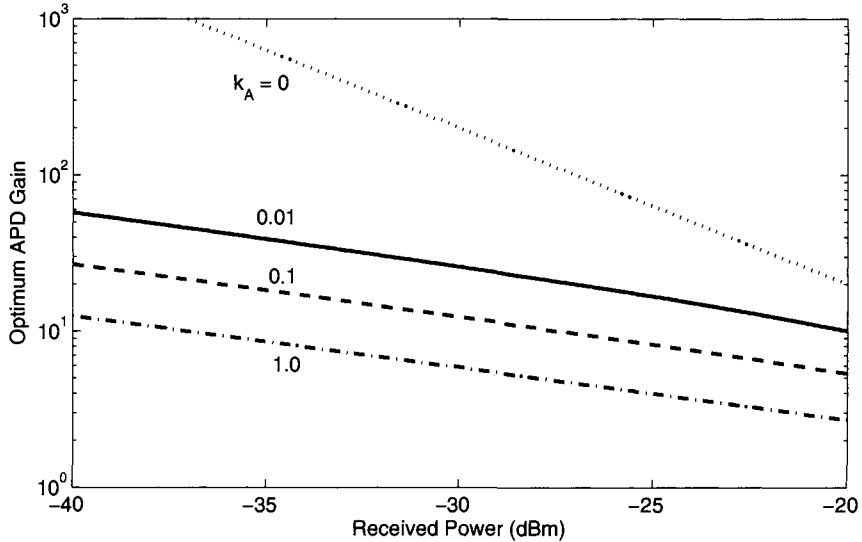


Figure 4.18: Optimum APD gain M_{opt} as a function of the incident optical power P_{in} for several values of k_A . Parameter values corresponding to a typical 1.55-μm InGaAs APD receiver were used.

The optimum value M_{opt} depends on a large number of the receiver parameters, such as the dark current, the responsivity R , and the ionization-coefficient ratio k_A . However, it is independent of receiver bandwidth. The most notable feature of Eq. (4.4.22) is that M_{opt} decreases with an increase in P_{in} . Figure 4.18 shows the variation of M_{opt} with P_{in} for several values of k_A by using typical parameter values $R_L = 1 \text{ k}\Omega$, $F_n = 2$, $R = 1 \text{ A/W}$, and $I_d = 2 \text{ nA}$ corresponding to a 1.55-μm InGaAs receiver. The optimum APD gain is quite sensitive to the ionization-coefficient ratio k_A . For $k_A = 0$, M_{opt} decreases inversely with P_{in} , as can readily be inferred from Eq. (4.4.22) by noting that the contribution of I_d is negligible in practice. By contrast, M_{opt} varies as $P_{\text{in}}^{-1/3}$ for $k_A = 1$, and this form of dependence appears to hold even for k_A as small as 0.01 as long as $M_{\text{opt}} > 10$. In fact, by neglecting the second term in Eq. (4.4.22), M_{opt} is well approximated by

$$M_{\text{opt}} \approx \left[\frac{4k_BTF_n}{k_AqR_L(R_dP_{\text{in}} + I_d)} \right]^{1/3} \quad (4.4.23)$$

for k_A in the range 0.01–1. This expression shows the critical role played by the ionization-coefficient ratio k_A . For Si APDs, for which $k_A \ll 1$, M_{opt} can be as large as 100. By contrast, M_{opt} is in the neighborhood of 10 for InGaAs receivers, since $k_A \approx 0.7$ for them. APD-based InGaAs receivers are useful for optical communication systems because of their higher sensitivity that allows them to operate at lower input power levels. However, with the advent of optical amplifiers, APDs are rarely employed in modern lightwave systems.

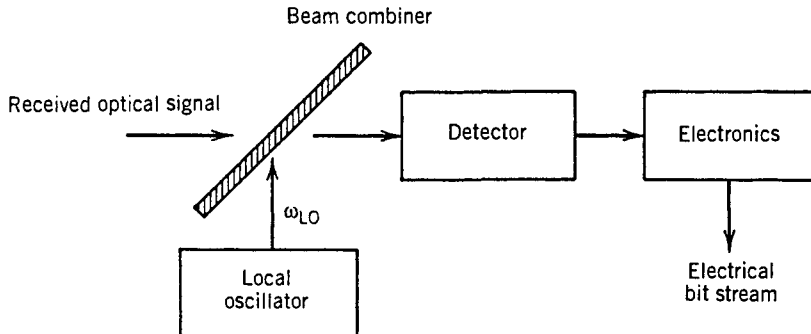


Figure 4.19: Schematic illustration of a coherent detection scheme.

4.5 Coherent Detection

It is clear from Section 4.4 that, even though shot noise sets the fundamental limit, it is the thermal noise that limits a photodetector in practice. The use of APDs helps to reduce the impact of thermal noise to some extent, but it also enhances the shot noise. One may ask if it is possible to design a detection scheme that is limited by shot-noise alone. The answer is provided by a technique known as *coherent detection*, so called because it combines the incoming optical signal coherently with a CW optical field before it falls on the detector. An added benefit is that such a technique can also be used for systems that encode information in the optical phase (such as the FSK and PSK modulation formats) because it converts phase variations into amplitude variations.

4.5.1 Local Oscillator

The basic idea behind coherent detection is shown schematically in Figure 4.19. A coherent field is generated locally at the receiver using a narrow-linewidth laser, called the *local oscillator* (LO), a term borrowed from the radio and microwave literature. It is combined with the incoming optical field using a beam splitter, typically a fiber coupler in practice. To see how such a mixing can improve the receiver performance, let us write the optical signal using complex notation as

$$E_s = A_s \exp[-i(\omega_0 t + \phi_s)], \quad (4.5.1)$$

where ω_0 is the carrier frequency, A_s is the amplitude, and ϕ_s is the phase. The optical field associated with the local oscillator is given by a similar expression,

$$E_{\text{LO}} = A_{\text{LO}} \exp[-i(\omega_{\text{LO}} t + \phi_{\text{LO}})], \quad (4.5.2)$$

where A_{LO} , ω_{LO} , and ϕ_{LO} represent the amplitude, frequency, and phase of the local oscillator, respectively. The scalar notation is used for both E_s and E_{LO} after assuming that the two fields are identically polarized. The optical power incident at the photodetector is given by $P = |E_s + E_{\text{LO}}|^2$. Using Eqs. (4.5.1) and (4.5.2),

$$P(t) = P_s + P_{\text{LO}} + 2\sqrt{P_s P_{\text{LO}}} \cos(\omega_{\text{IF}} t + \phi_s - \phi_{\text{LO}}), \quad (4.5.3)$$

where

$$P_s = A_s^2, \quad P_{\text{LO}} = A_{\text{LO}}^2, \quad \omega_{\text{IF}} = \omega_0 - \omega_{\text{LO}}. \quad (4.5.4)$$

The frequency $\nu_{\text{IF}} \equiv \omega_{\text{IF}}/2\pi$ is known as the *intermediate frequency* (IF). When $\omega_0 \neq \omega_{\text{LO}}$, the optical signal is demodulated in two stages. Its carrier frequency is first converted to an intermediate frequency ν_{IF} (typically 0.1–5 GHz). The resulting radio-frequency (RF) signal is then processed electronically to recover the bit stream. It is not always necessary to use an intermediate frequency. In fact, there are two different coherent detection techniques to choose from, depending on whether or not ω_{IF} equals zero. They are known as *homodyne* and *heterodyne* detection techniques.

4.5.2 Homodyne Detection

In this coherent-detection technique, the local-oscillator frequency ω_{LO} is selected to coincide with the signal-carrier frequency ω_0 so that $\omega_{\text{IF}} = 0$. From Eq. (4.5.3), the photocurrent ($I = R_d P$, where R_d is the detector responsivity) is given by

$$I(t) = R_d(P_s + P_{\text{LO}}) + 2R_d\sqrt{P_s(t)P_{\text{LO}}} \cos(\phi_s - \phi_{\text{LO}}). \quad (4.5.5)$$

Typically, $P_{\text{LO}} \gg P_s$, and $P_s + P_{\text{LO}} \approx P_{\text{LO}}$. The last term in Eq. (4.5.5) contains the information transmitted and is used by the decision circuit. Consider the case in which the local-oscillator phase is locked to the signal phase so that $\phi_s = \phi_{\text{LO}}$. The homodyne signal is then given by

$$I_p(t) = 2R_d\sqrt{P_s(t)P_{\text{LO}}}. \quad (4.5.6)$$

The main advantage of homodyne detection is evident from Eq. (4.5.6) if we note that the signal current in the direct-detection case is given by $I_{dd}(t) = R_d P_s(t)$. Denoting the average signal power by \bar{P}_s , the average electrical power is increased by a factor of $4P_{\text{LO}}/\bar{P}_s$ with the use of homodyne detection. Since P_{LO} can be made much larger than \bar{P}_s , the power enhancement can exceed 20 dB. Although shot noise is also enhanced, it is shown later that homodyne detection improves the SNR by a large factor.

Another advantage of coherent detection is evident from Eq. (4.5.5). Because the last term in this equation contains the signal phase explicitly, it is possible to recover data transmitted using the phase or frequency of the optical carrier. Direct detection does not allow this because all information in the signal phase is lost. Several modulation formats requiring phase encoding are discussed in Chapter 10.

A disadvantage of homodyne detection also results from its phase sensitivity. Since the last term in Eq. (4.5.5) contains the local-oscillator phase ϕ_{LO} explicitly, clearly ϕ_{LO} should be controlled. Ideally, ϕ_s and ϕ_{LO} should stay constant except for the intentional modulation of ϕ_s . In practice, both ϕ_s and ϕ_{LO} fluctuate with time in a random manner. However, their difference $\phi_s - \phi_{\text{LO}}$ can be forced to remain nearly constant through an optical phase-locked loop. The implementation of such a loop is not simple and makes the design of optical homodyne receivers quite complicated. In addition, matching of the transmitter and local-oscillator frequencies puts stringent requirements on the two optical sources.

4.5.3 Heterodyne Detection

In the case of heterodyne detection the local-oscillator frequency ω_{LO} is chosen to differ from the signal-carrier frequency ω_0 such that the intermediate frequency ω_{IF} is in the microwave region ($\nu_{\text{IF}} \sim 1 \text{ GHz}$). Using Eq. (4.5.3) together with $I = R_d P$, the photocurrent is now given by

$$I(t) = R_d(P_s + P_{\text{LO}}) + 2R_d\sqrt{P_s P_{\text{LO}}} \cos(\omega_{\text{IF}}t + \phi_s - \phi_{\text{LO}}). \quad (4.5.7)$$

Since $P_{\text{LO}} \gg P_s$ in practice, the direct-current (dc) term is nearly constant and can be removed easily using bandpass filters. The heterodyne signal is then given by the alternating-current (ac) term in Eq. (4.5.7) or by

$$I_{\text{ac}}(t) = 2R_d\sqrt{P_s P_{\text{LO}}} \cos(\omega_{\text{IF}}t + \phi_s - \phi_{\text{LO}}). \quad (4.5.8)$$

Similar to the case of homodyne detection, information can be transmitted through amplitude, phase, or frequency modulation of the optical carrier. More importantly, the local oscillator still amplifies the received signal by a large factor, thereby improving the SNR. However, the SNR improvement is lower by a factor of 2 (or by 3 dB) compared with the homodyne case. This reduction is referred to as the heterodyne-detection penalty. The origin of the 3-dB penalty can be seen by considering the signal power (proportional to the square of the current). Because of the ac nature of I_{ac} , the electrical power is reduced by a factor of 2 when I_{ac}^2 is averaged over a full cycle at the intermediate frequency (recall that the average of $\cos^2 \theta$ over θ is $\frac{1}{2}$).

The advantage gained at the expense of the 3-dB penalty is that the receiver design is simplified considerably because an optical phase-locked loop is no longer needed. Fluctuations in both ϕ_s and ϕ_{LO} still need to be controlled using narrow-linewidth semiconductor lasers for both optical sources. However, the linewidth requirements are relatively moderate when an asynchronous demodulation scheme is employed. This feature makes the heterodyne-detection scheme quite suitable for practical implementation in coherent lightwave systems.

4.5.4 Signal-to-Noise Ratio

The advantage of coherent detection for lightwave systems can be made more quantitative by considering the SNR of the receiver current. For this purpose, it is necessary to extend the analysis of Section 4.4 to the case of heterodyne detection. The receiver current fluctuates because of shot noise and thermal noise. The variance σ^2 of current fluctuations is obtained by adding the two contributions so that

$$\sigma^2 = \sigma_s^2 + \sigma_T^2, \quad (4.5.9)$$

where

$$\sigma_s^2 = 2q(I + I_d)\Delta f, \quad \sigma_T^2 = (4k_B T / R_L)F_n\Delta f. \quad (4.5.10)$$

It is important to note that the I in Eq. (4.5.10) is the total current generated at the detector and is given by Eq. (4.5.5) or Eq. (4.5.7), depending on whether homodyne or heterodyne detection is employed. In practice, $P_{\text{LO}} \gg P_s$, and I in Eq. (4.5.10) can be replaced by the dominant term $R P_{\text{LO}}$ for both cases.

The SNR is obtained by dividing the average signal power by the average noise power. In the heterodyne case, it is given by

$$\text{SNR} = \frac{\langle I_{\text{ac}}^2 \rangle}{\sigma^2} = \frac{2R_d^2 \bar{P}_s P_{\text{LO}}}{2q(R_d P_{\text{LO}} + I_d)\Delta f + \sigma_T^2}. \quad (4.5.11)$$

In the homodyne case, the SNR is larger by a factor of 2 if we assume that $\phi_s = \phi_{\text{LO}}$ in Eq. (4.5.5). The main advantage of coherent detection can be seen from Eq. (4.5.11). Since the local-oscillator power P_{LO} can be controlled at the receiver, it can be made large enough that the receiver noise is dominated by shot noise. More specifically, $\sigma_s^2 \gg \sigma_T^2$ when

$$P_{\text{LO}} \gg \sigma_T^2 / (2qR_d\Delta f). \quad (4.5.12)$$

Under the same conditions, the dark-current contribution to the shot noise is negligible ($I_d \ll R_p P_{\text{LO}}$). The SNR is then given by

$$\text{SNR} \approx \frac{R_d \bar{P}_s}{q\Delta f} = \frac{\eta \bar{P}_s}{h\nu\Delta f}, \quad (4.5.13)$$

where $R_d = \eta q/h\nu$ was used from Eq. (4.1.3). The main point to emphasize is that the use of coherent detection allows one to achieve the shot-noise limit even for $p-i-n$ receivers whose performance is generally limited by thermal noise. Moreover, in contrast with the case of APDs, this limit is realized without adding any excess shot noise.

It is useful to express the SNR in terms of the number of photons, N_p , received within a single bit. At the bit rate B , the signal power \bar{P}_s is related to N_p as $\bar{P}_s = N_p h\nu B$. Typically, $\Delta f \approx B/2$. Using these values in Eq. (4.5.13), the SNR is given by a simple expression

$$\text{SNR} = 2\eta N_p. \quad (4.5.14)$$

In the case of homodyne detection, SNR is larger by a factor of 2 and is given by $\text{SNR} = 4\eta N_p$.

4.6 Receiver Sensitivity

Among a group of optical receivers, a receiver is said to be more sensitive if it achieves the same performance with less optical power incident on it. The performance criterion for digital receivers is governed by the *bit-error rate* (BER), defined as the probability of incorrect identification of a bit by the decision circuit of the receiver. Hence, a BER of 2×10^{-6} corresponds to on average 2 errors per million bits. A commonly used criterion for digital optical receivers requires the BER to be below 1×10^{-9} . The receiver sensitivity is then defined as the minimum average received power \bar{P}_{rec} required by the receiver to operate at a BER of 10^{-9} . Since \bar{P}_{rec} depends on the BER, let us begin by calculating the BER.

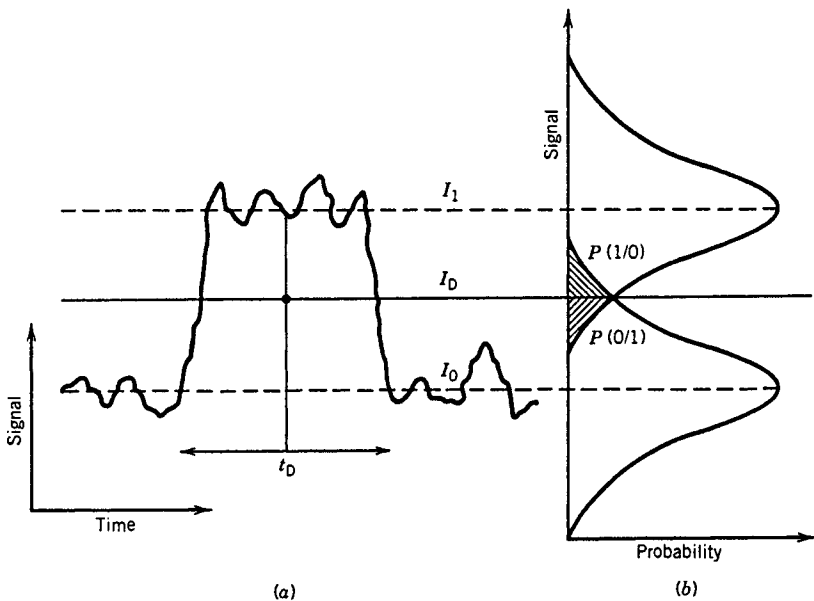


Figure 4.20: (a) Fluctuating signal generated at the receiver. (b) Gaussian probability densities of 1 and 0 bits. The dashed region shows the probability of incorrect identification.

4.6.1 Bit-Error Rate

Figure 4.20(a) shows schematically the fluctuating signal received by the decision circuit, which samples it at the decision instant t_D determined through clock recovery. The sampled value I fluctuates from bit to bit around an average value I_1 or I_0 , depending on whether the bit corresponds to 1 or 0 in the bit stream. The decision circuit compares the sampled value with a threshold value I_D and calls it bit 1 if $I > I_D$ or bit 0 if $I < I_D$. An error occurs if $I < I_D$ for bit 1 because of receiver noise. An error also occurs if $I > I_D$ for bit 0. Both sources of errors can be included by defining the *error probability* as

$$\text{BER} = p(1)P(0|1) + p(0)P(1|0), \quad (4.6.1)$$

where $p(1)$ and $p(0)$ are the probabilities of receiving bits 1 and 0, respectively, $P(0|1)$ is the probability of deciding 0 when 1 is received, and $P(1|0)$ is the probability of deciding 1 when 0 is received. Since 1 and 0 bits are equally likely to occur, $p(1) = p(0) = 1/2$, and the BER becomes

$$\text{BER} = \frac{1}{2}[P(0|1) + P(1|0)]. \quad (4.6.2)$$

Figure 4.20(b) shows how $P(0|1)$ and $P(1|0)$ depend on the probability density function $p(I)$ of the sampled value I . The functional form of $p(I)$ depends on the statistics of noise sources responsible for current fluctuations. Thermal noise i_T in Eq. (4.4.6) is well described by Gaussian statistics with zero mean and variance σ_T^2 . The statistics of shot-noise contribution i_s in Eq. (4.4.6) is also approximately Gaussian for

$p-i-n$ receivers although that is not the case for APDs [90]–[92]. A common approximation treats i_s as a Gaussian random variable for both $p-i-n$ and APD receivers but with different variance σ_s^2 given by Eqs. (4.4.5) and (4.4.17), respectively. Since the sum of two Gaussian random variables is also a Gaussian random variable, the sampled value I has a Gaussian probability density function with variance $\sigma^2 = \sigma_s^2 + \sigma_T^2$. However, both the average and the variance are different for 1 and 0 bits since I_p in Eq. (4.4.6) equals I_1 or I_0 , depending on the bit received. If σ_1^2 and σ_0^2 are the corresponding variances, the conditional probabilities are given by

$$P(0|1) = \frac{1}{\sigma_1 \sqrt{2\pi}} \int_{-\infty}^{I_D} \exp\left(-\frac{(I - I_1)^2}{2\sigma_1^2}\right) dI = \frac{1}{2} \operatorname{erfc}\left(\frac{I_1 - I_D}{\sigma_1 \sqrt{2}}\right), \quad (4.6.3)$$

$$P(1|0) = \frac{1}{\sigma_0 \sqrt{2\pi}} \int_{I_D}^{\infty} \exp\left(-\frac{(I - I_0)^2}{2\sigma_0^2}\right) dI = \frac{1}{2} \operatorname{erfc}\left(\frac{I_D - I_0}{\sigma_0 \sqrt{2}}\right), \quad (4.6.4)$$

where erfc stands for the complementary error function, defined as [93]

$$\operatorname{erfc}(x) = \frac{2}{\sqrt{\pi}} \int_x^{\infty} \exp(-y^2) dy. \quad (4.6.5)$$

By substituting Eqs. (4.6.3) and (4.6.4) in Eq. (4.6.2), the BER is given by

$$\text{BER} = \frac{1}{4} \left[\operatorname{erfc}\left(\frac{I_1 - I_D}{\sigma_1 \sqrt{2}}\right) + \operatorname{erfc}\left(\frac{I_D - I_0}{\sigma_0 \sqrt{2}}\right) \right]. \quad (4.6.6)$$

Equation (4.6.6) shows that the BER depends on the *decision threshold* I_D . In practice, I_D is optimized to minimize the BER. The minimum occurs when I_D is chosen such that

$$\frac{(I_D - I_0)^2}{2\sigma_0^2} = \frac{(I_1 - I_D)^2}{2\sigma_1^2} + \ln\left(\frac{\sigma_1}{\sigma_0}\right). \quad (4.6.7)$$

The last term in this equation is negligible in most cases of practical interest, and I_D is approximately obtained from

$$(I_D - I_0)/\sigma_0 = (I_1 - I_D)/\sigma_1 \equiv Q. \quad (4.6.8)$$

An explicit expression for I_D is

$$I_D = \frac{\sigma_0 I_1 + \sigma_1 I_0}{\sigma_0 + \sigma_1}. \quad (4.6.9)$$

When $\sigma_1 = \sigma_0$, $I_D = (I_1 + I_0)/2$, which corresponds to setting the decision threshold in the middle. This is the situation for most $p-i-n$ receivers whose noise is dominated by thermal noise ($\sigma_T \gg \sigma_s$) and is independent of the average current. By contrast, shot noise is larger for bit 1 than for bit 0, since σ_s^2 varies linearly with the average current. In the case of APD receivers, the BER can be minimized by setting the decision threshold in accordance with Eq. (4.6.9).

The BER with the optimum setting of the decision threshold is obtained by using Eqs. (4.6.6) and (4.6.8) and depends only on the Q parameter as

$$\text{BER} = \frac{1}{2} \operatorname{erfc}\left(\frac{Q}{\sqrt{2}}\right) \approx \frac{\exp(-Q^2/2)}{Q\sqrt{2\pi}}, \quad (4.6.10)$$

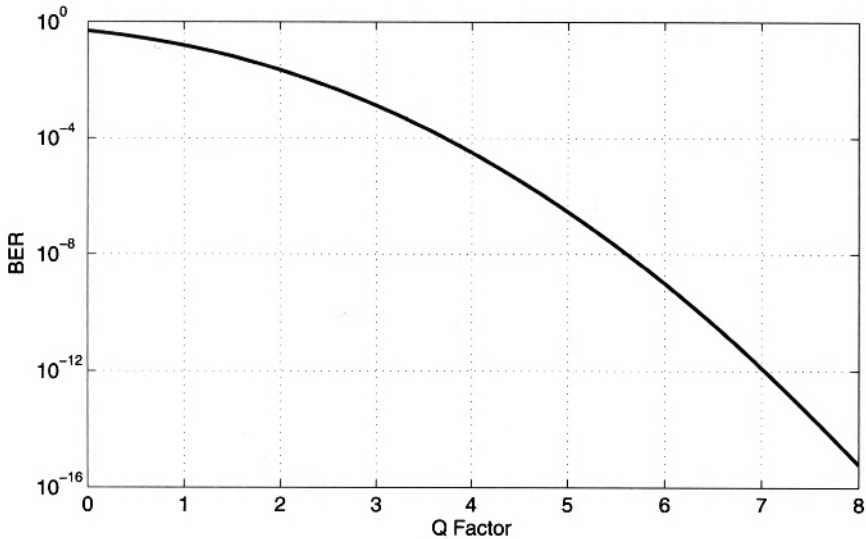


Figure 4.21: Bit-error rate versus the Q parameter.

where the Q factor is obtained from Eqs. (4.6.8) and (4.6.9) and is given by

$$Q = \frac{I_1 - I_0}{\sigma_1 + \sigma_0}. \quad (4.6.11)$$

The approximate form of BER is obtained by using the asymptotic expansion [93] of $\text{erfc}(Q/\sqrt{2})$ and is reasonably accurate for $Q > 3$. Figure 4.21 shows how the BER varies with the Q parameter. The BER improves as Q increases and becomes lower than 10^{-12} for $Q > 7$. The receiver sensitivity corresponds to the average optical power for which $Q \approx 6$, since $\text{BER} \approx 10^{-9}$ when $Q = 6$. Next subsection provides an explicit expression for the receiver sensitivity.

4.6.2 Minimum Received Power

Equation (4.6.10) can be used to calculate the minimum optical power that a receiver needs to operate reliably with a BER below a specified value. For this purpose the Q parameter should be related to the incident optical power. For simplicity, consider the case in which 0 bits carry no optical power so that $P_0 = 0$, and hence $I_0 = 0$. The power P_1 in 1 bits is related to I_1 as

$$I_1 = MR_d P_1 = 2MR_d \bar{P}_{\text{rec}}, \quad (4.6.12)$$

where \bar{P}_{rec} is the average received power defined as $\bar{P}_{\text{rec}} = (P_1 + P_0)/2$. The APD gain M is included in Eq. (4.6.12) for generality. The case of $p-i-n$ receivers can be considered by setting $M = 1$.

The RMS noise currents σ_1 and σ_0 include the contributions of both shot noise and thermal noise and can be written as

$$\sigma_1 = (\sigma_s^2 + \sigma_T^2)^{1/2} \quad \text{and} \quad \sigma_0 = \sigma_T, \quad (4.6.13)$$

where σ_s^2 and σ_T^2 are given by Eqs. (4.4.17) and (4.4.9), respectively. Neglecting the contribution of dark current, the noise variances become

$$\sigma_s^2 = 2qM^2F_A R_d(2\bar{P}_{\text{rec}})\Delta f, \quad (4.6.14)$$

$$\sigma_T^2 = (4k_B T / R_L) F_n \Delta f. \quad (4.6.15)$$

By using Eqs. (4.6.11)–(4.6.13), the Q factor is given by

$$Q = \frac{I_1}{\sigma_1 + \sigma_0} = \frac{2MR_d\bar{P}_{\text{rec}}}{(\sigma_s^2 + \sigma_T^2)^{1/2} + \sigma_T}. \quad (4.6.16)$$

For a specified value of BER, Q is determined from Eq. (4.6.10) and the receiver sensitivity \bar{P}_{rec} is found from Eq. (4.6.16). A simple analytic expression for \bar{P}_{rec} is obtained by solving Eq. (4.6.16) for a given value of Q and is given by [3]

$$\bar{P}_{\text{rec}} = \frac{Q}{R_d} \left(qF_A Q \Delta f + \frac{\sigma_T}{M} \right). \quad (4.6.17)$$

Equation (4.6.17) shows how \bar{P}_{rec} depends on various receiver parameters and how it can be optimized. Consider first the case of a $p-i-n$ receiver by setting $M = 1$. Since thermal noise σ_T generally dominates for such a receiver, \bar{P}_{rec} is given by the simple expression

$$(\bar{P}_{\text{rec}})_{\text{pin}} \approx Q\sigma_T / R_d. \quad (4.6.18)$$

From Eq. (4.6.15), σ_T^2 depends not only on receiver parameters such as R_L and F_n but also on the bit rate through the receiver bandwidth Δf (typically, $\Delta f = B/2$). Thus, \bar{P}_{rec} increases as \sqrt{B} in the thermal-noise limit. As an example, consider a $1.55-\mu\text{m}$ $p-i-n$ receiver with $R = 1 \text{ A/W}$. If we use $\sigma_T = 100 \text{ nA}$ as a typical value and $Q = 6$ corresponding to a BER of 10^{-9} , the receiver sensitivity is given by $\bar{P}_{\text{rec}} = 0.6 \mu\text{W}$ or -32.2 dBm .

Equation (4.6.17) shows how receiver sensitivity improves with the use of APD receivers. If thermal noise remains dominant, \bar{P}_{rec} is reduced by a factor of M , and the received sensitivity is improved by the same factor. However, shot noise increases considerably for APD, and Eq. (4.6.17) should be used in the general case in which shot-noise and thermal-noise contributions are comparable. Similar to the case of SNR discussed in Section 4.4.3, the receiver sensitivity can be optimized by adjusting the APD gain M . By using F_A from Eq. (4.4.18) in Eq. (4.6.17), it is easy to verify that \bar{P}_{rec} is minimum for an optimum value of M given by [3]

$$M_{\text{opt}} = k_A^{-1/2} \left(\frac{\sigma_T}{Qq\Delta f} + k_A - 1 \right)^{1/2} \approx \left(\frac{\sigma_T}{k_A Q q \Delta f} \right)^{1/2}, \quad (4.6.19)$$

and the minimum value is given by

$$(\bar{P}_{\text{rec}})_{\text{APD}} = (2q\Delta f / R_d) Q^2 (k_A M_{\text{opt}} + 1 - k_A). \quad (4.6.20)$$

The improvement in receiver sensitivity obtained by the use of an APD can be estimated by comparing Eqs. (4.6.18) and (4.6.20). It depends on the ionization-coefficient ratio k_A and is larger for APDs with a smaller value of k_A . For InGaAs APD receivers, the sensitivity is typically improved by 6–8 dB; such an improvement is sometimes called the APD advantage. Note that \bar{P}_{rec} for APD receivers increases linearly with the bit rate B ($\Delta f \approx B/2$), in contrast with its \sqrt{B} dependence for $p-i-n$ receivers. The linear dependence of \bar{P}_{rec} on B is a general feature of shot-noise-limited receivers. For an ideal receiver for which $\sigma_T = 0$, the receiver sensitivity is obtained by setting $M = 1$ in Eq. (4.6.17) and is given by

$$(\bar{P}_{\text{rec}})_{\text{ideal}} = (q\Delta f/R_d)Q^2. \quad (4.6.21)$$

A comparison of Eqs. (4.6.20) and (4.6.21) shows sensitivity degradation caused by the excess-noise factor in APD receivers.

Alternative measures of receiver sensitivity are sometimes used. For example, the BER can be related to the SNR and to the average number of photons N_p contained within the “1” bit. In the thermal-noise limit $\sigma_0 \approx \sigma_1$. By using $I_0 = 0$, Eq. (4.6.11) provides $Q = I_1/2\sigma_1$. As $\text{SNR} = I_1^2/\sigma_1^2$, it is related to Q by the simple relation $\text{SNR} = 4Q^2$. Since $Q = 6$ for a BER of 10^{-9} , the SNR must be at least 144 or 21.6 dB for achieving $\text{BER} \leq 10^{-9}$. The required value of SNR changes in the shot-noise limit. In the absence of thermal noise, $\sigma_0 \approx 0$, since shot noise is negligible for a “0” bit if the dark-current contribution is neglected. Since $Q = I_1/\sigma_1 = (\text{SNR})^{1/2}$ in the shot-noise limit, an SNR of 36 or 15.6 dB is enough to obtain $\text{BER} = 1 \times 10^{-9}$. It was shown in Section 4.4.2 that $\text{SNR} \approx \eta N_p$ [see Eq. (4.4.15) and the following discussion] in the shot-noise limit. By using $Q = (\eta N_p)^{1/2}$ in Eq. (4.6.10), the BER is given by

$$\text{BER} = \frac{1}{2} \operatorname{erfc} \left(\sqrt{\eta N_p / 2} \right). \quad (4.6.22)$$

For a receiver with 100% quantum efficiency ($\eta = 1$), $\text{BER} = 1 \times 10^{-9}$ when $N_p = 36$. In practice, most optical receivers require $N_p \sim 1000$ to achieve a BER of 10^{-9} , as their performance is severely limited by thermal noise.

4.6.3 Quantum Limit of Photodetection

The BER expression (4.6.22) obtained in the shot-noise limit is not totally accurate, since its derivation is based on the Gaussian approximation for the receiver noise statistics. For an ideal detector (no thermal noise, no dark current, and 100% quantum efficiency), $\sigma_0 = 0$, as shot noise vanishes in the absence of incident power, and thus the decision threshold can be set quite close to the 0-level signal. Indeed, for such an ideal receiver, 1 bits can be identified without error as long as even one photon is detected. An error is made only if a 1 bit fails to produce even a single electron–hole pair. For such a small number of photons and electrons, shot-noise statistics cannot be approximated by a Gaussian distribution, and the exact Poisson statistics should be used. If N_p is the average number of photons in each 1 bit, the probability of generating m electron–hole pairs is given by the Poisson distribution [94]

$$P_m = \exp(-N_p) N_p^m / m!. \quad (4.6.23)$$

The BER can be calculated by using Eqs. (4.6.2) and (4.6.23). The probability $P(1|0)$ that a 1 is identified when 0 is received is zero since no electron–hole pair is generated when $N_p = 0$. The probability $P(0|1)$ is obtained by setting $m = 0$ in Eq. (4.6.23), since a 0 is decided in that case even though 1 is received. Since $P(0|1) = \exp(-N_p)$, the BER is given by the simple expression

$$\text{BER} = \exp(-N_p)/2. \quad (4.6.24)$$

For $\text{BER} < 10^{-9}$, N_p must exceed 20. Since this requirement is a direct result of quantum fluctuations associated with the incoming light, it is referred to as the quantum limit. Each 1 bit must contain at least 20 photons to be detected with a $\text{BER} < 10^{-9}$. This requirement can be converted into power by using $P_1 = N_p h\nu B$, where B is the bit rate and $h\nu$ the photon energy. The receiver sensitivity, defined as $\bar{P}_{\text{rec}} = (P_1 + P_0)/2 = P_1/2$, is given by

$$\bar{P}_{\text{rec}} = N_p h\nu B/2 = \bar{N}_p h\nu B. \quad (4.6.25)$$

The quantity \bar{N}_p expresses the receiver sensitivity in terms of the average number of photons/bit and is related to N_p as $\bar{N}_p = N_p/2$ when 0 bits carry no energy. Its use as a measure of receiver sensitivity is quite common. In the quantum limit $\bar{N}_p = 10$. The power can be calculated from Eq. (4.6.25). For example, for a $1.55\text{-}\mu\text{m}$ receiver ($h\nu = 0.8\text{ eV}$), $\bar{P}_{\text{rec}} = 13\text{ nW}$ or -48.9 dBm at $B = 10\text{ Gb/s}$. Most receivers operate away from the quantum limit by 20 dB or more. This is equivalent to saying that \bar{N}_p typically exceeds 1000 photons in practical receivers.

4.7 Sensitivity Degradation

The sensitivity analysis in Section 4.6 is based on the consideration of receiver noise only. In particular, the analysis assumes that the optical signal incident on the receiver consists of an ideal bit stream such that 1 bits consist of an optical pulse of constant energy while no energy is contained in 0 bits. In practice, the optical signal emitted by a transmitter deviates from this ideal situation. Moreover, it can be degraded during its transmission through the fiber link. An example of such degradation is provided by the noise added at optical amplifiers. The minimum average optical power required by the receiver increases because of such nonideal conditions. This increase in the average received power is referred to as the *power penalty*. In this section we focus on the sources of power penalties that can lead to sensitivity degradation even without signal transmission through the fiber. Several transmission-related power-penalty mechanisms are discussed in Section 5.4.

4.7.1 Extinction Ratio

A simple source of a power penalty is related to the energy carried by 0 bits. Some power is emitted by most transmitters even in the off state. In the case of semiconductor lasers, the off-state power P_0 depends on the bias current I_b and the threshold current I_{th} . If $I_b < I_{\text{th}}$, the power emitted during 0 bits is due to spontaneous emission, and generally $P_0 \ll P_1$, where P_1 is the on-state power. By contrast, P_0 can be a significant

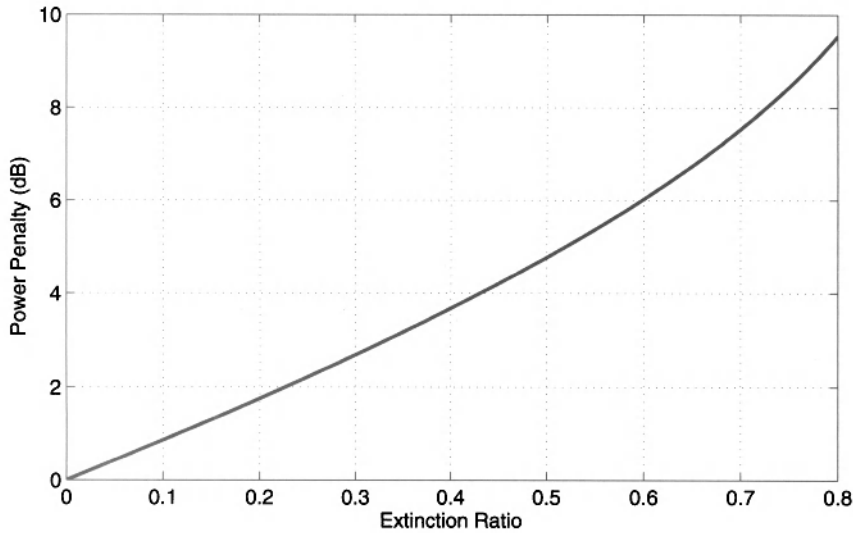


Figure 4.22: Power penalty versus the extinction ratio r_{ex} .

fraction of P_1 if the laser is biased close to but above threshold. The *extinction ratio* is defined as

$$r_{ex} = P_0/P_1. \quad (4.7.1)$$

The power penalty can be obtained by using Eq. (4.6.11). For a *p-i-n* receiver $I_1 = R_d P_1$ and $I_0 = R_d P_0$, where R_d is the responsivity (the APD gain can be included by replacing R_d with MR_d). By using the definition $\bar{P}_{rec} = (P_1 + P_0)/2$ for the receiver sensitivity, the Q factor is given by

$$Q = \left(\frac{1 - r_{ex}}{1 + r_{ex}} \right) \frac{2R_d \bar{P}_{rec}}{\sigma_1 + \sigma_0}. \quad (4.7.2)$$

In general, σ_1 and σ_0 depend on \bar{P}_{rec} because of the dependence of the shot-noise contribution on the received optical signal. However, both of them can be approximated by the thermal noise σ_T when receiver performance is dominated by thermal noise. By using $\sigma_1 \approx \sigma_0 \approx \sigma_T$ in Eq. (4.7.2), \bar{P}_{rec} is given by

$$\bar{P}_{rec}(r_{ex}) = \left(\frac{1 + r_{ex}}{1 - r_{ex}} \right) \frac{\sigma_T Q}{R_d}. \quad (4.7.3)$$

This equation shows that \bar{P}_{rec} increases when $r_{ex} \neq 0$. The power penalty is defined as the ratio $\delta_{ex} = \bar{P}_{rec}(r_{ex})/\bar{P}_{rec}(0)$. It is commonly expressed in decibel (dB) units by using

$$\delta_{ex} = 10 \log_{10} \left(\frac{\bar{P}_{rec}(r_{ex})}{\bar{P}_{rec}(0)} \right) = 10 \log_{10} \left(\frac{1 + r_{ex}}{1 - r_{ex}} \right). \quad (4.7.4)$$

Figure 4.22 shows how the power penalty increases with r_{ex} . A 1-dB penalty occurs for $r_{ex} = 0.12$ and increases to 4.8 dB for $r_{ex} = 0.5$. In practice, for lasers biased below

threshold, r_{ex} is typically below 0.05, and the corresponding power penalty (<0.4 dB) is negligible. Nonetheless, it can become significant if the semiconductor laser is biased above threshold. An expression for $\bar{P}_{\text{rec}}(r_{\text{ex}})$ can be obtained [3] for APD receivers by including the APD gain and the shot-noise contribution to σ_0 and σ_1 in Eq. (4.7.2). The optimum APD gain is lower than that in Eq. (4.6.19) when $r_{\text{ex}} \neq 0$. The sensitivity is also reduced because of the lower optimum gain. Normally, the power penalty for an APD receiver is larger by about a factor of 2 for the same value of r_{ex} .

4.7.2 Intensity Noise

The noise analysis of Section 4.4 is based on the assumption that the optical power incident on the receiver does not fluctuate. In practice, light emitted by any transmitter exhibits power fluctuations. Such fluctuations, called intensity noise, were discussed in Section 3.3.3 in the context of semiconductor lasers. The optical receiver converts power fluctuations into current fluctuations which add to those resulting from shot noise and thermal noise. As a result, the receiver SNR is degraded and is lower than that given by Eq. (4.4.19). An exact analysis is complicated, as it involves the calculation of photocurrent statistics [95]. A simple approach consists of adding a third term to the current variance given by Eq. (4.4.10), so that

$$\sigma^2 = \sigma_s^2 + \sigma_T^2 + \sigma_I^2, \quad (4.7.5)$$

where

$$\sigma_I = R_d \langle (\Delta P_{\text{in}}^2) \rangle^{1/2} = R_d P_{\text{in}} r_I. \quad (4.7.6)$$

The parameter r_I , defined as $r_I = \langle (\Delta P_{\text{in}}^2) \rangle^{1/2} / P_{\text{in}}$, is a measure of the noise level of the incident optical signal. It is related to the *relative intensity noise* (RIN) of the transmitter as

$$r_I^2 = \frac{1}{2\pi} \int_{-\infty}^{\infty} \text{RIN}(\omega) d\omega, \quad (4.7.7)$$

where $\text{RIN}(\omega)$ is given by Eq. (3.5.32). As discussed in Section 3.3.3, r_I is simply the inverse of the SNR of light emitted by the transmitter. Typically, the transmitter SNR is better than 20 dB, and $r_I < 0.01$.

As a result of the dependence of σ_0 and σ_1 on the parameter r_I , the parameter Q in Eq. (4.6.11) is reduced in the presence of intensity noise. Since Q should be maintained to the same value to maintain the BER, it is necessary to increase the received power. This is the origin of the power penalty induced by intensity noise. To simplify the following analysis, the extinction ratio is assumed to be zero, so that $I_0 = 0$ and $\sigma_0 = \sigma_T$. By using $I_1 = RP_1 = 2R\bar{P}_{\text{rec}}$ and Eq. (4.7.5) for σ_I , Q is given by

$$Q = \frac{2R_d \bar{P}_{\text{rec}}}{(\sigma_T^2 + \sigma_s^2 + \sigma_I^2)^{1/2} + \sigma_T}, \quad (4.7.8)$$

where

$$\sigma_s = (4qR_d \bar{P}_{\text{rec}} \Delta f)^{1/2}, \quad \sigma_I = 2r_I R \bar{P}_{\text{rec}}, \quad (4.7.9)$$

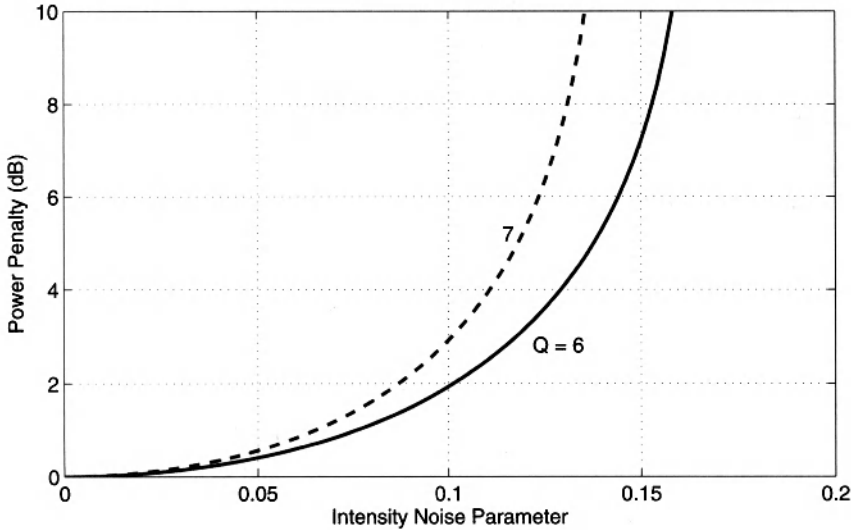


Figure 4.23: Power penalty versus the intensity noise parameter r_I .

and σ_T is given by Eq. (4.4.9). Equation (4.7.8) is easily solved to obtain the following expression for the receiver sensitivity:

$$\bar{P}_{\text{rec}}(r_I) = \frac{Q\sigma_T + Q^2 q \Delta f}{R_d(1 - r_I^2 Q^2)}. \quad (4.7.10)$$

The power penalty, defined as the increase in \bar{P}_{rec} when $r_I \neq 0$, is given by

$$\delta_I = 10 \log_{10}[\bar{P}_{\text{rec}}(r_I)/\bar{P}_{\text{rec}}(0)] = -10 \log_{10}(1 - r_I^2 Q^2). \quad (4.7.11)$$

Figure 4.23 shows the power penalty as a function of r_I for maintaining $Q = 6$ and 7 corresponding to a BER of 10^{-9} and 10^{-12} , respectively. The penalty is negligible for $r_I < 0.01$ as δ_I is below 0.02 dB. Since this is the case for most optical transmitters, the effect of transmitter noise is negligible in practice. The power penalty exceeds 2 dB for $r_I = 0.1$ and becomes infinite when $r_I = 1/Q$. An infinite power penalty implies that the receiver cannot operate at the specific BER even if the incident optical power is increased indefinitely. In the case of Figure 4.21, an infinite power penalty corresponds to a saturation of the BER curve above the 10^{-9} level for $Q = 6$, a feature referred to as the BER floor. In this respect, the effect of intensity noise is qualitatively different than the extinction ratio, for which the power penalty remains finite for all values of r_{ex} such that $r_{\text{ex}} < 1$.

The preceding analysis assumes that the intensity noise at the receiver is the same as at the transmitter. This is not typically the case when the optical signal propagates through a fiber link. The intensity noise added by in-line optical amplifiers often becomes a limiting factor for most long-haul lightwave systems (see Chapter 7). When a multimode semiconductor laser is used, fiber dispersion can lead to degradation of

the receiver sensitivity through the mode-partition noise. Another phenomenon that can enhance intensity noise is optical feedback from parasitic reflections occurring all along the fiber link. Such transmission-induced power-penalty mechanisms are considered in Section 5.4.

4.7.3 Timing Jitter

The calculation of receiver sensitivity in Section 4.5 is based on the assumption that the signal is sampled at the peak of the voltage pulse. In practice, the decision instant is determined by the clock-recovery circuit (see Figure 4.12). Because of the noisy nature of the input to the clock-recovery circuit, the sampling time fluctuates from bit to bit. Such fluctuations are called *timing jitter* [96]–[99]. The SNR is degraded because fluctuations in the sampling time lead to additional fluctuations in the signal. This can be understood by noting that if the bit is not sampled at the bit center, the sampled value is reduced by an amount that depends on the timing jitter Δt . Since Δt is a random variable, the reduction in the sampled value is also random. The SNR is reduced as a result of such additional fluctuations, and the receiver performance is degraded. The SNR can be maintained by increasing the received optical power. This increase is the power penalty induced by timing jitter.

To simplify the following analysis, let us consider a $p-i-n$ receiver dominated by thermal noise σ_T and assume a zero extinction ratio. By using $I_0 = 0$ in Eq. (4.6.11), the Q factor is given by

$$Q = \frac{I_1 - \langle \Delta i_j \rangle}{(\sigma_T^2 + \sigma_j^2)^{1/2} + \sigma_T}, \quad (4.7.12)$$

where $\langle \Delta i_j \rangle$ is the average value and σ_j is the RMS value of the current fluctuation Δi_j induced by timing jitter Δt . If $h_{\text{out}}(t)$ governs the shape of the current pulse,

$$\Delta i_j = I_1 [h_{\text{out}}(0) - h_{\text{out}}(\Delta t)], \quad (4.7.13)$$

where the ideal sampling instant is taken to be $t = 0$.

Clearly, σ_j depends on the shape of the signal pulse at the decision current. A simple choice [96] corresponds to $h_{\text{out}}(t) = \cos^2(\pi Bt/2)$, where B is the bit rate. Here Eq. (4.3.6) is used as many optical receivers are designed to provide that pulse shape. Since Δt is likely to be much smaller than the bit period $T_B = 1/B$, it can be approximated as

$$\Delta i_j = (2\pi^2/3 - 4)(B\Delta t)^2 I_1 \quad (4.7.14)$$

by assuming that $B\Delta t \ll 1$. This approximation provides a reasonable estimate of the power penalty as long as the penalty is not too large [96]. This is expected to be the case in practice. To calculate σ_j , the probability density function of the timing jitter Δt is assumed to be Gaussian, so that

$$p(\Delta t) = \frac{1}{\tau_j \sqrt{2\pi}} \exp\left(-\frac{\Delta t^2}{2\tau_j^2}\right), \quad (4.7.15)$$

where τ_j is the RMS value (standard deviation) of Δt . The probability density of Δi_j can be obtained by using Eqs. (4.7.14) and (4.7.15) and noting that Δi_j is proportional

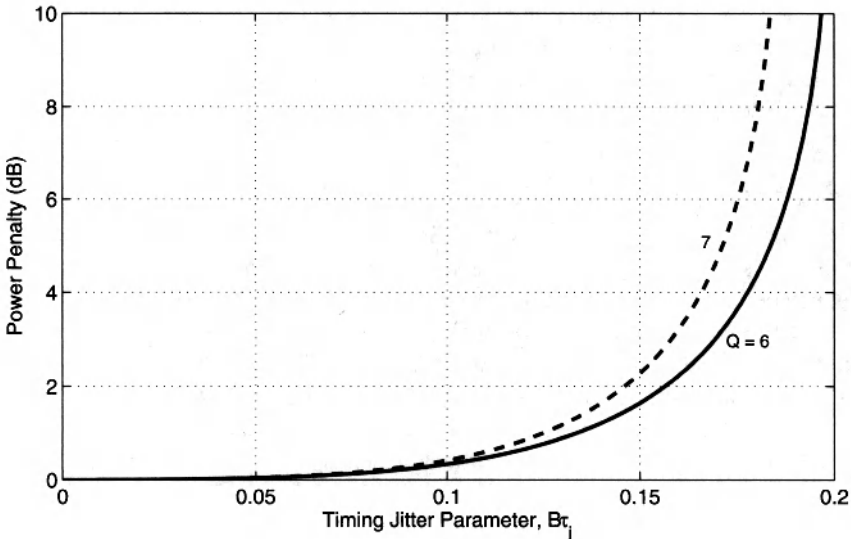


Figure 4.24: Power penalty versus the timing jitter parameter $B\tau_j$.

to $(\Delta t)^2$. The result is

$$p(\Delta i_j) = \frac{1}{\sqrt{\pi b \Delta i_j I_1}} \exp\left(-\frac{\Delta i_j}{b I_1}\right), \quad (4.7.16)$$

where

$$b = (4\pi^2/3 - 8)(B\tau_j)^2. \quad (4.7.17)$$

Equation (4.7.16) is used to calculate $\langle \Delta i_j \rangle$ and $\sigma_j = \langle (\Delta i_j)^2 \rangle^{1/2}$. The integration over Δi_j is easily done to obtain

$$\langle \Delta i_j \rangle = b I_1 / 2, \quad \sigma_j = b I_1 / \sqrt{2}. \quad (4.7.18)$$

By using Eqs. (4.7.12) and (4.7.18) and noting that $I_1 = 2R_d \bar{P}_{\text{rec}}$, where R_d is the responsivity, the receiver sensitivity is given by

$$\bar{P}_{\text{rec}}(b) = \left(\frac{\sigma_T Q}{R_d}\right) \frac{1 - b/2}{(1 - b/2)^2 - b^2 Q^2/2}. \quad (4.7.19)$$

The power penalty, defined as the increase in \bar{P}_{rec} , is given by

$$\delta_j = 10 \log_{10} \left(\frac{\bar{P}_{\text{rec}}(b)}{\bar{P}_{\text{rec}}(0)} \right) = 10 \log_{10} \left(\frac{1 - b/2}{(1 - b/2)^2 - b^2 Q^2/2} \right). \quad (4.7.20)$$

Figure 4.24 shows how the power penalty varies with the parameter $B\tau_j$, which has the physical significance of the fraction of the bit period over which the decision time fluctuates (one standard deviation). The power penalty is negligible for $B\tau_j < 0.1$ but

increases rapidly beyond $B\tau_j = 0.1$. A 2-dB penalty occurs for $B\tau_j = 0.16$. Similar to the case of intensity noise, the jitter-induced penalty becomes infinite beyond $B\tau_j = 0.2$. The exact value of $B\tau_j$ at which the penalty becomes infinite depends on the model used to calculate the jitter-induced power penalty. Equation (4.7.20) is obtained by using a specific pulse shape and a specific jitter distribution. It is also based on the use of Eqs. (4.6.10) and (4.7.12), which assumes Gaussian statistics for the receiver current. As evident from Eq. (4.7.16), jitter-induced current fluctuations are not Gaussian in nature. A more accurate calculation shows that Eq. (4.7.20) underestimates the power penalty [98]. The qualitative behavior, however, remains the same. In general, the RMS value of the timing jitter should be below 10% of the bit period for a negligible power penalty. A similar conclusion holds for APD receivers, for which the penalty is generally larger [99].

4.8 Receiver Performance

The receiver performance is characterized by measuring the BER as a function of the average optical power received. The average optical power corresponding to a BER of 10^{-9} is a measure of receiver sensitivity. Figure 4.25 shows the receiver sensitivity measured in various transmission experiments [100]–[111] by sending a long sequence of pseudorandom bits (typical sequence length $2^{15} - 1$) over a single-mode fiber and then detecting it by using either a *p-i-n* or an APD receiver. The experiments were performed at the 1.3- or 1.55- μm wavelength, and the bit rate varied from 100 MHz to 10 GHz. The theoretical quantum limit at these two wavelengths is also shown in Figure 4.25 by using Eq. (4.6.25). A direct comparison shows that the measured receiver sensitivities are worse by 20 dB or more compared with the quantum limit. Most of the degradation is due to the thermal noise that is unavoidable at room temperature and generally dominates the shot noise. Some degradation is due to fiber dispersion, which leads to power penalties; sources of such penalties are discussed in the following chapter.

The dispersion-induced sensitivity degradation depends on both the bit rate B and the fiber length L and increases with BL . This is the reason why the sensitivity degradation from the quantum limit is larger (25–30 dB) for systems operating at high bit rates. The receiver sensitivity at 10 Gb/s is typically worse than -25 dBm [111]. It can be improved by 5–6 dB by using APD receivers. In terms of the number of photons/bit, APD receivers require nearly 1000 photons/bit compared with the quantum limit of 10 photons/bit. The receiver performance is generally better for shorter wavelengths in the region near 0.85 μm , where silicon APDs can be used; they perform satisfactorily with about 400 photons/bit; an experiment in 1976 achieved a sensitivity of only 187 photons/bit [112]. It is possible to improve the receiver sensitivity by using coding schemes. A sensitivity of 180 photons/bit was realized in a 1.55- μm system experiment [113] after 305 km of transmission at 140 Mb/s.

It is possible to isolate the extent of sensitivity degradation occurring as a result of signal propagation inside the optical fiber. The common procedure is to perform a separate measurement of the receiver sensitivity by connecting the transmitter and receiver directly, without the intermediate fiber. Figure 4.26 shows the results of such a

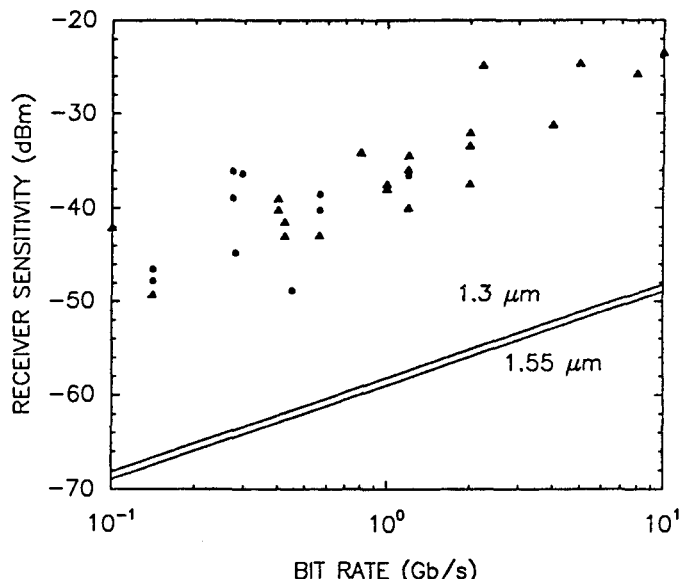


Figure 4.25: Measured receiver sensitivities versus the bit rate for *p-i-n* (circles) and APD (triangles) receivers in transmission experiments near 1.3- and 1.55- μm wavelengths. The quantum limit of receiver sensitivity is also shown for comparison (solid lines).

measurement for a 1.55- μm field experiment in which the RZ-format signal consisting of a pseudorandom bit stream in the form of solitons (sequence length $2^{23} - 1$) was propagated over more than 2000 km of fiber [114]. In the absence of fiber (0-km curve), a BER of 10^{-9} is realized for -29.5 dBm of received power. However, the launched signal is degraded considerably during transmission, resulting in about a 3-dB penalty for a 2040-km fiber link. The power penalty increases rapidly with further propagation. In fact, the increasing curvature of BER curves indicates that the BER of 10^{-9} would be unreachable after a distance of 2600 km. This behavior is typical of most lightwave systems. The eye diagram seen in Figure 4.26 is qualitatively different than that appearing in Figure 4.14. This difference is related to the use of the RZ format.

The performance of an optical receiver in actual lightwave systems may change with time. Since it is not possible to measure the BER directly for a system in operation, an alternative is needed to monitor system performance. As discussed in Section 4.3.3, the eye diagram is best suited for this purpose; closing of the eye is a measure of degradation in receiver performance and is associated with a corresponding increase in the BER. Figures 4.14 and 4.26 show examples of the eye diagrams for lightwave systems making use of the NRZ and RZ formats, respectively. The eye is wide open in the absence of optical fiber but becomes partially closed when the signal is transmitted through a long fiber link. Closing of the eye is due to amplifier noise, fiber dispersion, and various nonlinear effects, all of which lead to considerable distortion of optical pulses as they propagate through the fiber. The continuous monitoring of the

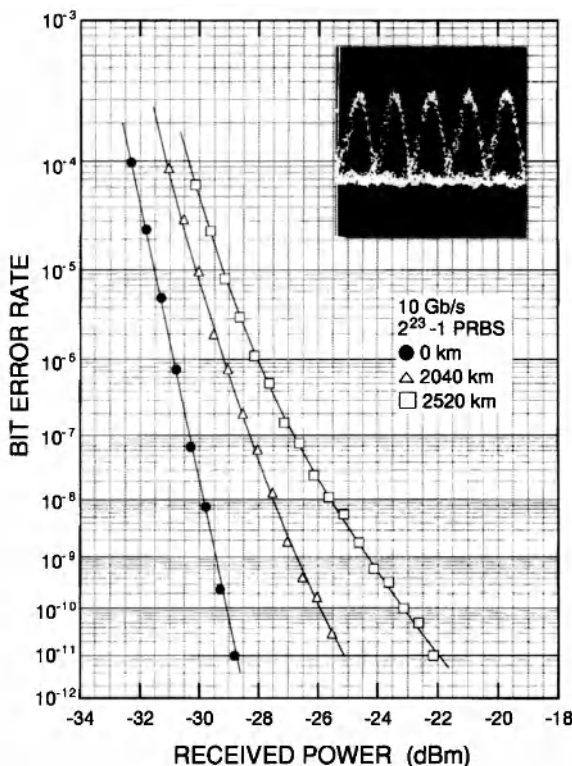


Figure 4.26: BER curves measured for three fiber-link lengths in a $1.55-\mu\text{m}$ transmission experiment at 10 Gb/s. Inset shows an example of the eye diagram at the receiver. (After Ref. [114]; ©2000 IEEE; reprinted with permission.)

eye pattern is common in actual systems as a measure of receiver performance.

The performance of optical receivers operating in the wavelength range $1.3\text{--}1.6\ \mu\text{m}$ is severely limited by thermal noise, as seen clearly from the data in Figure 4.25. The use of APD receivers improves the situation, but to a limited extent only, because of the excess noise factor associated with InGaAs APDs. Most receivers operate away from the quantum limit by 20 dB or more. The effect of thermal noise can be considerably reduced by using coherent-detection techniques in which the received signal is mixed coherently with the output of a narrow-linewidth laser. The receiver performance can also be improved by amplifying the optical signal before it is incident on the photodetector. We discuss optical amplifiers in Chapter 7.

Problems

- 4.1** Calculate the responsivity of a $p-i-n$ photodiode at 1.3 and $1.55\ \mu\text{m}$ if the quantum efficiency is 80%. Why is the photodiode more responsive at $1.55\ \mu\text{m}$?

- 4.2** Photons at a rate of $10^{10}/\text{s}$ are incident on an APD with responsivity of 6 A/W . Calculate the quantum efficiency and the photocurrent at the operating wavelength of $1.5 \mu\text{m}$ for an APD gain of 10.
- 4.3** Show by solving Eqs. (4.2.3) and (4.2.4) that the multiplication factor M is given by Eq. (4.2.7) for an APD in which electrons initiate the avalanche process. Treat α_e and α_h as constants.
- 4.4** The raised-cosine pulse shape of Eq. (4.3.6) can be generalized to generate a family of such pulses by defining

$$h_{\text{out}}(t) = \frac{\sin(\pi B t)}{\pi B t} \frac{\cos(\pi \beta B t)}{1 - (2\beta B t)^2},$$

where the parameter β varies between 0 and 1. Derive an expression for the transfer function $H_{\text{out}}(f)$ given by the Fourier transform of $h_{\text{out}}(t)$. Plot $h_{\text{out}}(t)$ and $H_{\text{out}}(f)$ for $\beta = 0, 0.5$, and 1.

- 4.5** Consider a $0.8\text{-}\mu\text{m}$ receiver with a silicon $p-i-n$ photodiode. Assume 20 MHz bandwidth, 65% quantum efficiency, 1 nA dark current, 8 pF junction capacitance, and 3 dB amplifier noise figure. The receiver is illuminated with $5 \mu\text{W}$ of optical power. Determine the RMS noise currents due to shot noise, thermal noise, and amplifier noise. Also calculate the SNR.
- 4.6** The receiver of Problem 4.6 is used in a digital communication system that requires a SNR of at least 20 dB for satisfactory performance. What is the minimum received power when the detection is limited by (a) shot noise and (b) thermal noise? Also calculate the noise-equivalent power in the two cases.
- 4.7** The excess noise factor of avalanche photodiodes is often approximated by M^x instead of Eq. (4.4.18). Find the range of M for which Eq. (4.4.18) can be approximated within 10% by $F_A(M) = M^x$ by choosing $x = 0.3$ for Si, 0.7 for InGaAs, and 1.0 for Ge. Use $k_A = 0.02$ for Si, 0.35 for InGaAs, and 1.0 for Ge.
- 4.8** Derive Eq. (4.4.22). Plot M_{opt} versus k_A by solving the cubic polynomial on a computer by using $R_L = 1 \text{ k}\Omega$, $F_n = 2$, $R = 1 \text{ A/W}$, $P_{\text{in}} = 1 \mu\text{W}$, and $I_d = 2 \text{ nA}$. Compare the results with the approximate analytic solution given by Eq. (4.4.23) and comment on its validity.
- 4.9** Derive an expression for the optimum value of M for which the SNR becomes maximum by using $F_A(M) = M^x$ in Eq. (4.4.19).
- 4.10** Derive an expression for the SNR of a homodyne receiver by taking into account both the shot noise and the thermal noise.
- 4.11** Consider a $1.55\text{-}\mu\text{m}$ heterodyne receiver with a $p-i-n$ photodiode of 90% quantum efficiency connected to a $50\text{-}\Omega$ load resistance. How much local-oscillator power is needed to operate in the shot-noise limit? Assume that shot-noise limit is achieved when the thermal-noise contribution at room temperature to the noise power is below 1%.
- 4.12** Prove that the SNR of an ideal PSK homodyne receiver (perfect phase locking and 100% quantum efficiency) approaches $4\bar{N}_p$, where \bar{N}_p is the average number

of photons/bit. Assume that the receiver bandwidth equals half the bit rate and that the receiver operates in the shot-noise limit.

- 4.13** Prove that the bit-error rate (BER) given by Eq. (4.6.6) is minimum when the decision threshold is set close to a value given by Eq. (4.6.9).
- 4.14** A $1.3\text{-}\mu\text{m}$ digital receiver is operating at 100 Mb/s and has an effective noise bandwidth of 60 MHz . The $p\text{-}i\text{-}n$ photodiode has negligible dark current and 90% quantum efficiency. The load resistance is $100\text{ }\Omega$ and the amplifier noise figure is 3 dB . Calculate the receiver sensitivity corresponding to a BER of 10^{-9} . How much does it change if the receiver is designed to operate reliably up to a BER of 10^{-12} ?
- 4.15** Calculate the receiver sensitivity (at a BER of 10^{-9}) for the receiver in Problem 4.12 in the shot-noise and thermal-noise limits. How many photons are incident during bit 1 in the two limits if the optical pulse can be approximated by a square pulse?
- 4.16** Derive an expression for the optimum gain M_{opt} of an APD receiver that would maximize the receiver sensitivity by taking the excess-noise factor as M^x . Plot M_{opt} as a function of x for $\sigma_T = 0.2\text{ }\mu\text{A}$ and $\Delta f = 1\text{ GHz}$ and estimate its value for InGaAs APDs.
- 4.17** Derive an expression for the sensitivity of an APD receiver by taking into account a finite extinction ratio for the general case in which both shot noise and thermal noise contribute to the receiver sensitivity. You can neglect the dark current.
- 4.18** Derive an expression for the intensity-noise-induced power penalty of a $p\text{-}i\text{-}n$ receiver by taking into account a finite extinction ratio. Shot-noise and intensity-noise contributions can both be neglected compared with the thermal noise in the off state but not in the on state.
- 4.19** Use the result of Problem 4.16 to plot the power penalty as a function of the intensity-noise parameter r_I [see Eq. (4.7.6) for its definition] for several values of the extinction ratio. When does the power penalty become infinite? Explain the meaning of an infinite power penalty.
- 4.20** Derive an expression for the timing-jitter-induced power penalty by assuming a parabolic pulse shape $I(t) = I_p(1 - B^2t^2)$ and a Gaussian jitter distribution with a standard deviation τ . You can assume that the receiver performance is dominated by thermal noise. Calculate the tolerable value of $B\tau$ that would keep the power penalty below 1 dB .

References

- [1] S. D. Personick, *Bell Syst. Tech. J.* **52**, 843 (1973); **52**, 875 (1973).
- [2] T. P. Lee and T. Li, in *Optical Fiber Telecommunications I*, S. E. Miller and A. G. Chynoweth, Eds., Academic Press, San Diego, CA, 1979, Chap. 18.
- [3] R. G. Smith and S. D. Personick, in *Semiconductor Devices for Optical Communications*, H. Kressel, Ed., Springer, New York, 1980.

- [4] B. L. Kasper, in *Optical Fiber Telecommunications II*, S. E. Miller and I. P. Kaminow, Eds., Academic Press, San Diego, CA, 1988, Chap. 18.
- [5] S. B. Alexander, *Optical Communication Receiver Design*, Vol. TT22, SPIE Press, Bellingham, WA, 1997.
- [6] R. J. Keyes, *Optical and Infrared Detectors*, Springer, New York, 1997.
- [7] S. Donati, *Photodetectors: Devices, Circuits and Applications*, Prentice Hall, Upper Saddle River, NJ, 1999.
- [8] H. S. Nalwa, Ed., *Photodetectors and Fiber Optics*, Academic Press, San Diego, CA, 2001.
- [9] J. C. Campbell, in *Optical Fiber Telecommunications*, Vol. 5A, I. P. Kaminow, T. Li, and A. E. Willner, Eds., Academic Press, San Diego, CA, 2008, Chap. 8.
- [10] R. S. Tucker, A. J. Taylor, C. A. Burrus, G. Eisenstein, and J. M. Westfield, *Electron. Lett.* **22**, 917 (1986).
- [11] K. Kishino, S. Ünlü, J. I. Chyi, J. Reed, L. Arsenault, and H. Morkoç, *IEEE J. Quantum Electron.* **27**, 2025 (1991).
- [12] C. C. Barron, C. J. Mahon, B. J. Thibeault, G. Wang, W. Jiang, L. A. Coldren, and J. E. Bowers, *Electron. Lett.* **30**, 1796 (1994).
- [13] I.-H. Tan, J. Dudley, D. I. Babić, D. A. Cohen, B. D. Young, E. L. Hu, J. E. Bowers, B. I. Miller, U. Koren, and M. G. Young, *IEEE Photon. Technol. Lett.* **6**, 811 (1994).
- [14] I.-H. Tan, C.-K. Sun, K. S. Giboney, J. E. Bowers, E. L. Hu, B. I. Miller, and R. J. Kapik, *IEEE Photon. Technol. Lett.* **7**, 1477 (1995).
- [15] Y.-G. Wey, K. S. Giboney, J. E. Bowers, M. J. Rodwell, P. Silvestre, P. Thiagarajan, and G. Robinson, *J. Lightwave Technol.* **13**, 1490 (1995).
- [16] K. Kato, S. Hata, K. Kwano, J. Yoshida, and A. Kozen, *IEEE J. Quantum Electron.* **28**, 2728 (1992).
- [17] K. Kato, A. Kozen, Y. Muramoto, Y. Itaya, N. Nagatsuma, and M. Yaita, *IEEE Photon. Technol. Lett.* **6**, 719 (1994).
- [18] K. Kato, *IEEE Trans. Microwave Theory Tech.* **47**, 1265 (1999).
- [19] T. Takeuchi, T. Nakata, K. Makita, and M. Yamaguchi, *Electron. Lett.* **36**, 972 (2000).
- [20] M. Achouche, V. Magnin, J. Harari, D. Carpentier, E. Derouin, C. Jany, and D. Decoster, *IEEE Photon. Technol. Lett.* **18**, 556 (2006).
- [21] A. Beling, J. C. Campbell, H.-G. Bach, G. G. Mekonnen, and D. Schmidt, *J. Lightwave Technol.* **26**, 16 (2008).
- [22] K. S. Giboney, R. L. Nagarajan, T. E. Reynolds, S. T. Allen, R. P. Mirin, M. J. W. Rodwell, and J. E. Bowers, *IEEE Photon. Technol. Lett.* **7**, 412 (1995).
- [23] H. Ito, T. Furuta, S. Kodama, and T. Ishibashi, *Electron. Lett.* **36**, 1809 (2000).
- [24] G. E. Stillman and C. M. Wolfe, in *Semiconductors and Semimetals*, Vol. 12, R. K. Willardson and A. C. Beer, Eds., Academic Press, San Diego, CA, 1977, pp. 291–393.
- [25] H. Melchior, in *Laser Handbook*, Vol. 1, F. T. Arecchi and E. O. Schulz-Dubois, Eds., North-Holland, Amsterdam, 1972, pp. 725–835.
- [26] J. C. Campbell, A. G. Dentai, W. S. Holden, and B. L. Kasper, *Electron. Lett.* **19**, 818 (1983).
- [27] B. L. Kasper and J. C. Campbell, *J. Lightwave Technol.* **5**, 1351 (1987).
- [28] L. E. Tarof, *Electron. Lett.* **27**, 34 (1991).
- [29] L. E. Tarof, J. Yu, R. Bruce, D. G. Knight, T. Baird, and B. Oosterbrink, *IEEE Photon. Technol. Lett.* **5**, 672 (1993).
- [30] J. Yu, L. E. Tarof, R. Bruce, D. G. Knight, K. Visvanatha, and T. Baird, *IEEE Photon. Technol. Lett.* **6**, 632 (1994).

- [31] C. L. F. Ma, M. J. Deen, and L. E. Tarof, *IEEE J. Quantum Electron.* **31**, 2078 (1995).
- [32] K. A. Anselm, H. Nie, C. Lenox, P. Yuan, G. Kinsey, J. C. Campbell, B. G. Streetman, *IEEE J. Quantum Electron.* **34**, 482 (1998).
- [33] T. Nakata, I. Watanabe, K. Makita, and T. Torikai, *Electron. Lett.* **36**, 1807 (2000).
- [34] F. Capasso, in *Semiconductor and Semimetals*, Vol. 22D, W. T. Tsang, Ed., Academic Press, San Diego, CA, 1985, pp. 1–172.
- [35] I. Watanabe, S. Sugou, H. Ishikawa, T. Anan, K. Makita, M. Tsuji, and K. Taguchi, *IEEE Photon. Technol. Lett.* **5**, 675 (1993).
- [36] T. Kagawa, Y. Kawamura, and H. Iwamura, *IEEE J. Quantum Electron.* **28**, 1419 (1992); *IEEE J. Quantum Electron.* **29**, 1387 (1993).
- [37] S. Hanatani, H. Nakamura, S. Tanaka, T. Ido, and C. Notsu, *Microwave Opt. Tech. Lett.* **7**, 103 (1994).
- [38] I. Watanabe, M. Tsuji, K. Makita, and K. Taguchi, *IEEE Photon. Technol. Lett.* **8**, 269 (1996).
- [39] I. Watanabe, T. Nakata, M. Tsuji, K. Makita, T. Torikai, and K. Taguchi, *J. Lightwave Technol.* **18**, 2200 (2000).
- [40] A. R. Hawkins, W. Wu, P. Abraham, K. Streubel, and J. E. Bowers, *Appl. Phys. Lett.* **70**, 303 (1997).
- [41] C. Lenox, H. Nie, P. Yuan, G. Kinsey, A. L. Homles, B. G. Streetman, and J. C. Campbell, *IEEE Photon. Technol. Lett.* **11**, 1162 (1999).
- [42] T. Nakata, T. Takeuchi, I. Watanabe, K. Makita, and T. Torikai, *Electron. Lett.* **36**, 2033 (2000).
- [43] J. Burm, K. I. Litvin, D. W. Woodard, W. J. Schaff, P. Mandeville, M. A. Jaspan, M. M. Gitin, and L. F. Eastman, *IEEE J. Quantum Electron.* **31**, 1504 (1995).
- [44] J. B. D. Soole and H. Schumacher, *IEEE J. Quantum Electron.* **27**, 737 (1991).
- [45] J. H. Kim, H. T. Griem, R. A. Friedman, E. Y. Chan, and S. Roy, *IEEE Photon. Technol. Lett.* **4**, 1241 (1992).
- [46] R.-H. Yuang, J.-I. Chyi, Y.-J. Chan, W. Lin, and Y.-K. Tu, *IEEE Photon. Technol. Lett.* **7**, 1333 (1995).
- [47] O. Vendier, N. M. Jokerst, and R. P. Leavitt, *IEEE Photon. Technol. Lett.* **8**, 266 (1996).
- [48] M. C. Hargis, S. E. Ralph, J. Woodall, D. McInturff, A. J. Negri, and P. O. Haugsjaa, *IEEE Photon. Technol. Lett.* **8**, 110 (1996).
- [49] W. A. Wohlmuth, P. Fay, C. Caneau, and I. Adesida, *Electron. Lett.* **32**, 249 (1996).
- [50] A. Bartels, E. Peiner, G.-P. Tang, R. Klockenbrink, H.-H. Wehmann, and A. Schlachetzki, *IEEE Photon. Technol. Lett.* **8**, 670 (1996).
- [51] Y. G. Zhang, A. Z. Li, and J. X. Chen, *IEEE Photon. Technol. Lett.* **8**, 830 (1996).
- [52] E. Droge, E. H. Bottcher, S. Kollakowski, A. Strittmatter, D. Bimberg, O. Reimann, and R. Steingruber, *Electron. Lett.* **34**, 2241 (1998).
- [53] A. Umbach, T. Engel, H. G. Bach, S. van Waasen, E. Dröge, A. Strittmatter, W. Ebert, W. Passenberg, R. Steingrüber, W. Schlaak, G. G. Mekonnen, G. Unterbörsch, and D. Bimberg, *IEEE J. Quantum Electron.* **35**, 1024 (1999).
- [54] J. W. Shi, Y. H. Chen, K. G. Gan, Y. J. Chiu, C. K. Sun, and J. E. Bowers, *IEEE Photon. Technol. Lett.* **14**, 363 (2002).
- [55] R. G. Swartz, in *Optical Fiber Telecommunications II*, S. E. Miller and I. P. Kaminow, Eds., Academic Press, San Diego, CA, 1988, Chap. 20.
- [56] K. Kobayashi, in *Optical Fiber Telecommunications II*, S. E. Miller and I. P. Kaminow, Eds., Academic Press, San Diego, CA, 1988, Chap. 11.

- [57] T. Horimatsu and M. Sasaki, *J. Lightwave Technol.* **7**, 1612 (1989).
- [58] O. Wada, H. Hamaguchi, M. Makiuchi, T. Kumai, M. Ito, K. Nakai, T. Horimatsu, and T. Sakurai, *J. Lightwave Technol.* **4**, 1694 (1986).
- [59] M. Makiuchi, H. Hamaguchi, T. Kumai, O. Aoki, Y. Oikawa, and O. Wada, *Electron. Lett.* **24**, 995 (1988).
- [60] K. Matsuda, M. Kubo, K. Ohnaka, and J. Shibata, *IEEE Trans. Electron. Dev.* **35**, 1284 (1988).
- [61] H. Yano, K. Aga, H. Kamei, G. Sasaki, and H. Hayashi, *J. Lightwave Technol.* **8**, 1328 (1990).
- [62] H. Hayashi, H. Yano, K. Aga, M. Murata, H. Kamei, and G. Sasaki, *IEE Proc.* **138**, Pt. J, 164 (1991).
- [63] H. Yano, G. Sasaki, N. Nishiyama, M. Murata, and H. Hayashi, *IEEE Trans. Electron. Dev.* **39**, 2254 (1992).
- [64] Y. Akatsu, M. Miyugawa, Y. Miyamoto, Y. Kobayashi, and Y. Akahori, *IEEE Photon. Technol. Lett.* **5**, 163 (1993).
- [65] K. Takahata, Y. Muramoto, H. Fukano, K. Kato, A. Kozen, O. Nakajima, and Y. Matsuoka, *IEEE Photon. Technol. Lett.* **10**, 1150 (1998).
- [66] S. Chandrasekhar, L. M. Lunardi, A. H. Gnauck, R. A. Hamm, and G. J. Qua, *IEEE Photon. Technol. Lett.* **5**, 1316 (1993).
- [67] E. Sano, M. Yoneyama, H. Nakajima, and Y. Matsuoka, *J. Lightwave Technol.* **12**, 638 (1994).
- [68] H. Kamitsuna, *J. Lightwave Technol.* **13**, 2301 (1995).
- [69] L. M. Lunardi, S. Chandrasekhar, C. A. Burrus, and R. A. Hamm, *IEEE Photon. Technol. Lett.* **7**, 1201 (1995).
- [70] M. Yoneyama, E. Sano, S. Yamahata, and Y. Matsuoka, *IEEE Photon. Technol. Lett.* **8**, 272 (1996).
- [71] E. Sano, K. Kurishima, and S. Yamahata, *Electron. Lett.* **33**, 159 (1997).
- [72] W. P. Hong, G. K. Chang, R. Bhat, C. K. Nguyen, and M. Koza, *IEEE Photon. Technol. Lett.* **3**, 156 (1991).
- [73] P. Fay, W. Wohlmuth, C. Caneau, and I. Adesida, *Electron. Lett.* **31**, 755 (1995).
- [74] G. G. Mekonnen, W. Schlaak, H. G. Bach, R. Steingruber, A. Seeger, T. Enger, W. Passenberg, A. Umbach, C. Schramm, G. Unterborsch, and S. van Waasen, *IEEE Photon. Technol. Lett.* **11**, 257 (1999).
- [75] K. Takahata, Y. Muramoto, H. Fukano, K. Kato, A. Kozen, S. Kimura, Y. Imai, Y. Miyamoto, O. Nakajima, and Y. Matsuoka, *IEEE J. Sel. Topics Quantum Electron.* **6**, 31 (2000).
- [76] N. Shimizu, K. Murata, A. Hirano, Y. Miyamoto, H. Kitabayashi, Y. Umeda, T. Akeyoshi, T. Furuta, and N. Watanabe, *Electron. Lett.* **36**, 1220 (2000).
- [77] U. Dümler, M. Möller, A. Bielik, T. Ellermeyer, H. Langenhagen, W. Walthes, and J. Mejri, *Electron. Lett.* **42**, 21 (2006).
- [78] A. Momtaz, D. Chung, N. Kocaman, J. Cao, M. Caresosa, B. Zhang, and I. Fujimori, *IEEE J. Solid-State Circuits* **42**, 872 (2007).
- [79] Y. Oikawa, H. Kuwatsuka, T. Yamamoto, T. Ihara, H. Hamano, and T. Minami, *J. Lightwave Technol.* **12**, 343 (1994).
- [80] T. Ohyama, S. Mino, Y. Akahori, M. Yanagisawa, T. Hashimoto, Y. Yamada, Y. Muramoto, and T. Tsunetsugu, *Electron. Lett.* **32**, 845 (1996).
- [81] Y. Kobayashi, Y. Akatsu, K. Nakagawa, H. Kikuchi, and Y. Imai, *IEEE Trans. Microwave Theory Tech.* **43**, 1916 (1995).

- [82] K. Emura, *Solid-State Electron.* **43**, 1613 (1999).
- [83] M. Bitter, R. Bauknecht, W. Hunziker, and H. Melchior, *IEEE Photon. Technol. Lett.* **12**, 74 (2000).
- [84] W. R. Bennett, *Electrical Noise*, McGraw-Hill, New York, 1960.
- [85] D. K. C. MacDonald, *Noise and Fluctuations: An Introduction*, Wiley, New York, 1962.
- [86] F. N. H. Robinson, *Noise and Fluctuations in Electronic Devices and Circuits*, Oxford University Press, Oxford, 1974.
- [87] W. Schottky, *Ann. Phys.* **57**, 541 (1918).
- [88] J. B. Johnson, *Phys. Rev.* **32**, 97 (1928).
- [89] H. Nyquist, *Phys. Rev.* **32**, 110 (1928).
- [90] R. J. McIntyre, *IEEE Trans. Electron. Dev.* **13**, 164 (1966); **19**, 703 (1972).
- [91] P. P. Webb, R. J. McIntyre, and J. Conradi, *RCA Rev.* **35**, 235 (1974).
- [92] P. Balaban, *Bell Syst. Tech. J.* **55**, 745 (1976).
- [93] M. Abramowitz and I. A. Stegun, Eds., *Handbook of Mathematical Functions*, Dover, New York, 1970.
- [94] B. E. A. Saleh and M. Teich, *Fundamentals of Photonics*, Wiley, New York, 1991.
- [95] L. Mandel and E. Wolf, *Optical Coherence and Quantum Optics*, Cambridge University Press, New York, 1995.
- [96] G. P. Agrawal and T. M. Shen, *Electron. Lett.* **22**, 450 (1986).
- [97] J. J. O'Reilly, J. R. F. DaRocha, and K. Schumacher, *IEE Proc.* **132**, Pt. J, 309 (1985).
- [98] K. Schumacher and J. J. O'Reilly, *Electron. Lett.* **23**, 718 (1987).
- [99] T. M. Shen, *Electron. Lett.* **22**, 1043 (1986).
- [100] T. P. Lee, C. A. Burrus, A. G. Dentai, and K. Ogawa, *Electron. Lett.* **16**, 155 (1980).
- [101] D. R. Smith, R. C. Hooper, P. P. Smyth, and D. Wake, *Electron. Lett.* **18**, 453 (1982).
- [102] J. Yamada, A. Kawana, T. Miya, H. Nagai, and T. Kimura, *IEEE J. Quantum Electron.* **18**, 1537 (1982).
- [103] M. C. Brain, P. P. Smyth, D. R. Smith, B. R. White, and P. J. Chidgey, *Electron. Lett.* **20**, 894 (1984).
- [104] M. L. Snodgrass and R. Klinman, *J. Lightwave Technol.* **2**, 968 (1984).
- [105] S. D. Walker and L. C. Blank, *Electron. Lett.* **20**, 808 (1984).
- [106] C. Y. Chen, B. L. Kasper, H. M. Cox, and J. K. Plourde, *Appl. Phys. Lett.* **46**, 379 (1985).
- [107] B. L. Kasper, J. C. Campbell, A. H. Gnauck, A. G. Dentai, and J. R. Talman, *Electron. Lett.* **21**, 982 (1985).
- [108] B. L. Kasper, J. C. Campbell, J. R. Talman, A. H. Gnauck, J. E. Bowers, and W. S. Holden, *J. Lightwave Technol.* **5**, 344 (1987).
- [109] R. Heidemann, U. Scholz, and B. Wedding, *Electron. Lett.* **23**, 1030 (1987).
- [110] M. Shikada, S. Fujita, N. Henmi, I. Takano, I. Mito, K. Taguchi, and K. Minemura, *J. Lightwave Technol.* **5**, 1488 (1987).
- [111] S. Fujita, M. Kitamura, T. Torikai, N. Henmi, H. Yamada, T. Suzuki, I. Takano, and M. Shikada, *Electron. Lett.* **25**, 702 (1989).
- [112] P. K. Runge, *IEEE Trans. Commun.* **24**, 413 (1976).
- [113] L. Pophillat and A. Levasseur, *Electron. Lett.* **27**, 535 (1991).
- [114] M. Nakazawa, H. Kubota, K. Suzuki, E. Yamada, and A. Sahara, *IEEE J. Sel. Topics Quantum Electron.* **6**, 363 (2000).

Chapter 5

Lightwave Systems

The preceding three chapters focused on the three main components of a fiber-optic communication system—optical fibers, optical transmitters, and optical receivers. In this chapter we consider the issues related to system design and performance when the three components are put together to form a practical lightwave system. Section 5.1 provides an overview of various system architectures. The design guidelines for fiber-optic communication systems are discussed in Section 5.2 by considering the effects of fiber losses and group-velocity dispersion. The power and the rise-time budgets are also described in this section. Section 5.3 focuses on long-haul systems for which the nonlinear effects become quite important. This section also covers various terrestrial and undersea lightwave systems that have been developed since 1980. Issues related to system performance are treated in Section 5.4 with emphasis on performance degradation occurring as a result of signal transmission through the optical fiber. In Section 5.5 we emphasize the importance of computer-aided design for lightwave systems.

5.1 System Architectures

From an architectural standpoint, fiber-optic communication systems can be classified into three broad categories—point-to-point links, distribution networks, and local-area networks [1]–[9]. This section focuses on the main characteristics of these three system architectures.

5.1.1 Point-to-Point Links

Point-to-point links constitute the simplest kind of lightwave systems. Their role is to transport information, available in the form of a digital bit stream, from one place to another as accurately as possible. The link length can vary from less than a kilometer (short haul) to thousands of kilometers (long haul), depending on the specific application. For example, optical data links are used to connect computers and terminals within the same building or between two buildings with a relatively short transmission distance (<10 km). The low loss and the wide bandwidth of optical fibers are not of

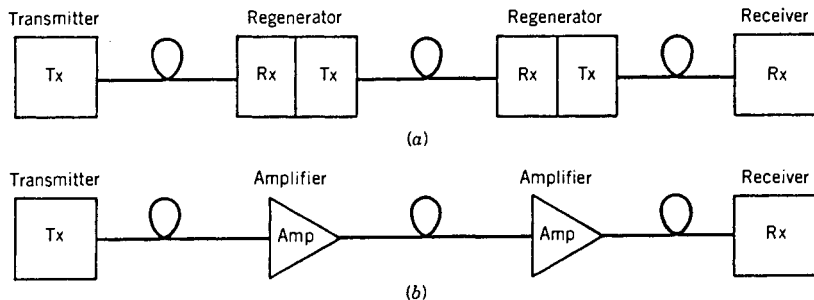


Figure 5.1: Point-to-point fiber links with periodic loss compensation through (a) regenerators and (b) optical amplifiers. A regenerator consists of a receiver followed by a transmitter.

primary importance for such data links; fibers are used mainly because of their other advantages, such as immunity to electromagnetic interference. In contrast, undersea lightwave systems are used for high-speed transmission across continents with a link length of several thousands of kilometers. Low losses and a large bandwidth of optical fibers are important factors in the design of transoceanic systems from the standpoint of reducing the overall operating cost.

When the link length exceeds a certain value, in the range 20–100 km depending on the operating wavelength, it becomes necessary to compensate for fiber losses, as the signal would otherwise become too weak to be detected reliably. Figure 5.1 shows two schemes used commonly for loss compensation. Until 1990, optoelectronic repeaters, called *regenerators* because they regenerate the optical signal, were used exclusively. As seen in Figure 5.1(a), a regenerator is nothing but a receiver-transmitter pair that detects the incoming optical signal, recovers the electrical bit stream, and then converts it back into optical form by modulating an optical source. Fiber losses can also be compensated by using optical amplifiers, which amplify the optical bit stream directly without requiring conversion of the signal to the electric domain. The advent of optical amplifiers around 1990 revolutionized the development of fiber-optic communication systems. Such amplifiers are especially valuable for WDM systems (see Chapter 6) as they can amplify a large number of channels simultaneously.

Optical amplifiers solve the loss problem but they add noise (see Chapter 7) and worsen the impact of fiber dispersion and nonlinearity because signal degradation keeps on accumulating over multiple amplification stages. Indeed, periodically amplified lightwave systems are often limited by fiber dispersion unless dispersion-compensation techniques (discussed in Chapter 8) are used. Optoelectronic repeaters do not suffer from this problem as they regenerate the original bit stream and thus effectively compensate for all sources of signal degradation automatically. However, their repeated use in WDM systems (every 80 km or so) is not cost effective. Although considerable research effort is being directed toward developing all-optical regenerators (see Chapter 11), most terrestrial systems employ a combination of the two techniques shown in Figure 5.1 and place an optoelectronic regenerator after a certain number of optical amplifiers. Submarine systems are often designed to operate over a distance of more than 5000 km using only cascaded optical amplifiers.

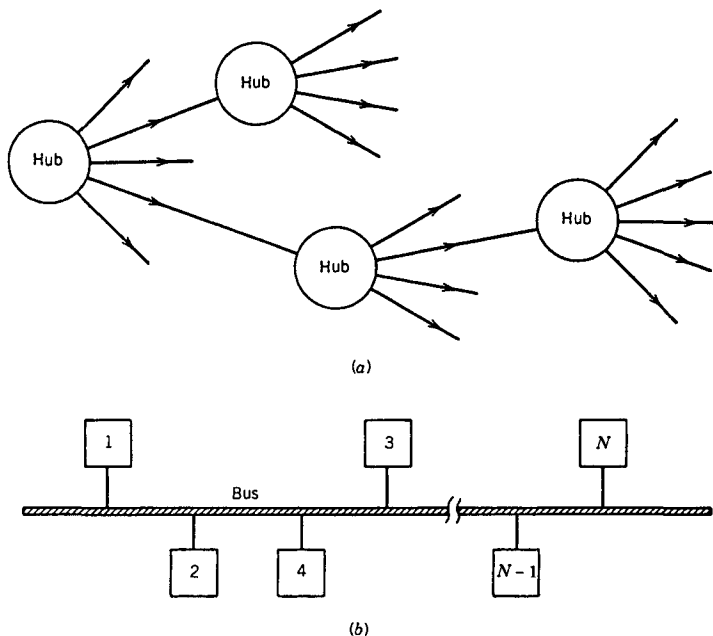


Figure 5.2: (a) Hub topology and (b) bus topology for distribution networks.

The spacing L between regenerators or optical amplifiers (see Figure 5.1), often called the *repeater spacing*, is a major design parameter simply because the system cost reduces as L increases. However, as discussed in Section 2.4, the distance L depends on the bit rate B because of fiber dispersion. The bit rate–distance product, BL , is generally used as a measure of the system performance for point-to-point links. The BL product depends on the operating wavelength, since both fiber losses and fiber dispersion are wavelength dependent. The first three generations of lightwave systems correspond to three different operating wavelengths near 0.85, 1.3, and 1.55 μm . Whereas the BL product was ~ 1 (Gb/s)-km for the first-generation systems operating near 0.85 μm , it becomes ~ 1 (Tb/s)-km for the third-generation systems operating near 1.55 μm and can exceed 1000 (Tb/s)-km for the fourth-generation systems.

5.1.2 Distribution Networks

Many applications of optical communication systems require that information is not only transmitted but also distributed to a group of subscribers. Examples include local-loop distribution of telephone services and broadcast of multiple video channels over cable television (CATV, short for common-antenna television). Considerable effort is directed toward the integration of audio and video services through a broadband digital network. The resulting bit stream can be transmitted using a variety of standards developed for this purpose. Transmission distances are relatively short ($L < 50$ km), but the bit rate can be as high as 100 Gb/s.

Figure 5.2 shows two topologies for distribution networks. In the case of *hub topology*, channel distribution takes place at central locations (or hubs), where an automated cross-connect facility switches channels in the electrical domain. Such networks are called *metropolitan-area networks* (MANs), or simply metro networks, as hubs are typically located in major cities [10]. The role of fiber is similar to the case of point-to-point links. Since the fiber bandwidth is generally much larger than that required by a single hub office, several offices can share a single fiber headed for the main hub. Telephone networks employ hub topology for distribution of audio channels within a city. A concern for the hub topology is related to its reliability—outage of a single fiber cable can affect the service to a large portion of the network. Additional point-to-point links can be used to guard against such a possibility by connecting important hub locations directly.

In the case of *bus topology*, a single fiber cable carries the multichannel optical signal throughout the area of service. Distribution is done by using optical taps, which divert a small fraction of the optical power to each subscriber. A simple CATV application of bus topology consists of distributing multiple video channels within a city. The use of optical fiber permits distribution of a large number of channels (100 or more) because of its large bandwidth compared with coaxial cables. The advent of *high-definition television* (HDTV) also requires lightwave transmission because of a large bandwidth associated with each video channel.

A problem with the bus topology is that the signal loss increases exponentially with the number of taps and limits the number of subscribers served by a single optical bus. Even when fiber losses are neglected, the power available at the N th tap is given by [1]

$$P_N = P_T C [(1 - \delta)(1 - C)]^{N-1}, \quad (5.1.1)$$

where P_T is the transmitted power, C is the fraction of power coupled out at each tap, and δ accounts for insertion losses, assumed to be the same at each tap. The derivation of Eq. (5.1.1) is left as an exercise for the reader. If we use $\delta = 0.05$, $C = 0.05$, $P_T = 1 \text{ mW}$, and $P_N = 0.1 \mu\text{W}$ as illustrative values, N should not exceed 60. A solution to this problem is offered by optical amplifiers which can boost the optical power of the bus periodically and thus permit distribution to a large number of subscribers as long as the effects of fiber dispersion remain negligible.

5.1.3 Local-Area Networks

Many applications of fiber-optic communication technology require networks in which a large number of users within a local area (e.g., a university campus) are interconnected in such a way that any user can access the network randomly to transmit data to any other user [11]–[13]. Such networks are called *local-area networks* (LANs). Optical-access networks used in a local subscriber loop also fall in this category. Since the transmission distances are relatively short ($<10 \text{ km}$), fiber losses are not of much concern for LAN applications. The major motivation behind the use of optical fibers is the large bandwidth offered by fiber-optic communication systems.

The main difference between MANs and LANs is related to the random access offered to multiple users of a LAN. The system architecture plays an important role

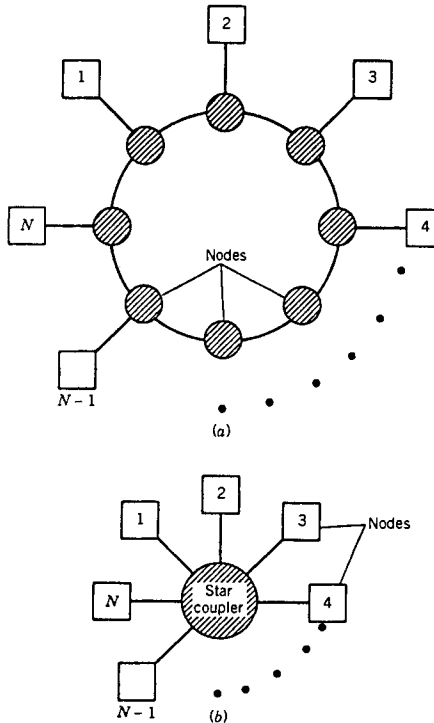


Figure 5.3: (a) Ring topology and (b) star topology for local-area networks.

for LANs, since the establishment of predefined protocol rules is a necessity in such an environment. Three commonly used topologies are known as bus, ring, and star configurations. The bus topology is similar to that shown in Figure 5.2(b). A well-known example of bus topology is provided by the *Ethernet*, a network protocol used to connect multiple computers and used by the *Internet*. The Ethernet operates at speeds of up to 10 Gb/s (10 GbE) by using a protocol based on *carrier-sense multiple access* (CSMA) with collision detection. A new standard known as 100 Gb Ethernet (officially IEEE 802.3ba) became operational in 2010. Its advent boosts the traffic speed on the Internet to a bit rate of 100 Gb/s. Figure 5.3 shows the ring and star topologies for LAN applications. In the ring topology [14], consecutive nodes are connected by point-to-point links to form a closed ring. Each node can transmit and receive the data by using a transmitter-receiver pair, which also acts as a repeater. A token (a predefined bit sequence) is passed around the ring. Each node monitors the bit stream to listen for its own address and to receive the data. It can also transmit by appending the data to an empty token. The use of ring topology for fiber-optic LANs has been commercialized with the standardized interface known as the fiber distributed data interface, FDDI for short [14].

In the *star topology* all nodes are connected through point-to-point links to a central node called a hub, or simply a star. Such LANs are further subclassified as *active-star*

or *passive-star* networks, depending on whether the central node is an active or passive device. In the active-star configuration, all incoming optical signals are converted to the electrical domain through optical receivers. The electrical signal is then distributed to drive individual node transmitters. Switching operations can also be performed at the central node since distribution takes place in the electrical domain. In the passive-star configuration, distribution takes place in the optical domain through devices such as directional couplers. Since the input from one node is distributed to many output nodes, the power transmitted to each node depends on the number of users. Similar to the case of bus topology, the number of users supported by passive-star LANs is limited by distribution losses. For an ideal $N \times N$ star coupler, the power reaching each node is simply P_T/N (if we neglect transmission losses) since the transmitted power P_T is divided equally among N users. For a passive star composed of directional couplers (see Section 8.2.4), the power is further reduced because of insertion losses and can be written as [1]

$$P_N = (P_T/N)(1 - \delta)^{\log_2 N}, \quad (5.1.2)$$

where δ is the insertion loss of each directional coupler. If we use $\delta = 0.05$, $P_T = 1$ mW, and $P_N = 0.1$ μ W as illustrative values, N can be as large as 500. This value of N should be compared with $N = 60$ obtained for the case of bus topology by using Eq. (5.1.1). A relatively large value of N makes star topology attractive for LAN applications.

5.2 Design Guidelines

The design of fiber-optic communication systems requires a clear understanding of the limitations imposed by the loss, dispersion, and nonlinearity of the fiber. Since fiber properties are wavelength dependent, the choice of operating wavelength is a major design issue. In this section we discuss how the bit rate and the transmission distance of a single-channel system are limited by fiber loss and dispersion; Chapter 6 is devoted to multichannel systems. We also consider the power and rise-time budgets and illustrate them through specific examples [9]. The power budget is also called the link budget, and the rise-time budget is sometimes referred to as the bandwidth budget.

5.2.1 Loss-Limited Lightwave Systems

Except for some short-haul fiber links, fiber losses play an important role in the system design. Consider an optical transmitter that is capable of launching an average power \bar{P}_{tr} . If the signal is detected by a receiver that requires a minimum average power \bar{P}_{rec} at the bit rate B , the maximum transmission distance is limited by

$$L = \frac{10}{\alpha_f} \log_{10} \left(\frac{\bar{P}_{\text{tr}}}{\bar{P}_{\text{rec}}} \right), \quad (5.2.1)$$

where α_f is the net loss (in dB/km) of the fiber cable, including splice and connector losses. The bit-rate dependence of L arises from the linear dependence of \bar{P}_{rec} on the bit rate B . Noting that $\bar{P}_{\text{rec}} = \bar{N}_p h \nu B$, where $h\nu$ is the photon energy and \bar{N}_p is the average

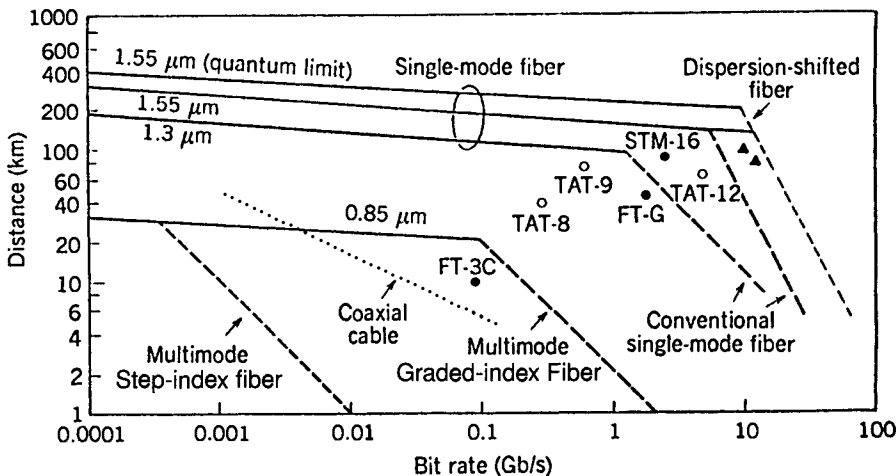


Figure 5.4: Loss (solid lines) and dispersion (dashed lines) limits on transmission distance L as a function of bit rate B for the three wavelength windows. The dotted line corresponds to coaxial cables. Circles denote commercial lightwave systems; triangles show laboratory experiments. (After Ref. [1]; ©1988 Academic Press; reprinted with permission.)

number of photons/bit required by the receiver, the distance L decreases logarithmically as B increases at a given operating wavelength.

The solid lines in Figure 5.4 show the dependence of L on B for three common operating wavelengths of 0.85, 1.3, and 1.55 μm by using $\alpha_f = 2.5, 0.4$, and 0.25 dB/km , respectively. The transmitted power is taken to be $\bar{P}_{\text{tr}} = 1 \text{ mW}$ at the three wavelengths, whereas $\bar{N}_p = 300$ at $\lambda = 0.85 \mu\text{m}$ and $\bar{N}_p = 500$ at 1.3 and 1.55 μm . The smallest value of L occurs for first-generation systems operating at 0.85 μm because of relatively large fiber losses near that wavelength. The repeater spacing of such systems is limited to 10–25 km, depending on the bit rate and the exact value of the loss parameter. In contrast, a repeater spacing of more than 100 km is possible for lightwave systems operating near 1.55 μm .

It is interesting to compare the loss limit of 0.85- μm lightwave systems with that of electrical communication systems based on coaxial cables. The dotted line in Figure 5.4 shows the bit-rate dependence of L for coaxial cables by assuming that the loss increases as \sqrt{B} . The transmission distance is larger for fiber-optic systems at small bit rates ($B < 5 \text{ Mb/s}$), but fiber-optic systems take over at bit rates in excess of 5 Mb/s. Since a longer transmission distance translates into a smaller number of repeaters in a long-haul point-to-point link, fiber-optic communication systems offer an economic advantage when the operating bit rate exceeds 10 Mb/s.

The system requirements typically specified in advance are the bit rate B and the transmission distance L . The performance criterion is specified through the BER, a typical requirement being $\text{BER} < 10^{-9}$. The first decision of the system designer concerns the choice of the operating wavelength. As a practical matter, the cost of components is lowest near 0.85 μm and increases as wavelength shifts toward 1.3 and 1.55 μm .

Figure 5.4 can be quite helpful in determining the appropriate operating wavelength. Generally speaking, a fiber-optic link can operate near $0.85 \mu\text{m}$ if $B < 200 \text{ Mb/s}$ and $L < 20 \text{ km}$. This is the case for many LAN applications. On the other hand, the operating wavelength is by necessity in the $1.55\text{-}\mu\text{m}$ region for long-haul lightwave systems operating at bit rates in excess of 2 Gb/s . The curves shown in Figure 5.4 provide only a guide to the system design. Many other issues need to be addressed while designing a realistic fiber-optic communication system. Among them are the choice of the operating wavelength, selection of appropriate transmitters, receivers, and fibers, and the issues of cost, performance, and system reliability.

5.2.2 Dispersion-Limited Lightwave Systems

In Section 2.4 we discussed how fiber dispersion limits the bit rate–distance product BL because of pulse broadening. When the dispersion-limited transmission distance is shorter than the loss-limited distance of Eq. (5.2.1), the system is said to be dispersion-limited. The dashed lines in Figure 5.4 show the dispersion-limited transmission distance as a function of the bit rate. Since the physical mechanisms leading to dispersion limitation can be different for different operating wavelengths, let us examine each case separately.

Consider first the case of $0.85\text{-}\mu\text{m}$ lightwave systems, which often use multimode fibers to minimize the system cost. As discussed in Section 2.1, the most limiting factor for multimode fibers is intermodal dispersion. In the case of step-index multimode fibers, Eq. (2.1.6) provides an upper bound on the BL product. It is plotted in Figure 5.4 using $n_1 = 1.46$ and $\Delta = 0.01$. Even at a low bit rate of 1 Mb/s , such multimode systems are dispersion-limited, and their transmission distance is limited to below 10 km . For this reason, multimode step-index fibers are rarely used in the design of fiber-optic communication systems. Considerable improvement can be realized by using graded-index fibers for which intermodal dispersion limits the BL product to values given by Eq. (2.1.11). The condition $BL = 2c/(n_1\Delta^2)$ is plotted in Figure 5.4 and shows that $0.85\text{-}\mu\text{m}$ lightwave systems are loss-limited, rather than dispersion-limited, for bit rates up to 100 Mb/s when graded-index fibers are used. The first generation of terrestrial systems took advantage of such an improvement and used graded-index fibers. The first commercial system became available in 1980 and operated at a bit rate of 45 Mb/s with a repeater spacing of less than 10 km .

The second generation of lightwave systems used primarily single-mode fibers near the minimum-dispersion wavelength occurring at about $1.31 \mu\text{m}$. The most limiting factor for such systems is dispersion-induced pulse broadening dominated by a relatively large source spectral width. As discussed in Section 2.4.3, the BL product is then limited by Eq. (2.4.26). The value of $|D|$ depends on how close the operating wavelength is to the zero-dispersion wavelength of the fiber and is typically $\sim 1 \text{ ps}/(\text{km-nm})$. Figure 5.4 shows the dispersion limit for $1.3\text{-}\mu\text{m}$ lightwave systems by choosing $|D|\sigma_\lambda = 2 \text{ ps/km}$ so that $BL \leq 125 \text{ (Gb/s)-km}$. As seen there, such systems are generally loss-limited for bit rates up to 1 Gb/s but become dispersion-limited at higher bit rates.

Third- and fourth-generation lightwave systems operate near $1.55 \mu\text{m}$ to take advantage of the smallest fiber losses occurring in this wavelength region. However,

dispersion becomes a major problem for such systems because $D \approx 16 \text{ ps}/(\text{km-nm})$ near $1.55 \mu\text{m}$ for standard silica fibers. Semiconductor lasers operating in a single longitudinal mode provide a solution to this problem. The dispersion limit is then given by Eq. (2.4.30). Figure 5.4 shows this limit by choosing $B^2L = 4000 \text{ (Gb/s)}^2\text{-km}$. As seen there, such $1.55\text{-}\mu\text{m}$ systems become dispersion-limited only for $B > 5 \text{ Gb/s}$. In practice, the frequency chirp imposed on the optical pulse during direct modulation provides a much more severe limitation. Qualitatively speaking, the frequency chirp manifests through a broadening of the pulse spectrum. If we use Eq. (2.4.26) with $D = 16 \text{ ps}/(\text{km-nm})$ and $\sigma_\lambda = 0.1 \text{ nm}$, the BL product is limited to $150 \text{ (Gb/s)}\text{-km}$. As a result, the frequency chirp limits the transmission distance to 75 km at $B = 2 \text{ Gb/s}$, even though loss-limited distance exceeds 150 km . The frequency-chirp problem is often solved by using an external modulator for systems operating at bit rates $> 5 \text{ Gb/s}$.

A solution to the dispersion problem is offered by *dispersion-shifted fibers* for which dispersion and loss both are minimum near $1.55 \mu\text{m}$. Figure 5.4 shows the improvement by using Eq. (2.4.30) with $|\beta_2| = 2 \text{ ps}^2/\text{km}$. Such systems can be operated at 20 Gb/s with a repeater spacing of about 80 km . Further improvement is possible by operating the lightwave system very close to the zero-dispersion wavelength, a task that is not always feasible because of variations in the dispersive properties of the fiber along the transmission link. In practice, the frequency chirp makes it difficult to achieve even the limit indicated in Figure 5.4. By 1989, two laboratory experiments had demonstrated transmission over 81 km at 11 Gb/s [15] and over 100 km at 10 Gb/s [16] by using low-chirp semiconductor lasers together with dispersion-shifted fibers. The triangles in Figure 5.4 show that such systems operate quite close to the fundamental limits set by fiber dispersion. Transmission over longer distances requires the use of dispersion management, a technique discussed in Chapter 8.

5.2.3 Power Budget

The purpose of the *power budget* is to ensure that enough power will reach the receiver to maintain reliable performance during the entire system lifetime. The minimum average power required by the receiver is the receiver sensitivity \bar{P}_{rec} (see Section 4.6). The average launch power \bar{P}_{tr} is generally known for any transmitter. The power budget takes an especially simple form in decibel units with optical powers expressed in dBm units (see Appendix A). More specifically,

$$\bar{P}_{\text{tr}} = \bar{P}_{\text{rec}} + C_L + M_s, \quad (5.2.2)$$

where C_L is the total channel loss and M_s is the *system margin*. The purpose of system margin is to allocate a certain amount of power to additional sources of power penalty that may develop during system lifetime because of component degradation or other unforeseen events. A system margin of $3\text{--}4 \text{ dB}$ is typically allocated during the design process.

The channel loss C_L should take into account all possible sources of power loss, including connector and splice losses. If α_f is the fiber loss in decibels per kilometer, C_L can be written as

$$C_L = \alpha_f L + \alpha_{\text{con}} + \alpha_{\text{splice}}, \quad (5.2.3)$$

Table 5.1 Power budget of a 0.85- μm lightwave system

Quantity	Symbol	Laser	LED
Transmitter power	\bar{P}_{tr}	0 dBm	-13 dBm
Receiver sensitivity	\bar{P}_{rec}	-42 dBm	-42 dBm
System margin	M_s	6 dB	6 dB
Available channel loss	C_L	36 dB	23 dB
Connector loss	α_{con}	2 dB	2 dB
Fiber cable loss	α_f	3.5 dB/km	3.5 dB/km
Maximum fiber length	L	9.7 km	6 km

where α_{con} and α_{splice} account for the connector and splice losses throughout the fiber link. Sometimes splice loss is included within the specified loss of the fiber cable. The connector loss α_{con} includes connectors at the transmitter and receiver ends but must include other connectors if used within the fiber link.

Equations (5.2.2) and (5.2.3) can be used to estimate the maximum transmission distance for a given choice of the components. As an illustration, consider the design of a fiber link operating at 100 Mb/s and requiring a maximum transmission distance of 8 km. As seen in Figure 5.4, such a system can be designed to operate near 0.85 μm provided that a graded-index multimode fiber is used for the optical cable. The operation near 0.85 μm is desirable from the economic standpoint. Once the operating wavelength is selected, a decision must be made about the appropriate transmitters and receivers. The GaAs transmitter can use a semiconductor laser or an LED as an optical source. Similarly, the receiver can be designed to use either a $p-i-n$ or an avalanche photodiode. Keeping the low cost in mind, let us choose a $p-i-n$ receiver and assume that it requires 2500 photons/bit on average to operate reliably with a BER below 10^{-9} . Using the relation $\bar{P}_{\text{rec}} = \bar{N}_p h\nu B$ with $\bar{N}_p = 2500$ and $B = 100 \text{ Mb/s}$, the receiver sensitivity is given by $\bar{P}_{\text{rec}} = -42 \text{ dBm}$. The average launch power for LED and laser-based transmitters is typically 50 μW and 1 mW, respectively.

Table 5.1 shows the power budget for the two transmitters by assuming that the splice loss is included within the cable loss. The transmission distance L is limited to 6 km in the case of LED-based transmitters. If the system specification is 8 km, a more expensive laser-based transmitter must be used. The alternative is to use an avalanche photodiode (APD) receiver. If the receiver sensitivity improves by more than 7 dB when an APD is used in place of a $p-i-n$ photodiode, the transmission distance can be increased to 8 km even for an LED-based transmitter. Economic considerations would then dictate the choice between the laser-based transmitters and APD receivers.

5.2.4 Rise-Time Budget

The purpose of the *rise-time budget* is to ensure that the system is able to operate properly at the intended bit rate. Even if the bandwidth of the individual system components exceeds the bit rate, it is still possible that the total system may not be able to operate at that bit rate. The concept of rise time is used to allocate the bandwidth among various components. The rise time T_r of a linear system is defined as the time during which the

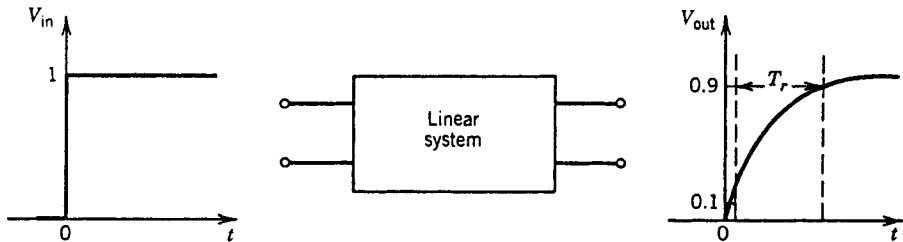


Figure 5.5: Rise time T_r associated with a bandwidth-limited linear system.

response increases from 10 to 90% of its final output value when the input is changed abruptly. Figure 5.5 illustrates the concept graphically.

An inverse relationship exists between the bandwidth Δf and the rise time T_r associated with a linear system. This relationship can be understood by considering a simple RC circuit as an example of the linear system. When the input voltage across an RC circuit changes instantaneously from 0 to V_0 , the output voltage changes as

$$V_{\text{out}}(t) = V_0[1 - \exp(-t/RC)], \quad (5.2.4)$$

where R is the resistance and C is the capacitance of the RC circuit. The rise time is found to be given by

$$T_r = (\ln 9)RC \approx 2.2RC. \quad (5.2.5)$$

The transfer function $H(f)$ of the RC circuit is obtained by taking the Fourier transform of Eq. (5.2.4) and is of the form

$$H(f) = (1 + i2\pi f RC)^{-1}. \quad (5.2.6)$$

The bandwidth Δf of the RC circuit corresponds to the frequency at which $|H(f)|^2 = 1/2$ and is given by the well-known expression $\Delta f = (2\pi RC)^{-1}$. By using Eq. (5.2.5), Δf and T_r are related as

$$T_r = \frac{2.2}{2\pi\Delta f} = \frac{0.35}{\Delta f}. \quad (5.2.7)$$

The inverse relationship between the rise time and the bandwidth is expected to hold for any linear system. However, the product $T_r\Delta f$ would generally be different than 0.35. One can use $T_r\Delta f = 0.35$ in the design of optical communication systems as a conservative guideline. The relationship between the bandwidth Δf and the bit rate B depends on the digital format. In the case of return-to-zero (RZ) format (see Section 1.2), $\Delta f = B$ and $BT_r = 0.35$. By contrast, $\Delta f \approx B/2$ for the nonreturn-to-zero (NRZ) format and $BT_r = 0.7$. In both cases, the specified bit rate imposes an upper limit on the maximum rise time that can be tolerated. The communication system must be designed to ensure that T_r is below this maximum value, i.e.,

$$T_r \leq \begin{cases} 0.35/B & \text{for RZ format,} \\ 0.70/B & \text{for NRZ format.} \end{cases} \quad (5.2.8)$$

The three components of fiber-optic communication systems have individual rise times. The total rise time of the whole system is related to the individual component rise times approximately as [17]

$$T_r^2 = T_{\text{tr}}^2 + T_{\text{fiber}}^2 + T_{\text{rec}}^2, \quad (5.2.9)$$

where T_{tr} , T_{fiber} , and T_{rec} are the rise times associated with the transmitter, fiber, and receiver, respectively. The rise times of the transmitter and the receiver are generally known to the system designer. The transmitter rise time T_{tr} is determined primarily by the electronic components of the driving circuit and the electrical parasitics associated with the optical source. Typically, T_{tr} is a few nanoseconds for LED-based transmitters but can be shorter than 0.1 ns for laser-based transmitters. The receiver rise time T_{rec} is determined primarily by the 3-dB electrical bandwidth of the receiver front end. Equation (5.2.7) can be used to estimate T_{rec} if the front-end bandwidth is specified.

The fiber rise time T_{fiber} should in general include the contributions of both the intermodal dispersion and group-velocity dispersion (GVD) through the relation

$$T_{\text{fiber}}^2 = T_{\text{modal}}^2 + T_{\text{GVD}}^2. \quad (5.2.10)$$

For single-mode fibers, $T_{\text{modal}} = 0$ and $T_{\text{fiber}} = T_{\text{GVD}}$. In principle, one can use the concept of fiber bandwidth discussed in Section 2.4.4 and relate T_{fiber} to the 3-dB fiber bandwidth $f_{3\text{dB}}$ through a relation similar to Eq. (5.2.7). In practice it is not easy to calculate $f_{3\text{dB}}$, especially in the case of modal dispersion. The reason is that a fiber link consists of many concatenated fiber sections (typical length 5 km), which may have different dispersion characteristics. Furthermore, mode mixing occurring at splices and connectors tends to average out the propagation delay associated with different modes of a multimode fiber. A statistical approach is often necessary to estimate the fiber bandwidth and the corresponding rise time [18]–[21].

In a phenomenological approach, T_{modal} can be approximated by the time delay ΔT given by Eq. (2.1.5) in the absence of mode mixing, i.e.,

$$T_{\text{modal}} \approx (n_1 \Delta/c)L, \quad (5.2.11)$$

where $n_1 \approx n_2$ was used. For graded-index fibers, Eq. (2.1.10) is used in place of Eq. (2.1.5), resulting in $T_{\text{modal}} \approx (n_1 \Delta^2/8c)L$. In both cases, the effect of mode mixing is included by changing the linear dependence on L by a sublinear dependence L^q , where q has a value in the range 0.5–1, depending on the extent of mode mixing. A reasonable estimate based on the experimental data is $q = 0.7$. The contribution T_{GVD} can also be approximated by ΔT given by Eq. (2.3.4), so that

$$T_{\text{GVD}} \approx |D|L\Delta\lambda, \quad (5.2.12)$$

where $\Delta\lambda$ is the spectral width of the optical source (taken as a full width at half maximum). The dispersion parameter D may change along the fiber link if different sections have different dispersion characteristics; an average value should be used in Eq. (5.2.12) in that case.

As an illustration of the rise-time budget, consider a 1.3-μm lightwave system designed to operate at 1 Gb/s over a single-mode fiber with a repeater spacing of 50 km.

The rise times for the transmitter and the receiver have been specified as $T_{\text{tr}} = 0.25$ ns and $T_{\text{rec}} = 0.35$ ns. The source spectral width is specified as $\Delta\lambda = 3$ nm, whereas the average value of D is 2 ps/(km-nm) at the operating wavelength. From Eq. (5.2.12), $T_{\text{GVD}} = 0.3$ ns for a link length $L = 50$ km. Modal dispersion does not occur in single-mode fibers. Hence $T_{\text{modal}} = 0$ and $T_{\text{fiber}} = 0.3$ ns. The system rise time is estimated by using Eq. (5.2.9) and is found to be $T_r = 0.524$ ns. The use of Eq. (5.2.8) indicates that such a system cannot be operated at 1 Gb/s when the RZ format is employed for the optical bit stream. However, it would operate properly if digital format is changed to the NRZ format. If the use of RZ format is a prerequisite, the designer must choose different transmitters and receivers to meet the rise-time budget requirement. The use of the NRZ format was prevalent during the 1990s, but the RZ format has become the format of choice for long-haul systems operating at a bit rate of 40 Gb/s, especially when the information is coded in the phase of the optical carrier.

5.3 Long-Haul Systems

With the advent of optical amplifiers, fiber losses can be compensated by inserting amplifiers periodically along a long-haul fiber link (see Figure 5.1). At the same time, the effects of fiber dispersion (GVD) can be reduced by using dispersion management (see Chapter 8). Since neither the fiber loss nor the GVD is then a limiting factor, one may ask how many in-line amplifiers can be cascaded in series, and what limits the total link length. This topic is covered in Chapter 7. Here we focus on the factors that limit the performance of amplified fiber links and provide a few design guidelines. The section also outlines the progress realized in the development of terrestrial and undersea lightwave systems since 1980 when the first system was installed.

5.3.1 Performance-Limiting Factors

The most important consideration in designing a periodically amplified fiber link is related to the *nonlinear effects* occurring inside all optical fibers [22] (see Section 2.6). For single-channel lightwave systems, the dominant nonlinear phenomenon that limits the system performance is *self-phase modulation* (SPM). When optoelectronic regenerators are used, the SPM effects accumulate only over one repeater spacing (typically <100 km) and are of little concern if the launch power satisfies Eq. (2.6.15) with $N_A = 1$, or the condition $P_{\text{in}} \ll 22$ mW. In contrast, the SPM effects accumulate over long lengths (~ 1000 km) when in-line amplifiers are used periodically for loss compensation. A rough estimate of the limitation imposed by the SPM is again obtained from Eq. (2.6.15). This equation predicts that the peak power should be below 2.2 mW for 10 cascaded amplifiers when the nonlinear parameter $\gamma = 2 \text{ W}^{-1}/\text{km}$. The condition on the average power depends on the modulation format and the shape of optical pulses. It is nonetheless clear that the average power should be reduced to below 1 mW for SPM effects to remain negligible for a lightwave system designed to operate over a distance of more than 1000 km. The limiting value of the average power also depends on the type of fiber in which light is propagating through the effective core area A_{eff} .

The SPM effects are most dominant inside dispersion-compensating fibers for which A_{eff} is typically close to $20 \mu\text{m}^2$.

The forgoing discussion of the SPM-induced limitations is too simplistic to be accurate since it completely ignores the role of fiber dispersion. In fact, as the dispersive and nonlinear effects act on the optical signal simultaneously, their mutual interplay becomes quite important [22]. The effect of SPM on pulses propagating inside an optical fiber can be included by using the nonlinear Schrödinger (NLS) equation of Section 2.6. This equation is given by [see Eq. (2.6.18)]

$$\frac{\partial A}{\partial z} + \frac{i\beta_2}{2} \frac{\partial^2 A}{\partial t^2} = -\frac{\alpha}{2}A + i\gamma|A|^2A, \quad (5.3.1)$$

where fiber losses are included through the α term. This term can also include periodic amplification of the signal by treating α as a function of z . The NLS equation is used routinely for designing modern lightwave systems.

Because of the nonlinear nature of Eq. (5.3.1), it should be solved numerically in general. A numerical approach is indeed adopted (see Appendix D) for quantifying the impact of SPM on the performance of long-haul lightwave systems [23]–[31]. The use of a large-effective-area fiber (LEAF) helps by reducing the nonlinear parameter γ defined as $\gamma = 2\pi n_2/(\lambda A_{\text{eff}})$. Appropriate chirping of input pulses can also be beneficial for reducing the SPM effects. This feature has led to the adoption of a new modulation format known as the chirped RZ or CRZ format. Numerical simulations show that, in general, the launch power must be optimized to a value that depends on many design parameters such as the bit rate, total link length, and amplifier spacing. In one study, the optimum launch power was found to be about 1 mW for a 5-Gb/s signal transmitted over 9000 km with 40-km amplifier spacing [27].

The combined effects of GVD and SPM also depend on the sign of the dispersion parameter β_2 . In the case of anomalous dispersion ($\beta_2 < 0$), the nonlinear phenomenon of *modulation instability* [22] can affect the system performance drastically [28]. This problem can be overcome by using a combination of fibers with normal and anomalous GVD such that the average dispersion over the entire fiber link is “normal.” However, a new kind of modulation instability, referred to as *sideband instability* [32], can occur in both the normal and anomalous GVD regions. It has its origin in the periodic variation of the signal power along the fiber link when equally spaced optical amplifiers are used to compensate for fiber losses. Since the quantity $\gamma|A|^2$ in Eq. (5.3.1) is then a periodic function of z , the resulting nonlinear-index grating can initiate a four-wave-mixing process that generates sidebands in the signal spectrum. It can be avoided by making the amplifier spacing nonuniform.

Another factor that plays a crucial role is the noise added by optical amplifiers. Similar to the case of electronic amplifiers, the noise of optical amplifiers is quantified through an amplifier noise figure F_n (see Chapter 7). The nonlinear interaction between the amplified spontaneous emission and the signal can lead to a large spectral broadening through the nonlinear phenomena such as cross-phase modulation and four-wave mixing [33]. Because the noise has a much larger bandwidth than the signal, its impact can be reduced by using optical filters. Numerical simulations indeed show a considerable improvement when optical filters are used after every in-line amplifier [27].

The polarization effects that are totally negligible in the traditional “nonamplified” lightwave systems become of concern for long-haul systems with in-line amplifiers. The polarization-mode dispersion (PMD) issue has been discussed in Section 2.3.5. In addition to PMD, optical amplifiers can also induce polarization-dependent gain and loss [26]. Although the PMD effects must be considered during system design, their impact depends on the design parameters such as the bit rate and the transmission distance. For bit rates as high as 10-Gb/s, the PMD effects can be reduced to an acceptable level with a proper design. However, PMD becomes of major concern for 40-Gb/s systems for which the bit slot is only 25 ps wide. The use of a PMD-compensation technique is often necessary at such high bit rates.

The fourth generation of lightwave systems began in 1995 when lightwave systems employing amplifiers first became available commercially. Of course, the laboratory demonstrations began as early as 1989. Many experiments used a recirculating fiber loop to demonstrate system feasibility as it was not practical to use long lengths of fiber in a laboratory setting. Already in 1991, an experiment showed the possibility of data transmission over 21,000 km at 2.5 Gb/s, and over 14,300 km at 5 Gb/s, by using the recirculating-loop configuration [34]. In a system trial carried out in 1995 by using actual submarine cables and repeaters [35], a 5.3-Gb/s signal was transmitted over 11,300 km with 60 km of amplifier spacing. This system trial led to the deployment of a commercial transpacific cable (TPC-5) that began operating in 1996.

The bit rate of fourth-generation systems was extended to 10 Gb/s beginning in 1992. As early as 1995, a 10-Gb/s signal was transmitted over 6480 km with 90-km amplifier spacing [36]. With a further increase in the distance, the SNR decreased below the value needed to maintain the BER below 10^{-9} . One may think that the performance should improve by operating close to the zero-dispersion wavelength of the fiber. However, an experiment, performed under such conditions, achieved a distance of only 6000 km at 10 Gb/s even with 40-km amplifier spacing [37], and the situation became worse when the RZ modulation format was used. Starting in 1999, the single-channel bit rate was pushed toward 40 Gb/s in several experiments [38]–[40], and by 2002 such systems became available commercially. The design of 40-Gb/s lightwave systems requires the use of several new ideas including the CRZ format, dispersion management with GVD-slope compensation, and distributed Raman amplification. Even then, the combined effects of the higher-order dispersion, PMD, and SPM degrade the system performance considerably at a bit rate of 40 Gb/s.

5.3.2 Terrestrial Lightwave Systems

An important application of fiber-optic communication links is for enhancing the capacity of telecommunication networks worldwide. Indeed, it is this application that started the field of optical fiber communications in 1977 and has propelled it since then by demanding systems with higher and higher capacities. Here we focus on the status of commercial systems by considering the terrestrial and undersea systems separately.

After a successful Chicago field trial in 1977, terrestrial lightwave systems became available commercially beginning in 1980 [41]–[43]. Table 5.2 lists the operating characteristics of several terrestrial systems developed since then. The first-generation systems operated near 0.85 μm and used multimode graded-index fibers as the trans-

Table 5.2 Terrestrial lightwave systems

System	Year	λ (μm)	B (Mb/s)	L (km)	Voice Channels
FT-3	1980	0.85	45	< 10	672
FT-3C	1983	0.85	90	< 15	1,344
FT-3X	1984	1.30	180	< 25	2,688
FT-G	1985	1.30	417	< 40	6,048
FT-G-1.7	1987	1.30	1,668	< 46	24,192
STM-16	1991	1.55	2,488	< 85	32,256
STM-64	1996	1.55	9,953	< 90	129,024
STM-256	2002	1.55	39,813	< 90	516,096

mission medium. As seen in Figure 5.4, the BL product of such systems is limited to 2 (Gb/s)-km. A commercial lightwave system (FT-3C) operating at 90 Mb/s with a repeater spacing of about 12 km realized a BL product of nearly 1 (Gb/s)-km; it is shown by a filled circle in Figure 5.4. The operating wavelength moved to 1.3 μm in second-generation lightwave systems to take advantage of low fiber losses and low dispersion near this wavelength. The BL product of 1.3- μm lightwave systems is limited to about 100 (Gb/s)-km when a multimode semiconductor laser is used inside the transmitter. In 1987, a commercial 1.3- μm lightwave system provided data transmission at 1.7 Gb/s with a repeater spacing of about 45 km. A filled circle in Figure 5.4 shows that this system operates quite close to the dispersion limit.

The third generation of lightwave systems became available commercially in 1991. Such systems operate near 1.55 μm at bit rates in excess of 2 Gb/s, typically at 2.488 Gb/s, corresponding to the OC-48 level of the SONET, or the STS-16 level of the SDH, specifications. The switch to the 1.55- μm wavelength helps to increase the loss-limited transmission distance to more than 100 km because of fiber losses of less than 0.25 dB/km in this wavelength region. However, the repeater spacing was limited to below 100 km because of the high GVD of standard telecommunication fibers. In fact, the deployment of third-generation lightwave systems was possible only after the development of distributed feedback (DFB) semiconductor lasers, which reduce the impact of fiber dispersion by reducing the source spectral width to below 100 MHz (see Section 2.4).

The fourth generation of lightwave systems appeared around 1996. Such systems operate in the 1.55- μm region at a bit rate as high as 40 Gb/s by using dispersion-shifted fibers in combination with optical amplifiers. However, more than 50 million kilometers of the standard telecommunication fiber is already installed in the worldwide telephone network. Economic reasons dictate that the fourth generation of lightwave systems make use of this existing base. Two approaches are being used to solve the dispersion problem. First, several dispersion-management schemes (discussed in Chapter 8) make it possible to extend the bit rate to 10 Gb/s while maintaining an amplifier spacing of up to 100 km. Second, several 10-Gb/s signals can be transmitted simultaneously by using the WDM technique discussed in Chapter 6. Moreover, if the WDM technique is combined with dispersion management, the total transmission

distance can approach several thousand kilometers provided that fiber losses are compensated periodically by using optical amplifiers. Such WDM lightwave systems were deployed commercially worldwide beginning in 1996 and allowed a system capacity of 1.6 Tb/s by 2000 for the 160-channel commercial WDM systems.

The fifth generation of lightwave systems began to emerge around 2001 [44]–[52]. The bit rate of each channel in this generation of WDM systems is 40 Gb/s (corresponding to the STM-256 or OC-768 level). Several new techniques developed in recent years make it possible to transmit a 40-Gb/s optical signal over long distances. New dispersion-shifted fibers have been developed with smaller PMD levels. Their use in combination with tunable dispersion-compensating techniques can compensate the GVD for all channels simultaneously. The use of Raman amplification helps to reduce the noise and improves the SNR at the receiver. The use of a forward-error correction (FEC) technique (see Section 5.5) helps to increase the transmission distance by reducing the required SNR. The number of WDM channels can be increased by using the L and S bands located on the long- and short-wavelength sides of the conventional C band occupying the 1530–1570-nm spectral region. In a 2001 experiment, 77 channels, each operating at 42.7-Gb/s, were transmitted over 1200 km by using the C and L bands simultaneously, resulting in a 3-Tb/s capacity [44]. In another 2001 experiment, the system capacity was extended to 10.2 Tb/s by transmitting 256 channels over 100 km at 42.7 Gb/s per channel using only the C and L bands, resulting in a spectral efficiency of 1.28 (b/s)/Hz [45]. The bit rate was 42.7 Gb/s in both of these experiments because of the overhead associated with the FEC technique.

Starting in 2002, the research focus shifted toward advanced modulation formats in which information is coded using optical phase rather than amplitude of the carrier wave (see Chapter 10). This approach has led to considerable improvement in the spectral efficiency of WDM systems. In a 2007 experiment [52], 25.6-Tb/s transmission was realized over 240 km of optical fibers using 160 WDM channels that spanned both the C and L bands with 50-GHz channel spacing. Each channel contained two polarization-multiplexed 85.4-Gb/s signals coded with the DQPSK format, resulting in a spectral efficiency of 3.2 b/s/Hz. By 2010, transmission at a total bit rate of 69.1 Tb/s was demonstrated over 240 km of fiber using 432 WDM channels, each operating at 171 Gb/s with a 7% FEC overhead [53].

5.3.3 Undersea Lightwave Systems

Undersea or submarine transmission systems are used for intercontinental communications and are capable of providing a network spanning the whole earth [54]–[56]. Reliability is of major concern for such systems as repairs are expensive. Generally, undersea systems are designed for a 25-year service life, with at most three failures during operation. Figure 1.5 shows the multitude of undersea systems deployed worldwide. Table 5.3 lists several high-capacity undersea fiber-optic cable systems installed after the year 2000. Most of them transport multiple WDM channels, each operating at 10 Gb/s, and employ several fiber pairs within each cable to further enhance the system capacity to beyond 1 Tb/s.

The first undersea fiber-optic cable (TAT-8) was a second-generation system. It was installed in 1988 in the Atlantic Ocean, with a repeater spacing of up to 70 km,

Table 5.3 High-capacity undersea lightwave systems

System Name	Year	Capacity (Gb/s)	Length (km)	WDM Channels	Fiber Pairs
TAT-14	2001	640	15,428	16	4
SEA-ME-WE 3	2001	960	39,000	48	2
AC-2	2001	1280	6,400	32	4
VSNL Transatlantic	2001	2560	13,000	64	4
FLAG	2001	4800	28,000	60	8
Apollo	2003	3200	13,000	80	4
SEA-ME-WE 4	2005	1280	18,800	64	2
Asia-America Gateway	2008	1920	20,000	96	2
India-ME-WE	2009	3840	13,000	96	4

and transported a single channel a bit rate of 280 Mb/s. The system design was on the conservative side, mainly to ensure reliability. The same technology was used for the first transpacific lightwave system (TPC-3), which became operational in 1989. By 1990 the third-generation lightwave systems had been developed. The TAT-9 submarine system used this technology in 1991; it was designed to operate near $1.55\text{ }\mu\text{m}$ at a bit rate of 560 Mb/s with a repeater spacing of about 80 km. The increasing traffic across the Atlantic Ocean led to the deployment of the TAT-10 and TAT-11 lightwave systems by 1993 with the same technology.

The advent of optical amplifiers prompted their use in the next generation of undersea systems. The TAT-12 cable, installed in 1995, employed optical amplifiers in place of optoelectronic regenerators and operated at a bit rate of 5.3 Gb/s with an amplifier spacing of about 50 km. The bit rate was slightly larger than the STM-32 bit rate of 5 Gb/s because of the overhead associated with the forward-error-correction technique discussed in Section 5.5. The design of such lightwave systems becomes quite complex because of the cumulative effects of fiber dispersion and nonlinearity, which must be controlled over long distances. The transmitter power and the dispersion profile along the link must be optimized to combat such effects.

A second category of undersea lightwave systems requires repeaterless transmission over several hundred kilometers [55]. Such systems are used for interisland communication or for looping a shoreline such that the signal is regenerated on the shore periodically after a few hundred kilometers of undersea transmission. The dispersive and nonlinear effects are of less concern for such systems than for transoceanic lightwave systems, but fiber losses become a major issue. The reason is easily appreciated by noting that the cable loss exceeds 100 dB over a distance of 500 km even under the best operating conditions. In the 1990s several laboratory experiments demonstrated repeaterless transmission at 2.5 Gb/s over more than 500 km by using two in-line amplifiers that were pumped remotely from the transmitter and receiver ends with high-power pump lasers. Another amplifier at the transmitter boosted the launched power to close to 100 mW.

Such high input powers exceed the threshold level for stimulated Brillouin scattering (SBS), a nonlinear phenomenon discussed in Section 2.6. The suppression of SBS

is often realized by modulating the phase of the optical carrier such that the carrier linewidth is broadened to 200 MHz or more from its initial value of <10 MHz [57]. Directly modulated DFB lasers can also be used for this purpose. In a 1996 experiment, a 2.5-Gb/s signal was transmitted over 465 km by direct modulation of a DFB laser [58]. Chirping of the modulated signal broadened the spectrum enough that an external phase modulator was not required provided that the launched power was kept below 100 mW. The bit rate of repeaterless undersea systems can be increased to 10 Gb/s by employing the same techniques used at 2.5 Gb/s. In a 1996 experiment [59], the 10-Gb/s signal was transmitted over 442 km by using two remotely pumped in-line amplifiers. Two external modulators were used, one for SBS suppression and another for signal generation. In a 1998 experiment, a 40-Gb/s signal was transmitted over 240 km using the RZ format and an alternating polarization format [60].

The use of the WDM technique in combination with optical amplifiers, dispersion management, and error correction has revolutionized the design of submarine fiber-optic systems [61]–[68]. In 1998, a submarine cable known as AC-1 was deployed across the Atlantic Ocean with a capacity of 80 Gb/s using the WDM technology. An identically designed system (PC-1) crossed the Pacific Ocean. The use of dense WDM, in combination with multiple fiber pairs per cable, resulted in systems with large capacities. By 2001, several systems with a capacity of >1 Tb/s became operational across the Atlantic Ocean (see Table 5.3). These systems employ a ring configuration and cross the Atlantic Ocean twice to ensure fault tolerance. The VSNL Transatlantic submarine system can achieve a total capacity of 2.56 Tb/s and spans a total distance of 13,000 km. Another system, known as Apollo, is capable of carrying traffic at speeds of up to 3.2 Tb/s by transmitting 80 channels (each operating at 10 Gb/s) over 4 fiber pairs.

The pace slowed down after 2001 with the bursting of the “telecom bubble.” However, the development of undersea systems has continued within industrial laboratories. In a 2003 experiment, transmission over 9400 km of 40 channels (each operating at 42.7 Gb/s with a 70-GHz channel spacing) was realized using phase modulation (with the DPSK format), FEC coding, and distributed Raman amplification [62]. By 2009, another experiment transmitted 72 channels, each operating at 100 Gb/s, over 10,000 km using the QPSK modulation format with digital processing in a coherent receiver [63]. On the commercial side, a field trial was carried out as early as 2004 in which 96 channels at 10 Gb/s were transmitted successfully over a distance of 13,000 km [64]. As seen in Table 5.3, several new transoceanic systems have been deployed worldwide in recent years. A few others such as Europe–India Gateway were in various stages of completion in 2010.

5.4 Sources of Power Penalty

The sensitivity of the optical receiver in a realistic lightwave system is affected by several physical phenomena which, in combination with fiber dispersion, degrade the SNR at the decision circuit. Among the phenomena that degrade the receiver sensitivity are modal noise, dispersion broadening and intersymbol interference, mode-partition noise, frequency chirp, and reflection feedback. In this section we discuss how the

system performance is affected by fiber dispersion by considering the extent of power penalty resulting from these phenomena.

5.4.1 Modal Noise

Modal noise is associated with multimode fibers and was studied extensively during the 1980s [69]–[82]. Its origin can be understood as follows. Interference among various propagating modes in a multimode fiber creates a *speckle pattern* at the photodetector. The nonuniform intensity distribution associated with the speckle pattern is harmless in itself, as the receiver performance is governed by the total power integrated over the detector area. However, if the speckle pattern fluctuates with time, it will lead to fluctuations in the received power that would degrade the SNR. Such fluctuations are referred to as *modal noise*. They invariably occur in multimode fiber links because of mechanical disturbances such as vibrations and microbends. In addition, splices and connectors act as spatial filters. Any temporal changes in spatial filtering translate into speckle fluctuations and enhancement of the modal noise. Modal noise is strongly affected by the source spectral bandwidth $\Delta\nu$ since mode interference occurs only if the coherence time ($T_c \approx 1/\Delta\nu$) is longer than the intermodal delay time ΔT given by Eq. (2.1.5). For LED-based transmitters $\Delta\nu$ is large enough ($\Delta\nu \sim 5$ THz) that this condition is not satisfied. Most lightwave systems that use multimode fibers also use LEDs to avoid the modal-noise problem.

Modal noise becomes a serious problem when semiconductor lasers are used in combination with multimode fibers. Attempts have been made to estimate the extent of sensitivity degradation induced by modal noise [71]–[73] by calculating the BER after adding modal noise to the other sources of receiver noise. Figure 5.6 shows the power penalty at a BER of 10^{-12} calculated for a $1.3\text{-}\mu\text{m}$ lightwave system operating at 140 Mb/s. The graded-index fiber has a $50\text{-}\mu\text{m}$ core diameter and supports 146 modes. The power penalty depends on the mode-selective coupling loss occurring at splices and connectors. It also depends on the longitudinal-mode spectrum of the semiconductor laser. As expected, power penalty decreases as the number of longitudinal modes increases because of a reduction in the coherence time of the emitted light.

Modal noise can also occur in single-mode systems if short sections of fiber are installed between two connectors or splices during repair or normal maintenance [73]–[76]. A higher-order mode can be excited at the fiber discontinuity occurring at the first splice and then converted back to the fundamental mode at the second connector or splice. Since a higher-order mode cannot propagate far from its excitation point, this problem can be avoided by ensuring that the spacing between two connectors or splices exceeds 2 m. Generally speaking, modal noise is not a problem for properly designed and maintained single-mode fiber-optic communication systems.

With the development of the vertical-cavity surface-emitting laser (VCSEL), the modal-noise issue has resurfaced in recent years [77]–[81]. The use of such lasers in short-haul optical data links, making use of multimode fibers (even those made of plastic), is of considerable interest because of the high bandwidth associated with VCSELs. Indeed, rates of several gigabits per second have been demonstrated in laboratory experiments with plastic fibers [83]. However, VCSELs have a long coherence length as they oscillate in a single longitudinal mode. In a 1994 experiment the BER measure-

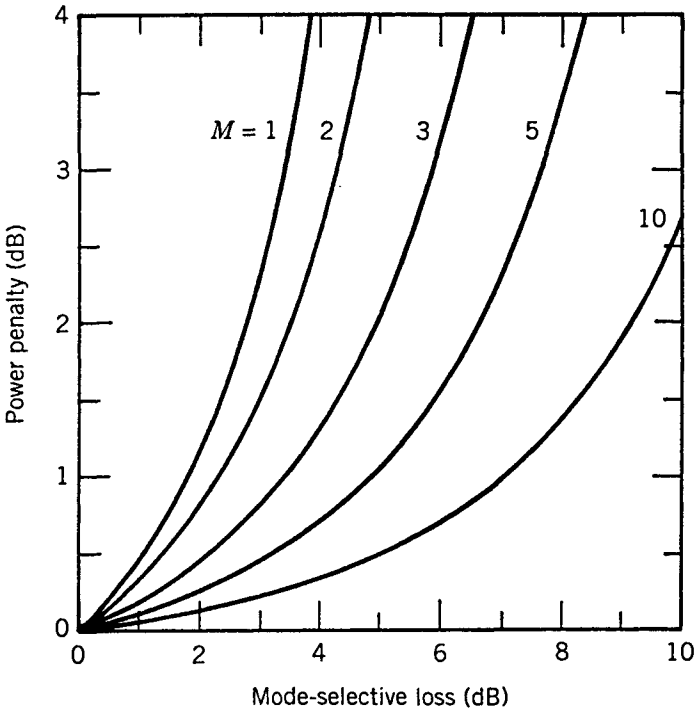


Figure 5.6: Modal-noise power penalty versus mode-selective loss. The parameter M is defined as the total number of longitudinal modes whose power exceeds 10% of the peak power. (After Ref. [71]; ©1986 IEEE; reprinted with permission.)

ments showed an error floor at a level of 10^{-7} even when the mode-selective loss was only 1 dB [78]. This problem can be avoided to some extent by using larger-diameter VCSELs which oscillate in several transverse modes and thus have a shorter coherence length. Computer models are generally used to estimate the power penalty for optical data links under realistic operating conditions [80]. Analytic tools such as the saddle-point method can also provide a reasonable estimate of the BER [81].

5.4.2 Mode-Partition Noise

As discussed in Section 3.3, multimode semiconductor lasers exhibit *mode-partition noise* (MPN), a phenomenon occurring because of an anticorrelation among pairs of longitudinal modes. In particular, various longitudinal modes fluctuate in such a way that individual modes exhibit large intensity fluctuations even though the total intensity remains relatively constant. MPN would be harmless in the absence of fiber dispersion, as all modes would remain synchronized during transmission and detection. In practice, different modes become unsynchronized, since they travel at slightly different speeds inside the fiber because of group-velocity dispersion. As a result of such desynchronization, the receiver current exhibits additional fluctuations, and the SNR at the

decision circuit becomes worse than that expected in the absence of MPN. A power penalty must be paid to improve the SNR to the same value that is necessary to achieve the required BER (see Section 4.5). The effect of MPN on system performance has been studied extensively for multimode semiconductor lasers [84]–[92].

In the case of multimode semiconductor lasers, the power penalty can be calculated by following an approach similar to that of Section 4.6.2 and is given by [84]

$$\delta_{\text{mpn}} = -5 \log_{10}(1 - Q^2 r_{\text{mpn}}^2), \quad (5.4.1)$$

where r_{mpn} is the relative noise level of the received power in the presence of MPN. A simple model for estimating the parameter r_{mpn} assumes that laser modes fluctuate in such a way that the total power remains constant under CW operation [84]. It also assumes that the average mode power is distributed according to a Gaussian distribution of RMS width σ_λ and that the pulse shape at the decision circuit of the receiver is described by a cosine function. Different laser modes are assumed to have the same cross-correlation coefficient γ_{cc} , i.e.,

$$\gamma_{\text{cc}} = \frac{\langle P_i P_j \rangle}{\langle P_i \rangle \langle P_j \rangle} \quad (5.4.2)$$

for all i and j such that $i \neq j$. The angular brackets denote an average over power fluctuations associated with mode partitioning. A straightforward calculation shows that r_{mpn} is given by [87]

$$r_{\text{mpn}} = (k/\sqrt{2})\{1 - \exp[-(\pi BLD\sigma_\lambda)^2]\}, \quad (5.4.3)$$

where the mode-partition coefficient k is related to γ_{cc} as $k = \sqrt{1 - \gamma_{\text{cc}}}$. The model assumes that mode partition can be quantified in terms of a single parameter k with values in the range 0–1. The numerical value of k is difficult to estimate and is likely to vary from laser to laser. Experimental measurements suggest that the values of k are in the range 0.6–0.8 and vary for different mode pairs [89].

Equations (5.4.1) and (5.4.3) can be used to calculate the MPN-induced power penalty. Figure 5.7 shows the power penalty at a BER of 10^{-9} ($Q = 6$) as a function of the normalized dispersion parameter $BLD\sigma_\lambda$ for several values of the mode-partition coefficient k . For any value of k , δ_{mpn} increases rapidly with an increase in $BLD\sigma_\lambda$ and becomes infinite when $BLD\sigma_\lambda$ reaches a critical value. For $k > 0.5$, the MPN-induced power penalty becomes quite large if $BLD\sigma_\lambda$ exceeds 0.15. However, it can be reduced to a negligible level ($\delta_{\text{mpn}} < 0.5$ dB) by designing the optical communication system such that $BLD\sigma_\lambda < 0.1$. As an example, consider a $1.3\text{-}\mu\text{m}$ lightwave system. If we assume that the operating wavelength is matched to the zero-dispersion wavelength to within 10 nm, $D \approx 1 \text{ ps}/(\text{km-nm})$. A typical value of σ_λ for multimode semiconductor lasers is 2 nm. The MPN-induced power penalty would be negligible if the BL product were below 50 (Gb/s)-km. At $B = 2 \text{ Gb/s}$ the transmission distance is then limited to 25 km. The situation becomes worse for $1.55\text{-}\mu\text{m}$ lightwave systems for which $D \approx 16 \text{ ps}/(\text{km-nm})$ unless dispersion-shifted fibers are used. In general, the MPN-induced power penalty is quite sensitive to the spectral bandwidth of the multimode laser and can be reduced by reducing the bandwidth. In one study [92], a reduction in

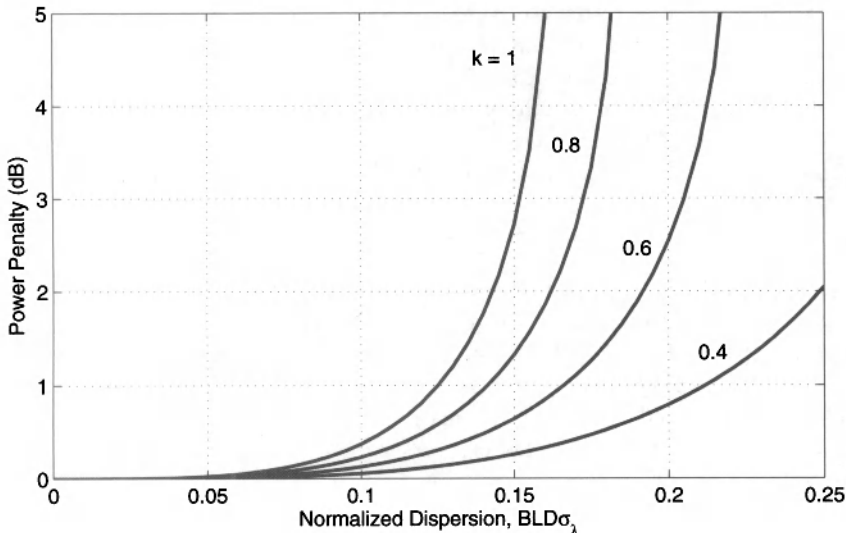


Figure 5.7: MPN-induced Power penalty versus $BLD\sigma_\lambda$ for a multimode semiconductor laser of RMS spectral width σ_λ . Different curves correspond to different values of the mode-partition coefficient k .

the carrier lifetime from 340 to 130 ps, realized by *p*-doping of the active layer, reduced the bandwidth of 1.3- μ m semiconductor lasers by only 40% (from 5.6 to 3.4 nm), but the power penalty decreased from an infinite value (BER floor above 10^{-9} level) to a mere 0.5 dB.

5.4.3 Reflection Feedback and Noise

In most fiber-optic communication systems, some light is invariably reflected back because of refractive-index discontinuities occurring at splices, connectors, and fiber ends. The effects of such unintentional feedback have been studied extensively [93]–[104] because they can degrade the performance of lightwave systems considerably. Even a relatively small amount of optical feedback affects the operation of semiconductor lasers [97] and can lead to excess noise in the transmitter output. Even when an isolator is used between the transmitter and the fiber, multiple reflections between splices and connectors can generate additional intensity noise and degrade receiver performance [99]. This subsection is devoted to the effect of reflection-induced noise on receiver sensitivity.

Most reflections in a fiber link originate at glass-air interfaces whose reflectivity can be estimated by using $R_f = (n_f - 1)^2 / (n_f + 1)^2$, where n_f is the refractive index of the fiber material. For silica fibers $R_f = 3.6\%$ (-14.4 dB) if we use $n_f = 1.47$. This value increases to 5.3% for polished fiber ends since polishing can create a thin surface layer with a refractive index of about 1.6. In the case of multiple reflections occurring between two splices or connectors, the reflection feedback can increase con-

siderably because the two reflecting surfaces act as mirrors of a Fabry–Perot interferometer. When the resonance condition is satisfied, the reflectivity increases to 14% for unpolished surfaces and to over 22% for polished surfaces. Clearly, a considerable fraction of the signal transmitted can be reflected back unless precautions are taken to reduce the optical feedback. A common technique for reducing reflection feedback is to use index-matching oil or gel near glass–air interfaces. Sometimes the tip of the fiber is curved or cut at an angle so that the reflected light deviates from the fiber axis. Reflection feedback can be reduced to below 0.1% by such techniques.

Semiconductor lasers are extremely sensitive to optical feedback [101]; their operating characteristics can be affected by feedback as small as -80 dB [97]. The most dramatic effect of feedback is on the laser linewidth, which can narrow or broaden by several order of magnitude, depending on the exact location of the surface where feedback originates [93]. The reason behind such a sensitivity is related to the fact that the phase of the reflected light can perturb the laser phase significantly even for relatively weak feedback levels. Such feedback-induced phase changes are detrimental mainly for coherent communication systems. The performance of direct-detection lightwave systems is affected by intensity noise rather than phase noise.

Optical feedback can increase the intensity noise significantly. Several experiments have shown a feedback-induced enhancement of the intensity noise occurring at frequencies corresponding to multiples of the external-cavity mode spacing [94]–[96]. In fact, there are several mechanisms through which the relative intensity noise (RIN) of a semiconductor laser can be enhanced by the external optical feedback. In a simple model [98], the feedback-induced enhancement of the intensity noise is attributed to the onset of multiple, closely spaced, external-cavity longitudinal modes whose spacing is determined by the distance between the laser output facet and the glass–air interface where feedback originates. The number and the amplitudes of the external-cavity modes depend on the amount of feedback. In this model, the RIN enhancement is due to intensity fluctuations of the feedback-generated side modes. Another source of RIN enhancement has its origin in the feedback-induced chaos in semiconductor lasers. Numerical simulations of the rate equations show that the RIN can be enhanced by 20 dB or more when the feedback level exceeds a certain value [102]. Even though the feedback-induced chaos is deterministic in nature, it manifests as an apparent RIN increase.

Experimental measurements of the RIN and the BER in the presence of optical feedback confirm that the feedback-induced RIN enhancement leads to a power penalty in lightwave systems [105]–[107]. Figure 5.8 shows the results of the BER measurements for a VCSEL operating at 958 nm. Such a laser operates in a single longitudinal mode because of an ultrashort cavity length ($\sim 1 \mu\text{m}$) and exhibits a RIN near -130 dB/Hz in the absence of reflection feedback. However, the RIN increases by as much as 20 dB when the feedback exceeds the -30 -dB level. The BER measurements at a bit rate of 500 Mb/s show a power penalty of 0.8 dB at a BER of 10^{-9} for -30 -dB feedback, and the penalty increases rapidly at higher feedback levels [107].

The power penalty can be calculated by following the analysis of Section 4.6.2 and is given by

$$\delta_{\text{ref}} = -10 \log_{10}(1 - r_{\text{eff}}^2 Q^2), \quad (5.4.4)$$

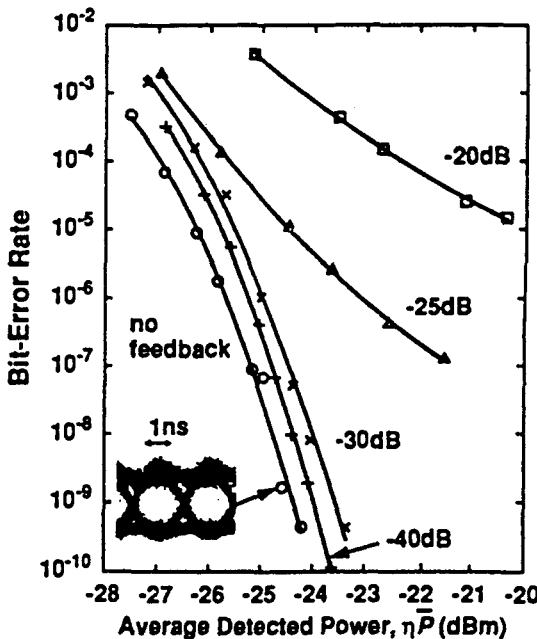


Figure 5.8: Experimentally measured BER at 500 Mb/s for a VCSEL under optical feedback. The BER is measured at several feedback levels. (After Ref. [107]; ©1993 IEEE; reprinted with permission.)

where r_{eff} is the effective intensity noise over the receiver bandwidth Δf and is obtained from

$$r_{\text{eff}}^2 = \frac{1}{2\pi} \int_{-\infty}^{\infty} \text{RIN}(\omega) d\omega = 2(\text{RIN})\Delta f. \quad (5.4.5)$$

In the case of feedback-induced external-cavity modes, r_{eff} can be calculated by using a simple model and is found to be [98]

$$r_{\text{eff}}^2 \approx r_I^2 + N/(\text{MSR})^2, \quad (5.4.6)$$

where r_I is the relative noise level in the absence of reflection feedback, N is the number of external-cavity modes, and MSR is the factor by which the external-cavity modes remain suppressed. Figure 5.9 shows the reflection-noise power penalty as a function of MSR for several values of N by choosing $r_I = 0.01$. The penalty is negligible in the absence of feedback ($N = 0$). However, it increases with an increase in N and a decrease in MSR . In fact, the penalty becomes infinite when MSR is reduced below a critical value. Thus, reflection feedback can degrade system performance to the extent that the system cannot achieve the desired BER despite an indefinite increase in the power received. Such reflection-induced BER floors have been observed experimentally [96] and indicate the severe impact of reflection noise on the performance of lightwave systems. An example of the reflection-induced BER floor is seen in Figure 5.8, where the BER remains above 10^{-9} for feedback levels in excess of -25 dB. Generally

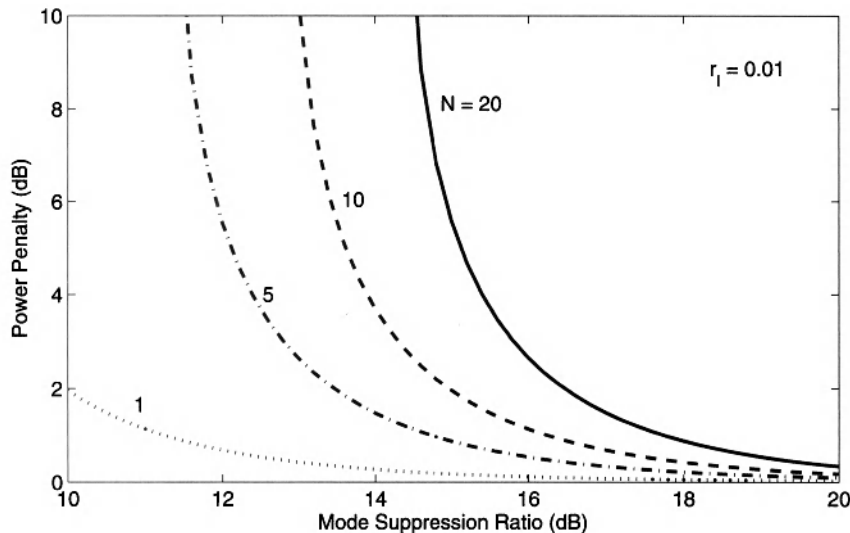


Figure 5.9: Feedback-induced power penalty as a function of MSR for several values of N and $r_I = 0.01$. Reflection feedback into the laser is assumed to generate N side modes of the same amplitude.

speaking, most lightwave systems operate satisfactorily when the reflection feedback is below -30 dB. In practice, the problem can be nearly eliminated by using an optical isolator within the transmitter module.

Even when an isolator is employed, reflection noise can be a problem for lightwave systems. In long-haul fiber links, fiber dispersion can convert phase noise into intensity noise, leading to performance degradation [100]. Similarly, two reflecting surfaces anywhere along the fiber link act as a Fabry–Perot interferometer which can convert phase noise into intensity noise [99]. Such a conversion can be understood by noting that multiple reflections inside a Fabry–Perot interferometer lead to a phase-dependent term in the transmitted intensity which fluctuates in response to phase fluctuations. As a result, the RIN of the signal incident on the receiver is higher than that occurring in the absence of reflection feedback. Most of the RIN enhancement occurs over a narrow frequency band whose spectral width is governed by the laser linewidth (~ 100 MHz). Since total noise is obtained by integrating over the receiver bandwidth, it can affect system performance considerably at bit rates larger than 1 Gb/s. The power penalty can still be calculated by using Eq. (5.4.4). A simple model that includes only two reflections between the reflecting interfaces shows that r_{eff} is proportional to $(R_1 R_2)^{1/2}$, where R_1 and R_2 are the reflectivities of the two interfaces [99]. Figure 4.21 can be used to estimate the power penalty. It shows that power penalty can become infinite and lead to BER floors when r_{eff} exceeds 0.2. Such BER floors have been observed experimentally [99]. They can be avoided only by eliminating or reducing parasitic reflections along the entire fiber link. It is therefore necessary to employ connectors and splices that reduce reflections through the use of index matching or other techniques.

5.4.4 Dispersive Pulse Broadening

Dispersion-induced pulse broadening affects the receiver performance in two ways. First, a part of the pulse energy spreads beyond the allocated bit slot and leads to inter-symbol interference. Second, the pulse energy within the bit slot is reduced when the optical pulse broadens. Such a decrease in pulse energy reduces the SNR at the decision circuit. As the SNR should remain constant to maintain the system performance, the receiver requires more average power. This is the origin of dispersion-induced power penalty δ_d .

An exact calculation of δ_d is difficult, as it depends on many details such as the extent of pulse shaping at the receiver. A rough estimate is obtained by following the analysis of Section 3.3.1, where broadening of Gaussian pulses is discussed. Equation (3.3.9) shows that the optical pulse remains Gaussian, but its peak power is reduced by a pulse-broadening factor given in Eq. (3.3.10). If we define the power penalty δ_d as the increase (in decibels) in the received power that would compensate the peak-power reduction, δ_d is given by

$$\delta_d = 10 \log_{10} b_f, \quad (5.4.7)$$

where b_f is the pulse broadening factor. As in Section 3.3.4, we consider the case of broadband and narrowband optical sources separately.

Consider first a lightwave system designed with a relatively broadband optical source. The broadening factor b_f in this case is obtained from Eq. (2.4.24) and has the form

$$b_f = \sigma/\sigma_0 = [1 + (DL\sigma_\lambda/\sigma_0)^2]^{1/2}, \quad (5.4.8)$$

where σ_λ is the RMS width of the source spectrum. The RMS width σ_0 of the optical pulse at the transmitter end is a design parameter. It can be related to the duty cycle d_c of RZ pulses as $4\sigma_0 = d_c T_b$, where $T_b \equiv 1/B$ is the duration of the bit slot at a given bit rate B . Using $\sigma_0 = d_c/(4B)$ in Eq. (5.4.8) and using Eq. (5.4.7), the power penalty becomes

$$\delta_d = 5 \log_{10} [1 + (4BLD\sigma_\lambda/d_c)^2]. \quad (5.4.9)$$

This result should be compared with the condition (3.3.40) found in Section 3.3.4. If we assume that input pulses are wide enough to occupy the entire bit slot ($d_c = 1$), the power penalty is negligible for $4BLD\sigma_\lambda \ll 1$, becomes 1.5 dB when $4BLD\sigma_\lambda = 1$, and increases rapidly beyond that.

In the case of a long-haul system designed with a narrowband source and chirp-free pulses, the broadening factor is obtained from Eq. (2.4.29). If we use again $\sigma_0 = d_c/(4B)$, the power penalty is given by

$$\delta_d = 5 \log_{10} [1 + (8\beta_2 B^2 L/d_c^2)^2]. \quad (5.4.10)$$

Figure 5.10 shows power penalty as a function of the dimensionless parameter combination $\mu = |\beta_2|B^2L$ for three values of d_c . Although the power penalty is negligible for values of $\mu < 0.05$ and $d_c > 0.5$, it increases rapidly as μ increases and exceeds 5 dB for $\mu = 0.1$ and $d_c = 0.5$. It is thus important to keep μ below 0.1. As an example, the operating distance of a 10-Gb/s lightwave system is limited to below 50 km because of dispersion when standard fibers are used with $|\beta_2| \approx 20 \text{ ps}^2/\text{km}$, but this value can be

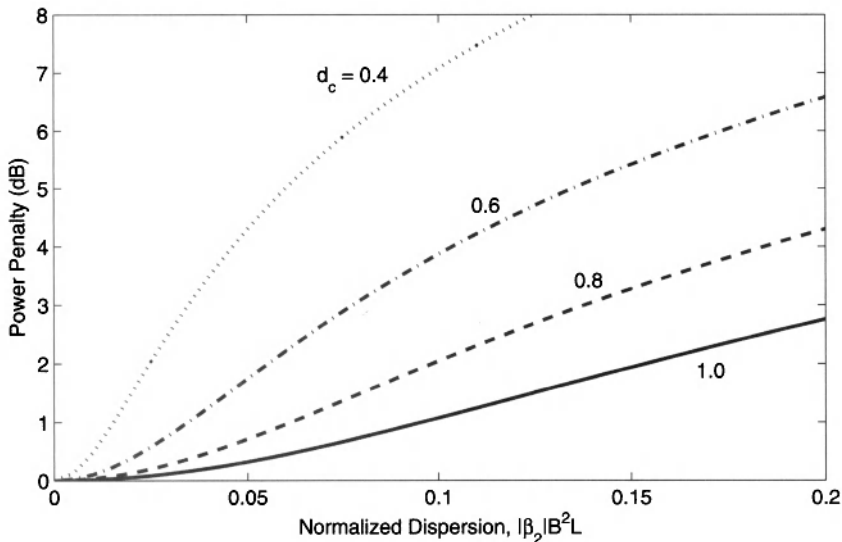


Figure 5.10: Dispersion-induced power penalty function as a function of $\mu = |\beta_2|B^2L$ for three values of duty cycle associated with an RZ bit stream.

increased considerably through dispersion management. It should be stressed that Eq. (5.4.10) provides only a rough estimate as its derivation is based on the assumptions of a Gaussian pulse shape.

5.4.5 Frequency Chirping

The preceding discussion of dispersion-induced power penalty assumed that the input pulses were unchirped. An initial chirp on optical pulses is known to limit the performance of 1.55-μm lightwave systems when directly modulated semiconductor lasers are used to generate the digital bit stream [108]–[121]. As discussed in Section 2.4.2, frequency chirping can enhance the dispersion-induced broadening of optical pulses and thus may degrade the performance of a long-haul lightwave system more than that expected when unchirped pulses are employed.

An exact calculation of the chirp-induced power penalty δ_c is difficult because frequency chirp depends on both the shape and the width of the optical pulse [110]–[113]. However, if we assume a Gaussian pulse shape and a linear chirp, the analysis of Section 2.4.2 can be used to estimate the chirp-induced power penalty. If we use Eq. (2.4.17) for the pulse broadening factor in Eq. (5.4.7) together with $T_0 = \sqrt{2}d_c/(4B)$, the power penalty is given by

$$\delta_c = 5 \log_{10} [(1 + 8C\beta_2 B^2 L/d_c^2)^2 + (8\beta_2 B^2 L/d_c^2)^2]. \quad (5.4.11)$$

Figure 5.11 shows the chirp-induced power penalty as a function of $|\beta_2|B^2L$ for several values of the chirp parameter C with $d_c = 1$. The parameter β_2 is taken to be

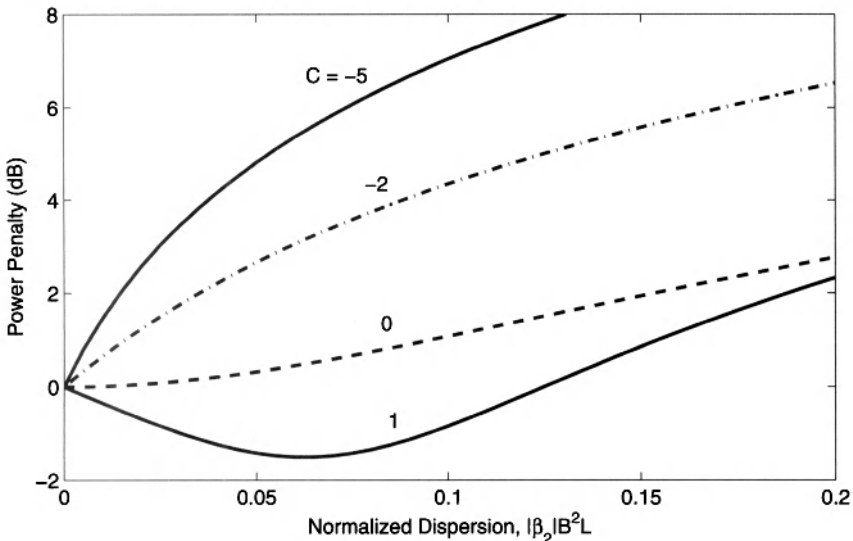


Figure 5.11: Chirp-induced power penalty as a function of $|\beta_2|B^2L$ for several values of the chirp parameter C . Gaussian pulses are assumed to be linearly chirped.

negative, as is the case for 1.55- μm lightwave systems. The $C = 0$ curve corresponds to the case of a chirp-free pulse. Power penalty is negligible (<0.1 dB) in this ideal case as long as $|\beta_2|B^2L < 0.05$. However, the penalty can exceed 5 dB if the transmitted pulses are chirped such that $C = -6$ (a typical value for semiconductor lasers). To keep the penalty below 0.1 dB, the system should be designed with $|\beta_2|B^2L < 0.002$. For standard optical fibers with $\beta_2 \approx -20 \text{ ps}^2/\text{km}$, B^2L is limited to $100 \text{ (Gb/s)}^2\text{-km}$, indicating that even at $B = 2.5 \text{ Gb/s}$, the transmission distance is limited to below 16 km because of frequency chirping. Interestingly, system performance can be improved by ensuring that $\beta_2C < 0$. As discussed in Section 3.3, each optical pulse then undergoes an initial compression phase. As C is negative for semiconductor lasers, fibers with “normal” dispersion ($\beta_2 > 0$) can provide better performance whenever directly modulated semiconductor lasers are employed. For this reason, fibers with normal GVD are often employed in metropolitan area networks. Alternatively, one can make use of dispersion compensation and ensure that the average value of β_2 is close to zero.

5.4.6 Eye-Closure Penalty

An alternative measure of system performance is provided by the extent the “eye opening” in the eye diagram is affected by the dispersive and nonlinear effects accumulated inside the fiber link. As discussed in Section 4.3, an electrical filter with a bandwidth smaller than the bit rate is used inside the receiver to reshape pulses before they reach the decision circuit. Figure 4.14 shows the eye diagram looks like for an NRZ-format bit stream. When RZ format is employed, the pattern still has the appearance of an eye, even though the top horizontal rail is missing. Even in the case of the DPSK format,

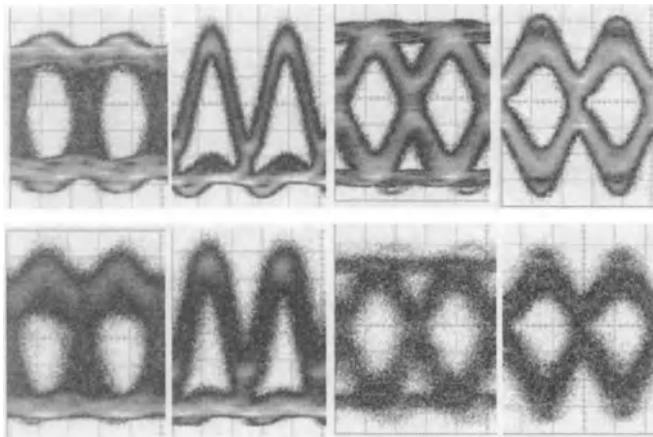


Figure 5.12: Measured eye diagrams at 40 Gb/s under back-to-back conditions (top row) and after a 263-km-long fiber link (bottom row). In both rows successive traces corresponds to NRZ, RZ, NRZ-DPSK, and RZ-DPSK formats, respectively. (After Ref. [122]; ©2004 IEEE.)

the eye diagram retains its shape. The top row in Figure 5.12 shows the measured eye diagrams at 40 Gb/s in the case of NRZ, CSRZ, NRZ-DPSK, and RZ-DPSK formats under the back-to-back condition in which the transmitter is directly connected to the receiver.

As the optical bit stream is transmitted through a fiber link, the accumulation of dispersive and nonlinear effects distorts optical pulses. These distortions manifest in the eye diagram through a reduced opening of the eye. The bottom row in Figure 5.12 shows the measured eye diagrams at 40 Gb/s after a 263-km-long fiber link for the same four modulation formats [122]. As seen there, eye opening is reduced for all formats. Since the decision threshold is set in the center of the open portion of the eye, any reduction in eye opening indicates an increase in the BER. This observation relates eye closure to the BER and suggests that its magnitude can provide a measure of the system performance. More precisely, the eye-closure penalty is quantified (in dB) as

$$\delta_{\text{eye}} = -10 \log_{10} \left(\frac{\text{eye opening after transmission}}{\text{eye opening before transmission}} \right). \quad (5.4.12)$$

Before Eq. (5.4.12) can be used, we need to clarify what one means by eye opening. Ideally, the eye amplitude peaks in the center of the bit slot and it provides an appropriate measure of eye opening. However, in practice, timing jitter makes it difficult to sample each pulse precisely at the location where pulse amplitude is maximum. If we allow an uncertainty of up to 10% on each side of the decision threshold, we should consider a rectangle of the largest area with a base of $0.2T_b$, where T_b is the duration of each symbol, that can be fitted within the open portion of the eye. The height of this rectangle then measures eye opening. This approach is commonly adopted for numerical simulations.

5.5 Forward Error Correction

As seen in the preceding section, receiver sensitivity and the BER of a lightwave system are degraded by many factors that are not always controllable in practice. Depending on details of the system design and objectives, it is entirely possible that a specified BER cannot be achieved. Under such conditions, the use of an error-correction scheme remains the only viable alternative.

Error control is not a new concept and is employed widely in electrical systems dealing with the transfer of digital data from one device to another [123]–[126]. The techniques used for controlling errors can be divided into two groups. In one group, errors are detected but not corrected. Rather, each packet of bits received with errors is retransmitted. This approach is suitable when data bits are transmitted in the form of packets (as is the case for the protocol used by the Internet) and they do not arrive at the destination in a synchronous fashion. In the other group, errors are detected as well as corrected at the receiver end without any retransmission of bits. This approach is referred to as forward error correction (FEC) and is best suited for lightwave systems operating with a synchronous protocol such as SONET or SDH.

Historically, lightwave systems did not employ FEC until the use of in-line optical amplifiers became common [127]–[129]. The use of FEC accelerated with the advent of WDM technology. As early as 1996, FEC was employed for a WDM system designed to operate over more than 425 km without any in-line amplifier or regenerator [130]. Since then, the FEC technique has been used in many WDM systems and is now considered almost routine [131]–[134].

5.5.1 Error-Correcting Codes

The basic idea behind any error-control technique is to add extra bits to the signal at the transmitter end in a judicious manner using a suitable coding algorithm [123]–[126]. A simple example is provided by the so-called parity bit that is added to the 7-bit ASCII code. In this example, the parity bit is chosen to be 0 or 1 depending on whether the number of 1 bits in the 7-bit sequence is even or odd. If a single bit is in error at the receiving end, an examination of the parity bit reveals the error.

The situation is somewhat different in the case of an optical bit stream, but the basic idea remains the same. An encoder within the transmitter adds additional control bits using a suitable code. At the receiver end, a decoder uses these control bits to detect errors, while correcting them simultaneously. How many errors can be corrected depends on the coding scheme employed. In general, more errors can be corrected by adding more control bits to the signal. Clearly, there is a limit to this process since the bit rate of the signal increases after the decoder. If B_e is the effective bit rate after coding a signal at the bit rate B , the *FEC overhead* associated with the error-correcting code is $B_e/B - 1$. The concept of *redundancy* is also used for FEC codes as the bits added by the coding scheme do not carry any information. Redundancy of a code is defined as $\rho = 1 - B_e/B$.

Many different types of error-correcting codes have been developed, often classified under names such as linear, cyclic, Hamming, Reed–Solomon, convolutional, product, and turbo codes [131]. Among these, Reed–Solomon (RS) codes have at-

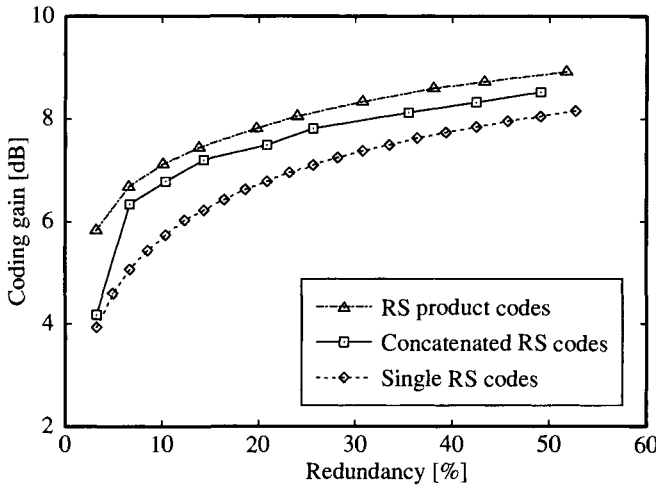


Figure 5.13: Coding gain as a function of code redundancy (overhead) for single, concatenated, and product-type RS codes. (After Ref. [132]; ©2002 IEEE.)

tracted most attention in the context of lightwave systems [132]. An RS code is denoted as $\text{RS}(n, k)$, where k is the size of a packet of bits that is converted through coding into a larger packet with n bits. The value of n is chosen such that $n = 2^m - 1$, where m is an integer. The RS code recommended by ITU for submarine applications uses $m = 8$ and is written as $\text{RS}(255, 239)$. The FEC overhead for this code is only 6.7%. Many other RS codes can be used if a higher overhead is permitted. For example, the code $\text{RS}(255, 207)$ has an overhead of 23.2% but it allows for more robust error control. The choice of the code depends on the level of improvement in the BER required for the system to operate reliably. It is common to quantify this improvement through the *coding gain*, a concept we discuss next.

5.5.2 Coding Gain

Coding gain is a measure of the improvement in BER realized through FEC. Since BER is related to the Q factor as indicated in Eq. (4.6.10), it is often expressed in terms of the equivalent value of Q that corresponds to the BER realized after the FEC decoder. The coding gain in decibel units is defined as [132]

$$G_c = 20 \log_{10}(Q_c/Q), \quad (5.5.1)$$

where Q_c and Q are related to the BERs obtained with and without FEC as

$$\text{BER}_c = \frac{1}{2} \operatorname{erfc}(Q_c/\sqrt{2}), \quad \text{BER} = \frac{1}{2} \operatorname{erfc}(Q/\sqrt{2}). \quad (5.5.2)$$

The factor of 20 appears in Eq. (5.5.1) in place of 10 because Q^2 is traditionally used for expressing the Q factor in decibel units. As an example, if the FEC decoder improves the BER from its original value of 10^{-3} to 10^{-9} , the value of Q increases from about 3

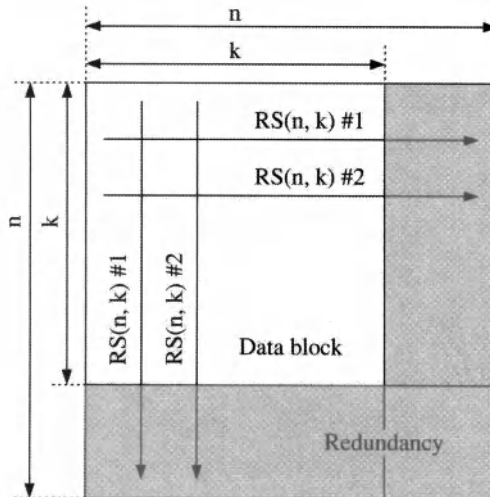


Figure 5.14: Schematic illustration of a RS product code. The same code is applied along the rows and columns of a block of bits. (After Ref. [132]; ©2002 IEEE.)

to 6, resulting in a coding gain of 6 dB. The coding gain is sometimes defined in terms of the SNR [131]. The two definitions differ by a small amount of $10 \log_{10}(B_e/B)$.

As one would expect, the magnitude of coding gain increases with the FEC overhead (or redundancy). The dashed line in Figure 5.13 shows this behavior. The coding gain is about 5.5 dB for 10% overhead and increases sublinearly, reaching only 8 dB even for a 50% overhead. It can be improved by concatenating two or more RS codes or by employing the RS product codes, but in all cases the coding gain begins to saturate as overhead increases. In the case of a RS product code, more than 6 dB of coding gain can be realized with only 5% overhead. The basic idea behind an RS product code is shown in Figure 5.14. As seen there, a block of data with k^2 bits is converted into n^2 bits by applying the same RS(n, k) code both along the rows and columns. As a result, the overhead of $n^2/k^2 - 1$ for a RS product code is larger, but it also allows more error control.

5.6 Computer-Aided Design

The design of a fiber-optic communication system involves optimization of a large number of parameters associated with transmitters, optical fibers, in-line amplifiers, and receivers. The design aspects discussed in Section 5.2 are too simple to provide the optimized values for all system parameters. The power and the rise-time budgets are only useful for obtaining a conservative estimate of the transmission distance (or repeater spacing) and the bit rate. The system margin in Eq. (5.2.2) is used as a vehicle to include various sources of power penalties discussed in Section 5.4. Such a simple approach fails for modern high-capacity systems designed to operate over long distances using optical amplifiers.

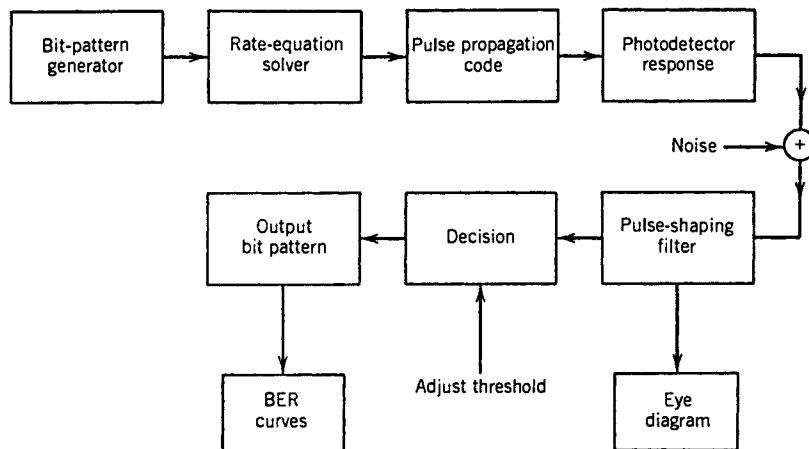


Figure 5.15: Steps involved in computer modeling of fiber-optic communication systems.

An alternative approach uses computer simulations and provides a much more realistic modeling of fiber-optic communication systems [136]–[149]. The computer-aided design techniques are capable of optimizing the whole system and can provide the optimum values of various system parameters such that the design objectives are met at a minimum cost. Figure 5.15 illustrates the various steps involved in the simulation process. The approach consists of generating an optical bit pattern at the transmitter, transmitting it through the fiber link, detecting it at the receiver, and then analyzing it through the tools such as the eye diagram and the Q factor.

Each step in the block diagram shown in Figure 5.15 can be carried out numerically by using the material given in Chapters 2–4. The input to the optical transmitter is a pseudorandom sequence of electrical pulses which represent 1 and 0 bits. The length N of the pseudorandom bit sequence determines the computing time and should be chosen judiciously. Typically, $N = 2^M$ with M is in the range of 6 to 10. The optical bit stream can be obtained by solving the rate equations that govern the modulation response of semiconductor lasers (see Section 3.3). The equations governing the modulation response should be used if an external modulator is used. Chirping is automatically included in both cases.

The most time-consuming part of system simulations is propagation of the optical bit stream through the fiber link which may contain multiple fiber sections with optical amplifiers inserted in between. Changes to the bit stream occurring in each fiber section are calculated by solving the NLS equation (5.3.1) so that both the dispersive and nonlinear effects are fully included. The noise added by optical amplifiers should also be included at the location of each amplifier.

The optical bit stream is converted into the electrical domain at the photodetector where shot and thermal noises are added as discussed in Section 4.4. The electrical bit stream is then passed through a pulse-shaping filter whose bandwidth is also a design parameter. An eye diagram is constructed using this filtered bit stream. The effect of varying system parameters can be studied by monitoring the eye degradation or by

calculating the Q parameter given in Eq. (4.6.11). Such an approach can be used to obtain the power penalty associated with various mechanisms discussed in Section 5.4. It can also be used to investigate trade-offs that would optimize the overall system performance. Numerical simulations reveal the existence of an optimum extinction ratio for which the system penalty is minimum.

Computer-aided design has another important role to play. A long-haul lightwave system may contain many repeaters, both optical and electrical. Transmitters, receivers, and amplifiers used at repeaters, although chosen to satisfy nominal specifications, are never identical. Similarly, fiber cables are constructed by splicing many different pieces (typical length 4–8 km) which have slightly different loss and dispersion characteristics. The net result is that many system parameters vary around their nominal values. For example, the dispersion parameter D , responsible not only for pulse broadening but also for other sources of power penalty, can vary significantly in different sections of the fiber link because of variations in the zero-dispersion wavelength and the transmitter wavelength. A statistical approach is often used to estimate the effect of such inherent variations on the performance of a realistic lightwave system. The idea behind such an approach is that it is extremely unlikely that all system parameters would take their worst-case values at the same time. Thus, repeater spacing can be increased well above its worst-case value if the system is designed to operate reliably at the specific bit rate with a high probability (say 99.9%).

The importance of computer-aided design for fiber-optic communication systems became apparent during the 1990s when the dispersive and nonlinear effects in optical fibers became of paramount concern with increasing bit rates and transmission distances. All modern lightwave systems are designed using numerical simulations, and several software packages are available commercially. Appendix D provides details on the simulation package available on the CD included with this book (courtesy of OptiWave Corporation). The CD also contains many additional problems designed specifically for a better understanding of the material covered in this book. The reader is encouraged to use the software on this CD to develop additional skills.

Problems

- 5.1** A distribution network uses an optical bus to distribute the signal to 10 users. Each optical tap couples 10% of the power to the user and has 1-dB insertion loss. Assuming that the station 1 transmits 1 mW of power over the optical bus, calculate the power received by the stations 8, 9, and 10.
- 5.2** A cable-television operator uses an optical bus to distribute the video signal to its subscribers. Each receiver needs a minimum of 100 nW to operate satisfactorily. Optical taps couple 5% of the power to each subscriber. Assuming 0.5 dB insertion loss for each tap and 1 mW transmitter power, estimate the number of subscribers that can be added to the optical bus?
- 5.3** A star network uses directional couplers with 0.5-dB insertion loss to distribute data to its subscribers. If each receiver requires a minimum of 100 nW and each

transmitter is capable of emitting 0.5 mW, calculate the maximum number of subscribers served by the network.

- 5.4** Make the power budget and calculate the maximum transmission distance for a 1.3- μm lightwave system operating at 100 Mb/s and using an LED for launching 0.1 mW of average power into the fiber. Assume 1-dB/km fiber loss, 0.2-dB splice loss every 2 km, 1-dB connector loss at each end of fiber link, and 100-nW receiver sensitivity. Allow 6-dB system margin.
- 5.5** A 1.3- μm long-haul lightwave system is designed to operate at 1.5 Gb/s. It is capable of coupling 1 mW of average power into the fiber. The 0.5-dB/km fiber-cable loss includes splice losses. The connectors at each end have 1-dB losses. The InGaAs $p-i-n$ receiver has a sensitivity of 250 nW. Make the power budget and estimate the repeater spacing.
- 5.6** Prove that the rise time T_r and the 3-dB bandwidth Δf of a RC circuit are related by $T_r\Delta f = 0.35$.
- 5.7** Consider a super-Gaussian optical pulse with the power distribution
- $$P(t) = P_0 \exp[-(t/T_0)^{2m}],$$
- where the parameter m controls the pulse shape. Derive an expression for the rise time T_r of such a pulse. Calculate the ratio T_r/T_{FWHM} , where T_{FWHM} is the full width at half maximum, and show that for a Gaussian pulse ($m = 1$) this ratio equals 0.716.
- 5.8** Prove that for a Gaussian optical pulse, the rise time T_r and the 3-dB optical bandwidth Δf are related by $T_r\Delta f = 0.316$.
- 5.9** Make the rise-time budget for a 0.85- μm , 10-km fiber link designed to operate at 50 Mb/s. The LED transmitter and the Si $p-i-n$ receiver have rise times of 10 and 15 ns, respectively. The graded-index fiber has a core index of 1.46, $\Delta = 0.01$, and $D = 80 \text{ ps}/(\text{km}\cdot\text{nm})$. The LED spectral width is 50 nm. Can the system be designed to operate with the NRZ format?
- 5.10** A 1.3- μm lightwave system is designed to operate at 1.7 Gb/s with a repeater spacing of 45 km. The single-mode fiber has a dispersion slope of $0.1 \text{ ps}/(\text{km}\cdot\text{nm}^2)$ in the vicinity of the zero-dispersion wavelength occurring at $1.308 \mu\text{m}$. Calculate the wavelength range of multimode semiconductor lasers for which the mode-partition-noise power penalty remains below 1 dB. Assume that the RMS spectral width of the laser is 2 nm and the mode-partition coefficient $k = 0.7$.
- 5.11** Generalize Eq. (5.4.1) for the case of APD receivers by including the excess-noise factor in the form $F(M) = M^x$.
- 5.12** Consider a 1.55- μm lightwave system operating at 1 Gb/s by using multimode semiconductor lasers of 2 nm (RMS) spectral width. Calculate the maximum transmission distance that would keep the mode-partition-noise power penalty below 2 dB. Use $k = 0.8$ for the mode-partition coefficient.
- 5.13** Use Eq. (5.4.11) to determine the maximum transmission distance for a 1.55- μm lightwave system operating at 4 Gb/s such that the chirp-induced power penalty

is below 1 dB. Assume that $C = -6$ for the single-mode semiconductor laser and $\beta_2 = -20 \text{ ps}^2/\text{km}$ for the single-mode fiber.

- 5.14** Repeat the preceding problem in the case of 8-Gb/s bit rate.
- 5.15** Use the results of Problem 4.18 to obtain an expression of the reflection-induced power penalty in the case of a finite extinction ratio r_{ex} . Reproduce the penalty curves shown in Figure 5.8 for the case $r_{\text{ex}} = 0.1$.
- 5.16** Consider a Fabry–Perot interferometer with two surfaces of reflectivity R_1 and R_2 . Follow the analysis of Ref. [99] to derive an expression of the relative intensity noise RIN(ω) of the transmitted light as a function of the linewidth of the incident light. Assume that R_1 and R_2 are small enough that it is enough to consider only a single reflection at each surface.
- 5.17** Follow the analysis of Ref. [136] to obtain an expression for the total receiver noise by including thermal noise, shot noise, intensity noise, mode-partition noise, chirp noise, and reflection noise.

References

- [1] P. S. Henry, R. A. Linke, and A. H. Gnauck, in *Optical Fiber Telecommunications II*, S. E. Miller and I. P. Kaminow, Eds., Academic Press, Boston, CA, 1988, Chap. 21.
- [2] P. E. Green, Jr., *Fiber-Optic Networks*, Prentice Hall, Upper Saddle River, NJ, 1993.
- [3] I. P. Kaminow and T. L. Koch, Eds., *Optical Fiber Telecommunications III* Academic Press, San Diego, CA, 1997.
- [4] I. P. Kaminow and T. Li, Eds., *Optical Fiber Telecommunications*, Vol. 4B, Academic Press, Boston, 2002.
- [5] B. Mukherjee, *Optical WDM Networks*, Springer, New York, 2006.
- [6] C. F. Lam, Ed., *Passive Optical Networks: Principles and Practice*, Academic Press, San Diego, CA, 2007.
- [7] I. P. Kaminow, T. Li, and A. E. Willner, Eds., *Optical Fiber Telecommunications*, Vol. 5B, Academic Press, Boston, 2008.
- [8] R. Ramaswami, K. Sivarajan, and G. Sasaki, *Optical Networks: A Practical Perspective*, 3rd ed., Morgan Kaufmann, San Francisco, 2009.
- [9] G. E. Keiser, *Optical Fiber Communications*, 4th ed., McGraw-Hill, New York, 2010.
- [10] L. Paraschis, O. Gerstel, and M. Y. Frankel, in *Optical Fiber Telecommunications*, Vol. 5B, I. P. Kaminow and T. Li, and A. E. Willner, Eds., Academic Press, Boston, 2008, Chap. 12.
- [11] E. Harstead and P. H. Van Heyningen, in *Optical Fiber Telecommunications*, Vol. 4B, I. P. Kaminow and T. Li, Eds., Academic Press, Boston, 2002.
- [12] R. E. Wagner, in *Optical Fiber Telecommunications*, Vol. 5B, I. P. Kaminow and T. Li, and A. E. Willner, Eds., Academic Press, Boston, 2008, Chap. 10.
- [13] K. Bergman, in *Optical Fiber Telecommunications*, Vol. 5B, I. P. Kaminow and T. Li, and A. E. Willner, Eds., Academic Press, Boston, 2008, Chap. 19.
- [14] F. E. Ross, *IEEE J. Sel. Areas Commun.* **7**, 1043 (1989).
- [15] J. L. Gimlett, M. Z. Iqbal, J. Young, L. Curtis, R. Spicer, and N. K. Cheung, *Electron. Lett.* **25**, 596 (1989).

- [16] S. Fujita, M. Kitamura, T. Torikai, N. Henmi, H. Yamada, T. Suzuki, I. Takano, and M. Shikada, *Electron. Lett.* **25**, 702 (1989).
- [17] C. Kleekamp and B. Metcalf, *Designer's Guide to Fiber Optics*, Cahners, Boston, 1978.
- [18] M. Eve, *Opt. Quantum Electron.* **10**, 45 (1978).
- [19] P. M. Rodhe, *J. Lightwave Technol.* **3**, 145 (1985).
- [20] D. A. Nolan, R. M. Hawk, and D. B. Keck, *J. Lightwave Technol.* **5**, 1727 (1987).
- [21] R. D. de la Iglesia and E. T. Azpitarte, *J. Lightwave Technol.* **5**, 1768 (1987).
- [22] G. P. Agrawal, *Nonlinear Fiber Optics*, 4th ed., Academic Press, San Diego, CA, 2001.
- [23] J. P. Hamaide, P. Emplit, and J. M. Gabriagues, *Electron. Lett.* **26**, 1451 (1990).
- [24] A. Mecozzi, *J. Opt. Soc. Am. B* **11**, 462 (1994).
- [25] A. Naka and S. Saito, *J. Lightwave Technol.* **12**, 280 (1994).
- [26] E. Lichtman, *J. Lightwave Technol.* **13**, 898 (1995).
- [27] F. Matera and M. Settembre, *J. Lightwave Technol.* **14**, 1 (1996); *Opt. Fiber Technol.* **4**, 34 (1998).
- [28] N. Kikuchi and S. Sasaki, *Electron. Lett.* **32**, 570 (1996).
- [29] D. Breuer, K. Obermann, and K. Petermann, *IEEE Photon. Technol. Lett.* **10**, 1793 (1998).
- [30] F. M. Madani and K. Kikuchi, *J. Lightwave Technol.* **17**, 1326 (1999).
- [31] A. Sano, Y. Miyamoto, S. Kuwahara, and H. Toba, *J. Lightwave Technol.* **18**, 1519 (2000).
- [32] F. Matera, A. Mecozzi, M. Romagnoli, and M. Settembre, *Opt. Lett.* **18**, 1499 (1993).
- [33] C. Lorattanasane and K. Kikuchi, *IEEE J. Quantum Electron.* **33**, 1084 (1997).
- [34] N. S. Bergano, J. Aspell, C. R. Davidson, P. R. Trischitta, B. M. Nyman, and F. W. Kerfoot, *Electron. Lett.* **27**, 1889 (1991).
- [35] T. Otani, K. Goto, H. Abe, M. Tanaka, H. Yamamoto, and H. Wakabayashi, *Electron. Lett.* **31**, 380 (1995).
- [36] M. Murakami, T. Takahashi, M. Aoyama, M. Amemiya, M. Sumida, N. Ohkawa, Y. Fukuda, T. Imai, and M. Aiki, *Electron. Lett.* **31**, 814 (1995).
- [37] T. Matsuda, A. Naka, and S. Saito, *Electron. Lett.* **32**, 229 (1996).
- [38] T. N. Nielsen, A. J. Stentz, K. Rottwitt, D. S. Vengsarkar, Z. J. Chen, P. B. Hansen, J. H. Park, K. S. Feder, S. Cabot, et al., *IEEE Photon. Technol. Lett.* **12**, 1079 (2000).
- [39] T. Zhu, W. S. Lee, and C. Scaphill, *Electron. Lett.* **37**, 15 (2001).
- [40] T. Matsuda, M. Murakami, and T. Imai, *Electron. Lett.* **37**, 237 (2001).
- [41] R. J. Sanferrare, *AT&T Tech. J.* **66** (1), 95 (1987).
- [42] C. Fan and L. Clark, *Opt. Photon. News* **6** (2), 26 (1995).
- [43] I. Jacobs, *Opt. Photon. News* **6** (2), 19 (1995).
- [44] B. Zhu, L. Leng, L. E. Nelson, Y. Qian, L. Cowsar, et al., *Electron. Lett.* **37**, 844 (2001).
- [45] S. Bigo, E. Lach, Y. Frignac, D. Hamoir, P. Sillard, et al., *Electron. Lett.* **37**, 448 (2001).
- [46] Y. Inada, H. Sugahara, K. Fukuchi, T. Ogata, and Y. Aoki, *IEEE Photon. Technol. Lett.* **14**, 1366 (2002).
- [47] B. Zhu, L. E. Nelson, S. Stulz, A. H. Gnauck, C. Doerr, J. Leuthold, L. Grner-Nielsen, M. O. Pedersen, J. Kim, and R. L. Lingle, *J. Lightwave Technol.* **22**, 208 (2004).
- [48] S. Bigo, *IEEE J. Sel. Topics Quantum Electron.* **10**, 329 (2004).
- [49] D. F. Grosz, A. Agarwal, S. Banerjee, D. N. Maywar, and A. P. Kung, *J. Lightwave Technol.* **22**, 423 (2004).
- [50] H. Suzuki, M. Fujiwara, and K. Iwatsuki, *J. Lightwave Technol.* **24**, 1998 (2006).
- [51] A. Gladisch, R.-P. Braun, D. Breuer, A. Ehrhardt, H.-M. Foisel, et al., *Proc. IEEE* **94**, 869 (2006).

- [52] A. H. Gnauck, G. Charlet, P. Tran, P. J. Winzer, C. R. Doerr, J. C. Centanni, E. C. Burrows, T. Kawanishi, T. Sakamoto, and K. Higuma, *J. Lightwave Technol.* **26**, 79 (2008).
- [53] A. Sano, H. Masuda, T. Kobayashi, et al., Proc. Opt. Fiber Commun. Conf., Paper PDPB7, 2010.
- [54] J. M. Sipress, Special issue, *AT&T Tech. J.* **73** (1), 4 (1995).
- [55] E. K. Stafford, J. Mariano, and M. M. Sanders, *AT&T Tech. J.* **73** (1), 47 (1995).
- [56] N. Bergano, in *Optical Fiber Telecommunications*, Vol. 4B, I. P. Kaminow and T. Li, Eds., Academic Press, Boston, CA, 2002.
- [57] P. B. Hansen, L. Eskildsen, S. G. Grubb, A. M. Vengsarkar, S. K. Korotky, et al., *Electron. Lett.* **31**, 1460 (1995).
- [58] L. Eskildsen, P. B. Hansen, S. G. Grubb, A. M. Vengsarkar, T. A. Strasser, et al., *IEEE Photon. Technol. Lett.* **8**, 724 (1996).
- [59] P. B. Hansen, L. Eskildsen, S. G. Grubb, A. M. Vengsarkar, S. K. Korotky, et al., *Electron. Lett.* **32**, 1018 (1996).
- [60] K. I. Suzuki, N. Ohkawa, M. Murakami, and K. Aida, *Electron. Lett.* **34**, 799 (1998).
- [61] J.-X. Cai, M. Nissov, C. R. Davidson, A. N. Pilipetskii, G. Mohs, et al., *J. Lightwave Technol.* **20**, 2247 (2002).
- [62] T. Tsuritani, K. Ishida, A. Agata, K. Shinonomura, I. Morita, et al., *J. Lightwave Technol.* **22**, 215 (2004).
- [63] G. Charlet, M. Salsi, P. Tran, M. Bertolini, H. Mardoyan, J. Renaudier, O. Bertran-Pardo, and S. Bigo, Optical Fiber Commun. Conf., Paper PDPB6 (Optical Society of America, 2009).
- [64] B. Bakhshi, M. Manna, G. Mohs, D. I. Kovsh, R. L. Lynch, et al., *J. Lightwave Technol.* **22**, 233 (2004).
- [65] N. Bergano, *J. Lightwave Technol.* **23**, 4125 (2005).
- [66] J.-X. Cai, C. R. Davidson, M. Nissov, H. Li, W. T. Anderson, et al., *J. Lightwave Technol.* **24**, 191 (2006).
- [67] A. N. Pilipetskii, *IEEE J. Sel. Topics Quantum Electron.* **12**, 484 (2006).
- [68] O. Gautheron, *C. R. Physique* **9**, xxx (2008).
- [69] P. E. Couch and R. E. Epworth, *J. Lightwave Technol.* **1**, 591 (1983).
- [70] T. Kanada, *J. Lightwave Technol.* **2**, 11 (1984).
- [71] A. M. J. Koonen, *IEEE J. Sel. Areas Commun.* **4**, 1515 (1986).
- [72] P. Chan and T. T. Tjhung, *J. Lightwave Technol.* **7**, 1285 (1989).
- [73] P. M. Shankar, *J. Opt. Commun.* **10**, 19 (1989).
- [74] G. A. Olson and R. M. Fortenberry, *Fiber Integ. Opt.* **9**, 237 (1990).
- [75] J. C. Goodwin and P. J. Vella, *J. Lightwave Technol.* **9**, 954 (1991).
- [76] C. M. Olsen, *J. Lightwave Technol.* **9**, 1742 (1991).
- [77] K. Abe, Y. Lacroix, L. Bonnell, and Z. Jakubczyk, *J. Lightwave Technol.* **10**, 401 (1992).
- [78] D. M. Kuchta and C. J. Mahon, *IEEE Photon. Technol. Lett.* **6**, 288 (1994).
- [79] C. M. Olsen and D. M. Kuchta, *Fiber Integ. Opt.* **14**, 121 (1995).
- [80] R. J. S. Bates, D. M. Kuchta, and K. P. Jackson, *Opt. Quantum Electron.* **27**, 203 (1995).
- [81] C.-L. Ho, *J. Lightwave Technol.* **17**, 1820 (1999).
- [82] G. C. Papen and G. M. Murphy, *J. Lightwave Technol.* **13**, 817 (1995).
- [83] H. Kosaka, A. K. Dutta, K. Kurihara, Y. Sugimoto, and K. Kasahara, *IEEE Photon. Technol. Lett.* **7**, 926 (1995).
- [84] K. Ogawa, *IEEE J. Quantum Electron.* **18**, 849 (1982).
- [85] W. R. Throssell, *J. Lightwave Technol.* **4**, 948 (1986).

- [86] J. C. Campbell, *J. Lightwave Technol.* **6**, 564 (1988).
- [87] G. P. Agrawal, P. J. Anthony, and T. M. Shen, *J. Lightwave Technol.* **6**, 620 (1988).
- [88] C. M. Olsen, K. E. Stubkjaer, and H. Olesen, *J. Lightwave Technol.* **7**, 657 (1989).
- [89] M. Mori, Y. Ohkuma, and N. Yamaguchi, *J. Lightwave Technol.* **7**, 1125 (1989).
- [90] W. Jiang, R. Feng, and P. Ye, *Opt. Quantum Electron.* **22**, 23 (1990).
- [91] R. S. Fyath and J. J. O'Reilly, *IEE Proc.* **137**, Pt. J, 230 (1990).
- [92] W.-H. Cheng and A.-K. Chu, *IEEE Photon. Technol. Lett.* **8**, 611 (1996).
- [93] G. P. Agrawal, *IEEE J. Quantum Electron.* **20**, 468 (1984).
- [94] G. P. Agrawal, N. A. Olsson, and N. K. Dutta, *Appl. Phys. Lett.* **45**, 597 (1984).
- [95] T. Fujita, S. Ishizuka, K. Fujito, H. Serizawa, and H. Sato, *IEEE J. Quantum Electron.* **20**, 492 (1984).
- [96] N. A. Olsson, W. T. Tsang, H. Temkin, N. K. Dutta, and R. A. Logan, *J. Lightwave Technol.* **3**, 215 (1985).
- [97] R. W. Tkach and A. R. Chraplyvy, *J. Lightwave Technol.* **4**, 1655 (1986).
- [98] G. P. Agrawal and T. M. Shen, *J. Lightwave Technol.* **4**, 58 (1986).
- [99] J. L. Gimlett and N. K. Cheung, *J. Lightwave Technol.* **7**, 888 (1989).
- [100] S. Yamamoto, N. Edagawa, H. Taga, Y. Yoshida, and H. Wakabayashi, *J. Lightwave Technol.* **8**, 1716 (1990).
- [101] G. P. Agrawal and N. K. Dutta, *Semiconductor Lasers*, 2nd ed., Van Nostrand Reinhold, New York, 1993.
- [102] A. T. Ryan, G. P. Agrawal, G. R. Gray, and E. C. Gage, *IEEE J. Quantum Electron.* **30**, 668 (1994).
- [103] K. Petermann, *IEEE J. Sel. Topics Quantum Electron.* **1**, 480 (1995).
- [104] R. S. Fyath and R. S. A. Waily, *Int. J. Opt.* **10**, 195 (1995).
- [105] M. Shikada, S. Takano, S. Fujita, I. Mito, and K. Minemura, *J. Lightwave Technol.* **6**, 655 (1988).
- [106] R. Heidemann, *J. Lightwave Technol.* **6**, 1693 (1988).
- [107] K.-P. Ho, J. D. Walker, and J. M. Kahn, *IEEE Photon. Technol. Lett.* **5**, 892 (1993).
- [108] D. A. Frisch and I. D. Henning, *Electron. Lett.* **20**, 631 (1984).
- [109] R. A. Linke, *Electron. Lett.* **20**, 472 (1984); *IEEE J. Quantum Electron.* **21**, 593 (1985).
- [110] T. L. Koch and J. E. Bowers, *Electron. Lett.* **20**, 1038 (1984).
- [111] F. Koyama and Y. Suematsu, *IEEE J. Quantum Electron.* **21**, 292 (1985).
- [112] A. H. Gnauck, B. L. Kasper, R. A. Linke, R. W. Dawson, T. L. Koch, T. J. Bridges, E. G. Burkhardt, R. T. Yen, D. P. Wilt, J. C. Campbell, K. C. Nelson, and L. G. Cohen, *J. Lightwave Technol.* **3**, 1032 (1985).
- [113] G. P. Agrawal and M. J. Potasek, *Opt. Lett.* **11**, 318 (1986).
- [114] P. J. Corvini and T. L. Koch, *J. Lightwave Technol.* **5**, 1591 (1987).
- [115] J. J. O'Reilly and H. J. A. da Silva, *Electron. Lett.* **23**, 992 (1987).
- [116] S. Yamamoto, M. Kuwazuru, H. Wakabayashi, and Y. Iwamoto, *J. Lightwave Technol.* **5**, 1518 (1987).
- [117] D. A. Atlas, A. F. Elrefaei, M. B. Romeiser, and D. G. Daut, *Opt. Lett.* **13**, 1035 (1988).
- [118] K. Hagimoto and K. Aida, *J. Lightwave Technol.* **6**, 1678 (1988).
- [119] H. J. A. da Silva, R. S. Fyath, and J. J. O'Reilly, *IEE Proc.* **136**, Pt. J, 209 (1989).
- [120] J. C. Cartledge and G. S. Burley, *J. Lightwave Technol.* **7**, 568 (1989).
- [121] J. C. Cartledge and M. Z. Iqbal, *IEEE Photon. Technol. Lett.* **1**, 346 (1989).
- [122] D. Sandel, S. Bhandare, A. F. Abas, B. Milivojevic, R. Noé, M. Guy, and M. Lapointe, *IEEE Photon. Technol. Lett.* **16**, 2568 (2004).

- [123] J. Baylis, *Error-Correcting Codes: A Mathematical Introduction*, Chapman and Hall, New York, 1998.
- [124] I. S. Reed and X. Chen, *Error-Control Coding for Data Networks*, Kluwer, Norwell, MA, 1999.
- [125] S. Gravano, *Introduction to Error-Control Code*, Oxford University Press, New York, 2001.
- [126] W. C. Huffman, *Fundamentals of Error-Correcting Codes*, Cambridge University Press, New York, 2003.
- [127] S. Yamamoto, H. Takahira, and M. Tanaka, *Electron. Lett.* **30**, 254 (1994).
- [128] J. L. Pamart, E. Lefranc, S. Morin, G. Balland, Y. C. Chen, T. M. Kissell, J. L. Miller, *Electron. Lett.* **30**, 342 (1994).
- [129] J. E. J. Alphonsus, P. B. Hansen, L. Eskildsen, D. A. Truxal, S. G. Grubb, D. J. DiGiovanni, T. A. Strasser, and E. C. Beck, *IEEE Photon. Technol. Lett.* **7**, 1495 (1995).
- [130] S. Sian, S. M. Webb, K. M. Guild, and D. R. Terrence, *Electron. Lett.* **32**, 50 (1996).
- [131] P. V. Kumar, M. Z. Win, H.-F. Lu, and C. N. Georghiades, in *Optical Fiber Telecommunications*, Vol. 4B, I. P. Kaminow and T. L. Koch, Eds., Academic Press, San Diego, CA, 2002, Chap. 17.
- [132] A. Agata, K. Tanaka, and N. Edagawa, *J. Lightwave Technol.* **20**, 2189 (2002).
- [133] B. V. Vasic, I. B. Djordjevic, and R. Kostuk, *J. Lightwave Technol.* **21**, 438 (2003).
- [134] I. B. Djordjevic, S. Sankaranarayanan, and B. V. Vasic, *J. Lightwave Technol.* **22**, 695 (2004).
- [135] N. W. Spellmeyer, J. C. Gottschalk, D. O. Caplan, and M. L. Stevens, *IEEE Photon. Technol. Lett.* **16**, 1579 (2004).
- [136] T. M. Shen and G. P. Agrawal, *J. Lightwave Technol.* **5**, 653 (1987).
- [137] A. F. Elrefaeia, J. K. Townsend, M. B. Romeiser, and K. S. Shanmugan, *IEEE J. Sel. Areas Commun.* **6**, 94 (1988).
- [138] M. K. Moaveni and M. Shafi, *J. Lightwave Technol.* **8**, 1064 (1990).
- [139] M. C. Jeruchim, P. Balaban, and K. S. Shamugan, *Simulation of Communication Systems*, Plenum Press, New York, 1992.
- [140] K. Hinton and T. Stephens, *IEEE J. Sel. Areas Commun.* **11**, 380 (1993).
- [141] A. J. Lowery and P. C. R. Gurney, *Appl. Opt.* **37**, 6066 (1998).
- [142] A. J. Lowery, O. Lenzmann, I. Koltchanov, et al., *IEEE J. Sel. Topics Quantum Electron.* **6**, 282 (2000).
- [143] F. Matera and M. Settembre, *IEEE J. Sel. Topics Quantum Electron.* **6**, 308 (2000).
- [144] X. Liu and B. Lee, *IEEE Photon. Technol. Lett.* **11**, 1549 (2003).
- [145] O. Sinkin, R. Holzlochner, J. Zweck, and C. R. Menyuk, *J. Lightwave Technol.* **21**, 61 (2003).
- [146] J. Leibrich and W. Rosenkranz, *IEEE Photon. Technol. Lett.* **15**, 395 (2003).
- [147] T. Kremp and W. Freude, *J. Lightwave Technol.* **23**, 149 (2005).
- [148] R. Scarmozzino, in *Optical Fiber Telecommunications*, Vol. 5A, I. P. Kaminow and T. Li, and A. E. Willner, Eds., Academic Press, Boston, 2008, Chap. 20.
- [149] X. Liu, F. Buchali, and R. W. Tkach, *J. Lightwave Technol.* **27**, 3632 (2009).

Chapter 6

Multichannel Systems

In principle, the capacity of an optical communication system can exceed 10 Tb/s because of a large frequency associated with the optical carrier. In practice, however, the bit rate was limited to 10 Gb/s or less until 1990 because of the limitations imposed by the dispersive and nonlinear effects and by the speed of electronic components. Since then, transmission of multiple optical channels over the same fiber has provided a simple way for extending the system capacity to beyond 1 Tb/s. Channel multiplexing can be done in the time or the frequency domain through time-division multiplexing (TDM) and frequency-division multiplexing (FDM), respectively. The TDM and FDM techniques can also be used in the electrical domain (see Section 1.2.2). To make the distinction explicit, it is common to refer to the two optical-domain techniques as *optical TDM* (OTDM) and *wavelength-division multiplexing* (WDM), respectively. The development of multichannel systems attracted considerable attention during the early 1990s, and WDM systems became available commercially by 1996.

This chapter is organized as follows. Sections 6.1 to 6.3 are devoted to WDM lightwave systems by considering in different sections the architectural aspects of such systems, the optical components needed for their implementation, and the performance issues such as interchannel crosstalk. Section 6.4 focuses on the basic concepts behind OTDM systems and issues related to their practical implementation. Subcarrier multiplexing, a scheme in which FDM is implemented in the microwave domain, is discussed in Section 6.5. The technique of code-division multiplexing is the focus of Section 6.6.

6.1 WDM Lightwave Systems

WDM corresponds to the scheme in which multiple optical carriers at different wavelengths are modulated by using independent electrical bit streams (which may themselves use TDM and FDM techniques in the electrical domain) and are then transmitted over the same fiber. The optical signal reaching the receiver is then demultiplexed into separate channels by using a suitable optical device. The WDM technique allows us to exploit the large bandwidth offered by optical fibers. For example, hundreds of 40-

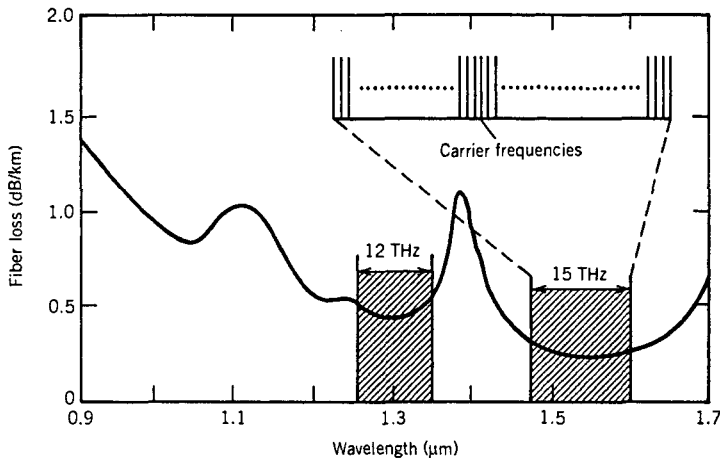


Figure 6.1: Low-loss transmission windows of silica fibers in the wavelength regions near 1.3 and 1.55 μm . The inset shows the WDM technique schematically.

Gb/s channels can be transmitted over the same fiber when channel spacing is reduced to near 100 GHz. Figure 6.1 shows the low-loss transmission windows of standard fibers centered near 1.3 and 1.55 μm . If the OH peak is eliminated using the so-called “dry” fibers, the total capacity of a WDM system may exceed 50 Tb/s.

The concept of WDM has been pursued since the first commercial lightwave system became available in 1980. In its simplest form, WDM was used as early as 1982 to transmit two channels in different transmission windows of an optical fiber. For example, an existing 0.85- μm lightwave system could be upgraded in capacity by adding another channel near 1.3 μm , resulting in a channel spacing of 450 nm. Considerable attention was directed during the 1980s toward reducing the channel spacing, and multichannel systems with a channel spacing of less than 0.1 nm had been demonstrated by 1990 [1]–[4]. However, it was during the decade of the 1990s that WDM systems were developed most aggressively [5]–[11]. Commercial WDM systems operating at 20–40 Gb/s first appeared around 1995, but their total capacity exceeded 1.6 Tb/s by the year 2000. Such systems employ hundreds of closely-spaced wavelengths and are referred to as dense WDM systems. Several laboratory experiments demonstrated in 2001 a system capacity of more than 10 Tb/s although their transmission distance was limited to below 200 km. By 2008, capacity of WDM systems approached 30 Tb/s [12]. Clearly, the advent of the WDM technique has led to a virtual revolution in designing lightwave systems. This section focuses on WDM systems by classifying them into three categories introduced in Section 5.1.

6.1.1 High-Capacity Point-to-Point Links

For long-haul fiber links forming the backbone of a telecommunication network, the role of WDM is simply to increase the total bit rate [13]. Figure 6.2 shows schematically such a point-to-point, high-capacity, WDM link. The output of several trans-

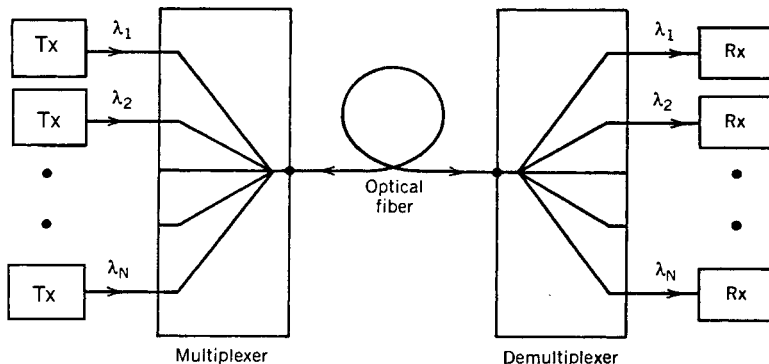


Figure 6.2: Multichannel point-to-point fiber link. Separate transmitter-receiver pairs are used to send and receive the signal at different wavelengths

mitters, each operating at its own carrier frequency (or wavelength), is multiplexed together. The multiplexed signal is launched into the optical fiber for transmission to the other end, where a demultiplexer sends each channel to its own receiver. When N channels at bit rates B_1, B_2, \dots, B_N are transmitted simultaneously over a fiber of length L , the total bit rate-distance product, BL , becomes

$$BL = (B_1 + B_2 + \dots + B_N)L. \quad (6.1.1)$$

For equal bit rates, the system capacity is enhanced by a factor of N . An early experiment in 1985 demonstrated the BL product of 1.37 (Tb/s)-km by transmitting 10 channels at 2 Gb/s over 68.3 km of standard fiber with a channel spacing of 1.35 nm [3].

The ultimate capacity of WDM fiber links depends on how closely channels can be packed in the wavelength domain. The minimum channel spacing is limited by interchannel crosstalk, an issue covered in Section 6.3. It is common to introduce a measure of the *spectral efficiency* of a WDM system as

$$\eta_s = B/\Delta\nu_{\text{ch}}, \quad (6.1.2)$$

where B is the channel bit rate and $\Delta\nu_{\text{ch}}$ is the channel spacing in frequency units. Attempts are made to make η_s as large as possible. For direct-detection systems, channel spacing must be larger than the bit rate B . In practice, spectral efficiency is often < 0.6 b/s/Hz, resulting in waste of considerable channel bandwidth.

The channel frequencies (or wavelengths) of WDM systems were initially standardized by the International Telecommunication Union (ITU) on a 100-GHz grid in the frequency range 186–196 THz (covering the C and L bands in the wavelength range 1530–1612 nm). For this reason, channel spacing for most commercial WDM systems is 100 GHz (0.8 nm at 1552 nm). This value leads to a spectral efficiency of only 0.1 b/s/Hz at a bit rate of 10 Gb/s. More recently, ITU has specified WDM channels with a frequency spacing of 50 GHz. The use of this channel spacing in combination with the bit rate of 40 Gb/s can increase spectral efficiency of direct-detection systems to 0.8 b/s/Hz. As discussed in Chapter 10, the use of coherent detection allows $\eta_s > 1$ b/s/Hz, and by 2009, values as large as 8 b/s/Hz have been realized [14].

Table 8.1 High-capacity WDM transmission experiments

Year	Channels <i>N</i>	Bit Rate <i>B</i> (Gb/s)	Capacity <i>NB</i> (Tb/s)	Distance <i>L</i> (km)	<i>NBL</i> Product [(Pb/s)-km]
2001	256	40	10.24	100	1.02
2001	273	40	10.92	117	1.28
2006	154	80	12.32	240	2.96
2007	320	80	25.60	240	6.14
2007	204	100	20.40	240	4.90
2009	320	100	32.00	580	18.56
2010	432	160	69.12	240	16.59

What is the ultimate capacity of WDM systems? The low-loss region of the state-of-the-art dry fibers (i.e., fibers with reduced OH-absorption near $1.4\text{ }\mu\text{m}$) extends over 300 nm in the wavelength region covering $1.3\text{--}1.6\text{ }\mu\text{m}$ (see Figure 6.1). The minimum channel spacing can be 25 GHz (0.2 nm) or less for 100-Gb/s channels if coherent detection is employed. Since 1500 channels with 0.2-nm spacing can be accommodated over a 300-nm bandwidth, the resulting capacity can be as large as 150 Tb/s. If we assume that such a WDM signal can be transmitted over 4000 km by using optical amplifiers with dispersion management, the effective *BL* product may eventually exceed 600 (Pb/s)-km with the use of WDM technology. This should be contrasted with the third-generation commercial lightwave systems, which transmitted a single channel over 80 km or so at a bit rate of up to 2.5 Gb/s, resulting in *BL* values of at most 0.2 (Tb/s)-km. Clearly, the use of WDM has the potential of improving the performance of modern lightwave systems by a factor of more than one million.

In practice, many factors limit the use of the entire low-loss window. Most optical amplifiers have a finite bandwidth (see Chapter 7). The number of channels is often limited by the bandwidth over which amplifiers can provide nearly uniform gain. The bandwidth of erbium-doped fiber amplifiers (EDFAs) is often limited to 40 nm even with the use of gain-flattening techniques (see Section 7.2.5). The use of Raman amplification in combination with EDFAs can extend the usable bandwidth to near 100 nm. Among other factors that limit the number of channels are (i) stability and tunability of distributed feedback (DFB) semiconductor lasers, (ii) signal degradation during transmission because of various nonlinear effects, and (iii) interchannel crosstalk during demultiplexing. In practice, high-capacity WDM fiber links require many high-performance components, such as transmitters integrating multiple DFB lasers, channel multiplexers and demultiplexers with add-drop capability, and large-bandwidth constant-gain amplifiers.

Experimental results on WDM systems can be divided into two groups based on whether the transmission distance is ~ 100 km or exceeds 1000 km. Since the 1985 experiment in which ten 2-Gb/s channels were transmitted over 68 km [3], both the number of channels and the bit rate of individual channels have increased considerably. A capacity of 340 Gb/s was demonstrated in 1995 by transmitting 17 channels, each operating at 20 Gb/s, over 150 km [16]. This was followed within a year by several

Table 8.1 High-capacity WDM Transoceanic Systems

Year	Channels <i>N</i>	Bit Rate <i>B</i> (Gb/s)	Capacity <i>NB</i> (Tb/s)	Distance <i>L</i> (km)	<i>NBL</i> Product [(Pb/s)-km]
2001	120	20	2.40	6,200	14.88
2002	256	10	2.56	11,000	28.16
2003	373	10	3.73	11,000	41.03
2004	150	40	6.00	6,120	36.72
2008	164	100	16.4	2,550	41.82
2009	72	100	7.20	7,040	50.69

experiments that realized a capacity of 1 Tb/s. By 2001, the capacity of WDM systems exceeded 10 Tb/s in several laboratory experiments. In one experiment, 273 channels, spaced 0.4-nm apart and each operating at 40 Gb/s, were transmitted over 117 km using three in-line amplifiers, resulting in a total bit rate of 11 Tb/s and a *BL* product of 1.3 (Pb/s)-km [17]. Table 8.1 lists several WDM transmission experiments in which system capacity exceeded 10 Tb/s [12]. The record capacity in 2010 occurred for a 69-Tb/s WDM system that transmitted 432 channels at 160 Gb/s over a distance of 240 km [15]. The shift in the bit rate of each channel toward 100 Gb/s after 2007 is due to the 100-Gb/s Ethernet transport standard developed in recent years.

The second group of WDM experiments involves transmission distances of more than 5000 km for submarine applications [18]–[22]. In a 1996 experiment, 100-Gb/s transmission (20 channels at 5 Gb/s) over 9100 km was realized using polarization scrambling with the forward-error correction (FEC) technique [18]. The pace of rapid development is evident when we note that, by 2001, a 2.4-Tb/s WDM signal (120 channels, each at 20 Gb/s) was transmitted over 6200 km, resulting in a *NBL* product of 15 (Pb/s)-km [19]. This should be compared with the first fiber-optic cable laid across the Atlantic ocean (TAT-8); it operated at 0.27 Gb/s with $NBL \approx 1.5$ (Tb/s)-km. The use of WDM had improved the capacity of undersea systems by a factor of 10,000 by 2001. Table 8.2 lists several WDM transmission experiments performed since 2001 [21]. The record *NBL* product of 101.8 (Pb/s)-km was realized in a 2010 experiment that transmitted 96 channels at 100 Gb/s over a distance of 10,608 km [23].

On the commercial side, WDM systems with a capacity of 40 Gb/s (16 channels at 2.5 Gb/s or 4 channels at 10 Gb/s) became available in 1996. Such a 16-channel system covered a wavelength range of about 12 nm in the 1.55-μm region with a channel spacing of 0.8 nm. WDM systems operating at 160 Gb/s (16 channels at 10 Gb/s) appeared in 1998. By 2001, dense WDM systems with a capacity of 1.6 Tb/s (realized by multiplexing 160 channels, each operating at 10 Gb/s) became available. After 2001, bursting of the so-called “telecom bubble” slowed down the demand of new WDM systems considerably. Nevertheless, fourth-generation WDM systems employing Raman amplification of a large number of 40-Gb/s channels had reached the commercial stage by 2003. This should be contrasted with the 10-Gb/s capacity of the third-generation systems available before the advent of the WDM technique. After 2007, commercial WDM systems have also moved toward a bit rate of 100 Gb/s per channel.

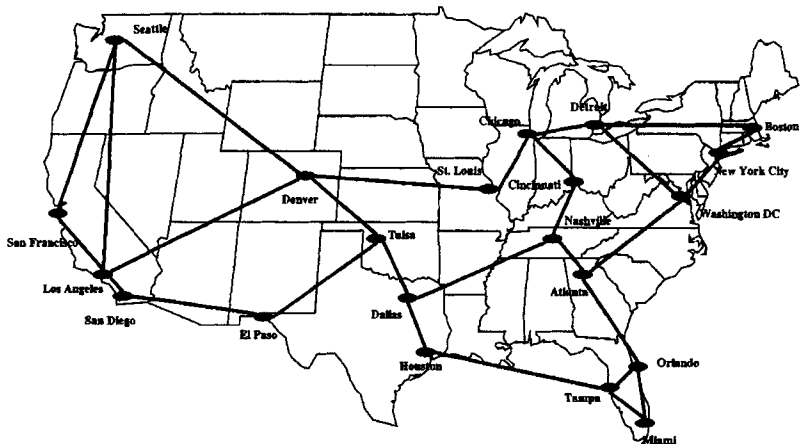


Figure 6.3: An example of a wide-area network in the form of several interconnected SONET rings. (After Ref. [24]; ©2000 IEEE; reproduced with permission.)

6.1.2 Wide-Area and Metro-Area Networks

Optical networks, as discussed in Section 5.1, are used to connect a large group of users spread over a geographical area. They can be classified as a local-area network (LAN), metropolitan-area network (MAN), or a wide-area network (WAN) depending on the area they cover [7]–[10]. All three types of networks can benefit from the WDM technology. They can be designed using the hub, ring, or star topology. A ring topology is most practical for MANs and WANs, while the star topology is commonly used for LANs. At the LAN level, a broadcast star is used to combine multiple channels. At the next level, several LANs are connected to a MAN by using passive wavelength routing. At the highest level, several MANs connect to a WAN whose nodes are interconnected in a mesh topology. At the WAN level, the network makes extensive use of switches and wavelength-shifting devices so that it is dynamically configurable.

Consider first a WAN covering a wide area (e.g., a country). Historically, telecommunication and computer networks (such as the Internet) occupying the entire U.S. geographical region have used a hub topology shown schematically in Figure 6.3. Such networks are often called mesh networks [24]. Hubs or nodes located in large metropolitan areas house electronic switches, which connect any two nodes either by creating a “virtual circuit” between them or by using *packet switching* through protocols such as TCP/IP (transmission control protocol/Internet protocol) and *asynchronous transfer mode* (ATM). With the advent of WDM during the 1990s, the nodes were connected through point-to-point WDM links, but the switching was being done electronically even in 2001. Such transport networks are termed “opaque” networks because they require optical-to-electronic conversion. As a result, neither the bit rate nor the modulation format can be changed without changing the switching equipment.

An all-optical network in which a WDM signal can pass through multiple nodes (possibly modified by adding or dropping certain channels) is called optically “trans-

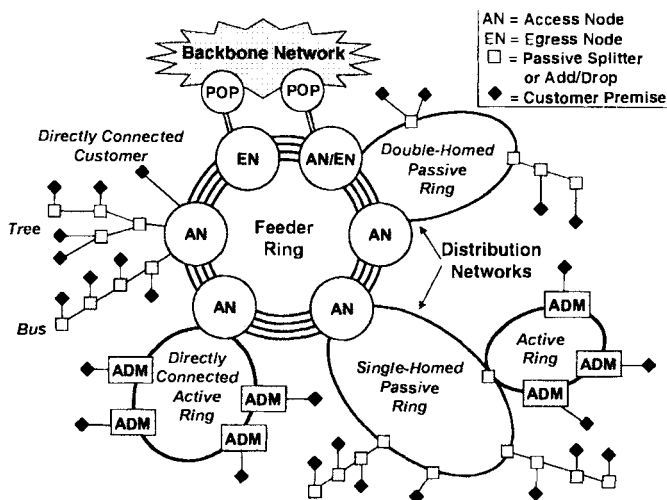


Figure 6.4: A WDM network with a feeder ring connected to several local distribution networks. (After Ref. [25]; ©1999 IEEE; reproduced with permission.)

parent.” Transparent WDM networks are desirable as they do not require demultiplexing and optical-to-electronic conversion of all WDM channels. As a result, they are not limited by the electronic-speed bottleneck and may help in reducing the cost of installing and maintaining the network. The nodes in a transparent WDM network (see Figure 6.3) switch channels using optical cross-connects. Such devices were still in their infancy in 2001.

An alternative topology implements a regional WDM network in the form of several interconnected rings. Figure 6.4 shows such a scheme schematically [25]. The feeder ring connects to the backbone of the network through an egress node. This ring employs four fibers to ensure robustness. Two of the fibers are used to route the data in the clockwise and counterclockwise directions. The other two fibers are called protection fibers and are used in case a point-to-point link fails (self-healing). The feeder ring supplies data to several other rings through access nodes. An add-drop multiplexer can be used at all nodes to drop and to add individual WDM channels. Dropped channels can be distributed to users using bus, tree, or ring networks. Notice that nodes are not always directly connected and require data transfer at multiple hubs. Such networks are called multihop networks.

Metro networks or MANs connect several central offices within a metropolitan area. The ring topology is also used for such networks. The main difference from the ring shown in Figure 6.4 stems from the scaling and cost considerations. The traffic flows in a metro ring at a modest bit rate compared with a WAN ring forming the backbone of a nationwide network. Typically, each channel operates at 2.5 Gb/s. To reduce the cost, a coarse WDM technique is used (in place of dense WDM common in the backbone rings) by using a channel spacing in the 2- to 10-nm range. Moreover, often just two fibers are used inside the ring, one for carrying the data and the other for protecting against a failure. Most metro networks were using electrical switching in 2001

although optical switching is the ultimate goal. In a test-bed implementation of an optically switched metro network, called the *multiwavelength optical network* (MONET), several sites within the Washington, DC, area of the United States were connected using a set of eight standard wavelengths in the $1.55\text{-}\mu\text{m}$ region with a channel spacing of 200 GHz [26]. MONET incorporated diverse switching technologies [synchronous digital hierarchy (SDH), asynchronous transfer mode (ATM), etc.] into an all-optical ring network using cross-connect switches based on the LiNbO_3 technology. Since then, several advances have improved considerably the state of the art of metro networks [27].

6.1.3 Multiple-Access WDM Networks

Multiple-access networks offer a random bidirectional access to each subscriber. Each user can receive and transmit information to any other user of the network at all times. Telephone networks provide one example; they are known as subscriber loop, local-loop, or access networks. Another example is provided by the Internet used for connecting multiple computers. In 2009, both the local-loop and computer networks were using electrical techniques to provide bidirectional access through circuit or packet switching. The main limitation of such techniques is that each node on the network must be capable of processing the entire network traffic. Since it is difficult to achieve electronic processing speeds in excess of 10 Gb/s, such networks are inherently limited by the electronics.

The use of WDM permits a novel approach in which the channel wavelength itself can be used for switching, routing, or distributing each channel to its destination, resulting in an all-optical network. Since wavelength is used for multiple access, such a WDM approach is referred to as *wavelength-division multiple access* (WDMA). A considerable amount of research and development work was done during the 1990s for developing WDMA networks [28]–[31]. Broadly speaking, WDMA networks can be classified into two categories, called single-hop and multihop all-optical networks [7]. Every node is directly connected to all other nodes in a single-hop network, resulting in a fully connected network. In contrast, multihop networks are only partially connected such that an optical signal sent by one node may require several hops through intermediate nodes before reaching its destination. In each category, transmitters and receivers can have their operating frequencies either fixed or tunable.

Several architectures can be used for all-optical multihop networks [7]–[10]. Hypercube architecture provides one example—it has been used for interconnecting multiple processors in a supercomputer [32]. The hypercube configuration can be easily visualized in three dimensions such that eight nodes are located at eight corners of a simple cube. In general, the number of nodes N must be of the form 2^m , where m is the dimensionality of the hypercube. Each node is connected to m different nodes. The maximum number of hops is limited to m , while the average number of hops is about $m/2$ for large N . Each node requires m receivers. The number of receivers can be reduced by using a variant, known as the deBruijn network, but it requires more than $m/2$ hops on average. Another example of a multihop WDM network is provided by the *shuffle network* or its bidirectional equivalent—the Banyan network.

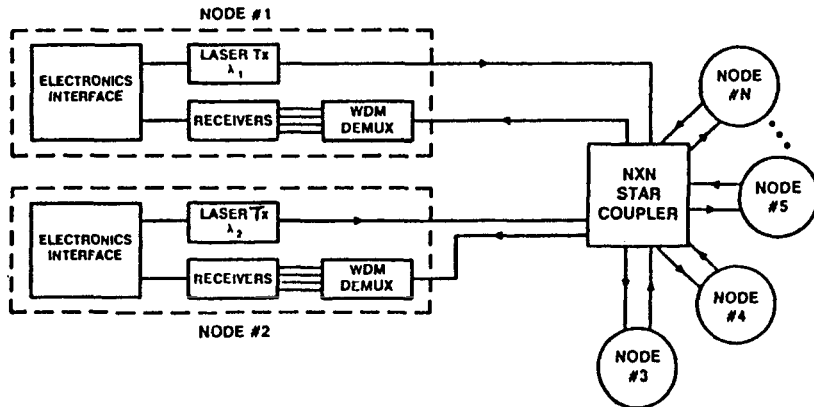


Figure 6.5: Schematic of the Lambdanet with N nodes. Each node consists of one transmitter and N receivers. (After Ref. [33]; ©1990 IEEE; reprinted with permission.)

Figure 6.5 shows an example of the single-hop WDM network based on the use of a *broadcast star*. This network, called the *Lambdanet* [33], is an example of the *broadcast-and-select* network. The new feature of the Lambdanet is that each node is equipped with one transmitter emitting at a unique wavelength and N receivers operating at the N wavelengths, where N is the number of nodes. The output of all transmitters is combined in a passive star and distributed to all receivers equally. Each node receives the entire traffic flowing across the network. A tunable optical filter can be used to select the desired channel. In the case of the Lambdanet, each node uses a bank of receivers in place of a tunable filter. This feature creates a nonblocking network whose capacity and connectivity can be reconfigured electronically depending on the application. The network is also transparent to the bit rate or the modulation format. Different users can transmit data at different bit rates with different modulation formats. The flexibility of the Lambdanet makes it suitable for many applications. The main drawback of the Lambdanet is that the number of users is limited by the number of available wavelengths. Moreover, each node requires many receivers (equal to the number of nodes), resulting in a considerable investment in hardware costs.

A tunable receiver can reduce the cost and complexity of the Lambdanet. This is the approach adopted for the *Rainbow network* [34]. This network can support up to 32 nodes, each of which can transmit 1-Gb/s signals over 10–20 km. It makes use of a central passive star (see Figure 6.5) together with the high-performance parallel interface for connecting multiple computers. A tunable optical filter is used to select the unique wavelength associated with each node. The main shortcoming of the Rainbow network is that tuning of receivers is a relatively slow process, making it difficult to use packet switching. An example of the WDM network that uses packet switching is provided by the *Starnet*. It can transmit data at bit rates of up to 1.25 Gb/s per node over a 10-km diameter while maintaining an SNR close to 24 dB [35].

WDM networks making use of a passive star coupler are often called *passive optical networks* (PONs) because they avoid active switching. PONs have the potential

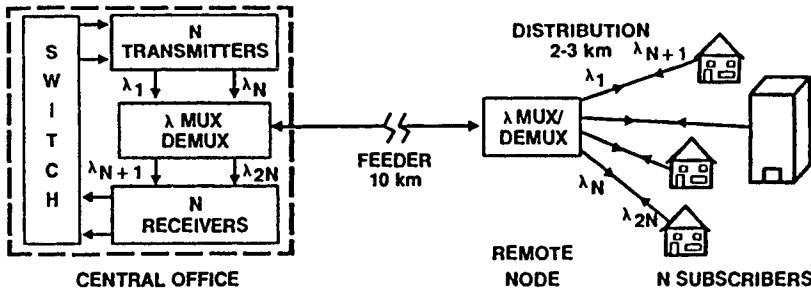


Figure 6.6: Passive photonic loop for local-loop applications. (After Ref. [36]; ©1988 IEE; reprinted with permission.)

for bringing optical fibers to the home (or at least to the curb). In one scheme, called a *passive photonic loop* [36], multiple wavelengths are used for routing signals in the local loop. Figure 6.6 shows a block diagram of such a network. The central office contains N transmitters emitting at wavelengths $\lambda_1, \lambda_2, \dots, \lambda_N$ and N receivers operating at wavelengths $\lambda_{N+1}, \dots, \lambda_{2N}$ for a network of N subscribers. The signals to each subscriber are carried on separate wavelengths in each direction. A remote node multiplexes signals from the subscribers to send the combined signal to the central office. It also demultiplexes signals for individual subscribers. The remote node is passive and requires little maintenance if passive WDM components are used. A switch at the central office routes signals depending on their wavelengths.

Since 2001, access networks for telecommunication applications have evolved considerably [37]–[39]. Proposed architectures include broadband PON (B-PON), Gb/s-PON (G-PON), and Gigabit Ethernet PON (GE-PON). The goal is to provide broadband access to each user and to deliver audio, video, and data channels on demand, while keeping the cost down. Indeed, many low-cost WDM components are being developed for this purpose. Some of these are covered in the next section devoted to WDM components.

6.2 WDM Components

The implementation of WDM technology for fiber-optic communication systems requires several new optical components [40]. Among them are multiplexers that combine the output of several transmitters and launch it into an optical fiber (see Figure 6.2); demultiplexers which split the received multichannel signal into individual channels destined to different receivers; star couplers that mix the output of several transmitters and broadcast the mixed signal to multiple receivers (see Figure 6.5); tunable optical filters which filter out one channel at a specific wavelength that can be changed by tuning the passband of the optical filter; multiwavelength optical transmitters whose wavelength can be tuned over a few nanometers; add–drop multiplexers and optical routers that can distribute a WDM signal to different ports.

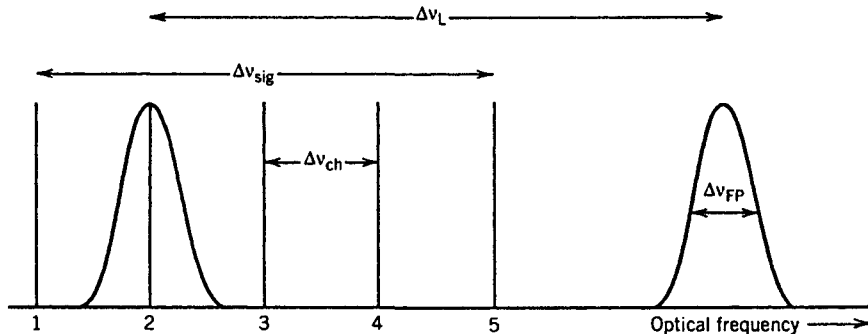


Figure 6.7: Channel selection through a tunable optical filter.

6.2.1 Tunable Optical Filters

It is instructive to consider optical filters first since they are often the building blocks of more complex WDM components. The role of a tunable optical filter in a WDM system is to select a desired channel at the receiver. Figure 6.7 shows the selection mechanism schematically. The filter bandwidth must be large enough to transmit the desired channel but, at the same time, small enough to block the neighboring channels.

All optical filters require a wavelength-selective mechanism and can be classified into two broad categories depending on whether optical interference or diffraction is the underlying physical mechanism. Each category can be further subdivided according to the scheme adopted. In this section we consider four kinds of optical filters; Figure 6.8 shows an example of each kind. The desirable properties of a tunable optical filter include: (1) wide tuning range to maximize the number of channels that can be selected, (2) negligible crosstalk to avoid interference from adjacent channels, (3) fast tuning speed to minimize the access time, (4) small insertion loss, (5) polarization insensitivity, (6) stability against environmental changes (humidity, temperature, vibrations, etc.), and (7) last but not the least, low cost.

Fabry–Perot Filters

A Fabry–Perot (FP) interferometer—a cavity formed by using two mirrors—can act as a tunable optical filter if its length is controlled electronically by using a piezoelectric transducer [see Figure 6.8(a)]. The transmittivity of a FP filter peaks at wavelengths that correspond to the longitudinal-mode frequencies given in Eq. (3.3.5). Hence, the frequency spacing between two successive transmission peaks, known as the *free spectral range*, is given by

$$\Delta v_L = c / (2n_g L), \quad (6.2.1)$$

where n_g is the group index of the intracavity material for a FP filter of length L .

If the filter is designed to pass a single channel (see Figure 6.7), the combined bandwidth of the multichannel signal, $\Delta v_{\text{sig}} = N\Delta v_{\text{ch}} = NB/\eta_s$, must be less than Δv_L , where N is the number of channels, η_s is the spectral efficiency, and B is the bit rate. At the same time, the filter bandwidth Δv_{FP} (the width of the transmission peak in

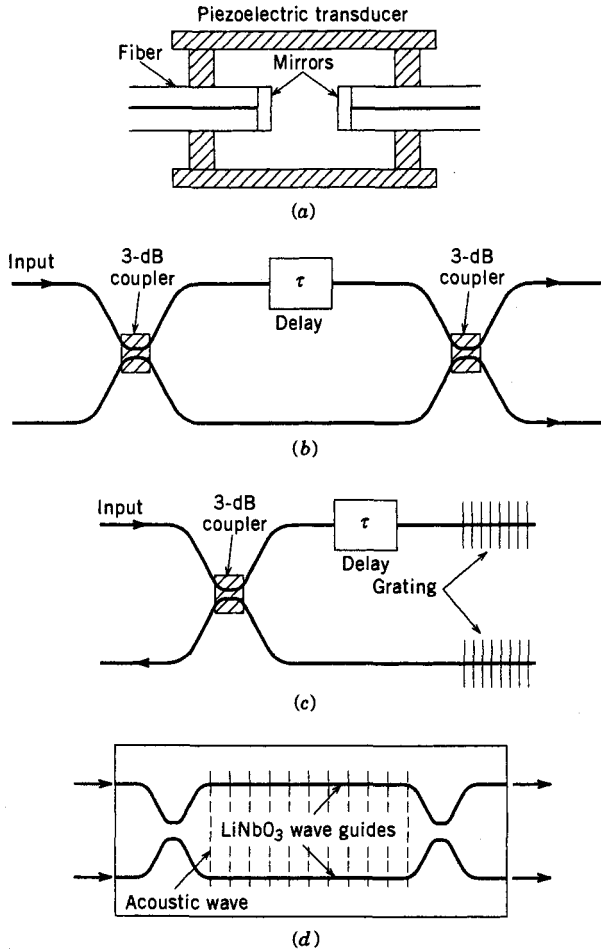


Figure 6.8: Four kinds of filters based on various interferometric and diffractive devices: (a) Fabry-Perot filter; (b) Mach-Zehnder filter; (c) grating-based Michelson filter; (d) acousto-optic filter. The shaded area represents a surface acoustic wave.

Figure 6.7) should be large enough to pass the entire frequency contents of the selected channel. Typically, $\Delta v_{FP} \sim B$. The number of channels is thus limited by

$$N < \eta_s (\Delta v_L / \Delta v_{FP}) = \eta_s F, \quad (6.2.2)$$

where $F = \Delta v_L / \Delta v_{FP}$ is the *finesse* of the FP filter. The concept of finesse is well known in the theory of FP interferometers [41]. If internal losses are neglected, the finesse is given by $F = \pi\sqrt{R}/(1-R)$ and is determined solely by the mirror reflectivity R , assumed to be the same for both mirrors [41].

Equation (6.2.2) provides a remarkably simple condition for the number of channels that a FP filter can resolve. As an example, if $\eta_s = \frac{1}{3}$, a FP filter with 99% reflecting

mirrors can select up to 104 channels. Channel selection is made by changing the filter length L electronically. The length needs to be changed by only a fraction of the wavelength to tune the filter. The filter length L itself is determined from Eq. (6.2.1) together with the condition $\Delta v_L > \Delta v_{\text{sig}}$. As an example, for a 10-channel WDM signal with 0.8-nm channel spacing, $\Delta v_{\text{sig}} \approx 1 \text{ THz}$. If $n_g = 1.5$ is used for the group index, L should be smaller than $100 \mu\text{m}$. Such a short length together with the requirement of high mirror reflectivities underscores the complexity of the design of FP filters for WDM applications.

A practical all-fiber design of FP filters uses the air gap between two optical fibers (see Figure 6.8). The two fiber ends forming the gap are coated to act as high-reflectivity mirrors [42]. The entire structure is enclosed in a piezoelectric chamber so that the gap length can be changed electronically for tuning and selecting a specific channel. The advantage of fiber FP filters is that they can be integrated within the system without incurring coupling losses. Such filters were used in commercial WDM fiber links starting in 1996. The number of channels is typically limited to below 100 ($F \approx 155$ for the 98% mirror reflectivity) but can be increased using two FP filters in tandem. Although tuning is relatively slow because of the mechanical nature of the tuning mechanism, it suffices for some applications.

Tunable FP filters can also be made using several other materials such as liquid crystals and semiconductor waveguides [43]–[48]. Liquid-crystal-based filters make use of the anisotropic nature of liquid crystals that makes it possible to change the refractive index electronically. A FP cavity is still formed by enclosing the liquid-crystal material within two high-reflectivity mirrors, but the tuning is done by changing the refractive index rather than the cavity length. Such FP filters can provide high finesse ($F \sim 300$) with a bandwidth of about 0.2 nm [43]. They can be tuned electrically over 50 nm, but switching time is typically $\sim 1 \text{ ms}$ or more when nematic liquid crystals are used. It can be reduced to below $10 \mu\text{s}$ by using smectic liquid crystals [44].

Thin dielectric films are commonly used for making narrow-band interference filters [45]. The basic idea is quite simple. A stack of suitably designed thin films acts as a high-reflectivity mirror. If two such mirrors are separated by a spacer dielectric layer, a FP cavity is formed that acts as an optical filter. The bandpass response can be tailored for a multicavity filter formed by using multiple thin-film mirrors separated by several spacer layers. Tuning can be realized in several different ways. In one approach, an InGaAsP/InP waveguide permits electronic tuning [46]. Silicon-based FP filters can be tuned using thermo-optic tuning [47]. Micromechanical tuning has also been used for InAlGaAs-based FP filters [48]. Such filters exhibited a tuning range of 40 nm with $< 0.35 \text{ nm}$ bandwidth in the $1.55-\mu\text{m}$ region.

Mach-Zehnder Filters

A chain of Mach-Zehnder (MZ) interferometers can also be used for making a tunable optical filter [49]–[51]. A MZ interferometer can be constructed simply by connecting the two output ports of a 3-dB coupler to the two input ports of another 3-dB coupler [see Figure 6.8(b)]. The first coupler splits the input signal equally into two parts, which acquire different phase shifts (if the arm lengths are made different) before they interfere at the second coupler. Since the relative phase shift is wavelength dependent,

the transmittivity $T(v)$ is also wavelength dependent. In fact, we can use Eq. (7.5.5) to find that $T(v) = |H(v)|^2 = \cos^2(\pi v \tau)$, where $v = \omega/2\pi$ is the frequency and τ is the relative delay in the two arms of the MZ interferometer [52]. A cascaded chain of such MZ interferometers with relative delays adjusted suitably acts as an optical filter that can be tuned by changing the arm lengths slightly. Mathematically, the transmittivity of a chain of M such interferometers is given by

$$T(v) = \prod_{m=1}^M \cos^2(\pi v \tau_m), \quad (6.2.3)$$

where τ_m is the relative delay in the m th member of the chain.

A commonly used method implements the relative delays τ_m such that each MZ stage blocks the alternate channels successively. This scheme requires $\tau_m = (2^m \Delta v_{ch})^{-1}$ for a channel spacing of Δv_{ch} . The resulting transmittivity of a 10-stage MZ chain has channel selectivity as good as that offered by a FP filter having a finesse of 1600. Moreover, such a filter is capable of selecting closely spaced channels. The MZ chain can be built by using fiber couplers or by using silica waveguides on a silicon substrate. The silica-on-silicon technology was exploited extensively during the 1990s to make many WDM components. Such devices are referred to as *planar lightwave circuits* because they use planar optical waveguides formed on a silicon substrate [53]–[56]. Tuning in MZ filters is realized through a chromium heater deposited on one arm of each MZ interferometer. Since the tuning mechanism is thermal, its use results in a slow response with a switching time of about 1 ms.

Grating-Based Filters

A separate class of tunable optical filters makes use of the wavelength selectivity provided by a Bragg grating. Fiber Bragg gratings provide a simple example of grating-based optical filters [57]. In its simplest form, a fiber grating acts as a reflection filter whose central wavelength can be controlled by changing the grating period, and whose bandwidth can be tailored by changing the grating strength or by chirping the grating period slightly. The reflective nature of fiber gratings is often a limitation in practice and requires the use of an *optical circulator*. A phase shift in the middle of the grating can convert a fiber grating into a narrowband transmission filter [58]. Many other schemes can be used to make transmission filters based on fiber gratings. In one approach, fiber gratings are used as mirrors of a FP filter, resulting in transmission filters whose free spectral range can vary over a wide range 0.1–10 nm [59]. In another design, a grating is inserted in each arm of a MZ interferometer to provide a transmission filter [57]. Other kinds of interferometers, such as the *Sagnac* and *Michelson* interferometers, can also be used to realize transmission filters. Figure 6.8(c) shows an example of the Michelson interferometer made by using a 3-dB fiber coupler and two fiber gratings acting as mirrors for the two arms of the Michelson interferometer [60]. Most of these schemes can also be implemented in the form of a planar lightwave circuit by forming silica waveguides on a silicon substrate.

Many other grating-based filters have been developed for WDM systems [61]–[68]. In one scheme, borrowed from the DFB-laser technology, the InGaAsP/InP material

system is used to form planar waveguides functioning near $1.55\text{ }\mu\text{m}$. The wavelength selectivity is provided by a built-in grating whose Bragg wavelength is tuned electrically through electrorefraction [61]. A phase-control section, similar to that used for multisegment DFB lasers, have also been used to tune distributed Bragg reflector (DBR) filters. Multiple gratings, each tunable independently, can also be used to make tunable filters [62]. Such filters can be tuned quickly (in a few nanoseconds) and can be designed to provide net gain since one or more amplifiers can be integrated with the filter. They can also be integrated with the receiver, as they use the same semiconductor material. These two properties of InGaAsP/InP filters make them quite attractive for WDM applications.

The spectral response of a fiber grating can be tuned either by heating or by compressing the grating so that either the effective mode index or the physical grating period changes in a prescribed manner. Tuning over a range of 40 nm was realized in 2002 by using the compression technique [66]. Another problem with grating filters is that they do not exhibit periodic filtering characteristics because a grating has a single stop band centered at the Bragg wavelength. This property can be changed by making a superstructure or sampled grating [68]. Such gratings contain multiple subgratings, separated by sections with a uniform refractive index, and are called superstructure gratings because of their doubly periodic nature. They are discussed in Section 8.4 in the context of dispersion compensation.

Acousto-Optic Filters

In another class of tunable filters, the grating is formed dynamically by using acoustic waves. Such filters, called *acousto-optic filters*, exhibit a wide tuning range ($> 100\text{ nm}$) and are quite suitable for WDM applications [69]–[73]. The physical mechanism behind the operation of acousto-optic filters is the *photoelastic effect* through which an acoustic wave propagating through an acousto-optic material creates periodic changes in the refractive index (corresponding to the regions of local compression and rarefaction). In effect, the acoustic wave creates a periodic index grating that can diffract an optical beam. Wavelength selectivity stems from this acoustically induced grating. When a transverse electric (TE) wave with the propagation vector \mathbf{k} is diffracted from this grating, its polarization can be changed from TE to transverse magnetic (TM) if the *phase-matching condition* $\mathbf{k}' = \mathbf{k} \pm \mathbf{K}_a$ is satisfied, where \mathbf{k}' and \mathbf{K}_a are the wave vectors associated with the TM and acoustic waves, respectively.

Acousto-optic tunable filters can be made by using bulk components as well as waveguides, and both kinds are available commercially. For WDM applications, the LiNbO₃ waveguide technology is often used since it can produce compact, polarization-independent, acousto-optic filters with a bandwidth of about 1 nm and a tuning range over 100 nm [70]. The basic design, shown schematically in Figure 6.8(d), uses two polarization beam splitters, two LiNbO₃ waveguides, a surface-acoustic-wave transducer, all integrated on the same substrate. The incident WDM signal is split into its orthogonally polarized components by the first beam splitter. The channel whose wavelength λ satisfies the Bragg condition $\lambda = (\Delta n)\Lambda_a$ is directed to a different output port by the second beam splitter because of an acoustically induced change in its polarization direction; all other channels go to the other output port. The TE–TM index difference

Δn is about 0.07 in LiNbO₃. Near $\lambda = 1.55 \mu\text{m}$, the acoustic wavelength Λ_a should be about $22 \mu\text{m}$. This value corresponds to a frequency of about 170 MHz if we use the acoustic velocity of 3.75 km/s for LiNbO₃. Such a frequency can be easily applied. Moreover, its exact value can be changed electronically to change the wavelength that satisfies the Bragg condition. Tuning is relatively fast because of its electronic nature and can be accomplished in a switching time of less than 10 μs . Acousto-optic tunable filters are also suitable for wavelength routing and optical cross-connect applications in dense WDM systems.

Amplifier-Based Filters

Another category of tunable optical filters operates on the principle of amplification of a selected channel. Any amplifier with a gain bandwidth smaller than the channel spacing can be used as an optical filter. Tuning is realized by changing the wavelength at which the gain peak occurs. Stimulated Brillouin scattering (SBS), occurring naturally in silica fibers [74], can be used for selective amplification of one channel, but the gain bandwidth is quite small (< 100 MHz). The SBS phenomenon involves interaction between the optical and acoustic waves and is governed by a phase-matching condition similar to that found for acousto-optic filters. As discussed in Section 2.6, SBS occurs only in the backward direction and results in a frequency shift of about 10 GHz in the $1.55\text{-}\mu\text{m}$ region.

To use the SBS amplification as a tunable optical filter, a continuous-wave (CW) pump beam is launched at the receiver end of the optical fiber in a direction opposite to that of the multichannel signal, and the pump wavelength is tuned to select the channel. The pump beam transfers a part of its energy to a channel down-shifted from the pump frequency by exactly the Brillouin shift. A tunable pump laser is a prerequisite for this scheme. The bit rate of each channel is even then limited to 100 MHz or so. In a 1989 experiment in which a 128-channel WDM network was simulated by using two 8×8 star couplers [75], a 150-Mb/s channel could be selected with a channel spacing as small as 1.5 GHz.

Semiconductor optical amplifiers (SOAs) can also be used for channel selection provided that a DFB structure is used to narrow the gain bandwidth [76]. A built-in grating can easily provide a filter bandwidth below 1 nm. Tuning is achieved using a *phase-control section* in combination with a shift of Bragg wavelength through electrorefraction. In fact, such amplifiers are nothing but multisectioin semiconductor lasers with antireflection coatings. In one experimental demonstration, two channels operating at 1 Gb/s and separated by 0.23 nm could be separated by selective amplification (> 10 dB) of one channel [77]. Four-wave mixing in an SOA can also be used to form a tunable filter whose center wavelength is determined by the pump laser [78].

6.2.2 Multiplexers and Demultiplexers

Multiplexers and demultiplexers are the essential components of any WDM system. Similar to the case of optical filters, demultiplexers require a wavelength-selective mechanism and can be classified into two broad categories. Diffraction-based demultiplexers employ an angularly dispersive element, such as a diffraction grating, which

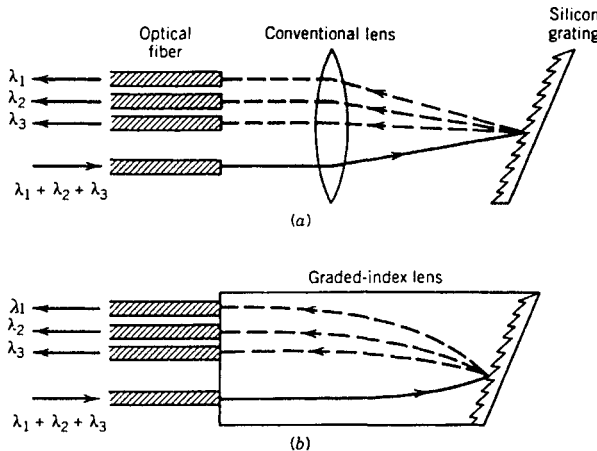


Figure 6.9: Grating-based demultiplexer making use of (a) a conventional lens and (b) a graded-index lens.

disperses incident light spatially into various wavelength components. Interference-based demultiplexers make use of devices such as optical filters and directional couplers. In both cases, the same device can be used as a multiplexer or a demultiplexer, depending on the direction of propagation, because of the inherent reciprocity of optical waves in dielectric media.

Grating-based demultiplexers use the phenomenon of Bragg diffraction from an optical grating [79]–[82]. Figure 6.9 shows the design of two such demultiplexers. The input WDM signal is focused onto a reflection grating, which separates various wavelength components spatially, and a lens focuses them onto individual fibers. Use of a graded-index lens simplifies alignment and provides a relatively compact device. The focusing lens can be eliminated altogether by using a concave grating. For a compact design, the concave grating can be integrated within a silicon slab waveguide [1]. In a different approach, multiple elliptical Bragg gratings are etched using the silicon technology [79]. The idea behind this approach is simple. If the input and output fibers are placed at the two foci of the elliptical grating, and the grating period Λ is adjusted to a specific wavelength λ_0 by using the Bragg condition $2\Delta n_{\text{eff}} = \lambda_0$, where n_{eff} is the effective index of the waveguide mode, the grating would selectively reflect that wavelength and focus it onto the output fiber. Multiple gratings need to be etched, as each grating reflects only one wavelength. Because of the complexity of such a device, a single concave grating etched directly onto a silica waveguide is more practical. Such a grating can be designed to demultiplex up to 120 channels with a wavelength spacing of 0.3 nm [81].

A problem with grating demultiplexers is that their bandpass characteristics depend on the dimensions of the input and output fibers. In particular, the core size of output fibers must be large to ensure a flat passband and low insertion losses. For this reason, most early designs of multiplexers used multimode fibers. In a 1991 design, a microlens array was used to solve this problem and to demonstrate a 32-channel multi-

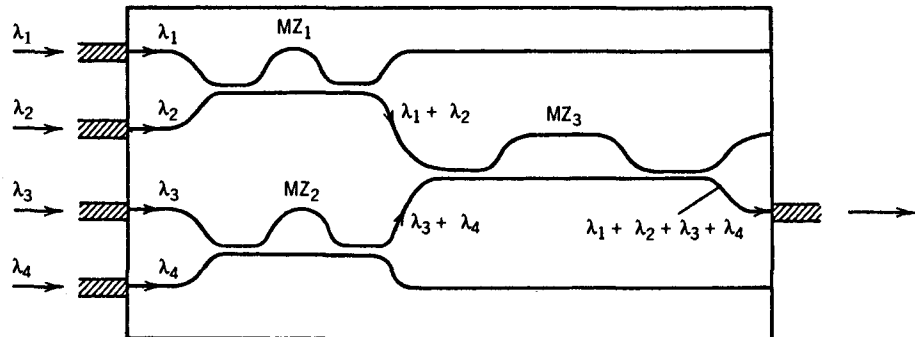


Figure 6.10: Layout of an integrated four-channel waveguide multiplexer based on Mach-Zehnder interferometers. (After Ref. [84]; ©1988 IEEE; reprinted with permission.)

plexer for single-mode fiber applications [83]. The fiber array was produced by fixing single-mode fibers in V-shaped grooves etched into a silicon wafer. The microlens transforms the relatively small mode diameter of fibers ($\sim 10 \mu\text{m}$) into a much wider diameter (about $80 \mu\text{m}$) just beyond the lens. This scheme provides a multiplexer that can work with channels spaced by only 1 nm in the wavelength region near $1.55 \mu\text{m}$ while accommodating a channel bandwidth of 0.7 nm.

Filter-based demultiplexers use the phenomenon of optical interference to select the wavelength [1]. Demultiplexers based on the MZ filter have attracted the most attention. Similar to the case of a tunable optical filter, several MZ interferometers are combined to form a WDM demultiplexer [84]–[86]. A 128-channel multiplexer fabricated with the silica-waveguide technology was fabricated by 1989 [85]. Figure 6.10 illustrates the basic concept by showing the layout of a four-channel multiplexer. It consists of three MZ interferometers. One arm of each MZ interferometer is made longer than the other to provide a wavelength-dependent phase shift between the two arms. The path-length difference is chosen such that the total input power from two input ports at different wavelengths appears at only one output port. The whole structure can be fabricated on a silicone substrate using SiO_2 waveguides in the form of a planar lightwave circuit.

Fiber Bragg gratings can also be used for making all-fiber demultiplexers. In one approach, a $1 \times N$ fiber coupler is converted into a demultiplexer by forming a *phase-shifted grating* at the end of each output port, opening a narrowband transmission window ($\sim 0.1 \text{ nm}$) within the stop band [58]. The position of this window is varied by changing the amount of phase shift so that each arm of the $1 \times N$ fiber coupler transmits only one channel. The fiber-grating technology can be applied to form Bragg gratings directly on a planar silica waveguide. This approach has attracted attention since it permits integration of Bragg gratings within planar lightwave circuits. Such gratings were incorporated in an asymmetric MZ interferometer (unequal arm lengths) resulting in a compact multiplexer [87].

It is possible to construct multiplexers by using multiple directional couplers. The basic scheme is similar to that shown in Figure 6.10 but simpler as MZ interferometers

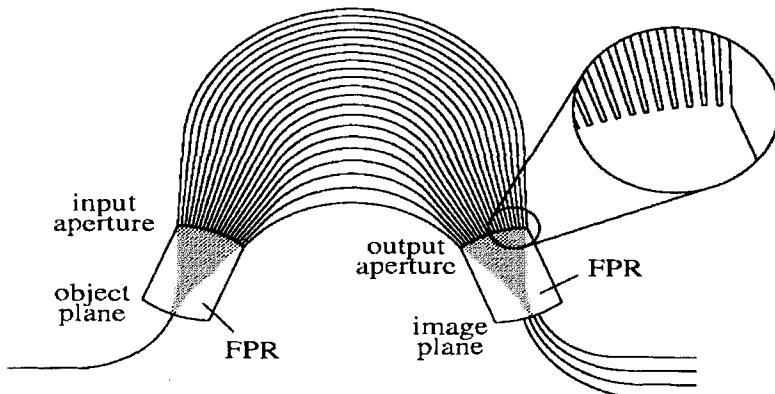


Figure 6.11: Schematic of a waveguide-grating demultiplexer consisting of an array of waveguides between two free-propagation regions (FPR). (After Ref. [89]; ©1996 IEEE; reprinted with permission.)

are not used. Furthermore, an all-fiber multiplexer made by using fiber couplers avoids coupling losses that occur whenever light is coupled into or out of an optical fiber. A fused biconical taper can also be used for making fiber couplers [88]. Multiplexers based on fiber couplers can be used only when channel spacing is relatively large (> 10 nm) and are thus suitable mostly for coarse WDM applications.

From the standpoint of system design, integrated demultiplexers with low insertion losses are preferred. An interesting approach uses a *phased array* of optical waveguides that acts as a grating. Such gratings are called *arrayed waveguide* gratings (AWGs) and have attracted considerable attention because they can be fabricated using the silicon, InP, or LiNbO₃ technology [89]–[95]. In the case of silica-on-silicon technology, they are useful for making planar lightwave circuits [93]. AWGs can be used for a variety of WDM applications and are discussed later in the context of WDM routers.

Figure 6.11 shows the design of a waveguide-grating demultiplexer, also known as a phased-array demultiplexer [89]. The incoming WDM signal is coupled into an array of planar waveguides after passing through a free-propagation region in the form of a lens. In each waveguide, the WDM signal experiences a different phase shift because of different lengths of waveguides. Moreover, the phase shifts are wavelength dependent because of the frequency dependence of the mode-propagation constant. As a result, different channels focus to different output waveguides when the light exiting from the array diffracts in another free-propagation region. The net result is that the WDM signal is demultiplexed into individual channels. Such demultiplexers were developed during the 1990s and became available commercially by 1999. They are able to resolve up to 256 channels with spacing as small as 0.2 nm. A combination of several suitably designed AWGs can increase the number of channels to more than 1000 while maintaining a 10-GHz resolution [96].

The performance of multiplexers is judged mainly by the amount of insertion loss for each channel. The performance criterion for demultiplexers is more stringent. First, the performance of a demultiplexer should be insensitive to the polarization of the

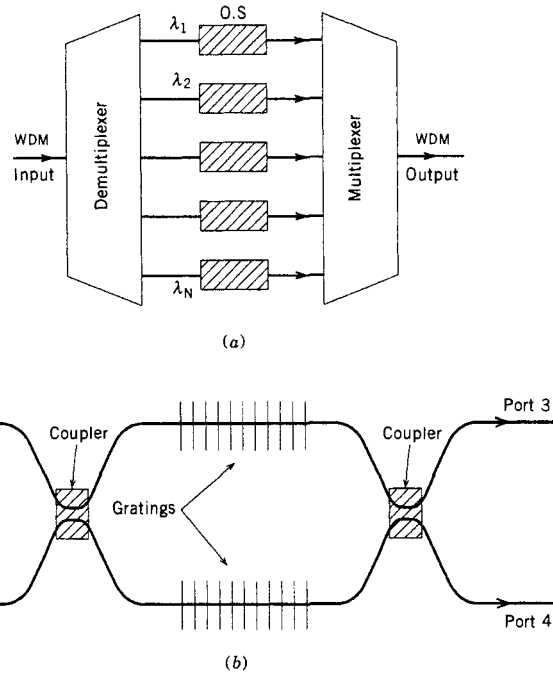


Figure 6.12: (a) A generic add–drop multiplexer based on optical switches (OS); (b) an add–drop filter made with a Mach–Zehnder interferometer and two identical fiber gratings.

incident WDM signal. Second, a demultiplexer should separate each channel without any leakage from the neighboring channels. In practice, some power leakage is likely to occur, especially in the case of dense WDM systems with small interchannel spacing. Such power leakage is referred to as crosstalk and should be quite small (< -20 dB) for a satisfactory system performance. The issue of interchannel crosstalk is discussed in Section 6.3.

6.2.3 Add–Drop Multiplexers and Filters

Add–drop multiplexers are needed for wide-area and metro-area networks in which one or more channels need to be dropped or added, while preserving the integrity of other channels [97]. Figure 6.12(a) shows a reconfigurable optical add–drop multiplexer (ROADM) schematically; it houses a bank of optical switches between a demultiplexer–multiplexer pair. The demultiplexer separates all channels, optical switches drop, add, or pass individual channels, and the multiplexer combines the entire signal back again. Any demultiplexer design discussed in the preceding subsection can be used to make such ROADMs. It is even possible to amplify the WDM signal and equalize the channel powers at the add–drop multiplexer since each channel can be individually controlled [98]. The new component in such multiplexers is the optical switch, which can be made using a variety of technologies including LiNbO₃ and InGaAsP waveguides.

If a single channel needs to be demultiplexed, and no active control of individual channels is required, one can use a much simpler multiport device designed to send a single channel to one port while all other channels are transferred to another port. Such devices avoid the need for demultiplexing all channels and are called add–drop filters because they filter out a specific channel without affecting the WDM signal. If only a small portion of the channel power is filtered out, such a device acts as an “optical tap” as it leaves the contents of the WDM signal intact.

Several kinds of add–drop filters have been developed since the advent of WDM technology [99]–[110]. The simplest scheme uses a series of interconnected directional couplers, forming a MZ chain similar to that of a MZ filter discussed earlier. However, in contrast with the MZ filter of Section 6.2.1, the relative delay τ_m in Eq. (6.2.3) is made the same for each MZ interferometer. Such a device is sometimes referred to as a *resonant coupler* because it resonantly couples out a specific wavelength channel to one output port while the remainder of the channels appear at the other output port. Its performance can be optimized by controlling the coupling ratios of various directional couplers [101]. Although resonant couplers can be implemented in an all-fiber configuration using fiber couplers, the silica-on-silicon waveguide technology provides a compact alternative for designing such add–drop filters [102].

The wavelength selectivity of Bragg gratings can also be used to make add–drop filters. In one approach, referred to as the *grating-assisted* directional coupler, a Bragg grating is fabricated in the middle of a directional coupler [107]. Such devices can be made in a compact form using InGaAsP/InP or silica waveguides. However, an all-fiber device is often preferred for avoiding coupling losses. In a common approach, two identical Bragg gratings are formed on the two arms of a MZ interferometer made using two 3-dB fiber couplers. The operation of such an add–drop filter can be understood from Figure 6.12(b). Assume that the WDM signal is incident on port 1 of the filter. The channel, whose wavelength λ_g falls within the stop band of the two identical Bragg gratings, is totally reflected and appears at port 2. The remaining channels are not affected by the gratings and appear at port 4. The same device can add a channel at the wavelength λ_g if the signal at that wavelength is injected from port 3. If the add and drop operations are performed simultaneously, it is important to make the gratings highly reflecting (close to 100%) to minimize the crosstalk. As early as 1995, such an all-fiber, add–drop filter exhibited the drop-off efficiency of more than 99%, while keeping the crosstalk level below 1% [103]. The crosstalk can be reduced below -50 dB by cascading several such devices [104].

Several other schemes use gratings to make add–drop filters. In one scheme, a waveguide with a built-in, phase-shifted grating is used to add or drop one channel from a WDM signal propagating in a neighboring waveguide [99]. In another, two identical AWGs are connected in series such that an optical amplifier connects each output port of one with the corresponding input port of the other [100]. The gain of amplifiers is adjusted such that only the channel to be dropped experiences amplification when passing through the device. Such a device is close to the generic add–drop multiplexer shown in Figure 6.12(a) with the only difference that optical switches are replaced with optical amplifiers.

In another category of add–drop filters, optical circulators are used in combination with a fiber grating [108]–[110]. Such a device is simple in design and can be made by

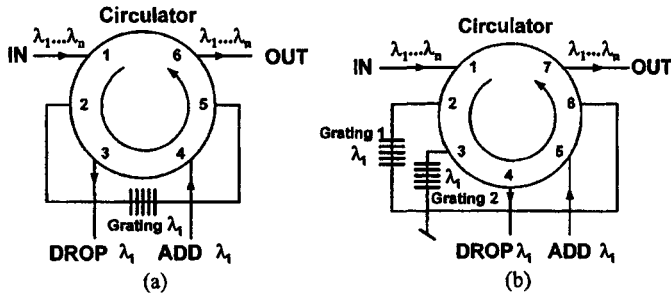


Figure 6.13: (a) Two designs of add–drop multiplexers using a single optical circulator in combination with fiber gratings. (After Ref. [108]; ©2001 IEEE; reprinted with permission.)

connecting two ends of a fiber grating to two 3-port optical circulators. The channel reflected by the grating appears at the unused port of the input-end circulator. The same-wavelength channel can be added by injecting it from the output-end circulator. The device can also be made by using only one circulator provided it has more than three ports. Figure 6.13 shows two such schemes [108]. Scheme (a) uses a six-port circulator. The WDM signal entering from port 1 exits from port 2 and passes through a Bragg grating. The dropped channel appears at port 3 while the remaining channels re-enter the circulator at port 5 and leave the device from port 6. The channel to be added enters from port 4. Scheme (b) works in a similar way but uses two identical gratings to reduce the crosstalk level. Many other variants are possible.

6.2.4 Star Couplers

The role of a star coupler, as seen in Figure 6.5, is to combine the optical signals entering from its multiple input ports and divide it equally among its output ports. In contrast with demultiplexers, star couplers do not contain wavelength-selective elements, as they do not attempt to separate individual channels. The number of input and output ports need not be the same. For example, in the case of video distribution, a relatively small number of video channels (say 100) may be sent to thousands of subscribers. The number of input and output ports is generally the same for the broadcast-and-select LANs in which each user wishes to receive all channels (see Figure 6.5). Such a passive star coupler is referred to as an $N \times N$ broadcast star, where N is the number of input (or output) ports. A reflection star is sometimes used for LAN applications by reflecting the combined signal back to its input ports. Such a geometry saves considerable fiber when users are distributed over a large geographical area.

Several kinds of star couplers have been developed for LAN applications [111]–[117]. An early approach made use of multiple 3-dB fiber couplers [112]. A 3-dB fiber coupler divides two input signals between its two output ports, the same functionality needed for a 2×2 star coupler. Higher-order $N \times N$ stars can be formed by combining several 2×2 couplers as long as N is a multiple of 2. Figure 6.14 shows an 8×8 star formed by interconnecting 12 fiber couplers. The complexity of such star couplers grows enormously with the number of ports.

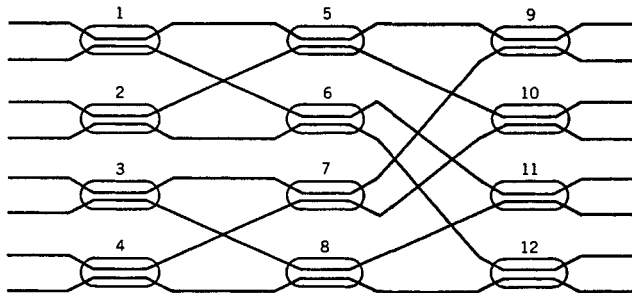


Figure 6.14: An 8×8 star coupler formed by using twelve 2×2 single-mode fiber couplers.

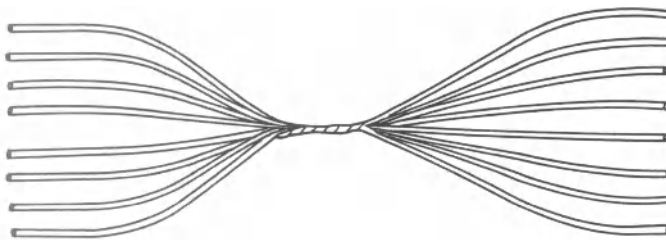


Figure 6.15: A star coupler formed by using the fused biconical tapering method.

Fused biconical-taper couplers can be used to make compact, monolithic, star couplers. Figure 6.15 shows schematically a star coupler formed using this technique. The idea is to fuse together a large number of fibers and elongate the fused portion to form a biconically tapered structure. In the tapered portion, signals from each fiber mix together and are shared almost equally among its output ports. Such a scheme works relatively well for multimode fibers [111] but is limited to only a few ports in the case of single-mode fibers. Fused 2×2 couplers were made as early as 1981 using single-mode fibers [88]; they can also be designed to operate over a wide wavelength range. Higher-order stars can be made using a combinatorial scheme similar to that shown in Figure 6.12 [113].

A common approach for fabricating a compact broadcast star makes use of the silica-on-silicon technology in which two arrays of planar SiO_2 waveguides, separated by a central slab region, are formed on a silicon substrate. Such a star coupler was first demonstrated in 1989 in a 19×19 configuration [114]. The SiO_2 channel waveguides were $200 \mu\text{m}$ apart at the input end, but the final spacing near the central region was only $8 \mu\text{m}$. The 3-cm-long star coupler had an efficiency of about 55%. A fiber amplifier can be integrated with the star coupler to amplify the output signals before broadcasting [115]. The silicon-on-insulator technology has been used for making star couplers. A 5×9 star made by using silicon rib waveguides exhibited low losses (1.3 dB) with relatively uniform coupling [116].

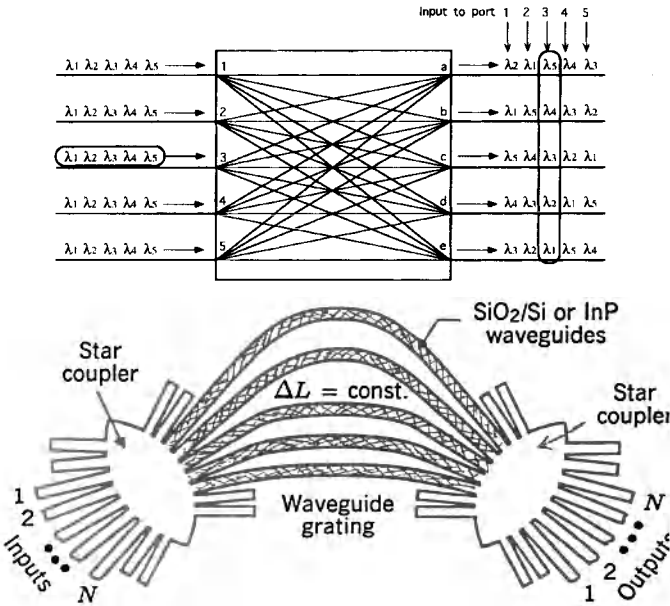


Figure 6.16: (a) Schematic illustration of a wavelength router and (b) its implementation using an AWG. (After Ref. [93]; ©1999 IEEE; reprinted with permission.)

6.2.5 Wavelength Routers

An important WDM component is an $N \times N$ wavelength router, a device that combines the functionality of a star coupler with multiplexing and demultiplexing operations. Figure 6.16(a) shows the operation of such a wavelength router schematically for $N = 5$. The WDM signals entering from N input ports are demultiplexed into individual channels and directed toward the N output ports of the router in such a way that the WDM signal at each port is composed of channels entering at different input ports. This operation results in a cyclic form of demultiplexing. Such a device is an example of a passive router since its use does not involve any active element requiring electrical power. It is also called a *static router* since the routing topology is not dynamically reconfigurable. Despite its static nature, such a WDM device has many potential applications in WDM networks.

The most common design of a wavelength router uses a AWG demultiplexer shown in Figure 6.11 modified to provide multiple input ports. Such a device, called the *waveguide-grating router* (WGR), is shown schematically in Figure 6.16(b). It consists of two $N \times M$ star couplers such that M output ports of one star coupler are connected with M input ports of another star coupler through an array of M waveguides that acts as an AWG [89]. Such a device is a generalization of the MZ interferometer in the sense that a single input is divided coherently into M parts (rather than two), which acquire different phase shifts and interfere in the second free-propagation region to come out of N different ports depending on their wavelengths. The symmetric nature of the WGR

permits to launch N WDM signals containing N different wavelengths simultaneously, and each WDM signal is demultiplexed to N output ports in a periodic fashion.

The physics behind the operation of a WGR requires a careful consideration of the phase changes as different wavelength signals diffract through the free-propagation region inside star couplers and propagate through the waveguide array [89]–[95]. The most important part of a WGR is the waveguide array designed such that the length difference ΔL between two neighboring waveguides remains constant from one waveguide to next. The phase difference for a signal of wavelength λ , traveling from the p th input port to the q th output port through the m th waveguide (compared to the path connecting central ports), can be written as [9]

$$\phi_{pqm} = (2\pi m/\lambda)(n_1 \delta_p + n_2 \Delta L + n_1 \delta'_q), \quad (6.2.4)$$

where n_1 and n_2 are the refractive indices in the regions occupied by the star couplers and waveguides, respectively. The lengths δ_p and δ'_q depend on the location of the input and output ports. When the condition

$$n_1(\delta_p + \delta'_q) + n_2 \Delta L = Q\lambda \quad (6.2.5)$$

is satisfied for some integer Q , the channel at the wavelength λ acquires phase shifts that are multiples of 2π while passing through different waveguides. As a result, all fields coming out of the M waveguides will interfere constructively at the q th port. Other wavelengths entering from the p th port will be directed to other output ports determined by the condition (6.2.5). Clearly, the device acts as a demultiplexer since a WDM signal entering from the p th port is distributed to different output ports depending on the channel wavelengths.

The routing function of a WGR results from the periodicity of the transmission spectrum. This property is also easily understood from Eq. (6.2.5). The phase condition for constructive interference can be satisfied for many integer values of Q . Thus, if Q is changed to $Q + 1$, a different wavelength will satisfy Eq. (6.2.5) and will be directed toward the same port. The frequency difference between these two wavelengths is the free spectral range (FSR), analogous to that of FP filters. For a WGR, it is given by

$$\text{FSR} = \frac{c}{n_1(\delta_p + \delta'_q) + n_2 \Delta L}. \quad (6.2.6)$$

Strictly speaking, FSR is not the same for all ports, an undesirable feature from a practical standpoint. However, when δ_p and δ'_q are designed to be relatively small compared with ΔL , FSR becomes nearly constant for all ports. In that case, a WGR can be viewed as N demultiplexers working in parallel with the following property. If the WDM signal from the first input port is distributed to N output ports in the order $\lambda_1, \lambda_2, \dots, \lambda_N$, the WDM signal from the second input port will be distributed as $\lambda_N, \lambda_1, \dots, \lambda_{N-1}$, and the same cyclic pattern is followed for other input ports.

The optimization of a WGR requires precise control of many design parameters for reducing the crosstalk and maximizing the coupling efficiency. Despite the complexity of the design, WGRs are routinely fabricated in the form of a compact commercial device (each dimension ~ 1 cm) using either silica-on-silicon technology or InGaAsP/InP

technology [89]–[95]. WGRs with 128 input and output ports were available by 1996 in the form of a planar lightwave circuit and were able to operate on WDM signals with a channel spacing as small as 0.2 nm while maintaining crosstalk below 16 dB. The number of channels could be increased to 256 by 2000 by employing silica waveguides with a relatively large core-cladding index difference of 1.5% while maintaining the 25-GHz channel spacing [118]. A combination of several suitably designed AWGs can increase the number of channels to more than 1,000 while maintaining the 10-GHz resolution [96]. The only negative aspect of such devices is that insertion losses for AWG demultiplexers can exceed 10 dB.

6.2.6 WDM Transmitters and Receivers

Most WDM systems use a large number of DFB lasers whose frequencies are chosen to match the ITU frequency grid precisely. This approach becomes impractical when the number of channels becomes large. Two solutions are possible. In one approach, single-mode narrowband lasers with a tuning range of 10 nm or more are employed (see Section 3.2.3). The use of such lasers reduces the inventory and maintenance problems. Alternatively, multiwavelength transmitters which generate light at 8 or more fixed wavelengths simultaneously can be used. Although such WDM transmitters attracted attention in the 1990s [119]–[125], it was only after 2001 that monolithically integrated WDM transmitters, operating near $1.55\text{ }\mu\text{m}$ with a channel spacing of 1 nm or less, were developed and commercialized using the InP-based photonic integrated-circuit (PIC) technology [126]–[131].

Several different techniques have been pursued for designing WDM transmitters. In one approach, the output of several DFB or DBR semiconductor lasers, independently tunable through Bragg gratings, is combined by using passive waveguides [119]–[121]. A built-in amplifier boosts the power of the multiplexed signal to increase the transmitted power. In a 1996 device, 16 gain-coupled DFB lasers were integrated, and their wavelengths were controlled by changing the width of the ridge waveguides and by tuning over a 1-nm range using a thin-film resistor [120]. In a different approach, sampled gratings with different periods are used to tune the wavelengths precisely of an array of DBR lasers [122]. The complexity of such devices makes it difficult to integrate more than 16 lasers on the same chip.

In a different approach, a waveguide grating is integrated within the laser cavity to provide lasing at several wavelengths simultaneously. An AWG is often used for multiplexing the output of several optical amplifiers or DBR lasers [123]–[125]. In a 1996 demonstration of the basic idea, simultaneous operation at 18 wavelengths (spaced apart by 0.8 nm) was realized using an intracavity AWG [123]. Figure 6.17 shows the laser design schematically. Spontaneous emission of the amplifier located on the left side is demultiplexed into 18 spectral bands by the AWG through the technique of spectral slicing. The amplifier array on the right side selectively amplifies the set of 18 wavelengths, resulting in a laser emitting at all wavelengths simultaneously. A 16-wavelength transmitter with 50-GHz channel spacing was built in 1998 by this technique [124]. In another approach, the AWG was not a part of the laser cavity but was used to multiplex the output of 10 DBR lasers, all produced on the same chip in

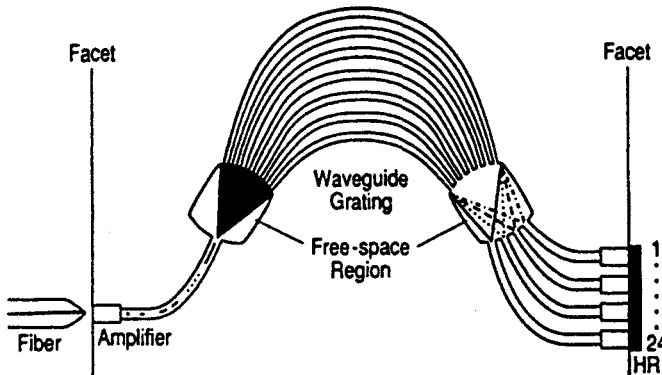


Figure 6.17: Schematic of a WDM laser made by integrating an AWG inside the laser cavity. (After Ref. [123]; ©1996 IEEE; reprinted with permission.)

an integrated fashion [125]. AWGs fabricated with the silica-on-silicon technology can also be used although they cannot be integrated on the InP substrate.

The PIC approach was followed intensively after 2001. In a 2002 transmitter, 12 tunable DFB lasers were integrated on the same InP chip and their outputs were combined using a micro-electro-mechanical system (MEMS) within a butterfly module [126]. Such a transmitter provided up to 20 mW of fiber-coupled power at ITU wavelengths within the C band with spacing of 50 GHz set precisely by a wavelength locker. Such a device is not fully integrated because it employs discrete lenses to couple light from lasers to the MEMS. By 2005, fully integrated large-scale PIC transmitter chips had been developed and commercialized [128]. Figure 6.18 shows the architecture of such a 10-channel transmitter incorporating more than 50 functions on a single chip. The outputs of a tunable DFB laser array pass through electroabsorption modulators (EAMa) (driven by 10-Gb/s electrical bit streams) and variable optical attenuators before they are combined by an AWG multiplexer. An optical power-monitor (OPM) array is also integrated within the chip to ensure power All laser wavelengths, separated in frequency by 200 GHz, fall on the ITU grid within the C band. A 10-channel receiver PIC chip was also developed to match this WDM transmitter. By 2006, this approach was extended to fabricate 40-channel WDM transmitters with 40-Gb/s bit rate per channel [129]. More recently, transmitters suitable for phase-encoded (DQPSK) bit streams have been developed by integrating multiple MZ interferometers within the InP chip [131].

Fiber lasers can also be designed to provide multiwavelength output and therefore act as a CW WDM source [132]–[136]. A ring-cavity fiber laser containing a frequency shifter (e.g., an acousto-optic device) and an optical filter with periodic transmission peaks (such as a FP filter, a sampled grating, or an AWG) can provide its output at a comb of frequencies set to coincide with the ITU grid. Up to 16 wavelengths were obtained by 2000 by this technique, although the power is not generally uniform across them. By 2009, 50-wavelength fiber lasers covering the entire C band with 100-GHz channel spacing were developed [136]. The output at all wavelengths exhibited the

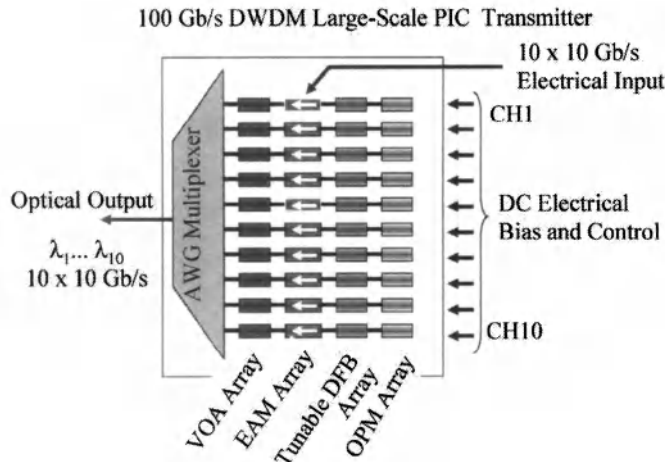


Figure 6.18: Schematic of a 10-channel WDM transmitter made with the large-scale PIC technology. (After Ref. [128]; ©2005 IEEE; reprinted with permission.)

same polarization with a narrow spectral bandwidth (<0.2 MHz). The main disadvantage of fiber lasers is that a demultiplexer is needed to separate the channels before data is imposed on them using individual modulators.

A unique approach to WDM sources exploits the technique of spectral slicing for realizing WDM transmitters and is capable of providing more than 1000 channels [137]–[140]. The output of a coherent, wide-bandwidth source is sliced spectrally using a mutipeak optical filter such as an AWG. In one implementation of this idea [137], picosecond pulses from a mode-locked fiber laser are first broadened spectrally to bandwidth as large as 200 nm through supercontinuum generation by exploiting the nonlinear effects in an optical fiber [74]. Spectral slicing of the output by an AWG then produces many WDM channels with a channel spacing of 1 nm or less. In a 2000 experiment, this technique produced 1000 channels with 12.5-GHz channel spacing [139]. In another experiment, 150 channels with 25-GHz channel spacing were realized within the C band covering the range 1530–1560 nm [140]. The SNR of each channel exceeded 28 dB, indicating that the source was suitable for dense WDM applications.

The generation of supercontinuum is not necessary if a mode-locked laser producing femtosecond pulses is employed. The spectral width of such pulses is quite large to begin with and can be enlarged to 50 nm or more by chirping them using 10–15 km of standard telecommunication fiber. Spectral slicing of the output by a demultiplexer can again provide many channels, each of which can be modulated independently. This technique also permits simultaneous modulation of all channels using a single modulator before the demultiplexer if the modulator is driven by a suitable electrical bit stream composed through TDM. A 32-channel WDM source was demonstrated in 1996 by using this method [138]. Since then, this technique has been used to provide sources with more than 1000 channels.

On the receiver end, multichannel WDM receivers have been developed because

their use can simplify the system design and reduce the overall cost [141]–[145]. Monolithic receivers integrate a photodiode array with a demultiplexer on the same chip. Typically, A planar concave-grating demultiplexer or a WGR is integrated with the photodiode array. Even electronic amplifiers can be integrated within the same chip. The design of such monolithic receivers is similar to the transmitter shown in Figure 6.17 except that no cavity is formed and the amplifier array is replaced with a photodiode array. Such a WDM receiver was first fabricated in 1995 by integrating an eight-channel WGR (with 0.8-nm channel spacing), eight $p-i-n$ photodiodes, and eight preamplifiers using heterojunction bipolar transistor technology [141]. By 2007, PIC receivers with a large number of photodiodes became available [130].

6.3 System Performance Issues

The most important issue in the design of WDM lightwave systems is the *interchannel crosstalk*. The system performance degrades whenever crosstalk leads to transfer of power from one channel to another. Such a transfer can occur because of the nonlinear effects in optical fibers, a phenomenon referred to as *nonlinear crosstalk* as it depends on the nonlinear nature of the communication channel. However, some crosstalk occurs even in a perfectly linear channel because of the imperfect nature of various WDM components such as optical filters, demultiplexers, and switches. In this section we discuss both the linear and nonlinear crosstalk mechanisms and also consider other performance issues relevant for WDM systems.

6.3.1 Heterowavelength Linear Crosstalk

Linear crosstalk can be classified into two categories depending on its origin [146]–[155]. Optical filters and demultiplexers often let leak a fraction of the signal power from neighboring channels that interferes with the detection process. Such crosstalk is called *heterowavelength* or *out-of-band* crosstalk and is less of a problem because of its incoherent nature than the *homowavelength* or *in-band* crosstalk that occurs during routing of the WDM signal from multiple nodes. This subsection focuses on the heterowavelength crosstalk.

Consider the case in which a tunable optical filter is used to select a single channel among the N channels incident on it. If the optical filter is set to pass the m th channel, the optical power reaching the photodetector can be written as $P = P_m + \sum_{n \neq m}^N T_{mn}P_n$ where P_m is the power in the m th channel and T_{mn} is the filter transmittivity for channel n when channel m is selected. Crosstalk occurs if $T_{mn} \neq 0$ for $n \neq m$. It is called out-of-band crosstalk because it belongs to the channels lying outside the spectral band occupied by the channel detected. Its incoherent nature is also apparent from the fact that it depends only on the power of the neighboring channels.

To evaluate the impact of such crosstalk on system performance, one should consider the power penalty, defined as the additional power required at the receiver to counteract the effect of crosstalk. The photocurrent generated in response to the inci-

dent optical power is given by

$$I = R_m P_m + \sum_{n \neq m}^N R_n T_{mn} P_n \equiv I_{\text{ch}} + I_X, \quad (6.3.1)$$

where $R_m = \eta_m q / h\nu_m$ is the photodetector responsivity for channel m at the optical frequency ν_m and η_m is the quantum efficiency. The second term I_X in Eq. (6.3.1) denotes the crosstalk contribution to the receiver current I . Its value depends on the bit pattern and becomes maximum when all interfering channels carry 1 bits simultaneously (the worst case).

A simple approach to calculating the crosstalk power penalty is based on the eye closure (see Section 4.3.3) occurring as a result of the crosstalk [146]. The eye closes most in the worst case for which I_X is maximum. In practice, I_{ch} is increased to maintain the system performance. If I_{ch} needs to be increased by a factor δ_X , the peak current corresponding to the top of the eye is $I_1 = \delta_X I_{\text{ch}} + I_X$. The decision threshold is set at $I_D = I_1/2$. The *eye opening* from I_D to the top level would be maintained at its original value $I_{\text{ch}}/2$ if

$$(\delta_X I_{\text{ch}} + I_X) - I_X - \frac{1}{2}(\delta_X I_{\text{ch}} + I_X) = \frac{1}{2}I_{\text{ch}}, \quad (6.3.2)$$

or when $\delta_X = 1 + I_X/I_{\text{ch}}$. The quantity δ_X is just the power penalty for the m th channel. By using I_X and I_{ch} from Eq. (6.3.1), δ_X can be written (in dB) as

$$\delta_X = 10 \log_{10} \left(1 + \frac{\sum_{n \neq m}^N R_n T_{mn} P_n}{R_m P_m} \right), \quad (6.3.3)$$

where the powers correspond to their on-state values. If the peak power is assumed to be the same for all channels, the crosstalk penalty becomes power independent. Further, if the photodetector responsivity is nearly the same for all channels ($R_m \approx R_n$), δ_X is well approximated by

$$\delta_X \approx 10 \log_{10} (1 + X), \quad (6.3.4)$$

where $X = \sum_{n \neq m}^N T_{mn}$ is a measure of the out-of-band crosstalk; it represents the fraction of total power leaked into a specific channel from all other channels. The numerical value of X depends on the transmission characteristics of the specific optical filter. For a FP filter, X can be obtained in a closed form [147].

The preceding analysis of crosstalk penalty is based on the eye closure rather than the bit-error rate (BER). One can obtain an expression for the BER if I_X is treated as a random variable in Eq. (6.3.1). For a given value of I_X , the BER is obtained by using the analysis of Section 4.5.1. In particular, the BER is given by Eq. (4.5.6) with the on- and off-state currents given by $I_1 = I_{\text{ch}} + I_X$ and $I_0 = I_X$ if we assume that $I_{\text{ch}} = 0$ in the off-state. The decision threshold is set at $I_D = I_{\text{ch}}(1 + X)/2$, which corresponds to the worst-case situation in which all neighboring channels are in the on state. The final BER is obtained by averaging over the distribution of the random variable I_X . The distribution of I_X has been calculated for a FP filter and is generally far from being Gaussian. The crosstalk power penalty δ_X can be calculated by finding the increase

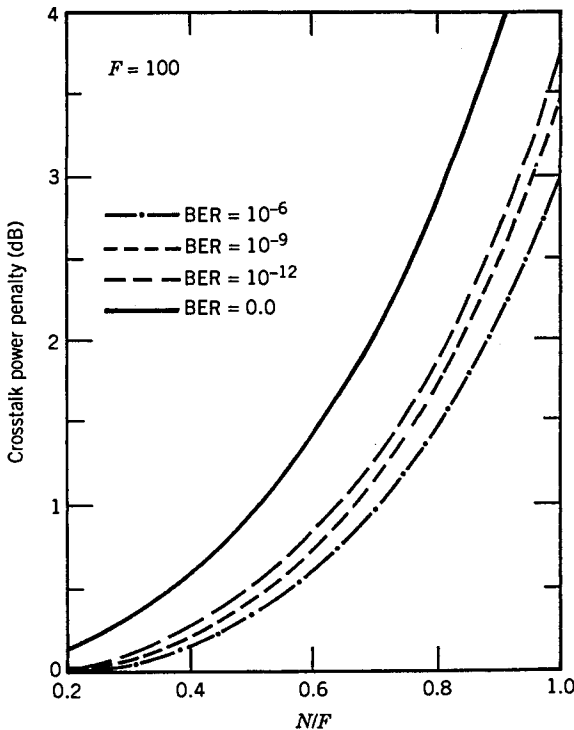


Figure 6.19: Crosstalk power penalty at four different values of the BER for a FP filter of finesse $F = 100$. (After Ref. [147]; ©1990 IEEE; reprinted with permission.)

in I_{ch} needed to maintain a certain value of BER. Figure 6.19 shows the calculated penalty for several values of BER plotted as a function of N/F [147] with the choice $F = 100$. The solid curve corresponds to the error-free case ($\text{BER} = 0$). The power penalty can be kept below 0.2 dB to maintain a BER of 10^{-9} for values of N/F as large as 0.33. From Eq. (6.2.2) the channel spacing can be as little as three times the bit rate for such FP filters.

6.3.2 Homowavelength Linear Crosstalk

Homowavelength or in-band crosstalk results from WDM components used for routing and switching along an optical network and has been of concern since the advent of WDM systems [148]–[155]. Its origin can be understood by considering a static wavelength router such as a WGR (see Figure 6.16). For an $N \times N$ router, there exist N^2 combinations through which N -wavelength WDM signals can be split. Consider the output at one wavelength, say λ_m . Among the $N^2 - 1$ interfering signals that can accompany the desired signal, $N - 1$ signals have the same carrier wavelength λ_m , while the remaining $N(N - 1)$ belong to different carrier wavelengths and are likely to be eliminated as they pass through other WDM components. The $N - 1$ crosstalk signals at the same wavelength (in-band crosstalk) originate from incomplete filtering through

a WGR because of its partially overlapping transmission peaks [149]. The total optical field, including only the in-band crosstalk, can be written as

$$E_m(t) = \left(E_m + \sum_{n \neq m}^N E_n \right) \exp(-i\omega_m t), \quad (6.3.5)$$

where E_m is the desired signal and $\omega_m = 2\pi c/\lambda_m$. The coherent nature of the in-band crosstalk is obvious from Eq. (6.3.5).

To see the impact of in-band crosstalk on system performance, we should again consider the power penalty. The receiver current $I = R|E_m(t)|^2$ in this case contains interference or beat terms similar to the case of optical amplifiers (see Section 7.5). One can identify two types of beat terms; signal–crosstalk beating with terms like $E_m E_n$ and crosstalk–crosstalk beating with terms like $E_k E_n$, where $k \neq m$ and $n \neq m$. The latter terms are negligible in practice and can be ignored. The receiver current is then given approximately as

$$I(t) \approx RP_m(t) + 2R \sum_{n \neq m}^N \sqrt{P_m(t)P_n(t)} \cos[\phi_m(t) - \phi_n(t)], \quad (6.3.6)$$

where $P_n = |E_n|^2$ is the power and $\phi_n(t)$ is the phase. In practice, $P_n \ll P_m$ for $n \neq m$ because a WGR is built to reduce the crosstalk. Since phases are likely to fluctuate randomly, we can write Eq. (6.3.6) as $I(t) = R(P_m + \Delta P)$, treat the crosstalk as intensity noise, and use the approach of Section 4.7.2 for calculating the power penalty. In fact, the result is the same as in Eq. (4.6.11) and can be written as

$$\delta_X = -10 \log_{10}(1 - r_X^2 Q^2), \quad (6.3.7)$$

where

$$r_X^2 = \langle (\Delta P)^2 \rangle / P_m^2 = X(N-1), \quad (6.3.8)$$

and $X = P_n/P_m$ is the crosstalk level defined as the fraction of power leaking through the WGR and is taken to be the same for all $N-1$ sources of coherent in-band crosstalk by assuming equal powers. An average over the phases was performed by replacing $\cos^2 \theta = \frac{1}{2}$. In addition, r_X^2 was multiplied by another factor of $\frac{1}{2}$ to account for the fact that P_n is zero on average half of the times (during 0 bits). Experimental measurements of power penalty for a WGR agree with this simple model [149].

The impact of in-band crosstalk can be estimated from Figure 4.21, where power penalty δ_X is plotted as a function of r_X . To keep the power penalty below 2 dB, $r_X < 0.07$ is required, a condition that limits $X(N-1)$ to below -23 dB from Eq. (6.3.8). Thus, the crosstalk level X must be below -38 dB for $N=16$ and below -43 dB for $N=100$, rather stringent requirements.

The calculation of crosstalk penalty in the case of dynamic wavelength routing through optical cross-connects becomes quite complicated because of a large number of crosstalk elements that a signal can pass through in such WDM networks [150]. The worst-case analysis predicts a large power penalty (> 3 dB) when the number of crosstalk elements becomes more than 25 even if the crosstalk level of each component is only -40 dB. Clearly, the linear crosstalk is of primary concern in the design of WDM networks and should be controlled. Several techniques have been proposed for this purpose [156]–[158].

6.3.3 Nonlinear Raman Crosstalk

Several nonlinear effects in optical fibers [74] can lead to interchannel and intrachannel crosstalk that affects the system performance considerably [159]–[165]. Section 2.6 discussed such nonlinear effects and their origin from a physical point of view. This subsection focuses on the Raman crosstalk.

As discussed in Section 2.6, stimulated Raman scattering (SRS) is generally not of concern for single-channel systems because of its relatively high threshold (about 500 mW near 1.55 μm). The situation is quite different for WDM systems in which the fiber acts as a Raman amplifier (see Section 7.3) such that the long-wavelength channels are amplified by the short-wavelength channels as long as the wavelength difference is within the bandwidth of the Raman gain. The Raman gain spectrum of silica fibers is so broad that amplification can occur for channels spaced as far apart as 100 nm. The shortest-wavelength channel is most depleted as it can pump many channels simultaneously. Such an energy transfer among channels can be detrimental for system performance as it depends on the bit pattern—amplification occurs only when 1 bits are present in both channels simultaneously. The Raman-induced crosstalk degrades the system performance and is of considerable concern for WDM systems [166]–[173].

Raman crosstalk can be avoided if channel powers are made so small that SRS-induced amplification is negligible over the entire fiber length. It is thus important to estimate the limiting value of the channel power. A simple model considers the depletion of the highest-frequency channel in the worst case in which 1 bits of all channels overlap completely simultaneously [159]. The amplification factor for each channel is $G_m = \exp(g_m L_{\text{eff}})$, where L_{eff} is the effective interaction length as defined in Eq. (2.6.2) and $g_m = g_R(\Omega_m)P_{\text{ch}}/A_{\text{eff}}$ is the Raman gain at $\Omega_m = \omega_1 - \omega_m$. For $g_m L_{\text{eff}} \ll 1$, the shortest-wavelength channel at ω_1 is depleted by a fraction $g_m L_{\text{eff}}$ due to Raman amplification of the m th channel. The total depletion for a M -channel WDM system is given by

$$D_R = \sum_{m=2}^M g_R(\Omega_m) P_{\text{ch}} L_{\text{eff}} / A_{\text{eff}}. \quad (6.3.9)$$

The summation in Eq. (6.3.9) can be carried out analytically if the Raman gain spectrum (see Figure 2.17) is approximated by a triangular profile such that g_R increases linearly for frequencies up to 15 THz with a slope $S_R = dg_R/d\nu$ and then drops to zero. Using $g_R(\Omega_m) = m S_R \Delta\nu_{\text{ch}}$, the fractional power loss for the shortest-wavelength channel becomes [159]

$$D_R = \frac{1}{2} M(M-1) C_R P_{\text{ch}} L_{\text{eff}}, \quad (6.3.10)$$

where $C_R = S_R \Delta\nu_{\text{ch}} / (2A_{\text{eff}})$. In deriving this equation, channels were assumed to have a constant spacing $\Delta\nu_{\text{ch}}$ and the Raman gain for each channel was reduced by a factor of 2 to account for random polarization states of different channels.

A more accurate analysis should consider not only depletion of each channel because of power transfer to longer-wavelength channels but also its own amplification by shorter-wavelength channels. If all other nonlinear effects are neglected along with

GVD, evolution of the power P_n associated with the n th channel is governed by the following equation (see Section 7.3):

$$\frac{dP_n}{dz} + \alpha P_n = C_R P_n \sum_{m=1}^M (n-m) P_m, \quad (6.3.11)$$

where α is assumed to be the same for all channels. This set of M coupled nonlinear equations can be solved analytically. For a fiber of length L , the result is given by [166]

$$P_n(L) = P_n(0) e^{-\alpha L} \frac{P_t \exp[(n-1)C_R P_t L_{\text{eff}}]}{\sum_{m=1}^M P_m(0) \exp[(m-1)C_R P_t L_{\text{eff}}]}, \quad (6.3.12)$$

where $P_t = \sum_{m=1}^M P_m(0)$ is the total input power in all channels. This equation shows that channel powers follow an exponential distribution because of Raman-induced coupling among all channels.

The depletion factor D_R for the shorter-wavelength channel ($n = 1$) is obtained using $D_R = (P_{10} - P_1)/P_{10}$, where $P_{10} = P_1(0) \exp(-\alpha L)$ is the channel power expected in the absence of SRS. In the case of equal input powers in all channels, $P_t = M P_{\text{ch}}$ in Eq. (6.3.12), and D_R is given by

$$D_R = 1 - \exp \left[-\frac{1}{2} M(M-1) C_R P_{\text{ch}} L_{\text{eff}} \right] \frac{M \sinh(\frac{1}{2} M C_R P_{\text{ch}} L_{\text{eff}})}{\sinh(\frac{1}{2} M^2 C_R P_{\text{ch}} L_{\text{eff}})}. \quad (6.3.13)$$

In the limit $M^2 C_R P_{\text{ch}} L_{\text{eff}} \ll 1$, this complicated expression reduces to the simple result in Eq. (6.3.10). In general, Eq. (6.3.10) overestimates the Raman crosstalk.

The Raman-induced power penalty is obtained using $\delta_R = -10 \log(1 - D_R)$ because the input channel power must be increased by a factor of $(1 - D_R)^{-1}$ to maintain the same system performance. Figure 6.20 shows how the power penalty increases with an increase in the channel power and the number of channels. The channel spacing is assumed to be 100 GHz. The slope of the Raman gain is estimated from the gain spectrum to be $S_R = 4.9 \times 10^{-18} \text{ m}/(\text{W-GHz})$ while $A_{\text{eff}} = 50 \mu\text{m}^2$ and $L_{\text{eff}} \approx 1/\alpha = 21.74 \text{ km}$. As seen from Figure 6.20, the power penalty becomes quite large for WDM systems with a large number of channels. If a value of at most 1 dB is considered acceptable, the limiting channel power P_{ch} exceeds 10 mW for 20 channels, but its value is reduced to below 1 mW when the number of WDM channels is larger than 70.

The foregoing analysis provides only a rough estimate of the Raman crosstalk as it neglects the fact that signals in each channel consist of a random sequence of 0 and 1 bits. A statistical analysis shows that the Raman crosstalk is lower by about a factor of 2 when signal modulation is taken into account [161]. The GVD effects that were neglected in the above analysis also reduce the Raman crosstalk since pulses in different channels travel at different speeds because of the group-velocity mismatch [167]. On the other hand, periodic amplification of the WDM signal can magnify the impact of SRS-induced degradation. The reason is that in-line amplifiers add noise which experiences less Raman loss than the signal itself, resulting in degradation of the SNR. The Raman crosstalk under realistic operating conditions was calculated in a 2003 study [173]. Numerical simulations showed that it can be reduced by inserting opti-

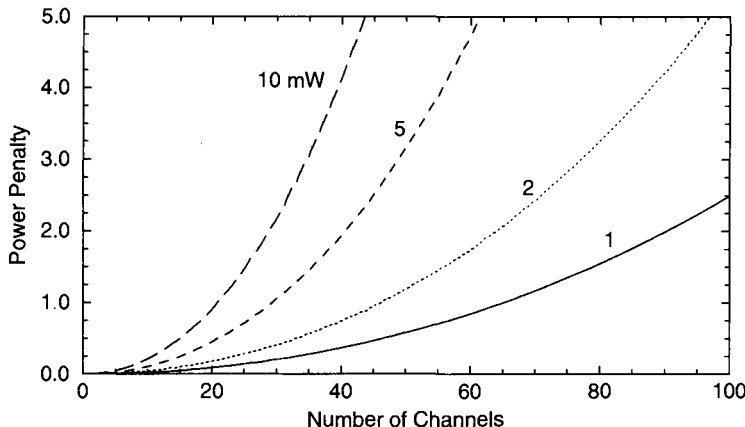


Figure 6.20: Raman-induced power penalty as a function of channel number for several values of P_{ch} . Channels are 100 GHz apart and launched with equal powers.

cal filters along the fiber link that block the low-frequency noise below the longest-wavelength channel [171]. Raman crosstalk can also be reduced using the technique of midway spectral inversion [168].

6.3.4 Stimulated Brillouin Scattering

Stimulated Brillouin scattering (SBS) can also transfer energy from a high-frequency channel to a low-frequency one when the channel spacing equals the Brillouin shift. However, in contrast with the case of SRS, such an energy transfer is easily avoided with the proper design of multichannel communication systems. The reason is that the Brillouin-gain bandwidth is extremely narrow (~ 20 MHz) compared with the Raman-gain bandwidth (~ 5 THz). Thus, the channel spacing must match almost exactly the *Brillouin shift* (about 10 GHz in the 1.55- μm region) for SBS to occur; such an exact match is easily avoided. Furthermore, as discussed in Section 2.6, the two channels must be counterpropagating for Brillouin amplification to occur.

Although SBS does not induce interchannel crosstalk when all channels propagate in the forward direction, it nonetheless limits the channel powers. The reason is that a part of the channel power can be transferred to a backward-propagating Stokes wave generated from noise when the threshold condition $g_B P_{\text{th}} L_{\text{eff}} / A_{\text{eff}} \approx 21$ is satisfied (see Section 2.6). This condition is independent of the number and the presence of other channels. However, the threshold for each channel can be reached at low power levels. Figure 6.21 shows how the output power and power reflected backward through SBS vary in a 13-km-long dispersion-shifted fiber as the injected CW power is increased from 0.5 to 50 mW [174]. No more than 3 mW could be transmitted through the fiber in this experiment after the *Brillouin threshold*. For a fiber with $A_{\text{eff}} = 50 \mu\text{m}^2$ and $\alpha = 0.2 \text{ dB/km}$, the threshold power is below 2 mW when the fiber length is long enough ($> 20 \text{ km}$) that L_{eff} can be replaced by $1/\alpha$.

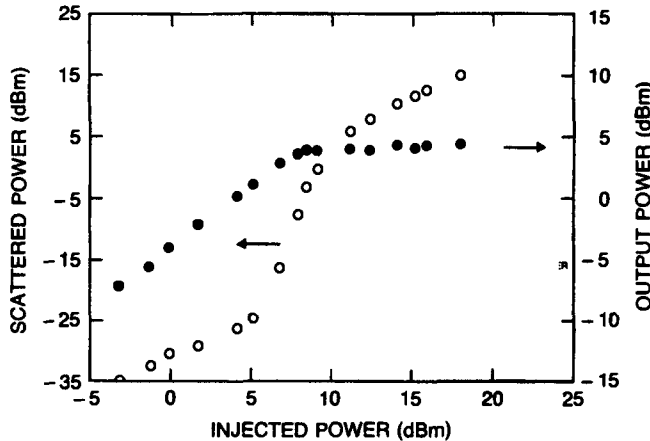


Figure 6.21: Output signal power (solid circles) and reflected SBS power (empty circles) as a function of power injected. (After Ref. [174]; ©1992 IEEE; reprinted with permission.)

The preceding estimate applies to CW signals as it neglects the effects of signal modulation resulting in a random sequence of 0 and 1 bits. In general, the Brillouin threshold depends on the modulation format as well as on the ratio of the bit rate to the Brillouin-gain bandwidth [175]. It increases to above 5 mW for lightwave systems operating near 10 Gb/s. Some applications require launch powers in excess of 10 mW. Several schemes have been proposed for raising the Brillouin threshold [176]–[183]. They rely on increasing either the Brillouin-gain bandwidth Δv_B or the spectral width of optical carrier. The former has a value of about 20 MHz for silica fibers, while the latter is typically < 10 MHz for DFB lasers used in WDM systems. The bandwidth of an optical carrier can be increased without affecting the system performance by modulating its phase at a frequency much lower than the bit rate. Typically, the modulation frequency Δv_m is in the range of 200–400 MHz. As the effective Brillouin gain is reduced by a factor of $(1 + \Delta v_m / \Delta v_B)$, the SBS threshold increases by the same factor. Since typically $\Delta v_B \sim 20$ MHz, the launched power can be increased by more than a factor of 10 by this technique.

If the Brillouin-gain bandwidth Δv_B of the fiber itself can be increased from its nominal value of 20 MHz to more than 200 MHz, the SBS threshold can be increased without requiring a phase. One technique uses sinusoidal strain along the fiber length for this purpose. The applied strain changes the Brillouin shift v_B by a few percent in a periodic manner. The resulting Brillouin-gain spectrum is much broader than that occurring for a fixed value of v_B . The strain can be applied during cabling of the fiber. In one fiber cable, Δv_B was found to increase from 50 to 400 MHz [176]. The Brillouin shift v_B can also be changed by making the core radius nonuniform along the fiber length since the longitudinal acoustic frequency depends on the core radius. The same effect can be realized by changing the dopant concentration along the fiber length. This technique increased the SBS threshold of one fiber by 7 dB [177]. A side effect of varying the core radius or the dopant concentration is that the GVD parameter β_2

also changes along the fiber length. It is possible to vary both of them simultaneously in such a way that β_2 remains relatively uniform [179]. Phase modulation induced by a supervisory channel through the nonlinear phenomenon of cross-phase modulation (XPM) can also be used to suppress SBS [181]. XPM induced by neighboring channels can also help [178], but it is hard to control and is itself a source of crosstalk. In practice, a frequency modulator integrated within the transmitter provides the best method for suppressing SBS. Threshold levels >200 mW have been realized with this technique [180].

6.3.5 Cross-Phase Modulation

The SPM and XPM both affect the performance of WDM systems. The effects of SPM has been discussed in Sections 5.3 in the context of single-channel systems; they also apply to individual channels of a WDM system. The phenomenon of XPM is an important mechanism of nonlinear crosstalk in WDM lightwave systems and has been studied extensively in this context [184]–[197].

As discussed in Section 2.6, XPM originates from the intensity dependence of the refractive index, which produces an intensity-dependent phase shift as the signal propagates through the optical fiber. The phase shift for a specific channel depends not only on the power of that channel but also on the power of other channels [74]. The total phase shift for the j th channel is given by (see Section 2.6)

$$\phi_j^{NL} = \frac{\gamma}{\alpha} \left(P_j + 2 \sum_{m \neq j}^N P_m \right), \quad (6.3.14)$$

where the first term is due to SPM and L_{eff} has been replaced with $1/\alpha$ assuming $\alpha L \gg 1$. The parameter γ is in the range $1\text{--}10 \text{ W}^{-1}\text{km}^{-1}$ depending on the type of fiber used, larger values occurring for dispersion-compensating fibers. The nonlinear phase shift depends on the bit pattern of various channels and can vary from zero to its maximum value $\phi_{\max} = (\gamma/\alpha)(2N - 1)P_j$ for N channels, if we assume equal channel powers.

Strictly speaking, the XPM-induced phase shift should not affect system performance if the GVD effects were negligible. However, any dispersion in fiber converts pattern-dependent phase shifts to power fluctuations, reducing the SNR at the receiver. This conversion can be understood by noting that time-dependent phase changes lead to frequency chirping that affects dispersion-induced broadening of the signal. Figure 6.22 shows XPM-induced fluctuations for a CW probe launched with a 10-Gb/s pump channel modulated using the NRZ format. The probe power fluctuates by as much as 6% after 320 km of dispersive fiber. The root-mean-square (RMS) value of fluctuations depends on the channel power and can be reduced by lowering it. As a rough estimate, if we use the condition $\phi_{\max} < 1$, the channel power is restricted to

$$P_{\text{ch}} < \alpha / [\gamma(2N - 1)]. \quad (6.3.15)$$

For typical values of α and γ , P_{ch} should be below 10 mW even for five channels and reduces to below 1 mW for more than 50 channels.

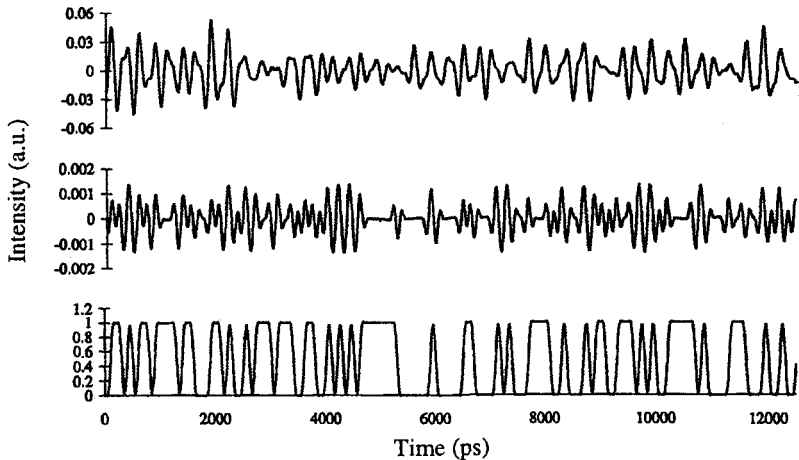


Figure 6.22: XPM-induced power fluctuations on a CW probe for a 130-km link (middle) and a 320-km link (top) with dispersion management. An NRZ bit stream in the pump channel is shown at the bottom. (After Ref. [187], ©1999 IEEE; reprinted with permission.)

The preceding analysis provides only a rough estimate as it ignores the fact that pulses belonging to different channels travel at different speeds and walk through each other at a rate that depends on their wavelength difference. Since XPM can occur only when pulses overlap in the time domain, its impact is reduced considerably by the walk-off effects. As a faster-moving pulse belonging to one channel collides with and passes through a specific pulse in another channel, the XPM-induced chirp shifts the pulse spectrum first toward red and then toward blue. In a lossless fiber, collisions of two pulses are perfectly symmetric, resulting in no net spectral shift at the end of the collision. In a loss-managed system with optical amplifiers placed periodically along the link, power variations make collisions between pulses of different channels asymmetric, resulting in a net frequency shift that depends on the channel spacing. Such frequency shifts lead to timing jitter (the speed of a channel depends on its frequency because of GVD) since their magnitude depends on the bit pattern as well as on the channel wavelengths. The combination of XPM-induced amplitude and timing jitter degrades the SNR at the receiver, especially for closely spaced channels, and leads to XPM-induced power penalty that depends on channel spacing and the type of fibers used for the WDM link. The power penalty increases for fibers with large GVD and for WDM systems designed with a small channel spacing and can exceed 5 dB even for 100-GHz spacing.

How can one control the XPM-induced crosstalk in WDM systems? Clearly, the use of low-GVD fibers will reduce this problem to some extent but is not practical because of the onset of FWM (see next subsection). In practice, dispersion management is employed in virtually all WDM systems such that the local dispersion is relatively large. Careful selection of the dispersion-map parameters may help from the XPM standpoint but may not be optimum from the SPM point of view [186]. A simple approach to XPM suppression consists of introducing relative time delays among the

WDM channels after each map period such that the “1” bits in neighboring channels are unlikely to overlap most of the time [191]. The use of RZ format is quite helpful in this context because all 1 bits occupy only a fraction of the bit slot. In a 10-channel WDM experiment, time delays were introduced by using 10 fiber gratings spaced apart by varying distances chosen to enhance XPM suppression [193]. The BER floor observed after 500 km of transmission disappeared after the XPM suppressors (consisting of 10 Bragg gratings) were inserted every 100 km. The residual power penalty at a BER of 10^{-10} was below 2 dB for all channels.

6.3.6 Four-Wave Mixing

As discussed in Section 2.6, the nonlinear phenomenon of FWM requires phase matching. It becomes a major source of nonlinear crosstalk whenever the channel spacing and fiber dispersion are small enough to satisfy the phase-matching condition approximately [74]. This is the case when a WDM system operates close to the zero-dispersion wavelength of dispersion-shifted fibers. For this reason, several techniques have been developed for reducing the impact of FWM in WDM systems [161].

The physical origin of FWM-induced crosstalk and the resulting system degradation can be understood by noting that FWM generates a new wave at the frequency $\omega_{ijk} = \omega_i + \omega_j - \omega_k$, whenever three waves at frequencies ω_i , ω_j , and ω_k copropagate inside the fiber. For an N -channel system, i , j , and k can vary from 1 to N , resulting in a large combination of new frequencies generated by FWM. In the case of equally spaced channels, the new frequencies coincide with the existing frequencies, leading to coherent in-band crosstalk. When channels are not equally spaced, most FWM components fall in between the channels and lead to incoherent out-of-band crosstalk. In both cases, the system performance is degraded because of a loss in the channel power, but the coherent crosstalk degrades system performance much more severely.

The FWM process in optical fibers is governed by a set of four coupled equations whose general solution requires a numerical approach [74]. If we neglect the phase shifts induced by SPM and XPM, assume that the three channels participating in the FWM process remain nearly undepleted, and include fiber losses, the amplitude A_F of the FWM component at the frequency ω_F is governed by

$$\frac{dA_F}{dz} = -\frac{\alpha}{2}A_F + d_F \gamma A_i A_j A_k^* \exp(-i\Delta kz), \quad (6.3.16)$$

where $A_m(z) = A_m(0) \exp(-\alpha z/2)$ for $m = i, j, k$ and $d_F = 2 - \delta_{ij}$ is the degeneracy factor defined such that its value is 1 when $i = j$ but doubles when $i \neq j$. This equation can be easily integrated to obtain $A_F(z)$. The power transferred to the FWM component in a fiber of length L is given by [198]

$$P_F = |A_F(L)|^2 = \eta_F (d_F \gamma L)^2 P_i P_j P_k e^{-\alpha L}, \quad (6.3.17)$$

where $P_m = |A_m(0)|^2$ is the launched power in the m th channel and η_F is a measure of the FWM efficiency defined as

$$\eta_F = \left| \frac{1 - \exp[-(\alpha + i\Delta k)L]}{(\alpha + i\Delta k)L} \right|^2. \quad (6.3.18)$$

The FWM efficiency η_F depends on the channel spacing through the phase mismatch governed by

$$\Delta k = \beta_F + \beta_k - \beta_i - \beta_j \approx \beta_2(\omega_i - \omega_k)(\omega_j - \omega_k), \quad (6.3.19)$$

where the propagation constants were expanded in a Taylor series around $\omega_c = (\omega_i + \omega_j)/2$ and β_2 is the GVD parameter at that frequency. If the GVD of the transmission fiber is relatively large, ($|\beta_2| > 5 \text{ ps}^2/\text{km}$), η_F nearly vanishes for typical channel spacings of 50 GHz or more. In contrast, $\eta_F \approx 1$ close to the zero-dispersion wavelength of the fiber, resulting in considerable power in the FWM component, especially at high channel powers. In the case of equal channel powers, P_F increases as P_{ch}^3 . This cubic dependence of the FWM component limits the channel powers to below 1 mW if FWM is nearly phase matched. Since the number of FWM components for an M -channel WDM system increases as $M^2(M - 1)/2$, the total power in all FWM components can be quite large.

A simple scheme for reducing the FWM-induced degradation consists of designing WDM systems with unequal channel spacings [161]. The main impact of FWM in this case is to reduce the channel power. This power depletion results in a power penalty that is relatively small compared with the case of equal channel spacings. Experimental measurements on WDM systems confirm the advantage of unequal channel spacings. In a 1999 experiment, this technique was used to transmit 22 channels, each operating at 10 Gb/s, over 320 km of dispersion-shifted fiber with 80-km amplifier spacing [199]. Channel spacings ranged from 125 to 275 GHz in the 1532- to 1562-nm wavelength region and were determined using a periodic allocation scheme [200]. The zero-dispersion wavelength of the fiber was close to 1548 nm, resulting in near phase matching of many FWM components. Nonetheless, the system performed quite well with less than 1.5-dB power penalty for all channels.

The use of a nonuniform channel spacing is not always practical because many WDM components, such as optical filters and waveguide-grating routers, require equal channel spacings. A practical solution is offered by the periodic dispersion-management technique discussed in Chapter 8. In this case, fibers with normal and anomalous GVD are combined to form a dispersion map such that GVD is high locally all along the fiber even though its average value is quite low. As a result, the FWM efficiency η_F is negligible throughout the fiber, resulting in little FWM-induced crosstalk. The use of dispersion management is common for suppressing FWM in WDM systems because of its practical simplicity. In fact, new kinds of fibers, called *nonzero-dispersion-shifted* fibers (NZDSFs), were designed and marketed after the advent of WDM systems. Typically, GVD is in the range of 4 to 8 ps/(km-nm) in such fibers to ensure that the FWM-induced crosstalk is minimized.

6.3.7 Other Design Issues

The design of WDM communication systems requires careful consideration of many transmitter and receiver characteristics. An important issue concerns the stability of the carrier frequency (or wavelength) associated with each channel. The frequency of light emitted from DFB or DBR semiconductor lasers can change considerably because of

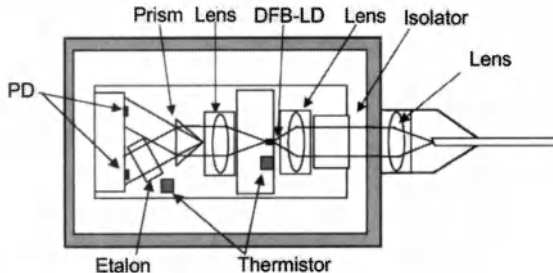


Figure 6.23: Schematic of a DFB laser-diode (LD) module with a built-in étalon for monitoring and stabilizing the laser wavelength; PD stands for photodiode. (After Ref. [207]; ©2004 IEEE.)

changes in the operating temperature ($\sim 10 \text{ GHz}/^\circ\text{C}$). Similar changes can also occur with the aging of lasers [201]. Such frequency changes are generally not of concern for single-channel systems. In the case of WDM lightwave systems it is important that the carrier frequencies of all channels remain stable, at least relatively, so that the channel spacing does not fluctuate with time.

A number of techniques have been used for frequency stabilization [202]–[209]. A common technique uses *electrical feedback* provided by a frequency discriminator using an atomic or molecular resonance to lock the laser frequency to the resonance frequency. For example, one can use ammonia, krypton, or acetylene for semiconductor lasers operating in the $1.55\text{-}\mu\text{m}$ region, as all three have resonances near that wavelength. Frequency stability to within 1 MHz can be achieved by this technique. Another technique makes use of the *optogalvanic effect* to lock the laser frequency to an atomic or molecular resonance. A phase-locked loop can also be used for frequency stabilization. In another scheme, a Michelson interferometer, calibrated by using a frequency-stabilized master DFB laser, provides a set of equally spaced reference frequencies [203]. A FP filter, an AWG, or any other filter with a comb-like periodic transmission spectrum can also be used for this purpose because it provides a reference set of equally spaced frequencies [204]. A fiber grating is useful for frequency stabilization but a separate grating is needed for each channel as its reflection spectrum is not periodic [205].

Figure 6.23 shows a DFB laser module in which both the optical power and the wavelength of the laser are monitored and maintained at constant values [207]. Light from the back facet of the DFB laser is split into two branches using a prism. An FP étalon in one branch serves as a wavelength reference; it is designed such that one of its transmission peaks occurs precisely at the wavelength at which the laser is designed to operate. The use of a FP étalon as a wavelength reference suffers from one problem. Variations in the étalon temperature can shift its transmission peaks in an uncontrolled manner. This problem is solved by monitoring the temperature of the étalon and adjusting the feedback signal accordingly. With this approach, the wavelength of the laser module drifted by less than 1 pm even when the module temperature varied from 5 to 70°C . Reliability tests indicated that wavelength drift for such lasers should be less than 5 pm during a 25-year operating period.

An important issue in the design of WDM networks is related to the loss of signal

power that occurs because of insertion, distribution, and transmission losses. Optical amplifiers are used to compensate for such losses but not all channels are amplified by the same factor unless the gain spectrum is flat over the entire bandwidth of the WDM signal. Although gain-flattening techniques are commonly employed, channel powers can still deviate by 10 dB or more when the WDM signal passes through many optical amplifiers before being detected. It may then become necessary to control the power of individual channels (through selective attenuation) at each node within a WDM network to make the channel powers nearly uniform. The issue of power management in WDM networks is quite complex and requires attention to many details [210]–[212]. The buildup of amplifier noise can also become a limiting factor when the WDM signal passes through a large number of amplifiers. In general, management of a WDM network requires attention to many details [7]–[10].

6.4 Time-Division Multiplexing

As discussed in Section 1.2, TDM is commonly performed in the electrical domain to obtain digital hierarchies for telecommunication systems. In this sense, even single-channel lightwave systems carry multiple TDM channels. The electrical TDM becomes difficult to implement at bit rates above 40 Gb/s because of the limitations imposed by high-speed electronics. A solution is offered by the *optical* TDM (OTDM), a scheme that can increase the bit rate of a single optical carrier to values above 1 Tb/s. The OTDM technique was studied extensively during the 1990s [213]–[219], and further research has continued in recent years in the context of WDM systems with channel bit rates of 100 Gb/s or more [220]–[224]. Its deployment requires new types of optical transmitters and receivers based on all-optical multiplexing and demultiplexing techniques. In this section we first discuss these new techniques and then focus on the design and performance issues related to OTDM lightwave systems.

6.4.1 Channel Multiplexing

In OTDM lightwave systems, several optical signals at a bit rate B share the same carrier frequency and are multiplexed optically to form a composite bit stream at the bit rate NB , where N is the number of channels. Several multiplexing techniques can be used for this purpose [219]. Figure 6.24 shows the design of an OTDM transmitter based on the delay-line technique. It requires a laser capable of generating a periodic pulse train at the repetition rate equal to the single-channel bit rate B . Moreover, the laser should produce pulses of width T_p such that $T_p < T_B = (NB)^{-1}$ to ensure that each pulse will fit within its allocated time slot T_B . The laser output is split equally into N branches, after amplification if necessary. A modulator in each branch blocks the pulses representing 0 bits and creates N independent bit streams at the bit rate B .

Multiplexing of N bit streams is achieved by a delay technique that can be implemented optically in a simple manner. In this scheme, the bit stream in the n th branch is delayed by an amount $(n - 1)/(NB)$, where $n = 1, \dots, N$. The output of all branches is then combined to form a composite signal. It should be clear that the multiplexed bit stream produced using such a scheme has a bit slot corresponding to the bit rate NB .

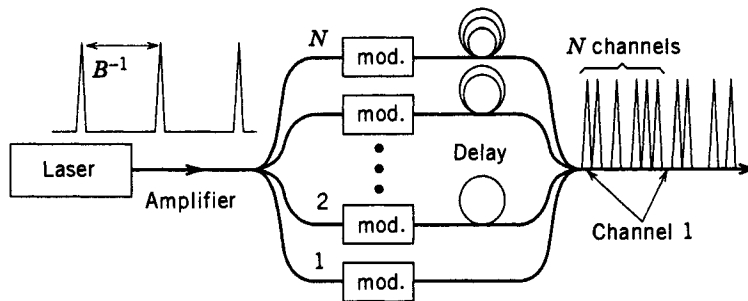


Figure 6.24: Design of an OTDM transmitter based on optical delay lines.

Furthermore, N consecutive bits in each interval of duration B^{-1} belong to N different channels, as required by the TDM scheme (see Section 1.2).

The entire OTDM multiplexer (except for modulators which require LiNbO₃ or semiconductor waveguides) can be built using single-mode fibers. Splitting and recombining of signals in N branches can be accomplished with $1 \times N$ fused fiber couplers. The optical delay lines can be implemented using fiber segments of controlled lengths. As an example, a 1-mm length difference introduces a delay of about 5 ps. Note that the delay lines can be relatively long (10 cm or more) because only the length difference has to be matched precisely. For a precision of 0.1 ps, typically required for a 40-Gb/s OTDM signal, the delay lengths should be controlled to within 20 μ m. Such precision is hard to realize using optical fibers.

An alternative approach makes use of planar lightwave circuits fabricated using the silica-on-silicon technology [53]–[56]. Such devices can be made polarization insensitive while providing a precise control of the delay lengths. However, the entire multiplexer cannot be built in the form of a planar lightwave circuit as modulators cannot be integrated with this technology. A simple approach consists of inserting an InP chip containing an array of electroabsorption modulators in between the silica waveguides that are used for splitting, delaying and combining the multiple channels (see Figure 6.24). The main problem with this approach is the spot-size mismatch as the optical signal passes from Si to InP waveguide (and vice versa). This problem can be solved by integrating spot-size converters with the modulators. Such an integrated OTDM multiplexer was used in a 160-Gb/s experiment in which 16 channels, each operating at 10 Gb/s were multiplexed [218]. In a different approach, a cascaded nonlinear process inside periodically poled LiNbO₃ waveguides (resulting in FWM) is employed [222].

An important difference between the OTDM and WDM techniques should be apparent from Figure 6.24: The OTDM technique requires the use of the RZ format. Historically, the NRZ format used before the advent of lightwave technology was retained even for optical communication systems. Starting in the late 1990s, the RZ format began to appear in dispersion-managed WDM systems. The use of OTDM requires optical sources emitting a train of short optical pulses at a repetition rate as high as 40 GHz. Two types of lasers are commonly used for this purpose [219]. In one approach, gain switching or mode locking of a semiconductor laser provides 10–20 ps pulses at a high repetition rate, which can be compressed using a variety of techniques.

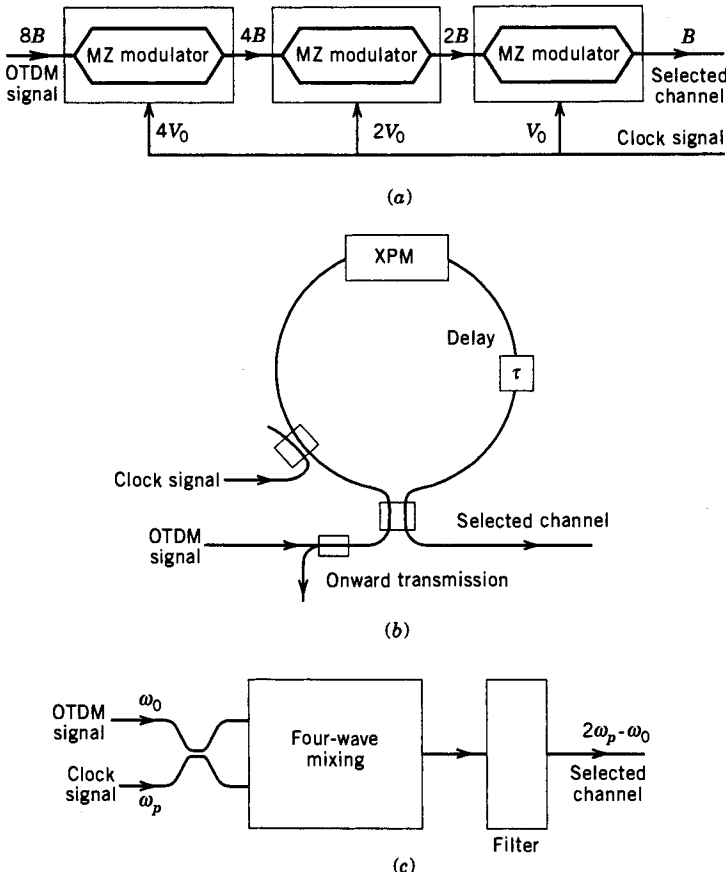


Figure 6.25: Demultiplexing schemes for OTDM signals based on (a) cascaded LiNbO₃ modulators, (b) XPM in a nonlinear optical-loop mirror, and (c) FWM in a nonlinear medium.

In another approach, a fiber laser is harmonically mode locked using an intracavity LiNbO₃ modulator [52]. Such lasers can provide pulse widths ~ 1 ps at a repetition rate of up to 40 GHz.

6.4.2 Channel Demultiplexing

Demultiplexing of individual channels from an OTDM signal requires electro-optic or all-optical techniques. Several schemes have been developed, each having its own merits and drawbacks [216]–[224]. Figure 6.25 shows three schemes discussed in this section. All demultiplexing techniques require a *clock signal*—a periodic pulse train at the single-channel bit rate. The clock signal is in the electric form for electro-optic demultiplexing but consists of an optical pulse train for all-optical demultiplexing.

The electro-optic technique uses several MZ-type LiNbO₃ modulators in series. Each modulator halves the bit rate by rejecting alternate bits in the incoming signal.

Thus, an 8-channel OTDM system requires three modulators, driven by the same electrical clock signal (see Figure 6.25), but with different voltages equal to $4V_0$, $2V_0$, and V_0 , where V_0 is the voltage required for π phase shift in one arm of the MZ interferometer. Different channels can be selected by changing the phase of the clock signal. The main advantage of this technique is that it uses commercially available components. However, it has several disadvantages, the most important being that it is limited by the speed of modulators. The electro-optic technique also requires a large number of expensive components, some of which need high drive voltage.

Several all-optical techniques make use of a *nonlinear optical loop mirror* (NOLM) constructed using a fiber loop whose ends are connected to the two output ports of a 3-dB fiber coupler as shown in Figure 6.25(b). Such a device is also referred to as the Sagnac interferometer. The NOLM is called a mirror because it reflects its input entirely when the counterpropagating waves experience the same phase shift over one round trip. However, if the symmetry is broken by introducing a relative phase shift of π between them, the signal is fully transmitted by the NOLM. The demultiplexing operation of an NOLM is based on the XPM [74], the same nonlinear phenomenon that can lead to crosstalk in WDM systems.

Demultiplexing of an OTDM signal by an NOLM can be understood as follows. The clock signal consisting of a train of optical pulses at the single-channel bit rate is injected into the loop such that it propagates only in the clockwise direction. The OTDM signal enters the NOLM after being equally split into counterpropagating directions by the 3-dB coupler. The clock signal introduces a phase shift through XPM for pulses belonging to a specific channel within the OTDM signal. In the simplest case, optical fiber itself introduces XPM. The power of the optical signal and the loop length are made large enough to introduce a relative phase shift of π . As a result, a single channel is demultiplexed by the NOLM. In this sense, an NOLM is the TDM counterpart of the WDM add-drop multiplexers discussed in Section 6.2.3. All channels can be demultiplexed simultaneously by using several NOLMs in parallel [214]. Fiber nonlinearity is fast enough that such a device can respond at femtosecond time scales. Demultiplexing of a 6.3-Gb/s channel from a 100-Gb/s OTDM signal was demonstrated in 1993. By 1998, the NOLM was used to demultiplex a 640-Gb/s OTDM signal [225].

The third scheme for demultiplexing in Figure 6.25 makes use of FWM in a nonlinear medium [52]. The OTDM signal is launched together with the clock signal (at a different wavelength) into a nonlinear medium. The clock signal plays the role of the pump for the FWM process. FWM produces a pulse at the idler wavelength only in time slots in which a clock pulse overlaps with the signal pulses of the channel that needs to be demultiplexed. As a result, the pulse train at the new wavelength is an exact replica of the channel that needs to be demultiplexed. An optical filter is used to separate the demultiplexed channel from the OTDM and clock signals. A polarization-preserving fiber is often used as the nonlinear medium for FWM because of the ultrafast nature of its nonlinearity and its ability to preserve the state of polarization despite environmental fluctuations. As early as 1996, error-free demultiplexing of 10-Gb/s channels from a 500-Gb/s OTDM signal was demonstrated by using clock pulses of about 1 ps duration [226]. This scheme can also amplify the demultiplexed channel (by up to 40 dB) through parametric amplification inside the same fiber [227].

6.4.3 System Performance

The transmission distance of OTDM signals is limited in practice by fiber dispersion because of the use of short optical pulses (~ 1 ps) dictated by a relatively high bit rate. In fact, an OTDM signal carrying N channels at the bit rate B is equivalent to transmitting a single channel at the composite bit rate of NB , and the bit rate–distance product NBL is restricted by the dispersion limits found in Section 2.4.3. As an example, it is evident from Figure 2.12 that a 200-Gb/s system is limited to $L < 50$ km even when the system is designed to operate exactly at the zero-dispersion wavelength of the fiber. Thus, OTDM systems require not only dispersion-shifted fibers but also the use of dispersion-management techniques capable of reducing the impact of both the second- and third-order dispersive effects (see Chapter 8). Even then, PMD becomes a limiting factor for long fiber lengths and its compensation is often necessary. The intrachannel nonlinear effects also limit the performance of OTDM systems because the use of intense pulses is often necessary for OTDM systems [217].

In spite of the difficulties inherent in designing OTDM systems operating at bit rates exceeding 100 Gb/s, many laboratory experiments have realized high-speed transmission using the OTDM technique [219]. In a 1996 experiment, a 100-Gb/s OTDM signal, consisting of 16 channels at 6.3 Gb/s, was transmitted over 560 km by using optical amplifiers (80-km spacing) together with dispersion management. The laser source in this experiment was a mode-locked fiber laser producing 3.5-ps pulses at a repetition rate of 6.3 GHz (the bit rate of each multiplexed channel). A multiplexing scheme similar to that shown in Figure 6.24 was used to generate the 100-Gb/s OTDM signal. The total bit rate was later extended to 400 Gb/s (forty 10-Gb/s channels) by using a supercontinuum pulse source producing 1-ps pulses [228]. Such short pulses are needed since the bit slot is only 2.5-ps wide at 400 Gb/s. It was necessary to compensate for the dispersion slope (third-order dispersion β_3) as 1-ps pulses were severely distorted and exhibited oscillatory tails extending to beyond 5 ps (typical characteristic of the third-order dispersion) in the absence of such compensation. Even then, the transmission distance was limited to 40 km.

OTDM transmission at a bit rate of 160 Gb/s drew considerable attention after 2000 because it was considered a natural update for 40-Gb/s systems [220]–[224]. In a 2001 field trial, a 160-Gb/s OTDM signal was transmitted over 116 km [230]. By 2006, transmission over 4320 km has been demonstrated using a recirculating loop [221]. This experiment employed the DPSK format and also demonstrated the long-term stability of OTDM systems with properly designed components. In another set of experiments the objective was to realize a single-channel bit rate of 1 Tb/s or more. In a 2000 experiment, a 1.28-Tb/s OTDM signal could be transmitted over 70 km but it required compensation of second-, third-, and fourth-order dispersions simultaneously [229]. More recently, the DQPSK format was employed to show OTDM transmission over 240 km at 1.28-Tb/s and over 160 km at a bit rate of 2.56 Tb/s [221].

A simple method for realizing high bit rates exceeding 1 Tb/s consists of combining the OTDM and WDM techniques. For example, a WDM signal consisting of M separate optical carriers such that each carrier carries N OTDM channels at the bit rate B has the total capacity $B_{\text{tot}} = MNB$. The dispersion limitations of such a system are set by the OTDM-signal bit rate of NB . In a 1999 experiment, this approach was used

to realize a total capacity of 3 Tb/s by using $M = 19$, $N = 16$, and $B = 10$ Gb/s [219]. The channels were spaced 450 GHz apart to avoid overlap between neighboring WDM channels, and the 70-nm WDM signal occupied both the C and L bands. The OTDM bit rate was extended to 320 Gb/s in a 2004 experiment that transmitted 10 such channels over a limited distance of 40 km [231]. By 2009, five channels, each operating at 320 Gb/s, were transmitted over 525 km by using a time-domain optical Fourier transformation technique [232]. With the use of new modulation formats and coherent detection, the total capacity of such OTDM/WDM systems should exceed 10 Tb/s. However, many factors such as various nonlinear effects in fibers and the practicality of dispersion compensation over a wide bandwidth are likely to limit the performance of such systems.

OTDM has also been used for designing transparent optical networks capable of connecting multiple nodes for random bidirectional access [215]. Its use is especially practical for packet-based networks employing the ATM or TCP/IP protocol [233]–[235]. Similar to the case of WDM networks, both single-hop and multihop architectures have been considered. Single-hop OTDM networks use passive star couplers to distribute the signal from one node to all other nodes. In contrast, multihop OTDM networks require signal processing at each node to route the traffic. A packet-switching technique is commonly used for such networks.

6.5 Subcarrier Multiplexing

In some LAN and MAN applications the bit rate of each channel is relatively low but the number of channels can become quite large. An example is provided by common-antenna (cable) television (CATV) networks. The basic concept behind *subcarrier multiplexing* (SCM) is borrowed from microwave technology, which employs multiple microwave carriers for transmitting multiple CATV channels (electrical FDM) over coaxial cables or free space. The total bandwidth is limited to well below 1 GHz when coaxial cables are used to transmit a multichannel microwave signal. However, if the microwave signal is transmitted optically by using optical fibers, the signal bandwidth can easily exceed 10 GHz for a single optical carrier. Such a scheme is referred to as SCM, since multiplexing is done by using microwave subcarriers rather than the optical carrier. It has been used commercially by the CATV industry since 1992 and can be combined with TDM or WDM. A combination of SCM and WDM can realize bandwidths in excess of 1 THz. The SCM technique essentially sends a radio or microwave signal over optical fibers and is also referred to as *radio over fibers*.

Figure 6.26 shows schematically a SCM lightwave system designed with a single optical carrier. The main advantage of SCM is the flexibility and the upgradability offered by it in the design of broadband networks. One can use analog or digital modulation, or a combination of the two, to transmit multiple voice, data, and video signals to a large number of users. Each user can be served by a single subcarrier, or the multi-channel signal can be distributed to all users as done commonly by the CATV industry. The SCM technique has been studied extensively because of its wide-ranging practical applications [236]–[239]. In this section we describe both the analog and digital SCM systems with emphasis on their design and performance.

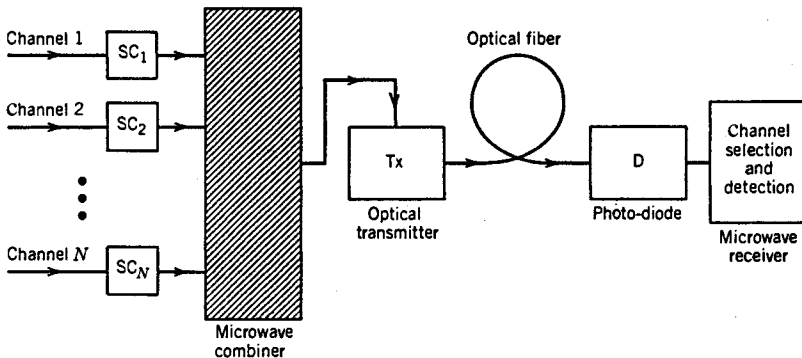


Figure 6.26: Schematic illustration of subcarrier multiplexing. Multiple microwave subcarriers (SC) are modulated, and the composite electrical signal is used to modulate an optical carrier at the transmitter (Tx).

6.5.1 Analog and Digital SCM Systems

This book focuses mostly on digital modulation techniques as they are employed almost universally for lightwave systems. An exception occurs in the case of SCM systems designed for video distribution. Until 2000, most CATV networks distributed television channels by using analog techniques based on frequency modulation (FM) or amplitude modulation with vestigial sideband (AM-VSB) formats [237]. As the wave form of an analog signal must be preserved during transmission, analog SCM systems require a high SNR at the receiver and impose strict linearity requirements on the optical source and the communication channel.

In analog SCM lightwave systems, each microwave subcarrier is modulated using an analog format, and the output of all subcarriers is summed using a microwave power combiner (see Figure 6.26). The composite signal is used to modulate the intensity of a semiconductor laser directly by adding it to the bias current. The transmitted power can be written as

$$P(t) = P_b \left[1 + \sum_{j=1}^N m_j a_j \cos(2\pi f_j t + \phi_j) \right], \quad (6.5.1)$$

where P_b is the output power at the bias level and m_j , a_j , f_j , and ϕ_j are, respectively, the modulation index, amplitude, frequency, and phase associated with the j th microwave subcarrier; a_j , f_j , or ϕ_j is modulated to impose the signal depending on whether AM, FM, or phase modulation (PM) is used.

The power at the receiver would also be in the form of Eq. (6.5.1) if the communication channel were perfectly linear. In practice, the analog signal is distorted during its transmission through the fiber link. The distortion is referred to as *intermodulation distortion* (IMD) and is similar in nature to the FWM distortion discussed in Section 6.3. Any nonlinearity in the response of the semiconductor laser used inside the optical transmitter or in the propagation characteristics of fibers generates new frequencies of the form $f_i + f_j$ and $f_i + f_j \pm f_k$, some of which lie within the transmission bandwidth and distort the analog signal. The new frequencies are referred to as the *intermodula-*

tion products (IMPs). These are further subdivided as two-tone IMPs and triple-beat IMPs, depending on whether two frequencies coincide or all three frequencies are distinct. The triple-beat IMPs tend to be a major source of distortion because of their large number. An N -channel SCM system generates $N(N - 1)(N - 2)/2$ triple-beat terms compared with $N(N - 1)$ two-tone terms. The second-order IMD must also be considered if subcarriers occupy a large bandwidth.

IMD has its origin in several distinct nonlinear mechanisms. The dynamic response of semiconductor lasers is governed by the rate equations (see Section 3.5), which are intrinsically nonlinear. The solution of these equations provides expressions for the second- and third-order IMPs originating from this intrinsic nonlinearity. Their contribution is largest whenever the IMP frequency falls near the relaxation-oscillation frequency. A second source of IMD is the nonlinearity of the power-current curve. The magnitude of resulting IMPs can be calculated by expanding the output power in a Taylor series around the bias power [237]. Several other mechanisms, such as fiber dispersion, frequency chirp, and mode-partition noise can cause IMD, and their impact on the SCM systems has been studied extensively [240].

The IMD-induced degradation of the system performance depends on the inter-channel interference created by IMPs. Depending on the channel spacing among microwave subcarriers, some of the IMPs fall within the bandwidth of a specific channel and affect the signal recovery. It is common to introduce composite second-order (CSO) and composite triple-beat (CTB) distortion by adding the power for all IMPs that fall within the passband of a specific channel [237]. The CSO and CTB distortion values are normalized to the carrier power of that channel and expressed in dBc units, where the “c” in dBc denotes normalization with respect to the carrier power. Typically, CSO and CTB distortion values should be below -60 dBc for negligible impact on the system performance; both of them increase rapidly with an increase in the modulation index.

System performance depends on the SNR associated with the demodulated signal. In the case of SCM systems, the *carrier-to-noise ratio* (CNR) is often used in place of SNR. The CNR is defined as the ratio of RMS carrier power to RMS noise power at the receiver and can be written as

$$\text{CNR} = \frac{(mR\bar{P})^2/2}{\sigma_s^2 + \sigma_T^2 + \sigma_I^2 + \sigma_{\text{IMD}}^2}, \quad (6.5.2)$$

where m is the modulation index, R is the detector responsivity, \bar{P} is the average received optical power, and σ_s , σ_T , σ_I , and σ_{IMD} are the RMS values of the noise currents associated with the shot noise, thermal noise, intensity noise, and IMD, respectively. The expressions for σ_s^2 and σ_T^2 are given in Section 4.4.1. The RMS value σ_I of the intensity noise can be obtained from Section 4.7.2. If we assume that the relative intensity noise (RIN) of the laser is nearly uniform within the receiver bandwidth,

$$\sigma_I^2 = (\text{RIN})(R\bar{P})^2(2\Delta f). \quad (6.5.3)$$

The RMS value of σ_{IMD} depends on the CSO and CTB distortion values.

The CNR requirements of SCM systems depend on the modulation format. In the case of AM-VSB format, the CNR should typically exceed 50 dB for satisfactory

performance. Such large values can be realized only by increasing the received optical power \bar{P} to a relatively large value (> 0.1 mW). This requirement has two effects. First, the power budget of AM-analog SCM systems is extremely limited unless the transmitter power is increased above 10 mW. Second, the intensity-noise contribution to the receiver noise dominates the system performance as σ_i^2 increases quadratically with \bar{P} . In fact, the CNR becomes independent of the received optical power when σ_i dominates. From Eqs. (6.5.2) and (6.5.3) the limited value of CNR is given by

$$\text{CNR} \approx \frac{m^2}{4(\text{RIN})\Delta f}. \quad (6.5.4)$$

As an example, the RIN of the transmitter laser should be below -150 dB/Hz to realize a CNR of 50 dB if $m = 0.1$ and $\Delta f = 50$ MHz are used as the representative values. Larger values of RIN can be tolerated only by increasing the modulation index m or by decreasing the receiver bandwidth. Indeed, DFB lasers with low values of the RIN were developed during the 1990s for CATV applications. In general, the DFB laser is biased high above threshold to provide a bias power P_b in excess of 5 mW because its RIN decreases as P_b^{-3} . High values of the bias power also permit an increase in the modulation index m .

The intensity noise can become a problem even when the transmitter laser is selected with a low RIN value to provide a large CNR in accordance with Eq. (6.5.4). The reason is that the RIN can be enhanced during signal transmission inside optical fibers. One such mechanism is related to multiple reflections between two reflecting surfaces along the fiber link. The two reflective surfaces act as an FP interferometer which converts the laser-frequency noise into intensity noise. The reflection-induced RIN depends on both the laser linewidth and the spacing between reflecting surfaces. It can be avoided by using fiber components (splices and connectors) with negligible parasitic reflections (< -40 dB) and by using lasers with a narrow linewidth (< 1 MHz). Another mechanism for the RIN enhancement is provided by the dispersive fiber itself. Because of GVD, different frequency components travel at slightly different speeds. As a result, frequency fluctuations are converted into intensity fluctuations during signal transmission. The dispersion-induced RIN depends on laser linewidth and increases quadratically with fiber length. Fiber dispersion also enhances CSO and CTB distortion for long link lengths [237]. It becomes necessary to use a dispersion-management technique (see Chapter 8) for such SCM systems.

The CNR requirement can be relaxed by changing the modulation format from AM to FM. The bandwidth of a FM subcarrier is considerably larger (30 MHz in place of 4 MHz). However, the required CNR at the receiver is much lower (about 16 dB in place of 50 dB) because of the so-called FM advantage that yields a studio-quality video signal (> 50 -dB SNR) with only 16-dB CNR. As a result, the optical power needed at the receiver can be as small as $10 \mu\text{W}$. The RIN is not much of a problem for such systems as long as the RIN value is below -135 dB/Hz. In fact, the receiver noise of FM systems is generally dominated by the thermal noise. Both the AM and FM techniques have been used successfully for analog SCM lightwave systems [237].

During the 1990s, the emphasis of SCM systems shifted from analog to digital modulation. The frequency-shift keying (FSK) format was used for modulating microwave subcarriers [236] as early as 1990 but its use requires coherent detection (see

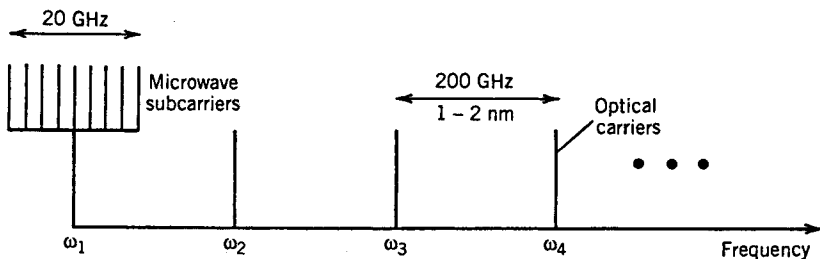


Figure 6.27: Frequency allocation in a multiwavelength SCM network.

Section 4.5). Moreover, a single digital video channel requires a bit rate of 100 Mb/s or more, in contrast with analog channels that occupy a bandwidth of only 6 MHz. For this reason, other modulation formats such as quadrature AM (QAM) and quadrature PSK (QPSK) have been explored. A multilevel QAM format is used often in practice with typically 64 levels. Such a signal requires a lower CNR compared with that needed for analog AM-VSB systems. The capacity of an SCM system can be increased considerably by employing hybrid techniques that mix analog and digital formats.

The hybrid SCM systems that combine the analog AM-VSB format with the digital QAM format have attracted attention because they can transmit a large number of video channels over the same fiber simultaneously [238]. The performance of such systems is affected by the clipping noise, multiple optical reflections, and the nonlinear mechanisms such as self-phase modulation (SPM) and SBS, all of which limit the total power and the number of channels that can be multiplexed. Nevertheless, hybrid SCM systems can transport up to 80 analog and 30 digital channels using a single optical transmitter. If only QAM format is employed, the number of digital channels is limited to about 80. In a 2000 experiment, 78 channels with the 64-QAM format were transmitted over 740 km [239]. Each channel had a bit rate of 30 Mb/s, resulting in a total capacity of 2.34 Gb/s. Such a SCM system can transport up to 500 compressed video channels. Further increase in the system capacity can be realized by combining the SCM and WDM techniques, a topic discussed next.

6.5.2 Multiwavelength SCM Systems

The combination of WDM and SCM provides the potential of designing broadband passive optical networks capable of providing integrated services (video, data, etc.) to a large number of subscribers [241]–[247]. In this scheme, shown schematically in Figure 6.27, multiple optical carriers are launched into the same optical fiber through the WDM technique. Each optical carrier carries multiple SCM channels using several microwave subcarriers. One can mix analog and digital signals using different subcarriers or different optical carriers. Such networks are extremely flexible and easy to upgrade as the demand grows. As early as 1990, 16 DFB lasers with a wavelength spacing of 2 nm in the 1.55- μm region were modulated with 100 analog video channels and six 622-Mb/s digital channels [242]. Video channels were multiplexed using the SCM technique such that one DFB laser carried 10 SCM channels over the band-

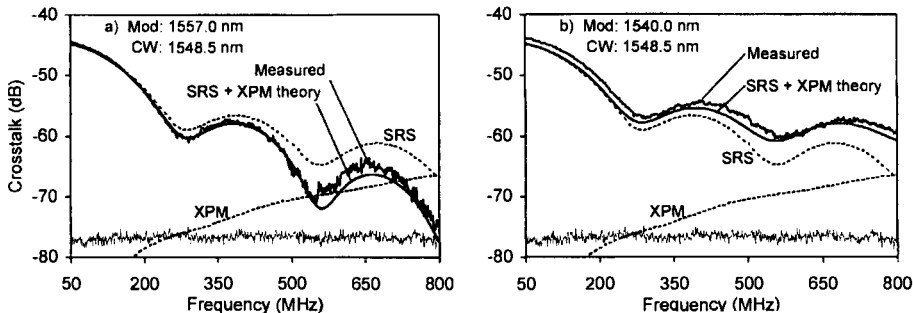


Figure 6.28: Predicted and measured crosstalk acquired over 25 km of fiber at 11-mW average power. The CW laser acts as a probe and its wavelength is (a) lower or (b) higher by 8.5 nm than the signal wavelength. (After Ref. [249]; ©1999 IEEE; reprinted with permission.)

width 300–700 MHz. The potential of such WDM systems was demonstrated in a 2000 experiment in which a broadcast-and-select network was capable of delivering 10,000 channels, each operating at 20 Gb/s [243]. The network used 32 wavelengths (on the ITU grid) each of which could carry 310 microwave subcarriers by modulating at a composite bit rate of 20 Gb/s. In a 2002 experiment, 8 WDM channels were transmitted over 800 km of fiber [245]. Each optical channel delivered 1.04-Gb/s payload using 35 subcarriers, each carrying a 32.2-Mb/s signal in the 256-QAM format.

The limiting factor for multiwavelength SCM networks is interchannel crosstalk resulting from both the linear and nonlinear processes [248]–[252]. The nonlinear effects that produce interchannel crosstalk are SRS and XPM, both of which have been analyzed. Figure 6.28 shows the crosstalk measured in a two-channel experiment together with the theoretical prediction of the SRS- and XPM-induced crosstalk levels [249]. One channel is modulated and carries the actual signal while the other operates continuously (CW) but its power is low enough that it acts as a probe. The wavelength difference $\lambda_{\text{mod}} - \lambda_{\text{CW}}$ is ± 8.5 nm in the two cases shown in Figure 6.28. The probe power varies with time because of SRS and XPM, and the crosstalk is defined as the ratio of radio-frequency (RF) powers in the two channels. The XPM-induced crosstalk increases and the Raman-induced crosstalk decreases with the modulation frequency but each has the same magnitude in the two cases shown in Figure 6.28. The two crosstalks add up in phase only when $\lambda_{\text{mod}} < \lambda_{\text{CW}}$, resulting in a larger value of the total crosstalk in that case. The asymmetry seen in Figure 6.28 is due to SRS and depends on whether the CW probe channel is being depleted or is being amplified by the other channel.

The linear crosstalk results from the phenomenon of optical beat interference. It occurs when two or more users transmit simultaneously on the same optical channel using different subcarrier frequencies. As the optical carrier frequencies are then slightly different, their beating produces a beat note in the photocurrent. If the beat-note frequency overlaps an active subcarrier channel, an interference signal would limit the detection process in a way similar to IMD. Statistical models have been used to estimate the probability of channel outage because of optical beat interference [50].

Multiwavelength SCM systems are quite useful for LAN and MAN applications [241]. They can provide multiple services (telephone, analog and digital TV channels, computer data, etc.) with only one optical transmitter and one optical receiver per user because different services can use different microwave subcarriers. This approach lowers the cost of terminal equipment in access networks. Different services can be offered without requiring synchronization, and microwave subcarriers can be processed using commercial electronic components. Each user is assigned a unique wavelength for transmitting multiple SCM messages but can receive multiple wavelengths. The main advantage of multiwavelength SCM is that the network can serve NM users, where N is the number of optical wavelengths and M is the number of microwave carriers by using only N distinct transmitter wavelengths. The optical wavelengths can be relatively far apart (coarse WDM) for reducing the cost of the terminal equipment. In another approach, the hybrid fiber/coaxial (HFC) technology is used to provide broadband integrated services to the subscriber. Digital video transport systems operating at 10 Gb/s by combining the WDM and SCM techniques became available in 1996. The use of WDM and SCM for personal communication networks is quite appealing. High spectral efficiency A multi-user architecture was demonstrated in 2008 capable of delivering a 1-Gb/s SCM signal per WDM channel in the 16-QAM format [253].

6.5.3 Orthogonal Frequency-Division multiplexing

Orthogonal frequency-division multiplexing (OFDM) is a well-known multiplexing technique in the context of cell phones and other wireless applications [254]–[256]. Its use for WDM systems, pursued since 2005, falls in the category of SCM systems, because OFDM, by its very nature, employs a large number of microwave subcarriers. The main difference from the SCM techniques discussed earlier in this section is the orthogonality of these subcarriers, a feature that allows their much tighter packing and thus improves the spectral efficiency considerably.

The basic idea behind OFDM makes use of the discrete Fourier transform (DFT) operation [257]–[261]. Figure 6.30 shows schematically the designs of typical OFDM transmitters and receivers. As seen there, the electrical bit stream undergoes considerable digital signal processing (DSP) both at the transmitter and receiver ends. The most important part is the DFT and inverse DFT (IDFT) operations. At the transmitter end, serial data is parallelized (S/P operation) and converted into a symbol stream. The number N of parallel streams is chosen in the form of $N = 2^n$ to perform the inverse DFT operation with the help of a fast Fourier transform algorithm, the integer n being typically in the range of 6 to 10. Each parallel stream represents a microwave subcarrier after the IDFT operation. After inserting a cyclic prefix or guardband (GI operation), a digital-to-analog converter (D/A operation) is employed to obtain a composite signal containing all subcarriers. After upshifting signal frequencies by f_{LO} using a microwave oscillator (LO1), the signal takes the form

$$s(t) = \sum_{m=-\infty}^{\infty} \sum_{k=1}^N c_{km} s_k(t - mT_s), \quad s_k(t) = h(t) \exp[-2\pi i(f_{LO} + f_k)t], \quad (6.5.5)$$

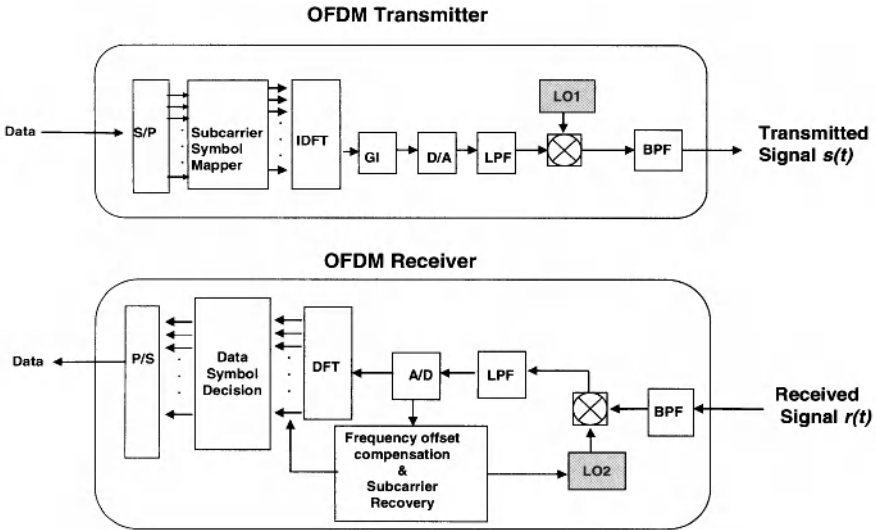


Figure 6.29: Schematic designs of optical OFDM transmitters and receivers. LPF, BPF, and LO stand for low-pass filter, bandpass filter, and local oscillator, respectively. Other symbols are explained in the text. (After Ref. [260]; ©2008 OSA.)

where $s_k(t)$ represents the k th subcarrier at frequency $f_{LO} + f_k$, T_s is the OFDM symbol duration, and $h(t) = 1$ in the interval $0 < t \leq T_s$ but zero outside of it. This composite signal is used to modulate an optical carrier at a specific frequency on the ITU grid. At the receiver end, all operations are reversed to recover the original data bit stream.

To understand the origin of the orthogonality of subcarriers, first note that the DFT frequencies associated with a periodic time-dependent function (period T_s) are given by $f_k = (k - 1)/T_s$, where the integer k takes values from 1 to N . The subcarriers thus form a comb of uniformly spaced frequencies. The orthogonality of subcarriers follows from the relation

$$\langle s_k(t) s_l^*(t) \rangle = \frac{1}{T_s} \int_0^{T_s} s_k(t) s_l^*(t) dt = \delta_{kl}, \quad (6.5.6)$$

where angle brackets denote averaging over the entire OFDM symbol duration. It is important to note that $T_s = NT_b$, where T_b is the bit slot, because the input bit stream is divided into N parallel streams. Since N often exceeds 100 and can be close to 1000, T_s is much longer than T_b . In other words, the symbol rate of each subcarrier is B/N . The OFDM technique permits us to send an input bit stream in the form of N symbol streams, each on its own subcarrier. The spectra of two neighboring symbol streams overlap considerably. However, they can still be demodulated at the receiver because of the orthogonality of these subcarriers.

A major advantage of the OFDM technique is that linear distortions of the transmitted signal, including those induced by fiber dispersion, are reduced dramatically because many low-speed symbol streams are transmitted in parallel rather than one high-speed bit stream. This becomes clear by noting that, since symbol duration of each subcarrier is much longer than the bit duration, dispersive effects are less of a

problem to begin with and can be removed easily at the receiver end if a cyclic prefix is added to each symbol. In this approach, the symbol duration T_s is increased by a certain amount, and this guardband at the front end is used to store a copy of the signal from the back end in a cyclic fashion. Although the increase in T_s reduces the symbol rate of each subcarrier, resulting in a net decrease of the total bit rate, the OFDM system becomes much more resistant to intersymbol interference induced by linear distortions[257]–[261].

The dispersion-tolerant nature of OFDM was demonstrated in a 2007 experiment, that transmitted a 8-Gb/s bit stream by using 128 subcarriers with the QPSK format [257]. The resulting optical OFDM signal could be transmitted over 1000 km of standard telecommunication fiber (using a recirculating fiber loop) without requiring any dispersion compensation. This experiment employed two narrowband lasers (one at the transmitter and the other at the receiver) with line widths of around 20 kHz. Such narrowband lasers are needed because of a relatively low symbol rate of subcarriers and the coherent detection used for them. A transmission distance of 4160 km at a bit rate of 25.8 Gb/s was realized in another OFDM experiment in which 256 subcarriers were used [259]. The experiment implemented a phase-noise compensation scheme by inserting a radio-frequency (RF) pilot at the transmitter. This compensation scheme is discussed later in Section 10.6.4 where we focus on coherent OFDM systems. Non-linear crosstalk resulting from FWM become quite critical for OFDM systems because of a relatively small frequency spacing among subcarriers. However, with suitable modifications of the existing DSP hardware, such distortions can be reduced considerably with a combination of pre- and post-compensation at the transmitter and receiver ends [258].

6.6 Code-Division Multiplexing

A multiplexing scheme, well known in the domain of wireless communications, makes use of the *spread-spectrum technique* [262]. It is referred to as *code-division multiplexing* (CDM) because each channel is coded in such a way that its spectrum spreads over a much wider region than occupied by the original signal [263]. Although spectrum spreading may appear counterintuitive from a spectral point of view, this is not the case because all users share the same spectrum. In fact, CDM is used often for cell phones as it provides the most flexibility in a multiuser environment. It is also relative secure because it is difficult to jam or intercept the signal in view of its coded nature. The term *code-division multiple access* (CDMA) is often employed in place of CDM to emphasize the asynchronous and random nature of multiuser connections.

Even though the use of CDMA for fiber-optic communications attracted attention during the 1980s [264]–[266], it was only after 1995 that optical CDM (OCDM) was pursued seriously [267]–[286]. It can be easily combined with the WDM technique. Conceptually, the difference between the WDM, TDM, and CDM can be understood as follows. The WDM and TDM techniques partition the channel bandwidth or the time slots among users. In contrast, all users share the entire bandwidth and all time slots in a random fashion in the case of CDM. The transmitted data can still be recovered

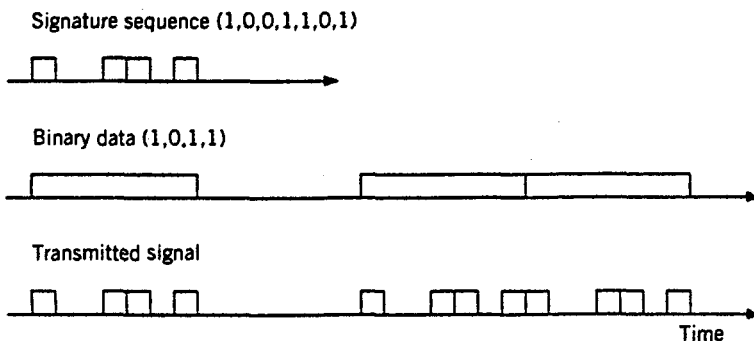


Figure 6.30: Coding of binary data in CDM systems using a signature sequence in the form of a 7-chip code.

because of the orthogonal nature of the codes employed. In this respect, CDM is similar to the OFDM technique discussed earlier [255].

The new components needed for any CDM system are the encoder and decoder located at the transmitter and receiver ends, respectively. The encoder spreads the signal spectrum over a much wider range than the minimum bandwidth necessary for transmission by means of a unique code. The decoder uses the same code for compressing the signal spectrum and recovering the data. Several methods can be used for encoding depending on whether it is done in the time domain, spectral domain, or both. The codes employed are referred to as being two dimensional when both time and frequency are involved. The time-domain codes include direct-sequence encoding and time hopping. The spectral codes can be implemented using the amplitude or the phase of various spectral components. In this section we discuss several encoding schemes used in recent experiments.

6.6.1 Time-Domain Encoding

Figure 6.30 shows an example of time-domain coding for optical CDMA systems. Each bit of data is coded using a signature sequence consisting of a large number, say M , of shorter bits, called “chips” borrowing the terminology used for wireless ($M = 7$ in the example shown). The effective bit rate (or the chip rate) increases by the factor of M because of coding. The signal spectrum is spread over a much wider region related to the bandwidth of individual chips. For example, the signal spectrum becomes broader by a factor of 64 if $M = 64$. Of course, the same spectral bandwidth is used by many users distinguished on the basis of different signature sequences assigned to them. The recovery of individual signals sharing the same bandwidth requires that the signature sequences come from a family of the orthogonal codes. The orthogonal nature of such codes ensures that each signal can be decoded accurately at the receiver end [271]. Transmitters are allowed to transmit messages at arbitrary times. The receiver recovers messages by decoding the received signal using the same signature sequence that was used at the transmitter. The decoding is accomplished using an optical correlation technique.

The encoders for signature-sequence coding typically use a delay-line scheme [264] that looks superficially similar to that shown in Figure 6.24 for multiplexing several OTDM channels. The main difference is that a single modulator, placed after the laser, imposes the data on the pulse train. The resulting pulse train is split into several branches (equal to the number of code chips), and optical delay lines are used to encode the channel. At the receiver end, the decoder consists of the delay lines in the reverse order (matched-filter detection) such that it produces a peak in the correlation output whenever the user's code matches with a sequence of time chips in the received signal. Chip patterns of other users also produce a peak through cross-correlation but the amplitude of this peak is lower than the autocorrelation peak produced when the chip pattern matches precisely. An array of fiber Bragg gratings, designed with identical stop bands but different reflectivities, can also act as encoders and decoders [270]. Different gratings introduce different delays depending on their relative locations and produce a coded version of the signal. Such grating-based devices provide encoders and decoders in the form of a compact all-fiber device (except for the optical circulator needed to put the reflected coded signal back onto the transmission line).

The CDM pulse trains consisting of 0 and 1 chips suffer from two problems. First, only unipolar codes can be used simply because optical intensity or power cannot be negative. The number of such codes in a family of orthogonal codes is often not very large until the code length is increased to beyond 100 chips. Second, the cross-correlation function of the unipolar codes is relatively high, making the probability of an error also large. Both of these problems can be solved if the optical phase is used for coding in place of the amplitude. Such schemes are being pursued and belong to coherent CDMA [286]. An advantage of coherent CDMA is that many families of bipolar orthogonal codes, developed for wireless systems and consisting of 1 and -1 chips, can be employed in the optical domain. When a CW laser source is used in combination with a phase modulator, another CW laser (local oscillator) is required at the receiver for coherent detection (see Section 4.5). On the other hand, if ultrashort optical pulses are used as individual chips, whose phase is shifted by π in chip slots corresponding to a -1 in the code, it is possible to decode the signal without using coherent detection.

In a 2001 experiment, a coherent CDMA system was able to recover the 2.5 Gb/s signal transmitted using a 64-chip code [274]. A sampled fiber grating was used for coding and decoding the data. Such a grating consists of an array of equally spaced smaller gratings so that a single pulse is split into multiple chips during reflection. Moreover, the phase of preselected chips can be changed by π so that each reflected pulse is converted into a phase-encoded train of chips. The decoder consists of a matched grating such that the reflected signal is converted into a single pulse through autocorrelation (constructive interference) for the signal bit while the cross-correlation or destructive interference produces no signal for signals belonging to other channels. The experiment used a NOLM (the same device used for demultiplexing of OTDM channels in Section 6.4) for improving the system performance. The NOLM passed the high-intensity autocorrelation peak but blocked the low-intensity cross-correlation peaks. The receiver was able to decode the 2.5-Gb/s bit stream from the 160-Gchip/s pulse train with less than 3-dB penalty at a BER of less than 10^{-9} . In 2002, this approach was used to demonstrate a four-channel WDM system, employing OCDM with 255 chips and quaternary phase coding at a chip rate of 320 Gchip/s [275].

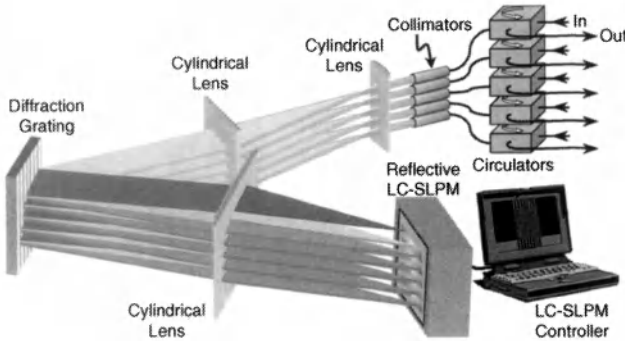


Figure 6.31: schematic of a CDMA encoder for spectral phase encoding. LC and SLPM stands for liquid crystal and spatial light-phase modulator, respectively. (After Ref. [279]; ©2005 IEEE; reprinted with permission.)

6.6.2 Frequency-Domain Encoding

Spectral encoding involves modifications of the amplitude or the phase of various spectral components of a short pulse according to a preassigned code. Phase encoding has attracted most attention and has been implemented in several experiments and field trials [278]–[283]. It can be implemented using several different schemes. A bulk-optics approach, shown schematically in Figure 6.31, employs a diffraction grating with a reflective, liquid crystal, spatial light-phase modulator (SLPM). The grating diffracts spectral components in different directions, and the SLPM changes their phases using a preset code. If binary coding with phase values of 0 and π is employed, SLPM simply changes the phase by π of some code-selected spectral components [279]. The same grating combines all spectral components during the return path, and a circulator directs the resulting, temporally broadened, spectrally-coded, optical pulse to its output port.

The encoder shown in Figure 6.31 is not practical for real systems because of its bulky nature. For this reason, several integrated versions have been developed. In one experiment [281], the spectral phase encoder consisted of multiple microring resonators coupled to two input and output waveguides (or buses), as shown schematically in Figure 6.32(a). Each set of four microring resonators (diameter ~ 0.1 mm) is designed to transfer one specific wavelength from input to output bus. Multiple thermo-optic phase shifters are used to change the phase of various spectral components from 0 to π , depending on the code employed; they also serve as bandpass filters. The 2006 experiment employed 8 frequencies on a 10-GHz frequency grid for implementing an 8-chip code and distributed 5-Gb/s signals to six users with a spectral efficiency of 0.375 b/s/Hz. In a 2007 field trial [283], the spectral phase encoder, shown schematically in Figure 6.32(b), employed phase modulators between two AWGs, which divided the spectrum of 0.7-ps pulse into 63 parts and then combined these parts back after phase shifts imposed on them as required by the CDMA code. The same device was used as a decoder at the receiver end with complimentary phase shifts that made the optical phase uniform across the entire pulse spectrum.

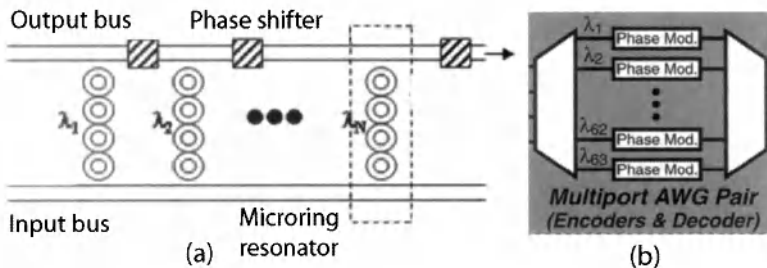


Figure 6.32: Integrated spectral phase encoders based on (a) microring resonators and (b) AWGs with phase modulators. (After Ref. [281]; ©2006 IEEE; reprinted with permission.)

6.6.3 Frequency Hopping

Spectrum spreading can also be accomplished using the technique of frequency hopping in which the carrier frequency is shifted periodically according to a preassigned code [267]. The situation differs from WDM in the sense that a fixed frequency is not assigned to a given channel. Rather, all channels share the entire bandwidth by using different carrier frequencies at different times according to a two-dimensional code. Such a spectrally encoded signal can be represented in the form of a matrix shown schematically in Figure 6.33. The matrix rows correspond to assigned frequencies and the columns correspond to time slots. The matrix element m_{ij} equals 1 if and only if the frequency ω_i is transmitted in the interval t_j . Different users are assigned different frequency-hop patterns (or codes) to ensure that two users do not transmit at the same frequency during the same time slot. The code sequences that satisfy this property are said to be orthogonal codes. In the case of asynchronous transmission, complete orthogonality cannot be ensured. Such systems make use of pseudo-orthogonal codes with maximum autocorrelation and minimum to ensure a BER as low as possible. In general, the BER of such CDMA systems remains relatively high (typically $> 10^{-6}$), but it can be improved using a forward-error correction scheme.

Frequency hopping in CDM lightwave systems requires a rapid change in the carrier frequency. It is difficult to make tunable semiconductor lasers whose wavelength can be changed over a wide range in a subnanosecond time scale. One possibility consists of hopping the frequency of a microwave subcarrier and then use the SCM technique for transmitting the CDM signal. This approach has the advantage that coding and decoding is done in the electrical domain, where the existing commercial microwave components can be used.

Several all-optical techniques have been developed for frequency hopping. They can be classified as coherent or incoherent depending on the type of optical source used for the CDMA system. In the case of incoherent CDMA, a broadband optical source such as an LED (or spontaneous emission from a fiber amplifier) is used in combination with a multipeak optical filter (such as an AWG) to create multiwavelength output [267]. Optical switches are then used to select different wavelengths for different chip slots. This technique can also be used to make CDMA add-drop multiplexers [239]. An array of fiber gratings having different Bragg wavelengths can

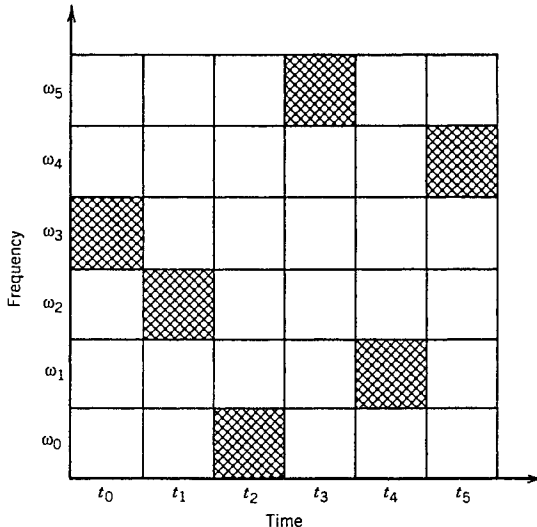


Figure 6.33: Frequency hopping in CDM lightwave systems. Filled square show frequencies for different time slots. A specific frequency-hop sequence (3, 2, 0, 5, 1, 4) is shown.

also be used for spectral encoding and decoding. A single chirped Moiré grating can replace the grating array because several gratings are written at the same location in such fiber gratings [57]. In a 2000 experiment, several Moiré gratings were used to demonstrate recovery of 622-Mb/s CDMA channels [272]. An integrated version of CDMA encoders, based on silica-on-silicon AWGs, has also been developed [277]. In this device, variable delay lines are incorporated between two AWGs.

In another approach called *coherence multiplexing* [268], a broadband optical source is used in combination with an unbalanced MZ interferometer that introduces a delay longer than the coherence time in one of its branches. Such CDMA systems rely on coherence to discriminate among channels and are affected severely by the optical beat noise. In a demonstration of this technique, four 1-Gb/s channels were multiplexed. The optical source was an SOA operating below the laser threshold so that its output had a bandwidth of 17 nm. A differential-detection technique was used to reduce the impact of optical beat noise. Indeed, bit-error rates below 10^{-9} could be achieved by using differential detection even when all four channels were operating simultaneously.

The coherent CDMA systems designed with spectral encoding have a distinct advantage that the CDMA signal can be overlaid over a WDM signal such that both signals occupy the same wavelength range. Figure 6.34 shows schematically how such a hybrid scheme works [273]. The spectrum of the received signal consists of a broadband CDMA background and multiple sharp narrowband peaks that correspond to various WDM channels. The CDMA background does not affect the detection of WDM channels much because of its low amplitude. The CDMA receiver employs a notch filter to remove the WDM signal before decoding it. The hybrid WDM–CDMA scheme is spectrally efficient as it makes use of the unused extra bandwidth around each WDM channel.

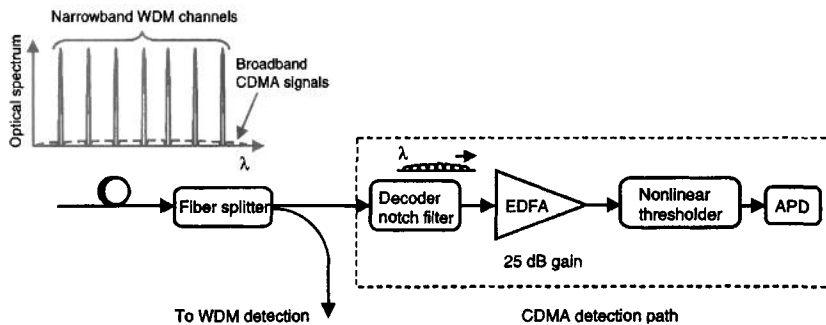


Figure 6.34: Receiver for a hybrid WDM–CDMA system sharing the same spectral bandwidth. A notch filter is used within the decoder to remove the WDM signal. (After Ref. [273]; ©2001 IEEE; reprinted with permission.)

WDM systems in which each channel is transmitted using CDM are of considerable interest. In this case, spectral efficiency is at a premium because the CDM-signal bandwidth should not exceed channel spacing. In a 2002 experiment, spectral efficiency of 1.6 (b/s)/Hz and a capacity of 6.4 Tb/s were realized in the C band alone using the combination of CDMA and WDM techniques [276]. This system employed the QPSK format for optical encoding and decoding with ultrafast optical time-gating. By 2009, a field trial demonstrated successful operation of a WDM–CDMA system capable of distributing 10-Gb/s signals to eight users simultaneously over 100 km with the 16-chip encoders and decoders based on sampled fiber gratings [286].

Problems

- 6.1 Dry fibers have acceptable losses over a spectral region extending from 1.3 to 1.6 μm . Estimate the capacity of a WDM system covering this entire region using 40-Gb/s channels spaced apart by 50 GHz.
- 6.2 The C and L spectral bands cover a wavelength range from 1.53 to 1.61 μm . How many channels can be transmitted through WDM when the channel spacing is 25 GHz? What is the effective bit rate–distance product when a WDM signal covering the two bands using 10-Gb/s channels is transmitted over 2000 km?
- 6.3 A 128×128 broadcast star is made by using 2×2 directional couplers, each having an insertion loss of 0.2 dB. Each channel transmits 1 mW of average power and requires 1 μW of average received power for operation at 1 Gb/s. What is the maximum transmission distance for each channel? Assume a cable loss of 0.25 dB/km and a loss of 3 dB from connectors and splices.
- 6.4 A Fabry–Perot filter of length L has equal reflectivities R for the two mirrors. Derive an expression for the transmission spectrum $T(v)$ considering multiple round trips inside the cavity containing air. Use it to show that the finesse is given by $F = \pi\sqrt{R}/(1 - R)$.

- 6.5** A Fabry–Perot filter is used to select 100 channels spaced apart by 0.2 nm. What should be the length and the mirror reflectivities of the filter? Assume 10-Gb/s bit rate, a refractive index of 1.5 and an operating wavelength of 1.55 μm .
- 6.6** The action of a fiber coupler is governed by the matrix equation $\mathbf{E}_{\text{out}} = \mathbf{T}\mathbf{E}_{\text{in}}$, where \mathbf{T} is the 2×2 transfer matrix and \mathbf{E} is a column vector whose two components represent the input (or output) fields at the two ports. Assuming that the total power is preserved, show that the transfer matrix \mathbf{T} is given by

$$\mathbf{T} = \begin{pmatrix} \sqrt{1-f} & i\sqrt{f} \\ i\sqrt{f} & \sqrt{1-f} \end{pmatrix},$$

where f is the fraction of the power transferred to the cross port.

- 6.7** Explain how a Mach–Zehnder interferometer works. Prove that the transmission through a chain of M such interferometers is given by $T(v) = \prod_{m=1}^M \cos^2(\pi v \tau_m)$, where τ_m is the relative delay. Use the result of the preceding problem for the transfer matrix of a 3-dB fiber coupler.
- 6.8** Consider a fiber coupler with the transfer matrix given in Problem 8.6. Its two output ports are connected to each other to make a loop of length L . Find an expression for the transmittivity of the fiber loop. What happens when the coupler splits the input power equally? Provide a physical explanation.
- 6.9** The reflection coefficient of a fiber grating of length L is given by

$$r_g(\delta) = \frac{i\kappa \sin(qL)}{q \cos(qL) - i\delta \sin(qL)},$$

where $q^2 = \delta^2 - \kappa^2$, $\delta = (\omega - \omega_B)(\bar{n})/c$ is the detuning from the Bragg frequency ω_B , and κ is the coupling coefficient. Plot the reflectivity spectrum using $\kappa = 8 \text{ cm}^{-1}$ and $\bar{n} = 1.45$, and a Bragg wavelength of 1.55 μm for $L = 3, 5$, and 8 mm. Estimate the grating bandwidth in GHz in the three cases.

- 6.10** You have been given ten 3-dB fiber couplers. Design a 4×4 demultiplexer with as few couplers as possible.
- 6.11** Explain how an array of planar waveguides can be used for demultiplexing WDM channels. Use diagrams as necessary.
- 6.12** Use a single fiber coupler and two fiber gratings to design an add–drop filter. Explain how such a device functions.
- 6.13** Use a waveguide-grating router to design an integrated WDM transmitter. How would the design change for a WDM receiver?
- 6.14** What is meant by the in-band linear crosstalk? Derive an expression for the power penalty induced by such crosstalk for a waveguide-grating router.
- 6.15** Explain how stimulated Raman scattering can cause crosstalk in multichannel lightwave systems. Derive Eq. (6.3.10) after approximating the Raman gain spectrum by a triangular profile.
- 6.16** Solve the set of M equations in Eq. (6.3.11) and show that the channel powers are given by Eq. (6.3.12).

- 6.17** Derive Eq. (6.3.14) by considering the nonlinear phase change induced by both self- and cross-phase modulations.
- 6.18** Solve Eq. (6.3.16) and show that the FWM efficiency is given by Eq. (6.3.18). Estimate its value for a 50-km fiber with $\alpha = 0.2 \text{ dB/km}$ and $\beta_2 = -1 \text{ ps}^2/\text{km}$ assuming 50-GHz channel spacing.
- 6.19** Derive an expression for the CNR of analog SCM lightwave systems by including thermal noise, shot noise, and intensity noise. Show that the CNR saturates to a constant value at high power levels.
- 6.20** Consider an analog SCM lightwave system operating at $1.55 \mu\text{m}$. It uses a receiver of 90% quantum efficiency, 10 nA dark current, and thermal-noise RMS current of 0.1 mA over a 50-MHz bandwidth. The RIN of the transmitter laser is -150 dB/Hz . Calculate the average received power necessary to obtain 50-dB CNR for an AM-VSB system with a modulation index of 0.2.

References

- [1] H. Ishio, J. Minowa, and K. Nosu, *J. Lightwave Technol.* **2**, 448 (1984).
- [2] G. Winzer, *J. Lightwave Technol.* **2**, 369 (1984).
- [3] N. A. Olsson, J. Hegarty, R. A. Logan, L. F. Johnson, K. L. Walker, L. G. Cohen, B. L. Kasper, and J. C. Campbell, *Electron. Lett.* **21**, 105 (1985).
- [4] C. A. Brackett, *IEEE J. Sel. Areas Commun.* **8**, 948 (1990).
- [5] P. E. Green, Jr., *Fiber-Optic Networks*, Prentice-Hall, Upper Saddle River, NJ, 1993.
- [6] J.-P. Laude, *DWDM Fundamentals, Components, and Applications*, Artech House, Norwood, MA, 2002.
- [7] B. Mukherjee, *Optical WDM Networks*, Springer, New York, 2006.
- [8] T. E. Stern, G. Ellinas, and K. Bala, *Multiwavelength Optical Networks: Architectures, Design, and Control*, Cambridge University Press, New York, 2009.
- [9] R. Ramaswami, K. Sivarajan, and G. Sasaki, *Optical Networks: A Practical Perspective*, 3rd ed., Morgan Kaufmann, San Francisco, 2009.
- [10] A. Stavdas, Ed., *Core and Metro Networks*, Wiley, Hoboken, NJ, 2000.
- [11] G. E. Keiser, *Optical Fiber Communications*, 4th ed., McGraw-Hill, New York, 2010.
- [12] A. H. Gnauck, R. W. Tkach, A. R. Chraplyvy, and T. Li, *J. Lightwave Technol.* **26**, 1032 (2008).
- [13] J. Zyskind et al., in *Optical Fiber Telecommunications*, Vol. 4B, I. P. Kaminow and T. Li, Eds., Academic Press, Boston, 2002, Chap. 5.
- [14] X. Zhou, J. Yu, M.-F. Huang, et al., Proc. Opt. Fiber Commun. Conf., Paper PDPB9, 2010.
- [15] A. Sano, H. Masuda, T. Kobayashi, et al., Proc. Opt. Fiber Commun. Conf., Paper PDPB7, 2010.
- [16] A. R. Chraplyvy, A. H. Gnauck, R. W. Tkach, R. M. Derosier, C. R. Giles, B. M. Nyman, G. A. Ferguson, J. W. Sulhoff, and J. L. Zyskind, *IEEE Photon. Technol. Lett.* **7**, 98 (1995).
- [17] K. Fukuchi, T. Kasamatsu, M. Morie, R. Ohhira, T. Ito, K. Sekiya, D. Ogasahara, and T. Ono, Proc. Optical Fiber Commun. Conf., Paper PDP24, 2001.
- [18] N. S. Bergano and C. R. Davidson, *J. Lightwave Technol.* **14**, 1287 (1996).

- [19] N. S. Bergano, in *Optical Fiber Telecommunications*, Vol. 4B, I. P. Kaminow and T. Li, Eds., Academic Press, Boston, 2002.
- [20] N. S. Bergano, *J. Lightwave Technol.* **23**, 5125 (2005).
- [21] A. N. Pilipetskii, *J. Lightwave Technol.* **24**, 484 (2006).
- [22] S. Bigo, in *Optical Fiber Telecommunications*, Vol. 5B, I. P. Kaminow, T. Li, and A. E. Willner, Eds., Academic Press, Boston, 2008, Chap. 14.
- [23] J.-X. Cai, Y. Cai, C. Davidson, et al., Proc. Opt. Fiber Commun. Conf., Paper PDPB10 (2010).
- [24] I. S. Binetti, A. Bragheri, E. Iannone, and F. Bentivoglio, *J. Lightwave Technol.* **18**, 1677 (2000).
- [25] A. A. M. Saleh and J. M. Simmons, *J. Lightwave Technol.* **17**, 2431 (1999).
- [26] W. T. Anderson, J. Jackel, G. K. Chang, H. Dai, X. Wei, M. Goodman, C. Allyn, M. Alvarez, and O. Clarke, et al., *J. Lightwave Technol.* **18**, 1988 (2000).
- [27] L. Paraschis, O. Gerstel, and M. Y. Frankel, in *Optical Fiber Telecommunications*, Vol. 5B, I. P. Kaminow, T. Li, and A. E. Willner, Eds., Academic Press, Boston, 2008, Chap. 12.
- [28] P. E. Green, Jr., *IEEE J. Sel. Areas Commun.* **14**, 764 (1996).
- [29] I. P. Kaminow, in *Optical Fiber Telecommunications*, Vol. 3A, I. P. Kaminow and T. L. Koch, Eds., Academic Press, Boston, 1997, Chap. 15.
- [30] T. Pfeiffer, J. Kissing, J. P. Elbers, B. Deppisch, M. Witte, H. Schmuck, and E. Voges, *J. Lightwave Technol.* **18**, 1928 (2000).
- [31] N. Ghani, J. Y. Pan, and X. Cheng, in *Optical Fiber Telecommunications*, Vol. 4B, I. P. Kaminow and T. Li, Eds., Academic Press, Boston, 2002, Chap. 8.
- [32] P. W. Dowd, *IEEE Trans. Comput.* **41**, 1223 (1992).
- [33] M. S. Goodman, H. Kobrinski, M. P. Vecchi, R. M. Bulley, and J. L. Gimlett, *IEEE J. Sel. Areas Commun.* **8**, 995 (1990).
- [34] E. Hall, J. Kravitz, R. Ramaswami, M. Halvorson, S. Tenbrink, and R. Thomsen, *IEEE J. Sel. Areas Commun.* **14**, 814 (1996).
- [35] D. Sadot and L. G. Kazovsky, *J. Lightwave Technol.* **15**, 1629 (1997).
- [36] S. S. Wagner, H. Kobrinski, T. J. Robe, H. L. Lemberg, and L. S. Smoot, *Electron. Lett.* **24**, 344 (1988).
- [37] C. Lin, Ed., *Broadband Optical Access Networks and Fiber-to-the-Home*, Wiley, Hoboken, NJ, 2006.
- [38] J. Prat, Ed., *Next-Generation FTTH Passive Optical Networks*, Springer, New York, 2008.
- [39] R. E. Wagner, in *Optical Fiber Telecommunications*, Vol. 5B, Chap. 10, I. P. Kaminow, T. Li, and A. E. Willner, Eds., Academic Press, Boston, 2008.
- [40] G. P. Agrawal, *Lightwave Technology: Components and Devices*, Chap. 8 Wiley, Hoboken, NJ, 2006.
- [41] M. Born and E. Wolf, *Principles of Optics*, 7th ed., Cambridge University Press, New York, 1999.
- [42] J. Stone and L. W. Stulz, *Electron. Lett.* **23**, 781 (1987).
- [43] K. Hirabayashi, H. Tsuda, and T. Kurokawa, *J. Lightwave Technol.* **11**, 2033 (1993).
- [44] A. Sneh and K. M. Johnson, *J. Lightwave Technol.* **14**, 1067 (1996).
- [45] J. Ciosek, *Appl. Opt.* **39**, 135 (2000).
- [46] H. K. Tsang, M. W. K. Mak, L. Y. Chan, J. B. D. Soole, C. Youtsey, and I. Adesida, *J. Lightwave Technol.* **17**, 1890 (1999).

- [47] M. Iodice, G. Cocorullo, F. G. Della Corte, and I. Rendina, *Opt. Commun.* **183**, 415 (2000).
- [48] J. Pfeiffer, J. Peerlings, R. Riemenschneider, et al., *Mat. Sci. Semicond. Process.* **3**, 409 (2000).
- [49] K. Takiguchi, K. Okamoto, and K. Moriwaki, *J. Lightwave Technol.* **14**, 2003 (1996).
- [50] E. L. Wooten, R. L. Stone, E. W. Miles, and E. M. Bradley, *J. Lightwave Technol.* **14**, 2530 (1996).
- [51] T. Mizuno, M. Oguma, T. Kitoh, Y. Inoue, and H. Takahashi, *IEEE Photon. Technol. Lett.* **18**, 325 (2006).
- [52] G. P. Agrawal, *Applications of Nonlinear Fiber Optics*, 2nd ed., Academic Press, Boston, 2008.
- [53] Y. Hibino, F. Hanawa, H. Nakagome, M. Ishii, and N. Takato, *J. Lightwave Technol.* **13**, 1728 (1995).
- [54] M. Kawachi, *IEE Proc.* **143**, 257 (1996).
- [55] Y. P. Li and C. H. Henry, *IEE Proc.* **143**, 263 (1996).
- [56] K. Okamoto, *Opt. Quantum Electron.* **31**, 107 (1999).
- [57] R. Kashyap, *Fiber Bragg Gratings*, 2nd ed., Academic Press, Boston, 2009.
- [58] G. P. Agrawal and S. Radic, *IEEE Photon. Technol. Lett.* **6**, 995 (1994).
- [59] G. E. Town, K. Sugde, J. A. R. Williams, I. Bennion, and S. B. Poole, *IEEE Photon. Technol. Lett.* **7**, 78 (1995).
- [60] F. Bilodeau, K. O. Hill, B. Malo, D. C. Johnson, and J. Albert, *IEEE Photon. Technol. Lett.* **6**, 80 (1994).
- [61] T. Numai, S. Murata, and I. Mito, *Appl. Phys. Lett.* **53**, 83 (1988); **54**, 1859 (1989).
- [62] J.-P. Weber, B. Stoltz, and M. Dasler, *Electron. Lett.* **31**, 220 (1995).
- [63] K. N. Park, Y. T. Lee, M. H. Kim, K. S. Lee, and Y. H. Won, *IEEE Photon. Technol. Lett.* **10**, 555 (1998).
- [64] A. Iocco, H. G. Limberger, R. P. Salathé, L. A. Everall, K. E. Chisholm, J. A. R. Williams, and I. Bennion, *J. Lightwave Technol.* **17**, 1217 (1999).
- [65] B. Ortega, J. Capmany, and J. L. Cruz, *J. Lightwave Technol.* **17**, 1241 (1999).
- [66] C. S. Goh, S. Y. Set, and K. Kikuchi, *IEEE Photon. Technol. Lett.* **14**, 1306 (2002).
- [67] H. Lee and G. Agrawal, *Opt. Express* **12**, 5595 (2004).
- [68] H. Li, M. Li, Y. Sheng, and J. E. Rothenberg, *J. Lightwave Technol.* **25**, 2739 (2007).
- [69] D. A. Smith, R. S. Chakravarthy, et al., *J. Lightwave Technol.* **14**, 1005 (1996).
- [70] J. L. Jackel, M. S. Goodman, J. E. Baran, et al., *J. Lightwave Technol.* **14**, 1056 (1996).
- [71] H. Herrmann, K. Schafer, and C. Schmidt, *IEEE Photon. Technol. Lett.* **10**, 120 (1998).
- [72] T. E. Dimmick, G. Kakarantzas, T. A. Birks, and P. S. J. Russell, *IEEE Photon. Technol. Lett.* **12**, 1210 (2000).
- [73] J. Sapriel, D. Charissoux, V. Voloshinov, and V. Molchanov, *J. Lightwave Technol.* **20**, 892 (2002).
- [74] G. P. Agrawal, *Nonlinear Fiber Optics*, 4th ed., Academic Press, Boston, 2007.
- [75] R. W. Tkach, A. R. Chraplyvy, and R. M. Derosier, *IEEE Photon. Technol. Lett.* **1**, 111 (1989).
- [76] K. Margari, H. Kawaguchi, K. Oe, Y. Nakano, and M. Fukuda, *IEEE J. Quantum Electron.* **24**, 2178 (1988).
- [77] T. Numai, S. Murata, and I. Mito, *Appl. Phys. Lett.* **53**, 1168 (1988).
- [78] S. Dubovitsky and W. H. Steier, *J. Lightwave Technol.* **14**, 1020 (1996).

- [79] C. H. Henry, R. F. Kazarinov, Y. Shani, R. C. Kistler, V. Pol, and K. J. Orlowsky, *J. Lightwave Technol.* **8**, 748 (1990).
- [80] K. A. McGreer, *IEEE Photon. Technol. Lett.* **8**, 553 (1996).
- [81] S. J. Sun, K. A. McGreer, and J. N. Broughton, *IEEE Photon. Technol. Lett.* **10**, 90 (1998).
- [82] F. N. Timofeev, E. G. Churin, P. Bayvel, V. Mikhailov, D. Rothnie, and J. E. Midwinter, *Opt. Quantum Electron.* **31**, 227 (1999).
- [83] D. R. Wisely, *Electron. Lett.* **27**, 520 (1991).
- [84] B. H. Verbeek, C. H. Henry, N. A. Olsson, K. J. Orlowsky, R. F. Kazarinov, and B. H. Johnson, *J. Lightwave Technol.* **6**, 1011 (1988).
- [85] K. Oda, N. Tokato, T. Kominato, and H. Toba, *IEEE Photon. Technol. Lett.* **1**, 137 (1989).
- [86] N. Takato, T. Kominato, A. Sugita, K. Jinguiji, H. Toba, and M. Kawachi, *IEEE J. Sel. Areas Commun.* **8**, 1120 (1990).
- [87] Y. Hibino, T. Kitagawa, K. O. Hill, F. Bilodeau, B. Malo, J. Albert, and D. C. Johnson, *IEEE Photon. Technol. Lett.* **8**, 84 (1996).
- [88] B. S. Kawasaki, K. O. Hill, and R. G. Gaumont, *Opt. Lett.* **6**, 327 (1981).
- [89] M. K. Smit and C. van Dam, *IEEE J. Sel. Topics Quantum Electron.* **2**, 236 (1996).
- [90] R. Mestric, M. Renaud, M. Bachamann, B. Martin, and F. Goborit, *IEEE J. Sel. Topics Quantum Electron.* **2**, 251 (1996).
- [91] H. Okayama, M. Kawahara, and T. Kamijoh, *J. Lightwave Technol.* **14**, 985 (1996).
- [92] C. Dragone, *J. Lightwave Technol.* **16**, 1895 (1998).
- [93] A. Kaneko, T. Goh, H. Yamada, T. Tanaka, and I. Ogawa, *IEEE J. Sel. Topics Quantum Electron.* **5**, 1227 (1999).
- [94] K. Kato and Y. Tohmori, *IEEE J. Sel. Topics Quantum Electron.* **6**, 4 (2000).
- [95] C. R. Doerr and K. Okamoto, in *Optical Fiber Telecommunications*, Vol. 5A, I. P. Kaminow, T. Li, and A. E. Willner, Eds., Academic Press, Boston, 2008, Chap. 9.
- [96] K. Takada, M. Abe, T. Shibata, and K. Okamoto, *IEEE Photon. Technol. Lett.* **13**, 577 (2001).
- [97] M. D. Feuer, D. C. Kipler, and S. L. Woodward, in *Optical Fiber Telecommunications*, Vol. 5B, I. P. Kaminow, T. Li, and A. E. Willner, Eds., Academic Press, Boston, 2008, Chap. 8.
- [98] F. Shehadeh, R. S. Vodhanel, M. Krain, C. Gibbons, R. E. Wagner, and M. Ali, *IEEE Photon. Technol. Lett.* **7**, 1075 (1995).
- [99] H. A. Haus and Y. Lai, *J. Lightwave Technol.* **10**, 57 (1992).
- [100] M. Zirngibl, C. H. Joyner, and B. Glance, *IEEE Photon. Technol. Lett.* **6**, 513 (1994).
- [101] M. Kuznetsov, *J. Lightwave Technol.* **12**, 226 (1994).
- [102] H. H. Yaffe, C. H. Henry, M. R. Serbin, and L. G. Cohen, *J. Lightwave Technol.* **12**, 1010 (1994).
- [103] F. Bilodeau, D. C. Johnson, S. Thériault, B. Malo, J. Albert, and K. O. Hill, *IEEE Photon. Technol. Lett.* **7**, 388 (1995).
- [104] T. Mizuuchi, T. Kitayama, K. Shimizu, and K. Ito, *J. Lightwave Technol.* **16**, 265 (1998).
- [105] T. Augustsson, *J. Lightwave Technol.* **16**, 1517 (1998).
- [106] S. Rotolo, A. Tanzi, S. Brunazzi, et al., *J. Lightwave Technol.* **18**, 569 (2000).
- [107] C. Riziotis and M. N. Zervas, *J. Lightwave Technol.* **19**, 92 (2001).
- [108] A. V. Tran, W. D. Zhong, R. C. Tucker, and R. Lauder, *IEEE Photon. Technol. Lett.* **13**, 582 (2001).
- [109] I. Y. Kuo and Y. K. Chen, *IEEE Photon. Technol. Lett.* **14**, 867 (2002).
- [110] A. V. Tran, C. J. Chae, and R. C. Tucker, *IEEE Photon. Technol. Lett.* **15**, 975 (2003).

- [111] E. G. Rawson and M. D. Bailey, *Electron. Lett.* **15**, 432 (1979).
- [112] M. E. Marhic, *Opt. Lett.* **9**, 368 (1984).
- [113] D. B. Mortimore and J. W. Arkwright, *Appl. Opt.* **30**, 650 (1991).
- [114] C. Dragone, C. H. Henry, I. P. Kaminow, and R. C. Kistler, *IEEE Photon. Technol. Lett.* **1**, 241 (1989).
- [115] M. I. Irshid and M. Kavehrad, *IEEE Photon. Technol. Lett.* **4**, 48 (1992).
- [116] P. D. Trinh, S. Yegnanarayanan, and B. Jalali, *IEEE Photon. Technol. Lett.* **8**, 794 (1996).
- [117] J. M. H. Elmighrani and H. T. Mouftah, *IEEE Commun. Mag.* **38** (2), 58 (2000).
- [118] Y. Hida, Y. Hibino, M. Itoh, A. Sugita, A. Himeno, and Y. Ohmori, *Electron. Lett.* **36**, 820 (2000).
- [119] T. P. Lee, C. E. Zah, R. Bhat, et al., *J. Lightwave Technol.* **14**, 967 (1996).
- [120] G. P. Li, T. Makino, A. Sarangan, and W. Huang, *IEEE Photon. Technol. Lett.* **8**, 22 (1996).
- [121] T. L. Koch, in *Optical Fiber Telecommunications*, Vol. 3B, I. P. Kaminow and T. L. Koch, Eds., Academic Press, Boston, 1997, Chap. 4.
- [122] S. L. Lee, I. F. Jang, C. Y. Wang, C. T. Pien, and T. T. Shih, *IEEE J. Sel. Topics Quantum Electron.* **6**, 197 (2000).
- [123] M. Zirngibl, C. H. Joyner, C. R. Doerr, L. W. Stulz, and H. M. Presby, *IEEE Photon. Technol. Lett.* **8**, 870 (1996).
- [124] R. Monnard, A. K. Srivastava, C. R. Doerr, et al., *Electron. Lett.* **34**, 765 (1998).
- [125] S. Menezo, A. Rigny, A. Talneau, et al., *IEEE J. Sel. Topics Quantum Electron.* **6**, 185 (2000).
- [126] B. Pezeshki, E. Vail, J. Kubicky, et al., *IEEE Photon. Technol. Lett.* **14**, 1457 (2002).
- [127] G. W. Yoffe, S. Y. Zou, B. Pezeshki, S. A. Rishton, and M. A. Emanuel, *IEEE Photon. Technol. Lett.* **16**, 735 (2004).
- [128] R. Nagarajan, C. H. Joyner, R. P. Schneide, et al., *IEEE J. Sel. Topics Quantum Electron.* **11**, 50 (2005).
- [129] R. Nagarajan, M. Kato, J. Pleumeekers, et al., *Electron. Lett.* **42**, 771 (2006).
- [130] D. Welch, F. A. Kish, S. Melle, et al., *IEEE J. Sel. Topics Quantum Electron.* **13**, 22 (2007).
- [131] M. Kato, P. Evans, S. Corzine, et al., Proc. Opt. Fiber Commun. Conf., Paper OThN2, 2009.
- [132] A. Bellemare, M. Karasek, M. Rochette, S. LaRochelle, and M. Tetu, *J. Lightwave Technol.* **18**, 825 (2000).
- [133] J. Yao, J. Yao, Z. Deng, and J. Liu, *IEEE Photon. Technol. Lett.* **17**, 756 (2005).
- [134] A. Zhang, H. Liu, M. S. Demokan, and H. Y. Tam, *IEEE Photon. Technol. Lett.* **17**, 2535 (2005).
- [135] D. Chen, S. Qin, Y. Gao and S. Gao, *Electron. Lett.* **43**, 524 (2007).
- [136] Y. Kim, S. Doucet, and S. LaRochelle, *IEEE Photon. Technol. Lett.* **20**, 1718 (2008).
- [137] T. Morioka, K. Uchiyama, S. Kawanishi, S. Suzuki, and M. Saruwatari, *Electron. Lett.* **31**, 1064 (1995).
- [138] M. C. Nuss, W. H. Knox, and U. Koren, *Electron. Lett.* **32**, 1311 (1996).
- [139] H. Takara, T. Ohara, K. Mori, et al., *Electron. Lett.* **36**, 2089 (2000).
- [140] E. Yamada, H. Takara, T. Ohara, et al., *Electron. Lett.* **37**, 304 (2001).
- [141] S. Chandrasekhar, M. Zirngibl, A. G. Dentai, et al., *IEEE Photon. Technol. Lett.* **7**, 1342 (1995).
- [142] T. Ohyama, Y. Akahori, T. Yamada, et al., *Electron. Lett.* **38**, 1576 (2002).

- [143] N. Kikuchi, Y. Shibata, H. Okamoto, et al., *Electron. Lett.* **39**, 312 (2003).
- [144] W. Tong, V. M. Menon, F. Xia, and S. R. Forrest, *IEEE Photon. Technol. Lett.* **16**, 1170 (2004).
- [145] X. Duan, Y. Huang, H. Huang, X. Ren, Q. Wang, Y. Shang, X. Ye, and S. Cai, *J. Lightwave Technol.* **27**, 4697 (2009).
- [146] P. A. Rosher and A. R. Hunwicks, *IEEE J. Sel. Areas Commun.* **8**, 1108 (1990).
- [147] P. A. Humblet and W. M. Hamdy, *IEEE J. Sel. Areas Commun.* **8**, 1095 (1990).
- [148] E. L. Goldstein and L. Eskildsen, *IEEE Photon. Technol. Lett.* **7**, 93 (1995).
- [149] H. Takahashi, K. Oda, and H. Toba, *J. Lightwave Technol.* **14**, 1097 (1996).
- [150] J. Zhou, R. Cadeddu, E. Casaccia, C. Cavazzoni, and M. J. O'Mahony, *J. Lightwave Technol.* **14**, 1423 (1996).
- [151] M. Gustavsson, L. Gillner, and C. P. Larsen, *J. Lightwave Technol.* **15**, 2006 (1997).
- [152] K. Durnani and M. J. Holmes, *J. Lightwave Technol.* **18**, 1871 (2000).
- [153] I. T. Monroy and E. Tangdiongga, *Crosstalk in WDM Communication Networks*, Kluwer, Norwell, MA, 2002.
- [154] S.-G. Park and S. S. Lee, *IEEE Photon. Technol. Lett.* **18**, 2698 (2006).
- [155] B. Baekelandt, C. Melange, J. Bauwelincx, P. Ossieur, T. De Ridder, X.-Z. Qiu, and J. Vandewege, *IEEE Photon. Technol. Lett.* **20**, 587 (2008).
- [156] M. J. Minardi and M. A. Ingram, *Electron. Lett.* **28**, 1621 (1992).
- [157] K.-P. Ho and J. M. Khan, *J. Lightwave Technol.* **14**, 1127 (1996).
- [158] Z. Li and G. Li, *IEEE Photon. Technol. Lett.* **18**, 811 (2006).
- [159] A. R. Chraplyvy, *J. Lightwave Technol.* **8**, 1548 (1990).
- [160] N. Shibata, K. Nosu, K. Iwashita, and Y. Azuma, *IEEE J. Sel. Areas Commun.* **8**, 1068 (1990).
- [161] F. Forghieri, R. W. Tkach, and A. R. Chraplyvy, in *Optical Fiber Telecommunications*, Vol. 3A, I. P. Kaminow and T. L. Koch, Eds., Academic Press, Boston, 1997, Chap. 8.
- [162] J. Kani, M. Jinno, T. Sakamoto, S. Aisawa, M. Fukui, K. Hattori, and K. Oguchi, *J. Lightwave Technol.* **17**, 2249 (1999).
- [163] P. Bayvel and R. I. Killey, in *Optical Fiber Telecommunications*, Vol. 4B, I. P. Kaminow and T. Li, Eds., Academic Press, Boston, 2002, Chap. 13.
- [164] M. Wu and W. I. Way, *J. Lightwave Technol.* **22**, 1483 (2004).
- [165] J. Toulouse, *J. Lightwave Technol.* **23**, 3625 (2005).
- [166] D. N. Christodoulides and R. B. Jander, *IEEE Photon. Technol. Lett.* **8**, 1722 (1996).
- [167] J. Wang, X. Sun, and M. Zhang, *IEEE Photon. Technol. Lett.* **10**, 540 (1998).
- [168] M. E. Marhic, F. S. Yang, and L. G. Kazovsky, *J. Opt. Soc. Am. B* **15**, 957 (1998).
- [169] A. G. Grandpierre, D. N. Christodoulides, and J. Toulouse, *IEEE Photon. Technol. Lett.* **11**, 1271 (1999).
- [170] K.-P. Ho, *J. Lightwave Technol.* **19**, 159 (2000).
- [171] C. M. McIntosh, A. G. Grandpierre, D. N. Christodoulides, J. Toulouse, and J. M. P. Delvaux, *IEEE Photon. Technol. Lett.* **13**, 302 (2001).
- [172] Z. Jiang and C. Fan, *J. Lightwave Technol.* **20**, 953 (2003).
- [173] T. Yamamoto and S. Norimatsu, *J. Lightwave Technol.* **20**, 2229 (2003).
- [174] X. P. Mao, R. W. Tkach, A. R. Chraplyvy, R. M. Jopson, and R. M. Derosier, *IEEE Photon. Technol. Lett.* **4**, 66 (1992).
- [175] D. A. Fishman and J. A. Nagel, *J. Lightwave Technol.* **11**, 1721 (1993).
- [176] N. Yoshizawa and T. Imai, *J. Lightwave Technol.* **11**, 1518 (1993).
- [177] K. Shiraki, M. Ohashi, and M. Tateda, *J. Lightwave Technol.* **14**, 50 (1996).

- [178] Y. Horiuchi, S. Yamamoto, and S. Akiba, *Electron. Lett.* **34**, 390 (1998).
- [179] K. Tsujikawa, K. Nakajima, Y. Miyajima, and M. Ohashi, *IEEE Photon. Technol. Lett.* **10**, 1139 (1998).
- [180] L. E. Adams, G. Nykolak, T. Tanbun-Ek, A. J. Stentz, A. M. Sergent, P. F. Sciortino, and L. Eskildsen, *Fiber Integ. Opt.* **17**, 311 (1998).
- [181] S. S. Lee, H. J. Lee, W. Seo, and S. G. Lee, *ptl13*, 741 (2001).
- [182] M. Li, X. Chen, J. Wang, et al., *Opt. Express* **15**, 8290 (2007).
- [183] T. Sakamoto, T. Matsui, K. Shiraki, and T. Kurashima, *J. Lightwave Technol.* **26**, 4401 (2009).
- [184] T. Chiang, N. Kagi, M. E. Marhic, and L. G. Kazovsky, *J. Lightwave Technol.* **14**, 249 (1996).
- [185] G. Bellotti, M. Varani, C. Francia, and A. Bononi, *IEEE Photon. Technol. Lett.* **10**, 1745 (1998).
- [186] A. V. T. Cartaxo, *J. Lightwave Technol.* **17**, 178 (1999).
- [187] R. Hui, K. R. Demarest, and C. T. Allen, *J. Lightwave Technol.* **17**, 1018 (1999).
- [188] L. E. Nelson, R. M. Jopson, A. H. Gnauck, and A. R. Chraplyvy, *IEEE Photon. Technol. Lett.* **11**, 907 (1999).
- [189] M. Shtaif, M. Eiselt, and L. D. Garett, *IEEE Photon. Technol. Lett.* **13**, 88 (2000).
- [190] J. J. Yu and P. Jeppesen, *Opt. Commun.* **184**, 367 (2000).
- [191] G. Bellotti and S. Bigo, *IEEE Photon. Technol. Lett.* **12**, 726 (2000).
- [192] R. I. Killey, H. J. Thiele, V. Mikhailov, and P. Bayvel, *IEEE Photon. Technol. Lett.* **12**, 804 (2000).
- [193] G. Bellotti, S. Bigo, P. Y. Cortes, S. Gauchard, and S. LaRochelle, *IEEE Photon. Technol. Lett.* **12**, 1403 (2000).
- [194] S. Betti and M. Giacconi, *IEEE Photon. Technol. Lett.* **13**, 43 (2001); **13**, 305 (2001).
- [195] Q. Lin and G. P. Agrawal, *IEEE J. Quantum Electron.* **40**, 958 (2004).
- [196] K.-P. Ho and H. C. Wang, *J. Lightwave Technol.* **24**, 396 (2006).
- [197] O. V. Sinkin, V. S. Grigoryan, and C. R. Menyuk, *J. Lightwave Technol.* **25**, 2959 (2007).
- [198] N. Shibata, R. P. Braun, and R. G. Waarts, *IEEE J. Quantum Electron.* **23**, 1205 (1987).
- [199] H. Suzuki, S. Ohteru, and N. Takachio, *IEEE Photon. Technol. Lett.* **11**, 1677 (1999).
- [200] J. S. Lee, D. H. Lee, and C. S. Park, *IEEE Photon. Technol. Lett.* **10**, 825 (1998).
- [201] H. Mawatari, M. Fukuda, F. Kano, Y. Tohmori, Y. Yoshikuni, and H. Toba, *J. Lightwave Technol.* **17**, 918 (1999).
- [202] T. Ikegami, S. Sudo, and Y. Sakai, *Frequency Stabilization of Semiconductor Laser Diodes*, Artec House, Boston, 1995.
- [203] M. Guy, B. Villeneuve, C. Latrasse, and M. Têtu, *J. Lightwave Technol.* **14**, 1136 (1996).
- [204] H. J. Lee, G. Y. Lyu, S. Y. Park, and J. H. Lee, *IEEE Photon. Technol. Lett.* **10**, 276 (1998).
- [205] Y. Park, S. T. Lee, and C. J. Chae, *IEEE Photon. Technol. Lett.* **10**, 1446 (1998).
- [206] T. Ono and Y. Yano, *IEEE J. Quantum Electron.* **34**, 2080 (1998).
- [207] H. Nasu, T. Takagi, T. Shinagawa, M. Oike, T. Nomura and A. Kasukawa, *J. Lightwave Technol.* **22**, 1344 (2004).
- [208] H. Nasu, T. Mukaihara, T. Takagi, M. Oike, T. Nomura, and A. Kasukawa, *IEEE J. Sel. Topics Quantum Electron.* **11**, 157 (2005).
- [209] Y. Tissot, H. G. Limberger, and R.-P. Salathe, *IEEE Photon. Technol. Lett.* **19**, 1702 (2007).
- [210] J. Zhou and M. J. O'Mahony, *IEE Proc.* **143**, 178 (1996).

- [211] Y. S. Fei, X. P. Zheng, H. Y. Zhang, Y. L. Guo, and B. K. Zhou, *IEEE Photon. Technol. Lett.* **11**, 1189 (1999).
- [212] K. J. Zhang, D. L. Hart, K. I. Kang, and B. C. Moore, *Opt. Express* **40**, 1199 (2001).
- [213] A. D. Ellis, D. M. Patrick, D. Flannery, R. J. Manning, D. A. O. Davies, and D. M. Spirit, *J. Lightwave Technol.* **13**, 761 (1995).
- [214] E. Bødtker and J. E. Bowers, *J. Lightwave Technol.* **13**, 1809 (1995).
- [215] V. W. S. Chan, K. L. Hall, E Modiano, and K. A. Rauschenbach, *J. Lightwave Technol.* **16**, 2146 (1998).
- [216] S. Kawanishi, *IEEE J. Quantum Electron.* **34**, 2064 (1998).
- [217] M. Nakazawa, H. Kubota, K. Suzuki, E. Yamada, and A. Sahara, *IEEE J. Sel. Topics Quantum Electron.* **6**, 363 (2000).
- [218] T. G. Ulmer, M. C. Gross, K. M. Patel, et al., *J. Lightwave Technol.* **18**, 1964 (2000).
- [219] M. Saruwatari, *IEEE J. Sel. Topics Quantum Electron.* **6**, 1363 (2000).
- [220] J. P. Turkiewicz, E. Tangdiongga, G. Lehmann, et al., *J. Lightwave Technol.* **23**, 225 (2005).
- [221] H.-G. Weber, R. Ludwig, S. Ferber, et al., *J. Lightwave Technol.* **24**, 4616 (2006).
- [222] T. Ohara, H. Takara, I. Shake, et al., *IEEE J. Sel. Topics Quantum Electron.* **13**, 40 (2007).
- [223] H. Murai, M. Kagawa, H. Tsuji, and K. Fujii, *IEEE J. Sel. Topics Quantum Electron.* **13**, 70 (2007).
- [224] K. Igarashi and K. Kikuchi, *IEEE J. Sel. Topics Quantum Electron.* **14**, 551 (2008).
- [225] T. Yamamoto, E. Yoshida, and M. Nakazawa, *Electron. Lett.* **34**, 1013 (1998).
- [226] T. Morioka, H. Takara, S. Kawanishi, T. Kitoh, and M. Saruwatari, *Electron. Lett.* **32**, 833 (1996).
- [227] J. Hansryd and P. A. Andrekson, *IEEE Photon. Technol. Lett.* **13**, 732 (2001).
- [228] S. Kawanishi, H. Takara, T. Morioka, O. Kamatani, K. Takaguchi, T. Kitoh, and M. Saruwatari, *Electron. Lett.* **32**, 916 (1996).
- [229] M. Nakazawa, T. Yamamoto, and K. R. Tamura, *Electron. Lett.* **36**, 2027 (2000).
- [230] U. Feiste, R. Ludwig, C. Schubert, et al., *Electron. Lett.* **37**, 443 (2001).
- [231] A. Suzuki, X. Wang, Y. Ogawa, and S. Nakamura, Proc. Eur. Conf. Optical Commun. Paper Th4.1.7, 2004.
- [232] P. Guan, M. Okazaki, T. Hirano, T. Hirooka, and M. Nakazawa, *IEEE Photon. Technol. Lett.* **21**, 1579 (2009).
- [233] K. L. Deng, R. J. Runser, P. Toliver, I. Glesk, and P. R. Prucnal, *J. Lightwave Technol.* **18**, 1892 (2000).
- [234] S. A. Hamilton, B. S. Robinson, T. E. Murphy, S. J. Savage, and E. P. Ippen, *J. Lightwave Technol.* **20**, 2086 (2002).
- [235] K. VLachos, N. Pleros, C. Bintjas, G. Theophilopoulos, and H. Avramopoulos, *J. Lightwave Technol.* **21**, 1857 (2003).
- [236] R. Gross and R. Olshansky, *J. Lightwave Technol.* **8**, 406 (1990).
- [237] M. R. Phillips and T. E. Darcie, in *Optical Fiber Telecommunications*, Vol 3A, I. P. Kaminow and T. L. Koch, Eds., Academic Press, Boston, 1997, Chap. 14.
- [238] S. Ovadia, H. Dai, and C. Lin, *J. Lightwave Technol.* **16**, 2135 (1998).
- [239] M. C. Wu, J. K. Wong, K. T. Tsai, Y. L. Chen, and W. I. Way, *IEEE Photon. Technol. Lett.* **12**, 1255 (2000).
- [240] A. J. Rainal, *J. Lightwave Technol.* **14**, 474 (1996).
- [241] W. I. Way, *Broadband Hybrid Fiber Coax Acess System Technologies*, Academic Press, Boston, 1998.

- [242] W. I. Way, S. S. Wagner, M. M. Choy, C. Lin, R. C. Menendez, H. Tohme, A. Yi-Yan, A. C. Von Lehman, R. E. Spicer, et al., *IEEE Photon. Technol. Lett.* **2**, 665 (1990).
- [243] M. Ogawara, M. Tsukada, J. Nishikido, A. Hiramatsu, M. Yamaguchi, and T. Matsunaga, *IEEE Photon. Technol. Lett.* **12**, 350 (2000).
- [244] R. Hui, B. Zhu, R. Huang, C. T. Allen, K. R. Demarest, and D. Richards, *J. Lightwave Technol.* **20**, 417 (2002).
- [245] G. C. Wilson, J.-M. Delavaux, A. Srivastava, Cyril Hullin, C. McIntosh, C. G. Bethea, and C. Wolf, *IEEE Photon. Technol. Lett.* **14**, 1184 (2002).
- [246] W.-P. Lin, M.-S. Kao, and S. Chi, *J. Lightwave Technol.* **21**, 319 (2003).
- [247] T. Kuri and K. Kitayama, *J. Lightwave Technol.* **21**, 3167 (2003).
- [248] S. L. Woodward, X. Lu, T. E. Darcie, and G. E. Bodeep, *IEEE Photon. Technol. Lett.* **8**, 694 (1996).
- [249] M. R. Phillips and D. M. Ott, *J. Lightwave Technol.* **17**, 1782 (1999).
- [250] F. S. Yang, M. E. Marhic, and L. G. Kazovsky, *J. Lightwave Technol.* **18**, 512 (2000).
- [251] G. Rossi, T. E. Dimmick, and D. J. Blumenthal, *J. Lightwave Technol.* **18**, 1639 (2000).
- [252] W. H. Chen and W. I. Way, *J. Lightwave Technol.* **22**, 1679 (2004).
- [253] J. Y. Ha, A. Wonfor, P. Ghiggino, R. V. Penty and I.H. White, *Electron. Lett.* **44**, 20082467 (2008).
- [254] A. R. S. Bahai, B. R. Saltzberg, and M. Ergen, *Multi-carrier Digital Communications: Theory And Applications Of OFDM*, 2nd ed., Springer, New York, 2004.
- [255] H. Schulze and C. Lueders, *Theory and Applications of OFDM and CDMA: Wideband Wireless Communications*, Wiley, Hoboken, NJ, 2005.
- [256] Y. Li and G. L. Stuber, *Orthogonal Frequency Division Multiplexing for Wireless Communications*, Springer, New York, 2006.
- [257] W. Shieh, X. Yi, and Y. Tang, *Electron. Lett.* **43**, 183 (2007).
- [258] A. J. Lowery, *Opt. Express* **15**, 12965 (2007).
- [259] S. L. Jansen, I. Morita, T. C. W. Schenk, N. Takeda, and H. Tanaka, *J. Lightwave Technol.* **26**, 6 (2008).
- [260] W. Shieh, H. Bao, and Y. Tang, *Opt. Express* **16**, 841 (2008).
- [261] J. Armstrong, *J. Lightwave Technol.* **27**, 189 (2009).
- [262] A. J. Viterbi, *CDMA: Principles of Spread Spectrum Communication*, Addison-Wesley, Reading, MA, 1995.
- [263] M. A. Abu-Rgheff, *Introduction to CDMA Wireless Communications*, Academic Press, Boston, 2007.
- [264] P. R. Prucnal, M. Santoro, and F. Tan, *J. Lightwave Technol.* **4**, 307 (1986).
- [265] G. J. Foschinni and G. Vannucci, *J. Lightwave Technol.* **6**, 370 (1988).
- [266] J. A. Salehi, A. M. Weiner, and J. P. Heritage, *J. Lightwave Technol.* **8**, 478 (1990).
- [267] M. Kavehrad and D. Zaccarina, *J. Lightwave Technol.* **13**, 534 (1995).
- [268] D. D. Sampson, G. J. Pendock, and R. A. Griffin, *Fiber Integ. Opt.* **16**, 129 (1997).
- [269] H. P. Sardesai, C. C. Desai, and A. M. Weiner, *J. Lightwave Technol.* **16**, 1953 (1998).
- [270] G. E. Town, K. Chan, and G. Yoffe, *IEEE J. Sel. Topics Quantum Electron.* **5**, 1325 (1999).
- [271] S. Kim, K. Yu, and N. Park, *J. Lightwave Technol.* **18**, 502 (2000).
- [272] L. R. Chen and P. W. Smith, *IEEE Photon. Technol. Lett.* **12**, 1281 (2000).
- [273] S. Shen and A. M. Weiner, *IEEE Photon. Technol. Lett.* **13**, 82 (2001).
- [274] P. C. Teh, P. Petropoulos, M. Ibsen, and D. J. Richardson, *J. Lightwave Technol.* **19**, 1352 (2001).

- [275] P. C. Teh, M. Ibsen, J. H. Lee, P. Petropoulos, and D. J. Richardson, *IEEE Photon. Technol. Lett.* **14**, 227 (2002).
- [276] H. Sotobayashi, W. Chujo, and K. I. Kitayama, *J. Lightwave Technol.* **22**, 250 (2004).
- [277] K. Takiguchi and M. Itoh, *IEEE J. Sel. Topics Quantum Electron.* **11**, 300 (2005).
- [278] Z. Jiang, D. S. Seo, D. E. Leaird, R. V. Roussev, C. Langrock, M. M. Fejer, and A. M. Weiner, *J. Lightwave Technol.* **23**, 1979 (2005).
- [279] R. P. Scott, W. Cong, V. J. Hernandez, K. Li, B. H. Kolner, J. P. Heritage, and S. J. Ben Yoo, *J. Lightwave Technol.* **23**, 3232 (2005).
- [280] W. Cong, R. P. Scott, V. J. Hernandez, N. K. Fontaine, B. H. Kolner, J. P. Heritage, and S. J. Ben Yoo, *IEEE Photon. Technol. Lett.* **18**, 1567 (2006).
- [281] A. Agarwal, P. Toliver, R. Menendez, T. Banwell, J. Jackel, and S. Etemad, *IEEE Photon. Technol. Lett.* **18**, 1952 (2006).
- [282] J. P. Heritage and A. M. Weiner, *IEEE J. Sel. Topics Quantum Electron.* **13**, 1351 (2007).
- [283] R. P. Scott, V. J. Hernandez, N. K. Fontaine, et al., *IEEE J. Sel. Topics Quantum Electron.* **13**, 1455 (2007).
- [284] X. Wang, N. Wada, T. Miyazaki, G. Cincotti, and K. I. Kitayama, *J. Lightwave Technol.* **25**, 207 (2007); *IEEE J. Sel. Topics Quantum Electron.* **13**, 1463 (2007).
- [285] C.-S. Brès and P. R. Prucnal, *J. Lightwave Technol.* **25**, 2911 (2007).
- [286] N. Kataoka, N. Wada, X. Wang, G. Cincotti, A. Sakamoto, Y. Terada, T. Miyazaki, and K. I. Kitayama, *J. Lightwave Technol.* **27**, 299 (2009).

Chapter 7

Loss Management

As seen in Chapters 5 and 6, the transmission distance of any fiber-optic communication system is eventually limited by fiber losses. Until 1995, this loss limitation was mostly overcome using optoelectronic repeaters, devices in which the optical signal is first converted into an electric form using a receiver and then regenerated using a transmitter. Such regenerators become quite complex and expensive for WDM systems because they require demultiplexing of individual WDM channels. An alternative approach to loss management makes use of optical amplifiers, which amplify the entire WDM signal directly without requiring conversion of each channel to the electric domain. Several kinds of optical amplifiers were developed during the 1980s, and the use of optical amplifiers for lightwave systems became widespread during the 1990s. By 1996, optical amplifiers became a part of the fiber-optic cables laid across the Atlantic and Pacific oceans. This chapter is devoted to the management of fiber losses in long-haul systems. In Section 7.1 we discuss the common technique in which optical amplifiers are used periodically along a fiber link and identify the two schemes known as lumped and distributed amplification schemes. Section 7.2 is devoted to erbium-doped fiber amplifiers, used routinely as lumped amplifiers. Section 7.3 focuses on Raman amplifiers that have been developed for distributed amplification of lightwave signals. The signal-to-noise ratio of amplified lightwave systems is considered in Sections 7.4 and 7.5, whereas Section 7.6 deals with the receiver sensitivity. The impact of amplifier noise on the transmitted signal is studied in Section 7.7. The final section focuses on issues relevant for periodically amplified lightwave systems.

7.1 Compensation of Fiber Losses

Fiber losses must be compensated for lightwave systems designed to operate over more than 100 km or so because their cumulative effects eventually make the signal so weak that information cannot be recovered at the receiver. In some cases, the use of two lumped amplifiers, one at the transmitter end and the other at the receiver end, can extend the system range to up to 400 km. Since long-haul and submarine lightwave systems extend over thousands of kilometers, fiber losses must be compensated in such

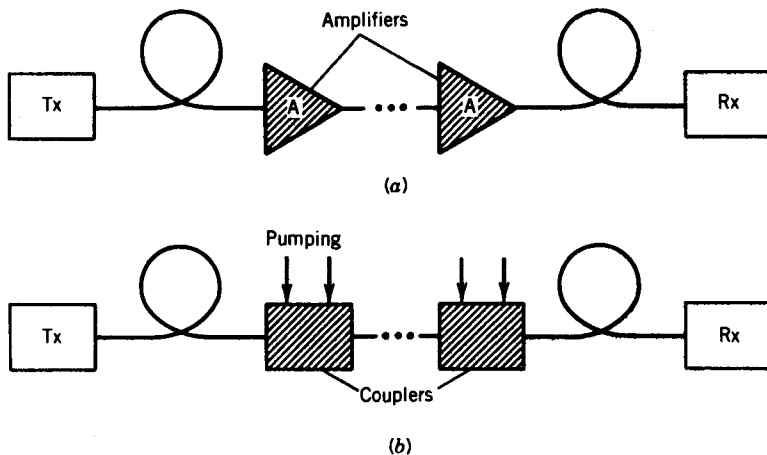


Figure 7.1: Schematic of fiber-loss management using (a) lumped or (b) distributed amplification schemes. Tx and Rx stand for optical transmitters and receivers, respectively.

systems using a chain of amplifiers that boosts the signal power periodically back to its original value.

7.1.1 Periodic Amplification Scheme

Until 1990, the only loss-management technique available to the system designer consisted of inserting an optoelectronic regenerator (often called a *repeater*) within the fiber link every 80 km or so. A repeater is nothing but a receiver-transmitter pair. In such a device, the optical bit stream is first converted into the electric domain and then regenerated with the help of an optical transmitter. This technique becomes quite cumbersome and expensive for WDM systems as it requires demultiplexing of individual channels at each repeater. A better solution to the fiber-loss problem is to make use of optical amplifiers because they can amplify multiple WDM channels simultaneously. Figure 7.1(a) shows how amplifiers can be cascaded in a periodic manner to form a chain, and thus enable one to transmit an optical bit stream over distances as long as 10,000 km, while retaining the signal in its original optical form.

Depending on the amplification scheme used, one can divide amplifiers into two categories known as lumped and distributed amplifiers. Most systems employ lumped erbium-doped fiber amplifiers (EDFAs) in which losses accumulated over 60 to 80 km of fiber lengths are compensated using short lengths (~ 10 m) of erbium-doped fibers [1]–[4]. In contrast, the distributed amplification scheme shown in Figure 7.1(b) uses the transmission fiber itself for signal amplification by exploiting the nonlinear phenomenon of stimulated Raman scattering (SRS). Such amplifiers are known as Raman amplifiers and have been used for lightwave systems since 2002. Their use for loss compensation requires that one or more pump lasers at suitable wavelengths inject optical power periodically, as shown in Figure 7.1(b).

To understand the periodic amplification scheme, we make use of Eq. (5.3.1) that governs propagation of optical signals inside a fiber link. The loss parameter α appearing in this equation reduces not only the signal power but it also impacts the strength of the nonlinear effects. This can be seen mathematically by introducing

$$A(z, t) = B(z, t) \exp(-\alpha z/2) \quad (7.1.1)$$

in Eq. (5.3.1) and writing it in terms of $B(z, t)$ as

$$\frac{\partial B}{\partial z} + \frac{i\beta_2}{2} \frac{\partial^2 B}{\partial t^2} = i\gamma e^{-\alpha z} |B|^2 B. \quad (7.1.2)$$

The physical interpretation of the preceding two equations is clear. Equation (7.1.1) shows that the optical power $|A(z, t)|^2$ decreases exponentially as $e^{-\alpha z}$ at a distance z because of fiber losses. As seen from Eq. (7.1.2), this decrease in the signal power also makes the nonlinear effects weaker, as expected intuitively.

The loss in signal power is quantified in terms of the average power defined as

$$P_{av}(z) = \lim_{T \rightarrow \infty} \frac{1}{T} \int_{T/2}^{T/2} |A(z, t)|^2 dt = P_{av}(0) e^{-\alpha z}, \quad (7.1.3)$$

where we used Eq. (7.1.1) and assumed that no other source of energy losses exists so that the integral $\int |B(z, t)|^2 dt$ over the entire bit stream remains constant in spite of changes in the shape of individual pulses. The average power decreases by a factor of $e^{\alpha L}$ over a fiber of length L . This factor exceeds 20 dB for a 100-km-long fiber cable even in the spectral region near 1.55 μm , where α has the smallest value of around 0.2 dB/km. Numerical values of α depend on the operating wavelength and may exceed 0.4 dB/km in the spectral region near 1.3 μm .

Any loss-management technique based on optical amplification degrades the signal-to-noise ratio (SNR) of the optical bit stream since all amplifiers add noise to the signal through spontaneous emission. This noise can be included by adding a noise term to the NLS equation together with the gain term. With the addition of such terms, Eq. (5.3.1) takes the form

$$\frac{\partial A}{\partial z} + \frac{i\beta_2}{2} \frac{\partial^2 A}{\partial t^2} = i\gamma |A|^2 A + \frac{1}{2} [g_0(z) - \alpha] A + f_n(z, t), \quad (7.1.4)$$

where $g_0(z)$ is the gain coefficient whose functional form depends on the amplification scheme used. The last term $f_n(z, t)$ in Eq. (7.1.4) accounts for the fluctuations induced by spontaneous emission. It vanishes on average, that is, $\langle f_n(z, t) \rangle = 0$, where angle brackets denote the ensemble average over the random process. If this process is assumed to be Markovian with Gaussian statistics, its statistical properties are completely described by the correlation function [5]

$$\langle f_n^*(z, t) f_n(z', t') \rangle = n_{sp} h v_0 g_0 \delta(z - z') \delta(t - t'), \quad (7.1.5)$$

where $h v_0$ is the photon energy and the spontaneous emission factor n_{sp} is defined in Section 7.2. The two delta functions in Eq. (7.1.5) ensure that all spontaneous-emission events are independent of each other both in time and at different points along the amplifier length. We ignore in this section the implications of the noise term in Eq. (7.1.4).

7.1.2 Lumped Versus Distributed Amplification

When EDAs are used periodically along a fiber link, the length l_a of each amplifier (typically $l_a < 0.1$ km) is much shorter than the spacing L_A between two amplifiers. Since $g_0 = 0$ everywhere except within each amplifier, one can solve the standard NLS equation (7.1.2) in each fiber section of length L_A . As seen from Eq. (7.1.3), losses in each section reduce the average power by a factor of $\exp(\alpha L_A)$ and they can be fully compensated by operating each lumped amplifier such that its gain $G_A = \exp(g_0 l_a) = \exp(\alpha L_A)$. Thus, in a loss-managed long-haul system, EDAs are inserted periodically after a distance L_A and their gain is adjusted such that $G_A = \exp(\alpha L_A)$. It is not necessary that amplifier spacing be uniform throughout the link. In the case of nonuniform spacing, if the n th amplifier is placed at a distance L_n from the transmitter, its gain G_n is chosen to be $G_n = \exp[\alpha(L_n - L_{n-1})]$ so that each amplifier fully compensates the losses of each fiber span preceding it.

In the case of distributed amplification, Eq. (7.1.4) should be solved along the entire fiber link, after $g_0(z)$ has been determined for a given pumping scheme. Similar to Eq. (7.1.1), it is useful to write the general solution of Eq. (7.1.4) in the form

$$A(z, t) = \sqrt{p(z)} B(z, t), \quad (7.1.6)$$

where $p(z)$ governs variations in the time-averaged power of the optical bit stream along the link length because of fiber losses and signal amplification. Substituting Eq. (7.1.6) in Eq. (7.1.4), $p(z)$ is found to satisfy a simple ordinary differential equation

$$\frac{dp}{dz} = [g_0(z) - \alpha]p, \quad (7.1.7)$$

whereas $B(z, t)$ satisfies Eq. (7.1.2) with $p(z)$ replacing the factor $e^{-\alpha z}$.

If $g_0(z)$ were constant and equal to α for all z , the average power of the optical signal would remain constant along the fiber link. This is the ideal situation in which the fiber is effectively lossless. In practice, distributed gain is realized by injecting pump power periodically into the fiber link (see Figure 7.1). Since pump power does not remain constant because of considerable fiber losses at the pump wavelength, $g(z)$ cannot be kept constant along the fiber. However, even though fiber losses cannot be compensated everywhere locally, they can be compensated fully over a distance L_A provided the following condition is satisfied:

$$\int_0^{L_A} g_0(z) dz = \alpha L_A. \quad (7.1.8)$$

Every distributed amplification scheme is designed to satisfy Eq. (7.1.8). The distance L_A is referred to as the *pump-station spacing*.

As mentioned earlier, stimulated Raman scattering is often used to provide distributed amplification. The scheme works by launching CW power at several wavelengths from a set of high-power semiconductor lasers located at the pump stations [57]. The wavelengths of pump lasers should be in the vicinity of $1.45 \mu\text{m}$ for amplifying optical signals in the $1.55\text{-}\mu\text{m}$ spectral region. These wavelengths and pump-power levels are chosen to provide a uniform gain over the entire C band (or C and L

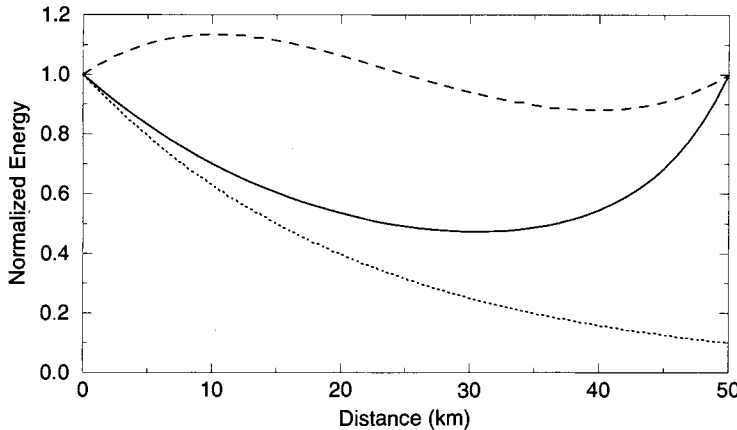


Figure 7.2: Variations in average signal power between two neighboring pump stations for backward (solid line) and bidirectional (dashed line) pumping schemes with $L_A = 50$ km. The lumped-amplifier case is shown by the dotted line.

bands in the case of dense WDM systems). Backward pumping is commonly used for distributed Raman amplification because such a configuration minimizes the transfer of pump-intensity noise to the amplified signal.

7.1.3 Bidirectional Pumping Scheme

The use of a bidirectional pumping scheme is beneficial in some cases. To provide physical insight, consider the case in which one pump laser is used at both ends of a fiber section of length L_A . In this case, the gain coefficient at a distance z can be written as

$$g(z) = g_1 \exp(-\alpha_p z) + g_2 \exp[-\alpha_p(L_A - z)], \quad (7.1.9)$$

where α_p is the fiber loss at the pump wavelength and the constants g_1 and g_2 are related to the pump powers injected at the two ends. Assuming equal pump powers and integrating Eq. (7.1.7), the average power of the optical signal, normalized to its fixed value at the pump stations, is found to vary as

$$p(z) = \exp \left[\alpha L_A \left(\frac{\sinh[\alpha_p(z - L_A/2)] + \sinh(\alpha_p L_A/2)}{2 \sinh(\alpha_p L_A/2)} \right) - \alpha z \right]. \quad (7.1.10)$$

In the case of backward pumping, $g_1 = 0$ in Eq. (7.1.9), and the solution of Eq. (7.1.7) is found to be

$$p(z) = \exp \left\{ \alpha L_A \left[\frac{\exp(\alpha_p z) - 1}{\exp(\alpha_p L_A) - 1} \right] - \alpha z \right\}, \quad (7.1.11)$$

where g_2 was again chosen to ensure that $p(L_A) = 1$.

The solid line in Figure 7.2 shows how $p(z)$ varies along the fiber in the case of backward pumping for $L_A = 50$ km using $\alpha = 0.2$ dB/km and $\alpha_p = 0.25$ dB/km. The

case of bidirectional pumping is shown with a dashed line. The case of lumped amplification is also shown for comparison by a dotted line. Whereas average signal power varies by a factor of 10 in the lumped case, it varies by less than a factor of 2 in the case of backward-pumped distributed amplification. Moreover, it varies by less than 15% in the case of a bidirectional pumping scheme, showing that this scheme is close to the ideal situation in which fiber losses are compensated fully all along the fiber. The range over which $p(z)$ varies depends on the pump-station spacing L_A . For example, $p(z)$ varies by a factor of 100 or more when $L_A = 100$ km if lumped amplification is used but by less than a factor of 2 when a bidirectional pumping scheme is employed.

Optical amplifiers developed so far include semiconductor optical amplifiers, doped-fiber amplifiers, Raman amplifiers, and parametric amplifiers. Among these, semiconductor optical amplifiers are rarely used as in-line amplifiers because of issues related to insertion losses, polarization sensitivity, and nonlinear effects such as cross-gain saturation and interchannel crosstalk. Although they are attracting renewed attention in recent years for applications in coarse WDM systems, semiconductor optical amplifiers are not discussed further in this chapter. Parametric amplifiers, making use of four-wave mixing inside an optical fiber, have attracted considerable attention in recent years [6]–[9]. These are also not discussed here as they are still far from being deployed in actual lightwave systems. In contrast, doped-fiber amplifiers are used routinely and Raman amplifiers have also been deployed in some WDM systems. These two types of amplifiers are discussed in detail in the following two sections.

7.2 Erbium-Doped Fiber Amplifiers

An important class of lumped optical amplifiers makes use of rare-earth elements as a gain medium by doping the fiber core during the manufacturing process. Although doped-fiber amplifiers were studied as early as 1964 [10], their use became practical only 25 years later, after their fabrication techniques were perfected [11]. In such amplifiers, properties such as the operating wavelength and the gain bandwidth are determined by the dopants while silica plays the role of a host medium. Among the rare-earth elements, erbium is the most practical element to realize fiber amplifiers operating in the wavelength region near $1.5\ \mu\text{m}$, and erbium-doped fiber amplifiers (EDFAs) have been studied extensively [1]–[4]. Their deployment in WDM systems after 1995 revolutionized fiber-optic communications and led to lightwave systems with capacities exceeding 1 Tb/s.

7.2.1 Pumping and Gain Spectrum

The fiber core inside an EDFA contains erbium ions (Er^{3+}), and pumping them at a suitable wavelength provides the optical gain through population inversion. The gain spectrum depends on the pumping scheme as well as on the presence of other dopants, such as germania and alumina, within the fiber core. The amorphous nature of silica broadens the energy levels of Er^{3+} into bands. Figure 7.3(a) shows a few energy bands of Er^{3+} in silica glasses. Many transitions can be used to pump an EDFA. Efficient EDFA pumping is possible using semiconductor lasers operating near 0.98- and 1.48-

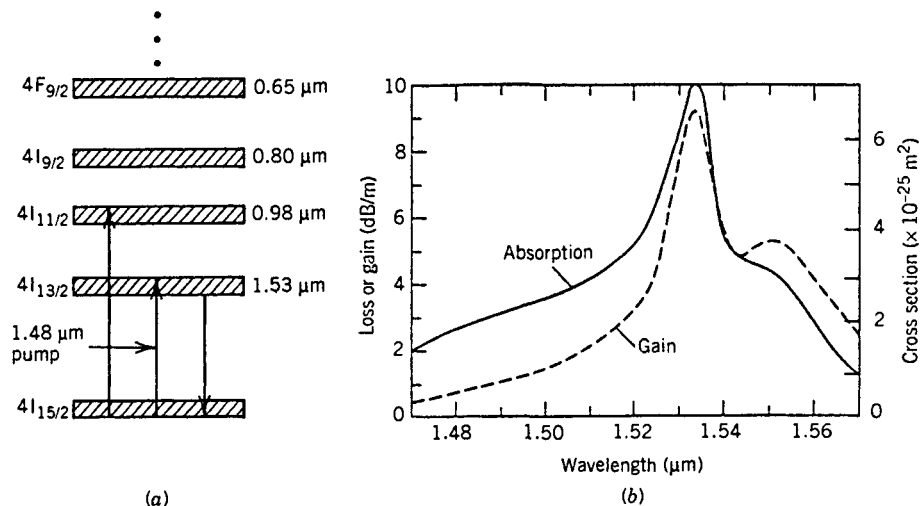


Figure 7.3: (a) Energy-level diagram of erbium ions in silica fibers; (b) absorption and gain spectra of an EDFA whose core was codoped with germania. (After Ref. [16]; ©1991 IEEE.)

μm wavelengths. Indeed, the development of such pump lasers was fueled with the advent of EDFAs. It is possible to realize a 30-dB gain with only 15 to 20 mW of absorbed pump power. Efficiencies as high as 11 dB/mW were achieved by 1990 with 0.98-μm pumping [12]. Most EDFAs use 980-nm pump lasers for such lasers are commercially available and can provide more than 100 mW of pump power. Pumping at 1480 nm requires longer fibers and higher powers because it uses the tail of the absorption band shown in Fig. 7.3(b).

EDFAs can be designed to operate in such a way that the pump and signal beams propagate in opposite directions, a configuration referred to as backward pumping to distinguish it from the forward-pumping configuration. The performance is nearly the same in the two pumping configurations when the signal power is small enough for the amplifier to remain unsaturated. In the saturation regime, the power-conversion efficiency is generally better in the backward-pumping configuration [13], mainly because of the important role played by the amplified spontaneous emission (ASE). In the bidirectional-pumping configuration, an EDFA is pumped in both directions simultaneously by using two semiconductor lasers located at the two fiber ends. This configuration requires two pump lasers but has the advantage that the population inversion, and hence the small-signal gain, is relatively uniform along the entire amplifier length.

Figure 7.3(b) shows the gain and absorption spectra of an EDFA whose core was doped with germania [16]. The gain spectrum is quite broad and has a double-peak structure. Its shape is affected considerably by the amorphous nature of silica and by the presence of other dopants within the fiber core such as alumina [14]–[16]. The gain spectrum is homogeneously broadened for isolated erbium ions. However, structural disorders lead to inhomogeneous broadening of the gain spectrum, whereas *Stark split-*

ting of various energy levels is responsible for homogeneous broadening. Mathematically, the gain should be averaged over the distribution of atomic transition frequencies ω_0 resulting in the effective gain of the form is given by

$$g_0(z, \omega) = \int_{-\infty}^{\infty} g(z, \omega, \omega_0) f(\omega_0) d\omega_0, \quad (7.2.1)$$

where $f(\omega_0)$ is the distribution function whose form also depends on the presence of other dopants within the fiber core.

The factor by which a weak input signal is amplified is obtained by integrating Eq. (damp.1) over the amplifier length L . If we neglect fiber losses because of small fiber lengths (~ 10 m) employed to make EDFA, the amplification factor is given by $G(\omega) = \exp[\int_0^L g_0(z, \omega) dz]$. Although $G(\omega)$ is also often referred to as the gain spectrum, one should not confuse it with $g_0(z, \omega)$. It can vary from amplifier to amplifier because it also depends on the amplifier length. In practice, both the bandwidth and the flatness of $G(\omega)$ are important for WDM systems. This issue is discussed later in this section.

7.2.2 Two-Level Model

The gain of an EDFA depends on a large number of device parameters such as erbium-ion concentration, amplifier length, core radius, and pump power [16]–[20]. A three-level rate-equation model used commonly for lasers can be adapted for EDFA [2]. It is sometimes necessary to add a fourth level to include the *excited-state absorption*. In general, the resulting equations must be solved numerically.

Considerable insight can be gained by using a simple two-level model that is valid when ASE and excited-state absorption are negligible. The model assumes that the top level of the three-level system remains nearly empty because of a rapid transfer of the pumped population to the excited state. It is, however, important to take into account the different emission and absorption cross sections for the pump and signal fields. The population densities of the two states, N_1 and N_2 , satisfy the following two rate equations [2]:

$$\frac{\partial N_2}{\partial t} = (\sigma_p^a N_1 - \sigma_p^e N_2) \phi_p + (\sigma_s^a N_1 - \sigma_s^e N_2) \phi_s - \frac{N_2}{T_1}, \quad (7.2.2)$$

$$\frac{\partial N_1}{\partial t} = (\sigma_p^e N_2 - \sigma_p^a N_1) \phi_p + (\sigma_s^e N_2 - \sigma_s^a N_1) \phi_s + \frac{N_2}{T_1}, \quad (7.2.3)$$

where σ_j^a and σ_j^e are the absorption and emission cross sections at the frequency ω_j with $j = p, s$. Further, T_1 is the spontaneous lifetime of the excited state (about 10 ms for EDFA). The quantities ϕ_p and ϕ_s represent the photon flux for the pump and signal waves, defined such that $\phi_j = P_j / (a_j h \nu_j)$, where P_j is the optical power, σ_j is the transition cross section at the frequency ν_j , and a_j is the cross-sectional area of the fiber mode for $j = p, s$.

The pump and signal powers vary along the amplifier length because of absorption, stimulated emission, and spontaneous emission. If the contribution of spontaneous

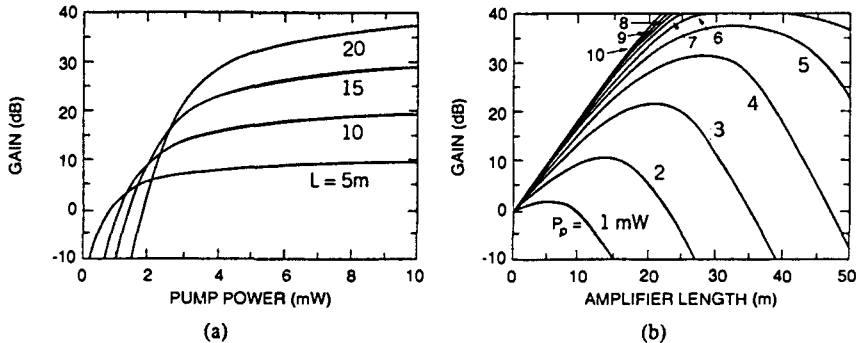


Figure 7.4: Small-signal gain as a function of (a) pump power and (b) amplifier length for an EDFA assumed to be pumped at 1.48 μm . (After Ref. [16]; ©1991 IEEE.)

emission is neglected, P_s and P_p satisfy the simple equations

$$\frac{\partial P_s}{\partial z} = \Gamma_s(\sigma_s^e N_2 - \sigma_s^a N_1)P_s - \alpha P_s, \quad (7.2.4)$$

$$s \frac{\partial P_p}{\partial z} = \Gamma_p(\sigma_p^e N_2 - \sigma_p^a N_1)P_p - \alpha' P_p, \quad (7.2.5)$$

where α and α' take into account fiber losses at the signal and pump wavelengths, respectively. These losses can be neglected for typical amplifier lengths of 10–20 m but they must be included in the case of distributed amplification. The confinement factors Γ_s and Γ_p account for the fact that the doped region within the core provides the gain for the entire fiber mode. The parameter $s = \pm 1$ in Eq. (7.2.5) depending on the direction of pump propagation; $s = -1$ in the case of a backward-propagating pump.

Equations (7.2.2)–(7.2.5) can be solved analytically, in spite of their complexity, after some justifiable approximations [17]. For lumped amplifiers, the fiber length is short enough that both α and α' can be set to zero. Noting that $N_1 + N_2 = N_t$ where N_t is the total ion density, only one equation, say Eq. (7.2.2) for N_2 , need be solved. Noting again that the absorption and stimulated-emission terms in the field and population equations are related, the steady-state solution of Eq. (7.2.2), obtained by setting the time derivative to zero, can be written as

$$N_2(z) = -\frac{T_1}{a_d h \nu_s} \frac{\partial P_s}{\partial z} - \frac{s T_1}{a_d h \nu_p} \frac{\partial P_p}{\partial z}, \quad (7.2.6)$$

where $a_d = \Gamma_s a_s = \Gamma_p a_p$ is the cross-sectional area of the doped portion of the fiber core. Substituting this solution into Eqs. (7.2.4) and (7.2.5) and integrating them over the fiber length, the powers P_s and P_p at the fiber output can be obtained in an analytical form. This model has been extended to include the ASE propagation in both the forward and backward directions [20].

Although the preceding approach is essential when the total signal power inside the amplifier is large enough to cause gain saturation, a much simpler treatment is

applicable in the so-called small-signal regime in which the EDFA remains saturated. In that case, the ϕ_s term in Eqs. (7.2.2) and (7.2.3) can be neglected, and the gain coefficient, $g(z) = (\sigma_s^e N_2 - \sigma_s^a N_1)$, does not depend on the signal power P_s . Equation (7.2.4) can then be readily integrated. The total amplifier gain G for an EDFA of length L is then given by

$$G = \exp \left[\Gamma_s \int_0^L [g(z) - \alpha] dz \right]. \quad (7.2.7)$$

Figure 7.4 shows the small-signal gain at $1.55 \mu\text{m}$ as a function of the pump power and the amplifier length by using typical parameter values. For a given amplifier length L , the amplifier gain initially increases exponentially with the pump power, but the increase becomes much smaller when the pump power exceeds a certain value [corresponding to the “knee” in Figure 7.4(a)]. For a given pump power, the amplifier gain becomes maximum at an optimum value of L and drops sharply when L exceeds this optimum value. The reason is that the latter portion of the amplifier remains unpumped and absorbs the amplified signal. Since the optimum value of L depends on the pump power P_p , it is necessary to choose both L and P_p appropriately. Figure 7.4(b) shows that a 35-dB gain can be realized at a pump power of 5 mW for $L = 30 \text{ m}$ and $1.48-\mu\text{m}$ pumping. It is possible to design amplifiers such that high gain is obtained for amplifier lengths as short as a few meters. The qualitative features shown in Figure 7.4 are observed in all EDFA; the agreement between theory and experiment is generally quite good [19].

The foregoing analysis assumes that both pump and signal waves are in the form of CW beams. In practice, EDFA are pumped by using CW semiconductor lasers, but the signal is in the form of a pulse train (containing a random sequence of 1 and 0 bits), and the duration of individual pulses is inversely related to the bit rate. The question is whether all pulses experience the same gain or not. It turns out that the gain remains constant with time in an EDFA for even microsecond long pulses. The reason is related to a relatively large value of the fluorescence time associated with the excited erbium ions ($T_1 \sim 10 \text{ ms}$). When the time scale of signal-power variations is much shorter than T_1 , erbium ions are unable to follow such fast variations. As single-pulse energies are typically much below the saturation energy ($\sim 10 \mu\text{J}$), EDFA respond to the average power. As a result, gain saturation is governed by the average signal power, and amplifier gain does not vary from pulse to pulse for a WDM signal. This is an extremely useful feature of EDFA.

In some applications such as packet-switched networks, signal power may vary on a time scale comparable to T_1 . Amplifier gain in that case is likely to become time dependent, an undesirable feature from the standpoint of system performance. A gain-control mechanism that keeps the amplifier gain pinned at a constant value consists of making the EDFA oscillate at a controlled wavelength outside the range of interest (typically below $1.5 \mu\text{m}$). Since the gain remains clamped at the threshold value for a laser, the signal is amplified by the same factor despite variations in the signal power. In one implementation of this scheme, an EDFA was forced to oscillate at $1.48 \mu\text{m}$ by fabricating two fiber Bragg gratings acting as high-reflectivity mirrors at the two ends of the amplifier [21].

7.2.3 Amplifier Noise

Amplifier noise is the ultimate limiting factor for system applications [22]–[25]. All amplifiers degrade the signal-to-noise ratio (SNR) of the amplified signal because of spontaneous emission that adds noise to the signal during its amplification. Because of this amplified spontaneous emission (ASE), the SNR is degraded, and the extent of degradation is quantified through a parameter F_n , called the *amplifier noise figure*. In analogy with the electronic amplifiers, it is defined as

$$F_n = \frac{(\text{SNR})_{\text{in}}}{(\text{SNR})_{\text{out}}}, \quad (7.2.8)$$

where SNR refers to the electric power generated when the optical signal is converted into an electric current. In general, F_n depends on several detector parameters that govern thermal noise associated with the detector (see Section 4.4.1). A simple expression for F_n can be obtained by considering an ideal detector whose performance is limited by shot noise only [26].

Consider an amplifier with the gain G such that the output and input powers are related by $P_{\text{out}} = GP_{\text{in}}$. The SNR of the input signal is given by

$$(\text{SNR})_{\text{in}} = \frac{\langle I \rangle^2}{\sigma_s^2} = \frac{(R_d P_{\text{in}})^2}{2q(R_d P_{\text{in}})\Delta f} = \frac{P_{\text{in}}}{2h\nu\Delta f}, \quad (7.2.9)$$

where $\langle I \rangle = R_d P_{\text{in}}$ is the average photocurrent, $R_d = q/h\nu$ is the responsivity of an ideal photodetector with unit quantum efficiency (see Section 4.1), and

$$\sigma_s^2 = 2q(R_d P_{\text{in}})\Delta f \quad (7.2.10)$$

is obtained from Eq. (4.4.5) for the shot noise by setting the dark current $I_d = 0$. Here Δf is the detector bandwidth. To evaluate the SNR of the amplified signal, we should add the contribution of ASE to the receiver noise.

The spectral density of ASE is nearly constant (white noise) and can be written as [26]

$$S_{\text{ASE}}(\nu) = n_{\text{sp}} h\nu_0 (G - 1), \quad (7.2.11)$$

where ν_0 is the carrier frequency of the signal being amplified. The parameter n_{sp} is called the *spontaneous emission factor* (or the population-inversion factor) and is given by

$$n_{\text{sp}} = \sigma_e N_2 / (\sigma_e N_2 - \sigma_a N_1). \quad (7.2.12)$$

where N_1 and N_2 are the atomic populations for the ground and excited states, respectively. The effect of spontaneous emission is to add fluctuations to the amplified signal; these are converted to current fluctuations during the photodetection process.

It turns out that the dominant contribution to the receiver noise comes from the beating of spontaneous emission with the signal [26]. The spontaneously emitted radiation mixes with the amplified signal and produces the current $I = R_d | \sqrt{G}E_{\text{in}} + E_{\text{sp}} |^2$ at the photodetector of responsivity R . Noting that E_{in} and E_{sp} oscillate at different frequencies with a random phase difference, it is easy to see that the beating of spontaneous emission with the signal will produce a noise current $\Delta I = 2R_d(GP_{\text{in}})^{1/2}|E_{\text{sp}}| \cos \theta$,

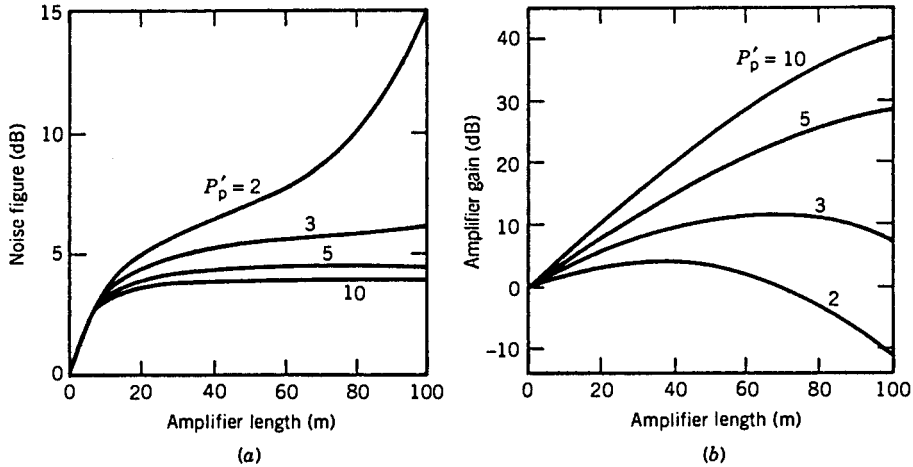


Figure 7.5: (a) noise figure and (b) amplifier gain as a function of the length for several pumping levels. (After Ref. [25]; ©1990 IEE.)

where θ is a rapidly varying random phase. Averaging over the phase, the variance of the photocurrent can be written as

$$\sigma^2 = 2q(R_dGP_{\text{in}})\Delta f + 4(R_dGP_{\text{in}})(R_dS_{\text{ASE}})\Delta f, \quad (7.2.13)$$

where $\cos^2 \theta$ was replaced by its average value $\frac{1}{2}$. The SNR of the amplified signal is thus given by

$$(\text{SNR})_{\text{out}} = \frac{(R_dGP_{\text{in}})^2}{\sigma^2} \approx \frac{GP_{\text{in}}}{(4S_{\text{ASE}} + 2h\nu)\Delta f}. \quad (7.2.14)$$

The amplifier noise figure is obtained by substituting Eqs. (7.2.9) and (7.2.14) in Eq. (7.2.8) and is given by

$$F_n = 2n_{\text{sp}} \left(1 - \frac{1}{G} \right) + \frac{1}{G} \approx 2n_{\text{sp}}, \quad (7.2.15)$$

where the last approximation is valid for $G \gg 1$. This equation shows that the SNR of the amplified signal is degraded by 3 dB even for an ideal amplifier for which $n_{\text{sp}} = 1$. For most practical amplifiers, F_n exceeds 3 dB and can be as large as 6–8 dB.

The preceding analysis assumed that n_{sp} was constant along the amplifier length. In the case of an EDFA, both N_1 and N_2 vary with z . The spontaneous-emission factor can still be calculated for an EDFA by using the two-level model discussed earlier, but the noise figure depends both on the amplifier length L and the pump power P_p , just as the amplifier gain does. Figure 7.5(a) shows the variation of F_n with the amplifier length for several values of P_p/P_p^{sat} when a 1.53- μm signal is amplified with an input power of 1 mW. The amplifier gain under the same conditions is also shown in Figure 7.5(b). The results show that a noise figure close to 3 dB can be obtained for a high-gain amplifier [22].

The experimental results confirm that F_n close to 3 dB is possible in EDFA s. A noise figure of 3.2 dB was measured in a 30-m-long EDFA pumped at $0.98 \mu\text{m}$ with 11 mW of power [23]. A similar value was found for another EDFA pumped with only 5.8 mW of pump power at $0.98 \mu\text{m}$ [24]. In general, it is difficult to achieve high gain, low noise, and high pumping efficiency simultaneously. The main limitation is imposed by the ASE traveling backward toward the pump and depleting the pump power. Incorporation of an internal isolator alleviates this problem to a large extent. In one implementation, 51-dB gain was realized with a 3.1-dB noise figure at a pump power of only 48 mW [27].

The measured values of F_n are generally larger for EDFA s pumped at $1.48 \mu\text{m}$. A noise figure of 4.1 dB was obtained for a 60-m-long EDFA when pumped at $1.48 \mu\text{m}$ with 24 mW of pump power [23]. The reason for a larger noise figure for $1.48\text{-}\mu\text{m}$ pumped EDFA s can be understood from Figure 7.5(a), which shows that the pump level and the excited level lie within the same band for $1.48\text{-}\mu\text{m}$ pumping. It is difficult to achieve complete population inversion ($N_1 \approx 0$) under such conditions. It is nonetheless possible to realize $F_n < 3.5$ dB for pumping wavelengths near $1.46 \mu\text{m}$.

Relatively low noise levels of EDFA s make them an ideal choice for WDM light-wave systems. In spite of low noise, the performance of long-haul fiber-optic communication systems employing multiple EDFA s is often limited by the amplifier noise. The noise problem is particularly severe when the system operates in the anomalous-dispersion region of the fiber because a nonlinear phenomenon known as the modulation instability [28] enhances the amplifier noise [29] and degrades the signal spectrum [30]. Amplifier noise also introduces timing jitter. These issue are discussed later in this chapter.

7.2.4 Multichannel Amplification

The bandwidth of EDFA s is large enough that they have proven to be the optical amplifier of choice for WDM applications. The gain provided by them is nearly polarization insensitive. Moreover, the interchannel crosstalk does not occur in EDFA s because of a relatively large value of T_1 (about 10 ms) compared with typical bit durations (0.1 ns at a bitrate of 10 Gb/s) in lightwave systems. The sluggish response of EDFA s ensures that their gain cannot be modulated at frequencies much larger than 10 kHz.

A second source of interchannel crosstalk is cross-gain saturation occurring because the gain of a specific channel is saturated not only by its own power (self-saturation) but also by the power of neighboring channels. This mechanism of crosstalk is common to all optical amplifiers including EDFA s [31]–[33]. It can be avoided by operating the amplifier in the unsaturated regime. Experimental results support this conclusion. In a 1989 experiment [31], negligible power penalty was observed when an EDFA was used to amplify two channels operating at 2 Gb/s and separated by 2 nm as long as the channel powers were low enough to avoid the gain saturation.

The main practical limitation of an EDFA stems from the spectral nonuniformity of the amplifier gain. Even though the gain spectrum of an EDFA is relatively broad, as seen in Fig. 7.3, the gain is far from uniform (or flat) over a wide wavelength range. As a result, different channels of a WDM signal are amplified by different amounts. This problem becomes quite severe in long-haul systems employing a cascaded chain of ED-

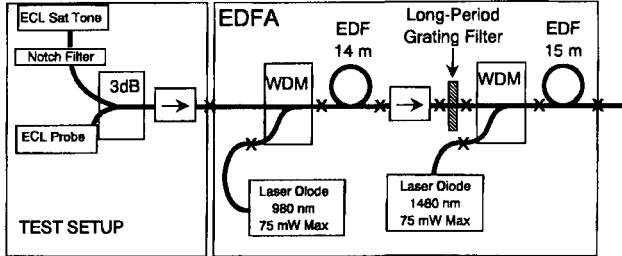


Figure 7.6: Schematic of an EDFA designed to provide uniform gain over the 1530–1570-nm bandwidth using an optical filter containing several long-period fiber gratings. The two-stage design helps to reduce the noise level. (After Ref. [37]; ©1997 IEEE.)

FAs. The reason is that small variations in the amplifier gain for individual channels grow exponentially over a chain of in-line amplifiers. Even a 0.2-dB gain difference grows to 20 dB over a chain of 100 in-line amplifiers, making channel powers vary by up to a factor of 100, an unacceptable variation range in practice. To amplify all channels by nearly the same amount, the double-peak nature of the EDFA gain spectrum forces one to pack all channels near one of the gain peaks, thereby reducing the usable gain bandwidth considerably.

The entire bandwidth of 40 nm or so can be used if the gain spectrum is flattened by introducing wavelength-selective losses. The basic idea behind gain flattening is quite simple. If an optical filter whose transmission losses mimic the gain profile (high in the high-gain region and low in the low-gain region) is inserted after the doped fiber, the output power will become nearly constant for all channels. Although fabrication of such a filter is not simple, several gain-flattening techniques have been developed [2]. Among others, thin-film interference filters, Mach-Zehnder filters, acousto-optic filters, and long-period fiber gratings have been used for flattening the gain profile and equalizing channel gains [34]–[36].

The gain-flattening techniques can be divided into active and passive categories. The filter-based methods are passive in the sense that channel gains cannot be adjusted in a dynamic fashion. The location of the optical filter itself requires some thought because of high losses associated with it. Placing it before the amplifier increases the noise, while placing it after the amplifier reduces the output power. Often a two-stage configuration shown in Fig. 7.6 is used. The second stage acts as a power amplifier but the noise figure is mostly determined by the first stage whose noise is relatively low because of its low gain. A combination of several long-period fiber gratings acting as the optical filter in the middle of two stages resulted by 1997 in an EDFA whose gain was flat to within 1 dB over the 40-nm bandwidth in the wavelength range of 1530–1570 nm [37].

Ideally, an optical amplifier should provide the same gain for all channels under all possible operating conditions. This is not the case in general. For instance, if the number of channels being transmitted changes, the gain of each channel will change since it depends on the total signal power (because of gain saturation). An active control of channel gains is thus desirable for WDM applications. Many techniques have been

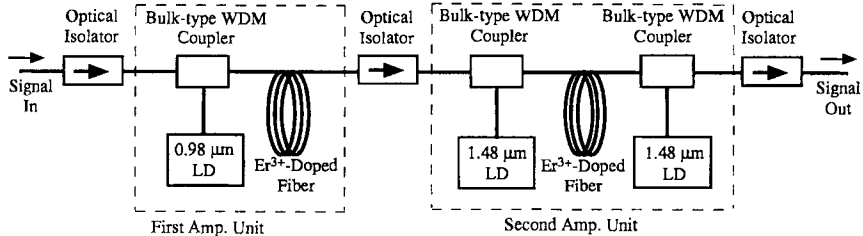


Figure 7.7: Schematic of an L-band EDFA providing uniform gain over the 1570–1610-nm bandwidth with a two-stage design. (After Ref. [44]; ©1999 IEEE.)

developed for this purpose. The most commonly used technique stabilizes the gain dynamically by incorporating within the amplifier a laser that operates outside the used bandwidth. Such devices are called gain-clamped EDFAs (as their gain is clamped by a built-in laser) and have been studied extensively [38]–[43].

WDM lightwave systems capable of transmitting more than 80 channels appeared by 1998. Such systems use the C and L bands simultaneously and need uniform amplifier gain over a bandwidth exceeding 60 nm. Moreover, the use of the L band requires optical amplifiers capable of providing gain in the wavelength range 1570–1610 nm. It turns out that EDFAs can provide gain over this wavelength range, with a suitable design. An L-band EDFA requires long fiber lengths (>100 m) to keep the inversion level relatively low. Figure 7.7 shows an L-band amplifier with a two-stage design [44]. The first stage is pumped at 980 nm and acts as a traditional EDFA (fiber length 20–30 m) capable of providing gain in the range 1530–1570 nm. In contrast, the second stage has 200-m-long doped fiber and is pumped bidirectionally using 1480-nm lasers. An optical isolator between the two stages passes the ASE from the first stage to the second stage (necessary for pumping the second stage) but blocks the backward-propagating ASE from entering the first stage. Such cascaded, two-stage amplifiers can provide flat gain over a wide bandwidth while maintaining a relatively low noise level. As early as 1996, flat gain to within 0.5 dB was realized over the wavelength range of 1544–1561 nm [45]. The second EDFA was codoped with ytterbium and phosphorus and was optimized such that it acted as a power amplifier. Since then, EDFAs providing flat gain over the entire C and L bands have been made [2]. Raman amplification can also be used for the L band. Combining Raman amplification with one or two EDFAs, uniform gain can be realized over a 75-nm bandwidth covering the C and L bands [46].

A parallel configuration has also been developed for EDFAs capable of amplifying over the C and L bands simultaneously [47]. In this approach, the incoming WDM signal is split into two branches, which amplify the C-band and L-band signals separately using an optimized EDFA in each branch. The two-arm design has produced a relatively uniform gain of 24 dB over a bandwidth as large as 80 nm when pumped with 980-nm semiconductor lasers while maintaining a noise figure of about 6 dB [2]. The two-arm or two-stage amplifiers are complex devices and contain multiple components, such as optical filters and isolators, within them for optimizing the amplifier performance. An alternative approach to broadband EDFAs uses a *fluoride* fiber in place of silica fibers as the host medium in which erbium ions are doped. Gain flatness over

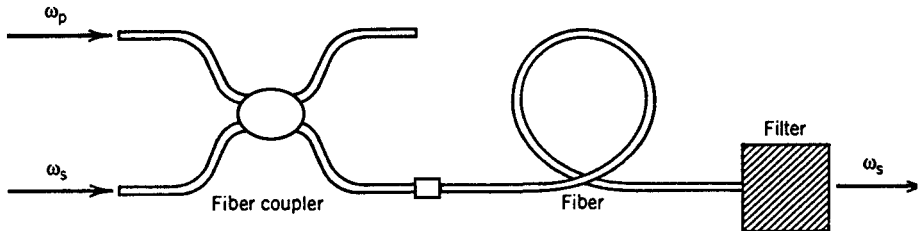


Figure 7.8: Schematic of a fiber-based Raman amplifier.

a 76-nm bandwidth has been realized by doping a *tellurite* fiber with erbium ions [48]. Although such EDFA s are simpler in design compared with multistage amplifiers, they suffer from the splicing difficulties because of the use of nonsilica glasses.

High-capacity lightwave systems as well as coarse WDM systems (channel spacing >5 nm) are likely to make use of the short-wavelength region—the so-called S band, extending from 1470 to 1520 nm—in addition to the C and L bands. Thulium-doped fiber amplifiers were initially developed for this purpose, and they are capable of providing flat gain in the wavelength range 1480–1510 nm when pumped using 1420-nm and 1560-nm semiconductor lasers [49]. More recently, attention has focused on EDFA s that can provide gain simultaneously in all three bands with a suitable design [50]–[53]. Semiconductor optical amplifiers are also being considered for coarse WDM systems. However, fiber-based Raman amplifiers are also likely to be deployed because they can provide amplification in any spectral region with a suitable choice of pump lasers; we turn to them in the next section.

7.3 Raman Amplifiers

Fiber-based Raman amplifiers [54]–[58] make use of *stimulated Raman scattering* (SRS) occurring in silica fibers [28]. Figure 7.8 shows how a fiber can be used as a Raman amplifier in the forward-pumping configuration. The pump and signal beams at frequencies ω_p and ω_s are injected into the fiber through a fiber coupler. As discussed in Sections 2.6.1, during the SRS process, a pump photon gives up its energy to create another photon of reduced energy at the signal frequency; the remaining energy is absorbed by the silica material in the form of molecular vibrations (optical phonons). The energy is transferred continuously from the pump to the signal through SRS as the two beams copropagate inside the fiber. The pump and signal beams counterpropagate in the backward-pumping configuration often used in practice.

7.3.1 Raman Gain and Bandwidth

The Raman-gain spectrum of silica fibers is shown in Figure 2.17; its broadband nature is a consequence of the amorphous nature of glass. The Raman-gain coefficient g_R is related to the optical gain $g(z)$ as $g = g_R I_p(z)$, where I_p is the pump intensity. In terms

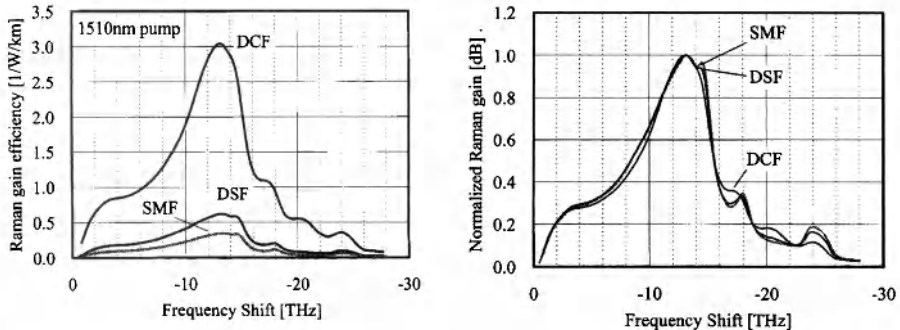


Figure 7.9: Raman-gain spectra (ratio g_R/a_p) for standard (SMF), dispersion-shifted (DSF) and dispersion-compensating (DCF) fibers. Normalized gain profiles are also shown. (After Ref. [54]; ©2001 IEEE.)

of the pump power $P_p(z)$, the gain can be written as

$$g(\omega, z) = g_R(\omega)[P_p(z)/a_p], \quad (7.3.1)$$

where a_p is the cross-sectional area of the pump beam inside the fiber. Since a_p can vary considerably for different types of fibers, the ratio g_R/a_p is a measure of the Raman-gain efficiency [54]. This ratio is plotted in Fig. 7.9 for three different fibers. A dispersion-compensating fiber (DCF) can be 8 times more efficient than a standard silica fiber (SMF) because of its smaller core diameter. The frequency dependence of the Raman gain is almost the same for the three kinds of fibers as evident from the normalized gain spectra shown in Figure 7.9. The gain peaks for a Stokes shift of about 13.2 THz. The gain bandwidth Δv_g is nearly 6 THz if we define it as the FWHM of the dominant peak in Figure 7.9.

The large bandwidth of fiber Raman amplifiers makes them attractive for fiber-optic communication systems. However, a relatively large pump power is required to realize an amplification factor $G > 20$ dB. As an example, if we use $G = \exp(gL)$ by ignoring pump losses in the unsaturated region, $gL \approx 6.7$ is required for $G = 30$ dB. By using the measured value of $g_R = 6 \times 10^{-14}$ m/W at the gain peak near 1.55 μm with $a_p = 50 \mu\text{m}^2$, the required pump power is more than 5 W for a 1-km-long fiber. It can be reduced for longer fibers, but then fiber losses must be included.

Raman amplifiers are called lumped or distributed depending on their design. In the lumped case, a discrete device is made by spooling 1–2 km of a especially prepared fiber that has been doped with Ge or phosphorus for enhancing the Raman gain. The fiber is pumped at a wavelength near 1.45 μm for amplification of 1.55- μm signals. In the case of distributed Raman amplification, the same fiber that is used for signal transmission is also used for signal amplification. The pump light is often injected in the backward direction and provides gain over relatively long lengths (> 50 km). The main drawback in both cases from the system standpoint is that high-power lasers are required for pumping. Early experiments often used a tunable color-center laser as a pump; such lasers are too bulky for system applications. For this reason, Raman amplifiers were rarely used during the 1990 when EDFAs became available. The

situation changed around 2000 with the availability of compact high-power semiconductor lasers. Since then, both the discrete and distributed Raman amplifiers have been employed in designing lightwave systems.

7.3.2 Raman-Induced Signal Gain

Consider the simplest situation in which a single CW pump beam is launched into an optical fiber used to amplify a CW signal. Variations in the pump and signal powers along the amplifier length can be studied by solving the two coupled equations given in Section 2.6.1. In terms of pump and signal powers, these equations take the form

$$dP_s/dz = -\alpha_s P_s + (g_R/a_p)P_p P_s, \quad (7.3.2)$$

$$dP_p/dz = -\alpha_p P_p - (\omega_p/\omega_s)(g_R/a_p)P_s P_p, \quad (7.3.3)$$

where α_s and α_p represent fiber losses at the signal and pump frequencies, respectively. The frequency ratio ω_p/ω_s results from different energies of pump and signal photons and disappears if these equations are written in terms of photon numbers.

Consider first the case of small-signal amplification for which pump depletion can be neglected [the last term in Eq. (7.3.3)]. Substituting $P_p(z) = P_p(0)\exp(-\alpha_p z)$ in Eq. (7.3.2), the signal power at the output of an amplifier of length L is given by

$$P_s(L) = P_s(0) \exp(g_R P_0 L_{\text{eff}}/a_p - \alpha_s L), \quad (7.3.4)$$

where $P_0 = P_p(0)$ is the input pump power and $L_{\text{eff}} = [1 - \exp(-\alpha_p L)]/\alpha_p$. Because of fiber losses at the pump wavelength, the effective length of the amplifier is less than the actual length L ; $L_{\text{eff}} \approx 1/\alpha_p$ for $\alpha_p L \gg 1$. Since $P_s(L) = P_s(0) \exp(-\alpha_s L)$ in the absence of Raman amplification, the amplifier gain is given by

$$G_A = \frac{P_s(L)}{P_s(0) \exp(-\alpha_s L)} = \exp(g_0 L), \quad (7.3.5)$$

where the small-signal gain g_0 is defined as

$$g_0 = g_R \left(\frac{P_0}{a_p} \right) \left(\frac{L_{\text{eff}}}{L} \right) \approx \frac{g_R P_0}{a_p \alpha_p L}. \quad (7.3.6)$$

The last relation holds for $\alpha_p L \gg 1$. The amplification factor G_A becomes length independent for large values of $\alpha_p L$. Figure 7.10 shows variations of G_A with P_0 for several values of input signal powers for a 1.3-km-long Raman amplifier operating at 1.064 μm and pumped at 1.017 μm . The amplification factor increases exponentially with P_0 initially but then starts to deviate for $P_0 > 1 \text{ W}$ because of gain saturation. Deviations become larger with an increase in $P_s(0)$ as gain saturation sets in earlier along the amplifier length. The solid lines in Figure 7.10 are obtained by solving Eqs. (7.3.2) and (7.3.3) numerically to include pump depletion.

As the pump supplies energy for signal amplification, it begins to get depleted. A decrease in pump power P_p reduces the optical gain in Eq. (7.3.1). This reduction in gain is referred to as gain saturation. An approximate expression for the saturated

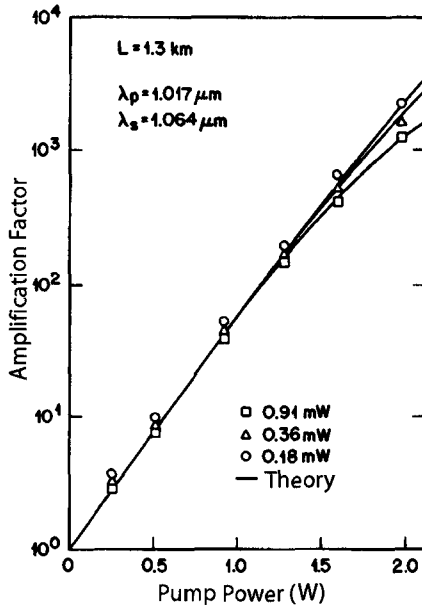


Figure 7.10: Variation of amplifier gain G_0 with pump power P_0 in a 1.3-km-long Raman amplifier for three values of the input power. Solid lines show the theoretical prediction. (After Ref. [59]; ©1981 Elsevier.)

amplifier gain G_s can be obtained assuming $\alpha_s = \alpha_p$ in Eqs. (7.3.2) and (7.3.3). The result is given by [28]

$$G_s = \frac{(1 + r_0)e^{-\alpha_s L}}{r_0 + G_A^{-(1+r_0)}}, \quad r_0 = \frac{\omega_p}{\omega_s} \frac{P_s(0)}{P_p(0)}. \quad (7.3.7)$$

Figure 7.11 shows the saturation characteristics by plotting G_s/G_A as a function of $G_A r_0$ for several values of G_A . The amplifier gain is reduced by 3 dB when $G_A r_0 \approx 1$. This condition is satisfied when the power of the amplified signal becomes comparable to the input pump power P_0 . In fact, P_0 is a good measure of the saturation power. Since typically $P_0 \sim 1$ W, and channel powers in a WDM system are ~ 1 mW, Raman amplifiers operate in the unsaturated regime, and Eq. (7.3.6) can be used in place of Eq. (7.3.7).

7.3.3 Multiple-Pump Raman Amplification

Starting in 1998, the use of multiple pumps for Raman amplification was pursued for developing broadband optical amplifiers required for WDM lightwave systems operating in the $1.55\text{-}\mu\text{m}$ region [60]–[65]. Dense WDM systems (100 or more channels) typically require optical amplifiers capable of providing uniform gain over a 70–80-nm wavelength range. In a simple approach, hybrid amplifiers made by combining erbium doping with Raman gain were used. In one implementation of this idea [46], nearly

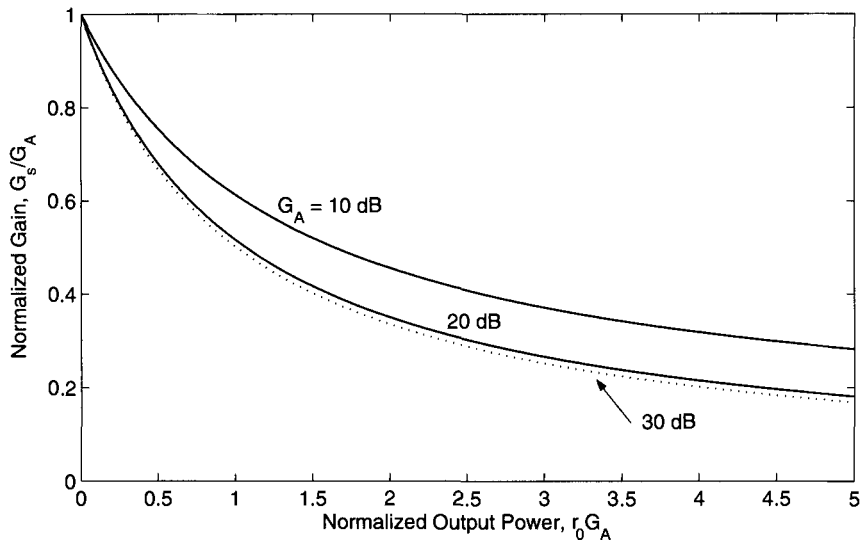


Figure 7.11: Gain–saturation characteristics of Raman amplifiers for several values of the unsaturated amplifier gain G_A .

80-nm bandwidth was realized by combining an EDFA with two Raman amplifiers, pumped simultaneously at three different wavelengths (1,471, 1,495, and 1,503 nm) using four pump modules, each module launching more than 150 mW of power into the fiber. The combined gain of 30 dB was nearly uniform over the wavelength range of 1.53–1.61 μm .

Broadband amplification over 80 nm or more can also be realized by using a pure Raman-amplification scheme [54]. In this case, a relatively long span (typically $>5\text{ km}$) of a fiber with a relatively narrow core (such as a DCF) is pumped using multiple pump lasers. Alternatively, one can use the transmission fiber itself as the Raman-gain medium. In the latter scheme, the entire long-haul fiber link is divided into multiple segments (60 to 100 km long), each one pumped backward using a pump module consisting of multiple pump lasers. The Raman gain accumulated over the entire segment length compensates for fiber losses of that segment in a distributed manner.

The basic idea behind multipump Raman amplifiers makes use of the property that the Raman gain exists at any wavelength as long as the pump wavelength is suitably chosen. Thus, even though the gain spectrum for a single pump is not very wide and is flat only over a few nanometers (see Figure 7.9), it can be broadened and flattened considerably by using several pumps of different wavelengths. Each pump creates the gain that mimics the spectrum shown in Figure 7.9(b), and superposition of several such spectra can create relatively flat gain over a wide spectral region when pump wavelengths and power levels are chosen judiciously. Figure 7.12(a) shows an example for the case in which five pump lasers operating at wavelengths of 1,420, 1,435, 1,450, 1,465, and 1,495 nm are used for pumping the Raman amplifier [54]. The individual

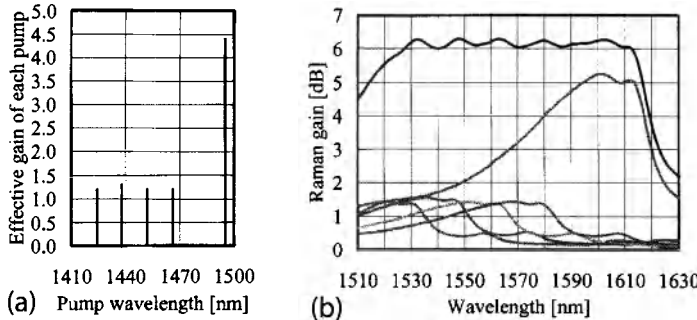


Figure 7.12: Composite Raman gain (b) for a Raman amplifier pumped with five lasers with different wavelengths and relative powers (a) chosen to provide nearly uniform gain over an 80-nm bandwidth. Other curves show the Raman gain provided by individual pumps. (After Ref. [54]; ©2001 IEEE.)

pump powers are chosen to provide different gain spectra shown in part (b) such that the total Raman gain is nearly uniform over a 80-nm bandwidth (top trace).

Raman gain spectra with a bandwidth of more than 100 nm have been realized using multiple pump lasers [61]–[65]. In a 2000 demonstration of this technique, 100 WDM channels with 25-GHz channel spacing, each operating at a bit rate of 10 Gb/s, were transmitted over 320 km [63]. All channels were amplified simultaneously by pumping each 80-km fiber span in the backward direction using four semiconductor lasers. Such a distributed Raman amplifier provided 15-dB gain at a pump power of 450 mW. An undesirable feature of SRS is that the Raman gain is polarization-sensitive. In general, the gain is maximum when the signal and pump are polarized along the same direction but is nearly zero when they are orthogonally polarized. The polarization problem can be solved by pumping a Raman amplifier such that two orthogonally polarized lasers are used at each pump wavelength, or by depolarizing the output of each pump laser.

The design of broadband Raman amplifiers suitable for WDM applications requires consideration of several factors. The most important among them is the inclusion of pump–pump interactions. In general, multiple pump beams are also affected by the Raman gain, and some power from each short-wavelength pump is invariably transferred to each longer-wavelength pump. An appropriate model that includes pump interactions, Rayleigh backscattering, and spontaneous Raman scattering considers each frequency component separately and requires the solution of the following set of coupled equations [62]:

$$\begin{aligned} \frac{dP_f(v)}{dz} = & \int_{\mu>v} g'(\mu, v)[P_f(\mu) + P_b(\mu)][P_f(v) + 2h\nu n_{sp}(\mu - v)] d\mu \\ & - \int_{\mu<v} g'(\nu, \mu)[P_f(\mu) + P_b(\mu)][P_f(v) + 4h\nu n_{sp}(\nu - \mu)] d\mu, \\ & - \alpha(v)P_f(v) + r_s P_b(v), \end{aligned} \quad (7.3.8)$$

where $g' = g_R/A_{\text{eff}}$, μ and ν denote optical frequencies, and the subscripts f and b denote forward- and backward-propagating waves, respectively. A similar equation

holds for the backward propagating waves. The parameter n_{sp} accounts for spontaneous Raman scattering that acts as a noise to the amplified signal. It is defined as

$$n_{\text{sp}}(\Omega) = [1 - \exp(-\hbar\Omega/k_B T)]^{-1}, \quad (7.3.9)$$

where $\Omega = |\mu - v|$ is the Raman shift and T denotes absolute temperature of the amplifier. In Eq. (7.3.8), the first and second terms account for the Raman-induced power transfer into and out of each frequency band. The factor of 4 in the second term results from the polarization-independent nature of spontaneous Raman scattering [54]. Fiber losses and Rayleigh backscattering are included through the last two terms and are governed by the parameters α and r_s , respectively.

To design broadband Raman amplifiers, the entire set of such equations is solved numerically to find the channel gains, and input pump powers are adjusted until the gain is nearly the same for all channels. Such amplifiers can amplify 100 channels or more over an 80-nm bandwidth with a ripple of less than 0.1 dB and are suitable for dense WDM systems covering both the C and L bands. Several laboratory experiments have used broadband Raman amplifiers to demonstrate transmission over long distances at high bit rates. In a 2009 experiment, 135 channels, each operating at 111 Gb/s, were transmitted over 6,248 km by using distributed Raman amplification inside a 240-km recirculating fiber loop [66].

7.3.4 Noise Figure of Raman Amplifiers

Spontaneous Raman scattering adds to the amplified signal and appears as a noise because of random phases associated with all spontaneously generated photons. This noise mechanism is similar to the spontaneous emission that affects the performance of EDFA except that, in the Raman case, it depends on the phonon population in the vibrational state, which in turn depends on temperature of the Raman amplifier.

On a more fundamental level, one should consider the evolution of signal with the noise added by spontaneous Raman scattering by solving Eq. (7.1.4). If we neglect the dispersive and nonlinear terms in this equation for simplicity, we need to solve

$$\frac{dA}{dz} = \frac{1}{2}g_0(z)A - \frac{\alpha_s}{2}A + f_n(z, t), \quad (7.3.10)$$

where $g_0(z) = g_R P_p(z)/a_p$ is the gain coefficient, $P_p(z)$ is the local pump power, and $f_n(z, t)$ takes into account the noise added through spontaneous Raman scattering. Since each scattering event is independent of others, this noise can be modeled as a Gaussian stochastic process for which $\langle f_n(z, t) \rangle = 0$ and the second moment is given by Eq. (7.1.5) with n_{sp} given in Eq. (7.3.8).

Equation (7.3.10) can be easily integrated to obtain $A(L) = \sqrt{G(L)}A(0) + A_{\text{sp}}$, where $G(L)$ is the amplification factor and the contribution of spontaneous Raman scattering is given by

$$A_{\text{sp}} = \sqrt{G(L)} \int_0^L \frac{f_n(z, t)}{\sqrt{G(z)}} dz, \quad G(z) = \exp \left(\int_0^z [g_0(z') - \alpha_s] dz' \right). \quad (7.3.11)$$

It is clear from this equation that the ASE contribution added to the signal depends on the distributed nature of the Raman gain. It is easy to show that $a_n(t)$ vanishes on average and its second moment is given by

$$\langle a_n(t)a_n(t') \rangle = G(L) \int_0^L dz \int_0^L dz' \frac{\langle f_n(z,t)f_n(z',t') \rangle}{\sqrt{G(z)G(z')}} = S_{\text{ASE}}\delta(t-t'), \quad (7.3.12)$$

where the spectral density of ASE noise is defined as

$$S_{\text{ASE}} = n_{\text{sp}}h\nu_0G(L) \int_0^L \frac{g_0(z)}{G(z)} dz. \quad (7.3.13)$$

We can calculate the power of the ASE contribution using $P_{\text{ASE}} = \langle |A_{\text{sp}}|^2 \rangle$ together with Eq. (7.1.5). The result is found to be

$$P_{\text{ASE}} = n_{\text{sp}}h\nu_0g_R\Delta\nu_o \frac{G(L)}{a_p} \int_0^L \frac{P_p(z)}{G(z)} dz, \quad (7.3.14)$$

where $\Delta\nu_o$ is the bandwidth of the Raman amplifier or of the optical filter, if such a filter is used to reduce the noise. The total noise power is higher by factor of 2 when both polarization components are considered.

The noise figure can now be calculated following the procedure used for EDFAs and is found to be

$$F_n = \frac{P_{\text{sp}}}{Gh\nu_0\Delta f} = n_{\text{sp}} \frac{g_R\Delta\nu_o}{a_p\Delta f} \int_0^L \frac{P_p(z)}{G(z)} dz. \quad (7.3.15)$$

This equation shows that the noise figure of a Raman amplifier depends not only on the optical and electrical bandwidths but also on the pumping scheme. It is quite useful for lumped Raman amplifiers for which fiber length is ~ 1 km and the net signal gain exceeds 10 dB. In the case of distributed amplification, the length of the fiber section typically exceeds 50 km, and pumping is such that $G(z) < 1$ throughout the fiber length. In this case, F_n predicted by Eq. (7.3.15) can be very large. It is common to introduce an *effective noise figure* using the definition $F_{\text{eff}} = F_n \exp(-\alpha_s L)$. Physically, this concept can be understood by noting that a passive fiber reduces the SNR of an optical signal by a factor of $\exp(-\alpha_s L)$ because of the reduction in signal power [64]. To find the effective noise figure of a Raman amplifier, one should remove the contribution of the passive fiber.

It should be stressed that F_{eff} can be less than 1 (or negative on the decibel scale). In fact, it is this feature of distributed Raman amplification that makes it so attractive for long-haul WDM lightwave systems. Physically speaking, the distributed gain counteracts fiber losses in the transmission fiber itself and results in a SNR that is improved, compared with the case in which losses are compensated at the end of fiber using lumped amplifiers. The forward pumping results in even less noise because Raman gain is then concentrated toward the input end of the fiber.

The performance of modern Raman amplifiers is affected by several factors that need to be controlled [6]. A few among them are double Rayleigh backscattering [67]–[71], pump-noise transfer [72], and polarization-mode dispersion [73]–[75]. The last

one has its origin in the polarization dependence of the Raman-gain coefficient g_R in silica fibers. Its impact can be reduced in practice by employing the technique of polarization scrambling [54]. In this technique, the pump polarization is changed randomly so that the signal experiences different local gain in different parts of the fiber, resulting effectively in an average gain that is independent of the signal polarization. The use of spun fibers for Raman amplifiers can also reduce the polarization impairments [76].

7.4 Optical Signal-To-Noise Ratio

The ASE noise added by each amplifier to the signal reduces the SNR of the amplified signal. As we have seen in Chapter 4, the performance of a lightwave system is dictated by the electrical SNR obtained after the signal has been converted into an electric form using a photodetector. However, the concept of optical SNR, defined as the ratio of optical power to the ASE power (within a certain bandwidth), is also useful as it can provide design guidelines. In this section we focus on the optical SNR and consider electrical SNR in the next section.

7.4.1 Lumped Amplification

In a chain of cascaded lumped amplifiers (see Figure 7.1), ASE accumulates from amplifier to amplifier and can build up to high levels [2]. The ASE power added by any amplifier is attenuated in succeeding fiber sections, but it is also amplified by all following amplifiers. The net effect is that one can simply add the ASE powers of all amplifiers at the end of a fiber link. Assuming that all amplifiers are spaced apart by the same distance L_A and are operated with the same gain $G = \exp(\alpha L_A)$, the total ASE power for a chain of N_A amplifiers is given by

$$P_{\text{ASE}}^{\text{tot}} = 2N_A S_{\text{ASE}} \Delta v_o = 2n_{\text{sp}} h v_0 N_A (G - 1) \Delta v_o, \quad (7.4.1)$$

where, as before, the factor of 2 takes into account the unpolarized nature of ASE and Δv_o is the bandwidth of the optical filter.

Clearly, ASE power can become quite large for large values of G and N_A . A side effect of high ASE levels is that, at some point, ASE begins to saturate amplifiers. Then, signal power is reduced while, at the same time, noise power keeps on increasing, resulting in severe degradation of the SNR. The ASE power can be controlled, and SNR can be improved, by reducing the amplifier spacing L_A . At first sight, this approach appears counterintuitive since it increases the number N_A of amplifiers. However, noting that $N_A = L_T / L_A = \alpha L_T / \ln G$ for a link of total length L_T , we find that $P_{\text{ASE}}^{\text{tot}}$ scales with G as $(G - 1) / \ln G$, and can be lowered by simply reducing the gain G of each amplifier. Thus, increasing the number of amplifiers while reducing their separation is an effective technique for controlling ASE noise. This feature explains why distributed amplification helps to improve the performance of a lightwave system.

In practice, one may want to minimize the number of lumped amplifiers for economical reasons. In this situation, the system should be designed with an amplifier spacing that is relatively large but still small enough to operate the system reliably and

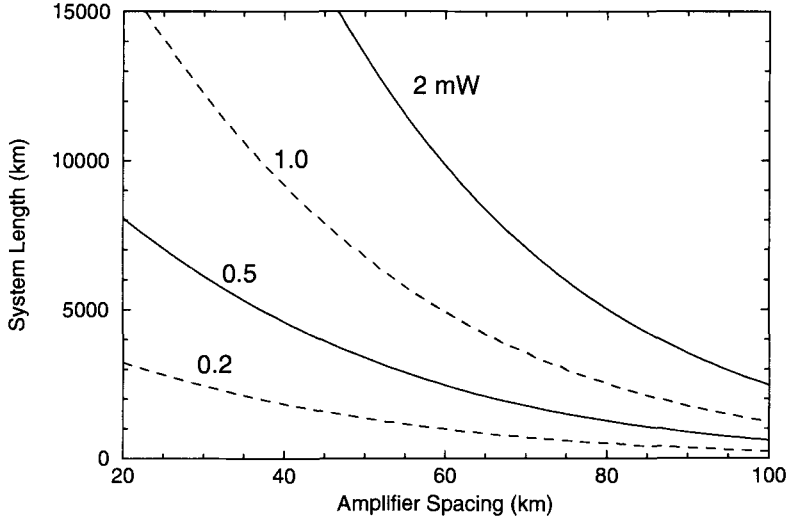


Figure 7.13: Maximum ASE-limited system length as a function of amplifier spacing L_A for several values of average signal power launched into a periodically amplified fiber link.

to realize a target value of optical SNR. From Eq. (7.4.1), the optical SNR can be written as

$$\text{SNR}_o = \frac{P_{\text{in}}}{P_{\text{ASE}}^{\text{tot}}} = \frac{P_{\text{in}} \ln G}{2n_{\text{sp}} h \nu_0 \Delta \nu_o \alpha L_T (G-1)}, \quad (7.4.2)$$

where P_{in} is the input average power. Figure 7.13 shows the total system length L_T as a function of L_A for several values of input powers using $\alpha = 0.2 \text{ dB/km}$, $n_{\text{sp}} = 1.6$, $\Delta \nu_o = 100 \text{ GHz}$, and assuming that an optical SNR of 20 is required for the system to function properly. For a given input power, amplifier spacing L_A becomes smaller as the system length increases. Although amplifier spacing can be improved by increasing the input power P_{in} , in practice, the maximum power that can be launched is limited by the onset of various nonlinear effects discussed in Chapter 4. Typically, P_{in} is limited to close to 1 mW. At such power levels, L_A should be in the range of 40 to 50 km for submarine lightwave systems with lengths of 6,000 km or more, but it can be increased to 80 km or so for terrestrial systems with link lengths under 3,000 km.

7.4.2 Distributed Amplification

In the case of distributed amplification, pump power is injected periodically at pump stations spaced apart by L_A and is chosen such that the signal power recovers at each pump station to its input value, that is, $P_s(nL_A) = P_{\text{in}}$. One can use an approach similar to that employed for lumped amplifiers for calculating the optical SNR and finding the optimum pump-station spacing. The optical SNR of the amplified signal in this case takes the form

$$\text{SNR}_o = \frac{P_s(L_T)}{N_A P_{\text{ASE}}} = \frac{P_{\text{in}}}{2N_A S_{\text{ASE}} \Delta \nu_o}, \quad (7.4.3)$$

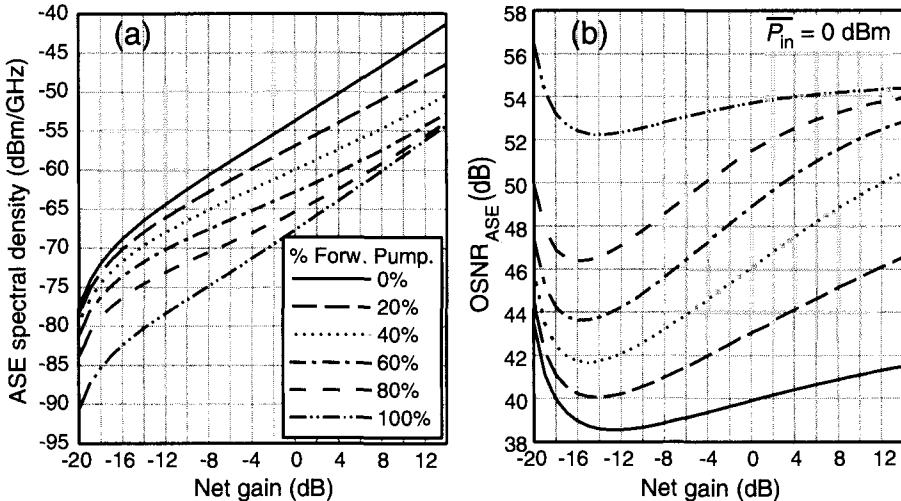


Figure 7.14: (a) ASE spectral density and (b) optical SNR as a function of net gain for a 100-km-long, bidirectionally pumped, distributed Raman amplifier when $P_{in} = 1 \text{ mW}$. The fraction of pump power in the forward direction varies from 0 to 100%. (After Ref. [55]; ©2003 Springer.)

where $L_T = N_A L_A$ is the link length, N_A is the number of pump stations, and S_{ASE} is given in Eq. (7.3.13).

A new feature of distributed amplification is that the pump power can be injected in the forward, backward, or both directions. Since the functional form of gain $g(z)$ depends on the pumping scheme, and S_{ASE} in Eq. (7.3.13) depends on $g(z)$, we can control the optical SNR to some extent by adopting a suitable pumping scheme. Figure 7.14 shows how (a) ASE spectral density and (b) optical SNR vary with the net gain $G(L)$ for several different pumping schemes, assuming that a 1-mW input signal is transmitted through a 100-km-long, bidirectionally pumped, distributed Raman amplifier [55]. The fraction of forward pumping varies from 0 to 100%. Fiber losses are 0.26 and 0.21 dB/km at the pump and signal wavelengths, respectively. Other parameters used were $n_{sp} = 1.13$, $h\nu_0 = 0.8 \text{ eV}$, and $g_R = 0.68 \text{ W}^{-1}/\text{km}$. The optical SNR is highest in the case of purely forward pumping (about 54 dB or so), but it degrades by as much as 15 dB as the fraction of backward pumping is increased from 0 to 100%. This can be understood by noting that the ASE generated near the input end experiences accumulated losses over the full length of the fiber in the case of forward pumping, whereas it experiences only a fraction of such losses in the case of backward pumping.

Figure 7.14(b) shows the optical SNR for a single 100-km-long section but it illustrates clearly the benefits of distributed amplification. If N_A such sections are employed to form a long-haul fiber link, SNR is reduced by a factor of N_A , as seen from Eq. (7.4.3). Even when $N_A = 100$ and the total link length $L_T = 10,000 \text{ km}$, SNR_o remains larger than 20 dB. Such high values of optical SNR are difficult to maintain for long fiber links when EDFAs are used.

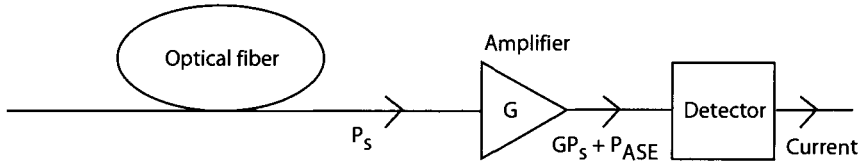


Figure 7.15: Schematic of the optical preamplification scheme. An amplifier is placed just before the detector to improve receiver sensitivity. The amplifier adds ASE to the signal and generates additional noise in the receiver current.

7.5 Electrical Signal-To-Noise Ratio

Optical SNR, although useful for design purposes, is not what governs the BER at the receiver. In this section, we focus on the electrical SNR of the current generated when an ASE-degraded optical signal is incident on a photodetector. For simplicity of discussion, we use the configuration shown in Figure 7.15 and assume that a single optical amplifier is used before the receiver to amplify a low-power signal before it is detected. This configuration is sometimes used to improve the receiver sensitivity through optical preamplification.

7.5.1 ASE-Induced Current Fluctuations

When the contribution of ASE noise to the signal field E_s is included, the photocurrent generated at the receiver can be written as

$$I = R_d(|\sqrt{G}E_s + E_{cp}|^2 + |E_{op}|^2) + i_s + i_T, \quad (7.5.1)$$

where G is the amplifier gain, i_s and i_T are current fluctuations induced by the shot noise and thermal noise, respectively, E_{cp} is the part of the ASE copolarized with the signal, and E_{op} is the orthogonally polarized part of the ASE. It is necessary to separate the ASE into two parts because only the copolarized part of the ASE can beat with the signal.

The ASE-induced current noise has its origin in the beating of E_s with E_{cp} and the beating of ASE with itself. To understand this beating phenomenon more clearly, notice that the ASE occurs over a broader bandwidth than the signal bandwidth Δv_s . It is useful to divide the ASE bandwidth Δv_o into M bins, each of bandwidth Δv_s , and write E_{cp} in the form

$$E_{cp} = \sum_{m=1}^M (S_{ASE}\Delta v_s)^{1/2} \exp(i\phi_m - i\omega_m t), \quad (7.5.2)$$

where ϕ_m is the phase of the noise component at the frequency $\omega_m = \omega_l + m(2\pi\Delta v_s)$ and ω_l is the lower boundary of the filter passband. The spectral density of ASE for a lumped amplifier is given in Eq. (7.2.11). A form identical to that of Eq. (7.5.2) applies for E_{op} .

Using $E_s = \sqrt{P_s} \exp(i\phi_s - i\omega_s t)$ and E_{cp} from Eq. (7.5.2) in Eq. (7.5.1) and including all beating terms, the current I can be written in the form

$$I = R_d G P_s + i_{\text{sig-sp}} + i_{\text{sp-sp}} + i_s + i_T, \quad (7.5.3)$$

where $i_{\text{sig-sp}}$ and $i_{\text{sp-sp}}$ represent current fluctuations resulting from signal-ASE and ASE-ASE beating, respectively, and are given by

$$i_{\text{sig-sp}} = 2R_d(G P_s S_{\text{ASE}} \Delta v_s)^{1/2} \sum_{m=1}^M \cos[(\omega_s - \omega_m)t + \phi_m - \phi_s], \quad (7.5.4)$$

$$i_{\text{sp-sp}} = 2R_d S_{\text{ASE}} \Delta v_s \sum_{m=1}^M \sum_{n=1}^M \cos[(\omega_n - \omega_m)t + \phi_m - \phi_n]. \quad (7.5.5)$$

Since these two noise currents fluctuate rapidly with time, we need to find their averages and variances. It is easy to see that $\langle i_{\text{sig-sp}} \rangle$ vanishes. However, $\langle i_{\text{sp-sp}} \rangle$ has a finite value resulting from the terms in the double sum for which $m = n$. This average value is given by

$$\langle i_{\text{sp-sp}} \rangle = 2R_d S_{\text{ASE}} \Delta v_s M \equiv 2R_d S_{\text{ASE}} \Delta v_o \equiv R_d P_{\text{ASE}}. \quad (7.5.6)$$

Variances of the two noise currents can also be calculated by squaring them and averaging over time. We write the final result directly as details are available in several texts [1]–[3]:

$$\sigma_{\text{sig-sp}}^2 = 4R_d^2 G P_s S_{\text{ASE}} \Delta f, \quad (7.5.7)$$

$$\sigma_{\text{sp-sp}}^2 = 4R_d^2 S_{\text{ASE}}^2 \Delta f (\Delta v_o - \Delta f/2), \quad (7.5.8)$$

where Δf is the effective noise bandwidth of the receiver. The total variance σ^2 of current fluctuations can be written as

$$\sigma^2 = \sigma_{\text{sig-sp}}^2 + \sigma_{\text{sp-sp}}^2 + \sigma_s^2 + \sigma_T^2, \quad (7.5.9)$$

where σ_T^2 is due to thermal noise and the shot-noise variance has an additional contribution resulting from the average in Eq. (7.5.6), that is,

$$\sigma_s^2 = 2q[R_d(G P_s + P_{\text{ASE}})]\Delta f, \quad (7.5.10)$$

where $P_{\text{ASE}} = 2S_{\text{ASE}} \Delta v_o$ is the total ASE power entering the receiver.

7.5.2 Impact of ASE on SNR

We can now calculate the electrical SNR at the receiver. Noting from Eq. (7.5.3) that $\langle I \rangle = R_d(G P_s + P_{\text{ASE}})$, the SNR is given by

$$\text{SNR}_e = \frac{\langle I \rangle^2}{\sigma^2} = \frac{R_d^2(G P_s + P_{\text{ASE}})^2}{\sigma_{\text{sig-sp}}^2 + \sigma_{\text{sp-sp}}^2 + \sigma_s^2 + \sigma_T^2}. \quad (7.5.11)$$

The important question is whether the SNR_e is improved or degraded because of signal amplification before its detection. To answer this question, we compare Eq. (7.5.11) with the SNR realized in the absence of optical amplifier. Setting $G = 1$ and $P_{\text{ASE}} = 0$, this SNR is given by

$$\text{SNR}'_e = \frac{R_d^2 P_s^2}{\sigma_s^2 + \sigma_T^2}. \quad (7.5.12)$$

Consider first the case of an ideal receiver with no thermal noise and 100% quantum efficiency so that $R_d = q/h\nu_0$. In this case, SNR without an amplifier is given by $\text{SNR}'_e = P_s / (2h\nu_0\Delta f)$. When an optical amplifier is used, the current variance is dominated by $\sigma_{\text{sig-sp}}^2$. Neglecting $\sigma_{\text{sp-sp}}^2$ and P_{ASE} in Eq. (7.5.11), the SNR is found to be

$$\text{SNR}_e = \frac{GP_s}{(4S_{\text{ASE}} + 2h\nu_0)\Delta f}. \quad (7.5.13)$$

Using S_{ASE} from Eq. (7.2.11), the noise figure of an optical amplifier is found to be given by Eq. (7.2.15).

In practice, thermal noise exceeds shot noise by a large amount, and it should be included before concluding that an optical amplifier always degrades SNR_e . Neglecting shot noise in Eq. (7.5.12) and retaining only the dominant term $\sigma_{\text{sig-sp}}^2$ in Eq. (7.5.11), we find that

$$\frac{\text{SNR}_e}{\text{SNR}'_e} = \frac{G\sigma_T^2}{4R_d^2 P_s S_{\text{ASE}} \Delta f}. \quad (7.5.14)$$

As this ratio can be made quite large by lowering P_s and increasing the amplifier gain G , electrical SNR can be improved by 20 dB or more compared with its value possible without amplification. This apparent contradiction can be understood by noting that the receiver noise, dominated by $\sigma_{\text{sig-sp}}^2$, is so large in magnitude that thermal noise can be neglected in comparison to it. In other words, optical preamplification of the signal helps to mask the thermal noise, resulting in an improved SNR. In fact, if we retain only the dominant noise term, the electrical SNR of the amplified signal becomes

$$\text{SNR}_e = \frac{GP_s}{4S_{\text{ASE}}\Delta f} = \frac{GP_s\Delta\nu_o}{2P_{\text{ASE}}\Delta f}. \quad (7.5.15)$$

This should be compared with the optical SNR of GP_s/P_{ASE} . As seen in Eq. (7.5.15), electrical SNR is higher by a factor of $\Delta\nu_o/(2\Delta f)$ under identical conditions since ASE noise contributes only over the receiver bandwidth Δf that is much narrower than the filter bandwidth $\Delta\nu_o$.

7.5.3 Noise Buildup in an Amplifier Chain

As mentioned earlier, long-haul lightwave systems require cascading of multiple optical amplifiers in a periodic fashion. The buildup of ASE noise is the most critical factor for such systems for two reasons. First, in a cascaded chain of optical amplifiers, the ASE accumulates over many amplifiers and degrades the SNR as the number of amplifiers increases [77]–[80]. Second, as the level of ASE grows, it begins to saturate optical amplifiers and reduce the gain of amplifiers located further down the fiber link. The

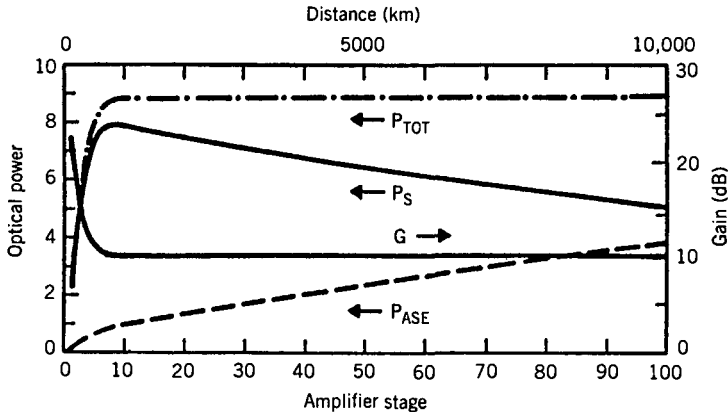


Figure 7.16: Variation of the signal power P_s and the ASE power P_{ASE} along a cascaded chain of optical amplifiers. The total power P_{TOT} becomes nearly constant after a few amplifiers. (After Ref. [78]; ©1991 IEEE.)

net result is that the signal level drops while the ASE level increases. Numerical simulations show that the system is self-regulating in the sense that the total power obtained by adding the signal and ASE powers ($P_{TOT} = P_s + P_{ASE}$) remains relatively constant. Figure 7.16 shows this self-regulating behavior for a cascaded chain of 100 amplifiers with 100-km spacing and 35-dB small-signal gain. The power launched by the transmitter is 1 mW. The other parameters are $n_{sp} = 1.3$ and $G_0 \exp(-\alpha L_A) = 3$. The signal and ASE powers become comparable after 10,000 km. Clearly, ASE-induced gain saturation should be avoided as much as possible. We assume this to be the case in the following discussion.

To estimate the SNR associated with a long-haul lightwave system, we assume that all amplifiers are spaced apart by a constant distance L_A , and the amplifier gain $G \equiv \exp(\alpha L_A)$ is just large enough to compensate for fiber losses in each fiber section. The total ASE power for a chain of N_A amplifiers is then given by Eq. (7.4.1) and can be used to find the optical SNR using $\text{SNR}_o = P_{in}/P_{ASE}$. To calculate the electrical SNR, we need to find the current variance at the receiver. If we assume that the receiver noise is dominated by the signal-ASE beat noise and include only this dominant contribution, the electrical SNR is found to be

$$\text{SNR}_e = \frac{R_d^2 P_{in}^2}{N_A \sigma_{\text{sig-sp}}^2} = \frac{P_{in}}{4N_A S_{\text{ASE}} \Delta f}, \quad (7.5.16)$$

where we used Eq. (7.5.7). This equation shows that the electrical SNR is reduced by a factor of N_A simply because ASE noise is increased by that factor. However, one should not conclude from this equation that the system performance can be improved by placing fewer amplifiers along the link. As discussed in Section 7.4.1, if we reduce the number of amplifiers, each amplifier would add more noise because it has to operate with a higher gain. The results shown in Figure 7.13 also apply here because the optical and electrical SNRs are related to each other as $\text{SNR}_e/\text{SNR}_o = \Delta v_o/(2\Delta f)$.

7.6 Receiver Sensitivity and Q Factor

So far we have considered input signals with constant power. Optical signals in any lightwave system are in the form of a pseudo-random bit stream consisting of 0 and 1 bits. This section focuses on such a realistic situation and evaluates the effects of amplifier noise on the BER and the receiver sensitivity.

7.6.1 Bit-Error Rate

The calculation of BER for lightwave systems employing optical amplifiers follows the approach outlined in Section 4.6.1. More specifically, BER is given by Eq. (4.6.10). However, the conditional probabilities $P(0|1)$ and $P(1|0)$ require knowledge of the probability density function (PDF) for the current I corresponding to symbols 0 and 1. Strictly speaking, the PDF does not remain Gaussian when optical amplifiers are used, and one should employ a more complicated form of the PDF for calculating the BER [81]–[83]. However, the results are much simpler if the actual PDF is approximated by a Gaussian. We assume this to be the case in this subsection.

With the Gaussian approximation for the receiver noise, we can use the analysis of Section 4.6.1 to find that the BER is given by Eq. (4.6.10), and the Q factor can still be defined as

$$Q = \frac{I_1 - I_0}{\sigma_1 + \sigma_0}. \quad (7.6.1)$$

However, the noise currents σ_1 and σ_0 should now include the beating terms introduced in Section 6.3.1 and are obtained using

$$\sigma_1^2 = \sigma_{\text{sig-sp}}^2 + \sigma_{\text{sp-sp}}^2 + \sigma_s^2 + \sigma_T^2, \quad \sigma_0^2 = \sigma_{\text{sp-sp}}^2 + \sigma_T^2. \quad (7.6.2)$$

In the case of 0 bits, σ_s^2 and $\sigma_{\text{sig-sp}}^2$ can be neglected as these two noise contributions are signal-dependent and nearly vanish for 0 bits if we assume a high extinction ratio for the bit stream. As the Q factor specifies the BER completely, one can realize a BER below 10^{-9} by ensuring that Q exceeds 6. The value of Q should exceed 7 if the BER needs to be below 10^{-12} .

Several other approximations can be made while calculating the Q factor. A comparison of Eqs. (7.5.7) and (7.5.10) shows that σ_s^2 can be neglected in comparison with $\sigma_{\text{sig-sp}}^2$ in most cases of practical interest. The thermal noise σ_T^2 can also be neglected in comparison with the dominant beating term whenever the average optical power at the receiver is relatively large (>0.1 mW). The noise currents σ_1 and σ_0 are then well approximated by

$$\sigma_1 = (\sigma_{\text{sig-sp}}^2 + \sigma_{\text{sp-sp}}^2)^{1/2}, \quad \sigma_0 = \sigma_{\text{sp-sp}}. \quad (7.6.3)$$

An important question is how receiver sensitivity is affected by optical amplification. Since the thermal noise does not appear in Eq. (7.6.3), one would expect that receiver performance would not be limited by it, and one may need much fewer photons per bit compared with thousands of photons required when thermal noise dominates. This is indeed the case, as also observed during the 1990s in several experiments that required about 100 to 150 photons/bit [84]–[87]. On the other hand, as discussed in

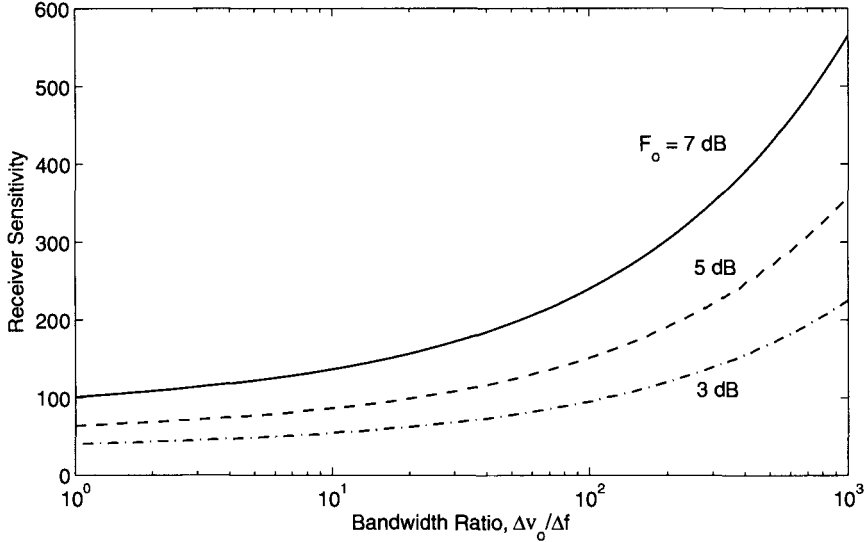


Figure 7.17: Receiver sensitivity \bar{N}_p as a function of optical filter bandwidth (normalized to the receiver bandwidth) for several values of amplifier-noise figure F_o .

Section 4.6.3, only 10 photons/bit are needed, on average, in the quantum limit. Even though we do not expect this level of performance when optical amplifiers are used because of the additional noise introduced by them, it is useful to inquire about the minimum number of photons in this case.

To calculate the receiver sensitivity, we assume for simplicity that no energy is contained in 0 bits so that $I_0 \approx 0$. Clearly, $I_1 = 2R_d\bar{P}_{\text{rec}}$, where \bar{P}_{rec} is the average power incident on the receiver. Using Eq. (7.5.7) and (7.5.8) in Eq. (7.6.3) together with Eq. (7.6.1), we obtain

$$\bar{P}_{\text{rec}} = h\nu_0 F_o \Delta f [Q^2 + Q(\Delta v_o / \Delta f - \frac{1}{2})^{1/2}]. \quad (7.6.4)$$

The receiver sensitivity can be written in terms of the average number of photons/bit, \bar{N}_p , by using the relation $\bar{P}_{\text{rec}} = \bar{N}_p h\nu_0 B$. If we accept $\Delta f = B/2$ as a typical value of the receiver bandwidth, \bar{N}_p is given by

$$\bar{N}_p = \frac{1}{2} F_o [Q^2 + Q(r_f - \frac{1}{2})^{1/2}], \quad (7.6.5)$$

where $r_f = \Delta v_o / \Delta f$ is the factor by which the optical filter bandwidth exceeds the receiver bandwidth.

Equation (7.6.5) is a remarkably simple expression for the receiver sensitivity. It shows clearly why amplifiers with a small noise figure must be used. It also shows how narrowband optical filters can improve the receiver sensitivity by reducing r_f . Figure 7.17 shows \bar{N}_p as a function of r_f for several values of the noise figure F_o using $Q = 6$, a value required to maintain a BER of 10^{-9} . The minimum value of F_o is 2 for an ideal amplifier. The minimum value of r_f is also 2 since Δv_o should be wide enough

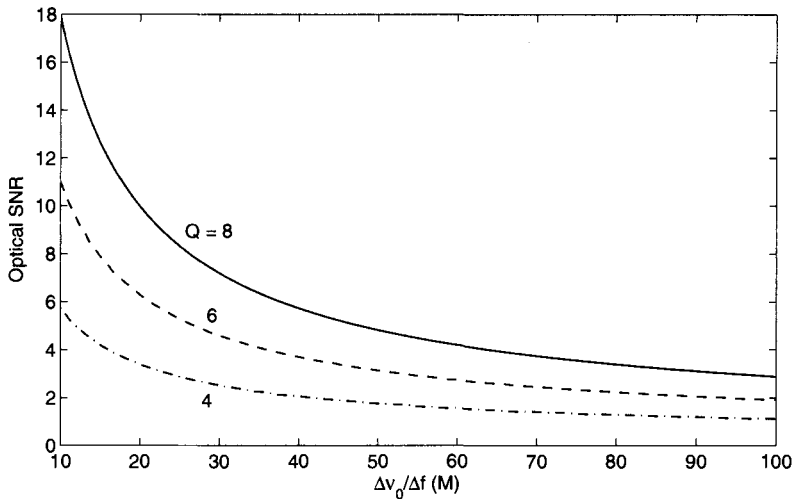


Figure 7.18: Required optical SNR as a function of M for several values of the Q factor.

to pass a signal at the bit rate B . Using $Q = 6$ with $F_o = 2$ and $r_f = 2$, the best receiver sensitivity from Eq. (7.6.5) is $\bar{N}_p = 43.3$ photons/bit. This value should be compared with $\bar{N}_p = 10$, the value obtained for an ideal receiver operating in the quantum-noise limit.

Even though the ASE itself has a Gaussian PDF, the detector current generated at the receiver does not follow Gaussian statistics because of the contribution of ASE–ASE beating. It is possible to calculate the probability density function of the 0 and 1 bits in terms of the modified Bessel function [81]–[83], and experimental measurements agree with the theoretical predictions. However, the Gaussian approximation is often used in practice for calculating the receiver sensitivity.

7.6.2 Relation between Q Factor and Optical SNR

The Q factor appearing in the calculation of BER and the optical SNR calculated in Section 6.2 are related to each other. To show this relationship in a simple form, we consider a lightwave system dominated by amplifier noise and assume that 0 bits carry no energy (except ASE). Then, $I_0 \approx 0$ and $I_1 = R_d P_1$, where P_1 is the peak power level during each 1 bit. Using the definition of total ASE power together with Eqs. (7.5.7) and (7.5.8), we obtain

$$\sigma_{\text{sig-sp}}^2 = 4R_d^2 P_1 P_{\text{ASE}}/M, \quad \sigma_{\text{sp-sp}}^2 = R_d^2 P_{\text{ASE}}^2/M, \quad (7.6.6)$$

where we assumed $M = \Delta v_o / \Delta f \gg 1$.

Using the two variances from Eq. (7.6.6) in Eq. (7.6.3), we can obtain σ_1 and σ_0 . If we calculate Q with the help of Eq. (7.6.1), the result is found to be [81]

$$Q = \frac{\text{SNR}_o \sqrt{M}}{\sqrt{2\text{SNR}_o + 1} + 1}, \quad (7.6.7)$$

where $\text{SNR}_o \equiv P_1/P_{\text{ASE}}$ is the optical SNR. This relation can be easily inverted to find

$$\text{SNR}_o = \frac{2Q^2}{M} + \frac{2Q}{\sqrt{M}}. \quad (7.6.8)$$

These equations show that $Q = 6$ can be realized for relatively low values of optical SNR. For example, we only need $\text{SNR}_o = 7.5$ when $M = 16$ to maintain $Q = 6$. Figure 7.18 shows how optical SNR varies with M for values of Q in the range of 4 to 8. As seen there, the required optical SNR increases rapidly as M is reduced to below 10.

7.7 Role of Dispersive and Nonlinear Effects

So far we have considered amplifier noise without paying attention to how this noise interacts with the dispersive and nonlinear effects that also occur as an optical signal propagates along the fiber link. In reality, ASE noise propagates with the signal and is affected by the same dispersive and nonlinear mechanisms that affect the optical signal. This section shows that ASE noise can be enhanced considerably if the conditions are suitable for modulation instability to occur. Moreover, ASE noise affects optical pulses and induces not only energy fluctuations but also timing jitter.

7.7.1 Noise Growth through Modulation Instability

Consider a long-haul lightwave system with lumped amplifiers placed periodically along the link. Each amplifier adds ASE noise that propagates with the signal in multiple fiber sections. In a purely linear system, the noise power would not change. However, the nonlinear term in the NLS equation (7.1.2) couples the ASE and signal and modifies both of them through the three nonlinear effects, SPM, XPM, and FWM, discussed in Section 2.6. In particular, the phenomenon of modulation instability [28] degrades the system performance by amplifying the ASE noise and converting phase fluctuations into intensity noise [88]–[96].

To study how ASE noise is affected by modulation instability, we solve Eq. (7.1.2) assuming that a CW signal with power P_0 enters the fiber with noise superimposed on it. Writing the solution in the form

$$B(z, t) = [\sqrt{P_0} + a(z, t)] \exp(i\phi_{\text{NL}}), \quad (7.7.1)$$

where $\phi_{\text{NL}} = \gamma P_0 \int_0^z e^{-\alpha z} dz$ is the SPM-induced nonlinear phase shift, and assuming that noise is much weaker than the signal ($|a|^2 \ll P_0$), we obtain

$$\frac{\partial a}{\partial z} + \frac{i\beta_2}{2} \frac{\partial^2 a}{\partial t^2} = i\gamma P_0 e^{-\alpha z} (a + a^*). \quad (7.7.2)$$

This linear equation is easier to solve in the Fourier domain because it reduces to the following set of two ordinary differential equations:

$$\frac{db_1}{dz} = \frac{i}{2} \beta_2 \Omega^2 b_1 + i\gamma P_0 e^{-\alpha z} (b_1 + b_1^*), \quad (7.7.3)$$

$$\frac{db_2}{dz} = \frac{i}{2} \beta_2 \Omega^2 b_2 + i\gamma P_0 e^{-\alpha z} (b_2 + b_2^*), \quad (7.7.4)$$

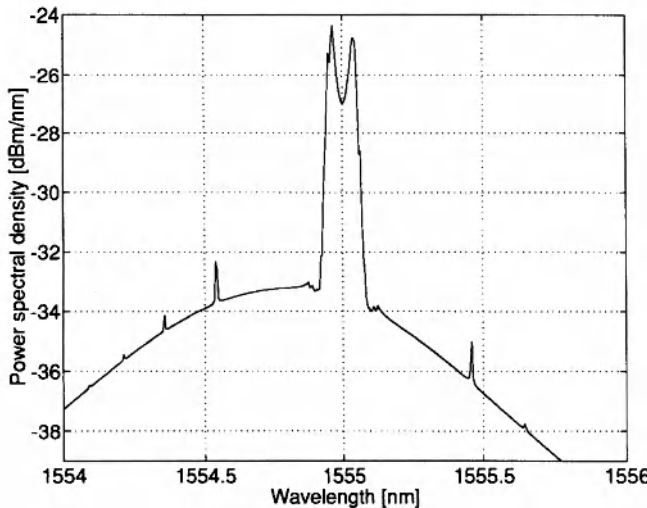


Figure 7.19: Optical spectrum showing effects of modulation instability at the end of a 2,500-km fiber link consisting of 50 amplifiers. (After Ref. [96]; ©1999 IEEE.)

where $b_1(z) = \tilde{a}(z, \Omega)$, $b_2(z) = \tilde{a}^*(z, -\Omega)$, \tilde{a} represents the Fourier transform of a , and $\Omega = \omega_n - \omega_0$ represents the shift of the noise frequency ω_n from the signal carrier frequency ω_0 . These equations show that SPM couples the spectral components of ASE noise located symmetrically around ω_0 . When Ω falls within the gain bandwidth of modulation instability, the corresponding noise components are amplified. In the FWM picture, two photons of energy $\hbar\omega_0$ from the signal are converted into two new photons with energies $\hbar(\omega_0 + \Omega)$ and $\hbar(\omega_0 - \Omega)$.

The coupled equations (7.7.3) and (7.7.4) can be solved easily when fiber losses are negligible ($\alpha = 0$) so that the last term is z -independent [88]. They can also be solved when $\alpha \neq 0$, but the solution involves the Hankel functions [91] or modified Bessel functions of complex order and argument [95]. A matrix method is also used for solving these equations numerically. To calculate the buildup of ASE noise in a long chain of amplifiers, one must add additional noise after each amplifier, propagate it in subsequent fiber sections, and sum the contribution for all amplifiers. This procedure allows one to calculate the optical spectrum as well as the relative intensity noise (RIN) spectrum at the receiver end [93]. Figure 7.19 shows an example of a numerically simulated optical spectrum at the end of a 2,500-km fiber link with 50 amplifiers placed 50 km apart [96]. A 1-mW signal at the 1.55- μm wavelength is transmitted through a fiber link using parameter values of $\beta_2 = -1 \text{ ps}^2/\text{km}$, $\gamma = 2 \text{ W}^{-1}/\text{km}$, and $\alpha = 0.22 \text{ dB/km}$. Optical filters with 8-nm bandwidths filter the ASE after every amplifier. The broad pedestal represents the ASE spectrum expected even in the absence of nonlinear effects. The double-peak structure near the signal wavelength is due to modulation instability. The weak satellite peaks result from the nonlinear index grating formed by periodic variations of signal power along the fiber link.

7.7.2 Noise-Induced Signal Degradation

We next focus on the degradation of optical signal as it propagates through a fiber link in which ASE noise is added by amplifiers periodically. For this purpose, we consider a single pulse representing bit 1 in a fixed time slot and ask how its energy and position are affected by noise. Although changes in pulse energy are expected, ASE can also induce timing jitter in a bit stream by shifting optical pulses from their original location within the time slot in a random fashion. Such a jitter was first studied in 1986 in the context of solitons and is called the Gordon–Haus jitter [97]. It was recognized later that timing jitter occurs in any lightwave system employing optical amplifiers and it imposes a fundamental limitation on all long-haul systems [98]–[104].

The physical origin of ASE-induced jitter can be understood by noting that optical amplifiers affect not only the amplitude but also the phase of the amplified signal. Time-dependent variations in the optical phase shift the signal frequency from its original value ω_0 by a small amount after each amplifier. Since the group velocity of an optical pulse depends on its carrier frequency (because of dispersion), the speed at which a pulse propagates through the fiber is affected by each amplifier in a random fashion. Such speed changes produce random shifts in the pulse position at the receiver and are responsible for the ASE-induced timing jitter.

In general, one should solve Eq. (7.1.2) numerically to study how much signal is affected by noise. However, such a Monte–Carlo approach is quite cumbersome in practice as this equation should be solved multiple times to collect a large enough statistical sample. The moment method [28] allows one to perform the average over ASE noise analytically. It makes use of three moments E , q and Ω , representing pulse energy, pulse-center position within the bit slot, and shift in the carrier frequency, respectively, and defined as [100]

$$q(z) = \frac{1}{E} \int_{-\infty}^{\infty} t |B(z, t)|^2 dt, \quad (7.7.5)$$

$$\Omega(z) = \frac{i}{2E} \int_{-\infty}^{\infty} \left(B^* \frac{\partial B}{\partial t} - B \frac{\partial B^*}{\partial t} \right) dt, \quad (7.7.6)$$

where $E(z) \equiv \int_{-\infty}^{\infty} |B(z, t)|^2 dt$. As the loss term has been removed from Eq. (7.1.2), we expect E to remain constant along the fiber in the absence of ASE noise.

Differentiating E , q , and Ω with respect to z and using Eq. (7.1.2), we find that they change in each passive fiber section as [101]

$$\frac{dE}{dz} = 0, \quad \frac{dq}{dz} = \beta_2 \Omega, \quad \frac{d\Omega}{dz} = 0. \quad (7.7.7)$$

A simple integration shows that while pulse energy E and frequency Ω do not change during propagation, pulse position shifts if the pulse enters the fiber with a finite value of Ω . This is easily understood if we recall that Eq. (7.1.2) is written in a frame moving with the group velocity v_g of the pulse, that is, the center of the pulse remains stationary as long as the carrier frequency ω_0 remains fixed. However, if this frequency shifts by Ω , the group velocity changes, and the pulse center shifts by $q(z) = \beta_2 \Omega z$.

Consider now what happens when pulse enters the k th amplifier along the fiber link. Because of ASE added by the amplifier, E , Ω , and q change by random amounts

δE_k , $\delta \Omega_k$, and δq_k , respectively. If we include these random changes, Eqs. (7.7.7) take the form

$$\frac{dE}{dz} = \sum_k \delta E_k \delta(z - z_k), \quad (7.7.8)$$

$$\frac{dq}{dz} = \beta_2 \Omega + \sum_k \delta q_k \delta(z - z_k), \quad (7.7.9)$$

$$\frac{d\Omega}{dz} = \sum_k \delta \Omega_k \delta(z - z_k), \quad (7.7.10)$$

where the sum is over the total number of amplifiers encountered by the pulse before it arrives at z . These equations show that frequency fluctuations induced by amplifiers manifest as position fluctuations because of GVD; some jitter occurs even when $\beta_2 = 0$. Clearly, ASE-induced timing jitter would be large for fibers with large dispersion and can be reduced by operating a lightwave system near the zero-dispersion wavelength of the fiber.

We next consider the statistics of fluctuations δE_k , δq_k , and $\delta \Omega_k$. Let $B(z_k, t)$ be the field entering the k th amplifier. After amplification, this field can be written as $B(z_k, t) + b_k(t)$, where $b_k(t)$ is the ASE-induced change in the optical field. This change vanishes on average but its correlation function is given by

$$\langle b_j^*(t) b_k(t') \rangle = S_{\text{ASE}} \delta_{jk} \delta(t - t'), \quad (7.7.11)$$

where S_{ASE} is the spectral density of ASE and δ_{jk} indicates that fluctuations at two different amplifiers are not correlated. We can calculate the change in E , q , and Ω occurring after the k th amplifier by applying Eqs. (7.7.5) and (7.7.6) at the end of that amplifier. After some simplifications, we obtain the following relations for these changes:

$$\delta E_k = \int_{-\infty}^{\infty} (B^* b_k + B b_k^* + |b_k|^2) dt, \quad (7.7.12)$$

$$\delta q_k = \frac{1}{E_k} \int_{-\infty}^{\infty} (t - q_k) (B^* b_k + B b_k^*) dt, \quad (7.7.13)$$

$$\delta \Omega_k = \frac{i}{E_k} \int_{-\infty}^{\infty} b_k^* \left(\frac{\partial B}{\partial t} + i \Omega_k B \right) dt + \text{c.c.} \quad (7.7.14)$$

We can now perform the average over the random variable b_k using Eq. (7.7.11) together with $\langle b_k \rangle = 0$. Random variables δq_k and $\delta \Omega_k$ vanish on average, but $\langle \delta E_k \rangle = S_{\text{ASE}}$. Their correlation function and variances can also be calculated and are found to be

$$\langle (\delta q_k)^2 \rangle = \frac{2S_{\text{ASE}}}{E_k^2} \int_{-\infty}^{\infty} (t - q_k)^2 |V(z_k, t)|^2 dt, \quad (7.7.15)$$

$$\langle (\delta \Omega_k)^2 \rangle = \frac{2S_{\text{ASE}}}{E_k^2} \int_{-\infty}^{\infty} \left| \frac{\partial V}{\partial t} \right|^2 dt, \quad (7.7.16)$$

$$\langle \delta q_k \delta \Omega_k \rangle = \frac{iS_{\text{ASE}}}{2E_k^2} \int_{-\infty}^{\infty} (t - q_k) V \frac{\partial V^*}{\partial t} dt + \text{c.c.}, \quad (7.7.17)$$

where $V = B \exp[i\Omega_k(t - q_k)]$. These equations apply for any pulse shape. However, they require a knowledge of the optical field $B(z, t)$ at each amplifier. In the most general case, this field can be obtained by solving Eq. (7.1.2) numerically. Such a semi-analytic approach is quite useful in practice as it solves the NLS equation numerically only once while performing the average over ASE noise in an analytic fashion [100].

7.7.3 Noise-Induced Energy Fluctuations

As a simple application of the moment method, we calculate the variance of pulse-energy fluctuations. As noted before, $\langle \delta E_k \rangle = S_{\text{ASE}}$. Calculating $\langle \delta E_k^2 \rangle$ from Eq. (7.7.12) and performing the average with the help of Eq. (7.7.11), we obtain the relatively simple result

$$\langle \delta E_k^2 \rangle = 2S_{\text{ASE}}E_k + S_{\text{ASE}}^2. \quad (7.7.18)$$

If we use the definition of energy variance,

$$\sigma_E^2 = \langle \delta E_k^2 \rangle - \langle \delta E_k \rangle^2, \quad (7.7.19)$$

the standard deviation $\sigma_E \equiv (2S_{\text{ASE}}E_k)^{1/2}$ depends on the pulse energy E_k before the amplifier. As a numerical example, for an amplifier with 20 dB gain and $n_{\text{sp}} = 1.5$ (noise figure about 4.8 dB), 1-pJ input pulses have a relative fluctuation level σ_E/E of about 0.6% in the spectral region near 1.55 μm.

The important question is how this noise accumulates along the fiber link. We can calculate energy variance for a long fiber link with multiple amplifiers by considering what happens to pulse energy in the fiber section before the k th amplifier. As seen from Eq. (7.7.7), E remains unchanged within a passive fiber as the loss term has been removed from Eq. (7.1.2). This leads to a recurrence relation $E_k = E_{k-1} + \delta E_k$ that can be used to obtain the final energy at the end of the last amplifier in the form

$$E_f = E_0 + \sum_{k=1}^{N_A} \delta E_k, \quad (7.7.20)$$

where E_0 is the input pulse energy and N_A is the number of amplifiers along the fiber link assumed to be spaced apart equally.

The average value is found from Eq. (7.7.20) to be

$$\langle E_f \rangle = E_0 + \sum_{k=1}^{N_A} \langle \delta E_k \rangle = E_0 + N_A S_{\text{ASE}}. \quad (7.7.21)$$

The second moment can also be calculated as

$$\langle E_f^2 \rangle = E_0^2 + 2E_0 \sum_{k=1}^{N_A} \langle \delta E_k \rangle + \sum_{k=1}^{N_A} \sum_{j=1}^{N_A} \langle \delta E_j \delta E_k \rangle. \quad (7.7.22)$$

Using the fact that fluctuations at each amplifier follow an independent random process and thus are uncorrelated, we obtain

$$\langle E_f^2 \rangle = E_0^2 + 4N_A S_{\text{ASE}}E_0 + N_A^2 S_{\text{ASE}}^2. \quad (7.7.23)$$

The standard deviation of energy fluctuations follows from Eqs. (7.7.19), (7.7.21), (7.7.23) and is given by

$$\sigma_E = \sqrt{2N_A S_{\text{ASE}} E_0}. \quad (7.7.24)$$

As expected on physical grounds, σ_E scales with the number of amplifiers as $\sqrt{N_A}$, or with the link length as $\sqrt{L_T}$ since $L_T = N_A L_A$ for an amplifier spacing of L_A . Even for a relatively long fiber link with 100 cascaded amplifiers, the level of energy fluctuations remains below 10% for typical parameter values.

7.7.4 Noise-Induced Timing Jitter

Let us now calculate the timing jitter at the end of a fiber link with a cascaded chain of N_A amplifiers. Equation (7.7.9) can be integrated in a straightforward manner to obtain the total jitter at the end of the fiber link in the form

$$q_f = \sum_{n=1}^{N_A} \delta q_n + d_a \sum_{n=1}^{N_A} \sum_{k=1}^{n-1} \delta \Omega_k, \quad (7.7.25)$$

where $d_a = \bar{\beta}_2 L_A$ is the accumulated dispersion in each fiber section with average dispersion $\bar{\beta}_2$. Timing jitter is calculated from this equation using

$$\sigma_t^2 = \langle q_f^2 \rangle - \langle q_f \rangle^2, \quad (7.7.26)$$

where angle brackets denote averaging over the random variables δq_k and $\delta \Omega_k$. Since both of them vanish on average, it follows that $\langle q_f \rangle = 0$. However, the variance σ_t^2 remains finite.

The averages appearing in Eq. (7.7.25) can be carried out analytically. Since the whole procedure is well known [101], we only state the final result

$$\sigma_t^2 = (S_{\text{ASE}}/E_0) T_0^2 N_A [(1 + (C_0 + N_A d_a / T_0^2)^2)]. \quad (7.7.27)$$

In the case of perfect dispersion compensation such that $d_a = 0$, the jitter variance increases linearly with the number of amplifiers. In contrast, when $d_a \neq 0$, it increases with N_A in a cubic fashion. For such long-haul systems, the dominant term in Eq. (7.7.11) varies as $N_A^3 d_a^2$. This is a general feature of ASE-induced jitter [97]. The cubic dependence of timing jitter on system length shows that even relatively small frequency fluctuations can induce enough jitter in long-haul systems that they may become inoperable, especially when fiber dispersion is not compensated.

Residual dispersion of a fiber link can lead to considerable timing jitter in CRZ systems, as seen from Eq. (7.7.27). Figure 7.20 shows the timing jitter as a function of the total system length $L_T = N_A L_A$ for a 10-Gb/s system using four values of $\bar{\beta}_2$ with $T_m = 30$ ps, $L_A = 50$ km, $C_0 = 0.2$, and $S_{\text{ASE}}/E_0 = 10^{-4}$. The ASE-induced jitter becomes a significant fraction of the pulse width for values of $|\bar{\beta}_2|$ as small as 0.2 ps²/km because of the cubic dependence of σ_t^2 on the system length L_T . Such jitter would lead to large power penalties, if left uncontrolled. The use of distributed amplification lowers the noise level in lightwave systems. One would thus expect timing jitter to be reduced if Raman amplification is employed in place of lumped amplifiers. This indeed turns out to be the case [104].

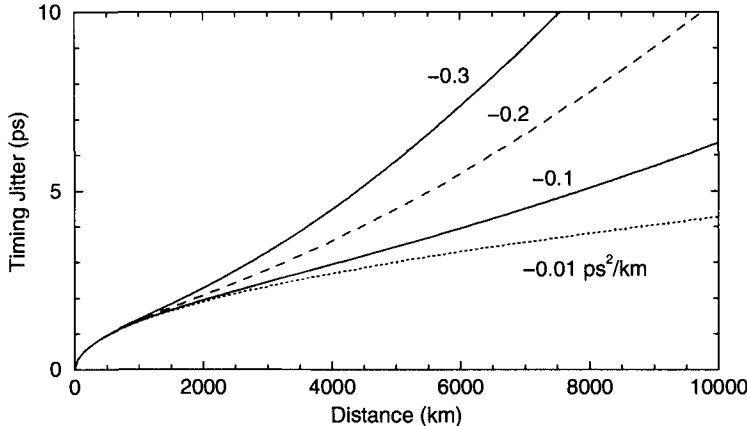


Figure 7.20: ASE-induced timing jitter as a function of system length for several values of the average dispersion $\bar{\beta}_2$.

7.8 Periodically Amplified Lightwave Systems

Many experiments performed during the early 1990s employed a chain of cascaded in-line optical amplifiers for increasing the length of long-haul fiber links [105]–[110]. These experiments showed that fiber dispersion becomes the limiting factor in periodically amplified lightwave systems. Indeed, the experiments were feasible only because the system was operated close to the zero-dispersion wavelength of the fiber link. Moreover, the residual dispersion was tailored along the link in such a way that the total dispersion over the entire link length was quite small at the operating wavelength. By 1992, total system length could be increased to beyond 10,000 km with such dispersion-management techniques. In a 1991 experiment, an effective transmission distance of 21,000 km at 2.5 Gb/s and of 14,300 km at 5 Gb/s was realized using a recirculating fiber loop [111]. By 2010, 96 channels, each channel operating at 100 Gb/s, could be transmitted over 10,600 km by using a phase-based modulation format [112].

A rough estimate of dispersion-limited system length can be obtained if launched power is assumed to be low enough that one can neglect the nonlinear effects during signal transmission. Since amplifiers compensate only for fiber losses, dispersion limitations discussed in Section 2.4.3 and shown in Figure 2.13 apply for each channel of a WDM system if L is replaced by L_T . From Eq. (2.4.30), the dispersion limit for systems making use of standard fibers ($\beta_2 \approx -20 \text{ ps}^2/\text{km}$ at $1.55 \mu\text{m}$) is $B^2 L < 3,000 \text{ (Gb/s)}^2 \cdot \text{km}$. Such a system length is limited to below 2 km at 40 Gb/s and this length increases to only 30 km at 10 Gb/s. An increase by a factor of 20 can be realized by using dispersion-shifted fibers with $|\beta_2| \approx 1 \text{ ps}^2/\text{km}$. To extend the distance to beyond 6,000 km at 10 Gb/s, average GVD along the link should be smaller than $|\bar{\beta}_2| = 0.1 \text{ ps}^2/\text{km}$.

7.8.1 Numerical Approach

The preceding estimate is crude since it does not include the impact of nonlinear effects discussed in Section 2.6. Even though power levels are kept relatively modest for each channel, the nonlinear effects can become quite important because of their accumulation over long distances. For single-channel systems, the most dominant nonlinear phenomenon that limits the system performance is SPM. An estimate of power limitation imposed by the SPM can be obtained from Eq. (2.6.14). If we use $\alpha = 0.2 \text{ dB/km}$ and $\gamma = 2 \text{ W}^{-1}/\text{km}$ as typical values, and assume that the fiber link contains 100 amplifiers with 50-km spacing, the input power should be below 0.25 mW (-6 dBm) for the resulting 5,000-km-long system. Such power levels may not be high enough to maintain the required Q factor when ASE noise accumulated over 100 amplifiers is taken into account. The only solution would then be to decrease the number of the cascaded amplifiers.

An analytic estimate of the SPM-limited distance provides only a rough guideline as it ignores not only fiber dispersion but also the accumulation of ASE noise along the link. In reality, the nonlinear and dispersive effects act on a noisy optical signal simultaneously, and their mutual interplay is quite important. For this reason, the most practical approach for designing modern lightwave system consists of solving the NLS equation (7.1.4) directly using a suitable numerical technique. Numerical simulations indeed show that the accumulation of the nonlinear effects often limits the system length in practical lightwave systems and requires optimization of various design parameters such as amplifier spacing, input power launched into fiber, and dispersion properties of fibers used to construct the transmission link [113]–[129]. Indeed, several software packages dealing with the design of lightwave systems are available commercially. One such package, marketed by Optiwave and called OptiSystem, is provided on the compact disk enclosed with this book (see Appendix D).

The main advantage of a computer-aided design technique for designing modern lightwave systems is that such an approach is capable of optimizing the whole system and can provide the optimum values of various system parameters such that the design objectives are met at a minimum cost. Figure 7.21 illustrates the various steps involved in the simulation process. The approach consists of generating an optical bit pattern at the transmitter, transmitting it through the fiber link, detecting it at the receiver, and then analyzing it through the tools such as the eye diagram and the Q factor.

At the transmitter end, a pseudorandom bit sequence (PRBS) is used to create an RZ or NRZ electrical bit stream. The length N of the thus bit stream determines the computing time and should be chosen judiciously. Typically, $N = 2^M$, where M is in the range of 6 to 10. The optical bit stream is obtained by solving the rate equations that govern the modulation response of a semiconductor laser, if direct modulation is employed (see Section 3.4). A different set of equations governing the dynamics of an external modulator should be used if such a device is used to convert the CW laser light into an optical bit stream (as in Figure 7.21). Chirping of optical pulses is automatically included in both cases. Deformation of the optical bit stream during its transmission through the optical fiber is calculated by solving the NLS equation (7.1.4). The method most commonly used for solving this equation is known as the split-step Fourier method [28].

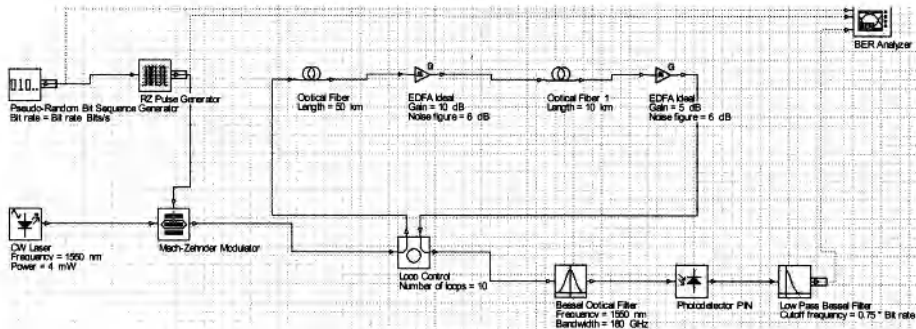


Figure 7.21: Layout of a typical lightwave system for modeling based on the software package OptiSystem.

The noise added by optical amplifiers should be included in any realistic simulation. In the case of lumped amplifiers, Eq. (7.1.4) is solved without the gain and noise terms in each fiber section, and ASE noise is added to the signal at the location of each amplifier through Eq. (7.2.11). In the case of distributed amplification, noise must be added throughout the fiber length and it should satisfy the correlation function given in Eq. (7.1.5). There are two equivalent techniques for adding ASE noise to the signal during numerical simulations. In one case, noise is added in the time domain, while ensuring that it follows Gaussian statistics and has a spectral density given by Eq. (7.2.11) in the lumped case and by Eq. (7.1.5) in the distributed case. In an alternative approach, noise is added in the frequency domain. In the case of lumped amplifiers, the spectral amplitude at the amplifier output is given by

$$\tilde{A}_{\text{out}}(\nu) = \sqrt{G} \tilde{A}_{\text{in}}(\nu) + \tilde{\alpha}_n(\nu), \quad (7.8.1)$$

where a tilde represents the Fourier transform. The noise $\tilde{\alpha}_n(\nu)$ is assumed to be frequency-independent (white noise) over the whole amplifier bandwidth, or the filter bandwidth if an optical filter is used after each amplifier. Mathematically, $\tilde{\alpha}_n(\nu)$ is a complex Gaussian random variable whose real and imaginary parts have the spectral density $S_{\text{ASE}}/2$.

After adding noise at each amplifier, the NLS equation is solved in the following fiber section, and the procedure is repeated until the last amplifier is reached. A suitable receiver model converts optical signal into the electric domain and filters it using a filter whose bandwidth Δf is close to but smaller than the bit rate B (typically $\Delta f/B = 0.6\text{--}0.8$). The resulting electric bit stream is used to find the instantaneous values of currents, I_0 and I_1 , for 0 and 1 bits, respectively, by sampling it at the center of each bit slot. An eye diagram is also constructed using the filtered bit stream. The system performance is quantified through the Q factor, defined in Eq. (4.6.11) and related directly to the BER through Eq. (4.6.10). The calculation of the Q factor requires that the NLS equation be solved a large number of times with different seeds for the amplifier noise. Such an approach can be used to investigate trade-offs that would optimize overall system performance.

Computer-aided design has another important role to play. A long-haul lightwave system may contain many repeaters, both optical and electrical. Transmitters, receivers, and amplifiers used at repeaters, although chosen to satisfy nominal specifications, are never identical. Similarly, fiber cables are constructed by splicing many different pieces (with a typical length of 4 to 8 km) that have slightly different loss and dispersion characteristics. The net result is that many system parameters vary around their nominal values. For example, the dispersion parameter D , responsible not only for pulse broadening but also for other sources of power penalty, can vary significantly in different sections of the fiber link because of variations in the zero-dispersion wavelength and the transmitter wavelength. A statistical approach is often used to estimate the effect of such inherent variations on the performance of a realistic lightwave system. The idea behind such an approach is that it is extremely unlikely that all system parameters would take their worst-case values at the same time. Thus, repeater spacing can be increased well above its worst-case value if the system is designed to operate reliably at the specific bit rate with a high probability (say, 99.9%).

7.8.2 Optimum Launched Power

The importance of computer-aided design for fiber-optic communication systems became apparent during the 1990s with the advent of optical amplifiers. Amplifiers not only added ASE noise to the signal but also allow the dispersive and nonlinear effects to accumulate over long lengths. Moreover, amplifier noise often forces one to increase the channel power to more than 1 mW in order to maintain a high SNR (and a high Q factor consistent with the BER requirements). Since noise limits the Q factor at low power levels whereas nonlinear effects limit it at high power levels, it is evident that

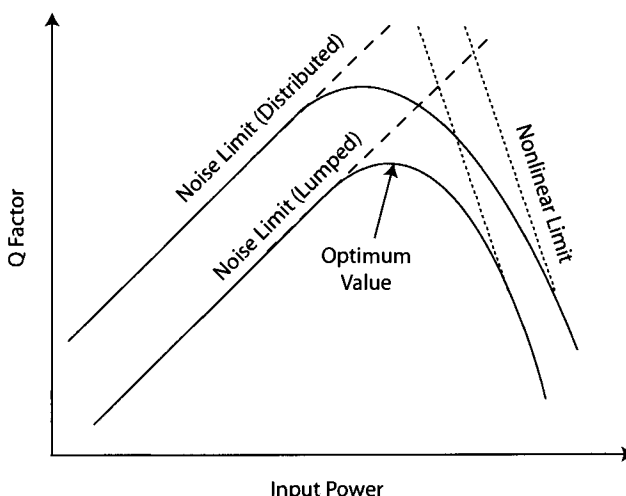


Figure 7.22: Schematic illustration of Q -factor variations with launched power in long-haul systems employing lumped or distributed amplification. The dashed and dotted lines show the ASE and nonlinear limits, respectively.

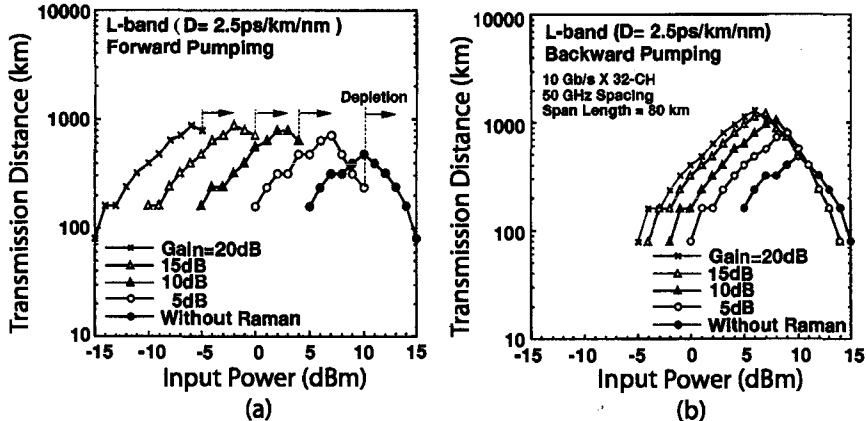


Figure 7.23: Maximum transmission distance as a function of input power when losses are compensated using a hybrid amplification scheme. The Raman gain is varied from 0 to 20 dB in the cases of (a) forward and (b) backward pumping. Arrows mark the maximum power at which pump depletion becomes significant. (After Ref. [128]; ©2001 IEEE.)

a lightwave system would have the largest value of Q at an optimum value of the average power launched into the fiber at the input end. Figure 7.22 shows schematically how the Q factor varies with the average input power for a long-haul lightwave system limited by the nonlinear effects. The Q factor increases initially with launched power, reaches a peak value, and then decreases with a further increase in the power because of the onset of the nonlinear effects.

Figure 7.22 also illustrates why the use of distributed amplification, in place of lumped amplifiers, improves system performance. Since the level of ASE noise is lower in the case of distributed amplification, such systems exhibit a higher optical SNR (or the Q factor) at a given power level (dashed line). As a result, the power level at which Q peaks is smaller compared with the lumped case. From a practical perspective, one can trade off a higher Q with a larger transmission distance. In other words, distributed amplification helps to increase the link length. This feature is shown in Figure 7.23, where numerical results are shown for a 32-channel WDM system [128] by plotting the maximum possible transmission distance as a function of input power assuming that a value of $Q = 7$ must be maintained at the end to ensure a BER below 10^{-12} . The fiber link is divided into 80-km sections, and the 20-dB loss of each section is compensated using a forward or backward pumping configuration.

Several features of Figure 7.23 are noteworthy. As expected from Figure 7.22, transmission distance is maximum at an optimum value of input power. This optimum value is largest (about 10 mW), and the distance is smallest (about 480 km) in the case of pure lumped amplification. As the amount of Raman gain increases, the optimum power is reduced and transmission distance increases. The same signal can be transmitted over more than 1,000 km when all losses are compensated through Raman amplification. The optimum value of input power drops below -5 dBm in the case of forward pumping. The more than two-fold increase in the link length with the use of

Raman amplification is due to a reduced ASE noise that is added to the signal during its transmission.

Some terrestrial lightwave systems serving the backbone of a wide-area network should operate over more than 3,000 km (called ultra-long-haul systems). This can be realized by employing forward error correction because the minimum value of Q required at the receiver then drops to close to 3 (rather than being 7, as assumed in Figure 7.23). Indeed, by 2004, a WDM system with 128 channels, each channel operating at 10 Gb/s, was able to transmit information over 4,000 km when it was designed to compensate losses through forward Raman pumping in each 100-km section of dispersion-shifted fibers [130]. Even when standard fibers were employed, the system could be operated over 3,200 km with a pump-station spacing of 80 km. In both cases, it was necessary to employ forward error correction with 7% overhead. The average power launched into the fiber link was only -5 dBm . Such low power was enough to maintain an optical SNR of more than 15 dB for all channels because of a low noise level associated with distributed Raman amplification in the forward-pumping configuration. It was also important to compensate for fiber dispersion along the fiber link. In general, system performance can be improved with dispersion management. We turn to this issue in Chapter 8.

Problems

- 7.1 The Lorentzian profile of the gain coefficient $g(v)$ has a 3-dB bandwidth of 1 THz. Calculate the 3-dB bandwidth when such an optical amplifier is operated to provide 20- and 30-dB signal gains. Neglect gain saturation.
- 7.2 An optical amplifier can amplify a $1\text{-}\mu\text{W}$ signal to the 1-mW level. What is the output power when a 1-mW signal is incident on the same amplifier? Assume that the gain coefficient saturates as $g = g_0(1 + P/P_s)^{-1}$ and the saturation power is 10 mW .
- 7.3 Explain the gain mechanism in EDFA s. Use Eqs. (7.2.2) and (7.2.3) to derive an expression for the small-signal gain in the steady state.
- 7.4 Discuss the origin of gain saturation in fiber Raman amplifiers. Solve Eqs. (7.3.2) and (7.3.3) with $\alpha_s = \alpha_p$ and derive Eq. (7.3.7) for the saturated gain.
- 7.5 A Raman amplifier is pumped in the backward direction using 1 W of power. Find the output power when a $1\text{-}\mu\text{W}$ signal is injected into the 5-km-long amplifier. Assume losses of 0.2 and 0.25 dB/km at the signal and pump wavelengths, respectively, $A_{\text{eff}} = 50 \mu\text{m}^2$, and $g_R = 6 \times 10^{-14} \text{ m/W}$. Neglect gain saturation.
- 7.6 Starting with the differential equation $\partial A / \partial z = g_0 A / 2 + f_n(z, t)$ and Eq. (7.1.5), prove that the spectral density of ASE noise added by a lumped amplifier of length l_a is given by $S_{\text{ASE}} = n_{\text{sp}} h \nu_0 [\exp(g_0 l_a) - 1]$.
- 7.7 Repeat the preceding problem for a distributed amplifier for which g_0 is a function of z and prove that the noise spectral density is given by Eq. (7.3.13).

- 7.8** Derive an expression for the optical SNR at the end of a fiber link containing N_A amplifiers spaced apart by a distance L_A . Assume that an optical filter of bandwidth $\Delta\nu_o$ is used to control the ASE noise.
- 7.9** Calculate the optical SNR at the output end of a 4,000-km lightwave system designed using 50 EDFA's with 4.5-dB noise figure. Assume a fiber-cable loss of 0.25 dB/km at 1.55 μm , an input power of 1 mW, and a 2-nm-bandwidth for the optical filter.
- 7.10** Explain the concept of noise figure for an optical amplifier. Use Eq. (7.5.9) for the total variance of current fluctuations and prove that the minimum noise figure is 3 dB for an ideal amplifier with high gain ($G \gg 1$) and complete inversion ($n_{sp} = 1$).
- 7.11** What is meant by the effective noise figure of a distributed Raman amplifier? Why is this noise figure always negative on a decibel scale?
- 7.12** Calculate the receiver sensitivities at a BER of 10^{-9} and 10^{-12} by using Eq. (7.6.4). Assume that the receiver operates at 1.55 μm with a 8-GHz bandwidth. The preamplifier has a noise figure of 4 dB, and a 1-nm optical filter is installed between the preamplifier and the detector.
- 7.13** Solve Eqs. (7.7.3) and (7.7.4) in the case $\alpha = 0$ for a fiber of length L and show that the result can be written in a matrix form. Give explicit expressions for all matrix elements in terms of fiber parameters. You may consult Ref. [88].
- 7.14** Use the definitions of moments in Eqs. (7.7.5) and (7.7.6) and prove that q and Ω evolve with z as indicated in Eqs. (7.7.9) and (7.7.10).
- 7.15** Use Eqs. (7.7.11) and (7.7.12) and prove that energy fluctuations at the end of N_A cascaded amplifiers have the variance $\sigma_E^2 = 2N_A S_{ASE} E_0$, where E_0 is the input pulse energy. Assume that each amplifier fully compensates losses of the preceding fiber section.
- 7.16** Use the results of the preceding problem to calculate the noise level σ_E/E_0 for a 1.55- μm fiber link consisting of 50 amplifiers spaced 80-km apart. Assume $E_0 = 0.1$ pJ, a noise figure of 4.8 dB for each amplifier, and fiber losses of 0.25 dB/km.

References

- [1] E. Desurvire, *Erbium-Doped Fiber Amplifiers: Principles and Applications*, Wiley, Hoboken, NJ, 1994.
- [2] P. C. Becker, N. A. Olsson, and J. R. Simpson, *Erbium-Doped Fiber Amplifiers: Fundamentals and Technology*, Academic Press, Boston, 1999.
- [3] E. Desurvire, D. Bayart, B. Destheux, and S. Bigo, *Erbium-Doped Fiber Amplifiers: Device and System Developments*, Wiley, Hoboken, NJ, 2002.
- [4] G. P. Agrawal, *Applications of Nonlinear Fiber Optics*, 2nd ed., Academic Press, Boston, 2008, Chap. 4.
- [5] H. A. Haus, *Electromagnetic Noise and Quantum Optical Measurements*, Springer, New York, 2000, Chap. 6

- [6] G. P. Agrawal, *Lightwave Technology: Components and Devices*, Wiley, Hoboken, NJ, 2004, Chap. 3.
- [7] F. Yaman, Q. Lin, S. Radic, and G. P. Agrawal, *J. Lightwave Technol.* **25**, 3088 (2006).
- [8] P. Kylemark, J. Ren, M. Karlsson, S. Radic, C. J. McKinstry, and P. A. Andrekson, *J. Lightwave Technol.* **25**, 870 (2007).
- [9] M. E. Marhic, *Fiber Optical Parametric Amplifiers, Oscillators and Related Devices*, Cambridge University Press, New York, 2007.
- [10] C. J. Koester and E. Snitzer, *Appl. Opt.* **3**, 1182 (1964).
- [11] S. B. Poole, D. N. Payne, R. J. Mears, M. E. Fermann, and R. E. Laming, *J. Lightwave Technol.* **4**, 870 (1986).
- [12] M. Shimizu, M. Yamada, H. Horiguchi, T. Takeshita, and M. Okayasu, *Electron. Lett.* **26**, 1641 (1990).
- [13] R. I. Laming, J. E. Townsend, D. N. Payne, F. Meli, G. Grasso, and E. J. Tarbox, *IEEE Photon. Technol. Lett.* **3**, 253 (1991).
- [14] W. J. Miniscalco, *J. Lightwave Technol.* **9**, 234 (1991).
- [15] J. L. Zyskind, E. Desurvire, J. W. Sulhoff, and D. J. DiGiovanni, *IEEE Photon. Technol. Lett.* **2**, 869 (1990).
- [16] C. R. Giles and E. Desurvire, *J. Lightwave Technol.* **9**, 271 (1991).
- [17] A. A. M. Saleh, R. M. Jopson, J. D. Evankow, and J. Aspell, *IEEE Photon. Technol. Lett.* **2**, 714 (1990).
- [18] B. Pedersen, A. Bjarklev, O. Lumholt, and J. H. Povlsen, *IEEE Photon. Technol. Lett.* **3**, 548 (1991).
- [19] K. Nakagawa, S. Nishi, K. Aida, and E. Yoneda, *J. Lightwave Technol.* **9**, 198 (1991).
- [20] R. M. Jopson and A. A. M. Saleh, *Proc. SPIE* **1581**, 114 (1992).
- [21] E. Delevalque, T. Georges, J. F. Bayon, M. Monerie, P. Niay, and P. Benarge, *Electron. Lett.* **29**, 1112 (1993).
- [22] R. Olshansky, *Electron. Lett.* **24**, 1363 (1988).
- [23] M. Yamada, M. Shimizu, M. Okayasu, T. Takeshita, M. Horiguchi, Y. Tachikawa, and E. Sugita, *IEEE Photon. Technol. Lett.* **2**, 205 (1990).
- [24] R. I. Laming and D. N. Payne, *IEEE Photon. Technol. Lett.* **2**, 418 (1990).
- [25] K. Kikuchi, *Electron. Lett.* **26**, 1851 (1990).
- [26] A. Yariv, *Opt. Lett.* **15**, 1064 (1990); H. Kogelnik and A. Yariv, *Proc. IEEE* **52**, 165 (1964).
- [27] R. I. Laming, M. N. Zervas, and D. N. Payne, *IEEE Photon. Technol. Lett.* **4**, 1345 (1992).
- [28] G. P. Agrawal, *Nonlinear Fiber Optics*, 4th ed., Academic Press, Boston, 2007.
- [29] K. Kikuchi, *IEEE Photon. Technol. Lett.* **5**, 221 (1993).
- [30] M. Murakami and S. Saito, *IEEE Photon. Technol. Lett.* **4**, 1269 (1992).
- [31] E. Desurvire, C. R. Giles, and J. R. Simpson, *J. Lightwave Technol.* **7**, 2095 (1989).
- [32] K. Inoue, H. Toba, N. Shibata, K. Iwatsuki, A. Takada, and M. Shimizu, *Electron. Lett.* **25**, 594 (1989).
- [33] C. R. Giles, E. Desurvire, and J. R. Simpson, *Opt. Lett.* **14**, 880 (1990).
- [34] K. Inoue, T. Korninaro, and H. Toba, *IEEE Photon. Technol. Lett.* **3**, 718 (1991).
- [35] S. H. Yun, B. W. Lee, H. K. Kim, and B. Y. Kim, *IEEE Photon. Technol. Lett.* **11**, 1229 (1999).
- [36] R. Kashyap, *Fiber Bragg Gratings*, Academic Press, Boston, 1999.
- [37] P. F. Wysocki, J. B. Judkins, R. P. Espindola, M. Andrejco, A. M. Vengsarkar, and K. Walker, *IEEE Photon. Technol. Lett.* **9**, 1343 (1997).

- [38] X. Y. Zhao, J. Bryce, and R. Minasian, *IEEE J. Sel. Topics Quantum Electron.* **3**, 1008 (1997).
- [39] R. H. Richards, J. L. Jackel, and M. A. Ali, *IEEE J. Sel. Topics Quantum Electron.* **3**, 1027 (1997).
- [40] G. Luo, J. L. Zyskind, J. A Nagel, and M. A. Ali, *J. Lightwave Technol.* **16**, 527 (1998).
- [41] M. Karasek and J. A. Valles, *J. Lightwave Technol.* **16**, 1795 (1998).
- [42] A. Bononi and L. Barbieri, *J. Lightwave Technol.* **17**, 1229 (1999).
- [43] M. Karasek, M. Menif, and R. A. Rusch, *J. Lightwave Technol.* **19**, 933 (2001).
- [44] H. Ono, M. Yamada, T. Kanamori, S. Sudo, and Y. Ohishi, *J. Lightwave Technol.* **17**, 490 (1999).
- [45] P. F. Wysocki, N. Park, and D. DiGiovanni, *Opt. Lett.* **21**, 1744 (1996).
- [46] M. Masuda and S. Kawai, *IEEE Photon. Technol. Lett.* **11**, 647 (1999).
- [47] M. Yamada, H. Ono, T. Kanamori, S. Sudo, and Y. Ohishi, *Electron. Lett.* **33**, 710 (1997).
- [48] M. Yamada, A. Mori, K. Kobayashi, H. Ono, T. Kanamori, K. Oikawa, Y. Nishida, and Y. Ohishi, *IEEE Photon. Technol. Lett.* **10**, 1244 (1998).
- [49] T. Kasamatsu, Y. Yano, and T. Ono, *J. Lightwave Technol.* **20**, 1826 (2002).
- [50] H. Ono, M. Yamada, and M. Shimizu, *J. Lightwave Technol.* **21**, 2240 (2003).
- [51] J. B. Rosolem, A. A. Juriollo, R. Arradi, A. D. Coral, J. C. R. F. Oliveira, and Mu. A. Romero, *J. Lightwave Technol.* **24**, 3691 (2006).
- [52] M. Foroni, F. Poli, A. Cucinotta and S. Selleri, *Opt. Lett.* **31**, 3228 (2006); *Electron. Lett.* **43**, 329 (2007).
- [53] C.-M. Hung, N.-K. Chen, and Y. Lai, *Opt. Express* **15**, 1454 (2007).
- [54] S. Namiki and Y. Emori, *IEEE J. Sel. Topics Quantum Electron.* **7**, 3 (2001).
- [55] J. Bromage, P. J. Winzer, and R. J. Essiambre, in *Raman Amplifiers for Telecommunications*, M. N. Islam, Ed., Springer, New York, 2003, Chap. 15.
- [56] C. Headley and G. P. Agrawal, Eds., *Raman Amplification in Fiber Optical Communication Systems*, Academic Press, Boston, 2004.
- [57] J. Bromage, *J. Lightwave Technol.* **22**, 79 (2004).
- [58] J. Chen, X. Liu, C. Lu, Y. Wang, and Z. Li, *J. Lightwave Technol.* **24**, 935 (2006).
- [59] M. Ikeda, *Opt. Commun.* **39**, 148 (1981).
- [60] H. Masuda, S. Kawai, K. Suzuki, and K. Aida, *IEEE Photon. Technol. Lett.* **10**, 516 (1998).
- [61] Y. Emori, K. Tanaka, and S. Namiki, *Electron. Lett.* **35**, 1355 (1999).
- [62] H. D. Kidorf, K. Rottwitt, M. Nissov, M. X. Ma, and E. Rabarijaona, *IEEE Photon. Technol. Lett.* **12**, 530 (1999).
- [63] H. Suzuki, J. Kani, H. Masuda, N. Takachio, K. Iwatsuki, Y. Tada, and M. Sumida, *IEEE Photon. Technol. Lett.* **12**, 903 (2000).
- [64] K. Rottwitt and A. J. Stentz, in *Optical Fiber Telecommunications*, Vol. 4A, I. Kaminow and T. Li, Eds., Academic Press, Boston, 2002, Chap. 5.
- [65] G. Qin, R. Jose, and Y. Ohishi, *J. Lightwave Technol.* **25**, 2727 (2007).
- [66] H. Masuda, E. Yamazaki, A. Sano, et al., Proc. Opt. Fiber Commun. Conf., Paper PDPCB5 (2009).
- [67] P. Wan and J. Conradi, *J. Lightwave Technol.* **14**, 288 (1996).
- [68] P. B. Hansen, L. Eskildsen, A. J. Stentz, T. A. Strasser, J. Judkins, J. J. DeMarco, R. Pedrazzani, and D. J. DiGiovanni, *IEEE Photon. Technol. Lett.* **10**, 159 (1998).
- [69] M. Nissov, K. Rottwitt, H. D. Kidorf, and M. X. Ma, *Electron. Lett.* **35**, 997 (1999).

- [70] S. A. E. Lewis, S. V. Chernikov, and J. R. Taylor, *IEEE Photon. Technol. Lett.* **12**, 528 (2000).
- [71] C. H. Kim, J. Bromage, and R. M. Jopson, *IEEE Photon. Technol. Lett.* **14**, 573 (2002).
- [72] C. R. S. Fludger, V. Handerek, and R. J. Mears, *J. Lightwave Technol.* **19**, 1140 (2001).
- [73] S. Popov, E. Vanin, and G. Jacobsen, *Opt. Lett.* **27**, 848 (2002).
- [74] Q. Lin and G. P. Agrawal, *Opt. Lett.* **27**, 2194 (2002); *Opt. Lett.* **28**, 227 (2003).
- [75] Q. Lin and G. P. Agrawal, *J. Opt. Soc. Am. B* **32**, 1616 (2003).
- [76] S. Sergeyev, S. Popov, and A. T. Friberg, *Opt. Express* **16**, 14380 (2008).
- [77] Y. Yamamoto and T. Mukai, *Opt. Quantum Electron.* **21**, S1 (1989).
- [78] C. R. Giles and E. Desurvire, *J. Lightwave Technol.* **9**, 147 (1991).
- [79] G. R. Walker, N. G. Walker, R. C. Steele, M. J. Creaner, and M. C. Brain, *J. Lightwave Technol.* **9**, 182 (1991).
- [80] S. Ryu, S. Yamamoto, H. Taga, N. Edagawa, Y. Yoshida, and H. Wakabayashi, *J. Lightwave Technol.* **9**, 251 (1991).
- [81] D. Marcuse, *J. Lightwave Technol.* **8**, 1816 (1990); *J. Lightwave Technol.* **9**, 505 (1991).
- [82] P. A. Humblet and M. Azizoglu, *J. Lightwave Technol.* **9**, 1576 (1991).
- [83] B. Chan and J. Conradi, *J. Lightwave Technol.* **15**, 680 (1997).
- [84] T. Saito, Y. Sunohara, K. Fukagai, S. Ishikawa, N. Henmi, S. Fujita, and Y. Aoki, *IEEE Photon. Technol. Lett.* **3**, 551 (1991).
- [85] A. H. Gnauck and C. R. Giles, *IEEE Photon. Technol. Lett.* **4**, 80 (1992).
- [86] J. Nakagawa, T. Mizuochi, K. Takano, K. Motoshima, K. Shimizu, and T. Kitayama, *Electron. Lett.* **32**, 48 (1996).
- [87] P. B. Hansen, A. J. Stentz, L. Eskildsen, S. G. Grubb, T. A. Strasser, J. R. Pedrazzani, *Electron. Lett.* **32**, 2164 (1996).
- [88] M. Yu, G. P. Agrawal, and C. J. McKinstry, *J. Opt. Soc. Am. B* **12**, 1126 (1995).
- [89] M. O. van Deventer, S. Wingstrand, B. Hermansson, A. Bolle, P. Jalderot, C. Backdahl, and J. Karlsson, *Opt. Fiber Technol.* **2**, 183 (1996).
- [90] C. Lorattanasane and K. Kikuchi, *IEEE J. Quantum Electron.* **33**, 1084 (1997).
- [91] A. Carena, V. Curri, R. Gaudino, P. Poggolini, and S. Benedetto, *IEEE Photon. Technol. Lett.* **9**, 535 (1997).
- [92] R. A. Saunders, B. A. Patel, and D. Garthe, *IEEE Photon. Technol. Lett.* **9**, 699 (1997).
- [93] R. Q. Hui, M. O'Sullivan, A. Robinson, and M. Taylor, *J. Lightwave Technol.* **15**, 1071 (1997).
- [94] M. Midrio, *J. Opt. Soc. Am. B* **14**, 2910 (1997).
- [95] E. Ciaramella and M. Tamburini, *IEEE Photon. Technol. Lett.* **11**, 1608 (1999).
- [96] M. Norgia, G. Giuliani, and S. Donati, *J. Lightwave Technol.* **17**, 1750 (1999).
- [97] J. P. Gordon and H. A. Haus, *Opt. Lett.* **11**, 665 (1986).
- [98] R. J. Essiambre and G. P. Agrawal, *J. Opt. Soc. Am. B* **14**, 314 (1997).
- [99] E. Iannone, F. Matera, A. Mecozzi, and M. Settembre, *Nonlinear Optical Communication Networks*, Wiley, New York, 1998, Chap. 5.
- [100] V. S. Grigoryan, C. R. Menyuk, and R. M. Mu, *J. Lightwave Technol.* **17**, 1347 (1999).
- [101] J. Santhanam, C. J. McKinstry, T. I. Lakoba, and G. P. Agrawal, *Opt. Lett.* **26**, 1131 (2001).
- [102] C. J. McKinstry, J. Santhanam, and G. P. Agrawal, *J. Opt. Soc. Am. B* **19**, 640 (2002).
- [103] J. Santhanam and G. P. Agrawal, *IEEE J. Sel. Topics Quantum Electron.* **7**, 632 (2002).
- [104] E. Poutrina and G. P. Agrawal, *J. Lightwave Technol.* **20**, 762 (2002).

- [105] N. Edagawa, Y. Toshida, H. Taga, S. Yamamoto, K. Mochizuchi, and H. Wakabayashi, *Electron. Lett.* **26**, 66 (1990).
- [106] S. Saito, T. Imai, and T. Ito, *J. Lightwave Technol.* **9**, 161 (1991).
- [107] S. Saito, *J. Lightwave Technol.* **10**, 1117 (1992).
- [108] T. Imai, M. Murakami, T. Fukuda, M. Aiki, and T. Ito, *Electron. Lett.* **28**, 1484 (1992).
- [109] M. Murakami, T. Kataoka, T. Imai, K. Hagimoto, and M. Aiki, *Electron. Lett.* **28**, 2254 (1992).
- [110] H. Taga, M. Suzuki, N. Edagawa, Y. Yoshida, S. Yamamoto, S. Akiba, and H. Wakabayashi, *Electron. Lett.* **28**, 2247 (1992).
- [111] N. S. Bergano, J. Aspell, C. R. Davidson, P. R. Trischitta, B. M. Nyman, and F. W. Kerfoot, *Electron. Lett.* **27**, 1889 (1991).
- [112] J.-X. Cai, Y. Cai, C. Davidson, et al., Proc. Opt. Fiber Commun. Conf., Paper PDPB10 (2010).
- [113] F. Matera and M. Settembre, *J. Lightwave Technol.* **14**, 1 (1996).
- [114] X. Y. Zou, M. I. Hayee, S. M. Hwang, and A. E. Willner, *J. Lightwave Technol.* **14**, 1144 (1996).
- [115] K. Inser and K. Petermann, *IEEE Photon. Technol. Lett.* **8**, 443 (1996); D. Breuer and K. Petermann, *IEEE Photon. Technol. Lett.* **9**, 398 (1997).
- [116] F. Forghieri, P. R. Prucnal, R. W. Tkach, and A. R. Chraplyvy, *IEEE Photon. Technol. Lett.* **9**, 1035 (1997).
- [117] F. Matera and M. Settembre, *Fiber Integ. Opt.* **15**, 89 (1996); *J. Opt. Commun.* **17**, 1 (1996); *Opt. Fiber Technol.* **4**, 34 (1998).
- [118] S. Bigo, A. Bertaina, M. W. Chbat, S. Gurib, J. Da Loura, J. C. Jacquinot, J. Hervo, P. Bouesselet, S. Borne, D. Bayart, L. Gasca, and J. L. Beylat, *IEEE Photon. Technol. Lett.* **10**, 1045 (1998).
- [119] D. Breuer, K. Obermann, and K. Petermann, *IEEE Photon. Technol. Lett.* **10**, 1793 (1998).
- [120] M. I. Hayee and A. E. Willner, *IEEE Photon. Technol. Lett.* **11**, 991 (1999).
- [121] A. Sahara, H. Kubota, and M. Nakazawa, *Opt. Commun.* **160**, 139 (1999).
- [122] R. Lebref, A. Ciani, F. Matera, and M. Tamburrini, *Fiber Integ. Opt.* **18**, 245 (1999).
- [123] F. M. Madani and K. Kikuchi, *J. Lightwave Technol.* **17**, 1326 (1999).
- [124] J. Kani, M. Jinno, T. Sakamoto, S. Aisawa, M. Fukui, K. Hattori, and K. Oguchi, *J. Lightwave Technol.* **17**, 2249 (1999).
- [125] C. M. Weinert, R. Ludwig, W. Pieper, H. G. Weber, D. Breuer, K. Petermann, and F. Kuppers, *J. Lightwave Technol.* **17**, 2276 (1999).
- [126] A. J. Lowery, O. Lenzmann, I. Koltchanov, R. Moosburger, R. Freund, A. Richter, S. Georgi, D. Breuer, and H. Hamster, *IEEE J. Sel. Topics Quantum Electron.* **6**, 282 (2000).
- [127] F. Matera and M. Settembre, *IEEE J. Sel. Topics Quantum Electron.* **6**, 308 (2000).
- [128] N. Takachio and H. Suzuki, *J. Lightwave Technol.* **19**, 60 (2001).
- [129] M. Suzuki and N. Edagawa, *J. Lightwave Technol.* **21**, 916 (2003).
- [130] D. F. Grosz, A. Agarwal, S. Banerjee, D. N. Maywar, and A. P. Küng, *J. Lightwave Technol.* **21**, 423 (2004).

Chapter 8

Dispersion Management

Optical amplifiers discussed in Chapter 7 solve the fiber-loss problem but, at the same time, make the dispersion problem worse because dispersive effects keep accumulating along the entire chain of amplifiers. Indeed, long-haul WDM systems making use of amplifiers are often limited by the dispersive and nonlinear effects rather than fiber losses. However, the dispersion problem can be managed in practice through a suitable dispersion-compensation scheme. This chapter focuses on several such techniques. Section 8.1 explains the basic idea behind dispersion management. Section 8.2 is devoted to special kinds of fibers developed for compensating dispersion in long-haul links. Several types of dispersion-equalizing filters are discussed in Section 8.3. The use of fiber gratings for dispersion management is considered in Section 8.4. The technique of optical phase conjugation, also known as midspan spectral inversion, is discussed in Section 8.5. In Section 8.6 we focus on several techniques employed at the transmitter or receiver end for managing the dispersion of medium-haul links. Section 8.7 is devoted to dispersion management in high-speed systems in which each channel operates at 40 Gb/s or more. The compensation of polarization-mode dispersion (PMD) is also discussed in this section.

8.1 Dispersion Problem and Its Solution

All long-haul lightwave systems employ single-mode optical fibers in combination with distributed feedback (DFB) semiconductor lasers with a relatively narrow line width (<0.1 GHz). As discussed in Section 2.4.3, the performance of such systems is often limited by pulse broadening induced by group-velocity dispersion (GVD) of silica fibers. Direct modulation of a DFB laser chirps optical pulses in an optical bit stream and broadens their spectrum enough that direct modulation cannot be used at bit rates above 2.5 Gb/s.

WDM systems operating at channel bit rates of 10 Gb/s or more often employ external modulators to avoid spectral broadening induced by frequency chirping. Under such conditions, the GVD-limited transmission distance at a given bit rate B is obtained

from Eq. (2.4.30) and is given by

$$L < \frac{1}{16|\beta_2|B^2} = \frac{\pi c}{8\lambda^2|D|B^2}, \quad (8.1.1)$$

where β_2 is related to the commonly used dispersion parameter D through Eq. (2.3.5). For “standard” telecommunication fibers D is about 16 ps/(km-nm) near $\lambda = 1.55 \mu\text{m}$. Equation (8.1.1) predicts that L cannot exceed 30 km at a bit rate of 10 Gb/s when such fibers are used for designing lightwave systems.

The existing worldwide fiber-cable network, installed during the 1980s, consists of more than 50 million kilometers of standard fiber. This fiber was suitable for second- and third-generation systems designed to operate at bit rates of up to 2.5 Gb/s with repeater spacing of under 80 km (without optical amplifiers). However, the same fiber could not be used for upgrading the existing transmission links to fourth-generation systems (operating at 10 Gb/s and employing optical amplifiers for loss compensation) because of the 30-km dispersion limit set by Eq. (8.1.1). Although it is possible to manufacture dispersion-shifted fibers, installation of new fibers is a costly solution to the dispersion problem, and it is not a viable alternative in practice. For this reason, several dispersion-management schemes were developed during the 1990s to address the upgrade problem [1]–[3].

One may think that the dispersion problem can be solved for new fiber links by employing dispersion-shifted fibers and operating the link close to the zero-dispersion wavelength of this fiber so that $|D| \approx 0$. Under such conditions, system performance is limited by third-order dispersion (TOD). The dashed line in Figure 2.13 shows the maximum possible transmission distance at a given bit rate B when $D = 0$. Indeed, such a system can operate over more than 1,000 km even at a bit rate of 40 Gb/s. However, this solution is not practical for WDM systems because of four-wave mixing (FWM). As discussed in Section 2.6.3, the nonlinear phenomenon of FWM becomes quite efficient for low values of the dispersion parameter D and limits performance of any system operating close to the zero-dispersion wavelength of the fiber. For this reason, some form of dispersion management is employed for all long-haul WDM systems [2]–[4].

The basic idea behind any dispersion-management scheme is quite simple and can be understood from the pulse-propagation equation (2.4.9) used in Section 2.4 for studying the impact of fiber dispersion and written here as

$$\frac{\partial A}{\partial z} + \frac{i\beta_2}{2} \frac{\partial^2 A}{\partial t^2} - \frac{\beta_3}{6} \frac{\partial^3 A}{\partial t^3} = 0, \quad (8.1.2)$$

where β_3 governs the effects of TOD. This equation ignores the nonlinear effects that will be included later. Assuming that signal power is low enough that all nonlinear effects can be neglected. It can be easily solved with the Fourier-transform method (see Section 2.4) and has the solution

$$A(z, t) = \frac{1}{2\pi} \int_{-\infty}^{\infty} \tilde{A}(0, \omega) \exp \left(\frac{i}{2} \beta_2 \omega^2 z + \frac{i}{6} \beta_3 \omega^3 z - i\omega t \right) d\omega, \quad (8.1.3)$$

where $\tilde{A}(0, \omega)$ is the Fourier transform of $A(0, t)$.

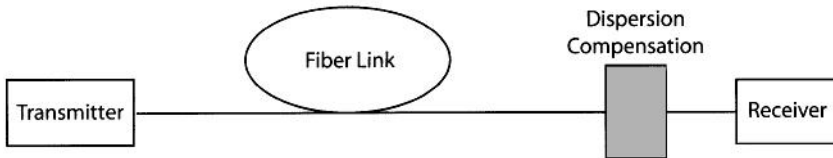


Figure 8.1: Schematic of a dispersion-compensation scheme in which an optical filter is placed before the receiver.

Dispersion-induced degradation of the optical signal is caused by the z -dependent phase factor acquired by spectral components of the pulse during propagation inside the fiber. Indeed, one can think of fiber as an optical filter with the transfer function

$$H_f(z, \omega) = \exp(i\beta_2 \omega^2 z/2 + i\beta_3 \omega^3 z/6). \quad (8.1.4)$$

All optical-domain dispersion-management schemes implement an optical “filter” whose transfer function $H(\omega)$ is chosen such that it cancels the phase factor associated with the fiber. As seen from Eq. (8.1.3), if $H(\omega) = H_f^*(L, \omega)$, the output signal can be restored to its input form at the end of a fiber link of length L . Moreover, if nonlinear effects are negligible, such a filter can be placed at the transmitter end, or at the receiver end, or anywhere along the fiber link.

Consider the simplest situation shown schematically in Figure 8.1, where a dispersion-compensating filter is placed just before the receiver. From Eq. (8.1.3), the optical field after the filter is given by

$$A(L, t) = \frac{1}{2\pi} \int_{-\infty}^{\infty} \tilde{A}(0, \omega) H(\omega) \exp\left(\frac{i}{2}\beta_2 \omega^2 L + \frac{i}{6}\beta_3 \omega^3 L - i\omega t\right) d\omega. \quad (8.1.5)$$

Expanding the phase of $H(\omega)$ in a Taylor series and retaining up to the cubic term, we obtain

$$H(\omega) = |H(\omega)| \exp[i\phi(\omega)] \approx |H(\omega)| \exp[i(\phi_0 + \phi_1 \omega + \frac{1}{2}\phi_2 \omega^2 + \frac{1}{6}\phi_3 \omega^3)], \quad (8.1.6)$$

where $\phi_m = d^m \phi / d\omega^m (m = 0, 1, \dots)$ is evaluated at the carrier frequency ω_0 . The constant phase ϕ_0 and the time delay ϕ_1 do not affect the pulse shape and can be ignored. The spectral phase introduced by the fiber can be compensated by choosing an optical filter such that $\phi_2 = -\beta_2 L$ and $\phi_3 = -\beta_3 L$. The signal will be restored perfectly only if $|H(\omega)| = 1$ and other higher-order terms in Eq. (8.1.6) are negligible. The same optical filter can also reduce amplifier noise if its bandwidth is chosen suitably.

8.2 Dispersion-Compensating Fibers

Optical filters whose transfer function has the form $H(\omega) = H_f^*(L, \omega)$ are not easy to design. The simplest solution is to use an especially designed fiber as an optical filter because it automatically has the desired form of the transfer function. This solution was suggested as early as 1980 [5] and it provides an all-optical, fiber-based solution

to the dispersion problem. During the 1990s, a special kind of fiber, known as the *dispersion-compensating fiber* (DCF), was developed for this purpose [6]–[12]. Such fibers are routinely used for upgrading old fiber links or for installing new WDM fiber links. Such a scheme works well even when the nonlinear effects are not negligible as long as the average optical power launched into the fiber link is optimized properly.

8.2.1 Conditions for Dispersion Compensation

Consider the situation shown in Figure 8.1 and assume that the optical bit stream propagates through two fiber segments of lengths L_1 and L_2 , the second of which is the DCF. Each fiber has a transfer function of the form given in Eq. (8.1.4). After passing through the two fibers, the optical field is given by

$$A(L, t) = \frac{1}{2\pi} \int_{-\infty}^{\infty} \tilde{A}(0, \omega) H_{f1}(L_1, \omega) H_{f2}(L_2, \omega) \exp(-i\omega t) d\omega, \quad (8.2.1)$$

where $L = L_1 + L_2$ is the total length. If the DCF is designed such that the product of the two transfer functions is 1, the pulse will fully recover its original shape at the end of DCF. If β_{2j} and β_{3j} are the GVD and TOD parameters for the two fiber segments ($j = 1, 2$), the conditions for perfect dispersion compensation are

$$\beta_{21}L_1 + \beta_{22}L_2 = 0, \quad \beta_{31}L_1 + \beta_{32}L_2 = 0. \quad (8.2.2)$$

These conditions can be written in terms of the dispersion parameter D and the dispersion slope S (defined in Section 2.3) as

$$D_1L_1 + D_2L_2 = 0, \quad S_1L_1 + S_2L_2 = 0. \quad (8.2.3)$$

The first condition is sufficient for compensating dispersion of a single channel since the TOD does not affect the bit stream much until pulse widths become shorter than 1 ps. Consider the upgrade problem for fiber links made with standard telecommunication fibers. Such fibers have $D_1 \approx 16 \text{ ps}/(\text{km-nm})$ near the 1.55-μm wavelength within the C band. Equation (8.2.3) shows that a DCF must exhibit normal GVD ($D_2 < 0$). For practical reasons, L_2 should be as small as possible. This is possible only if the DCF has a large negative value of D_2 . As an example, if we use $D_1 = 16 \text{ ps}/(\text{km-nm})$ and assume $L_1 = 50 \text{ km}$, we need a 8-km-long DCF when $D_2 = -100 \text{ ps}/(\text{km-nm})$. This length can be reduced to 5 km if the DCF is designed to have $D_2 = -160 \text{ ps}/(\text{km-nm})$. In practice, DCFs with larger values of $|D_2|$ are preferred to minimize extra losses incurred inside a DCF that must also be compensated using an optical amplifier.

Consider now a WDM system. The second condition in Eq. (8.2.3) must be satisfied if the same DCF must compensate dispersion over the entire bandwidth of a WDM system. The reason can be understood by noting that the dispersion parameters D_1 and D_2 in Eq. (8.2.3) are wavelength-dependent. As a result, the single condition $D_1L_1 + D_2L_2 = 0$ is replaced with a set of conditions

$$D_1(\lambda_n)L_1 + D_2(\lambda_n)L_2 = 0 \quad (n = 1, \dots, N), \quad (8.2.4)$$

where λ_n is the wavelength of the n th channel and N is the number of channels within the WDM signal. In the vicinity of the zero-dispersion wavelength of a fiber, D varies

with the wavelength almost linearly. Writing $D_j(\lambda_n) = D_j^c + S_j(\lambda_n - \lambda_c)$ in Eq. (8.2.4), where D_j^c is the value at the wavelength λ_c of the central channel, the dispersion slope of the DCF should satisfy

$$S_2 = -S_1(L_1/L_2) = S_1(D_2/D_1), \quad (8.2.5)$$

where we used the condition (8.2.3) for the central channel. This equation shows that the ratio S/D , called the *relative* dispersion slope, for the DCF should be equal to its value for the transmission fiber.

If we use typical values, $D \approx 16 \text{ ps}/(\text{km-nm})$ and $S \approx 0.05 \text{ ps}/(\text{km-nm}^2)$, we find that the ratio S/D is positive and about 0.003 nm^{-1} for standard fibers. Since D must be negative for a DCF, its dispersion slope S should be negative as well. Moreover, its magnitude should satisfy Eq. (8.2.5). For a DCF with $D \approx -100 \text{ ps}/(\text{km-nm})$, the dispersion slope should be about $-0.3 \text{ ps}/(\text{km-nm}^2)$. The use of *negative-slope* DCFs offers the simplest solution to the problem of dispersion-slope compensation for WDM systems with a large number of channels. Indeed, such DCFs were developed and commercialized during the 1990s for dense WDM systems [13]–[16]. In a 2001 experiment, broadband DCFs were used to transmit a 1-Tb/s WDM signal (101 channels, each operating at 10 Gb/s) over 9,000 km [16].

8.2.2 Dispersion Maps

It is not necessary to employ just two fiber sections as shown in Figure 8.1. In general, a fiber link may contain multiple types of fibers with different dispersion characteristics. The main impact of dispersion management from a mathematical standpoint is that the dispersion coefficients β_2 and β_3 appearing in Eq. (8.1.2) become z -dependent as they change from one fiber section to the next. As long as the nonlinear effects remain negligible, we can still solve this equation. If we neglect the TOD effects for simplicity, the solution given in Eq. (8.1.3) is modified to become

$$A(z, t) = \frac{1}{2\pi} \int_{-\infty}^{\infty} \tilde{A}(0, \omega) \exp\left(\frac{i}{2} d_a(z) \omega^2 - i\omega t\right) d\omega, \quad (8.2.6)$$

where $d_a(z) = \int_0^z \beta_2(z') dz'$ represents the total accumulated dispersion up to a distance z . Dispersion management requires that $d_a(L) = 0$ at the end of the fiber link so that $A(L, t) = A(0, t)$. In practice, the accumulated dispersion of a fiber link is quantified through $\bar{d}_a(z) = \int_0^z D(z') dz'$. It is related to d_a as $\bar{d}_a = (-2\pi c/\lambda^2) d_a$.

Figure 8.2 shows three possible schemes for managing dispersion in long-haul fiber links. In each case, the accumulated dispersion is shown along the fiber link in a schematic fashion. In the first configuration, known as *precompensation*, the dispersion accumulated over the entire link is compensated at the transmitter end. In the second configuration, known as *postcompensation*, a DCF of appropriate length is placed at the receiver end. In the third configuration, known as *periodic compensation*, dispersion is compensated in a periodic fashion all along the link. Each of these configurations is referred to as a dispersion map, as it provides a visual map of dispersion variations along the link length. One can construct a variety of dispersion maps by combining several different fibers.

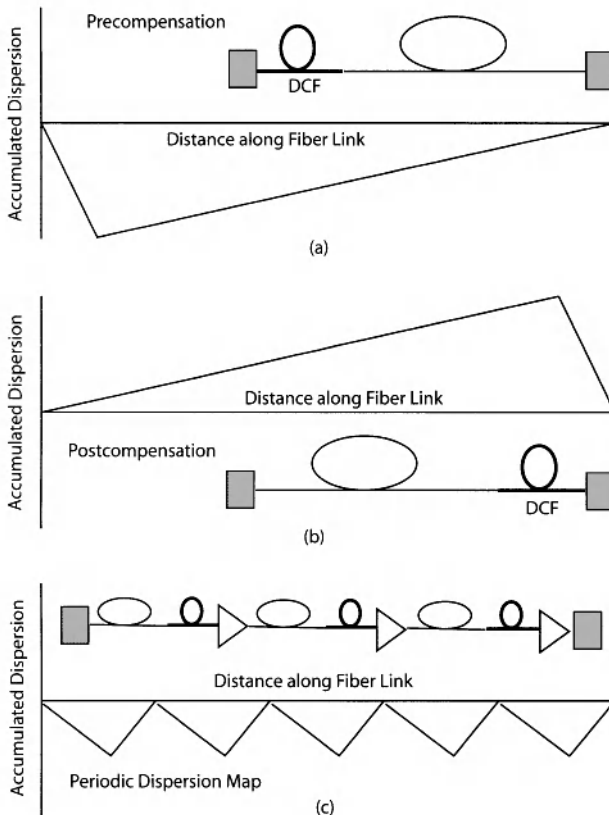


Figure 8.2: Schematic of three dispersion-management schemes: (a) precompensation, (b) postcompensation, and (c) periodic compensation. In each case, accumulated dispersion is shown along the link length.

A natural question is which dispersion map is the best from a system's standpoint. For a truly linear system (no nonlinear effects), all three schemes shown in Figure 8.2 are identical. In fact, any dispersion map for which $d_a(L) = 0$ at the end of a fiber link of length L would recover the original bit stream, no matter how much it became distorted along the way. However, nonlinear effects are always present, although their impact depends on the power launched into the fiber link. It turns out that the three configurations shown in Figure 8.2 behave differently when nonlinear effects are included, and the system performance can be improved by adopting an optimized dispersion map.

8.2.3 DCF Designs

There are two basic approaches to designing DCFs. In one case, the DCF supports a single mode and is fabricated with a relatively small value of the fiber parameter V . In the other approach, the V parameter is increased beyond the single-mode limit

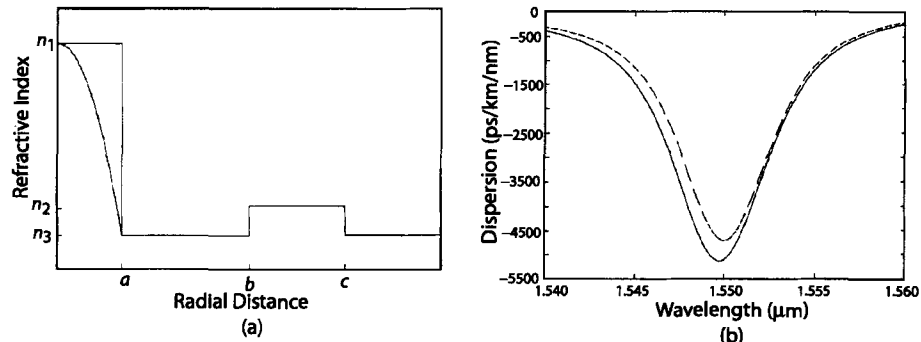


Figure 8.3: (a) Refractive-index profiles of two DCFs designed with two concentric cores. (b) Dispersion parameter as a function of wavelength for the same two designs. (After Ref. [7]; ©1996 IEEE.)

($V > 2.405$) so that the DCF supports two or more modes. We consider both designs in this section.

In the single-mode design, the V parameter of the fiber is close to 1. This is accomplished by reducing the core size and modifying the refractive-index profile through doping of the core and cladding regions. As discussed in Section 2.2.3, the fundamental mode of the fiber is weakly confined for $V \approx 1$. As a large fraction of the mode propagates inside the cladding region, the waveguiding contribution to total dispersion is enhanced considerably, resulting in large negative values of D . A depressed-cladding design is often used in practice for making DCFs [6]. Values of D below $-100 \text{ ps}/(\text{km-nm})$ can be realized by narrowing the central core and adjusting the design parameters of the depressed cladding region surrounding the core [11]. Dispersion slope S near 1,550 nm can also be made negative and varied considerably by adjusting the design parameters to match the ratio S/D of the DCF to different types of transmission fibers.

Unfortunately, such DCFs suffer from two problems, both resulting from their relatively narrow core diameter. First, they exhibit relatively high losses because a considerable fraction of the fundamental fiber mode resides in the cladding region ($\alpha \sim 0.5 \text{ dB/km}$). The ratio $|D|/\alpha$ is often used as a figure of merit for characterizing various DCFs [6]. Clearly, this ratio should be as large as possible, and values $>250 \text{ ps}/(\text{nm-dB})$ have been realized in practice. Second, the effective mode area A_{eff} is only $20 \mu\text{m}^2$ or so for DCFs. As the nonlinear parameter $\gamma \equiv 2\pi n_2/(\lambda A_{\text{eff}})$ is larger by a factor of 4 or so for DCFs compared with its value for standard fibers, the optical intensity is also larger at a given input power, and the nonlinear effects are enhanced considerably inside DCFs [11].

A practical solution for upgrading the existing terrestrial lightwave systems operating over standard fibers consists of adding a DCF module (with 6–8 km of DCF) to optical amplifiers spaced apart by 60 to 80 km. The DCF compensates for GVD, while the amplifier takes care of fiber losses. This scheme is quite attractive but suffers from the loss and nonlinearity problems. Insertion losses of a DCF module often exceed 5 dB. These losses can be compensated by increasing the amplifier gain, but only

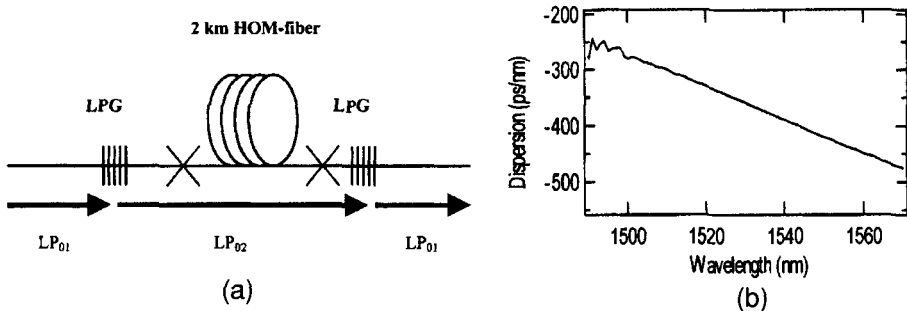


Figure 8.4: (a) Schematic of a DCF made using a higher-order mode (HOM) fiber and two long-period gratings (LPGs). (b) Measured wavelength dependence of the dispersion parameter for such a DCF. (After Ref. [19]; ©2001 IEEE.)

at the expense of enhanced amplified spontaneous emission (ASE). As input power should be kept relatively low to avoid the nonlinear effects, the transmission distance is limited by ASE noise.

Several new designs have been proposed to solve the problems associated with a standard DCF. In one design, shown schematically in Figure 8.3(a), the DCF is designed with two concentric cores, separated by a ring-shaped cladding region [7]. The relative core-cladding index difference is larger for the inner core ($\Delta_i \approx 2\%$) compared with the outer core ($\Delta_o \approx 0.3\%$), but the core sizes are chosen such that each core supports a single mode. The three size parameters a , b , and c and the three refractive indices n_1 , n_2 , and n_3 can be optimized to design DCFs with desired dispersion characteristics. The solid curve in Figure 8.3(b) shows the calculated values of D in the $1.55\text{-}\mu\text{m}$ region for a specific design with $a = 1\text{ }\mu\text{m}$, $b = 15.2\text{ }\mu\text{m}$, $c = 22\text{ }\mu\text{m}$, $\Delta_i = 2\%$, and $\Delta_o = 0.3\%$. The dashed curve corresponds to a parabolic index profile for the inner core. The mode diameter for both designs is about $9\text{ }\mu\text{m}$, a value close to that of standard fibers. However, as shown in Figure 8.3(b), the dispersion parameter can be as large as $-5,000\text{ ps/(km-nm)}$ for such DCFs. It has proven difficult to realize such high values of D experimentally. Nevertheless, a DCF with $D = -1,800\text{ ps/(km-nm)}$ was fabricated by 2000 [10]. For this value of D , a length of $<1\text{ km}$ is enough to compensate dispersion accumulated over 100 km of standard fiber. Insertion losses are negligible for such small lengths.

The problems associated with a single-mode DCF can also be solved by using a fiber that support higher-order modes (HOMs). Such HOM fibers are designed with values of $V > 2.5$. They have almost the same loss as a single-mode fiber but can be designed such that the dispersion parameter D has large negative values for the second or higher-order modes [17]–[21]. Indeed, values of D close to -770 ps/(km-nm) were measured as early as 1994 for elliptical-core DCFs [17]. A 1-km length of such a DCF can compensate the GVD accumulated over 45 km , while adding relatively little to the total link loss or to the nonlinear degradation.

The use of few-mode DCFs requires a mode-conversion device capable of transferring optical signal from the fundamental mode to a higher-order mode supported by

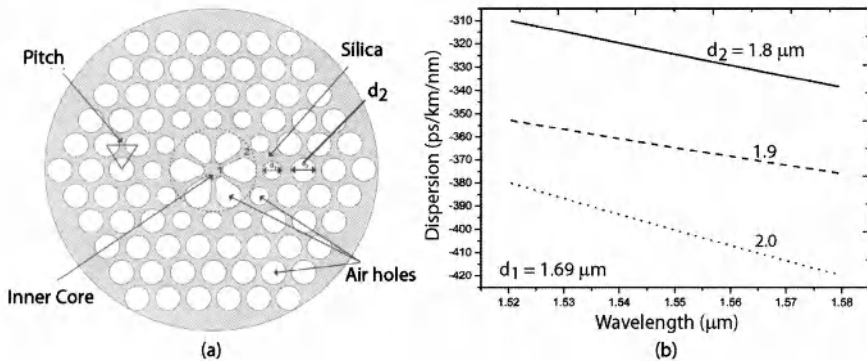


Figure 8.5: (a) Cross section of a dual-core photonic-crystal fiber and (b) wavelength dependence of its dispersion parameter for three values of d_2 when $d_1 = 1.69 \mu\text{m}$. (After Ref. [29]; ©2006 OSA.)

the DCF. Several such all-fiber devices have been developed [22]–[24]. The all-fiber nature of the mode-conversion device is important to keep the insertion loss of the device to an acceptable level. Additional requirements on a mode converter are that it should be polarization-insensitive and should operate over a broad bandwidth. Almost all practical mode-conversion devices use an HOM fiber with a fiber grating that provides coupling between the two modes [21]. The grating period Λ is chosen to match the effective-index difference $\delta\bar{n}$ between the two specific modes that are coupled by the grating ($\Lambda = \lambda / \delta\bar{n}$) and is typically $\sim 100 \mu\text{m}$. Such gratings are called long-period fiber gratings [24].

The HOM fibers are inherently polarization sensitive, and their use requires polarization controllers in front of each dispersion-compensating module. This problem can be solved by using fibers oscillating in a few modes and employing the higher-order LP₀₂ mode for dispersion compensation. Figure 8.4(a) shows schematically such a DCF spliced in between two long-period fiber gratings that convert the LP₀₁ mode into LP₀₂ mode at the input end and then back into the LP₀₁ mode at the output end [19]. The mode converters are designed to be >99% efficient over the entire C band. The measured dispersion characteristics of such a 2-km-long DCF are shown in Figure 8.4(b). The parameter D has a value of $-420 \text{ ps}/(\text{km}\cdot\text{nm})$ near 1,550 nm and this value changes considerably with wavelength because of a large dispersion slope associated with this fiber. This feature allows for broadband dispersion compensation by ensuring that the ratio S/D of the DCF is close to the fiber used for transmitting data. Other useful features of such a DCF are that the device is polarization-insensitive, exhibits relatively low insertion losses (<3.7 dB), and offers dispersion compensation over the entire C band. Such devices were close to reaching the commercial stage in 2004.

Another approach to DCF design makes use of photonic crystal fibers [25]–[31]. Such fibers contain a two-dimensional array of air holes around a central core that modifies their dispersion characteristics substantially, depending on the size of air holes and the spacing among them [25]. Dual-core photonic-crystal fibers can provide large negative values of D with dispersion slopes that make them quite suitable for broadband

dispersion compensation in WDM systems [27]–[30]. Figure 8.5(a) shows the cross section of one design for such fibers [29]. It contains an inner ring of air holes with a smaller diameter d_1 that is surrounded by multiple rings of air holes with a larger diameter d_2 . Calculated values of the dispersion parameter D as a function of wavelength are shown in Figure 8.5(b) for three values of d_2 when $d_1 = 1.68 \mu\text{m}$. Dispersion compensation over a much larger bandwidth can be realized with further modifications in the design of such fibers [31].

8.3 Fiber Bragg Gratings

The DCFs discussed in Section 7.2 suffer from high insertion losses because of their relatively long lengths. They also enhance the impact of nonlinear effects within a log-haul system. Both of these issues can be resolved to a large extent by using fiber-based Bragg gratings for dispersion compensation.

In a fiber Bragg grating, the refractive index inside the core changes in a period fashion along the grating length [24]. Because of this feature, the grating acts as an optical filter. More specifically, it develops a *stop band* in the form of a spectral region over which most of the incident light is reflected back. The stop band is centered at the Bragg wavelength λ_B that is related to the grating period Λ by the relation $\lambda_B = 2\bar{n}\Lambda$, where \bar{n} is the average mode index. The periodic nature of index variations couples the forward- and backward-propagating waves at wavelengths close to the Bragg wavelength and, as a result, provides frequency-dependent reflectivity to the incident signal over a bandwidth determined by the grating strength. In essence, a fiber grating acts as a reflection filter. Although the use of such gratings for dispersion compensation was proposed in the 1980s [32], it was only during the 1990s that fabrication technology advanced enough that their use became practical [24].

8.3.1 Constant-Period Gratings

In the simplest type of grating, the refractive index varies along the grating length in a periodic fashion as

$$n(z) = \bar{n} + n_g \cos(2\pi z/\Lambda), \quad (8.3.1)$$

where \bar{n} is the average value of the refractive index and n_g is the modulation depth. Typically, $n_g \sim 10^{-4}$ and $\Lambda \sim 0.5 \mu\text{m}$ for fiber gratings designed to operate near the 1550-nm spectral region. Bragg gratings are analyzed using two coupled-mode equations that describe the coupling between the forward- and backward-propagating waves at a given frequency $\omega = 2\pi c/\lambda$. These equations have the form [33]

$$dA_f/dz = i\delta A_f + i\kappa A_b, \quad (8.3.2)$$

$$dA_b/dz = -i\delta A_b - i\kappa A_f, \quad (8.3.3)$$

where A_f and A_b are the field amplitudes of the two waves and

$$\delta = \frac{2\pi\bar{n}}{\lambda} - \frac{2\pi}{\lambda_B}, \quad \kappa = \frac{\pi n_g \Gamma}{\lambda_B}. \quad (8.3.4)$$

Physically, δ represents detuning from the Bragg wavelength, κ is the coupling coefficient, and Γ is the confinement factor.

The coupled-mode equations can be solved analytically owing to their linear nature. Most of the input light is reflected when optical frequency is close to the Bragg wavelength. The transfer function of the grating, acting as a reflective filter, is found to be [33]

$$H(\omega) = \frac{A_b(0)}{A_f(0)} = \frac{i\kappa \sin(qL_g)}{q \cos(qL_g) - i\delta \sin(qL_g)}, \quad (8.3.5)$$

where $q^2 = \delta^2 - \kappa^2$ and L_g is the grating length. When incident wavelength falls in the region $-\kappa < \delta < \kappa$, q becomes imaginary, and most of the light is reflected back by the grating (reflectivity becomes nearly 100% for $\kappa L_g > 3$). This region constitutes the stop band of the grating.

As before, the dispersion characteristics of the grating are related to the frequency dependence of the phase of $H(\omega)$. It is easy to show that the phase is nearly linear inside the stop band. Thus, grating-induced dispersion exists mostly outside the stop band, a region in which grating transmits most of the incident signal. In this region ($|\delta| > \kappa$), the dispersion parameters of a fiber grating are given by [33]

$$\beta_2^g = -\frac{\text{sgn}(\delta)\kappa^2/v_g^2}{(\delta^2 - \kappa^2)^{3/2}}, \quad \beta_3^g = \frac{3|\delta|\kappa^2/v_g^3}{(\delta^2 - \kappa^2)^{5/2}}, \quad (8.3.6)$$

where v_g is the group velocity. Grating dispersion is anomalous ($\beta_2^g < 0$) on the high-frequency or “blue” side of the stop band, where δ is positive and the carrier frequency exceeds the Bragg frequency. In contrast, dispersion becomes normal ($\beta_2^g > 0$) on the low-frequency or “red” side of the stop band. The red side can be used for compensating the dispersion of standard fibers near 1.55 μm ($\beta_2 \approx -21 \text{ ps}^2/\text{km}$). Since β_2^g can exceed 1,000 ps^2/cm , a single 2-cm-long grating can compensate dispersion accumulated over 100 km of fiber. However, higher-order dispersion of the grating, nonuniform transmission, and rapid variations of $|H(\omega)|$ close to stop-band edges make constant-period fiber gratings far from being practical for dispersion compensation.

An *apodization technique* is used in practice to improve the grating response [24]. In an apodized grating, the index change n_g is nonuniform across the grating, resulting in a z -dependent κ . Typically, as shown in Figure 8.6(a), κ is uniform in the central region of length L_0 and tapers down to zero at both ends over a short length L_t for a grating of length $L \equiv L_0 + 2L_t$. Figure 8.6(b) shows the measured reflectivity spectrum of an apodized 7.5-cm-long grating [34]. The reflectivity exceeds 90% within the stop band designed to be about 0.17-nm wide. The sharp drop in the reflectivity at both edges of the stop band is due to apodization. In another approach, the grating is fabricated such that κ varies linearly over its entire length. In a 1996 experiment, such an 11-cm-long grating was used to compensate the GVD acquired by a 10-Gb/s signal over 100 km of standard fiber [35]. The coupling coefficient $\kappa(z)$ varied smoothly from 0 to 6 cm^{-1} over the grating length. Such a grating compensated GVD over 106 km for a 10-Gb/s signal with only a 2-dB power penalty at a bit-error rate (BER) of 10^{-9} . In the absence of the grating, the penalty was infinitely large because of the existence of a BER floor.

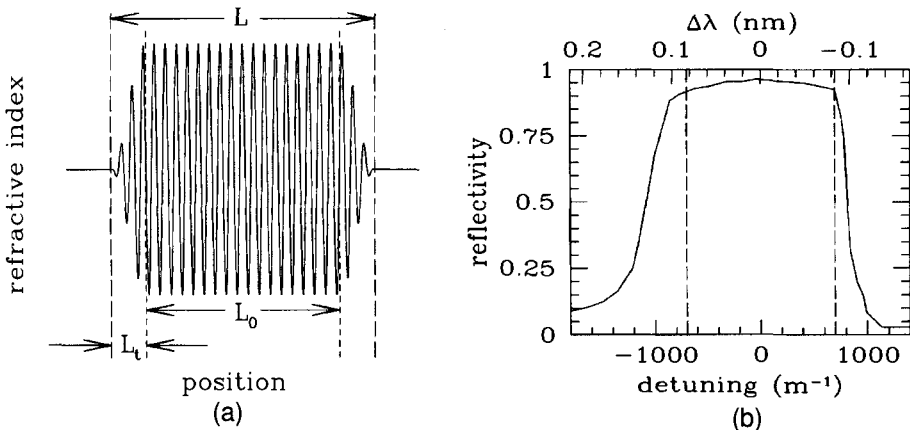


Figure 8.6: (a) Schematic variation of the refractive index in an apodized fiber grating. The length L_t of tapering region is chosen to be a small fraction of the total grating length L . (b) Measured reflectivity spectrum for such a 7.5-cm-long grating. (After Ref. [34]; ©1999 OSA.)

Tapering of the coupling coefficient along the grating length can also be used for dispersion compensation when the signal wavelength lies within the stop band, and the grating acts as a reflection filter. Numerical solutions of the coupled-mode equations for a uniform-period grating for which $\kappa(z)$ varies linearly from 0 to 12 cm^{-1} over the 12-cm length show that such a grating exhibits a V-shaped group-delay profile, centered at the Bragg wavelength. It can be used for dispersion compensation if the wavelength of the incident signal is offset from the center of the stop band such that the signal spectrum sees a linear variation of the group delay. Such a 8.1-cm-long grating was capable of compensating the GVD acquired over 257 km of standard fiber by a 10-Gb/s signal [36]. Although uniform gratings have been used for dispersion compensation [35]–[38], they suffer from a relatively narrow stop band (typically $<0.1 \text{ nm}$) and cannot be used at high bit rates. This shortcoming can be overcome by using chirped gratings, a topic we turn to next.

8.3.2 Chirped Fiber Gratings

Chirped fiber gratings have a relatively broad stop band and were proposed for dispersion compensation as early as 1987 [39]. The optical period $\bar{n}\Lambda$ in a chirped grating is not constant but changes over its length. Since the Bragg wavelength ($\lambda_B = 2\bar{n}\Lambda$) also varies along the grating length, different frequency components of an incident optical pulse are reflected at different points, depending on where the Bragg condition is satisfied locally. In essence, the stop band of a chirped fiber grating results from overlapping of many mini stop bands, each shifted as the Bragg wavelength shifts along the grating. The resulting stop band can be more than 10 nm wide, depending on the grating length. Such gratings can be fabricated using several different methods [24].

It is easy to understand the operation of a chirped fiber grating from Figure 8.7, where the low-frequency components of a pulse are delayed more because of increasing

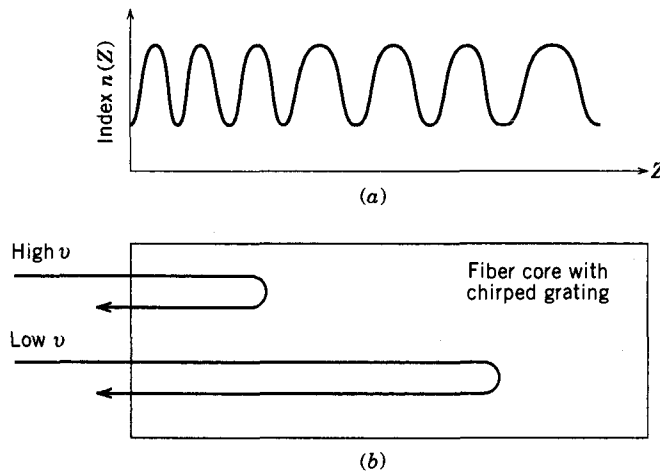


Figure 8.7: Dispersion compensation by a linearly chirped fiber grating: (a) index profile $n(z)$ along the grating length; (b) reflection of low and high frequencies at different locations within the grating because of variations in the Bragg wavelength.

optical period (and the Bragg wavelength). This situation corresponds to anomalous GVD. The same grating can provide normal GVD if it is flipped (or if the light is incident from the right). Thus, the optical period $\bar{n}\Lambda$ of the grating should decrease for it to provide normal GVD. From this simple picture, the dispersion parameter D_g of a chirped grating of length L_g can be determined by using the relation $T_R = D_g L_g \Delta\lambda$, where T_R is the round-trip time inside the grating and $\Delta\lambda$ is the difference in the Bragg wavelengths at the two ends of the grating. Since $T_R = 2\bar{n}L_g/c$, the grating dispersion is given by a remarkably simple expression

$$D_g = 2\bar{n}/(c\Delta\lambda). \quad (8.3.7)$$

As an example, $D_g \approx 5 \times 10^7$ ps/(km-nm) for a grating bandwidth $\Delta\lambda = 0.2$ nm. Because of such large values of D_g , a 10-cm-long chirped grating can compensate for the GVD acquired over 300 km of standard fiber.

Chirped fiber gratings were employed for dispersion compensation during the 1990s in several transmission experiments [40]–[44]. In a 10-Gbs/s experiment, a 12-cm-long chirped grating was used to compensate dispersion accumulated over 270 km of fiber [41]. Later, the transmission distance was increased to 400 km using a 10-cm-long apodized chirped fiber grating [42]. This represents a remarkable performance by an optical filter that is only 10 cm long. When compared to DCFs, fiber gratings offer lower insertion losses and do not enhance the nonlinear degradation of the signal.

It is necessary to apodize chirped gratings to avoid group-delay ripples that affect system performance. Mathematically, Eq. (8.3.1) for index variations across the grating takes the following form for an apodized chirped grating:

$$n(z) = \bar{n} + n_g a_g(z) \cos[2\pi(z/\Lambda_0)(1 + C_g z)], \quad (8.3.8)$$

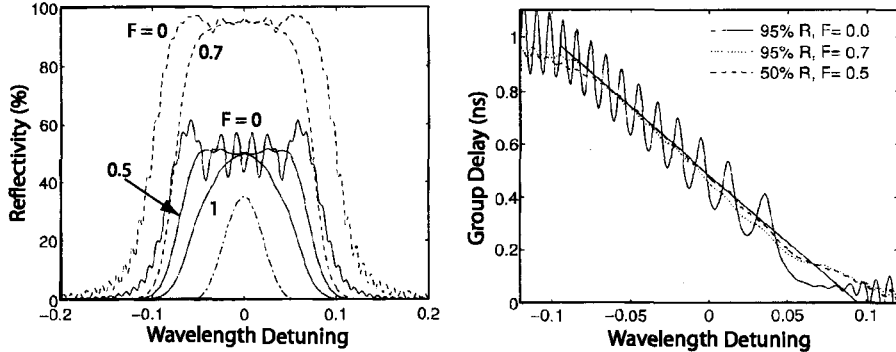


Figure 8.8: (a) Reflectivity and (b) group delay as a function of wavelength for linearly chirped fiber gratings with 50% (solid curves) or 95% (dashed curves) reflectivities and different values of apodization fraction F . The innermost curve shows for comparison the spectrum of a 100-ps pulse. (After Ref. [45]; ©1996 IEEE.)

where $a_g(z)$ is the apodization function, Λ_0 is the value of the grating period at $z = 0$, and C_g is the rate at which this period changes with z . The apodization function is chosen such that $a_g = 0$ at the two grating ends but becomes 1 in the central part of the grating. The fraction F of the grating length over which a_g changes from 0 to 1 plays an important role. Figure 8.8 shows the reflectivity and the group delay (related to the phase derivative $d\phi/d\omega$) calculated as a function of wavelength by solving the coupled-mode equations for several 10-cm-long gratings with different values of peak reflectivities and the apodization fraction F . The chirp rate $C_g = 6.1185 \times 10^{-4} \text{ m}^{-1}$ was constant in all cases [45]. The modulation depth n_g was chosen such that the grating bandwidth was wide enough to fit a 10-Gb/s signal within its stop band. Dispersion characteristics of such gratings can be further optimized by choosing the apodization profile $a_g(z)$ appropriately [46].

It is evident from Figure 8.8 that apodization reduces ripples in both the reflectivity and group-delay spectra. Since the group delay should vary with wavelength linearly to produce a constant GVD across the signal spectrum, it should be as ripple-free as possible. However, if the entire grating length is apodized ($F = 1$), the reflectivity ceases to be constant across the pulse spectrum, an undesirable situation. Also, reflectivity should be as large as possible to reduce insertion losses. In practice, gratings with 95% reflectivity and $F = 0.7$ provide the best compromise for 10-Gb/s systems [45]. Figure 8.9 shows the measured reflectivity and group delay spectra for a 10-cm-long grating whose bandwidth of 0.12 nm is chosen to ensure that a 10-Gb/s signal fits within its stop band [44]. The slope of the group delay (about 5,000 ps/nm) is a measure of the dispersion-compensation capability of the grating. Such a grating can recover a 10-Gb/s signal by compensating the GVD acquired over 300 km of the standard fiber.

It is clear from Eq. (8.3.7) that D_g of a chirped grating is ultimately limited by the bandwidth $\Delta\lambda$ over which GVD compensation is required, which in turn is determined by the bit rate B . This creates a dilemma because as the stop-band bandwidth is increased to accommodate a high-bit-rate signal, the grating dispersion D_g decreases.

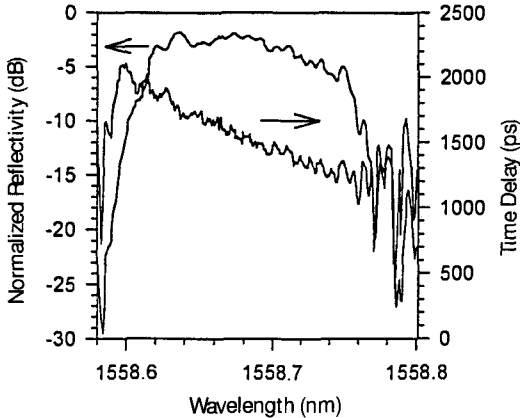


Figure 8.9: Measured reflectivity and group delay for a linearly chirped fiber grating with a bandwidth of 0.12 nm. (After Ref. [44]; ©1996 IEEE.)

Cascading of two or more gratings can solve this problem to some extent. In a 1996 experiment [43], two chirped fiber gratings were cascaded in series to compensate fiber dispersion over 537 km. In another 1996 experiment, the transmission distance of a 10-Gb/s signal was extended to 700 km by using a 10-cm-long chirped grating in combination with a phase-alternating duobinary scheme [44].

A drawback of chirped fiber gratings is that they work as a reflection filter. A 3-dB fiber coupler can be used to separate the reflected signal from the incident one. However, its use imposes a 6-dB loss that adds to other insertion losses. An optical circulator reduces insertion losses to below 2 dB. Several other techniques can be used. For example, two or more fiber gratings can be combined to form a transmission filter that provides dispersion compensation with relatively low insertion losses [47]. A single grating can be converted into a transmission filter by introducing a phase shift in the middle of the grating [48]. A Moiré grating, constructed by superimposing two chirped gratings formed on the same piece of fiber, also has a transmission peak within its stop band [49]. The bandwidth of such transmission filters is relatively small.

A major drawback of a fiber grating is that its transfer function exhibits a single peak. Thus, a single grating cannot compensate the dispersion of several WDM channels unless its design is modified. Several different approaches can be used to solve this problem. In one approach, chirped fiber gratings are fabricated with a wide stop band (>10 nm) by increasing their length. Such a grating can be used in a WDM system if the number of channels is small enough that the total signal bandwidth fits inside its stop band. In a 1999 experiment, a 6-nm-bandwidth chirped grating was used for a four-channel WDM system, each channel operating at 40 Gb/s [50]. When the WDM-signal bandwidth is much larger than that, one can use several cascaded chirped gratings in series such that each grating reflects one channel and compensates its dispersion [51]–[55]. The advantage of this technique is that the gratings can be tailored to match the dispersion experienced by each channel, resulting in automatic dispersion-slope compensation. Figure 8.10 shows the cascaded-grating scheme schematically for

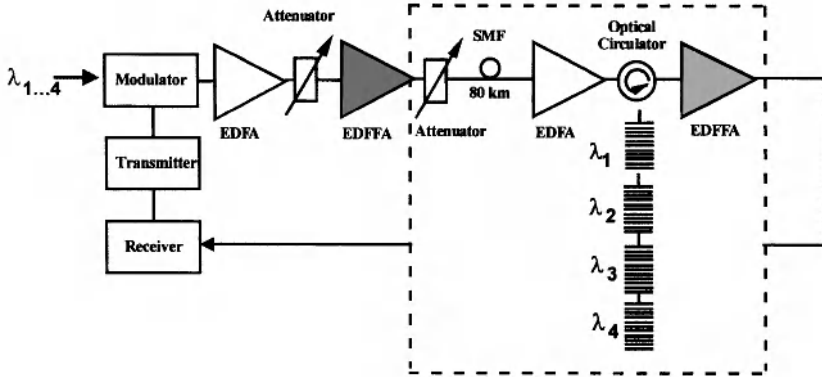


Figure 8.10: Cascaded gratings used for dispersion compensation in a WDM system. (After Ref. [54]; ©1999 IEEE.)

a four-channel WDM system [54]. Every 80 km, a set of four gratings compensates the GVD for all channels, while two optical amplifiers take care of all losses. By 2000, this approach was applied to a 32-channel WDM system with 18-nm bandwidth [55]. Six chirped gratings, each with a 6-nm-wide stop band, were cascaded to compensate GVD for all channels simultaneously.

8.3.3 Sampled Gratings

The cascaded-gratings approach becomes cumbersome as the number of channels in a WDM system becomes large. A new kind of fiber grating, referred to as the *sampled grating*, has been developed to solve this problem. Such devices have double periodicity and are also known as *superstructure gratings*. Fiber-based sampled gratings were first made in 1994 [56]. Since then, they have attracted considerable attention for dispersion compensation [57]–[66].

A sampled grating consists of multiple subgratings separated from each other by a section of uniform index (each subgrating is a sample, hence the name “sampled” grating). Figure 8.11 shows a sampled grating schematically. In practice, such a structure can be realized by blocking certain regions through an amplitude mask during fabrication of a long grating such that $\kappa = 0$ in the blocked regions. It can also be made by etching away parts of an existing grating. In both cases, $\kappa(z)$ varies periodically along z . It is this periodicity that modifies the stop band of a uniform grating. If the average index \bar{n} also changes with the same period, both δ and κ become periodic in the coupled-mode equations. The solution of these equation shows that a sampled grating has multiple stop bands separated from each other by a constant amount. The frequency spacing Δv_p among neighboring reflectivity peaks is set by the sample period Λ_s as $\Delta v_p = c/(2n_g\Lambda_s)$ and is controllable during the fabrication process. Moreover, if each subgrating is chirped, the dispersion characteristics of each reflectivity peak are governed by the amount of chirp introduced.

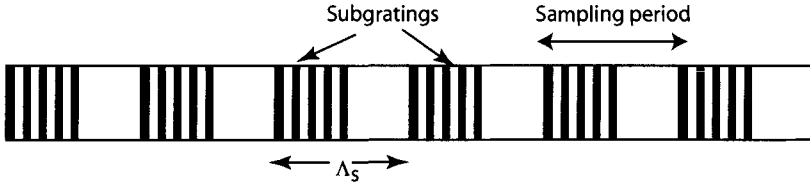


Figure 8.11: Schematic of a sampled grating. Darkened areas indicate regions with a higher refractive index.

A sampled grating is characterized by a periodic sampling function $S(z)$. The sampling period Λ_s of about 1 mm is chosen so that $\Delta\nu_p$ is close to 100 GHz (typical channel spacing for WDM systems). In the simplest kind of grating, the sampling function is a “rect” function such that $S(z) = 1$ over a section of length $f_s\Lambda_s$ and 0 over the remaining portion of length $(1 - f_s)\Lambda_s$. However, this is not the optimum choice because it leads to a transfer function in which each peak is accompanied by multiple subpeaks. The reason is related to the fact that the shape of the reflectivity spectrum is governed by the Fourier transform of $S(z)$. This can be seen by multiplying n_g in Eq. (8.3.1) with $S(z)$ and expanding $S(z)$ in a Fourier series to obtain

$$n(z) = \bar{n} + n_g \operatorname{Re} \left\{ \sum_m F_m \exp[2i(\beta_0 + m\beta_s)z] \right\}, \quad (8.3.9)$$

where F_m is the Fourier coefficient, $\beta_0 = \pi/\Lambda_0$ is the Bragg wave number, and β_s is related to the sampling period Λ_s as $\beta_s = \pi/\Lambda_s$. In essence, a sampled grating behaves as a collection of multiple gratings whose stop bands are centered at wavelengths $\lambda_m = 2\pi/\beta_m$, where $\beta_m = \beta_0 + m\beta_s$ and m is an integer. The peak reflectivity associated with different stop bands is governed by the Fourier coefficient F_m .

A multipeak transfer function, with nearly constant reflectivity for all peaks, can be realized by adopting a sampling function of the form $S(z) = \sin(az)/az$, where a is a constant. Such a “sinc” shape function was used in 1998 to fabricate 10-cm-long gratings with up to 16 reflectivity peaks separated by 100 GHz [58]. A 1999 experiment used such a sampled grating for a four-channel WDM system [59]. As the number of channels increases, it becomes more and more difficult to compensate the GVD of all channels at the same time because such a grating does not compensate for the dispersion slope of the fiber. This problem can be solved by introducing a chirp in the sampling period Λ_s , in addition to the chirping of the grating period Λ [60]. In practice, a linear chirp is used. The amount of chirp depends on the dispersion slope of the fiber as $\delta\Lambda_s/\Lambda_s = |S/D|\Delta\lambda_{ch}$, where $\Delta\lambda_{ch}$ is the channel bandwidth and $\delta\Lambda_s$ is the change in the sampling period over the entire grating length. Figure 8.12 shows the reflection and dispersion characteristics of a 10-cm-long sampled grating designed for 8 WDM channels with 100-GHz spacing. For this grating, each subgrating was 0.12 mm long and the 1-mm sampling period was changed by only 1.5% over the 10-cm grating length.

The preceding approach becomes impractical as the number N of WDM channels increases because it requires a large index modulation (n_g grows linearly with N). A solution is offered by sampled gratings in which the sampling function $S(z)$ modifies

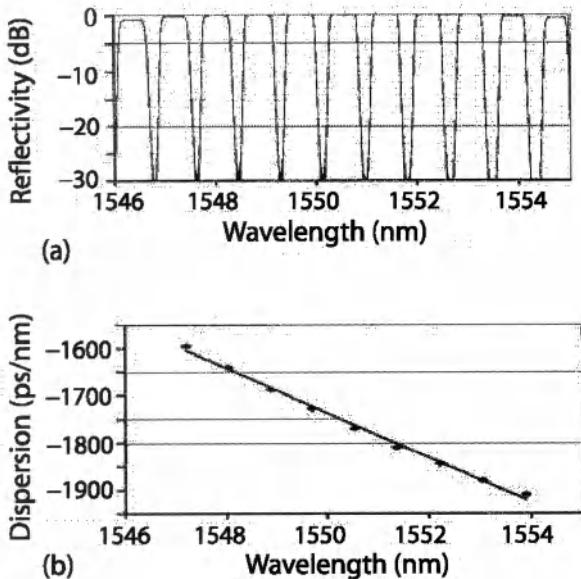


Figure 8.12: (a) Reflection and (b) dispersion characteristics of a chirped sampled grating designed for 8 channels spaced apart by 100 GHz. (After Ref. [60]; ©1999 IEEE.)

the phase of κ , rather than changing its amplitude; the modulation depth in this case grows only as \sqrt{N} . The phase-sampling technique has been used with success for making tunable semiconductor lasers [67]. Recently, it has been applied to fiber gratings [61]–[66]. In contrast with the case of amplitude sampling, index modulations exist over the entire grating length. However, the phase of modulation changes in a periodic fashion with a period Λ_s that itself is chirped along the grating length. Mathematically, index variations can be written in the form [64]

$$n(z) = \bar{n} + n_g \operatorname{Re}\{\exp[2i\pi(z/\Lambda_0) + i\phi_s(z)]\}, \quad (8.3.10)$$

where n_g is the constant modulation amplitude, Λ_0 is the average grating period, and the phase $\phi_s(z)$ varies in a periodic fashion. By expanding $\exp(i\phi_s)$ in a Fourier series, $n(z)$ can be written in the form of Eq. (8.3.9), where F_m depends on how the phase $\phi_s(z)$ varies in each sampling period. The shape of the reflectivity spectrum and dispersion characteristics of the grating can be tailored by controlling F_m and by varying the magnitude of chirp in the grating and sampling periods [64].

As an example, Figure 8.13(a) shows the measured reflectivity as a function of wavelength for a phase-sampled grating fabricated to compensate dispersion of 45 channels with 100 GHz spacing within the C band [65]. Figure 8.13(b) shows wavelength dependence of the group delay for the central channel located near 1543.9 nm. The magnitude of dispersion estimated from the slope of group delay is about -1374 ps/nm. Such a grating can compensate simultaneously dispersion acquired over 80 km of standard fiber for 45-channel WDM system. A phase mask was used to make this phase-sampled grating. The same technique was used to make an 81-channel grat-

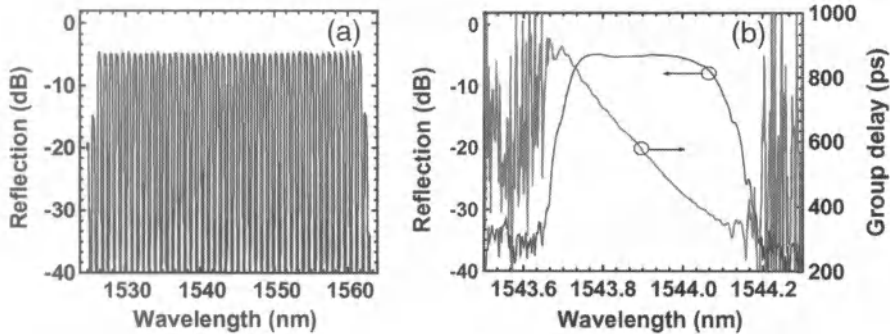


Figure 8.13: (a) Reflectivity spectrum of a phase-sampled grating fabricated to compensate dispersion of 45 channels in the C band with 100 GHz spacing. (b) Measured reflectivity and group delay as a function of wavelength for the central channel. (After Ref. [65]; ©2007 IEEE.)

ing. With the simultaneous use of two phase-sampling functions, such gratings can be designed to cover the S, C, and L bands [66].

8.4 Dispersion-Equalizing Filters

Fiber gratings constitute an example a whole class of optical filters that can be employed for compensating dispersion in long-haul systems. In this section we consider several other dispersion-equalizing filters that may be made using fibers or planar waveguides. Such a compact optical filter can be combined with an amplifier module such that both the loss and the dispersion of optical fibers are compensated simultaneously in a periodic fashion. Moreover, an optical filter can also reduce the amplifier noise if its bandwidth is much smaller than the amplifier bandwidth.

8.4.1 Gires–Tournois Filters

Any interferometer acts as an optical filter because it is sensitive to the frequency of input light by its very nature and exhibits frequency-dependent transmission and reflection characteristics. A simple example is provided by the Fabry–Perot interferometer. The only problem from the standpoint of dispersion compensation is that the transfer function of a Fabry–Perot filter affects both the amplitude and phase of passing light. As seen from Eq. (8.1.4), a dispersion-equalizing filter should affect the phase of light but not its amplitude.

This problem is easily solved by using a Gires–Tournois (GT) interferometer, which is simply a Fabry–Perot interferometer whose back mirror has been made 100% reflective. The transfer function of a GT filter is obtained by considering multiple round trips inside its cavity and is given by [68]

$$H(\omega) = H_0 e^{i\omega T_r} \left(\frac{1 - re^{-i\omega T_r}}{1 - re^{i\omega T_r}} \right). \quad (8.4.1)$$

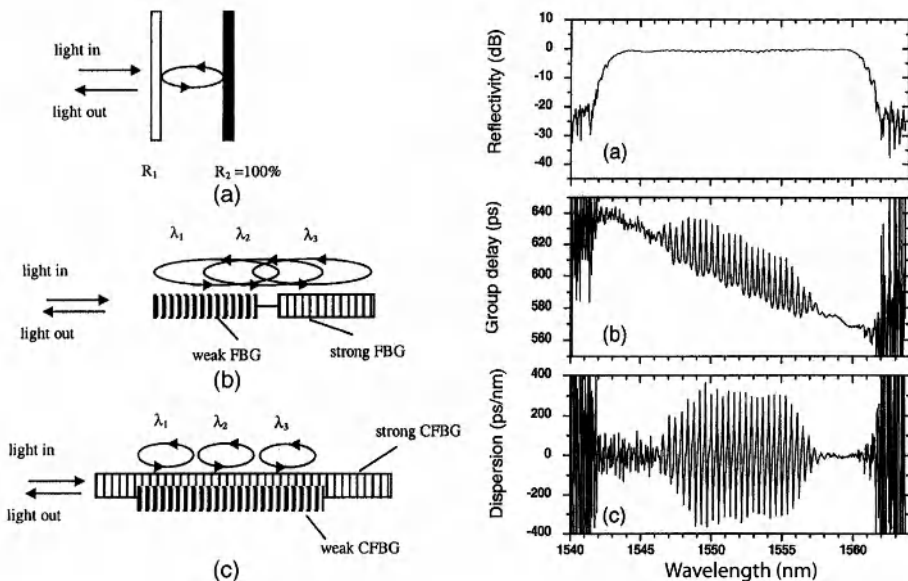


Figure 8.14: (a) Schematic of a distributed GT filter made using two superimposed fiber gratings. (b) Measured reflectivity, group delay, and dispersion as a function of wavelength for a 1-cm-long device. (After Ref. [71]; ©2003 OSA.)

where the constant H_0 takes into account losses, $|r|^2$ is the front-mirror reflectivity, and T_r is the round-trip time within the filter cavity. If losses are constant over the signal bandwidth, $|H_{GT}(\omega)|$ is frequency-independent, and only the spectral phase is modified by such a filter.

However, the phase $\phi(\omega)$ of $H_{GT}(\omega)$ is far from ideal. It is a periodic function, peaking at frequencies that correspond to longitudinal modes of the cavity. In the vicinity of each peak, a spectral region exists in which phase variations are nearly quadratic in ω . The group delay, $\tau_g = d\phi(\omega)/d\omega$, is also a periodic function. The quantity $\phi_2 \equiv d\tau_g/d\omega$, related to the slope of the group delay, represents the total dispersion of the GT filter. At frequencies corresponding to the longitudinal modes, ϕ_2 is given by

$$\phi_2 = 2T_r^2 r(1 - r)/(1 + r)^3. \quad (8.4.2)$$

As an example, for a 2-cm-thick GT filter designed with $r = 0.8$, $\phi_2 \approx 2,200 \text{ ps}^2$. Such a device can compensate the GVD acquired over 110 km of standard fiber.

Several experiments have shown the potential of GT filters as a compact dispersion compensator. In a 1991 experiment, such a device was used to transmit a 8-Gb/s signal over 130 km of standard fiber [69]. The GT filter had a 1-mm-long cavity with 70% reflectivity for the front mirror. The relatively high insertion loss of 8 dB was compensated by using an optical amplifier. However, 6-dB losses were due to the 3-dB fiber coupler that was used to separate the reflected signal from the incident signal. This amount can be reduced to below 1 dB using an optical circulator. The micro-electro-

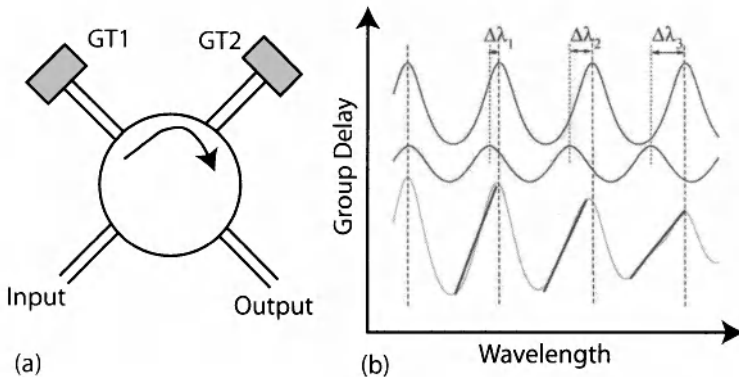


Figure 8.15: (a) Two GT filters cascaded using a circulator. (b) Group delay as a function of wavelength for individual GT filters and the resulting total group delay (gray curve). Dark lines show the slope of group delay. (After Ref. [74]; ©2004 IEEE.)

mechanical system (MEMS) technology has also been employed for fabricating a GT filter whose cavity length can be adjusted electronically [70].

In another approach, two mirrors of the GI filter are replaced with two fiber gratings, one of which is made nearly 100% reflective. The two gratings can even overlap physically, resulting in the so-called distributed GT filter [71]. Figure 8.14 shows schematically the basic idea behind such a device together with the measured reflectivity, group delay, and dispersion as a function of wavelength for a device consisting of a 1-cm-long grating with 98% reflectivity and another 6-mm-long grating with 11% reflectivity. Whereas the reflectivity is nearly constant over the 20-nm spectral window, group delay and dispersion exhibit a periodic pattern. The 50-GHz channel spacing results from a 2-nm shift in the Bragg wavelength of two gratings.

A GT filter can compensate dispersion for multiple channels simultaneously because, as seen in Eq. (8.4.1), it exhibits a periodic response at frequencies that correspond to the longitudinal modes of the underlying Fabry–Perot cavity. However, the periodic nature of the transfer function also indicates that ϕ_2 in Eq. (8.4.2) is the same for all channels. In other words, a GT filter cannot compensate for the dispersion slope of the transmission fiber without suitable design modifications. Several schemes have been proposed for dispersion slope compensation [72]–[74]. In one approach, two or more cavities are coupled such that the entire device acts as a composite GT filter [72]. In another design, GT filters are cascaded in series. In a 2004 experiment, cascaded GT filters were used to compensate dispersion of 40 channels (each operating at 10 Gb/s) over a length of 3,200 km [73].

Another approach employs two grating-based distributed GT filters [74], which are cascaded using a circulator as shown in Figure 8.15. This Figure also shows schematically the basic idea behind the dispersion slope compensation. A four-port circulator forces the input WDM signal to pass through the two filters in a sequential fashion. Two GT filters have different device parameters, resulting in group-delay profiles whose peaks are slightly shifted and have different amplitudes. This combination results in

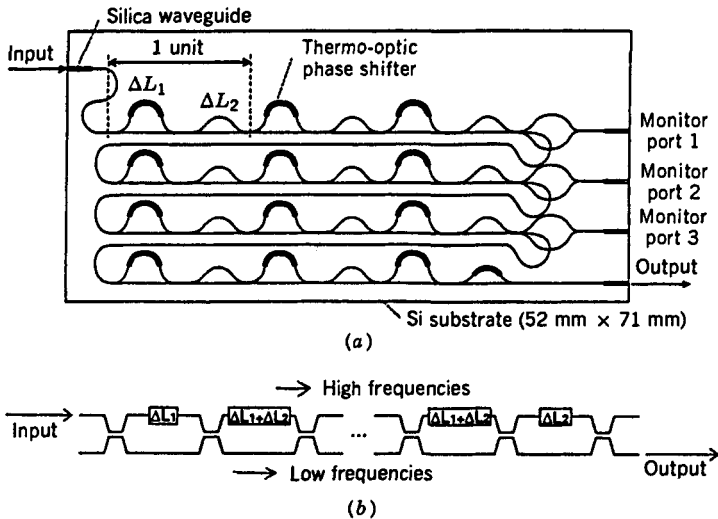


Figure 8.16: (a) A planar lightwave circuit made of a chain of Mach–Zehnder interferometers; (b) unfolded view of the device. (After Ref. [76]; ©1994 IEEE.)

a composite group-delay profile that exhibits different slopes (and hence a different dispersion parameter D) near each peak. Changes in D occurring from one peak to the next can be designed to satisfy the slope condition in Eq. (8.4.1) by choosing the filter parameters appropriately.

8.4.2 Mach–Zehnder Filters

A Mach–Zehnder (MZ) interferometer can also act as an optical filter. Such a fiber-based device can be constructed by connecting two fiber couplers in series. The first coupler splits the input signal into two parts, which acquire different phase shifts if optical path lengths are different, before they interfere at the second coupler. The signal may exit from either of the two output ports depending on its frequency and the arm lengths. In the case of two 3-dB couplers, the transfer function for the cross port is given by [33]

$$H_{\text{MZ}}(\omega) = \frac{1}{2}[1 + \exp(i\omega\tau)], \quad (8.4.3)$$

where τ is the extra delay in the longer arm of the MZ interferometer.

If we compare Eq. (8.4.3) with Eq. (8.1.4), we can conclude that a single MZ interferometer is not suitable for dispersion compensation. However, it turned out that a cascaded chain of several MZ interferometers acts as an excellent dispersion-equalizing filter [75]. Such filters have been fabricated in the form of a *planar lightwave circuit* using silica waveguides on a silicon substrate [76]–[81]. Figure 8.16(a) shows schematically a specific circuit design. This device was $52 \times 71 \text{ mm}^2$ in size and exhibited a chip loss of 8 dB [76]. It consists of 12 couplers with asymmetric arm lengths that are cascaded in series. A chromium heater is deposited on one arm of each MZ interferometer to provide thermo-optic control of the optical phase. The main advantage of such a

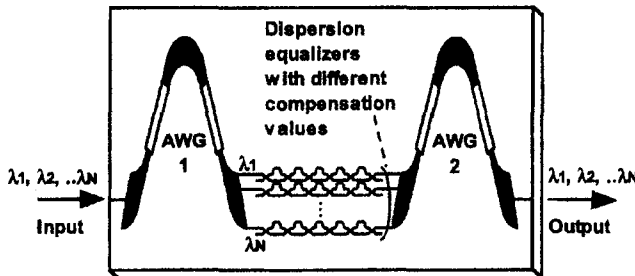


Figure 8.17: A planar lightwave circuit capable of compensating both the dispersion and dispersion slope. A separate MZ chain is employed for each WDM channel. (After Ref. [80]; ©2003 IEEE.)

device is that its dispersion-equalization characteristics can be controlled by changing the arm lengths and the number of MZ interferometers.

The operation of the MZ filter can be understood from the unfolded view shown in Figure 8.16(b). The device is designed such that the higher-frequency components propagate in the longer arm of the MZ interferometers. As a result, they experience more delay than the lower-frequency components taking the shorter route. The relative delay introduced by such a device is just the opposite of that introduced by a standard fiber exhibiting anomalous dispersion near $1.55\text{ }\mu\text{m}$. The transfer function $H(\omega)$ can be obtained analytically and is used to optimize the device design and performance [77]. In a 1994 implementation [78], a planar lightwave circuit with only five MZ interferometers provided a relative delay of 836 ps/nm. Such a device is only a few centimeters long, but it is capable of compensating dispersion acquired over 50 km of fiber. Its main limitations are a relatively narrow bandwidth ($\sim 10\text{ GHz}$) and sensitivity to input polarization. However, it acts as a programmable optical filter whose GVD as well as the operating wavelength can be adjusted. In one device, the GVD could be varied from $-1,006$ to 834 ps/nm [79].

It is not easy to compensate for the dispersion slope of the fiber with a single MZ chain. A simple solution is to demultiplex the WDM signal, employ a MZ chain designed suitably for each channel, and then multiplex the WDM channels back. Although this process sounds too complicated to be practical, all components can be integrated on a single chip using the silica-on-silicon technology [80]. Figure 8.17 shows the schematic of such a planar lightwave circuit. The use of a separate MZ chain for each channel allows the flexibility that the device can be tuned to match dispersion experienced by each channel. By 2008, the use of a lattice-form filer allowed tuning over a range of $\pm 500\text{ ps/nm}$ [81].

8.4.3 Other All-Pass Filters

It is possible to design several other types of filters that affect the signal phase but leave the signal amplitude intact. Such filters are known as all-pass filters (as they pass all of the optical power incident on them) and have attracted considerable attention within

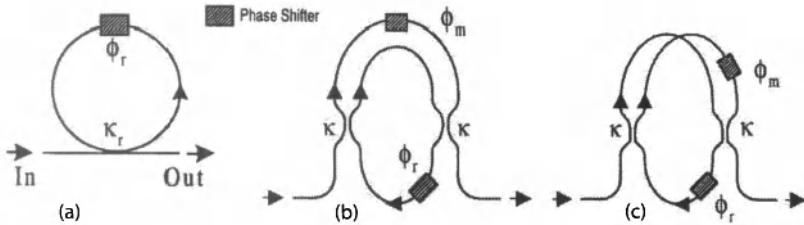


Figure 8.18: Three designs for all-pass filters based on ring resonators: (a) A simple ring resonator with a built-in phase shifter; (b) an asymmetric MZ configuration; (c) a symmetric MZ configuration. (After Ref. [87]; ©1999 IEEE.)

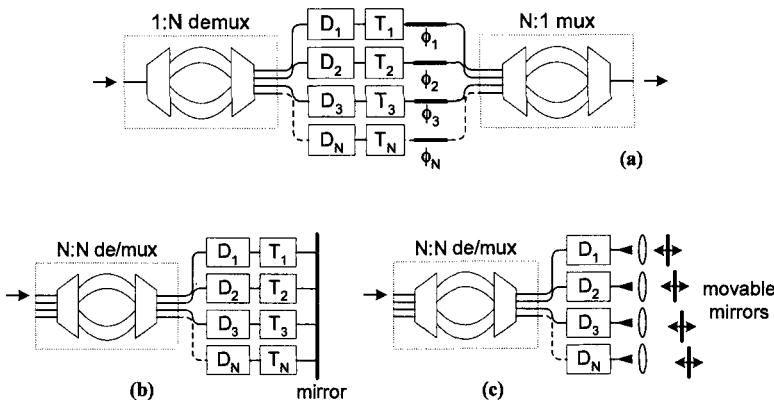


Figure 8.19: Three architectures for all-pass filters; boxes marked D and T stand for a dispersive element and a delay line. (After Ref. [85]; ©2003 IEEE.)

the context of dispersion compensation [82]–[85]. A ring resonator constitutes a simple example of an all-pass filter [33]. Indeed, ring resonators have been employed for this purpose since 1998 [86]–[88].

Figure 8.18 shows schematically three designs that use directional couplers and phase shifters to form a ring resonator [87]. Although a single ring can be employed for dispersion compensation, cascading of multiple rings increases the amount of dispersion. More complicated designs combine a MZ interferometer with a ring. The resulting device can compensate even the dispersion slope of a fiber. Such devices have been fabricated using the silica-on-silicon technology. With this technology, the phase shifters seen in Figure 8.18 are incorporated using thin-film chromium heaters. One such device exhibited dispersion that ranged from -378 to $-3,026$ ps/nm depending on the channel wavelength.

In general, all-pass filters such as those shown in Figure 8.18 suffer from a narrow bandwidth over which dispersion can be compensated. The amount of dispersion can be increased by using multiple stages but the bandwidth is reduced even further. A solution is provided by the filter architectures shown in Figure 8.19 [85] in which the WDM signal is split into individual channels using a demultiplexer. In (a), an array

of dispersive elements, followed by delay lines and phase shifters, is used to compensate for the dispersion of each channel. Individual channels are then multiplexed back. Configurations (b) and (c) simplify the design using a single mirror or an array of movable mirrors. Such designs, although more complicated, provide the most flexibility.

8.5 Optical Phase Conjugation

Although the use of optical phase conjugation (OPC) for dispersion compensation was proposed in 1979 [89], it was only in 1993 that the OPC technique was first implemented experimentally [90]–[93]. It has attracted considerable attention since then [94]–[107]. In contrast to other optical schemes discussed in this chapter, the OPC is a nonlinear optical technique. This section describes the principle behind it and discusses its implementation in practical lightwave systems.

8.5.1 Principle of Operation

The simplest way to understand how OPC can compensate the GVD is to take the complex conjugate of Eq. (8.1.2) and obtain

$$\frac{\partial A^*}{\partial z} - \frac{i\beta_2}{2} \frac{\partial^2 A^*}{\partial t^2} - \frac{\beta_3}{6} \frac{\partial^3 A^*}{\partial t^3} = 0. \quad (8.5.1)$$

A comparison of Eqs. (8.1.2) and (8.5.1) shows that the phase-conjugated field A^* propagates with the sign reversed for the GVD parameter β_2 . This observation suggests immediately that, if the optical field is phase-conjugated in the middle of the fiber link, as shown in Figure 8.20(a), second-order dispersion (GVD) accumulated over the first half will be compensated exactly in the second half of the fiber link. As the β_3 term does not change sign on phase conjugation, OPC cannot compensate for the TOD. In fact, it is easy to show by keeping the higher-order terms in the Taylor expansion in Eq. (2.4.4) that OPC compensates for all even-order dispersion terms, while leaving the odd-order terms unaffected.

The effectiveness of midspan OPC for dispersion compensation can also be verified by using Eq. (8.1.3) with $\beta_3 = 0$. The optical field just before OPC is obtained by substituting $z = L/2$ in this equation. The propagation of the phase-conjugated field A^* in the second-half section then yields

$$A^*(L, t) = \frac{1}{2\pi} \int_{-\infty}^{\infty} \tilde{A}^* \left(\frac{L}{2}, \omega \right) \exp \left(\frac{i}{4} \beta_2 L \omega^2 - i\omega t \right) d\omega, \quad (8.5.2)$$

where $\tilde{A}^*(L/2, \omega)$ is the Fourier transform of $A^*(L/2, t)$ and is given by

$$\tilde{A}^*(L/2, \omega) = \tilde{A}^*(0, -\omega) \exp(-i\omega^2 \beta_2 L/4). \quad (8.5.3)$$

By substituting Eq. (8.5.3) in Eq. (8.5.2), one finds that $A(L, t) = A^*(0, t)$. Thus, except for a phase reversal induced by the OPC, the input field is completely recovered, and the pulse shape is restored to its input form. Since the signal spectrum after OPC becomes the mirror image of the input spectrum, the OPC technique is also referred to as *midspan spectral inversion*.

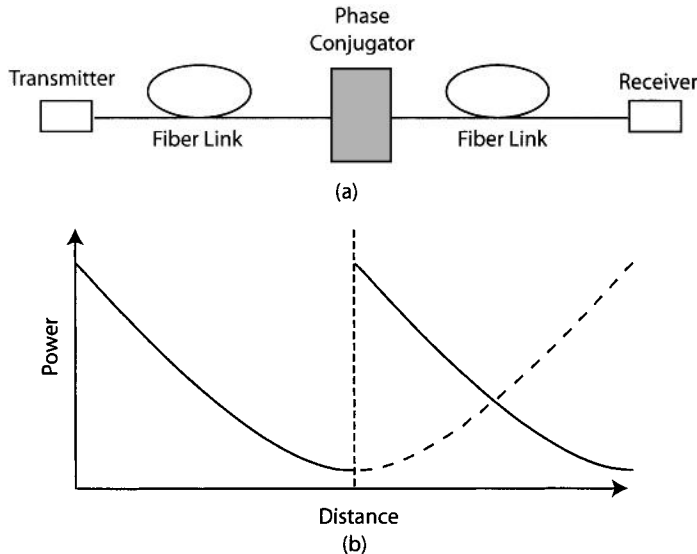


Figure 8.20: (a) Schematic of dispersion management through midspan phase conjugation. (b) Power variations inside the fiber link when an amplifier boosts the signal power at the phase conjugator. The dashed line shows the power profile required for SPM compensation.

8.5.2 Compensation of Self-Phase Modulation

As discussed in Section 2.6, the nonlinear phenomenon of SPM leads to the chirping of the transmitted signal that manifests itself through broadening of the signal spectrum. In most lightwave systems, SPM effects degrade the signal quality, especially when the signal is propagated over long distances using multiple optical amplifiers. It turns out that the OPC technique can compensate simultaneously for both the GVD and SPM simultaneously. This feature of OPC was noted in the early 1980s [108] and attracted considerable attention after 1993 [101].

It is easy to show that both the GVD and SPM are compensated perfectly in the absence of fiber losses. Pulse propagation in a lossy fiber is governed by Eq. (2.6.18) or by

$$\frac{\partial A}{\partial z} + \frac{i\beta_2}{2} \frac{\partial^2 A}{\partial t^2} = i\gamma|A|^2 A - \frac{\alpha}{2} A, \quad (8.5.4)$$

where α accounts for fiber losses. When $\alpha = 0$, A^* satisfies the same equation when we take the complex conjugate of Eq. (8.5.4) and change z to $-z$. In other words, the propagation of A^* is equivalent to sending the signal backward and undoing distortions induced by β_2 and γ . As a result, midspan OPC can compensate for both SPM and GVD simultaneously.

Fiber losses destroy this important property of midspan OPC. The reason is intuitively obvious if we note that the SPM-induced phase shift is power-dependent. As a result, much larger phase shifts are induced in the first half of the link than the second half, and OPC cannot compensate for the nonlinear effects. Equation

(8.5.4) can be used to study the impact of fiber losses. By making the substitution $A(z, t) = B(z, t)p(z)$, Eq. (8.5.4) can be written as

$$\frac{\partial B}{\partial z} + \frac{i\beta_2}{2} \frac{\partial^2 B}{\partial t^2} = i\gamma p(z)|B|^2 B, \quad (8.5.5)$$

where $p(z) = \exp(-\alpha z)$. The effect of fiber losses is mathematically equivalent to the loss-free case but with a z -dependent nonlinear parameter. By taking the complex conjugate of Eq. (8.5.5) and changing z to $-z$, it is easy to see that perfect SPM compensation can occur only if $p(z) = \exp(\alpha z)$ after phase conjugation ($z > L/2$). A general requirement for the OPC technique to work is $p(z) = p(L-z)$. This condition cannot be satisfied when $\alpha \neq 0$.

One may think that the problem can be solved by amplifying the signal after OPC so that the signal power becomes equal to the input power before it is launched in the second-half section of the fiber link. Although such an approach reduces the impact of SPM, it does not lead to perfect compensation of it. The reason can be understood by noting that the propagation of a phase-conjugated signal is equivalent to propagating a *time-reversed* signal [109]. Thus, perfect SPM compensation can occur only if the power variations are symmetric around the midspan point where the OPC is performed so that $p(z) = p(L-z)$ in Eq. (8.5.5). Optical amplification does not satisfy this property. Figure 8.20(b) shows the actual and required forms of $p(z)$. One can come close to SPM compensation if the signal is amplified often enough that the power does not vary by a large amount during each amplification stage. This approach is, however, not practical because it requires closely spaced amplifiers. The use of distributed Raman amplification with bidirectional pumping can also help because it can provide $p(z)$ close to 1 over the entire span.

Perfect compensation of both GVD and SPM can be realized by employing dispersion-decreasing fibers in which $|\beta_2|$ decreases along the fiber length. To see how such a scheme can be implemented, assume that β_2 in Eq. (8.5.5) is a function of z . By making the transformation $\xi = \int_0^z p(z) dz$, Eq. (8.5.5) can be written as [101]

$$\frac{\partial B}{\partial \xi} + \frac{i}{2} b(\xi) \frac{\partial^2 B}{\partial t^2} = i\gamma|B|^2 B, \quad (8.5.6)$$

where $b(z) = \beta_2(z)/p(z)$. Both GVD and SPM are compensated if $b(\xi) = b(\xi_L - \xi)$, where ξ_L is the value of ξ at $z = L$. This condition is automatically satisfied when $\beta_2(z)$ decreases in exactly the same way as $p(z)$ so that their ratio remains constant. Since $p(z)$ decreases exponentially, both GVD and SPM can be compensated in a dispersion-decreasing fiber whose GVD decreases as $e^{-\alpha z}$. This approach is quite general and applies even when in-line amplifiers are used.

8.5.3 Generation of Phase-Conjugated Signal

The implementation of the midspan OPC technique requires a nonlinear optical element that generates the phase-conjugated signal. The most commonly used method makes use of *four-wave mixing* (FWM) in a nonlinear medium. Since the optical fiber itself is a nonlinear medium [110], a simple approach is to use a special fiber

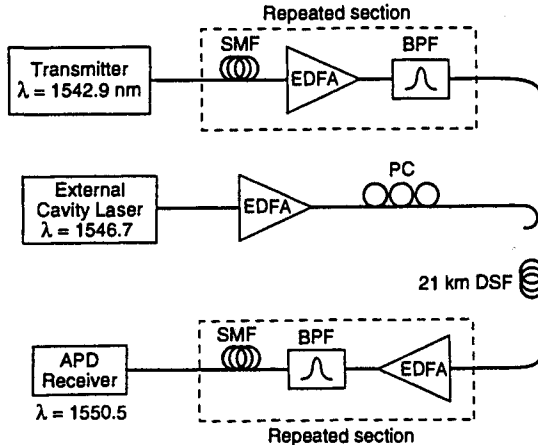


Figure 8.21: Experimental setup for dispersion compensation through midspan spectral inversion in a 21-km-long dispersion-shifted fiber. (After Ref. [91]; ©1993 IEEE.)

designed to maximize the FWM efficiency. The use of FWM requires launching of a pump beam at a frequency ω_p that is shifted from the signal frequency ω_s by a small amount ($\sim 0.5 \text{ THz}$). Such a device acts as a parametric amplifier and amplifies the signal, while also generating an idler at the frequency $\omega_c = 2\omega_p - \omega_s$ if the phase-matching condition is satisfied. The idler beam carries the same information as the signal but its phase is reversed with respect to the signal and its spectrum is inverted.

The phase-matching condition can be approximately satisfied if the zero-dispersion wavelength of the OPC fiber is chosen to nearly coincide with the pump wavelength. This was the approach adopted in a 1993 experiment [90] in which a 1,546-nm signal was phase-conjugated using FWM in a 23-km-long fiber pumped at 1,549 nm. A 6-Gb/s signal could be transmitted over 152 km by compensating dispersion through OPC in the middle of the fiber link. In another 1993 experiment [91], a 10-Gb/s signal was transmitted over 360 km with the setup shown in Figure 8.21. The midspan OPC was performed in a 21-km-long fiber by using a pump laser whose wavelength was tuned exactly to the zero-dispersion wavelength of the fiber. The pump and signal wavelengths differed by 3.8 nm, and a bandpass filter was used to separate the phase-conjugated signal from the pump.

Several factors need to be considered while implementing the midspan OPC technique in practice. First, since the signal wavelength changes from ω_s to $\omega_c = 2\omega_p - \omega_s$ at the phase conjugator, the GVD parameter β_2 becomes different in the second-half section. As a result, perfect compensation occurs only if the phase conjugator is slightly offset from the midpoint of the fiber link. The exact location L_p can be determined by using the condition $\beta_2(\omega_s)L_p = \beta_2(\omega_c)(L - L_p)$, where L is the total link length. By expanding $\beta_2(\omega_c)$ in a Taylor series around the signal frequency ω_s , L_p is found to be

$$\frac{L_p}{L} = \frac{\beta_2 + \delta_c \beta_3}{2\beta_2 + \delta_c \beta_3}, \quad (8.5.7)$$

where $\delta_c = \omega_c - \omega_s$ is the frequency shift of the signal induced by the OPC technique. For a typical wavelength shift of 6 nm, the phase-conjugator location changes by about 1%. The effect of residual dispersion and SPM in the phase-conjugation fiber itself can also affect the placement of a phase conjugator [98].

A second factor that needs to be addressed is that the FWM process in optical fibers is polarization-sensitive. As signal polarization is not controlled in optical fibers, it varies at the OPC in a random fashion. Such random variations affect FWM efficiency and make the standard FWM technique unsuitable for practical purposes. Fortunately, the FWM scheme can be modified to make it polarization-insensitive. In one approach, two orthogonally polarized pump beams at different wavelengths, located symmetrically on the opposite sides of the zero-dispersion wavelength λ_{ZD} of the fiber, are used [93]. This scheme has another advantage: The phase-conjugate wave can be generated at the frequency of the signal itself by choosing λ_{ZD} such that it coincides with the signal frequency. Polarization-insensitive OPC can also be realized by using a single pump in combination with a fiber grating and an *orthoconjugate mirror* [95], but the device works in the reflective mode and requires separation of the conjugate wave from the signal through an optical circulator.

Low efficiency of the OPC process can be of concern. In early experiments, the conversion efficiency η_c was below 1%, making it necessary to amplify the phase-conjugated signal [91]. However, the FWM process is not inherently a low-efficiency process and, in principle, it can even provide net gain [110]. Indeed, analysis of the FWM equations shows that η_c can be increased considerably by increasing the pump power; it can even exceed 100% by optimizing the power levels and the wavelength difference of the the pump and signal [96]. High pump powers require suppression of stimulated Brillouin scattering through modulation of pump phases. In a 1994 experiment, 35% conversion efficiency was realized with this technique [94].

The FWM process in a semiconductor optical amplifier (SOA) can also be used to generate the phase-conjugated signal. This approach was first used in a 1993 experiment to demonstrate the transmission of a 2.5-Gb/s signal over 100 km of standard fiber [92]. Later, in a 1995 experiment the same approach was used for transmitting a 40-Gb/s signal over 200 km of standard fiber [97]. The possibility of highly nondegenerate FWM inside SOAs was suggested in 1987, and this technique is used extensively in the context of wavelength conversion [111]. Its main advantage is that the phase-conjugated signal can be generated in a device of 1-mm length. The conversion efficiency is also typically higher than that of FWM in an optical fiber because of amplification, although this advantage is offset by the relatively large coupling losses resulting from the need to couple the signal back into the fiber. By a proper choice of the pump-signal detuning, conversion efficiencies of more than 100% (net gain for the phase-conjugated signal) have been realized through FWM in SOAs [112].

Periodically poled lithium-niobate (PPLN) waveguides have been used to make a compact, wideband, spectral inverter [113]. The phase-conjugated signal in such a device is generated through two cascaded second-order nonlinear processes that are quasi-phase-matched through periodic poling of the crystal. Such an OPC device exhibited only 7-dB insertion losses and was capable of compensating the dispersion of four 10-Gb/s channels simultaneously over 150 km of standard fiber. By 2003, a PPLN waveguide was used for simultaneous phase conjugation of 103 channels from the C-

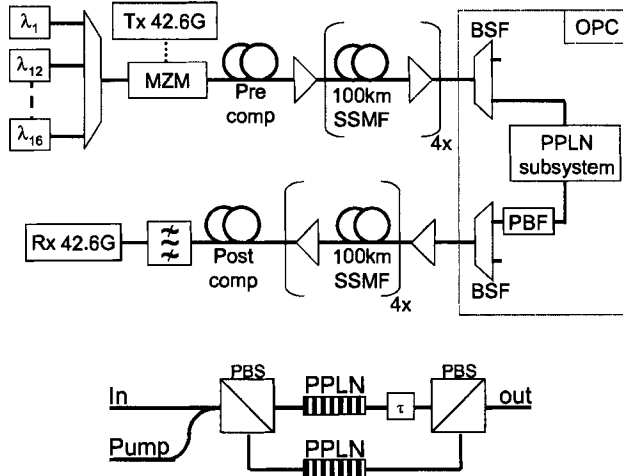


Figure 8.22: Experimental setup of a 16-channel WDM system, employing a PPLN-based phase conjugator to transmit data over 800 km of standard fiber; bottom part shows the polarization-diversity scheme employed. (After Ref. [106]; ©2006 IEEE.)

band to the L-band with a conversion efficiency of about -15 dB using a single pump at 1555 nm [114].

The OPC technique has been used for dispersion compensation in several recent experiments [106]. In a 2004 WDM experiment, a PPLN-based phase conjugator was used to demonstrate the transmission of 16 channels (each operating at 40 Gb/s) over 800 km of standard fiber. Amplifier spacing was 100 km and a single PPLN device was used midway after 4 amplifiers. Figure 8.22 shows the experimental setup schematically. A single pump at a wavelength of 1,546.12 nm phase-conjugated all 16 WDM channels as it inverted the signal spectrum around the pump wavelength. A polarization-diversity scheme shown in Figure 8.22 was employed to ensure that the OPC process was polarization-independent.

For long-haul applications, one may ask whether the OPC technique can compensate the GVD acquired over thousands of kilometers. This question has been studied extensively through numerical simulations. In one set of simulations, a 10-Gb/s signal could be transmitted over 6,000 km when the average launch power was kept below 3 mW to reduce the effects of fiber nonlinearity [99]. In another study, the amplifier spacing was found to play an important role; transmission over 9,000 km was feasible by keeping the amplifiers 40 km apart [102]. The choice of the operating wavelength with respect to the zero-dispersion wavelength was also critical. In the case of anomalous dispersion ($\beta_2 < 0$), periodic variations of the signal power along the fiber link can lead to the generation of additional sidebands through an instability known as *sideband instability* [115]. This instability can be avoided if the dispersion parameter is relatively large [$D > 10 \text{ ps}/(\text{km}\cdot\text{nm})$]. This is the case for standard fibers near $1.55 \mu\text{m}$.

In general, the maximum transmission distance for the OPC technique depends on many factors such as FWM efficiency, input power, and amplifier spacing [100]. If a

suitably designed periodic dispersion map is used in combination with OPC, it is possible to suppress the sideband instability and increase the transmission distance to beyond 10,000 km [104]. In a 2005 experiment, dispersion over 10,200 km was compensated for a 22 channels, operating at 20 Gb/s and separated by 50 GHz, using a mid-span PPLN-based phase conjugator [106]. The 94.5-km recirculating loop employed standard fibers with a dispersion of 16 ps/km/nm, and its losses were compensated through Raman amplification. This experiment employed the RZ-DPSK format, and the OPC also helped in reducing the nonlinear phase noise (see Section 10.5).

8.6 Channels at High Bit Rates

Commercial WDM systems in which individual channels operate at a bit rate of 40 Gb/s became available by 2002, and efforts were underway to increase the channel bit rate to 100 Gb/s and beyond. For such high-speed systems, the management of channel dispersion poses additional problems. In this section we focus on several relevant issues.

8.6.1 Tunable Dispersion Compensation

It is difficult to attain full GVD compensation for all channels in a WDM system. A small amount of residual dispersion remains uncompensated and often becomes a concern for long-haul systems. For a link of length L , this accumulated dispersion is given by $d_a = \int_0^L D(z) dz$, where $D(z)$ denotes local dispersion along the link. A post-compensation technique is often adopted in laboratory experiments. In this approach, the residual dispersion for individual channels is compensated by adding adjustable lengths of a DCF at the receiver end (dispersion trimming). This technique is not suitable for commercial WDM systems for several reasons. First, the exact amount of channel-dependent residual dispersion is not always known because of uncontrollable variations in the dispersion of fiber segments forming the transmission path. Second, even the path length may change in reconfigurable optical networks. Third, as the single-channel bit rate increases toward 40 Gb/s and beyond, the tolerable value of the residual dispersion becomes so small that even temperature-induced changes in GVD become a concern. For these reasons, the best approach is to adopt a tunable dispersion-compensation scheme that allows the dispersion control for each channel in a dynamic fashion.

Many techniques have been developed for tunable dispersion compensation over the last decade [116]–[135]. Several of them make use of a fiber Bragg grating whose dispersion is tuned by changing the optical period $\bar{n}\Lambda$ of the grating. In one scheme, the grating is chirped nonlinearly so that its Bragg wavelength increases nonlinearly along the grating length. Tunable dispersion is realized when such a grating is stretched with a piezoelectric transducer [116].

In a linearly chirped grating, the slope of group delay (responsible for dispersion) at a given wavelength does not change with stretching. However, this slope can be changed by a large factor when the chirp is nonlinear. Mathematically, stress-induced changes in the mode index \bar{n} change the local Bragg wavelength as $\lambda_B(z) = 2\bar{n}(z)\Lambda(z)$.

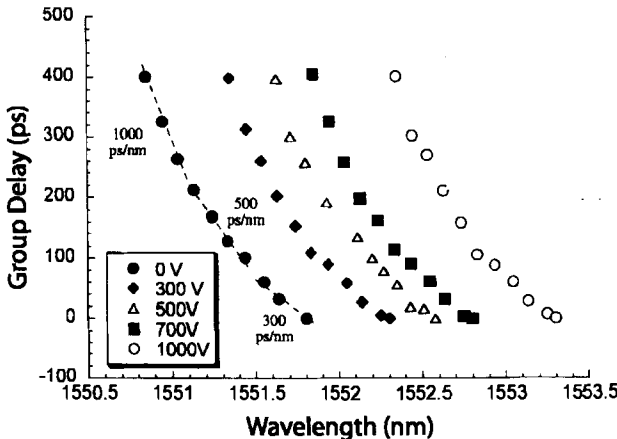


Figure 8.23: Group delay as a function of wavelength at several applied voltages for a nonlinearly chirped fiber grating. (After Ref. [116]; ©1999 IEEE.)

For such a grating, Eq. (8.3.7) is replaced with

$$D_g(\lambda) = \frac{d\tau_g}{d\lambda} = \frac{2}{c} \frac{d}{d\lambda} \left(\int_0^{L_g} \bar{n}(z) dz \right), \quad (8.6.1)$$

where τ_g is the group delay and L_g is the grating length. The value of D_g at any wavelength can be altered by changing the mode index \bar{n} (through heating or stretching), resulting in tunable dispersion characteristics for the Bragg grating.

The stretching technique has been used with success since 1999 to tune the dispersion provided by a nonlinearly chirped fiber grating [116]. The grating is placed on a mechanical stretcher and a piezoelectric transducer is used to stretch it by applying an external voltage. Figure 8.23 shows the group-delay characteristics of a 5-cm-long grating as the voltage is changed from 0 to 1,000 V. For a fixed channel wavelength, d_a can be changed from -300 to $-1,000$ ps/nm by changing the voltage, resulting in a tuning range of 700 ps/nm. The same technique can be extended to provide tunable compensation for multiple channels by using a sampled grating with nonlinear chirp. However, it suffers from a relatively large third-order dispersion that affects each channel. This problem can be solved by cascading two identical gratings in a fashion such that their chirps are opposite in nature [122].

In a different approach to realizing tunable dispersion, the grating is made with either no chirp or with a linear chirp, and a temperature gradient is used to produce a controllable chirp. Such distributed heating requires a thin-film heater deposited on the outer surface of the fiber whose core contains the grating. In a simple technique [118], film thickness is changed along the grating length to create a temperature gradient when a constant voltage is applied across the film. Figure 8.24(a) shows the reflection spectra of a 8-cm-long grating at three voltage levels. The total dispersion, calculated from the group delay $\tau_g(\lambda)$, is displayed in Figure 8.24(b) as a function of applied voltage. The grating is initially unchirped and has a narrow stop band that shifts and broadens as the

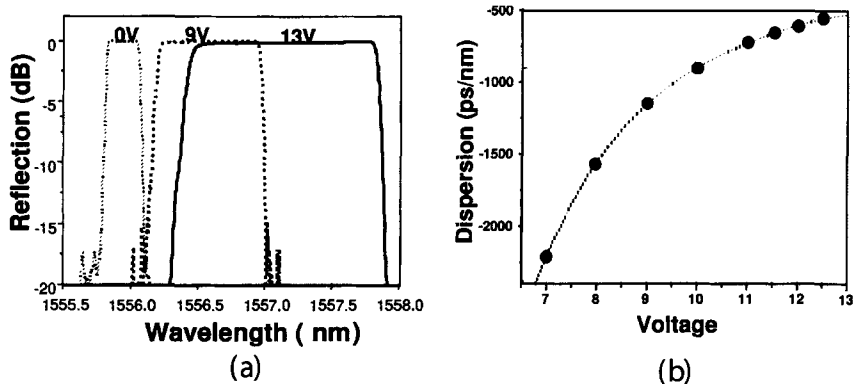


Figure 8.24: (a) Reflection spectrum and (b) total GVD as a function of voltage for a fiber grating with temperature gradient. (After Ref. [118]; ©2000 IEEE.)

grating is chirped through nonuniform heating. Physically, the Bragg wavelength λ_B changes along the grating because the optical period $\bar{n}(z)\Lambda$ becomes z -dependent when a temperature gradient is established along the grating. The total dispersion $D_g L_g$ can be changed in the range of -500 to $-2,200$ ps/nm by this approach. Such gratings can be used to provide tunable dispersion for 10-Gb/s systems. A segmented thin-film heater is sometimes used for creating a temperature gradient as it provides better temperature control along the grating length. Both the dispersion and dispersion slope of such a device can be controlled electronically. Moreover, in contrast to the stretching technique that requires large voltages, only a few volts are required for thermal tuning of a grating.

Cascaded, phase-apodized, chirped fiber gratings can also provide tunable dispersion with thermal tuning [133]. Figure 8.25 shows such a device schematically. It consists in two such gratings cascaded using a four-port optical circulator. Each phase-apodized grating consists of two superimposed gratings of different periods and thus acts as a distributed GT filter (see Section 8.4.1) with a group delay that varies peri-

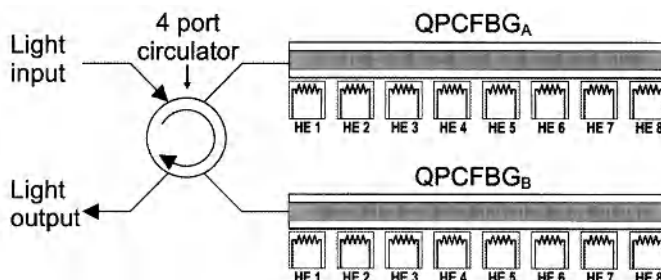


Figure 8.25: A tunable dispersion compensator based on quasi-periodic chirped fiber Bragg gratings (QPCFBG) acting as distributed GT filters. Multiple heating elements (HE) are used to tune the local Bragg wavelength of gratings. (After Ref. [133]; ©2008 IEEE.)

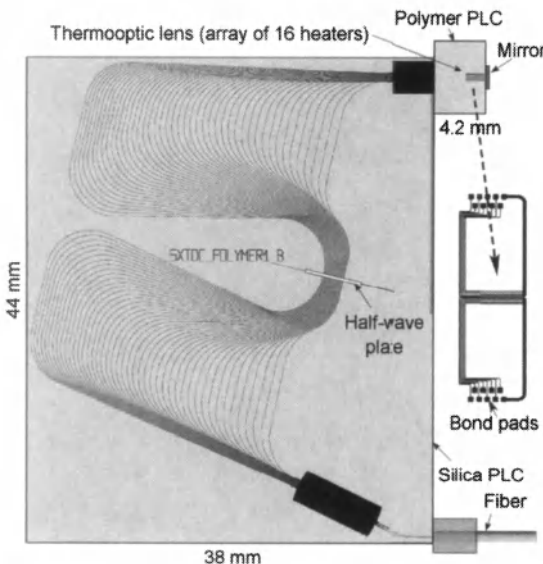


Figure 8.26: Schematic of a tunable dispersion compensator based on planar lightwave circuits. An AWG is attached to a polymer waveguide with 16 heaters that can be individually addressed to produce a parabolic heat distribution. (After Ref. [131]; ©2006 IEEE.)

odically with frequency with a period equal to the free spectral range of the GT filter. Dispersion tuning is realized with the help of multiple heating elements along the length of each grating that are used to change the local grating period. By adjusting the group delays in the two gratings with suitable temperature profiles, such a device can compensate simultaneously the dispersion of 32 channels, spaced apart by 50 GHz, while providing a tuning range of ± 800 ps/nm over a 30-GHz bandwidth.

As seen in Section 8.4.2, planar lightwave circuits, fabricated with the silica-on-silicon technology, can be used as tunable dispersion compensators [79]–[81]. The use of an arrayed waveguide grating (AWG) based on this technology provides another approach to realizing tunable dispersion. Figure 8.26 shows such a device schematically [131]. It consists of an AWG that is attached to a polymer-based planar lightwave circuit containing a thermo-optic lens. The AWG has a free-spectral range of 100 GHz so that it can demultiplex a WDM signal containing 100-GHz-spaced channels. The polymer PLC contains a 7.5- μ m-thick slab waveguide with an array of 16 heaters on top that can be individually addressed to produce a parabolic heat distribution. A mirror at the far end of the 4.2-mm-long polymer waveguide reflects all channels back toward the AWG. The dispersion of such a device could be tuned over a 1300-ps/nm range over a 40-GHz bandwidth. In another AWG-based approach shown in Figure 8.27, the demultiplexed channels are focused onto a array of liquid-crystal elements that reflect each channel back after imposing an electrically controllable phase shift on it [134]. Such a device was used to compensate dispersion of a WDM signal occupying the entire L band. In a 2009 experiment, the liquid-crystal array was replaced with lens-shaped trenches filled with optical resins [135].

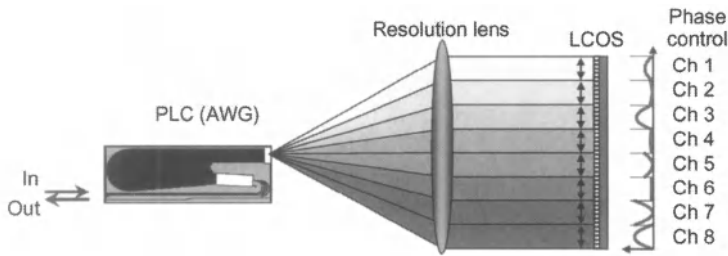


Figure 8.27: A tunable dispersion compensator in which a liquid-crystal array is used for tuning dispersion. (After Ref. [134]; ©2009 IEEE.)

8.6.2 Higher-Order Dispersion Management

When the bit rate of a single channel exceeds 40 Gb/s (through the use of time-division multiplexing, e.g.), the third- and higher-order dispersive effects begin to influence the optical signal. For example, the bit slot at a bit rate of 160 Gb/s is only 6.25 ps wide. An RZ optical signal at such a high bit rate consists of pulses of width <5 ps. Equation (2.4.33) can be used to estimate the maximum transmission distance L , limited by the TOD β_3 , when the second-order dispersion (GVD) is fully compensated. The result is found to be

$$L \leq 0.034(|\beta_3|B^3)^{-1}. \quad (8.6.2)$$

This limitation is shown in Figure 2.13 by the dashed line. At a bit rate of 200 Gb/s, L is limited to about 50 km and drops to only 3.4 km at 500 Gb/s if we use a typical value of $\beta_3 = 0.08 \text{ ps}^3/\text{km}$. Clearly, it is essential to develop devices that can compensate for both the GVD and TOD in a tunable fashion when the single-channel bit rate exceeds 100 Gb/s [136]–[151].

The simplest solution to TOD compensation is provided by DCFs designed to have a negative dispersion slope so that both β_2 and β_3 have opposite signs in comparison with the standard fibers. The necessary conditions for designing such fibers is given in Eq. (8.2.5). Thus, the DCFs used for the compensation of dispersion slope in WDM systems also provide control of third-order dispersion for each channel. The only problem with DCFs is that their dispersion characteristics are not easily tunable. As a result, system performance can be easily compromised if link dispersion changes because of temperature or other environmental changes.

The tunable compensation of dispersion slope is possible through optical filters. Planar lightwave circuits based on cascaded MZ interferometric filters have proved quite successful because of the programmable nature of such filters. As early as 1996, such a filter was designed to have a dispersion slope of -15.8 ps/nm^2 over a 170-GHz bandwidth and used to compensate third-order dispersion over 300 km of a dispersion-shifted fiber with $\beta_3 \approx 0.05 \text{ ps}/(\text{km}\cdot\text{nm}^2)$ at the operating wavelength [137]. Figure 8.28 compares the pulse shapes at the fiber output observed with and without β_3 compensation when a 2.1-ps pulse was transmitted over 100 km of such a fiber. The equalizing filter eliminates the oscillatory tail and reduces the width of the main peak from

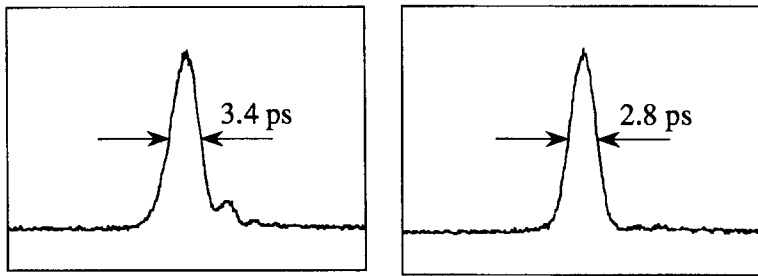


Figure 8.28: Pulse shapes after a 2.1-ps input pulse has propagated over 100 km of dispersion-shifted fiber ($\beta_2 = 0$). Left and right traces compare the improvement realized by compensating the third-order dispersion. (After Ref. [137]; ©1998 IEEE.)

3.4 to 2.8 ps. The residual increase in the pulse width from its input value of 2.1 ps is partly due to PMD.

Chirped fiber gratings are often preferred in practice because of their all-fiber nature. Long fiber gratings (~ 1 m) were developed by 1997 for this purpose [138]. In 1998, a nonlinearly chirped fiber grating was capable of compensating the TOD over 6 nm for distances as long as 60 km [139]. The cascading of several chirped gratings can provide a dispersion compensator that has arbitrary dispersion characteristics and is capable for compensating dispersion to all higher orders. Figure 8.29(a) shows a simple configuration for compensating the TOD β_3 of a fiber [140]. Two identical chirped fiber gratings are cascaded through an optical circulator, but one of them is flipped over so that their chirps are opposite in nature. As the group-delay slopes are equal but of opposite signs for the two gratings, the combination provides no net GVD. However, their TOD contributions add up to produce a nearly parabolic shape for the relative group delay, as shown in Figure 8.29(b).

An arrayed-waveguide grating [141] or a sampled fiber grating [60] can also compensate for second- and third-order dispersions simultaneously. Although a nonlinearly

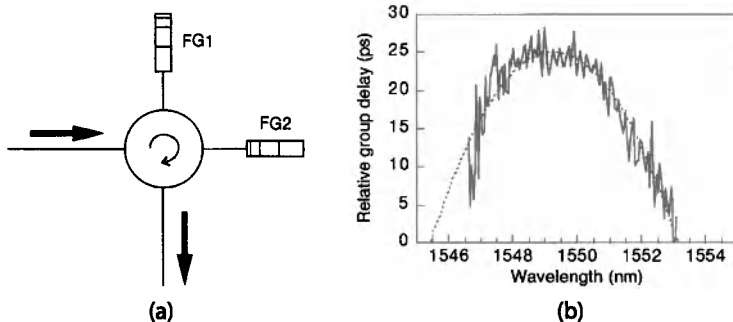


Figure 8.29: (a) Compensation of third-order dispersion by cascading two identical fiber gratings (FG). (b) Resulting group delay (solid curve) with a parabola (dotted curve) superimposed on it. (After Ref. [140]; ©2000 IEEE.)

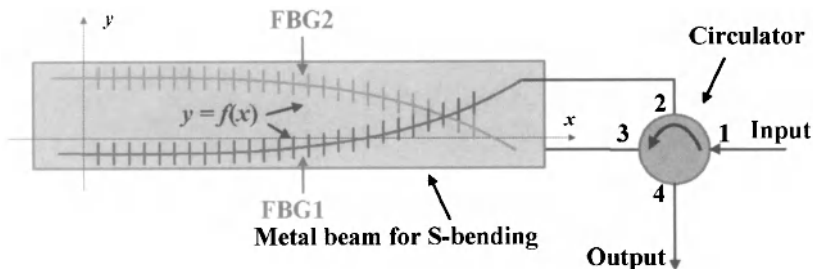


Figure 8.30: Schematic of a device used for tunable dispersion-slope compensation. Two uniform fiber Bragg gratings (FBG) are bent using a metal beam and cascaded using an optical circulator. (After Ref. [151]; ©2009 IEEE.)

chirped sampled grating can provide tunable dispersion for several channels simultaneously [142], its bandwidth is still limited. An arrayed-waveguide grating in combination with a spatial phase filter can provide dispersion-slope compensation over a bandwidth as large as 8 THz and should be suitable for 40-Gb/s multichannel systems [143]. The feasibility of transmitting a 100-Gb/s signal over 10,000 km has also been investigated using midspan optical phase conjugation in combination with third-order dispersion compensation [144].

Tunable compensation of dispersion slope can also be realized by integrating a segmented thin-film heater with a chirped fiber grating. In a 2004 experiment, a 4-cm-long grating was heated in a distributed fashion using 32 thin-film segments. A DCF module was used after the grating to ensure that accumulated second-order dispersion was zero at the center wavelength of the channel. It was possible to vary the dispersion slope from -20 to $+20$ ps/nm 2 by adjusting temperature distribution along the grating. In a different approach, two fiber gratings, linearly or nonlinearly chirped by applying a strain, were cascaded in series through an optical circulator [145]. Both gratings were mounted on a substrate that could be bent by moving a block. It was possible to change only the dispersion slope from nearly 0 to -58 ps/nm 2 over a bandwidth of 1.7 nm without affecting the Bragg wavelength of the grating.

Even unchirped fiber gratings can be used to realize tunable values of third-order dispersion. Figure 8.30 shows one design in which two unchirped gratings are mounted on a metal beam that can be bent by applying strain [151]. A four-port circulator was used to send the input signal through each grating in a cascaded fashion. The third-order dispersion of such a device could be tuned by adjusting the applied nonlinear strain, without changing the second-order dispersion. In this 2009 experiment, dispersion slope could be varied from -13.9 to -54.8 ps/nm 2 over a bandwidth of more than 2 nm.

Several experiments have explored the possibility of transmitting a single channel at bit rates of more than 200 Gb/s [152]–[157]. In a 1996 experiment [152], a 400-Gb/s signal was transmitted by transmitting 0.98-ps pulses inside a 2.5-ps time slot. Without compensation of third-order dispersion, the pulse broadened to 2.3 ps after 40 km and exhibited a long oscillatory tail extending over 6 ps, a characteristic feature of the third-order dispersion [110]. With partial compensation of third-order dispersion, the

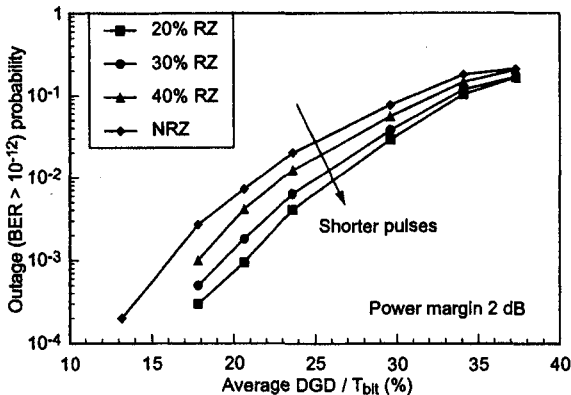


Figure 8.31: Outage probability as a function of average DGD (normalized to bit slot) for NRZ and RZ formats. Duty cycle is varied from 20 to 40% in the case of RZ pulses. (After Ref. [165]; ©2002 IEEE.)

oscillatory tail disappeared, and the pulse width reduced to 1.6 ps, making it possible to recover the 400-Gb/s data with high accuracy. Optical pulses shorter than 0.5 ps were used in 1998 to realize a bit rate of 640 Gb/s [153]. In a 2001 experiment, the bit rate was extended to 1.28 Tb/s by transmitting 380-fs pulses over 70 km of fiber [156]. The propagation of such short pulses requires compensation of second-, third-, and fourth-order dispersions simultaneously. The highest single-channel bit rate of 2.56 Tb/s was realized in a 2006 experiment in which a DQPSK signal (see Chapter 10) was transmitted over 160 km [157].

8.6.3 PMD Compensation

As discussed in Section 2.3.5, PMD leads to distortion of optical pulses because of random variations in the birefringence of an optical fiber along its length. This distortion occurs in addition to GVD-induced pulse broadening. The use of dispersion management can eliminate GVD-induced broadening but does not affect the PMD-induced degradation of an optical signal. For this reason, the control of PMD has become a major issue for modern dispersion-managed lightwave systems [158]–[172].

Before discussing the PMD-compensation technique, it is important to obtain an order-of-magnitude estimate of the maximum link length for uncompensated systems. Equation (2.3.17) shows that the RMS value of the differential group delay (DGD) for a link of length L is given by $\sigma_T = D_p \sqrt{L}$, where D_p is the PMD parameter. It is important to note that instantaneous values of DGD fluctuates with time over a wide range because of temperature and other environmental factors [159]. If DGD becomes so large that it exceeds the bit slot, a lightwave system stops functioning properly; this is referred to as fading or *outage* in analogy with a similar effect occurring in radio systems [158].

The performance of a PMD-limited system is quantified using the concept of the outage probability, which should be below a prescribed value (often set near 10^{-5}

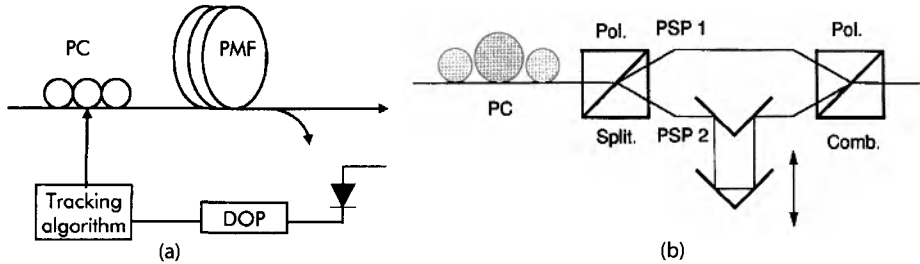


Figure 8.32: Schematic of two optical PMD compensators. PC, PMF, DOP, and PSP stand for polarization-maintaining fiber, degree of polarization, and principal state of polarization, respectively. (After Ref. [180]; ©2004 IEEE.)

or 5 min/year) for acceptable system performance. An accurate estimate of outage probability requires extensive numerical simulations [162]–[172]. In general, outage probability depends on the modulation format, among other things. Figure 8.31 shows outage probability as a function of average DGD for the NRZ and RZ formats assuming that outage occurs when the power penalty exceeds 2 dB to maintain a BER of 10^{-12} . In general, the performance is better for the RZ format with shorter pulses. The main conclusion is that the RMS value of DGD should only be a small fraction of the bit slot at a given bit rate B . The exact value of this fraction varies in the range of 0.1 to 0.15 depending on the modulation format and other design details of a lightwave system. If we use 10% as a conservative criterion for this ratio and use $B\sigma_T = 0.1$, the system length and the bit rate are related to the PMD parameter D_p of the fiber by the condition

$$B^2 L < (10 D_p)^{-2}. \quad (8.6.3)$$

We can use this condition to estimate the maximum PMD-limited distance over which a system can operate at a given bit rate B . In the case of “old” fiber links installed using standard fibers, the condition (8.6.3) becomes $B^2 L < 10^4$ (Gb/s)²-km, if we use $D_p = 1 \text{ ps}/\sqrt{\text{km}}$ as a representative value. Such fibers require PMD compensation at $B = 10 \text{ Gb/s}$ when the link length exceeds even 100 km. In contrast, modern fibers have typically D_p below $0.1 \text{ ps}/\sqrt{\text{km}}$. For systems designed using such fibers, $B^2 L$ can exceed 10^6 (Gb/s)²-km. As a result, PMD compensation is not necessary at 10 Gb/s but may be required at 40 Gb/s if the link length exceeds 600 km. It should be stressed that Eq. (8.6.3) provides only an order-of-magnitude estimate. Moreover, this condition can be relaxed when the technique of forward error correction (FEC) is employed at the receiver [165].

The preceding discussion shows that PMD can limit the performance of long-haul systems when the channel bit rate exceeds 10 Gb/s. For this reason, techniques for compensating PMD attracted attention as early as 1994 and have continued to evolve since then [173]–[188]. Here, we focus on optical techniques; electrical techniques are covered in the following section. Figure 8.32 shows the basic idea behind optical PMD compensation [180]. It consists of a polarization controller followed with a birefringent element such as a polarization-maintaining fiber. A feedback loop that measures degree of polarization uses this information to adjust the polarization controller.

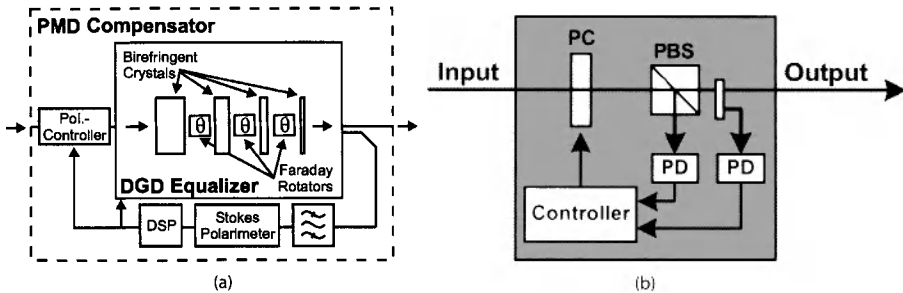


Figure 8.33: PMD compensators based on (a) birefringent crystals and (b) polarizers. DSP, PC, PBS, and PD stand for digital signal processor, polarization controller, polarization beam splitter, and photodiode, respectively. (After Ref. [184]; ©2005 IEEE.)

The performance of the simple PMD compensator shown in Figure 8.32(a) is limited by the fixed DGD provided by its birefringent element. Several other designs employ a variable DGD using a tunable delay line similar to that shown in Figure 8.32(b). The PMD-distorted signal is separated into its two components using a polarization controller and a polarization beam splitter. The two components are combined after introducing an adjustable delay in one branch through a variable delay line. A feedback loop is still needed to obtain an error signal that is used to adjust the polarization controller in response to environmental changes. The success of this technique depends on the ratio L/L_{PMD} for a fiber of length L , where $L_{\text{PMD}} = (T_0/D_p)^2$ and T_0 is the pulse width [189]. Considerable improvement is expected as long as this ratio does not exceed 4. Because L_{PMD} is close to 10,000 km for $D_p \approx 0.1 \text{ ps}/\sqrt{\text{km}}$ and $T_0 = 10 \text{ ps}$, such a PMD compensator can work over transoceanic distances for 10-Gb/s systems.

PMD compensation can also be realized using devices that do not employ optical fibers. Examples include LiNbO₃-based distributed compensator [179], ferroelectric liquid crystals, optical all-pass filters [181], birefringent chirped fiber gratings [116], and yttrium orthovanadate (YVO₄) crystals. Figure 8.33(a) shows a PMD compensator based on YVO₄ crystals that has been used successfully for lightwave systems operating at a bit rate of 160 Gb/s [184]. It consists of multiple birefringent YVO₄ crystals of different lengths separated from each other by Faraday rotators. More precisely, the length of each crystal is one half of the previous one. Because of this feature and the use of tunable Faraday rotators, such a device was capable of providing tunable DGD ranging from 0.31 to 4.70 ps in steps of 0.63 ps. In the 160-Gb/s experiment, a LiNbO₃-based polarization controller was used to scramble the state of polarization at the transmitter end and to ensure the detection of changes in instantaneous DGD at the receiver end.

Several other kinds of PMD compensators have been developed. A virtually imaged phased array, a device also sometimes used for GVD compensation, can be used for PMD compensation after suitable changes [186]. Such a device converts the frequency-dependent Jones matrix of the fiber link that is responsible for PMD to a frequency-independent constant matrix in a dynamic fashion. In a recent 160-Gb/s experiment, a polarizer-based PMD compensator shown in Figure 8.33(b) was employed with suc-

cess [188]. In this device, the orthogonally polarized components of the optical signal are detected using photodiodes, and the resulting currents are used to adjust a polarization controller in a dynamic fashion.

It should be stressed that most PMD compensators help to mitigate only the first-order PMD effects. At high bit rates, optical pulses are short enough, and their spectrum becomes wide enough, that the PSPs cannot be assumed to remain constant over the whole pulse spectrum. Higher-order PMD effects become of concern for lightwave systems operating at bit rates of 40 Gb/s or more. The compensation of second- and even third-order PMD may be necessary in some cases. In most cases, a first-order PMD compensator can increase the tolerable value of DGD by more than a factor of 3, resulting in a substantial increase in the transmission distance for PMD-compensated systems. In practice, a single PMD compensator cannot be used for all WDM channels. Rather, a separate PMD compensator is required for each channel. This fact makes PMD compensation along the fiber link a costly proposition for WDM systems. An electrical equalizer built into the receiver provide an alternative practical solution for both GVD and PMD compensation. We turn to this topic next.

8.7 Electronic Dispersion Compensation

Although electronic dispersion compensation attracted attention as early as 1990 because of its potentially low cost and ease of implementation in the form of a integrated-circuit chip within the receiver [190], it was only after 2000 that it advanced enough to become usable in real lightwave systems. [191]. The main limitation of electronic techniques is related to the speed of electronic circuits. Recent advances in digital signal processing (DSP) have made electronic compensation a practical tool not only for GVD but also for PMD.

8.7.1 Basic Idea behind GVD Precompensation

The philosophy behind electronic techniques for GVD compensation is that, even though the optical signal has been degraded by GVD, one should be able to equalize the effects of dispersion electronically if the fiber acts as a *linear system*. As we saw in Section 8.1.1, when the GVD effects dominate, the transfer function of a fiber link of length L can be written as

$$H_f(\omega) = \exp(i\omega^2 d_a/2), \quad d_a = \int_0^L \beta_2(z) dz, \quad (8.7.1)$$

where d_a is the dispersion accumulated along the entire fiber link. If the electric signal generated at the receiver recovers both the amplitude and phase of the optical signal, one may be able to compensate for GVD by passing it through a suitable electrical filter. Unfortunately, the use of direct detection recovers only the amplitude, making it impossible to apply such a filter.

The situation is different in the case of coherent detection. It is relatively easy to compensate for dispersion if a heterodyne receiver is used for signal detection. Such a

receiver first converts the optical signal into a microwave signal at the intermediate frequency ω_{IF} , while preserving both the amplitude and phase information. A microwave bandpass filter whose impulse response is governed by the transfer function,

$$H(\omega) = \exp[-i(\omega - \omega_{IF})^2 d_a/2], \quad (8.7.2)$$

restores the signal to its original form [192]. Indeed, as early as 1992, a 31.5-cm-long microstrip line was used for dispersion equalization [193]. Its use made it possible to transmit an 8-Gb/s signal over 188 km of standard fiber. In a 1993 experiment, the technique was extended to homodyne detection [194], and a 6-Gb/s signal could be recovered at the receiver after propagating over 270 km of standard fiber. Microstrip lines can be designed to compensate for GVD acquired over fiber lengths as long as 4,900 km for a lightwave system operating at a bit rate of 2.5 Gb/s [195].

In the case of direct-detection receivers, no linear equalization technique based on optical filters can recover a signal that has spread outside its allocated bit slot. Nevertheless, several nonlinear equalization techniques have been developed that permit recovery of the degraded signal [191]. In one method, the decision threshold, normally kept fixed at the center of the eye diagram, is varied from bit to bit depending on the preceding bits. In another, the decision about a given bit is made after examining the analog waveform over a multiple-bit interval surrounding the bit in question [190]. More recently, analog and digital signal processing techniques have been employed with considerable success.

Another possibility consists of processing the electrical signal at the transmitter such that it precompensates for the dispersion experienced within the fiber link. In this section, we focus first on the precompensation techniques and then consider the analog and digital techniques employed at the receiver end.

8.7.2 Precompensation at the Transmitter

Noting from Section 2.4.2 that the dispersion-induced pulse broadening is accompanied by a frequency chirp imposed on optical pulses, a simple scheme prechirps each optical pulse in the opposite direction by the correct amount. Prechirping in time can change the spectral amplitude $\tilde{A}(0, \omega)$ of input pulses in such a way that GVD-induced degradation is eliminated, or at least reduced substantially. Clearly, if the spectral amplitude is modified as

$$\tilde{A}(0, \omega) \rightarrow \tilde{A}(0, \omega) \exp(-i\omega^2 d_a/2), \quad (8.7.3)$$

the GVD will be compensated exactly, and the pulse will retain its shape at the fiber output. Although, it is not easy to implement this transformation, one can come close to it by prechirping optical pulses. For this reason, the prechirping technique attracted attention as early as 1988 and has been implemented in several experiments to increase the fiber-link length [198]–[205].

Prechirp Technique

Figure 8.34 can help us in understanding how prechirping helps. Without prechirp, optical pulses spread monotonically because of chirping induced by dispersion. How-

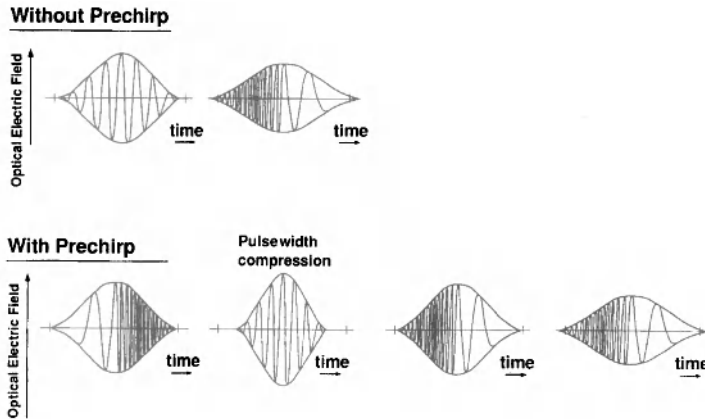


Figure 8.34: Changes in the electric field and pulse envelope with propagation for pulses with and without prechirp. (After Ref. [201]; ©1994 IEEE.)

ever, as discussed in Section 2.4.2 and shown in Figure 8.34, for values of C such that $\beta_2 C < 0$, a chirped pulse compresses initially before its width increases. For this reason, a suitably chirped pulse can propagate over longer distances before it broadens outside its allocated bit slot. As a rough estimate of the improvement, assume that pulse broadening by a factor of up to $\sqrt{2}$ is tolerable. Using Eq. (2.4.17), the maximum transmission distance is found to be

$$L = \frac{C + \sqrt{1 + 2C^2}}{1 + C^2} L_D, \quad (8.7.4)$$

where $L_D = T_0^2 / |\beta_2|$ is the dispersion length. For unchirped Gaussian pulses, $C = 0$ and $L = L_D$. However, L increases by 36% for $C = 1$. The maximum improvement by a factor of $\sqrt{2}$ occurs for $C = 1/\sqrt{2}$. These features clearly illustrate that the prechirp technique requires careful optimization. Even though the pulse shape is rarely Gaussian in practice, the prechirp technique can increase the transmission distance by 50% or more. As early as 1986, a super-Gaussian model predicted such an improvement [196].

In the case of direct modulation [197], the semiconductor laser chirps each optical pulse automatically through the carrier-induced index changes. Unfortunately, the chirp parameter C is negative for directly modulated semiconductor lasers. Since β_2 in the 1.55-μm wavelength region is also negative for standard fibers, the condition $\beta_2 C < 0$ is not satisfied. In fact, as seen in Figure 3.3, the chirp induced by direct modulation reduces the transmission distance drastically when standard fibers are used. In contrast, if dispersion-shifted fibers with normal GVD ($\beta_2 > 0$) are employed, the same chirp helps to improve the system performance. Indeed, such fibers are routinely employed for metro networks to incorporate prechirping-induced dispersion compensation.

In the case of external modulation, optical pulses are nearly chirp-free. The prechirp technique in this case imposes a frequency chirp on each pulse with a positive value of the chirp parameter C so that the condition $\beta_2 C < 0$ is satisfied. In a simple approach,

the carrier frequency of the DFB laser is first modulated (FM) before the laser output is passed to an external modulator for amplitude modulation (AM). The resulting optical signal exhibits simultaneous AM and FM [201]. This technique falls in the category of electronic compensation because the FM of the optical carrier is realized by modulating the current injected into the DFB laser by a small amount (~ 1 mA). Although such a direct modulation of the DFB laser also modulates the optical power sinusoidally, the magnitude is small enough that it does not interfere with the detection process.

To see how FM of the optical carrier generates a signal that consists of chirped pulses, we assume for simplicity that the pulse shape is Gaussian. The optical signal can then be written in the form

$$E(0,t) = A_0 \exp(-t^2/T_0^2) \exp[-i\omega_0(1 + \delta \sin \omega_m t)t], \quad (8.7.5)$$

where the carrier frequency ω_0 of the pulse is modulated sinusoidally at the frequency ω_m with a modulation depth δ . Near the pulse center, $\sin(\omega_m t) \approx \omega_m t$, and Eq. (8.7.5) becomes

$$E(0,t) \approx A_0 \exp\left[-\frac{1+iC}{2}\left(\frac{t}{T_0}\right)^2\right] \exp(-i\omega_0 t), \quad (8.7.6)$$

where the chirp parameter C is given by

$$C = 2\delta\omega_m\omega_0 T_0^2. \quad (8.7.7)$$

Both the sign and magnitude of the chirp parameter C can be controlled by changing the FM parameters δ and ω_m .

Phase modulation of the optical carrier also leads to a positive chirp, as can be verified by replacing Eq. (8.7.5) with

$$E(0,t) = A_0 \exp(-t^2/T_0^2) \exp[-i\omega_0 t + i\delta \cos(\omega_m t)] \quad (8.7.8)$$

and using $\cos x \approx 1 - x^2/2$. An advantage of the phase-modulation technique is that the external modulator itself can modulate the carrier phase. The simplest solution is to employ an external modulator whose refractive index can be changed electronically in such a way that it imposes a frequency chirp with $C > 0$ [198]. As early as 1991, a 5-Gb/s signal was transmitted over 256 km [199] using a LiNbO₃ modulator such that values of C were in the range of 0.6 to 0.8. Other types of modulators, such as an electroabsorption modulator [200] or a Mach–Zehnder modulator [202], can also chirp the optical pulse with $C > 0$, and have been used to demonstrate transmission beyond the dispersion limit [203]. With the development of DFB lasers integrated with an electroabsorption modulator, the implementation of the prechirp technique became quite practical. In a 1996 experiment, a 10-Gb/s NRZ signal was transmitted over 100 km of standard fiber using such a transmitter [204]. By 2005, link length of up to 250 km became possible through chirp management at the transmitter end [205].

Prechirping of an bit stream can also be accomplished through amplification of the optical signal. This technique, first demonstrated in 1989, amplifies the transmitter output using a semiconductor optical amplifier (SOA) operating in the gain-saturation regime [206]–[210]. Physically speaking, gain saturation leads to time-dependent variations in the carrier density, which, in turn, chirp the amplified pulse through changes

in the refractive index. The amount of chirp depends on the input pulse shape and is nearly linear over most of the pulse. The SOA not only amplifies the pulse but also chirps it such that the chirp parameter $C > 0$. Because of this chirp, the input pulse can be compressed in a fiber with $\beta_2 < 0$. Such a compression was observed in an experiment in which 40-ps input pulses were compressed to 23 ps when they were propagated over 18 km of standard fiber [206].

The potential of this technique for dispersion compensation was demonstrated in a 1989 experiment by transmitting a 16-Gb/s signal over 70 km of fiber [207]. From Eq. (8.1.1), in the absence of amplifier-induced chirp, the transmission distance at 16 Gb/s is limited to about 14 km for a fiber with $D = 15 \text{ ps}/(\text{km-nm})$. The use of the amplifier in the gain-saturation regime increased the transmission distance five-fold. It has the added benefit that it can compensate for the coupling and insertion losses that invariably occur in a transmitter by amplifying the signal before it is launched into the optical fiber. Moreover, this technique can be used for the simultaneous compensation of fiber losses and GVD if SOAs are used as in-line amplifiers [210].

A nonlinear medium can also be used to prechirp the pulse. As discussed in Section 2.6.2, the nonlinear phenomenon of SPM chirps an optical pulse as it propagates down a fiber. Thus, a simple prechirp technique consists of passing the transmitter output through a fiber of suitable length before launching it into the communication link. From Eq. (4.1.5), the phase of the optical signal is modulated by SPM as

$$A(0,t) = \sqrt{P(t)} \exp[i\gamma L_m P(t)], \quad (8.7.9)$$

where $P(t)$ is the power of the pulse and L_m is the length of the nonlinear fiber. In the case of Gaussian pulses for which $P(t) = P_0 \exp(-t^2/T_0^2)$, the chirp is nearly linear, and Eq. (8.7.9) can be approximated by

$$A(0,t) \approx \sqrt{P_0} \exp \left[-\frac{1+iC}{2} \left(\frac{t}{T_0} \right)^2 \right] \exp(-i\gamma L_m P_0), \quad (8.7.10)$$

where the chirp parameter is given by $C = 2\gamma L_m P_0$. For $\gamma > 0$, the chirp parameter C is positive, and is thus suitable for dispersion compensation. The transmission fiber itself can be used for chirping the pulse. This approach was suggested in a 1986 study; it indicated the possibility of doubling the transmission distance by optimizing the average power of the input signal [211].

Novel Modulation Formats

The dispersion problem can also be alleviated to some extent by adopting a suitable modulation format for the transmitted signal. In an interesting approach, referred to as *dispersion-supported transmission*, the frequency-shift keying (FSK) format was employed for signal transmission [212]–[216]. The FSK signal is generated by switching the laser wavelength by a constant amount $\Delta\lambda$ between 1 and 0 bits while leaving the power unchanged. During propagation inside the fiber, the two wavelengths travel at slightly different speeds. The time delay between the 1 and 0 bits is determined by the wavelength shift $\Delta\lambda$ and is given by $\Delta T = DL\Delta\lambda$. The wavelength shift $\Delta\lambda$ is chosen such that $\Delta T = 1/B$. Figure 8.35 shows schematically how the one-bit delay produces

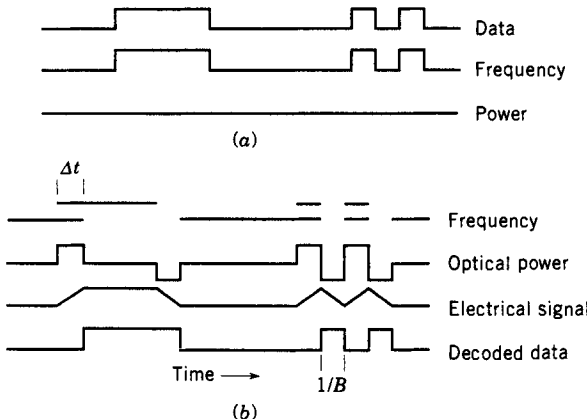


Figure 8.35: Dispersion compensation using FSK coding: (a) Optical frequency and power of the transmitted signal; (b) frequency and power of the received signal and the electrically decoded data. (After Ref. [212]; ©1994 IEEE.)

a three-level optical signal at the receiver. In essence, because of fiber dispersion, the FSK signal is converted into a signal whose amplitude is modulated. The signal can be decoded at the receiver by using an electrical integrator in combination with a decision circuit [212].

Several transmission experiments have shown the usefulness of the dispersion-supported transmission scheme [212]–[214]. All these experiments were concerned with increasing the transmission distance of a $1.55\text{-}\mu\text{m}$ lightwave system operating at 10 Gb/s or more over standard fibers exhibiting large GVD (about 17 ps/km/nm). In a 1994 experiment, transmission of a 10-Gb/s signal over 253 km of standard fiber was realized with this approach [212]. By 1998, in a 40-Gb/s field trial, the signal was transmitted over 86 km of standard fiber [214]. These values should be compared with the prediction of Eq. (8.1.1). Clearly, the transmission distance can be improved by a large factor by employing the FSK technique when the system is properly designed [216].

Another approach to increasing the transmission distance consists of employing a modulation format for which the signal bandwidth at a given bit rate is smaller compared with that of the standard on-off keying. One scheme makes use of *duobinary coding* [217]. This coding scheme reduces the signal bandwidth by 50% by adding two successive bits in the digital bit stream, thus forming a three-symbol duobinary code at half the bit rate. Since both the 01 and 10 combinations add to 1, the signal phase must be modified to distinguish between the two (see Section 10.1). Since the GVD-induced degradation depends on signal bandwidth, transmission distance is considerably larger for a duobinary signal [218]–[223].

In a 1994 experiment designed to compare the binary and duobinary schemes, a 10-Gb/s signal could be transmitted over distances 30 to 40 km longer by replacing binary coding with duobinary coding [218]. The duobinary scheme can be combined with the prechirp technique. Indeed, transmission of a 10-Gb/s signal over 160 km of a standard fiber was realized in 1994 by combining duobinary coding with an external

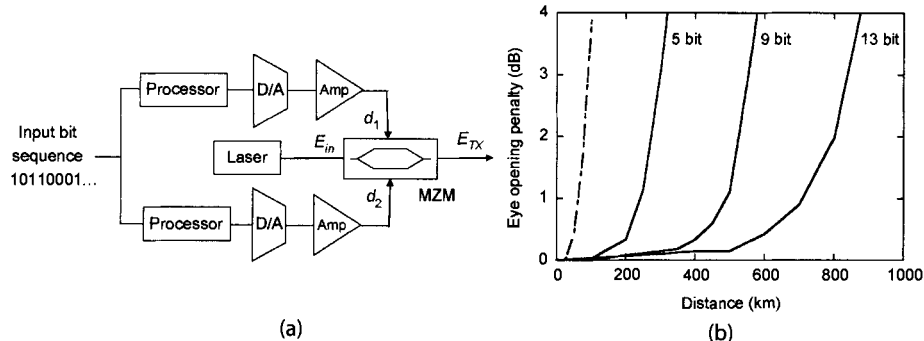


Figure 8.36: (a) Transmitter design and (b) eye-opening penalty versus distance for an electronic precompensation scheme. (After Ref. [224]; ©2005 IEEE.)

modulator capable of producing a frequency chirp with $C > 0$ [218]. Since chirping increases the signal bandwidth, it is hard to understand why it would help. It appears that phase reversals occurring in practice when a duobinary signal is generated are primarily responsible for improvement realized with duobinary coding [219]. Another dispersion-management scheme, called the *phase-shaped* binary transmission, has also been proposed to take advantage of phase reversals [220]. The use of duobinary transmission increases signal-to-noise requirements and requires decoding at the receiver. Despite these shortcomings, it is useful for upgrading the existing terrestrial lightwave systems to bit rates of 10 Gb/s and more [221]–[223].

Digital Signal Processing

Considerable progress has been made in recent years to implement the transformation given in Eq. (8.7.3) electronically within the transmitter as accurately as possible [224]–[226]. The basic idea is that this transformation is equivalent to a convolution in the time domain that can be carried out electronically using digital signal processing.

Figure 8.36(a) shows the scheme proposed in 2005. It makes use of digital signal processing together with digital-to-analog conversion to determine the exact amplitude and phase of each bit and then generate the entire bit stream by applying the resulting electronic signal to a dual-drive Mach–Zehnder modulator. The time-domain convolution that corresponds to the transformation given in Eq. (8.7.3) is calculated by using a look-up table of the incoming bit sequence stored in memory. The accuracy of the convolution depends on the number of consecutive bits employed for calculating it. Figure 8.36(b) shows the numerically estimated eye opening penalty as a function of fiber length when 5, 9, and 13 consecutive bits are used for this purpose and compares it with the uncompensated case (dashed curve). In the uncompensated case, a penalty of 2 dB occurred at 80 km (accumulated dispersion $d_a = 1360 \text{ ps/nm}$). With the 13-bit electronic precompensation, the link length could be increased to close to 800 km ($d_a = 13,600 \text{ ps/nm}$), indicating the dramatic improvement possible with such a scheme. In principle, any link length can be realized by increasing the number of consecutive bits employed for calculating the convolution more and more accurately.

A field-programmable gate array was used for digital signal processing in a 2007 experiment [225].

In a different approach to this problem, GVD was precompensated using only intensity modulation of the optical signal [226]. At a first sight, such an approach should fail because the transformation given in Eq. (8.7.3) cannot be realized through pure intensity modulation. However, in the case of direct detection, the phase information at the receiver is discarded. One can thus use the phase at the receiver end as an additional degree of freedom. For a given optical power pattern at the receiver, it is possible to find the predistorted injection current required for direct modulation of a semiconductor laser that will provide that pattern, provided one knows the specific relation between the intensity and phase for that laser. In the 2009 experiment, an artificial neural network was used to find the injection current, which was then used to modulate directly a semiconductor laser. The resulting 10-Gb/s signal could be transmitted over 190-km of standard fiber ($d_a \approx 3,500 \text{ ps/nm}$). Numerical simulations showed that dispersion precompensation over up to 350 km of fiber was possible with this technique.

8.7.3 Dispersion Compensation at the Receiver

Electronic dispersion compensation within the receiver is most attractive because it requires only suitably designed integrated-circuit chips [191]. With recent advances in the analog and digital signal processing, this approach has become realistic for modern lightwave systems [227]–[241]. The main difficulty lies in the fact that electronic logic circuits must operate at a high speed close to the bit rate, or the symbol rate if more than one bit/symbol is transmitted using advanced modulation formats (see Chapter 10). Dispersion-equalizing circuits operating at bit rates of 10 Gb/s were realized by 2000, and by 2007 such circuits were being used for systems operating at 40 Gb/s [234].

Direct-Detection Receivers

Since direct detection recovers only the amplitude of the transmitted signal, no linear equalization technique can recover a signal that has spread outside its allocated bit slot. Nevertheless, several nonlinear signal processing techniques, developed originally for radio and cable networks, have been adopted for lightwave systems. Two commonly used ones are known as the *feed-forward equalizer* (FFE) and the *decision-feedback equalizer* (DFE), and both of them have been realized in the form of integrated-circuit chips operating at bit rates of up to 40 Gb/s. Figure 8.37 shows a design in which the two equalizers are combined in series.

A feed-forward equalizer consists of a transversal filter in which the incoming electrical signal $x(t)$ is split into a number of branches using multiple tapped delay lines and their outputs are then combined back to obtain

$$y(t) = \sum_{m=0}^{N-1} c_m x(t - mT_c), \quad (8.7.11)$$

where N is the total number of taps, T_c is the delay time (about 50% of the bit slot), and c_m is the relative weight of m th tap. Tap weights are adjusted in a dynamic fashion

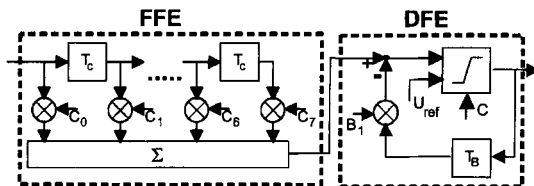


Figure 8.37: Electronic dispersion equalizer combining feed-forward and decision-feedback equalizers in series. (After Ref. [229]; ©2004 IEEE.)

using a control algorithm such that the receiver performance is improved [229]. The error signal for the control electronics may correspond to maximization of the “eye opening” or of the Q factor provided by an eye monitor within the receiver.

A decision-feedback equalizer, as its name suggests, makes use of the feedback provided by a decision circuit. More precisely, a fraction of the voltage at the output of the decision circuit is subtracted from the incoming signal. Often, such a circuit is combined with a feed-forward equalizer, as shown in Figure 8.37, to improve the overall performance [234]. Although digital signal processing (DSP) can be employed for both equalizers, such electronic circuits are realized in practice using analog signal processing because they consume less power. An advantage of such circuits is that they can also compensate for PMD simultaneously [233].

Another electronic equalizer, known as the *maximum likelihood signal estimator* (MLSE), is based on digital signal processing and thus requires an analog-to-digital converter after the photodetector [234]. It makes use of the Viterbi algorithm, conceived in 1967 and used widely in cellular networks. This algorithm works by examining multiple bits simultaneously and finding the most likely bit sequence for them. As it is not based on a specific form of distortion, an MLSE equalizer can compensate for both the GVD and PMD simultaneously.

A 2007 study was devoted to understand to what extent different electronic equalizers improve the performance of 10.7-Gb/s systems, making use of on-off keying with the RZ or the NRZ format, when they are affected by the GVD and PMD individually or simultaneously [233]. Figure 8.38 shows the measured optical SNR penalty as a function of fiber length ($D = 17 \text{ ps/km/nm}$) when the signal was affected only by GVD (negligible PMD along the link). Several points are noteworthy. First, the penalty is considerably smaller for the NRZ format compared with the RZ format in all cases. This is understood by recalling from Section 2.4 that optical pulses are wider (or signal bandwidth is smaller) in the case of the NRZ format. Second, the signal can be transmitted over longer distances when an electronic equalizer is employed. Assuming that at most a 2-dB penalty can be tolerated, the distance is 54% and 43% longer in the case of the NRZ and RZ formats, respectively, when the combination of FFE and DFE is employed. Third, the MLSE equalizer works better in both cases. In the case of the NRZ format, the fiber length increases from 50 to 110 km at the 2-dB penalty point.

The results for PMD compensation showed that the RZ format is more tolerant of the PMD than the NRZ format. The use of electronic equalizers improved considerably the PMD level that could be tolerated, and the most improved occurred again for

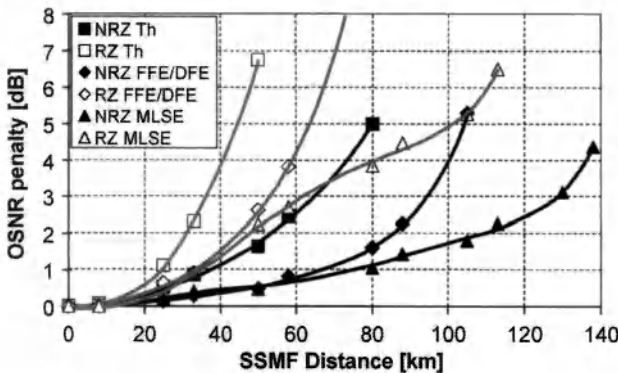


Figure 8.38: Measured optical SNR penalty as a function of fiber length ($D = 17 \text{ ps/km/nm}$) for RZ and NRZ formats when signal is affected only by GVD. (After Ref. [233]; ©2007 IEEE.)

the MLSE equalizer. However, when both the GVD and PMD were present simultaneously, the tolerable PMD level was comparable for the RZ and NRZ formats.

Coherent-Detection Receivers

Electronic compensation of dispersion can be carried out much more readily if both the signal amplitude and phase are detected at the receiver. Moreover, the compensation of PMD requires that this information be available for both polarization components of the received optical signal. The use of coherent detection makes this possible, and several experiments have implemented this approach in recent years [237]–[241].

Figure 8.39 shows a coherent receiver in which the use of phase and polarization diversity with four photodiodes permits the recovery of the amplitudes and phases for both polarization components. A polarization beam splitter splits the incoming signal into its orthogonally polarized components, E_x and E_y , which are then combined with the output of a local oscillator using two 3×3 couplers acting as 90° hybrids [237]. The four photodiodes recover the real and imaginary parts of $E_x E_{lo}^*$ and $E_y E_{lo}^*$, respectively, from which both the amplitude and phases can be obtained. The local oscillator converts the optical signal to the microwave domain while keeping its amplitude and phase intact.

Compensation of GVD is easily implemented in the frequency domain [240] using an all-pass filter whose transfer function is the inverse of that given in Eq. (8.7.1). This step requires digitization of the complex field, computation of its numerical Fourier transform, multiplication by $H(\omega)$, and then inverse Fourier transform of the resulting digital signal. All these steps can be implemented with digital signal processing.

GVD can also be compensated in the time domain by converting the transfer function in Eq. (8.7.1) to an impulse response by taking its Fourier transform:

$$h(t) = \sqrt{\frac{2\pi}{id_a}} \exp\left(-\frac{it^2}{2d_a}\right). \quad (8.7.12)$$

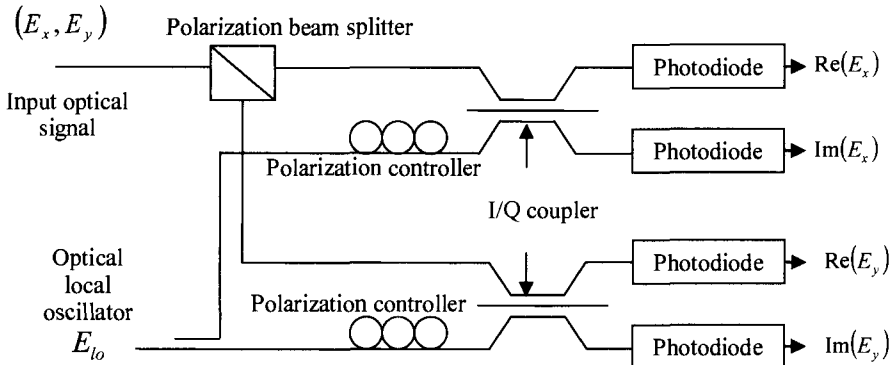


Figure 8.39: Schematic of a coherent receiver that recovers the real and imaginary parts of the polarization components E_x and E_y of the optical signal using a local oscillator. (After Ref. [239]; ©2008 OSA.)

It is not easy to implement this impulse response digitally because its infinite duration makes it noncausal. However, if the impulse response is truncated appropriately, it can be implemented using a finite-impulse-response filter with a tapped delay line [239]. The required number of taps depends both on the symbol rate and d_a ; it exceeds 200 for a 10 Gbaud signal transmitted over 4000 km of optical fiber.

Compensation of PMD can be carried out in the time domain using the inverse of the Jones matrix that corresponds to propagation of optical signal through the fiber link [240]. However, it is not easy to find this matrix. Moreover, the effects of PMD change in a dynamic fashion, indicating that this matrix also changes with time. In the case of modulation formats such as DPSK and QPSK (see Section 10.1), one solution is to construct the inverse matrix from the received signal itself using an algorithm known as the *constant modulus algorithm* [237]. Such an algorithm was used with success in a 2007 experiment in which a 42.8-Gb/s signal, modulated using the so-called dual-polarization QPSK (DP-QPSK) format was transmitted over 6400 km at a symbol rate of 10.7 Gbaud.

In the case of differential formats such as DPSK, the phase of the optical signal at the receiver can also be recovered without using a local oscillator by a technique known as self-coherent (see Section 10.2). In this scheme, the use of a Mach-Zender interferometer with one-bit delay between its two arms allows phase recovery. The same scheme can be employed even for traditional RZ and NRZ systems (making use of on-off keying) to recover the optical phase at the receiver and use it to construct the full optical field. Figure 8.40 shows how two photodetectors after the Mach-Zender interferometer can be used to reconstruct the field and use it for dispersion compensation with suitable electrical processing [241]. This technique was employed in a 2009 experiment in which a 10-Gb/s signal could be transmitted over nearly 500 km of standard fiber in spite of more than 8,000 ps/nm of dispersion accumulated over the fiber link. Numerical simulations indicated that dispersion over more than 2000 km of fiber link can be compensated with this approach.

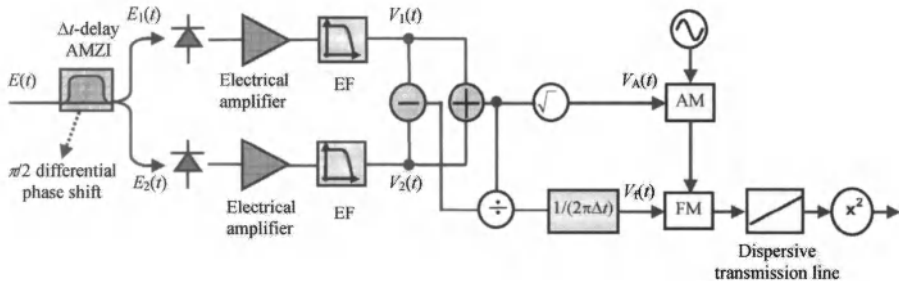


Figure 8.40: A receiver in which an asymmetric Mach–Zender interferometer (AMZI) recovers both the amplitude and phase of the optical signal and uses them for electronic dispersion compensation. (After Ref. [241]; ©2009 IEEE.)

Digital Backpropagation

Knowledge of the full optical field at the receiver permits another approach that can compensate not only for the dispersive effects but also for all kinds of nonlinear effects that degrade the signal during its transmission through the fiber link. This approach is known as *digital backpropagation* and is based on a simple idea: numerical backpropagation of the received signal, implemented with digital signal processing, should recover fully the original optical field at the transmitter end if all fiber-link parameters are known. This idea is attracting attention in recent years because of its potential for compensating for all degradations simultaneously [242]–[245].

It is not easy to implement backpropagation of the received signal digitally in real time because of the speed limit of current electronics [242]. In practice, each WDM channel is translated to the baseband (without the optical carrier) using coherent detection, resulting in a complex signal $E_k = A_k \exp(i\phi_k)$ for the k th channel. The analog-to-digital converter should sample this field with sufficient temporal resolution. The number of sample points per symbol is relatively small (2 to 4) with the current state of digital signal processing, and one must adopt up-sampling to ensure sufficient temporal resolution. However, it is not possible to process the entire time-domain signal simultaneously. A parallel scheme is typically employed using a finite-impulse-response filter, instead of the conventional Fourier transform technique. This scheme was used in a 2008 experiment in which three 6-Gbaud WDM channels were transmitted over 760 km using the binary PSK format and was found to perform better than two other dispersion-compensation techniques [244].

The compensation of polarization-multiplexed WDM channels is more complicated because it requires the recovery of both polarization components of the optical signal for each channel and their digital backpropagation by solving two coupled NLS equations. In a 2009 experiment [245], a detection scheme similar to that of Figure 8.39, was employed to recover the amplitudes and phases of the two polarization components after three 6-Gbaud WDM channels were transmitted over 1440 km of using a 80-km-long recirculating fiber loop. The digitized complex amplitudes were backpropagated with the split-step Fourier method [110]. The Q factor of the central channel after backpropagation depended on the step size. It increased from a low value of 4.5 dB to near

14 dB with a relatively large step size of 20 km. These results show that digital back-propagation is likely to become a practical technique with continuing improvements in the speed of electronics.

Problems

- 8.1** What is the dispersion-limited transmission distance for a 1.55- μm lightwave system making use of direct modulation at 10 Gb/s? Assume that frequency chirping broadens the Gaussian-shape pulse spectrum by a factor of 6 from its transform-limited width. Use $D = 17 \text{ ps}/(\text{km-nm})$ for fiber dispersion.
- 8.2** How much improvement in the dispersion-limited transmission distance is expected if an external modulator is used in place of direct modulation for the lightwave system of Problem 7.1?
- 8.3** Solve Eq. (8.1.2) by using the Fourier transform method. Use the solution to find an analytic expression for the pulse shape after a Gaussian input pulse has propagated to $z = L$ in a fiber with $\beta_2 = 0$.
- 8.4** Use the results of preceding problem and plot the pulse shape after a Gaussian pulse with a full width at half-maximum (FWHM) of 1 ps is transmitted over 20 km of dispersion-shifted fiber with $\beta_2 = 0$ and $\beta_3 = 0.08 \text{ ps}^3/\text{km}$. How would the pulse shape change if the sign of β_3 is inverted?
- 8.5** Use Eq. (8.1.3) to plot the pulse shapes for $C = -1, 0$, and 1 when 50-ps (FWHM) chirped Gaussian pulses are transmitted over 100 km of standard fiber with $D = 16 \text{ ps}/(\text{km-nm})$. You can neglect third-order dispersion.
- 8.6** The transfer function of an optical filter is given by

$$H(\omega) = \exp[-(1 + ib)\omega^2/\omega_f^2].$$

What is the impulse response of this filter? Use Eq. (8.1.5) to find the pulse shape at the filter output when an unchirped Gaussian pulse is launched at the input end of a fiber of length L . How would you optimize the filter to minimize the effect of fiber dispersion?

- 8.7** Use the results of the preceding problem to compare the pulse shapes before and after the filter when 30-ps (FWHM) Gaussian pulses are propagated over 100 km of fiber with $\beta_2 = -20 \text{ ps}^2/\text{km}$. Assume that the filter bandwidth is the same as the pulse spectral width and that the filter parameter b is optimized. What is the optimum value of b ?
- 8.8** Prove by using Eq. (8.1.5) that a DCF can provide dispersion compensation over the entire C band when the ratio S/D for the DCF is matched to that of the fiber used to construct the transmission link.
- 8.9** Solve Eqs. (8.3.2) and (8.3.3) and show that the transfer function of a Bragg grating is indeed given by Eq. (8.3.5).
- 8.10** Write a computer program to solve Eqs. (8.3.2) and (8.3.3) for chirped fiber gratings for which both δ and κ vary with z . Use it to plot the amplitude and

phase of the reflectivity of a grating in which the period varies linearly by 0.01% over the 10-cm length. Assume $\kappa L = 4$ and the Bragg wavelength of $1.55 \mu\text{m}$ at the input end of the grating.

- 8.11 Use the dispersion relation $q^2 = \delta^2 - \kappa^2$ of a Bragg grating to show that the second- and third-order dispersion parameters of the grating are given by Eq. (8.3.6).
- 8.12 Explain how a chirped fiber grating compensates for GVD. Derive an expression for the GVD parameter of such a grating when the grating period varies linearly by $\delta\Lambda$ over the grating length L .
- 8.13 A 5-cm-long sampled grating is designed with a sampling period of 1 mm. Each period contains a 0.4-mm-long subgrating with $0.5\text{-}\mu\text{m}$ modulation period. Plot the reflectivity spectrum by solving Eqs. (8.3.2) and (8.3.3) with $\kappa = 0.6 \text{ cm}^{-1}$.
- 8.14 Derive Eq. (8.4.1) for a Gires–Tournois filter and prove that it provides the dispersion given in Eq. (8.4.2).
- 8.15 Derive Eq. (8.4.1) for a Gires–Tournois filter and prove that it provides the dispersion given in Eq. (8.4.2).
- 8.16 Consider a lossless ring resonator formed using a directional coupler and find an expression for its transfer function. Prove its all-pass nature and find the phase shift provided by it as a function of frequency.
- 8.17 Explain how optical phase conjugation can be used to compensate for fiber dispersion. Prove that the FWM process inverts the signal spectrum.
- 8.18 Prove that both SPM and GVD can be compensated through midspan OPC only if the fiber loss $\alpha = 0$.
- 8.19 Prove that the phase conjugator should be located at a distance given in Eq. (8.5.7) when the frequency ω_c of the phase-conjugated field does not coincide with the signal frequency ω_s .
- 8.20 The prechirp technique is used for dispersion compensation in a 10-Gb/s light-wave system operating at $1.55 \mu\text{m}$ and transmitting the 1 bits as chirped Gaussian pulses of 40-ps width (FWHM). Pulse broadening by up to 50% can be tolerated. What is the optimum value of the chirp parameter C , and how far can the signal be transmitted for this optimum value? Use $D = 17 \text{ ps}/(\text{km-nm})$.
- 8.21 The prechirp technique of preceding Problem is implemented through frequency modulation of the optical carrier. Determine the modulation frequency for a maximum change of 10% from the average value.
- 8.22 Start the OptiPerformer software provided on the CD and open the file “40 Gbps - RZ and NRZ.osp” file in the folder Ch8. Run the program and plot the Q factor as a function of input power for the RZ and NRZ formats. Explain why Q peaks at a certain value of input power and why this value is higher for the RZ format. Study the eye diagrams at the peak Q in the two cases. Which format is better for 40-Gb/s systems and why?

References

- [1] A. Gnauck and R. Jopson, in *Optical Fiber Telecommunications*, Vol. 3A, I. P. Kaminow and T. L. Koch, Eds., Academic Press, Boston, 1997, Chap. 7.
- [2] J. Zyskind, R. Barry, G. Pendock, M. Cahill, and J. Ranka, in *Optical Fiber Telecommunications*, Vol. 4B, I. P. Kaminow and T. Li, Eds., Academic Press, Boston, 2002, Chap. 7.
- [3] A. E. Willner and B. Hoanca, in *Optical Fiber Telecommunications IV*, Vol. 4B, I. P. Kaminow and T. Li, Eds., Academic Press, Boston, 2002, Chap. 14.
- [4] M. Suzuki and N. Edagawa, *J. Lightwave Technol.* **21**, 916 (2003).
- [5] C. Lin, H. Kogelnik, and L. G. Cohen, *Opt. Lett.* **5**, 476 (1980).
- [6] A. J. Antos and D. K. Smith, *J. Lightwave Technol.* **12**, 1739 (1994).
- [7] K. Thyagarajan, R. K. Varshney, P. Palai, A. K. Ghatak, and I. C. Goyal, *IEEE Photon. Technol. Lett.* **8**, 1510 (1996).
- [8] M. Onishi, T. Kashiwada, Y. Ishiguro, Y. Koyano, M. Nishimura, and H. Kanamori, *Fiber Integ. Opt.* **16**, 277 (1997).
- [9] J. Liu, Y. L. Lam, Y. C. Chan, Y. Zhou, and J. Yao, *Fiber Integ. Opt.* **18**, 63 (1999).
- [10] J.-L. Auguste, R. Jindal, J.-M. Blondy, M. Clapeau, J. Marcou, B. Dussardier, G. Monnom, D. B. Ostrowsky, B. P. Pal, and K. Thyagarajan, *Electron. Lett.* **36**, 1689 (2000).
- [11] L. Grüner-Nielsen, S. N. Knudsen, B. Edvold, T. Veng, D. Magnussen, C. C. Larsen, and H. Damsgaard, *Opt. Fiber Technol.* **6**, 164 (2000).
- [12] L. Grüner-Nielsen, M. Wandel, P. Kristensen, C. Jørgensen, L. V. Jørgensen, B. Edvold, B. Palsdottir, and D. Jakobsen, *J. Lightwave Technol.* **23**, 3566 (2005).
- [13] R. W. Tkach, R. M. Derosier, A. H. Gnauck, A. M. Vengsarkar, D. W. Peckham, J. J. Zyskind, J. W. Sulhoff, and A. R. Chraplyvy, *IEEE Photon. Technol. Lett.* **7**, 1369 (1995).
- [14] H. Taga, M. Suzuki, N. Edagawa, S. Yamamoto, and S. Akiba, *IEEE J. Quantum Electron.* **34**, 2055 (1998).
- [15] C. D. Chen, T. Kim, O. Mizuhara, T. V. Nguyen, K. Ogawa, R. E. Tench, L. D. Tzeng, and P. D. Yeates, *Electron. Lett.* **35**, 648 (1999).
- [16] B. Bakhshi, M. F. Arend, M. Vaa, W. W. Patterson, R. L. Maybach, and N. S. Bergano, *Proc. Optical Fiber Commun. Conf.*, Paper PD2, 2001.
- [17] C. D. Poole, J. M. Wiesenfeld, D. J. DiGiovanni, and A. M. Vengsarkar, *J. Lightwave Technol.* **12**, 1746 (1994).
- [18] M. Eguchi, M. Koshiwa, and Y. Tsuji, *J. Lightwave Technol.* **14**, 2387 (1996).
- [19] S. Ramachandran, B. Mikkelsen, L. C. Cowsar, et al., *IEEE Photon. Technol. Lett.* **13**, 632 (2001).
- [20] M. Eguchi, *J. Opt. Soc. Am. B* **18**, 737 (2001).
- [21] S. Ramachandran, *J. Lightwave Technol.* **23**, 3426 (2005).
- [22] R. C. Youngquist, J. L. Brooks, and H. J. Shaw, *Opt. Lett.* **9**, 177 (1984).
- [23] C. D. Poole, C. D. Townsend, and K. T. Nelson, *J. Lightwave Technol.* **9**, 598 (1991).
- [24] R. Kashyap, *Fiber Bragg Gratings*, 2nd ed., Academic Press, Boston, 2009.
- [25] T. A. Birks, D. Mogilevtsev, J. C. Knight, and P. St. J. Russell, *IEEE Photon. Technol. Lett.* **11**, 674 (1999).
- [26] L. P. Shen, W.-P. Huang, G. X. Chen, and S. S. Jian, *IEEE Photon. Technol. Lett.* **15**, 540 (2003).
- [27] Y. Ni, L. Zhang, L. An, J. Peng, and C. Fan, *IEEE Photon. Technol. Lett.* **16**, 1516 (2004).
- [28] T. Fujisawa, K. Saitoh, K. Wada, and M. Koshiba, *Opt. Express* **14**, 893 (2006).

- [29] S. Yang, Y. Zhang, L. He, and S. Xie, *Opt. Lett.* **31**, 2830 (2006).
- [30] T. Matsui, K. Nakajima, and I. Sankawa, *J. Lightwave Technol.* **25**, 757 (2007).
- [31] S. Kim and C.-S. Kee, *Opt. Express* **17**, 15885 (2009).
- [32] D. K. W. Lam, B. K. Garside, and K. O. Hill, *Opt. Lett.* **7**, 291 (1982).
- [33] G. P. Agrawal, *Lightwave Technology: Components and Devices*, Wiley, Hoboken, NJ, 2004.
- [34] B. J. Eggleton, C. M. de Sterke, and R. E. Slusher, *J. Opt. Soc. Am. B* **16**, 587 (1999).
- [35] B. J. Eggleton, T. Stephens, P. A. Krug, G. Dhosi, Z. Brodzeli, and F. Ouellette, *Electron. Lett.* **32**, 1610 (1996).
- [36] T. Stephens, P. A. Krug, Z. Brodzeli, G. Dhosi, F. Ouellette, and L. Poladian, *Electron. Lett.* **32**, 1599 (1996).
- [37] N. M. Litchinister, B. J. Eggleton, and D. B. Pearson, *J. Lightwave Technol.* **15**, 1303 (1997).
- [38] K. Hinton, *J. Lightwave Technol.* **15**, 1411 (1997).
- [39] F. Ouellette, *Opt. Lett.* **12**, 622, (1987).
- [40] K. O. Hill, S. Thériault, B. Malo, F. Bilodeau, T. Kitagawa, D. C. Johnson, J. Albert, K. Takiguchi, T. Kataoka, and K. Hagimoto, *Electron. Lett.* **30**, 1755 (1994).
- [41] P. A. Krug, T. Stephens, G. Yoffe, F. Ouellette, P. Hill, and G. Dhosi, *Electron. Lett.* **31**, 1091 (1995).
- [42] W. H. Loh, R. I. Laming, X. Gu, M. N. Zervas, M. J. Cole, T. Widdowson, and A. D. Ellis, *Electron. Lett.* **31**, 2203 (1995).
- [43] W. H. Loh, R. I. Laming, N. Robinson, A. Cavaciuti, F. Vaninetti, C. J. Anderson, M. N. Zervas, and M. J. Cole, *IEEE Photon. Technol. Lett.* **8**, 944 (1996).
- [44] W. H. Loh, R. I. Laming, A. D. Ellis, and D. Atkinson, *IEEE Photon. Technol. Lett.* **8**, 1258 (1996).
- [45] D. Atkinson, W. H. Loh, J. J. O'Reilly, and R. I. Laming, *IEEE Photon. Technol. Lett.* **8**, 1085 (1996).
- [46] K. Ennser, M. N. Zervas, and R. I. Laming, *IEEE J. Quantum Electron.* **34**, 770 (1998).
- [47] S. V. Chernikov, J. R. Taylor, and R. Kashyap, *Opt. Lett.* **20**, 1586 (1995).
- [48] G. P. Agrawal and S. Radic, *IEEE Photon. Technol. Lett.* **6**, 995 (1994).
- [49] L. Zhang, K. Sugden, I. Bennion, and A. Molony, *Electron. Lett.* **31**, 477 (1995).
- [50] A. H. Gnauck, J. M. Wiesenfeld, L. D. Garrett, R. M. Derosier, F. Forghieri, V. Gusmeroli, and D. Scarano, *IEEE Photon. Technol. Lett.* **11**, 1503 (1999).
- [51] L. D. Garrett, A. H. Gnauck, F. Forghieri, V. Gusmeroli, and D. Scarano, *IEEE Photon. Technol. Lett.* **11**, 484 (1999).
- [52] K. Hinton, *Opt. Fiber Technol.* **5**, 145 (1999).
- [53] X. F. Chen, Z. B. Ma, C. Guang, Y. Meng, and X. L. Yang, *Microwave Opt. Tech. Lett.* **23**, 352 (1999).
- [54] I. Riant, S. Gurib, J. Gourhant, P. Sansonetti, C. Bungarzeau, and R. Kashyap, *IEEE J. Sel. Topics Quantum Electron.* **5**, 1312 (1999).
- [55] L. D. Garrett, A. H. Gnauck, R. W. Tkach, et al., *IEEE Photon. Technol. Lett.* **12**, 356 (2000).
- [56] B. J. Eggleton, P. A. Krug, L. Poladian, and F. Ouellette, *Electron. Lett.* **30**, 1620 (1994).
- [57] F. Ouellette, P. A. Krug, T. Stephens, G. Dhosi, and B. Eggleton, *Electron. Lett.* **31**, 899 (1995).
- [58] M. Ibsen, M. K. Durkin, M. J. Cole, and R. I. Laming, *IEEE Photon. Technol. Lett.* **10**, 842 (1998).

- [59] M. Ibsen, A. Fu, H. Geiger, and R. I. Laming, *Electron. Lett.* **35**, 982 (1999).
- [60] W. H. Loh, F. Q. Zhou, and J. J. Pan, *IEEE Photon. Technol. Lett.* **11**, 1280 (1999).
- [61] J. E. Rothenberg, H. Li, Y. Li, J. Popelek, Y. Wang, R. B. Wilcox, and J. Zweiback, *IEEE Photon. Technol. Lett.* **14**, 1309 (2002).
- [62] A. V. Buryak, K. Y. Kolossovski, and D. Y. Stepanov, *IEEE J. Quantum Electron.* **39**, 91 (2003).
- [63] H. Li, Y. Sheng, Y. Li, and J. E. Rothenberg, *J. Lightwave Technol.* **21**, 2074 (2003).
- [64] H. J. Lee and G. P. Agrawal, *IEEE Photon. Technol. Lett.* **15**, 1091 (2003); *Opt. Express* **12**, 5595 (2004).
- [65] H. Li, M. Li, Y. Sheng, and J. E. Rothenberg, *J. Lightwave Technol.* **25**, 2739 (2007).
- [66] H. Li, M. Li, and J. Hayashi, *Opt. Lett.* **34**, 938 (2009).
- [67] H. Ishii, F. Kano, Y. Tohmori, Y. Kondo, T. Tamamura, and Y. Yoshikuni, *IEEE J. Sel. Topics Quantum Electron.* **1**, 401 (1995).
- [68] L. J. Cimini, L. J. Greenstein, and A. A. M. Saleh, *J. Lightwave Technol.* **8**, 649 (1990).
- [69] A. H. Gnauck, C. R. Giles, L. J. Cimini, J. Stone, L. W. Stulz, S. K. Korotky, and J. J. Veselka, *IEEE Photon. Technol. Lett.* **3**, 1147 (1991).
- [70] C. K. Madsen, J. A. Walker, J. E. Ford, K. W. Goossen, T. N. Nielsen, and G. Lenz, *IEEE Photon. Technol. Lett.* **12**, 651 (2000).
- [71] X. Shu, K. Chisholm, and K. Sugden, *Opt. Lett.* **28**, 881 (2003).
- [72] M. Jablonski, Y. Takushima, and K. Kikuchi, *J. Lightwave Technol.* **19**, 1194 (2001).
- [73] D. Yang, C. Lin, W. Chen, and G. Barbarossa, *IEEE Photon. Technol. Lett.* **16**, 299 (2004).
- [74] X. Shu, K. Chisholm, and K. Sugden, *IEEE Photon. Technol. Lett.* **16**, 1092 (2004).
- [75] T. Ozeki, *Opt. Lett.* **17**, 375 (1992).
- [76] K. Takiguchi, K. Okamoto, S. Suzuki, and Y. Ohmori, *IEEE Photon. Technol. Lett.* **6**, 86 (1994).
- [77] M. Sharma, H. Ibe, and T. Ozeki, *J. Lightwave Technol.* **12**, 1759 (1994).
- [78] K. Takiguchi, K. Okamoto, and K. Moriwaki, *IEEE Photon. Technol. Lett.* **6**, 561 (1994).
- [79] K. Takiguchi, K. Okamoto, and K. Moriwaki, *J. Lightwave Technol.* **14**, 2003 (1996).
- [80] K. Takiguchi, K. Okamoto, T. Goh, and M. Itoh, *J. Lightwave Technol.* **21**, 2463 (2003).
- [81] K. Takiguchi, H. Takahashi, and T. Shibata, *Opt. Lett.* **33**, 1243 (2008).
- [82] C. K. Madsen and L. H. Zhao, *Optical Filter Design and Analysis: A Signal Processing Approach*, Wiley, New York, 1999.
- [83] G. Lenz and C. K. Madsen, *J. Lightwave Technol.* **17**, 1248 (1999).
- [84] C. K. Madsen, *J. Lightwave Technol.* **18**, 880 (2000).
- [85] C. K. Madsen, *J. Lightwave Technol.* **21**, 2412 (2003).
- [86] C. K. Madsen and G. Lenz, *IEEE Photon. Technol. Lett.* **10**, 994 (1998).
- [87] C. K. Madsen, G. Lenz, A. J. Bruce, M. A. Capuzzo, L. T. Gomez, and R. E. Scotti, *IEEE Photon. Technol. Lett.* **11**, 1623 (1999).
- [88] O. Schwebel, *J. Lightwave Technol.* **22**, 1380 (2004).
- [89] A. Yariv, D. Fekete, and D. M. Pepper, *Opt. Lett.* **4**, 52 (1979).
- [90] S. Watanabe, N. Saito, and T. Chikama, *IEEE Photon. Technol. Lett.* **5**, 92 (1993).
- [91] R. M. Jopson, A. H. Gnauck, and R. M. Derosier, *IEEE Photon. Technol. Lett.* **5**, 663 (1993).
- [92] M. C. Tatham, G. Sherlock, and L. D. Westbrook, *Electron. Lett.* **29**, 1851 (1993).
- [93] R. M. Jopson and R. E. Tench, *Electron. Lett.* **29**, 2216 (1993).

- [94] S. Watanabe and T. Chikama, *Electron. Lett.* **30**, 163 (1994).
- [95] C. R. Giles, V. Mizrahi, and T. Erdogan, *IEEE Photon. Technol. Lett.* **7**, 126 (1995).
- [96] S. Wabnitz, *IEEE Photon. Technol. Lett.* **7**, 652 (1995).
- [97] A. D. Ellis, M. C. Tatham, D. A. O. Davies, D. Nesser, D. G. Moodie, and G. Sherlock, *Electron. Lett.* **31**, 299 (1995).
- [98] M. Yu, G. P. Agrawal, and C. J. McKinstry, *IEEE Photon. Technol. Lett.* **7**, 932 (1995).
- [99] X. Zhang, F. Ebskamp, and B. F. Jorgensen, *IEEE Photon. Technol. Lett.* **7**, 819 (1995).
- [100] X. Zhang and B. F. Jorgensen, *Electron. Lett.* **32**, 753 (1996).
- [101] S. Watanabe and M. Shirasaki, *J. Lightwave Technol.* **14**, 243 (1996).
- [102] C. Lorattanasane and K. Kikuchi, *J. Lightwave Technol.* **15**, 948 (1997).
- [103] T. Merker, P. Meissner, and U. Feiste, *IEEE J. Sel. Topics Quantum Electron.* **6**, 258 (2000).
- [104] P. Kaewplung, T. Angkaew, and K. Kikuchi, *J. Lightwave Technol.* **21**, 1465 (2003).
- [105] G. L. Woods, P. Papaparaskova, M. Shtaif, I. Brener, and D. A. Pitt, *IEEE Photon. Technol. Lett.* **16**, 677 (2004).
- [106] S. L. Jansen, D. van den Borne, P. M. Krumrich, S. Spälter, G.-D. Khoe, and H. de Waardt, *IEEE J. Sel. Topics Quantum Electron.* **12**, 505 (2006).
- [107] J. Li, K. Xu, G. Zhou, J. Wu, and J. Lin, *J. Lightwave Technol.* **25**, 1986 (2007).
- [108] R. A. Fisher, B. R. Suydam, and D. Yevick, *Opt. Lett.* **8**, 611 (1983).
- [109] R. A. Fisher, Ed., *Optical Phase Conjugation*, Academic Press, Boston, 1983.
- [110] G. P. Agrawal, *Nonlinear Fiber Optics*, 4th ed., Academic Press, Boston, 2007.
- [111] G. P. Agrawal, in *Semiconductor Lasers: Past, Present, Future*, G. P. Agrawal, Ed., AIP Press, Woodbury, NY, 1995, Chap. 8.
- [112] A. D'Ottavi, F. Martelli, P. Spano, A. Mecozzi, and S. Scotti, *Appl. Phys. Lett.* **68**, 2186 (1996).
- [113] M. H. Chou, I. Brener, G. Lenz, et al., *IEEE Photon. Technol. Lett.* **12**, 82 (2000).
- [114] J. Yamawaku, H. Takara, T. Ohara, K. Sato, A. Takada, T. Morioka, O. Tadanaga, H. Miyazawa, and M. Asobe, *Electron. Lett.* **39**, 1144 (2003).
- [115] F. Matera, A. Mecozzi, M. Romagnoli, and M. Settembre, *Opt. Lett.* **18**, 1499 (1993).
- [116] A. E. Willner, K. M. Feng, J. Cai, S. Lee, J. Peng, and H. Sun, *IEEE J. Sel. Topics Quantum Electron.* **5**, 1298 (1999).
- [117] M. J. Erro, M. A. G. Laso, D. Benito, M. J. Garde, and M. A. Muriel, *IEEE J. Sel. Topics Quantum Electron.* **5**, 1332 (1999).
- [118] B. J. Eggleton, A. Ahuja, P. S. Westbrook, J. A. Rogers, P. Kuo, T. N. Nielsen, and B. Mikkelsen, *J. Lightwave Technol.* **18**, 1418 (2000).
- [119] T. Inui, T. Komukai, and M. Nakazawa, *Opt. Commun.* **190**, 1 (2001).
- [120] S. Matsumoto, T. Ohira, M. Takabayashi, K. Yoshiara, and T. Sugihara, *IEEE Photon. Technol. Lett.* **13**, 827 (2001).
- [121] L. M. Lunardi, D. J. Moss, et al., *J. Lightwave Technol.* **20**, 2136 (2002).
- [122] Z. Pan, Y. W. Song, C. Yu, Y. Wang, Q. Yu, J. Popelek, H. Li, Y. Li, and A. E. Willner, *J. Lightwave Technol.* **20**, 2239 (2002).
- [123] Y. W. Song, Z. Pan, et al., *J. Lightwave Technol.* **20**, 2259 (2002).
- [124] S. Ramachandran, S. Ghalmi, S. Chandrasekhar, I. Ryazansky, M. F. Yan, F. V. Dimarcello, W. A. Reed, and P. Wisk, *IEEE Photon. Technol. Lett.* **15**, 727 (2003).
- [125] D. J. Moss, M. Lamont, S. McLaughlin, G. Randall, P. Colbourne, S. Kiran, and C. A. Hulse, *IEEE Photon. Technol. Lett.* **15**, 730 (2003).

- [126] T. Sano, T. Iwashima, M. Katayama, T. Kanie, M. Harumoto, M. Shigehara, H. Suganuma, and M. Nishimura, *IEEE Photon. Technol. Lett.* **15**, 1109 (2003).
- [127] X. Shu, K. Sugden, P. Rhead, J. Mitchell, I. Felmeri, G. Lloyd, K. Byron, Z. Huang, I. Khrushchev, and I. Bennion, *IEEE Photon. Technol. Lett.* **15**, 1111 (2003).
- [128] N. Q. Ngo, S. Y. Li, R. T. Zheng, S. C. Tjin, and P. Shum, *J. Lightwave Technol.* **21**, 1568 (2003).
- [129] X. Chen, X. Xu, M. Zhou, D. Jiang, X. Li, J. Feng, and S. Xie, *IEEE Photon. Technol. Lett.* **16**, 188 (2004).
- [130] J. Kim, J. Bae, Y.-G. Han, S. H. Kim, J.-M. Jeong, and S. B. Lee, *IEEE Photon. Technol. Lett.* **16**, 849 (2004).
- [131] C. R. Doerr, R. Blum, L. L. Buhl, M. A. Cappuzzo, E. Y. Chen, A. Wong-Foy, L. T. Gomez, and H. Bulthuis, *IEEE Photon. Technol. Lett.* **18**, 1222 (2006).
- [132] C. R. Doerr, S. Chandrasekhar, and L. L. Buhl, *IEEE Photon. Technol. Lett.* **20**, 560 (2008).
- [133] S. Doucet, S. LaRochelle, and M. Morin, *J. Lightwave Technol.* **26**, 2899 (2008).
- [134] S. Sohma, K. Mori, H. Masuda, A. Takada, K. Seno, K. Suzuki, and N. Ooba, *IEEE Photon. Technol. Lett.* **21**, 1271 (2009).
- [135] Y. Ikuma and T. Tsuda, *J. Lightwave Technol.* **27**, 5202 (2009).
- [136] M. Onishi, T. Kashiwada, Y. Koyano, Y. Ishiguro, M. Nishimura, and H. Kanamori, *Electron. Lett.* **32**, 2344 (1996).
- [137] K. Takiguchi, S. Kawanishi, H. Takara, A. Himeno, and K. Hattori, *J. Lightwave Technol.* **16**, 1647 (1998).
- [138] M. Durkin, M. Ibsen, M. J. Cole, and R. I. Laming, *Electron. Lett.* **33**, 1891 (1997).
- [139] T. Komukai and M. Nakazawa, *Opt. Commun.* **154**, 5 (1998).
- [140] T. Komukai, T. Inui, and M. Nakazawa, *IEEE J. Quantum Electron.* **36**, 409 (2000).
- [141] H. Tsuda, K. Okamoto, T. Ishii, K. Naganuma, Y. Inoue, H. Takenouchi, and T. Kurokawa, *IEEE Photon. Technol. Lett.* **11**, 569 (1999).
- [142] Y. Xie, S. Lee, Z. Pan, J. X. Cai, A. E. Willner, V. Grubsky, D. S. Starodubov, E. Salik, and J. Feinberg, *IEEE Photon. Technol. Lett.* **12**, 1417 (2000).
- [143] H. Takenouchi, T. Ishii, and T. Goh, *Electron. Lett.* **37**, 777 (2001).
- [144] P. Kaewplung, R. Angkaew, and K. Kikuchi, *IEEE Photon. Technol. Lett.* **13**, 293 (2001).
- [145] C. S. Goh, S. Y. Set, and K. Kikuchi, *IEEE Photon. Technol. Lett.* **16**, 524 (2004).
- [146] S. Matsumoto, M. Takabayashi, K. Yoshiara, T. Sugihara, T. Miyazaki, and F. Kubota, *IEEE Photon. Technol. Lett.* **16**, 1095 (2004).
- [147] T. Inui, T. Komukai, K. Mori, and T. Morioka, *J. Lightwave Technol.* **23**, 2039 (2005).
- [148] J. Kwon, S. Kim, S. Roh, and B. Lee, *IEEE Photon. Technol. Lett.* **18**, 118 (2006).
- [149] B. Dabarsyah, C. S. Goh, S. K. Khijwania, S. Y. Set, K. Katoh, and K. Kikuchi, *J. Lightwave Technol.* **25**, 2711 (2007).
- [150] X. Shu, E. Turitsyna, K. Sugden, and I. Bennion, *Opt. Express* **16**, 12090 (2008).
- [151] S. Kim, J. Bae, K. Lee, S. H. Kim, J.-M. Jeong, and S. B. Lee, *Opt. Express* **17**, 4336 (2009).
- [152] S. Kawanishi, H. Takara, T. Morioka, O. Kamatani, K. Takiguchi, T. Kitoh, and M. Saruwatari, *Electron. Lett.* **32**, 916 (1996).
- [153] M. Nakazawa, E. Yoshida, T. Yamamoto, E. Yamada, and A. Sahara, *Electron. Lett.* **34**, 907 (1998).
- [154] T. Yamamoto, E. Yoshida, K. R. Tamura, K. Yonenaga, and M. Nakazawa, *IEEE Photon. Technol. Lett.* **12**, 355, (2000).

- [155] M. D. Pelusi, X. Wang, F. Futami, K. Kikuchi, and A. Suzuki, *IEEE Photon. Technol. Lett.* **12**, 795 (2000).
- [156] M. Nakazawa, T. Yamamoto, and K. R. Tamura, *Electron. Lett.* **36**, 2027 (2000); T. Yamamoto and M. Nakazawa, *Opt. Lett.* **26**, 647 (2001).
- [157] H. G. Weber, R. Ludwig, S. Ferber, C. Schmidt-Langhorst, M. Kroh, V. Marembert, C. Boerner, and C. Schubert, *J. Lightwave Technol.* **24**, 4616 (2006).
- [158] C. D. Poole and J. Nagel, in *Optical Fiber Telecommunications*, Vol. 3A, I. P. Kaminow and T. L. Koch, Eds., Academic Press, San Diego, CA, 1997, Chap. 6.
- [159] M. Karlsson, J. Brentel, and P. A. Andrekson, *J. Lightwave Technol.* **18**, 941 (2000).
- [160] H. Kogelnik, R. M. Jopson, and L. E. Nelson, in *Optical Fiber Telecommunications*, Vol. 4A, I. P. Kaminow and T. Li, Eds., Academic Press, Boston, 2002, Chap. 15.
- [161] A. E. Willner, S. M. Reza, M. Nezam, L. Yan, Z. Pan, and M. C. Hauer, *J. Lightwave Technol.* **22**, 106 (2004).
- [162] H. Bülow, *IEEE Photon. Technol. Lett.* **10**, 696 (1998).
- [163] R. Khosravani and A. E. Willner, *IEEE Photon. Technol. Lett.* **13**, 296 (2001).
- [164] P. Lu, L. Chen, and X. Bao, *J. Lightwave Technol.* **20**, 1805 (2002).
- [165] H. Sunnerud, M. Karlsson, C. Xie, and P. A. Andrekson, *J. Lightwave Technol.* **20**, 2204 (2002).
- [166] J. N. Damask, G. Gray, P. Leo, G. Simer, K. Rochford, and D. Veasey, *IEEE Photon. Technol. Lett.* **15**, 48 (2003).
- [167] J. Kissing, T. Gravemann, and E. Voges, *IEEE Photon. Technol. Lett.* **15**, 611 (2003).
- [168] P. J. Winzer, H. Kogelnik, and K. Ramanan, *IEEE Photon. Technol. Lett.* **16**, 449 (2004).
- [169] E. Forestieri and G. Prati, *J. Lightwave Technol.* **22**, 988 (2004).
- [170] G. Biondini, W. L. Kath, and C. R. Menyuk, *J. Lightwave Technol.* **22**, 1201 (2004).
- [171] M. Boroditsky, M. Brodsky, N. J. Frigo, P. Magill, C. Antonelli, and A. Mecozzi, *IEEE Photon. Technol. Lett.* **17**, 345 (2005).
- [172] N. Cvijetic, S. G. Wilson, and D. Y. Qian, *J. Lightwave Technol.* **26**, 2118 (2008).
- [173] T. Takahashi, T. Imai, and M. Aiki, *Electron. Lett.* **30**, 348 (1994).
- [174] C. Francia, F. Bruyère, J. P. Thiéry, and D. Penninckx, *Electron. Lett.* **35**, 414 (1999).
- [175] R. Noé, D. Sandel, M. Yoshida-Dierolf, et al., *J. Lightwave Technol.* **17**, 1602 (1999).
- [176] T. Merker, N. Hahnenkamp, and P. Meissner, *Opt. Commun.* **182**, 135 (2000).
- [177] H. Y. Pua, K. Peddanarappagari, B. Zhu, C. Allen, K. Demarest, and R. Hui, *J. Lightwave Technol.* **18**, 832 (2000).
- [178] H. Sunnerud, C. Xie, M. Karlsson, R. Samuelsson, and P. A. Andrekson, *J. Lightwave Technol.* **20**, 368 (2002).
- [179] R. Noé, D. Sandel, and V. Mirvoda, *IEEE J. Sel. Topics Quantum Electron.* **10**, 341 (2004).
- [180] S. Lanne and E. Corbel, *J. Lightwave Technol.* **22**, 1033 (2004).
- [181] C. K. Madsen, M. Cappuzzo, E. J. Laskowski, et al., *J. Lightwave Technol.* **22**, 1041 (2004).
- [182] H. F. Haunstein, W. Sauer-Greff, A. Dittrich, K. Sticht, and R. Urbansky, *J. Lightwave Technol.* **22**, 1169 (2004).
- [183] P. B. Phua, H. A. Haus, and E. P. Ippen, *J. Lightwave Technol.* **22**, 1280 (2004).
- [184] S. Kieckbusch, S. Ferber, H. Rosenfeldt, et al., *J. Lightwave Technol.* **23**, 165 (2005).
- [185] L. Yan, X. S. Yao, M. C. Hauer, and A. E. Willner, *J. Lightwave Technol.* **24**, 3992 (2006).
- [186] H. Miao, A. M. Weiner, L. Mirkin, and P. J. Miller, *IEEE Photon. Technol. Lett.* **20**, 545 (2008).

- [187] A. Dogariu, P. N. Ji, L. Cimponeriu, and T. Wang, *Opt. Commun.* **282**, 3706 (2009).
- [188] M. Daikoku, T. Miyazaki, I. Morita, T. Hattori, H. Tanaka, and F. Kubota, *J. Lightwave Technol.* **27**, 451 (2009).
- [189] D. Mahgerefteh and C. R. Menyuk, *IEEE Photon. Technol. Lett.* **11**, 340 (1999).
- [190] J. H. Winters and R. D. Gitlin, *IEEE Trans. Commun.* **38**, 1439 (1990); J. H. Winters, *J. Lightwave Technol.* **8**, 1487 (1990).
- [191] A. Shanbhag, Q. Yu, and J. Choma, *Optical Fiber Telecommunications*, Vol. 5A, I. P. Kaminow and T. Li, and A. E. Willner, Eds., Academic Press, Boston, 2008, Chap. 18.
- [192] K. Iwashita and N. Takachio, *J. Lightwave Technol.* **8**, 367 (1990).
- [193] N. Takachio, S. Norimatsu, and K. Iwashita, *IEEE Photon. Technol. Lett.* **4**, 278 (1992).
- [194] K. Yonenaga and N. Takachio, *IEEE Photon. Technol. Lett.* **5**, 949 (1993).
- [195] S. Yamazaki, T. Ono, and T. Ogata, *J. Lightwave Technol.* **11**, 603 (1993).
- [196] G. P. Agrawal and M. J. Potasek, *Opt. Lett.* **11**, 318 (1986).
- [197] G. P. Agrawal, *Semiconductor Lasers*, 2nd ed., Van Nostrand Reinhold, New York, 1993.
- [198] F. Koyama and K. Iga, *J. Lightwave Technol.* **6**, 87 (1988).
- [199] A. H. Gnauck, S. K. Korotky, J. J. Veselka, J. Nagel, C. T. Kemmerer, W. J. Minford, and D. T. Moser, *IEEE Photon. Technol. Lett.* **3**, 916 (1991).
- [200] E. Devaux, Y. Sorel, and J. F. Kerdiles, *J. Lightwave Technol.* **11**, 1937 (1993).
- [201] N. Henmi, T. Saito, and T. Ishida, *J. Lightwave Technol.* **12**, 1706 (1994).
- [202] J. C. Cartledge, H. Debrégeas, and C. Rolland, *IEEE Photon. Technol. Lett.* **7**, 224 (1995).
- [203] J. A. J. Fells, M. A. Gibbon, I. H. White, et al., *Electron. Lett.* **30**, 1168 (1994).
- [204] K. Morito, R. Sahara, K. Sato, and Y. Kotaki, *IEEE Photon. Technol. Lett.* **8**, 431 (1996).
- [205] D. Mahgerefteh, Y. Matsui, C. Liao, et al., *Electron. Lett.* **41**, 543 (2005).
- [206] G. P. Agrawal and N. A. Olsson, *Opt. Lett.* **14**, 500 (1989).
- [207] N. A. Olsson, G. P. Agrawal, and K. W. Wecht, *Electron. Lett.* **25**, 603 (1989).
- [208] N. A. Olsson and G. P. Agrawal, *Appl. Phys. Lett.* **55**, 13 (1989).
- [209] G. P. Agrawal and N. A. Olsson, *IEEE J. Quantum Electron.* **25**, 2297 (1989).
- [210] G. P. Agrawal and N. A. Olsson, U.S. Patent 4,979,234 (1990).
- [211] M. J. Potasek and G. P. Agrawal, *Electron. Lett.* **22**, 759 (1986).
- [212] B. Wedding, B. Franz, and B. Junginger, *J. Lightwave Technol.* **12**, 1720 (1994).
- [213] B. Wedding, K. Koffers, B. Franz, D. Mathoorasing, C. Kazmierski, P. P. Monteiro, and J. N. Matos, *Electron. Lett.* **31**, 566 (1995).
- [214] W. Idler, B. Franz, D. Schlump, B. Wedding, and A. J. Ramos, *Electron. Lett.* **35**, 2425 (1998).
- [215] K. Perlicki and J. Siuzdak, *Opt. Quantum Electron.* **31**, 243 (1999).
- [216] J. A. V. Morgado and A. V. T. Cartaxo, *IEE Proc. Optoelect.* **148**, 107 (2001).
- [217] M. Schwartz, *Information, Transmission, Modulation, and Noise*, 4th ed., McGraw-Hill, New York, 1990, Sec. 3.10.
- [218] G. May, A. Solheim, and J. Conradi, *IEEE Photon. Technol. Lett.* **6**, 648 (1994).
- [219] D. Penninckx, L. Pierre, J.-P. Thiery, B. Clesca, M. Chbat, and J.-L. Beylat, *Electron. Lett.* **32**, 1023 (1996).
- [220] D. Penninckx, M. Chbat, L. Pierre, and J.-P. Thiery, *IEEE Photon. Technol. Lett.* **9**, 259 (1997).
- [221] K. Yonenaga and S. Kuwano, *J. Lightwave Technol.* **15**, 1530 (1997).
- [222] T. Ono, Y. Yano, K. Fukuchi, T. Ito, H. Yamazaki, M. Yamaguchi, and K. Emura, *J. Lightwave Technol.* **16**, 788 (1998).

- [223] W. Kaiser, T. Wuth, M. Wichers, and W. Rosenkranz, *IEEE Photon. Technol. Lett.* **13**, 884 (2001).
- [224] R. I. Killey, P. M. Watts, V. Mikhailov, M. Glick, and P. Bayvel, *IEEE Photon. Technol. Lett.* **17**, 714 (2005).
- [225] P. M. Watts, R. Waegemans, M. Glick, P. Bayvel, and R. I. Killey, *J. Lightwave Technol.* **25**, 3089 (2007).
- [226] S. Warm, C.-A. Bunge, T. Wuth, and K. Petermann, *IEEE Photon. Technol. Lett.* **21**, 1090 (2009).
- [227] F. Cariati, F. Martini, P. Chiappa, and R. Ballentin, *Electron. Lett.* **36**, 889 (2000).
- [228] A. J. Weiss, *IEEE Photon. Technol. Lett.* **15**, 1225 (2003).
- [229] F. Buchali and H. Bülow, *J. Lightwave Technol.* **22**, 1116 (2004).
- [230] V. Curri, R. Gaudino, A. Napoli, and P. Poggiolini, *IEEE Photon. Technol. Lett.* **16**, 2556 (2004).
- [231] O. E. Agazzi, M. R. Hueda, H. S. Carrer, and D. E. Crivelli, *J. Lightwave Technol.* **23**, 749 (2005).
- [232] T. Foggi, E. Forestieri, G. Colavolpe, and G. Prati, *J. Lightwave Technol.* **24**, 3073 (2006).
- [233] J. M. Gene, P. J. Winzer, S. Chandrasekhar, and H. Kogelnik, *J. Lightwave Technol.* **25**, 1735 (2007).
- [234] H. Bülow, F. Buchali, and A. Klekamp, *J. Lightwave Technol.* **26**, 158 (2008).
- [235] P. Poggiolini and G. Bosco, *J. Lightwave Technol.* **26**, 3041 (2008).
- [236] A. C. Singer, N. R. Shanbhag, and H.-M. Bae, *IEEE Sig. Proc. Mag.* **25** (6), 110 (2008).
- [237] S. J. Savory, G. Gavioli, R. I. Killey, and P. Bayvel, *Opt. Express* **15**, 2120 (2007).
- [238] E. Ip and J. M. Kahn, *J. Lightwave Technol.* **25**, 2033 (2007).
- [239] S. J. Savory, *Opt. Express* **16**, 804 (2008).
- [240] M. S. Alfiad, et al., *J. Lightwave Technol.* **27**, 3590 (2009).
- [241] M. E. McCarthy, J. Zhao, A. D. Ellis, and P. Gunning, *J. Lightwave Technol.* **27**, 5327 (2009).
- [242] X. Li, X. Chen, G. Goldfarb, E. Mateo, I. Kim, F. Yaman, and G. Li, *Opt. Express* **16**, 880 (2008).
- [243] E. Ip and J. M. Kahn, *J. Lightwave Technol.* **26**, 3416 (2008).
- [244] G. Goldfarb, E. M. G. Taylor, and G. Li, *IEEE Photon. Technol. Lett.* **20**, 1887 (2008).
- [245] Yaman and G. Li, *IEEE Photon. Journal* **1**, 144 (2009).

Chapter 9

Control of Nonlinear Effects

As we saw in Chapter 8, with the use of dispersion compensation, dispersion ceases to be a limiting factor for lightwave systems. Indeed, the performance of modern long-haul systems is typically limited by the nonlinear effects introduced in Section 2.6. In this chapter we focus on the techniques used to manage the nonlinear effects. Section 9.1 shows how nonlinear effects limit a long-haul fiber link and introduces the two main techniques used to reduce their impact. Section 9.2 focuses on the formation of optical soliton in fibers with constant dispersion and how they can be used to advantage for transmitting information. In soliton-based systems, optical pulses representing 1 bits are much shorter than the bit slot, and their shape inside the fiber is maintained by carefully balancing the dispersive and nonlinear effects. Dispersion-managed solitons are considered in Section 9.3 with an emphasis on dispersion maps that ensure the periodic evolution of such solitons over long link lengths. Section 9.4 deals with pseudo-linear systems in which fiber dispersion is used to broaden short optical pulses so much that their peak power is reduced by a large factor over most of the fiber link. Overlapping of neighboring pulses still produces intrachannel nonlinear effects, and the techniques used for controlling them are discussed in Section 9.5.

9.1 Impact of Fiber Nonlinearity

The use of dispersion management in combination with optical amplifiers can extend the length of a WDM system to several thousand kilometers. If the optical signal is regenerated electronically every 300 km or so, such a system works well as the nonlinear effects do not accumulate over long lengths. In contrast, if the signal is maintained in the optical domain by cascading many amplifiers, the nonlinear effects such as self-phase modulation (SPM) and cross-phase modulation (XPM) ultimately limit the system performance [1]. For this reason, the impact of nonlinear effects on the performance of dispersion-managed systems has been investigated extensively [2]–[32]. In this section we study how the nonlinear effects influence a dispersion-managed system and how their impact can be minimized with a suitable choice of system parameters.

9.1.1 System Design Issues

In the absence of nonlinear effects, the use of dispersion management ensures that each pulse is confined to its bit slot when the optical signal arrives at the receiver, even if pulses have spread over multiple slots during their transmission. Moreover, it is immaterial whether dispersion is compensated at the transmitter end, receiver end, or periodically within the fiber link. Any dispersion map can be used as long as the accumulated group-velocity dispersion (GVD) vanishes at the end of a link of length L ($d_a \equiv \int_0^L \beta_2(z) dz = 0$). The performance of such a system is only limited by the SNR degradation induced by amplifier noise. Since SNR can be improved by increasing input optical power, link length can be made arbitrarily long in principle.

However, the nonlinear effects are not negligible for long-haul WDM systems when channel powers exceed a few milliwatts, and the transmission distance is often limited by the nonlinear effects. Moreover, as seen in Section 7.8, an optimum power level exists at which the system performs best. Dispersion management is essential for long-haul systems to ensure that the system is not limited by GVD-induced pulse broadening. However, different dispersion maps can lead to different Q factors at the receiver end even when $d_a = 0$ for all of them [2]. This is so because the dispersive and nonlinear effects do not act on the signal independently. More specifically, degradation induced by the nonlinear effects depends on the local value of $d_a(z)$ at any distance z within the fiber link.

The major nonlinear phenomenon affecting the performance of a single isolated channel is the SPM. The propagation of an optical bit stream inside a dispersion-managed system is governed by the NLS equation (7.1.4) that can be written as

$$i \frac{\partial A}{\partial z} - \frac{\beta_2}{2} \frac{\partial^2 A}{\partial t^2} + \gamma |A|^2 A = \frac{i}{2} (g_0 - \alpha) A, \quad (9.1.1)$$

where we have ignored the noise term to simplify the following discussion. In a dispersion-managed system, the three fiber parameters (β_2 , γ , and α) are functions of z because of their different values in two or more fiber sections used to form the dispersion map. The gain parameter g_0 is also a function of z because of loss management. Its functional form depends on whether a lumped or a distributed amplification scheme is employed.

Equation (9.1.1) is solved numerically to analyze the performance of dispersion-managed systems. As was done in Section 7.1.2, it is useful to eliminate the gain and loss terms in this equation with the transformation $A(z, t) = \sqrt{P_0 p(z)} U(z, t)$ and write it in terms of $U(z, t)$ as

$$i \frac{\partial U}{\partial z} - \frac{\beta_2}{2} \frac{\partial^2 U}{\partial t^2} + \gamma P_0 p(z) |U|^2 U = 0, \quad (9.1.2)$$

where P_0 is the input peak power and $p(z)$ governs variations in the peak power of the signal along the fiber link through

$$p(z) = \exp \left(\int_0^z [g_0(z) - \alpha(z)] dz \right). \quad (9.1.3)$$

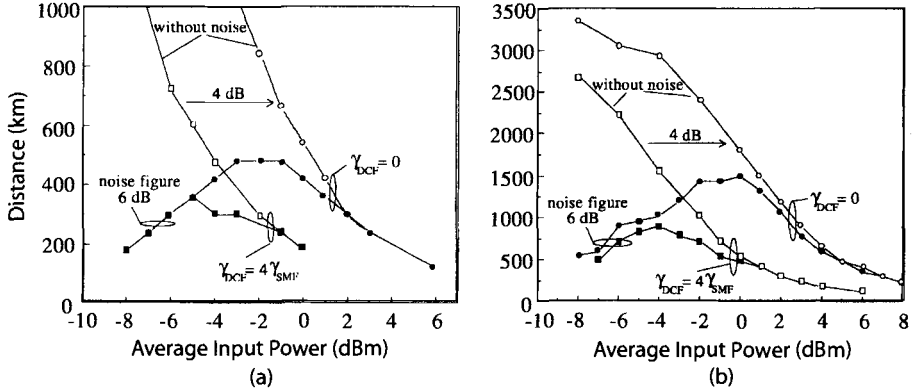


Figure 9.1: Maximum transmission distance as a function of average input power for a 40-Gb/s dispersion-managed system designed with the (a) NRZ and (b) RZ formats. The filled and empty symbols show numerical data obtained with and without amplifier noise, respectively. (After Ref. [8]; ©1997 IEEE.)

If losses are compensated in a periodic fashion, $p(z_m) = 1$, where $z_m = mL_A$ is the location of the m th amplifier and L_A is the amplifier spacing. In the case of lumped amplifiers, $g_0 = 0$ within the fiber link, and $p(z) = \exp[-\int_0^z \alpha(z) dz]$. Equation (9.1.2) shows that the effective nonlinear parameter $\gamma_e(z) \equiv \gamma p(z)$ is also z -dependent because of changes in the signal power induced by fiber losses and optical amplifiers. In particular, when lumped amplifiers are used, the nonlinear effects are strongest just after signal amplification and become negligible in the tail end of each fiber section between two amplifiers.

There are two major design issues for any dispersion-managed system: What is the optimum dispersion map and which modulation format provides the best performance? Both of these issues have been studied by solving the NLS equation (9.1.2) numerically [4]–[27]. Although attention was initially focused on the NRZ format, the performance of RZ and NRZ formats was compared starting in 1996, both numerically and experimentally, under realistic operating conditions [8]–[14]. As an example, Figure 9.1 shows the numerical results for the (a) NRZ and (b) RZ formats by plotting the maximum transmission distance L at which eye opening is reduced by 1 dB at the receiver of a 40-Gb/s system as average launched power is increased [8]. The periodic dispersion map consisted of 50 km of standard fiber with $D = 16 \text{ ps}/(\text{km-nm})$, $\alpha = 0.2 \text{ dB/km}$, and $\gamma = 1.31 \text{ W}^{-1}/\text{km}$, followed by 10 km of dispersion-compensating fiber (DCF) with $D = -80 \text{ ps}/(\text{km-nm})$, $\alpha = 0.5 \text{ dB/km}$, and $\gamma = 5.24 \text{ W}^{-1}/\text{km}$. Optical amplifiers with 6-dB noise figure were placed 60 km apart and compensated total fiber losses within each map period. The duty cycle was 50% in the case of the RZ format.

As discussed earlier and evident from Figure 9.1, distance can be continuously increased in the absence of amplifier noise by decreasing the launched power (open squares). However, when noise is included, an optimum power level exists for which the link length is maximum. This distance is less than 400 km when the NRZ format is employed but becomes larger by about a factor of 3 when the RZ format is implemented

with a 50% duty cycle. The reason behind this improvement can be understood by noting that the dispersion length is relatively small (<5 km) for RZ pulses propagating inside a standard fiber. As a result, RZ-format pulses spread quickly and their peak power is reduced considerably compared with the NRZ case. This reduction in the peak power lowers the impact of SPM.

Figure 9.1 also shows how the buildup of nonlinear effects within DCFs affects the system performance. In the case of RZ format, maximum distance is below 900 km at an input power level of -4 dBm because of the DCF-induced nonlinear degradation (filled squares). Not only DCFs have a larger nonlinear parameter because of their smaller core size, pulses are also compressed inside them to their original width, resulting in much higher peak powers. If the nonlinear effects can be suppressed within DCF, maximum distance can be increased close to 1,500 km by launching higher powers. This improvement can be realized in practice by using an alternate dispersion-compensating device requiring shorter lengths (such as a two-mode DCF or a fiber grating). In the case of NRZ format, the link length is limited to below 500 km even when nonlinear effects are negligible within DCFs.

As seen from Figure 9.1, the nonlinear effects play an important role in dispersion-managed systems whenever a DCF is used because its smaller core size enhances optical intensities (manifested through a larger value of the γ parameter). Placement of the amplifier after the DCF helps since the signal is then weak enough that the nonlinear effects are less important in spite of a small core area of DCFs. The optimization of system performance using different dispersion maps has been the subject of intense study. In a 1994 experiment, a 1,000-km-long fiber loop containing 31 fiber amplifiers was used to study three different dispersion maps [2]. The maximum transmission distance of 12,000 km at a bit rate of 5 Gb/s was realized for the case in which short sections of normal-GVD fibers were used to compensate for the anomalous GVD of long sections. In a 1995 experiment, the transmission distance of a 80-Gb/s signal, obtained by multiplexing eight 10-Gb/s channels with 0.8-nm channel spacing, was found to be limited to 1,171 km because of the onset of various nonlinear effects [3].

The choice between the RZ and NRZ formats is not always so obvious as it depends on many other design parameters. As early as 1995, an experiment as well as numerical simulations indicated that a 10-Gb/s signal can be transmitted over 2,245 km using the NRZ format with 90-km amplifier spacing, provided the link dispersion is not fully compensated [6]. A similar conclusion was reached in a 1999 experiment in which RZ and NRZ formats were compared for a 10-Gb/s system [14]. Figure 9.2 shows the recirculating loop used in this experiment. Because of cost considerations, most laboratory experiments employ a fiber loop in which the optical signal is forced to recirculate many times to simulate a long-haul lightwave system. Two optical switches determine how long a pseudorandom bit stream circulates inside the loop before it reaches the receiver. The loop length and the number of round trips set the total transmission distance. The loop shown in Figure 9.2 contains two 102-km sections of standard fiber and two 20-km DCFs. A filter with a 1-nm bandwidth reduces the buildup of broadband ASE noise. The 10-Gb/s signal could be transmitted over 2,040 km with both the RZ and NRZ formats when launched power was properly optimized. However, it was necessary to add a 38-km section of standard fiber in front of the receiver in the NRZ case so that dispersion was not fully compensated.

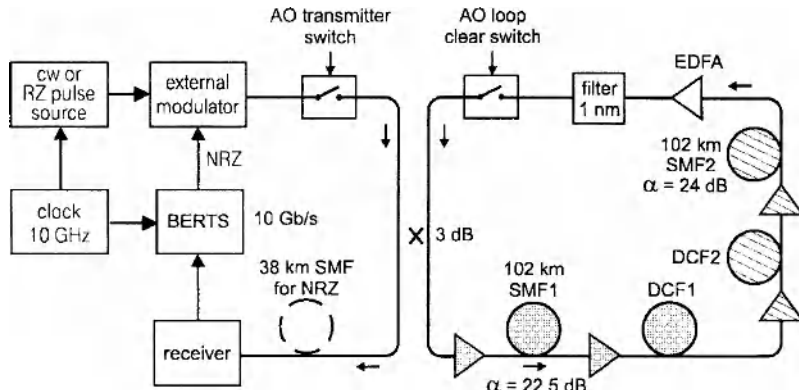


Figure 9.2: Recirculating fiber loop used to demonstrate the transmission of a 10-Gb/s signal over 2,040 km of standard fiber. Two acousto-optic (AO) switches control the timing of signal into and out of the loop. BERTS stands for bit-error-rate test set. (After Ref. [14]; ©1999 IEEE.)

Perfect compensation of GVD in each map period is not generally the best solution in the presence of nonlinear effects. A numerical approach is generally used to optimize the design of dispersion-managed lightwave systems [4]–[13]. In general, local GVD should be kept relatively large, while minimizing the average dispersion for all channels. In a 1998 experiment, a 40-Gb/s signal was transmitted over 2,000 km of standard fiber using a novel dispersion map [15]. The distance could be increased to 16,500 km at a lower bit rate of 10 Gb/s by placing an optical amplifier right after the DCF within the recirculating fiber loop [16]. Since the nonlinear effects were not negligible, it is believed that soliton properties played an important role in this experiment (see Section 9.2).

A systematic study based on the NLS equation (9.1.2) shows that although the NRZ format can be used at 10 Gb/s, the RZ format is superior in most practical situations for lightwave systems operating at bit rates of 40 Gb/s or higher [8]–[20]. Even at 10 Gb/s, the RZ format can be used to design systems that are capable of transmitting data over a distance of up to 10,000 km over standard fibers [22]. Such a performance is not realizable with the NRZ format. For this reason, the focus of this chapter is high-speed systems designed with the RZ format.

9.1.2 Semianalytic Approach

Although the NLS equation (9.1.2) must be solved numerically for a realistic modeling of lightwave systems, considerable insight can be gained by adopting a semianalytic approach in which the dispersive and nonlinear effects are considered for a single optical pulse representing an isolated 1 bit. In this case, Eq. (9.1.2) can be reduced to solving a set of two ordinary differential equations using a variational approach [17]. The moment method can also be employed for this purpose [1]. Both methods assume that each optical pulse maintains its shape even though its amplitude, width, and chirp may change during propagation. As was seen in Section 2.4, a chirped Gaussian pulse

maintains its functional form in the linear case ($\gamma = 0$). If the nonlinear effects are relatively weak in each fiber section compared with the dispersive effects, the pulse is likely to retain its Gaussian shape approximately even when nonlinear effects are included.

At a distance z inside the fiber, the envelope of a chirped Gaussian pulse has the form

$$U(z, t) = a \exp[-\frac{1}{2}(1 + iC)t^2/T^2 + i\phi], \quad (9.1.4)$$

where a is the amplitude, T is the width, C is the chirp, and ϕ is the phase. All four parameters vary with z . The variational or the moment method can be used to obtain four ordinary differential equations governing the evolution of these four parameters along the fiber link [1]. The phase equation can be ignored as it does not couple to the other three equations. The amplitude equation can be integrated to find that the product a^2T does not vary with z and is related to the input pulse energy E_0 as $E_0 = \sqrt{\pi}P_0a^2(z)T(z) = \sqrt{\pi}P_0T(0)$ as $a(0) = 1$. Thus, we only need to solve the following two coupled equations:

$$\frac{dT}{dz} = \frac{\beta_2(z)C}{T}, \quad (9.1.5)$$

$$\frac{dC}{dz} = (1 + C^2) \frac{\beta_2(z)}{T^2} + \frac{\gamma(z)p(z)E_0}{\sqrt{2\pi}T}. \quad (9.1.6)$$

Details of loss and dispersion managements appear in these equations through the z dependence of three parameters β_2 , γ , and p . Equations (9.1.5) and (9.1.6) require values of three pulse parameters at the input end, namely the width T_0 , chirp C_0 , and energy E_0 , before they can be solved. The pulse energy E_0 is related to the average power launched into the fiber link through the relation $P_{av} = \frac{1}{2}BE_0 = (\sqrt{\pi}/2)P_0(T_0/T_b)$, where T_b is the duration of bit slot at the bit rate B .

Consider first the linear case by setting $\gamma(z) = 0$. In this case, E_0 plays no role because pulse-propagation details are independent of the initial pulse energy. Equations (9.1.5) and (9.1.6) can be solved analytically in the linear case and have the following general solution:

$$T^2(z) = T_0^2 + 2 \int_0^z \beta_2(z)C(z) dz, \quad C(z) = C_0 + \frac{1 + C_0^2}{T_0^2} \int_0^z \beta_2(z) dz, \quad (9.1.7)$$

where details of the dispersion map are included through $\beta_2(z)$. This solution looks complicated but it is easy to perform integrations for a two-section dispersion map. The values of T and C at the end of the map period $z = L_{map}$ are given by

$$T_1 = T_0[(1 + C_0d)^2 + d^2]^{1/2}, \quad C_1 = C_0 + (1 + C_0^2)d, \quad (9.1.8)$$

where the dimensionless parameter d is defined as

$$d = \frac{1}{T_0^2} \int_0^{L_{map}} \beta_2(z) dz = \frac{\bar{\beta}_2 L_{map}}{T_0^2}, \quad (9.1.9)$$

and $\bar{\beta}_2$ is the average value of the dispersion parameter over the map period L_{map} .

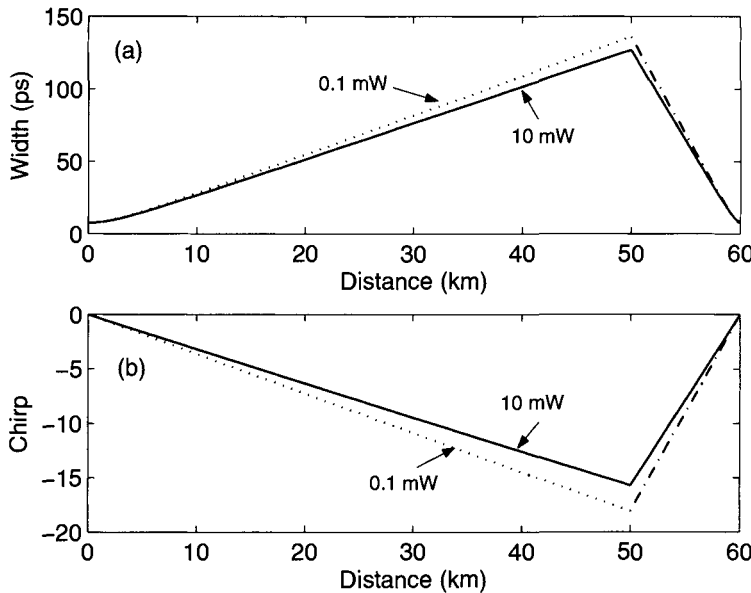


Figure 9.3: (a) Pulse width and (b) chirp at the end of successive amplifiers for several values of average input power for the 40-Gb/s system with a periodic dispersion map used in Figure 9.1.

As is evident from Eq. (9.1.8), when nonlinear effects are negligible, the final pulse parameters depend only on the average dispersion, and not on details of the dispersion map. This is exactly what one would expect when the theory of Section 2.6 is applied to a linear system. If the dispersion map is designed such that $\bar{\beta}_2 = 0$, both T and C return to their input values at $z = L_{\text{map}}$. In the case of a periodic dispersion map, each pulse would recover its original shape after each map period if $d = 0$. However, when the average GVD of the dispersion-managed link is not zero, T and C change after each map period, and pulse evolution is not periodic.

To study how the nonlinear effects governed by the γ term in Eq. (9.1.8) affect the pulse parameters, we can solve Eqs. (9.1.5) and (9.1.6) numerically. Figure 9.3 shows the evolution of pulse width and chirp over the first 60-km span for an isolated pulse in a 40-Gb/s bit stream using the same two-section dispersion map employed for Figure 9.1 (50-km standard fiber followed with 10 km of DCF). Solid lines represent 10-mW launched power. Dotted lines show the low-power case for comparison. In the first 50-km section, pulse broadens by a factor of about 15, but it is compressed back in the DCF because of dispersion compensation. Although the nonlinear effects modify both the pulse width and chirp, changes are not large even for a 10-mW launched power. In particular, the width and chirp are almost recovered after the first 60-km span.

The situation changes considerably if the pulse is allowed to propagate over many map periods. Figure 9.4 shows the pulse width and chirp after each amplifier (spaced 60-km apart) over a distance of 3,000 km (50 map periods). At a relatively low power level of 1 mW, the input values are almost recovered after each map period as dispersion is fully compensated. However, as the launched power is increased beyond 1 mW, the

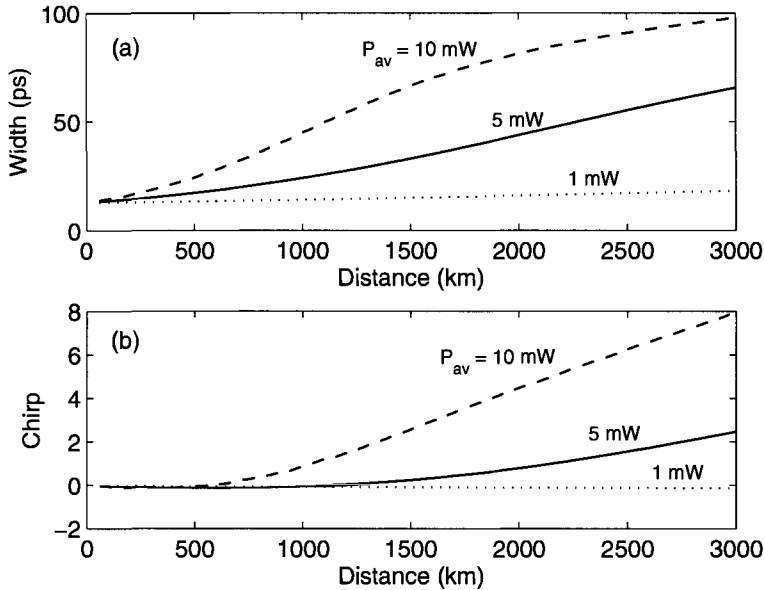


Figure 9.4: (a) Pulse width and (b) chirp at the end of successive amplifiers for three values of average input power for a 40-Gb/s system with the periodic dispersion map used in Figure 9.1.

nonlinear effects start to dominate, and the pulse width and chirp begin to deviate considerably from their input values, in spite of dispersion compensation. Even for $P_{av} = 5 \text{ mW}$, pulse width becomes larger than the bit slot after a distance of about 1,000 km, and the situation is worse for $P_{av} = 10 \text{ mW}$. Thus, the optimum power level is close to 1 mW if the objective is to minimize the impact of nonlinear effects. This conclusion is in agreement with the results shown in Figure 9.1 and obtained by solving the NLS equation directly, after including the effect of amplifier noise.

9.1.3 Soliton and Pseudo-linear Regimes

As the preceding discussion shows, when the nonlinear term in Eq. (9.1.6) is not negligible, pulse parameters do not return to their input values after each map period even for perfect dispersion compensation ($d = 0$). Eventually, the buildup of nonlinear distortion affects each pulse within the optical bit stream so much that the system cannot operate beyond a certain distance. As seen in Figure 9.1, this limiting distance can be under 500 km depending on the system design. For this reason, the management of nonlinear effects is an important issue for long-haul lightwave systems. It turns out that the parameters associated with a dispersion map (length and GVD of each section) can be controlled to manage the nonlinearity problem. Two main techniques have evolved, and systems employing them are said to operate in the *pseudo-linear* and *soliton* regimes.

It was noted in several experiments that a nonlinear system performs best when GVD compensation is only 90 to 95% so that some residual dispersion remains after

each map period. In fact, if the input pulse is initially chirped such that $\bar{\beta}_2 C < 0$, the pulse at the end of the fiber link may even be shorter than the input pulse. This behavior is expected for a linear system (see Section 2.6) and follows from Eq. (9.1.8) for $C_0 d < 0$. It also persists for weakly nonlinear systems. This observation has led to the adoption of the chirped RZ (CRZ) format for dispersion-managed fiber links.

To understand how the system and fiber parameters affect the evolution of an optical signal inside a fiber link, consider a lightwave system in which dispersion is compensated only at the transmitter and receiver ends. Since fiber parameters are constant over most of the link, it is useful to introduce the dispersion and nonlinear length scales as

$$L_D = T_0^2 / |\beta_2|, \quad L_{NL} = (\gamma P_0)^{-1}, \quad (9.1.10)$$

respectively. Introducing a normalized time τ as $\tau = t/T_0$, the NLS equation (9.1.2) can be written in the form

$$iL_D \frac{\partial U}{\partial z} - \frac{s}{2} \frac{\partial^2 U}{\partial \tau^2} + \frac{L_D}{L_{NL}} p(z) |U|^2 U = 0, \quad (9.1.11)$$

where $s = \text{sign}(\beta_2) = \pm 1$, depending on the sign of β_2 . If we use $\gamma = 2 \text{ W}^{-1}/\text{km}$ as a typical value, the nonlinear length $L_{NL} \sim 100 \text{ km}$ at peak-power levels in the range of 2 to 4 mW. In contrast, the dispersion length L_D can vary over a wide range (from ~ 1 to 10,000 km), depending on the bit rate of the system and the type of fibers used to construct it. As a result, one can encounter the following three situations.

If $L_D \gg L_{NL}$ and link length $L < L_D$, the dispersive effects play a minor role, but the nonlinear effects cannot be ignored when $L > L_{NL}$. This is the situation for systems operating at a bit rate of 2.5 Gb/s or less. For example, L_D exceeds 1,000 km at $B = 2.5 \text{ Gb/s}$ even for standard fibers with $\beta_2 = -21 \text{ ps}^2/\text{km}$ and can exceed 10,000 km for dispersion-shifted fibers. Such systems can be designed to operate over long distances by reducing the peak power and increasing the nonlinear length accordingly. The use of a dispersion map is also helpful for this purpose.

If L_D and L_{NL} are comparable and much shorter than the link length, both the dispersive and nonlinear terms are equally important in the NLS equation (9.1.11). This is often the situation for 10-Gb/s systems operating over standard fibers because L_D becomes $\sim 100 \text{ km}$ when T_0 is close to 50 ps. The use of optical solitons is most beneficial in the regime in which L_D and L_{NL} have similar magnitudes. A soliton-based system confines each pulse tightly to its original bit slot by employing the RZ format with a low duty cycle and maintains this confinement through a careful balance of frequency chirps induced by GVD and SPM. Since GVD is used to offset the impact of nonlinear effects, dispersion is never fully compensated in soliton-based systems. It will be seen in Section 9.2 that solitons can be formed only in the anomalous-GVD regime. A dispersion map can still be used but the average dispersion of the fiber link should be controlled. Solitons formed under such conditions are known as dispersion-managed solitons and are covered in Section 9.3.

If $L_D \ll L_{NL}$, we enter a new regime in which dispersive effects dominate locally, and the nonlinear effects can be treated in a perturbative manner. This situation is encountered in lightwave systems whose individual channels operate at a bit rate of 40 Gb/s or more. The bit slot is only 25 ps at 40 Gb/s. If T_0 is $< 10 \text{ ps}$ and standard

fibers are employed, L_D is reduced to below 5 km. A lightwave system operating under such conditions is said to operate in the quasi-linear or pseudo-linear regime. In such systems, input pulses broaden so rapidly that they spread over several neighboring bits. The extreme broadening reduces their peak power by a large factor. Since the nonlinear term in the NLS equation (9.1.2) scales with the peak power, its impact is considerably reduced. Interchannel nonlinear effects (discussed in Chapter 9) are reduced considerably in pseudo-linear systems because of an averaging effect that produces a nearly constant total power in all bit slots. In contrast, overlapping of neighboring pulses enhances the *intrachannel* nonlinear effects. As nonlinear effects remain important, such systems are called *pseudo-linear* [25]. Of course, pulses must be compressed back at the receiver end to ensure that they occupy their original time slot before the optical signal arrives at the receiver. This can be accomplished by compensating the accumulated dispersion with a DCF or another dispersion-equalizing filter. Section 9.4 is devoted to pseudo-linear systems.

9.2 Solitons in Optical Fibers

Solitons form in optical fibers because a balance between the chirps induced by GVD and SPM, both of which limit the system performance when acting independently. To understand how such a balance is possible, we follow the analysis of Sections 2.4 and 2.6. As shown there, the GVD broadens an optical pulse during its propagation inside an optical fiber, except when the pulse is initially chirped in the right way (see Figure 2.12). More specifically, a chirped pulse is compressed during earlier stages of propagation whenever β_2 and the chirp parameter C happen to have opposite signs so that $\beta_2 C$ is negative. As discussed in Section 2.6.2, SPM imposes a chirp on the optical pulse such that $C > 0$. If $\beta_2 < 0$, the condition $\beta_2 C < 0$ is readily satisfied. Moreover, as the SPM-induced chirp is power-dependent, it is not difficult to imagine that under certain conditions, SPM and GVD may cooperate in such a way that the SPM-induced chirp is just right to cancel the GVD-induced broadening of the pulse. In this situation, an optical pulse propagates undistorted in the form of a soliton [33]–[35].

9.2.1 Properties of Optical Solitons

To find the conditions under which solitons can form, we assume that pulses are propagating in the region of anomalous GVD and choose $s = -1$ in Eq. (9.1.11). We also set $p(z) = 1$, a condition requiring perfect distributed amplification. Introducing a normalized distance in the form $\xi = z/L_D$, Eq. (9.1.11) takes the form

$$i \frac{\partial U}{\partial \xi} + \frac{1}{2} \frac{\partial^2 U}{\partial \tau^2} + N^2 |U|^2 U = 0, \quad (9.2.1)$$

where the parameter N is defined as

$$N^2 = \frac{L_D}{L_{NL}} = \frac{\gamma P_0 T_0^2}{|\beta_2|}. \quad (9.2.2)$$

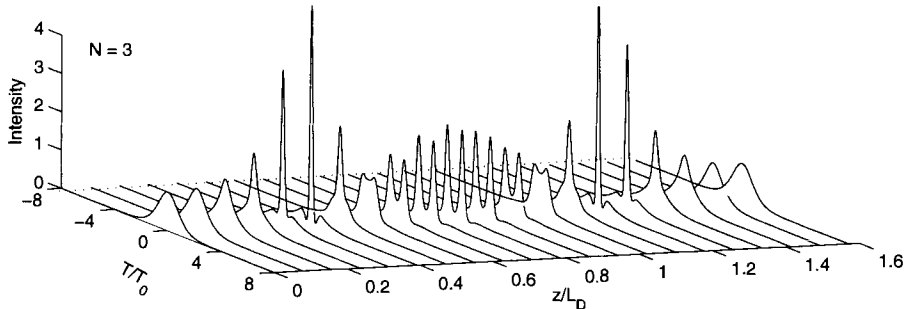


Figure 9.5: Evolution of a third-order soliton over one soliton period. The power profile $|u|^2$ is plotted as a function of z/L_D .

It represents a dimensionless combination of the pulse and fiber parameters. Even the single parameter N appearing in Eq. (9.2.1) can be removed by introducing $u = NU$ as a renormalized amplitude. With this change, the NLS equation takes on its canonical form [1]

$$i \frac{\partial u}{\partial \xi} + \frac{1}{2} \frac{\partial^2 u}{\partial \tau^2} + |u|^2 u = 0. \quad (9.2.3)$$

The NLS equation (9.2.3) belongs to a special class of nonlinear partial differential equations that can be solved exactly with a mathematical technique known as the *inverse scattering method* [36]–[38]. It was first solved in 1971 by this method [39]. The main result can be summarized as follows. When an input pulse having an initial amplitude

$$u(0, \tau) = N \operatorname{sech}(\tau) \quad (9.2.4)$$

is launched into the fiber, its shape remains unchanged during propagation when $N = 1$ but follows a periodic pattern for integer values of $N > 1$ such that the input shape is recovered at $\xi = m\pi/2$, where m is an integer.

An optical pulse whose parameters satisfy the condition $N = 1$ is called the *fundamental soliton*. Pulses corresponding to other integer values of N are called higher-order solitons. The parameter N represents the order of the soliton. Noting that $\xi = z/L_D$, the soliton period z_0 , defined as the distance over which higher-order solitons first recover their original shape, is given by $z_0 = (\pi/2)L_D$. The *soliton period* z_0 and the *soliton order* N play an important role in the theory of optical solitons. Figure 9.5 shows the evolution of a third-order soliton over one soliton period by solving the NLS equation (9.2.1) numerically with $N = 3$. The pulse shape changes considerably but returns to its original form at $z = z_0$. Only a fundamental soliton maintains its shape during propagation inside optical fibers. In a 1973 study, Eq. (9.2.1) was solved numerically to show that optical solitons can form in optical fibers [40].

The solution corresponding to the fundamental soliton can be obtained by solving Eq. (9.2.3) directly, without recourse to the inverse scattering method. The approach consists of assuming that a solution of the form

$$u(\xi, \tau) = V(\tau) \exp[i\phi(\xi)] \quad (9.2.5)$$

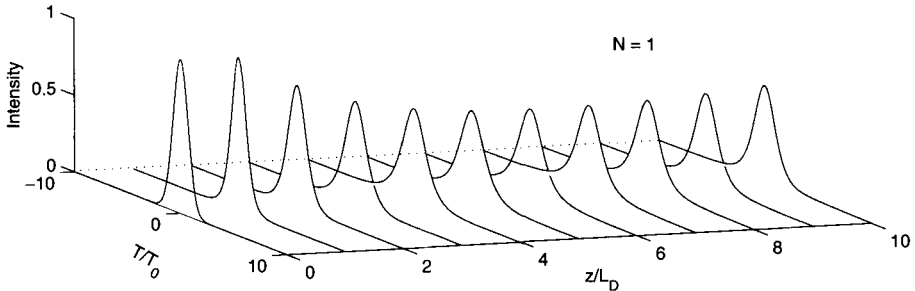


Figure 9.6: Evolution of a Gaussian pulse with $N = 1$ over the range $\xi = 0$ to 10. The pulse evolves toward the fundamental soliton by changing its shape, width, and peak power.

exists, where V must be independent of ξ for Eq. (9.2.5) to represent a fundamental soliton that maintains its shape during propagation. The phase ϕ can depend on ξ but is assumed to be time-independent. When Eq. (9.2.5) is substituted in Eq. (9.2.3) and the real and imaginary parts are separated, we obtain two real equations for V and ϕ . These equations show that ϕ should be of the form $\phi(\xi) = K\xi$, where K is a constant. The function $V(\tau)$ is then found to satisfy the nonlinear differential equation

$$\frac{d^2V}{d\tau^2} = 2V(K - V^2). \quad (9.2.6)$$

This equation can be solved by multiplying it with $2(dV/d\tau)$ and integrating over τ . The result is found to be

$$(dV/d\tau)^2 = 2KV^2 - V^4 + C, \quad (9.2.7)$$

where C is a constant of integration. Using the boundary condition that both V and $dV/d\tau$ should vanish for any optical pulse at $|\tau| \rightarrow \infty$, C can be set to zero.

The constant K in Eq. (9.2.7) is determined using the boundary condition that $V = 1$ and $dV/d\tau = 0$ at the soliton peak, assumed to occur at $\tau = 0$. Its use provides $K = \frac{1}{2}$, resulting in $\phi = \xi/2$. Equation (9.2.7) is easily integrated to obtain $V(\tau) = \text{sech}(\tau)$. We have thus found the well-known “sech” solution [36]–[38]

$$u(\xi, \tau) = \text{sech}(\tau) \exp(i\xi/2) \quad (9.2.8)$$

for the fundamental soliton by integrating the NLS equation directly. It shows that the input pulse acquires a phase shift $\xi/2$ as it propagates inside the fiber, but its amplitude remains unchanged. It is this property of a fundamental soliton that makes it an ideal candidate for optical communications. In essence, the effects of fiber dispersion are exactly compensated by the fiber nonlinearity when the input pulse has a “sech” shape and its width and peak power are related by Eq. (9.2.2) in such a way that $N = 1$.

An important property of optical solitons is that they are remarkably stable against perturbations. Thus, even though the fundamental soliton requires a specific shape and a certain peak power corresponding to $N = 1$ in Eq. (9.2.2), it can be created even when the pulse shape and the peak power deviate from the ideal conditions. Figure 9.6

shows the numerically simulated evolution of a Gaussian input pulse for which $N = 1$ but $u(0, \tau) = \exp(-\tau^2/2)$. As seen there, the pulse adjusts its shape and width as it propagates down the fiber in an attempt to become a fundamental soliton and attains a “sech” profile for $\xi \gg 1$. Similar behavior is observed when N deviates from 1. It turns out that the N th-order soliton can form when the input value of N is in the range $N - \frac{1}{2}$ to $N + \frac{1}{2}$ [41]. In particular, the fundamental soliton can be excited for values of N in the range of 0.5 to 1.5.

It is surprising that an optical fiber can force any input pulse to evolve toward a soliton. A simple way to understand this behavior is to think of optical solitons as the temporal modes of a nonlinear waveguide. Higher intensities in the pulse center create a temporal waveguide by increasing the refractive index only in the central part of the pulse. Such a waveguide supports temporal modes just as the core-cladding index difference leads to spatial modes of optical fibers. When the input pulse does not match a temporal mode precisely but it is close to it, most of the pulse energy can still be coupled to that temporal mode. The rest of the energy spreads in the form of *dispersive waves*. It will be seen later that such dispersive waves affect system performance and should be minimized by matching the input conditions as close to the ideal requirements as possible. When solitons adapt to perturbations adiabatically, perturbation theory developed specifically for solitons can be used to study how the soliton amplitude, width, frequency, speed, and phase evolve along the fiber.

The NLS equation can be solved with the inverse scattering method even when an optical fiber exhibits normal dispersion [42]. The intensity profile of the resulting solutions exhibits a dip in a uniform background, and it is the dip that remains unchanged during propagation inside an optical fiber [43]. For this reason, such solutions of the NLS equation are called *dark* solitons. Even though dark solitons were observed during the 1980s and their properties have been studied thoroughly [44]–[51], most experiments have employed bright solitons with a “sech” shape. In the following discussion we focus on the fundamental soliton given in Eq. (9.2.8).

9.2.2 Loss-Managed Solitons

We have seen in the preceding section that solitons use SPM to maintain their width even in the presence of fiber dispersion. However, this property holds only if soliton energy remains constant inside the fiber. It is not difficult to see that a decrease in pulse energy because of fiber losses would produce soliton broadening because a reduced peak power weakens the SPM effect necessary to counteract the GVD. When optical amplifiers are used periodically for compensating fiber losses, soliton energy changes in a periodic fashion. Such energy variations are included in the NLS equation (9.1.11) through the periodic function $p(z)$. In the case of lumped amplifiers, $p(z)$ decreases exponentially between two amplifiers and can vary by 20 dB or more over each period. The important question is whether solitons can maintain their shape and width in spite of such large energy fluctuations. It turns out that solitons can remain stable over long distances, provided amplifier spacing L_A is kept much smaller than the dispersion length L_D [52].

In general, changes in soliton energy are accompanied by changes in pulse width. Large rapid variations in $p(z)$ can destroy a soliton if its width changes rapidly through

the emission of dispersive waves. The concept of the *path-averaged* soliton [52] makes use of the fact that solitons evolve little over a distance that is short compared with the dispersion length (or soliton period). Thus, when $L_A \ll L_D$, the width of a soliton remains virtually unchanged even if its peak power varies considerably in each section between two amplifiers. In effect, one can replace $p(z)$ by its average value \bar{p} in Eq. (9.1.11) when $L_A \ll L_D$. Noting that \bar{p} is just a constant that modifies γP_0 , we recover the standard NLS equation.

From a practical viewpoint, a fundamental soliton can be excited if the input peak power P_s (or energy) of the path-averaged soliton is chosen to be larger by a factor of $1/\bar{p}$. If we introduce the amplifier gain as $G = \exp(\alpha L_A)$ and use $\bar{p} = L_A^{-1} \int_0^{L_A} e^{-\alpha z} dz$, the energy enhancement factor for loss-managed solitons is given by

$$f_{LM} = \frac{P_s}{P_0} = \frac{1}{\bar{p}} = \frac{\alpha L_A}{1 - \exp(-\alpha L_A)} = \frac{G \ln G}{G - 1}. \quad (9.2.9)$$

Thus, soliton evolution in lossy fibers with periodic lumped amplification is identical to that in lossless fibers provided (1) amplifiers are spaced such that $L_A \ll L_D$ and (2) the launched peak power is larger by a factor f_{LM} . As an example, $G = 10$ and $f_{LM} \approx 2.56$ when $L_A = 50$ km and $\alpha = 0.2$ dB/km.

The condition $L_A \ll L_D$ is vague for designing soliton systems. The question is how close L_A can be to L_D before the system may fail to work. The semianalytic approach of Section 9.1.2 can be extended to study how fiber losses affect the evolution of solitons. However, we should replace Eq. (9.1.4) with

$$U(z, t) = a \operatorname{sech}(t/T) \exp[-iCt^2/T^2 + i\phi], \quad (9.2.10)$$

to ensure that the “sech” shape of a soliton is maintained. Using the variational or the moment method, we obtain the following two coupled equations:

$$\frac{dT}{dz} = \frac{\beta_2 C}{T}, \quad (9.2.11)$$

$$\frac{dC}{dz} = \left(\frac{4}{\pi^2} + C^2 \right) \frac{\beta_2}{T^2} + \frac{2\gamma p(z)E_0}{\pi^2 T}, \quad (9.2.12)$$

where $E_0 = 2P_0T_0$ is the input pulse energy. A comparison with Eqs. (9.1.5) and (9.1.6) obtained for Gaussian pulses shows that the width equation remains unchanged; the chirp equation also has the same form but different coefficients.

As a simple application of the moment equations, we use them for finding the soliton-formation condition in the ideal case of $p(z) = 1$. If the pulse is initially unchirped, both derivatives in Eqs. (9.2.11) and (9.2.12) vanish at $z = 0$ if β_2 is negative and the pulse energy is chosen to be $E_0 = 2|\beta_2|/(\gamma T_0)$. Under such conditions, the width and chirp of the pulse will not change with z , and the pulse will form a fundamental soliton. Using $E_0 = 2P_0T_0$, it is easy to see that this condition is equivalent to setting $N = 1$ in Eq. (9.2.2).

To include fiber losses, we set $p(z) = \exp(-\alpha z)$ in each fiber section of length L_A in a periodic fashion. Figure 9.7 shows how the soliton width and chirp change at successive amplifiers for several values of L_A in the range 25 to 100 km, assuming

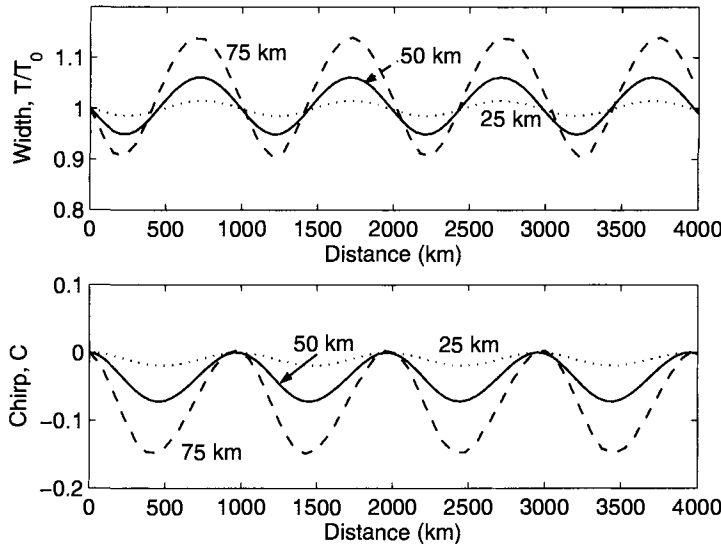


Figure 9.7: Evolution of pulse with T and chirp C along the fiber length for three amplifier spacings (25, 50, and 75 km) when $L_D = 100$ km.

$L_D = 100$ km. Such values of dispersion length are realized for a 10-Gb/s soliton system, for example, when $T_0 = 20$ ps and $\beta_2 = -4$ ps²/km. When amplifier spacing is 25 km, both the width and chirp remain close to their input values. As L_A is increased to 50 km, they oscillate in a periodic fashion, and oscillation amplitude increases as L_A increases. For example, the width can change by more than 10% when $L_A = 75$ km. The oscillatory behavior can be understood by performing a linear stability analysis of Eqs. (9.2.11) and (9.2.12). However, if L_A/L_D exceeds 1 considerably, the pulse width starts to increase exponentially in a monotonic fashion. Figure 9.7 shows that $L_A/L_D \leq 0.5$ is a reasonable design criterion when lumped amplifiers are used for loss management.

The variational equations such as Eqs. (9.2.11) and (9.2.12) only serve as a guideline, and their solutions are not always trustworthy, because they completely ignore the dispersive radiation generated as solitons are perturbed. For this reason, it is important to verify their predictions through direct numerical simulations of the NLS equation itself. Figure 9.8 shows the evolution of a loss-managed soliton over a distance of 10,000 km, assuming that solitons are amplified every 50 km. When the input pulse width corresponds to a dispersion length of 200 km, the soliton is preserved quite well even after 10,000 km because the condition $L_A \ll L_D$ is well satisfied. However, if the dispersion length is reduced to 25 km, the soliton is unable to sustain itself because of the excessive emission of dispersive waves.

How does the limitation on amplifier spacing affect the design of soliton systems? The condition $L_A < L_D$ can be related to the width T_0 through $L_D = T_0^2/|\beta_2|$. The resulting condition is

$$T_0 > \sqrt{|\beta_2|L_A}. \quad (9.2.13)$$

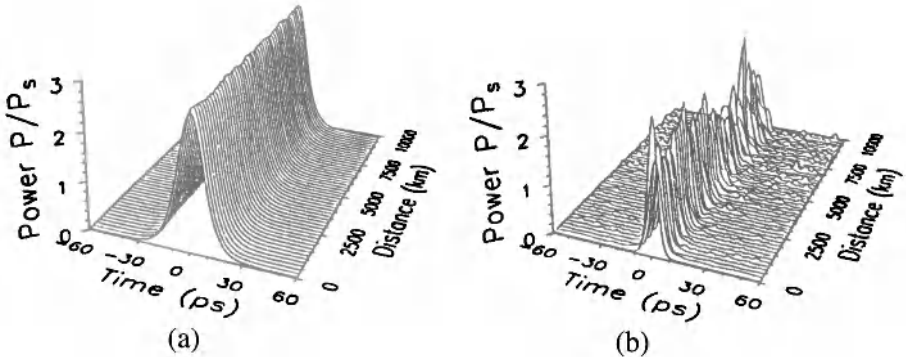


Figure 9.8: Evolution of loss-managed solitons over 10,000 km for (a) $L_D = 200$ km and (b) 25 km with $L_A = 50$ km, $\alpha = 0.22$ dB/km, and $\beta_2 = -0.5$ ps²/km.

The pulse width T_0 must be a small fraction of the bit slot $T_b = 1/B$ to ensure that the neighboring solitons are well separated. Mathematically, the soliton solution in Eq. (9.2.8) is valid only when a single pulse propagates by itself. It remains approximately valid for a train of pulses only when individual solitons are well isolated. This requirement can be used to relate the soliton width T_0 to the bit rate B using $T_b = 2q_0T_0$, where $2q_0$ is a measure of separation between two neighboring pulses in an optical bit stream. Typically, q_0 exceeds 4 to ensure that pulse tails do not overlap significantly. Using $T_0 = (2q_0B)^{-1}$ in Eq. (9.2.13), we obtain the following design criterion:

$$B^2L_A < (4q_0^2|\beta_2|)^{-1}. \quad (9.2.14)$$

Choosing typical values, $\beta_2 = -2$ ps²/km, $L_A = 50$ km, and $q_0 = 5$, we obtain $T_0 > 10$ ps and $B < 10$ GHz. Clearly, the use of path-averaged solitons imposes a severe limitation on both the bit rate and the amplifier spacing for soliton communication systems. To operate even at 10 Gb/s, one must reduce either q_0 or L_A if β_2 is kept fixed. Both of these parameters cannot be reduced much below the values used in obtaining the preceding estimate.

A partial solution to this problem was suggested in 2000 when it was proposed that one could prechirp the soliton to relax the condition $L_A \ll L_D$, even though the standard soliton solution in Eq. (9.2.8) has no chirp [53]. The basic idea consists of finding a periodic solution of Eqs. (9.2.11) and (9.2.12) that repeats itself at each amplifier using the periodic boundary conditions

$$T(z = L_A) = T_0, \quad C(z = L_A) = C_0. \quad (9.2.15)$$

The input pulse energy E_0 and input chirp C_0 can be used as two adjustable parameters. A perturbative solution of Eqs. (9.2.11) and (9.2.12) shows that the pulse energy must be increased by a factor close to the energy enhancement factor f_{LM} in Eq. (9.2.9). At the same time, the input chirp that provides a periodic solution is related to this factor as

$$C_0 = \frac{4}{\pi^2} \left[\frac{1}{2} - \frac{(f_{LM} - 1)}{\ln G} \right]. \quad (9.2.16)$$

Numerical results based on the NLS equation show that with a proper prechirping of input solitons, amplifier spacing can exceed $2L_D$. However, dispersive waves eventually destabilize a soliton over long fiber lengths when L_A is made significantly larger than the dispersive length.

The condition $L_A \ll L_D$ can also be relaxed considerably by employing distributed amplification. As discussed in Section 7.1, a distributed-amplification scheme is superior to lumped amplification because its use provides a nearly lossless fiber by compensating losses locally at every point along the fiber link. As early as 1988, solitons were transmitted over 4,000 km of lossy fiber using periodic Raman amplification inside a 42-km recirculating fiber loop [54]. The distance could later be increased to 6,000 km with further optimization. This experiment was the first to demonstrate that solitons could be transmitted over transoceanic distances in principle. Starting in 1989, lumped amplifiers were used for loss-managed soliton systems. In a 1991 experiment, 2.5-Gb/s solitons were transmitted over 12,000 km by using a 75-km recirculating loop [55]. In this experiment, the performance was limited mainly by the timing jitter induced by amplifier noise. During the 1990s, several schemes for reducing the timing jitter were discovered and employed for improving the performance of soliton systems [33]–[35]. The technique of Raman amplification has become quite common in recent years for both the soliton and nonsoliton systems.

9.3 Dispersion-Managed Solitons

As we saw in Chapter 8, dispersion management is employed commonly for modern WDM systems. Since such systems use fiber sections with both normal and anomalous GVDs, one may ask what happens to solitons in this case. It turns out that solitons can form even when the GVD parameter β_2 varies along the link length but their properties are quite different. This section is devoted to such dispersion-managed solitons. We first consider dispersion-decreasing fibers and then focus on fiber links with periodic dispersion maps.

9.3.1 Dispersion-Decreasing Fibers

An interesting scheme relaxes completely the restriction $L_A \ll L_D$ imposed normally on loss-managed solitons by employing a new kind of fiber in which GVD varies along the fiber length [56]. Such fibers are called *dispersion-decreasing* fibers (DDFs) and are designed such that the decreasing GVD counteracts the reduced SPM experienced by solitons weakened from fiber losses.

Soliton evolution in a DDF is governed by Eq. (9.1.2) except that β_2 is a continuous function of z . Introducing the normalized distance and time variables as

$$\xi = T_0^{-2} \int_0^z \beta_2(z) dz, \quad \tau = t/T_0, \quad (9.3.1)$$

we can write this equation in the form

$$i \frac{\partial U}{\partial \xi} + \frac{1}{2} \frac{\partial^2 U}{\partial \tau^2} + N^2(z)|U|^2 U = 0, \quad (9.3.2)$$

where $N^2(z) = \gamma P_0 T_0^2 p(z)/|\beta_2(z)|$. If the GVD profile is chosen such that $|\beta_2(z)| = |\beta_2(0)|p(z)$, N becomes a constant, and Eq. (9.3.2) reduces the standard NLS equation obtained earlier with $p(z) = 1$. As a result, fiber losses have no effect on a soliton in spite of its reduced energy when DDFs are used. More precisely, lumped amplifiers can be placed at any distance and are not limited by the condition $L_A \ll L_D$, provided the GVD decreases exponentially in the fiber section between two amplifiers as

$$|\beta_2(z)| = |\beta_2(0)| \exp(-\alpha z). \quad (9.3.3)$$

This result can be understood qualitatively by noting from Eq. (9.2.2) that the requirement $N = 1$ can be maintained, in spite of power losses, if both $|\beta_2|$ and γ decrease exponentially at the same rate. The fundamental soliton then maintains its shape and width even in a lossy fiber.

Fibers with a nearly exponential GVD profile have been fabricated [57]. A practical technique for making such DDFs consists of reducing the core diameter along the fiber length in a controlled manner during the fiber-drawing process. Variations in the fiber diameter change the waveguide contribution to β_2 and reduce its magnitude. Typically, GVD can be varied by a factor of 10 over a length of 20 to 40 km. The accuracy realized by the use of this technique is estimated to be better than 0.1 ps²/km [58]. The propagation of solitons in DDFs has been observed in several experiments [58]–[60]. In a 40-km DDF, solitons preserved their width and shape in spite of energy losses of more than 8 dB [59]. In a recirculating loop made using DDFs, a 6.5-ps soliton train at 10 Gb/s could be transmitted over 300 km [60].

In an alternative approach, the exponential GVD profile of a DDF is approximated with a staircase profile by splicing together several constant-dispersion fibers with different β_2 values. This approach was studied during the 1990s, and it was found that most of the benefits of DDFs can be realized using as few as four fiber segments [61]–[65]. How should one select the length and the GVD of each fiber used for emulating a DDF? The answer is not obvious, and several methods have been proposed. In one approach, power deviations are minimized in each section [61]. In another approach, fibers of different GVD values D_m and different lengths L_{map} are chosen such that the product $D_m L_{\text{map}}$ is the same for each section. In a third approach, D_m and L_{map} are selected to minimize the shading of dispersive waves [62]. Advantages offered by DDFs for soliton systems include a lower timing jitter [1] and a reduced noise level [66]. In spite of these benefits, DDFs are rarely used in practice.

9.3.2 Periodic Dispersion Maps

Periodic dispersion maps consisting of alternating-GVD fibers are attractive because their use lowers the average dispersion of the entire link, while keeping the GVD of each section large enough that the FWM crosstalk remains negligible in WDM systems. However, the use of dispersion management forces each soliton to propagate in the normal-dispersion regime of a fiber during each map period. At first sight, such a scheme should not even work because the normal-GVD fibers do not support solitons and lead to considerable broadening and chirping of the pulse. So, why should solitons survive in a dispersion-managed fiber link? An intense theoretical effort devoted to this

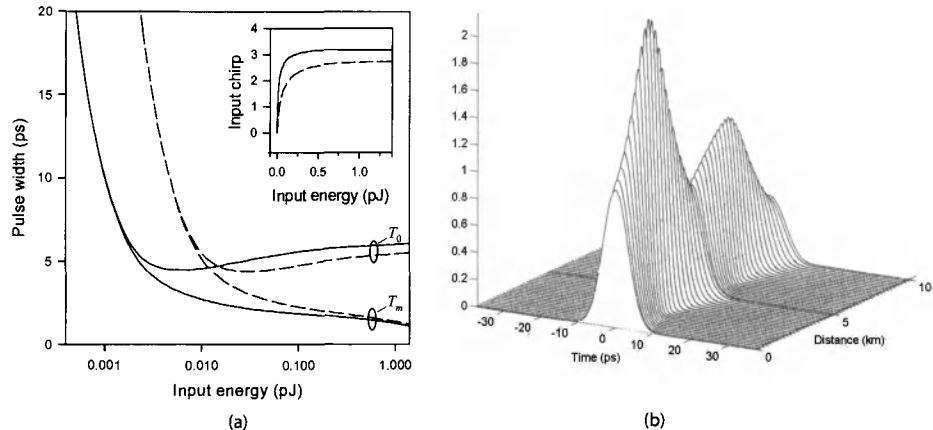


Figure 9.9: (a) Changes in T_0 (upper curve) and T_m (lower curve) with input pulse energy E_0 for $\alpha = 0$ (solid lines) and 0.25 dB/km (dashed lines). The inset shows the input chirp C_0 in the two cases. (b) Evolution of the DM soliton over one map period for $E_0 = 0.1 \text{ pJ}$ and $L_A = 80 \text{ km}$.

issue led to the discovery of dispersion-managed (DM) solitons [67]–[90]. Physically speaking, if the dispersion length associated with each fiber section used to form the map is a fraction of the nonlinear length, the pulse would evolve in a linear fashion over a single map period. On a longer length scale, solitons can still form if the SPM effects are balanced by the average dispersion. As a result, solitons can survive in an average sense, even though not only the peak power but also the width and shape of such solitons oscillate periodically.

We focus on a simple dispersion map consisting of two fibers with opposite GVD characteristics. Soliton evolution is governed by Eq. (9.1.2) in which β_2 is a piecewise continuous function of z taking values β_{2a} and β_{2n} in the anomalous and normal GVD sections of lengths l_a and l_n , respectively. The map period $L_{\text{map}} = l_a + l_n$ can be different from the amplifier spacing L_A . Clearly, the properties of DM solitons will depend on several map parameters even when only two types of fibers are used in each map period. Numerical simulations show that a nearly periodic solution can often be found by adjusting input pulse parameters (width, chirp, and peak power) even though these parameters vary considerably in each map period. The shape of such DM solitons is closer to a Gaussian profile rather than the “sech” shape associated with standard solitons [68]–[70].

Numerical solutions, although essential, do not lead to much physical insight. Several techniques have been used to solve the NLS equation (9.1.2) approximately. A common approach makes use of the variational method [71]–[73]. Another approach expands $B(z, t)$ in terms of a complete set of the Hermite–Gauss functions that are solutions of the linear problem [74]. A third approach solves an integral equation, derived in the spectral domain using perturbation theory [76]–[78].

Here we focus on the variational equations (9.1.5) and (9.1.6) used earlier in Section 9.1.2. Because the shape of DM solitons is close to a Gaussian pulse, they can be applied for them. These two equations should be solved with the periodic boundary

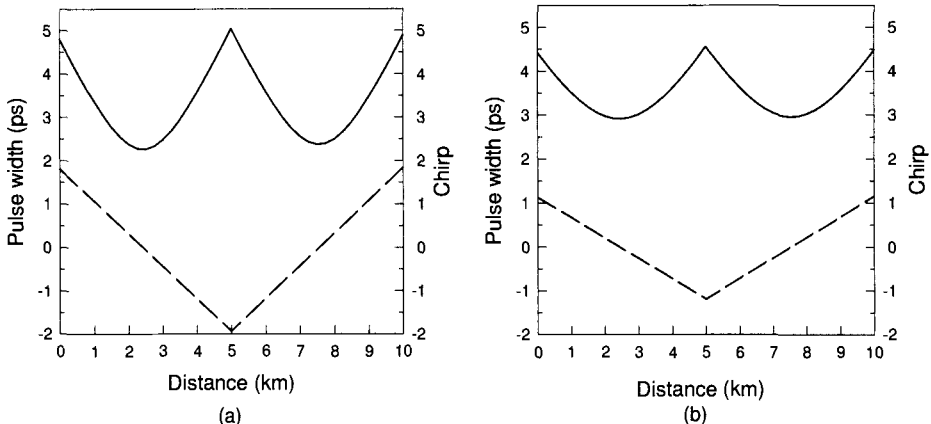


Figure 9.10: Variations of pulse width and chirp (dashed line) over one map period for DM solitons with the input energy (a) $E_0 = 0.1 \text{ pJ}$ and (b) E_0 close to E_c .

conditions given in Eq. (9.2.15) to ensure that the DM soliton recovers its initial state after each amplifier. The periodic boundary conditions fix the values of the initial width T_0 and the chirp C_0 at $z = 0$ for which a soliton can propagate in a periodic fashion for a given value of pulse energy E_0 . A new feature of the DM solitons is that the input pulse width depends on the dispersion map and cannot be chosen arbitrarily. In fact, T_0 cannot fall below a critical value that is set by the map itself.

Figure 9.9 shows how the pulse width T_0 and the chirp C_0 of allowed periodic solutions vary with input pulse energy for a specific dispersion map. The minimum value T_m of the pulse width occurring in the middle of the anomalous-GVD section of the map is also shown. The map is suitable for 40-Gb/s systems and consists of alternating fibers with GVD of -4 and $4 \text{ ps}^2/\text{km}$ and lengths $l_a \approx l_n = 5 \text{ km}$ such that the average GVD is $-0.01 \text{ ps}^2/\text{km}$. The solid lines show the case of ideal distributed amplification for which $p(z) = 1$. The lumped-amplification case is shown by the dashed lines in Figure 9.9, assuming 80-km amplifier spacing and 0.25 dB/km losses in each fiber section.

Several conclusions can be drawn from Figure 9.9. First, both T_0 and T_m decrease rapidly as pulse energy is increased. Second, T_0 attains its minimum value at a certain pulse energy E_c while T_m keeps decreasing slowly. Third, T_0 and T_m differ by a large factor for $E_0 \gg E_c$. This behavior indicates that pulse width changes considerably in each fiber section when this regime is approached. An example of pulse breathing is shown in Figure 9.9(b) for $E_0 = 0.1 \text{ pJ}$ in the case of lumped amplification. The input chirp C_0 is relatively large ($C_0 \approx 1.8$) in this case. The most important feature of Figure 9.9 is the existence of a minimum value of T_0 for a specific value of the pulse energy. The input chirp $C_0 = 1$ at that point. It is interesting to note that the minimum value of T_0 does not depend much on fiber losses and is about the same for the solid and dashed curves, although the value of E_c is much larger in the lumped amplification case because of fiber losses.

Both the pulse width and the peak power of DM solitons vary considerably within

each map period. Figure 9.10(a) shows the width and chirp variations over one map period for the DM soliton of Figure 9.9(b). The pulse width varies by more than a factor of 2 and becomes minimum nearly in the middle of each fiber section where frequency chirp vanishes. The shortest pulse occurs in the middle of the anomalous-GVD section in the case of ideal distributed amplification in which fiber losses are compensated fully at every point along the fiber link. For comparison, Figure 9.10(b) shows the width and chirp variations for a DM soliton whose input energy is close to E_c where the input pulse is shortest. Breathing of the pulse is reduced considerably together with the range of chirp variations. In both cases, the DM soliton is quite different from a standard fundamental soliton as it does not maintain its shape, width, or peak power. Nevertheless, its parameters repeat from period to period at any location within the map. For this reason, DM solitons can be used for optical communications in spite of oscillations in the pulse width. Moreover, such solitons perform better from a system standpoint.

9.3.3 Design Issues

Figures 9.9 and 9.10 show that Eqs. (9.1.5) and (9.1.6) permit periodic propagation of many different DM solitons in the same map by choosing different values of E_0 , T_0 , and C_0 . How should one choose among these solutions when designing a soliton system? Pulse energies much smaller than E_c (corresponding to the minimum value of T_0) should be avoided because a low average power would then lead to rapid degradation of SNR as amplifier noise builds up with propagation. On the other hand, when $E_0 \gg E_c$, large variations in the pulse width in each fiber section would induce XPM-induced interaction between two neighboring solitons if their tails begin to overlap considerably. For this region, the region near $E_0 = E_c$ is most suited for designing DM soliton systems. Numerical solutions of the NLS equation (9.1.2) confirm this conclusion.

The 40-Gb/s system design used for Figures 9.9 and 9.10 was possible only because the map period L_{map} was chosen to be much smaller than the amplifier spacing of 80 km, a configuration referred to as the *dense* dispersion management. When L_{map} is increased to 80 km using $l_a \approx l_b = 40$ km, while keeping the same value of average dispersion, the minimum pulse width supported by the map increases by a factor of 3. The bit rate is then limited to below 20 Gb/s.

It is possible to find the values of T_0 and T_m by solving Eqs. (9.1.5) and (9.1.6) approximately. Equation (9.1.6) shows that $T^2(z) = T_0^2 + 2 \int_0^z \beta_2(z)C(z)dz$ any point within the map. The chirp equation cannot be integrated analytically but the numerical solutions show that $C(z)$ varies almost linearly in each fiber section. As seen in Figure 9.10, $C(z)$ changes from C_0 to $-C_0$ in the first section and then back to C_0 in the second section. Noting that the ratio $(1 + C^2)/T^2$ is related to the spectral width that changes little over one map period when the nonlinear length is much larger than the local dispersion length, we average it over one map period and obtain the following relation between T_0 and C_0 :

$$T_0 = T_{\text{map}} \sqrt{\frac{1 + C_0^2}{|C_0|}}, \quad T_{\text{map}} = \left(\frac{|\beta_{2n}\beta_{2a}l_n l_a|}{\beta_{2n}l_n - \beta_{2a}l_a} \right)^{1/2}, \quad (9.3.4)$$

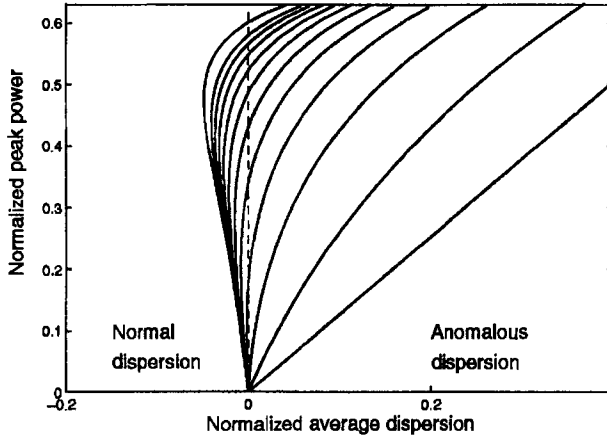


Figure 9.11: Peak power of DM solitons as a function of $\bar{\beta}_2/\beta_{2a}$. The map strength is zero for the straight line, increases in step of 2 until 20, and becomes 25 for the leftmost curve. (After Ref. [71]; ©1998 OSA.)

where T_{map} is a parameter with dimensions of time involving only the four map parameters [87]. It provides a time scale associated with an arbitrary dispersion map in the sense that the stable periodic solutions supported by it have input pulse widths that are close to T_{map} (within a factor of 2 or so). The minimum value of T_0 occurs for $|C_0| = 1$ and is given by $T_0^{\min} = \sqrt{2}T_{\text{map}}$.

It is useful to look for other combinations of the four map parameters that may play an important role in designing a DM soliton system. Two parameters that are useful for this purpose are defined as [71]

$$\bar{\beta}_2 = \frac{\beta_{2n}l_n + \beta_{2a}l_a}{l_n + l_a}, \quad S_{\text{map}} = \frac{\beta_{2n}l_n - \beta_{2a}l_a}{T_{\text{FWHM}}^2}, \quad (9.3.5)$$

where $T_{\text{FWHM}} \approx 1.665T_m$ is the FWHM at the location where pulse width is minimum in the anomalous-GVD section. Physically, $\bar{\beta}_2$ represents the average GVD of the entire link, while the map strength S_{map} is a measure of how much GVD changes abruptly between two fibers in each map period. The solutions of Eqs. (9.1.5) and (9.1.6) as a function of map strength S for different values of $\bar{\beta}_2$ reveal the surprising feature that DM solitons can exist even when the average GVD is normal, provided the map strength exceeds a critical value S_{cr} [79]–[83].

As an example, Figure 9.11 shows DM-soliton solutions for several values of S_{map} by plotting peak power as a function of the dimensionless ratio $\bar{\beta}_2/\beta_{2a}$ [71]. Periodic solutions in the normal-GVD regime exist only when S_{map} exceeds a critical value of 4.8, indicating that pulse width for such solutions changes by a large factor in each fiber section. Moreover, when $S_{\text{map}} > S_{\text{cr}}$, a periodic solution can exist for two different values of the input pulse energy in a small range of positive values of $\bar{\beta}_2 > 0$. Numerical solutions of Eq. (9.3.2) confirm these predictions, except that the critical value of the map strength is found to be 3.9.

For map strengths below a critical value (about 3.9 numerically), the average GVD is anomalous for DM solitons. In that case, one is tempted to compare them with standard solitons forming in a uniform-GVD fiber link with $\beta_2 = \bar{\beta}_2$. For relatively small values of S_{map} , variations in the pulse width and chirp are small enough that one can ignore them. The main difference between the average-GVD and DM solitons then stems from the higher peak power required to sustain DM solitons. The energy enhancement factor for DM solitons is defined as [67]

$$f_{\text{DM}} = E_0^{\text{DM}} / E_0^{\text{av}} \quad (9.3.6)$$

and can exceed 10 depending on the system design. The larger energy of DM solitons benefits a soliton system in several ways. Among other things, it improves the SNR and decreases the timing jitter.

Dispersion-management schemes were used for solitons as early as 1992 although they were referred to by names such as partial soliton communication and dispersion allocation [91]. In the simplest form of dispersion management, a relatively short segment of dispersion-compensating fiber (DCF) is added periodically to the transmission fiber, resulting in dispersion maps similar to those used for nonsoliton systems. It was found in a 1995 experiment that the use of DCFs reduced the timing jitter considerably [92]. In fact, in this 20-Gb/s experiment, the timing jitter became low enough when the average dispersion was reduced to a value near $-0.025 \text{ ps}^2/\text{km}$ that the 20-Gb/s signal could be transmitted over transoceanic distances.

A large number of experiments have shown the benefits of DM solitons for light-wave systems [93]–[101]. In one experiment, the use of a periodic dispersion map enabled the transmission of a 20-Gb/s soliton bit stream over 5,520 km of a fiber link containing amplifiers at 40-km intervals [93]. In another 20-Gb/s experiment [94], solitons could be transmitted over 9,000 km without using any in-line optical filters since the periodic use of DCFs reduced timing jitter by more than a factor of 3. A 1997 experiment focused on the transmission of DM solitons using dispersion maps such that solitons propagated most of the time in the normal-GVD regime [95]. This 10-Gb/s experiment transmitted signals over 28,000 km using a recirculating fiber loop consisting of 100 km of normal-GVD fiber and 8 km of anomalous-GVD fiber such that the average GVD was anomalous (about $-0.1 \text{ ps}^2/\text{km}$). Periodic variations in the pulse width were also observed in such a fiber loop [96]. In a later experiment, the loop was modified to yield the average-GVD value of zero or a slightly positive value [97]. Stable transmission of 10-Gb/s solitons over 28,000 km was still observed. In all cases, experimental results were in excellent agreement with those of numerical simulations [98].

An important application of dispersion management consists of upgrading the existing terrestrial networks designed with standard fibers [99]–[101]. A 1997 experiment used fiber gratings for dispersion compensation and realized 10-Gb/s soliton transmission over 1,000 km. Longer transmission distances were realized using a recirculating fiber loop [100] consisting of 102 km of standard fiber with anomalous GVD ($\beta_2 \approx -21 \text{ ps}^2/\text{km}$) and 17.3 km of DCF with normal GVD ($\beta_2 \approx 160 \text{ ps}^2/\text{km}$). The map strength S was quite large in this experiment when 30-ps (FWHM) pulses were launched into the loop. By 1999, 10-Gb/s DM solitons could be transmitted over

16,000 km of standard fiber when soliton interactions were minimized by choosing the location of amplifiers appropriately [16].

9.3.4 Timing Jitter

We saw in Section 7.7.4 that noise added by optical amplifiers perturbs the position of each optical pulse in its time slot. Timing jitter induced by amplifier noise is especially severe for soliton-based systems and it limits the total transmission distance of any long-haul soliton link. This limitation was first pointed out in 1986 in the context of standard constant-width solitons. It persists even for DM soliton systems, although jitter is reduced for them [102]–[114]. In all cases, the dominant source of timing jitter is related to changes in the soliton carrier frequency, occurring because of phase fluctuations induced by amplifier noise.

The moment method of Section 7.7.2 can be used to calculate the variance of fluctuations in the frequency and pulse position. Since pulse shape remains approximately Gaussian for DM solitons, the analysis applies for them with minor changes. The final result can be written as [111]

$$\sigma_t^2 = \frac{S_{\text{ASE}} T_m^2}{E_0} [N_A(1 + C_0^2) + N_A(N_A - 1)C_0 d + \frac{1}{6}N_A(N_A - 1)(2N_A - 1)d^2], \quad (9.3.7)$$

where N_A is the number of amplifiers along the link and the dimensionless parameter d is defined as in Eq. (9.1.9), except that the minimum width T_m should be used in place of T_0 . The first term inside the square brackets results from direct position fluctuations of a soliton within each amplifier. The second term is related to the cross-correlation between frequency and position fluctuations. The third term is solely due to frequency fluctuations. For a soliton system designed with $L_{\text{map}} = L_A$ and $N_A \gg 1$, jitter is dominated by the last term in Eq. (9.3.7) because of its N_A^3 dependence and is approximately given by

$$\frac{\sigma_t^2}{T_m^2} \approx \frac{S_{\text{ASE}}}{3E_0} N_A^3 d^2 = \frac{S_{\text{ASE}} L_T^3}{3E_0 L_D^2 L_A}, \quad (9.3.8)$$

where $L_D = T_m^2 / |\bar{\beta}_2|$ and $N_A = L_T / L_A$ for a lightwave system with the total transmission distance L_T .

Because of the cubic dependence of σ_t^2 on the system length L_T , the timing jitter can become an appreciable fraction of the bit slot for long-haul systems, especially at bit rates exceeding 10 Gb/s for which the bit slot is shorter than 100 ps. Such jitter would lead to large power penalties if left uncontrolled. In practice, jitter should be less than 10% of the bit slot. Figure 9.12 shows how timing jitter increases with L_T for a 20-Gb/s DM soliton system, designed using a dispersion map consisting of 10.5 km of anomalous-GVD fiber and 9.7 km of normal-GVD fiber [$D = \pm 4 \text{ ps}/(\text{km-nm})$]. Optical amplifiers with $n_{\text{sp}} = 1.3$ (or a noise figure of 4.1 dB) are placed every 80.8 km (4 map periods) along the fiber link for compensating 0.2-dB/km losses. Variational equations were used to find the input pulse parameters for which solitons recover periodically after each map period ($T_0 = 6.87 \text{ ps}$, $C_0 = 0.56$, and $E_0 = 0.4 \text{ pJ}$). The nonlinear parameter γ was $1.7 \text{ W}^{-1}/\text{km}$.

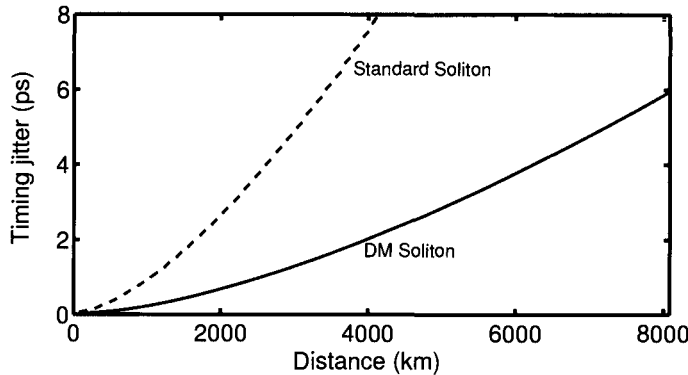


Figure 9.12: ASE-induced timing jitter as a function of length for a 20-Gb/s system designed with DM (solid curve) and standard (dashed line) solitons.

An important question is whether the use of dispersion management is helpful or harmful from the standpoint of timing jitter. The timing jitter for standard solitons can also be found in a closed form using the moment method and is given by [111]

$$\sigma_t^2 = \frac{S_{\text{ASE}} T_0^2}{3E_s} [N_A + \frac{1}{6} N_A(N_A - 1)(2N_A - 1)d^2], \quad (9.3.9)$$

where we have used E_s for the input soliton energy to emphasize that it is different from the DM soliton energy E_0 used in Eq. (9.3.7). For a fair comparison of the DM and standard solitons, we consider an identical soliton system except that the dispersion map is replaced by a single fiber whose GVD is constant and equal to the average value $\bar{\beta}_2$. The soliton energy E_s can be found by using $E_0 = 2P_0T_0$ with $P_0 = |\bar{\beta}_2|/(\gamma T_0^2)$ and is given by

$$E_s = 2f_{\text{LM}}|\bar{\beta}_2|/(\gamma T_0), \quad (9.3.10)$$

where the factor f_{LM} is the enhancement factor resulting from loss management ($f_{\text{LM}} \approx 3.8$ for a 16-dB gain). The dashed line in Figure 9.12 shows the timing jitter using Eqs. (9.3.9) and (9.3.10). A comparison of the two curves shows that the jitter is considerably smaller for DM solitons. The physical reason behind the jitter reduction is related to the enhanced energy of the DM solitons. In fact, the energy ratio E_0/E_s equals the energy enhancement factor f_{DM} introduced earlier in Eq. (9.3.6). From a practical standpoint, the reduced jitter of DM solitons permits much longer transmission distances as evident from Figure 9.12. Note that Eq. (9.3.9) also applies for DDFs because the GVD variations along the fiber can be included through the parameter d defined in Eq. (9.1.9).

For long-haul soliton systems, the number of amplifiers is large enough that the N_A^3 term dominates in Eq. (9.3.9), and the timing jitter for standard solitons is approximately given by [103]

$$\frac{\sigma_t^2}{T_0^2} = \frac{S_{\text{ASE}} L_T^3}{9E_s L_D^2 L_A}. \quad (9.3.11)$$

Comparing Eqs. (9.3.8) and (9.3.11), we find that timing jitter is reduced by a factor of $(f_{\text{DM}}/3)^{1/2}$ when DM solitons are used.

To find a simple design rule, we can use Eq. (9.3.11) with the condition $\sigma_t < b_j/B$, where b_j is the fraction of the bit slot by which a soliton can move without affecting the system performance adversely. Using $B = (2q_0T_0)^{-1}$ and E_s from Eq. (9.3.10), the bit rate–distance product BL_T for standard solitons is found to be limited by

$$BL_T < \left(\frac{9b_j^2 f_{\text{LM}} L_A}{S_{\text{ASE}} q_0 \gamma \bar{\beta}_2} \right)^{1/3}. \quad (9.3.12)$$

For DM solitons the energy enhancement factor f_{LM} is replaced by $f_{\text{LM}} f_{\text{DM}}/3$. The tolerable value of b_j depends on the acceptable BER and on details of the receiver design; typically, $b_j < 0.1$. To see how amplifier noise limits the total transmission distance, consider a standard soliton system operating at 10 Gb/s with parameter values $T_0 = 10$ ps, $q_0 = 5$, $\alpha = 0.2$ dB/km, $\gamma = 2 \text{ W}^{-1}/\text{km}$, $\bar{\beta}_2 = -1 \text{ ps}/(\text{km-nm})$, $n_{\text{sp}} = 1.5$, $L_A = 50$ km, and $b_j = 0.08$. Using $G = 10$ dB, we find $f_{\text{LM}} = 2.56$ and $S_{\text{ASE}} = 2.16 \times 10^{-6}$ pJ. With these values, BL_T must be below 70 (Tb/s)-km, and the transmission distance is limited to below 7,000 km at 10 Gb/s. This value can be increased to beyond 10,000 km for DM solitons.

9.3.5 Control of Timing Jitter

As the timing jitter ultimately limits the performance of a soliton system, it is essential to find a solution to the timing-jitter problem before the use of solitons can become practical. Several techniques were developed during the 1990s for controlling timing jitter [115]–[136]. This subsection is devoted to a brief discussion of them.

The use of optical filters for controlling the timing jitter of solitons was proposed as early as 1991 [115]–[117]. This approach makes use of the fact that the ASE occurs over the entire amplifier bandwidth but the soliton spectrum occupies only a small fraction of it. The bandwidth of optical filters is chosen such that the soliton bit stream passes through the filter but most of the ASE is blocked. If an optical filter is placed after each amplifier, it improves the SNR because of the reduced ASE and also reduces the timing jitter simultaneously. This was indeed found to be the case in a 1991 experiment [116] but the reduction in timing jitter was less than 50%.

The filter technique can be improved dramatically by allowing the center frequency of the successive optical filters to slide slowly along the link. Such *sliding-frequency* filters avoid the accumulation of ASE within the filter bandwidth and, at the same time, reduce the growth of timing jitter [118]. The physical mechanism behind the operation of such filters can be understood as follows. As the filter passband shifts, solitons shift their spectrum as well to minimize filter-induced losses. In contrast, the spectrum of ASE cannot change. The net result is that the ASE noise accumulated over a few amplifiers is filtered out later when the soliton spectrum has shifted by more than its own bandwidth.

The moment method can be extended to include the effects of optical filters by noting that each filter modifies the soliton field such that

$$U_f(z_f, t) = \frac{1}{2\pi} \int_{-\infty}^{\infty} H_f(\omega - \omega_f) \tilde{U}(z_f, \omega) e^{-i\omega t} d\omega, \quad (9.3.13)$$

where $\tilde{U}(z_f, \omega)$ is the pulse spectrum and H_f is the transfer function of the optical filter located at z_f . The filter passband is shifted by ω_f from the soliton carrier frequency. If we approximate the filter spectrum by a parabola over the soliton spectrum and use $H_f(\omega - \omega_f) = 1 - b(\omega - \omega_f)^2$, it is easy to see that the filter introduces an additional loss for the soliton that should be compensated by increasing the gain of optical amplifiers. The analysis of timing jitter shows that sliding-frequency filters reduce jitter considerably for both the standard and DM solitons [131].

Solitons can also be controlled in the time domain using the technique of *synchronous* amplitude modulation, implemented in practice using a LiNbO₃ modulator [121]. The technique works by introducing additional losses for those solitons that have shifted from their original position (center of the bit slot). The modulator forces solitons to move toward its transmission peak where the loss is minimum. Mathematically, the action of the modulator is to change the soliton amplitude as

$$U(z_m, t) \rightarrow T_m(t - t_m) U(z_m, t), \quad (9.3.14)$$

where $T_m(\tau)$ is the transmission coefficient of the modulator located at $z = z_m$. The moment method or perturbation theory can be used to show that timing jitter is reduced considerably by modulators.

The synchronous modulation technique can also be implemented by using a phase modulator [122]. One can understand the effect of periodic phase modulation by recalling that a frequency shift is associated with all time-dependent phase variations. Since a change in soliton frequency is equivalent to a change in the group velocity, phase modulation induces a temporal displacement. Synchronous phase modulation is implemented in such a way that the soliton experiences a frequency shift only if it moves away from the center of the bit slot, which confines it to its original position despite the timing jitter induced by ASE and other sources. Intensity and phase modulations can be combined together to further improve system performance [123].

Synchronous modulation can be combined with optical filters to control solitons simultaneously in both the time and frequency domains. In fact, this combination permits arbitrarily long transmission distances [124]. The use of intensity modulators also permits a relatively large amplifier spacing by reducing the impact of dispersive waves. This property of modulators was exploited in 1995 to transmit a 20-Gb/s soliton train over 150,000 km with an amplifier spacing of 105 km [125]. Synchronous modulators also help in reducing the soliton interaction and in clamping the level of amplifier noise. The main drawback of modulators is that they require a clock signal that is synchronized with the original bit stream.

A relatively simple approach uses post-compensation of accumulated dispersion for reducing timing jitter [126]. The basic idea can be understood from Eq. (9.3.7) or Eq. (9.3.9) obtained for the timing jitter of DM and standard solitons, respectively. The cubic term that dominates the jitter at long distances depends on the accumulated

dispersion through the parameter d . If a fiber is added at the end of the link such that it reduces the accumulated dispersion, it should help in reducing the jitter. It is easy to include the contribution of the post-compensation fiber to the timing jitter using the moment method. In the case of DM solitons, the jitter variance at the end of a post-compensation fiber of length L_c and GVD β_{2c} is given by [111]

$$\sigma_c^2 = \sigma_t^2 + (S_{\text{ASE}} T_m^2 / E_0) [2N_A C_0 d_c + N_A (N_A - 1) dd_c + N_A d_c^2], \quad (9.3.15)$$

where σ_t^2 is given by Eq. (9.3.7) and $d_c = \beta_{2c} L_c / T_m^2$. If we define $y = -d_c / (N_A d)$ as the fraction by which the accumulated dispersion $N_A d$ is compensated and retain only the dominant cubic terms in Eq. (9.3.15), this equation can be written as

$$\sigma_c^2 = N_A^3 d^2 T_m^2 (S_{\text{ASE}} / E_0) (y^2 - y + 1/3). \quad (9.3.16)$$

The minimum value occurs for $y = 0.5$ for which σ_c^2 is reduced by a factor of 4. Thus, the timing jitter of solitons can be reduced by a factor of 2 by postcompensating the accumulated dispersion by 50%. The same conclusion holds for standard solitons [126].

Several other techniques can be used for controlling timing jitter. One approach consists of inserting a fast saturable absorber periodically along the fiber link. Such a device absorbs low-intensity light, such as ASE and dispersive waves, but leaves the solitons intact by becoming transparent at high intensities. To be effective, it should respond at a time scale shorter than the soliton width. It is difficult to find an absorber that can respond at such short time scales. A nonlinear optical loop mirror can act as a fast saturable absorber and reduce the timing jitter of solitons, while also stabilizing their amplitude [127]. Re-timing of a soliton train can also be accomplished by taking advantage of cross-phase modulation [128]. The technique overlaps the soliton data stream and another pulse train composed of only 1 bits (an optical clock) inside a fiber where cross-phase modulation (XPM) induces a nonlinear phase shift on each soliton in the signal bit stream. Such a phase modulation translates into a net frequency shift only when the soliton does not lie in the middle of the bit slot. Similar to the case of synchronous phase modulation, the direction of the frequency shift is such that the soliton is confined to the center of the bit slot. Other nonlinear effects such as stimulated Raman scattering [129] and four-wave mixing (FWM) can also be exploited for controlling the soliton parameters [130]. The technique of distributed amplification also helps in reducing timing jitter [114].

9.4 Pseudo-linear Lightwave Systems

Pseudo-linear lightwave systems operate in the regime in which the local dispersion length is much shorter than the nonlinear length in all fiber sections of a dispersion-managed link. This approach is most suitable for systems operating at bit rates of 40 Gb/s or more and employing relatively short optical pulses that spread over multiple bits quickly as they propagate along the link. This spreading reduces the peak power and lowers the impact of SPM on each pulse. There are several ways one can design such systems. In one case, pulses spread throughout the link and are compressed back at the receiver end using a dispersion-compensating device. In another, pulses

are spread even before the optical signal is launched into the fiber link using a DCF (precompensation) and they compress slowly within the fiber link, without requiring any post-compensation.

A third possibility is to employ periodic in-line compensation. In this case, the dispersion map is chosen such that each pulse broadens by a large factor in the first section but it is compressed in the following section with opposite dispersion characteristics. An optical amplifier restores the signal power after the second section, and the whole process repeats itself. Often, a small amount of dispersion is left uncompensated in each map period. This residual dispersion per span can be used to control the impact of intrachannel nonlinear effects in combination with the amounts of pre- and post-compensation.

As optical pulses spread considerably outside their assigned bit slot in all pseudo-linear systems, they overlap considerably and interact with each other through the nonlinear term in the NLS equation. It turns out that the spreading of bits belonging to different WDM channels produces an averaging effect that reduces the *interchannel* nonlinear effects considerably [25]. However, at the same time, an enhanced nonlinear interaction among the bits of the same channel produces new *intrachannel* nonlinear effects that limit the system performance, if left uncontrolled. Thus, pseudo-linear systems are far from being linear. The important question is whether pulse spreading helps to lower the overall impact of fiber nonlinearity and allows higher launched powers into the fiber link. The answer to this question turned out to be affirmative. In this section we focus on the intrachannel nonlinear effects and study how they affect a pseudo-linear lightwave system.

9.4.1 Origin of Intrachannel Nonlinear Effects

All pseudo-linear systems suffer from the nonlinear interaction among the neighboring overlapping pulses. Starting in 1999, such intrachannel nonlinear effects were studied extensively [137]–[149]. In a numerical approach, one solves the NLS equation (9.1.2) for a pseudo-random bit stream with the input

$$U(0, t) = \sum_{m=1}^M U_m(0, t - t_m), \quad (9.4.1)$$

where $t_m = mT_b$, T_b is the duration of the bit slot, M is the total number of bits included in numerical simulations. Here, U_m governs the shape of input pulses, and $U_m = 0$ if the m th pulse represents a 0 bit.

Even though numerical simulations are essential for a realistic system design, considerable physical insight can be gained with a semianalytic approach that focuses on three neighboring pulses. If we write the total field as $U = U_1 + U_2 + U_3$ in Eq. (9.1.2), it reduces to the following set of three coupled NLS equations [25]:

$$i \frac{\partial U_1}{\partial z} - \frac{\beta_2}{2} \frac{\partial^2 U_1}{\partial t^2} + \gamma P_0 p(z) [(|U_1|^2 + 2|U_2|^2 + 2|U_3|^2)U_1 + U_2^2 U_3^*] = 0, \quad (9.4.2)$$

$$i \frac{\partial U_2}{\partial z} - \frac{\beta_2}{2} \frac{\partial^2 U_2}{\partial t^2} + \gamma P_0 p(z) [(|U_2|^2 + 2|U_1|^2 + 2|U_3|^2)U_2 + 2U_1 U_2^* U_3] = 0, \quad (9.4.3)$$

$$i \frac{\partial U_3}{\partial z} - \frac{\beta_2}{2} \frac{\partial^2 U_3}{\partial t^2} + \gamma P_0 p(z) [(|U_3|^2 + 2|U_1|^2 + 2|U_2|^2) U_3 + U_2^2 U_1^*] = 0. \quad (9.4.4)$$

These three coupled equations show explicitly the origin of intrachannel nonlinear effects. The first nonlinear term corresponds to SPM. The next two terms result from XPM induced by the other two pulses. Since these terms represent XPM interaction between pulses belonging to the same channel, this phenomenon is referred to as intrachannel XPM. The last term is FWM-like and is responsible for intrachannel FWM. Although it may seem odd that FWM can occur among pulses of the same channel, one should remember that the spectrum of each pulse has modulation side bands located on both sides of the carrier frequency. If different sidebands of two or more overlapping pulses are present simultaneously in the same temporal window, they can interact through FWM and transfer energy among the interacting pulses. This phenomenon can also create new pulses in the time domain. Such pulses are referred to as a *shadow* pulse [137] or a *ghost* pulse [138]. They impact the system performance considerably, especially those created in the 0-bit time slots [146].

The preceding method can be extended to the case of more than three pulses. Assuming that Eq. (9.4.1) can be used at any distance z , the NLS equation (9.1.2) can be written as

$$\sum_{j=1}^M \left(i \frac{\partial U_j}{\partial z} - \frac{\beta_2}{2} \frac{\partial^2 U_j}{\partial t^2} \right) = -\gamma P_0 p(z) \sum_{j=1}^M \sum_{k=1}^M \sum_{l=1}^M U_j U_k^* U_l. \quad (9.4.5)$$

The triple sum on the right side includes all the nonlinear effects. SPM occurs when $j = k = l$. The terms responsible for XPM correspond to $j = k \neq l$ and $j \neq k = l$. The remaining terms lead to intrachannel FWM. Each nonlinear term in the triple sum on the right side of Eq. (9.4.5) provides its contribution in a temporal region near $t_j + t_l - t_k$, a relation analogous to the phase-matching condition among waves of different frequencies [25]. This relation can be used to identify all nonlinear terms that can contribute to a specific pulse. It is important to note that, whereas the total energy of all pulses remains constant during propagation, the energy of any individual pulse can change because of intrachannel FWM.

When a single pulse surrounded by several zero bits on both sides, we can set $U_1 = U_3 = 0$ in Eqs. (9.4.2) through (9.4.4). The resulting equation for U_2 is identical to the original NLS equation (9.1.2). The SPM effects in this case have been studied in Section 9.1 through Eqs. (9.1.5) and (9.1.6) obtained with the help of the moment method. As was found there, the impact of SPM is reduced considerably for pseudo-linear systems because of a much lower peak power of each pulse. It is also reduced because of spectral breathing occurring as pulse spectrum broadens and narrows from one fiber section to the next. However, the effects of intrachannel XPM and FWM are not negligible. Even though intrachannel XPM affects only the phase of each pulse, this phase shift is time-dependent and affects the carrier frequency of the pulse. As discussed later, the resulting frequency chirp leads to timing jitter through fiber dispersion [140].

In the following discussion, we study the impact of intrachannel XPM and FWM on the performance of a pseudo-linear system. This impact depends on the choice of the dispersion map, among other things [25]. In general, the optimization of a dispersion-managed system requires the adjustment of many design parameters, such as launch

power, amplifier spacing, and the location of DCFs [139]. In a 2000 experiment, a 40-Gb/s signal could be transmitted over transoceanic distances, in spite of its use of standard fibers, through a synchronous modulation technique [22]. In a 2002 experiment, distance could be increased to 10^6 km using synchronous modulation in combination with all-optical regeneration [150].

9.4.2 Intrachannel Cross-Phase Modulation

It turns out that intrachannel XPM introduces timing jitter in a pseudo-linear system. To understand its origin, consider two isolated 1 bits by setting $U_3 = 0$ in Eqs. (9.4.2) through (9.4.4). The optical field associated with each pulse satisfies an equation of the form

$$i \frac{\partial U_n}{\partial z} - \frac{\beta_2}{2} \frac{\partial^2 U_n}{\partial t^2} + \gamma P_0 p(z) (|U_n|^2 + 2|U_{3-n}|^2) U_n = 0, \quad (9.4.6)$$

where $n = 1$ or 2 . Clearly, the last term is due to XPM. If we ignore the effects of GVD for the moment, this term shows that, over a short distance Δz , the phase of each pulse is shifted nonlinearly by the other pulse by the amount

$$\phi_n(z, t) = 2\gamma P_0 p(z) \Delta z |U_{3-n}(z, t)|^2. \quad (9.4.7)$$

As this phase shift depends on pulse shape, it varies across the pulse and produces a frequency chirp

$$\delta\omega_n \equiv -\frac{\partial\phi_n}{\partial t} = -2\gamma P_0 p(z) \Delta z \frac{\partial}{\partial t} |U_{3-n}(z, t)|^2. \quad (9.4.8)$$

This frequency shift is known as the XPM-induced chirp.

Similar to the case of ASE-induced frequency shift discussed in Section 7.7.2, an XPM-induced shift in the carrier frequency of the pulse translates into a shift in the pulse position through changes in the group velocity of the pulse. If all pulses were to shift in time by the same amount, this effect would be harmless. However, the time shift depends on the pattern of bits surrounding each pulse that varies from bit to bit depending on the data transmitted. As a result, pulses shift in their respective time slots by different amounts, a feature referred to as XPM-induced timing jitter. As will be seen later, XPM also introduces some amplitude fluctuations.

A more quantitative estimate of the XPM effects makes use of the moment or the variational method. In this case, we must include the expected frequency and temporal shifts and assume that Eq. (9.4.6) has the following solution:

$$U_n(z, t) = a_n \exp[-\frac{1}{2}(1+iC_m)(t-t_n)^2/T_n^2 - i\Omega_n(t-t_n) + i\phi_n], \quad (9.4.9)$$

where t_n represents the position and Ω_n represents the frequency shift for the n th pulse. In the moment method, these two quantities are calculated using

$$t_n = \frac{1}{E_0} \int_{-\infty}^{\infty} t |U_n|^2 dt, \quad \Omega_n = \frac{i}{2E_0} \int_{-\infty}^{\infty} t \left(U_n^* \frac{\partial U_n}{\partial t} - U_n \frac{\partial U_n^*}{\partial t} \right) dt, \quad (9.4.10)$$

where E_0 is the input energy of each pulse.

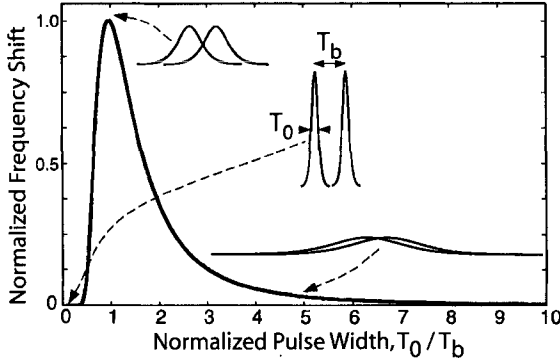


Figure 9.13: Normalized XPM-induced frequency shift as a function of pulse width T_0 for two Gaussian pulses separated by T_b . The insets show schematically the extent of overlap between two pulses in three cases. (After Ref. [138]; ©1999 OSA.)

Noting that each pulse in Eq. (9.4.9) is quantified through six parameters, such an approach leads to 12 first-order differential equations. The two phase equations can be ignored if we neglect interactions that are phase-dependent. The amplitude equations are not needed since $E_0 = \sqrt{\pi}a_n^2T_n$ relates a_n to T_n . Furthermore, only the frequency difference $\Delta\Omega = \Omega_1 - \Omega_2$ and the pulse separation $\Delta t = t_1 - t_2$ are relevant for describing the intrachannel XPM effects. One is thus left with the following set of six equations:

$$\frac{dT_n}{dz} = \frac{\beta_2(z)C_n}{T_n}, \quad (9.4.11)$$

$$\frac{dC_n}{dz} = (1 + C_n^2)\frac{\beta_2(z)}{T_n^2} + \frac{\gamma(z)p(z)E_0}{\sqrt{2\pi}T_n} \left[1 - \frac{2T_n^3}{T_a^3}(1 - \mu^2)e^{-\mu^2/2} \right], \quad (9.4.12)$$

$$\frac{d\Delta\Omega}{dz} = \gamma(z)p(z)E_0 \frac{8\mu}{\pi T_a^2} e^{-\mu^2/2}, \quad (9.4.13)$$

$$\frac{d\Delta t}{dz} = \beta_2(z)\Delta\Omega, \quad (9.4.14)$$

where $n = 1$ or 2 , $\mu = \Delta t/T_a$, and $T_a^2 = \frac{1}{2}(T_1^2 + T_2^2)$.

A comparison of Eqs. (9.4.11) and (9.4.12) with Eqs. (9.1.5) and (9.1.6) shows that, although the width equation remains unchanged, overlapping of two neighboring pulses modifies the chirp equation. However, any change in the chirp also affects the pulse width, as the two equations are coupled. Moreover, changes in pulse width would manifest through changes in pulse amplitude since $E_0 = \sqrt{\pi}a_n^2T_n$ remains constant for each pulse. Thus, the amplitude of any 1 bit would depend whether it is surrounded by 0 or 1 bits. As this pattern varies randomly in an optical bit stream, pulse amplitude would vary from bit to bit. This is the origin of XPM-induced amplitude jitter.

Equations (9.4.13) and (9.4.14) show that XPM-induced timing jitter results from the frequency shift $\Delta\Omega$. If $\Delta\Omega$ were to vanish, the pulse separation would remain fixed at its initial value, and no jitter would occur. At a bit rate B , two neighboring

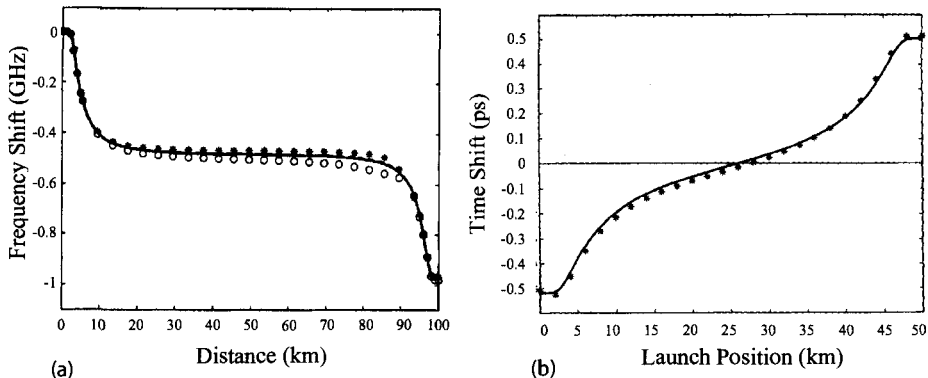


Figure 9.14: (a) XPM-induced frequency shift over one map period and (b) temporal shift in pulse spacing as a function of launch position within the anomalous-GVD fiber for two 5-ps Gaussian pulses separated by 25 ps. The curves almost coincide for two launch conditions. Symbols show the numerical results obtained from the NLS equation. (After Ref. [142]; ©2001 OSA.)

pulses are initially spaced by $\Delta t = T_b \equiv B^{-1}$. When both pulses have the same initial width T_0 , clearly $T_a = T_0$. Equation (9.4.13) shows that the amount of frequency shift depends on the ratio $x = T_0/T_b$ as $F(x) = x^{-3} \exp[-1/(2x^2)]$. Figure 9.13 shows how this function varies with x [138]. It peaks near $x = 1$, indicating that frequency shift $\Delta\Omega$ is largest when pulse widths are comparable to their temporal spacing. For pulses much smaller than the bit slot, $x \ll 1$, and $\Delta\Omega$ nearly vanishes. This is expected on physical grounds because the tails of such narrow pulses do not overlap significantly, and pulses cannot interact through XPM. What is surprising is that $\Delta\Omega$ is also relatively small when pulses are much wider than their spacing so that $x \gg 1$. Intuitively, one would guess this to be the worse situation since pulses almost completely overlap under such conditions. The reason is related to the fact that the XPM-induced frequency chirp in Eq. (9.4.8) depends on the slope of the pulse power. This slope is smaller for wider pulses and also changes sign, resulting in an averaging effect. The main conclusion is that XPM-induced timing jitter can be reduced by stretching optical pulses over multiple bit slots. This is precisely what is done in pseudo-linear lightwave systems.

The frequency shift $\Delta\Omega$ and pulse spacing Δt change with z as two pulses propagate inside the fiber link. Such changes are studied by solving Eqs. (9.4.11) through (9.4.14) numerically for a given dispersion map [142]. Figure 9.14(a) shows $\Delta\Omega/2\pi$ along a 100-km link formed by using two 50-km fiber sections with $D = \pm 10 \text{ ps}/(\text{km-nm})$. The nonlinear parameter $\gamma = 2 \text{ W}^{-1}/\text{km}$ for both fibers. Losses are assumed to be compensated through distributed amplification so that $p(z) = 1$. Two Gaussian pulses have 5-ps width (FWHM) at the input and are separated by 25 ps. The solid curve shows the case in which pulses are launched at the input end of the section with anomalous GVD. The almost coinciding dashed curve corresponds to the case in which the dispersion map is made symmetric by launching pulses at the midpoint of this section. Stars and circles show the results obtained in these two cases by solving the NLS equation directly. Most of the frequency shift occurs near the two ends of the map period where

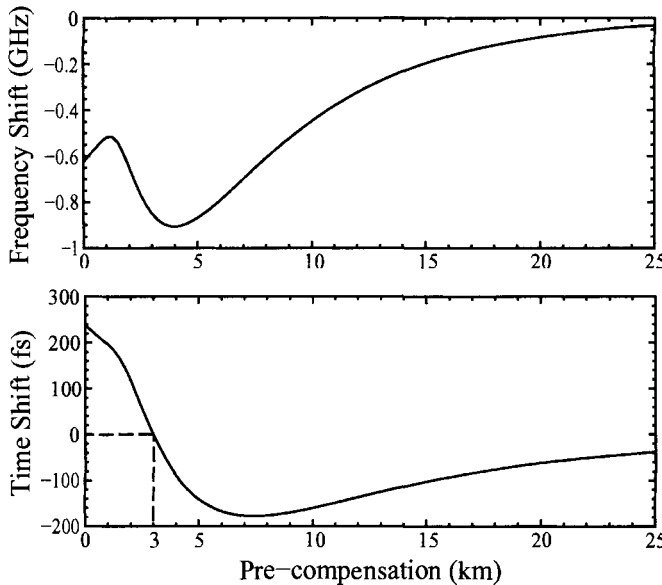


Figure 9.15: Frequency and time shifts after 100 km as a function of DCF length used for precompensation. (After Ref. [25]; ©2002 Elsevier.)

pulses are relatively short and overlap only partially.

Even though the frequency shift is nearly the same for the symmetric and asymmetric maps, the shift in pulse spacing Δt from its initial 25-ps value depends considerably on the exact location where input pulses are launched. This is evident from Figure 9.14(b) that shows this shift as a function of the launch position within the anomalous-GVD fiber. Timing shift can be positive or negative depending on whether the first fiber section exhibits anomalous or normal dispersion. The reason is related to the fact that two pulses attract each other in the case of anomalous GVD but they repel each other for normal GVD. As the frequency shift in Figure 9.14(a) grows monotonically, it is the second section that produces the most shift [142]. The most important feature of this figure is that pulse position does not shift at all for a symmetric dispersion map. In this case, timing shifts produced in the two sections completely cancel each other. This cancellation can occur only when distributed amplification is used, and we can set $p(z) \approx 1$. In the case of lumped amplification, large power variations make the XPM effects much stronger in the first section of a periodic dispersion map.

When lumped amplification is used, the dispersion map is not symmetric. However, it is possible to cancel the XPM-induced time shift by suitably chirping input pulses before launching them into the fiber link. Experimentally, a fiber of suitable length is used to chirp the pulse. This technique is equivalent to the precompensation technique discussed in Section 8.2. Figure 9.15 shows the frequency and temporal shifts acquired after one map period as a function of fiber length used for precompensation. The 100-km-long map consists of a 75-km section with $\beta_2 = -5 \text{ ps}^2/\text{km}$, followed with a 25-km DCF section with $\beta_2 = 20 \text{ ps}^2/\text{km}$. The same DCF is used for precompensation. Even

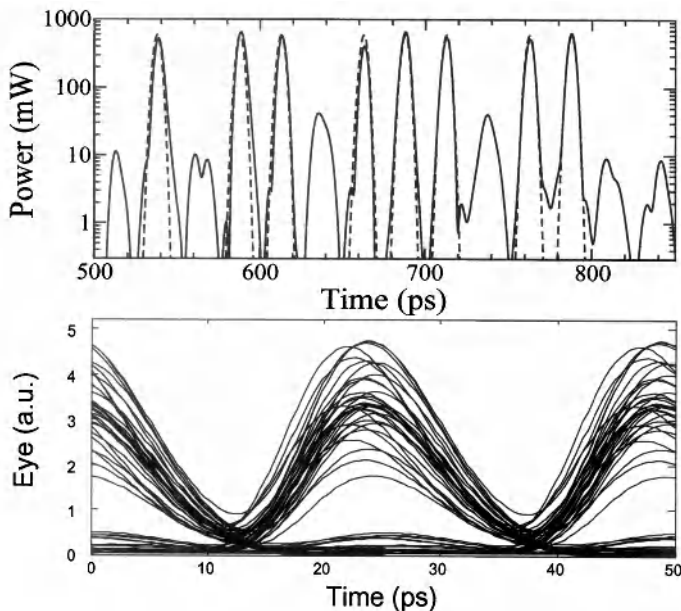


Figure 9.16: Bit stream and eye diagram at the end of a 80-km fiber with $D = 17 \text{ ps}/(\text{km-nm})$. The dashed curve shows for comparison the input bit stream. (After Ref. [25]; ©2002 Elsevier.)

though there is always a net frequency shift after one map period, the temporal shift vanishes when the length of precompensation fiber is about 3 km.

9.4.3 Intrachannel Four-Wave Mixing

The impact of intrachannel FWM is quite different from intrachannel XPM because this nonlinear process can transfer energy from one pulse to neighboring pulses. In particular, it can create new pulses in bit slots that represent 0's and contain no pulse initially. Such FWM-generated pulses (called ghost or shadow pulses) are undesirable for any lightwave system because they lead to additional errors if their amplitude becomes substantial [137]. Ghost pulses were observed as early as 1992 when a pair of ultrashort pulses, each stretched to 90 ps, was propagated through an optical fiber [151]. However, this phenomenon attracted attention only after 1999 when it was found to impact the performance of lightwave systems employing strong dispersion management [25].

As an example of the system degradation caused by intrachannel FWM [25], Figure 9.16 shows the results of numerical simulations for a 40-Gb/s system at the end of a 80-km-long standard fiber with $D = 17 \text{ ps}/(\text{km-nm})$. The 5-ps Gaussian input pulses were first chirped by propagating them through a precompensation fiber with $DL = -527 \text{ ps/nm}$. Other parameters are identical to those used for Figure 9.15. Because of the rapid broadening of input pulses, timing jitter is reduced considerably. However, ghost

pulses appear in all 0 slots, and they degrade the eye diagram considerably. Amplitude fluctuations seen in this figure also result from intrachannel FWM.

Compared with the case of XPM, analytic treatment of intrachannel FWM is more involved. A perturbative approach has been used with considerable success to describe the impact of intrachannel nonlinearities [140], but its accuracy decreases rapidly for large timing jitter. Its main advantages are: one does not need to assume a specific pulse shape and it can be extended easily even to the case of a pseudorandom bit stream [143]–[145]. The main idea is to assume that the solution of the NLS equation (9.1.2) can be written in the form

$$U(z, t) = \sum_{j=1}^M U_j(z, t - t_j) + \sum_{j=1}^M \sum_{k=1}^M \sum_{l=1}^M \Delta U_{jkl}(z, t), \quad (9.4.15)$$

where M the number of bits, U_j represents the amplitude of the j th bit located at $t = t_j$ initially, and ΔU_{jkl} is the perturbation created by the nonlinear term. The first term in Eq. (9.4.15) represents the zeroth-order solution obtained by neglecting the nonlinear term in the NLS equation ($\gamma = 0$). This solution can be obtained in an analytic form. The second term represents the contribution of all nonlinear effects. It can also be obtained in a closed form by employing first-order perturbation theory [140].

In the case of Gaussian input pulses of width T_0 , the perturbation produced by the nonlinear term is given by [25]

$$\begin{aligned} \Delta U_{jkl}(L, t_j + t_l - t_k) &= \gamma P_0 \exp\left(-\frac{t^2}{6T_0^2}\right) e^{i\Delta\phi} \int_0^L \frac{ip(z) dz}{\sqrt{1+2id+3d^2}} \\ &\times \exp\left(-\frac{3[2t/3+(t_j-t_k)][2t/3+(t_l-t_k)]}{T_0^2(1+3id)} - \frac{(t_j-t_l)^2}{T_0^2(1+2id+3d^2)}\right), \end{aligned} \quad (9.4.16)$$

where $\Delta\phi = \phi_k + \phi_l - \phi_j$ is related to the phases of individual pulses and the parameter $d(z)$ is defined as $d(z) = T_0^{-2} \int_0^z \beta_2(z) dz$. All intrachannel nonlinear effects produced by SPM, XPM, and FWM are included in this perturbative solution. The number of terms that must be included in the triple sum in Eq. (9.4.15) scales as M^3 for a bit stream with M bits. The integral in Eq. (9.4.16) can be performed analytically in some limiting cases. For example, if we consider a constant-dispersion fiber, set $p(z) = 1$ assuming ideal distributed amplification, and consider a fiber length L much longer than the dispersion length $L_D = T_0^2 / |\beta_2|$, we obtain [140]

$$\Delta U_{jkl}(L, t_j + t_l - t_k) = (i\gamma P_0 L D / \sqrt{3}) \exp(-t^2 / 6T_0^2) e^{i\Delta\phi} E_1(ir_{jkl} L D / L), \quad (9.4.17)$$

where $r_{jkl} = (t_j - t_k)(t_l - t_k) / T_0^2$ and $E_1(x)$ represents the exponential integral function.

Further insight can be gained by considering the simplest case of two pulses located at $t_1 = T_b$ and $t_2 = 2T_b$. In this case, j , k , and l take values 1 or 2, and 8 terms are contained in the triple sum in Eq. (9.4.15). The SPM effects are governed by the combinations 111 and 222. The effects of intrachannel XPM are governed by the four combinations 112, 122, 211, and 221. The remaining two combinations, 121 and 212, produce intrachannel FWM and perturbations that are located not at the original position of the input pulses but at locations 0 and $3T_b$. If these two time slots contain pulses

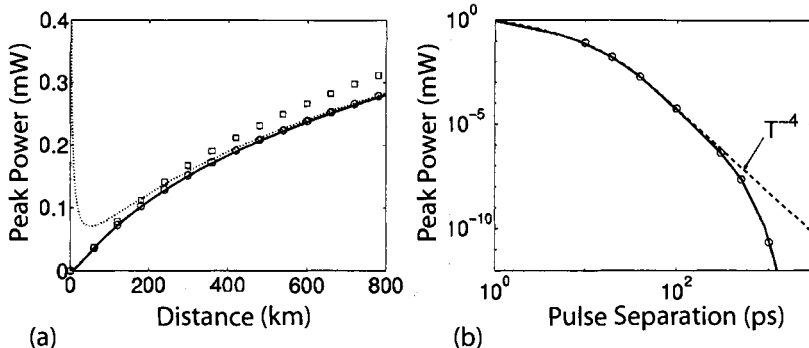


Figure 9.17: Peak power of a ghost pulse as a function of (a) link length L and (b) pulse separation T_b . The dotted curves indicate asymptotic approximations. Symbols show for comparison the results of numerical simulations. (After Ref. [140]; ©2000 IEEE.)

(and represent 1 bits), this perturbation beats with them and manifests as amplitude jitter. In contrast, if they represent 0 bits, a ghost pulse appears in these time slots.

Ghost pulses impact the detection process considerably depending on their power level. The peak power of the ghost pulse located at $t = 0$ is found from Eq. (9.4.17), after setting $j = l = 1$ and $k = 2$, to be

$$P_g(L) = |\Delta U_{121}(L, 0)|^2 = \frac{1}{3}(\gamma P_0 L_D)^2 \exp(-t^2/3T_0^2) \left| E_1 \left(\frac{2iT_b^2}{|\beta_2|L} \right) \right|^2, \quad (9.4.18)$$

where we used $t_1 = T_b$ and $t_2 = 2T_b$ for the location of two pulses whose overlapping generated the ghost pulse through intrachanneel FWM. Figure 9.17 shows (a) how the peak power grows with the link length L for a 40-Gb/s signal ($T_b = 25$ ps) and (b) how it decreases at $L = 20$ km with the duration T_b of the bit slot, when a bit stream is launched with 10-mW average power into a link made of standard fibers [140]. The dotted curve is obtained when $E_1(x)$ is replaced with its asymptotic approximation in which $|E_1(x)| \sim \ln(|1/x|)$. Such a logarithmic growth of P_g with L holds only for links with constant dispersion. The power transferred to ghost pulses can be reduced by increasing T_b . Indeed, Eq. (9.4.18) predicts that P_g varies with T_b as T_b^{-4} when we use an asymptotic approximation in which $|E_1(x)| \sim 1/x$ for large value of x . As seen in Figure 9.17, the predictions of this equation are in good agreement with the numerical simulations based on the NLS equation.

The preceding results change considerably when a periodic dispersion map is employed [142]–[147]. Even though peak power or energy of each ghost pulse grows in a logarithmic fashion during a single map period [142], it can still build up rapidly along the link because of a resonance related to the periodic nature of loss and dispersion variations [145]. Physically speaking, the amplitudes of ghost pulse generated in each map period add up in phase because of this resonance. As a result, the total peak power at the end of a link length L grows as

$$P_t(L) = |\Delta U_{121}(L, 0)|^2 \equiv P_g(L_{\text{map}})(L/L_{\text{map}})^2, \quad (9.4.19)$$

where L_{map} is the map period. Such quadratic growth of the ghost-pulse energy becomes of considerable concern for long-haul systems.

Intrachannel FWM also leads to amplitude fluctuations. Physically speaking, whenever the perturbation ΔU_{jkl} falls within the bit slots occupied by 1 bits, it beats with the amplitude of that bit. This beating modifies the amplitude of each 1 bit by an amount that depends not only on the pseudo-random bit pattern but also on the relative phases of neighboring pulses. In the case of a periodic dispersion map, energy fluctuations grow only linearly with length of the fiber link [145]. Moreover, they can be reduced considerably by adopting a distributed amplification scheme such that the average power does not vary much along the link.

9.5 Control of Intrachannel Nonlinear Effects

It is clear from Section 9.4 that intrachannel XPM and FWM can limit the performance of a pseudo-linear system. Both of these effects may occur even for systems making use of DM solitons because pulses overlap partially during each map period. It is thus important to find ways to reduce their impact through a proper system design. In this section we focus on several such schemes.

9.5.1 Optimization of Dispersion Maps

The design of any lightwave system requires an appropriate dispersion map. There are two main choices. In one, dispersion accumulates along most of the link length and is compensated using DCFs only at the transmitter and receiver ends (pre- and post-compensation). In the other, dispersion is compensated periodically along the link (in-line compensation), either completely or partially. In the later situation, DCFs may be used at the two ends for compensating the residual dispersion. Both types of dispersion maps have been used for 40-Gb/s experiments.

In a 1998 experiment, dispersion accumulated over a 150-km link with $D = 2.3 \text{ ps}/(\text{km}\cdot\text{nm})$ was fully compensated through pre- or post-compensation [152]. Pre-compensation worked only if the launch power was below 5 dBm. Much higher powers could be launched (up to 12 dBm) in the case of post-compensation, while keeping the penalty below 0.5 dB. A similar dispersion map was employed in a 2000 experiment in which a 40-Gb/s signal was transmitted over 800 km by amplifying it periodically every 80 km [153]. This experiment used standard fibers and compensated the entire accumulated dispersion ($d_a > 12 \text{ ns/nm}$) at the receiver end. It also operated in the pseudo-linear regime as it employed 2.5-ps pulses to generate the 40-Gb/s bit stream. The amplifier spacing was increased to 120 km in a later experiment [154]. Figure 9.18(a) shows the measured Q factor as a function of launched power after 3, 4, 5, and 6 amplifiers. At a distance of 600 km, Q^2 exceeded 15.6 dB (a value needed to keep the BER below 10^{-9}) over a large power range from 4 to 11 dBm. However, when link length was 720 km, this value of Q^2 was obtained only for an input power level close to 8 dBm. As seen in Figure 9.18(b), much longer distances could be realized by reducing the spacing between amplifiers to 80 km.

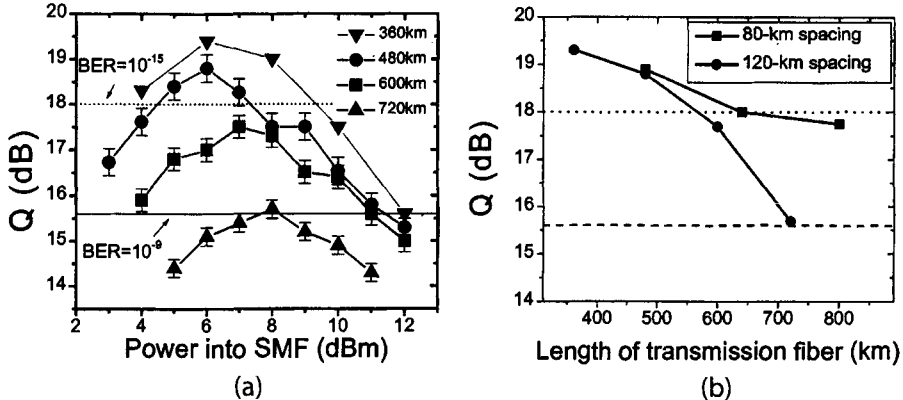


Figure 9.18: Measured Q factors (symbols) in a 40-Gb/s experiment (a) as a function of launched power after 3, 4, 5, and 6 amplifiers spaced 120 km apart and (b) as a function of distance for amplifier spacings of 80 and 120 km. The dashed and dotted lines show the value of Q needed to maintain a BER below 10^{-9} and 10^{-15} . (After Ref. [154]; ©2000 IEEE.)

A recirculating-loop configuration is often used in practice for 40-Gb/s experiments employing periodic dispersion maps [155]–[158]. In an experiment operating in the pseudo-linear regime [155], dispersion accumulated over 100 km of dispersion-shifted fiber was compensated using a higher-order-mode DCF (see Section 8.2). The span loss of 22 dB was compensated using a hybrid amplification scheme, with 15 dB of distributed Raman gain realized through backward pumping. In this experiment, 40-Gb/s data could be transmitted over 1,700 km while maintaining a BER below 10^{-9} . The same approach was used in another loop experiment in which loop length was 75 km, and the DCF did not fully compensate its dispersion [156]. The residual dispersion of -1.4 ps/nm per round trip was compensated outside the loop, just before the receiver. The DCF location was changed within the loop to simulate the pre- and post-compensation situations. In general, post-compensation provided better performance in the case of the RZ format. The FWM theory of Section 9.4.3 shows that the power transferred to ghost pulses is sensitive to the amount of precompensation. In this experiment, the transmission distance was limited to about 700 km.

Several 40-Gb/s experiments designed the dispersion map such that the system operated in the DM-soliton regime. In one set of experiments, the average GVD of a 106-km-long recirculating loop was varied to optimize system performance [157]. It was found that the system could be operated over more than 1,500 km by adjusting the launched power as long as the average dispersion was anomalous in the range of 0 to $0.1 \text{ ps}/(\text{km-nm})$. Much better performance was realized in another experiment in which a 40-Gb/s signal in the form of DM solitons could be transmitted over 6,400 km [158]. In general, soliton systems are found to be limited by XPM-induced timing jitter, whereas pseudo-linear systems are limited by FWM-generated ghost pulses [159].

The optimization of a dispersion map is not a trivial task as it involves varying a large number of design parameters (lengths and dispersion of individual fibers used to make the map, the amount of pre- and post-compensation employed, pulse width,

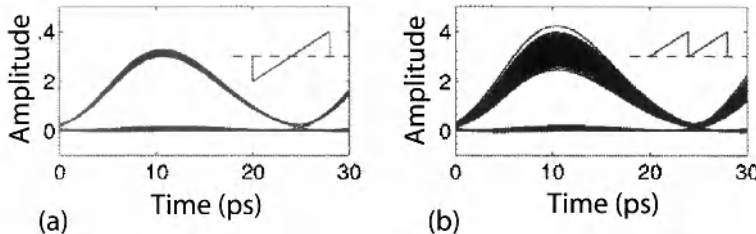


Figure 9.19: Numerically simulated eye diagrams at 1,600 km for (a) symmetric and (b) asymmetric dispersion maps. (After Ref. [160]; ©2001 IEEE.)

etc.) for a given set of system parameters (such as bit rate, link length, amplifier spacing). Extensive numerical simulations reveal several interesting features [25]. Both the pseudo-linear and DM-soliton regimes can be used to design 40-Gb/s systems, but the dispersion map for them is generally quite different. When fiber dispersion is relatively small along most of the link [$D < 4 \text{ ps}/(\text{km-nm})$], the soliton regime works best with an RZ duty cycle near 50% and requires some residual dispersion per map period. The system can also be designed in the pseudo-linear regime if the duty cycle is reduced to below 30% and the amount of pre- and post-compensation is suitably optimized. In contrast, when dispersion is large along most of the link (as is the case when standard single-mode fibers are employed), operation in the pseudo-linear regime may be more desirable for designing a 40-Gb/s system. Even though a single-channel soliton system may operate at 40 Gb/s over longer lengths under some conditions [149], the pseudo-linear regime is often preferred for WDM systems [25].

It turns out that the intrachannel nonlinear effects can be controlled with a suitable choice of the dispersion map [160]–[166]. As discussed earlier, XPM-induced timing jitter can be reduced considerably by making the dispersion map symmetric. In fact, as seen in Figure 9.19, both timing and amplitude jitters can be reduced by making the accumulated dispersion $d_a(z) = \int_0^z D(z) dz$ symmetric over the link such that $d_a(z) = d_a(L - z)$ [160]. In practice, this can be realized by compensating 50% of dispersion at the transmitter end and the remaining 50% at the receiver end. Such a map was used for numerical simulations shown in Figure 9.19 for which 2.5-ps Gaussian pulses with a 25-ps bit slot were propagated over 1,600 km of standard fiber with $D = 17 \text{ ps}/(\text{km-nm})$. Equation (9.4.16) can be used to understand why jitter may be reduced for symmetric maps by noting that the limits of integration should be changed from $-L/2$ to $L/2$ for such maps [160]. As discussed earlier, timing jitter results from XPM-induced frequency shifts that cancel for a symmetric map. Indeed, timing jitter would vanish under such conditions if $p(z) = 1$ in Eq. (9.4.16). The residual jitter seen in Figure 9.19 is due to variations in the average power of the signal along the link induced by a lumped amplification scheme. The amplitude jitter depends on the relative phase between the existing pulse in a bit slot and the nonlinear perturbation ΔU produced in that bit slot by other neighboring pulses. The in-phase part of the perturbation nearly vanishes for symmetric maps, resulting in reduced amplitude fluctuations.

If a periodic dispersion map is employed with two fiber sections of equal lengths but opposite dispersions, the jitter reduction can be realized by reversing the two fibers in

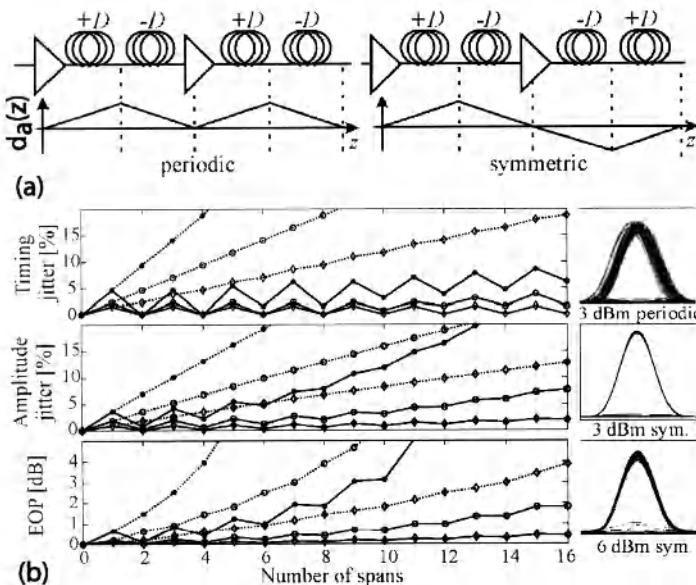


Figure 9.20: (a) Design of symmetric and asymmetric fiber links with corresponding changes in accumulated dispersion. (b) Timing jitter, amplitude jitter, and eye-opening penalty over 16 spans (each 80 km long) for symmetric (solid curves) and asymmetric (dashed) links. Launched power is 3, 6, and 9 dBm for diamonds, circles, and squares, respectively. Eye diagrams are also shown for all three cases. (After Ref. [161]; ©2004 IEEE.)

every alternate map period. Figure 9.20 shows the reduction realized in the amplitude and timing jitters at three power levels [161] with such symmetrization of the dispersion map. The calculated eye-opening penalty (EOP) is also shown. Each span employs two 40-km fiber sections with $D = \pm 17$ ps/(km-nm), $\alpha = 0.2$ dB/km, and $\gamma = 1.1$ W $^{-1}$ /km. In the case of a conventional periodic dispersion map, both the amplitude and timing jitters increase linearly with the link length and become so large that the EOP exceeds 4 dB after 700 km for a launched power of 6 dBm. In contrast, when the map is made symmetric, jitter accumulated over one span is cancelled to a large extent in the following span. As a result, the net timing jitter oscillates and increases much more slowly for symmetric maps. With a simple change that involves only flipping the fibers in alternate spans, the same system can operate over more than 1,200 km with negligible penalty. The length of two fiber sections in the dispersion map does not need to be equal for the cancellation of jitter to occur. The concept of scaled translation symmetry can be used to show that both the amplitude and timing jitters can be reduced for a wide variety of maps [162], even when variations in the average power are not symmetric around the midpoint.

The use of optical phase conjugation can also reduce the intrachannel nonlinear effects [167]–[169]. As discussed in Section 8.5, such a device is equivalent to reversing the sign of the dispersion parameters of all fiber sections in the second half of the

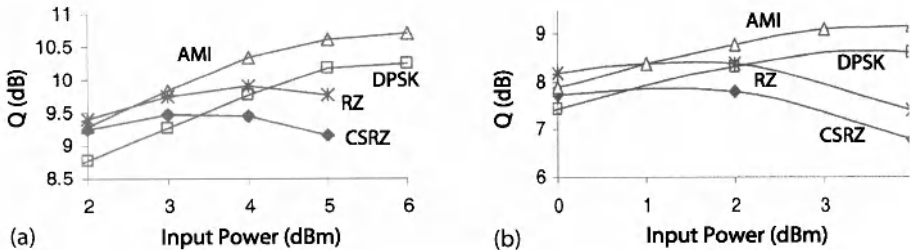


Figure 9.21: Power dependence of the Q factor found numerically for a 40-Gb/s channel at a distance of 1,000 km for four modulation formats and two dispersion maps (a) and (b). (After Ref. [173]; ©2003 IEEE.)

link. System-level experiments have confirmed that phase conjugation can reduce the impact of intrachannel nonlinear effects considerably [168].

9.5.2 Phase-Alteration Techniques

As the nonlinear perturbation in Eq. (9.4.16) depends on the phase of pulses generating it, the input phase of optical pulses forming the bit stream can be used to control the intrachannel nonlinear effects [170]. The basic idea consists of introducing a relative phase shift between any two neighboring bits, resulting in a modulation format referred to as the alternate-phase RZ (AP-RZ) format. Several other formats, such as carrier-suppressed RZ (CSRZ), duobinary RZ, RZ-DPSK, and alternate-mark-inversion (AMI) RZ, can also be employed. The last format was used in a 2003 experiment to transmit a 40-Gb/s signal over 2,000 km [171]. The improvement in the Q factor was typically less than 1 dB when compared with the standard RZ format.

The important question is which phase-alteration technique is the optimum choice for suppressing the intrachannel nonlinear effects. Since ghost pulses generated through intrachannel FWM are often the limiting factor for pseudo-linear systems, one can ask which technique reduces their amplitude most [172]–[174]. Four modulation formats were compared in a numerical study [173], whose results are shown in Figure 9.21. The Q factor is plotted for a 40-Gb/s system at a distance of 1000 km for two dispersion maps with a 100-km map period. The map (a) consists of three sections such that $D = 19 \text{ ps}/(\text{km-nm})$ for the first and third sections (each 30 km long) but $D = -28 \text{ ps}/(\text{km-nm})$ for the 40-km-long middle section. The map (b) employs 100 km of standard fiber with $D = 17 \text{ ps}/(\text{km-nm})$ whose dispersion is compensated using DCFs. The duty cycle is typically 66% for the CSRZ format but only 33% for the standard RZ format. As seen in Figure 9.21, both the DPSK and AMI formats provide better performance compared with RZ and CSRZ formats. This can be understood by noting that the amplitude of ghost pulses generated through various combinations of the subscripts j , k , and l in Eq. (9.4.16) depends on the phase of neighboring bits, among other things. The amount of improvement realized with the use of DPSK and AP-RZ formats depends on the launched power. In general, more power can be launched when phase-alteration techniques are employed.

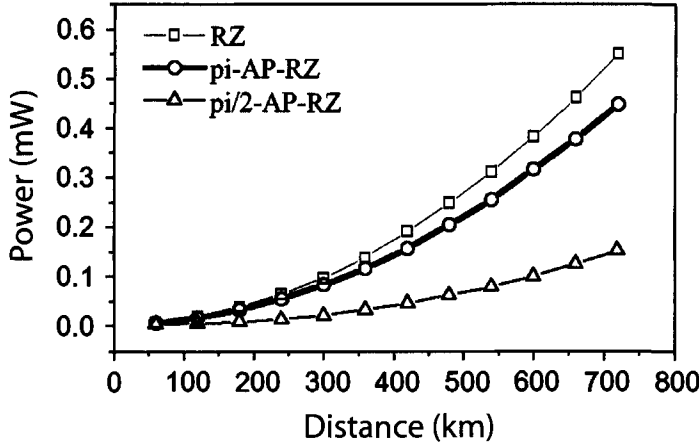


Figure 9.22: Growth of power in 0 bits as function of distance for a 40-Gb/s signal with 6.25-ps pulses and three RZ-type formats. (After Ref. [174]; ©2004 IEEE.)

The CSRZ format is an example of the AP-RZ format for which the phase difference $\delta\phi$ between two neighboring bits is fixed at a value of π . Clearly, one can choose $\delta\phi$ in the range of 0 to π , although the optical carrier may then not be suppressed completely. A numerical study shows that the optimum value of $\delta\phi$ is close to $\pi/2$, as this choice minimizes the buildup of ghost pulses generated through intrachannel FWM [174]. Figure 9.22 shows the standard deviation of power in 0 bits (calculated numerically) as the function of distance for a 40-Gb/s signal with 25% duty-cycle pulses. The dispersion map consists of 60 km of standard fiber, followed by 12 km of a DCF. As expected from the theory of Section 9.4.3, power in 0 bits increases rapidly in a quadratic fashion for a standard RZ signal ($\delta\phi = 0$). The growth is reduced slightly in the case of the CSRZ format ($\delta\phi = \pi$). However, it is suppressed by a large amount for $\delta\phi = \pi/2$. Experimental results support this conclusion.

9.5.3 Polarization Bit Interleaving

Another technique for controlling the intrachannel nonlinear effects alternates the polarization of neighboring bits in an RZ signal. It makes use of the fact that both the XPM and FWM processes depend on the state of polarization (SOP) of the interacting waves. The technique of polarization bit interleaving was first used in 1991 for reducing interaction between neighboring solitons [175]. In another approach, used commonly for increasing the spectral efficiency of WDM systems, neighboring channels are orthogonally polarized [176]. However, this scheme is quite different from the one considered in this section in which neighboring bits of a single channel are orthogonally polarized through time-domain interleaving [177]–[181].

Figure 9.23 shows two schemes that can be used for polarization alternation on a bit by bit basis [181]. In both of them, a pulse carver is used to create an uncoded train of RZ pulses at the bit rate rate. In scheme (a), a phase modulator operating

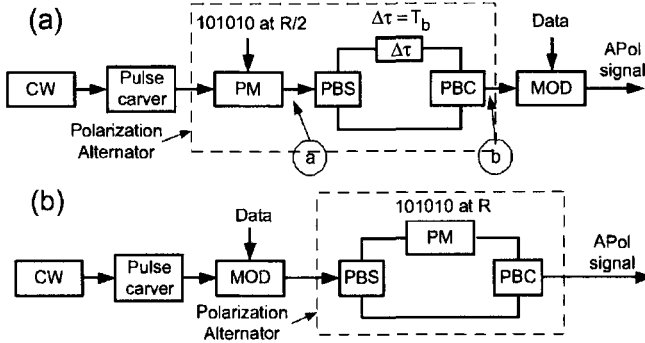


Figure 9.23: Schematic illustration of two schemes for alternating polarization such that neighboring bits are orthogonally polarized. Acronyms PM, PBS, PBC, MOD, and APol stand for phase modulator, polarization beam splitter, polarization beam combiner, data modulator, and alternate polarization, respectively. (After Ref. [181]; ©2004 IEEE.)

at half the bit rate first imposes a phase shift on this pulse train, which is split into its orthogonally polarized components that are combined back after one bit delay. A data modulator then codes the RZ signal. In scheme (b), in contrast, the pulse train is first coded with the data. It is then split into its orthogonally polarized components that are combined back after a phase modulator first imposes a phase shift on one of the components. The second scheme is much easier to implement in practice. The signal spectrum is affected considerably with polarization alternation. In particular, the spectra of orthogonally polarized components have side bands spaced apart by the bit rate B , but they are shifted by $B/2$.

Considerable reduction in the power level of ghost pulses generated through intra-channel FWM was observed in a 40-Gb/s recirculating-loop experiment [181]. The loop included four spans of 82.3 km, each span formed with 70 km or so of standard fiber followed with a DCF that left a residual dispersion of 40 ps/nm per span. Backward Raman pumping was used for compensating span losses in a distributed fashion. Figure 9.24 shows the measured BER as a function of launch power after a distance of 2,000 km (six round trips in the loop). Four curves correspond to four different modulation formats. The duty cycle of RZ and CSRZ bit streams was 33% and 66%, respectively.

Several features of Figure 9.24 are noteworthy. First, the minimum BER was $>10^{-4}$ for both the RZ and CSRZ formats when all bits had the same SOP and it was realized at a relatively low value of launch power. When the polarization-alternation technique was implemented, the BER improved considerably and its minimum value occurred at a higher power level (about 1 dBm). These results indicate that the Q^2 factor improves by 4.5 dB when neighboring bits are orthogonally polarized and can be understood as follows. With polarization alternation, intrachannel nonlinear impairments are reduced significantly and lead to a much lower BER for the RZ format, as evident from Figure 9.24. Since the duty cycle was 66% for the CSRZ signal, and each 1 bit had a wider pulse width, its performance was slightly lower than the RZ signal (with a 33% duty cycle) under the same operating conditions. The main conclusion

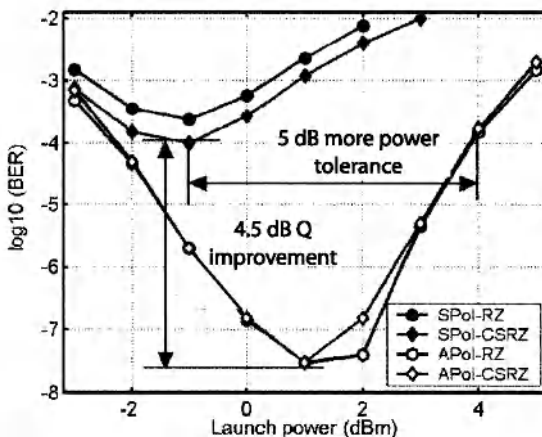


Figure 9.24: BER measured as a function of launch power at a distance of 2,000 km in the case of four different modulation formats. SPol and APol stand for the same- and alternate-polarization bit patterns. (After Ref. [181]; ©2004 IEEE.)

is that the use of polarization alternation in the time domain helps considerably to reduce the intrachannel nonlinear effects in high-speed lightwave systems operating at bit rates of 40 Gb/s or more. A low-duty RZ format is often the optimum choice for such systems so that the system operates in the pseudo-linear regime.

Problems

- 9.1 Solve the NLS equation (9.1.2) numerically using the same dispersion map employed for Figure 9.1. Consider a 40-Gb/s system designed using RZ pulses of Gaussian shape with a 6.25-ps width (FWHM). Use a 128-bit bit pattern to construct curves similar to those shown in Figure 9.1(a), assuming that the maximum distance corresponds to a 1-dB penalty in the eye opening. Is this system design better than the 50% duty cycle used for Figure 9.1? Justify your answer in physical terms.
- 9.2 Derive Eqs. (9.1.5) and (9.1.6) using the moment method.
- 9.3 Repeat the derivation of Eqs. (9.1.5) and (9.1.6) with the variational method.
- 9.4 Write a computer program for solving Eqs. (9.1.5) and (9.1.6) using Fortran, Matlab, or another programming language. Use it to reproduce the results shown in Figures 9.3 and 9.4.
- 9.5 A 10-Gb/s soliton system is operating at $1.55 \mu\text{m}$ using fibers with a constant dispersion of $D = 2 \text{ ps}/(\text{km}\cdot\text{nm})$. The effective core area of the fiber is $50 \mu\text{m}^2$. Calculate the peak power and the pulse energy required for fundamental solitons of 30-ps width (FWHM). Use $n_2 = 2.6 \times 10^{-20} \text{ m}^2/\text{W}$.
- 9.6 The soliton system of the preceding problem needs to be upgraded to 40 Gb/s. Calculate the pulse width, peak power, and energy of the solitons when soliton

width (FWHM) is 20% of the bit slot. What is the average launched power for this system?

- 9.7 Verify by direct substitution that the soliton solution given in Eq. (9.2.8) satisfies the NLS equation.
- 9.8 Solve the NLS equation numerically (9.2.1) and plot the evolution of the fourth- and fifth-order solitons over one soliton period. Compare your results with those shown in Figure 9.5 and comment on the main differences.
- 9.9 Verify numerically by propagating a fundamental soliton over 100 dispersion lengths that the shape of the soliton does not change on propagation. Repeat the simulation using a Gaussian input pulse shape with the same peak power and explain the results.
- 9.10 A 10-Gb/s soliton lightwave system is designed with $T_0/T_b = 0.1$ to ensure well-separated solitons in the RZ bit stream. Calculate pulse width, peak power, pulse energy, and the average power of the RZ signal, assuming $\beta_2 = -1 \text{ ps}^2/\text{km}$ and $\gamma = 2 \text{ W}^{-1}/\text{km}$.
- 9.11 Prove that the energy of standard solitons should be increased by the factor $G \ln G / (G - 1)$ when fiber loss α is compensated periodically using optical amplifiers. Here, $G = \exp(\alpha L_A)$ is the amplifier gain and L_A is the spacing between amplifiers.
- 9.12 A 10-Gb/s soliton communication system is designed with 50-km amplifier spacing. What should the peak power of the input pulse be to ensure that a fundamental soliton is maintained in an average sense in a fiber with 0.2 dB/km loss? Assume 100-ps pulse width (FWHM), $\beta_2 = -0.5 \text{ ps}^2/\text{km}$, and $\gamma = 2 \text{ W}^{-1}/\text{km}$. What is the average launched power for such a system?
- 9.13 Calculate the maximum bit rate for a soliton system designed with $q_0 = 5$, $\beta_2 = -1 \text{ ps}^2/\text{km}$, and $L_A = 50 \text{ km}$. Assume that the condition (9.2.14) is satisfied when $B^2 L_A$ is at the 20% level. What is the soliton width at the maximum bit rate?
- 9.14 Use the NLS equation (9.1.2) to prove that solitons remain unperturbed by fiber losses when fiber dispersion decreases exponentially as $\beta_2(z) = \beta_2(0) \exp(-\alpha z)$.
- 9.15 Solve Eqs. (9.1.5) and (9.1.6) numerically by imposing the periodicity condition given in Eq. (9.2.15). Plot T_0 and C_0 as a function of input pulse energies in the range of 0.1 to 10 ps for a dispersion map made using 70 km of the standard fiber with $D = 17 \text{ ps}/(\text{km-nm})$ and 10 km of DCF with $D = -115 \text{ ps}/(\text{km-nm})$. Use $\gamma = 2 \text{ W}^{-1}/\text{km}$ and $\alpha = 0.2 \text{ dB/km}$ for the standard fiber and $\gamma = 6 \text{ W}^{-1}/\text{km}$ and $\alpha = 0.5 \text{ dB/km}$ for the DCF.
- 9.16 Calculate the map strength S and the map parameter T_{map} for the map used in the preceding problem when 1-pJ input pulses are launched. Estimate the maximum bit rate that this map can support.
- 9.17 Explain in physical terms how intrachannel XPM among optical pulses representing 1 bits produces timing and amplitude jitter.

9.18 What is meant by a ghost pulse? Explain how such a pulse is generated through intrachannel FWM in a pseudo-linear system.

References

- [1] G. P. Agrawal, *Nonlinear Fiber Optics*, 4th ed., Academic Press, Boston, 2007.
- [2] H. Taga, S. Yamamoto, N. Edagawa, Y. Yoshida, S. Akiba, and H. Wakabayashi, *J. Lightwave Technol.* **12**, 1616 (1994).
- [3] S. Sekine, N. Kikuchi, S. Sasaki, and Y. Uchida, *Electron. Lett.* **31**, 1080 (1995).
- [4] A. Naka and S. Saito, *J. Lightwave Technol.* **13**, 862 (1995).
- [5] N. Kikuchi and S. Sasaki, *J. Lightwave Technol.* **13**, 868 (1995).
- [6] N. Kikuchi, S. Sasaki, and K. Sekine *Electron. Lett.* **31**, 375 (1995); N. Kikuchi and S. Sasaki, *Electron. Lett.* **32**, 570 (1996).
- [7] F. Matera and M. Settembre, *J. Lightwave Technol.* **14**, 1 (1996); *Opt. Fiber Technol.* **4**, 34 (1998).
- [8] D. Breuer and K. Petermann, *IEEE Photon. Technol. Lett.* **9**, 398 (1997).
- [9] F. Forghieri, P. R. Prucnal, R. W. Tkach, and A. R. Chraplyvy, *IEEE Photon. Technol. Lett.* **9**, 1035 (1997).
- [10] A. Sahara, H. Kubota, and M. Nakazawa, *IEEE Photon. Technol. Lett.* **9**, 1179 (1997).
- [11] T. Matsuda, A. Naka, and S. Saito, *J. Lightwave Technol.* **16**, 340 (1998).
- [12] A. Sano, Y. Miyamoto, T. Kataoka, and K. Hagimoto, *J. Lightwave Technol.* **16**, 977 (1998).
- [13] D. Breuer, K. Obermann, and K. Petermann, *IEEE Photon. Technol. Lett.* **10**, 1793 (1998).
- [14] C. Caspar, H.-M. Foisel, A. Gladisch, N. Hanik, F. Küppers, R. Ludwig, A. Mattheus, W. Pieper, B. Strelbel, and H. G. Weber, *IEEE Photon. Technol. Lett.* **10**, 481 (1999).
- [15] D. S. Govan, W. Forysiak, and N. J. Doran, *Opt. Lett.* **23**, 1523 (1998).
- [16] I. S. Penketh, P. Harper, S. B. Alleston, A. M. Niculae, I. Bennion I, and N. J. Doran, *Opt. Lett.* **24**, 802 (1999).
- [17] S. K. Turitsyn and E. G. Shapiro, *Opt. Fiber Technol.* **4**, 151 (1998).
- [18] F. M. Madani and K. Kikuchi, *J. Lightwave Technol.* **17**, 1326 (1999).
- [19] C. M. Weinert, R. Ludwig, W. Pieper, H. G. Weber, D. Breuer, K. Petermann, and F. Küppers, *J. Lightwave Technol.* **17**, 2276 (1999).
- [20] M. Nakazawa, H. Kubota, K. Suzuki, E. Yamada, and A. Sahara, *IEEE J. Sel. Topics Quantum Electron.* **6**, 363 (2000).
- [21] M. Murakami, T. Matsuda, H. Maeda, and T. Imai, *J. Lightwave Technol.* **18**, 1197 (2000).
- [22] A. Sahara, T. Inui, T. Komukai, H. Kubota, and M. Nakazawa, *J. Lightwave Technol.* **18**, 1364 (2000).
- [23] T. Hoshida, O. Vassilieva, K. Yamada, S. Choudhary, R. Pecqueur, H. Kuwahara, *J. Lightwave Technol.* **20**, 1989 (2002).
- [24] B. Konrad, K. Petermann, J. Berger, R. Ludwig, C. M. Weinert, H. G. Weber, and B. Schmauss, *J. Lightwave Technol.* **20**, 2129 (2002).
- [25] R.-J. Essiambre, G. Raybon, and B. Mikkelsen, in *Optical Fiber Telecommunications*, Vol. 4B, I. P. Kaminow and T. Li, Eds., Academic Press, Boston, 2002, Chap. 6.
- [26] Z. Jiang and C. Fan, *J. Lightwave Technol.* **21**, 953 (2003).

- [27] M. Wu, and W. I. Way, *J. Lightwave Technol.* **22**, 1483 (2004).
- [28] X. S. Xiao, S. M. Gao, Y. Tian, and C. X. Yang, *J. Lightwave Technol.* **24**, 2083 (2006); *J. Lightwave Technol.* **25**, 929 (2007).
- [29] S. Chandrasekhar and X. Liu, *IEEE Photon. Technol. Lett.* **19**, 1801 (2007).
- [30] A. Bononi, P. Serena, and A. Orlandini, *J. Lightwave Technol.* **26**, 3617 (2008).
- [31] A. Bononi, P. Serena, and M. Bellotti, *J. Lightwave Technol.* **27**, 3974 (2009).
- [32] Z. Tao, W. Yan, S. Oda, T. Hoshida, and J. C. Rasmussen, *Opt. Express* **17**, 13860 (2009).
- [33] A. Hasegawa and M. Matsumoto, *Optical Solitons in Fibers*, Springer, New York, 2002.
- [34] Y. S. Kivshar and G. P. Agrawal, *Optical Solitons: From Fibers to Photonic Crystals*, Academic Press, Boston, 2003, Chap. 3.
- [35] L. F. Mollenauer and J. P. Gordon, *Solitons in Optical Fibers: Fundamentals and Applications*, Academic Press, Boston, 2006.
- [36] M. J. Ablowitz and P. A. Clarkson, *Solitons, Nonlinear Evolution Equations, and Inverse Scattering*, Cambridge University Press, New York, 1991.
- [37] G. L. Lamb, Jr., *Elements of Soliton Theory*, Dover, New York, 1994.
- [38] T. Miwa, *Mathematics of Solitons*, Cambridge University Press, New York, 1999.
- [39] V. E. Zakharov and A. B. Shabat, *Sov. Phys. JETP* **34**, 62 (1972).
- [40] A. Hasegawa and F. Tappert, *Appl. Phys. Lett.* **23**, 142 (1973).
- [41] J. Satsuma and N. Yajima, *Prog. Theor. Phys.* **55**, 284 (1974).
- [42] V. E. Zakharov and A. B. Shabat, *Sov. Phys. JETP* **37**, 823 (1973).
- [43] A. Hasegawa and F. Tappert, *Appl. Phys. Lett.* **23**, 171 (1973).
- [44] W. J. Tomlinson, R. J. Hawkins, A. M. Weiner, J. P. Heritage, and R. N. Thurston, *J. Opt. Soc. Am. B* **6**, 329 (1989).
- [45] P. Emplit, M. Haelterman, and J. P. Hammaide, *Opt. Lett.* **18**, 1047 (1993).
- [46] M. Nakazawa and K. Suzuki, *Electron. Lett.* **31**, 1084 (1995); *Electron. Lett.* **31**, 1076 (1995).
- [47] R. Leners, P. Emplit, D. Foursa, M. Haelterman, and R. Kashyap, *J. Opt. Soc. Am. B* **14**, 2339 (1997).
- [48] Y. S. Kivshar and B. Luther-Davies, *Phys. Rep.* **298**, 81 (1998).
- [49] Y. Chen and J. Atai, *IEEE J. Quantum Electron.* **34**, 1301 (1998).
- [50] M. Stratmann, M. Bohm, and F. Mitschke, *Electron. Lett.* **37**, 1182 (2001).
- [51] Y. S. Kivshar and G. P. Agrawal, Eds., *Optical Solitons: From Fibers to Photonic Crystals*, Academic Press, Boston, 2003, Chap. 4.
- [52] Y. Kodama and A. Hasegawa, *Opt. Lett.* **7**, 339 (1982); **8**, 342 (1983).
- [53] Z. M. Liao, C. J. McKinstry, and G. P. Agrawal, *J. Opt. Soc. Am. B* **17**, 514 (2000).
- [54] L. F. Mollenauer and K. Smith, *Opt. Lett.* **13**, 675 (1988).
- [55] L. F. Mollenauer, B. M. Nyman, M. J. Neubelt, G. Raybon, and S. G. Evangelides, *Electron. Lett.* **27**, 178 (1991).
- [56] K. Tajima, *Opt. Lett.* **12**, 54 (1987).
- [57] V. A. Bogatyryov, M. M. Bubnov, E. M. Dianov, and A. A. Sysoliatin, *Pure Appl. Opt.* **4**, 345 (1995).
- [58] D. J. Richardson, R. P. Chamberlin, L. Dong, and D. N. Payne, *Electron. Lett.* **31**, 1681 (1995).
- [59] A. J. Stentz, R. Boyd, and A. F. Evans, *Opt. Lett.* **20**, 1770 (1995).
- [60] D. J. Richardson, L. Dong, R. P. Chamberlin, A. D. Ellis, T. Widdowson, and W. A. Pender, *Electron. Lett.* **32**, 373 (1996).
- [61] W. Forysiak, F. M. Knox, and N. J. Doran, *Opt. Lett.* **19**, 174 (1994).

- [62] T. Georges and B. Charbonnier, *Opt. Lett.* **21**, 1232 (1996); *IEEE Photon. Technol. Lett.* **9**, 127 (1997).
- [63] S. Cardianal, E. Desurvire, J. P. Hamaide, and O. Audouin, *Electron. Lett.* **33**, 77 (1997).
- [64] A. Hasegawa, Y. Kodama, and A. Murata, *Opt. Fiber Technol.* **3**, 197 (1997).
- [65] S. Kumar, Y. Kodama, and A. Hasegawa, *Electron. Lett.* **33**, 459 (1997).
- [66] S. Kumar, *IEEE Photon. Technol. Lett.* **16**, 810 (2004).
- [67] N. J. Smith, F. M. Knox, N. J. Doran, K. J. Blow, and I. Bennion, *Electron. Lett.* **32**, 54 (1996).
- [68] M. Nakazawa, H. Kubota, and K. Tamura, *IEEE Photon. Technol. Lett.* **8**, 452 (1996).
- [69] M. Nakazawa, H. Kubota, A. Sahara, and K. Tamura, *IEEE Photon. Technol. Lett.* **8**, 1088 (1996).
- [70] A. B. Grudinin and I. A. Goncharenko, *Electron. Lett.* **32**, 1602 (1996).
- [71] A. Berntson, N. J. Doran, W. Forysiak, and J. H. B. Nijhof, *Opt. Lett.* **23**, 900 (1998).
- [72] J. N. Kutz, P. Holmes, S. G. Evangelides, and J. P. Gordon, *J. Opt. Soc. Am. B* **15**, 87 (1998).
- [73] S. K. Turitsyn, I. Gabitov, E. W. Laedke, V. K. Mezentsev, S. L. Musher, E. G. Shapiro, T. Schafer, and K. H. Spatschek, *Opt. Commun.* **151**, 117 (1998).
- [74] T. I. Lakoba and D. J. Kaup, *Phys. Rev. E* **58**, 6728 (1998).
- [75] S. K. Turitsyn and E. G. Shapiro, *J. Opt. Soc. Am. B* **16**, 1321 (1999).
- [76] I. R. Gabitov, E. G. Shapiro, and S. K. Turitsyn, *Phys. Rev. E* **55**, 3624 (1997).
- [77] M. J. Ablowitz and G. Bioindini, *Opt. Lett.* **23**, 1668 (1998).
- [78] C. Paré and P. A. Bélanger, *Opt. Lett.* **25**, 881 (2000).
- [79] J. H. B. Nijhof, N. J. Doran, W. Forysiak, and F. M. Knox, *Electron. Lett.* **33**, 1726 (1997).
- [80] V. S. Grigoryan and C. R. Menyuk, *Opt. Lett.* **23**, 609 (1998).
- [81] J. N. Kutz and S. G. Evangelides, *Opt. Lett.* **23**, 685 (1998).
- [82] Y. Chen and H. A. Haus, *Opt. Lett.* **23**, 1013 (1998).
- [83] J. H. B. Nijhof, W. Forysiak, and N. J. Doran, *Opt. Lett.* **23**, 1674 (1998).
- [84] S. K. Turitsyn, J. H. B. Nijhof, V. K. Mezentsev, and N. J. Doran, *Opt. Lett.* **24**, 1871 (1999).
- [85] S. K. Turitsyn, M. P. Fedoruk, and A. Gornakova, *Opt. Lett.* **24**, 969 (1999).
- [86] L. J. Richardson, W. Forysiak, and N. J. Doran, *IEEE Photon. Technol. Lett.* **13**, 209 (2001).
- [87] E. Poutrina and G. P. Agrawal, *Opt. Commun.* **206**, 193 (2002).
- [88] S. Waiyapot, S. K. Turitsyn, and V. K. Mezentsev, *J. Lightwave Technol.* **20**, 2220 (2002).
- [89] C. Xie, L. F. Mollenauer, and N. Mamysheva, *J. Lightwave Technol.* **21**, 769 (2003).
- [90] E. Poutrina and G. P. Agrawal, *J. Lightwave Technol.* **21**, 990 (2003).
- [91] H. Kubota and M. Nakazawa, *Opt. Commun.* **87**, 15 (1992); M. Nakazawa and H. Kubota, *Electron. Lett.* **31**, 216 (1995).
- [92] M. Suzuki, I. Morita, N. Edagawa, S. Yamamoto, H. Taga, and S. Akiba, *Electron. Lett.* **31**, 2027 (1995).
- [93] A. Naka, T. Matsuda, and S. Saito, *Electron. Lett.* **32**, 1694 (1996).
- [94] I. Morita, M. Suzuki, N. Edagawa, S. Yamamoto, H. Taga, and S. Akiba, *IEEE Photon. Technol. Lett.* **8**, 1573 (1996).
- [95] J. M. Jacob, E. A. Golovchenko, A. N. Pilipetskii, G. M. Carter, and C. R. Menyuk, *IEEE Photon. Technol. Lett.* **9**, 130 (1997).
- [96] G. M. Carter and J. M. Jacob, *IEEE Photon. Technol. Lett.* **10**, 546 (1998).

- [97] V. S. Grigoryan, R. M. Mu, G. M. Carter, and C. R. Menyuk, *IEEE Photon. Technol. Lett.* **10**, 45 (2000).
- [98] R. M. Mu, C. R. Menyuk, G. M. Carter, and J. M. Jacob, *IEEE J. Sel. Topics Quantum Electron.* **6**, 248 (2000).
- [99] A. B. Grudinin, M. Durkin, M. Isben, R. I. Laming, A. Schiffini, P. Franco, E. Grandi, and M. Romagnoli, *Electron. Lett.* **33**, 1572 (1997).
- [100] F. Favre, D. Le Guen, and T. Georges, *J. Lightwave Technol.* **17**, 1032 (1999).
- [101] M. Zitelli, F. Favre, D. Le Guen, and S. Del Burgo, *IEEE Photon. Technol. Lett.* **9**, 904 (1999).
- [102] J. P. Gordon and H. A. Haus, *Opt. Lett.* **11**, 665 (1986).
- [103] D. Marcuse, *J. Lightwave Technol.* **10**, 273 (1992).
- [104] N. J. Smith, W. Forysiak, and N. J. Doran, *Electron. Lett.* **32**, 2085 (1996).
- [105] G. M. Carter, J. M. Jacob, C. R. Menyuk, E. A. Golovchenko, A. N. Pilipetskii, *Opt. Lett.* **22**, 513 (1997).
- [106] S. Kumar and F. Lederer, *Opt. Lett.* **22**, 1870 (1997).
- [107] J. N. Kutz and P. K. A. Wai, *IEEE Photon. Technol. Lett.* **10**, 702 (1998).
- [108] T. Okamawari, A. Maruta, and Y. Kodama, *Opt. Lett.* **23**, 694 (1998); *Opt. Commun.* **149**, 261 (1998).
- [109] V. S. Grigoryan, C. R. Menyuk, and R. M. Mu, *J. Lightwave Technol.* **17**, 1347 (1999).
- [110] M. F. S. Ferreira and S. C. V. Latas, *J. Lightwave Technol.* **19**, 332 (2001).
- [111] J. Santhanam, C. J. McKinstrie, T. I. Lakoba, and G. P. Agrawal, *Opt. Lett.* **26**, 1131 (2001).
- [112] C. J. McKinstrie, J. Santhanam, and G. P. Agrawal, *J. Opt. Soc. Am. B* **19**, 640 (2002).
- [113] J. Santhanam and G. P. Agrawal, *IEEE J. Sel. Topics Quantum Electron.* **7**, 632 (2002).
- [114] E. Poutrina and G. P. Agrawal, *IEEE Photon. Technol. Lett.* **14**, 39 (2002); *J. Lightwave Technol.* **20**, 762 (2002).
- [115] A. Mecozzi, J. D. Moores, H. A. Haus, and Y. Lai, *Opt. Lett.* **16**, 1841 (1991).
- [116] L. F. Mollenauer, M. J. Neubelt, M. Haner, E. Lichtman, S. G. Evangelides, and B. M. Nyman, *Electron. Lett.* **27**, 2055 (1991).
- [117] Y. Kodama and A. Hasegawa, *Opt. Lett.* **17**, 31 (1992).
- [118] L. F. Mollenauer, J. P. Gordon, and S. G. Evangelides, *Opt. Lett.* **17**, 1575 (1992).
- [119] V. V. Afanasjev, *Opt. Lett.* **18**, 790 (1993).
- [120] M. Romagnoli, S. Wabnitz, and M. Midrio, *Opt. Commun.* **104**, 293 (1994).
- [121] M. Nakazawa, E. Yamada, H. Kubota, and K. Suzuki, *Electron. Lett.* **27**, 1270 (1991).
- [122] N. J. Smith, W. J. Firth, K. J. Blow, and K. Smith, *Opt. Lett.* **19**, 16 (1994).
- [123] S. Bigo, O. Audouin, and E. Desurvire, *Electron. Lett.* **31**, 2191 (1995).
- [124] M. Nakazawa, K. Suzuki, E. Yamada, H. Kubota, Y. Kimura, and M. Takaya, *Electron. Lett.* **29**, 729 (1993).
- [125] G. Aubin, E. Jeanny, T. Montalant, J. Moulu, F. Pirio, J.-B. Thomine, and F. Devaux, *Electron. Lett.* **31**, 1079 (1995).
- [126] W. Forysiak, K. J. Blow, and N. J. Doran, *Electron. Lett.* **29**, 1225 (1993).
- [127] M. Matsumoto, H. Ikeda, and A. Hasegawa, *Opt. Lett.* **19**, 183 (1994).
- [128] T. Widdowson, D. J. Malyon, A. D. Ellis, K. Smith, and K. J. Blow, *Electron. Lett.* **30**, 990 (1994).
- [129] S. Kumar and A. Hasegawa, *Opt. Lett.* **20**, 1856 (1995).
- [130] V. S. Grigoryan, A. Hasegawa, and A. Maruta, *Opt. Lett.* **20**, 857 (1995).
- [131] M. Matsumoto, *J. Opt. Soc. Am. B* **15**, 2831 (1998); *Opt. Lett.* **23**, 1901 (1998).

- [132] S. K. Turitsyn and E. G. Shapiro, *J. Opt. Soc. Am. B* **16**, 1321 (1999).
- [133] S. Waiyapot and M. Matsumoto, *IEEE Photon. Technol. Lett.* **11**, 1408 (1999).
- [134] M. F. S. Ferreira and S. H. Sousa, *Electron. Lett.* **37**, 1184 (2001).
- [135] M. Matsumoto, *Opt. Lett.* **23**, 1901 (2001).
- [136] J. Santhanam and G. P. Agrawal, *J. Opt. Soc. Am. B* **20**, 284 (2003).
- [137] R.-J. Essiambre, B. Mikkelsen, and G. Raybon, *Electron. Lett.* **35**, 1576 (1999).
- [138] P. V. Mamyshev and N. A. Mamysheva, *Opt. Lett.* **24**, 1454 (1999).
- [139] M. Zitelli, F. Matera, and M. Settembre, *J. Lightwave Technol.* **17**, 2498 (1999).
- [140] A. Mecozzi, C. B. Clausen, and M. Shtaif, *IEEE Photon. Technol. Lett.* **12**, 392 (2000).
- [141] R. I. Killey, H. J. Thiele, V. Mikhailov, and P. Bayvel, *IEEE Photon. Technol. Lett.* **12**, 1624 (2000).
- [142] J. Mårtensson, A. Berntson, M. Westlund, A. Danielsson, P. Johannesson, D. Anderson, and M. Lisak, *Opt. Lett.* **26**, 55 (2001).
- [143] A. Mecozzi, C. B. Clausen, and M. Shtaif, *IEEE Photon. Technol. Lett.* **12**, 1633 (2000).
- [144] S. Kumar, *IEEE Photon. Technol. Lett.* **13**, 800 (2001); S. Kumar, J. C. Mauro, S. Raghavan, and D. Q. Chowdhury, *IEEE J. Sel. Topics Quantum Electron.* **18**, 626 (2002).
- [145] M. J. Ablowitz and T. Hirooka, *Opt. Lett.* **25**, 1750 (2000); *IEEE J. Sel. Topics Quantum Electron.* **18**, 603 (2002).
- [146] P. Johannesson, D. Anderson, A. Berntson, and J. Mårtensson, *Opt. Lett.* **26**, 1227 (2001).
- [147] P. Bayvel and R. I. Killey, in *Optical Fiber Telecommunications*, Vol. 4B, I. P. Kaminow and T. Li, Eds., Academic Press, Boston, 2002, Chap. 13.
- [148] M. Daikoku, T. Otani, and M. Suzuki, *IEEE Photon. Technol. Lett.* **15**, 1165 (2003).
- [149] D. Duce, R. I. Killey, and P. Bayvel, *J. Lightwave Technol.* **22**, 1263 (2004).
- [150] G. Raybon, Y. Su, J. Leuthold, R.-J. Essiambre, T. Her, C. Joergensen, P. Steinurzel, and K. D. K. Feder, Proc. Opt. Fiber Commun., Paper FD-10, 2002.
- [151] M. K. Jackson, G. R. Boyer, J. Paye, M. A. Franco, and A. Mysyrowicz, *Opt. Lett.* **17**, 1770 (1992).
- [152] D. Breuer, H. J. Ehrke, F. Küppers, R. Ludwig, K. Petermann, H. G. Weber, and K. Weich, *IEEE Photon. Technol. Lett.* **10**, 822 (1998).
- [153] A. H. Gnauck, S.-G. Park, J. M. Wiesenfeld, and L. D. Garrett, *Electron. Lett.* **35**, 2218 (1999).
- [154] S.-G. Park, A. H. Gnauck, J. M. Wiesenfeld, and L. D. Garrett, *IEEE Photon. Technol. Lett.* **12**, 1085 (2000).
- [155] S. Ramachandran, G. Raybon, B. Mikkelsen, M. Yan, and L. Cowsar, and R. J. Essiambre, Digest Europ. Conf. Opt. Commun., Amsterdam, 2001, p. 282.
- [156] R. I. Killey, V. Mikhailov, S. Appathurai, and P. Bayvel, *J. Lightwave Technol.* **20**, 2282 (2002).
- [157] Y. Takushima, T. Douke, X. Wang, and K. Kikuchi, *J. Lightwave Technol.* **20**, 360 (2002).
- [158] R. Holzlöhner, H. N. Ereifej, V. S. Grigoryan, G. M. Carter, and C. R. Menyuk, *J. Lightwave Technol.* **20**, 1124 (2002).
- [159] A. Pizzinat, A. Schiffini, F. Alberti, F. Matera, A. N. Pinto, and P. Almeida, *J. Lightwave Technol.* **20**, 1673 (2002).
- [160] A. Mecozzi, C. B. Clausen, M. Shtaif, S.-G. Park, and A. H. Gnauck, *IEEE Photon. Technol. Lett.* **13**, 445 (2001).
- [161] A. G. Striegler and B. Schmauss, *J. Lightwave Technol.* **22**, 1877 (2004).
- [162] H. Wei and D. V. Plant, *Opt. Express* **12**, 4282 (2004).

- [163] A. S. Lenihan, O. V. Sinkin, B. S. Marks, G. E. Tudury, R. J. Runser, A. Goldman, C.R. Menyuk, and G. M. Carter, *IEEE Photon. Technol. Lett.* **17**, 1588 (2005).
- [164] P. Minzioni and A. Schiffini, *Opt. Express* **13**, 8460 (2005).
- [165] F. Zhang, C. A. Bunge, K. Petermann, and A. Richter, *Opt. Express* **14**, 6613 (2006).
- [166] M. Shtaif, *IEEE Photon. Technol. Lett.* **20**, 620 (2008).
- [167] A. Chowdhury and R. J. Essiambre, *Opt. Lett.* **29**, 1105 (2004).
- [168] A. Chowdhury, G. Raybon, R.-J. Essiambre, J. H. Sinsky, A. Adamiecki, J. Leuthold, C. R. Doerr, and S. Chandrasekhar, *J. Lightwave Technol.* **23**, 172 (2005).
- [169] S. L. Jansen, D. van den Borne, P. M. Krumrich, S. Spälder, G.-D. Khoe, and H. de Waardt, *IEEE J. Sel. Topics Quantum Electron.* **12**, 505 (2006).
- [170] K. S. Cheng and J. Conradi, *IEEE Photon. Technol. Lett.* **14**, 98 (2002).
- [171] P. J. Winzer, A. H. Gnauck, G. Raybon, S. Chandrasekhar, Y. Su, and J. Leuthold, *IEEE Photon. Technol. Lett.* **15**, 766 (2003).
- [172] X. Liu, X. Wei, A. H. Gnauck, C. Xu, and L. K. Wickham, *Opt. Lett.* **13**, 1177 (2002).
- [173] A. V. Kanaev, G. G. Luther, V. Kovanic, S. R. Bickham, and J. Conradi, *J. Lightwave Technol.* **21**, 1486 (2003).
- [174] S. Appathurai, V. Mikhailov, R. I. Killey, and P. Bayvel, *J. Lightwave Technol.* **22**, 239 (2004).
- [175] S. G. Evangelides, L. F. Mollenauer, J. P. Gordon, and N. S. Bergano, *J. Lightwave Technol.* **10**, 28 (1992).
- [176] A. Agarwal, S. Banerjee, D. F. Grosz, A. P. Küng, D. N. Maywar, A. Gurevich, and T. H. Wood, *IEEE Photon. Technol. Lett.* **15**, 470 (2003).
- [177] F. Matera, M. Settembre, M. Tamburini, F. Favre, D. L. Guen, T. Georges, M. Henry, G. Michaud, P. Franco, A. Schiffini, M. Romagnoli, M. Guglielmucci, and S. Cascelli, *J. Lightwave Technol.* **17**, 2225 (1999).
- [178] B. Mikkelsen, G. Raybon, R. J. Essiambre, A. J. Stentz, T. N. Nielsen, D. W. Peckham, L. Hsu, L. Gruner-Nielsen, K. Dreyer, and J. E. Johnson, *IEEE Photon. Technol. Lett.* **12**, 1400 (2000).
- [179] A. Hodzic, B. Konrad, and K. Petermann, *IEEE Photon. Technol. Lett.* **15**, 153 (2003).
- [180] X. Liu, C. Xu, and X. Wei, *IEEE Photon. Technol. Lett.* **16**, 30 (2004).
- [181] C. Xie, I. Kang, A. H. Gnauck, L. Möller, L. F. Mollenauer, and A. R. Grant, *J. Lightwave Technol.* **22**, 806 (2004).

Chapter 10

Advanced Lightwave Systems

Lightwave systems discussed so far are based on a simple digital modulation scheme in which an electrical binary bit stream modulates the intensity of an optical carrier inside an optical transmitter (on-off keying or OOK). The resulting optical signal, after its transmission through the fiber link, falls directly on an optical receiver that converts it to the original digital signal in the electrical domain. Such a scheme is referred to as *intensity modulation with direct detection* (IM/DD). Many alternative schemes, well known in the context of radio and microwave communication systems [1]–[3], transmit information by modulating both the amplitude and the phase of a carrier wave. Although the use of such modulation formats for optical systems was considered in the 1980s [4]–[9], it was only after the year 2000 that phase modulation of optical carriers attracted renewed attention, motivated mainly by its potential for improving the spectral efficiency of WDM systems [10]–[16]. Depending on the receiver design, such systems can be classified into two categories. In coherent lightwave systems [14], transmitted signal is detected using homodyne or heterodyne detection requiring a local oscillator. In the so-called self-coherent systems [16], the received signal is first processed optically to transfer phase information into intensity modulations and then sent to a direct-detection receiver.

The motivation behind using phase encoding is two-fold. First, the sensitivity of optical receivers can be improved with a suitable design compared with that of direct detection. Second, phase-based modulation techniques allow a more efficient use of fiber bandwidth by increasing the spectral efficiency of WDM systems. This chapter pays attention to both aspects. Section 10.1 introduces new modulation formats and the transmitter and receiver designs used to implement them. Section 10.2 focuses on demodulation techniques employed at the receiver end. The bit-error rate (BER) is considered in Section 10.3 for various modulation formats and demodulation schemes. Section 10.4 focuses on the degradation of receiver sensitivity through mechanisms such as phase noise, intensity noise, polarization mismatch, and fiber dispersion. Non-linear phase noise is discussed in Section 10.5 together with the techniques used for its compensation. Section 10.6 reviews the recent progress realized with emphasis on improvements in the spectral efficiency. The topic of ultimate channel capacity is the focus of Section 10.7.

10.1 Advanced Modulation Formats

As discussed in Section 1.2.3, both the amplitude and the phase of an optical carrier can be employed for encoding the information that need to be transmitted. In the case of IM/DD systems, a binary ASK format is employed such that the peak amplitude (or intensity) of the carrier takes two values, one of them being close to zero (also called the OOK format). In this section we focus on phase-based modulation formats employed in modern lightwave systems.

10.1.1 Encoding of Optical Signals

Recall from Section 1.2.3 that the electric field $\mathbf{E}(t)$ associated with an optical carrier has the form

$$\mathbf{E}(t) = \hat{\mathbf{e}} \operatorname{Re}[a \exp(i\phi - i\omega_0 t)], \quad (10.1.1)$$

where $\hat{\mathbf{e}}$ is the polarization unit vector, a is the amplitude, ϕ is the phase, and ω_0 is the carrier frequency. Introducing the complex phasor as $A = a e^{i\phi}$, one can construct a constellation diagram in which the real and imaginary parts of A are plotted along the x and y axes, respectively. In the case of the OOK format, such a diagram has two points along the real axis, indicating that only the amplitude a changes from 0 to a_1 whenever a bit 1 is transmitted (with no change in the phase).

The simplest PSK format is the one in which phase of the optical carrier takes two distinct values (see Figure 1.11), typically chosen to be 0 and π . Such a format is called binary PSK, or BPSK. Coherent detection is a necessity for such a format because all information would be lost if the optical signal were detected directly without first mixing it coherently with a local oscillator. The use of PSK format requires the phase of the optical carrier to remain stable over a duration much longer than the bit duration, $T_b = 1/B$, at a given bit rate B . This requirement puts a stringent condition on tolerable spectral linewidths of both the transmitter laser and the local oscillator, especially when the bit rate is relatively small.

The phase-stability requirement can be relaxed considerably by using a variant of the PSK format, known as *differential* PSK or DPSK. In the case of DPSK, information is coded in the phase difference between two neighboring bits. If only two phase values are used (differential BPSK or DBPSK), the phase difference $\Delta\phi = \phi_k - \phi_{k-1}$ is changed by π or 0, depending on whether k th bit is a 1 or 0 bit. The advantage of a DPSK format is that the received signal can be demodulated successfully as long as the carrier phase remains relatively stable over a duration of two bits.

The BPSK format does not improve spectral efficiency because it employs only two distinct values of the carrier phase. If the carrier phase is allowed to take four distinct values, typically chosen to be 0, $\pi/2$, π , and $3\pi/2$, one can transmit 2 bits simultaneously. Such a format is called quadrature PSK (QPSK), and its differential version is termed DQPSK. Figure 10.1(a), where the QPSK format is shown using a constellation diagram, can help in understanding how two bits can be transmitted simultaneously. As shown there, one can assign the four possible combinations of two bits, namely 00, 01, 10, and 11, to four values of the carrier phase in a unique manner. As a result, the bit rate is effectively halved with the use of the QPSK (or DQPSK)

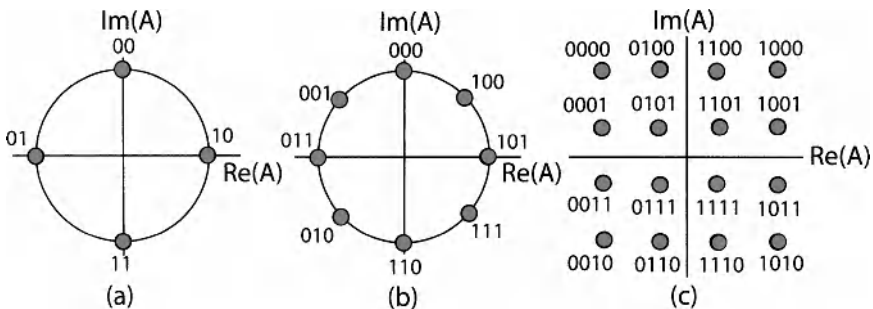


Figure 10.1: Constellation diagrams for (a) QPSK, (b) 8-PSK, and (c) 16-QAM modulation formats showing how multibit combinations are assigned to different symbols.

format. This effective bit rate is called the *symbol rate* and is expressed in units of baud. In this terminology, well known in the areas of radio and microwave communications, phase values represent “symbols” that are transmitted, and their number M represents the size of the alphabet. The symbol rate B_s is related to the bit rate B by the simple relation $B = \log_2(M)B_s$. Thus, if the QPSK format with $M = 4$ is employed at $B_s = 40$ Gbaud, information will be transmitted at a bit rate of 80 Gb/s, resulting in a two-fold improvement in the spectral efficiency of a WDM system. Of course, the bit rate is tripled if one employs 8 distinct values of carrier phase using the so-called 8-PSK format. Figure 10.1(b) shows the assignment of 3 bits to each symbol in this case.

Much more sophisticated modulation formats can be designed if the amplitude of the signal is also allowed to change from one symbol to next. An example is shown in Figure 1.11(d), where the amplitude can take two possible values with four possible phases for each amplitude. Another example is shown in Figure 10.1(c), where 16 symbols lying on a square grid are employed to transmit 4 bits simultaneously. This modulation format is known 16-QAM, where QAM stands for *quadrature amplitude modulation*. Clearly, this approach can be extended to reduce the symbol rate even further at a given bit rate by extending the number M of symbols employed. It should be emphasized that the assignment of bit combinations to various symbols in Figure 10.1 is not arbitrary. A coding scheme, known as Gray coding [2], maps different bit combinations to different symbols in such a way that only a single bit changes between two adjacent symbols separated by the shortest distance in the constellation diagram. If Gray coding is not done, a single symbol error can produce errors in multiple bits, resulting in an increase in the system BER.

Spectral efficiency can be enhanced further by a factor of two by exploiting the state of polarization (SOP) of the optical carrier. In the case of polarization-division multiplexing (PDM), each wavelength is used to transmit two orthogonally polarized bit streams at half the original bit rate. It may appear surprising that such a scheme can work because the SOP of a channel does not remain fixed inside an optical fiber and can vary in a random fashion because of birefringence fluctuations. However, it is easy to see that PDM can be employed successfully as long as the two PDM channels at each wavelength remain close to orthogonally polarized over the entire link length. This

can occur only if the effects of PMD and nonlinear depolarization remain relatively small over the entire link length. If coherent detection is employed at the receiver, it is possible to separate the two PDM channels with a suitable polarization-diversity scheme. The combination of QPSK (or DQPSK) and PDM reduces the symbol rate to one quarter of the actual bit rate and thus enhances the spectral efficiency by a factor of 4. Such a dual-polarization QPSK format is attractive because a 100-Gb/s signal can be transmitted over fiber links designed to carry 10-Gb/s signal with 50-GHz channel spacing and was in use for commercial systems by 2010.

One more design issue needs to be addressed. In the case of a purely phase-encoded signal, such as the QPSK format shown in Figure 10.1(a), the amplitude or power of the data stream is initially constant with time when the NRZ format is employed because each symbol occupies the entire time slot allotted to it. This situation has two implications. First, the average power launched into the each channel is enhanced considerably, an undesirable feature in general. Second, various dispersive and nonlinear effects induce time-dependent power variations during transmission of the data stream through the fiber that affect the system performance. An alternative is to employ a modulation format in which all symbol slots contain an optical pulse whose phase varies according to the data being transmitted. This situation is indicated by prefixing RZ to the format employed for data transmission (e.g., RZ-DQPSK).

10.1.2 Amplitude and Phase Modulators

The implementation of any PSK format requires an external modulator capable of changing the optical phase in response to an applied voltage though a physical mechanism known as electrorefraction [17]. Any electro-optic crystal with proper orientation can be used for phase modulation. A LiNbO₃ waveguide is commonly used in practice. The phase shift $\delta\phi$ occurring inside the waveguide is related to the index change δn by the simple relation

$$\delta\phi = (2\pi/\lambda)(\delta n)l_m, \quad (10.1.2)$$

where λ is the wavelength of input light and l_m is the modulator length. The index change δn is proportional to the applied voltage. Thus, any phase shift can be imposed on the optical carrier by applying the required voltage.

An amplitude modulator is also needed in most practical cases. It can be used to convert a CW signal from a DFB laser into a RZ pulse train. It can also be used to modulate the amplitude and phase of incident light simultaneously. A common design employs a Mach-Zehnder (MZ) interferometer for converting a voltage-induced phase shift into amplitude modulation of the input signal.

Figure 10.2 shows schematically the design of a LiNbO₃ MZ modulator. The input field A_i is split into two equal parts at a Y junction, which are recombined back by another Y junction after different phase shifts have been imposed on them by applying voltages across two waveguides that form the two arms of a MZ interferometer. It is common to express these phase shifts in the form $\phi_j(t) = \pi V_j(t)/V_\pi$, where V_j is the voltage applied across the j th arm ($j = 1, 2$) and V_π is the voltage required to produce a π phase shift. This parameter is known for any LiNbO₃ modulator and is typically in

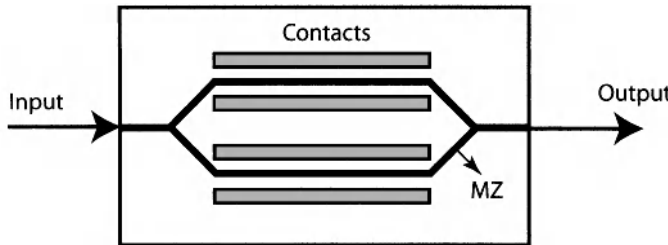


Figure 10.2: Schematic of a LiNbO₃ modulator. The Mach–Zehnder configuration converts an input CW beam into an encoded optical bit stream by applying appropriate voltages (gray contact pads) across the two arms of the interferometer.

the range of 3 to 5 V. In terms of the two phase shifts, the transmitted field is given by

$$A_t = \frac{1}{2} A_i (e^{i\phi_1} + e^{i\phi_2}). \quad (10.1.3)$$

The transfer function of the modulator is easily obtained in the form

$$t_m = A_t / A_i = \cos[\frac{1}{2}(\phi_1 - \phi_2)] \exp[i(\phi_1 + \phi_2)/2]. \quad (10.1.4)$$

It shows that a MZ modulator affects both the amplitude and the phase of the light incident on it. It can act as a pure amplitude modulator if we choose voltages in the two arms such that $V_2(t) = -V_1(t) + V_b$, where V_b is a constant bias voltage, because $\phi_1 + \phi_2$ then reduces to a constant. The power transfer function of the modulator in this case takes the form

$$T_m(t) = |t_m|^2 = \cos^2 \left(\frac{\pi}{2V_\pi} [2V_1(t) - V_b] \right). \quad (10.1.5)$$

Such a MZ modulator can act as a pure phase modulator that changes only the phase of input signal by an amount $\phi_1(t)$ if the same voltage is applied to the two arms such that $\phi_1 = \phi_2$.

Although a single MZ modulator can change both the amplitude and phase of input light simultaneously by choosing the arm voltages V_1 and V_2 appropriately, it does not modulate the two quadratures independently. A solution is provided by a *quadrature modulator* realized by nesting three MZ modulators in a way shown in Figure 10.3 such that each arm of the outer MZ interferometer contains its own MZ modulator. By choosing the applied voltages appropriately, one can cover the entire complex plane in the constellation diagram.

As an example, consider the QPSK modulation format. In this case, two internal MZ modulators are operated in the so-called push–pull regime [17] in which $\phi_2 = -\phi_1$ in Eq. (10.1.4). Further, the voltage is changed such that the transfer function t_m takes values ± 1 , corresponding to two phase shifts of 0 and π , depending on the data bits being transmitted. The outer modulator is biased such that it produces a constant $\pi/2$ phase shift between the signals in its two arms. The output then has four possible phase shifts given by $(\pm 1 \pm i)/\sqrt{2}$, which correspond to four phase values of $\pi/4$, $3\pi/4$,

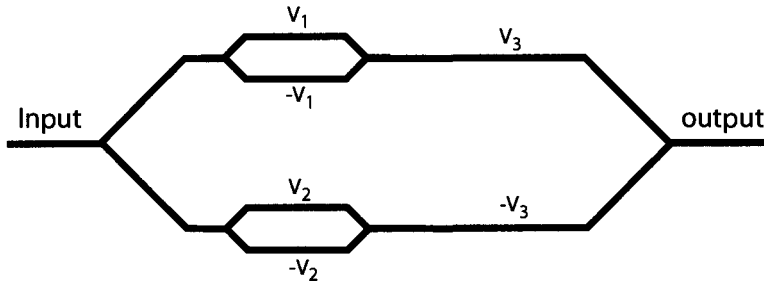


Figure 10.3: Schematic of a quadrature modulator used for generating the QPSK or the DQPSK format. The two inner MZ interferometers are driven by the electrical data streams while the voltage V_3 is used to introduce a constant $\pi/2$ phase shift between its two arms.

$5\pi/4$, and $7\pi/4$ and are suitable for creating a data stream with the QPSK modulation. A DQPSK symbol stream can also be created with such a modulator when the two internal MZ modulators are driven by an electrical signal that has been differentially encoded.

10.2 Demodulation Schemes

The use of phase encoding requires substantial changes at the receiver end. Conversion of the received optical signal into an electrical form suitable for reconstructing the original bit stream is called *demodulation*. When information is coded into phase of the optical carrier, direct detection cannot be used for demodulation because all phase information is lost during the detection process. Two techniques known as *coherent demodulation* and *delay demodulation* are used to convert phase information into intensity variations. As discussed in Section 4.5, coherent detection makes use of a local oscillator and can be implemented in two flavors known as homodyne and heterodyne schemes. Although simple in concept, homodyne detection is difficult to implement in practice, as it requires a local oscillator whose frequency matches the carrier frequency exactly and whose phase is locked to the incoming signal using an optical phase-locked loop. Heterodyne detection simplifies the receiver design but the electrical signal oscillates at microwave frequencies and must be demodulated to the baseband using techniques similar to those developed for microwave communication systems [1]–[3]. In this section we discuss three demodulation schemes used in practice.

10.2.1 Synchronous Heterodyne Demodulation

Figure 10.4 shows a synchronous heterodyne receiver schematically. The frequency of the local oscillator differs from the carrier frequency of the incident signal by the *intermediate frequency* (IF) chosen to be in the microwave region (~ 1 GHz). The current generated at the photodiode oscillates at the intermediate frequency and is passed through a bandpass filter (BPF) centered at this frequency ω_{IF} . The filtered current, in

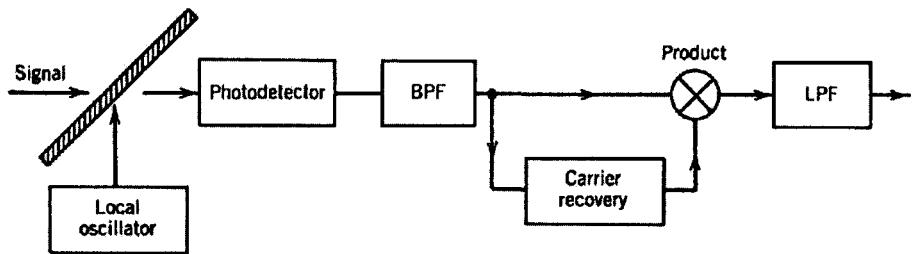


Figure 10.4: Block diagram of a synchronous heterodyne receiver. BPF and LPF stand for bandpass and low-pass filters.

the absence of noise, can be written as [see Eq. (4.5.8)]

$$I_f(t) = I_p \cos(\omega_{\text{IF}}t - \phi), \quad (10.2.1)$$

where $I_p = 2R_d\sqrt{P_s P_{\text{LO}}}$ and $\phi = \phi_s - \phi_{\text{LO}}$ is the phase difference between the signal and the local oscillator. The noise is also filtered by the BPF. Using the in-phase and out-of-phase quadrature components of the filtered Gaussian noise [1], the receiver noise is included through

$$I_f(t) = (I_p \cos \phi + i_c) \cos(\omega_{\text{IF}}t) + (I_p \sin \phi + i_s) \sin(\omega_{\text{IF}}t), \quad (10.2.2)$$

where i_c and i_s are Gaussian random variables of zero mean with variance σ^2 given in Eq. (4.5.9).

In the case of synchronous demodulation, a clock circuit is used to recover the microwave carrier $\cos(\omega_{\text{IF}}t)$ as shown in Figure 10.4. Then, $I_f(t)$ is multiplied by this clock signal and filtered by a low-pass filter. The resulting baseband signal is

$$I_d = \langle I_f \cos(\omega_{\text{IF}}t) \rangle = \frac{1}{2}(I_p \cos \phi + i_c), \quad (10.2.3)$$

where angle brackets denote low-pass filtering used for rejecting the ac components oscillating at $2\omega_{\text{IF}}$. Equation (10.2.3) shows that only the in-phase noise component affects the performance of a synchronous heterodyne receiver.

Synchronous demodulation requires recovery of the microwave carrier at the intermediate frequency ω_{IF} . Several electronic schemes can be used for this purpose, all requiring a kind of electrical phase-locked loop [19]. Two commonly used loops are the *squaring loop* and the *Costas loop*. A squaring loop uses a square-law device to obtain a signal of the form $\cos^2(\omega_{\text{IF}}t)$ that has a frequency component at $2\omega_{\text{IF}}$. This component can be used to generate a microwave signal at ω_{IF} .

A single-port receiver such as that shown in Figure 10.4 rejects half of the signal power P_s as well as half of the local-oscillator power P_{LO} during the mixing process. The loss in signal power is equivalent to a 3-dB power penalty. A solution is provided by balanced receivers. As shown in Figure 10.5 schematically, a balanced heterodyne receiver employs a 3-dB coupler with two photodetectors at its two output ports [20]–[22]. The operation of a balanced receiver can be understood by considering the photocurrents I_+ and I_- generated in each branch:

$$I_{\pm} = \frac{1}{2}R_d(P_s + P_{\text{LO}}) \pm R_d\sqrt{P_s P_{\text{LO}}} \cos(\omega_{\text{IF}}t + \phi). \quad (10.2.4)$$

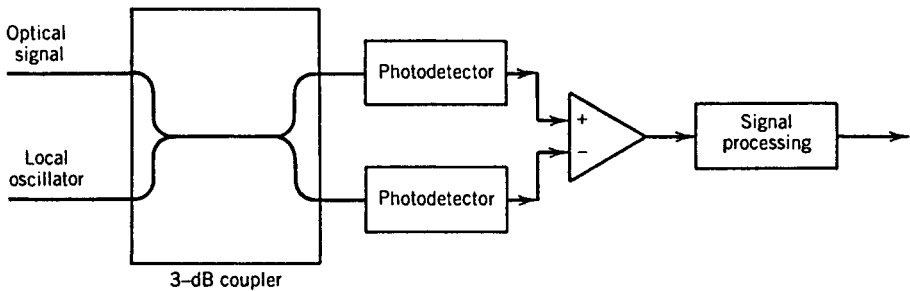


Figure 10.5: Schematic of a two-port balanced heterodyne receiver.

The difference of the two currents, $I_+ - I_-$, provides the heterodyne signal. The dc term is eliminated completely during the subtraction process when the two branches are balanced in such a way that they recombine the signal and local-oscillator powers in a synchronized fashion. More importantly, such a balanced receiver uses all of the signal power and thus avoids the 3-dB power penalty intrinsic to any single-port receiver. At the same time, as discussed later in Section 10.4.1, it helps to reduce the impact of intensity noise of a local oscillator, making it easier to operate the receiver in the shot-noise limit.

10.2.2 Asynchronous Heterodyne Demodulation

The design of a heterodyne receiver can be simplified considerably by adopting the asynchronous demodulation scheme that does not require recovery of the microwave carrier. Figure 10.6 shows such a heterodyne receiver schematically. As before, the current generated at the photodiode is passed through a BPF centered at the intermediate frequency ω_{IF} . The filtered signal $I_f(t)$ is converted to the baseband by an *envelope detector*, followed by a low-pass filter. The signal received by the decision circuit is just $I_d = |I_f|$. Using I_f from Eq. (10.2.2), it can be written as

$$I_d = |I_f| = [(I_p \cos \phi + i_c)^2 + (I_p \sin \phi + i_s)^2]^{1/2}. \quad (10.2.5)$$

The main difference is that both the in-phase and quadrature components of the receiver noise affect the signal. Although the SNR is somewhat degraded compared with the case of synchronous demodulation, sensitivity degradation resulting from the reduced SNR is relatively small (about 0.5 dB). As the phase-stability requirements are quite modest in the case of asynchronous demodulation, this scheme is often used for coherent lightwave systems. Similar to the case of synchronous receivers, it is common to employ a balanced receiver, such as that shown in Figure 10.5, in the asynchronous case as well to avoid rejecting half of the signal and local-oscillator powers during the mixing process.

The asynchronous demodulation can be employed readily for both the ASK and FSK formats. In the FSK case, the heterodyne receiver uses two separate branches to process the 1 and 0 bits whose carrier frequencies, and hence the intermediate frequencies, are different. The scheme can be used whenever the tone spacing is much larger

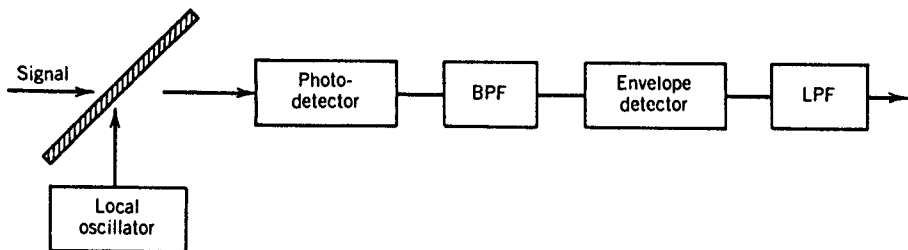


Figure 10.6: Block diagram of an asynchronous heterodyne receiver.

than the bit rates, so that the spectra of 1 and 0 bits have negligible overlap. The two BPFs have their center frequencies separated exactly by the tone spacing so that each BPF passes either 1 or 0 bits only. A single-filter receiver of Figure 10.6 can be used for FSK demodulation if its bandwidth is chosen to be wide enough to pass the entire bit stream. The signal is then processed by a frequency discriminator to identify 1 and 0 bits. This scheme works well only if the tone spacing is less than or comparable to the bit rate.

Asynchronous demodulation cannot be used in the case of any PSK-based format because the phase of the transmitter laser and the local oscillator are not locked and can drift with time. The use of DPSK format permits asynchronous demodulation by using a delay scheme in which the filtered electrical signal is multiplied by a replica of it that has been delayed by one bit period. A better option is to implement the delay demodulation scheme in the optical domain because it bypasses the need of a local oscillator.

10.2.3 Optical Delay Demodulation

In the case of differential phase encoding, a scheme known as *delay demodulation* can be employed. It makes use of a MZ interferometer whose two arms differ in lengths such that the signal in the longer arm is delayed by exactly one symbol duration ($T_s = 1/B_s$). Such a device is sometimes referred to as an optical delay interferometer. In contrast with a LiNbO₃ MZ modulator (see Figure 10.2) that typically has only one output port, a delay interferometer, shown schematically in Figure 10.7(a), is constructed by using two 3-dB couplers so that it has two output ports. When an optical field $A(t)$ is incident on one of the input ports, the powers at the two output ports are given by

$$P_{\pm}(t) = \frac{1}{4}|A(t) \pm A(t - T_s)|^2, \quad (10.2.6)$$

where the choice of sign depends on whether the bar or the cross port of the MZ interferometer is used for photodetection. Such a demodulation scheme is also called *self-coherent* because a delayed replica of the optical signal itself is used in place of a local oscillator required for coherent detection [16].

Although phase information can be recovered by processing only one output of the MZ interferometer with a single photodetector, such a scheme is rarely used because it rejects half of the received power. In practice, receiver performance is improved

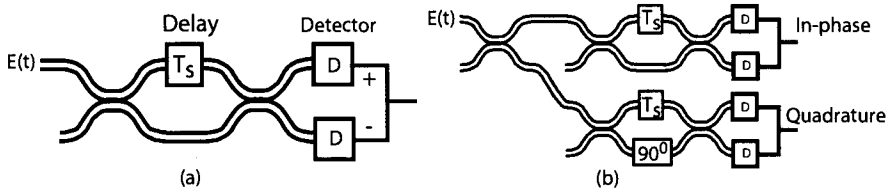


Figure 10.7: Receiver designs for processing (a) DBPSK and (a) DQPSK formats making use of optical delay demodulation with balanced detection. (After Ref. [15]; ©2008 OSA.)

considerably if two photodetectors are employed to detect both $P_{\pm}(t)$, and the resulting currents are subtracted. Such a balanced-detection scheme is shown schematically in Figure 10.7(a). Using $A(t) = \sqrt{P_0} \exp[i\phi(t)]$ in Eq. (10.2.6) with $I_{\pm} = R_d P_{\pm}(t)$, where R_d is the detector responsivity, the currents at the two photodetectors can be written as

$$I_{\pm}(t) = \frac{1}{2} R_d P_0 [1 \pm \cos(\Delta\phi)], \quad (10.2.7)$$

where $\Delta\phi(t) = \phi(t) - \phi(t - T_s)$ is the phase difference between the two neighboring symbols. After subtracting the two currents, the signal used by the decision circuit is given by

$$\Delta I = R_d \operatorname{Re}[A(t) A^*(t - T_s)] = R_d P_0 \cos(\Delta\phi). \quad (10.2.8)$$

In the BPSK case, $\Delta\phi = 0$ or π depending on the bits transmitted. Thus, one can reconstruct the original bit stream from temporal variations of the electrical signal.

The situation is more complicated in the case of the DQPSK format. Figure 10.7(b) shows the layout of a DQPSK receiver schematically. It employs two MZ interferometers with one-symbol delays but also introduces a relative phase shift of $\pi/2$ in one of them. The resulting two outputs of each MZ interferometer are then processed using the balanced detection scheme identical to that employed in the BPSK case. Because of the $\pi/2$ relative phase shift in one of the delay interferometers, two output currents correspond to the in-phase and quadrature components of the received optical field.

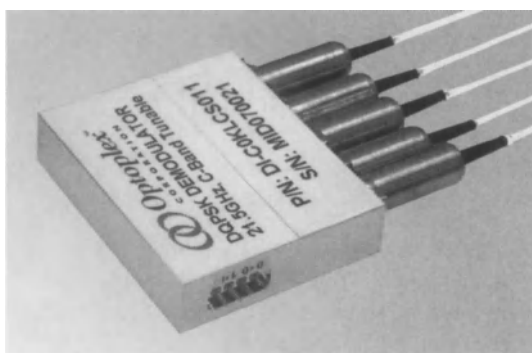


Figure 10.8: Photograph of a commercial DQPSK demodulator capable of operating at a symbol rate of 20 Gb/s. (Source: www.optoplex.com).

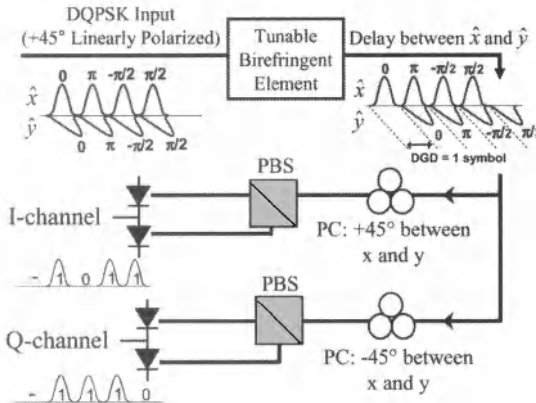


Figure 10.9: Schematic of a DQPSK receiver designed with a tunable birefringent element. PC and PBS stand for polarization controller and polarization beam splitter. (After Ref. [33]; ©2008 IEEE.)

Optical delay interferometers can be fabricated with several technologies, including planar silica waveguides [11], LiNbO₃ waveguides [31], and optical fibers [32]. In all cases, it is important that the optical delay is precisely controlled because any deviation from the required delay T_s leads to degradation in the system performance. Since the optical path length of two arms may change because of environmental fluctuations, an active control of temperature is often required in practice. Free-space optics has also been used with success. Figure 10.8 shows a commercial DQPSK demodulator based on free-space optics. It employs an athermal design and is capable of operating at a symbol rate of 20 Gb/s in the entire C and L telecommunication bands. By 2010, commercial devices were capable of generating or receiving dual-polarization DPSK (or DQPSK) signals suitable for 100-Gb/s WDM channels.

An alternative design with reduced complexity makes use of a tunable birefringent element whose length is chosen such that the orthogonally polarized components are delayed with respect to each other exactly by one-symbol duration T_s [33]. Figure 10.9 shows how such an element can be used to build a DQPSK receiver. When the input signal is polarized linearly at 45° with respect to the slow (or fast) axis of this element, and a polarization beam splitter (PBS) is used at its output to split the orthogonally polarized components, the two outputs behave similar to the two outputs of an optical delay interferometer. In the case of the DBPSK format, these two outputs can be fed directly to a balanced detector. In the case of the DQPSK format, the device output is first split equally into two parts and phase shifts of ±45° are introduced using a polarization controller such that the two parts undergo a relative phase shift of $\pi/2$. The use of two balanced detectors then allows one to process the in-phase and quadrature components of the incident optical field separately. The main advantage of using a birefringent element is that an active control of temperature is not necessary because the two polarization components share the same optical path within this element. Moreover, its tuning capability allows one to operate such a receiver at different symbol rates.

10.3 Shot Noise and Bit-Error Rate

The signal-to-noise ratio (SNR) and the resulting BER for a specific modulation format depend on the demodulation scheme employed [18]. This is so because the noise added to the signal is different for different demodulation schemes. In this section we consider the shot-noise limit and discuss BER for the three demodulation schemes of Section 10.2. Next section focuses on a more realistic situation in which system performance is limited by other noise sources introduced by lasers and optical amplifiers employed along the fiber link.

10.3.1 Synchronous Heterodyne Receivers

Consider first the case of the binary ASK format. The signal used by the decision circuit is given in Eq. (10.2.3) with $\phi = 0$. The phase difference $\phi = \phi_s - \phi_{\text{LO}}$ generally varies randomly because of phase fluctuations associated with the transmitter laser and the local oscillator. We consider such fluctuations later in Section 10.4 but neglect them here as our objective is to discuss the shot-noise limit. The decision signal for the ASK format then becomes

$$I_d = \frac{1}{2}(I_p + i_c), \quad (10.3.1)$$

where $I_p \equiv 2R_d(P_s P_{\text{LO}})^{1/2}$ takes values I_1 and I_0 , depending on whether a 1 or 0 bit is being detected. We assume no power is transmitted during the 0 bits and set $I_0 = 0$.

Except for the factor of $\frac{1}{2}$ in Eq. (10.3.1), the situation is analogous to the case of direct detection discussed in Section 4.6. The factor of $\frac{1}{2}$ does not affect the BER since both the signal and the noise are reduced by the same factor, leaving the SNR unchanged. In fact, one can use the same result [Eq. (4.6.10)],

$$\text{BER} = \frac{1}{2} \operatorname{erfc}(Q/\sqrt{2}), \quad (10.3.2)$$

where the Q factor, defined in Eq. (4.6.11), can be written as

$$Q = \frac{I_1 - I_0}{\sigma_1 + \sigma_0} \approx \frac{I_1}{2\sigma_1} = \frac{1}{2}(\text{SNR})^{1/2}. \quad (10.3.3)$$

In relating Q to SNR, we used $I_0 = 0$ and set $\sigma_0 \approx \sigma_1$. The latter approximation is justified for coherent receivers whose noise is dominated by shot noise induced by the local-oscillator and remains the same irrespective of the received signal power. As shown in Section 4.5, the SNR can be related to the number of photons N_p received during each 1 bit by the simple relation $\text{SNR} = 2\eta N_p$, where η is the quantum efficiency of the photodetectors employed.

The use of Eqs. (10.3.2) and (10.3.3) with $\text{SNR} = 2\eta N_p$ provides the following expression for the BER:

$$\text{BER} = \frac{1}{2} \operatorname{erfc}(\sqrt{\eta N_p / 4}). \quad (10.3.4)$$

One can use the same method to calculate the BER in the case of ASK homodyne receivers. Equations (10.3.2) and (10.3.3) still remain applicable. However, the SNR is improved by 3 dB in the homodyne case.

Equation (10.3.4) can be used to calculate the receiver sensitivity at a specific BER. Similar to the direct-detection case discussed in Section 4.6, we define the receiver sensitivity \bar{P}_{rec} as the average received power required for realizing a BER of 10^{-9} or less. From Eqs. (10.3.2) and (10.3.3), $\text{BER} = 10^{-9}$ when $Q \approx 6$, or when $\text{SNR} = 144$ (21.6 dB). We can use Eq. (4.5.13) to relate SNR to \bar{P}_{rec} if we note that $\bar{P}_{\text{rec}} = \bar{P}_s/2$ simply because signal power is zero during the 0 bits. The result is

$$\bar{P}_{\text{rec}} = 2Q^2hv\Delta f/\eta = 72hv\Delta f/\eta. \quad (10.3.5)$$

In the ASK homodyne case, \bar{P}_{rec} is smaller by a factor of 2 because of the 3-dB homodyne-detection advantage. As an example, for a $1.55\text{-}\mu\text{m}$ ASK heterodyne receiver with $\eta = 0.8$ and $\Delta f = 1$ GHz, the receiver sensitivity is about 12 nW and reduces to 6 nW if homodyne detection is used.

The receiver sensitivity is often quoted in terms of the number of photons N_p using Eqs. (10.3.4) because such a choice makes it independent of the receiver bandwidth and the operating wavelength. Furthermore, η is also set to 1 so that the sensitivity corresponds to an ideal photodetector. It is easy to verify that for realizing a BER of $= 10^{-9}$, N_p should be 72 and 36 in the heterodyne and homodyne cases, respectively. It is important to remember that N_p corresponds to the number of photons within a single 1 bit. The average number of photons per bit, \bar{N}_p , is reduced by a factor of 2 in the case of binary ASK format.

Consider now the case of the BPSK format. The signal at the decision circuit is given by Eq. (10.2.3), or by

$$I_d = \frac{1}{2}(I_p \cos \phi + i_c). \quad (10.3.6)$$

The main difference from the ASK case is that I_p is constant, but the phase ϕ takes values 0 or π depending on whether a 1 or 0 is being transmitted. In both cases, I_d is a Gaussian random variable but its average value is either $I_p/2$ or $-I_p/2$, depending on the received bit. The situation is analogous to the ASK case with the difference that $I_0 = -I_1$ in place of being zero. In fact, we can use Eq. (10.3.2) for the BER, but Q is now given by

$$Q = \frac{I_1 - I_0}{\sigma_1 + \sigma_0} \approx \frac{2I_1}{2\sigma_1} = (\text{SNR})^{1/2}, \quad (10.3.7)$$

where $I_0 = -I_1$ and $\sigma_0 = \sigma_1$ was used. By using $\text{SNR} = 2\eta N_p$, the BER is given by

$$\text{BER} = \frac{1}{2} \text{erfc}(\sqrt{\eta N_p}). \quad (10.3.8)$$

As before, the SNR is improved by 3 dB, or by a factor of 2, in the case of PSK homodyne detection.

The receiver sensitivity at a BER of 10^{-9} can be obtained by using $Q = 6$. For the purpose of comparison, it is useful to express the receiver sensitivity in terms of the number of photons N_p . It is easy to verify that $N_p = 18$ and 9 for heterodyne and homodyne BPSK detection, respectively. The average number of photons/bit, \bar{N}_p , equals N_p for the PSK format because the same power is transmitted during 1 and 0 bits. A PSK homodyne receiver is the most sensitive receiver, requiring only 9 photons/bit.

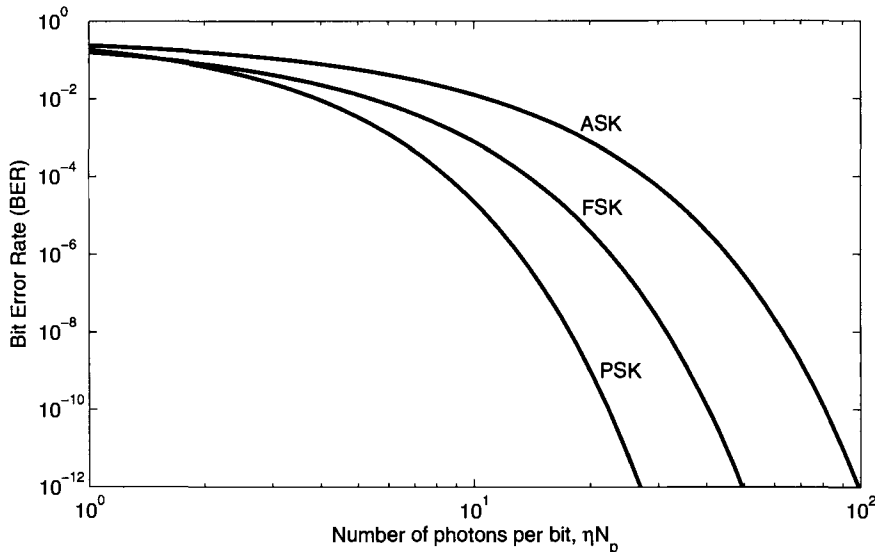


Figure 10.10: Changes in BER as a function of ηN_p for synchronous heterodyne receivers. The three curves compare the quantum limit for the ASK, FSK, and PSK formats.

For completeness, consider the case of binary FSK format for which heterodyne receivers employ a dual-filter scheme, each filter passing only 1 or 0 bits. The scheme is equivalent to two complementary ASK heterodyne receivers operating in parallel. This feature allows us to use Eqs. (10.3.2) and (10.3.3) for the FSK case as well. However, the SNR is improved by a factor of 2 compared with the ASK case because the same amount of power is received even during 0 bits. By using $\text{SNR} = 4\eta N_p$ in Eq. (10.3.3), the BER is given by $\text{BER} = \frac{1}{2} \text{erfc}(\sqrt{\eta N_p / 2})$. In terms of the number of photons, the sensitivity is given by $\bar{N}_p = \bar{N}_p = 36$. Figure 10.10 shows the BER as a function of ηN_p for the ASK, PSK, and FSK formats, demodulated by using a synchronous heterodyne receiver. It is interesting to compare the sensitivity of coherent receivers with that of a direct-detection receiver. Table 10.1 shows such a comparison. As discussed in Section 4.6.3, an ideal direct-detection receiver requires 10 photons/bit to operate at a BER of $\leq 10^{-9}$. This value is considerably superior to that of heterodyne schemes. However, it is never achieved in practice because of thermal noise, dark current, and many other factors, which degrade the sensitivity to the extent that $\bar{N}_p > 1000$ is usually required. In the case of coherent receivers, \bar{N}_p below 100 can be realized because shot noise can be made dominant by increasing the local-oscillator power.

10.3.2 Asynchronous Heterodyne Receivers

The BER calculation for asynchronous receivers is more complicated because the noise does not remain Gaussian when an envelope detector is used (see Figure 10.6). The reason can be understood from Eq. (10.2.5) showing the signal processed by the decision

Table 10.1 Sensitivity of synchronous receivers

Modulation Format	Bit-Error Rate	N_p	\bar{N}_p
ASK heterodyne	$\frac{1}{2}\operatorname{erfc}(\sqrt{\eta N_p/4})$	72	36
ASK homodyne	$\frac{1}{2}\operatorname{erfc}(\sqrt{\eta N_p/2})$	36	18
PSK heterodyne	$\frac{1}{2}\operatorname{erfc}(\sqrt{\eta N_p})$	18	18
PSK homodyne	$\frac{1}{2}\operatorname{erfc}(\sqrt{2\eta N_p})$	9	9
FSK heterodyne	$\frac{1}{2}\operatorname{erfc}(\sqrt{\eta N_p/2})$	36	36
Direct detection	$\frac{1}{2}\exp(-\eta N_p)$	20	10

circuit. In the case of an ideal ASK heterodyne receiver, ϕ can be set to zero so that (subscript d is dropped for simplicity)

$$I = [(I_p + i_c)^2 + i_s^2]^{1/2}. \quad (10.3.9)$$

Even though both i_c and i_s are Gaussian random variables with zero mean and the same standard deviation σ , where σ is the RMS noise current, the probability density function (PDF) of I is not Gaussian. It can be calculated by using a standard technique [23] and is found to be given by [24]

$$p(I, I_p) = \frac{I}{\sigma^2} \exp\left(-\frac{I^2 + I_p^2}{2\sigma^2}\right) I_0\left(\frac{I_p I}{\sigma^2}\right), \quad (10.3.10)$$

where $I_0(x)$ represents a modified Bessel function of the first kind and I varies in the range 0 to ∞ because the output of an envelope detector can have only positive values. This PDF is known as the *Rice distribution* [24]. When $I_p = 0$, the Rice distribution reduces to a *Rayleigh distribution*, well known in statistical optics [23].

The BER calculation follows the analysis of Section 4.6.1 with the only difference that the Rice distribution needs to be used in place of the Gaussian distribution. The BER is given by Eq. (4.6.2) with

$$P(0|1) = \int_{I_0}^{I_D} p(I, I_1) dI, \quad P(1|0) = \int_{I_D}^{\infty} p(I, I_0) dI. \quad (10.3.11)$$

where I_D is the decision level and I_1 and I_0 are values of I_p for 1 and 0 bits. The noise is the same for all bits ($\sigma_0 = \sigma_1 = \sigma$) because it is dominated by the local oscillator power. The integrals in Eq. (10.3.11) can be expressed in terms of Marcum's Q function [25], defined as [2]

$$Q_1(a, b) = \int_b^{\infty} x I_0(ax) \exp\left(-\frac{x^2 + a^2}{2}\right) dx. \quad (10.3.12)$$

The result for the BER is

$$\text{BER} = \frac{1}{2} \left[1 - Q_1\left(\frac{I_1}{\sigma}, \frac{I_D}{\sigma}\right) + Q_1\left(\frac{I_0}{\sigma}, \frac{I_D}{\sigma}\right) \right]. \quad (10.3.13)$$

The decision level I_D is chosen such that the BER is minimum for given values of I_1 , I_0 , and σ . It is difficult to obtain an exact analytic expression of I_D . However, under typical operating conditions, $I_0 \approx 0$, $I_1/\sigma \gg 1$, and I_D is well approximated by $I_1/2$. The BER then becomes

$$\text{BER} \approx \frac{1}{2} \exp(-I_1^2/8\sigma^2) = \frac{1}{2} \exp(-\text{SNR}/8). \quad (10.3.14)$$

Using $\text{SNR} = 2\eta N_p$, we obtain the final result,

$$\text{BER} = \frac{1}{2} \exp(-\eta N_p/4), \quad (10.3.15)$$

A comparison with Eq. (10.3.4), obtained in the case of synchronous ASK receivers shows that the BER is larger in the asynchronous case for the same value of ηN_p . However, the difference is so small that the receiver sensitivity at a BER of 10^{-9} is degraded by only 0.5 dB. If we assume that $\eta = 1$, Eq. (10.3.15) shows that $\text{BER} = 10^{-9}$ for $\bar{N}_p = 40$ ($\bar{N}_p = 36$ in the synchronous case).

Consider next the PSK format. As mentioned earlier, asynchronous demodulation cannot be used for it. However, DBPSK signals can be demodulated by implementing the delay-demodulation scheme in the microwave regime. The filtered current in Eq. (10.2.2) is divided into two parts, and one part is delayed by exactly one symbol period T_s . The product of two currents depends on the phase difference between any two neighboring bits and is used by the decision current to determine the bit pattern.

To find the PDF of the decision variable, we write Eq. (10.2.2) in the form $I_f(t) = \text{Re}[\xi(t) \exp(-i\omega_{\text{IF}}t)]$, where

$$\xi(t) = I_p \exp[i\phi(t)] + n(t) \equiv r(t) \exp[i\psi(t)]. \quad (10.3.16)$$

Here, $n = i_c + i i_s$ is a complex Gaussian random process. The current used by the decision circuit can now be written as

$$I_d(t) = \text{Re}[\xi(t)\xi^*(t-T_s)] = r(t)r(t-T_s) \cos[\omega_{\text{IF}}T_s + \psi(t) - \psi(t-T_s)]. \quad (10.3.17)$$

If $\omega_{\text{IF}}T_s$ is chosen to be a multiple of 2π and we can approximate ψ with ϕ , then $I_d = \pm r(t)r(t-T_s)$ as the phase difference takes its two values of 0 and π . The BER is thus determined by the PDF of the random variable $r(t)r(t-T_s)$.

It is helpful to write this product in the form $I_d = (r_+^2 - r_-^2)$, where $r_{\pm} = \frac{1}{2}[r(t) \pm r(t-T_s)]$. Consider the error probability when $\phi = 0$ for which $I_d > 0$ in the absence of noise. An error will occur if $r_+ < r_-$ because of noise. Thus, the conditional probability is given by

$$P(\pi|0) = P(I_d < 0) = P(r_+^2 < r_-^2). \quad (10.3.18)$$

This probability can be calculated because the PDFs of r_{\pm}^2 can be obtained by noting that $n(t)$ and $n(t-T_s)$ are uncorrelated Gaussian random variables. The other conditional probability, $P(0|\pi)$, can be found in the same manner. The final result is quite simple and is given by [4]

$$\text{BER} = \frac{1}{2} \exp(-\eta N_p). \quad (10.3.19)$$

A BER of 10^{-9} is obtained for $\eta N_p = 20$. As a reminder, the quantity ηN_p is just the SNR per bit in the shot-noise limit.

10.3.3 Receivers with Delay Demodulation

In the delay-demodulation scheme shown in Figure 10.7, one or more MZ interferometers with one-symbol delay are used at the receiver end. In the DBPSK case, a single MZ interferometer is employed. The outputs of the two detectors in this case have average currents given in Eq. (10.2.7). The decision variable is formed by subtracting the two currents such that $I_d = R_d P_0 \cos(\Delta\phi)$. The average currents for 0 and 1 bits are $R_d P_0$ and $-R_d P_0$ for $\Delta\phi = 0$ and π , respectively.

To see how the noise affects the two currents, note first from Eq. (10.2.8) that I_d can be written in the form

$$I_d = R_d \operatorname{Re}[A(t)A^*(t-T)], \quad (10.3.20)$$

where $A = \sqrt{P_0}e^{i\phi} + n(t)$ is the optical field entering the receiver. Here, $n(t)$ represent the noise induced by vacuum fluctuations that lead to the shot noise at the receiver. A comparison of Eq. (10.3.20) with Eq. (10.3.17), obtained in the case of a heterodyne detector with delay implemented in the microwave domain, shows the similarity between the two cases. Following the discussion presented there, one can conclude that the BER in the DBPSK case is again given by Eq. (10.3.19), or by $\text{BER} = \frac{1}{2} \exp(-\eta N_p)$. As before, the SNR per bit, ηN_p , sets the BER, and a BER of 10^{-9} is obtained for $\eta N_p = 20$.

The analysis is much more involved in the case of the DQPSK format. Proakis has developed a systematic approach for calculating error probabilities for a variety of modulation formats that includes the DQPSK format [2]. Although his analysis is for a heterodyne receiver with delay implemented in the microwave domain, the results apply as well to the case of optical delay demodulation. In particular, when the DQPSK format is implemented with the Gray coding, the BER is given by [2]

$$\text{BER} = Q_1(a, b) - \frac{1}{2} I_0(ab) \exp[-\frac{1}{2}(a^2 + b^2)], \quad (10.3.21)$$

$$a = [\eta N_p(2 - \sqrt{2})]^{1/2}, \quad b = [\eta N_p(2 + \sqrt{2})]^{1/2}, \quad (10.3.22)$$

where I_0 is the modified Bessel function of order zero and $Q_1(a, b)$ is Marcum's Q function introduced earlier in Eq. (10.3.12).

Figure 10.11 shows the BER curves for the DBPSK and DQPSK formats and compares them with the BER curve obtained in the case in which a heterodyne receiver is employed to detect the BPSK or the QPSK format (without differential encoding). When DBPSK is used in place of BPSK, the receiver sensitivity at a BER of 10^{-9} changes from 18 to 20 photons/bit, indicating a power penalty of less than 0.5 dB. In view of such a small penalty, DBPSK is often used in place of BPSK because its use avoids the need of a local oscillator and simplifies the receiver design considerably. However, a penalty of close to 2.4 dB occurs in the case of the DQPSK format for which receiver sensitivity changes from 18 to 31 photons/bit.

Because of the complexity of the BER expression in Eq. (10.3.21), it is useful to find its approximate analytic form. Using the upper and lower bounds on Marcum's Q function [34], Eq. (10.3.21) can be written in the following simple form [35]:

$$\text{BER} \approx \frac{\pi}{8}(a+b) \frac{I_0(ab)}{\exp(ab)} \operatorname{erfc}\left(\frac{b-a}{\sqrt{2}}\right). \quad (10.3.23)$$

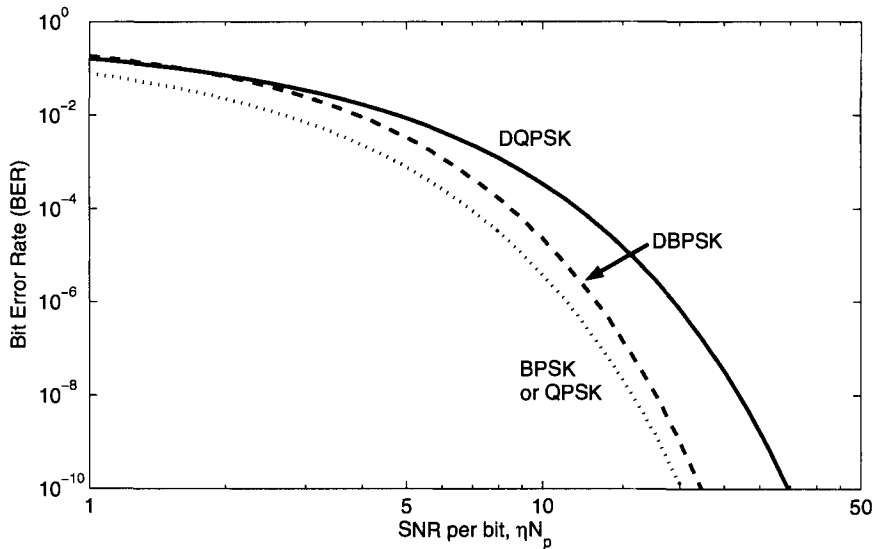


Figure 10.11: BER as a function of ηN_p in the shot-noise limit for DBPSK and DQPSK receivers with optical delay demodulation. The dotted curve shows for comparison the quantum limit of a heterodyne receiver in the absence of differential encoding.

This expression is accurate to within 1% for BER values below 3×10^{-2} . If we now employ asymptotic expansions $I_0(x) \approx (2\pi x)^{-1/2} \exp(x)$ and $\text{erfc}(x) \approx (\pi x)^{-1/2} \exp(-x^2)$, valid for large values of x , and use a and b from Eq. (10.3.22), we obtain [35]

$$\text{BER} \approx (1 + \sqrt{2})(8\sqrt{2}\pi\eta N_p)^{-1/2} \exp[-(2 - \sqrt{2})\eta N_p]. \quad (10.3.24)$$

This expression is accurate to within a few percent for values of $\eta N_p > 3$.

10.4 Sensitivity Degradation Mechanisms

The discussion in Section 10.3 assumed ideal operating conditions in which system performance is only limited by shot noise. Several other noise sources degrade the receiver sensitivity in practical coherent systems. In this section we consider a few important sensitivity degradation mechanisms and also discuss the techniques used to improve the performance with a proper receiver design.

10.4.1 Intensity Noise of Lasers

The effect of intensity noise of lasers on the performance of direct-detection receivers has been discussed in Section 4.7.2 and was found to be negligible in most cases of practical interest. This is not the case for coherent receivers [26]–[30]. To understand why intensity noise plays such an important role in heterodyne receivers, we follow the

analysis of Section 4.7.2 and write the current variance as

$$\sigma^2 = \sigma_s^2 + \sigma_T^2 + \sigma_I^2, \quad (10.4.1)$$

where $\sigma_I = RP_{\text{LO}}r_I$ and r_I is related to the *relative intensity noise* (RIN) of the local oscillator as defined in Eq. (4.6.7). If the RIN spectrum is flat up to the receiver bandwidth Δf , r_I^2 can be approximated by $2(\text{RIN})\Delta f$. The SNR is obtained by using Eq. (10.4.1) in Eq. (4.5.11) and is given by

$$\text{SNR} = \frac{2R^2\bar{P}_sP_{\text{LO}}}{2q(RP_{\text{LO}} + I_d)\Delta f + \sigma_T^2 + 2R^2P_{\text{LO}}^2(\text{RIN})\Delta f}. \quad (10.4.2)$$

The local-oscillator power P_{LO} should be large enough to make σ_T^2 negligible in Eq. (10.4.2) so that the heterodyne receiver operates in the shot-noise limit. However, an increase in P_{LO} increases the contribution of intensity noise quadratically in Eq. (10.4.2). If the intensity-noise contribution becomes comparable to shot noise, the SNR would decrease unless the signal power \bar{P}_s is increased to offset the increase in receiver noise. This increase in \bar{P}_s is the power penalty δ_I resulting from the local-oscillator intensity noise. If we neglect I_d and σ_T^2 in Eq. (10.4.2) for a receiver designed to operate in the shot-noise limit, the power penalty (in dB) is given by the simple expression

$$\delta_I = 10 \log_{10}[1 + (\eta/h\nu)P_{\text{LO}}(\text{RIN})]. \quad (10.4.3)$$

Figure 10.12 shows δ_I as a function of RIN for several values of P_{LO} using $\eta = 0.8$ and $h\nu = 0.8$ eV. The power penalty exceeds 2 dB when $P_{\text{LO}} = 1$ mW even for a local oscillator with a RIN of -160 dB/Hz, a value difficult to realize for DFB semiconductor lasers. Indeed, sensitivity degradation from local-oscillator intensity noise was observed in 1987 for a homodyne receiver [26]. The optical delay demodulation scheme also suffers from the intensity-noise problem.

Balanced detection provides a solution to the intensity-noise problem [20]. The reason can be understood from Figure 10.5 showing a balanced heterodyne receiver. The dc term is eliminated completely when the two branches are balanced in such a way that each branch receives equal signal and local-oscillator powers. More importantly, the intensity noise associated with the dc term is also eliminated during the subtraction process. The reason is related to the fact that the same local oscillator provides power to each branch. As a result, intensity fluctuations in the two branches are perfectly correlated and cancel out during subtraction of the photocurrents I_+ and I_- . It is noteworthy that intensity noise of a local oscillator affects even a balanced heterodyne receiver because the current difference, $I_+ - I_-$, still depends on the local-oscillator power. However, because this dependence is of the form of $\sqrt{P_{\text{LO}}}$, the intensity-noise problem is much less severe for a balanced heterodyne receiver.

Optical delay-demodulation schemes shown in Figure 10.7 also makes use of balanced detection. In this case, a local oscillator is not used, and it is the intensity noise of the transmitter laser that must be considered. The dc part of the photocurrents I_+ and I_- given in Eq. (10.2.7) is again canceled during the subtraction of the two currents, which helps to reduce the impact of intensity noise. However, now the current difference ΔI in Eq. (10.2.8) depends linearly on the signal power P_s . This situation is similar to the direct-detection case discussed in Section 4.7.2, and the impact of intensity noise is again not that severe.

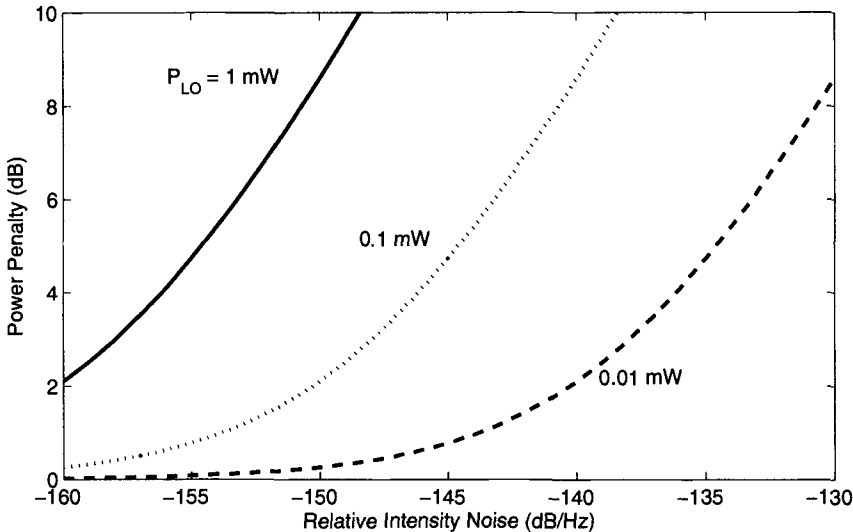


Figure 10.12: Power penalty versus RIN for three values of the local-oscillator power.

10.4.2 Phase Noise of Lasers

An important source of sensitivity degradation for lightwave systems making use of any PSK format is the phase noise associated with the transmitter laser (and the local oscillator in the case of coherent detection). The reason is obvious if we note that current generated at the receiver depends on the carrier phase, and any phase fluctuations introduce current fluctuations that degrade the SNR at the receiver. In the case of coherent detection, both the signal phase ϕ_s and the local-oscillator phase ϕ_{LO} should remain relatively stable to avoid the sensitivity degradation.

A measure of the duration over which the laser phase remains relatively stable is provided by the *coherence time* time related inversely to the laser linewidth $\Delta\nu$. To minimize the impact of phase noise, the coherence time should be much longer than the symbol duration T_s . In practice, it is common to use a dimensionless parameter $\Delta\nu T_s$ for characterizing the effects of phase noise on the performance of coherent lightwave systems. Since the symbol rate $B_s = 1/T_s$, this parameter is just the ratio $\Delta\nu/B_s$. In the case of heterodyne detection involving a local oscillator, $\Delta\nu$ represents the sum of the two linewidths, $\Delta\nu_T$ and $\Delta\nu_{LO}$, associated with the transmitter and the local oscillator, respectively.

Considerable attention has been paid to calculate the BER in the presence of phase noise and to estimate the dependence of power penalty on the ratio $\Delta\nu/B_s$ [36]–[51]. As an exact solution is not possible, either a Monte–Carlo-type numerical approach [51] is employed or a perturbation technique is used [43] to obtain approximate analytic results. Recently, the use of an approximation, called the phase-noise exponent commutation (PNEC), has resulted in simple analytic BER expressions for both the PSK and DPSK formats [50]. This approach also allows one to take into account the actual

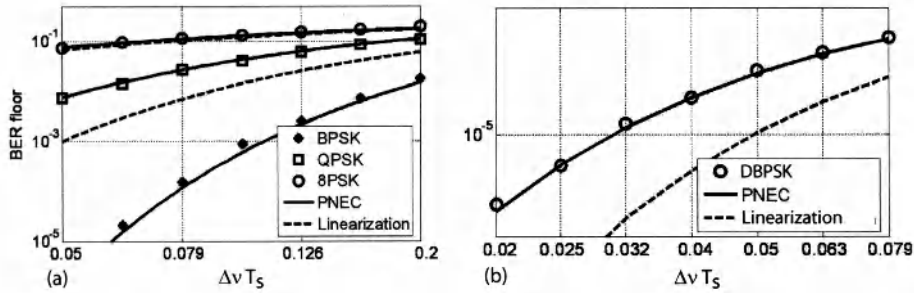


Figure 10.13: Changes in BER floor as a function of $\Delta v T_s$ for (a) three PSK formats and (b) the DBPSK format. PNEC approximation (solid lines) agrees well with numerical results (symbols). Dashed lines show results of a linearized theory. (After Ref. [50]; ©2009 IEEE.)

shape of RZ pulses commonly employed in modern lightwave systems.

The main conclusion in all cases is that the BER increases rapidly with the parameter $\Delta v T_s$. The increase in BER becomes so rapid for $\Delta v T_s > 0.01$ that a BER floor (see Section 4.7.2) appears above a BER at a certain value of this parameter. If this BER floor occurs at a level $> 10^{-9}$, the system BER will exceed this value irrespective of the amount of signal power reaching the receiver (an infinite power penalty). Figure 10.13 shows how the BER floor changes with $\Delta v T_s$ for BPSK, QPSK, 8PSK, and DBPSK formats [50]. In all cases, the BER floor is above the 10^{-9} level when $\Delta v T_s$ exceeds a value of about 0.02.

An important metric from a practical standpoint is the tolerable value of $\Delta v T_s$ for which power penalty remains below a certain value (say, 1 dB) at a BER of 10^{-9} . As expected, this value depends on the modulation format as well as on the demodulation technique employed. The linewidth requirements are most stringent for homodyne receivers. Although the tolerable value depends to some extent on the design of the phase-locked loop, typically $\Delta v T_s$ should be $< 5 \times 10^{-4}$ for homodyne receivers to ensure a power penalty of less than 1 dB [38].

The linewidth requirements are relaxed considerably for heterodyne receivers. For synchronous heterodyne receivers needed for the BPSK format, $\Delta v T_s < 0.01$ is required [41]. As seen from Figure 10.13(a), this requirement becomes more severe for the QPSK format. In contrast, $\Delta v T_s$ can exceed 0.1 for asynchronous ASK and FSK receivers [43]–[45]. The reason is related to the fact that such receivers use an envelope detector that throws away phase information. The effect of phase fluctuations is mainly to broaden the signal bandwidth. The signal can be recovered by increasing the bandwidth of the bandpass filter (BPF). In principle, any linewidth can be tolerated if the BPF bandwidth is suitably increased. However, a penalty must be paid because receiver noise increases with an increase in the BPF bandwidth.

The DBPSK format requires narrower linewidths compared with the asynchronous ASK and FSK formats when a delay-demodulation scheme is used. The reason is that information is contained in the phase difference between the two neighboring bits, and the phase should remain stable at least over the duration of two bits. Figure 10.13(b) and other estimates show that $\Delta v T_s$ should be less than 1% to operate with a < 1 dB

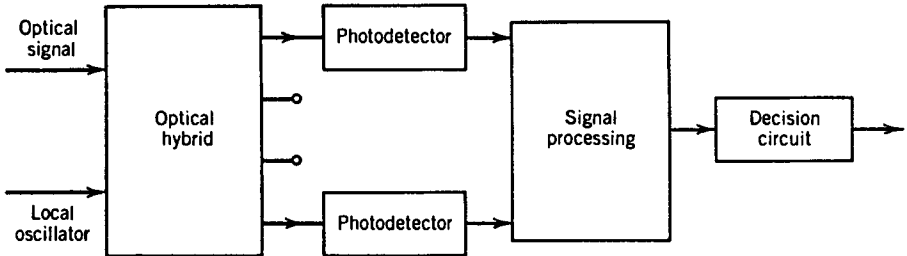


Figure 10.14: Schematic of a multiport phase-diversity receiver.

power penalty [38]. At a 10-Gb/s bit rate, the required linewidth is <10 MHz, but it increases by a factor of 4 at 40 Gb/s. Since DFB lasers with a linewidth of 10 MHz or less are available commercially, the use of the DBPSK format is quite practical at bit rates of 10 Gb/s or more. The requirement is much tighter for the DQPSK format for which the symbol rate B_s plays the role of the bit rate. An approximate analytic expression [49] for the BER predicts that a laser linewidth of <3 MHz may be required at 10 GBd. Of course, this value increases by a factor of 4 if the DQPSK format is used at a symbol rate of 40 GBd.

The preceding estimates of the required laser linewidth are based on the assumption that a BER of 10^{-9} or less is required for the system to operate reliably. Modern lightwave systems employing forward-error correction can operate at a raw BER of as high as 10^{-3} . In that case, the limiting value of the parameter $\Delta v T_s$ for < 1 dB power penalty may increase by a factor of 2 or more. However, if the allowed power penalty is reduced to a level below 0.2 dB, $\Delta v T_s$ again goes back to the limiting values discussed earlier.

An alternative approach solves the phase-noise problem for coherent receivers by adopting a scheme known as *phase-diversity receivers* [52]–[56]. Such receivers use multiple photodetectors whose outputs are combined to produce a signal that is independent of the phase difference $\phi_{IF} = \phi_s - \phi_{LO}$. Figure 10.14 shows schematically a multiport phase-diversity receiver. An optical component known as an *optical hybrid* combines the signal and local-oscillator inputs and provides its output through several ports with appropriate phase shifts introduced into different branches. The output from each port is processed electronically and combined to provide a current that is independent of ϕ_{IF} . In the case of a two-port homodyne receiver, the two output branches have a relative phase shift of 90° , so that their currents vary as $I_p \cos \phi_{IF}$ and $I_p \sin \phi_{IF}$. When the two currents are squared and added, the signal becomes independent of ϕ_{IF} . In the case of a three-port receiver, the three branches have relative phase shifts of 0, 120° , and 240° . Again, when the currents are added and squared, the signal becomes independent of ϕ_{IF} .

10.4.3 Signal Polarization Fluctuations

Polarization of the received optical signal plays no role in direct-detection receivers simply because the photocurrent generated in such receivers depends only on the num-

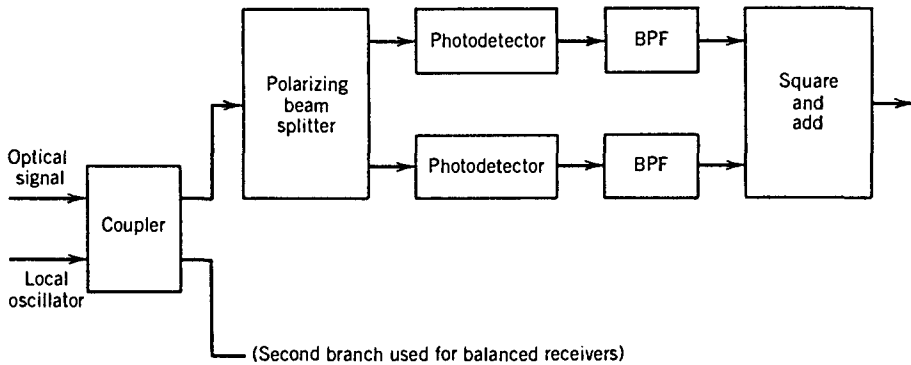


Figure 10.15: Schematic of a polarization-diversity coherent receiver.

ber of incident photons. This is not the case for coherent receivers, whose operation requires matching the state of polarization (SOP) of the local oscillator to that of the signal received. The polarization-matching requirement can be understood from the analysis of Section 4.5, where the use of scalar fields E_s and E_{LO} implicitly assumed the same SOP for the two optical fields. If \hat{e}_s and \hat{e}_{LO} represent the unit vectors along the direction of polarization of E_s and E_{LO} , respectively, the interference term in Eq. (4.5.3) contains an additional factor $\cos \theta$, where θ is the angle between \hat{e}_s and \hat{e}_{LO} . Since the interference term is used by the decision circuit to reconstruct the transmitted bit stream, any change in θ from its ideal value of $\theta = 0$ reduces the signal and affects the receiver performance. In particular, if the SOPs of E_s and E_{LO} are orthogonal to each other, the electrical signal disappears altogether (complete fading). Any change in θ affects the BER through changes in the receiver current and SNR.

The polarization state \hat{e}_{LO} of the local oscillator is determined by the laser and remains fixed. This is also the case for the transmitted signal before it is launched into the fiber. However, at the receiver end, the SOP of the optical signal differs from that of the signal transmitted because of fiber birefringence. Such a change would not be a problem if \hat{e}_s remained constant with time because one could match it with \hat{e}_{LO} by simple optical techniques. However, as discussed in Section 2.3.5, \hat{e}_s changes randomly inside most fiber links because of birefringence fluctuations related to environmental changes. Such changes occur on a time scale ranging from seconds to microseconds. They lead to random changes in the BER and render coherent receivers unusable, unless some scheme is devised to make the BER independent of polarization fluctuations.

Several schemes have been developed for solving the polarization-mismatch problem [57]–[62]. In one scheme [57], the polarization state of the received optical signal is tracked electronically and a feedback-control technique is used to match \hat{e}_{LO} with \hat{e}_s . In another, polarization scrambling or spreading is used to force \hat{e}_s to change randomly during a symbol period [58]–[61]. Rapid changes of \hat{e}_s are less of a problem than slow changes because, on average, the same power is received during each bit. A third scheme makes use of optical phase conjugation to solve the polarization problem [62]. The phase-conjugated signal can be generated inside a dispersion-shifted fiber through four-wave mixing. The pump laser used for four-wave mixing can also play the role of

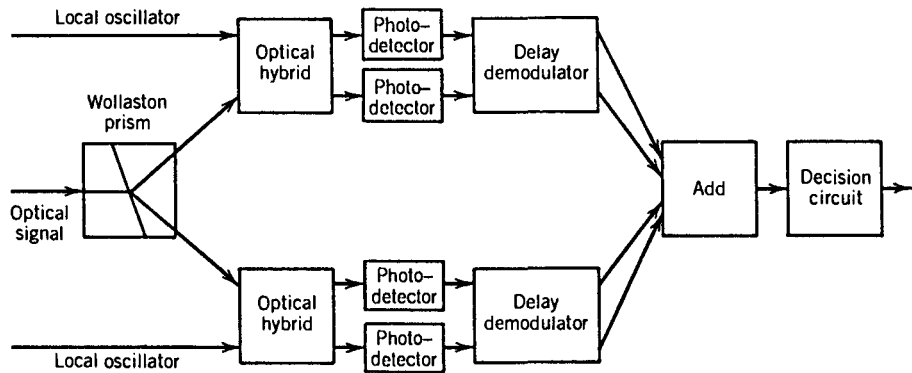


Figure 10.16: Four-port coherent DPSK receiver employing both phase and polarization diversity. (After Ref. [64]; ©1987 IEE.)

the local oscillator. The resulting photocurrent has a frequency component at twice the pump-signal detuning that can be used for recovering the bit stream.

The most commonly used approach solves the polarization problem by using a two-port receiver, similar to that shown in Figure 10.5, with the difference that the two branches process orthogonal polarization components. Such receivers are called *polarization-diversity receivers* [63]–[71], as their operation is independent of the SOP of the optical signal reaching the receiver. Figure 10.15 shows the block diagram of a polarization-diversity receiver. A polarization beam splitter is used to separate the orthogonally polarized components which are processed by separate branches of the two-port receiver. When the photocurrents generated in the two branches are squared and added, the electrical signal becomes polarization independent. The power penalty incurred in following this technique depends on the modulation and demodulation techniques used by the receiver. In the case of synchronous demodulation, the power penalty can be as large as 3 dB [66]. However, the penalty is only 0.4–0.6 dB for optimized asynchronous receivers [63].

The technique of polarization diversity can be combined with phase diversity to realize a receiver that is independent of both phase and polarization fluctuations of the signal received [65]. Figure 10.16 shows such a four-port receiver having four branches, each with its own photodetector. The performance of such receivers would be limited by the intensity noise of the local oscillator, as discussed in Section 10.4.1. The next step consists of designing a balanced, phase- and polarization-diversity, coherent receiver by using eight branches with their own photodetectors. Such a receiver was first demonstrated in 1991 using a compact bulk optical hybrid [67]. Soon after, the attention turned toward developing integrated balanced receivers. By 1995, a polarization-diversity receiver was fabricated using InP-based optoelectronic integrated circuits [70]. More recently, the attention has focused on coherent receivers that employ digital signal processing [72]–[75]. With this approach, even homodyne detection can be realized without relying on a phase-locked loop [75].

10.4.4 Noise Added by Optical Amplifiers

As discussed in Section 7.5, optical amplifiers degrade considerably the electrical SNR in the case of direct detection because of the noise added to the optical signal in the form of amplified spontaneous emission (ASE). As expected, amplifier noise also degrades the performance of coherent receivers. The extent of degradation depends on the number of amplifiers employed and becomes quite severe for long-haul systems that may employ tens of amplifiers along the fiber link. Even for relatively short fiber links without in-line amplifiers, an optical preamplifier is often used for the signal or the local oscillator. In the case of optical delay demodulation, the use of an optical preamplifier before the receiver is almost a necessity because the receiver performance would otherwise be limited by the thermal noise of photodetectors.

The noise analysis of Section 7.5 can be extended to heterodyne and delay-demodulation receivers [18]. Two new noise currents that contribute to the total receiver noise are $\sigma_{\text{sig-sp}}^2$ and $\sigma_{\text{sp-sp}}^2$ representing, respectively, the impact of beating between the signal and ASE and between ASE and ASE. Although a general analysis is quite complicated, if we assume that a narrowband optical filter is employed after the preamplifier to reduce ASE noise and retain only $\sigma_{\text{sig-sp}}^2$ that is the dominant noise term in practice, it turns out that the SNR of the signal is reduced from ηN_p to $\eta N_p/n_{\text{sp}}$, where n_{sp} is the spontaneous emission factor introduced in Section 7.2.4 and defined in Eq. (7.2.12). We can write n_{sp} in terms of the noise figure F_n of optical amplifiers using the relation $F_n \approx 2n_{\text{sp}}$ given in Eq. (7.2.15). If multiple amplifiers are employed, the SNR is degraded further because the effective noise figure of a chain of amplifiers increases with the number of amplifiers.

Another polarization issue must be considered because of the unpolarized nature of the amplifier noise. As discussed in Section 7.5.1, in addition to the ASE noise component copolarized with the signal, the orthogonally polarized part of the ASE also enters the receiver and adds additional noise. One can avoid this part by placing a polarizer before the photodetector so that the noise and the signal are in the same polarization state. This situation is referred to as *polarization filtering*. When polarization filtering is done at the receiver and a single optical preamplifier is used to amplify either the optical signal or the local oscillator, the BER for different modulation formats can be obtained from expressions given in Section 10.3 by replacing N_p with N_p/n_{sp} in them. The receiver sensitivity at a given BER is degraded by a factor of n_{sp} because the incident optical power must be increased by the same factor.

In the absence of polarization filtering, orthogonally polarized noise should be included and it leads to an increase in the BER. In the case of a DBPSK signal demodulated using an optical delay interferometer, the BER is found to be [18]

$$\text{BER} = \frac{1}{2} \exp(-\eta N_p)(1 + \eta N_p/4), \quad (10.4.4)$$

indicating that the BER is increased by a factor of $1 + \eta N_p/4$. The resulting increase in required SNR is not negligible because a BER of 10^{-9} is realized at a SNR of $\eta N_p = 22$ rather than 20. However, this increase corresponds to power penalty of less than 0.5 dB. When a DQPSK signal is received without polarization filtering, the BER is found to

be given by [18]:

$$\text{BER} = Q_1(a, b) - \frac{1}{2} I_0(ab) \exp[-\frac{1}{2}(a^2 + b^2)] \\ + [(b^2 - a^2)/8ab] I_1(ab) \exp[-\frac{1}{2}(a^2 + b^2)], \quad (10.4.5)$$

where $I_1(x)$ the modified Bessel function of order one. Compared with the case of polarization filtering in Eq. (10.3.21), another term is added to the BER because of additional current fluctuations produced by ASE polarized orthogonal to the signal. However, this increase is almost negligible and leads to a power penalty of < 0.1 dB.

10.4.5 Fiber Dispersion

As discussed in Sections 2.4 and 5.4, dispersive effects occurring inside optical fibers affect all lightwave systems. Such impairments result not only from group-velocity dispersion (GVD) governed by the parameter D but also from polarization-mode dispersion (PMD) governed by the parameter D_p . As expected, both of them affect the performance of coherent and self-coherent systems, although their impact depends on the modulation format employed and is often less severe compared with that for IM/DD systems [76]–[83]. The reason is easily understood by noting that coherent systems, by necessity, use a semiconductor laser operating in a single longitudinal mode with a narrow linewidth. Frequency chirping is also avoided by using external modulators.

The effect of fiber dispersion on the transmitted signal can be calculated by following the analysis of Section 2.4. In particular, Eq. (2.4.15) can be used to calculate the optical field at the fiber output for any modulation technique as long as the non-linear effects are negligible. In a 1988 study, the GVD-induced power penalty was calculated for various modulation formats through numerical simulations of the “eye-opening” degradation occurring when a pseudo-random bit sequence was propagated through a single-mode fiber [76]. A new method of calculating the BER in the presence of dispersive effects was proposed in 2000 and used to show that the eye degradation approach fails to predict the power penalty accurately [81]. This method can include preamplifier noise as well and has been used to calculate power penalties induced by GVD and PMD for a variety of modulation formats [82], including the DBPSK and DQPSK formats implemented with the delay-demodulation technique.

Figure 10.17(a) shows the GVD-induced power penalty as a function of DB^2L , where B is the bit rate and L is the fiber-link length, for several modulation formats [82]. Figure 10.17(b) shows the PMD-induced power penalty as a function of the dimensionless parameter $\Delta\tau/T_b$, where $T_b = 1/B$ is the bit duration and $\Delta\tau$ is average value of the differential group delay, after setting $D = 0$. The case of on-off keying (OOK) is shown for comparison. Also, both the RZ and NRZ cases are shown for each modulation format to emphasize how dispersive effects depend on them. Although the results depend to some extent on the specific shape of RZ pulses and the specific transfer functions employed for the optical and electrical filters in numerical simulations, they can be used for drawing qualitative conclusions.

As seen in Figure 10.17(a), the power penalties at a given value of DB^2L are smaller for the DBPSK format compared with the OOK format in both the RZ and NRZ cases but the qualitative behavior is quite similar. In particular, the penalty can be reduced to

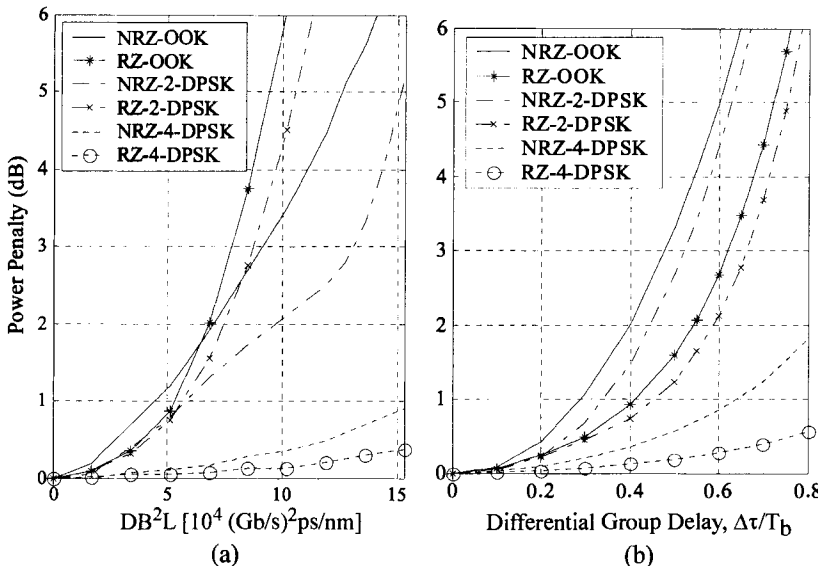


Figure 10.17: (a) GVD-induced and (b) PMD-induced power penalties for several modulation formats. Here, 2-DPSK and 4-DPSK stand for the DBPSK and DQPSK formats, respectively. (After Ref. [82]; ©2004 IEEE.)

below 1 dB in both cases by making $DB^2L < 5 \times 10^4$ (Gb/s)² ps/nm. In contrast, power penalties are reduced dramatically for the DQPSK format, and much larger values of DB^2L can be tolerated. The reason is easily understood by noting that at a given bit rate B the symbol rate B_s is reduced by a factor of 2. This allows the use of wider optical pulses and results in a smaller power penalty. The PMD-induced power penalty in Figure 10.17(b) shows a similar qualitative behavior for the same physical reason. These results indicate clearly that, as far as dispersion effects are concerned, their impact can be reduced considerably by adopting a format that allows transmission of multiple bits during the time slot allocated to a single symbol. This is the reason why the use of DQPSK format is becoming prevalent in modern, high-performance systems.

If dispersive effects begin to limit a coherent system, one can employ a variety of dispersion-management techniques discussed in Chapter 8. In the case of long-haul systems, periodic compensation of fiber dispersion with dispersion-compensating fibers is employed routinely. It is also possible to compensate for fiber dispersion through an electronic equalization technique implemented within the receiver [84]–[87]. This approach is attracting considerable attention since 2005 with the implementation of digital signal processing in digital coherent receivers.

10.5 Impact of Nonlinear Effects

All nonlinear effects [88] discussed in Chapter 9 in the context of IM/DD systems have the potential of limiting the performance of coherent or self-coherent lightwave sys-

tems, depending on the optical power launched into the fiber. The impact of stimulated Brillouin scattering (SBS) depends on both the modulation format and the bit rate, and its effects on coherent systems have been studied extensively [89]–[91]. The impact of stimulated Raman scattering on WDM coherent systems is less severe compared with IM/DD systems if information is encoded in the carrier phase because the Raman-induced power transfer depends only on the channel power. On the other hand, self-(SPM) and cross-phase modulations (XPM) play a much more important role because they convert intensity fluctuations into phase fluctuations. Because of the nonlinear origin of such fluctuations, the phase noise induced by them is known as the *nonlinear phase noise*. This section focuses mainly on this kind of noise.

10.5.1 Nonlinear Phase Noise

Gordon and Mollenauer in 1990 were the first to study the impact of nonlinear phase noise on the performance of a long-haul system employing fiber amplifiers [92]. By 1994, SPM-induced limitations for coherent systems were observed experimentally and studied in more detail theoretically [93]–[95]. In a 1993 experiment that employed synchronous heterodyne detection of a BPSK signal at a bit rate of 8 Gb/s, a drop in the total transmitted distance was observed at average input power levels as low as 1 mW [94]. With the revival of interest in phase-encoded formats after 2001, nonlinear phase noise attracted renewed attention, and by now its properties have been studied quite thoroughly [96]–[114].

The origin of nonlinear phase noise is easy to understand from Section 2.6.2 where the SPM-induced nonlinear phase shift has been analyzed. In general, one must solve the nonlinear Schrödinger (NLS) equation given in Eq. (2.6.18) numerically to see how the complex amplitude $A(z, t)$ of the optical signal evolves inside the fiber. However, this equation can be solved analytically in the limit of negligible dispersive effects ($\beta_2 \approx 0$), and the solution for a fiber of length L is given is given by

$$A(L, t) = A(0, t) \exp[-\alpha L + i\phi_{NL}(t)], \quad \phi_{NL}(t) = \gamma |A(0, t)|^2 L_{eff}, \quad (10.5.1)$$

where $L_{eff} = (1 - e^{-\alpha L})/\alpha$ is the effective fiber length defined earlier in Eq. (2.6.7). For fiber lengths longer than 50 km, we can use the approximation $L_{eff} = 1/\alpha$, where α is the fiber-loss parameter at the signal wavelength. The nonlinear parameter γ is around $2 \text{ W}^{-1}/\text{km}$ for telecommunication fibers in the wavelength region near $1.55 \mu\text{m}$.

If the input field is noisy because of amplifier noise added to it at preceding fiber spans, i.e., $A(0, t) = A_s(t) + n(t)$, it follows from Eq. (10.5.1) that fluctuations in the signal phase ϕ_s are enhanced inside the fiber because of the nonlinear phase shift ϕ_{NL} . This enhancement is also evident in Figure 10.18 where the initial noise $n(t)$ is shown by a circular cloud around the signal-field vector $A_s(t)$. SPM inside the fiber distorts the circular cloud into an elongated ellipse because a positive amplitude fluctuation leads to a larger nonlinear phase shift than the negative one. Mathematically, with the notation $A(L, t) = \bar{A}(t) \exp[i\phi(t)]$, the phase at the end of fiber is given by

$$\phi(t) \approx \phi_s + \gamma L_{eff} |A_s(t)|^2 + \delta\phi(t) + 2\gamma L_{eff} \text{Re}[A_s^*(t)n(t)], \quad (10.5.2)$$

where we have neglected a second-order noise term containing $n^2(t)$. The second term in this expression represents a deterministic, nonlinear shift in the signal phase that

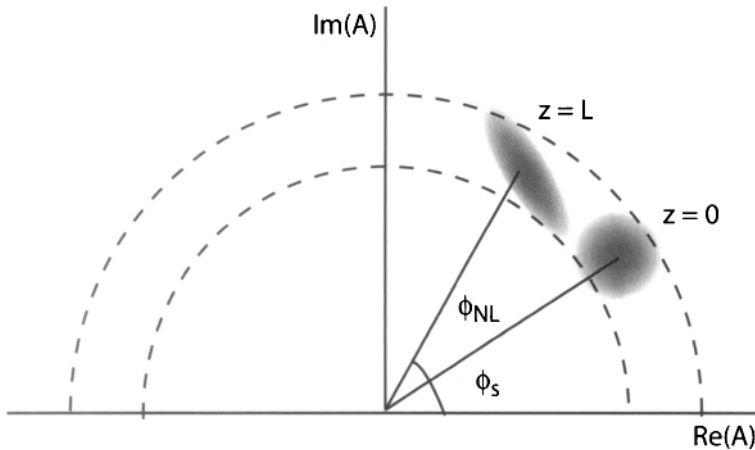


Figure 10.18: Schematic illustration of the SPM-induced enhancement of phase noise inside an optical fiber of length L . SPM distorts the initially circular noise cloud into an elongated ellipse. Two dashed semi-circles show the range of amplitude fluctuations.

does not vary from one symbol to next and cancels out during differential detection. It represents the average value of the nonlinear phase shift. The third term represents a linear phase noise that occurs even in the absence of SPM. The last term shows how the combination of amplifier noise and SPM leads to enhanced fluctuations in the signal phase. While the initial amplifier noise is of additive nature, nonlinear phase noise is multiplicative in Eq. (10.5.2). It is also “colored” because of a time-dependent signal. These features indicate that the nonlinear phase noise may not remain Gaussian even if $n(t)$ itself follows Gaussian statistics.

The analysis of nonlinear phase noise is much more complicated for long-haul systems that compensate fiber losses periodically using a lumped or distributed amplification scheme. In general, one must solve the stochastic NLS equation given in Eq. (7.1.4) along the entire fiber link to find the statistical properties of the optical field reaching the receiver, a challenging task even numerically. The situation becomes simpler if we neglect fiber dispersion ($\beta_2 = 0$) and assume that a lumped amplifier, with the gain $G_A = e^{\alpha L}$, compensates losses after every fiber span of length L . Every amplifier adds ASE noise that affects the signal and contributes to the nonlinear phase noise until the end of the entire fiber link. Since the nonlinear phase shift in each fiber section is additive, for a chain of N amplifiers, the nonlinear phase given in Eq. (10.5.1) becomes

$$\phi_{NL} = \gamma L_{\text{eff}} \left(\sum_{k=1}^N \left[|A(0, t) + \sum_{j=1}^k n_j|^2 \right] \right), \quad (10.5.3)$$

where $n_j(t)$ is the noise added by the j th amplifier. This expression can be used to find the probability density function (PDF) of the nonlinear phase noise after noting that the ASE noise added by one amplifier is independent of that added by other amplifiers [18].

As seen in Eq. (10.5.1), the signal phase contains two noise terms representing linear and nonlinear phase fluctuations. In practice, the PDF of the total phase $\phi(t)$

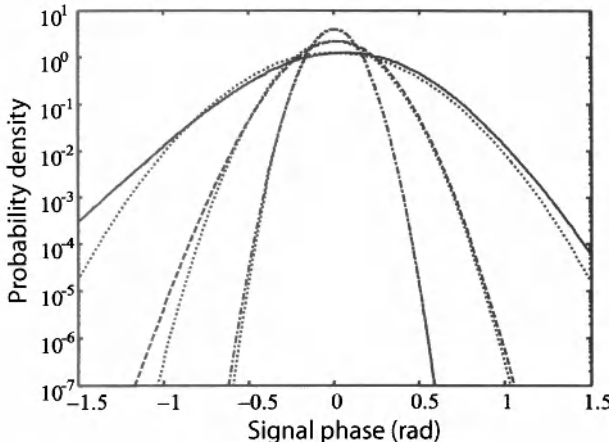


Figure 10.19: Probability density function of the signal phase for optical SNR values of 10, 15, and 20 dB for the signal power using $\langle \phi_{NL} \rangle = \sqrt{3}/2$. In each case, the dotted curve shows a Gaussian distribution with the same variance. (After Ref. [103]; ©2004 OSA.)

is of more interest because it controls the BER of a phase-encoded lightwave system. This case was studied in 1994 by Mecozzi, who succeeded in finding an approximate analytic expression for the BER in the case of the DPSK format [95]. An analytic expression for the PDF of the signal phase was found by 2004 in the form of an infinite series containing hypergeometric functions [103].

The PDF of phase noise can be used to calculate its variance. Neglecting the impact of intensity fluctuations and making some reasonable approximations, the phase variance is given by a remarkably simple expression [103]

$$\sigma_\phi^2 \approx \frac{S_{ASE}L_T}{2E_0} [1 + 2(\gamma P_0 L_T)^2 / 3], \quad (10.5.4)$$

where S_{ASE} is the ASE spectral density of noise given in Eq. (7.2.11), L_T is the total link length, E_0 is the pulse energy within the symbol slot, and P_0 is the corresponding peak power. The first term, representing the contribution of $\delta\phi$ in Eq. (10.5.2), grows linearly with L_T . The second term, having its origin in the nonlinear phase noise, grows cubically with L_T and shows why SPM plays a detrimental role in phase-encoded lightwave systems. The phase variance can be minimized by optimizing P_0 , or the average value $\langle \phi_{NL} \rangle$ of the nonlinear phase shift. It is easy to show by differentiating Eq. (10.5.4) that the optimum value of the $\langle \phi_{NL} \rangle$ is $\sqrt{3}/2$.

Figure 10.19 shows three examples of the phase PDFs for optical SNR values of 10, 15, and 20 dB for the received signal [103]. In each case, the dotted curve shows a Gaussian distribution with the same variance. Although the PDF of phase fluctuations becomes close to a Gaussian for SNR of 20 dB or more, it deviates from it for lower SNR values, especially in tails of the PDF that are important for estimating the BER. Nevertheless, the variance of phase fluctuations provides a rough measure of the impact of nonlinear phase noise on system performance and is often used as a guideline.

10.5.2 Effect of Fiber Dispersion

The preceding analysis of nonlinear phase noise is approximate as it neglects fiber dispersion. It is difficult to make much analytic progress because of the stochastic nature of the NLS equation in Eq. (7.1.4). However, the variance of phase noise can be calculated analytically [96] if we employ the variational formalism or the moment method of Section 7.7.2. Such an approach also allows one to take into account variations of the loss, dispersion, and nonlinear parameters along the fiber link that occur in a dispersion-managed fiber link.

One of the conclusions of such an approach is that the variance of phase fluctuations decreases as the dispersive effects become more and more dominant [106]. This is not surprising if we note that dispersion causes optical pulses to spread, resulting in a reduced peak power, and thus a reduced nonlinear phase noise. This argument also indicates that the best system design from the standpoint of nonlinear phase is one in which entire dispersion is compensated at the receiver end [111]. However, these arguments ignore the intrachannel XPM and FWM effects discussed in Section 9.4. As the dispersive effects broaden optical pulses, pulses in neighboring symbol slots begin to overlap and interact through XPM, a phenomenon that also leads to nonlinear phase noise. When the intrachannel XPM effects are taken into account properly, the variance of phase fluctuations does not decrease much with an increase in fiber dispersion [107]. However, what matters in the case of the RZ-DBPSK format is the variance of the phase difference for the two neighboring RZ pulses. A detailed analysis shows that this variance becomes relatively small for the DBPSK format because of a partial correlation between phase noises of adjacent pulses [108]. In this situation, the nonlinear phase noise resulting from intrachannel FWM provides the dominant contribution in the limit of large fiber dispersion.

The XPM-induced nonlinear phase noise is also important for WDM systems in which optical pulses belonging to different channels overlap periodically as they propagate inside the fiber at different speeds. This case has been analyzed using a perturbation approach [111]. Figure 10.20 compares predicted BERs for a WDM DBPSK-format system as the number of channels increases from 1 to 49 for three dispersion-management schemes. The 12.5-Gb/s channels (25-GHz channel spacing) are transmitted over 1600 km using 20 amplifiers separated by 80 km. Each fiber span consists of standard fibers with the parameters $\alpha = 0.25 \text{ dB/km}$, $\beta_2 = -21.6 \text{ ps}^2/\text{km}$, and $\gamma = 2 \text{ W}^{-1}/\text{km}$. Dispersion is compensated at amplifier locations by (a) 95%, (b) 100%, and (c) 0%; remaining dispersion compensated at the receiver. In the case of (a), BER of all channels can be reduced to near a 10^{-9} level by optimizing channel powers closed to 2 mW. In the case of 100% compensation (b), the interchannel XPM effects degrade the signal phase to the extent that a BER of at most 10^{-5} is realized even when channel powers are suitably optimized to near 1 mW. The entire dispersion is compensated once at the receiver end in (c). The BER improves in this case considerably but the optimum channel power decreases as the number of channels increases. Moreover, BER is very sensitive to this optimum value and decreases rapidly with small changes around it. In all cases, the situation is much worse for the DQPSK format. These results indicate that interchannel XPM effects limit the performance of phase-enclosed WDM systems quite severely.

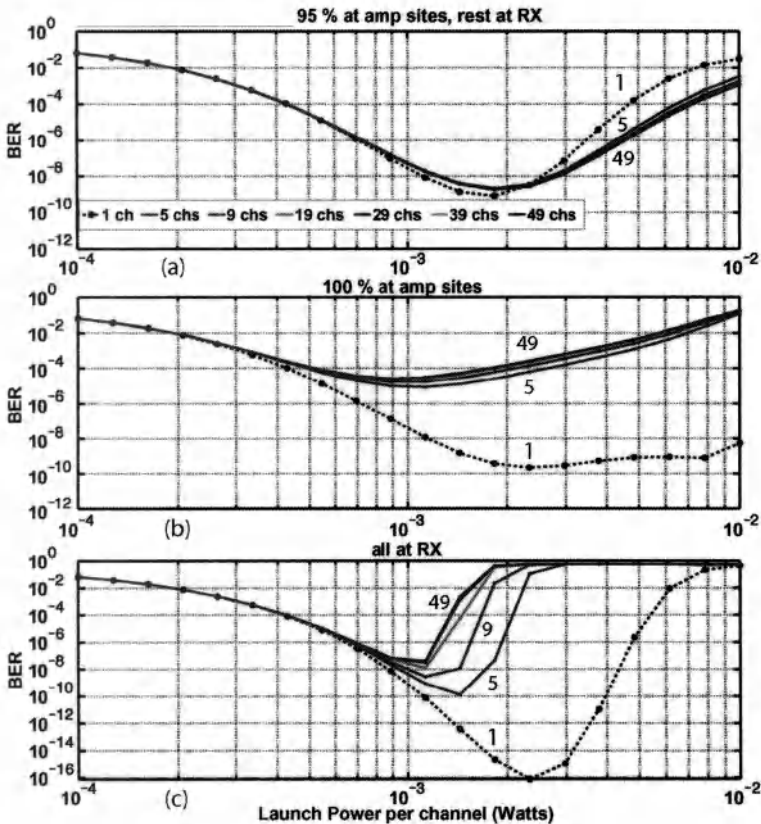


Figure 10.20: Predicted BERs as a function of launched channel power for a 49-channel WDM DBPSK system with (a) 95%, (b) 100%, and (c) 0% dispersion compensation at amplifiers with rest done at the receiver end. (After Ref. [111]; ©2007 IEEE.)

10.5.3 Compensation of Nonlinear Phase Noise

Given the serious impact of nonlinear phase noise on phase-encoded lightwave systems, the question is whether one can compensate for it with a suitable scheme. The answer turns out to be: yes, to some extent. Several compensation schemes have been proposed in recent years with varying degrees of success [115]–[127].

The basic reason why nonlinear phase noise can be compensated is easily understood from Eq. (10.5.1). It shows that the nonlinear phase shift is actually a deterministic process in the sense that it is linearly proportional to the instantaneous optical power. The only reason for this phase shift to be noisy is that the power itself is fluctuating. Thus, a simple approach to nonlinear phase compensation consists of using a nonlinear device that imposes a negative phase shift on the incoming optical signal in proportion to the optical power. In essence, such a device exhibits a negative value of the nonlinear parameter γ . In a 2002 proposal, this device was in the form of a periodically poled LiNbO₃ waveguide that provided a negative nonlinear phase shift

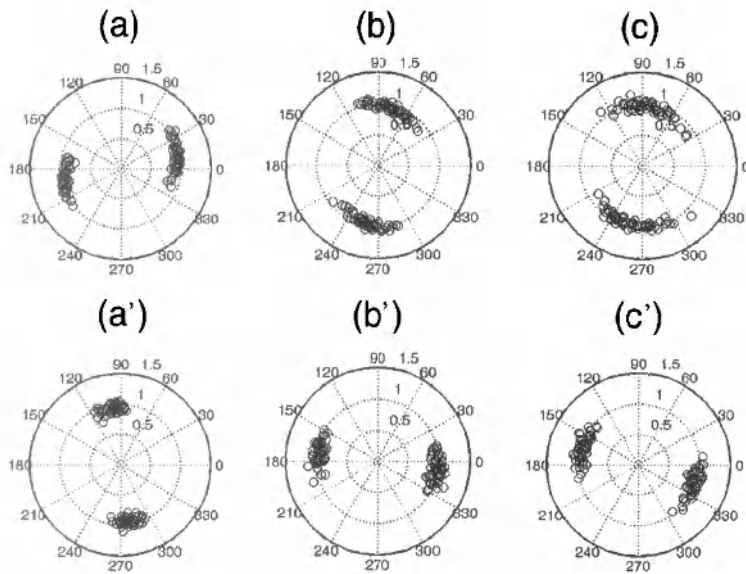


Figure 10.21: Phasor diagrams after 6000-km of transmission for (a) a single channel, (b) 5 channels with 100-GHz spacing, and (c) 5 channels with 50-GHz spacing. Bottom row shows reduction in phase noise with post-nonlinearity compensation. (After Ref. [115]; ©2002 OSA.)

through a cascaded second-order nonlinear process [115]. Such a scheme is referred to as *post-nonlinearity compensation* because it is implemented at the end of the fiber link.

In another implementation of this idea, optical power is first detected at the receiver end, and the resulting current is used to drive a LiNbO₃ phase modulator that imposes a negative phase shift proportional to the optical power on the received optical signal [116]. This scheme was implemented in a 2002 experiment using two phase modulators that processed orthogonally polarized components of the signal to impose a polarization-independent phase shift on the signal [117]. The compensation of SPM-induced phase shift was observed through a reduction in spectral broadening.

Extensive numerical simulations performed for single-channel and WDM systems indicate that a post-nonlinearity compensation scheme reduces the nonlinear phase noise but does not eliminate it [115]. The reason can be understood from Eq. (10.5.3). It shows that the nonlinear phase shift builds up along the fiber link, with the noise added by multiple amplifiers. Since intensity noise itself evolves along the fiber link, the use of optical power at the end of the link cannot cancel the nonlinear phase noise completely. As an example, Figure 10.21 shows, using phasor diagrams, the extent of phase-noise reduction after 6000-km transmission of DBPSK signals for WDM channels operating at 10 Gb/s. The dispersion-managed link consisted of 100-km fiber spans ($D = 6 \text{ ps/km/nm}$) with partial dispersion compensation at amplifiers, a pre-dispersion of 2300 ps/nm, and a post-dispersion of 150 ps/nm. Fiber losses of 23 dB during each span were assumed to be compensated through backward Raman ampli-

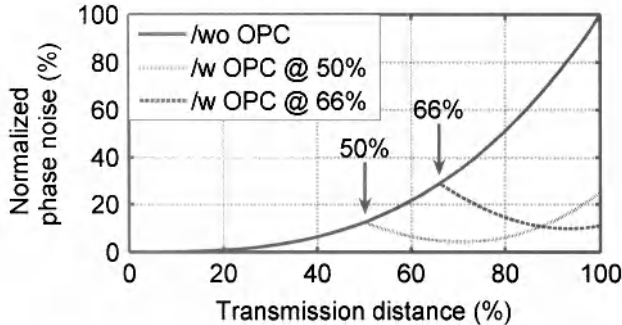


Figure 10.22: Normalized phase variance as a function of the link length. Solid curve shows its monotonic growth in the absence of OPC; its reduction after OPC is carried out at two locations is also shown. (After Ref. [125]; ©2006 IEEE.)

fication. Figure 10.21 shows that the effectiveness of the compensation scheme is reduced for closely spaced channels. The reason is related to the interchannel XPM process that generates additional nonlinear phase noise. This XPM-induced noise can be reduced by adopting the polarization interleaving technique that ensures that neighboring channels are orthogonally polarized.

The use of a phase modulator, driven by a current proportional to received optical power also reduces the nonlinear phase noise. However, one needs to optimize the fraction of received power that is sent to the detector. Also, one must ask whether phase modulator should be used at the end of the fiber link or placed within the link at an optimum distance. These issues have been analyzed and it is found that the phase variance can be reduced by a factor of 9 by placing the phase modulator at a distance of $2L_T/3$, where L_T is the total link length [118]. Even larger reduction factors are possible by placing two or more phase modulators at optimum locations within the fiber link. On the experimental side, a single phase modulator, placed at the end of a 1-km-long highly nonlinear fiber, reduced the phase noise of a single 10-Gb/s DBPSK channel considerably, resulting in a higher electrical SNR and an improved eye diagram [119].

Another scheme for phase-noise compensation [120]–[123] makes use of optical phase conjugation (OPC). As already discussed in Section 8.5, OPC can compensate the GVD and SPM effects simultaneously [128]. OPC can also compensate for the timing jitter included by amplifier noise [129]. Thus, it is not surprising that OPC is suitable for compensation of SPM-induced nonlinear phase noise. The only question is at what location along the fiber link should the phase conjugator be placed and to what extent is the phase noise compensated. As we saw in Section 8.5.1, dispersion compensation requires mid-span placement of the OPC device. However, such a choice is not optimum for phase-noise compensation [120]. As seen from Eq. (10.5.3), nonlinear phase noise builds up along the fiber link such that the second half of the fiber link contributes to it much more than the first half. Clearly, it is better if OPC is carried out in the second half of the fiber link.

The variance σ_ϕ^2 of nonlinear phase noise and its reduction with OPC can be cal-

culated using a variational [120], moment [122], or perturbation method [123]. These methods can also be used to find the optimum location of the phase conjugator. Figure 10.22 shows how much the OPC helps to reduce the phase variance for two different locations of the phase conjugator [125]. When it is placed exactly at the mid-point, the phase variance is reduced by a factor of 4 (or 6 dB). However, it can be reduced by 9.5 dB, or almost by a factor of 10, when the phase conjugator is placed at a distance of $0.66L_T$. Even larger reductions are possible by using two phase conjugators. A 12-dB reduction in phase variance occurs when they are placed at distances of $L_T/4$ and $3L_T/4$. This value can be increased to 14 dB by placing the phase conjugators at 40% and 80% of the total link length. One should keep in mind that the level of dispersion compensation provided by a phase conjugator also depends on its location. For example, in the case of two phase conjugators, 100% dispersion compensation occurs in the first configuration but it is reduced to a 80% level in the second configuration.

Experiments have been performed to observe the OPC-induced reduction in the nonlinear phase noise. In one experiment [121], a single 10.7-Gb/s DBPSK channel was transmitted over 800 km, with OPC taking place at various locations of the fiber link. The performance was characterized using a Q factor defined in terms of the observed BER as

$$Q = 20 \log_{10} \left(\sqrt{2} \operatorname{erfc}^{-1}(2\text{BER}) \right). \quad (10.5.5)$$

This Q factor improved by 4 dB when OPC was implemented at the midpoint of the link. In this experiment, the optimum location was the midpoint as improvement in the Q factor was reduced on either side of this location.

In another WDM experiment [121], 44 DQPSK channels, with 50-GHz spacing and 10.7-GHz symbol rate, were transmitted over 10,200 km using a recirculating loop configuration. Losses inside fibers were compensated using EDFAAs in combination with backward Raman amplification. Midpoint-OPC was carried out using a periodically poled LiNbO₃ waveguide. Figure 10.23(a) shows the Q factor as a function of distance, with and without OPC, for a typical channel. Without OPC, Q factor began to degrad rapidly after 6000 km, and the signal could not be transmitted error-free after 7800 km. Such a rapid degradation does not occur when OPC is employed, and the WDM system operates error free over 10,200 km. Figure 10.23(b) shows that the Q factors of all channels at a distance of 10,200 km remains above the FEC limit of 9.1 dB. These results clearly illustrate the potential of OPC-based compensation of nonlinear phase noise in real WDM systems.

Several other techniques can provide partial compensation of nonlinear phase noise. An electronic compensation scheme can be used inside the optical receiver simply by subtracting from the received phase a correction proportional to the incident power. With proper optimization, phase variance can be reduced by up to a factor of 4, resulting in doubling of the transmission distance [124]. Nonlinear phase noise within the fiber link can be controlled to some extent by optimizing the number and locations of in-line amplifiers [126]. The use of Wiener filtering has also been suggested for this purpose [127].

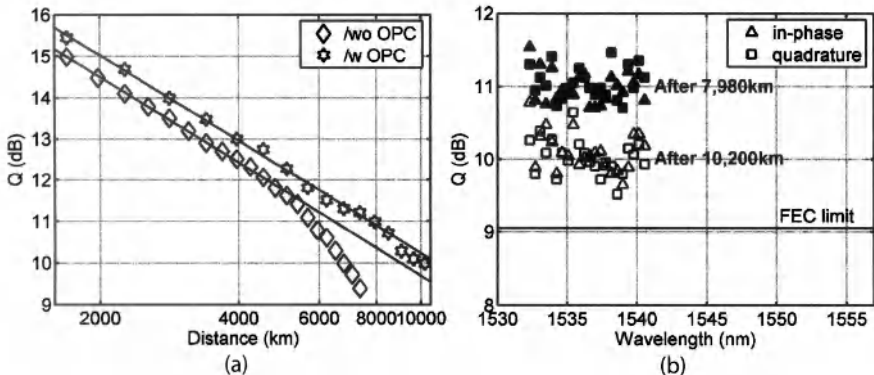


Figure 10.23: (a) Q factors as a function of distance, with and without OPC, for a typical channel of a 44-channel WDM system with the DQPSK format. (b) Q factors with OPC at two distances for all channels. The FEC limit is shown for comparison. (After Ref. [121]; ©2006 IEEE.)

10.6 Recent Progress

Many transmission experiments performed during the 1980s demonstrated that coherent receivers could function at lower power levels compared with that required for direct detection [4]–[9]. With the advent of optical amplifiers, this issue became irrelevant. However, as WDM systems began to transmit more and more channels within the 40-nm bandwidth of the C band, the issue of spectral efficiency led after 2001 to a renewed interest in phase-encoded lightwave systems. This section reviews the recent progress realized in designing such systems.

10.6.1 Systems with the DBPSK format

The DBPSK format was the first one employed for demonstrating hight-capacity WDM systems [130]–[146]. The reason is related to the adoption of the delay-demodulation scheme of Section 10.2.3 based on an optical interferometer; with its use, receiver design is similar to that employed for IM/DD receivers. Moreover, optical transmitters for generating a DBPSK signal require only one additional phase modulator. However, DBPSK format allows one to send only one bit per symbol, resulting in a symbol rate equal to the bit rate. Since any gain in spectral efficiency is relatively modest, why should one use the DBPSK format in place of the standard OOK format? The answer was provided by studies devoted to comparing the two formats [130]–[134]. It turns out that the nonlinear XPM effects are reduced considerably with the use of DBPSK [131]. As a result, this format improves the system performance considerably for dense WDM systems designed to provide a spectral efficiency $\eta_s > 0.4 \text{ b/s/Hz}$ [133].

This advantage was realized in 2002 when 64 WDM channels, each operating at 42.7 Gb/s, were transmitted over 4000 km using the RZ-DBPSK format. The use of 100-GHz channel spacing resulted in a 53-nm bandwidth of the WDM signal with $\eta_s = 0.4 \text{ b/s/Hz}$. By 2003, several experiments reported major advances by employing the DBPSK format [136]–[142]. In one experiment, a spectral efficiency of $\eta_s = 0.8$

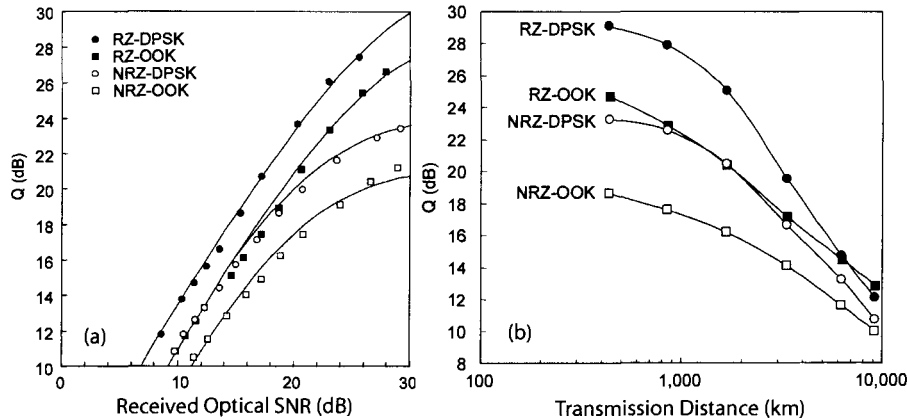


Figure 10.24: Comparison of Q factors (a) as a function of optical SNR and (b) as a function of distance for four modulation formats for a WDM system with 100 channels at 10.7 Gb/s. (After Ref. [134]; ©2003 IEEE.)

b/s/Hz was realized by transmitting 64 WDM channels, each operating at 42.7 Gb/s with a channel spacing of only 50 GHz, over 3200 km of fiber, resulting in a system capacity of 6.4 Tb/s [136]. In another, the objective was to demonstrate transmission of 40 channels (each at 40 Gb/s) over a trans-Pacific distance of 10,000 km [137]. These two experiments used a format known as CSRZ-DBPSK, where CSRZ stands for carrier-suppressed RZ, in which two neighboring RZ pulses have a relative phase difference of π , in addition to the phase shift required by the bit pattern. Another experiment transmitted 185 WDM channels, each operating at 10.7 Gb/s, over 8370 km using the RZ-DBPSK format [138]. Still another transmitted 373 WDM channels, each operating at 10.7 Gb/s, over 11,000 km using the same format [139]. Channels were spaced apart by 25 GHz ($\eta_s = 0.4$ b/s/Hz) and occupied a 80-nm bandwidth in the 1.55- μ m spectral region. In a later experiment, spectral efficiency could be increased to 0.65 b/s/Hz, but the number of channels was limited to 301 [141].

Spectral efficiency in the preceding experiments was limited to 0.8 b/s/Hz. However, a 2002 experiment managed to realize a spectral efficiency of 1.6 b/s/Hz by combining 40 DBPSK channels (each at 40 Gb/s) with optical code-division multiplexing, resulting in a system capacity of 6.4 Tb/s [143]. The bit rate of 160 Gb/s per channel was realized in a 2003 experiment in which six such channels were transmitted over 2000 km, with a spectral efficiency of 0.53 b/s/Hz, using the RZ-DBPSK format [144]. Of course, the 160-Gb/s signal containing 3.5-ps pulses has to be generated through an OTDM scheme. This experiment showed that the DBPSK format could be used even at a bit rate of 170.6 Gb/s that is required for 160-Gb/s systems when a forward-error correction scheme is implemented.

The advantages of the DBPSK format were quantified in a 2003 WDM experiment that transmitted 100 channels over transoceanic distances with a spectral efficiency of 0.22 b/s/Hz [134]. The experiment compared the DBPSK and OOK formats using both the RZ and NRZ bit streams at bit rate of 10.7 Gb/s. Figure 10.23(a) shows

the Q factors as a function of optical SNR (measured in a 0.1-nm bandwidth) for the 4 formats with noise added by an amplifier (before transmission). Figure 10.23(b) shows the degradation in Q factors as a function of transmission distance with the same launched average power in all cases (Q values were averaged over three widely separated channels). The RZ-DPSK format is superior initially to all other format, and this advantage is retained up to a distance of about 6300 km, after which RZ-OOK has a slightly higher Q factor. A faster reduction in Q for the RZ-DBPSK format indicates that the nonlinear effects were more serious in the later case. However, this situation changes for dense WDM systems with a spectral efficiency $\eta_s > 0.4$ b/s/Hz [133]. The reason appears to be that the XPM-induced degradation under such conditions becomes more severe for systems employing the OOK format [131].

10.6.2 Systems with the DQPSK format

An obvious advantage of the QPSK format is that it transmits 2 bits/symbol, resulting in a symbol rate that is only 50% of the actual bit rate and a doubling of the spectral efficiency η_s . As a result, QPSK format allows, in principle, $\eta_s \geq 1$ b/s/Hz. This feature led to a large number of experiments dealing with the DQPSK format [145]–[156]. In a 2002 experiment, 9 WDM channels were transmitted over 1000 km using a 25-GHz channel spacing with the RZ-DQPSK format [145]. The symbol rate of 12.5 Gbaud corresponded to a bit rate of 25 Gb/s, resulting in $\eta_s = 1$ b/s/Hz (if we ignore the overhead imposed by forward-error correction).

By 2003, an experiment used the DQPSK format to realize a spectral efficiency of 1.6 b/s/Hz [146]. It was able to transmit 8 channels at 40 Gb/s over 200 km with a channel spacing of 25 GHz. The symbol rate was only 10 Gbaud in this experiment because it also employed the PDM or dual-polarization technique in which two orthogonally polarized bit streams are generated at half the original bit rate. The combination of DQPSK and PDM reduces the symbol rate to one quarter of the actual bit rate and thus enhances the spectral efficiency by a factor of 4. As a result, a 40-Gb/s signal can be transmitted using components developed for 10-Gb/s channels.

The fiber-link length was limited to only 200 km in the preceding 2003 experiment [146]. This limitation is mainly due to the use of PDM. In a 2004 experiment, 64 WDM channels at a symbol rate of 12.5 Gbaud could be transmitted over 6500 km using the RZ-DQPSK format (without PDM) with a spectral efficiency of 1 b/s/Hz [147]. The distance could be increased to 10,200 km in a 2005 experiment in which mid-span OPC was employed to compensate fiber dispersion and to reduce simultaneously the impact of nonlinear phase noise [151]. However, the total capacity of this system was only 0.88 Tb/s. A much higher capacity of 5.94 Tb/s was realized in another 2005 experiment [152] that used DQPSK with PDM, but the link length was then limited to 324 km. The link length could be extended to 1700 km (with 1-dB margin) in a 2006 experiment that transmitted 40 channels at a bit rate of 85.6 Gb/s on a 50-GHz frequency grid [153]. This experiment also showed that the Q factors of the received signal were lower by 2.2 dB when the PDM technique was employed, and they decreased linearly with distance whether PDM was used or not.

In recent years, the total system capacity of DQPSK systems has exceeded 10 Tb/s. A capacity of 14 Tb/s was realized in a 2006 experiment that transmitted PDM 140

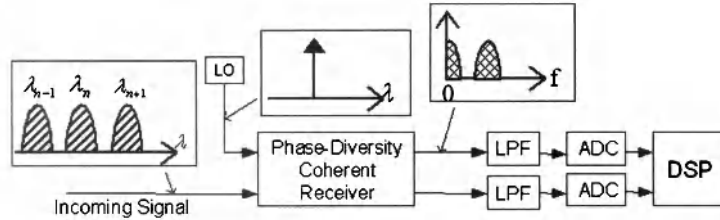


Figure 10.25: Components of a digital coherent receiver. LPF, ADC, and DSP stand for low-pass filter, analog-to-digital converter, and digital signal processing, respectively. (After Ref. [158]; ©2006 IEEE.)

channels (each operating at 111 Gb/s) within a 59-nm-wide wavelength window extending from 1561 to 1620 nm [154]. This experiment demonstrated a spectral efficiency of 2.0 b/s/Hz over a limited link length of 160 km. The system capacity was increased to 20.4 Tb/s within a year by expanding the wavelength range from 1536 to 1620 nm [155]. The link length length was 240 km with the same spectral efficiency. A system capacity of 25.6 Tb/s was realized in a 2007 experiment that transmitted 160 WDM channels over 240 km on a 50 GHz grid with a spectral efficiency of 3.2 b/s/Hz [156].

10.6.3 QAM and Related formats

The BPSK and QPSK formats discussed so far in this section encode the data in the phase of the optical carrier but they leave its amplitude unchanged from one symbol to next. In contrast, the QAM format employs both the amplitude and phase for data encoding. Moreover, the number of symbols ($M = 2^m$) employed can vary from 2 to more than 128 depending on the value of the integer m . An example of the 16-QAM format is shown in Figure 10.1 with 16 symbols ($m = 4$). In this notation, QPSK corresponds to 4-QAM.

A major difference from the cases of DBPSK and DQPSK formats is that the use of the QAM format requires coherent detection of the transmitted signal at the receiver end. A phase-locked loop is often used for this purpose, but phase synchronization between the local oscillator and the transmitter laser is a challenging task because of intrinsic phase noise of the two lasers [157]. This task becomes even more challenging in the presence of nonlinear phase noise. Nevertheless, such phase-locking techniques were developed after 2003. In a different approach, a phase-diversity homodyne scheme was employed without a phase-locked loop and the carrier phase was estimated with (DSP) on the homodyne signal [158]. Figure 10.25 shows the design of such a digital coherent receiver. An analog-to-digital converter is used to convert the filtered analog signal into a digital format suitable for DSP. Because of the use of DSP, such an approach can also compensate for distortions of the optical signal induced inside the fiber link through mechanisms such as chromatic dispersion.

In a 2005 experiment, coherent demodulation of a 40-Gb/s bit stream, encoded using the QPSK (or 4-QAM) format with polarization multiplexing and transmitted over 200 km, had been realized [159]. Because the symbol rate was 10 Gbaud, three WDM

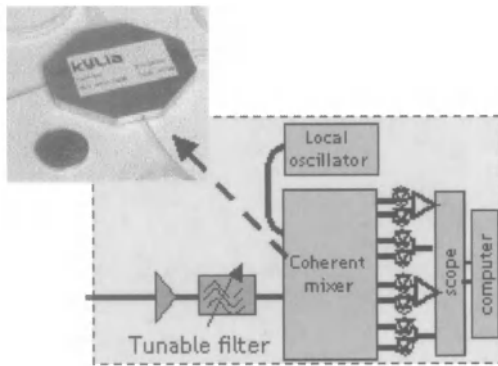


Figure 10.26: Design of the digital coherent receiver used for 100-Gb/s signals in the dual-polarization QPSK format. The inset shows the compact size of this receiver. (After Ref. [160]; ©2009 IEEE.)

channels could be separated by only only 16 GHz. The experiment employed a phase-diversity coherent receiver with digital signal processing (DSP). By 2008, 164 channels at 111 Gb/s were transmitted over 2550 km at a symbol rate of 27.75 Gbaud by combining the QPSK format with polarization multiplexing [160]. The channel spacing of 50 GHz required the use of both the C and L bands, but the experiment realized a record capacity-distance product of 41,800 (Tb/s)-km, while employing coherent detection. Figure 10.26 shows the design and the photograph of the digital coherent receiver used in this experiment; the inset shows the compact size that was possible because of the use of DSP within the receiver. By 2010, the dual-polarization QPSK format was in use for commercial systems.

Spectral efficiency of such systems can be improved further by transmitting more than 2 bits/symbol. In a 2006 experiment, a 128-QAM signal at 20 Mbaud was transmitted over 525 km and then detected using heterodyne detection with a frequency-stabilized fiber laser and an offset-locking technique [161]. This experiment did not employ the WDM technique, but it showed that up to 7 bits per symbol could be encoded successfully with the QAM format. In a later experiment, the symbol rate was increased to 1 Gbaud, and a 64-QAM signal was transmitted over 150 km of fiber [162]. This experiment employed heterodyne detection with a frequency-stabilized fiber laser and used an optical phase-lock loop. By 2008, this scheme was extended to transmit three WDM channels (each operating at 12 Gb/s) over 160 km with only 1.4-GHz channel spacing, resulting in a spectral efficiency of 8.6 b/s/Hz [163]. In another experiment, a single 40-Gb/s channel was transmitted over 100-km of standard fiber with the 16-QAM format and demodulated using a digital coherent receiver [164].

The state of the art has improved considerably for QAM-based WDM systems in recent years. In a 2008 experiment, 10-channels (each operating at 112 Gb/s) with 25-GHz spacing were transmitted over 315 km using the 16-QAM format with PDM, resulting in a symbol rate of 14 Gbaud and a spectral efficiency of 4.5 b/s/Hz [165]. By 2009, the fiber length was increased to 630 km, while the channel spacing could be reduced to 16.7 GHz so that the spectral efficiency was 6.7 b/s/Hz [166]. If the

FEC overhead is taken into account and the actual bit rate of 104 Gb/s is used, the spectral efficiency becomes 6.2 b/s/Hz, still a very respectable number. A high-capacity system was demonstrated in 2008 by transporting a 161 channels, each operating at a bit rate of 114 Gb/s, over 662 km of fiber [167]. It combined the 8-PSK format with polarization multiplexing, resulting in a symbol rate of 19 Gbaud. All 114 channels could be amplified by a single C-band EDFA because of the 25-GHz channel spacing employed in this experiment. A system capacity of 32 Tb/s was realized in a 2009 experiment that transmitted 320 WDM channels (each at 114 Gb/s) over 580 km of fiber by using the 8-QAM format with PDM [168]. By 2010, system capacity was more than doubled to 69.1 Tb/s by transmitting 432 channels (each at 171 Gb/s) over 240 km with a spectral efficiency of 6.4 b/s/Hz by using the 16-QAM format [169]. Another 2010 experiment realized 64-Tb/s capacity by transmitting 640 channels (each at 107 Gb/s) over 320 km with a spectral efficiency of 8 b/s/Hz in the 32-QAM format [170].

10.6.4 Systems Employing Orthogonal FDM

As discussed in Section 6.5.3, orthogonal FDM, or OFDM, is a subcarrier multiplexing technique that makes use of the FFT algorithm with DSP to transmit multiple bits simultaneously at orthogonal subcarrier frequencies located in the vicinity of the main carrier. This technique is widely used for cellular transmission at microwave frequencies and has recently been adopted for lightwave systems because it has the potential of improving their performance considerably [171]–[184]. Its main advantage is that the OFDM symbol rate is a small fraction of the actual bit rate because hundreds of bits are transmitted in parallel using multiple subcarriers separated by $1/T_s$. Moreover, no dispersion compensation is typically required because dispersion-induced distortions can be removed at the receiver through DSP of the electrical signal in the frequency domain [172].

The coherent optical OFDM technique was proposed in 2005 [171] and its advantages were studied soon after [172]–[174]. An experimental demonstration of this technique at a bit rate of 8 Gb/s employed 128 subcarriers with the QPSK format [175]. Such an optical OFDM signal was transmitted over 1000 km of standard telecommunication fiber (using a recirculating fiber loop) without any dispersion compensation. This experiment employed two narrowband lasers (one at the transmitter and the other at the receiver) with line widths of around 20 kHz. Such narrowband lasers are needed because of a relatively low symbol rate of subcarriers and the coherent detection used for them.

A transmission distance of 4160 km at a bit rate of 25.8 Gb/s was realized in a 2007 OFDM experiment in which 256 subcarriers were used [176]. This experiment implemented a phase-noise compensation scheme by inserting a radio-frequency (RF) pilot at the transmitter. Since this pilot is distorted by phase noise in exactly the same way as the OFDM signal, it can be used at the receiver to remove phase distortions from the OFDM signal. Figure 10.27 shows the effectiveness of this technique by comparing constellation diagrams with and without compensation of the phase noise using an RF pilot. An external-cavity semiconductor laser with a 100-kHz linewidth was used as the local oscillator at the receiver end.

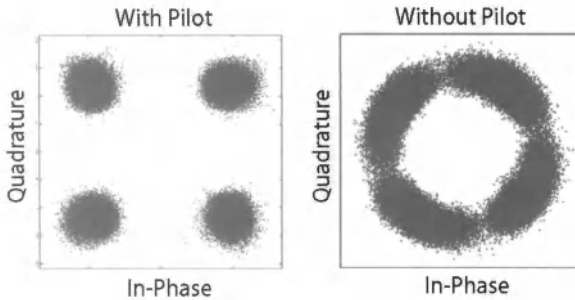


Figure 10.27: Constellation diagrams with and without compensation of the phase noise using an RF pilot. (After Ref. [176]; ©2008 IEEE.)

Some OFDM systems focus on the bit rate of 100 Gb/s that is required for the 100-GbE standard. The actual bit rate is slightly higher in practice because of the FEC overhead. By 2008, a bit rate of 107 Gb/s was realized for an OFDM system operating with 128 QPSK-encoded subcarriers [180]. The resulting OFDM signal could be transmitted over 1000 km of standard fiber without any dispersion compensation in the optical domain. The 37-GHz bandwidth of the OFDM signal led to a spectral efficiency of close to 3 b/s/Hz. In another experiment, a spectral efficiency of 2 b/s/Hz was realized by transmitting ten 121.9-Gb/s WDM channels over 1000 km of standard fiber through OFDM with 50-GHz channel spacing [182]. This experiment employed the 8-QAM format with PDM such that each 121.9 Gb/s channel occupied a bandwidth of only 22.8 GHz.

The spectral efficiency was increased to 4 b/s/Hz in a 2009 experiment that reduced the channel spacing to 25 GHz [184]. In this experiment, seven 132.2-Gb/s channels were transmitted over 1300 km of standard fiber using the 8-QAM format with PDM. The symbol length was 14.4 ns in the case of 128 subcarriers but it increased to 104 ns for 1024 subcarriers. Figure 10.28 shows the observed BER for the central channel after 1000 km of transmission as a function of the average input power/channel for three symbol lengths corresponding to the use of 128, 256, and 1024 subcarriers. The linear phase distortions were compensated in all cases using the RF-pilot technique, resulting in the same system performance at low input powers. However, as the channel power increased to beyond 0.2 mW, nonlinear phase distortions led to a considerable increase in BER in the case of 104-ns symbol length (1024 subcarriers). The BER was the lowest in the case of 128 subcarriers. One reason for this dependence on the symbol length is that the RF pilot is also affected by the SPM and XPM phenomena as the channel power is increased. Such nonlinear distortions of the RF pilot may reduce the effectiveness of the phase-noise compensation scheme.

The research on optical OFDM systems is progressing rapidly in several directions. In one case, the objective is to enhance the spectral efficiency of WDM systems. In a 2009 experiment, a spectral efficiency of 7 b/s/Hz was realized by transmitting 8 channels, each operating at 65.1 Gb/s, over 630 km of fiber by employing the 32-QAM format with PDM [185]. Channel spacing was only 8 GHz in this WDM experiment. In another case, the objective was to increase the system capacity. In a 2009 exper-

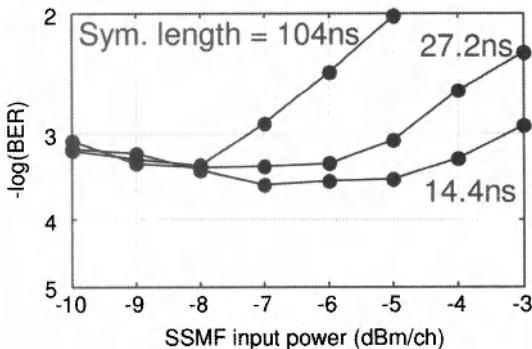


Figure 10.28: BER of the central channel after 1000 km as a function of input channel power for three symbol lengths (from lowest to highest) corresponding to the FFT size of 128, 256, and 1024. (After Ref. [184]; ©2009 IEEE.)

iment, OFDM was used to transmit 135 channels, each operating at 111 Gb/s, over 6248 km, resulting in a record capacity–distance product of 84,300 (Tb/s)-km [186]. This experiment employed the QPSK format and PDM together with distributed Raman amplification for the WDM signal extending from 1563 to 1620 nm.

Motivated by the future 1-Tb/s Ethernet systems, still another direction for lightwave systems is to transmit a single channel at a bit rate of 1 Tb/s or more [187]–[191]. Both the OTDM and OFDM techniques can be employed for this purpose. In the case of OFDM, such an objective requires the use of a large number of subcarriers so that the symbol rate per subcarrier is reasonable. In one 2009 experiment, 4104 spectrally overlapping subcarriers were employed to transmit a 1-Tb/s single channel over 600 km of standard fiber [189]. The entire OFDM signal occupied a bandwidth of 320.6 GHz, resulting in a spectral efficiency of 3.3 b/s/Hz. By 2010, OFDM systems were capable of operating at bit rates of up to 10.8 Tb/s [191].

10.7 Ultimate Channel Capacity

With the advent of wavelength-division multiplexing (WDM) technology, lightwave systems with a capacity of more than 1 Tb/s have become available commercially. Moreover, a system capacity of 69.1 Tb/s has been demonstrated in a 2010 laboratory experiment [169]. However, any communication channel has a finite bandwidth, and optical fibers are no exception. One may thus ask what limits the ultimate capacity of a fiber-optic communication system [192]–[200].

The performance of any communication system is ultimately limited by the noise in the received signal. This limitation can be stated more formally by using the concept of *channel capacity* introduced by Shannon in the context of information theory [201]. It turns out that a maximum possible bit rate exists for error-free transmission of a binary digital signal in the presence of Gaussian noise. This rate is called the channel capacity. More specifically, the capacity (in bits/s) of a noisy communication channel

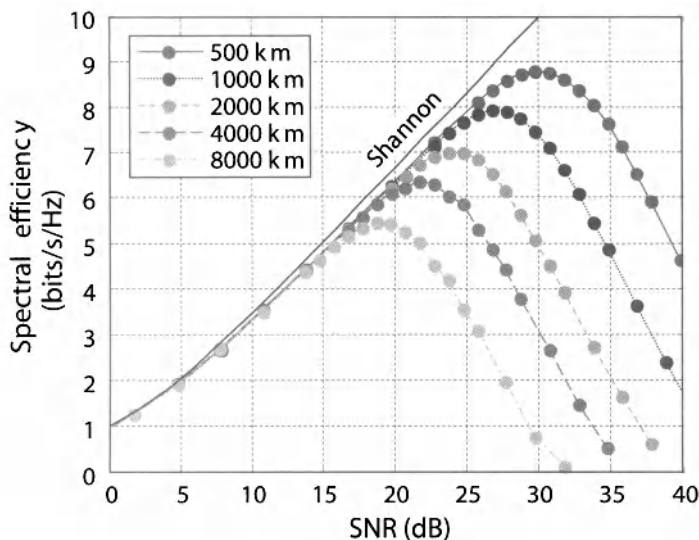


Figure 10.29: Spectral efficiency as a function of SNR calculated numerically including the nonlinear effects over transmission distances ranging from 500 to 8,000 km. (After Ref. [200]; ©2010 IEEE.)

of bandwidth W is given by [200]

$$C_s = W \log_2(1 + \text{SNR}) = W \log_2[1 + P_s/(N_0 W)], \quad (10.7.1)$$

where N_0 is the spectral density of noise and P_s is the average signal power related to the pulse energy in a symbol as $E_s = P_s/W$. Equation (10.7.1) is valid for a linear channel with additive noise. It shows that the channel capacity (or the bit rate) can exceed channel bandwidth if noise level is low enough to maintain a high signal-to-noise ratio (SNR). It is common to define the spectral efficiency of a WDM channel as $\eta_s = C_s/W$ that is a measure of bits transmitted per second per unit bandwidth and is measured in units of (b/s)/Hz. For a SNR of >30 dB, η_s exceeds 10 (b/s)/Hz according to Eq. (10.7.1).

It may appear surprising that Eq. (10.7.1) does not depend on the modulation format. We have seen in Section 10.1 that the number of bits that can be transmitted during each symbol is limited by the the number of symbols in the constellation diagram (or the alphabet size). In fact, the spectral efficiency is limited to $\log_2 M$ for an alphabet size of M . The reason why Eq. (10.7.1) is independent of M is that this equation is derived in the limit $M \rightarrow \infty$ such that symbols occupy the entire two-dimensional space in the constellation diagram with a Gaussian density distribution. Thus, it is important to keep in mind that the following discussion of channel capacity represents an upper limit of what can be realized in practice.

Even with this caveat, Eq. (10.7.1) does not always apply to fiber-optic communication systems because of the nonlinear effects occurring inside optical fibers. It can nonetheless be used to provide an upper limit on the system capacity. The total bandwidth of modern lightwave systems is limited by the bandwidth of optical amplifiers

and is below 10 THz (80 nm) even when both the C and L bands are used simultaneously. With the advent of new kinds of fibers and amplification techniques, one may expect that eventually this bandwidth may approach 50 THz if we use the entire low-loss region extending from 1.25 to 1.65 μm . If we divide this bandwidth into 1000 WDM channels, each 50 GHz wide, and assume that the SNR exceeds 100 for each channel, the maximum system capacity predicted by Eq. (10.7.1) is close to 350 Tb/s, assuming that the optical fiber acts as a linear channel. The highest capacity realized for WDM systems was 69.1 Tb/s in a 2010 experiment [169]. The preceding estimate shows that there is considerable room for improvement. The most limiting factor in practice is the spectral efficiency set by the alphabet size M . The use of a larger M should improve the capacity of future WDM systems.

The impact of the nonlinear effects on the channel capacity of lightwave systems has attracted attention in recent years [192]–[199]. A systematic approach was developed in a 2010 review on this topic [200]. Figure 10.29 shows how the nonlinear effects reduce the ultimate spectral efficiency from its value predicted by Eq. (10.7.1), when high signal powers are launched to ensure a high SNR at the receiver in spite of the buildup of amplifier noise along the fiber link. As one may expect, the spectral efficiency depends on the transmission distance, and it becomes worse as this distance increases. However, the most noteworthy feature of Figure 10.29 is that, for any transmission distance, a maximum value occurs at an optimum value of SNR that changes with distance. For example, the maximum spectral efficiency for a 1000-km-long link is limited to below 8 (b/s)/Hz, irrespective of the alphabet size of the modulation format employed. This is in sharp contrast to the prediction of Eq. (10.7.1) and reflects a fundamental limitation imposed by the nonlinear effects. We refer to Ref. [200] for details of the numerical procedure used to obtain Figure 10.29.

Problems

- 10.1** Sketch how the electric field of a carrier would change with time for the PSK format during 5 bits with the pattern 01010. Assume that the phase of the carrier is shifted by 180° during each 1 bit.
- 10.2** Explain what is meant by the DPSK format. Sketch how the electric field varies for this format using the same 5-bit pattern 01010 used in the preceding problem.
- 10.3** Draw the constellation diagrams for the QPSK and 8-PSK formats. Also show the bit combinations assigned to each symbol in the Gray-coding scheme.
- 10.4** Derive an expression for transfer function of a Mach–Zehnder modulator as a function of applied voltages V_1 and V_2 across its two arms. Under what conditions such a modulator acts as a pure amplitude modulator?
- 10.5** Sketch the design of an optical transmitter for the RZ-DQPSK format. Explain how such a transmitter works.
- 10.6** Sketch the design of an synchronous heterodyne receiver and derive an expression of the current used by the decision circuit in terms of the received signal power. Use noise currents in both quadratures.

- 10.7** Sketch the design of an asynchronous heterodyne receiver and derive an expression of the current used by the decision circuit in terms of the received signal power. Use noise currents in both quadratures.
- 10.8** Sketch the design of an optical delay-demodulator receiver for the RZ-DQPSK format. Explain how such a receiver can detect both quadratures of the optical field.
- 10.9** Derive an expression for the BER of a synchronous heterodyne ASK receiver after assuming that the in-phase noise component i_c has a probability density function

$$p(i_c) = \frac{1}{\sigma\sqrt{2}} \exp\left(-\frac{\sqrt{2}}{\sigma}|i_c|\right).$$

Determine the SNR required to achieve a BER of 10^{-9} .

- 10.10** Derive the Rice distribution given in Eq. (10.3.10)] when the signal current I is given by Eq. (10.3.9) for an asynchronous heterodyne ASK receiver. Assume that both quadrature components of noise obey Gaussian statistics with standard deviation σ .
- 10.11** Show that the BER of an asynchronous heterodyne ASK receiver [Eq. (10.3.13)] can be approximated as $\text{BER} = \frac{1}{2} \exp[-I_1^2/(8\sigma^2)]$ when $I_1/\sigma \gg 1$ and $I_0 = 0$. Assume $I_D = I_1/2$.
- 10.12** Consult Ref. [35] and show that the BER given in Eq. (10.3.21) for the DQPSK format can be approximated by Eq. (10.3.24). Plot the two expressions as a function of N_p .
- 10.13** Derive an expression for the SNR for heterodyne receivers in terms of the intensity noise parameter r_I by using Eq. (10.4.1). Prove that the optimum value of P_{LO} at which the SNR is maximum is given by $P_{\text{LO}} = \sigma_T/(Rr_I)$ when the dark-current contribution to the shot noise is neglected.
- 10.14** Explain the origin of nonlinear phase noise. Derive an expression for the output field $A(L, t)$ after a noisy input field $A(0, t) = A_s(t) + n(t)$ has propagated through a nonlinear fiber of length L .
- 10.15** Discuss two techniques that can be used to compensate the nonlinear phase noise in phase-encoded lightwave systems at least partially.

References

- [1] M. Schwartz, *Information Transmission, Modulation, and Noise*, 4th ed., McGraw-Hill, New York, 1990.
- [2] J. G. Proakis, *Digital Communications*, 4th ed., McGraw Hill, 2001.
- [3] L. W. Couch II, *Digital and Analog Communication Systems*, 7th ed., Prentice Hall, Upper Saddle River, NJ, 2006.
- [4] T. Okoshi and K. Kikuchi, *Coherent Optical Fiber Communications*, Kluwer Academic, Boston, 1988.
- [5] R. A. Linke and A. H. Gnauck, *J. Lightwave Technol.* **6**, 1750 (1988).

- [6] J. R. Barry and E. A. Lee, *Proc. IEEE* **78**, 1369 (1990).
- [7] P. S. Henry and S. D. Persoinick, Eds., *Coherent Lightwave Communications*, IEEE Press, Piscataway, NJ, 1990.
- [8] S. Betti, G. de Marchis, and E. Iannone, *Coherent Optical Communication Systems*, Wiley, New York, 1995.
- [9] S. Ryu, *Coherent Lightwave Communication Systems*, Artec House, Boston, 1995.
- [10] J. H. Sinsky, A. Adamiecki, A. H. Gnauck, C. A. Burrus, J. Leuthold, O. Wohlgemuth, S. Chandrasekhar, and A. Umbach, *J. Lightwave Technol.* **22**, 180 (2004).
- [11] A. H. Gnauck and P. J. Winzer, *J. Lightwave Technol.* **23**, 115 (2005).
- [12] P. J. Winzer and R.-J. Essiambre, *Proc. IEEE* **94**, 952 (2006); *J. Lightwave Technol.* **24**, 4711 (2006).
- [13] P. J. Winzer and R.-J. Essiambre, in *Optical Fiber Telecommunications*, Vol. 5B, I. P. Kaminow, T. Li, and A. E. Willner, Eds., Academic Press, Boston, 2008, Chap. 2.
- [14] K. Kikuchi, in *Optical Fiber Telecommunications*, Vol. 5B, I. P. Kaminow, T. Li, and A. E. Willner, Eds., Academic Press, Boston, 2008, Chap. 3.
- [15] E. Ip, A. Pak, T. Lau, D. J. F. Barros, and J. M. Kahn, *Opt. Express* **16**, 753 (2008).
- [16] X. Liu, S. Chandrasekhar, and A. Leven, in *Optical Fiber Telecommunications*, Vol. 5B, I. P. Kaminow, T. Li, and A. E. Willner, Eds., Academic Press, Boston, 2008, Chap. 4.
- [17] G. P. Agrawal, *Lightwave Technology: Components and Devices*, Wiley, Hoboken, NJ, 2004.
- [18] K.-P. Ho, *Phase-Modulated Optical Communication Systems*, Springer, New York, 2005.
- [19] F. M. Gardner, *Phaselock Techniques*, Wiley, Hoboken, NJ, 2005.
- [20] G. L. Abbas, V. W. Chan, and T. K. Yee, *J. Lightwave Technol.* **3**, 1110 (1985).
- [21] B. L. Kasper, C. A. Burrus, J. R. Talman, and K. L. Hall, *Electron. Lett.* **22**, 413 (1986).
- [22] S. B. Alexander, *J. Lightwave Technol.* **5**, 523 (1987).
- [23] J. W. Goodman, *Statistical Optics*, Wiley, New York, 1985.
- [24] S. O. Rice, *Bell Syst. Tech. J.* **23**, 282 (1944); **24**, 96 (1945).
- [25] J. I. Marcum, *IRE Trans. Inform. Theory* **6**, 259 (1960).
- [26] L. G. Kazovsky, A. F. Elrefaie, R. Welter, P. Crepso, J. Gimlett, and R. W. Smith, *Electron. Lett.* **23**, 871 (1987).
- [27] A. F. Elrefaie, D. A. Atlas, L. G. Kazovsky, and R. E. Wagner, *Electron. Lett.* **24**, 158 (1988).
- [28] R. Gross, P. Meissner, and E. Patzak, *J. Lightwave Technol.* **6**, 521 (1988).
- [29] W. H. C. de Krom, *J. Lightwave Technol.* **9**, 641 (1991).
- [30] Y.-H. Lee, C.-C. Kuo, and H.-W. Tsao, *Microwave Opt. Tech. Lett.* **5**, 168 (1992).
- [31] P. S. Cho, G. Harston, C. J. Kerr, A. S. Greenblatt, A. Kaplan, Y. Achiam, G. Levy-Yurista, M. Margalit, Y. Gross, J. B. Khurgin, *IEEE Photon. Technol. Lett.* **16**, 656 (2004).
- [32] F. Seguin and F. Gonthier, Proc. Opt. Fiber Commun. Conf. Digest, Paper OFL5 (2005).
- [33] L. Christen, Y. K. Lizé, S. Nuccio, L. Paraschis, and A. E. Willner, *IEEE Photon. Technol. Lett.* **20**, 1166-1168 (2008).
- [34] G. E. Corazza and G. Ferrari, *IEEE Trans. Inf. Theory* **48**, 3003 (2002).
- [35] G. Ferrari and G. E. Corazza, *Electron. Lett.* **40**, 1284 (2004).
- [36] K. Kikuchi, T. Okoshi, M. Nagamatsu, and H. Henmi, *J. Lightwave Technol.* **2**, 1024 (1984).
- [37] G. Nicholson, *Electron. Lett.* **20**, 1005 (1984).
- [38] L. G. Kazovsky, *J. Lightwave Technol.* **3**, 1238 (1985); *J. Lightwave Technol.* **4**, 415 (1986).

- [39] B. Glance, *J. Lightwave Technol.* **4**, 228 (1986).
- [40] I. Garrett and G. Jacobsen, *J. Lightwave Technol.* **4**, 323 (1986); **5**, 551 (1987).
- [41] T. G. Hodgkinson, *J. Lightwave Technol.* **5**, 573 (1987).
- [42] L. G. Kazovsky, P. Meissner, and E. Patzak, *J. Lightwave Technol.* **5**, 770 (1987).
- [43] G. J. Foschini, L. J. Greenstein, and G. Vannuchi, *IEEE Trans. Commun.* **36**, 306 (1988).
- [44] I. Garrett, D. J. Bond, J. B. Waite, D. S. L. Lettis, and G. Jacobsen, *J. Lightwave Technol.* **8**, 329 (1990).
- [45] L. G. Kazovsky and O. K. Tonguz, *J. Lightwave Technol.* **8**, 338 (1990).
- [46] C. Kaiser, M. Shafi, and P. Smith, *J. Lightwave Technol.* **11**, 1820 (1993).
- [47] G. Einarsson, J. Strandberg, and I. T. Monroy, *J. Lightwave Technol.* **13**, 1847 (1995).
- [48] M. T. Core and H. H. Tan, *IEEE Trans. Commun.* **50**, 21 (2002).
- [49] S. Savory and A. Hadjifotiou, *IEEE Photon. Technol. Lett.* **16**, 930 (2004).
- [50] Y. Atzman and M. Nazarathy, *J. Lightwave Technol.* **27**, 19 (2009).
- [51] P. Serena, N. Rossi, M. Bertolini, and A. Bononi, *J. Lightwave Technol.* **27**, 2404 (2009).
- [52] T. G. Hodgkinson, R. A. Harmon, and D.W. Smith, *Electron. Lett.* **21**, 867 (1985).
- [53] A. W. Davis and S. Wright, *Electron. Lett.* **22**, 9 (1986).
- [54] A. W. Davis, M. J. Pettitt, J. P. King, and S. Wright, *J. Lightwave Technol.* **5**, 561 (1987).
- [55] L. G. Kazovsky, R. Welter, A. F. Elrefaei, and W. Sessa, *J. Lightwave Technol.* **6**, 1527 (1988).
- [56] L. G. Kazovsky, *J. Lightwave Technol.* **7**, 279 (1989).
- [57] T. Okoshi, *J. Lightwave Technol.* **3**, 1232 (1985).
- [58] T. G. Hodgkinson, R. A. Harmon, and D. W. Smith, *Electron. Lett.* **23**, 513 (1987).
- [59] M. W. Maeda and D. A. Smith, *Electron. Lett.* **27**, 10 (1991).
- [60] P. Poggiolini and S. Benedetto, *IEEE Trans. Commun.* **42**, 2105 (1994).
- [61] S. Benedetto and P. Poggiolini, *IEEE Trans. Commun.* **42**, 2915 (1994).
- [62] G. P. Agrawal, *Quantum Semiclass. Opt.* **8**, 383 (1996).
- [63] B. Glance, *J. Lightwave Technol.* **5**, 274 (1987).
- [64] T. Okoshi and Y. C. Cheng, *Electron. Lett.* **23**, 377 (1987).
- [65] Y. H. Cheng, T. Okoshi, and O. Ishida, *J. Lightwave Technol.* **7**, 368 (1989).
- [66] B. Enning, R. S. Vodhanel, E. Dietrich, E. Patzak, P. Meissner, and G. Wenke, *J. Lightwave Technol.* **7**, 459 (1989).
- [67] R. Langenhorst, W. Pieper, M. Eiselt, D. Rhode, and H. G. Weber, *IEEE Photon. Technol. Lett.* **3**, 80 (1991).
- [68] T. Imai, *J. Lightwave Technol.* **9**, 650 (1991).
- [69] S. Ryu, S. Yamamoto, Y. Namihira, K. Mochizuki, and H. Wakabayashi, *J. Lightwave Technol.* **9**, 675 (1991).
- [70] F. Ghirardi, A. Bruno, B. Mersali, J. Brandon, L. Giraudet, A. Scavennec, and A. Carencio, *J. Lightwave Technol.* **13**, 1536 (1995).
- [71] A. T. Erdogan, A. Demir, and T. M. Oktem, *J. Lightwave Technol.* **26**, 1823 (2008).
- [72] T. Pfau, R. Peveling, J. Hauden, et al., *IEEE Photon. Technol. Lett.* **19**, 1988 (2007).
- [73] J. Renaudier, G. Charlet, M. Salsi, O. B. Pardo, H. Mardoyan, P. Tran, and S. Bigo, *J. Lightwave Technol.* **26**, 36 (2008).
- [74] K. Kikuchi and S. Tsukamoto, *J. Lightwave Technol.* **26**, 1817 (2008).
- [75] C. Zhang, Y. Mori, K. Igarashi, K. Katoh, and K. Kikuchi, *J. Lightwave Technol.* **27**, 224 (2009).
- [76] A. A. Elrefaei, R. E. Wagner, D. A. Atlas, and D. G. Daut, *J. Lightwave Technol.* **6**, 704 (1988).

- [77] K. Iwashita and N. Takachio, *J. Lightwave Technol.* **7**, 1484 (1989).
- [78] M. S. Kao and J. S. Wu, *J. Lightwave Technol.* **11**, 303 (1993).
- [79] E. Iannone, F. S. Locati, F. Matera, M. Romagnoli, and M. Settembre, *J. Lightwave Technol.* **11**, 1478 (1993).
- [80] B. Pal, R. Gangopadhyay, and G. Prati, *J. Lightwave Technol.* **18**, 530 (2000).
- [81] E. Forestieri, *J. Lightwave Technol.* **18**, 1493 (2000).
- [82] J. Wang and J. M. Khan, *J. Lightwave Technol.* **22**, 362 (2004).
- [83] K.-P. Ho and H.-C. Wang, *IEEE Trans. Commun.* **56**, 1422 (2008).
- [84] R. G. Priest and T. G. Giallorenzi, *Opt. Lett.* **12**, 622 (1987).
- [85] J. Winters, *J. Lightwave Technol.* **8**, 1487 (1990).
- [86] E. Ip and J. M. Khan, *J. Lightwave Technol.* **25**, 2033 (2007).
- [87] H. Bülow, F. Buchali, and A. Klekamp, *J. Lightwave Technol.* **26**, 158 (2008).
- [88] G. P. Agrawal, *Nonlinear Fiber Optics*, 4th ed., Academic Press, San Diego, CA, 2007.
- [89] Y. Aoki, K. Tajima, and I. Mito, *J. Lightwave Technol.* **6**, 710 (1988).
- [90] T. Sugie, *J. Lightwave Technol.* **9**, 1145 (1991); *Opt. Quantum Electron.* **27**, 643 (1995).
- [91] N. Ohkawa and Y. Hayashi, *J. Lightwave Technol.* **13**, 914 (1995).
- [92] J. P. Gordon and L. F. Mollenauer, *Opt. Lett.* **15**, 1351 (1990).
- [93] S. Ryu, *J. Lightwave Technol.* **10**, 1450 (1992).
- [94] N. Takachio, S. Norimatsu, K. Iwashita, and K. Yonenaga, *J. Lightwave Technol.* **12**, 247 (1994).
- [95] A. Mecozzi, *J. Lightwave Technol.* **12**, 1993 (1994).
- [96] C. J. McKinstry and C. Xie, *IEEE J. Sel. Topics Quantum Electron.* **8**, 616 (2002).
- [97] H. Kim and A. H. Gnauck, *IEEE Photon. Technol. Lett.* **15**, 320 (2003).
- [98] K.-P. Ho, *IEEE Photon. Technol. Lett.* **15**, 1213 (2003); *J. Opt. Soc. Am. B* **20**, 1875 (2003); *IEEE Photon. Technol. Lett.* **16**, 1403 (2004).
- [99] H. Kim, *J. Lightwave Technol.* **21**, 1770 (2003).
- [100] A. G. Green, P. P. Mitra, and L. G. L. Wegener, *Opt. Lett.* **28**, 2455 (2003).
- [101] M. Hanna, D. Boivin, P.-A. Lacourt, and J.-P. Goedgebuer, *J. Opt. Soc. Am. B* **21**, 24 (2004).
- [102] K.-P. Ho, *IEEE J. Sel. Topics Quantum Electron.* **10**, 421 (2004); *IEEE Photon. Technol. Lett.* **17**, 789 (2005).
- [103] A. Mecozzi, *Opt. Lett.* **29**, 673 (2004).
- [104] Y. Yadin, M. Shtaif, and M. Orenstein, *IEEE Photon. Technol. Lett.* **16**, 1307 (2004).
- [105] J. Wang and J. M. Kahn, *IEEE Photon. Technol. Lett.* **16**, 2165 (2004).
- [106] S. Kumar, *Opt. Lett.* **30**, 3278 (2005).
- [107] K.-P. Ho and H.-C. Wang, *Opt. Lett.* **31**, 2109 (2006).
- [108] F. Zhang, C.-A. Bunge, and K. Petermann, *Opt. Lett.* **31**, 1038 (2006).
- [109] P. Serena, A. Orlandini, and A. Bononi, *J. Lightwave Technol.* **24**, 2026 (2006).
- [110] Y. Yadin, M. Orenstein, and M. Shtaif, *IEEE Photon. Technol. Lett.* **19**, 164 (2007).
- [111] A. Demir, *J. Lightwave Technol.* **25**, 2002 (2009).
- [112] M. Bertolini, P. Serena, N. Rossi, and A. Bononi, *IEEE Photon. Technol. Lett.* **21**, 15 (2009).
- [113] M. Secondini, M. Frezzini, and E. Forestieri, *IEEE Photon. Technol. Lett.* **21**, 908 (2009).
- [114] S. Kumar, *J. Lightwave Technol.* **27**, 4722 (2009).
- [115] X. Liu, X. Wei, R. E. Slusher, and C. J. McKinstry, *Opt. Lett.* **27**, 1616 (2002).
- [116] C. Xu and X. Liu, *Opt. Lett.* **27**, 1619 (2002).

- [117] C. Xu, L. F. Mollenauer, and X. Liu, *Electron. Lett.* **38**, 1578 (2002).
- [118] K.-P. Ho, *Opt. Commun.* **221**, 419 (2003); *Opt. Commun.* **245**, 391 (2005).
- [119] J. Hansryd, J. van Howe, and C. Xu, *IEEE Photon. Technol. Lett.* **16**, 1975 (2004); *IEEE Photon. Technol. Lett.* **17**, 232 (2005).
- [120] C. J. McKinstry, S. Radic, and C. Xie, *Opt. Lett.* **28**, 1519 (2003).
- [121] S. L. Jansen, D. van den Borne, B. Spinnler, S. Calabro, H. Suche, P. M. Krummrich, W. Sohler, G.-D. Khoe, and H. de Waardt, *J. Lightwave Technol.* **24**, 54 (2006).
- [122] D. Boivin, G.-K. Chang, J. R. Barry, and M. Hanna, *J. Opt. Soc. Am. B* **23**, 2019 (2006).
- [123] S. Kumar and L. Liu, *Opt. Express* **15**, 2166 (2007).
- [124] K.-P. Ho and J. M. Kahn, *J. Lightwave Technol.* **22**, 779 (2004).
- [125] S. L. Jansen, D. van den Borne, P. M. Krummrich, S. Spälter, G.-D. Khoe, and H. de Waardt, *J. Lightwave Technol.* **24**, 505 (2006).
- [126] A. P. T. Lau and J. M. Kahn, *J. Lightwave Technol.* **24**, 1334 (2006).
- [127] X. Q. Qi, X. P. Zhang, and Q. F. Shao, *J. Lightwave Technol.* **26**, 3210 (2008).
- [128] S. Watanabe and M. Shirasaki, *J. Lightwave Technol.* **14**, 243 (1996).
- [129] R. J. Essiambre and G. P. Agrawal, *J. Opt. Soc. Am. B* **14**, 323 (1997).
- [130] M. Rohde, C. Caspar, N. Heimes, M. Konitzer, E.-J. Bachus, and N. Hanik, *Electron. Lett.* **36**, 1483 (2000).
- [131] J. Leibrich, C. Wree, and W. Rosenkranz, *IEEE Photon. Technol. Lett.* **14**, 155 (2002).
- [132] A. H. Gnauck, G. Raybon, S. Chandrasekhar, J. Leuthold, C. Doerr, L. Stulz, E. Burrows, *IEEE Photon. Technol. Lett.* **15**, 467 (2003).
- [133] C. Xu, X. Liu, L. F. Mollenauer, and X. Wei, *IEEE Photon. Technol. Lett.* **15**, 617 (2003).
- [134] T. Mizuuchi, K. Ishida, T. Kobayashi, J. Abe, K. Kinjo, K. Motoshima, and K. Kasahara, *J. Lightwave Technol.* **21**, 1933 (2003).
- [135] A. H. Gnauck, G. Raybon, S. Chandrasekhar, et al., Proc. Opt. Fiber Commun. Conf., Paper FC2 (2002).
- [136] B. Zhu, L. E. Nelson, S. Stulz, et al., Proc. Opt. Fiber Commun. Conf., Paper PDP19 (2003).
- [137] C. Rasmussen, T. Fjelde, J. Bennike, et al., Proc. Opt. Fiber Commun. Conf., Paper PDP18 (2003).
- [138] J. F. Marcerou, G. Vareille, L. Becouarn, P. Pecci, and P. Tran, Proc. Opt. Fiber Commun. Conf., Paper PDP20 (2003).
- [139] J. Cai, D. Foursa, C. Davidson, et al., Proc. Opt. Fiber Commun. Conf., Paper PDP22 (2003).
- [140] T. Tsuritani, K. Ishida, A. Agata, et al., Proc. Opt. Fiber Commun. Conf., Paper PDP23 (2003).
- [141] L. Becouarn, G. Vareille, P. Pecci, and J. F. Marcerou, Proc. Eur. Conf. Opt. Commun., Paper PD39 (2003).
- [142] T. Tsuritani, K. Ishida, A. Agata, et al., *J. Lightwave Technol.* **22**, 215 (2004).
- [143] H. Sotobayashi, W. Chujo, and K. Kitayama, *IEEE Photon. Technol. Lett.* **14**, 555 (2002).
- [144] A. H. Gnauck, G. Raybon, P.G. Bernasconi, J. Leuthold, C.R. Doerr, and L.W. Stulz, *IEEE Photon. Technol. Lett.* **15**, 467 (2003).
- [145] P. S. Cho, V. S. Grigoryan, Y. A. Godin, A. Salamon, and Y. Achiam, *IEEE Photon. Technol. Lett.* **15**, 473 (2003).
- [146] C. Wree, N. Hecker-Denschlag, E. Gottwald, P. Krummrich, J. Leibrich, E. D. Schmidt, B. Lankl, and W. Rosenkranz, *IEEE Photon. Technol. Lett.* **15**, 1303 (2003).

- [147] T. Tokle, C. R. Davidson, M. Nissov, J.-X. Cai, D. Foursa, and A. Pilipetskii, *Electron. Lett.* **40**, 444 (2004).
- [148] S. Bhandare, D. Sandel, A. F. Abas, B. Milivojevic, A. Hidayat, R. Noé, M. Guy, and M. Lapointe, *Electron. Lett.* **40**, 821 (2004).
- [149] N. Yoshikane and I. Morita, *J. Lightwave Technol.* **23**, 108 (2005).
- [150] B. Milivojevic, A. F. Abas, A. Hidayat, S. Bhandare, D. Sandel, R. Noé, M. Guy, and M. Lapointe, *IEEE Photon. Technol. Lett.* **17**, 495 (2005).
- [151] S. L. Jansen, D. van den Borne, C. Climent, et al., Proc. Opt. Fiber Commun. Conf., Paper PDP28 (2005).
- [152] S. Bhandare, D. Sandel, B. Milivojevic, A. Hidayat, A. A. Fauzi, H. Zhang, S. K. Ibrahim, F. Wüst, and R. Noé, *IEEE Photon. Technol. Lett.* **17**, 914 (2005).
- [153] D. van den Borne, S. L. Jansen, E. Gottwald, P. M. Krumrich, G. D. Khoe, and H. de Waardt, Proc. Opt. Fiber Commun. Conf., Paper PDP34 (2006).
- [154] A. Sano, H. Masuda, Y. Kisaka, et al., Proc. Eur. Conf. Opt. Commun., Paper Th4.1.1 (2006).
- [155] H. Masuda, A. Sano, T. Kobayashi, et al., Proc. Opt. Fiber Commun. Conf., Paper PDP20 (2007).
- [156] A. H. Gnauck, G. Charlet, P. Tran, et al., *J. Lightwave Technol.* **26**, 79 (2008).
- [157] E. Ip and J. M. Khan, *J. Lightwave Technol.* **23**, 4110 (2005).
- [158] D. S. Ly-Gagnon, S. Tsukamoto, K. Katoh, and K. Kikuchi, *J. Lightwave Technol.* **24**, 12 (2006).
- [159] S. Tsukamoto, D. S. Ly-Gagnon, K. Katoh, and K. Kikuchi, Proc. Opt. Fiber Commun. Conf., Paper PDP29 (2005).
- [160] G. Charlet, J. Renaudier, H. Mardoyan, P. Tran, O. B. Pardo, F. Verluise, M. Achouche, A. Boutin, F. Blache, J.-Y. Dupuy, and S. Bigo, *J. Lightwave Technol.* **27**, 153 (2009).
- [161] M. Nakazawa, M. Yoshida, K. Kasai and J. Hongou, *Electron. Lett.* **42**, 710 (2006).
- [162] J. Hongo, K. Kasai, M. Yoshida, and M. Nakazawa, *IEEE Photon. Technol. Lett.* **19**, 638 (2007).
- [163] M. Yoshida, H. Goto, T. Omiya, K. Kasai, and M. Nakazawa, Proc. Eur. Conf. Opt. Commun., Paper Mo.4.D.5 (2008).
- [164] Y. Mori, C. Zhang, K. Igarashi, K. Katoh, and K. Kikuchi, Proc. Eur. Conf. Opt. Commun., Paper Tu.I.E.4 (2008).
- [165] P. J. Winzer and A. H. Gnauck, Proc. Eur. Conf. Opt. Commun., Paper Th.3.E.5 (2008).
- [166] A. H. Gnauck, P. J. Winzer, C. R. Doerr, and L. L. Buhl, Proc. Opt. Fiber Commun. Conf., Paper PDPB8 (2009).
- [167] J. Yu, X. Zhou, M.-F. Huang, Y. Shao, et al., Proc. Eur. Conf. Opt. Commun., Paper Th.3.E.2 (2008).
- [168] X. Zhou, J. Yu, M.-F. Huang, et al., Proc. Opt. Fiber Commun. Conf., Paper PDPB4 (2009).
- [169] A. Sano, H. Masuda, T. Kobayashi, et al., Proc. Opt. Fiber Commun. Conf., Paper PDPB7, 2010.
- [170] X. Zhou, J. Yu, M.-F. Huang, et al., Proc. Opt. Fiber Commun. Conf., Paper PDPB9 (2010).
- [171] W. Shieh and C. Athaudage, *Electron. Lett.* **42**, 587 (2006).
- [172] A. J. Lowery and J. Armstrong, *Opt. Express* **14**, 2079 (2006).
- [173] I. B. Djordjevic and B. Vasic, *Opt. Express* **14**, 3767 (2006).
- [174] A. J. Lowery, S. Wang, and M. Premaratne, *Opt. Express* **15**, 13282 (2007).

- [175] W. Shieh, X. Yi, and Y. Tang, *Electron. Lett.* **43**, 183 (2007).
- [176] S. L. Jansen, I. Morita, T. C. W. Schenk, N. Takeda, and H. Tanaka, *J. Lightwave Technol.* **26**, 6 (2008).
- [177] S. L. Jansen, I. Morita, T. C. W. Schenk, and H. Tanaka, *J. Opt. Networking*, **7**, 173 (2008).
- [178] W. Shieh, X. Yi, Y. Ma and Q. Yang, *J. Opt. Networking* **7**, 234 (2008).
- [179] W. Shieh, H. Bao, and Y. Tang, *Opt. Express* **16**, 841 (2008).
- [180] W. Shieh, Q. Yang, and Y. Ma, *Opt. Express* **16**, 6378 (2008).
- [181] Q. Yang, Y. Tang, Y. Ma, and W. Shieh, *J. Lightwave Technol.* **27**, 168 (2009).
- [182] S. L. Jansen, I. Morita, T. C. W. Schenk, N. Takeda, and H. Tanaka, *J. Lightwave Technol.* **27**, 177 (2009).
- [183] J. Armstrong, *J. Lightwave Technol.* **27**, 189 (2009).
- [184] S. L. Jansen, A. A. Amin, H. Takahashi, I. Morita, and H. Tanaka, *IEEE Photon. Technol. Lett.* **21**, 802 (2009).
- [185] H. Takahashi, A. Al Amin, S. L. Jansen, I. Morita, and H. Tanaka, Proc. Opt. Fiber Commun. Conf., Paper PDPB7 (2009).
- [186] H. Masuda, E. Yamazaki, A. Sano, et al., Proc. Opt. Fiber Commun. Conf., Paper PDPB5 (2009).
- [187] C. Zhang, Y. Mori, K. Igarashi, K. Katoh, and K. Kikuchi, Proc. Opt. Fiber Commun. Conf., Paper OTuG3 (2009).
- [188] C. Schmidt-Langhorst, R. Ludwig, H. Hu, and C. Schubert, Proc. Opt. Fiber Commun. Conf., Paper OTuN5 (2009).
- [189] Y. Ma, Q. Yang, Y. Tang, S. Chen, and W. Shieh, *Opt. Express* **17**, 9421 (2009).
- [190] R. Dischler and F. Buchali, Proc. Opt. Fiber Commun. Conf., Paper PDPC2 (2009).
- [191] D. Hillerkuss et al., Proc. Opt. Fiber Commun. Conf., Paper PDPC1 (2010).
- [192] P. P. Mitra and J. B. Stark, *Nature* **411**, 1027 (2001).
- [193] A. Mecozzi and M. Shtaif, *IEEE Photon. Technol. Lett.* **13**, 1029 (2001).
- [194] J. Tang, *J. Lightwave Technol.* **19**, 1104 (2001); **19**, 1110 (2001).
- [195] E. E. Narimanov and P. P. Mitra, *J. Lightwave Technol.* **20**, 530 (2002).
- [196] K. S. Turitsyn, S. A. Derevyanko, I. V. Yurkevich, and S. K. Turitsyn, *Phys. Rev. Lett.* **91**, 203901 (2003).
- [197] I. B. Djordjevic, B. Vasic, M. Ivkovic, and I. Gabitov, *J. Lightwave Technol.* **23**, 3755 (2005).
- [198] M. Ivković, I. Djordjević, and B. Vasić, *J. Lightwave Technol.* **25**, 1163 (2007).
- [199] R.-J. Essiambre, G. J. Foschini, G. Kramer, and P. J. Winzer, *Phys. Rev. Lett.* **101**, 163901 (2008).
- [200] R.-J. Essiambre, G. Kramer, P. J. Winzer, G. J. Foschini, and B. Goebel, *J. Lightwave Technol.* **28**, 662 (2010).
- [201] C. E. Shannon, *Proc. IRE* **37**, 10 (1949).

Chapter 11

Optical Signal Processing

Current lightwave systems perform signal processing mostly in the electric domain. This approach is acceptable if signal processing is done at the transmitter and receiver ends but becomes impractical if it needs to be carried out at intermediate nodes of an optical network. For example, switching of individual WDM channels at an intermediate node may require a change in its carrier wavelength. An electric-domain implementation would require recovering the electric bit stream with an optical receiver and then recreating the WDM channel using an optical transmitter operating at the new wavelength. An all-optical approach would simply send the channel to a nonlinear optical device (called the wavelength converter) that changes the carrier wavelength without affecting its data contents. Another example is provided by optical regenerators that clean up an optical signal and amplify it without any optical to electrical conversion. This chapter focuses on a variety of signal processing devices that make use of the same nonlinear effects, such as self-phase modulation (SPM), cross-phase modulation (XPM), and four-wave mixing (FWM), that are otherwise harmful for lightwave systems. Section 11.1 describes several fiber- and semiconductor-based devices that are useful for optical signal processing. All-optical flip-flops and wavelength converters are covered in Sections 11.2 and 11.3, respectively. Several other applications are discussed in Section 11.4 including and format conversion and packet switching. Section 11.5 is devoted to optical regenerators.

11.1 Nonlinear Techniques and Devices

The main features of the three nonlinear phenomena, SPM, XPM, and FWM, that are useful for all-optical signal processing have been discussed in Section 2.7. All three can be implemented using a piece of optical fiber designed to enhance the nonlinear effects. Such fibers are known as *highly nonlinear fibers* and are designed such that the effective area of the fundamental mode is reduced considerably compared to that of standard fibers [1]. As a result, the nonlinear parameter γ , defined in Section 2.6.2 to scale inversely with the effective mode area A_{eff} , is enhanced considerably [2]. Its value

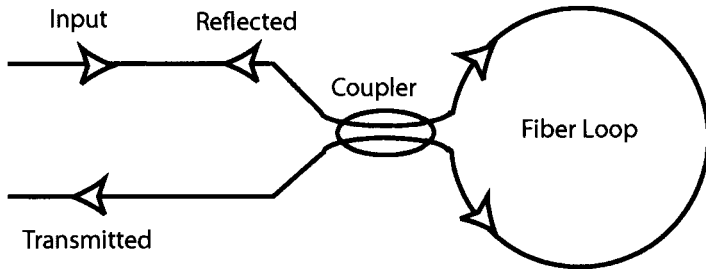


Figure 11.1: Schematic of an all-fiber Sagnac interferometer acting as a nonlinear optical loop mirror whose transmission depends on launched input power.

typically exceeds $10 \text{ W}^{-1}/\text{km}$ for silica-based highly nonlinear fibers and becomes even larger than $1000 \text{ W}^{-1}/\text{km}$ for especially designed non-silica fibers [3]–[6].

Several devices have been developed in recent years for the purpose of optical signal processing of telecommunication signals [7]. This section covers devices such as Sagnac interferometers, parametric amplifiers, semiconductor optical amplifiers, and bistable resonators.

11.1.1 Nonlinear Optical Loop Mirrors

A nonlinear optical loop mirror (NOLM) is an example of a Sagnac interferometer in which different nonlinear phase shifts acquired by counterpropagating waves inside a fiber loop are exploited for optical signal processing [8]–[10]. Figure 11.1 shows schematically how a Sagnac interferometer can be made by connecting a piece of long fiber to the two output ports of a fiber coupler to form a loop. The entering optical field is split into two counterpropagating parts that share the same optical path and interfere at the coupler coherently. The relative phase difference between the counterpropagating beams determines whether an input beam is reflected or transmitted by the Sagnac interferometer. In fact, if a 3-dB fiber coupler is used, any input is totally reflected, and the Sagnac loop acts as a perfect mirror. Such a device can be designed to transmit a high-power signal while reflecting it at low power levels, thus acting as an all-optical switch.

The physical mechanism behind nonlinear switching can be understood by considering a CW or a quasi-CW input beam. When such an optical signal is incident at one port of the fiber coupler, its split into two parts whose relative amplitude and phases depend on the transfer matrix of the coupler given by [11]

$$T_c = \begin{pmatrix} \sqrt{\rho} & i\sqrt{1-\rho} \\ i\sqrt{1-\rho} & \sqrt{\rho} \end{pmatrix}, \quad (11.1.1)$$

where ρ represents the fraction of the input power P_0 remaining in the bar port of the coupler. Using this transfer matrix, the transmittivity of an NOLM of length L is found to be [10]

$$T_S = 1 - 2\rho(1-\rho)\{1 + \cos[(1-2\rho)\gamma P_0 L]\}, \quad (11.1.2)$$

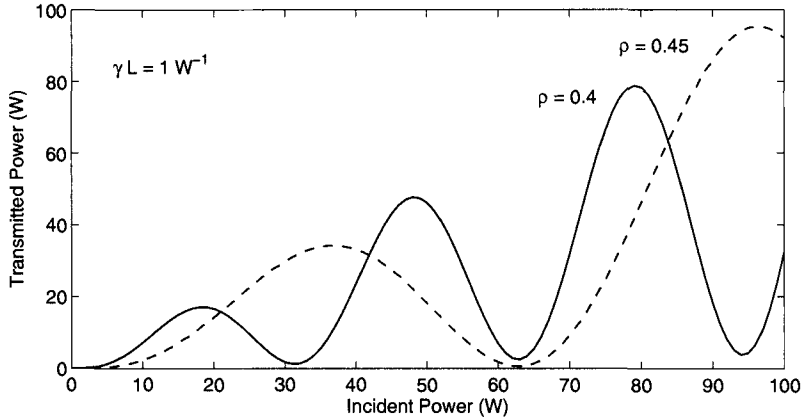


Figure 11.2: Transmitted power as a function of incident power for two values of ρ , showing the nonlinear response of an all-fiber Sagnac interferometer.

where P_0 is the input power. For $\rho = 0.5$, T_S equals zero, and all the input power is reflected back (hence the name *optical loop mirror*). Physically, if the power is equally divided between the counterpropagating waves, nonlinear phase shifts are the same for both waves, resulting in no relative phase difference between the counterpropagating waves. However, if the power-splitting factor ρ is different than 0.5, an NOLM exhibits different behavior at low and high powers and can act as an optical switch.

Figure 11.2 shows the transmitted power as a function of P_0 for two values of ρ . At low powers, little light is transmitted if ρ is close to 0.5 since $T_S \approx 1 - 4\rho(1 - \rho)$. At high powers, the SPM-induced phase shift leads to 100% transmission of the input signal whenever

$$|1 - 2\rho|\gamma P_0 L = (2m - 1)\pi, \quad (11.1.3)$$

where m is an integer. As seen in Figure 11.2, the device switches from low to high transmission periodically as input power increases. In practice, only the first transmission peak ($m = 1$) is likely to be used for switching because it requires the least power. The switching power for $m = 1$ can be estimated from Eq. (11.1.3) and is 31 W for a 100-m-long fiber loop when $\rho = 0.45$ and $\gamma = 10 \text{ W}^{-1}/\text{km}$. It can be reduced by increasing the loop length, but one should then consider the effects of fiber loss and GVD that were neglected in deriving Eq. (11.1.2).

The switching power of a Sagnac interferometer can also be reduced by incorporating a fiber amplifier within the loop [12]. If the amplifier is located close to the fiber coupler, its presence introduces an asymmetry as the counterpropagating pulses are not amplified simultaneously. Since the Sagnac interferometer is unbalanced by the amplifier, even a 50:50 coupler ($\rho = 0.5$) can be used. The switching behavior can be understood by noting that one wave is amplified at the entrance to the loop while the counterpropagating wave experiences amplification just before exiting the loop. Since the intensities of the two waves differ by a large amount throughout the loop, the differential phase shift can be quite large. Assuming that the clockwise wave is amplified

first by a factor G , the transmittivity is found to be

$$T_S = 1 - 2\rho(1-\rho)\{1 + \cos[(1-\rho-G\rho)\gamma P_0 L]\}. \quad (11.1.4)$$

The condition for complete transmission is obtained from Eq. (11.1.3) by replacing $(1-2\rho)$ with $(1-\rho-G\rho)$. For $\rho = 0.5$, the switching power is given by (using $m = 1$)

$$P_0 = 2\pi/[(G-1)\gamma L]. \quad (11.1.5)$$

Since the amplification factor G can be as large as 30 dB, the switching power is reduced by a factor of up to 1000. Such a device, referred to as the *nonlinear amplifying-loop mirror*, can switch at peak power levels below 1 mW. In a demonstration of the basic concept, 4.5 m of Nd-doped fiber was spliced within the 306-m fiber loop formed using a 3-dB coupler, and CW-like switching was observed using 10-ns pulses [12]. The switching power was about 0.9 W even when the amplifier provided only a 6-dB gain (a factor of 4). In a later experiment, the use of a semiconductor optical amplifier, providing different gains for counterpropagating waves inside a 17-m fiber loop, resulted in switching powers of less than 250 μ W when 10-ns pulses were injected into the loop [13].

From the standpoint of optical signal processing, XPM-induced switching is more important than SPM-induced switching because one can use another optical beam to control the switching process. In this important class of applications, a control (or a pump) beam is injected into the NOLM such that it propagates in only one direction and induces a nonlinear phase shift on one of the counterpropagating waves through XPM, while the other is not affected by it. In essence, the control signal is used to unbalance the Sagnac interferometer in a way similar to how an optical amplifier can be used to produce different SPM-induced phase shifts. As a result, the loop can be made using a 50:50 coupler so that a low-power CW beam is reflected in the absence of the control but transmitted when a control pulse is applied. Many experiments have shown the potential of XPM-induced switching [14]–[20].

When the signal and control wavelengths are not close to each other, we should consider the walk-off effects induced by the mismatch in their group velocities. In the absence of the GVD effects, the XPM-induced relative phase shift imposed on the signal by a control pulse is given by [2]

$$\phi_{XPM} = 2\gamma \int_0^L |A_c(t - d_w z)|^2 dz, \quad (11.1.6)$$

where A_c is the control-pulse amplitude and

$$d_w = v_{gc}^{-1} - v_{gs}^{-1} = \beta_2(\Delta\omega) \quad (11.1.7)$$

represents the group-velocity mismatch between the control and signal pulses separated in frequency by $\Delta\omega$.

The integral in Eq. (11.1.6) can be evaluated analytically for certain shapes of the control pulse. For example, for a “sech” control pulse with $A_c(t) = \sqrt{P_c} \operatorname{sech}(t/T_0)$, the phase shift is given by [15]

$$\phi_{XPM}(\tau) = 2\gamma P_c L_w [\tanh(\tau) - \tanh(\tau - L/L_w)], \quad (11.1.8)$$

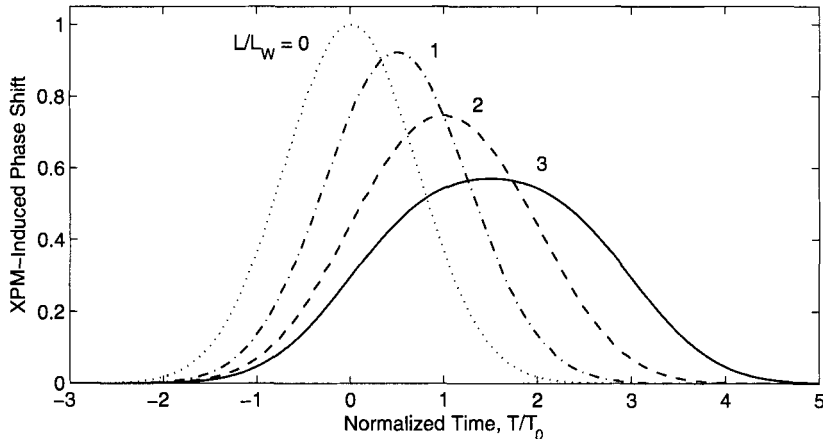


Figure 11.3: Temporal profile of the XPM-induced phase shift (normalized to ϕ_{\max}) as a function of T/T_0 for several values of L/L_w .

where $\tau = t/T_0$ and $L_w = T_0/d_w$ is the so-called walk-off length. In the case of Gaussian optical pulses with $|A_c(t)|^2 = P_c \exp(-t^2/T_0^2)$, the XPM-induced phase shift becomes

$$\phi_{\text{XPM}}(\tau) = \sqrt{\pi} \gamma P_c L_w [\text{erf}(\tau) - \text{erf}(\tau - L/L_w)], \quad (11.1.9)$$

where $\text{erf}(x)$ stands for the error function.

Figure 11.3 shows the XPM-induced phase shift, normalized to its maximum value $\phi_{\max} = 2\gamma P_c L$, as a function of τ for several values of L/L_w in the case of Gaussian pulses. The temporal phase profile mimics the pulse shape for small values of L/L_w , but its shape is distorted considerably as fiber length becomes larger than L_w . As one may expect, the maximum value of the phase shift is reduced by the walk-off effects, an undesirable feature that increases the required peak power. However, even more detrimental from a practical standpoint is the broadening of the phase profile because it leads to a switching window wider than the control pulses.

The problem of pulse walk-off can be solved by using a fiber whose zero-dispersion wavelength lies between the pump and signal wavelengths such that the two waves have the same group velocity ($d_w = 0$). Indeed, such a 200-m-long Sagnac loop was built in 1990 using polarization-maintaining fiber [16]. It was employed to switch the $1.54\text{-}\mu\text{m}$ signal using 120-ps pump pulses with 1.8-W peak power at $1.32\text{ }\mu\text{m}$. In a later experiment, 14-ps pump pulses, obtained from a gain-switched $1.55\text{-}\mu\text{m}$ DFB laser and amplified using a fiber amplifier, were able to switch a CW signal in the wavelength region near $1.32\text{ }\mu\text{m}$.

The pulse walk-off occurring because of wavelength difference between the pump and signal can also be avoided by using an orthogonally polarized pump at the same wavelength as that of the signal [17]. There is still a group-velocity mismatch because of polarization-mode dispersion, but it is relatively small. Moreover, it can be used to advantage by constructing a Sagnac loop in which the slow and fast axes of polarization-maintaining fibers are interchanged in a periodic fashion. In one imple-

mentation of this idea [18], a 10.2-m loop consisted of 11 such sections. Two orthogonally polarized pump and signal pulses (width about 230 fs) were injected into the loop and propagated as solitons. The pump pulse was polarized along the fast axis and delayed initially such that it overtook the signal pulse in the first section. In the second section, the signal pulse traveled faster because of the reversing of slow and fast axes and overtook the pump pulse. This process repeated in each section. As a result, two solitons collided multiple times inside the Sagnac loop, and the XPM-induced phase shift was enhanced considerably.

NLOMs can be employed for many applications. The main advantage of using the nonlinearity of fibers is its ultrafast nature that permits all-optical signal processing at femtosecond time scales. The advent of highly nonlinear fibers [2], in which the nonlinear parameter γ is enhanced by as much as a factor of 1000, has made the use of a Sagnac interferometer much more practical by reducing the required length of the nonlinear fiber loop.

An NOLM acts as a high-pass intensity filter in the sense that it reflects low-intensity signals but transmits high-intensity radiation without affecting it. A simple application of NLOMs consists of using them for pulse shaping and pulse cleanup. For example, if a short optical pulse contains a broad low-intensity pedestal, the pedestal can be removed by passing it through such a device [21]. Similarly, a pulse train corrupted by the amplified spontaneous emission during its amplification can be cleaned by passing it through an NOLM. The NOLM can also be used for pulse compression and for generating a train of short optical pulses at a high repetition rate by injecting a dual-wavelength signal [22].

An important application of NLOMs is for converting the wavelength of a WDM channel. As early as 1992, XPM induced by control pulses from a laser operating near 1533 nm was used to convert the 1554-nm CW radiation into a pulse train [23]. By 2000, an NOLM was used for wavelength conversion at a bit rate of 40 Gb/s [24]. Section 11.3 discusses the wavelength-conversion process in more detail. NLOMs are also useful for logic operations on digital bit streams. A polarization-maintaining Sagnac loop was used in 1991 to demonstrate elementary logic operation [25]. NLOMs can be used as analog-to-digital and digital-to-analog converters [26]. They are also useful for all-optical regeneration of WDM channels because they can reshape pulses while reducing the noise level [27]. The pulse-shaping capability of such interferometers can be improved significantly by concatenating several Sagnac loops in series [28].

11.1.2 Parametric Amplifiers

Parametric amplifiers make use of FWM inside a nonlinear medium, such as a highly nonlinear fiber [29]–[33], using the scheme shown schematically in Figure 11.4. The signal at the frequency ω_s that needs to be amplified is launched inside the fiber together with a CW pump of frequency ω_p . The FWM phenomenon creates an idler wave at the frequency $\omega_i = 2\omega_p - \omega_s$ if the phase-matching condition is satisfied for the four photons participating in the FWM process.

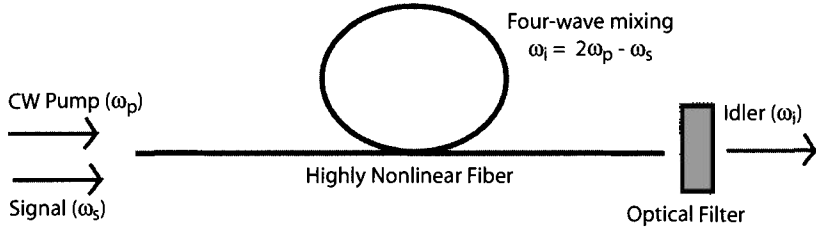


Figure 11.4: Schematic of an fiber-optic parametric amplifier. A CW beam acts as the pump that amplifies both the signal and idler waves simultaneously. An optical filter passes the signal or the idler depending on the application.

Single-Pump Parametric Amplifiers

To understand the amplification process, we use the well-known theory of FWM developed for optical fibers [2]. When a single pump is used at power levels much higher than the signal, and depletion of the pump is ignored, the FWM process is governed by two coupled linear equations written in the Fourier domain as

$$\frac{dA_s}{dz} = 2i\gamma A_p^2 \exp(-i\kappa z) A_i^*, \quad (11.1.10)$$

$$\frac{dA_i}{dz} = 2i\gamma A_p^2 \exp(-i\kappa z) A_s^*, \quad (11.1.11)$$

where $A_s(\omega_s, z)$ and $A_i(\omega_i, z)$ represent the signal and idler fields, A_p is the input pump field, and κ represents the total phase mismatch given by

$$\kappa = \beta(\omega_s) + \beta(\omega_i) - 2\beta(\omega_p) + 2\gamma P_0, \quad (11.1.12)$$

where $\beta(\omega)$ is the propagation constant of the fiber mode at frequency ω and $P_0 \equiv |A_p|^2$ is the input pump power. It follows from Eq. (11.1.11) that the amplitude of the idler field is related to the complex conjugate of the signal field or, equivalently, its spectrum is inverted with respect to the signal spectrum. As was seen in Section 8.5, this phase-conjugation property of FWM is useful for dispersion compensation.

Equations (11.1.10) and (11.1.11) can be solved easily to study how the signal and idler waves grow along the fiber length as a result of FWM. Using this solution, the signal and idler powers at the fiber output ($z = L$) are given by

$$P_s(L) = |A_s(L)|^2 = P_s(0)[1 + (1 + \kappa^2/4g^2)\sinh^2(gL)], \quad (11.1.13)$$

$$P_i(L) = |A_i(L)|^2 = P_i(0)(1 + \kappa^2/4g^2)\sinh^2(gL), \quad (11.1.14)$$

where the parametric gain g is defined as

$$g = \sqrt{(\gamma P_0)^2 - \kappa^2/4}. \quad (11.1.15)$$

The amplification factor is obtained from Eq. (11.1.13) and can be written using Eq. (11.1.15) in the form

$$G_s = \frac{P_s(L)}{P_s(0)} = 1 + \frac{\sinh^2(gL)}{(gL_{NL})^2}, \quad (11.1.16)$$

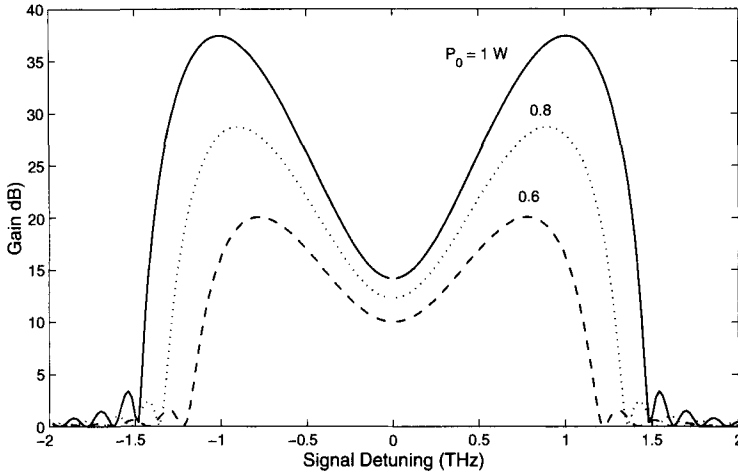


Figure 11.5: Gain spectra of a 0.5-km-long parametric amplifier at three pump power levels obtained numerically using $\beta_2 = -0.5 \text{ ps}^2/\text{km}$ and $\gamma = 10 \text{ W}^{-1}/\text{km}$.

where the nonlinear length is defined as $L_{\text{NL}} = (\gamma P_0)^{-1}$. The parametric gain depends on the phase mismatch κ and can become quite small if the phase-matching condition is not satisfied. On the other hand, when phase matching is perfect ($\kappa = 0$) and $gL \gg 1$, the amplifier gain increases exponentially with P_0 as

$$G_s \approx \frac{1}{4} \exp(2\gamma P_0 L). \quad (11.1.17)$$

In terms of the nonlinear length, the gain increases as $\exp(2L/L_{\text{NL}})$ for a parametric amplifier as long as gain saturation and pump depletion remain negligible. Notice that the amplifier length must be longer than the nonlinear length L_{NL} for realizing significant gain and that G_p exceeds 28 dB for $L = 4L_{\text{NL}}$. Since $L_{\text{NL}} = 10 \text{ m}$ for a fiber with $\gamma = 100 \text{ W}^{-1}/\text{km}$ and pumped with $P_0 = 1 \text{ W}$, such a 50-m-long parametric amplifier can provide more than 30-dB gain.

The gain spectrum is obtained from Eq. (11.1.16) by plotting G_p as a function of pump-signal detuning defined as $\delta = \omega_s - \omega_p$. Assuming that the pump wavelength is located close to the zero-dispersion wavelength of the fiber, and expanding $\beta(\omega)$ in a Taylor series around the pump frequency ω_p , we find from Eq. (11.1.12) that $\kappa \approx \beta_2 \delta^2 + 2\gamma P_0$, where β_2 is the GVD parameter at the pump frequency. Figure 11.5 shows the gain as a function of signal detuning from the pump wavelength at three pump-power levels for a 500-m-long parametric amplifier designed using a fiber with $\gamma = 10 \text{ W}^{-1}/\text{km}$ and $\beta_2 = -0.5 \text{ ps}^2/\text{km}$. Both the peak gain and the amplifier bandwidth increase as pump power is increased. The peak value of the gain is close to 38 dB at a 1-W pump level and occurs when the signal is detuned by 1 THz (about 8 nm) from the pump wavelength. Experimental results on Parametric Amplifiers agree with this simple FWM theory [31] as long as pump depletion is negligible

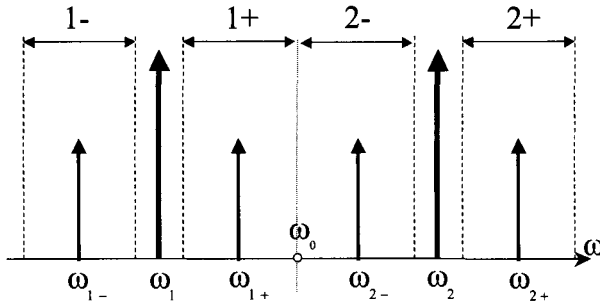


Figure 11.6: Spectral bands of a parametric amplifier pumped at two frequencies ω_1 and ω_2 located symmetrically around the zero-dispersion frequency ω_0 . A signal at ω_{1+} produces three dominant idlers through three distinct FWM processes.

Dual-Pump Parametric Amplifiers

A fundamental shortcoming of single-pump Parametric amplifiers is obvious from Figure 11.5. Because the gain is far from being uniform over the entire bandwidth, only a small portion of the gain spectrum near the two gain peaks can be used in practice. This problem can be solved by using two pumps whose wavelengths are chosen to produce a flat gain profile over a wide spectral range, while also allowing polarization-independent operation of the device [34]–[36].

A dual-pump parametric amplifier is fundamentally different from the conventional single-pump device. Its operating principle can be understood from Figure 11.6 where the two pumps are located on opposite sides of the zero-dispersion wavelength of the fiber. When either pump is used in isolation, parametric gain is narrowband and relatively small. More specifically, the pump in the anomalous region produces spectral features similar to those seen in Figure 11.5, whereas the pump in the normal region exhibits almost no gain. However, when both pumps are turned on simultaneously, the gain is not only larger but the spectral range over which gain is nearly uniform is also considerably wider. It is this central flat-gain region that turns parametric amplifiers into devices that are useful for lightwave systems.

Dual-pump parametric amplifiers provide uniform gain over a wide bandwidth by balancing three distinct processes that can produce parametric gain in multiple spectral regions [34]. Consider, as shown in Figure 11.6, two pumps at frequencies ω_1 and ω_2 , and a signal at the frequency ω_{1+} . First, the nondegenerate FWM produces an idler at ω_{2-} through the process $\omega_1 + \omega_2 \rightarrow \omega_{1+} + \omega_{2-}$. Second, the ω_1 pump generates an idler at ω_{1-} through a degenerate FWM process $\omega_1 + \omega_1 \rightarrow \omega_{1+} + \omega_{1-}$. If its wavelength lies in the anomalous-dispersion region of the fiber. The second pump can also produce a new idler through $\omega_2 + \omega_2 \rightarrow \omega_{2+} + \omega_{2-}$. Third, a Bragg-scattering process produces additional gain through the combinations denoted as [34]

$$\omega_1 + \omega_{1+} \rightarrow \omega_2 + \omega_{2-}, \quad \omega_2 + \omega_{1+} \rightarrow \omega_1 + \omega_{2+}. \quad (11.1.18)$$

Several other weak idler waves are also created but the three dominant idlers identified in Figure 11.6 must be considered for any dual-pump parametric amplifier. The relative

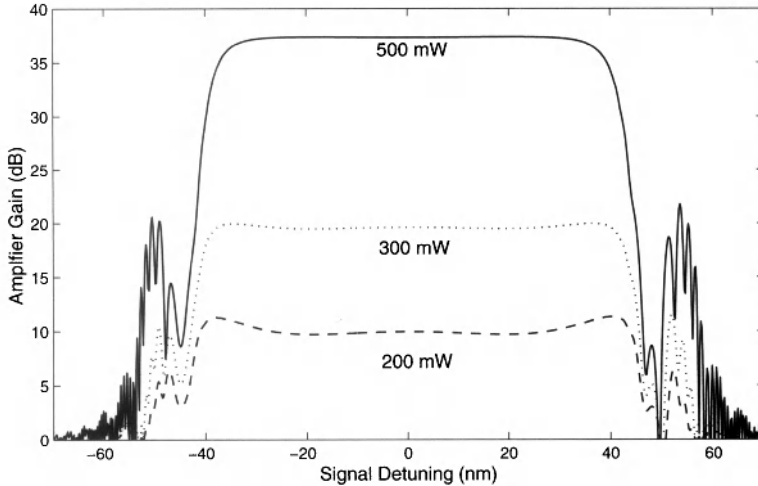


Figure 11.7: Theoretical gain spectra at three pump powers for a dual-pump parametric amplifier. Two pumps have equal powers and are located 35 nm away on each side of the zero-dispersion wavelength. Signal detuning is specified with respect to this wavelength.

strength of the three processes depends on the pump powers as well as on the detuning of the two pumps from the zero-dispersion wavelength. This feature allows one to produce a desired parametric response by simply choosing the pump wavelengths and powers appropriately.

The theory of dual-pump parametric amplifiers is somewhat involved because one must consider at least six fields at the frequencies shown in Figure 11.6 simultaneously for an accurate analysis. If we neglect pump depletion, Eqs. (11.1.10) and (11.1.11) found in the single-pump case are replaced by a set of four coupled equations [34]. It turns out that the gain spectrum depends on a larger number of parameters such as pump wavelengths, zero-dispersion wavelength, and the third- and fourth-order dispersion parameters of the fiber. In one configuration that can provide flat gain over a wide bandwidth, the two pump wavelengths are chosen almost symmetrically on the opposite sides of the zero-dispersion wavelength λ_0 . Figure 11.7 shows examples of the gain spectra in this case at three pump-power levels. A 500-m-long highly nonlinear fiber with $\gamma = 10 \text{ W}^{-1}/\text{km}$ and $\lambda_0 = 1570 \text{ nm}$ is assumed to be pumped using two lasers at wavelengths of 1,525 and 1,618 nm. The third- and fourth-order dispersion parameters of the fiber are $\beta_3 = 0.038 \text{ ps}^3/\text{km}$ and $\beta_4 = 1 \times 10^{-4} \text{ ps}^3/\text{km}$, respectively. When each pump provides 500 mW of power, a relatively large and uniform gain (38 dB) occurs over a bandwidth of more than 70 nm. The central flat gain region is mostly due to the nondegenerate FWM process. The other two FWM processes only affect the spectral wings and lead to oscillations seen in Figure 11.7.

Several experiments have shown that parametric amplifiers can provide flat gain over a wide bandwidth when pumped using the configuration shown in Figure 11.6. In one 2003 experiment [35], a gain of more than 40 dB was obtained over a bandwidth of 34 nm when a 1-km-long highly nonlinear fiber ($A_{\text{eff}} = 11 \mu\text{m}^2$) with its zero-

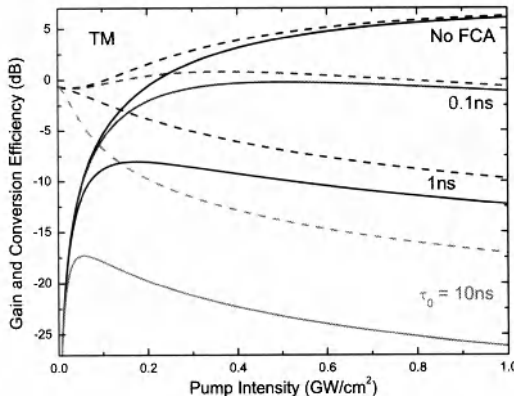


Figure 11.8: Signal gain (dashed lines) and idler conversion efficiency (solid curves) as a function of pump intensity for several values of carrier lifetime τ_c . The curve “No FCA” corresponds to the case $\tau_c = 0$. (After Ref. [40]; ©2006 OSA.)

dispersion wavelength at 1,583.5 nm was pumped with 600 and 200 mW of powers at 1,559 and 1,610 nm, respectively. Unequal input pump powers were used because the Raman gain transfers power from the shorter-wavelength pump to the other pump throughout the fiber length. The onset of SBS was avoided by modulating the pump phases at 10 GHz using a pseudorandom bit pattern.

Silicon-Based Parametric Amplifiers

It is not essential to employ optical fibers for making parametric amplifiers, and any material exhibiting a large third-order susceptibility can be used in place of fibers. Recently, silicon waveguides with nanoscale dimensions (also called photonic nanowires) have been used for this purpose with considerable success [37]–[44].

The theory of FWM in silicon waveguides is similar to that used earlier for optical fibers with some modifications [40]. The main change comes from the fact that when pumped in the spectral region of telecommunication interest near 1550 nm, the phenomenon of two-photon absorption (TPA) cannot be ignored because energy of pump photons exceeds one half of the bandgap. Moreover, TPA generates free carriers that not only induce additional absorption but also change the refractive index [45]. For this reason, Eqs. (11.1.10) and (11.1.11) should be modified to include the TPA and free-carrier effects, both of which degrade the efficiency of the FWM process. On the positive side, the nonlinear parameter γ is more than 10,000 times larger in silicon waveguides because of a much larger value of n_2 for silicon and a much smaller effective mode area of silicon waveguides. As a result, FWM can be observed in short devices with lengths of only ~ 1 cm.

The results of FWM theory extended to include the TPA and free-carrier effects reveal that idler generation can occur over a broad bandwidth (extending >300 nm) when pumped with a single pump whose wavelength nearly coincides with the zero-dispersion wavelength of the silicon waveguide [40]. However, it is not possible to

realize a net signal or idler amplification when the device is pumped continuously. The reason is related to the accumulation of TPA-generated free carriers whose population builds up substantially due to a relatively long lifetime of free carriers in silicon (typically >1 ns). Figure 11.8 shows the signal gain G_s (dashed lines) and the idler conversion efficiency, $\eta_c = P_i(L)/P_s(0)$ (solid curves), as a function of pump intensity for three values of the carrier lifetime τ_c ranging from 0.1 to 10 ns. The pump is launched at the zero-dispersion wavelength of 1551.3 nm and the signal wavelength is set at 1601.3 nm. Both G_s and η_c decrease for pump intensities >0.2 GW/cm² when τ_c exceeds 0.1 ns. This is so because more free carriers are created at high pump intensities and their density increases linearly with τ_c , resulting in higher losses for larger value of τ_c . For $\tau_c = 10$ ns, the maximum conversion efficiency is only -17.5 dB but it increases to 8 dB if τ_c is reduced to 1 ns.

Figure 11.8 indicates that, for a CW pump, signal amplification is possible only if the carrier lifetime is reduced to below 100 ps. Such a limitation does not exist for short optical pulses. For this reason, early experiments on FWM in silicon waveguides employed pulsed pumping to realize a net signal gain [38]. However, CW pumping is often desirable for signal processing applications. The limitation imposed by the carrier lifetime can be overcome to some extent by implementing a reversed-biased p-i-n junction that removes free carriers from the FWM region by accelerating them toward the electrodes [41]. On the positive side, a relatively short length of silicon waveguides permits FWM to occur over a broad wavelength range that can exceed 300 nm [40]. In a 2010 experiment, a bandwidth of more than 800 nm was realized by controlling the waveguide dispersion through device dimensions [44]. A detailed FWM theory shows that the magnitudes and signs of both the second- and fourth-order dispersions must be controlled for extending the bandwidth over which FWM can occur [2]. In the 2010 experiment, the width and height of the silicon waveguide were controlled to realize a wavelength difference of 837 nm between the signal and idler. However, the experiment employed a CW signal and a CW pump, and the conversion efficiency was limited to below 20 dB.

11.1.3 Nonlinear Effects in Semiconductor Optical Amplifiers

Semiconductor optical amplifiers (SOAs) were developed during the 1980s for their potential applications in lightwave systems [46]–[50]. Although, with the advent of the doped-fiber and Raman amplifiers, SOAs are rarely used for fiber-loss compensation in lightwave systems, they exhibit several nonlinear effects that make them useful for optical signal processing. Because of their relatively short lengths (~ 1 mm), their third-order susceptibility cannot be exploited for this purpose. However, gain saturation that is intrinsic to any amplifier can be used as a substitute.

Optical Gain and its Saturation in SOAs

Although semiconductor lasers can be used as amplifiers when biased below threshold, their bandwidth is inherently limited by multiple reflections at the facets. Most SOAs suppress this feedback using a tilted-stripe in combination with antireflection coatings at the facets. The 3-dB bandwidth can approach 100 nm for such an amplifier.

SOAs are pumped electrically by injecting electrons into its active region. If a CW optical signal is launched into its input end, this signal is amplified exponentially with the single-pass gain $G = \exp(gL)$ as long as the gain remains unsaturated. However, it is relatively easy to saturate the gain coefficient g , which is related to the electron density N by the relation

$$g(N) = \Gamma\sigma_g(N - N_0), \quad (11.1.19)$$

where Γ is confinement factor, σ_g is the gain cross section, and N_0 is the value of N at which the SOA becomes transparent. These three parameters characterize an SOA and depend on its design details.

To discuss gain saturation, we use a well-known rate equation for the carrier density in the form

$$\frac{dN}{dt} = \frac{I}{qV} - \frac{N}{\tau_c} - \frac{\sigma_g(N - N_0)}{\sigma_m h\nu} P, \quad (11.1.20)$$

where τ_c is the carrier lifetime and σ_m is the effective area of the waveguide mode. In the case of a CW beam or pulses much longer than τ_c , the steady-state value of N is obtained by setting $dN/dt = 0$ in Eq. (11.1.20). When the solution is substituted in Eq. (11.1.19), the optical gain is found to saturate as

$$g = \frac{g_0}{1 + P/P_s}, \quad (11.1.21)$$

where the small-signal gain g_0 is given by

$$g_0 = \Gamma\sigma_g[I\tau_c/(qV) - N_0], \quad (11.1.22)$$

and the saturation power P_s is defined as

$$P_s = h\nu\sigma_m/(\sigma_g\tau_c). \quad (11.1.23)$$

Typical values of P_s are in the range of 5 to 10 mW.

SOAs as Nonlinear Devices

Gain saturation that limits the usefulness of SOAs in lightwave systems as an optical amplifier also renders them quite useful for optical signal processing (while amplifying the signal simultaneously). Because of gain saturation induced by optical pulses, SOAs can be used for wavelength conversion, channel demultiplexing, and logic operations [51]–[53]. SOAs are not only extremely compact (active volume $< 1 \text{ mm}^3$), they can also be integrated monolithically with other devices on the same chip.

The most important feature of SOAs is that they exhibit a strong carrier-induced third-order nonlinearity with effective values of $n_2 \sim 10^{-13} \text{ m}^2/\text{W}$ that are seven orders of magnitude larger than that of silica fibers [54]–[56]. Although this nonlinearity does not respond on a femtosecond time scale, it is fast enough that it can be used to make devices operating at bit rates as fast as 40 Gb/s. The origin of this nonlinearity lies in gain saturation and the fact that any change in the carrier density affects not only the optical gain but also the refractive index within the active region of an SOA.

A simple way to understand the nonlinear response of an SOA is to consider what happens when a short optical pulse is launched into it. The amplitude $A(z,t)$ of the pulse envelope inside the SOA evolves as [54]

$$\frac{\partial A}{\partial z} + \frac{1}{v_g} \frac{\partial A}{\partial t} = \frac{1}{2}(1 - i\beta_c)gA, \quad (11.1.24)$$

where v_g is the group velocity and carrier-induced index changes are included through the linewidth enhancement factor β_c . The time dependence of g is governed by Eq. (11.1.20), which can be written in the form

$$\frac{\partial g}{\partial t} = \frac{g_0 - g}{\tau_c} - \frac{g|A|^2}{E_{\text{sat}}}, \quad (11.1.25)$$

where the saturation energy E_{sat} is defined as

$$E_{\text{sat}} = h\nu(\sigma_m/\sigma_g) = P_s\tau_c, \quad (11.1.26)$$

and g_0 is given by Eq. (11.1.22). Typically, $E_{\text{sat}} \sim 1 \text{ pJ}$.

Equations (11.1.24) and (11.1.25) govern amplification of optical pulses in SOAs. They can be solved analytically for pulses whose duration is short compared with the carrier lifetime ($\tau_p \ll \tau_c$). The first term on the right side of Eq. (11.1.25) can then be neglected during pulse amplification. By introducing the reduced time $\tau = t - z/v_g$ together with $A = \sqrt{P} \exp(i\phi)$, Eqs. (11.1.24) and (11.1.25) can be written as [54]

$$\frac{\partial P}{\partial z} = g(z, \tau)P(z, \tau), \quad (11.1.27)$$

$$\frac{\partial \phi}{\partial z} = -\frac{1}{2}\beta_c g(z, \tau), \quad (11.1.28)$$

$$\frac{\partial g}{\partial \tau} = -g(z, \tau)P(z, \tau)/E_{\text{sat}}. \quad (11.1.29)$$

Equation (11.1.27) can easily be integrated over the amplifier length L to yield

$$P_{\text{out}}(\tau) = P_{\text{in}}(\tau) \exp[h(\tau)], \quad (11.1.30)$$

where $P_{\text{in}}(\tau)$ is the input power and $h(\tau)$ is the total integrated gain defined as

$$h(\tau) = \int_0^L g(z, \tau) dz. \quad (11.1.31)$$

If Eq. (11.1.29) is integrated over the amplifier length after replacing gP by $\partial P/\partial z$, $h(\tau)$ satisfies [54]

$$\frac{dh}{d\tau} = -\frac{1}{E_{\text{sat}}} [P_{\text{out}}(\tau) - P_{\text{in}}(\tau)] = -\frac{P_{\text{in}}(\tau)}{E_{\text{sat}}} (e^h - 1). \quad (11.1.32)$$

Equation (11.1.32) can easily be solved to obtain $h(\tau)$. The amplification factor $G(\tau)$ is related to $h(\tau)$ as $G = \exp(h)$ and is given by

$$G(\tau) = \frac{G_0}{G_0 - (G_0 - 1) \exp[-E_0(\tau)/E_{\text{sat}}]}, \quad (11.1.33)$$

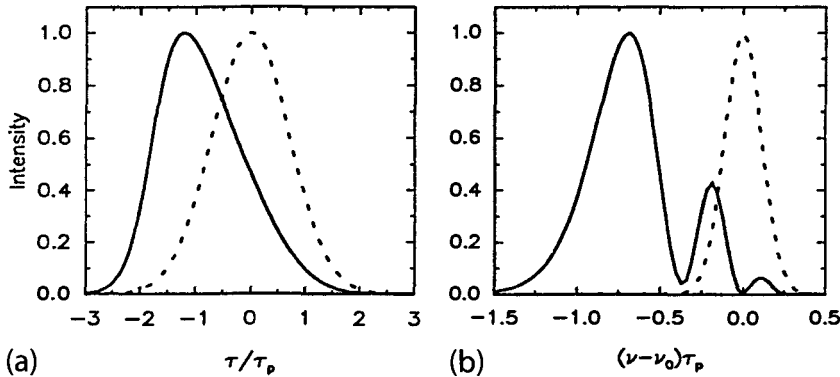


Figure 11.9: (a) Shape and (b) spectrum at the output of a semiconductor optical amplifier with $G_0 = 30$ dB and $\beta_c = 5$ for a Gaussian input pulse of energy $E_{\text{in}}/E_{\text{sat}} = 0.1$. The dashed curves show for comparison the shape and spectrum of the input pulse.

where G_0 is the unsaturated amplifier gain and $E_0(\tau) = \int_{-\infty}^{\tau} P_{\text{in}}(\tau') d\tau'$ is the partial energy of the input pulse defined such that $E_0(\infty)$ equals the input pulse energy E_{in} .

The solution (11.1.33) shows that the amplifier gain is different for different parts of the pulse. The leading edge experiences the full gain G_0 as the amplifier is not yet saturated. The trailing edge experiences the least gain since the whole pulse has saturated the amplifier gain. As seen from Eq. (11.1.28), gain saturation leads to a time-dependent phase shift across the pulse. This phase shift is found by integrating Eq. (11.1.28) over the amplifier length and is given by

$$\phi(\tau) = -\frac{1}{2}\beta_c \int_0^L g(z, \tau) dz = -\frac{1}{2}\beta_c h(\tau) = -\frac{1}{2}\beta_c \ln[G(\tau)]. \quad (11.1.34)$$

Since the pulse modulates its own phase through gain saturation, this phenomenon is referred to as *saturation-induced SPM* [54]. The frequency chirp is related to the phase derivative as

$$\Delta\nu_c = -\frac{1}{2\pi} \frac{d\phi}{d\tau} = \frac{\beta_c}{4\pi} \frac{dh}{d\tau} = -\frac{\beta_c P_{\text{in}}(\tau)}{4\pi E_{\text{sat}}} [G(\tau) - 1], \quad (11.1.35)$$

where Eq. (11.1.32) was used.

SPM and the associated frequency chirp are similar to the phenomena that occur when an optical pulse propagates through a fiber. Just as in optical fibers, the spectrum of the amplified pulse broadens and contains several peaks of different amplitudes [54]. Figure 11.9 shows the numerically calculated shape (a) and spectrum (b) of amplified pulses when a Gaussian pulse of energy such that $E_{\text{in}}/E_{\text{sat}} = 0.1$ is amplified by a SOA. The dominant spectral peak is shifted toward the red side and is broader than the input spectrum. It is also accompanied by one or more satellite peaks. The temporal and spectral changes depend on the level of amplifier gain. The experiments performed by using picosecond pulses from mode-locked semiconductor lasers have confirmed the behavior seen in Figure 11.9.

SOAs also exhibit XPM when a control pulse is used to change the phase of the signal being amplified by it. Similar to the case of optical fibers, the XPM-induced phase shift can be converted into intensity changes by employing either a Mach–Zender or a Sagnac interferometer. Such devices suffer less from the walk-off problem compared to optical fibers because their length is typically much small. When an SOA is placed within the Sagnac loop to impose the XPM-induced phase shift, the loop length can be 1 m or less because the loop is used only to propagate an input signal into counter-propagating directions. The speed of such devices is limited inherently by the carrier lifetime (typically >0.1 ns) but it can be overcome by a clever trick [57]–[60]. The trick consists of placing the SOA such that it is shifted from the center of the loop by a small but precise distance. It is this shift that governs the temporal window over which switching occurs rather than the carrier lifetime.

11.1.4 Bistable Optical Devices

Optical bistability is a major nonlinear phenomenon [61] that can be exploited for making bistable devices useful for optical signal processing. As the name implies, under certain conditions, the output of an optical device can have two discrete stable values for the same input. If the output can be switched between these two values through an external time-dependent control, the device acts as a time-domain switch. A simple device that exhibits optical bistability is a Fabry–Perot (FP) resonator containing a nonlinear medium [61]. A ring resonator can also be used for the same purpose. In fact, as early as 1983, a single-mode fiber was used as the nonlinear medium inside a ring cavity to realize an optically bistable device [62].

The origin of optical bistability in FP resonators can be understood by using the transmissivity of an FP resonator containing a nonlinear medium. Using R_m for the mirror reflectivities, we obtain

$$T_{\text{FP}}(v) = \frac{P_t}{P_i} = \frac{(1 - R_m)^2}{(1 - R_m)^2 + 4R_m \sin^2(\phi/2)}, \quad (11.1.36)$$

where $\phi = \delta + \phi_{\text{NL}}$ is the total phase shift during one round trip. The linear part, $\delta = (\Delta\omega)\tau_r$, depends on the round-trip time τ_r and the frequency detuning $\Delta\omega$ from a cavity resonance. The nonlinear contribution results from SPM and can be written as

$$\phi_{\text{NL}} = 2\gamma P_{\text{av}} L_m, \quad (11.1.37)$$

where γ is the nonlinear parameter, P_{av} is the average intracavity power, and L_m is the length of nonlinear medium. For high-finesse resonators, transmitted power $P_t \approx (1 - R_m)P_{\text{av}}$. If we use this relation in Eq. (11.1.36), the transmitted power is found to satisfy the transcendental equation

$$P_t \left\{ 1 + \frac{4R_m}{(1 - R_m)^2} \sin^2 \left[\frac{\delta}{2} + \frac{\gamma P_t L_m}{(1 - R_m)} \right] \right\} = P_i. \quad (11.1.38)$$

It is clear from this equation that multiple values of P_t are possible at a fixed value of the incident power P_i because of the nonlinear phase shift. The number of solutions

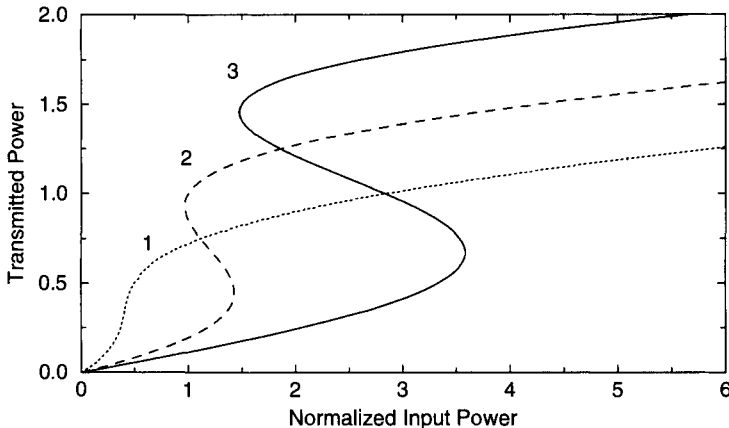


Figure 11.10: Bistable response of a fiber resonator with $R_m = 0.5$ for three values of detuning δ . Powers are normalized using $P_n = (2\gamma L_m)^{-1}$.

depends on the input power P_i . At low powers, only one solution exists. With increasing input power, the number of solutions increases from one to three, then to five and beyond. We focus on the case of three solutions since it requires the least input power.

Multiple solutions of Eq. (11.1.38) lead to dispersive optical bistability, a nonlinear phenomenon that has been observed using several different nonlinear media [61]. It occurs when the linear phase shift $\delta \neq 0$ so that little light is transmitted at low power levels. The nonlinear phase shift brings the signal onto a FP resonance, resulting in higher transmission. However, the transmitted power P_t does not increase linearly with P_i , as is evident from the nonlinear nature of Eq. (11.1.38). Figure 11.10 shows the expected behavior for three values of detuning. Over a certain range of δ , three solutions of Eq. (11.1.38) produce the well-known S-shaped curve associated with optical bistability. The middle branch with a negative slope is known to be unstable [61]. As a result, the transmitted power jumps up and down at specific values of P_i in such a way that it exhibits hysteresis. The low-output state is referred to as the “off” state, while high-output state corresponds to the “on” state. Such a device can be switched on and off by changing input power, input wavelength, or other controls that change the initial detuning δ . Indeed, any mechanism that changes the linear refractive index of the intracavity material can be used for controlling such an optical switch.

Optical bistability has been observed using several different nonlinear media including semiconductor waveguides, and optical fibers [61]. As early as 1978, a LiNbO₃ waveguide was used for this purpose by coating its two cleaved ends with silver to form an FP cavity [63]. Waveguides formed using multiple quantum wells were used during the 1980s [64]. In the case of optical fibers, SBS hampers the observation of optical bistability when CW beams or relatively broad optical pulses are used. Bistability in a fiber-ring resonator was first seen in a 1983 experiment in which SBS was avoided using picosecond pulses [62]. In a later experiment, SBS was suppressed by placing an optical isolator inside the ring cavity that allowed the propagation of light in a single

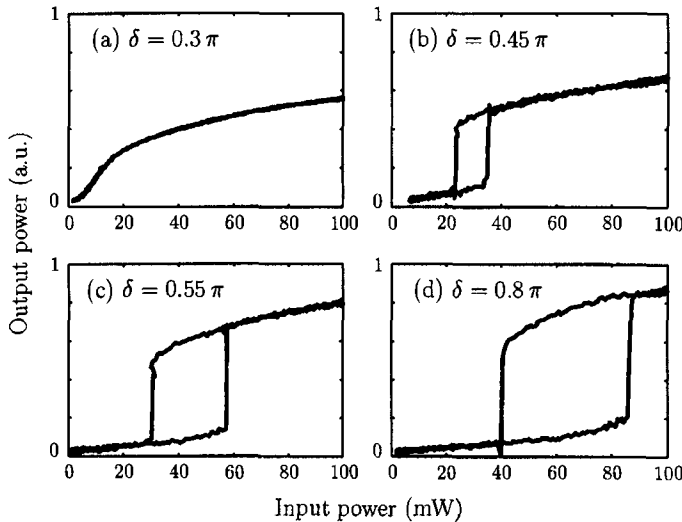


Figure 11.11: Hysteresis cycles observed in a fiber-ring resonator at four values (a–d) of detuning δ . (After Ref. [66]; ©1998 OSA.)

direction [65]. Bistable behavior was observed in this experiment at CW power levels below 10 mW. The nonlinear phase shift ϕ_{NL} at this power level was relatively small in magnitude (below 0.01 rad) but still large enough to induce bistability. An improved stabilization scheme was used in a 1998 experiment [66]. Figures 11.11(a) through (d) show the observed behavior at four values of the detuning δ . The experiment used mode-locked pulses (with a width of ~ 1 ps) emitted from a Ti:sapphire laser. The length of fiber-ring resonator (about 7.4 m) was adjusted precisely so that an entering laser pulse overlapped in time with another pulse already circulating inside the cavity (synchronous pumping).

The use of semiconductor lasers as optically bistable devices attracted considerable attention during the 1990s [67]. The main advantage is that such lasers employ an FP cavity by design and that the active semiconductor waveguide of the laser can provide sufficient nonlinearity for bistability to occur. Moreover, an external holding beam is not needed since lasers generate this beam internally. Thus, it is sufficient to send a control signal, provided the laser exhibits bistable behavior in some range of applied current. Most semiconductor lasers are not intrinsically bistable but can be made so by integrating one or more saturable-absorber sections within the laser cavity [68]–[71]. Even an SOA can be used as a bistable device. Indeed, SOAs were used during the 1980s for observing bistability and for realizing all-optical flip-flops [72], [73]. Even though SOAs require an external holding beam, the power required is relatively low as SOAs also provide optical amplification.

FP cavities, although common, are not essential for bistability as long as there is a built-in mechanism that can provide optical feedback. Distributed feedback (DFB) from a Bragg grating formed inside a nonlinear medium can serve this purpose and lead to optical bistability [74]. One can employ a fiber grating or a planar waveguide with

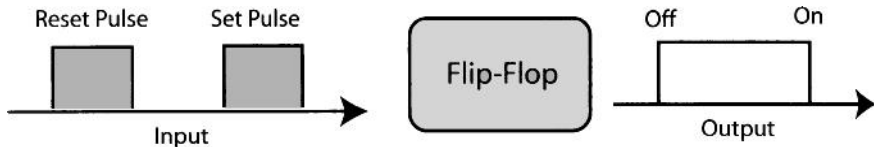


Figure 11.12: Schematic of an all-optical flip-flop. Set and reset pulses turn the flip-flop on and off, respectively.

the built-in grating for making time-domain switches. DFB semiconductor lasers and SOAs are a natural candidate for such devices and they have been used for this purpose since the 1980s [75]–[78]. The physical mechanism responsible for optical bistability is the dependence of the refractive index on the carrier density; as the carrier density within the active region decreases in response to gain saturation, the refractive index increases, leading to a shift of the stop band associated with the Bragg grating. This nonlinear shift of the stop band is equivalent to changing detuning in Figure 11.11. The stop band can also be shifted by changing the SOA gain through current injection. The next section show how such changes can be used for making all-optical flip-flops.

11.2 All-Optical Flip-Flops

Optical flip-flops constitute time-domain switches that can be turned on and off using an external control. Such devices attracted considerable attention during the 1980s because they mimic the functionality of electrical flip-flops and provide the most versatile solution for optical switching, optical memory, and optical logic elements [79]–[83].

All flip-flops require an optical bistable device that can be switched between its two output states through a control signal. Semiconductor lasers and SOAs are often used for making flip-flops because of their compact size, low power consumption, and potential for monolithic integration with other photonic devices. The external control can be electrical or optical for such devices. When an optical control is used, the device is referred to as an all-optical flip-flop. Figure 11.12 shows the basic idea behind such a device. The device output can be switched to the “on” state by sending an optical set signal in the form of a short pulse. At a later time, a reset pulse turns the flip-flop off. Unlike the switching scheme discussed in Section 11.1.1, the output remains on for the duration between the set and reset pulses. In this sense, a flip-flop retains memory of the set pulse and can be used as an optical memory element.

11.2.1 Semiconductor Lasers and SOAs

An InGaAsP semiconductor laser was used in a 1987 experiment [81] as a Fabry–Perot amplifier by biasing it at slightly below threshold (97% level). Two other 1.53- μm lasers with a frequency difference of only 1 GHz were used for holding and control beams. The flip-flop could be switched on and off, but the switching time in this experiment was relatively long ($>1 \mu\text{s}$). In a 2000 experiment [78], a DFB laser was biased below threshold, and the resulting SOA was employed as an optically bistable

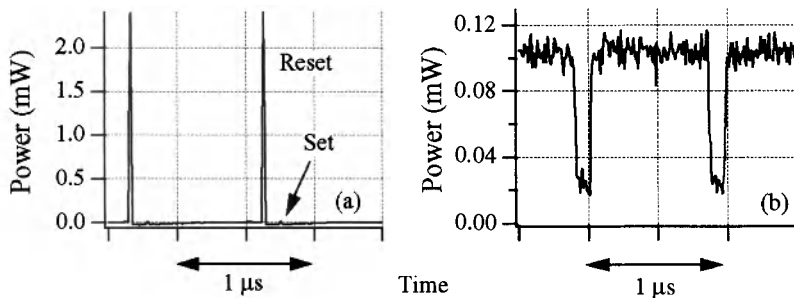


Figure 11.13: Operating characteristics of an optical flip-flop built using a DFB laser biased slightly below threshold. (a) Sequence of set (small peaks) and reset pulses; (b) output power as a function of time. (After Ref. [78]; ©2000 OSA.)

device. The holding beam at 1,547 nm was tuned toward the longer-wavelength side of the Bragg resonance. Set and reset pulses were 15-ns-wide and were obtained from two InGaAsP lasers operating at 1,567 and 1,306 nm, respectively. The set pulse had a peak power of only 22 μ W (0.33-pJ energy), while the peak power of reset pulses was close to 2.5 mW (36-pJ energy). Figure 11.13 shows (a) a sequence of two set and two reset pulses together with (b) the output of the flip-flop. Such a device is capable of switching on a time scale comparable to the carrier lifetime (\sim 1 ns).

The physical mechanism behind such a flip-flop is related to the shift in the stop band of the grating as the refractive index changes in response to variations in the carrier density. The set pulse saturates the SOA gain, reduces the carrier density, and thus increases the effective refractive index \bar{n} and shifts the Bragg wavelength to longer wavelengths as the two are related by $\lambda_B = 2\bar{n}\Lambda$, where Λ is the grating period. In contrast, the reset pulse is absorbed by the SOA. Resulting increase in the carrier density decreases the refractive index \bar{n} and shifts the Bragg wavelength toward shorter wavelengths. The wavelength of set pulses must be within the gain bandwidth of the SOA so that it can saturate the amplifier. The exact wavelength of the reset pulse is not important as long as it is shorter than the holding-beam wavelength by an amount large enough that it falls outside the gain bandwidth and is thus absorbed by the amplifier. Thus, both control signals have a broad wavelength range of operation. The polarization of the reset pulse does not play any role. The dependence on the polarization of the set pulse can be reduced by designing the SOA appropriately. As control signals operate independently from the holding beam, they can propagate in a direction opposite to that of the holding beam; their role is only to change the carrier density. This transparency to the direction should be useful for system design.

Optical flip-flops has been constructed in recent years using several other designs [84]–[101]. In a 1995 experiment, flip-flop operation at 1.2 GHz was realized using a vertical-cavity surface-emitting laser (VCSEL) by injecting optical set and reset pulses with orthogonal polarizations [84]. The physical mechanism behind this flip-flop is related to polarization bistability. More specifically, the state of polarization of the output is switched from TE to TM by using set and reset pulses. In another experiment [86], an optical flip-flop was realized by switching between two modes of a semiconductor

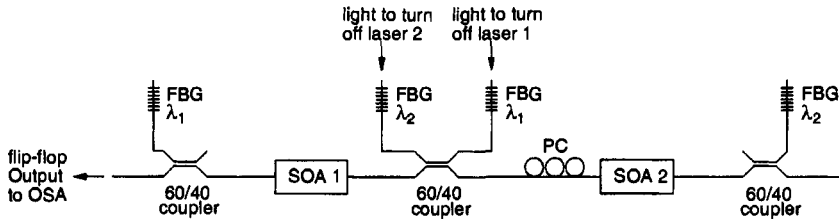


Figure 11.14: Optical flip-flop based on two coupled semiconductor lasers, each built using an SOA and two fiber gratings acting as mirrors. Each laser can be turned on and off by injecting light at a wavelength different than its own. (After Ref. [91]; ©2001 IEEE.)

laser. FWM in photorefractive crystals can also be used for making an optical flip-flop when the feedback is provided by placing the crystal in a ring cavity [87]. However, the speed of such a device is limited by the response time of the photorefractive crystal. A VSCEL laser biased below threshold was used as a bistable amplifier in 2009 to realize a flip-flop operating in the reflection mode [99].

In another scheme, injection of CW light into a DFB laser created optical bistability through the spatial hole burning effect [98]. Switching between the low- and high-power states was realized by injecting low-energy (~ 0.2 pJ) set and reset pulses into the DFB laser from opposite directions. Such a flip-flop could be switched on within a duration < 75 ps at repetition rates of up to 2 GHz.

Passive semiconductor waveguides can also be used for constructing an all-optical flip-flop [89]. Such devices cannot employ gain saturation as the nonlinear mechanism. Instead, they often operate below the bandgap of the semiconductor material and employ the optical Kerr effect to introduce intensity-dependent changes in the refractive index. A Bragg grating is also fabricated along the waveguide length to make the device bistable. Because of the electronic nature of the Kerr nonlinearity, such optical flip-flops can respond at time scales of picoseconds or shorter. This is the main advantage of passive waveguides compared with SOAs whose response time is limited by the carrier lifetime.

11.2.2 Coupled Semiconductor Lasers and SOAs

Several kinds of flip-flops have been made by coupling two lasers or SOAs. The use of two mutually synchronized semiconductor lasers was proposed in 1997 [88]. By 2001, two coupled semiconductor lasers were used for making flip-flops in which the output wavelength was switched between two values by selectively turning one of the lasers off [91]. Figure 11.14 shows the experimental scheme. Two lasers, each built using an SOA and two fiber Bragg gratings acting as mirrors, operate at different wavelengths, say, λ_1 and λ_2 . One of the lasers is selectively turned off using the technique of *gain quenching* by injecting light at a wavelength different than that at which the laser operates in isolation. As a result, the output wavelength can be switched between λ_1 and λ_2 using optical controls.

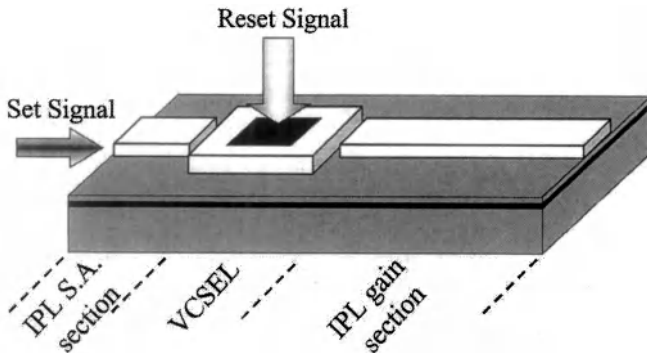


Figure 11.15: Schematic of an optical flip-flop in which a VCSEL is integrated with an in-plane laser (IPL) containing a short unbiased section acting as a saturable absorber (S.A.). Directions of set and reset pulses are also shown. (After Ref. [90]; ©2000 IEEE.)

An optical flip-flop in which two coupled lasers were integrated on the same chip has also been fabricated [90]. In this device shown schematically in Figure 11.15, a VCSEL is integrated with an edge-emitting laser. The two lasers share the same active region and are mutually coupled through gain saturation since they compete for the gain in this shared region. The edge-emitting laser contains a short unbiased section that acts as a saturable absorber and makes it bistable. This laser is biased such that its output is relatively weak (off state). A set pulse injected into the absorber switches the laser to the “on” state because it reduces cavity losses by saturating the absorber. The device can be turned off by injecting a reset pulse through the VCSEL if the pulse is intense enough to saturate the gain in the active region shared by the two lasers. As the intracavity intensity is reduced in response to lower gain, eventually it becomes too low to saturate the absorber; this results in increased cavity losses, and the device returns to the original “off” state. This cycle can be repeated to switch the flip-flop on and off using set and reset pulses. In another scheme, two active waveguides were coupled using a multimode-interference (MMI) coupler and two saturable absorbers were incorporated within a semiconductor laser cavity such that it exhibited bistability with respect to its two transverse modes when controlled by the set and reset pulses [96].

In an interesting scheme, optical feedback between an SOA and a DFB laser is employed to realize a flip-flop [97]. The bidirectional coupling between the two is exploited to realize bistable operating by injecting low-energy (~ 5 pJ) set and reset pulses from the opposite directions. The flip-flop exhibited an on-off ratio of more than 15 and could be operated at a repetition rate of 0.5 GHz using 150-ps-wide pulses. In another scheme shown schematically in Figure 11.16, two Mach-Zehnder (MZ) interferometers, with an SOA in one of their arms, were coupled to realize flip-flop operation. Coupling between the two interferometers provides the bistability by allowing switching between the two CW holding beams launched at different wavelengths. The whole device, named optical static random-access-memory (RAM) cell, could be integrated monolithically using a hybrid technology in which InP chips are flip-bonded

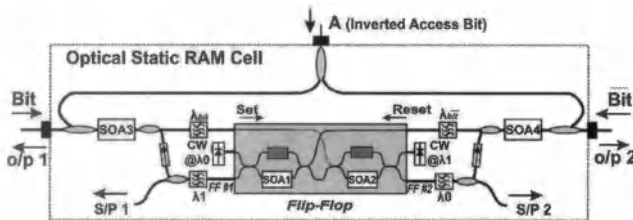


Figure 11.16: (a) Schematic of an integrated flip-flop made by coupling two MZ interferometers with SOAs in their arms. (After Ref. [100]; ©2009 IEEE.)

onto a silicon platform [100]. Such a device exhibited read and write functionality at a bit rate of 5 Gb/s.

In a 2010 experiment, a flip-flop was realized through heterogeneous integration of an InP microdisk laser (diameter 7.5 μm) that was coupled to a silicon waveguide, fabricated with the silicon-on-insulator technology [101]. At low bias currents, the laser operated in both the clockwise and counter-clockwise directions, but it operated in one direction only at high currents because the two effective lasers were coupled through their common gain medium. The bistable operation between the clockwise and counter-clockwise directions was exploited to make the flip-flop. More specifically, when the set and rest pulses were injected into the laser from the opposite directions, the laser switched its direction of operation. Such a device exhibited switching in 60 ps with only 1.8 fJ of injected pulse energy.

11.3 Wavelength Converters

Optical networks in which WDM channels are switched based on their carrier wavelengths require a device that can change the carrier wavelength of the channel without affecting its bit pattern that contains the information being transmitted. A large number of such devices have been developed based on both optical fibers and semiconductor materials. This section considers some of them and with focus on their performance from a system standpoint.

11.3.1 XPM-Based Wavelength Converters

We first focus on fiber-based wavelength converters in which the nonlinear phenomenon of XPM is employed for optical switching. The basic idea behind this technique has been discussed in Section 11.1.1 in the context of XPM-induced switching and is illustrated schematically in Figure 11.17. The data channel whose wavelength λ_2 needs to be changed is propagated inside a fiber of appropriate length together with a CW seed whose wavelength λ_1 is chosen to coincide with the desired wavelength of the converted signal. It acts as a pump and imposes an XPM-induced phase shift on the CW seed only in the time slots associated with the 1 bits. This phase shift is converted into amplitude modulation using an interferometer. In practice, a NOLM acting as a Sagnac interferometer is employed for this purpose [102]–[104]. The new feature in

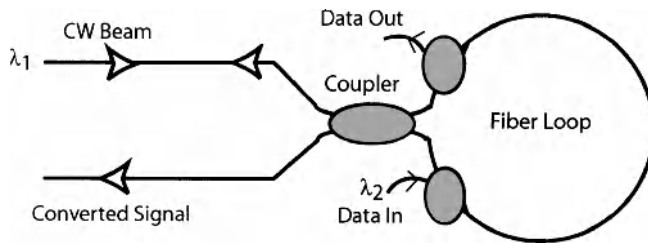


Figure 11.17: A wavelength converter making use of XPM-induced phase shifts inside a Sagnac interferometer to change the data wavelength from λ_2 to λ_1 .

Figure 11.17 is that the data channel is launched such that it affects the CW seed in only one direction, resulting in a differential phase shift that can be used to copy the bit pattern of the data channel onto the transmitted λ_1 signal.

In a 1994 experiment, the wavelength of a 10-Gb/s data channel was shifted by 8 nm using 4.5-km of dispersion-shifted fiber inside an NOLM [102]. By the year 2000, this technique provided wavelength converters capable of operating at bit rates of up to 40 Gb/s [24]. The NOLM was made using 3 km of dispersion-shifted fiber with its zero-dispersion wavelength at 1555 nm, and it was used to shift the wavelength of a 1547-nm channel by as much as 20 nm. The on-off ratio between the maximum and minimum transmission states was measured to be 25 dB. The optical eye diagrams of the original and wavelength-converted signals indicated that individual pulses were almost unaffected during wavelength conversion.

One may ask what limits the extent of wavelength shift when an NOLM is used for wavelength conversion. The answer is related to different group velocities associated with the two fields interacting through XPM. To estimate the maximum wavelength shift, let us assume that L should be less than the walk-off length L_w . Noting that, for two channels separated in frequency by $\delta\nu$, the walk-off parameter d_w is related to fiber dispersion as $d_w = |\beta_2|(2\pi\delta\nu)$, the condition $L < L_w$ reduces to

$$\delta\nu < T_0/(2\pi\beta_2 L). \quad (11.3.1)$$

The required fiber length is obtained from the requirement that $2\gamma P_0 L$ must equal π for wavelength conversion to occur. For a dispersion shifted fiber, L should exceed 1 km if the input peak power P_0 is limited to near 1 W. Using $L = 2$ km and $T_0 = 20$ ps with $\beta_2 = 1 \text{ ps}^2/\text{km}$, The frequency difference $\delta\nu$ is close to 1.5 THz, a value that corresponds to a wavelength difference of 12 nm.

The required fiber length can be reduced considerably by employing highly nonlinear fibers for which γ exceeds $10 \text{ W}^{-1}/\text{km}$. In a 2001 experiment [104], wavelength conversion of 0.5-ps pulses was realized using an NOLM with just 50 m of a highly nonlinear fiber with $\gamma = 20.4 \text{ W}^{-1}/\text{km}$. Because of such a short length of the fiber loop, the wavelength could be shifted by 26 nm even for such short pulses. The peak power of input pulses required for a π phase shift was close to 4 W in this experiment.

It is not essential to use an optical interferometer for XPM-based wavelength converters. In a simpler approach shown schematically in Figure 11.18, the bit stream

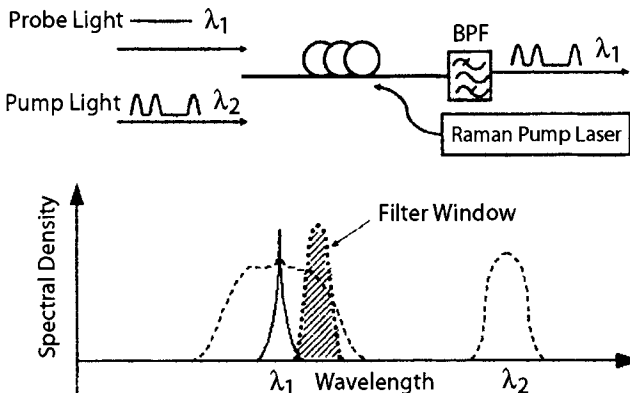


Figure 11.18: Schematic of an XPM-based wavelength converter; The bandpass filter (BPF) is offset from the probe wavelength to select only a part of the XPM-broadened spectrum. (From Ref. [110]; ©2005 IEEE.)

acting as the pump is launched into a nonlinear fiber together with a CW probe and the output is passed through a suitable optical filter [105]–[112]. Pump pulses at the wavelength λ_2 affect the spectrum of the CW probe (at the desired wavelength λ_1) through XPM only in the time slots associated with the 1 bits. If the passband of the optical filter is shifted from λ_1 by a suitable amount, the output is a replica of the original bit stream at the new wavelength. Any optical filter with a bandwidth larger than that of the data channel (0.5 nm or so) can be used for this purpose, including a fiber grating. In a 2000 experiment [105], the wavelength of a 40-Gb/s signal was shifted by several nanometers through XPM inside a 10-km-long fiber. This experiment employed a 4-m loop made of polarization-maintaining fiber as a notch filter. The magnitude of wavelength shift was limited by the 10-km length of the fiber in which XPM occurred.

Much larger wavelength shifts have been realized by employing highly nonlinear fibers. In a 2001 experiment [106], wavelength conversion at a bit rate of 80 Gb/s was performed by using such a 1-km-long fiber with $\gamma = 11 \text{ W}^{-1}/\text{km}$. The zero-dispersion wavelength of the fiber was 1552 nm with a relatively small dispersion slope near this wavelength. The 80-Gb/s data channel at the 1560-nm wavelength was first amplified to the 70-mW power level then coupled into the fiber together with a CW probe whose wavelength was varied in the range of 1525–1554 nm. A tunable optical filter with a 1.5-nm bandwidth was used at the fiber output to produce the wavelength-converted channel. Figure 11.19(a) shows the optical spectra just before and after the optical filter at a probe wavelength of 1545.6 nm. Before the filter, the probe spectrum shows multiple sidebands generated through XPM with a dominant peak at 1545.6 nm. After the filter, the carrier has been suppressed relative to the sidebands, resulting in a wavelength-converted signal with a bit stream identical to that of the original channel. The pulse width of the converted signal is shown in Figure 11.19(b) as a function of probe wavelength. As seen there, the width remains nearly unchanged over a wide bandwidth. The BER measurements indicated negligible power penalty for such a wavelength converter.

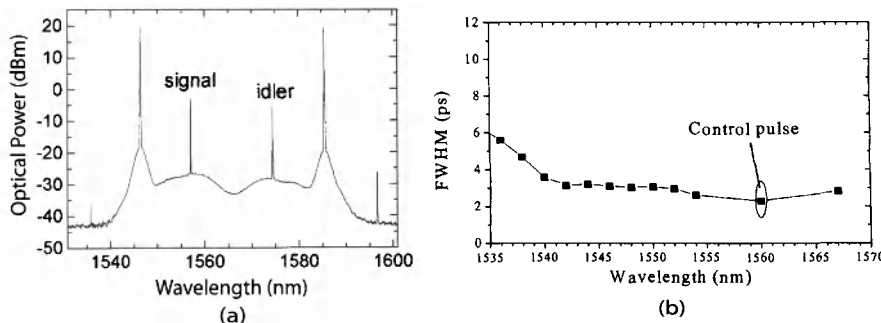


Figure 11.19: (a) Optical spectra measured before and after the tunable optical filter (TOF). (b) Pulse width of converted channel as a function of its wavelength. The width of original data channel is marked as control pulse. (From Ref. [106]; ©2001 IEEE.)

Wavelength conversion at a bit rate of 160 Gb/s was realized in a 2004 experiment in which a 0.5-km-long dispersion-shifted fiber was employed to produce the XPM-induced phase shift [108]. This fiber was followed with a fiber grating that acted as a notch filter and two other optical filters with bandwidths of 5 and 4 nm whose pass bands were offset from the carrier frequency of the input signal by 160 GHz. It was observed that the wavelength converter maintained the phase of the input signal, a desirable property from the system standpoint. The performance of such wavelength converters improves further if the Raman gain of the fiber is utilized to enhance the XPM-induced phase shift by pumping the fiber in the backward direction, as indicated in Figure 11.18. In a 2005 experiment, the efficiency improved by 21 dB when a 1-km-long highly nonlinear fiber was pumped with 600-mW of pump power [110].

Fiber lengths required to impose sufficient XPM-induced phase shifts can be reduced to below 10 m if microstructured fibers with an ultrasmall effective mode area are employed. Indeed, only 5.8 m of a highly nonlinear fiber was needed in a 2003 experiment in which a fiber grating was used as a narrowband tunable filter [107]. The wavelength of the converted channel was tunable over a 15-nm bandwidth in the normal dispersion region of the fiber. Such a large bandwidth was possible because of a reduction in the walk-off effects for short fibers. The use of normal dispersion eliminates the coherence degradation occurring in the case of anomalous dispersion because of the amplification of laser-intensity noise through modulation instability.

Even shorter fiber lengths are possible if one makes use of a nonsilica fiber with a relatively large value of the parameter n_2 . In a 2006 experiment, only a 1-m-long piece of bismuth-oxide fiber was used to change the wavelength of a 10-Gb/s NRZ signal by as much as 15 nm [111]. The fiber exhibited normal dispersion of $330 \text{ ps}^2/\text{km}$ with $\gamma \approx 1100 \text{ W}^{-1}/\text{km}$ at the 1550-nm wavelength. Because of its short length, the onset of SBS was not an issue as the SBS threshold was $>1 \text{ W}$. For the same reason, the walk-off effects were negligible. The wavelength conversion in this experiment was based on the XPM-induced nonlinear polarization rotation that makes the fiber act as a Kerr shutter [2]. More specifically, the data channel causing the XPM and the CW beam are launched such that their linear states of polarizations are oriented at 45° . The

XPM-induced phase shift changes the polarization of the CW beam only in time slots of 1 bits but leaves the polarization of 0 bits unchanged. A polarizer is used to select the wavelength-converted bits.

A practical issue with most wavelength converters is related to the polarization-sensitive nature of XPM in optical fibers. It is well known that the XPM-induced nonlinear phase shift depends on the relative states of polarization of the pump and probe waves [2], and it acquires its maximum value when the two waves are copolarized. The polarization state of a data channel in a lightwave system is not fixed and can change with time in a virtually random fashion, and such polarization changes would manifest as fluctuations in the peak power of wavelength-converted pulses. It turns out that a polarization-insensitive wavelength converter can be realized by twisting the highly nonlinear fiber in which XPM occurs such that the fiber acquires a constant circular birefringence. In a 2006 experiment [112], this technique was employed to convert the wavelength of a 160-Gb/s data channel with only 0.7-dB polarization sensitivity. Optical fibers exhibiting circular birefringence are useful for a variety of optical signal-processing applications [113].

11.3.2 FWM-Based Wavelength Converters

FWM-based wavelength converter requires a parametric amplifier such as the one shown in Figure 11.4. If the frequency ω_s of a signal needs to be converted to ω_i , it is launched inside the fiber together with a CW pump whose frequency ω_p is exactly in the middle so that the energy conservation condition, $2\omega_p = \omega_s + \omega_i$, is satisfied. As discussed in Section 11.1.2, such a FWM process generates an idler wave that mimics the bit pattern of the signal channel precisely because FWM occurs only during temporal slices allocated to 1 bits. No idler photons are produced during 0 bits because both the pump and signal photons must be present simultaneously for FWM to take place. As a result, if an optical filter is placed at the output end of the fiber that passes the idler but blocks the pump and signal, the output is a wavelength-converted replica of the original bit stream. Although the use of fibers for wavelength conversion was investigated as early as 1992 [114]–[116], the technique matured only after the advent of highly nonlinear fibers, whose use reduced the length of the fiber in which FWM takes place [117]–[127].

The conversion efficiency, defined as the ratio of output idler power at the end of a fiber of length L to the input signal power, is found from Eq. (11.1.14) to be

$$\eta_c = P_i(L)/P_s(0) = (\gamma P_0/g)^2 \sinh^2(gL). \quad (11.3.2)$$

This equation shows that η_c can exceed 1 when the phase-matching condition is nearly satisfied. In fact, $\eta_c = \sinh^2(\gamma P_0 L) \gg 1$ when $\kappa = 0$ and $\gamma P_0 L > 1$. Thus, FWM-based wavelength converters can amplify a bit stream, while switching its wavelength from ω_s to ω_i . This is an extremely useful feature of such wavelength converters. Of course, the signal is also amplified. In essence, one has two amplified copies of the input bit stream at two different wavelengths.

It follows from Eq. (11.3.2) that the conversion efficiency η_c depends on the phase mismatch κ and the fiber length L through the product κL . It turns out that the range

of detunings $\delta \equiv \omega_p - \omega_s$ over which κL can be made small shrinks rapidly for long fibers. This feature can be seen more clearly from the relation

$$\kappa = \beta_2 \delta^2 + 2\gamma P_0, \quad (11.3.3)$$

where $\beta_2 \approx (\omega_p - \omega_0)\beta_3$ and β_3 is the third-order dispersion parameter at the zero-dispersion frequency ω_0 of the fiber. For a given value of δ , the phase mismatch κ can be made zero by choosing the pump wavelength in the anomalous-dispersion regime such that $\beta_2 = -2\gamma P_0/\delta^2$. However, if the signal wavelength deviates from this specific value of δ , η_c decreases at a rate that depends on the fiber length L . As a result, the bandwidth over which wavelength conversion can be realized for a specific pump wavelength is relatively narrow for long fibers (< 10 nm for $L > 10$ km), but it can be increased to beyond 80 nm for fibers shorter than 100 m [30].

Experimental results on wavelength conversion are in agreement with this simple prediction of FWM theory. In the original 1992 experiment, the use of a 10-km-long dispersion-shifted fiber restricted the wavelength range to 8 nm or so [114]. By 1998, the use of a 720-m-long highly nonlinear fiber with a γ value of $10 \text{ W}^{-1}/\text{km}$ permitted wavelength conversion over 40 nm with only 600 mW of pump powers [29]. The conversion efficiency varied with signal wavelength but was as high as 28 dB, indicating that the wavelength-converted signal was amplified by up to a factor of 630 because of FWM-induced parametric amplification. An added advantage of the wide bandwidth is that such a device can be used to convert wavelengths of multiple channels simultaneously. In a 2000 experiment [30], simultaneous conversion of 26 channels covering wavelengths ranging from 1570 to 1611 nm bandwidth was realized using a 100-m-long section of a highly nonlinear fiber with $\gamma = 13.8 \text{ W}^{-1}/\text{km}$. The conversion efficiency was relatively low in this experiment (close to -19 dB) because the launched pump power was limited to 200 mW by the onset of SBS.

The onset of SBS becomes even more serious for wavelength converters that employ longer fibers and want to maintain a high conversion efficiency. The SBS threshold is around 5 mW for long fibers (> 10 km) and increases to near 50 mW for fiber lengths of 1 km or so. Since fiber-optic parametric amplifiers require pump power levels approaching 1 W, a suitable technique is needed that raises the threshold of SBS and suppresses it over the amplifier length. A common technique used in practice modulates the pump phase either at several fixed frequencies near 1 GHz [33], or over a broad frequency range using a pseudorandom pattern at a bit rate as high as 10 Gb/s [34]. This technique suppresses SBS by broadening the pump spectrum but it does not affect the parametric gain much. However, the SNR both the signal and idler is reduced when dispersive effects within the fiber convert phase modulation into amplitude modulation of the pump [118]. Pump-phase modulation also leads to broadening of the idler spectrum, making it twice as broad as the pump spectrum. Such broadening of the idler is of concern for wavelength converters: It is avoided in practice using dual-pump parametric amplifiers that also have other advantages.

As seen in Section 11.1.2, the dual-pump configuration provides nearly uniform gain over a wide bandwidth, while allowing polarization-independent operation of the device. The suppression of idler broadening can be understood by noting that the complex amplitude A_i of the idler field resulting from the FWM process has the form

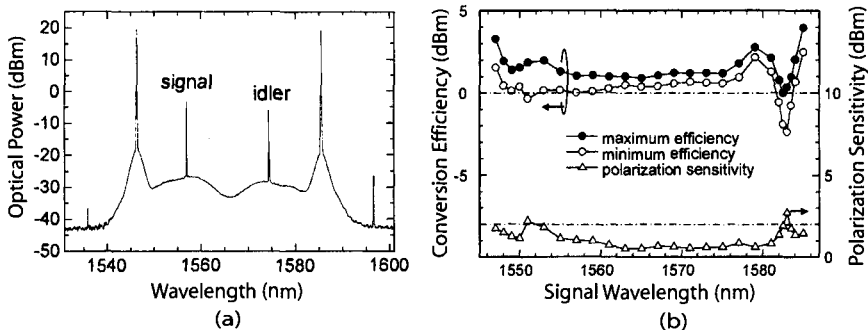


Figure 11.20: (a) Optical spectrum measured for a FWM-based wavelength converter. Two dominant peaks correspond to two orthogonally polarized pumps. (b) Conversion efficiency and its polarization sensitivity as a function of signal wavelength. (From Ref. [36]; ©2003 IEEE.)

$A_i \propto A_{p1}A_{p2}A_s^*$, where A_{p1} and A_{p2} are the pump amplitudes [2]. Clearly, the phase of the idler would vary with time if the two pumps are modulated either in phase or in a random manner. However, If the two pumps are modulated such that their phases are always equal but opposite in sign, the product $A_{p1}A_{p2}$ will not exhibit any modulation. As a result, even though the idler spectrum will be a mirror image of the signal spectrum, the bandwidth of the two spectra will be identical. A digital approach makes use of binary phase modulation so that the phase of both pumps is modulated in the same direction but takes only two discrete values, namely 0 and π . This approach works because the product $A_{p1}A_{p2}$ does not change under such a modulation scheme. The polarization problem is solved by using two orthogonally polarized pumps [34].

Figure 11.20(a) shows the optical spectrum recorded at the output when a 1557-nm signal was launched inside a dual-pump wavelength converter [36]. The two pumps had power levels of 118 and 148 mW at wavelengths of 1585.5 and 1546.5 nm, respectively. The power was higher at the shorter wavelength to offset the Raman-induced power transfer to the longer-wavelength pump. FWM occurred inside a 1-km-long highly nonlinear fiber ($\gamma = 18 \text{ W}^{-1}/\text{km}$). The zero-dispersion wavelength of the fiber was 1566 nm with a dispersion slope of $0.027 \text{ ps/nm}^2/\text{km}$ at this wavelength. The idler generated through FWM near 1570 nm had the same bit pattern as the signal. Its average power was also comparable to that of the signal, indicating nearly 100% efficiency for such a wavelength converter. In fact, as shown in Figure 11.20(b), high efficiency could be maintained over a bandwidth of 40 nm or so. The efficiency varied somewhat with the signal SOP but variations were below 2 dB over a 30-nm range. The wavelength of multiple channels can be converted simultaneously by such parametric amplifiers [119]. It is also noteworthy that a single signal channel creates multiple idlers at different wavelengths that carry the same information as the signal, resulting in the so-called wavelength multicasting.

Fiber-based wavelength converters have benefited considerably with the advent of photonic crystal fibers (PCFs) and non-silica fibers [121]–[127]. A 64-m-long PCF was used in a 2005 experiment [121]. It had a relatively constant dispersion over a 100-nm bandwidth centered near 1550 nm with a small effective mode area. These two

features permitted efficient wavelength conversion in spite of a relatively short length of the fiber. In a later experiment, a similar device was used with success for converting the wavelength of a 40-Gb/s signal coded with the DPSK format [122]. The highest conversion bandwidth of 100 nm was realized in another 2005 experiment in which the PCF length was reduced to only 20 m [123].

The shortest fiber length of only 40 cm for a wavelength converter was made possible with the advent of the bismuth-oxide fibers [124]. Such fibers exhibit a value of the Kerr nonlinearity n_2 that is 70 times larger than that of silica fibers. As a result, by reducing the core diameter to below 4 μm , the value of the nonlinear parameter γ can be increased to beyond 1000 W^{-1}/km . Such fibers exhibit FWM even when their length is below 1 m. Moreover, their SBS threshold is large enough that one does not have to modulate the pump phase. In the 2006 experiment the wavelength of a 40-Gb/s signal could be converted with -16 dB conversion efficiency by launching about 1 W of CW pump power into a 40-cm-long bismuth-oxide fiber. A PCF design was employed in 2007 for a 1-m-long bismuth-oxide fiber to realize wavelength conversion of 10-Gb/s channels over a 35-nm bandwidth [126].

11.3.3 Passive Semiconductor Waveguides

In place of optical fibers, passive semiconductor waveguides can be employed for wavelength conversion. FWM in silicon waveguides has been used for wavelength conversion in several recent experiments [38]–[44]. As discussed earlier in Section 11.1.2, the performance of such waveguides is limited by free carriers that are generated through TPA when the waveguide is pumped continuously near 1550 nm. For typical values of the carrier lifetime in silicon waveguides (>1 ns), the density of free carriers builds up to the extent that losses induced by them reduce the conversion efficiency to below -10 dB under CW pumping. For this reason, early experiments solved this problem by employing picosecond pump pulses.

CW pumping was employed in a 2006 experiment in which the use of 160-mW of pump power inside a 2.8-cm-long silicon waveguide provided a conversion efficiency of -10.6 dB for a 10-Gb/s channel [39]. The channel bit rate was soon extended to 40 Gb/s in a 2006 experiment in which the effective carrier lifetime was reduced by using a reversed-biased silicon waveguide [41]. A conversion efficiency of -8.6 dB at a pump power of 450 mW could be realized using a 8-cm-long waveguide with 25 V of reverse bias that decreased the density of free carriers by removing them from the region where FWM took place. In another experiment, the objective was to enhance the bandwidth over which wavelength conversion can be realized [42]. By controlling the waveguide dispersion through device dimensions, a bandwidth of more than 150 nm could be realized with pulsed pumping, but the conversion efficiency was limited to below -9.5 dB in this experiment. By 2009, 40-Gb/s wavelength conversion with CW pumping was realized over a bandwidth of more than 50 nm using a 1.1-cm-long silicon waveguide, but the conversion efficiency was only -18 dBm in this experiment [43]. These results show that it will be difficult to realize a net gain at the converted wavelength with silicon waveguides.

LiNbO_3 waveguides provide an alternative approach. They exhibit a finite second-order susceptibility $\chi^{(2)}$ that can be used for three-wave mixing, a process for which

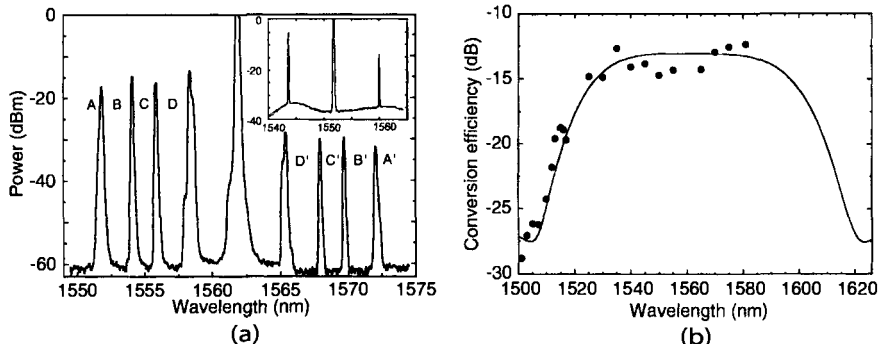


Figure 11.21: (a) Simultaneous wavelength conversion of four channels in a PPLN waveguide pumped at 1562 nm with 110-mW power. Inset shows 16% conversion efficiency realized at a pump power of 165 mW. (b) Conversion efficiencies measured as a function of signal wavelength are shown on the right together with the theoretical prediction. (After Ref. [129]; ©1999 IEEE.)

the idler frequency is given by $\omega_i = \omega_p - \omega_s$ when pump and signal waves interact inside the waveguide. This process is also called difference-frequency generation, and it requires a phase-matching condition to be satisfied. As early as 1993, a LiNbO₃ waveguide was used for wavelength conversion [128] by employing the technique of periodic poling in which the sign of $\chi^{(2)}$ is inverted periodically along the waveguide length for realizing quasi-phase matching.

Such devices require the use of a single-mode pump laser operating in the spectral region near 780 nm with 50–100 mW of power. In practice, it is difficult to simultaneously couple a 780-nm pump and a 1550-nm signal into the fundamental mode of the waveguide. An alternative scheme makes use of two cascaded second-order nonlinear processes occurring in a periodically poled LiNbO₃ (PPLN) waveguide using a pump laser operating near 1550 nm [129]–[137]. In such a wavelength converter, the pump at a frequency ω_p is first up-converted to $2\omega_p$ through second-harmonic generation, which then generates wavelength-shifted output through difference-frequency generation. Such a cascaded process mimics FWM, but is much more efficient than FWM based on third-order susceptibility. It is also less noisy than the FWM process occurring inside the active region of SOAs.

Multiple WDM channels can be converted simultaneously using a PPLN waveguide. Figure 11.21(a) shows the optical spectrum recorded in a 1999 experiment [129] in which four channels at wavelengths in the range of 1552 to 1558 nm were coupled into a PPLN waveguide together with a 1562-nm pump with 110 mW power. The four peaks on the right side of the pump peak represent the four wavelength-converted channels. The conversion efficiency is about 5% for all channels but it can be increased by increasing pump power. The inset shows wavelength conversion of a single channel with 16% efficiency at a pump power of 175 mW. The conversion efficiency depends on the wavelength separation between the pump and signal, as shown in Figure 11.21(b). The bandwidth of the flat region over which conversion efficiency is nearly constant is more than 60 nm. With a proper device design, conversion efficiencies of >70% have

been realized at a pump power of 150 mW [133].

LiNbO_3 devices can respond at femtosecond time scales and thus easily operate at bit rates of 40 Gb/s or more. Conversion of 160-Gb/s RZ signals was realized in a 2007 experiment [135] in which two pumps were used to realize tunable wavelength conversion. In this scheme, one pump at a fixed frequency ω_1 first combines with the signal at ω_s to generate the sum frequency $\omega_+ = \omega_1 + \omega_s$. This new wave then combines with the second pump at a tunable frequency ω_2 to generate the difference frequency $\omega_i = \omega_+ - \omega_2$. Such a scheme looks superficially similar to the dual-pump FWM in optical fibers but the idler frequency created by it, $\omega_i = \omega_1 - \omega_2 + \omega_s$, is different from that found in the fiber case. Its main advantage is that it provides additional control over the wavelength-conversion process.

11.3.4 SOA-Based Wavelength Converters

Several nonlinear techniques for wavelength conversion make use of SOAs [138]–[146]. FWM inside an SOA was used for this purpose during the 1990s, and it remains a strong candidate [141]. It is surprising that FWM can occur in SOAs because the carrier density cannot respond at the beat frequency of the pump and signal when the two differ by more than 10 GHz. The nonlinearity responsible for this process has its origin in fast intraband relaxation processes occurring at a time scale of 0.1 ps [147]. As a result, frequency shifts as large as 10 THz, corresponding to wavelength conversion over a range of 80 nm, are possible. For the same reason, this technique can work at bit rates as high as 100 Gb/s and is transparent to both the bit rate and the data format. Because of the gain provided by the amplifier, conversion efficiency can be quite high, resulting even in a net gain. An added advantage of this technique is the reversal of the frequency chirp since its use inverts the signal spectrum. The performance can be improved further using two SOAs in a tandem configuration.

A simple approach is based on cross-gain saturation, occurring when a weak field is amplified inside the SOA together with a strong field, and the amplification of the weak field is affected by the strong field [138]. To use this phenomenon, the WDM signal whose wavelength λ_1 needs to be converted is launched into the SOA together with a low-power CW beam at the wavelength λ_2 at which the converted signal is desired. Amplifier gain is mostly saturated by the λ_1 beam. As a result, the CW beam is amplified by a large amount during 0 bits (no saturation) but by a much smaller amount during 1 bits. Thus, the bit pattern of the incident signal is transferred to the new wavelength with reverse polarity (1 and 0 bits are interchanged).

The cross-gain saturation technique has been used in many experiments and can work at bit rates as high as 40 Gb/s [140]. It can provide net gain to the wavelength-converted signal. Its main disadvantages are (i) relatively low on–off contrast, (ii) degradation due to spontaneous emission, and (iii) phase distortion because of frequency chirping that invariably occurs in SOAs. The use of an absorbing medium in place of the SOA solves the polarity reversal problem. An electroabsorption modulator has been used for wavelength conversion with success [148]. It works on the principle of cross-absorption saturation. The device blocks the CW signal at λ_2 because of high absorption, except when the arrival of 1 bits at λ_1 saturates the absorption.

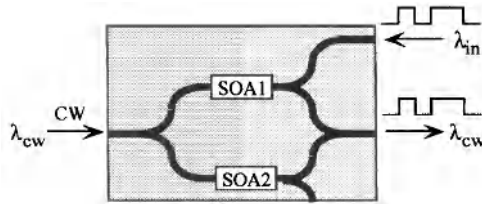


Figure 11.22: XPM-based wavelength conversion using two SOAs in wto arms of a MZ interferometer. (After Ref. [140]; ©1997 IEEE.)

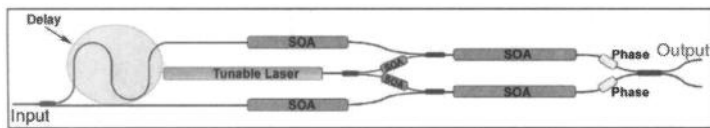


Figure 11.23: Schematic of a widely tunable wavelength converter with a monolithically integrated tunable semiconductor laser. (After Ref. [142]; ©2007 IEEE.)

The contrast problem can be solved by using a MZ interferometer, shown schematically in Figure 11.22, with an SOA in its each arm [140]. The CW signal at the wavelength λ_{cw} is split equally between the two arms but the WDM channel at the wavelength λ_{in} is sent through only one arm. During the 0 bits of this signal, the CW beam is blocked for a suitably balanced interferometer. However, during its 1 bits, the CW beam is directed toward the output port because of a change in the refractive index induced by the WDM signal. The net result is that the output of the MZ interferometer is an exact replica of the incident signal at the wavelength λ_{cw} . XPM is the physical mechanism involves in this wavelength-conversion scheme. It is preferable over cross-gain saturation because it does not reverse the bit pattern and results in a higher on-off contrast.

Other types of interferometers such as a Sagnac interferometer can also be used with similar results. The MZ interferometer is used in practice because it can be easily integrated on a single chip using InGaAsP/InP technology, resulting in a compact device. Figure 11.23 shows a schematic of a widely tunable, wavelength converter with a monolithically integrated tunable semiconductor laser [142]. In this device, the data channel whose wavelength needs to be converted is split into two parts that are fed into two arms of the interferometer with a suitable delay. Such a scheme permits the device to operate at a bit rate of 40 Gb/s in spite of a relatively slow gain recovery in two SOAs.

A much simpler configuration has been used in several recent experiments in which a single SOAs is employed with an optical bandpass filter at its output end whose pass-band is shifted from the probe wavelength by a small amount [143]–[146]. The basic idea is identical to that shown in Figure 11.18 except that an SOA replaces the optical fiber as a nonlinear element. In spite of a long gain-recover time of SOAs (~ 100 ps), such an XPM-based wavelength converter has been shown to work at bit rates as high as 320 Gb/s [144]. The physical process behind it has been termed transient XPM. How-

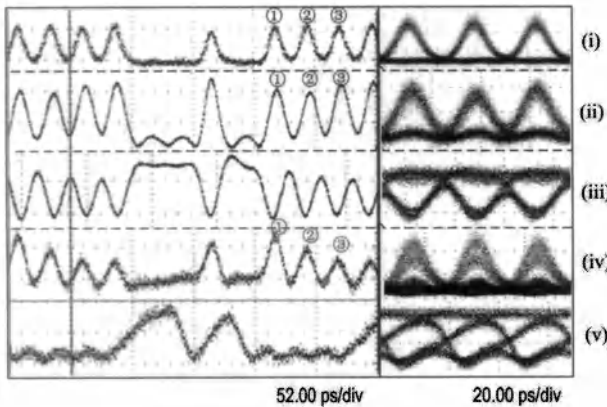


Figure 11.24: Bit patterns and the corresponding eye diagrams of the input (top) and wavelength-converted outputs at filer offsets of -0.3 , -0.1 , $+0.4$, and 0 nm using an SOA with a gain-recovery time of 60 ps. (After Ref. [146]; ©2008 IEEE.)

ever, one should keep in mind that cross-gain saturation plays an equally important role in the operation of such a device because it controls the magnitude of XPM-induced spectral broadening. In fact, depending on the exact location of the filter's passband, the wavelength-converted signal may exhibit a bit pattern that is inverted or noninverted with respect to that of the input data [146]. Recall that an inverted bit pattern has its origin in cross-gain saturation. The optical filter plays an important role in pulse shaping. It can even convert an inverted bit stream into a noninverted one [143].

Figure 11.24 shows the results of an experiment in which the wavelength of a 40-Gb/s RZ channel was down-shifted by about 6 nm using an SOA while the filer offset from the wavelength of the CW probe was varied from -0.3 to $+0.4$ nm. Top row (i) shows the input bit pattern and the corresponding eye diagram. Remaining 4 rows (ii to v) show the wavelength-converted output for a filer offset of -0.3 , -0.1 , $+0.4$, and 0 nm, respectively. The bit pattern is not inverted when the offset is -0.3 nm, but it becomes inverted when the offset is reduced to -0.1 nm. The eye diagrams are reasonable in both cases although amplitude jitter is enhanced because of pattern effects. The situation is worse for an offset of $+0.4$ nm. The worst-case situation (v) occurs for an offset of 0 nm because the effects of cross-gain saturation and slow gain recovery dominate in this case. Similar effects have been seen at higher bit rates but the transient XPM inside SOAs has been successfully used for converting wavelengths of channels operating at 160 and 320 Gb/s [144].

11.4 Ultrafast Optical Switching

Wavelength converters switch the entire bit stream at one wavelength to a different wavelength without affecting its temporal content. Some applications require selective switching of one or more bits to a different port [149]–[151]. An example is provided by *packet switching* in which a packet of tens or hundreds of bits is selected from a bit

stream. Another example is provided by the OTDM technique in which a selected bit of a high-speed bit stream is sent to another port in a periodic fashion. Such applications require time-domain switches that can be turned on for a specific duration using an external control.

11.4.1 Time-Domain Demultiplexing

As seen in Section 6.4, an OTDM signal consists of a high-speed bit stream that is composed of several channels, each operating at a lower bit rate and interwoven with others in a periodic fashion. If 10 channels, each operating at 40 Gb/s, are multiplexed in the time domain, every 10th bit of the composite 400-Gb/s bit stream belongs to the same channel. Demultiplexing a channel from such a high-speed OTDM signal requires optical switches that pick all the bits belonging to a specific channel and direct those bits to a different port. Such switches require an *optical clock* at the single-channel bit rate that is used to switch signal pulses selectively using a nonlinear phenomenon such as XPM or FWM (see Section 6.4.2).

Fiber-Based Demultiplexers

Figure 6.25 of Section 6.4.2 and discussion there show how XPM inside an NOLM or FWM inside a highly nonlinear fiber can be exploited for time-domain demultiplexing of OTDM channels. The FWM technique was used as early as 1996 to demultiplex 10-Gb/s channels from a 500-Gb/s bit stream using clock pulses of 1-ps duration [152]. A distinct advantage of using FWM is that the demultiplexed channel is also amplified through parametric gain inside the same fiber [153]. A problem with FWM-based demultiplexer is related to the polarization sensitivity of the FWM process itself because maximum parametric gain occurs only when the pump and signal are copolarized. If the state of polarization of a signal is not aligned with that of the pump and changes with time in an unpredictable manner, both the signal and idler power levels fluctuate, resulting in poor performance.

A polarization-diversity technique, in which the input signal is separated into two orthogonally polarized parts that are processed separately, can be used [154], but it adds considerable complexity. A simple scheme for solving the polarization problem was adopted in 2004. It consists of attaching a short piece of polarization-maintaining fiber (PMF) to the input port of the highly nonlinear fiber used for FWM and using an optical phase-locked loop for locking clock pulses to the peak position of incoming signal pulses [155]. As shown in Figure 11.25, the control clock pulses are polarized at 45° with respect to the principal axes of the polarization-maintaining fiber that also splits and separates randomly polarized signal pulses into two orthogonally polarized parts. Since two separate FWM processes take place simultaneously within the same nonlinear fiber, in essence, polarization diversity is realized with this simple experimental arrangement. Such an approach was capable of demultiplexing a 160-Gb/s bit stream into 10-Gb/s individual channels with <0.5 dB polarization sensitivity.

In another approach to solving the polarization problem, the nonlinear fiber in which FWM occurs is itself made birefringent [156]. Moreover, it is divided into two equal sections in which the fast and slow axes are reversed. A single pump in the form

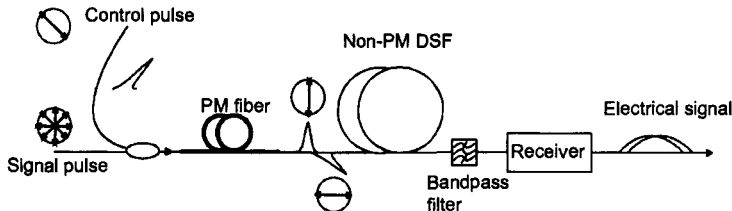


Figure 11.25: A polarization-insensitive FWM-based demultiplexing scheme; PM fiber and DSF stand for polarization-maintaining and dispersion-shifted fibers, respectively. (From Ref. [155]; ©2004 IEEE.)

of clock pulses, polarized at 45° with respect to the slow axis of the fiber, is launched together with the high-speed signal that needs to be demultiplexed. The orthogonally polarized components of the pump and signal interact through FWM and create the idler containing the demultiplexed channel. Even though the two polarization components separate from each other in the first section, they are brought back together in the second half of the fiber because of the reversal of the slow and fast axes in the second section. An optical filter at the end of the fiber blocks the pump and signal, resulting in the demultiplexed channel at the idler wavelength.

XPM-based demultiplexing based on NOLMs also suffers from the polarization issue. Several techniques can be employed for polarization-insensitive operation of an NOLM [157]–[160]. One among them is similar to that shown in Figure 11.25. A short piece of PMF is used to split the signal and clock pulses along its slow and fast axes. An optical bandpass filter centered at the signal wavelength is placed at one end of the NOLM so that it blocks the propagation of the clock pulse in one direction. However, this blocking occurs in the other direction only after the clock pulse has passed through the loop and has changed the phase of a specific signal pulse by π through XPM. As a result, data pulses belonging to the demultiplexed channel appear at the NOLM output, where a second PMF combines the two polarization components.

Similar to the case of wavelength conversion, it is not necessary to employ an NOLM for making use of XPM. In a 2001 experiment, a scheme is similar to that shown in Figure 11.18 was used for time-domain demultiplexing [161]. The only difference was that the role of probe at wavelength λ_1 was played by the OTDM data signal, while intense clock pulses at wavelength λ_2 played the role of the pump. The clock pulses shifted the spectrum through XPM of only those data pulses that overlap with them in the time domain. An optical filter was then used to select these pulses, resulting in a demultiplexed channel at the clock wavelength. This experiment used a 5-km-long fiber with its zero-dispersion wavelength at 1543 nm. The 14-ps control pulses at a repetition rate of 10 GHz had a wavelength of 1534 nm and were propagated with the 80-Gb/s OTDM signal at 1538.5 nm.

As seen in Section 11.1.1, the group-velocity mismatch between the signal and control pulses plays a major role in XPM-based optical switching. This mismatch can be reduced by locating the control and signal pulses on the opposite sides of the zero-dispersion wavelength of the fiber. In addition, the use of a highly nonlinear fiber not only reduces the required average power of control pulses but also helps with the prob-

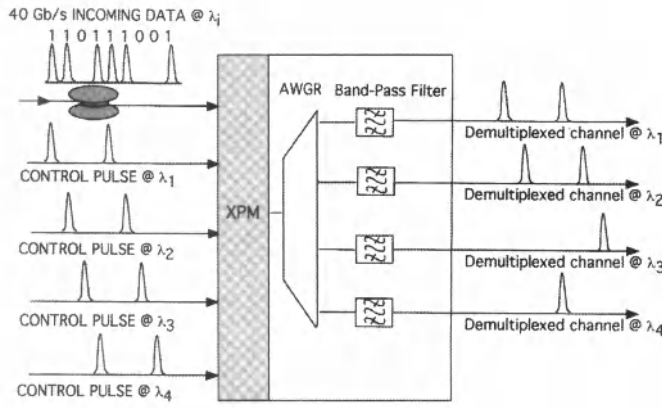


Figure 11.26: Simultaneous demultiplexing of 4 channels using 4 optical clocks at different wavelengths; AWGR stands for an arrayed-waveguide router. (From Ref. [162]; ©2002 IEEE.)

lem of group-velocity mismatch as much shorter lengths are needed. An added benefit of this technique is that it can be used to demultiplex multiple channels simultaneously by simply employing multiple control pulses at different wavelengths. Figure 11.26 shows such a scheme schematically [162]. It was implemented in a 2002 experiment to demultiplex four 10-Gb/s channels from a 40-Gb/s composite bit stream through XPM inside a 500-m-long highly nonlinear fiber. Only a 100-m-long fiber was employed in another experiment to demultiplex 10-Gb/s channels from a 160-Gb/s bit stream [163].

Much smaller fiber lengths can be employed by using microstructured fibers or a nonsilica fiber made of a material with high values of n_2 . Only a 1-m-long piece of bismuth-oxide fiber was needed in a 2005 experiment [164] because this fiber exhibited a value $\sim 1100 \text{ W}^{-1}/\text{km}$ for the nonlinear parameter γ . The train of 3.5-ps control pulses at a 10-GHz repetition rate was amplified to an average power level close to 0.4 W to ensure a high peak power ($P_0 > 10 \text{ W}$) so that the value of $\gamma P_0 L$ exceeded 10 even for the 1-m-long fiber. This experiment employed the fiber as a Kerr shutter [2] and made use of the XPM-induced nonlinear birefringence that changed the state of polarization of selected signal pulses such that only they were transmitted through the polarizer placed at the output end of the fiber. Because the walk-off effects were negligible for the short fiber, the measured switching window was narrow enough (only 2.6-ps wide) to demultiplex a 160-Gb/s bit stream.

Polarization-independent operation can be realized by using a linearly birefringent PMF or a spun fiber exhibiting circular birefringence [176]. A 30-m-long photonic crystal fiber exhibiting linear birefringence was employed in a 2006 experiment [165]. Clock pulses were polarized at 45° to the slow axis of the fiber so that their energy was divided equally between the slow and fast axes. The SOP of both the data and clock pulses evolved periodically with different beat lengths because of their different wavelengths. As a result, their relative SOP varied in a nearly random fashion. This feature resulted in an averaging of the XPM effect and produced an output that was independent of the signal polarization. In a later experiment, a high-speed polarization

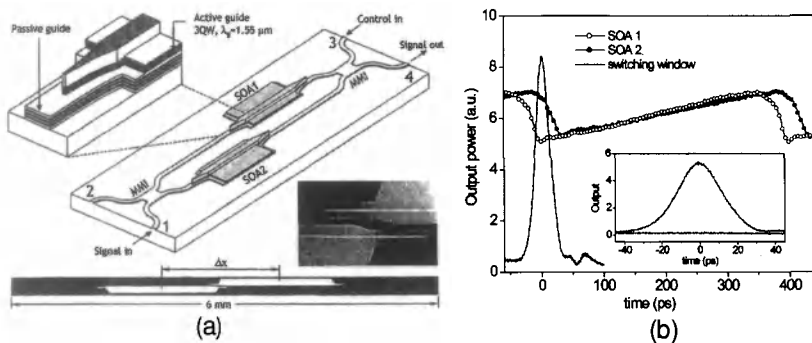


Figure 11.27: (a) A TOAD demultiplexer with two SOAs placed asymmetrically. Insets show the device structure. (b) Gain variations inside two SOAs and the resulting switching window. (After Ref. [175]; ©2001 IEEE.)

scrambler was employed to randomize the SOP of 160-Gb/s data pulses but the SOP of the 10-Gb/s clock pulses was kept fixed [166]. The XPM-induced spectral broadening occurred inside a 2-m-long bismuth-oxide fiber. Because of polarization scrambling, the performance of such a demultiplexer exhibited little sensitivity to the input SOP of the data bit stream.

SOA-Based Demultiplexers

The main limitation of a fiber-based demultiplexer stems from the weak fiber nonlinearity requiring long lengths. Although, the required fiber length can be reduced by using highly nonlinear fibers, the use of an SOA provides an alternative. Both the XPM and FWM schemes have been shown to work with SOAs [167]–[171]. An electro-absorption modulator has also been used for demultiplexing purposes [172]. In the case of an NOLM, an SOA is inserted within the fiber loop. The XPM-induced phase shift occurs because of changes in the refractive index induced by the clock pulses as they saturate the SOA gain. As the phase shift occurs selectively only for the data bits belonging to a specific channel, that channel is demultiplexed. The refractive-index change induced by the SOA is large enough that a relative phase shift of π can be induced at moderate power levels by an SOA of <1-mm length.

SOAs suffer from a relatively slow temporal response governed by the carrier lifetime (~ 100 ps). A faster response can be realized by using a gating scheme. For example, by placing an SOA asymmetrically within the NOLM such that the counter-propagating signals enter the SOA at different times, the device can be made to respond at a time scale ~ 1 ps. Such a device is referred to as the terahertz optical asymmetrical demultiplexer (TOAD). Its operation at bit rates as high as 250 Gb/s was demonstrated by 1994 [173]. An MZ interferometer with two SOAs in its two branches can also demultiplex an OTDM signal at high speeds and can be fabricated in the form an integrated compact chip using the InP technology. The silica-on-silicon technology has also been used to make a compact MZ demultiplexer in a symmetric configuration that was capable of demultiplexing a 168-Gb/s signal [174]. If the SOAs are placed in

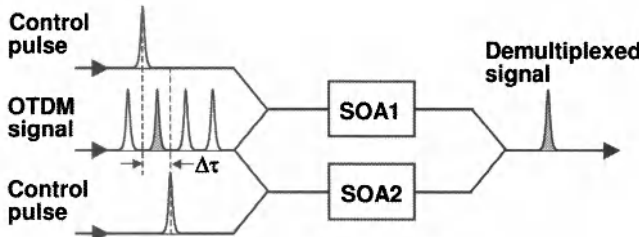


Figure 11.28: A demultiplexer based on the symmetric MZ configuration in which clock pulses are fed to two SOAs with a short relative delay. (After Ref. [178]; ©2009 IEEE.)

an asymmetric fashion, the device operates similar to a TOAD device. Figure 11.27(a) shows such a MZ device fabricated with the InGaAsP/InP technology [175]. The offset between the two SOAs plays a critical role in this device and is typically < 1 mm.

The operating principle behind the MZ-TOAD device can be understood from Figure 11.27. The clock signal (control) enters from port 3 of the MZ interferometer and is split into two branches. It enters the SOA1 first, saturates its gain, and opens the MZ switch through XPM-induced phase shift. A few picoseconds later, the SOA2 is saturated by the clock signal. The resulting phase shift closes the MZ switch. The duration of the switching window can be precisely controlled by the relative location of the two SOAs as shown in Figure 11.27(b). Such a device is not limited by the carrier lifetime and can operate at high bit rates when designed properly.

Several other SOA-based schemes have been implemented in recent years. In a 2006 experiment, transient XPM, discussed earlier in the context of wavelength conversion, was used to demultiplex 40-Gb/s channels from a 320-Gb/s OTDM bit stream [113]. This scheme employs an optical filter that is shifted from the clock wavelength by a suitable amount and works in a way identical to that of a wavelength converter. By 2007, it was extended to operate on a 640-Gb/s OTDM signal consisting of 0.8-ps-wide optical pulses [177]. In a 2009 experiment, a symmetric MZ configuration, shown schematically in Figure 11.28, was used for demultiplexing a 640-Gb/s bit stream [178]. The clock pulses at a repetition rate of 40 Gb/s were injected in both arms with a relative delay of about 1.4 ps. As seen in Figure 11.27, such a device can act as a gate that opens only for the duration of this relative delay despite of a slow response of two SOAs.

11.4.2 Data-Format Conversion

As we saw in Section 1.2.3, both the RZ and NRZ formats can be employed when is used for data transmission. The NRZ format is often employed in WDM networks as it is most efficient spectrally. The use of RZ format, or one of its variants such as the carrier-suppressed RZ (CSRZ) format, becomes necessary at high bit rates, and it is the format of choice for OTDM systems. In a network environment, the conversion among these formats may become necessary. Several techniques for conversion between the NRZ and RZ formats make use of the nonlinear effects occurring inside fibers or SOAs.

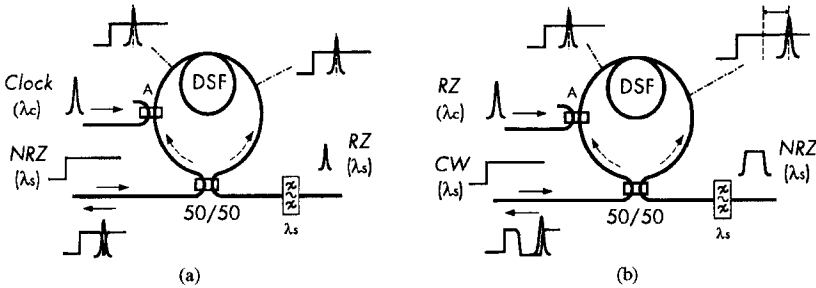


Figure 11.29: (a) NRZ-to-RZ and (b) RZ-to-NRZ conversion using an NOLM; DSF stands for dispersion-shifted fiber. (From Ref. [179]; ©1997 IEEE.)

Figure 11.29 shows how XPM inside an NOLM can be used for conversion between the NRZ and RZ formats [179]. In the case of NRZ-to-RZ conversion, the phase of NRZ pulses is shifted inside the loop by launching an optical clock (a regular train of pulses at the bit rate) such that it propagates in one direction only. In the case of RZ-to-NRZ conversion, the phase of a CW beam is shifted by the RZ data pulses propagating in one direction only. The main limitation is set by the walk-off effects that govern the switching window of the NOLM. An SOA-based NOLM has also been used to convert the RZ or NRZ bit stream into one with the CSRZ format [184].

Several other schemes have been developed in recent years for fiber-based format conversion [180]–[182]. In a 2005 experiment, the XPM-induced wavelength shift inside a nonlinear fiber was used for RZ-to-NRZ conversion [180]. The scheme is similar to that shown in Figure 11.18 (in the context of wavelength conversion), the only difference being that the optical filter is centered exactly at the wavelength of the CW probe. The RZ signal acts as the pump and modulates the phase of the CW probe. The resulting chirp shifts the wavelength of pulses representing 1 bits. The filter blocks these pulses but lets pass the 0 bits. The resulting bit stream is a polarity-reversed NRZ version of the original RZ signal.

A similar scheme can be adopted for NRZ-to-RZ conversion [181]. In this case, an optical clock acting as the pump is sent through the fiber together with the NRZ signal. The XPM interaction between the two broadens the signal spectrum. The optical filter is offset from the signal wavelength similar to the case of wavelength conversion. The output is an RZ version of the signal at the same wavelength. Such a scheme suffers from polarization sensitivity, because the nonlinear process of XPM itself is polarization dependent [2]. It can be made polarization insensitive by employing a polarization-diversity loop. The polarization of the clock (control) is oriented at 45° with respect to the principal axes of the polarizing beam splitter (PBS) so that its power is divided equally in two counterpropagating directions. The NRZ signal with a random SOP is also divided into two orthogonally polarized parts. The same PBS combines the two parts. An optical circulator directs the output toward an optical filter whose passband is offset properly.

A scheme for RZ-to-NRZ conversion makes use of only SPM-induced spectral broadening inside a normally dispersive optical fiber [182]. The RZ pulses are chirped

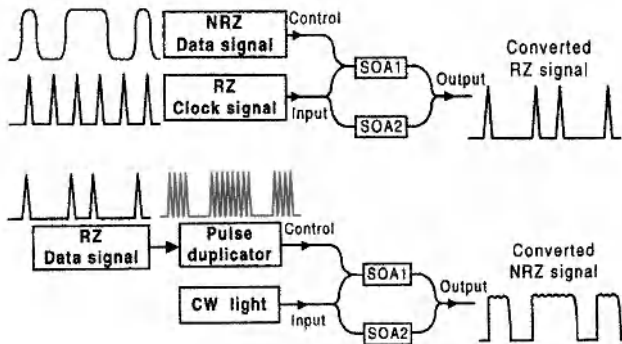


Figure 11.30: (a) NRZ-to-RZ and (b) RZ-to-NRZ conversion using two SOAs inside a MZ interferometer. (From Ref. [183]; ©2003 IEEE.)

through SPM and undergo considerable broadening inside the fiber. If the fiber length is chosen such that this pulse broadening is large enough to fill the entire bit slot, the output is an NRZ version of the original bit stream.

Several schemes make use of the nonlinear effects inside SOAs for format conversion [183]–[192]. A MZ interferometer with SOAs in its two arms was employed in a 2003 experiment [183]. Figure 11.30 shows the underlying idea schematically. In the case of NRZ-to-RZ conversion, input RZ signal is injection into into the control port, while an RZ clock at the same bit rate is fed into the interferometer designed to block clock pulses in the absence of the control signal. The phase shift induced by the NRZ signal converts clock pulses into an RZ signal. In the case of RZ-to-NRZ conversion, a pulse duplicator is employed to make multiple shifted copies of the input RZ signal (within one bit period) before it is injected into the control port. Multiple copies maintain the XPM-induced phase shift over the entire bit duration converting a CW beam into a NRZ signal. An SOA inside a Sagnac loop placed with a fixed offset from the loop center can be used to create a fast switch in a way similar to that shown in Figure 11.27. Such a loop was used in 2004 for converting the NRZ and RZ formats into the CSRZ format at a bit rate of 10 Gb/s [184]. It can also be used for NRZ-to-RZ conversion [185].

Similar to the case of wavelength conversion, it is not necessary to use an interferometer. Format conversion can be realized using FWM, XPM, or cross-gain saturation inside a single SOA. These nonlinear processes can also be used to realize conversion of RZ and NRZ formats to BPSK or DPSK formats [186]–[188]. In some cases, SOAs can be operated at a bit rate of up to 40 Gb/s. For example, XPM inside a single SOA was used in a 2007 experiment to convert a 42.6-Gb/s NRZ signal to the RZ format [189]. In another experiment, an optical filter was placed after the SOA to convert a 40-Gb/s NRZ signal such that its passband was offset from the signal wavelength by an optimum amount [190]. A 40-Gb/s RZ signal can also be converted to the NRZ format using cross-gain saturation [192]. The main point to note is that SOAs are quite useful for optical signal processing.

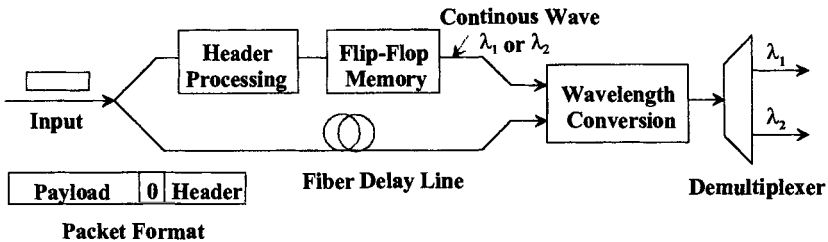


Figure 11.31: Design of an 1×2 all-optical packet switch directing its output to two different output ports depending on the header address. (After Ref. [193]; ©2003 IEEE.)

11.4.3 Packet Switching

Optical packet switching is a complicated process requiring many components for buffering, header processing, and switching [151]. Packet-switched networks route information in the form of packets consisting of hundreds of bits. Each packet begins with a header that contains the destination information. When a packet arrives at a node, a router reads the header and sends it toward its destination. Considerable progress has been made in recent years in realizing such an all-optical router by using optical flip-flops and other time-domain switches [193]–[199].

The basic element of an optical router is a packet switch that can direct each incoming packet to different output ports depending on the information in the header. Figure 11.31 shows one implementation of such a packet switch [193]. Optical power of the input packet is split into two branches using a directional coupler. One branch processes the header, while the other delivers the payload and simply contains a fiber-delay line to compensate for the latency in the header branch. Between the header and the payload, a few 0 bits are inserted that serve as the guard time. The entire switch is composed of three units. The header-processing unit is a time-domain switch (e.g., an NOLM). The flip-flop memory unit is implemented using two coupled lasers that switch the output between two wavelengths, say, λ_1 and λ_2 . The third unit is simply a wavelength converter; it converts the wavelength of the incoming data packet to the output wavelength of the flip-flop. With the use of a demultiplexer, the switch directs output at different wavelengths to different ports depending on the header information. By 2008, such a packet switch could be operated at a bit rate of 160 Gb/s [196] using a flip-flop design similar to that shown in Figure 11.16. Both the flip-flop and the wavelength converter employed SOAs in this experiment.

In another packet-switching scheme, a single DFB laser was used as an optical flip-flop capable of switching between its low- and high-power states by injecting the set and reset pulses [197]. In this case, multiple DFB lasers operating at different wavelengths can be used simultaneously such that a set pulse from the header processor turns on a specific flip-flop, resulting in a header output at that wavelength. As before, a wavelength converter and demultiplexer can then direct the packet to different output ports.

A monolithic tunable optical router was realized in 2010 by integrating more than 200 devices on a single InP chip [199]. The 8×8 packet switch was capable of oper-

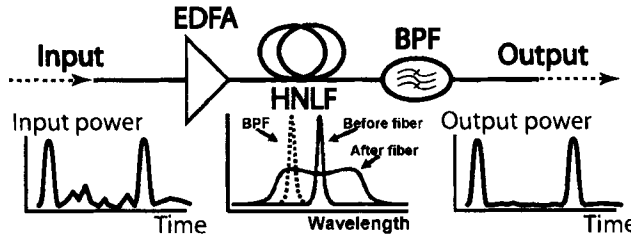


Figure 11.32: An SPM-based 2R regenerator (top) and its action on a bit stream (bottom). HNLF stands for a highly nonlinear fiber. (From Ref. [206]; ©2006 IEEE.)

ating at 40-Gb/s, corresponding to a throughput of 320 Gb/s. The 1.45-cm-long router (with a width of 4.25 mm) integrated 8 wavelength converters (using SOAs in a MZ configuration) with a passive 8×8 arrayed-waveguide grating router. Such photonic integrated circuits show that packet switching is reaching a stage where a single chip will be able to route packets optically.

11.5 Optical Regenerators

An important application of optical signal processing is for regenerating optical signals degraded during transmission though fibers and amplifiers [149]. An ideal optical regenerator transforms the degraded bit stream into its original form by performing three functions: reamplification, reshaping, and retiming. Such devices are referred as *3R regenerators* to emphasize that they perform all three functions. With this terminology, optical amplifiers can be classified as 1R regenerators because they only reamplify the bit stream. Devices that perform the first two functions are called *2R regenerators*. Since 2R and 3R regenerators have to work at time scales shorter than the bit slot in order to carry out pulse reshaping and retiming, they must operate at time scales of 10 ps or less, depending on the bit rate of the optical signal. As nonlinear effects in optical fibers respond at femtosecond time scales, highly nonlinear fibers are often employed for such devices [200]. However, the use of SOAs is also being pursued in view of their low-power requirements.

11.5.1 Fiber-Based 2R Regenerators

All three major nonlinear effects, SPM, XPM, and FWM, can be employed for optical regeneration. An SPM-based 2R regenerator, proposed in 1998 for regenerating RZ signals [201], has been studied extensively in recent years [202]–[211]. Figure 11.32 shows the underlying idea behind this scheme. The distorted noisy signal is first amplified by an EDFA before it propagates through a highly nonlinear fiber, where its spectrum broadens considerably because of SPM-induced frequency chirp. It is subsequently passed through a bandpass filter (BPF), whose center wavelength is chosen judiciously, resulting in an output bit stream with much reduced noise and much improved pulse characteristics.

It may appear surprising at first sight that spectral filtering of a bit stream whose phase has been modified nonlinearly improves the signal in the time domain. However, it is easy to see why this scheme would remove noise from the 0 bits. As the noise power in 0 bits is relatively low, the spectrum does not broaden much during 0 bits. If the passband of the optical filter is offset enough from the peak of the input spectrum, this noise would be blocked by the filter. In practice, this offset is chosen such that pulses representing 1 bits pass through the filter without much distortion. The noise level of 1 bits is also reduced because a small change in the peak power does not affect the pulse spectrum significantly, resulting in a much cleaner output bit stream.

To understand the operation of SPM-based regenerators, one may employ the analysis given in Chapter 4 of Ref. [2]. If we neglect the dispersive effects within the highly nonlinear fiber, only the phase of the the optical field is affected by SPM within the fiber such that

$$U(L, t) = U(0, t) \exp[i\gamma P_0 L_{\text{eff}} |U(0, t)|^2], \quad (11.5.1)$$

where $L_{\text{eff}} = (1 - e^{-\alpha L})/\alpha$ is the effective length for a fiber of length L with the loss parameter α , P_0 is the peak power of pulses, and $U(0, t)$ represents bit pattern of the input bit stream. As an optical filter acts in the spectral domain, the optical field after the filter can be written as

$$U_f(t) = \mathcal{F}^{-1}\{H_f(\omega - \omega_f)\mathcal{F}[U(L, t)]\}, \quad (11.5.2)$$

where \mathcal{F} is the Fourier-transform operator and $H_f(\omega - \omega_f)$ is the transfer function of a filter offset from the carrier frequency of pulses by ω_f .

The performance of an SPM-based regenerator depends on three parameters: the maximum nonlinear phase shift $\phi_{\text{NL}} \equiv \gamma P_0 L_{\text{eff}}$, the filter-passband offset ω_f , and the filter bandwidth $\delta\omega$, which must be large enough to accommodate the entire signal so that the width of optical pulses remains intact. This leaves only two design parameters whose optimum values were investigated in a 2005 study [205] using Gaussian-shape pulses and a Gaussian transfer function for the filter. In general, ϕ_{NL} should not be too large because, if the spectrum becomes too broad, filter-induced losses become too large. Its optimum value is close to $3\pi/2$ because the SPM-broadened spectrum then exhibits two peaks with a sharp dip at the original carrier frequency of the pulse [2]. Noting that $\phi_{\text{NL}} = L_{\text{eff}}/L_{NL}$, where L_{NL} is the nonlinear length, the optimum length L_{eff} is close to $5L_{NL}$. The optimum value of the filter offset in this case is found to be $\omega_f = 3/T_0$, where T_0 is the half-width of Gaussian pulses with the power profile $P(t) = P_0 \exp(-t^2/T_0^2)$.

Figure 11.33 shows a numerical example of the noise reduction provided by SPM-based 2R regenerators [205] in the case of $\phi_{\text{NL}} = 5$ and 2-ps-wide Gaussian pulses (appropriate for a 160-Gb/s bit stream). Each input pulse could have up to 10% variations in its peak power (average value 1 mW) but its width was changed to keep the same pulse energy. At the output end, the noise power is reduced from 10% to 0.6% of the average peak power, and the amplitude of power variations is reduced from 10% to 4.6%. The reason behind a large reduction in noise power is related to almost complete blocking of noise pulses in 0-bit time slots. For example, a noise pulse with 0.1-mW peak power in Figure 11.33(a) is nearly blocked by the regenerator.

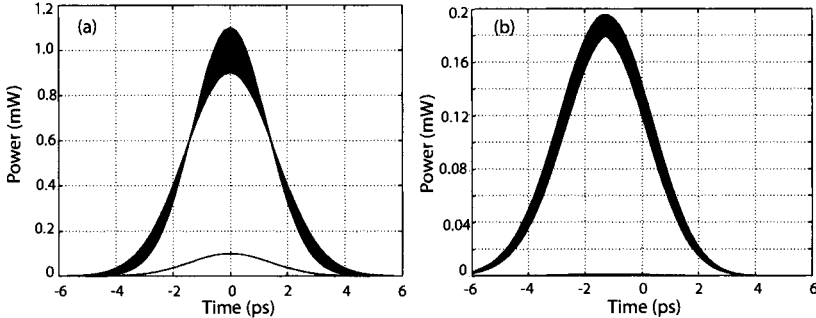


Figure 11.33: Numerically simulated pulse shapes at (a) input and (b) output ends of a SPM-based 2R regenerator designed with $\phi_{NL} = 5$. The noise pulse with 10% amplitude is almost completely blocked by the regenerator. (From Ref. [205]; ©2005 IEEE.)

The preceding analysis holds as long as dispersive effects are negligible. At high bit rates, pulses become so short that such effects may not remain negligible. However, one must distinguish between the cases of normal and anomalous dispersion. The anomalous-GVD case was studied during the 1990s in the context of soliton-based systems. In this case, SPM and GVD occur inside the transmission fiber itself. Soliton regenerators with a design similar to that shown in Figure 11.32 have also been considered [212] but they operate differently because the optical filter is centered on the carrier frequency itself. In the case of normal GVD, the SPM-based regenerator is designed with a filter offset from the carrier frequency but it is important to include the dispersive effects. Considerable theoretical work has shown that the optimization of a 2R regenerator is quite sensitive to the magnitude of dispersion [209]–[211]. Experiments performed at a bit rate of 40 Gb/s also show that the optimum power launched into the fiber depends on the fiber length and filter offset, and it must be optimized for such regenerators to work well [202].

The required fiber length can be reduced considerably by employing nonsilica fibers with large values of n_2 . A 2.8-m-long piece of chalcogenide (As_2Se_3) fiber was employed in a 2005 experiment [204]. This fiber exhibited high normal dispersion near 1550 nm with $\beta_2 > 600 \text{ ps}^2/\text{km}$. However, it turned out that this large value actually helped the device performance, rather than hindered it. The large value of the nonlinear parameter ($\gamma \approx 1200 \text{ W}^{-1}/\text{km}$) reduced the required peak power to $\sim 1 \text{ W}$, whereas large values of β_2 reduced the dispersion length L_D close to 18 m for 5.8-ps pulses employed in the experiment. The optimum fiber length under these conditions was close to 3 m. Figure 11.34 shows the impact of fiber dispersion on the SPM-broadened spectrum and the resulting changes in the transfer function of the regenerator for a fixed position of the optical filter. Improvements in the transfer function result from the reduced amplitude of spectral oscillations, resulting in a relatively smooth spectrum. Even the presence of two-photon absorption in chalcogenide fibers, a normally undesirable phenomenon, helps in improving the device performance [207].

In a 2006 experiment, 1-m length of a bismuth-oxide fiber was employed in combination with a tunable 1-nm bandpass filter [208]. The center wavelength of the filter

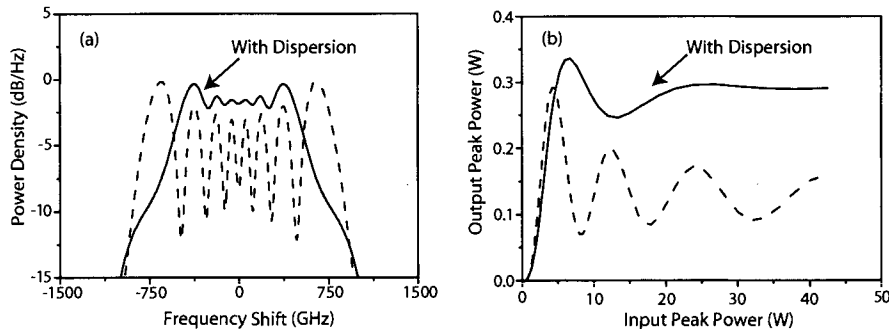


Figure 11.34: Effects of normal dispersion on (a) pulse spectrum and (b) power-transfer function for an SPM-based 2R regenerator made with a 2.8-m-long piece of chalcogenide fiber. Dashed curves show, for comparison, the dispersion-free case. (From Ref. [204]; ©2005 OSA.)

was offset by 1.7 nm from the carrier wavelength of the incoming 10-Gb/s bit stream. Losses were negligible (about 0.8 dB) for such a short fiber that also exhibited a normal dispersion of $330 \text{ ps}^2/\text{km}$ at 1550 nm. The nonlinear parameter γ for this fiber was close to $1100 \text{ W}^{-1}/\text{km}$. Because of a high nonlinearity and normal dispersion, such a fiber performed well as a 2R regenerator when the peak power of input pulses was large enough (about 8 W) to induce significant spectral broadening. Figure 11.35 compares the measured power-transfer function with the theoretical prediction. A negligible output at low input powers and a relatively broad peak ensure that power fluctuations will be reduced considerably for both 0 and 1 bits.

The nonlinear phenomenon of XPM is also useful for optical regeneration. Any nonlinear device in which a combination of the SPM and XPM effects produces nonlinear power transfer characteristics similar to that seen in Figure 11.35 can be used as

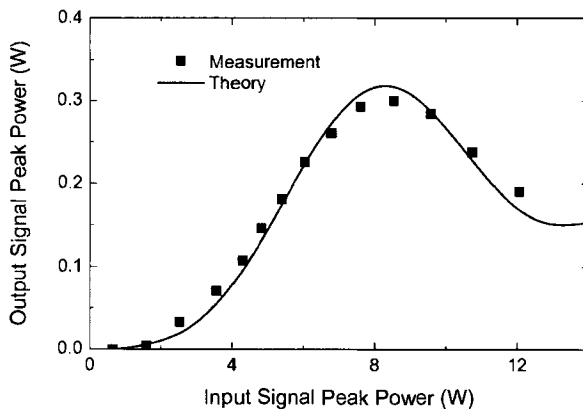


Figure 11.35: Measured and predicted power-transfer functions for an SPM-based regenerator made with a 1-m-long bismuth-oxide fiber. (From Ref. [208]; ©2006 IEEE.)

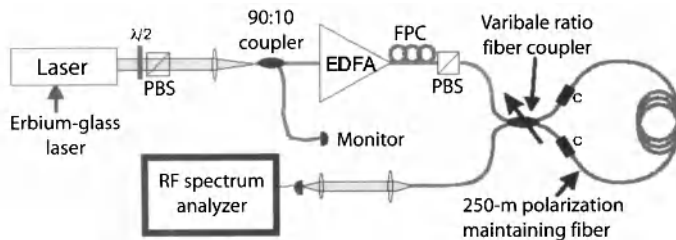


Figure 11.36: Experimental setup employed for a NOLM-based 2R regenerator; PBS and FPC stand for polarizing beam splitter and fiber polarization controller, respectively. (From Ref. [216]; ©2003 IEEE.)

a 2R regenerator. A NOLM is just such a nonlinear device, and it was used as early as 1992 for realizing optical regeneration [213]. In this experiment, the XPM-induced phase shift was employed to modify the NOLM transmission and to regenerate the bit stream. Soon after, such devices were analyzed [214] and employed for optical regeneration of pulses in soliton-based systems [179]. The use of a Kerr shutter where XPM is used to change the state of polarization provided regenerators operating at speeds of up to 40 Gb/s [215].

A highly asymmetric NOLM was employed in a 2003 experiment, and it reduced the signal noise by as much as 12 dB [216]. Figure 11.36 shows the experimental setup schematically. The NOLM was built using a fiber coupler whose splitting ratio could be varied to ensure that power levels in the counterpropagating directions differed substantially inside the Sagnac loop made with a 250-m-long polarization-maintaining fiber. For a splitting ratio of 90:10, the combination of SPM and XPM produced a relative phase shift in the two directions such that the power-transfer function of the NOLM exhibited a nearly flat region around 5 mW of input power, and the noise level was reduced considerably in this region. The optical SNR of a 40-Gb/s system could be improved by 3.9 dB with this approach [217]. In another system experiment, a 10-Gb/s signal could be propagated over 100,000 km using a NOLM as a 2R regenerator within a recirculating fiber loop [218]. Three cascaded NOLMs were used in a 2004 experiment to realize regeneration of 160-Gb/s signals [219].

FWM attracted attention for 2R regeneration starting in 2000, and several experiments have demonstrated its use in practice [220]–[226]. As we have seen in Section 8.1.2, FWM converts a fiber into a parametric amplifier. Similar to any amplifier, the gain of a parametric amplifier also saturates when signal power becomes large enough to saturate the amplifier [221]. Because of this gain saturation, fluctuations in the peak power of a pulse are reduced by a large factor. Figure 11.37(a) shows the improvement realized in the case of a parametric amplifier made using a 2.5-km-long dispersion-shifted fiber and pumped close to the zero-dispersion wavelength with 500-ps pulses (peak power 1.26 W). The FOPA exhibited a gain of 45 dB at low signal powers, but the gain saturated when the output signal power approached 200 mW. Because of it, noise power of the signal was reduced by more than a factor of 20. This is also evident from the temporal patterns seen in part (b).

Simple theory of Section 8.1.2 cannot be used for describing gain saturation in

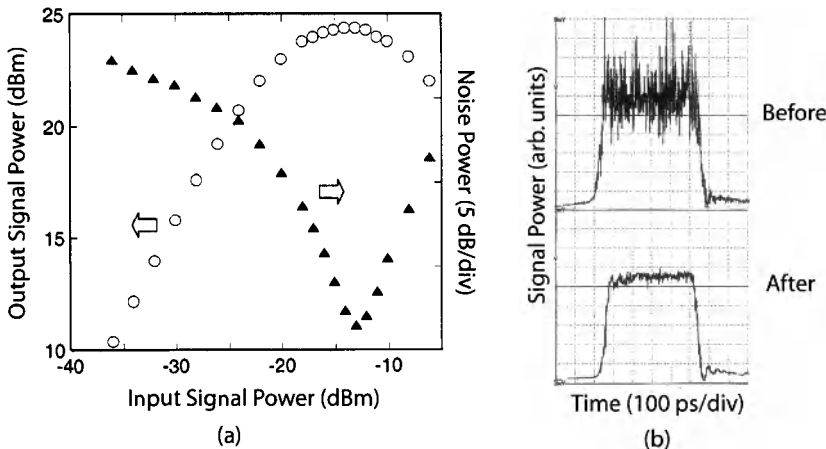


Figure 11.37: (a) Saturation of output signal power in a 2.5-km-long parametric amplifier (circles) and the resulting drop in the noise power (triangles); (b) power fluctuations at the input and output ends. (From Ref. [223]; ©2002 IEEE.)

parametric amplifiers because it assumes that the pump power remains nearly undepleted along the fiber. For a parametric amplifier to be useful as a 2R regenerator, the signal power must become large enough that the pump is depleted significantly. Moreover, large power levels of the signal and idler initiate a cascaded FWM process by acting as the pump and creating multiple other waves [220]. All of these idlers act as a wavelength-shifted replica of the signal and exhibit much less noise compared with the signal. Experimental results for a single-pump parametric amplifier agree with a theoretical model that takes into account pump depletion [222]. A dual-pump parametric amplifier has also been used as a 2R regenerator [225]. As seen in Section 8.1.2, multiple idlers at different wavelengths are generated in this case. The device performs better if one of the idlers is used as the regenerated signal.

The performance of FWM-based regenerators can be improved further by cascading two parametric amplifiers in series. In a 2006 experiment, the output of first parametric amplifier was filtered with an optical filter to select a higher-order idler that acted as the pump for the second-stage parametric amplifier [226]. A CW seed acted

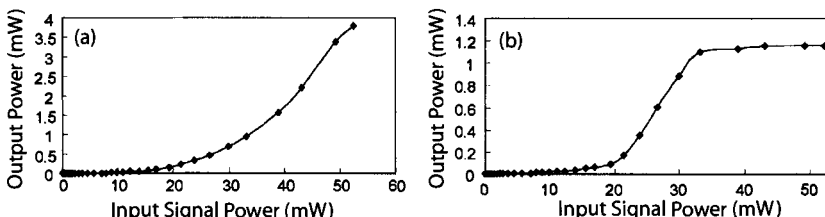


Figure 11.38: Measured transfer functions after the first (a) and second (b) stages for a two-stage FWM-based regenerator. (From Ref. [226]; ©2006 IEEE.)

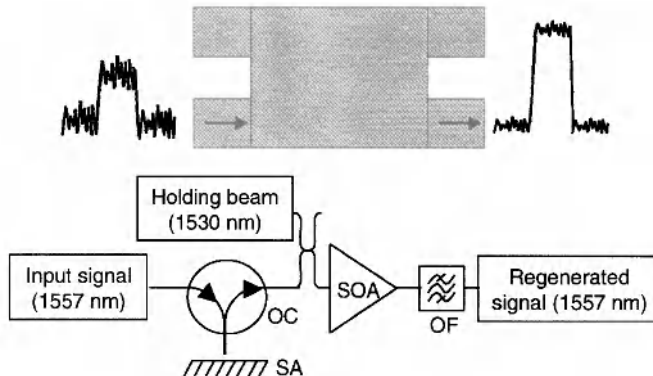


Figure 11.39: Two designs for SOA-based 2R regenerators; (top) an SOA with the MMI design; (bottom) an SOA combined with a saturable absorber (SA) using an optical circulator (OC); OF stands for an optical filter. (From Ref. [230]; ©2006 IEEE.)

as the signal and created its corresponding idler. This idler had the same bit pattern as the signal launched at the input end of the first parametric amplifier but with a much reduced noise level. Figure 11.38 shows the measured transfer functions after the first and second stages. A nearly step-function-like shape after the second stage indicates the extent of improvement possible with such a scheme.

11.5.2 SOA-Based 2R Regenerators

SOA-based wavelength converters can be used as 2R regenerators because they transfer the bit pattern of a degraded signal to a CW optical beam at the new wavelength. After this transfer process, the SNR of the new signal is much better than the original signal. Since SOAs also provide amplification and pulse shaping, the new bit stream has all the features provided by a 2R regenerator except that the signal wavelength has also changed. In a 2000 experiment [227], the optical SNR of a 40-Gb/s degraded signal was improved by 20 dB when an MZ interferometer with two SOAs in its arms was employed as a wavelength converter. Four additional SOAs were added near the input and output ports to ensure that the converted signal was amplified as well.

Several schemes exist that can provide 2R regeneration without a wavelength shift [228]–[231], and two of them are shown in Figure 11.39. A 2×2 MMI coupler was employed in a 2002 experiment [228]. Such an SOA acts a directional coupler that transfers a low-power signal to its cross port. In contrast, high-power signals not only saturate the SOA gain but they also exit through the bar port. As a result, noise level is reduced for both the 0 and 1 bits as they pass through the SOA. Second scheme in Figure 11.39 combines a saturable absorber (deposited on a mirror) with an SOA through an optical circulator [230]. Such a device acts as a 2R regenerator because low-power 0 bits are absorbed while high-power 1 bits are reflected and amplified by the SOA. Intensity noise of 1 bits is reduced considerably by the saturable absorber. The holding beam in Figure 11.39 helps to shorten the gain-recovery time of the SOA so that it can be operated at bit rates of 10 Gb/s or more. It is possible to integrate

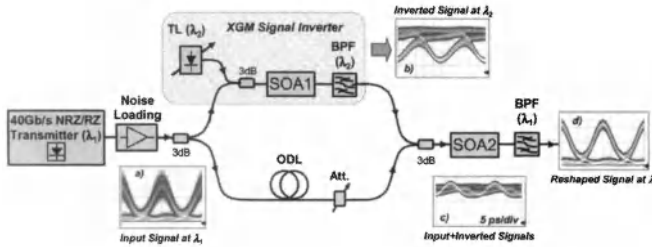


Figure 11.40: A 2R regenerator making use of cross-gain modulation (XGM) inside SOA2; SOA1 is used to generate a bit-inverted copy of incoming signal at a different wavelength. Four insets show eye diagrams at 4 places. (From Ref. [231]; ©2008 IEEE.)

saturable absorbers and SOAs on the same chip if we make use of the electroabsorption properties of InGaAsP quantum wells (the same material used for making SOAs) under reverse bias [229]. In this design a saturable absorber follows the SOA, and this cascading pattern is repeated if necessary. As before, 0 bits are absorbed while 1 bits pass through the absorbers.

Another scheme makes use of cross-gain saturation inside an SOA occurring when two optical fields are amplified simultaneously. The new feature of this scheme is that the degraded bit stream is launched inside the SOA together with an bit-inverted copy of it at a different wavelength [231]. This inverted copy is generated from the original signal using another SOA acting as a wavelength converter, as shown in Figure 11.40. The wavelength converter employs a bandpass filter with a wavelength offset chosen to create an inverted bit pattern similar to that shown in the third trace of Figure 11.24 (see Section 11.3.4). The two signals with inverted bit patterns are launched into the SOA2 such that the total power is nearly constant. Owing to cross-gain saturation, noise levels of both the 0 and 1 bits is reduced considerably for the output at the original-signal wavelength, resulting in a regenerated signal. This scheme works for and signal polarization and can be used at bit rates of 40 Gb/s or more.

11.5.3 Fiber-Based 3R Regenerators

As mentioned earlier, a 3R regenerator performs the retiming function, in addition to reamplification and reshaping, to reduce the timing jitter of the incoming bit stream. An optical modulator was used during the 1990s for this purpose in the context of soliton systems [232], and its use is often necessary for 3R regenerators [233]. An electrical clock signal, extracted from the input data itself, drives the modulator and provides the timing information related to the duration of each bit slot. An SPM-based 3R regenerator can be built by adding a modulator to the scheme shown in Figure 11.32. A schematic of such a device is shown in Figure 11.41. Numerical simulations for a fiber link containing such 3R regenerators at periodic intervals indeed show a considerable reduction in timing jitter [203]. As early as 2002, this approach was used to realize transmission of a 40-Gb/s over 1000,000 km using a 400-km-long recirculating fiber loop [234]. The 40-GHZ electric clock used to derive the modulator was recovered from the incoming bit stream itself. Another 2002 experiment used an SOA-

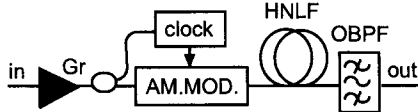


Figure 11.41: An SPM-based 3R regenerator; AM-MOD, HNLF, and OBPF stand for amplitude modulator, highly nonlinear fiber, and optical bandpass filter, respectively. (From Ref. [203]; ©2004 IEEE.)

based wavelength converter after a fiber-based regenerator to transmit a 40-Gb/s over 1000,000 km [235]

Several fiber-based schemes have been proposed for reducing the timing jitter of a bit stream [236]–[243]. In one scheme, a single phase modulator in combination with a dispersive fiber is found to be effective in reducing timing jitter [236]. In another, an optical AND gate is used to correlate data pulses with clock pulses that have been chirped and broadened inside a dispersive fiber [237]. The combination of a dispersion-compensating fiber and a fiber grating is also found to be effective in suppressing timing jitter induced by the intrachannel XPM effects [238]. In an interesting scheme, a sampled fiber grating is used first to broaden and reshape data pulses into a nearly rectangular shape [240]. These pulses are then launched into an NOLM acting as an optical switch and driven by narrow clock pulses. Clock pulses shift the phase of each data pulse through XPM and direct only its central part to the output port, resulting in regenerated data with much reduced timing jitter. In the absence of a fiber grating, such an optical switch does not reduce timing jitter much.

A simple design of a 3R regenerator makes use of XPM inside a highly nonlinear fiber, followed with an optical filter. Figure 11.42 shows the configuration adopted in a 2005 experiment [239] together with its principle of operation. The clock pulses at the wavelength λ_2 are narrower than signal pulses and are delayed such that each of them continues overlapping with a signal pulse over the entire fiber length in spite of their different speeds. The optical filter is set at λ_2 with a bandwidth narrower than the clock spectrum. As the signal power increases in parts (b) to (d), the XPM-induced wavelength shift of clock pulses reduces their transmission, resulting in a power-transfer function, shown in Figure 11.42(e). The output of such a device is a wavelength-converted signal with a reversal of 1 and 0 bits. In the experiment, the 10-Gb/s signal at a wavelength of 1534 nm was launched inside a 750-m-long highly nonlinear fiber together with 2.9-ps clock pulses at 1552 nm at a 10-GHz repetition rate. The regeneration 10-Gb/s signal improved the BER significantly because of reduced noise level and timing jitter.

The XPM-based scheme shown in Figure 11.42 has been analyzed in detail theoretically [241]. It turns out that the improvement in BER after the regenerator occurs only if the power-transfer function of the regenerator is different for 0 and 1 bits. The scheme of Figure 11.42 exhibits this feature because the wavelength shift of the clock depends on the derivative of the signal power [2] as $\delta\omega = -2\gamma L_{\text{eff}}(dP/dt)$. Data bits representing a logical 1 shift the clock spectrum through XPM, and the filter blocks these clock bits. On the other hand, 0 bits containing only noise produce little spectral shift of clock pulses, which pass through the filter unchanged. Timing jitter is

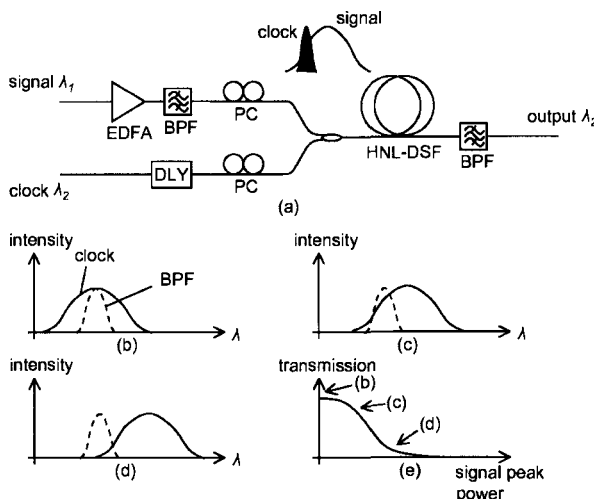


Figure 11.42: (a) Configuration of an XPM-based 3R regenerator and its operating principle. As signal power increases from (b) to (d), the XPM-induced wavelength shift reduces transmission, resulting in the response shown in part (e). (From Ref. [239]; ©2005 IEEE.)

eliminated because clock pulses now represent the data with reversed polarity.

An electro-absorption modulator acting as a saturable absorber can also eliminate timing jitter through the process of cross-absorption modulation [244]–[246]. In this scheme, a 2R regenerator is used first to reduce the noise level. The intense data pulses are then passed through a saturable absorber together with low-power clock pulses [246]. Clock pulses are absorbed when a logical 1 appears in the data stream but are transmitted otherwise. The resulting output is an inverted replica of the original bit stream with virtually no timing jitter.

11.5.4 SOA-Based 3R Regenerators

Similar to the case of optical fibers, one can combine any SOA-based 2R regenerator with a modulator driven by an electrical clock at the bit rate. In one 2009 experiment, the regenerator shown in 11.39 was combined with an electroabsorption modulator to provide retiming of an incoming 43-Gb/sbit stream [247]. The electrical clock needed for the modulator was extracted for the incoming signal itself using a clock recovery circuit consisting of a 40-GHz photodiode and a phase-locked loop. The cascadability of such a 3 regenerator was investigating by placing it inside a recirculating fiber loop whose length was varied from 100 to 300 km. A 43-Gb/s signal could be transmitted over 10,000 km when the loop length or regenerating spacing was 200 km or less.

One may ask if an optical clock can be used in place of the electrical one. As early as 2001, such an approach was used [248] to realize a 3R regenerator with the setup shown in Figure 11.43(a). The device is essentially a wavelength converter designed with a single SOA followed by an unbalanced MZ interferometer providing a relative delay of one bit period between its two arms. The optical signal at the wavelength λ_1

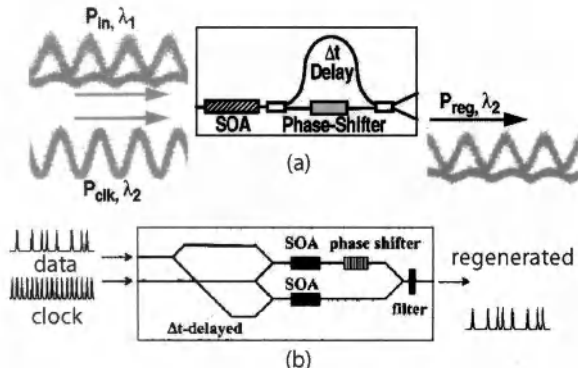


Figure 11.43: Two designs for SOA-based 3R regenerators. In both cases, the device acts as a wavelength converter but an optical clock at the bit rate of the signal is used in place of a CW beam. (From Ref. [248]; ©2001 IEEE.)

is launched into the SOA together with an optical clock at the bit rate of the signal but at a different wavelength λ_2 . The clock pulses are passed through the device in the absence of the signal (during 0 bits) but are blocked when the signal is on (during 1 bits). As a result, the bit pattern of the incoming signal is transferred to this clock with bit inversion, and the clock pulses now serve the role of the regenerated signal at a new wavelength.

Another scheme shown in Figure 11.43(b) uses the same idea but employs a balanced MZ interferometer with one SOA in its each arm [249]. This device is also a wavelength converter with the only change that an optical clock at the bit rate of the signal is used in place of a CW beam. An advantage of this scheme is that regeneration occurs without inversion of the incoming bit pattern. Figure 11.44 shows how such a 3R regenerator works. In essence, data pulses open an optical switch for a duration shorter than a bit slot but longer than their widths. Clock pulses are synchronized such that they appear within this switching window. The timing jitter is eliminated at the output end because regularly spaced clock pulses are used as a regenerated signal at

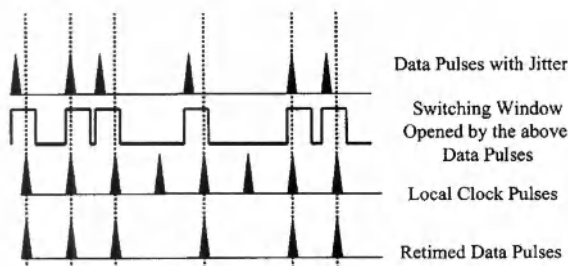


Figure 11.44: Schematic showing how timing jitter is eliminated in SOA-based 3R regenerators. Local optical clock is at the bit rate of data pulses but at a different wavelength. (From Ref. [249]; ©2001 IEEE.)

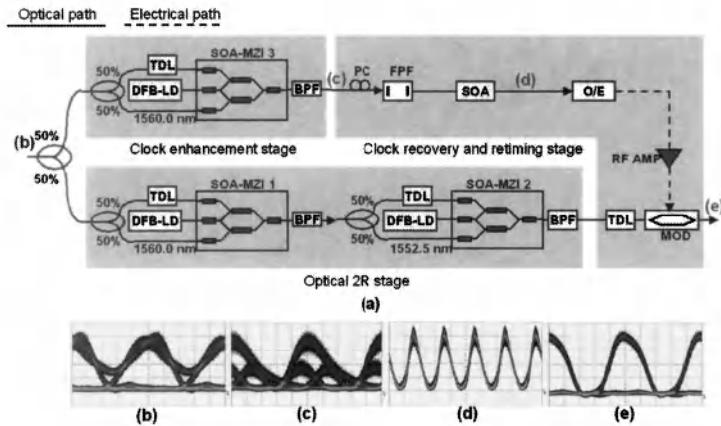


Figure 11.45: (a) An SOA-based 3R regenerator designed with three SOA-based 2R regenerators whose upper branch is used for clock recovery. (b–e) Eye diagrams at 4 locations marked in part (a). LD, TDL, and FPF stand for a laser diode, a tunable delay line, and a Fabry–Perot filter, respectively. (From Ref. [254]; ©2006 IEEE.)

a new wavelength associated with them. In the 2002 experiment, such a device was operated successfully at a bit rate of 84 Gb/s.

The use of an optical clock requires a mode-locked laser, capable of operating at the bit rate of incoming signal, but its pulse train should be synchronized with data pulses in the signal, a difficult task in practice. The alternative is to extract the optical clock from the signal itself. Considerable progress has been made in recent years to realize 3R regenerators that extract an optical clock extracted from the incoming signal. A simple idea is based on the concept of spectral filtering. If an optical signal is passed through a multipoint optical filter, such as an FP filter, whose relatively narrow transmission peaks are spaced by exactly the bit rate of the signal, the filtered spectrum would consist of a frequency comb that corresponds to a periodic train of optical pulses, or an optical clock with a repetition rate equal of the signal's bit rate. In a 2004 experiment, a tunable FP filter was used in combination with an SOA to extract a 40-Gb/s optical clock [250]; the SOA acted as an amplitude equalizer. The optical clock exhibited low amplitude noise (<0.5%) and low timing jitter (<0.5 ps). Several other schemes have been used for extracting optical clocks, including those based on electroabsorption modulators, self-pulsing DFB or quantum-dot lasers, mode-locked ring or semiconductor lasers, and FP-type SOAs [251]–[258].

In some cases, the recovered optical clock is converted to an electrical clock that is used to drive a modulator. Figure 11.45 shows an example of such a 3R regenerator [254]. It makes use of three SOA-based 2R regenerators based on a MZ configuration with six SOAs. One of them (upper branch) is followed with a Fabry–Perot filter for recovering the optical clock, which is converted into an electrical clock. The other two 2R regenerators (lower branch) are combined in series to improve the optical SNR and cancel the wavelength shift occurring after the first regenerator. Four patterns at bottom show the eye diagrams for the incoming 10-Gb/s signal, the signal before

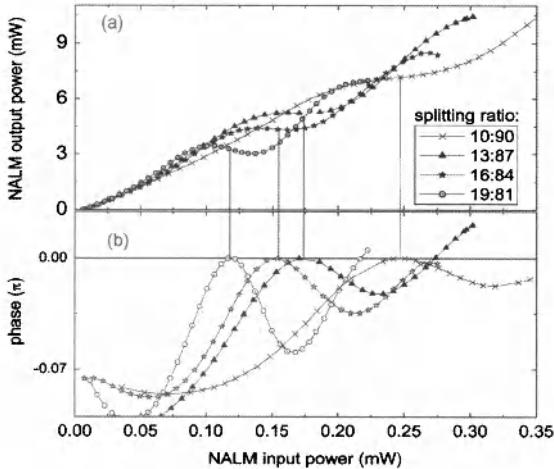


Figure 11.46: Measured (a) power and (b) phase transfer functions for several splitting ratios for a NOLM used for regenerating RZ-DPSK signals. (From Ref. [268]; ©2007 IEEE.)

clock recovery, the recovered clock, and the regenerated signal. Such a 3R regenerator was used in a recirculating fiber loop to realize transmission of a 10-Gb/s signal over 125,000 km without dispersion compensation. This experiment clearly shows the ultimate potential of SOAs for optical signal processing.

11.5.5 Regeneration of Phase-Encoded Signals

So far we have considered all-optical regeneration of NRZ or RZ bit streams. Most of the schemes discussed earlier do not work for regeneration of phase-encoded signals because their operation is based on different power levels associated with the 0 and 1 bits. As we saw in Chapter 10, it is common to employ a pulse in every bit slot whose phase takes two or more values depending on the format chosen. Recently, several techniques have been developed for regenerating RZ-DPSK signals [259]–[270].

In a 2005 study, an NOLM similar to that shown in Figure 11.36 was employed with one crucial difference: an attenuator with different losses in the counterpropagating directions was inserted near one end of the fiber loop [260]. This device works similar to an optical isolator and can be fabricated using polarizers and a Faraday rotator. Although much higher input powers are required, the power-transfer function exhibits a flat region around which the phase shift produced by the NOLM is also constant and relatively small. The experimental results were in agreement with the theoretical predictions [264].

A bidirectional EDFA (in place of a directional attenuator) at one end of the NOLM was used in a 2007 experiment to realize regeneration of RZ-DPSK signals [268]. The input signal was split asymmetrically at the fiber coupler such that each weaker subpulse was first amplified by the EDFA, while the stronger subpulse passed through it after traversing the Sagnac loop. As a result, the SPM-induced phase shift was much larger for the weaker subpulses. As the phase of output pulse is set by stronger sub-

pulses, the NOLM does not distort the phase of outgoing pulses much. Figure 11.46 shows the measured power and phase characteristics for a 3-km-long fiber loop ($\gamma = 2.5 \text{ W}^{-1}/\text{km}$) for several splitting ratios of the fiber coupler when the amplifier was pumped to provide a small-signal gain of 23 dB. As expected, the output power becomes nearly constant in a specific range of input powers, a feature that reduces noise of 1 bits. Since the phase is nearly constant in this region, amplitude noise of the signal can be suppressed without transferring it into phase jitter. At the same time, the relative phase shift between the 0 and 1 bits is so small ($< 0.07\pi$) that it does not affect decoding of the DPSK bit stream. Indeed, measured BERs for a 10-Gb/s RZ-DPSK bit stream were improved considerably with such a regenerator. The amplification can also be provided through the Raman gain by injecting pump light into the loop such that it propagates in one direction only [263].

The SPM-based 2R regenerator, shown in Figure 11.32, can also be adopted for the RZ-DPSK format with suitable modifications. For example, the signal phase can be almost preserved over long distances if the nonlinear fiber provides anomalous dispersion and a saturable absorber is inserted before it [261]. In this case, the combination of soliton effects and narrowband filtering reduces amplitude noise and reshapes RZ pulses without affecting the signal phase significantly. A FWM-based approach can also be used by pumping the fiber near the zero-dispersion wavelength and increasing the signal power so that the parametric gain is saturated and multiple idlers are generated through cascaded FWM. However, one should set the optical filter such that it selects the signal and rejects all idlers to minimize degradation of the information contained in signal phase. An XPM-based scheme has also been proposed for regenerating DPSK signals [259].

The preceding schemes regenerate RZ pulses by reducing amplitude noise (while preserving their phases) but they do not reduce the phase noise. A FWM-based approach accomplishes this task by making use of phase-sensitive amplification inside a Mach-Zehnder or Sagnac interferometer. A 6-km-long Sagnac loop (or NOLM) was employed in a 2005 experiment [262] to realize >13 dB of phase-sensitive gain at a pump power of 100 mW. Phase noise was reduced enough to improve the BER of the regenerated DPSK signal by a factor of 100. In a later experiment, the same loop was used to reduce both the amplitude and phase noises by a relatively large factor [266].

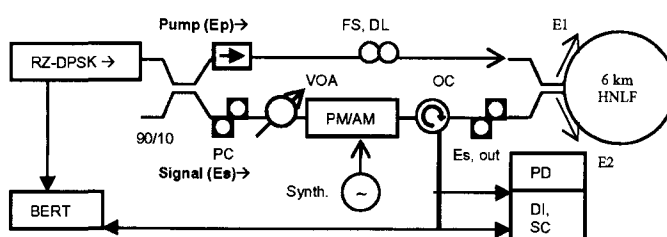


Figure 11.47: Experimental setup for regenerating RZ-DPSK signals through phase-sensitive amplification inside a Sagnac loop; BERT, FS-DL, VOA, OC, PD, DI, and SC stand for bit-error rate tester, fiber stretcher delay line, variable optical attenuator, optical circulator, photodiode, delay interferometer, and sampling oscilloscope, respectively. (From Ref. [266]; ©2006 OSA.)

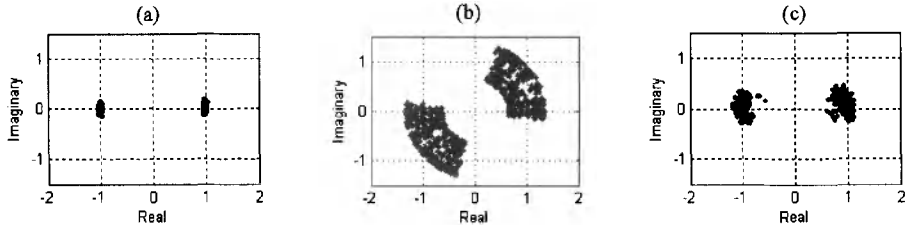


Figure 11.48: Constellation diagrams of the RZ-DPSK signal (a) before adding noise, (b) after adding noise, and (c) after phase-sensitive amplification. (From Ref. [266]; ©2006 OSA.)

Figure 11.47 shows the experimental setup employed for phase-sensitive amplification inside a Sagnac interferometer. The DPSK signal is first split into two parts using a 90:10 fiber coupler. The branch with 90% average power acts as a pump, while the low-power branch acts as the signal; a delay line in the pump branch ensures decorrelation between the two. Phase and amplitude noises are added to the signal before it enters the 6-km-long fiber loop, where a degenerate FWM process transfers power from the pump to the signal. The extent of power transfer depends on the relative phase difference between the pump and signal. It is this feature that reduces phase noise at the NOLM output. Figure 11.48 shows the extent of improvement realized with this scheme using constellation diagrams [266]. Both the amplitude and phase noises are reduced significantly after phase-sensitive amplification. A dual-pump parametric amplifier can also be employed for this purpose provided signal frequency is located exactly in the middle of the two pumps so that it coincides with the idler frequency [267].

The design of a fiber-based 3R regenerator for DPSK signals is shown in Figure 11.49. It adds a 1-bit delay interferometer in front of a 2R regenerator whose output is fed to fiber-based phase modulator driven by an optical clock recovered from the signal itself (or obtained from a pulsed optical source). The role of a delay interferometer is to convert the incoming DPSK signal into an RZ-ASK signal whose noise is reduced by the 2R amplitude regenerator. The regenerated data stream is finally used to modulate the phase of clock pulses through XPM inside an optical fiber. In a 2008 experiment [269], a 2.4-km-long highly nonlinear fiber was used as a phase modulator together with a fiber-based 2R generator. Such a device reduces both the amplitude and phase noises of the incoming DPSK bit stream. A 2009 experiment showed that it was capable of reducing the impact of nonlinear phase noise that affects a DPSK signal considerably [270].

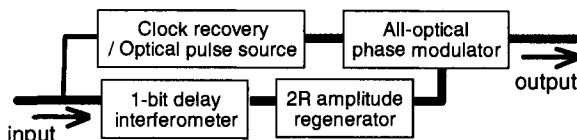


Figure 11.49: Block diagram of a fiber-based 3R regenerator for DPSK (top) signals. (From Ref. [269]; ©2008 OSA.)

Optical regeneration of RZ-DQPSK signals is also of considerable practical interest [271]–[273]. A 2-km-long NOLM was used for this purpose in a 2007 experiment to regenerate a 80-Gb/s signal [271]. Numerical simulations show that phase-sensitive amplification can also be used with success [272]. Even the scheme shown in Figure 11.49 can be generalized to the case of DQPSK signals, but it requires two delay interferometers, two 2R regenerators and two phase modulators to deal with four possible phases of a single symbol [273].

Problems

- 11.1** Use the transfer matrix given in Eq. (11.1.1) and prove that the transmittivity of an NOLM is indeed given by Eq. (11.1.2).
- 11.2** Repeat the preceding problem for the NOLM in which an amplifier is inserted within the loop right after the coupler and prove that the transmittivity is now given by Eq. (11.1.4).
- 11.3** Calculate the XPM-induced phase shift using Eqs. (11.1.6) when control pulses have a soliton shape with $A_c(t) = \text{sech}(t/T_0)$. Repeat the calculation for Gaussian control pulses. In both cases, express your answer in terms of the walk-off length defined as $L_w = T_0/d_w$.
- 11.4** Solve Eqs. (11.1.10) and (11.1.11) describing the FWM process and prove that the amplification factor of a parametric amplifier is given by Eq. (11.1.16).
- 11.5** Prove that the phase-mismatch parameter κ , defined in Eq. (11.1.12), reduces approximately to $\kappa = \beta_2 \delta^2 + 2\gamma P_0$ with $\delta = \omega_s - \omega_p$.
- 11.6** Solve Eqs. (11.1.27) and (11.1.29) analytically and prove that the amplification factor for an optical pulse is given by Eq. (11.1.33).
- 11.7** Solve Eq. (11.1.24) and (11.1.25) numerically and plot the output pulse shape and spectrum when a 50-ps Gaussian pulse with 1-pJ energy is amplified by an SOA having values $E_{\text{sat}} = 5 \text{ pJ}$ and $\tau_c = 100 \text{ ps}$ and $g_0 L = 6$, where L is the SOA length.
- 11.8** Reproduce the bistable curves shown in Figure 11.10 using Eq. (11.1.38) with $R_m = 0.5$. Calculate the powers at which such a device will turn on and off assuming $\delta = 3$, $\gamma = 20 \text{ W}^{-1}/\text{km}$, and $L_m = 100 \text{ m}$.
- 11.9** A 1-km-long fiber with $\gamma = 20 \text{ W}^{-1}/\text{km}$ is used for converting the wavelength of a 1550-nm channel to 1555 nm using XPM-induced spectral broadening. Estimate the center wavelength of the optical filter used after the fiber when peak power of the signal is 0.8 W.
- 11.10** Describe two techniques that can be used to convert an NRZ bit stream into a RZ bit stream.
- 11.11** Explain how the nonlinear phenomenon of SPM can be used for regeneration of optical bit streams. Use diagrams as necessary.

- 11.12** Reproduce a figure similar to that shown in Figure 11.33 numerically by applying Eq. (11.5.2) to a set of 10-ps-wide (FWHM) noisy Gaussian pulses. Use $\phi_{NL} = 5$ and a frequency shift of 80 GHz for the optical filter.

References

- [1] M. Hirano, T. Nakanishi, T. Okuno, and M. Onishi, *IEEE J. Sel. Topics Quantum Electron.* **15**, 103 (2008).
- [2] G. P. Agrawal, *Nonlinear Fiber Optics*, 4th ed. Academic Press, Boston, 2007.
- [3] K. Kikuchi, K. Taira, and N. Sugimoto, *Electron. Lett.* **38**, 166 (2002).
- [4] M. P. Fok and C. Shu, *IEEE J. Sel. Topics Quantum Electron.* **14**, 587 (2008).
- [5] M. D. Pelusi, V. G. Ta'eed, L. Fu, et al., *IEEE J. Sel. Topics Quantum Electron.* **14**, 529 (2008).
- [6] M. D. Pelusi, F. Luan, S. Madden, D.-Y. Choi, D. A. Bulla, B. Luther-Davies, and B. J. Eggleton, *IEEE Photon. Technol. Lett.* **22**, 3 (2010).
- [7] G. P. Agrawal, *Applications of Nonlinear Fiber Optics*, 2nd ed., Academic Press, Boston, 2008.
- [8] K. Otsuka, *Opt. Lett.* **8**, 471 (1983).
- [9] D. B. Mortimore, *J. Lightwave Technol.* **6**, 1217 (1988).
- [10] N. J. Doran and D. Wood, *Opt. Lett.* **13**, 56 (1988).
- [11] G. P. Agrawal, *Lightwave Technology: Components and Devices* (Wiley, New York, 2004).
- [12] M. E. Fermann, F. Haberl, M. Hofer, and H. Hochstrasser, *Opt. Lett.* **15**, 752 (1990).
- [13] A. W. O'Neil and R. P. Webb, *Electron. Lett.* **26**, 2008 (1990).
- [14] M. C. Farries and D. N. Payne, *Appl. Phys. Lett.* **55**, 25 (1989).
- [15] K. J. Blow, N. J. Doran, B. K. Nayar, and B. P. Nelson, *Opt. Lett.* **15**, 248 (1990).
- [16] M. Jinno and T. Matsumoto, *IEEE Photon. Technol. Lett.* **2**, 349 (1990); *Electron. Lett.* **27**, 75 (1991).
- [17] H. Avramopoulos, P. M. W. French, M. C. Gabriel, H. H. Houh, N. A. Whitaker, and T. Morse, *IEEE Photon. Technol. Lett.* **3**, 235 (1991).
- [18] J. D. Moores, K. Bergman, H. A. Haus, and E. P. Ippen, *Opt. Lett.* **16**, 138 (1991); *J. Opt. Soc. Am. B* **8**, 594 (1991).
- [19] M. Jinno and T. Matsumoto, *IEEE J. Quantum Electron.* **28**, 875 (1992).
- [20] H. Bülow and G. Veith, *Electron. Lett.* **29**, 588 (1993).
- [21] K. Smith, N. J. Doran, and P. G. J. Wigley, *Opt. Lett.* **15**, 1294 (1990).
- [22] S. V. Chernikov and J. R. Taylor, *Electron. Lett.* **29**, 658 (1993).
- [23] R. A. Betts, J. W. Lear, S. J. Frisken, and P. S. Atherton, *Electron. Lett.* **28**, 1035 (1992).
- [24] J. Yu, X. Zheng, C. Peucheret, A. T. Clausen, H. N. Poulsen, and P. Jeppesen, *J. Lightwave Technol.* **18**, 1001 (2000).
- [25] M. Jinno and T. Matsumoto, *Opt. Lett.* **16**, 220 (1991).
- [26] J. M. Jeong and M. E. Marhic, *Opt. Commun.* **91**, 115 (1992).
- [27] J. K. Lucek and K. Smith, *Opt. Lett.* **15**, 1226 (1993).
- [28] B. K. Nayar, N. Finlayson, and N. J. Doran, *J. Mod. Opt.* **40**, 2327 (1993).
- [29] G. A. Nowak, Y.-H. Kao, T. J. Xia, M. N. Islam, and D. Nolan, *Opt. Lett.* **23**, 936 (1998).
- [30] O. Aso, S. Arai, T. Yagi, M. Tadakuma, Y. Suzuki, and S. Namiki, *Electron. Lett.* **36**, 709 (2000).

- [31] J. Hansryd, P. A. Andrekson, M. Westlund, J. Li, and P. O. Hedekvist, *IEEE J. Sel. Topics Quantum Electron.* **8**, 506 (2002).
- [32] B. N. Islam and Ö Boyraz, *IEEE J. Sel. Topics Quantum Electron.* **8**, 527 (2002).
- [33] K. K. Y. Wong, K. Shimizu, M. E. Marhic, K. Uesaka, G. Kalogerakis, and L. G. Kazovsky, *Opt. Lett.* **28**, 692 (2003).
- [34] S. Radic and C. J. McKinstrie, *Opt. Fiber Technol.* **9**, 7 (2003).
- [35] S. Radic, C. J. McKinstrie, R. M. Jopson, J. C. Centanni, Q. Lin, and G. P. Agrawal, *Electron. Lett.* **39**, 838 (2003).
- [36] T. Tanemura and K. Kikuchi, *IEEE Photon. Technol. Lett.* **15**, 1573 (2003).
- [37] R. L. Espinola, J. I. Dadap, R. M. Osgood, Jr., S. J. McNab, and Y. A. Vlasov, *Opt. Express* **13**, 4341 (2005).
- [38] M. A. Foster, A. C. Turner, J. E. Sharping, B. S. Schmidt, M. Lipson, and A. L. Gaeta, *Nature* **441**, 960 (2006).
- [39] K. Yamada, H. Fukuda, T. Tsuchizawa, T. Watanabe, T. Shoji, and S. Itabashi, *IEEE Photon. Technol. Lett.* **18**, 1046 (2006).
- [40] Q. Lin, J. Zhang, P. M. Fauchet, and G. P. Agrawal, *Opt. Express* **14**, 4786 (2006).
- [41] Y.-H. Kuo, H. Rong, V. Sih, S. Xu, and M. Paniccia, *Opt. Express* **14**, 11721 (2006).
- [42] M. A. Foster, A. C. Turner, R. Salem, M. Lipson, and A. L. Gaeta, *Opt. Express* **15**, 12949 (2007).
- [43] B. G. Lee, A. Biberman, A. C. Turner-Foster, M. A. Foster, M. Lipson, A. L. Gaeta, and K. Bergman, *IEEE Photon. Technol. Lett.* **21**, 182 (2009).
- [44] A. C. Turner, M. A. Foster, R. Salem, A. L. Gaeta, and M. Lipson, *Opt. Express* **18**, 1904 (2010).
- [45] Q. Lin, O. J. Painter, and G. P. Agrawal, *Opt. Express* **15**, 16604 (2007).
- [46] T. Saitoh and T. Mukai, *IEEE J. Quantum Electron.* **23**, 1010 (1987).
- [47] N. A. Olsson, *J. Lightwave Technol.* **7**, 1071 (1989).
- [48] T. Saitoh and T. Mukai, in *Coherence, Amplification, and Quantum Effects in Semiconductor Lasers*, Y. Yamamoto, Ed., Wiley, New York, 1991, Chap. 7.
- [49] G. P. Agrawal and N. K. Dutta, *Semiconductor Lasers*, 2nd ed., Van Nostrand Reinhold, New York, 1993, Chap. 11.
- [50] L. H. Spiekman, *Optical Fiber Telecommunications*, Vol. 4A, I. P. Kaminow and T. Li, Eds., Academic Press, Boston, 2002, Chap. 14.
- [51] R. J. Manning, A. D. Ellis, A. J. Poustie, and K. J. Blow, *J. Opt. Soc. Am. B* **14**, 3204 (1997).
- [52] K. E. Stubkjaer, *IEEE J. Sel. Topics Quantum Electron.* **6**, 1428 (2000).
- [53] G. P. Agrawal and D. N. Maywar, in *Nonlinear Photonic Crystals*, Springer Series in Photonics, Vol. 10, Eds. R. E. Slusher and B. H. Eggleton, Springer, New York, 2003, Chap. 13.
- [54] G. P. Agrawal and N. A. Olsson, *IEEE J. Quantum Electron.* **25**, 2297 (1989).
- [55] G. P. Agrawal and N. A. Olsson, *Opt. Lett.* **14**, 500 (1989).
- [56] N. A. Olsson, G. P. Agrawal, and K. W. Wecht, *Electron. Lett.* **25**, 603 (1989).
- [57] M. Eiselt, *Electron. Lett.* **28**, 1505 (1992).
- [58] J. P. Sokoloff, P. R. Prucnal, I. Glesk, and M. Kane, *IEEE Photon. Technol. Lett.* **5**, 787 (1993).
- [59] M. Eiselt, W. Pieper, and H. G. Weber, *J. Lightwave Technol.* **13**, 2099 (1995).
- [60] I. Glesk, B. C. Wang, L. Xu, V. Baby, and P. R. Prucnal, in *Progress in Optics*, Vol. 45, E. Wolf, Ed., Elsevier, Amsterdam, 2003, Chap. 2.

- [61] H. M. Gibbs, *Optical Bistability: Controlling Light with Light*, Academic Press, Boston, 1984.
- [62] H. Nakatsuka, S. Asaka, H. Itoh, K. Ikeda, and M. Matsuoka, *Phys. Rev. Lett.* **50**, 109 (1983).
- [63] P. W. Smith, I. P. Kaminow, P. J. Maloney, and L. W. Stulz, *Appl. Phys. Lett.* **33**, 24 (1978); *Appl. Phys. Lett.* **34**, 62 (1979).
- [64] P. L. K. Wa, J. E. Sitch, N. J. Mason, and P. N. Robson, *Electron. Lett.* **21**, 26 (1985).
- [65] R. M. Shelby, M. D. Levenson, and S. H. Perlmutter, *J. Opt. Soc. Am. B* **5**, 347 (1988).
- [66] S. Coen, M. Haelterman, P. Emplit, L. Delage, L. M. Simohamed, and F. Reynaud, *J. Opt. Soc. Am. B* **15**, 2283 (1998).
- [67] H. Kawaguchi, *IEEE J. Sel. Topics Quantum Electron.* **3**, 1254 (1997).
- [68] C. Harder, K. Y. Lau, and A. Yariv, *IEEE J. Quantum Electron.* **18**, 1351 (1982).
- [69] M. Ueno and R. Lang, *J. Appl. Phys.* **58**, 1689 (1985).
- [70] H. F. Liu, Y. Hashimoto, and T. Kamiya, *IEEE J. Quantum Electron.* **24**, 43 (1988).
- [71] G. H. Duan, P. Landais, and J. Jacquet, *IEEE J. Quantum Electron.* **30**, 2507 (1994).
- [72] W. F. Sharfin and M. Dagenais, *Appl. Phys. Lett.* **48**, 321 (1986); **48**, 1510 (1986).
- [73] M. J. Adams, H. J. Westlake, and M. J. O'Mahony, in *Optical Nonlinearities and Instabilities in Semiconductors*, H. Haug, Ed., Academic Press, Boston, 1988, Chap. 15.
- [74] H. G. Winful, J. H. Marburger, and E. Garmire, *Appl. Phys. Lett.* **35**, 379 (1979).
- [75] M. J. Adams and R. Wyatt, *Proc. Inst. Elect. Eng.*, **134**, 35, 1987.
- [76] D. N. Maywar and G. P. Agrawal, *IEEE J. Quantum Electron.* **33**, 2029 (1997); *IEEE J. Quantum Electron.* **34**, 2364 (1998).
- [77] D. N. Maywar and G. P. Agrawal, *Opt. Express* **3**, 440 (1998).
- [78] D. N. Maywar and G. P. Agrawal, and Y. Nakano, *Opt. Express* **6**, 75 (2000).
- [79] K. Okumura, Y. Ogawa, H. Ito, and H. Inaba, *IEEE J. Quantum Electron.* **21**, 377 (1985).
- [80] S. Suzuki, T. Terakado, K. Komatsu, K. Nagashima, A. Suzuki, and M. Kondo, *J. Light-wave Technol.* **4**, 894 (1986).
- [81] K. Inoue, *Opt. Lett.* **12**, 918 (1987).
- [82] K. Otsuka, *Electron. Lett.* **24**, 800 (1988); *Opt. Lett.* **14**, 72 (1987).
- [83] L. L. Chern and J. K. McIver, *Opt. Lett.* **15**, 186 (1990).
- [84] H. Kawaguchi, *Electron. Lett.* **31**, 1150 (1995).
- [85] J. Zhou, M. Cada, G. P. Li, and T. Makino, *IEEE Photon. Technol. Lett.* **7**, 1125 (1995).
- [86] B. B. Jian, *Electron. Lett.* **32**, 349 (1996).
- [87] M. S. Petrovic, M. R. Belic, M. V. Jaric, and F. Kaiser, *Opt. Commun.* **138**, 349 (1997).
- [88] T. Chattopadhyay and M. Nakajima, *Opt. Commun.* **138**, 320 (1997).
- [89] K. Nakatsuhara, T. Mizumoto, R. Munakata, Y. Kigure, and Y. Naito, *IEEE Photon. Technol. Lett.* **10**, 78 (1998).
- [90] F. Robert, D. Fortusini, and C. L. Tang, *IEEE Photon. Technol. Lett.* **12**, 465 (2000).
- [91] M. T. Hill, H. de Waardt, G. D. Khoe, and H. J. S. Dorren, *IEEE J. Quantum Electron.* **37**, 405 (2001).
- [92] S.-H. Jeong, H.-C. Kim, T. Mizumoto, J. Wiedmann, S. Arai, M. Takenaka, and Y. Nakano, *IEEE J. Quantum Electron.* **38**, 706 (2002).
- [93] V. Van, T. A. Ibrahim, P. P. Absil, F. G. Johnson, R. Grover, and P.-T. Ho, *IEEE J. Sel. Topics Quantum Electron.* **8**, 705 (2002).
- [94] H. J. S. Dorren, D. Lenstra, Y. Liu, M. T. Hill, and G. D. Khoe, *IEEE J. Quantum Electron.* **39**, 141 (2003).

- [95] R. Clavero, F. Ramos, J. M. Martinez, and J. Marti, *IEEE Photon. Technol. Lett.* **17**, 843 (2005).
- [96] M. Takenaka, M. Raburn, and Y. Nakano, *IEEE Photon. Technol. Lett.* **17**, 968 (2005).
- [97] W. D’Oosterlinck, J. Buron, F. Öhman, G. Morthier, and R. Baets, *IEEE Photon. Technol. Lett.* **19**, 489 (2007).
- [98] K. Huybrechts, G. Morthier, and R. Baets, *Opt. Express* **16**, 11405 (2008).
- [99] A. M. Kaplan, G. P. Agrawal and D. N. Maywar, *Electron. Lett.* **45**, 127 (2009).
- [100] N. Pleros, D. Apostolopoulos, D. Petrantonakis, C. Stamatiadis, and H. Avramopoulos, *IEEE Photon. Technol. Lett.* **21**, 73 (2009).
- [101] L. Liu, R. Kumar, K. Huybrechts, et al., *Nature Photonics* **4**, 182 (2010).
- [102] K. A. Rauschenbach, K. L. Hall, J. C. Livas, and G. Raybon, *IEEE Photon. Technol. Lett.* **6**, 1130 (1994).
- [103] J. Yu, X. Zheng, C. Peucheret, A. T. Clausen, H. N. Poulsen, and P. Jeppesen, *J. Lightwave Technol.* **18**, 1007 (2000).
- [104] T. Sakamoto, F. Futami, K. Kikuchi, S. Takeda, Y. Sugaya, and S. Watanabe, *IEEE Photon. Technol. Lett.* **13**, 502 (2001).
- [105] B. E. Olsson, P. Öhlén, L. Rau, and D. J. Blumenthal, *IEEE Photon. Technol. Lett.* **12**, 846 (2000).
- [106] J. Yu and P. Jeppesen, *IEEE Photon. Technol. Lett.* **13**, 833 (2001).
- [107] J. H. Lee, Z. Yusoff, W. Belardi, M. Ibsen, T. M Monro, and D. J. Richardson, *IEEE Photon. Technol. Lett.* **15**, 437 (2003).
- [108] L. Rau, W. Wang, S. Camatel, H. Poulsen, and D. J. Blumenthal, *IEEE Photon. Technol. Lett.* **16**, 2520 (2004).
- [109] W. Mao, P. A. Andrekson, and J. Toulouse, *IEEE Photon. Technol. Lett.* **17**, 420 (2005).
- [110] W. Wang, H. N. Poulsen, L. Rau, H. F. Chou, J. E. Bowers, and D. J. Blumenthal, *J. Lightwave Technol.* **23**, 1105 (2005).
- [111] J. H. Lee, T. Nagashima, T. Hasegawa, S. Ohara, N. Sugimoto, and K. Kikuchi, *IEEE Photon. Technol. Lett.* **18**, 298 (2006).
- [112] T. Tanemura, J. H. Lee, D. Wang, K. Katoh, and K. Kikuchi, *Opt. Express* **14**, 1408 (2006).
- [113] T. Tanemura and K. Kikuchi, *J. Lightwave Technol.* **24**, 4108 (2006).
- [114] K. Inoue and H. Toba, *IEEE Photon. Technol. Lett.* **4**, 69 (1992).
- [115] K. Inoue, T. Hasegawa, K. Oda, and H. Toba, *Electron. Lett.* **29**, 1708 (1993).
- [116] K. Inoue, *J. Lightwave Technol.* **12**, 1916 (1994); *IEEE Photon. Technol. Lett.* **6**, 1451 (1993).
- [117] J. H. Lee, W. Belardi, K. Furusawa, P. Petropoulos, Z. Yusoff, T. M. Monro, and D. J. Richardson, *IEEE Photon. Technol. Lett.* **15**, 440 (2003).
- [118] F. Yaman, Q. Lin, S. Radic, and G. P. Agrawal, *IEEE Photon. Technol. Lett.* **17**, 2053 (2005).
- [119] Y. Wang, C. Yu, T. Luo, L. Yan, Z. Pan, and A. E. Willner, *J. Lightwave Technol.* **23**, 3331 (2005).
- [120] G. Kalogerakis, M. E. Marhic, K. Uessaka, K. Shimizu, Member, K. K.-Y. Wong, and L. G. Kazovsky, *J. Lightwave Technol.* **24**, 3683 (2006).
- [121] K. K. Chow, C. Shu, C. Lin, and A. Bjarklev, *IEEE Photon. Technol. Lett.* **17**, 624 (2005).
- [122] P. A. Andersen, T. Tokle, Y. Geng, C. Peucheret, and P. Jeppesen, *IEEE Photon. Technol. Lett.* **17**, 1908 (2005).
- [123] A. Zhang and M. S. Demokan, *Opt. Lett.* **30**, 2375 (2005).

- [124] J. H. Lee, T. Nagashima, T. Hasegawa, S. Ohara, N. Sugimoto, and K. Kikuchi, *J. Lightwave Technol.* **24**, 22 (2006).
- [125] M. P. Fok and C. Shu, *IEEE Photon. Technol. Lett.* **19**, 1166 (2007).
- [126] K. K. Chow, K. Kikuchi, T. Nagashima, T. Hasegawa, S. Ohara, and N. Sugimoto, *Opt. Express* **15**, 15418 (2007).
- [127] W. Astar, C.-C. Wei, Y.-J. Chen, J. Chen, and G. M. Carter, *Opt. Express* **16**, 12039 (2008).
- [128] C. Q. Xu, H. Okayama, and M. Kawahara, *Appl. Phys. Lett.* **63**, 3559 (1993).
- [129] M. H. Chou, I. Brener, M. M. Fejer, E. E. Chaban, and S. B. Christman, *IEEE Photon. Technol. Lett.* **11**, 653 (1999).
- [130] I. Cristiani, V. Degiorgio, L. Socci, F. Carbone, and M. Romagnoli, *IEEE Photon. Technol. Lett.* **14**, 669 (2002).
- [131] S. Yu, and W. Gu, *IEEE J. Quantum Electron.* **40**, 1744 (2004).
- [132] Y. L. Lee, B. Yu, C. Jung, Y. Noh, J. Lee, and D. Ko, *Opt. Express* **13**, 2988 (2005).
- [133] Y. Nishida, H. Miyazawa, M. Asobe, O. Tadanaga, and H. Suzuki, *IEEE Photon. Technol. Lett.* **17**, 1049 (2005).
- [134] C. Langrock, S. Kumar, J. E. McGeehan, A. E. Willner, and M. M. Fejer, *J. Lightwave Technol.* **24**, 2579 (2006).
- [135] H. Furukawa, A. Nirmalathas, N. Wada, S. Shinada, H. Tsuboya, and T. Miyazaki, *IEEE Photon. Technol. Lett.* **19**, 384 (2007).
- [136] J. Zhang, Y. Chen, F. Lu, and X. Chen, *Opt. Express* **16**, 6957 (2008).
- [137] A. Tehranchi, and R. Kashyap, *Opt. Express* **17**, 19113 (2009).
- [138] G.-H. Duan, in *Semiconductor Lasers: Past, Present, and Future*, G. P. Agrawal, Ed. (AIP Press, Woodbury, NY, 1995), Chap. 10.
- [139] T. Durhuus, B. Mikkelsen, C. Joergensen, S. L. Danielsen, and K. E. Stubkjaer, *J. Lightwave Technol.* **14**, 942 (1996).
- [140] C. Joergensen, S. L. Danielsen, K. E. Stubkjaer, et. al., *IEEE J. Sel. Topics Quantum Electron.* **3**, 1168 (1997).
- [141] C. Politi, D. Klonidis, and M. J. O'Mahony, *J. Lightwave Technol.* **24**, 1203 (2006).
- [142] V. Lal, M. L. Mašanović, J. A. Summers, G. Fish, and D. J. Blumenthal, *IEEE J. Sel. Topics Quantum Electron.* **13**, 49 (2007).
- [143] J. Leuthold, D. M. Marom, S. Cabot, J. J. Jaques, R. Ryf, and C. R. Giles, *J. Lightwave Technol.* **22**, 186 (2004).
- [144] Y. Liu, E. Tangdiongga, Z. Li, et al., *J. Lightwave Technol.* **24**, 230 (2006); *J. Lightwave Technol.* **25**, 103 (2007).
- [145] M. Matsuura, N. Kishi, and T. Miki, *J. Lightwave Technol.* **25**, 38 (2007).
- [146] J. Dong, X. Zhang, S. Fu, J. Xu, P. Shum, and D. Huang, *IEEE J. Sel. Topics Quantum Electron.* **14**, 770 (2008).
- [147] G. P. Agrawal, *J. Opt. Soc. Am. B* **5**, 147 (1988).
- [148] S. Hojfeldt, S. Bischoff, and J. Mork, *J. Lightwave Technol.* **18**, 1121 (2000).
- [149] P. Leclerc, B. Lavingne, and D. Chiaroni, in *Optical Fiber Telecommunications*, Vol. 4A, I. P. Kaminow and T. Li, Eds., Academic Press, Boston, 2002, Chap. 15.
- [150] K. Vlachos, N. Pleros, C. Bintjas, G. Theophilopoulos, and H. Avramopoulos, *J. Lightwave Technol.* **21**, 1857 (2003).
- [151] R. S. Tucker, in *Optical Fiber Telecommunications*, Vol. 5B, I. P. Kaminow and T. Li, and A. E. Willner, Eds., Academic Press, Boston, 2008, Chap. 17.

- [152] T. Morioka, H. Takara, S. Kawanishi, T. Kitoh, and M. Saruwatari, *Electron. Lett.* **32**, 832 (1996).
- [153] P. O. Hedekvist, M. Karlsson, and P. A. Andrekson, *J. Lightwave Technol.* **15**, 2051 (1997).
- [154] T. Hasegawa, K. Inoue, and K. Oda, *IEEE Photon. Technol. Lett.* **5**, 947 (1993).
- [155] T. Sakamoto, K. Seo, K. Taira, N. S. Moon, and K. Kikuchi, *IEEE Photon. Technol. Lett.* **16**, 563 (2004).
- [156] F. Yaman, Q. Lin, and G. P. Agrawal, *IEEE Photon. Technol. Lett.* **18**, 2335 (2006).
- [157] K. Uchiyama, T. Morioka, and M. Saruwatari, *Electron. Lett.* **31**, 1862 (1995).
- [158] B. E. Olsson and P. A. Andrekson, *IEEE Photon. Technol. Lett.* **9**, 764 (1997).
- [159] J. W. Lou, K. S. Jepsen, D. A. Nolan, S. H. Tarca, W. J. Bouton, A. F. Evans, and M. N. Islam, *IEEE Photon. Technol. Lett.* **12**, 1701 (2000).
- [160] T. Sakamoto, H. C. Lim, and K. Kikuchi, *IEEE Photon. Technol. Lett.* **14**, 1737 (2002).
- [161] B. E. Olsson and D. J. Blumenthal, *IEEE Photon. Technol. Lett.* **13**, 875 (2001).
- [162] L. Rau, W. Wang, B. E. Olsson, Y. Chiu, H. F. Chou, D. J. Blumenthal, and J. E. Bowers, *IEEE Photon. Technol. Lett.* **14**, 1725 (2002).
- [163] J. Li, B. E. Olsson, M. A. Karlsson, and P. A. Andrekson, *IEEE Photon. Technol. Lett.* **15**, 1770 (2003).
- [164] J. H. Lee, T. Tanemura, T. Nagashima, T. Hasegawa, S. Ohara, N. Sugimoto, and K. Kikuchi, *Opt. Lett.* **30**, 1267 (2005).
- [165] A. S. Lenihan, R. Salem, T. E. Murphy, and G. M. Carter, *IEEE Photon. Technol. Lett.* **18**, 1329 (2006).
- [166] R. Salem, A. S. Lenihan, G. M. Carter, and T. E. Murphy, *IEEE Photon. Technol. Lett.* **18**, 2254 (2006).
- [167] K. Uchiyama, S. Kawanishi, and M. Saruwatari, *IEEE Photon. Technol. Lett.* **10**, 890 (1998).
- [168] R. Hess, M. Caraccia-Gross, W. Vogt, et al., *IEEE Photon. Technol. Lett.* **10**, 166 (1998).
- [169] S. L. Jansen, M. Heid, S. Spälder, et al., *Electron. Lett.* **38**, 978 (2002).
- [170] C. Schubert, C. Schmidt, S. Ferber, R. Ludwig, and H. G. Weber, *Electron. Lett.* **39**, 1074 (2003).
- [171] C. Porzi, A. Bogoni, L. Poti, G. Contestabile, *IEEE Photon. Technol. Lett.* **17**, 633 (2005).
- [172] E. S. Awad, P. S. Cho, J. Goldhar, *IEEE Photon. Technol. Lett.* **17**, 1534 (2005).
- [173] J. Glesk, J. P. Sokoloff, and P. R. Prucnal, *Electron. Lett.* **30**, 339 (1994).
- [174] M. Nakazawa, H. Kubota, K. Suzuki, E. Yamada, and A. Sahara, *IEEE J. Sel. Topics Quantum Electron.* **6**, 363 (2000).
- [175] P. V. Studenkov, M. R. Gokhale, J. Wei, W. Lin, I. Glesk, P. R. Prucnal, and S. R. Forrest, *IEEE Photon. Technol. Lett.* **13**, 600 (2001).
- [176] E. Tangdiongga, Y. Liu, H. de Waardt, G. D. Khoe, and H. J. S. Dorren, *IEEE Photon. Technol. Lett.* **18**, 908 (2006).
- [177] E. Tangdiongga, Y. Liu, H. de Waardt, et al., *Opt. Lett.* **32**, 835 (2007).
- [178] T. Hirooka, M. Okazaki, T. Hirano, P. Guan, M. Nakazawa, and S. Nakamura, *IEEE Photon. Technol. Lett.* **21**, 1574 (2009).
- [179] S. Bigo, O. Leclerc, and E. Desurvire, *IEEE J. Sel. Topics Quantum Electron.* **3**, 1208 (1997).
- [180] S. H. Lee, K. Chow, and C. Shu, *Opt. Express* **13**, 1710 (2005).
- [181] C. H. Kwok and C. Lin, *IEEE J. Sel. Topics Quantum Electron.* **12**, 451 (2006); *IEEE Photon. Technol. Lett.* **19**, 1825 (2007).

- [182] S. H. Lee, K. Chow, and C. Shu, *Opt. Commun.* **263**, 152 (2006).
- [183] L. Xu, B. C. Wang, V. Baby, I. Glesk, and P. R. Prucnal, *IEEE Photon. Technol. Lett.* **15**, 308 (2003).
- [184] W. Li, M. Chen, Y. Dong, and S. Xie, *IEEE Photon. Technol. Lett.* **16**, 203 (2004).
- [185] C. G. Lee, Y. J. Kim, C. S. Park, H. J. Lee, and C. S. Park, *J. Lightwave Technol.* **23**, 834 (2005).
- [186] C. Yan, Y. Su, L. Yi, L. Leng, X. Tian, X. Xu, and Y. Tian, *IEEE Photon. Technol. Lett.* **18**, 2368 (2006).
- [187] K. Mishina, A. Maruta, S. Mitani, et al., *J. Lightwave Technol.* **24**, 3751 (2006).
- [188] H. Jiang, H. Wen, L. Han, Y. Guo, and H. Zhang, *IEEE Photon. Technol. Lett.* **19**, 1985 (2007).
- [189] X. Yang, A. Mishra, R. Manning, R. Webb, and A. Ellis, *Electron. Lett.* **43**, 890 (2007).
- [190] J. Dong, X. Zhang, J. Xu, and D. Huang, S. Fu, and P. Shum, *Opt. Express* **15**, 2907 (2007).
- [191] T. Silveira, A. Ferreira, A. Teixeira, and P. Monteiro, *IEEE Photon. Technol. Lett.* **20**, 1597 (2008).
- [192] L. Banchi, M. Presi, A. D'Errico, G. Contestabile, and E. Ciaramella, *J. Lightwave Technol.* **28**, 32 (2010).
- [193] H. J. S. Dorren, M. T. Hill, Y. Liu, et al., *J. Lightwave Technol.* **21**, 2 (2003).
- [194] Q. Lin, R. Jiang, C. F. Marki, C. J. McKinstry, R. Jopson, J. Ford, G. P. Agrawal, and S. Radic, *IEEE Photon. Technol. Lett.* **17**, 2376 (2005).
- [195] T. Tanemura, K. Takeda, Y. Kanema, and Y. Nakano, *Opt. Express* **14**, 10785 (2006).
- [196] J. Herrera, O. Raz, E. Tangdiongga, et al., *J. Lightwave Technol.* **26**, 176 (2008).
- [197] K. Huybrechts, T. Tanemura, Y. Nakano, R. Baets, and G. Morthier, *IEEE Photon. Technol. Lett.* **21**, 703 (2009).
- [198] T. Tanemura, K. Takeda, and Y. Nakano, *Opt. Express* **17**, 9454 (2009).
- [199] S. C. Nicholes, M. L. Măsanović, B. Jevremović, E. Lively, L. A. Coldren, and D. J. Blumenthal, *J. Lightwave Technol.* **28**, 641 (2010).
- [200] S. Radic, D. J. Moss, and B. J. Eggleton, in *Optical Fiber Telecommunications*, Vol. 5A, I. P. Kaminow, T. Li, and A. E. Willner, Eds., Academic Press, Boston, 2008, Chap. 20.
- [201] P. V. Mamyshev, *Proc. Eur. Conf. Opt. Commun.*, p. 475, 1998.
- [202] T. H. Her, G. Raybon, and C. Headley, *IEEE Photon. Technol. Lett.* **16**, 200 (2004).
- [203] M. Matsumoto, *J. Lightwave Technol.* **22**, 1472 (2004); *Opt. Express* **14**, 11018 (2006).
- [204] L. B. Fu, M. Rochette, V. G. Ta'eed, D. J. Moss, and B. J. Eggleton, *Opt. Express* **13**, 7637 (2005).
- [205] P. Johannisson and M. Karlsson, *IEEE Photon. Technol. Lett.* **17**, 2667 (2005).
- [206] M. Rochette, L. Fu, V. Ta'eed, D. J. Moss, and B. J. Eggleton, *IEEE J. Sel. Topics Quantum Electron.* **12**, 736 (2006).
- [207] M. R. E. Lamont, M. Rochette, D. J. Moss, and B. J. Eggleton, *IEEE Photon. Technol. Lett.* **18**, 1185 (2006).
- [208] J. H. Lee, T. Nagashima, T. Hasegawa, S. Ohara, N. Sugimoto, Y.-G. Han, S. B. Lee, and K. Kikuchi, *IEEE Photon. Technol. Lett.* **18**, 1296 (2006).
- [209] A. G. Striegler and B. Schmauss, *J. Lightwave Technol.* **24**, 2835 (2006).
- [210] L. A. Provost, C. Finot, P. Petropoulos, K. Mukasa, and D. J. Richardson, *Opt. Express* **15**, 5100 (2007).
- [211] P. P. Baveja, D. N. Maywar, and G. P. Agrawal, *J. Lightwave Technol.* **27**, 3831 (2009).
- [212] M. Matsumoto and O. Leclerc, *Electron. Lett.* **38**, 576 (2002).

- [213] M. Jinno, *J. Lightwave Technol.* **12**, 1648 (1994).
- [214] N. J. Smith and N. J. Doran, *J. Opt. Soc. Am. B* **12**, 1117 (1995).
- [215] W. A. Pender, T. Widdowson, and A. D. Ellis, *Electron. Lett.* **32**, 567 (1996).
- [216] M. Meissner, M. Rösch, B. Schmauss, and G. Leuchs, *IEEE Photon. Technol. Lett.* **15**, 1297 (2003).
- [217] M. Meissner, K. Sponsel, K. Cvecek, A. Benz, S. Weisser, B. Schmauss, and G. Leuchs, *IEEE Photon. Technol. Lett.* **16**, 2105 (2004).
- [218] P. Z. Huang, A. Gray, I. Khrushchev, and I. Bennion, *IEEE Photon. Technol. Lett.* **16**, 2526 (2004).
- [219] A. Bogoni, P. Ghelfi, M. Scaffardi, and L. Poti, *IEEE J. Sel. Topics Quantum Electron.* **10**, 192 (2004).
- [220] E. Ciaramella and T. Stefano, *IEEE Photon. Technol. Lett.* **12**, 849 (2000).
- [221] K. Inoue, *IEEE Photon. Technol. Lett.* **13**, 338 (2001).
- [222] E. Ciaramella, F. Curti, and T. Stefano, *IEEE Photon. Technol. Lett.* **13**, 142 (2001).
- [223] K. Inoue and T. Mukai, *J. Lightwave Technol.* **20**, 969 (2002).
- [224] A. Bogris and D. Syvridis, *J. Lightwave Technol.* **21**, 1892 (2003).
- [225] S. Radic, C. J. McKinstrie, R. M. Jopson, J. C. Centanni, and A. R. Chraplyvy, *IEEE Photon. Technol. Lett.* **15**, 957 (2003).
- [226] S. Yamashita and M. Shahed, *IEEE Photon. Technol. Lett.* **18**, 1054 (2006).
- [227] D. Wolfson, A. Kloch, T. Fjelde, C. Janz, B. Dagens, and M. Renaud, *IEEE Photon. Technol. Lett.* **12**, 332 (2000).
- [228] J. De Merlier, G. Morthier, S. Verstuyft, et al., *IEEE Photon. Technol. Lett.* **14**, 660 (2002).
- [229] F. Öhman, R. Kjær, L. J. Christiansen, K. Yvind, and J. Mørk, *IEEE Photon. Technol. Lett.* **18**, 1273 (2006).
- [230] M. Gay, L. Bramerie, D. Massoubre, A. OHare, A. Shen, J. L. Oudar, and J. C. Simon, *IEEE Photon. Technol. Lett.* **18**, 1067 (2006).
- [231] G. Contestabile, M. Presi, R. Proietti, and E. Ciaramella, *IEEE Photon. Technol. Lett.* **20**, 1133 (2008).
- [232] A. Sahara, T. Inui, T. Komukai, H. Kubota, and M. Nakazawa, *J. Lightwave Technol.* **18**, 1364 (2000).
- [233] O. Leclerc, B. Lavigne, E. Balmefrezol, P. Brindel, L. Pierre, D. Rouvillain, F. Seguinéau, *J. Lightwave Technol.* **21**, 2779 (2003).
- [234] G. Raybon, Y. Su, J. Leuthold, et al., Proc. Optical Fiber Commun., Paper FD10, 2002.
- [235] J. Leuthold, G. Raybon, Y. Su, et al., *Electron. Lett.* **38**, 890 (2002).
- [236] L. A. Jiang, M. E. Grein, H. A. Haus, and E. P. Ippen, *Opt. Lett.* **28**, 78 (2003).
- [237] J. A. Harrison, K. J. Blow, and A. J. Poustie, *Opt. Commun.* **240**, 221 (2004).
- [238] A. Striegler and B. Schmauss, *IEEE Photon. Technol. Lett.* **16**, 2574 (2004); *IEEE Photon. Technol. Lett.* **17**, 1310 (2005).
- [239] J. Suzuki, T. Tanemura, K. Taira, Y. Ozeki, and K. Kikuchi, *IEEE Photon. Technol. Lett.* **17**, 423 (2005).
- [240] F. Parmigiani, P. Petropoulos, M. Ibsen, and D. J. Richardson, *J. Lightwave Technol.* **24**, 357 (2006).
- [241] M. Rochette, J. L. Blows, and B. J. Eggleton, *Opt. Express* **14**, 6414 (2006).
- [242] Z. Zhu, M. Funabashi, Z. Pan, L. Paraschis, D. L. Harris, and S. J. B. Yoo, *J. Lightwave Technol.* **25**, 504 (2007).
- [243] C. Ito and J. C. Cartledge, *IEEE J. Sel. Topics Quantum Electron.* **14**, 616 (2008).

- [244] T. Otani, T. Miyazaki, and S. Yamamoto, *J. Lightwave Technol.* **20**, 195 (2002).
- [245] H. Murai, M. Kagawa, H. Tsuji, and K. Fujii, *IEEE Photon. Technol. Lett.* **17**, 1965 (2005).
- [246] M. Daikoku, N. Yoshikane, T. Otani, and H. Tanaka, *J. Lightwave Technol.* **24**, 1142 (2006).
- [247] G. Gavioli and P. Bayvel, *IEEE Photon. Technol. Lett.* **21**, 1014 (2009).
- [248] J. Leuthold, B. Mikkelsen, R. E. Behringer, G. Raybon, C. H. Joyner, and P. A. Besse, *IEEE Photon. Technol. Lett.* **13**, 860 (2001).
- [249] Y. Ueno, S. Nakamura, and K. Tajima, *IEEE Photon. Technol. Lett.* **13**, 469 (2001).
- [250] G. Contestabile, A. D'Errico, M. Presi, and E. Ciaramella, *IEEE Photon. Technol. Lett.* **16**, 2523 (2004).
- [251] Z. Hu, H.-F. Chou, K. Nishimura, L. Rau, M. Usami, J. E. Bowers, and D. J. Blumenthal, *IEEE J. Sel. Topics Quantum Electron.* **11**, 329 (2005).
- [252] S. Arahira and Y. Ogawa, *IEEE J. Quantum Electron.* **41**, 937 (2005); **43**, 1204 (2007).
- [253] I. Kim, C. Kim, G. Li, P. LiKamWa, and J. Hong, *IEEE Photon. Technol. Lett.* **17**, 1295 (2005).
- [254] Z. Zhu, M. Funabashi, P. Zhong, L. Paraschis, and S. J. B. Yoo, *IEEE Photon. Technol. Lett.* **18**, 2159 (2006).
- [255] B. Lavigne, J. Renaudier, F. Lelarge, O. Legouezigou, H. Gariah, and G.-H. Duan, *J. Lightwave Technol.* **25**, 170 (2007).
- [256] F. Wang, Y. Yu, X. Huang, and X. Zhang, *IEEE Photon. Technol. Lett.* **21**, 1109 (2009).
- [257] S. Arahira, H. Takahashi, K. Nakamura, H. Yaegashi, and Y. Ogawa, *IEEE J. Quantum Electron.* **45**, 476 (2009).
- [258] S. Pan and J. Yao, *J. Lightwave Technol.* **27**, 3531 (2009).
- [259] A. Striegler and B. Schmauss, *IEEE Photon. Technol. Lett.* **16**, 1083 (2004).
- [260] A. G. Striegler, M. Meissner, K. Cvecek, K. Sponsel, G. Leuchs, and B. Schmauss, *IEEE Photon. Technol. Lett.* **17**, 639 (2005).
- [261] M. Matsumoto, *IEEE Photon. Technol. Lett.* **17**, 1055 (2005); *J. Lightwave Technol.* **23**, 2696 (2005).
- [262] K. Croussore, I. Kim, Y. Han, C. Kim, G. Li, and S. Radic, *Opt. Express* **13**, 3945 (2005).
- [263] S. Boscolo, R. Bhamber, and S. K. Turitsyn, *IEEE J. Quantum Electron.* **42**, 619 (2006).
- [264] K. Cvecek, G. Onishchukov, K. Sponsel, A. G. Striegler, B. Schmauss, and G. Leuchs, *IEEE Photon. Technol. Lett.* **18**, 1801 (2006).
- [265] P. Vorreau, A. Marculescu, J. Wang, et al., *IEEE Photon. Technol. Lett.* **18**, 1970 (2006).
- [266] K. Croussore, I. Kim, C. Kim, and G. Li, *Opt. Express* **14**, 2085 (2006).
- [267] A. Bogris and D. Syvridis, *IEEE Photon. Technol. Lett.* **18**, 2144 (2006).
- [268] K. Cvecek, K. Sponsel, G. Onishchukov, B. Schmauss, and G. Leuchs, *IEEE Photon. Technol. Lett.* **19**, 146 (2007).
- [269] M. Matsumoto and H. Sakaguchi, *Opt. Express* **16**, 11169 (2008).
- [270] M. Matsumoto and Y. Morioka, *Opt. Express* **17**, 6913 (2009).
- [271] K. Cvecek, K. Sponsel, R. Ludwig, et al., *IEEE Photon. Technol. Lett.* **19**, 1475 (2007).
- [272] J. Yan, L. An, Z. Zheng, and X. Liu, *IET Optoelectron.* **3**, 158 (2009)
- [273] M. Matsumoto, *Opt. Express* **18**, 10 (2010).

Appendix A

System of Units

The international system of units (known as the SI, short for *Système International*) is used in this book. The three fundamental units in the SI are meter (m), second (s), and kilogram (kg). A prefix can be added to each of them to change its magnitude by a multiple of 10. Mass units are rarely required in this book. Most common measures of distance used are km (10^3 m) and Mm (10^6 m). On the other hand, common time measures are ns (10^{-9} s), ps (10^{-12} s), and fs (10^{-15} s). Other common units in this book are Watt (W) for optical power and W/m^2 for optical intensity. They can be related to the fundamental units through energy because optical power represents the rate of energy flow ($1 \text{ W} = 1 \text{ J/s}$). The energy can be expressed in several other ways using $E = h\nu = k_B T = mc^2$, where h is the Planck constant, k_B is the Boltzmann constant, and c is the speed of light. The frequency ν is expressed in hertz ($1 \text{ Hz} = 1 \text{ s}^{-1}$). Of course, because of the large frequencies associated with the optical waves, most frequencies in this book are expressed in GHz or THz.

In the design of optical communication systems the optical power can vary over several orders of magnitude as the signal travels from the transmitter to the receiver. Such large variations are handled most conveniently using decibel units, abbreviated dB, commonly used by engineers in many different fields. Any ratio R can be converted into decibels by using the general definition

$$R \text{ (in dB)} = 10 \log_{10} R. \quad (\text{A.1})$$

The logarithmic nature of the decibel allows a large ratio to be expressed as a much smaller number. For example, 10^9 and 10^{-9} correspond to 90 dB and -90 dB, respectively. Since $R = 1$ corresponds to 0 dB, ratios smaller than 1 are negative in the decibel system. Furthermore, negative ratios cannot be written using decibel units.

The most common use of the decibel scale occurs for power ratios. For instance, the signal-to-noise ratio (SNR) of an optical or electrical signal is given by

$$\text{SNR} = 10 \log_{10} (P_S/P_N), \quad (\text{A.2})$$

where P_S and P_N are the signal and noise powers, respectively. The fiber loss can also be expressed in decibel units by noting that the loss corresponds to a decrease in the

optical power during transmission and thus can be expressed as a power ratio. For example, if a 1-mW signal reduces to 1 μ W after transmission over 100 km of fiber, the 30-dB loss over the entire fiber span translates into a loss of 0.3 dB/km. The same technique can be used to define the insertion loss of any component. For instance, a 1-dB loss of a fiber connector implies that the optical power is reduced by 1 dB (by about 20%) when the signal passes through the connector. The bandwidth of an optical filter is defined at the 3-dB point, corresponding to 50% reduction in the signal power. The modulation bandwidth of light-emitting diodes (LEDs) in Section 3.2 and of semiconductor lasers in Section 3.5 is also defined at the 3-dB point, at which the modulated powers drops by 50%.

Since the losses of all components in a fiber-optic communication systems are expressed in dB, it is useful to express the transmitted and received powers also by using a decibel scale. This is achieved by using a derived unit, denoted as dBm and defined as

$$\text{power (in dBm)} = 10 \log_{10} \left(\frac{\text{power}}{1 \text{ mW}} \right), \quad (\text{A.3})$$

where the reference level of 1 mW is chosen simply because typical values of the transmitted power are in that range (the letter m in dBm is a reminder of the 1-mW reference level). In this decibel scale for the absolute power, 1 mW corresponds to 0 dBm, whereas powers below 1 mW are expressed as negative numbers. For example, a 10- μ W power corresponds to -20 dBm. The advantage of decibel units becomes clear when the power budget of lightwave systems is considered in Chapter 5. Because of the logarithmic nature of the decibel scale, the power budget can be made simply by subtracting various losses from the transmitter power expressed in dBm units.

Appendix B

Acronyms

Each scientific field has its own jargon, and the field of optical communications is not an exception. Although an attempt was made to avoid extensive use of acronyms, many still appear throughout the book. Each acronym is defined the first time it appears in a chapter so that the reader does not have to search the entire text to find its meaning. As a further help, we list all acronyms here, in alphabetical order.

AM	amplitude modulation
AON	all-optical network
APD	avalanche photodiode
ASE	amplified spontaneous emission
ASK	amplitude-shift keying
ATM	asynchronous transfer mode
AWG	arrayed-waveguide grating
BER	bit-error rate
BH	buried heterostructure
BPF	bandpass filter
BPSK	binary phase-shift keying
CATV	common-antenna (cable) television
CDM	code-division multiplexing
CDMA	code-division multiple access
CNR	carrier-to-noise ratio
CPFSK	continuous-phase frequency-shift keying
CRZ	chirped return-to-zero
CSMA	carrier-sense multiple access
CSRZ	carrier-suppressed return-to-zero
CSO	composite second-order
CVD	chemical vapor deposition
CW	continuous wave
CTB	composite triple beat
DBPSK	differential binary phase-shift keying
DBR	distributed Bragg reflector

DCF	dispersion-compensating fiber
DDF	dispersion-decreasing fiber
DFB	distributed feedback
DFT	discrete Fourier transform
DGD	differential group delay
DIP	dual in-line package
DM	dispersion-managed
DPSK	differential phase-shift keying
DQPSK	differential quadrature phase-shift keying
DSP	digital signal processing
EDFA	erbium-doped fiber amplifier
FDM	frequency-division multiplexing
FET	field-effect transistor
FM	frequency modulation
FP	Fabry–Perot
FFT	fast Fourier transform
FSK	frequency-shift keying
FWHM	full-width at half-maximum
FWM	four-wave mixing
GVD	group-velocity dispersion
HBT	heterojunction-bipolar transistor
HDTV	high-definition television
HEMT	high-electron-mobility transistor
HFC	hybrid fiber-coaxial
IC	integrated circuit
IF	intermediate frequency
IMD	intermodulation distortion
IM/DD	intensity modulation with direct detection
IMP	intermodulation product
ISDN	integrated services digital network
ISI	intersymbol interference
ITU	International Telecommunication Union
LAN	local-area network
LEAF	large effective-area fiber
LED	light-emitting diode
LO	local oscillator
LPE	liquid-phase epitaxy
LPF	low-pass filter
MAN	metropolitan-area network
MBE	molecular-beam epitaxy
MCSV	modified chemical vapor deposition
MEMS	micro-electro-mechanical system
MMI	multi-mode interference
MOCVD	metal-organic chemical vapor deposition
MONET	multiwavelength optical network
MPEG	motion-picture entertainment group

MPN	mode-partition noise
MQW	multiquantum well
MSK	minimum-shift keying
MSM	metal–semiconductor–metal
MSR	mode-suppression ratio
MTTF	mean time to failure
MZ	Mach–Zehnder
NA	numerical aperture
NEP	noise-equivalent power
NLS	nonlinear Schrödinger
NOLM	nonlinear optical-loop mirror
NRZ	nonreturn to zero
NSE	nonlinear Schrödinger equation
NSDSF	nonzero-dispersion-shifted fiber
OCDM	optical code-division multiplexing
OEIC	opto-electronic integrated circuit
OFDM	orthogonal frequency-division multiplexing
OOK	on–off keying
OPC	optical phase conjugation
OTDM	optical time-division multiplexing
OVD	outside-vapor deposition
OXC	optical cross-connect
PCM	pulse-code modulation
PDF	probability density function
PDM	polarization-division multiplexing
PIC	photonic integrated circuit
PM	phase modulation
PMD	polarization-mode dispersion
PON	passive optical network
PPLN	periodically poled lithium niobate
PSK	phase-shift keying
PSP	principal state of polarization
QAM	quadrature amplitude modulation
QPSK	quadrature phase-shift keying
RDF	reverse-dispersion fiber
RF	radio frequency
RIN	relative intensity noise
RMS	root mean square
RZ	return to zero
SAGM	separate absorption, grading, and multiplication
SAM	separate absorption and multiplication
SBS	stimulated Brillouin scattering
SCM	subcarrier multiplexing
SDH	synchronous digital hierarchy
SLM	single longitudinal mode
SNR	signal-to-noise ratio

SOA	semiconductor optical amplifier
SONET	synchronized optical network
SOP	state of polarization
SPM	self-phase modulation
SRS	stimulated Raman scattering
SSFS	soliton self-frequency shift
STM	synchronous transport module
STS	synchronous transport signal
TDM	time-division multiplexing
TE	transverse electric
TM	transverse magnetic
TOAD	terahertz optical asymmetric demultiplexer
TOD	third-order dispersion
TPA	two-photon absorption
VAD	vapor-axial deposition
VCSEL	vertical-cavity surface-emitting laser
VPE	vapor-phase epitaxy
VSB	vestigial sideband
WAN	wide-area network
WDM	wavelength-division multiplexing
WDMA	wavelength-division multiple access
WGR	waveguide-grating router
XPM	cross-phase modulation
YAG	yttrium aluminium garnet
YIG	yttrium iron garnet
ZDWL	zero-dispersion wavelength

Appendix C

General Formula for Pulse Broadening

The discussion of pulse broadening in Section 2.4 assumes the Gaussian-shape pulses and includes dispersive effects only up to the third order. In this appendix, a general formula is derived that can be used for pulses of arbitrary shape. Moreover, it makes no assumption about the dispersive properties of the fiber and can be used to include dispersion to any order. The basic idea behind the derivation consists of the observation that the pulse spectrum does not change in a linear dispersive medium irrespective of what happens to the pulse shape. It is thus better to calculate the changes in the pulse width in the spectral domain.

For pulses of arbitrary shapes, a measure of the pulse width is provided by the quantity $\sigma^2 = \langle t^2 \rangle - \langle t \rangle^2$, where the first and second moments are calculated using the pulse shape as indicated in Eq. (2.4.21). These moments can also be defined in terms of the pulse spectrum as

$$\langle t \rangle = \int_{-\infty}^{\infty} t |A(z, t)|^2 dt \equiv \frac{-i}{2\pi} \int_{-\infty}^{\infty} \tilde{A}^*(z, \omega) \tilde{A}_\omega(z, \omega) d\omega, \quad (\text{C.1})$$

$$\langle t^2 \rangle = \int_{-\infty}^{\infty} t^2 |A(z, t)|^2 dt \equiv \frac{1}{2\pi} \int_{-\infty}^{\infty} |\tilde{A}_\omega(z, \omega)|^2 d\omega, \quad (\text{C.2})$$

where $\tilde{A}(z, \omega)$ is the Fourier transform of $A(z, t)$ and the subscript ω denotes partial derivative with respect to ω . For simplicity of discussion, we normalize A and \tilde{A} such that

$$\int_{-\infty}^{\infty} |A(z, t)|^2 dt = \frac{1}{2\pi} \int_{-\infty}^{\infty} |\tilde{A}(z, \omega)|^2 d\omega = 1. \quad (\text{C.3})$$

As discussed in Section 2.4, when nonlinear effects are negligible, different spectral components propagate inside the fiber according to the simple relation

$$\tilde{A}(z, \omega) = \tilde{A}(0, \omega) \exp(i\beta z) = [S(\omega) e^{i\theta}] \exp(i\beta z), \quad (\text{C.4})$$

where $S(\omega)$ represents the spectrum of the input pulse and $\theta(\omega)$ accounts for the effects of input chirp. As seen in Eq. (2.4.13), the spectrum of chirped pulses acquires

a frequency-dependent phase. The propagation constant β depends on frequency because of dispersion. It can also depend on z when dispersion management is used or when fiber parameters such as the core diameter are not uniform along the fiber.

If we substitute Eq. (C.4) in Eqs. (C.1) and (C.2), perform the derivatives as indicated, and calculate $\sigma^2 = \langle t^2 \rangle - \langle t \rangle^2$, we obtain

$$\sigma^2 = \sigma_0^2 + [\langle t^2 \rangle - \langle t \rangle^2] + 2[\langle \tau \theta_\omega \rangle - \langle \tau \rangle \langle \theta_\omega \rangle], \quad (\text{C.5})$$

where the angle brackets now denote average over the input pulse spectrum such that

$$\langle f \rangle = \frac{1}{2\pi} \int_{-\infty}^{\infty} f(\omega) |S(\omega)|^2 d\omega. \quad (\text{C.6})$$

In Eq. (C.5), σ_0 is the root-mean-square (RMS) width of input pulses, $\theta_\omega = d\theta/d\omega$, and τ is the group delay defined as

$$\tau(\omega) = \int_0^L \frac{\partial \beta(z, \omega)}{\partial \omega} dz \quad (\text{C.7})$$

for a fiber of length L . Equation (C.5) can be used for pulses of arbitrary shape, width, and chirp. It makes no assumption about the form of $\beta(z, \omega)$ and thus can be used for dispersion-managed fiber links containing fibers with arbitrary dispersion characteristics.

As a simple application of Eq. (C.5), one can use it to derive Eq. (2.4.22). Assuming uniform dispersion and expanding $\beta(z, \omega)$ to third-order in ω , the group delay is given by

$$\tau(\omega) = (\beta_1 + \beta_2 \omega + \frac{1}{2} \beta_3 \omega^2)L. \quad (\text{C.8})$$

For a chirped Gaussian pulse, Eq. (2.4.13) provides the following expressions for S and θ :

$$S(\omega) = \sqrt{\frac{4\pi T_0^2}{1+C^2}} \exp\left[-\frac{\omega^2 T_0^2}{2(1+C^2)}\right], \quad \theta(\omega) = \frac{C\omega^2 T_0^2}{2(1+C^2)} - \tan^{-1} C. \quad (\text{C.9})$$

The averages in Eq. (C.5) can be performed analytically using Eqs. (C.8) and (C.9) and result in Eq. (2.4.22).

As another application of Eq. (C.5), consider the derivation of Eq. (2.4.23) that includes the effects of a wide source spectrum. For such a pulse, the input field can be written as $A(0, t) = A_0(t)f(t)$, where $f(t)$ represents the pulse shape and $A_0(t)$ is fluctuating because of the partially coherent nature of the source. The spectrum $S(\omega)$ now becomes a convolution of the pulse spectrum and the source spectrum such that

$$S(\omega) = \frac{1}{2\pi} \int_{-\infty}^{\infty} S_p(\omega - \omega_1) F(\omega_1) d\omega_1, \quad (\text{C.10})$$

where S_p is the pulse spectrum and $F(\omega_s)$ is the fluctuating field spectral component at the source with the correlation function of the form

$$\langle F^*(\omega_1) F(\omega_2) \rangle_s = G(\omega_1) \delta(\omega_1 - \omega_2). \quad (\text{C.11})$$

The quantity $G(\omega)$ represents the source spectrum. The subscript s in Eq. (C.11) is a reminder that the angle brackets now denote an ensemble average over the field fluctuations.

The moments $\langle t \rangle$ and $\langle t^2 \rangle$ are now replaced by $\langle\langle t \rangle\rangle_s$ and $\langle\langle t^2 \rangle\rangle_s$ where the outer angle brackets stand for the ensemble average over field fluctuations. Both of them can be calculated in the special case in which the source spectrum is assumed to be Gaussian, i.e.,

$$G(\omega) = \frac{1}{\sigma_\omega \sqrt{2\pi}} \exp\left(-\frac{\omega^2}{2\sigma_\omega^2}\right), \quad (\text{C.12})$$

where σ_ω is the RMS spectral width of the source. For example,

$$\begin{aligned} \langle\langle t \rangle\rangle_s &= \int_{-\infty}^{\infty} \tau(\omega) \langle |S(\omega)|^2 \rangle_s d\omega - i \int_{-\infty}^{\infty} \langle S^*(\omega) S_\omega(\omega) \rangle_s d\omega \\ &= L \iint_{-\infty}^{\infty} (\beta_1 + \beta_2 \omega + \frac{1}{2} \beta_3 \omega^2) |S_p(\omega - \omega_1)|^2 G(\omega_1) d\omega_1 d\omega \end{aligned} \quad (\text{C.13})$$

Since both the pulse spectrum and the source spectrum are assumed to be Gaussian, the integral over ω_1 can be performed first, resulting in another Gaussian spectrum. The integral over ω is then straightforward in Eq. (C.13) and yields

$$\langle\langle t \rangle\rangle_s = L \left[\beta_1 + \frac{\beta_3}{8\sigma_0^2} (1 + C^2 + V_\omega^2) \right], \quad (\text{C.14})$$

where $V_\omega = 2\sigma_\omega\sigma_0$. Repeating the same procedure for $\langle\langle t^2 \rangle\rangle_s$, we recover Eq. (2.4.13) for the ratio σ/σ_0 .

Appendix D

Software Package

The back cover of the book contains a software package for designing fiber-optic communication system on a compact disk (CD) provided by the Optiwave Corporation (Website: www.optiwave.com). The CD contains 32-bit and 64-bit versions of a program called OptiPerformer 8 based on the commercial software sold by Optiwave under the name OptiSystem 8.0. The CD also contains a set of problems for each chapter that are appropriate for the readers of this book. The reader is encouraged to try these numerical exercises as they will help in understanding many important issues involved in the design of realistic lightwave systems.

The CD should work on any PC running the Microsoft Windows software (XP, Vista, or Windows 7). The first step is to install the OptiPerformer. The installation procedure should be straightforward for most users. Simply insert the CD in the CD-ROM drive, and follow the instructions. If the installer does not start automatically, one may have to click on the "setup" program in the root directory of the CD. After the installation, the user simply has to click on the icon named `OptiPerformer.exe` to start the program.

The philosophy behind the computer-aid design of lightwave systems has been discussed in Section 5.6. Similar to the setup seen in Fig. 5.15, the main window of the program is used to layout the lightwave system using various components from the component library. Once the layout is complete, the optical bit stream is propagated through the fiber link by solving the nonlinear Schrödinger equation as discussed in Section 5.6. It is possible to record the temporal and spectral features of the bit stream at any location along the fiber link by inserting the appropriate data-visualization components.

The OptiSystem software can be used for solving many problems assigned at the end of each chapter. Consider, for example, the simple problem of the propagation of optical pulses inside optical fibers discussed in Section 2.4. Top part of Figure D.1 shows the layout for solving this problem. The input bit pattern should have the RZ format and be of the form "000010000" so that a single isolated pulse is propagated. The shape of this pulse can be specified directly or calculated using the Mach-Zehnder modulator module. The output of the modulator is connected to an optical fiber whose length and other parameters can be specified by the user. The fiber output can be

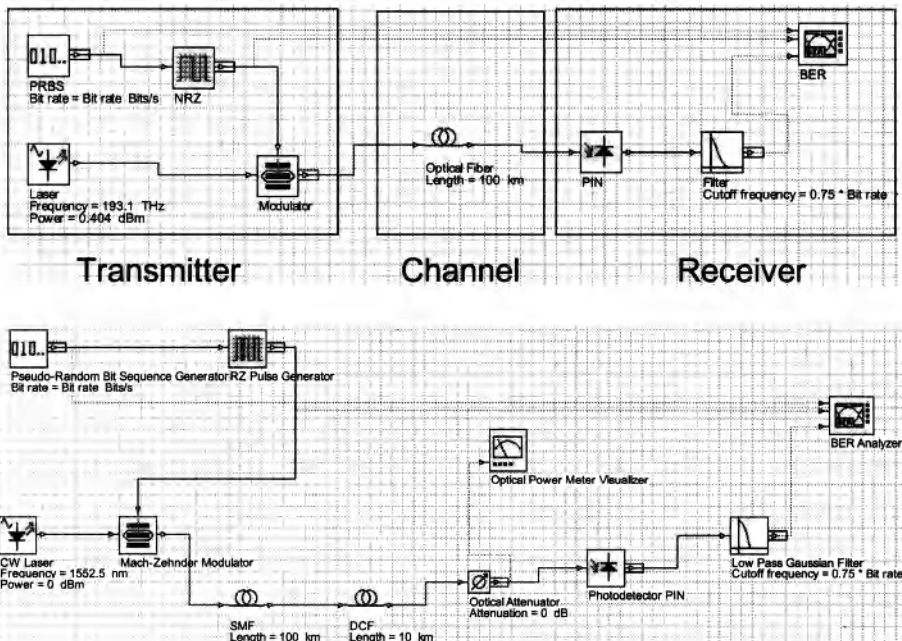


Figure D.1: Two examples of the layout for solving system-design problems with the Optiwave software supplied on the CD.

connected directly to temporal and spectral visualizers so that the shape and spectrum of the output pulse can be observed graphically. It can also be sent to a photodiode and electrical filter before using visualizers to record the pulse shape and its spectrum. If the nonlinear effects are turned off or input power is set to low enough for them remain negligible, the spectrum should not change but the pulse should exhibit considerable broadening. For Gaussian pulses, the results should agree with the theory of Section 2.4.

The OptiPerformer supplied on the CD does not allow one to create their own designs. Rather, a large number of prepared samples are provided in the directory **OptiPerformer Files**. Folders in this directory are arranged by chapters, and each chapter contains several files that can be run using the OptiPerformer software to solve the underlying design problem. Figure D.1 shows an example related to dispersion management. Most users of this book will benefit by solving these problems and analyzing the graphical output. A portable-data format (PDF) file is also included; it can be consulted to find more details about each problem.

Index

- absorption
 free-carrier, 85
 material, 72
 two-photon, 98, 521, 540, 555
- accelerated aging, 119
- acoustic waves, 60, 237
- activation energy, 120
- amplification
 distributed, 296, 298, 311, 319, 408, 423, 439
 lumped, 298, 318, 333, 419–423, 446
 parametric, 537, 538
 periodic, 296
 phase-sensitive, 566
 Raman, 338
- amplification factor, 312, 517, 524
- amplified spontaneous emission, 301, 307, 483
- amplifier
 cascaded, 296, 318, 324
 chain of, 318, 323
 distributed, 315
 dual-pump parametric, 519
 erbium-doped fiber, *see* EDFA
 Fabry–Perot, 529
 hybrid, 313
 in-line, 194
 lumped, 296, 317, 409
 parametric, 372, 516–521, 537, 557
 Raman, 309–318, 320
 semiconductor optical, 373
 silicon-based parametric, 521
 single-pump parametric, 517
 thulium-doped fiber, 310
- amplifier spacing, 318, 324, 374, 409, 419
- amplitude mask, 360
- amplitude-phase coupling, 98, 103
- amplitude-shift keying, *see* modulation format
- anticorrelation, 102, 202
- antireflection coating, 90, 114, 238, 522
- APD, 137–143
- bandwidth of, 139
- design of, 138
- enhanced shot noise in, 155
- excess noise factor for, 155
- gain of, 139
- optimum gain for, 156, 165
- physical mechanism behind, 137
- reach-through, 140
- responsivity of, 139
- SAM, 140, 141
- superlattice, 142
- apodization technique, 355, 358
- ASCII code, 8
- ATM protocol, 228, 230, 269
- Auger recombination, 81, 82, 97
- autocorrelation function, 101, 151, 279, 281
- avalanche breakdown, 139
- avalanche photodiode, *see* APD
- balanced detection, 477
- bandwidth
 amplifier, 307, 336
 APD, 139
 ASE, 321
 Brillouin-gain, 258
 electrical, 317
 fiber, 54, 193
 filter, 146, 233, 238, 336, 347, 363
 grating, 354, 357
 LED, 113, 114
 modulation, 99, 114
 noise, 152, 322
 parametric amplifier, 518
 photodetector, 131, 134
 Raman-amplifier, 310
 Raman-gain, 63
 RC circuit, 192
 receiver, 271, 471
 semiconductor laser, 99
 signal, 11, 269, 321, 390

- small-signal modulation, 98
- beat length, 36
- Beer's law, 55
- bending loss, 58
- BER floor, 355
- Bessel function, 32, 327, 329, 473, 475, 484
- biconical taper, 241, 245
- birefringence, 36, 44, 481
 - circular, 537, 547
 - degree of, 36
 - linear, 547
 - random, 45, 382
- bistability, 526–533
 - dispersive, 527
 - physical mechanism for, 529
 - polarization, 530
- bit rate-distance product, 3, 27, 28, 44, 53, 184, 189, 203, 225, 268, 432
- bit slot, 8, 51, 146, 208, 268, 386, 392
- bit-error rate, 19, 162–164, 212–214, 252, 325, 470–476
- Boltzmann constant, 112, 152
- Bragg condition, 88, 237, 239, 356
- Bragg diffraction, 88, 90, 237, 239
- Bragg wavelength, 92, 237, 238, 354, 375, 530
- Brillouin gain, 61
- Brillouin scattering, 59, 199, 486
 - spontaneous, 60
 - stimulated, 60, 238, 257, 521, 527, 538
 - suppression of, 538
 - threshold of, 536, 538, 540
- Brillouin shift, 60, 61, 238, 257
- Brillouin threshold, 257
- broadcast star, 231, 244–245
- butt coupling, 115
- cable television, 184, 269
- carrier lifetime, 82, 95, 97, 522–524, 540
- carrier-induced nonlinearity, 523
- carrier-sense multiple access, 186
- carrier-to-noise ratio, 271
- catastrophic degradation, 119
- CDMA systems, 277–283
- chemical-vapor deposition, 69
- chip rate, 278
- chirp
 - amplifier-induced, 388, 525
 - dispersion-induced, 49
 - fiber-induced, 389
 - linear, 361, 376
- modulation induced, 387
- modulation-induced, 190, 200
- modulator-induced, 108
- power penalty due to, 209
- SPM-induced, 416, 553
- XPM-induced, 260, 437
- chirp parameter, 48, 53, 108, 209, 387, 388
- chromium heater, 366, 368
- circuit switching, 228, 230
- circulator, 359, 364, 380, 381
- clipping noise, 273
- clock circuit, 465
- clock recovery, 147, 162, 171
- coaxial cable, 2, 188, 269
- code-division multiplexing, 277–283
- codes
 - bipolar, 279
 - duobinary, 390
 - error-correcting, 212
 - frequency hopping, 281
 - orthogonal, 278, 281
 - pseudo-orthogonal, 281
 - Reed-Solomon, 212
 - signature sequence, 278
 - spectral, 280
 - turbo, 212
 - two-dimensional, 281
 - unipolar, 279
- coherence function, 50
- coherence time, 282, 478
- coherent detection, 158–160, 462, 464
- coherent lightwave systems, 459–503
 - advantages of, 158
 - bit-error rate for, 470–476
 - dispersion effects in, 484
 - phase noise in, 478–480
 - polarization effects in, 480
 - sensitivity degradation for, 476–485
- computer-aided design, 214, 335, 337
- confinement factor, 38, 85, 95, 355, 523
- constellation diagram, 15, 460, 463
- conversion efficiency, 373, 522, 538, 541
- core–cladding interface, 25, 27, 58
- correlation length, 45
- Costas loop, 465
- coupled-mode equations, 354, 358, 360
- coupling coefficient, 355
- coupling efficiency, 87, 111, 113, 115
- critical angle, 25, 58, 110
- cross-correlation, 203, 279, 281

- cross-gain saturation, 307
cross-phase modulation, 65, 328, 407, 434–441, 514, 533, 543, 556
control of, 444–451
demultiplexing with, 267
interchannel, 259–261, 489
intrachannel, 436–441, 489
crosstalk, 251–264
Brillouin-induced, 257
EDFA-induced, 307
electrical, 108
filter-induced, 251–253
FWM-induced, 67, 261–262, 277
heterowavelength, 251
homowavelength, 251, 253
in-band, 253–254
linear, 251–254
nonlinear, 255–262
out-of-band, 251–253
Raman-induced, 64, 255–257, 274
router-induced, 253–254
XPM-induced, 66, 259–261, 274
crosstalk penalty, 252, 254
cutoff wavelength, 130
cyclic prefix, 275

dark current, 131, 152, 161
decision circuit, 147, 162, 208, 210, 390, 466, 471, 474, 481
decision threshold, 162, 163, 211, 252, 386
decision-feedback equalizer, 393
decoder, 279
CDMA, 278
spectral phase, 280
delay technique, 264
demodulation
asynchronous, 466
coherent, 464, 497
delay, 467, 475
DQPSK, 469
in optical domain, 467
incoherent, 466
schemes for, 464–469
self-coherent, 467
synchronous, 464
demultiplexer, 238–242
concave-grating, 251
diffraction-based, 238
electro-optic, 266
filter-based, 240
grating-based, 239
interference-based, 238
TDM, 266–267
terahertz optical asymmetrical, 548
waveguide-grating, 241
detector, *see* photodetector
difference-frequency generation, 541
diffusion coefficient, 101
digital backpropagation, 396
digital hierarchy, 12
digital signal processing, 275, 391, 393, 394, 482, 497, 499
directional coupler, 240, 243
dispersion, 38–46
accumulated, 349, 352, 408
anomalous, 195, 357, 374, 410, 519, 536, 555, 566
fiber, 484
fourth-order, 382, 520
grating, 355, 357, 358
group-velocity, 39–42, 86, 193, 194, 345, 408, 416–419, 484
higher-order, 355
intermodal, 26, 189, 193
material, 40–41, 85
multipath, 26, 27
normal, 195, 348, 357, 387, 410, 419, 424, 536
polarization-mode, 37, 44, 196, 462, 484
postcompensation of, 349, 375, 444
precompensation of, 349, 385, 440, 444
pulse broadening due to, 47–50
residual, 333, 373, 375, 435, 444, 450
second-order, 369, 379
temperature dependence of, 375
third-order, 43, 52, 268, 346, 376, 379, 381, 520
trimming of, 375
tunable, 375–382
waveguide, 40, 41, 351, 522
dispersion compensation
broadband, 348, 353, 382
condition for, 348
dynamic, 375–378
electronic, 385
module for, 351
perfect, 411
periodic, 349
polarization-mode, 382–385
receiver-end, 392

- third-order, 379
- tunable, 375–378
- dispersion length, 49, 387, 415, 434, 442
- dispersion management, 334, 408, 423–430
 - broadband, 348, 379
 - DCF for, 347–354
 - duobinary technique for, 390
 - fiber gratings for, 354–363
 - filters for, 363–369
 - FSK format for, 389
 - higher-order, 379–382
 - need for, 345–347
 - periodic, 262
 - phase conjugation for, 369–375
 - prechirping technique for, 386–389
 - WDM system, 375–385
- dispersion map, 349, 408, 435
 - optimization of, 409, 444
 - periodic, 375, 409, 424–430, 445
 - strength of, 428
 - symmetric, 447
 - two-section, 412
- dispersion parameter, 39, 47, 193, 337, 346, 348, 352, 374, 447
- dispersion relation, 60
- dispersion slope, 43, 51, 268, 349, 381, 539
 - compensation of, 361, 367, 375–382
 - negative, 349, 351
 - relative, 349
 - tunable, 377, 379, 381
- dispersion-compensating fiber, *see* fibers
- dispersion-decreasing fiber, *see* fiber
- dispersion-induced limitations, 50–53, 345–347
- dispersion-shifted fibers, *see* fibers
- dispersive waves, 419, 421, 434
- distributed amplification, *see* amplification
- distributed Bragg reflector, 89
- distributed feedback, *see* feedback
- distributed feedback lasers, 88
 - gain-coupled, 89, 248
 - linewidth saturation in, 103
 - multisection, 91
 - phase-shifted, 89
- DPSK format, 210, 448, 565
- duty cycle, 446, 448, 450
- EDFA
 - amplification characteristics of, 302
 - C-band, 309
 - cascaded chain of, 308
- gain spectrum of, 301
- gain-clamped, 309
- L-band, 309
- multichannel amplification in, 307
- noise in, 305
- parallel configuration for, 309
- properties of, 300–310
- pumping of, 300
- semiconductor lasers for, 300
- spectral nonuniformity of, 307
- two-stage, 309
- effective mode area, 38, 61, 351, 521, 536
- elasto-optic coefficient, 61
- electro-optic effect, 106
- electroabsorption, 107, 560, 562
- electron-hole recombination, 81, 83, 100
- electron-beam lithography, 90
- electrorefraction, 462
- electrostriction, 60
- encoder
 - CDMA, 278
 - spectral phase, 280
- encoding
 - frequency domain, 280
 - phase, 280, 460, 464
 - spectral, 280
 - time-domain, 278
 - time-frequency domain, 281
- envelope detector, 466, 479
- epitaxial growth, 80, 90, 107
- equalization technique, 392
- equalizing filter, *see* filter
- erbium-doped fiber amplifier, *see* EDFA
- error correction, 198, 212–214, 227, 281
- error function, 515
- error probability, *see* bit-error rate
- Ethernet, 71, 186, 501
- excess noise factor, 155
- excited-state absorption, 302
- extinction ratio, 107, 167
- eye closure, 252, 393, 484
- eye diagram, 148, 174, 210, 335, 386, 492, 534
- eye opening, 211, 391, 447
- Fabry–Perot cavity, 84, 135, 143, 263
- Fabry–Perot interferometer, *see* interferometer
- Faraday effect, 117
- Faraday rotator, 565
- fast axis, 36, 515, 546
- feed-forward equalizer, 392

- feedback
cavity, 84
distributed, 88, 345, 528
dual-loop, 118
electrical, 263
negative, 145
optical, 90, 117, 150, 204, 528
reflection, 204, 272
- fiber amplifier, *see* EDFA
fiber coupler, 241, 244, 265, 512, 567
fiber dispersion, *see* dispersion
fiber grating, *see* grating
fiber modes, 31–38
 effective index of, 34
 eigenvalue equation for, 33
 field distribution of, 36
 hybrid, 34
 propagation constant of, 34
 spot size of, 37
- fiber nonlinearity, *see* nonlinear effects
fiber-optic systems, *see* lightwave systems
fibers
 bandwidth of, 54
 birefringence of, 36
 bismuth-oxide, 536, 547, 555
 chalcogenide, 58, 555
 depressed-cladding, 68, 351
 design of, 67–73
 dispersion-compensating, 347–354, 409, 410, 429
 dispersion-decreasing, 42, 371, 423–424
 dispersion-flattened, 42
 dispersion-shifted, 42, 67, 68, 190, 197, 257, 261, 334, 346, 415, 481, 534
 dry, 7, 226
 elliptical-core, 352
 erbium-doped, 296
 fabrication of, 67–73
 fluoride, 58, 309
 four-wave mixing in, 371
 graded-index, 27–29, 71, 189, 191, 193
 highly nonlinear, 520, 534–536, 538, 539, 546, 554
 loss of, 55–59
 low-PMD, 45
 microstructured, 536
 modes of, *see* fiber modes
 multimode, 25–29, 189, 201
 nonlinear effects in, 59–67
 nonsilica, 555
- nonzero-dispersion-shifted, 262
parabolic-index, 27
PFBVE, 72
photonic crystal, 353, 539, 547
plastic, 29, 71–72, 201
PMMA, 72
polarization-maintaining, 37, 44, 515, 535, 545, 557
polycrystalline, 58
precompensation, 441
pulse propagation in, 46
reduced-slope, 43
reverse-dispersion, 43
silica, 68–71
single-mode, 34–38
spun, 547
standard, 346, 387, 410, 429, 450
tellurite, 310
wave propagation in, 29–34
- filter
 acousto-optic, 237, 308
 add-drop, 243
 all-pass, 367, 384
 amplifier-based, 238
 bandpass, 148, 160, 432, 464, 466, 467, 479, 553, 555
 cascaded, 365
 dispersion-compensating, 347
 electrical, 210
 equalizing, 363–369, 379
 Fabry–Perot, 233–235, 252, 363, 564
 finite-impulse-response, 396
 Gires–Tournois, 363
 grating, 236
 high-pass, 148
 in-line, 432
 interference, 308
 interferometric, 379
 low-pass, 146, 465
 Mach–Zehnder, 235, 240, 243, 308, 366
 microwave, 386
 narrowband, 326
 notch, 535, 536
 optical, 363–369, 432, 554, 561, 566
 raised-cosine, 147
 reflection, 354, 356
 sliding-frequency, 432
 surface-acoustic-wave, 148
 transversal, 392
 tunable optical, 233–238, 251

- finesse, 234
 flame hydrolysis, 69
 flip bonding, 150, 532
 flip-flop, 528
 laser-based, 529
 microdisk laser based, 533
 optical, 529–533
 passive-waveguide, 531
 physical mechanism behind, 530
 silicon-based, 533
 SOA-based, 529
 format conversion, 549
 forward error correction, *see* error correction
 four-wave mixing, 67, 261–262, 328, 346, 371,
 434, 481, 516–521, 537, 542, 557
 efficiency of, 261, 373
 intrachannel, 436, 441
 nondegenerate, 373
 Franz–Keldysh effect, 107
 free spectral range, 85, 233
 free-carrier effects, 521
 frequency chirping, 106, 108, 345, 415, 542
 frequency hopping, 281
 gain
 APD, 139, 156
 Brillouin, 238
 differential, 83
 distributed, 298, 317
 parametric, 517, 519
 polarization-dependent, 46, 196
 Raman, 310
 saturation of, 523, 529, 530, 557
 small-signal, 312, 523
 gain quenching, 531
 gain saturation, 307, 312, 522, 548
 gain-bandwidth product, 141, 142
 gain-flattening technique, 264, 308
 gain-recovery time, 559
 Gaussian distribution, 37, 473, 488
 Gaussian pulse, *see* pulse
 Gaussian random process, 101, 103, 465, 471
 Gaussian statistics, 151, 162, 173, 297
 ghost pulse, 436, 442, 443, 448
 Gordon–Haus jitter, *see* timing jitter
 graded-index fiber, *see* fibers
 grating
 acoustically induced, 237
 amplitude-sampled, 362
 apodized, 355, 357
 arrayed-waveguide, 241, 280, 282, 380
 birefringent, 384
 Bragg, 236, 239, 240, 243, 261, 354, 375,
 528, 531
 built-in, 88, 237, 238, 353, 529
 cascaded, 359
 chirped, 92, 356–363
 concave, 239
 DFB-laser, 88
 diffraction, 238, 280
 dispersion of, 357
 elliptical, 239
 fiber, 236, 240, 261, 279, 281, 304, 354–
 363, 373, 528, 531, 536, 561
 long-period, 308, 353
 Moiré, 282, 359
 nonlinear-index, 195, 329
 nonlinearly chirped, 380
 phase-sampled, 362
 phase-shifted, 240
 sampled, 92, 237, 279, 360, 380, 561
 superstructure, 92, 237, 360
 tunable, 536
 waveguide, 246
 grating period, 88, 92, 239, 353, 354, 361, 375
 Gray coding, 461, 475
 group delay, 362, 364, 365, 376
 differential, 382
 slope of, 364
 spectrum of, 358
 group velocity, 39, 330, 433
 group-velocity dispersion, *see* dispersion
 group-velocity mismatch, 514, 546
 GVD parameter, 39, 47, 348, 372, 416–419
 Hankel function, 329
 Hermite–Gauss function, 425
 heterodyne detection, 160, 385, 464, 498
 heterodyne receiver
 asynchronous, 466, 472–474
 balanced, 465
 intensity noise at, 476–477
 phase noise in, 478–480
 sensitivity degradation of, 476–485
 synchronous, 464, 470–472
 heterostructure design, 83, 113
 holding beam, 528, 530
 holographic technique, 90
 homodyne detection, 159, 386, 464, 471
 hypercube architecture, 230

- hysteresis, 527
- idler wave, 517, 519, 537, 539
- impact ionization, 137, 155
- impulse response, 54
- index-matching liquid, 116, 205
- injection locking, 106
- integrated circuits
- optoelectronic, 119, 148, 248, 482
 - photonic, 119, 553
- interdigitized electrode, 143
- interface scattering, 85
- interfacial gel polymerization, 71
- interferometer
- Fabry–Perot, 205, 207, 233, 263, 363
 - Gires–Tournois, 363
 - Mach–Zehnder, 106, 235, 240, 243, 267, 282, 366, 462, 467, 532, 543, 548, 562, 566
 - Michelson, 236, 263
 - optical delay, 467, 469, 567
 - Sagnac, 236, 267, 512–516, 533, 543, 566
- intermediate frequency, 159, 386, 464, 465
- intermodulation distortion, 271
- Internet, 71, 186
- Internet protocol, 269
- intersymbol interference, 102, 146, 208, 277
- inverse scattering method, 417, 419
- ionization coefficient ratio, 139, 157, 166
- ITU wavelength grid, 225
- Johnson noise, 152
- junction heating, 97
- Kerr effect, 531, 540
- Kerr shutter, 536, 547, 557
- Lambertian source, 111, 114
- Langevin noise, 100, 297
- laser linewidth, 478
- laser threshold, 84
- LED, 110–115
 - bandwidth of, 113
 - Burrus-type, 113
 - coupling efficiency for, 116
 - edge-emitting, 114
 - modulation response of, 112
 - reliability of, 120
 - resonant-cavity, 115
 - surface-emitting, 113, 115
- temperature dependence of, 112
- lens coupling, 115, 117
- light-emitting diodes, *see* LED
- lightwave systems
- advanced, 459–503
 - architectures for, 182
 - coherent, *see* coherent systems
 - components of, 17–20
 - DBPSK, 494
 - design of, 187–194, 408–416
 - dispersion-managed, 407–416
 - dispersion-limited, 50–53, 189, 345–347
 - DQPSK, 496
 - evolution of, 4–8
 - high-capacity, 224
 - high-speed, 375–385
 - history of, 1–4
 - long-haul, 194–200, 295, 324, 444–451
 - loss-limited, 187–189
 - loss-managed, 298–300
 - modulation formats for, 460–464
 - nonlinearity-limited, 334
 - numerical approach for, 335
 - OFDM, 499
 - periodically amplified, 334
 - point-to-point, 182–184
 - pseudo-linear, 416, 434–451
 - QAM-format, 497
 - self-coherent, 459–503
 - soliton-based, 555
 - SPM effects in, 407–416
 - subcarrier, 269–275
 - submarine, 295, 319
 - TDM, *see* TDM systems
 - terrestrial, 196–198, 319, 339, 351
 - ultra-long-haul, 339
 - undersea, 119, 198–200
 - WDM, *see* WDM systems
- LiNbO₃ technology, 373
- linewidth enhancement factor, 98, 103, 524
- load resistor, 145, 152
- local oscillator, 158–161, 460, 464, 466, 477
 - intensity noise of, 477
 - linewidth of, 478
- local-area network, *see* networks
- logic gates, 516
- Lorentzian spectrum, 61, 103
- loss
- bending, 58
 - cavity, 85, 95

- channel, 190
 compensation of, 295–300
 connector, 73, 190
 coupling, 241, 389
 DCF, 351, 352
 distribution, 187
 fiber, 55–59, 187, 295, 370, 450
 filter-induced, 554
 insertion, 185, 248, 359, 364, 373
 internal, 85, 234
 microbending, 73
 mode-selective, 201
 polarization-dependent, 46, 196
 splice, 73, 190
 loss management, 408, 419–423
 lumped amplification, *see* amplification
- Mach–Zehnder interferometer, *see* interferometer
 map period, 261, 411, 427
 map strength, 428
 Marcum Q function, 473, 475
 Markovian approximation, 101, 297
 matched-filter detection, 279
 material dispersion, *see* dispersion
 Maxwell's equations, 29
 mean time to failure, 119
 MEMS technology, 94, 365
 metropolitan-area network, *see* networks
 Michelson interferometer, *see* interferometer
 microdisk laser, 533
 microlens, 239
 microring resonator, 280
 microstrip line, 386
 microwave communication, 2, 269, 461, 464
 microwave subcarrier, 270, 275
 Mie scattering, 58
 MLSE equalizer, 393
 modal noise, 201
 mode
 fiber, *see* fiber modes
 fundamental, 351
 longitudinal, 85, 88, 201, 202, 364
 temporal, 419
 transverse, 532
 vibrational, 72
 mode converter, 353
 mode index, 34, 35, 239
 mode-locked fiber laser, 250, 268
 mode-partition noise, 102, 171, 202–204
 mode-suppression ratio, 88, 89, 206
 modulation
 amplitude, 14, 98, 106
 cross-phase, 65
 direct, 98, 104
 external, 106
 frequency, 14, 389
 large-signal, 104
 nonlinear phase, 64
 phase, 14, 98, 106, 388, 462
 pulse-code, 10
 pulse-duration, 10
 pulse-position, 10
 quadrature amplitude, 461
 self-phase, 64
 sinusoidal, 98, 113
 small-signal, 98
 synchronous, 433, 437
 modulation format, 13–15, 460–464
 AM-VSB, 270, 271
 ASK, 14
 BPSK, 460
 CRZ, 14, 415
 CSRZ, 211, 449, 450, 549
 DBPSK, 469, 494
 DPSK, 460
 DQPSK, 468, 475, 496
 duobinary, 359, 390
 FSK, 14, 272, 389, 466
 nonreturn-to-zero, *see* NRZ format
 NRZ-DPSK, 211
 OOK, 14
 PSK, 14, 460–464
 QAM, 273, 497
 QPSK, 273, 460, 463, 475
 return-to-zero, *see* RZ format
 modulation instability, 195, 328, 536
 gain bandwidth of, 329
 noise amplification by, 328
 modulator
 amplitude, 388, 433, 462
 electro-absorption, 562
 electroabsorption, 107, 388, 542, 562, 564
 external, 107, 345, 462
 frequency, 259
 intensity, 106
 LiNbO₃, 107, 433, 462
 Mach–Zehnder, 266, 388, 391, 462
 multiquantum-well, 109

- phase, 106, 279, 280, 433, 449, 462, 491, 561
phase modulator, 258
push-pull, 463
quadrature, 463
transfer function of, 463
moment method, 330, 411, 437
Morse code, 2
multimode-interference coupler, 532, 559
multiplexer
 add-drop, 242–244
 TDM, 264
 WDM, *see* demultiplexer
multiplexing
 code-division, 277–283
 coherence, 282
 electric-domain, 11
 frequency-division, 11
 orthogonal frequency-division, 275, 499
 polarization-division, 461, 496, 499
 subcarrier, 269–275, 499
 time-division, 11, 264–269, 379
 wavelength-division, 223–251
- network protocol
 ATM, 228
 CSMA, 186
 Ethernet, 186
 TCP/IP, 228
- network topology, 185, 186
- networks
 access, 230
 active-star, 186
 all-optical, 230
 broadcast, 184, 228
 CATV, 184, 269–273
 distribution, 184, 228
 local-area, 112, 115, 185, 228
 local-loop, 230
 mesh, 228
 metro, 185
 metropolitan-area, 228
 multihop, 229
 passive-star, 187
 WDM, *see* WDM networks
 wide-area, 228
- neural network, 392
- noise
 amplification of, 328
 amplifier, 195, 305, 363, 483, 486, 492
 amplitude, 318–320
 ASE, 324, 328, 330, 335, 338, 352
 beat, 282
 electrical amplifier, 153
 filtered, 465
 Gaussian, 325, 465, 501
 intensity, 101, 169, 205, 329, 466, 476–477, 566
 intensity, 100–102
 laser, 100–104
 mode-partition, 102, 202–204
 non-Gaussian, 327
 nonlinear phase, 486–493
 $1/f$, 104
 phase, 102–104, 207, 478–480, 566, 567
 quantization, 9
 Raman amplifier, 316
 receiver, 151–157, 161, 465, 477
 shot, 100, 151, 160, 322
 spontaneous-emission, 305
 thermal, 152, 160, 165, 322, 323, 325
 white, 151, 152, 305
noise figure, 153, 305, 306, 322, 409
 amplifier-chain, 323
 effective, 317
- nonlinear depolarization, 462
- nonlinear effects
 amplifier-induced, 328–333
 control of, 444–451
 DCF-induced, 410
 impact of, 407–451, 485–493
 interchannel, 255–262, 416
 intrachannel, 268, 435
 second-order, 373
 third-order, 59–67, 523
- nonlinear length, 415, 434, 518, 554
- nonlinear optical loop mirror, 267, 434, 512–516, 533, 557
- nonlinear parameter, 64, 259, 351, 371, 409, 439, 526, 540, 555
- nonlinear phase noise, 486–493
 compensation of, 490
 impact of dispersion, 489
 SPM-induced, 486
 variance of, 488
 XPM-induced, 489
- nonlinear polarization rotation, 536
- nonlinear Schrödinger equation, 66, 195, 335, 408, 416–419, 486, 587
- nonradiative recombination, 81

- NRZ format, 13, 147, 148, 192, 194, 210, 259, 265, 383, 409, 410, 549
 NRZ-to-RZ conversion, 550
 numerical aperture, 26, 71, 111, 114, 115
 Nyquist noise, 152
- OFDM, *see* multiplexing
 on-off keying, 14, 393, 459, 549
 optical amplifiers, *see* amplifiers
 optical beat interference, 274
 optical bistability, *see* bistability
 optical circulator, 236, 373
 optical clock, 267, 545, 550, 562
 optical communication systems, *see* lightwave systems
 optical data links, 182, 201
 optical detector, *see* photodetector
 optical feedback, *see* feedback
 optical fibers, *see* fibers
 optical filter, *see* filter
 optical isolator, 117, 204, 207, 565
 optical networks, *see* networks
 optical phase conjugation, *see* phase conjugation
 optical phonons, 310
 optical receiver, *see* receiver
 optical transmitter, *see* transmitter
 optoelectronic integration, 119, 148
 optoelectronic repeater, 183
 optogalvanic effect, 263
 orthoconjugate mirror, 373
 outage probability, 382
 outside-vapor deposition, 69
- p-n* junction, 82, 132
 packet switching, 228, 230, 269, 552
 parametric amplifier, *see* amplifier
 paraxial approximation, 28
 passive photonic loop, 232
 periodic poling, 373, 541
 phase conjugation, 67, 369–375, 381, 481
 fiber-based, 371
 midspan, 369
 polarization-insensitive, 373
 PPLN based, 374
 phase shift
 nonlinear, 65, 526, 528, 537
 SPM-induced, 328, 370, 513, 526, 565
 voltage-induced, 462
 XPM-induced, 516, 526, 533, 536, 557
 phase-alternation technique, 448
 phase-locked loop, 263, 464, 479, 482, 498
 phase-matching condition, 67, 237, 372, 518, 537
 phase-shift keying, *see* modulation format
 photodetector
 avalanche, *see* APD
 balanced, 469
 bandwidth of, 131
 MSM, 143, 144
 quantum efficiency of, 129
 responsivity of, 129
 traveling-wave, 136
 photodiode
 p-i-n, 133
 p-n, 132
 waveguide, 136
 photoelastic effect, 237
 photon lifetime, 95
 photonic nanowire, 521
 photorefractive crystal, 531
 piezoelectric transducer, 375
 pigtail, 115
 planar lightwave circuit, 150, 236, 240, 248, 265, 366, 379
 plastic optical fiber, *see* fibers
 PMD, *see* dispersion
 compensation of, 196, 382–385
 first-order, 45, 385
 pulse broadening induced by, 45
 second-order, 46, 385
 PMD compensator, 384
 PMD parameter, 45, 383
 point-to-point links, 182–184
 WDM, 224–227
 Poisson statistics, 151, 166
 polarization bit interleaving, 449–451
 polarization diversity, 462, 482
 polarization filtering, 483
 polarization scrambling, 227, 481, 548
 polarization-mode dispersion, *see* PMD
 population inversion, 83, 307
 population-inversion factor, 305
 power budget, 190–191, 272
 power penalty
 chirp-induced, 209
 dispersion-induced, 208, 484
 extinction ratio, 168
 eye-closure, 210, 447
 feedback-induced, 205

- filter-induced, 252
- FWM-induced, 261
- heterodyne-detection, 160
- intensity-noise, 170
- modal-noise, 201
- mode-partition noise, 202–204
- phase-noise, 479
- phase-noise-induced, 478
- PMD-induced, 484
- Raman-induced, 256
- RIN-induced, 170, 477
- router-induced, 254
- sources of, 200–210
- timing-jitter, 172
- XPM-induced, 260
- prechirp technique, 386–389
- preform, 69, 71
- pseudorandom bit pattern, 104, 335, 410, 442, 521, 538
- pulse**
 - chirped, 47, 412
 - clock, 548, 561, 563
 - Gaussian, 47, 49, 208, 389, 412, 419, 425
 - ghost, *see* ghost pulse
 - hyperbolic secant, 418, 425
 - shadow, 436
 - super-Gaussian, 53, 387
 - ultrashort, 250
- pulse broadening, 208, 345, 408
 - general formula for, 584
- GVD-induced, 49
- PMD-induced, 45
- source-induced, 50
- pulse-code modulation, *see* modulation**
- pump depletion, 312, 518
- pump-station spacing, 298, 319
- pumping
 - backward, 299, 311, 320, 450
 - bidirectional, 299, 300
 - forward, 320
- Q factor, 163–173, 202, 213, 325–328, 336, 448, 470**
- quantum dot, 106
- quantum efficiency, 470
 - differential, 97
 - external, 97, 110, 143
 - internal, 82, 97, 110
 - photodetector, 129
 - total, 97, 111
- quantum limit, 166, 173
- quantum well, 93, 108, 115
 - modulation-doped, 106
 - multi, 97, 103
 - strained, 98
- quasi-phase matching, 373, 541
- Raman amplification, 255, 299, 312**
 - broadband, 313
 - distributed, 317
 - multiple-pump, 313
- Raman amplifier, *see* amplifier**
- Raman crosstalk, *see* crosstalk**
- Raman gain, 63, 255, 310, 338, 536, 566**
- Raman scattering, 59, 255–257, 486**
 - spontaneous, 62, 315, 316
 - stimulated, 62, 296, 298, 310, 434
- Raman shift, 62, 316**
- rare-earth elements, 300
- rate equation, 95, 100, 302
- Rayleigh distribution, 473
- Rayleigh scattering, 58
- receiver**
 - APD, 154
 - asynchronous, 482
 - balanced, 465, 466, 468, 477
 - coherent detection, 394
 - components of, 19
 - delay-demodulation, 475
 - design of, 144
 - digital coherent, 482, 498
 - direct detection, 392
 - DQPSK, 469
 - front end of, 144
 - heterodyne, 464, 465, 472
 - homodyne, 470, 471, 477, 479
 - integrated, 148
 - noise in, 151–157
 - packaging of, 150
 - performance of, 173–175
 - phase-diversity, 480, 498
 - polarization-diversity, 482
 - sensitivity of, 161–175
 - WDM, 248
- receiver noise, *see* noise**
- receiver sensitivity, 161–175, 200–210, 325, 326, 470–485**
- recirculating loop, 196, 334, 410, 423, 429, 445, 562, 565**
- refractive index**

- carrier-induced change in, 98
- effective, 530
- periodic, 354
- regenerator, 296
 - 2R, 553–560
 - 3R, 560–565
 - all-optical, 553–568
 - DPSK-Signal, 565
 - fiber-based, 553–559
 - FWM-based, 557
 - optoelectronic, 183, 194
 - SOA-based, 559–560
 - soliton, 555
 - SPM-based, 553–556
 - XPM-based, 557
- relative intensity noise, 101, 329
- relaxation oscillations, 99, 101, 103
- repeater spacing, 184, 337, 346
- resonator
 - Fabry–Perot, 85, 526
 - ring, 368, 526, 527
- responsivity, 468
 - APD, 139, 155
 - LED, 111
 - photodetector, 129
- Rice distribution, 473
- RIN, 169, 205, 271, 477
 - dispersion-induced, 272
 - feedback-induced, 205
 - reflection-induced, 272
- rise time, 130, 191–194
- rise-time budget, 191–194
- router
 - all-optical, 552
 - static, 246
 - waveguide-grating, 246
 - WDM, 246
- RZ format, 13, 148, 192, 194, 210, 261, 265, 383, 409, 410, 451, 549
 - alternate mark inversion, 448
 - carrier-suppressed, 448
- RZ-to-NRZ conversion, 550
- Sagnac interferometer, *see* interferometer
- Sagnac loop, 512–516, 526, 566
- sampling period, 361
- sampling theorem, 9
- saturable absorber, 434, 528, 559, 562, 566
- saturation
 - cross-absorption, 542
 - cross-gain, 542, 544, 551, 560
 - gain, 518, 522, 525, 531, 532
- saturation energy, 304, 524
- saturation velocity, 132
- SBS, *see* Brillouin scattering
- Schottky barrier, 143
- second-harmonic generation, 541
- self-phase modulation, 64, 65, 194, 273, 328, 335, 370–371, 389, 408, 415–419, 434, 436, 486, 525, 553
- Sellmeier equation, 40
- semiconductor lasers
 - bistability in, 528
 - broad-area, 86
 - buried heterostructure, 87
 - characteristics of, 94–97
 - coupled, 531
 - coupled-cavity, 90
 - coupling efficiency for, 116
 - DFB, *see* distributed feedback lasers, 529
 - EDFA pumping by, 300
 - feedback sensitivity of, 117, 205
 - flip-flop, 529
 - frequency stability of, 263
 - gain in, 82
 - index-guided, 86
 - intensity noise of, 477
 - linewidth of, 102
 - longitudinal modes of, 85
 - mode-locked, 525, 564
 - modulation response of, 98–99
 - modulator-integrated, 107
 - multiquantum-well, 97
 - multisection, 238
 - noise in, 100–104
 - packaging of, 120
 - quantum-dot, 564
 - reliability of, 119
 - self-pulsing, 564
 - SNR of, 101
 - structures for, 86
 - surface-emitting, 93
 - temperature sensitivity of, 95
 - threshold of, 84
 - tunable, 91
- semiconductor optical amplifiers, 514
 - demultiplexing with, 548
 - filters based on, 238
 - flip-flop, 529
 - gain saturation in, 522

- nonlinear effects in, 522–526
shot noise, *see* noise
shot-noise limit, 466, 474, 477
sideband instability, 195, 374
signal
 analog, 8–11, 270–272, 497
 audio, 8, 11, 184
 binary, 8
 clock, 266, 465
 crosstalk, 253
 CSRZ, 450
 DBPSK, 474
 digital, 8–11, 272, 497
 duobinary, 390
 FSK, 390
 heterodyne, 160, 466
 homodyne, 159
 microwave, 269, 386, 465
 multichannel, 233
 OFDM, 499
 OTDM, 545, 549
 phase-conjugated, 369, 371, 373
 phase-encoded, 462
 spectrally encoded, 281
 studio-quality video, 272
 time-reversed, 371
 video, 8, 11, 184, 269
WDM, 239, 242, 246, 247, 256, 269, 307,
 359, 368
signal-to-noise ratio, 9, 101, 153–156, 160, 260,
 297, 305, 318, 408
 electrical, 321–324
 optical, 318–320, 327
signature sequence, 278
silica-on-silicon technology, 236, 241, 243, 245,
 247, 249, 265, 367
silicon optical bench, 117
silicon waveguide, *see* waveguide
silicon-on-insulator technology, 245, 533
slope efficiency, 97, 118
slow axis, 36, 515, 546
SNR, *see* signal-to-noise ratio
soliton
 bright, 419
 dispersion-managed, 424–430
 fundamental, 417
 higher-order, 417
 loss-managed, 419–423
 order of, 417
 path-averaged, 420
 periodic amplification of, 419–423
 properties of, 416–419
soliton period, 417
soliton systems
 amplifier spacing for, 419–423
 dispersion management for, 423–430
 jitter control in, 432–434
 timing jitter in, 430–434
SONET, 12, 197, 212
source–fiber coupling, 115
spatial hole burning, 98, 531
spatial light modulator, 280
spatial phase filter, 381
speckle pattern, 201
spectral broadening
 chirp-induced, 345
 SPM-induced, 550, 553
 XPM-induced, 548
spectral efficiency, 8, 15, 225, 233
 CDMA, 280, 283
 DPSK format, 494
 OFDM format, 500
 QAM format, 498
spectral filtering, 554
spectral hole burning, 98
spectral inversion, 369
spectral slicing, 248, 250
splice loss, *see* loss
split-step Fourier method, 335, 396
spontaneous emission, 80, 95, 100, 112, 297
 amplified, 305, 323, 327, 352, 516
spontaneous emission factor, 95, 297, 305, 483
spot-size converter, 87, 117
spread-spectrum technique, 277
SRS, *see* Raman scattering
star coupler, 186, 231, 244–245, 269
star topology, 186
Stark splitting, 302
stimulated emission, 80, 95
Stokes shift, 60
stop band, 240, 354–356, 359, 376, 529, 530
subcarrier multiplexing, *see* multiplexing
supercontinuum, 250, 268
surface recombination, 81
susceptibility, 30
 second-order, 540
 third-order, 541
switching
 NOLM-based, 512
 nonlinear, 512

- packet, 544, 552
- SOA-based, 529
- SPM-induced, 513
- ultrafast, 544–551
- XPM-induced, 514
- switching time, 529
- symbol rate, 461, 469, 494, 496, 498
- synchronous digital hierarchy, 12, 197, 230
- synchronous optical network, *see* SONET
- synchronous transport module, 13
- system design, *see* lightwave systems
- system margin, 190, 214
- TCP/IP protocol, 269
- TDM systems, 264–269
 - demultiplexer for, 266–267
 - multiplexer for, 264
 - performance of, 268
- telecommunication fiber links, 196–200
- thermal noise, *see* noise
- thermoelectric cooler, 96, 118, 120
- thin-film heater, 376, 381
- third-order dispersion, *see* dispersion, 538
- three-wave mixing, 540
- threshold condition, 85
- threshold current, 95, 96
- time-division multiplexing, *see* multiplexing
- time-domain demultiplexing, 545–549
- timing jitter, 260, 430–434, 447, 560
 - ASE-induced, 330, 333
 - control of, 432–434
 - electrical, 171–173
 - Gordon–Haus, 330, 430
 - receiver, 171–173
 - XPM-induced, 437, 446
- total internal reflection, 25, 27, 58, 110
- transfer function
 - fiber, 54, 347, 385
 - filter, 363, 386, 554
 - grating, 355, 361
 - LED, 113
 - linear channel, 147
 - Mach–Zehnder, 366, 367
 - modulator, 463
 - power, 557, 561, 565
 - RC circuit, 192
 - semiconductor laser, 99
- transistor
 - field-effect, 149
 - heterojunction-bipolar, 149, 251
- high-electron-mobility, 149
- transit time, 131, 134, 139
- transmitter, 115–121
 - components of, 18
 - driving circuitry in, 118
 - monolithic, 119
 - OEIC, 119
 - optical feedback in, 117
 - packaging of, 119
 - precircling at, 386
 - reliability of, 119
 - source–fiber coupling in, 115
 - WDM, 248
- triple-beat distortion, 271
- two-photon absorption, *see* absorption
- V parameter, 34, 350, 352
- vapor-axial deposition, 69
- variational method, 412, 425, 437
- Vernier effect, 92
- vertical-cavity surface-emitting lasers, 93, 201, 205, 530, 532
- vestigial sideband, 270
- Viterbi algorithm, 393
- walk-off effect, 260, 514, 515, 536, 550
- wall-plug efficiency, 97, 111
- waveguide
 - LiNbO₃, 106, 373, 462, 527, 540
 - nonlinear, 419
 - PPLN, 373, 541
 - ridge, 86, 248
 - semiconductor, 528, 531, 540
 - silicon, 521, 533, 540
 - temporal, 419
- waveguide dispersion, *see* dispersion
- waveguide grating, *see* grating
- waveguide photodiode, 136
- waveguide-grating router, 251, 262
- wavelength converter, 373, 533–544
 - dual-pump, 539
 - FWM-based, 537
 - LiNbO₃-based, 540
 - silicon-based, 540
 - SOA-based, 542
 - XPM-based, 533, 534
- wavelength multicasting, 539
- wavelength routing, 246
- wavelength-division multiplexing, *see* multiplexing, WDM systems

- WDM components, 232–251
WDM networks
 all-optical, 228
 Banyan, 230
 broadcast, 228–230
 deBruijn, 230
 distribution, 228–230
 Lambdanet, 231
 multihop, 230
 multiple-access, 230–232
 router for, 246
 shuffle, 230
 transport, 228
WDM systems, 223–232, 262, 296
 coarse, 310
 components for, 232, 251
crosstalk in, 251–264
DCF for, 349
dense, 299, 316
dispersion-managed, 375–385
point-to-point links, 224–227
spectral efficiency of, 225
subcarrier-multiplexed, 273
Wiener–Khinchin theorem, 151

XPM-induced phase shift, *see* phase shift
XPM-induced switching, *see* switching
XPM-induced wavelength shift, 561

zero-dispersion wavelength, 41, 51, 52, 55, 189,
 262, 331, 334, 337, 346, 348, 372,
 515, 518, 520, 521, 534, 535, 557

WILEY SERIES IN MICROWAVE AND OPTICAL ENGINEERING

KAI CHANG, Editor

Texas A&M University

FIBER-OPTIC COMMUNICATION SYSTEMS, Fourth Edition • *Govind P. Agrawal*

ASYMMETRIC PASSIVE COMPONENTS IN MICROWAVE INTEGRATED CIRCUITS •

Hee-Ran Ahn

COHERENT OPTICAL COMMUNICATIONS SYSTEMS • *Silvello Betti, Giancarlo De Marchis, and Eugenio Iannone*

PHASED ARRAY ANTENNAS: FLOQUET ANALYSIS, SYNTHESIS, BFNs, AND ACTIVE ARRAY SYSTEMS • *Arun K. Bhattacharyya*

HIGH-FREQUENCY ELECTROMAGNETIC TECHNIQUES: RECENT ADVANCES AND APPLICATIONS • *Asoke K. Bhattacharyya*

RADIO PROPAGATION AND ADAPTIVE ANTENNAS FOR WIRELESS COMMUNICATION LINKS: TERRESTRIAL, ATMOSPHERIC, AND IONOSPHERIC • *Nathan Blaunstein and Christos G. Christodoulou*

COMPUTATIONAL METHODS FOR ELECTROMAGNETICS AND MICROWAVES •
Richard C. Booton, Jr.

ELECTROMAGNETIC SHIELDING • *Salvatore Celozzi, Rodolfo Araneo, and Giampiero Lovat*

MICROWAVE RING CIRCUITS AND ANTENNAS • *Kai Chang*

MICROWAVE SOLID-STATE CIRCUITS AND APPLICATIONS • *Kai Chang*

RF AND MICROWAVE WIRELESS SYSTEMS • *Kai Chang*

RF AND MICROWAVE CIRCUIT AND COMPONENT DESIGN FOR WIRELESS SYSTEMS •
Kai Chang, Inder Bahl, and Vijay Nair

MICROWAVE RING CIRCUITS AND RELATED STRUCTURES, Second Edition • *Kai Chang and Lung-Hwa Hsieh*

MULTIRESOLUTION TIME DOMAIN SCHEME FOR ELECTROMAGNETIC ENGINEERING •
Yinchao Chen, Qunsheng Cao, and Raj Mittra

DIODE LASERS AND PHOTONIC INTEGRATED CIRCUITS • *Larry Coldren and Scott Corzine*
EM DETECTION OF CONCEALED TARGETS • *David J. Daniels*

RADIO FREQUENCY CIRCUIT DESIGN • *W. Alan Davis and Krishna Agarwal*

MULTICONDUCTOR TRANSMISSION-LINE STRUCTURES: MODAL ANALYSIS TECHNIQUES •
J. A. Brandão Faria

PHASED ARRAY-BASED SYSTEMS AND APPLICATIONS • *Nick Fourikis*

SOLAR CELLS AND THEIR APPLICATIONS, Second Edition • *Lewis M. Fraas and Larry D. Partain*

FUNDAMENTALS OF MICROWAVE TRANSMISSION LINES • *Jon C. Freeman*

OPTICAL SEMICONDUCTOR DEVICES • *Mitsuo Fukuda*

MICROSTRIP CIRCUITS • *Fred Gardiol*

HIGH-SPEED VLSI INTERCONNECTIONS, Second Edition • *Ashok K. Goel*

FUNDAMENTALS OF WAVELETS: THEORY, ALGORITHMS, AND APPLICATIONS •
Jaideva C. Goswami and Andrew K. Chan

- HIGH-FREQUENCY ANALOG INTEGRATED CIRCUIT DESIGN • Ravender Goyal (ed.)
- ANALYSIS AND DESIGN OF INTEGRATED CIRCUIT ANTENNA MODULES •
K. C. Gupta and Peter S. Hall
- PHASED ARRAY ANTENNAS, Second Edition • R. C. Hansen
- STRIPLINE CIRCULATORS • Joseph Helszajn
- THE STRIPLINE CIRCULATOR: THEORY AND PRACTICE • Joseph Helszajn
- LOCALIZED WAVES • Hugo E. Hernández-Figueroa, Michel Zamboni-Rached, and
Erasmo Recami (eds.)
- MICROSTRIP FILTERS FOR RF/MICROWAVE APPLICATIONS • Jia-Sheng Hong and
M. J. Lancaster
- MICROWAVE APPROACH TO HIGHLY IRREGULAR FIBER OPTICS • Huang Hung-Chia
- NONLINEAR OPTICAL COMMUNICATION NETWORKS • Eugenio Iannone, Francesco Matera,
Antonio Mecozzi, and Marina Settembre
- FINITE ELEMENT SOFTWARE FOR MICROWAVE ENGINEERING • Tatsuo Itoh, Giuseppe Pelosi,
and Peter P. Silvester (eds.)
- INFRARED TECHNOLOGY: APPLICATIONS TO ELECTROOPTICS, PHOTONIC DEVICES, AND
SENSORS • A. R. Jha
- SUPERCONDUCTOR TECHNOLOGY: APPLICATIONS TO MICROWAVE, ELECTRO-OPTICS,
ELECTRICAL MACHINES, AND PROPULSION SYSTEMS • A. R. Jha
- OPTICAL COMPUTING: AN INTRODUCTION • M. A. Karim and A. S. S. Awwal
- INTRODUCTION TO ELECTROMAGNETIC AND MICROWAVE ENGINEERING • Paul R. Karmel,
Gabriel D. Colef, and Raymond L. Camisa
- MILLIMETER WAVE OPTICAL DIELECTRIC INTEGRATED GUIDES AND CIRCUITS •
Shiban K. Koul
- ADVANCED INTEGRATED COMMUNICATION MICROSYSTEMS • Joy Laskar, Sudipto
Chakraborty, Manos Tentzeris, Franklin Bien, and Anh-Vu Pham
- MICROWAVE DEVICES, CIRCUITS AND THEIR INTERACTION • Charles A. Lee and
G. Conrad Dalman
- ADVANCES IN MICROSTRIP AND PRINTED ANTENNAS • Kai-Fong Lee and Wei Chen (eds.)
- SPHEROIDAL WAVE FUNCTIONS IN ELECTROMAGNETIC THEORY • Le-Wei Li, Xiao-Kang Kang,
and Mook-Seng Leong
- ARITHMETIC AND LOGIC IN COMPUTER SYSTEMS • Mi Lu
- OPTICAL FILTER DESIGN AND ANALYSIS: A SIGNAL PROCESSING APPROACH •
Christi K. Madsen and Jian H. Zhao
- THEORY AND PRACTICE OF INFRARED TECHNOLOGY FOR NONDESTRUCTIVE TESTING •
Xavier P. V. Maldague
- METAMATERIALS WITH NEGATIVE PARAMETERS: THEORY, DESIGN, AND MICROWAVE
APPLICATIONS • Ricardo Marqués, Ferran Martín, and Mario Sorolla
- OPTOELECTRONIC PACKAGING • A. R. Mickelson, N. R. Basavanhally, and Y. C. Lee (eds.)
- OPTICAL CHARACTER RECOGNITION • Shunji Mori, Hirobumi Nishida, and Hiromitsu Yamada
- ANTENNAS FOR RADAR AND COMMUNICATIONS: A POLARIMETRIC APPROACH •
Harold Mott
- INTEGRATED ACTIVE ANTENNAS AND SPATIAL POWER COMBINING • Julio A. Navarro and
Kai Chang
- ANALYSIS METHODS FOR RF, MICROWAVE, AND MILLIMETER-WAVE PLANAR TRANSMIS-
SION LINE STRUCTURES • Cam Nguyen

LASER DIODES AND THEIR APPLICATIONS TO COMMUNICATIONS AND INFORMATION PROCESSING • *Takahiro Numai*

FREQUENCY CONTROL OF SEMICONDUCTOR LASERS • *Motoichi Ohtsu* (ed.)

WAVELETS IN ELECTROMAGNETICS AND DEVICE MODELING • *George W. Pan*

OPTICAL SWITCHING • *Georgios Papadimitriou, Chrisoula Papazoglou, and Andreas S. Pomportsis*

MICROWAVE IMAGING • *Matteo Pastorino*

ANALYSIS OF MULTICONDUCTOR TRANSMISSION LINES • *Clayton R. Paul*

INTRODUCTION TO ELECTROMAGNETIC COMPATIBILITY, Second Edition • *Clayton R. Paul*

ADAPTIVE OPTICS FOR VISION SCIENCE: PRINCIPLES, PRACTICES, DESIGN AND APPLICATIONS • *Jason Porter, Hope Queener, Julianna Lin, Karen Thorn, and Abdul Awwal* (eds.)

ELECTROMAGNETIC OPTIMIZATION BY GENETIC ALGORITHMS • *Yahya Rahmat-Samii and Eric Michielssen* (eds.)

INTRODUCTION TO HIGH-SPEED ELECTRONICS AND OPTOELECTRONICS •

Leonard M. Riazat

NEW FRONTIERS IN MEDICAL DEVICE TECHNOLOGY • *Arye Rosen and Harel Rosen* (eds.)

ELECTROMAGNETIC PROPAGATION IN MULTI-MODE RANDOM MEDIA • *Harrison E. Rowe*

ELECTROMAGNETIC PROPAGATION IN ONE-DIMENSIONAL RANDOM MEDIA •

Harrison E. Rowe

HISTORY OF WIRELESS • *Tapan K. Sarkar, Robert J. Mailloux, Arthur A. Oliner, Magdalena Salazar-Palma, and Dipak L. Sengupta*

PHYSICS OF MULTIANTENNA SYSTEMS AND BROADBAND PROCESSING • *Tapan K. Sarkar, Magdalena Salazar-Palma, and Eric L. Mokole*

SMART ANTENNAS • *Tapan K. Sarkar, Michael C. Wicks, Magdalena Salazar-Palma, and Robert J. Bonneau*

NONLINEAR OPTICS • *E. G. Sauter*

APPLIED ELECTROMAGNETICS AND ELECTROMAGNETIC COMPATIBILITY • *Dipak L. Sengupta and Valdis V. Liepa*

COPLANAR WAVEGUIDE CIRCUITS, COMPONENTS, AND SYSTEMS • *Rainee N. Simons*

ELECTROMAGNETIC FIELDS IN UNCONVENTIONAL MATERIALS AND STRUCTURES • *Onkar N. Singh and Akhlesh Lakhtakia* (eds.)

ANALYSIS AND DESIGN OF AUTONOMOUS MICROWAVE CIRCUITS • *Almudena Suárez*

ELECTRON BEAMS AND MICROWAVE VACUUM ELECTRONICS • *Shulim E. Tsimring*

FUNDAMENTALS OF GLOBAL POSITIONING SYSTEM RECEIVERS: A SOFTWARE APPROACH, Second Edition • *James Bao-yen Tsui*

RF/MICROWAVE INTERACTION WITH BIOLOGICAL TISSUES • *André Vander Vorst, Arye Rosen, and Youji Kotsuka*

InP-BASED MATERIALS AND DEVICES: PHYSICS AND TECHNOLOGY • *Osamu Wada and Hideki Hasegawa* (eds.)

COMPACT AND BROADBAND MICROSTRIP ANTENNAS • *Kin-Lu Wong*

DESIGN OF NONPLANAR MICROSTRIP ANTENNAS AND TRANSMISSION LINES • *Kin-Lu Wong*

PLANAR ANTENNAS FOR WIRELESS COMMUNICATIONS • *Kin-Lu Wong*

FREQUENCY SELECTIVE SURFACE AND GRID ARRAY • *T. K. Wu* (ed.)

ACTIVE AND QUASI-OPTICAL ARRAYS FOR SOLID-STATE POWER COMBINING • *Robert A. York and Zoya B. Popović* (eds.)

OPTICAL SIGNAL PROCESSING, COMPUTING AND NEURAL NETWORKS • *Francis T. S. Yu and Suganda Jutamulia*

ELECTROMAGNETIC SIMULATION TECHNIQUES BASED ON THE FDTD METHOD •

Wenhu Yu, Xiaoling Yang, Yongjun Liu, and Raj Mittra

SiGe, GaAs, AND InP HETEROJUNCTION BIPOLAR TRANSISTORS • *Jian Yuan*

PARALLEL SOLUTION OF INTEGRAL EQUATION-BASED EM PROBLEMS • *Yu Zhang and Tapan K. Sarkar*

ELECTRODYNAMICS OF SOLIDS AND MICROWAVE SUPERCONDUCTIVITY • *Shu-Ang Zhou*

Fiber-Optic Communication Systems, Fourth Edition
by Govind P. Agrawal
Copyright © 2010 John Wiley & Sons, Inc.

CUSTOMER NOTE: IF THIS BOOK IS ACCOMPANIED BY SOFTWARE,
PLEASE READ THE FOLLOWING BEFORE OPENING THE PACKAGE.

This software contains files to help you utilize the models described in the accompanying book. By opening the package, you are agreeing to be bound by the following agreement:

This software product is protected by copyright and all rights are reserved by the author and John Wiley & Sons, Inc. You are licensed to use this software on a single computer. Copying the software to another medium or format for use on a single computer does not violate the U.S. Copyright Law. Copying the software for any other purpose is a violation of the U.S. Copyright Law.

This software product is sold as is without warranty of any kind, either express or implied, including but not limited to the implied warranty of merchantability and fitness for a particular purpose. Neither Wiley nor its dealers or distributors assumes any liability of any alleged or actual damages arising from the use of or the inability to use this software. (Some states do not allow the exclusion of implied warranties, so the exclusion may not apply to you.)

